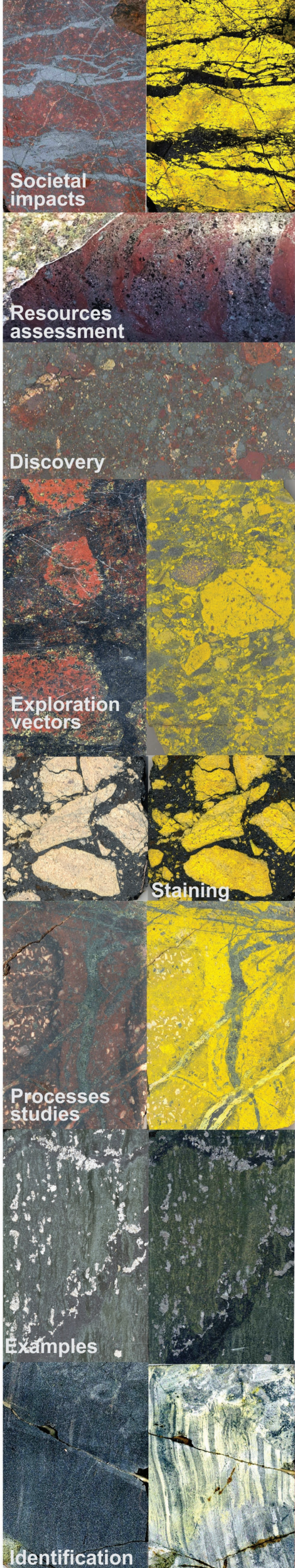


# GAC Special Paper 52

# Mineral Systems with Iron Oxide Copper-gold (IOCG) and Affiliated Deposits

## Guest Editors

Louise Corriveau
Eric G. Potter and A. Hamid Mumin

GEOLOGICAL ASSOCIATION OF CANADA
ASSOCIATION GÉOLOGIQUE DU CANADA

Mineral Deposits Division
Geological Association of Canada

CANADA 1842 GEOLOGICAL SURVEY - COMMISSION GÉOLOGIQUE

AGC-AMC-AIH QUÉBEC 2019 Où les géosciences convergent
GAC-MAC-IAH QUÉBEC 2019 Where geosciences converge

DEMCo

**Library and Archives Canada Cataloguing in Publication**
**Title: Mineral systems with iron oxide copper-gold (IOCG) and affiliated deposits / guest editors, Louise Corriveau, Eric G. Potter, A. Hamid Mumin.**
**Names: Corriveau, Louise, 1957- editor. | Potter, E.G., editor. | Mumin, A. Hamid, 1954- editor. | Geological Association of Canada, publisher.**
**Series: Geological Association of Canada special paper ; 52.**
**Description: Series statement: Geological Association of Canada special paper ; 52 | Includes bibliographical references and index.**
**Identifiers: Canadiana (print) 20220164959 | Canadiana (ebook) 20220164991 | ISBN 9781897095959 (softcover) | ISBN 9781897095966 (PDF)**
**Subjects: LCSH: Minerals. Classification: LCC QE372.2 .M56 2022 | DDC 549—dc23**

**Keywords:** Iron oxide copper-gold (IOCG), iron oxide-apatite (IOA), IOA-REE, iron-rich cobalt-bismuth, albitite-hosted uranium, iron skarn, five-element veins, critical metals, strategic metals, specialty metals, Ag-Au-Cu-U-REE, Co-Bi-Au, Bi-Co-Ni-Ag-As, U-Th, polymetallic, rare earth elements (REE), uranium, iron oxides, arsenides, sulphides, ore deposits, mineral systems, metallogenesis, metal pathways, ore deposit model, metasomatism, magmatic-hydrothermal processes, metasomatic iron and alkali-calcic (MIAC), iron oxide and alkali-calcic alteration (IOAA), breccia, alteration facies, mineralization, alkali metasomatism, albitization, albitite, HT Na-Ca-Fe, HT Ca-Fe, HT Ca-K-Fe, HT K-Fe, LT K-Fe, LT Ca-Mg-Fe, K-felsite, K-skarn, albite, apatite, biotite, britholite, clinopyroxene, amphibole, magnetite, K-feldspar, hematite, chlorite, sericite, carbonate, barite, fluorite, pyrite, gold, chalcopyrite, arsenopyrite, bornite, chalcocite, evaporite, batholith, A-type magmatism, diorite, magmatic fluids, fluid mixing, prograde, retrograde, high geotherm, gravity high, magnetic high, residual Bouguer gravity, total magnetic intensity grid, Great Bear magmatic zone, NICO, Josette REE, Olympic Copper-Gold Province, Olympic Dam, Cloncurry, Ernest Henry, Norrbotten, Bafq, Central Andes, Mina Justa, Mantoverde, Candelaria, El Espino, Middle-Lower Yangtze River Metallogenic Belt (MLYRMB), eastern Junggar, eastern Tianshan, Mesozoic, Proterozoic, field geology, alteration mapping, geochemistry, mineralogy, mineral chemistry, geophysics, economic geology, mineral potential assessment, mineral exploration, process studies.

Publisher *
The Geological Association of Canada
c/o Dept. of Earth Sciences
Memorial University of Newfoundland
St. John's, NL A1B 3X5 CANADA
Phone 709 864-7660
Fax 709 864-2532
Email : gac@mun.ca
Website www.gac.ca

ISSN 0072-1042

**GAC® Book Editor: Reginald Wilson**
**Layout Editor: Étienne Girard**



**Suggested citation for papers within this Special Paper 52 volume**
Authors of papers, 2022, Title of paper, in Corriveau, L., Potter, E.G. and Mumin, A.H., eds., Mineral systems with iron oxide copper-gold (IOCG) and affiliated deposits: Geological Association of Canada, Special Paper 52, p. X-X.

***Citation suggérée pour les articles au sein de ce volume du Special Paper 52***
*Auteurs de l'article, 2022, Titre de l'article : dans Corriveau, L., Potter, E.G. et Mumin, A.H., eds., Mineral systems with iron oxide copper-gold (IOCG) and affiliated deposits: Association géologique du Canada, Special Paper 52, p. X-X.*

# Mineral Systems with Iron Oxide Copper-gold (IOCG) and Affiliated Deposits

*Edited by Louise Corriveau, Eric G. Potter and A. Hamid Mumin*

# Sponsors

**The Geological Association of Canada and Mineral Deposits Division**

The Geological Association of Canada (GAC®) and its Mineral Deposit Division (MDD) are Canadian geoscience organizations that promote and advance geosciences and economic geology in Canada through publications, awards, prestigious medals, conferences, meetings and exhibitions led by their national and international academic, private sector and government community members. The Association and its MDD division are pleased to publish this comprehensive review of the geological, geochemical, mineralogical and geophysical footprints of mineral systems comprising iron oxide copper-gold (IOCG), iron oxide-apatite (IOA), and related deposits that host critical metals as primary commodities and byproducts. This knowledge transfer on the geoscience of metasomatic deposits containing critical metals contributes to government, industry and academia efforts in securing critical and strategic metal resources for the economic prosperity and social well-being of the nation and our global community. In addition, the GAC® "flagship" journal, *Geoscience Canada*, welcomes technical papers of broad interest to the geoscience community. The GAC® Short Course Notes and Special Paper series are based on annual meeting short courses and symposia, and are intended to extend the duration of knowledge transfer beyond the meeting itself. The MDD newsletter, *The Gangue*, provides members and the geoscience community at large a forum to share ideas, describe interesting mineral occurrences or expand on deposit models. MDD also supports student involvement in field trips.

**L'Association géologique du Canada et sa division des gîtes minéraux**

L'Association géologique du Canada (GAC®) et sa division des gîtes minéraux (MDD) sont des organismes géoscientifiques canadiens qui contribuent à la promotion et au développement des géosciences et de la géologie économique au Canada par le biais de publications, prix, médailles prestigieuses, conférences, congrès et exhibits réalisés par ses membres des milieux académiques, de l'industrie et gouvernementaux au national et à l'international. Par le bias de ce volume, elles ont le plaisir de publier cette synthèse des empreintes géologiques, géochimiques, minéralogiques et géophysiques de systèmes minéralisateurs à gîtes à oxydes de fer cuivre-or (IOCG), gîtes à oxydes de fer-apatite (IOA) et gîtes affiliés comportant des métaux critiques comme principaux produits et sous-produits. En ciblant des gîtes à métaux critiques multiples, le volume représente une contribution géoscientifique fondamentale à la prospérité économique et au bien-être social du pays. La revue phare du GAC®, Géosciences Canada, publie des articles techniques d'intérêt général pour la communauté géoscientifique. Les séries de Notes de cours intensifs et Special Paper du GAC® prolongent le transfert de connaissances amorcé lors des cours intensifs et des symposiums aux congrès annuels. Le bulletin du MDD, The Gangue, offre aux membres et à la communauté géoscientifique en général un forum pour le partage d'idées, la description de gîtes d'intérêt et le development de modèles métallogéniques. La division soutient également la participation des étudiants aux excursions sur le terrain.

**GAC-MAC-IAH 2019**

The Geological Association of Canada (GAC®), the Mineralogical Association of Canada (MAC) and the Canadian National Chapter of the International Association of Hydrogeologists (IAH/CNC) welcomed national and global geoscientists to the GAC®-MAC-IAH/CNC meeting in 2019 in Québec City. Under the theme *Where Geosciences Converge*, the three Associations promoted life-long learning through symposia, special sessions, short courses and field trips, fostered networking with successful social activities and poster sessions and recognized excellence in geosciences with awards, prestigious medals and student grants. Experts from the Geological Survey of Canada, DEMCo, the China University of Geosciences, Red Pine Exploration and the Deutsches GeoForschungs Zentrum joined forces to deliver a symposium and a short course on Ore systems with IOA, IOCG, skarn and polymetallic albitite-hosted deposits in memory of Dr. Patrick Williams. Thanks to a well attended Short Course and the sponsorships of the Mineral Deposit Division (MDD) and DEMCo, the GAC-MAC-AIH 2019 committee is pleased to sponsor the publication of the GAC Special Paper 52. The Local Organizing Committee is fully committed to supporting students interested in gaining field-based regional perspectives in geoscience including in economic geology.

**AGC-AMC-AIH 2019**

L'Association géologique du Canada (AGC®), l'Association minéralogique du Canada (AMC) et le chapitre national canadien de l'Association internationale des hydrogéologues (AIH/CNC) ont accueilli les géoscientifiques de par le monde et du Canada au congrès de l'AGC-AMC-AIH/CNC en 2019 à Québec. Sous le thème Là où les géosciences convergent, ce congrès des trois associations a stimulé l'apprentissage continu à travers sa série de symposiums, sessions spéciales, cours intensifs et excursions de terrain et a favorisé le réseautage avec ses activités sociales et ses sessions d'affiches fort réussies. Les associations y ont reconnu l'excellence en géosciences avec moults prix, médailles prestigieuses et bourses aux étudiants. Des experts de la Commission géologique du Canada, de DEMCo, de l'Université des géosciences de Chine, de Red Pine Exploration et du Deutsches GeoForschungs Zentrum ont uni leurs efforts pour présenter un symposium et un cours intensif sur les systèmes minéralisateurs à gîtes IOA, IOCG, skarn et polymétalliques au sein d'albitite en mémoire du Dr Patrick Williams. Le comité GAC-MAC-AIH 2019 est heureux de parrainer la publication du GAC Special Paper 52 avec les recettes du cours intensif résultant d'une forte participation au cours et aux parrainages de la Division des gîtes minéraux (MDD) et de DEMCo. Le comité organisateur local vise aussi à appuyer les étudiants désireux d'acquérir une perspective régionale basée sur le terrain en géosciences, y compris en métallogénie.

**DEMCo, the Denendeh Exploration and Mining Company of the Dene First Nations**

The Denendeh Exploration and Mining Company, DEMCo, is an exploration/mining company 100% owned by the 27 Dene First Nations in partnership with the Denendeh Investments Incorporated. DEMCo owns extensive properties in the Camsell River IOA-IOCG district of the Great Bear magmatic zone and undertook a recovery program of historic drill cores in addition to regional- and deposit-scale exploration. The company shared its vast geological and geophysical datasets with the Geological Survey of Canada, helped co-organized the GAC-MAC-AIH 2019 IOCG-related symposium and sponsored the IOCG-related short course. The funds now serve to sponsor this GAC Special Paper 52.

The Dene Nations support and promote mineral exploration and environmental studies as means to walk, explore, take care of and benefit from the land. This important endeavour fosters empowerment, economic growth and prosperity for the Dene First Nations and Canadians in general. Modern re-examination of historic mining camps such as those of the Camsell River district can lead to discoveries, including for critical metals as illustrated in this GAC Special Paper 52. Building on our collective strengths is a great opportunity for all to engage in the field-driven geosciences of mineral systems with IOCG and affiliated critical metal deposits for effective and respectful resource development with and among First Nations.

**Denendeh Exploration and Mining Company, DEMCo, des Premières Nations dénées**

La Denendeh Exploration and Mining Company, DEMCo, est une société d'exploration minière détenue à 100 % par les 27 Premières Nations dénées en partenariat avec la Denendeh Investments Incorporated. DEMCo possède de vastes propriétés dans le district IOA-IOCG de la rivière Camsell de la zone magmatique du Grand lac de l'Ours, TNO. La compagnie mène un vaste programme d'exploration régionale et à l'échelle des anciennes mines et de récupération de carottes de forage historiques. La société a partagé ses ensembles de données géologiques et géophysiques avec la Commission géologique du Canada pour ses recherches en cours, a aidé à co-organiser le symposium du AGC-AMC-AIH/CNC 2019 sur les IOCG et gîtes affiliés et a parrainé le cours intensif qui y était associé. Les fonds appuient maintenant la publication du Special Paper 52 de l'AGC.

Les Pemières Nations dénées soutiennent et promeuvent l'exploration minérale et les études environnementales comme moyens de marcher et explorer le territoire tout en prenant soin et en bénéficiant des ressources de la Terre et en favorisant l'émancipation, la croissance économique et la prospérité des Premières Nations dénées et des canadiens en général. Le ré-examen moderne d'anciens camps miniers comme ceux du district de la rivière Camsell peut mener à de nouvelles découvertes, notamment en métaux critiques, comme l'illustre le présent Special Paper 52 de l'AGC. S'appuyer les uns les autres nous donne l'opportunité de s'engager dans les géosciences à la lumière des données de terrain pour contribuer efficacement et respectueusement au développement des ressources des systèmes minéralisateurs à gîtes IOCG et à métaux critiques affiliés avec et parmi les Premières Nations.

## Acknowledgments

This GAC Special Paper 52 is a contribution of the Geological Survey of Canada's Targeted Geoscience Initiative (TGI) and Geomapping for Energy and Minerals (GEM) programs in collaboration with researchers from the Bureau de la Recherche géologique et minière (BRGM, France), Geological Survey of South Australia, Geoscience Australia, Geological Survey of Iran, Brandon Univ., Laval Univ., Université du Québec à Montréal, Karlsruhe Institute of Technology, Guangzhou Institute of Geochemistry, China Univ. of Geosciences (Wuhan), Chang'an Univ., Chinese Academy of Sciences, Univ. of Hong Kong, Univ. of Isfahan, Jadavpur Univ., BHP-Olympic Dam, Red Pine Exploration, SOQUEM and Agnico Eagle Mines Limited. Additional organisations and researchers generously volunteered time and effort to the research, data acquisition, reviews and editing of papers or gave permission to publish photos that led to this volume. In particular, the editors thank the Northwest Territories Geological Survey, Fortune Minerals Limited, DEMCo, Alberta Star Development Corporation, Community Government of Gamètì, Tłı̨chǫ Government, Tłı̨chǫ Lands Protection Department, Dél̨ı̨nę Renewable Resource Council, Délı̨nę Land Corporation, Wek'èezhìi Land and Water Board, Polar Continental Shelf Program, Aurora Research Institute, Ernest Henry Mining, NSERC-Agnico Eagle Industrial Research Chair in Mineral Exploration, as well as the industry, university and government research partners and collaborators of the volume contributors.

The editors gratefully acknowledge the Geological Association of Canada and its Mineral Deposits Division for sponsoring this Special Paper 52 and the in-kind support of the Geological Survey of Canada. Additional contributions from DEMCo and the GAC-MAC-AIH 2019 Local Organizing Committee are much appreciated. The Geological Association of Canada acknowledges the dedication of reviewers Pedro Acosta-Góngora, Erin Adlakha, Fernando Barra, Olivier Blein, Adrienne Brotodewo, Jim Craven, Sophie Decrée, Paul Duuring, Randy Enkin, Michael Gadd, Robin Goad, Xiaowen Huang, Charlie Jefferson, Dawn Kellet, Colter Kelly, Crystal Laflamme, Chris Lawley, David Lentz, Vladimir Lisitsin, Anne McCafferty, Isabelle McMartin, Nick Oliver, Suzanne Paradis, Jeanne Percival, Duane Petts, Nicolas Piette-Lauzière, Raphaël Quentin de Gromard, Anthony Reid, Anne-Aurélie Sappin, Tobias Schlegel, Roger Skirrow and Xin-Fu Zhao, of editors Reginald Wilson, Louise Corriveau, Eric Potter and Hamid Mumin and of lay-out editor Étienne Girard.

# Dedications

## Patrick John Williams (1957–2018)

Patrick was a shining beacon showing us the way forward through IOCG short courses and conferences, from -30°C in Yellowknife to +30°C in his home town of Townsville, Australia. He reviewed and edited our papers and those of our peers rigorously, sharing his knowledge and insights so that we could always benefit from his vast experience and expertise. We still go back to his reviews, his recommendations, his suggestions. Pat faced challenges in his steady, systematic, and rigorous manner. He took on the most challenging of ore deposit types, IOCG, and wrote a number of seminal papers. He systemically climbed the Scottish mountains >3000 feet as reported scrupulously in his Munro's Tables. Patrick is appreciated by all who knew him for his caring and deeply involved approach to teaching, mentoring and organizing, and will be remembered for his lasting contributions to economic geology research and our geoscience community.

Patrick was the Director of Clump Mountain Geoscience Pty Ltd based in North Queensland, Australia. Prior to this, he was a senior lecturer in economic geology and Director of the Economic Geology Research Unit at James Cook University (Australia). Recognized by the economic geology community as the world leader in the field of IOCG deposits, he was commissioned by the Society of Economic Geologist to lead the synthesis paper *Iron oxide copper-gold deposits: geology, space-time distribution, and possible mode of origin* for the Economic Geology 100$^{th}$ Anniversary Volume. He shared with Special Paper 52 contributors a love for field studies in economic geology research. His contributions provided perspectives on the tectonic settings, geology, geochemistry and physical property of IOCG deposits, and their alteration systems. He also shared widely his view on classification of IOCG deposits, and his first-hand knowledge of IOCGs in Australia. Patrick's knowledge and insights have greatly benefitted Canadian geoscience and exploration, and indeed have given a tremendous boost to the entire global geoscience effort. An extensive obituary was published in Mineralium Deposita for which he was editor between 2008 and 2012.

**Thanks Pat!**

## Sunil S. Gandhi (1935–2017)

Sunil pioneered research on settings prospective for IOCG deposits across Canada and was instrumental in the discovery of the NICO Au-Co-Bi-Cu deposit in 1994 in the Northwest Territories. He envisioned the importance of these ore systems well before they became accepted nationaly. His fieldwork and research in the 1980s and 1990s focused on the Great Bear magmatic zone, East Arm and Central Mineral Belt regional metallogeny. He was also among the first to suggest linkages between IOA veins and IOCG systems. Today, we are walking in his footsteps.

Sunil began his geological career in India, earning his BSc and MSc degrees at Bombay (Mumbai) and Karnatak Universities, then completed a second MSc degree at McGill University in 1960 followed by his PhD thesis in 1967 at McGill. After working for the exploration industry in Québec, Saskatchewan and Labrador (involved in discovery of the Michelin deposit), Sunil joined the GSC as research scientist (1977–1996) to carry out annual assessments of uranium resources in Canada as part of the Uranium Resource Assessment Group (URAG). His research led him to world-wide conferences and field excursions, notably in Europe, China and Australia. After leaving the GSC in 1997, Sunil became a geological consultant, specializing in exploration concepts and target selection, mainly for uranium, gold, and IOCG-type deposits in Canada and India while conducting research and maintaining uranium and IOCG deposit databases for the GSC. He was a consummate collaborator, freely sharing his ideas, data, and photographs with academic and industry colleagues and was revising papers to his last days, committed to getting his last paper in Ore Geology Reviews, published posthumously in 2018. This paper led to new research directions, a new graduate student and new collaborators as he too showed us the way forward.

**Thanks Sunil!**

# Preface

**Louise Corriveau, Eric G. Potter and A. Hamid Mumin**

**Editors**

The Geological Association of Canada published the Short Course Notes 20 (SCN 20) *Exploring for iron oxide copper-gold deposits: Canada and global analogues* in 2010. All copies having been sold, the editors, Louise Corriveau and Hamid Mumin joined forced with Eric Potter and volunteered to update the volume. It was meant to be simple and quick... Instead, it became a totally new volume with 13 new papers and 3 papers that update existing Short Course Notes 20 contributions. We also provide a reproduction in memoriam of Patrick Williams' paper on magnetite-group IOCG deposits. The new team of collaborators was set in place for the IOCG-related short courses at the SGA 2017 and the GAC®-MAC-IAH/CNC 2019 meetings in Québec City, convened respectively by L. Corriveau, P.J. Williams and A.H. Mumin and by L. Corriveau, E. Potter, D. Harlov and X.-F. Zhao.

Special Paper 52 focuses on field-driven geosciences with over 70 full pages of photos from field exposures, rock slabs, cobaltinitrite-stained rock slabs, drill cores and thin sections. Abundant geological, chemical and geophysical maps and hundreds of geochemical and mineral chemistry diagrams highlight the footprints of archetypical case examples from systems across the Great Bear magmatic zone (NICO and Sue Diane deposits, Port Radium-Echo Bay district, Terra mine and Grouard Lake regions of the Camsell River district), Kwyjibo district (Josette REE deposit), Wanapitei district (Scadding mine) and Romanet Horst in Canada, the Olympic Copper-Gold Province (Olympic Dam and Punt Hill deposits, Emmie Bluff, Murdie Murdie and Titan prospects) and Cloncurry district (Ernest Henry deposit) in Australia, the Cenral Andes (Mina Justa, Mantoverde, Candelaria, El Espino), the Middle-Lower Yangtze River Metallogenic Belt, Eastern Junngar and Eastern Tianshan districts in China, the Bafq district in Iran, the Singhbhum Shear Zone district in India, and the Norrbotten district in Sweden. Geochemical modeling of publically available datasets from the Southeast Missouri district (USA) and Kwyjibo district (Canada) were also processed. BHP-Olympic Dam made available to this research group 20,000 whole-rock analyses. This collaboration has led to the publication in this volume of a new geological map of the Olympic Dam deposit, with a series of plan views, sections and geochemical diagrams illustrating the distribution and evolution of its metals, minerals, cations, alteration and mineralization indices, and magnetic susceptibility and density. Variations within mineralized systems with iron oxide and alkali-calcic alteration, as well as iron oxide- and iron-poor variants that include iron sulphide, iron carbonate and iron silicate rich deposits provide an overview of the broad range of related deposits that fall within metasomatic iron and alkali-calcic mineral systems.

Leading experts invited to contribute to this volume all share a love for field geology and expand their field-driven research with state-of-the art analytical, geochemical and/or geophysical modeling tools. Some had contributed to the flagship IOCG deposit volumes published by Porter Geoconsultancy, others to our Short Course Notes 20, and all joined forces to share their knowledge at short courses or symposiums. All papers have been peer reviewed as highlighted in the acknowledgments above and subsequently thoroughly edited by us, the guest editors and Reginald Wilson, GAC book editor. The papers are edited to Canadian English spelling largely following A.J. Weatherston, O.E. Inglis, J. Gray, D. Busby, and B. Couture in their 2016 Guide to authors of the Geological Survey of Canada, Open File Report 8095. Canadians mix British and American English spelling; apologies Pat, this usage drove you crazy! Units quoted throughout the volumes are metric, using standard international abbreviations. A volume on IOCGs and the affiliated deposits could not happened without a *Thank you to Mike Porter, you are a source of inspiration including for writing this preface and for organizing and editing our second GAC volume.* Our scientific IOCG-IOA knowledge base needs exhaustive books such as the Porter Geoconsultancy volumes and the GAC Short Course Notes 20 and GAC Special Paper 52.

Please enjoy the GAC Special Paper 52 volume. We hope to see you in the field, learning from each other and planting the seeds of future contributions as we discuss and argue standing over outcrops and drill cores. This volume would not have been possible without field work and those on whose work our research is built. To explorationists, prospectors and developers, public servants, faculties, grad and undergrad students, environmental geoscientists, land-use planners, First Nations, communities and managers, we hope that great successes will arise from our public-private-academic sector collaborations and holistic approaches to mineral systems with IOCG, IOA and affiliated critical metal deposits.

**Thank you to all!**

# Mineral Systems with Iron Oxide Copper-gold (Ag-Bi-Co-U-REE) and Affiliated Deposits: Introduction and Overview

**Louise Corriveau**
*Natural Resources Canada, Geological Survey of Canada, Québec City, Canada; .*
*louise.corriveau@rncan-nrcan.gc.ca.*

**A. Hamid Mumin**
*Department of Geology, Brandon University, Brandon, Manitoba, Canada.*

**Eric G. Potter**
*Natural Resources Canada, Geological Survey of Canada, Ottawa, Ontario, Canada.*

*Recommended citation: Corriveau, L., Mumin, A.H., and Potter, E.G., 2022, Mineral systems with iron oxide copper-gold (Ag-Bi-Co-U-REE) and affiliated deposits: introduction and overview, in Corriveau, L., Potter, E.G. and Mumin, A.H., eds., Mineral systems with iron oxide copper-gold (IOCG) and affiliated deposits: Geological Association of Canada, Special Paper 52, p. 1-26.*

## Abstract

Iron oxide copper-gold (IOCG) deposits host economic quantities of Cu ± Au and may also yield Ag, Co, Bi, Fe, Mo, Ni, PGE, Pb, REE, U, V, Zn and industrial minerals. Iron oxide-apatite (IOA) deposits are sources of iron ore, and can in some cases contain REE ores. Affiliated deposits include, cobalt-bismuth variants of IOCG deposits rich in critical metals, iron and polymetallic skarn deposits, albitite-hosted uranium and Au-Co-U deposits, molybdenum-rhenium and iron sulphide-copper-graphite or copper-gold deposits. All these deposit types form within regional-scale iron oxide and alkali-calcic alteration systems. An individual ore system will not encompass this entire array of deposits, as system evolution and metal endowment depend on tectonics, volcanic activity, depth and geodynamic settings. The large resource potential for base, precious, REE, strategic, critical and nuclear metals, and the clustering of deposits in districts along extensive geological provinces, make IOCG and affiliated deposits attractive targets for modern exploration. This Special Paper of the Geological Association of Canada documents these ore systems globally, and more specifically their settings, alteration facies, breccia types and mineral chemistry. Examples discussed include the Olympic Copper-Gold Province and Cloncurry district (Australia), the Great Bear magmatic zone (Canada), the Central Andes (South America), the Bafq district (Iran), and the Middle-Lower Yangtze River Metallogenic Belt,Kangdian, eastern Tianshan and eastern Junggar districts (China). Complementary information is sourced from the southeast Missouri district (USA), Singhbhum Shear Zone (India), Norbotten district (Sweden), Bayan Obo deposit (China), and Central Mineral Belt, Kwyjibo district and Romanet Horst (Canada).

The diagnostic alteration facies and breccias associated with these ore systems reflect regional chemical and textural modification of host rocks, resulting from progressive and efficient metasomatic fluid-rock reactions across very steep physicochemical gradients sustained by heat ingress and the ascent and evolution of large hypersaline fluid plumes. Field examples and processing of large lithochemical and geophysical databases illustrate the footprints of these ore systems and enable the development of new petrological mapping protocols, discriminant diagrams and lithogeochemical tools for their characterization. By documenting alteration facies, paragenetic sequences, mineral chemistry, structural controls, and geophysical and geochemical signatures, and framing them into ore genetic models and deposit classes, the examples provide effective vectors to mineralization and address critical issues in exploring for these deposits worldwide.

## Résumé

Les gîtes à cuivre-or et oxydes de fer (IOCG) renferment des quantités économiques de cuivre avec ou sans or et peuvent aussi contenir du Ag, Co, Bi, Fe, Mo, Ni, EGP, Pb, ETR, U, V, Zn et des minéraux industriels. Les gîtes à oxydes de fer et apatite (IOA) contiennent du minerai de fer et parfois de terres rares. Des variantes IOCG à cobalt et bismuth et autres métaux critiques, du skarn riche en fer ou polymétallique, des gîtes à uranium et Au-Co-U encaissés dans des albitites, des gîtes de molybdène-rhénium et d'autres à sulfures de fer, cuivre- graphite ou à cuivre-or sont affiliés aux gîtes IOA et IOCG. Tous se forment au sein de systèmes minéralisateurs à oxydes de fer et altération alcali-calcique d'échelle régionale. Toutefois, chaque système ne formera pas tous les types de gîtes, dépendant de son évolution et de son contenu en métaux, eux-mêmes une fonction de facteurs variés dont la tectonique, l'activité volcanique, la profondeur et le contexte géodynamique. L'important potentiel en ressources (métaux de base, précieux, stratégiques, critiques et nucléaires de même que terres rares) de ces gîtes et les grappes de gîtes qu'ils forment le long de vastes provinces géologiques font des gîtes IOCG et affiliés des cibles attrayantes pour l'exploration. Ce volume de la série Special Paper de l'Association géologique du Canada documente ces systèmes minéralisateurs dans leur ensemble et plus particulièrement leurs contextes, facies d'altération, brèches et chimie minérale. Les exemples discutés incluent la province cuivre-or d'Olympic et le district de Cloncurry (Australie), la zone magmatique du Grand lac de l'Ours (Canada), les Andes centrales (Amérique du Sud), le district iranien de Bafq et les districts de Kangdian, de l’est du Tianshan, de l’est du Junggar et de la ceinture métallogénique du fleuve Yangtsé moyen-inférieur de Chine. Des informations complémentaires proviennent également des districts du sud-est du Missouri (États-Unis) et de Norbotten (Suède), de la zone de cisaillement de Singhbhum (Inde), du gîte de Bayan Obo (Chine) et du Horst de Romanet, district de Kwyjibo et de la Ceinture centrale de minéraux du Labrador (Canada).

Les faciès d’altération et les brèches associés aux systèmes étudiés reflètent les modifications de la composition et des textures des roches hôtes à l’échelle régionale suite à la progression de réactions métasomatiques fluides-roches à travers de forts gradients physicochimiques soutenus par de forts apports de chaleur et l’ascension et l’évolution de larges panaches de fluides hypersalins. Des exemples de terrain et le traitement de grandes bases de données lithogéochimiques et géophysiques illustrent les empreintes de ces systèmes. Leur caractérisation est bonifiée par de nouveaux protocoles de cartographie pétrologique, diagrammes discriminants et outils lithogéochimiques. En documentant les faciès d’altération, les séquences paragénétiques, la chimie minérale, les contrôles structuraux, ainsi que les signatures géophysiques et géochimiques et en les encadrant dans des modèles génétiques et des classifications de gîtes, les exemples fournissent des vecteurs efficaces de la minéralisation et abordent des problèmes critiques dans l’exploration de ces gisements à l’échelle globale.

## Introduction

The iron oxide copper-gold (IOCG) deposit type comprises an extraordinary range of epigenetic polymetallic hydrothermal deposits that contain >15 vol % iron oxides and include copper ± gold as economic metals (Williams, 2010). All IOCG deposits are hosted within continental upper crustal ore systems characterized by regional-scale hydrothermal iron oxide and alkali-calcic alteration (IOAA; Fig. 1; Porter, 2010; Corriveau et al., 2016). The incremental and multiphase evolution of these systems in tectonically active volcano-plutonic environments and sedimentary basins can lead to a vast array of deposit types in addition to IOCG deposits sensu stricto, many with economic concentrations of iron, base (Cu, Pb, Ni, Zn), precious (Au, Ag, platinum-group elements) and strategic and critical metals, including Co, Bi, Mo, Nb, REE, Sb, Se, Te, and U as well as industrial minerals (see definition of critical metals in Skirrow et al., 2013; Fortier et al., 2018). For example, the Olympic Dam deposit in Australia has a mineral resource of 10 billion tonnes containing ~80 Mt Cu, 2600 kt $U_3O_8$, ~110 Moz Au, and ~320 Moz Ag. It is the world’s largest mineable uranium resource, and is ranked fifth in copper and third in gold resources (Table 1; BHP, 2017, 2018a, b). Mine operations currently separate but do not process vast quantities of REE (currently metallurgically non-economic) as well as iron (magnetite and hematite).

Examples of deposit types within IOAA systems (Table 1; Fig. 1) include: 1) iron oxide-apatite (IOA) deposits and their rare – earth elements (REE) variants, notably the Josette heavy REE IOA deposit (Canada) and the REE-mineralized Pea Ridge IOA deposit (US) (Table 1; Clark et al., 2010; Perreault and Lafrance, 2015; Aleinikoff et al., 2016; Day et al., 2016); 2) polymetallic and iron skarn deposits such as the U-REE (-Th) Mary Kathleen skarn deposit (about 0.025% $ThO_2$; Oliver et al., 1999; Mernagh and Miezitis, 2008); 3) iron oxide or iron silicate Co-Bi-Au (± Cu) deposits such as the Au-Co-Bi-Cu NICO (Canada) with potential Sb, Se and Te byproducts and local enrichments in W, and the Blackbird deposit (US) of the Idaho Cobalt Belt (Table 1; Goad et al., 2000; Slack, 2013: R. Goad, pers. comm., 2020), 4) iron oxide-uranium (IOU) deposits (Hitzman and Valenta, 2005), 5) polymetallic (Ag, Au, Co, Cu, Ni, U) albitite-hosted deposits (Wilde, 2013; Montreuil et al., 2015; Potter et al., 2019b), and 6) the Cu-Mo-Re±Au Kalman and Merlin deposits and the Tick Hill Au deposit in Australia (Table 1; Babo et al., 2017; Mudd et al., 2017). Cobalt and magnetite byproducts are also expected for the E1 IOCG deposit (EXCO Resources Ltd, 2012). Nickel occurs at the Jaguar deposit and GT-34 prospect (Garcia et al., 2020; Ferreira Filho et al., 2021).

Each mineral system may not form the entire array of deposit types but a vast array of mineralization types is regularly observed. The systems, and their mining districts form metallogenic provinces over hundreds of kilometres (Sillitoe, 2003; Mumin et al., 2010; Williams, 2010b; Yu et al., 2011; Williams et al., 2015; Montreuil et al., 2016b; Potter et al., 2019a; Chen and Zhao, 2022; Fabris, 2022; Skirrow, 2022; Zhao et al., 2022). These provinces are known to also host iron-sulphide-copper-graphite deposits (Mumin and Trott, 2003), iron-sulphide-copper-gold deposits (ISCG; Belperio, 2016), and

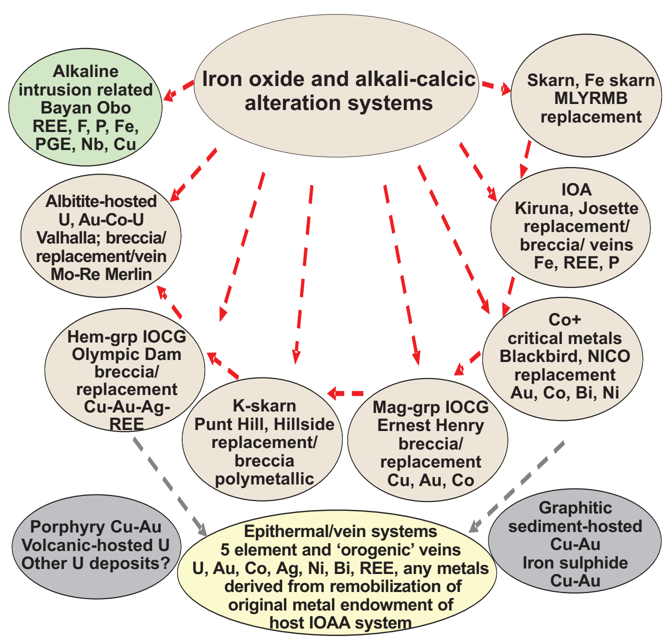


**Figure 1.** Continuum of deposit types within typical iron oxide and alkali-calcic alteration systems and continuum of these systems with other deposit types. Grp: group; MLYRMB: Middle-Lower Yangtze River Metallogenic Belt.

five-element and other vein-type deposits (Mumin et al., 2010; Gandhi et al., 2018; Potter et al., 2019a). A continuum exists between IOAA and epithermal and porphyry systems, and IOAA systems with epithermal caps have been identified worldwide (Fig. 1; Mumin et al., 2007, 2010; Kreiner and Barton, 2011, 2017; Corriveau et al., 2022a–d). In addition, a few high metamorphic grade (upper amphibolite and granulite facies) IOAA systems and their IOCG and IOA mineralization have been recognized in Australia and Canada; at least one of them still bears an epithermal cap (Corriveau and Spry, 2014; Corriveau et al., 2018a). Outlier metal endowment leading to deposits can result from remobilization of existing IOAA system metal endowment into ores through renewed tectonic or magmatic activities (Aleinikoff et al., 2016; Corriveau et al., 2022b). Globally, the polymetallic nature, variety of deposit types and potential for large tonnages make IOAA systems attractive for modern exploration.

Since definition of the IOCG deposit type (Hitzman et al., 1992), advances in our ability to comprehend and explore for these systems have led to new discoveries of deposits and districts. Operating mines have opened worldwide — Canada being a notable exception (Fig. 2). This Geological Association of Canada Special Paper furthers our understanding of ore deposits within IOAA systems in mining districts and prospective terranes, focusing on Proterozoic to Phanerozoic examples.

**Table 1.** Resources and reserves of selected deposits (see Corriveau et al., 2018b for more resources information on IOCG and affiliated deposits).

| Deposit | Total resources and total ore reserves |
|---|---|
| Olympic Dam | 10,070 Mt at 0.62% Cu, 0.21 kg/t $U^3O^8$, 0.27 g/t Au, 1.0 g/t Ag, open cut; 1,041 Mt at 1.68% Cu, 0.47 kg/t $U^3O^8$, 0.63 g/t Au, 3 g/t Ag, underground ore (+ ~0.3% LREE, 0.01% HREE) (BHP, 2020; K. Ehrig, personal communication, 2018) |
| Salobo | 346 Mt at 0.6% Cu, 0.3 g/t Au (Burns et al., 2017) |
| Candelaria | 501 Mt at 0.54% Cu, 0.13 g/t Au, 2.06 g/t Ag (Couture et al., 2017) |
| Ernest Henry | 167 Mt at 1.1% Cu, 0.5 g/t Au (pre-mining resource Williams and Skirrow, 2000) 87.1 Mt at 1.17% Cu, 0.62 g/t Au (2020 underground resource; Glencore, 2020) |
| Prominent Hill | 210 Mt at 1.2% Cu, 0.5 g/t Au, 2.8 g/t Ag + 31 Mt at 0.1% Cu, 1.5 g/t Au, 1.1 g/t Ag (+ 103 ppm U, + REE) (OZ Minerals, 2014a, 2019) |
| Bayan Obo | 57.4 Mt at 6% $REE_2O_3$ 2.2 Mt at 0.13% $Nb_2O_5$ 1500 Mt at 35% Fe (Smith and Chengyu, 2000; Fan et al., 2015) |
| NICO | 33 Mt at 1.02 g/t Au, 0.12% Co, 0.14% Bi, 0.04% Cu[1] (Burgess et al., 2014) |
| Sue Dianne | 8.4 Mt at 0.80% Cu, 0.07 g/t Au, 3.2g/t Ag[2] (Hennessey and Puritch, 2008) |
| Josette (Kwyjbo) | 6.92 Mt at 2.72% $REE_2O_3$ (measured + indicated) + 1.33 Mt at 3.64% $REE_2O_3$ (inferred) (Gagnon et al., 2018) |
| Merlin | 6.4 Mt at 1.5% Mo, 26 g/t Re[1] (Chinova Resources, 2014) |

Mt: million tonnes of ore; [1]: total mineral reserves; [2]: indicated resources

Archean settings, for which the Carajás district in Brazil is the archetype, are described in Xavier et al. (2010, 2017), Melo et al. (2016) and Schutesky et al. (2020).

This introductory paper briefly reviews IOCG, IOA and affiliated deposit types and their ore systems, updates classification and deposit type continuums, and addresses the topics to be discussed in subsequent chapters. It also illustrates how synergies between government, private sector and academia are critical in exploration for these diverse deposit types, and examines the social benefits stemming from discoveries, public geosciences and mineral exploration. An emphasis is placed on citing the chapters of this volume to highlight their contributions to this Special Paper. In terms of editing, this and all other papers of this volume have been peer reviewed including by the Geological Association of Canada editor, Reginald Wilson, and edited to Canadian English following Weatherston et al. (2016).

## Iron Oxide and Alkali-calcic Alteration Systems

Williams (2010a) classified IOCG and affiliated deposits using a descriptive approach that is best suited to applied exploration. He avoided genetic classifications considering the many variants and unknowns in the genesis of IOCG and affiliated deposits, let alone the need for a classification of mineral occurrences in under-explored and largely uncharted prospective settings. This classification scheme embraces the fact that many systems having IOCG deposits include components representing more than one deposit type. Since then, other classifications and criteria have been put forward (Groves et al., 2010; Chen, 2013; Barton, 2014; Hofstra et al., 2021) and the continuum of IOCG-associated deposits has been much better documented (Mumin et al., 2010; Kreiner and Barton, 2011, 2017). Nevertheless, the Williams (2010a) classification has stood the test of time for IOAA systems with only minor adjustment needed, as illustrated at the end of this chapter.

To clarify deposit classification and cover the range of IOCG and affiliated deposits, Porter (2010) put forward the umbrella term “iron oxide-alkali altered deposits”. Corriveau et al. (2016) replaced “deposits” by “systems” and “altered” by “alteration”, leaving “iron oxide and alkali alteration systems”. However, further revisions were needed to reflect the presence of calcic minerals, and in some cases the significant addition of calcium during alteration associated with IOA and IOCG deposits (e.g. Tornos et al., 2017; del Real et al., 2018; Blein et al., 2022). As a result, the umbrella term used in this volume is iron oxide and alkali-calcic alteration (IOAA) systems.

### *Alteration Facies and Metasomatic Reaction Paths*

Evolving fluid columns that lead to IOAA systems originate from highly saline and volatile-rich fluids that ascend through the upper crust. The original fluids rise along fault zones and other major crustal discontinuities, permeate through country rocks, and alter them intensely over 10s to 100s of cubic kilometres, chemically and texturally transforming host rocks into a series of distinctive alteration facies (this volume). Fluid and


**Figure 2.** Distribution of IOCG, IOA and affiliated deposits and their districts (increased font size) (Williams et al., 2005; Corriveau et al., 2018b and references therein) on geological map of the world (Chorlton, 2007).

metal sources are varied. Many systems are driven by magmatic-hydrothermal H–C–O–S-Cl-F fluids and magmatic heat, with very significant to minor addition of crustal fluids such as meteoric water, and oxidized, bittern, sulphate-rich basinal brines in which fluid mixing leads to ambiguity concerning fluid sources, or even an apparent(?) lack of a magmatic fluid source (cf. Haynes et al., 1995; Bastrakov et al., 2007; Baker et al., 2008; Oliver et al., 2008; Chen, 2013; Richards and Mumin, 2013a, b; Barton, 2014; Richards et al., 2017; Skirrow, 2022; Zhao et al., 2022). At the scale and intensity with which alteration proceeds across ore systems, one source of metals and fluids is intrinsically the host rocks (e.g. carbonate for C-derived fluids, sedimentary rocks for $H_2O$, S, etc.), as illustrated throughout this volume.

Where alteration is most intense, the composition of the host rocks, whether volcanic, volcaniclastic, hypabyssal intrusive or sedimentary, has little influence on the final mineral parageneses and bulk composition of the altered rocks (Corriveau et al., 2016; Blein et al., 2022). Where alteration is weak to moderate, the country rock composition affects the abundance of particular minerals, but ultimately, if significantly altered, all rock types are transformed into "facies" characterized by regular sets of mineral assemblages and compositional ranges including metal associations (Corriveau et al., 2016, 2022a–d).

Building on the early works of Hitzman et al. (1992), Marschik and Fontboté (2001), Williams et al. (2005), Monteiro et al. (2008), and others that described the main alteration types, Corriveau et al. (2010b, 2016) introduced six main alteration facies to characterize the range of alteration types that develop as highly saline fluid columns rise through the upper crust and temperatures decline (high- to low-temperatures: HT to LT; Fig. 3). The prograde evolution as defined in Corriveau et al. (2022d) is regular and predictable, though the intensity to which any alteration facies develops is variable at the scale of a system, a district, or an entire belt, leading to variations in deposit types within districts (e.g. IOA dominant versus IOCG dominant districts; Corriveau et al., 2018b, 2022b; Zhao et al., 2022).

The main facies, some of their most common transitions and the associated deposit types (Fig. 2) consist of:

1) Na (albite, scapolite) alteration produces albitite and serves as host to U and Au-Co-U deposits. The albitite (i.e. rocks composed of >80 modal % albite) and albite alteration commonly forms vast corridors along fault zones and above subvolcanic intrusions. The albitite predates or forms simultaneously with local skarn (garnet, clinopyroxene) and predates iron skarn deposits (Corriveau et al., 2022b; Zhao et al., 2022). Albitite (Na) alteration grades to Na-Ca (albite, scapolite) and HT Na-Ca-Fe (albite, amphibole, magnetite, apatite).
2) HT Ca-Fe [amphibole (actinolite and hornblende), magnetite and apatite] alteration leads to IOA deposits (Blein et al., 2022; Daliran et al., 2022; Zhao et al., 2022). REE mineralization occurs where systems hosting IOA have transitioned to HT Ca-K-Fe, HT K-Fe or LT K-Fe alteration facies, and the original metal endowment was remobilized such as in the Missouri and Kwyjibo districts (Day et al., 2016; Corriveau et al., 2022a). Where intense, HT Ca-K-Fe alteration may host cobalt- and bismuth-rich variants of IOCG deposits that are dominated by arsenopyrite rather than copper-iron-sulphides. This transitional facies is most extensive in sedimentary sequences containing carbonate

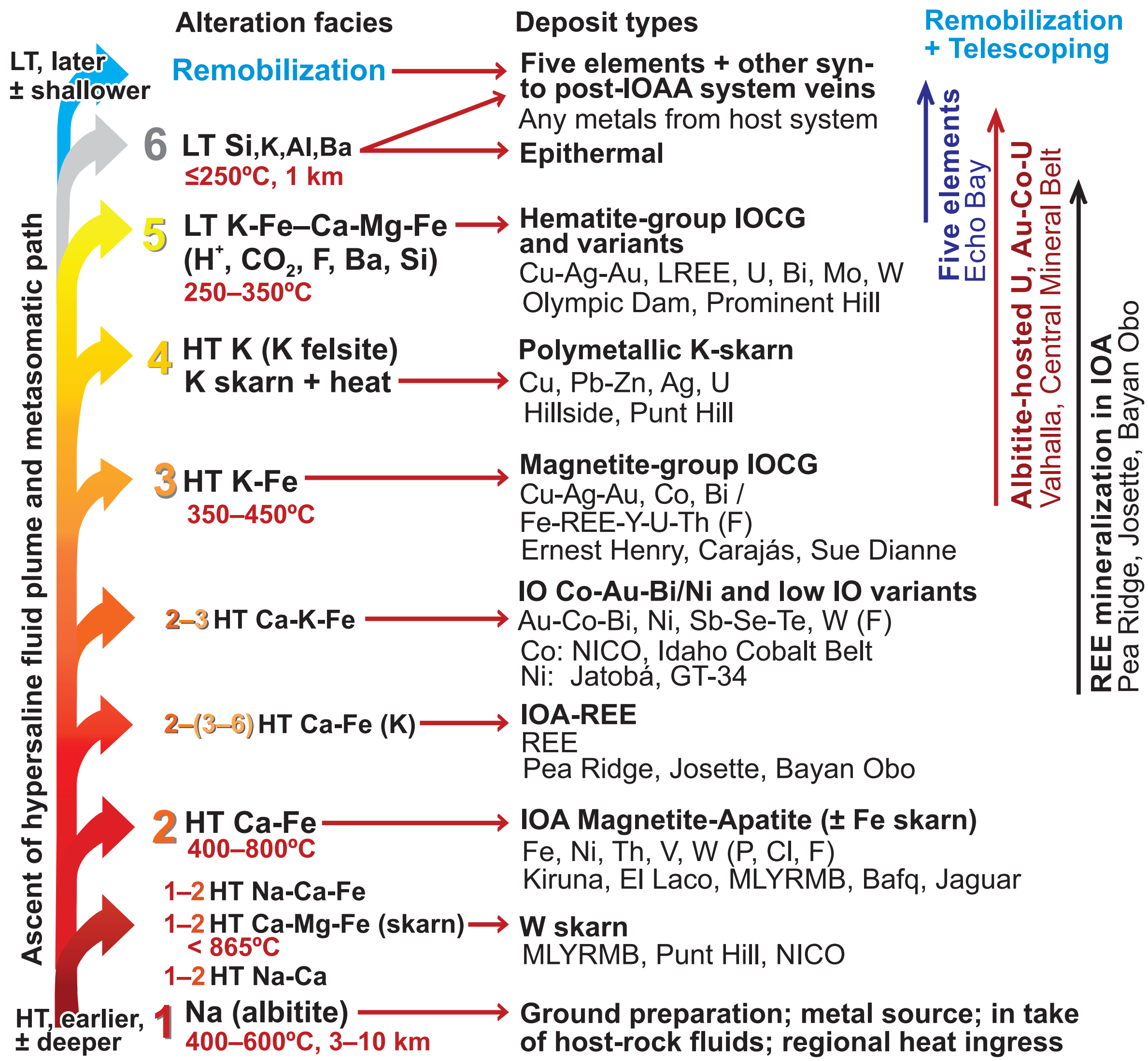


FIGURE 3. Ore deposit model for IOAA systems (modified from Corriveau et al., 2016). Albitite-hosted uranium deposits form when deep albitite is overprinted by lower temperature fluids. Rare earth element ores are commonly a result of remobilization of early REE endowment of mature IOA deposits that had previously evolved to K-bearing facies (Corriveau et al., 2022b, IO: iron oxide).

rocks; mineralization is largely stratabound (Slack, 2013; Montreuil et al., 2016b). Some iron oxide-rich to iron-oxide-poor nickel-dominant variants occur in host sequences with mafic-ultramafic rocks such as Jatoba and GT-34 (Garcia et al., 2020; Veloso et al., 2020). Brittle-ductile deformation is common during the development of HT Ca-Fe and HT Ca-K-Fe alteration facies, whereas ductile folding locally occurs in HT Ca-Fe facies (Montreuil et al., 2016a; Corriveau et al., 2022c, d).

3) HT K-Fe (K-feldspar, biotite, magnetite) alteration hosts polymetallic magnetite-group IOCG deposits (e.g. Cloncurry deposit; Williams et al., 2005; Williams, 2010a). Biotite-rich HT K-Fe alteration facies and associated mineralization commonly form stratabound replacement zones and are not systematically associated with extensive brecciation (e.g. NICO, Candelaria, Dahongshan and Lala deposits; Montreuil et al., 2016b; Zhao et al., 2017b, 2022; del Real et al., 2018; Zeng et al., 2018). However, K-feldspar-rich HT K-Fe alteration facies is regularly associated with brecciation and precipitation of copper sulphides in veins or disseminations (Clark et al., 2010; Corriveau et al., 2010b, 2022b, d; Williams, 2010b; Jébrak, 2022). This association suggests that brecciation results from the build-up of hydraulic pressure, potentially aided through sealing of the system by cover sequences (e.g. a rhyolite cap at NICO; Goad et al., 2000; Montreuil et al., 2016b). Tectonic controls may enhance brecciation such as at the Sue Dianne deposit (Mumin et al., 2010).

4) K-skarn (clinopyroxene, garnet, K-feldspar) and K-felsite (K-feldspar) alteration may be superimposed on calcium-rich rocks (e.g. carbonates or early carbonate alteration) where heat ingress transforms carbonates into skarn as the system transitions from magnetite to hematite. Polymetallic skarn with or without IOCG characteristics may form

(e.g. Hillside and Punt Hill deposits in the Olympic Copper-Gold Province, and the Mile Lake prospect in the GBMZ; Mumin et al., 2010; Ismail et al., 2014; Fabris et al., 2018; Blein et al., 2022; Corriveau et al., 2022b).

5) LT K-Fe, hydrolytic- to $CO_2$-rich alteration (K-feldspar, white mica, hematite ± carbonates such as calcite, dolomite, siderite and ankerite, chlorite, barite, epidote, and quartz). In association with this facies or following it, hydrolytic to $CO_2$-rich alteration parageneses with Ca-Mg, Ca-Fe or Fe-Mg are common and form a distinct LT Ca-Mg-Fe hydrolytic to $CO_2$-rich facies (Facies 5b). The LT K-Fe facies and Ca-Mg-Fe variants hosts polymetallic hematite-group IOCG deposits with and without U and REE (e.g. Olympic Dam deposit; Williams et al., 2005; Ehrig et al., 2012, 2017; Corriveau et al., 2022a, c; Skirrow, 2022).

6) LT K-Si-Al±Fe-Ba (phyllic, silicic, advanced argillic) alteration includes LT K, LT Si and LT K-Al alteration. The LT K (phyllic) alteration, with sericite ± quartz and pyrite as the dominant alteration assemblage, is commonly found at the summit of IOAA systems. It varies from minor phyllic overprints to complete replacement of host rocks (Mumin at al., 2010). The LT Fe-Si±Ba assemblages include pervasive late-stage silicification, and extensive quartz veins, stockworks and breccias ± hematite, carbonates, barite, base metal sulphides and arsenides, precious metals and uraninite. These late-stage veins can be distal to system cores or cut earlier high-temperature alteration. They are the epithermal manifestation of magmatic-hydrothermal IOAA systems that form IOCG and IOA deposits (Mumin et al., 2010; Richards and Mumin, 2013a, b; Zhao et al., 2022).

The Na, Na-Ca, HT Na-Ca-Fe and HT Ca-Fe facies are early, laterally extensive and commonly form deep within IOAA systems. These alteration facies may not be exposed or intersected in drilling as they are not the immediate host to deposits unless replaced, or brecciated and replaced, by fertile alteration facies and mineralization. In such cases, their presence may be largely obscured in large deposits and require extensive exploration to recognize.

The definition of these alteration facies differs from some-previous works by taking into account the significant iron oxide components in the alteration parageneses. Excluding iron oxides from alteration (by considering it as mineralization), leads to misinterpretation. For example, using the term potassic alteration, which is common in porphyry deposits, for a K-Fe alteration facies in IOCG deposits negates the significant impact of the abundant iron oxides on chemical composition and geophysical properties, and the significance of the mineral assemblages as vector fto ores (Corriveau et al., 2016, 2022b; Katona and Fabris, 2022). A similar point was brought up by Skirrow (2010) and some of his earlier papers, concerning the use of traditional descriptors such as "hydrolytic" alteration for the LT K-Fe alteration facies, as it did not capture the hematite-rich and "potassic" nature of this alteration. Mineralogical descriptors such as "hematite-sericite-chlorite-carbonate" were then preferred. But as mineral contents are highly variable, mineralogical descriptors became impossible to use efficiently during regional-scale alteration mapping, hence the need to bring the terminology for alteration types to a more comprehensive level, by applying the notion of alteration facies, labelling the alteration facies by their diagnostic descriptor and general high- or low-temperature origin.

Though the mineral contents of all these assemblages can be highly variable, they form consistent paragenetic sets that have diagnostic compositional ranges in major elements (Montreuil et al., 2013; Blein et al., 2022; Corriveau et al., 2022a). Interpretation of large databases to understand mineral potential and ore genesis regionally (e.g. Corriveau et al., 2015; Acosta-Góngora et al., 2018a) is greatly facilitated by a good understanding of alteration facies development and how these facies represent efficient proxies for the partitioning of elements and metal migration and deposition as the systems evolve (Acosta-Góngora et al., 2019; Blein et al., 2022; Corriveau et al., 2022a). This approach furthers earlier geochemical tools provided for IOAA systems by Benavides et al. (2008a, b) and Montreuil et al. (2013). In addition, the alteration facies remain diagnostic even after metamorphism to upper amphibolite and granulite facies, due to the largely isochemical nature of such metamorphism, as illustrated in Blein and Corriveau (2017) and Corriveau et al. (2018a).

The footprints of IOAA systems are controlled by lithospheric architecture, tectonic activity, rock permeability and reactivity, magma emplacement (as nuclei or drivers for the systems), ingress of high or low-temperature fluids, and by the sequential, cyclical or telescoped build-up of the systems, causing prograde and retrograde assemblages to form (e.g. Skirrow, 2010, 2022; Corriveau et al., 2016). The geodynamic settings in which these deposits form are commonly tectonically and volcanically active and can include faulting and caldera collapse (e.g. Hildebrand et al., 2010; Zhao et al., 2022).

The prograde metasomatic reactions are the result of the extreme chemical disequilibrium induced across the upper crust as fluid columns, highly saline at first, collect at depth from single or multiple sources such as above large magma chambers, and ascend along major fault zones, splays, crustal discontinuities and permeable or chemically reactive rocks. Other fluid sources can be involved and may have great importance in the ultimate metal endowment of deposits (Barton, 2014; Schlegel et al., 2018; Huang et al., 2022; Zhao et al., 2022), though they may not radically transform the sequence of alteration facies per se. Fluid-rock reactions and associated metal dissolution and transport toward deposition sites are a key source of metals (e.g. Oliver et al., 2004, 2008; Acosta-Góngora et al., 2018b). Repeated injections of magmas and orthomagmatic fluids reheat the systems and cause overprinting of high-temperature alteration facies on lower-temperature facies. They can also bring additional metals to the main fluid column. Emplacement of sub-volcanic intrusions increases heat and fluid influx, and generates subsidiary hydrothermal cells that coalesce with the main system. In parallel, ingress of low-temperature fluids also significantly modifies the thermal gradient of a system, brings additional metals, and can induce alteration telescoping and metal precipitation (e.g. Skirrow, 2022).

Syn-metasomatic tectonic activity and caldera collapse combined with magma emplacement induces faulting and telescoping, repetition or overprinting of alteration facies. Hence, in this volume, the term tectonic telescoping is used to describe the abrupt disruption of the prograde metasomatic record of a system in which early alteration types are cut, replaced or brecciated by later-stage alteration facies without an in situ record of the normal alteration facies sequence. Such telescoping in alteration facies can be induced by tectonic activity in the form of basin inversion tectonics or more local tectonic activity such as those related to caldera collapse, etc. In the process, higher-temperature facies can be brought into the lower-temperature fields of the system, or faulting may provide deeper ingress of low-temperature fluids, induce fluid mixing or changes in physicochemical conditions at local to system scales. The importance of differential uplift and exhumation of earlier, hotter and deeper parts of the systems, as well as mixing of the fluid column and reaction of earlier alteration types with oxidized, surface-derived or basin-derived fluids, has been discussed by Skirrow (2010), Montreuil et al. (2015) and Corriveau et al. (2016), among others. In this volume, many chapters review these topics and the importance of telescoping in the evolution of ore systems (Chen and Zhao, 2022; Daliran et al., 2022; Skirrow, 2022 and references therein; Zhao et al., 2022).

*Deposit Continuum*

A continuum from IOAA systems to porphyry copper and epithermal deposits occurs globally and is well illustrated in the Port Radium-Echo Bay district of the GBMZ (Mumin et al., 2007, 2010; Richards and Mumin, 2013a, b) and at province scale by Tiddy and Giles (2020). A variety of polymetallic epithermal veins host various combinations of Cu, U, Co, Bi, Ag and other metals, peripheral to, or at high structural levels, within IOAA systems. Many such veins not only form late as a regular outcome of fluid evolution within IOAA systems, but can also form at much later stages through remobilization and additional metal ingress associated with subsequent intrusive and orogenic events (Davis et al., 2011; Dufréchou et al., 2015; Perreault and Lafrance, 2015; Gandhi et al., 2018).

*Geological Settings and Magmatism*

In contrast to other hydrothermal deposit types that have deposit-scale associations with a specific causative sedimentary basin, volcanic centre, intrusion, fault zone or shear zone such as SEDEX, VMS and porphyry deposits, IOCG, IOA and affiliated deposits have a regional-scale spatial and genetic association with high temperature granitic or intermediate plutonic suites (continental I- to A-type magmatism) and crustal-scale fault zones and splays (Williams et al., 2005; Groves et al., 2010; Porter, 2010; Montreuil et al., 2016a, b; Ootes et al., 2017; Tiddy and Giles, 2020). Corriveau and Mumin (2010) provide an overview of the geodynamic settings, lithospheric attributes and characteristics of some IOA, IOCG and affiliated deposits of interest for exploration in frontier terranes (Table 2).

**Table 2.** Characteristics of IOAA systems with IOCG, IOA and affiliated critical metal deposits (this volume).

1) Polymetallic iron oxide-rich and iron sulphide-poor metasomatic systems with polymetallic and Fe skarn, Fe-, REE- or Ni-IOA, IOCG, iron-rich Co-Bi or Ni, albitite-hosted U or Au-Co-U, Mo-Re, and affiliated deposit types.
2) Archean to Phanerozoic in age.
3) Consecutive alteration facies with magnetite and/or hematite (> 15%) and alkali-calcic mineral assemblages evolving from Na (albitite), HT Na-Ca-Fe, HT Ca-Fe, HT Ca-K-Fe, HT K-Fe, K-felsite or K-skarn, LT K-Fe, LT Ca-Mg-Fe facies to epithermal and vein systems; extensive brecciation.
4) Metal remobilization by younger processes can lead to IOA-REE ores, five-element veins and additional deposit types.
5) Source of base metals (Cu, Fe, Ni, Pb, Zn), precious metals (Au, Ag, PGE), strategic and critical metals (REE, including HREE, Bi, Co, U, V), magnetite and industrial minerals.
6) Low to moderate ore grades; potential for very large tonnages.
7) Occurs in any host rocks, but largely in continental volcano-plutonic arc and back-arc terranes.
8) Associated with, but either proximal or distal to large-scale granitic to dioritic intrusive suites (A- to I-types), alkaline-carbonatite stocks and (or) crustal-scale fault zones and splays.
9) Structural control on ore deposition adjacent to, along, or at intersection of faults, unconformities and other discontinuities.
10) Linkages to extensional episodes during or following compressional tectonic regimes and basin inversion.
11) Triggered by the ascent of voluminous fluid plumes pooled at mid-crust from varied sources and recharge during ascent by fluid/volatile released from host rocks and external fluid sources; mantle to surface 'connection'.
12) Continuum with metasomatic iron and alkali-calcic (MIAC) systems with iron silicates, iron carbonates or iron sulphides instead of iron oxides and components poor in iron .
13) Skarn-porphyry copper-epithermal continuums.
14) Under-explored districts; exploration optimized through IOAA metasomatic framework for the disparate mineralization types.

A suprasubduction zone setting is invoked for most IOAA districts discussed in this volume: Gawler craton (Tiddy and Giles, 2020), the Central Andes (Chen and Zhao, 2022), the Bafq district in Iran (Daliran et al., 2022), the Great Bear magmatic zone (Corriveau et al., 2022c, d), and the eastern Tianshan, eastern Junggar districts and Middle-Lower Yangtze River Metallogenic Belt in China (Zhao et al., 2022). In addition, similarities between the Great Bear magmatic zone and Olympic Copper-Gold Province IOAA systems include discrete tholeiitic basalt to A-type rhyolite volcanic centers with sub-volcanic intrusions that formed synchronous with the IOAA systems, followed by voluminous ignimbritic flare-up and batholith emplacement postdating the IOAA systems (Montreuil et al., 2016a, c; Ootes et al., 2017; Wade et al., 2019; Tiddy and Giles, 2020).

Both the Great Bear magmatic zone and the Olympic Copper-Gold Province had their early arc magmatism terminated (e.g. rollback subduction ceasing due to the collision of a buoyant oceanic plateau; Tiddy and Giles, 2020). This was followed by tectonic inversion of extensional basins and high-temperature and low-pressure metamorphism, renewed magmatism (e.g. calc-alkaline to shoshonitic evolving to A-type volcanic and intrusive rocks in the Great Bear; Ootes et al., 2017; deposition of the Lower Gawler Range Volcanics and onset of emplacement of A-type granites during flat-slab subduction in the Gawler Craton; Tiddy and Giles, 2020), and development of IOAA systems and IOCG deposits. Subsequently, magmatism evolved from being constrained to local volcanic centers to the emplacement of voluminous (A-type) granitic batholiths accompanied by an ignimbrite flare-up (Great Bear batholith and post-IOAA Sloan group in the Great Bear and Upper Gawler Range Volcanics in the Gawler Craton; Ootes et al., 2017; Wade et al., 2019). Slab steepening and retreat led to progressive younging of the magmatic activity and the genesis of porphyry and epithermal deposits to the west of the Olympic Copper-Gold Province in the Gawler Craton. Westward migration of the magmatic front is also observed in the Great Bear with many of the younger intrusions being under a sedimentary cover (Hayward and Corriveau, 2014). A supra-subduction zone environment that includes tectonic inversion is also documented in the Eastern Tianshan district in China and for the Central Andes (Chen and Zhao, 2022; Zhao et al., 2022). Alternative models for the geodynamic setting of the Olympic Copper-Gold Province are discussed in Tiddy and Giles (2020).

Four distinct geological settings for melting of asthenosphere and deep lithosphere in arc or post-subduction settings lead to variations in resultant arc magma chemistry that directly influence associated ore systems. In subduction zones, arc magmas with high $fS_2$ and low $fO_2$ generate barren porphyry systems, magmas with high $fS_2$ and $fO_2$ generate fertile arc porphyry systems, and magmas with low $fS_2$ and high $fO_2$ generate S-poor porphyry or IOCG deposits. Post-subduction settings such as arc-rifting, back-arc and distal extensional settings with low $fS_2$ and high $fO_2$ magmas can generate post-subduction porphyry copper-gold, alkali epithermal gold, and IOCG deposits (Richards and Mumin, 2013a, b).

Though continuums exist between IOAA and porphyry systems, major IOCG deposits are most commonly Proterozoic in age (with exceptions such as the Chilean Iron Belt) and porphyry deposits Phanerozoic, a result of secular evolution of Earth, from Archean to present, according to Richards and Mumin (2013a, b). In this model, Precambrian IOAA systems are considered less enriched in sulphides due to the lack of ocean sulphate, a key factor in the production of the oxidized sulphur-enriched arc magmas needed for the formation of sulphur-rich (pyrite) porphyry copper systems. Hence arc magmas of similar composition but generated in the Proterozoic and Archean will lead to IOCG deposits (stabilization of hydrothermal iron oxides rather than abundant pyrite). Another reason invoked for the overall paucity of giant porphyry deposits in rocks older than the Phanerozoic is a lack of preservation of such near-surface deposit types (Cooke et al., 2005). However, Precambrian porphyry deposits are known and interpreted to be underexplored (Sinclair, 2007) and Corriveau et al. (2007, 2018a) and Corriveau and Spry (2014) have pointed out that the large extent of high-grade metamorphism across Proterozoic terranes may hamper the global recognition of porphyry and other volcanoplutonic-hosted ore systems.

*Ages*

Ages of known deposits within IOAA systems range from Archean to Phanerozoic (Table 3). The Carajás district in Brazil is amongst the oldest at 2.71–2.68 Ga. The youngest deposits include El Laco in the Chilean Andes (IOA deposit) at 2 Ma, Cerro de Mercado at 0.04 Ga and Peña Colorada at 0.06 Ga in Mexico, and Oueb Belif at 9 Ma and Salmi at 0.02 Ga in Tunisia and Turkey, respectively. Phanerozoic deposits are common in the Central Andes (e.g. Chilean Iron Belt at 0.122–0.115 Ga), and in China and South Korea with the Middle Yangtze River Metallogenic Belt at 0.13 Ga and the Yangyang deposit at 0.21 Ga, respectively.

**Table 3.** Ages of IOA, IOCG and affiliated deposits.

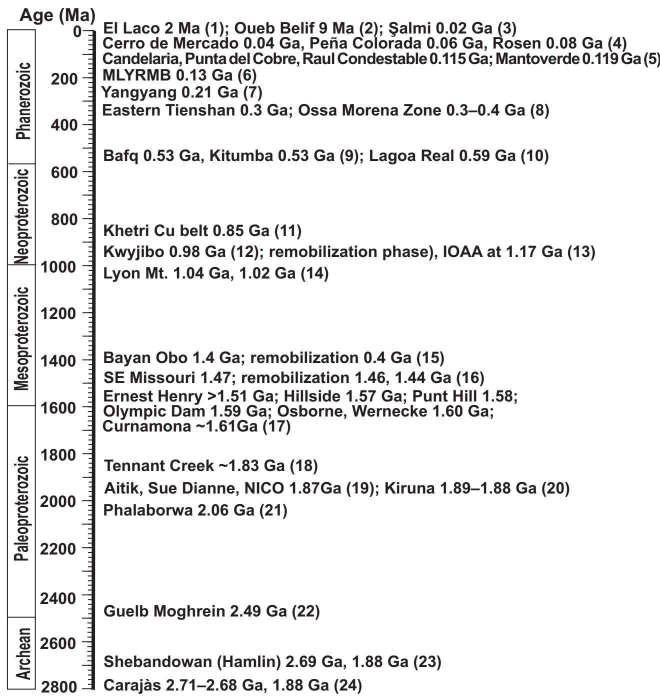


1: Nyström and Henríquez (1994); 2: Decrée et al. (2013); 3: Yılmazer et al. (2014); 4: Corona-Esquivel et al. (2011), Sillitoe et al. (2020); 5: Mathur et al. (2002), Sillitoe (2003), Gelcich et al. (2005), del Real et al. (2018); 6: Mao et al. (2011), Zhou et al. (2013); 7: Seo et al. (2015); 8: Carriedo and Tornos (2010); 9: Torab and Lehmann (2007), Porter (2010), Stosch et al. (2011), Huang et al. (2013); 10: Lobato et al. (2015); 11: Knight et al. (2002); 12: Gauthier et al. (2004), Clark et al. (2010); 13: Corriveau et al. (2007); 14: Selleck et al. (2004), Valley et al. (2009, 2011); 15: Fan et al. (2014, 2015); 16: Aleinikoff et al. (2016), Neymark et al. (2016); 17: Mark et al. (2000), Williams and Skirrow (2000), Gauthier et al. (2001), Thorkelson et al. (2001), Reid et al. (2011), Skirrow et al. (2011); 18: Skirrow (2000); 19: Gandhi et al. (2001), Wanhainen et al. (2003), Montreuil et al. (2016a, c); 20: Romer et al. (1994); 21: Reischmann (1995); 22: Kolb et al. (2010); 23: Forslund (2012); 24: Tallarico et al. (2004), Moreto et al. (2015).

## The IOCG (±U) Deposit Type

Notwithstanding the diverse nature of known IOCG deposits and their host environments (Table 2; this volume), some common definitive characteristics can be identified, including the following:

- polymetallic, hydrothermal ores with >15% magnetite and/or hematite (i.e. not simply pervasive iron staining);
- copper with or without gold as principle economic metals,

though the principal commodities vary greatly and may include combinations of base (Cu, Fe, ±Ni, Pb, Zn), precious (Au, Ag, PGE), and strategic (Co, Bi, V) metals, REE, and uranium;
- iron oxides with Fe/Ti ratios greater than those in most igneous rocks and bulk crust, especially in nelsonites and igneous Fe-Ti deposits;
- strong structural and stratigraphic control;
- regional- to deposit-scale, intense, pervasive, Na, Ca-Fe, K-Fe and Fe alteration;
- abundant hydrothermal-structural breccia zones; and
- presence of regional-scale high-temperature magmas (e.g. A-type granite, additional mafic magma) or of alkaline magmas, and the pooling of magmatic-hydrothermal fluids to initiate the chain reactions that form the IOAA systems.

The mineralization styles are diverse and consist of strata-bound to discordant breccia zones, stockworks, veins, disseminations, replacement zones and mantos (this volume). In essence, they reflect the expected suite of deposit characteristics that can be associated with large to giant magmatic-hydrothermal systems (Mumin et al., 2010; Richards and Mumin, 2013a, b), though taken individually many of the above characteristics are not solely restricted to magmatic-hydrothermal systems. Immediate ore hosts are intensely metasomatized by K-Fe alteration facies at high temperatures (magnetite, K-feldspar, biotite assemblages) and (or) at low temperature (hematite, K-feldspar, sericite, chlorite and carbonate-bearing assemblages) (Mumin et al., 2010; Williams, 2010a, b; Corriveau et al., 2022a, d; Skirrow, 2022). The ore and host alteration facies form within any host rocks, at any stratigraphic level, and commonly among units of different ages. Within a single system, deposits can be hosted in volcanic, sedimentary, intrusive and metamorphic rocks.

Iron oxide metasomatism has to be significant for a deposit to be classified as an IOCG deposit, although the iron oxide and copper-gold enrichments may not be directly spatially correlated. Prospects and hydrothermal systems featuring iron metasomatism in the form of iron oxide staining, minor iron oxide disseminations and minor to significant iron carbonate alteration, or having mineralization that does not contain economic copper (but otherwise bear most of the other characteristics of IOCG deposits), are best referred to as IOCG variants or affiliated deposits until significant iron oxide is found within the deposit itself. These deposits, such as the K-skarn Punt Hill deposit in Australia, can be parts of IOAA systems or their continuums (Fig. 1; Corriveau et al., 2022a, b).

One of the exceptional characteristics of many IOCG deposits is the great spatial extent of high-temperature alteration facies compared to other magmatic-hydrothermal deposits such as porphyry copper-type systems. Other things being equal (e.g. similar size and composition of source magmas), Richards and Mumin (2013a) attribute the great extent of high-temperature alteration to emplacement within "hot rocks". The causes of hotter host rocks are varied and include higher geothermal gradients in the past (i.e. at 2.0 Ga the geothermal gradient would be twice the current value), extensional regime, hydrothermal sealing of the systems, and (or) geotherm rise through ascent of the voluminous hot saline fluid plume formation within the high-temperature metasomatic aureoles of underlying batholiths.

Williams (2010a) subdivided IOCG deposits into three groups: magnetite group (e.g. Ernest Henry, Candelaria, Sossego, Salobo, Guelb Moghrein, Boss in Fig. 2), magnetite-to-hematite group (e.g. Sue Dianne, Raul-Condestable, Mantoverde; Fig. 2), and hematite group (e.g. Olympic Dam, Carrapateena, Prominent Hill, Mina Justa; Fig. 2). Cobalt-rich but low-copper variants of magnetite-group IOCG deposits also form, such as the NICO Au-Co-Bi-Cu deposit in Canada (Acosta-Góngora et al., 2015a, b; Corriveau et al., 2016; Montreuil et al., 2016b). The main ore minerals of IOCG deposits include copper sulphides and more rarely As-, Pb-, Zn- and Ni-sulphides, Ag-, Cu-, Ni- and Co-arsenides, Ag-, Bi- and Co tellurides, electrum, REE-bearing and U-bearing phosphates or oxides, and native Bi, Cu, Ag and Au (Corriveau, 2007; Ehrig et al., 2012). Accessory minerals are numerous, with 90 species identified at Olympic Dam alone (Ehrig et al., 2012).

Uranium is currently mined at Olympic Dam and was mined at several vein-type deposits in the GBMZ. Uranium also occurs in the Prominent Hill, Carrapateena, Oak Dam and Khamsin deposits of the Olympic Copper-Gold Province (Davidson et al., 2007; OZ Minerals, 2014a, b, 2019), in the Wernecke Breccia (Hunt et al., 2010), in the GBMZ IOAA systems (Somarin and Mumin, 2012; Ootes et al., 2013; Montreuil et al., 2015; Gandhi et al., 2018; Potter et al., 2019b, 2022), in the Kwyjibo district (Clark et al., 2005, 2010; Magrina et al., 2005) and in the New Jersey inlier and Adirondack district (Scrub Oaks and Mineville deposits; Foose and McLelland, 1995; Williams et al., 2005) of the Grenville Province.

### Iron Oxide±Apatite (IOA) Deposit Types

Iron oxide-apatite deposits (containing 30–60 wt% Fe) with or without REE mineralization are also called Kiruna type deposits and abbreviated to IOA (also termed volcanic-hosted iron and porphyrite iron in historic and some current Chinese literature; Zhao et al., 2022). As per all other deposits within these systems, mineral proportions greatly vary in IOA deposits; as such, within the broad IOA group we include deposits in which iron oxide is abundant but apatite may be minor or absent, e.g. the magnetite-dominant component of the Oak Dam East deposit, and many of the iron oxide-rich but sulphide-poor deposits of the Olympic Copper-Gold Province beyond the Acropolis deposit (see Skirrow, 2022). Key IOA-type deposits (see Corriveau et al., 2018b and references therein for a more complete listing) include:
- Kiirunavaara (682 Mt, 47.5% Fe), Norbotten district, Sweden;
- Oak Dam East (~560 Mt, 41–56% Fe) (+ Cu, U, Au), Olympic Copper-Gold Province, Australia;
- Marcona (~1940 Mt, 55.4% Fe) (+ Cu), central Andes province, Chile and Peru;
- El Laco (734 Mt, 49% Fe), high Andes, Chile; and

- Pea Ridge (161 Mt, ~ 54% Fe; 0.2Mt, 12% REE), southeast Missouri district, Granite-Rhyolite Province, USA.

The first Canadian REE-rich IOA deposit to be discovered was the Josette deposit of the Kwyjibo district in the Grenville Province of Québec (Table 1). This district hosts a variety of IOA, IOCG, and affiliated prospects. The alteration facies are described in detail by Clark et al. (2010). Two IOA deposits were historically mined from the Grenville Province in Ontario: the Marmoraton (28 Mt of 42% Fe) and Hilton deposits (Sangster et al., 2012) and other prospects (Lac Marmont, south of the Kwyjibo district; Bondy gneiss complex) are known (Clark et al., 2010; Corriveau et al., 2018a).

Systems with iron oxide-apatite deposits have the same alteration assemblages as systems with IOCG deposits, but have different proportions of alteration facies at deposit- to regional-scales; Na, skarn, HT Na-Ca-Fe and HT Ca-Fe alteration facies are dominant. Iron skarn mineralization occurs among or in association with IOA ores and can originate from similar fluids (Zhao et al., 2017a; Liu et al., 2018; Zeng, 2020; Zeng et al., 2020). The IOA deposits, associated skarn and HT Ca-Fe alteration zones are poor in sulphides (the Jaguar nickel deposit is a notable exception) and uranium unless overprinted by fertile HT Ca-K-Fe and/or K-Fe alteration accompanied by chalcopyrite and uranium (Montreuil et al., 2016c; Zhao et al., 2017b). In the Middle Lower Yangtze River Metallogenic Belt, iron skarn such as those of the Jinshandian deposit formed in evaporite-bearing sedimentary host sequence and coeval IOA deposits in volcanic rocks (Zeng, 2020; Zeng et al., 2020).

Iron oxide-apatite deposits that did not evolve to potassic-bearing alteration facies are commonly devoid of REE ore and apatite is commonly poor in REE (e.g. Lac Marmont; Clark et al., 2005, 2010). The REE-endowed IOA deposits are typically replaced by, or spatially associated with, HT Ca-K-Fe, HT K-Fe, or LT K-Fe alteration, as observed at the Bayan Obo deposit in China, the Pea Ridge deposit in southeastern Missouri, and the Josette deposit (Kwyjibo district) in Québec (Perreault and Lafrance, 2015; Aleinikoff et al., 2016; Huang et al., 2022). Detailed research at Josette and Pea Ridge illustrates that the REE ore stems from remobilization of early REE endowment of the IOA mineralization, either by fluids associated with a late-stage intrusion or by a metamorphic event. Detailed studies of apatite illustrate the process by which REE-enriched minerals are formed by progressive migration of REEs during pseudomorphic replacement of apatite by REE-poor apatite (Harlov et al., 2005; Bonyadi et al., 2011).

Magnetite only or magnetite-apatite IOA assemblages may form at depth within two types of IOAA systems: those that have evolved to IOCG mineralization (Great Bear, Olympic Dam, Oak Dam, and Kwyjibo including the Josette deposit; Clark et al., 2010; Mumin et al., 2010; Ehrig et al., 2017; Corriveau et al., 2022a, b), or those that have cooled without maturing to IOCG mineralization, such as what is currently observed in the Middle-Lower Yangtze River Metallogenic Belt, where IOA and some iron skarn deposits dominate (Zhao et al., 2022 and references therein). Some IOA mineralization also precipitated near surface, such as at El Laco (Tornos et al., 2017 and references therein).

The IOA ores are commonly fine grained and massive, although veins, stockworks, and breccia also occur. Conclusive field evidence of metasomatic attributes (i.e. replacement, breccia filling, fluidization, brecciation) is common, and protolith textures may be preserved or destroyed by alteration (Corriveau et al., 2022b–d; Daliran et al., 2022; Zhao et al., 2022). The deposits are frequently associated with andesitic magmatism, forming at shallow depth above the roof of intrusions (Hildebrand, 1986; Zeng, 2020; Zhao et al., 2022). They can contain fluid inclusions similar in chemistry to IOCG deposits, a component of which includes extremely high temperature (>800 °C) hydrosaline liquids and hypersaline (>90 wt%) fluids (Zeng, 2020) and iron oxide melt inclusions may occur in coeval andesite (Tornos et al., 2017). Highly saline magmatic-hydrothermal fluids stem in part from coeval magmas and interact with host rocks, resulting in mineral assemblages that can crystallize at very high temperatures (600–800°C or greater). The characteristics of these deposits and their magnetite chemistry are discussed in Zhao et al. (2022) and Huang et al. (2022).

Ore deposit models for IOA deposits are diverse (Chen, 2013; Knipping et al., 2015; Tornos et al., 2016, 2017; Zhao et al., 2016, 2017a, 2022; Lentz et al., 2019; Bain et al., 2020; Zeng, 2020) and invoke:

- metasomatism (magmatic-hydrothermal alteration) related to highly saline fluids exsolved from magma chambers and/or to heated basinal fluids or evaporite-derived;
- iron oxide magmas (immiscible from silicate magmas); melt attributes include iron oxide melt inclusions in coeval andesite;
- hypersaline fluids/hydrosaline liquids and iron oxide-salt melts;
- fluidization of hydrothermal precipitates;
- flotation of igneous magnetite; and
- syntexis of carbonate or partial melting of evaporite-bearing carbonate rocks.

The flotation model proposed by Knipping et al. (2015) involves the capture and entrainment of magnetite microlites by chlorine- and iron-rich fluids that exsolved from magmas during decompression (i.e. magma ascent), nucleated along the magnetite microlites, and rose along major active fault zones carrying their magnetite crystal mush. Deposition of the igneous magnetite (and apatite) is interpreted as forming the main body of these deposits. Coeval with magnetite deposition, a drop in fluid pressure initiates hydrothermal crystallization of magnetite at lower temperatures with a composition distinct from that of magmatic-derived magnetite (Rojas et al., 2018). Amphibole-bearing mineral assemblages also form. This new model invokes metal entrapment by exsolved magmatic fluids, the ponding of magmatic brines at depth and the ability of these evolving fluids to carry metal loads towards surface (e.g. Nadeau et al., 2013; Nadeau, 2015). However, like the iron oxide magma model, the flotation model has yet to explain the early formation of regional-scale albitite zones associated with IOA ores, as it proposes that increasing sodium and potassium concentrations in the brine during decompression would reduce the potential for sodic and potassic alteration (Simon et al., 2017).

The emplacement of immiscible iron oxide magma would clearly distinguish the genesis of IOA deposits from IOCG deposits (Tornos et al., 2016, 2017). As discussed in Corriveau et al. (2022b) and Huang et al. (2022), any processes invoked for the genesis of IOA deposits must also be capable of producing not only the range of alteration facies found in IOAA systems but also the alteration sequence starting with the pre-IOA ore albitite and HT Na-Ca-Fe and skarn facies. Although the presence of hydrothermal fluids associated with IOA deposits is acknowledged as having induced iron oxide and alkali-calcic alteration (e.g. Tornos et al., 2016, 2017; Barra et al., 2017), currently only models involving the ascent of highly saline to hypersaline fluids (magmatic-hydrothermal or non-magmatic brines or a combination of both) satisfy the prerequisite of having early, commonly deeper and regional-scale albitization (Corriveau et al., 2022b; Daliran et al., 2022; Huang et al., 2022; Zhao et al., 2022). In addition, the igneous origin has commonly been disputed based on the observation of incremental hydrothermal alteration of host rocks by magnetite, and the extreme ability magnetite has to pseudomorph host-rock textures, as seen in andesite flows at El Laco in Chili (e.g. Sillitoe and Burrows, 2002) and in porphyritic andesite and sedimentary structures in the GBMZ (e.g. Hildebrand, 1986; Corriveau et al., 2022b–d). Emplacement of metasomatic magnetite mushes through fluidization breccia is also documented in the Cloncurry district (Rusk et al., 2010) and in the GBMZ (Corriveau et al., 2022b, d).

## Polymetallic Albitite-hosted Deposits

Albitite-hosted uranium deposits consist of uranium enrichment within albitite, but field relationships in non-metamorphosed examples clearly demonstrate that the uranium mineralization postdates the crystallization of albitite; mineralization is genetically related to the host IOAA systems but not to the albitization process itself, except for its porosity development as further described below. These deposits are also called Na-metasomatic uranium, metasomatic uranium and orogenic uranium. In this paper, the Na-metasomatic uranium term is clearly avoided as the uranium precipitation is not related to Na metasomatism per se. As for the orogenic uranium term, it is not a class included in any of the formal uranium deposit classifications (e.g. by the International Atomic Energy Agency) and was proposed for an area that was previously described as containing metasomatic uranium (e.g. Mount Isa in Australia; McGloin et al., 2016). Similarities also exist with albitite-hosted Au-Cu-U veins from India (Ray, 1990; Bhukia area, Mukherjee et al., 2016; Khetri and Ladera area of Rajasthan, Knight et al., 2002).

In Canada (Fig. 4), two albitite-hosted uranium deposits are known, both in the Central Mineral Belt of Labrador. The Michelin deposit has total resources of 37.5 Mt at 0.10% $U_3O_8$ and the Upper C deposit at Moran Lake has 6.92 Mt at 0.29% U (indicated) + 2.84 Mt at 0.20% U (inferred) resources (Paladin Energy, 2015; Sparkes, 2017). The deposits and prospects along the belt display footprints characteristic of IOAA systems in which early and likely deep albitite has been thrust-faulted into the field of lower temperature alteration facies and served as host to uranium mineralization (Acosta-Góngora et al., 2019).

The Southern Breccia and Cole prospects of the GBMZ are also prospective exploration targets (Montreuil et al., 2015, 2016b; Potter et al., 2019b). These deposits and prospects occur within regional-scale albitite alteration zones associated with IOAA systems as documented worldwide (Wilde, 2013). These include the prospects from the Romanet Horst and potentially those of the Wanapitei region in the Huronian basin in Canada (e.g. Scadding gold mine; Schandl and Gorton, 2007; Corriveau et al., 2014; Montreuil et al., 2015; MacDonald Mines Exploration Ltd, 2019; Potter et al., 2019b; Blein et al., 2022), the Kuusamo deposit in Finland (Pankka and Vanhanen, 1992), the Valhalla deposit in the Mount Isa Inlier in Australia (Polito et al., 2009), the Itataia deposit in Brazil (Verissimo et al., 2016), and some deposits along the Singhbhum Shear Zone, India (Pal et al., 2009). Some of these Au-Co-U deposits within albitite have locally been referred to as orogenic Au, although the original metal endowment was likely that of the host IOAA systems (e.g. Kuusamo in Finland; Laraboué, Larafella in Burkina Faso; Eilu et al., 2015).

Spatial and temporal associations of albitite with uranium mineralization and with IOCG deposits are well documented; the albitite forms structural, porous, damaged, fractured and brecciated corridors for fluid channeling and ore precipitation (Montreuil et al., 2015; Potter et al., 2019b, and references therein). The precipitation of uranium within albitite takes place in conjunction with telescoping (i.e. contraction) of the

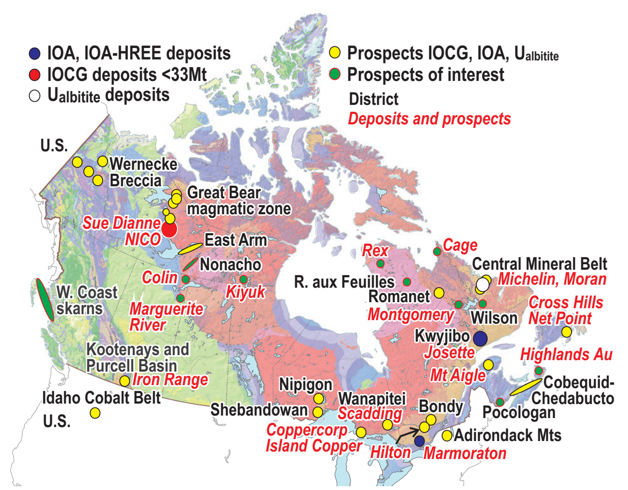


**FIGURE 4.** Canadian settings with known deposits in red on a map distinguishing Precambrian rocks in pink from Phanerozoic rocks in blue and green (modified from Corriveau, 2007 and Corriveau et al., 2018b). Colin refers to a series of mineral occurrences in northeastern Alberta (Rukhlov, 2011).

alteration sequence, as albitite zones are exposed to conditions conducive to precipitation of high- to low-temperature K-Fe alteration facies. An example of this process is the magnetite-K-feldspar-bearing U-Mo-Cu mineralization in the Southern Breccia (Montreuil et al., 2015, 2016b; Blein et al., 2022). Uranium also precipitates in association with LT Ca-Mg-Fe alteration facies, such as in quartz-carbonate veins formed during the evolution of an IOAA system (e.g. Romanet Horst; Corriveau et al., 2014), or during subsequent orogenic or intrusive events (e.g. late uranium-bearing chlorite-hematite vein, Southern Breccia; Potter et al., 2019b, 2022; prospects in the Central Mineral Belt of Labrador; Sparkes, 2017). Potter et al. (2019b) propose that primary uranium enrichment in the Southern Breccia mineralization zones was likely sourced and transported as chloride and fluoride species by high temperature, reducing fluids. As with many ore systems hosting uranium mineralization, several generations of uranium dissolution, enrichment and/or reprecipitation occur, as documented at the Olympic Dam deposit by Macmillan et al. (2016).

## Skarn, Iron Skarn and Potassic Skarn

Skarn in IOAA systems forms in carbonate-bearing sedimentary sequences and locally occurs in association with IOA deposits, in the form of iron skarn and skarn-bearing IOA deposits (e.g. Middle Yangtze River Metallogenic Belt; Zhao et al., 2017a, 2022; Liu et al., 2018). Such skarn forms prior to, or coeval with, albitite or as albitite transitions to the HT Ca-Fe alteration facies within carbonate rocks. Local skarn also forms where later-stage carbonate veins and alteration have been transformed into new skarn due to renewed heating of the system through emplacement of magmas or high temperature fluids (e.g. spectacular exposures in the Wangbaoshan iron deposit, Daye district, Middle-Lower Yangtze River Metallogenic Belt, China; Hu et al., 2020).

Potassium feldspar-bearing skarn also occurs among IOCG deposits and within IOAA systems. Early skarn can be overprinted by subsequent K or K-Fe alteration, or a K-skarn facies can form through precipitation of K-feldspar coeval with skarn assemblages which can lead to Cu-Au-rich or Ag-Zn K-skarn deposits (components of Hillside and Punt Hill in Australia; components of Sossego in Brazil and Raul-Condestable in Peru; Hannukainen and Kaunisvaara in Scandinavia; Mile Lake Breccia; De Haller et al., 2006; Monteiro et al., 2008; Mumin et al., 2010; Baker et al., 2011, 2014; Ismail et al., 2014; Fabris et al., 2018; Fabris, 2022). The skarn may be coeval with the development of regional IOAA systems (Punt Hill; Reid et al., 2011; Fabris et al., 2018: Fabris, 2022) or can precede them and serve as hosts for IOA, IOCG or U, Th, REE mineralization (e.g. Mary Kathleen in Australia; Oliver et al., 1999; Mernagh and Miezitis, 2008).

## Other Deposit Types within IOAA Systems

Iron oxide, IOA, IOCG and affiliated deposits that form in IOAA systems, including those associated with carbonatites, can have significant resources of Nb, P, REE, PGE, Mo and vermiculite such as at the Bayan Obo and Phalaborwa deposits (Table 1; Groves and Vielreicher, 2001; Porter, 2010; Chinova Resources, 2014; Babo et al., 2017), and in the Romanet Horst of Canada (Clark and Wares, 2004). Five-element and other polymetallic veins have long been recognized within the GBMZ and the East Arm basin (Robinson and Ohmoto, 1973; Badham, 1975; Badham and Muda, 1980; Gandhi et al., 2013). These veins were previously mined for U, Ag and Cu and are now recognized as parts of a large polymetallic IOAA system, being formed late within the IOAA system evolution or subsequently through the remobilization of their original metal endowment (Mumin et al., 2007, 2010; Gandhi et al., 2013, 2018; Potter et al., 2019a). The association of IOAA systems with carbonatites and late mineralized veins is of interest because they provide easily recognized targets for potential IOAA systems and their deposit types in frontier territories, including metamorphic terranes (Corriveau, 2007; Corriveau and Mumin, 2010; Dufréchou et al., 2015).

## Canadian IOCG and IOA Districts

Detailed reviews of Canadian settings prospective for IOA, IOCG and affiliated deposits can be found in Corriveau (2007), Corriveau et al. (2010a) and Gandhi (2015). Precambrian districts include (Figs. 2, 4): the GBMZ, East Arm basin and Nonacho basin in the Northwest Territories; the Wernecke Breccia in Yukon; the Belt-Purcell Basin (e.g. Iron Range prospect) in British Columbia; the Kwyjibo district (e.g. Josette REE deposit), the Bondy gneiss complex and other targets of the Grenville Province (e.g. regions of the past-producing Marmoraton and Hilton iron mine); the Rex lineament in the Superior Province; the Romanet Horst (Québec) and to the south the region hosting the Montgomery Lake copper-gold prospect (Newfoundland-Labrador) of the Labrador Trough; the Mid-Continent Rift, Shebandowan greenstone belt, and Wanapitei district in the Southern Province in Ontario; and the Central Mineral Belt in Labrador (Fig. 4; Gandhi, 1978; Meyer et al., 2003; Gauthier et al., 2004; Clark et al., 2005; Corriveau, 2007; Schandl and Gorton, 2007; Corriveau et al., 2010a, 2014, 2018a, 2022a–d; Hunt et al., 2010; Lulin et al., 2010; Mumin et al., 2010; Sangster et al., 2011, 2012; Forslund, 2012; Galicki et al., 2012; Potter et al., 2013a, 2019a; Sparkes, 2017; Adlakha et al., 2019; Conliffe, 2020; Corriveau and Potter, in press). The Rex lineament and Shebandowan greenstone belt settings are Archean (Fig. 4). An IOCG model has also been proposed for many other mineral occurrences and settings (Furic and Jébrak, 2005; Mumin and Perrin, 2005; Tremblay and Koziol, 2007; Sangster et al., 2011, 2012; Turner, 2012).

Phanerozoic examples include those of the Appalachian Orogen (e.g. Cobequib-Chedabucto district and Highlands Gold occurrences of Nova Scotia; the Pocologan area of New Brunswick; Koorae, Net Point and Cross Hills prospects of Newfoundland; and Mont-de-l'Aigle prospect of Quebec (New-Brunswick Department of Mines, 2003; Simard et al., 2006; Corriveau, 2007; Kontak et al., 2008; MacHattie and O'Reilly, 2009; Belperio, 2010; Corriveau et al., 2010a; Galicki et al., 2012; Courage, 2013;

Baldwin, 2019). All these prospects form along a network of faults that have a history of reactivation and may have served as preferential pathways for the development of IOAA systems across terranes (e.g. Piette-Lauzière et al., 2019).

In the Cordillera, the 0.2 Ga Minto Cu-Au-Ag deposit, with indicated resources of 48 Mt at 1.09% Cu, 0.39 g/t Au and 3.73 g/t Ag, occurs within a volcanic-arc hosted magnetite-biotite-altered and predominantly granodioritic pluton (Hood, 2012). The Cu-Au-Ag-Pb metal association hosted by K-Fe-P-U-Th-enriched and Si-Al-Ca-Na-depleted magnetite-biotite alteration assemblages (Hood, 2012) are consistent with magnetite-group IOCG deposits. Such a model was proposed by Quin and Mercer (2008) but since then this deposit and the related Carmacks copper deposit have been interpreted as metamorphosed remnants of a Late Triassic belt of porphyry deposits (Kovacs et al., 2020).

The first two IOCG deposits discovered in Canada since recognition of the IOCG class are the Sue Dianne and NICO deposit in the southern GBMZ; NICO is fully permitted and operation awaits completion of an all-weather road. In the northern GBMZ, two IOCG districts have reached advanced exploration stages (Port Radium-Echo Bay and Camsell River), but many showings and fertile areas remain underexplored throughout the belt. The GBMZ also extends under Proterozoic and Phanerozoic sedimentary basins, including the uranium-bearing Hornby Bay Basin (Gebert et al., 2007), and the Dessert Lake Basin (Bleeker and LeCheminant, 2008). Some of the most prospective geophysical anomalies interpreted as potential ore systems by Hayward et al. (2013) occur below these sedimentary basins and remain under-explored. In terms of REE mineralization, the most regularly REE enriched prospects of the GBMZ fall along its reactivated eastern boundary (the Wopmay fault zone; e.g. Ham and JLD prospect; Corriveau et al., 2015, 2022a). Their IOA mineralization displays intense recrystallization (De Toni, 2016).

## From Under-explored Territories to Mines

*Discovery Timelines and Success Stories*

The discovery of multiple deposits in the Olympic Copper-Gold Province of the Gawler craton in Australia is a good case example of persistence in exploration, feedback between government, academia and private sector results, and timeline of discoveries. Drill holes first intersected the Olympic Dam deposit in July 1975, but the first publications on deposit geology, potential controls on ore deposition, and the role of geophysics and structural lineaments as vectors to mineralization were not released for nearly 10 years (Roberts and Hudson, 1983; O'Driscoll, 1986; Oreskes and Einaudi, 1990; Reeve et al., 1990; Haynes et al., 1995; Haynes, 2006). Another 10 years followed before the IOCG deposit type was recognized as a unique class, incorporating several other known but atypical deposits (Hitzman et al., 1992). The current resource of the Olympic Dam deposit is now reported at more than 10 billion tonnes (Table 1), and the deposit is still open at depth.

Three decades after the discovery of the Olympic Dam deposit, concurrent with a major Geoscience Australia project, a second economic IOCG deposit was discovered in the Olympic Copper-Gold metallogenic province, namely Prominent Hill (Table 1, Fig. 2; Belperio et al., 2007; Skirrow and Davidson, 2007; OZ Minerals, 2014a; Schlegel and Heinrich, 2015). Another 5 years elapsed before discovery of the Carrapateena deposit (total resources of 134 Mt at 1.5% Cu, 0.6 g/t Au, 6.3 g/t Ag (+U); Skirrow, 2010; OZ Minerals, 2019), followed by Hillside in 2009 (total resources of 337 Mt at 0.6% Cu, 0.14g/t Au, 15.7% Fe; Ismail et al., 2014; Rex Minerals Ltd, 2015), and Khamsin in 2012 (total resources of 202 Mt at 0.6% Cu, 0.1 g/t Au, 1.7 g/t Ag, 86 ppm U; OZ Minerals, 2014b). Renewed exploration in the Oak Dam deposit region is now leading to additional major discoveries decades after the seminal paper of Davidson et al. (2007) (BHP, 2018). Skirrow et al. (2002) coined the term Olympic Copper-Gold Province to highlight the prospectivity of the whole province (see also Reid, 2019; Tiddy and Giles, 2020; Skirrow, 2022).

In parallel, the discovery of the Merlin Mo-Re-Cu-Au deposit in the Cloncurry district (Babo et al., 2017) and the renewed interest for uranium and REE in the Mary Kathleen deposit (Salles et al., 2017) illustrate how varied commodities can be in IOAA systems.

The IOCG and affiliated deposits have greatly increased Australian resources in copper, gold, uranium, cobalt, molybdenum and rhenium, and provide significant employment with extended mine lives (Table 1). With such large potential resources, the discovery of IOCG deposits could significantly renew Canada's 21st century mineral inventory as they have in Australia, Brazil and South America (Table 1; Corriveau et al., 2018b).

*Synergies as a Tool for Increasing Discoveries of Under-represented IOAA Deposit Types*

Many producing mining districts reached peak production in the 20th century. In parallel, many deposit types remain under-represented in Canada and globally, in particular IOCG and affiliated deposits. Renewing mineral resources for the 21st century requires: 1) targeting exploration and public geoscience towards these under-represented and still untapped deposit types and host systems; 2) diversifying exploration into uncharted and commonly under-valued terranes; 3) reassessing baseline geological and environmental data to include IOAA systems; and 4) expanding exploration tools and geo-environmental models (e.g. Canadian Minerals and Metals Plan, 2018; OZ Minerals exploration challenge). Successes in discoveries where government, academia and private sector have targeted the same district together is nowhere better illustrated than in the Olympic Copper-Gold Province of Australia.

Impediments to discoveries include concealment by sedimentary or volcanic cover, lack of infrastructure, and remoteness, but the most common obstacles are likely high-grade metamorphism and the former lack of an effective system-scale ore deposit model. The impact of metamorphism is well illustrated in the 1500 by 500 km Grenville Province. This belt remains one of the most under-explored regions of Canada even though the province and its extensions in the Granite-Rhyolite Province and as inlier in the Appalachian orogen host six known IOCG-IOA districts, namely the Southeast Missouri district, Adirondack belt, Kwyjibo district (e.g. Josette REE deposit), New Jersey district, southern Central Metasedimentary Belt (e.g. Marmoraton and Hilton deposits) and the Bondy gneiss complex (Corriveau et al., 2007, 2018a, 2022a, b; Day et al., 2016). Many of these are within populated regions or within ~50 km of transportation routes.

In Canada, the GBMZ, Romanet Horst and Central Mineral Belt are recognized as the most prospective settings for IOCG deposits, a result of metal endowment and extensive collaborative research between government, academia and industry (see Mumin et al., 2007, 2010; Corriveau and Mumin, 2010; Jackson and Ootes, 2012; Corriveau et al., 2014; this volume; Slack et al., 2016). Other prospective settings targeted for joint government, academia and private sector include the East Arm basin (Gandhi et al., 2013; Potter et al., 2013a, 2019a), the Wernecke breccias in Yukon (Hunt et al., 2010), the Iron Range in British Columbia (Galicki et al., 2012), the Eden Lake region in Manitoba (Mumin and Perrin, 2005; Mumin, 2010), the Central Mineral Belt in Labrador (Hinchey and LaFlamme, 2009; Sparkes, 2017; Acosta-Góngora et al., 2018a, b), and the Cobequid-Chedabucto Fault Zone and other fault zones in Nova Scotia (Kontak et al., 2008; Corriveau et al., 2010a; Baldwin, 2019; Piette-Lauzière et al., 2019). Other settings may be as prospective, but without extensive research and access to properties it is hard to make informed decisions in a regional synthesis.

*Timeline for Proof of Concepts in Prospective Settings*

Canada has the type of geological terranes known worldwide to host significant IOCG and affiliated deposits (see criteria in Skirrow, 2022) and yet does not have a single producing IOCG or IOA mine. While Australia was efficiently exploring for IOCG deposits and significantly expanding its resources in multiple metals, Canada remained largely at a proof of concept stage.

Proof of concept in the GBMZ was initiated through waves of government and industry mapping, government and academic research and mineral exploration long before IOCG deposits came into vogue. Pioneer IOCG work started in the early 1980s, building on the 1930s to 1960s classic mapping and industry exploration that led to mining of the Great Bear Lake uranium-silver veins. In the northern GBMZ, mapping of albite and magnetite-apatite-amphibole alteration zones in the Camsell River district led to the demonstration by Hildebrand (1984, 1986) that these alteration zones were hydrothermal in origin and not magmatic as previously interpreted (Badham and Morton, 1976; further textural evidence presented in Corriveau et al., 2022b–d). Here, stunning cross-sectional field exposures facilitated the resolution of conflicting models, which has not yet been achieved elsewhere.

In the southern GBMZ, Gandhi (1978) presented exploration guides to uranium in the Bear and Slave structural provinces. Subsequently, he identified, characterized and studied a series of magnetite-apatite and vein-type prospects across the GBMZ and in the East Arm of Great Slave Lake, collaborating with industry to provide key geoscientific data for today's exploration (Gandhi, 1992; Gandhi and Halliday, 1993). In 1994, an airborne multiparameter survey by the Geological Survey of Canada (Gandhi et al., 1996) documented Canada's largest hydrothermal potassium anomaly above what is now the NICO deposit. Since then, partnerships between industry, government and academia have provided geoscientific support for the NICO development (Goad et al., 2000; Corriveau et al., 2010a, b, 2016; Mumin et al., 2010; Burgess et al., 2014; Hayward et al., 2016; Montreuil et al., 2016b). Furthermore, Fortune Minerals provided logistical support as well as unpublished geophysical data (used for the Hayward et al. (2013, 2016) models) to government to study the entire southern GBMZ.

Confirmation of polymetallic IOCG mineralization has stimulated new exploration in the GBMZ, sharing of expertise and knowledge, collaborative research and training, and access to mineral properties and base camps for regional mapping. The synergies between industry, governments and academia has now expanded to DEMCo, the Denendeh exploration and mining company of the Dene First Nations. Such collaborations have greatly advanced the geological knowledge of the belt and contributed to the publication of numerous lithological, structural, alteration and breccia maps at regional and local scales (Hildebrand, 2011, 2017; Jackson and Ootes, 2012; Potter et al., 2013b; Hildebrand et al., 2014; Gandhi et al., 2014; Mumin, 2015; Montreuil et al., 2016b; Corriveau et al., 2022a). Without such synergies, the advances outlined in this Special Paper and in the earlier Short Course Notes 20 (Corriveau and Mumin, 2010) could not have been possible.

*Disparate Deposit Type Models within a District: IOAA?*

Impediments to discoveries in Canada and beyond can also include exploration strategies based on inadequate assessment of deposit models. Many IOAA systems worldwide remain unrecognized or under-valued. The intrinsic metasomatic variations across these systems commonly lead to clusters of mineral prospects having distinct host rocks, alteration attributes, metal associations, mineralization styles and deformation types, as shown throughout this volume. An unfortunate outcome is that the myriad of prospects is commonly interpreted as resulting from a variety of distinct syngenetic to epigenetic ore systems; this obscures the district mineral potential for IOCG and affiliated deposits, as illustrated in Potter et al. (2019a).

Models historically favoured for prospects in the GBMZ, the Romanet Horst, the East Arm of Great Slave Lake and the Idaho Co-Cu-Au belt (Hildebrand, 1986; Gandhi, 1994; Skanderberg, 2001; Mumin et al., 2010; Potter et al., 2013a, 2019a; Slack, 2013; Desrochers, 2014; Corriveau et al., 2014; Bretzlaff and Kerswill, 2016) include among others:

- volcanogenic massive sulfides;
- sedimentary iron formation-hosted Au;
- SEDEX type;
- volcaniclastic-hosted Au-Cu-Ag;
- diatreme, skarn, and ironstone-hosted Au;

- intrusion-related, unconformity-type and volcanic-hosted uranium;
- vein-type epithermal with one or more of Cu, Ag, Au, Pb, Zn, Co, Bi, Ni or U;
- IOA (or Kiruna);
- granite-related hydrothermal replacement; and
- synmetamorphic vein and replacement deposit types.

While many of these models may remain valid for some of the deposits, there is clear evidence in all cases for a greater connection to large-scale metasomatic (magmatic-hydrothermal) processes within the host districts, and in many cases encompassing the deposits in question. Their alteration facies and metal enrichments display the diagnostic features of IOAA systems and the range of their deposit types. In addition, many historic prospects in these provinces have significant spatial extents and "accessory" commodities (REE, U, Bi, Co, Cu, Au, Fe-V, P, F, etc.). The latter are elements to consider when exploring for deposits within IOAA systems, considering the endowment of critical metals in the systems worldwide.

*Broadening the Mineral Potential of Known Districts*

A lack of sufficient field exposure or regional-scale exploration hampers the discovery of the full spectrum of deposits within a single district. For example, it took decades before Na, Na-Ca-Fe and Fe-rich HT Ca-Fe alteration (magnetite-apatite) was found at Olympic Dam and surrounding area, though Na and Na-Ca alteration were known in the Moonta-Wallaroo and Mount Woods districts of the province (Skirrow, 2010, 2022; Corriveau et al., 2022d). Most notable is the recent discovery of remnants of early magnetite-apatite assemblages in the deepest drill hole of the deposit (Apukhtina et al., 2017; Ehrig et al., 2017; Corriveau et al., 2022d). In Iran, new discoveries of IOCG mineralization have significantly expanded the mineral potential of the Bafq district (Daliran et al., 2022). This district, as many others worldwide, illustrates that polymetallic prospects with U, Au, Ag, Cu, Co and REE metal associations in close proximity to regional-scale albitite or 'Kiruna-type' occurrences can be explained, predicted and explored for within the framework of IOAA ore systems (Fig. 3). In addition, epithermal alteration types and mineral occurrences associated with the genesis of these ore systems are recognized in the GBMZ, Andes, Yangtze district and at Olympic Dam (Mumin et al., 2010; Kreiner and Barton, 2011, 2017; Ehrig et al., 2012; Richards and Mumin, 2013a; Li et al., 2015). The epithermal veins display a variety of U, Au, Ag, Co and/or REE associations. The presence of extremely disparate mineral occurrences within magmatic-hydrothermal districts is, therefore, considered a key criterion when re-examining the mineral potential of under-explored settings for IOCG and affiliated deposits worldwide (e.g. Corriveau, 2007; Acosta-Góngora et al., 2019; Potter et al., 2019a; Blein et al., 2022).

Geophysical studies are assisting with the interpretation and prioritization of prospective targets. Predictive mineral potential tools and a paragenetic ore deposit model arose from the Targeted Geoscience Initiative (TGI) program as they did from projects conducted by Geoscience Australia (Corriveau et al., 2010b, 2022b; Schofield, 2012; Hayward et al., 2013, 2016; Montreuil et al., 2013, 2015, 2016b; Potter et al., 2013a; Enkin et al., 2016). These tools were shown to be efficient at broadening the range of mineral targets in the GBMZ, the East Arm of Great Slave Lake, and the Romanet Horst in Quebec (Geomapping for Energy and Minerals, and Mineral and Energy Resource Assessment programs; Corriveau et al., 2014, 2016 and references therein; Potter et al., 2019a). They are now being applied to the Central Mineral Belt (TGI program; Acosta-Góngora et al., 2018a, 2019), and to high-grade metamorphic terranes (Blein and Corriveau, 2017; Corriveau et al., 2018a). In the Romanet Horst, a classic region for albitite-hosted uranium mineralization (Kish and Cuney, 1981) and to the South, conclusive evidence was found for IOCG potential within the same metasomatic system that hosts historic uranium mineralization (Corriveau et al., 2014; Conliffe, 2020; see also Clark and Wares, 2004 and Setterfield et al., 2006).

*Social Benefits*

Renewed exploration for IOCG deposits and affiliated is creating millions of dollars in economic benefits to Canada and its northern communities, and the possibility of long-term benefits linked to development of mines and associated environmental monitoring and remediation (Burgess et al., 2014; Beaulieu, 2019). Feasibility and permitting also come with extensive and regional-scale environmental studies. Increased prospectivity through government research and surveys also provides key opportunities for First Nations to conduct their own mineral exploration and baseline environmental studies, gain employment in the mining and environmental remediation industry, make informed decisions on land use, and manage the lands (Beaulieu, 2019). For example, DEMCO, a Dene First Nation mineral exploration company, not only conducted mineral exploration in the Camsell River district but also salvaged drill cores from historic exploration sites, saving millions of dollars in exploration costs (Bowdidge and Dunford, 2015).

Benefits related to IOCG research and exploration extend across Canada where industry follows in the footsteps of exploration successes worldwide (Fig. 4). Research- and mining-related environmental studies support branches of governments that regulate the exploration/mining industry and assess resources for land use decisions (Gebert et al., 2007). In this respect, recognition of the extensive metasomatic alteration associated with IOCG deposits has direct implications for environmental baseline studies. The spatial extent of natural metal enrichment is large, and can be exposed at surface for as much as several hundred km$^2$, such as in the Port Radium-Echo Bay district (GBMZ). In these areas, documenting metal enrichment from the unusual metasomatic alteration is as important for long-term environmental assessment and monitoring as it is for the initial exploration.

The non-traditional character of IOCG and affiliated deposits within broader IOAA systems challenges exploration and forces us to: 1) re-evaluate entire "new" geological terranes; 2) explore new research avenues in economic geology;

3) develop and revise metallogenic models for exploration; 4) adapt exploration expertise and strategies, in particular those acquired in Archean greenstone belts; 5) reassess the potential of former iron and uranium deposits; and 6) keep an open mind to the wide range of associated deposit types that will form in large magmatic-hydrothermal systems.

Many IOCG and affiliated critical metal deposits occur in areas where communities have never or rarely been exposed to exploration and mining. However, mineral resources must be replenished, and the polymetallic nature of IOCG and affiliated deposits comprising precious, base, critical and nuclear metals, makes them particularly well suited for today's world. Hence, this Special Paper is also meant to provide geoscience knowledge for informed societal decisions and knowledge sharing (e.g. Watari et al., 2020). Collectively, the variety of IOCG and affiliated deposits (Table 1), their mine life, the polymetallic nature of the ore, the variety of critical metals they host, and the number of people employed by mining such deposits, all underscore the exciting exploration potential of prospective settings worldwide (Huston et al., 2012).

## Critical Geoscience Issues Addressed in the Volume

In terms of understanding the genesis of IOCG and affiliated deposits, major advances have been achieved on several fronts since the publication of the Geological Association of Canada's Short Course Notes 20 (Corriveau et al., 2010b). Some of these topics are addressed within this Special Paper.

Archetypical magnetite- and hematite-group deposits are covered in four chapters. The Olympic Dam deposit and the Ernest Henry deposit of the Cloncurry district in Australia provide templates for IOCG breccia zones, veins, disseminations and massive iron oxide lenses with polymetallic enrichments. In their papers on the settings, alteration associations, fluid sources and deposit characteristics of "magnetite-group" and "hematite-group" deposits, Patrick Williams, Roger Skirrow, Louise Corriveau and colleagues collectively describe alteration types and zonation, mineral assemblages of mineralized systems hosting IOCG deposits, and possible continuums with uranium deposits (Corriveau et al., 2022a–d; Skirrow, 2022; Williams, 2022). Corriveau et al. (2022a, d) provide a new map and extensive plan views of alteration zoning at the Olympic Dam deposit as well as extensive information on the geochemical footprints of the deposit. Processes such as host-rock leaching, fluid mixing and wall-rock reactions are highlighted. In addition, Skirrow (2022) and Fabris (2022) provide detailed reviews of geodynamic settings and magmatic suites, especially of the Hiltaba Suite granites and the Gawler Range Volcanics rocks, which are associated with the Olympic Dam deposit and other deposits within the Olympic Copper-Gold Province.

Corriveau et al. (2022b, d) combine the description of the archetypical magnetite- and hematite-group IOCG deposits (Ernest Henry and Olympic Dam) with those of similar deposits, such as the remarkable, glacially exposed regional-scale cross-sections of host IOAA systems from the GBMZ. This comparison illustrates how exploring for IOCG deposits requires looking beyond iron oxide breccias and focussing on the metasomatic development of the ore system itself from the regional to the deposit scale. Corriveau et al. (2022b) illustrate the progressive fluid-rock reactions and metal fluxing associated with the prograde, retrograde and cyclical build-up and tectonic telescoping of alteration facies, and how these processes lead to a variety of deposit types having diverse morphology, mineral assemblages, mineral contents, sequences of alteration facies, and metal associations. This and many other chapters within the book also document how diversity is exacerbated by successive emplacement of magmas and episodes of fluid mixing from a variety of sources (e.g. Skirrow, 2022).

Other Proterozoic examples and Phanerozoic case studies further describe the realm of field characteristics of IOA, IOCG and affiliated deposits, and the geological parameters and processes that control mineralization and distribution of deposits. Daliran et al. (2022), Zhao et al. (2022) and Chen and Zhao (2022) all target districts that combine IOA and IOCG deposits. Yet, in some cases, significant IOA deposits have not been discovered within the vicinity of significant IOCG deposits, and vice versa. Fundamental differences in district-scale physicochemical conditions and evolution of systems may be one explanation (Williams, 2010a, b; Corriveau et al., 2022b; Zhao et al., 2022). The contribution of Chen and Zhao (2022), based on Andean IOCG deposits, illustrates the importance of continental magmatic arcs, orogen-scale faults, tectonic inversion, extensional relapse, and modified subcontinental lithosphere in the development of IOCG districts.

Field geology still represents the leading edge in gaining new perspectives on prospective geological settings — if conducted with a good understanding of what to look for, what to sample, and what to do for follow-up studies. To this end, Corriveau et al. (2022c) provide examples of mapping protocols, and alteration facies nomenclature, styles, morphology and field relationships. This chapter and Corriveau et al. (2022d) focus on regrouping metasomatic paragenetic sets as alteration facies to simplify mapping and characterization of IOAA systems and deposits and assessing mineral potential.

Jébrak (2022) uses examples of breccia zones from around the world to illustrate the characteristics of these breccias and the methods to characterize them. He also discusses beeccia origins and processes in order to maximize the use of breccia as exploration guides.

The identification of IOAA systems requires an in-depth understanding of their field attributes (rock types, parageneses, modal mineralogy, potentially preserved textures and structures). However, in the same way that alteration facies have very diagnostic ranges in composition that can be easily illustrated by their Na, Ca, Fe, K, Mg and Si+Al cationic proportions, whole-rock composition can be used to identify IOAA systems from the processing of lithogeochemical databases. Blein et al. (2022) and Corriveau et al. (2022a) processed large databases from the Olympic Copper-Gold Province (e.g. Olympic Dam deposit) in Australia, the GBMZ, Romanet Horst, and Central Mineral Belt in Canada and the Southeast Missouri district in the United States to illustrate the lithogeochemical metasomatic evolution and footprints of IOAA systems as metal pathways to ores. This approach helps understand the transfer of elements from sources to deposition sites, the metal fluxing from crustal rocks during extensive alteration, and deposits that form via single stage evolution versus the influx of metals from distinct sources and the tectonic telescoping of IOAA components at regional to deposit scales.

Criteria for identifying terranes prospective for IOA, IOCG and affiliated deposits are reviewed in Williams (2010a, b, 2022) and Skirrow (2022) while Patrick Williams' classification of deposit types published in 2010 has been updated in Figure 5 to take into account all the new material in this volume and references therein. Additional information on iron oxide-poor deposits, their associated alteration facies and their classification is provided in Corriveau et al. (2022b) and Hofstra et al. (2021).

Many granitic volcano-plutonic terranes remain under-explored and under-mapped worldwide. In the Olympic Copper-Gold Province of the Gawler Craton, private and public sectors have tackled the poor field exposures with unprecedented geophysical surveys at deposit to lithospheric and mantle scales. Katona and Fabris (2022) provide a robust characterization of the geophysical footprints of IOCG deposits in the Olympic Copper-Gold Province, along with new exploration guidelines for such terranes that can be applied globally to most IOAA systems.

Using a combination of field geology and in situ analysis of uraninite, Potter et al. (2022) explore uranium enrichment processes in IOAA systems from the GBMZ, in particular the chemically distinct primary uranium enrichment in HT K-Fe alteration that may be a source of this metal during later, more oxidizing alteration facies (LT K-Fe–Ca-Mg-Fe).

The application of indicator mineral methods to IOCG exploration has greatly expanded since Beaudoin and Dupuis (2010). Building on the use of magnetite as a mineral indicator for exploration, Huang et al. (2022) review the importance of magnetite chemistry as an indicator of crystallization conditions and ore genesis processes.

## Concluding Remarks

Ore formation processes within IOAA systems remain a challenging field of research in economic geology. Collectively, the chapters within this volume illustrate the field, mineralogical, chemical and geophysical footprints of iron-oxide and alkali-calcic alteration systems and their IOA, IOCG, skarn, albitite-hosted uranium, and affiliated critical metal deposits. Case studies are global and remain largely under-explored (e.g. the Great Bear magmatic zone, the Cloncurry district, the Olympic Copper-Gold Province, the Bafq district, the Andes, and the Kangdian and Middle-Lower Yangtze River Metallogenic Belt districts). The case examples help to formulate practical mapping protocols and exploration tools, assess ore deposit models and study the thermal, metal and fluid transfer from mantle to crust, the roles of crustal and lithospheric architecture and geodynamic settings, and the multiple catalysts for regional-scale alteration and ore deposition within these giant metasomatic systems.

## Acknowledgments

This paper is a synergistic product of the Geological Survey of Canada Targeted Geoscience Initiative and Geomapping for Energy and Minerals programs, in collaboration with the Northwest Territories Geological Survey and the Newfoundland and Labrador Geological Survey. We are grateful to Alberta Star Development Corporation, Fortune Minerals Limited, Hunter Bay Resources, DEMCo, Energizer Resources Inc., Honey Badgers Exploration Inc., Diamonds North, Brandon University, NSERC, graduate and undergraduate students, industry, university and government colleagues and research associates from across Canada who generously contributed time, effort and funding for this research. We thank reviewers Colter Kelly, Roger Skirrow and Jeanne Percival for their valued comments for this chapter, and all contributors for making this special paper possible. This is Natural Resources Canada Land and Minerals Sector contribution 20190067.

## References

Acosta-Góngora, G.P., Gleeson, S.A., Samson, I., Ootes, L., and Corriveau, L., 2015a, Gold refining by bismuth melts in the iron oxide-dominated NICO Au-Co-Bi (±Cu±W) deposit, NWT, Canada: Economic Geology, v. 110, p. 291-314.

Acosta-Góngora, P., Gleeson, S., Samson, I., Corriveau, L., Ootes, L., Taylor, B.E., Creaser, R.A., and Muehlenbachs, K., 2015b, Genesis of the Paleoproterozoic NICO iron-oxide-cobalt-gold-bismuth deposit, Northwest Territories, Canada: evidence from isotope geochemistry and fluid inclusions: Precambrian Research, v. 268, p. 168-193.

Acosta-Góngora, P., Duffet, C., Sparkes, G.W., and Potter, E.G., 2018a, Central Mineral Belt uranium geochemistry database, Newfoundland and Labrador: Geological Survey of Canada, Open File 8352, 8 p.

Acosta-Góngora, P., Gleeson, S., Samson, I., Corriveau, L., Ootes, L., Jackson, S.E., Taylor, B.E., and Girard, I., 2018b, Origin of sulfur and crustal recycling of copper in polymetallic (Cu-Au-Co-Bi-U± Ag) iron-oxide-dominated systems of the Great Bear magmatic zone, NWT, Canada: Mineralium Deposita, v. 53, p. 353-376.

Acosta-Góngora, P., Potter, E.G., Corriveau, L., Lawley, C.J.M., and Sparkes, G.W., 2019, Geochemistry of U±Cu±Mo±V mineralization, Central Mineral Belt, Labrador: differentiating between mineralization styles using a principal component analysis approach, *in* Rogers, N., ed., Targeted Geoscience Initiative: 2018 report of activities: Geological Survey of Canada, Open File 8549, p. 381-391.

Adlakha, E., Landry, K., Terekhova, A., Hanley, J., Falck, H., and Martel, E., 2019, Hydrothermal history and metallogeny of the Nonacho Basin, *in* Gervais, S.D., Irwin, D., and Terlaky, V., compilers, 47th Annual Yellowknife Geoscience Forum Abstracts: Northwest Territories Geological Survey, YKGSF Abstracts Volume 2019, p. 1-2.

Aleinikoff, J.N., Selby, D., Slack, J.F., Day, W.C., Pillers, R.M., Cosca, M.A., Seeger, C.M., Fanning, C.M., and Samson, I.M., 2016, U-Pb, Re-Os, and Ar/Ar geochronology of REE-rich breccia pipes and associated host rocks from the Mesoproterozoic Pea Ridge Fe-REE-Au deposit, St. Francois Mountains, Missouri: Economic Geology, v. 111, p. 1883-1914.

Apukhtina, O.B., Kamenetsky, V.S., Ehrig,K., Kamenetsky, M.B., Maas, R., Thompson, J., McPhie, J., Ciobanu, C.L., and Cook, N.J., 2017, Early, deep magnetite-fluorapatite mineralization at the Olympic Dam Cu-U-Au-Ag deposit, South Australia: Economic Geology, v. 112, p. 1531-1542.

Babo, J., Spandler, C., Oliver, N., Brown, M., Rubenach, M., and Creaser, R.A., 2017, The high-grade Mo-Re Merlin deposit, Cloncurry District, Australia: paragenesis and geochronology of hydrothermal alteration and ore formation: Economic Geology, v. 112, p. 397-422.

Badham, J.PN., 1975, Mineralogy, paragenesis and origin of the Ag–Ni, Co arsenide mineralization, Camsell River, N.W.T., Canada: Mineralium Deposita, v. 10, p. 153-175.

Badham, J.P.N., and Morton, R.D., 1976, Magnetite-apatite intrusions and calc-alkaline magmatism, Camsell River, N.W.T.: Canadian Journal of Earth Sciences, v. 13, p. 348-354.

Badham, J.P.N., and Muda, M.M.Z., 1980, Mineralogy and paragenesis of hydrothermal mineralizations in the East Arm of Great Slave Lake: Economic Geology, v. 75, p. 1120-1238.

Baker, H., Pattinson, D., and Reardon, C., 2011, Technical review of the Kaunisvaara iron project, Sweden: SRK Consulting, National Instrument 43-101 Technical Report, available at www.sedar.com.

Baker, H., MacDougall, C., and Pattinson, D., 2014, Technical review of the Hannukainen iron-copper-gold project, Kolari District, Finland: SRK Consulting, National Instrument 43-101 Technical Report, available at www.sedar.com.

Baker, T., Mustard, R., Fu, B., Williams, P.J., Dong, G., Fisher, L., Mark, G., and Ryan, C.G., 2008, Mixed messages in iron oxide–copper–gold systems of the Cloncurry district, Australia: insights from PIXE analysis of halogens and copper in fluid inclusions: Mineralium Deposita, v. 43, p. 599-608.

Baldwin, G., 2019, The Highlands Gold occurrences, eastern Cape Breton Highlands, Nova Scotia: an unrecognized IOCG district?: Geological Association of Canada-Mineralogical Association of Canada, Abstracts, v. 42, p. 58.

Bain, W.M., Steele-MacInnis, M., Li, K., Li, L., Mazdab, F.K., and Marsh, E.E., 2020, A fundamental role of carbonate–sulfate melts in the formation of iron oxide–apatite deposits: Nature Geoscience, v. 13, p. 751-757.

Barra, F., Reich, M., Selby, D., Rojas, P., Simon, A., Salazar, E., and Palma, G., 2017, Unraveling the origin of the Andean IOCG clan: a Re-Os isotope approach: Ore Geology Reviews, v. 81, p. 62-78.

Barton, M.D., 2014, Iron oxide(–Cu–Au–REE–P–Ag–U–Co) systems, *in* Holland, H.D. and Turekian, K.K., eds., Treatise on geochemistry, Second Edition, volume 13: Elsevier, p. 515-541.

Bastrakov, E.N., and Skirrow, R.G., 2007, Fluid evolution and origins of iron oxide–Cu–Au prospects in the Olympic Dam district, Gawler Craton, South Australia: Economic Geology, v. 102, p. 1415-1440.

Beaudoin, G., and Dupuis, C., 2010, Iron oxides trace element fingerprinting of mineral deposit types, *in* Corriveau, L. and Mumin, A.H., eds., Exploring for iron oxide copper-gold deposits: Canada and global analogues: Geological Association of Canada, Short Course Notes, No. 20, p. 111-125.

Beaulieu, D., 2019, A Dene perspective on resource development in Canada for, by and among First Nations: Geological Association of Canada-Mineralogical Association of Canada, Abstracts, v. 42, p. 13.

Belperio, A.P., 2010, Nova Scotia IOCG project: Nova Scotia Department of Natural Resources, Minerals and Resources Branch, Open File Report ME 2010-005, 50 p.

Belperio, A.P., 2016, Exploration for IOCG and ISCG copper-gold giants: how different can they be?: Presentation available at minotaurexploration.com.au.

Belperio, A.P., Flint, R., and Freeman, H., 2007, Prominent Hill: a hematite-dominated, iron oxide copper-gold system: Economic Geology, v. 102, p. 1499-1510.

Benavides, J., Kyser, T.K., Clark, A.C., Stanley, C., and Oates, C., 2008a, Application of molar element ratio analysis of lag talus composite sample to the exploration for iron oxide-copper-gold mineralization: Mantoverde area, northern Chile: Geochemistry: Exploration, Environment Analysis, v. 8, p. 369-380.

Benavides, J., Kyser, T.K., Clark, A.C., Stanley, C., and Oates, C., 2008b, Exploration guidelines for copper-rich iron oxide-copper-gold deposits in the Mantoverde area, northern Chile: the integration of host-rock molar element ratios and oxygen isotope compositions: Geochemistry: Exploration, Environment, Analysis, v. 8, p. 343-367.

BHP, 2017, BHP annual report 2017: BHP Limited [online] available from www.bhp.com.

BHP, 2018, BHP copper exploration program update: BHP Limited [online] available on November 2018 from www.bhp.com.

BHP, 2020, BHP annual report 2020: BHP Limited [online] available from www.bhp.com.

Bleeker, W., and LeCheminant, A.N., 2008, The Proterozoic Dessert Lake red-bed basin, a target for uranium exploration – an update, *in* Jackson, V. and Irwin, D., compilers, 36th Annual Yellowknife Geoscience Forum Astracts, Northwest Territories Geoscience Office, YKGSF Abstract Volume 2008, p. 65.

Blein, O., and Corriveau, L., 2017, Recognizing IOCG alteration facies at granulite facies in the Bondy Gneiss Complex of the Grenville Province: Proceedings of the 14th SGA Biennial Meeting, 20-23 August 2017, Québec City, p. 907-911.

Blein, O., Corriveau, L., Montreuil, J.-F., Ehrig, K., Fabris, A., Reid, A., and Pal, D., 2022, Geochemical signatures of metasomatic ore systems hosting IOCG, IOA, albitite-hosted uranium and affiliated deposits: a tool for process studies and mineral exploration, *in* Corriveau, L., Potter, E.G. and Mumin, A.H., eds., Mineral systems with iron oxide copper-gold (IOCG) and affiliated deposits: Geological Association of Canada, Special Paper 52, p. 263-298.

Bonyadi, Z., Davidson, G.J., Mehrabi, B., Meffre, S., and Ghazban, F., 2011, Significance of apatite REE depletion and monazite inclusions in the brecciated Se-Chahun iron oxide–apatite deposit, Bafq district, Iran: insights from paragenesis and geochemistry: Chemical Geology, v. 281, p. 253-269.

Bowdidge, C., and Dunford, A., 2015, Camsell River property, Northwest Territories 86E09 and 86F12: Northwest Territories Geological Survey, Assessment Report 033952, 73 p.

Bretzlaff, R., and Kerswill, J.A., 2016, Mineral occurrences of the Great Bear magmatic zone: Geological Survey of Canada, Open File 7959, 7 p.

Burgess, H., Gowans, R.M., Hennessey, B.T., Lattanzi, C.R., and Puritch, E., 2014, Technical report on the feasibility study for the NICO gold–cobalt–bismuth–copper deposit, Northwest Territories, Canada: Fortune Minerals Ltd., NI 43-101 Technical Report No. 1335, 385 p., available at www.sedar.com.

Burns, N., Davis, C., Diedrich, C., and Tagami, M., 2017, Salobo copper-gold mine Carajás, Pará State, Brazil: 43-101 Technical Report, Wheaton Precious Metals, 126 p., available at www.sedar.com.

Canadian Minerals and Metals Plan, 2018, Mining ideas for the Canadian Minerals and Metals Plan: a discussion paper: Government of Canada, 30 p.

Carriedo, J., and Tornos, F., 2010, The iron oxide copper-gold belt of the Ossa Morena zone, southwest Iberia: implications for IOCG genetic models, *in* Porter, T.M., ed., Hydrothermal iron oxide copper-gold and related deposits: a global perspective, v. 4: PGC Publishing, Adelaide, p. 441-460.

Chen, H., 2013, External sulphur in IOCG mineralization: implications on definition and classification of the IOCG clan: Ore Geology Reviews, v. 51, p. 74-78.

Chen, H., and Zhao, L., 2022, Mineralization, alteration, and fluid compositions in selected Andean IOCG deposits, *in* Corriveau, L., Potter, E.G. and Mumin, A.H., eds., Mineral systems with iron oxide copper-gold (IOCG) and affiliated deposits: Geological Association of Canada, Special Paper 52, p. 365-381.

Chinova Resources, 2014, Merlin molybdenum / rhenium project, 2014: Available at www.chinovaresources.com .

Chorlton, L.B. (compiler), 2007, Generalized geology of the world: bedrock domains and major faults in GIS format: Geological Survey of Canada, Open File 5529, 48 p.

Clark, T., and Wares, R., 2004, Synthèse lithotectonique et métallogénique de l'Orogène du Nouveau-Québec (Fosse du Labrador): Ministère des Ressources naturelles et de la Faune, Québec, MM 2004-01, p. 1-177.

Clark, T., Gobeil, A., and David, J., 2005, Iron oxide-Cu-Au–type and related mineralization in the Manitou Lake area, Grenville Province, Quebec: variations in composition and alteration style, *in* Corriveau, L. and Clark, T., eds., The Grenville Province: a geological and mineral resources perspective derived from government and academic research initiative: Canadian Journal of Earth Sciences, v. 42, p. 1829-1847.

Clark, T., Gobeil, A., and Chevé, S., 2010, Alterations in IOCG-type and related deposits in the Manitou Lake area, Eastern Grenville Province, Québec, *in* Corriveau, L. and Mumin, A.H., eds., Exploring for iron oxide copper-gold deposits: Canada and global analogues: Geological Association of Canada, Short Course Notes, No. 20, p. 127-146.

Cloncurry, Queensland, Australia: implications for IOCG genesis, *in* Porter, T.M., ed., Hydrothermal iron oxide copper-gold and related deposits: a global perspective, v. 3: PGC Publishing, Adelaide, p. 201-218.

Conliffe, J., 2020, Petrology and geochemistry of the Montgomery Lake showing: evidence of IOCG type mineralization in the eastern Labrador Trough: Newfoundland and Labrador Department of Natural Resources Geological Survey, Report 201, 103120.

Cooke, D.R., Hollings, P., and Walshe, J.L., 2005, Giant porphyry deposits: characteristics, distribution, and tectonic controls: Economic Geology, v. 100, p. 801-818.

Corona-Esquivel, R., Tritlla, J., and Levresse, G., 2011, Formation ages of the two Phanerozoic IOCG belts in México: Proceedings of the 11th SGA Biennial Meeting, Antofagasta, Chile, p. 473-475.

Corriveau, L., 2007, Iron oxide copper-gold deposits: a Canadian perspective, *in* Goodfellow, W., ed., Mineral deposits of Canada: a synthesis of major deposit-types, district metallogeny, the evolution of geological provinces, and exploration methods: Geological Association of Canada-Mineral Deposits Division, Special Volume 5, p. 307-328.

Corriveau, L., and Mumin, A.H., 2010, Exploring for iron oxide copper–gold deposits: the need for case studies, classifications and exploration vectors, *in* Corriveau, L. and Mumin, A.H., eds., Exploring for iron oxide copper-gold deposits: Canada and global analogues: Geological Association of Canada, Short Course Notes, No. 20, p. 1-12.

Corriveau, L., and Potter, E.G., in press, Advancing exploration for iron oxide-copper-gold and affiliated deposits in Canada: context, scientific overview, outcomes and impacts, *in* Pehrsson, S., Wodicka. N., Rogers, N. and Percival, J., eds., Canada's northern shield: new perspectives from the Geo-Mapping for Energy and Minerals Program: Geological Survey of Canada, Bulletin 612.

Corriveau, L., and Spry, P., 2014, Metamorphosed hydrothermal ore deposits, *in* Holland, H.D. and Turekian, K.K., eds., Treatise on geochemistry, second edition: Elsevier, v. 13, p. 175-194.

Corriveau, L., Perreault, S., and Davidson, A., 2007, Prospectivity of the Grenville Province: a perspective, *in* Goodfellow, W., ed., Mineral deposits of Canada: a synthesis of major deposit-types, district metallogeny, the evolution of geological provinces, and exploration methods: Geological Association of Canada-Mineral Deposits Division, Special Volume 5, p. 819-848.

Corriveau, L., Mumin, A.H., and Setterfield, T., 2010a, IOCG environments in Canada: characteristics, geological vectors to ore and challenges, *in* Porter, T.M., ed., Hydrothermal iron oxide copper-gold and related deposits: a global perspective, v. 4: PGC Publishing, Adelaide, p. 311-344.

Corriveau, L., Williams, P.J., and Mumin, H., 2010b, Alteration vectors to IOCG mineralization – from uncharted terranes to deposits, *in* Corriveau, L. and Mumin, A.H., eds., Exploring for iron oxide copper-gold deposits: Canada and global analogues: Geological Association of Canada, Short Course Notes, No. 20, p. 89-110.

Corriveau, L., Nadeau, O., Montreuil, J.-F., and Desrochers, J.-P., 2014, Report of activities for the Core Zone: strategic geomapping and geoscience to assess the mineral potential of the Labrador Trough for multiple metals IOCG and affiliated deposits, Canada: Geological Survey of Canada, Open File 7714, 12 p.

Corriveau, L., Lauzière, K., Montreuil, J.-F., Potter, E.G., Hanes, R., and Prémont, S., 2015, Dataset of geochemical data from iron oxide alkali-altered mineralizing systems of the Great Bear magmatic zone (NWT): Geological Survey of Canada, Open File 7643, 19p., 6 geochemical datasets.

Corriveau, L., Montreuil, J.-F., and Potter, E.G., 2016, Alteration facies linkages among IOCG, IOA and affiliated deposits in the Great Bear magmatic zone, Canada, *in* Slack, J., Corriveau, L. and Hitzman, M., eds., Proterozoic iron oxide-apatite (± REE) and iron oxide-copper-gold and affiliated deposits of Southeast Missouri, USA, and the Great Bear magmatic zone, Northwest Territories, Canada: Economic Geology, v. 111, p. 2045-2072.

Corriveau, L., Blein, O., Gervais, F., Trapy, P.H., De Souza, S., and Fafard, D., 2018a, Iron-oxide and alkali-calcic alteration, skarn and epithermal mineralizing systems of the Grenville Province: the Bondy gneiss complex in the Central Metasedimentary Belt of Quebec as a case example – a field trip to the 14th Society for Geology Applied to Mineral Deposits (SGA) biennial meeting: Geological Survey of Canada, Open File 8349, 136 p.

Corriveau, L., Potter, E.G., Montreuil, J.-F., Blein, O., Ehrig, K., and De Toni, A., 2018b, Iron-oxide and alkali-calcic alteration ore systems and their polymetallic IOA, IOCG, skarn, albitite-hosted U±Au±Co, and affiliated deposits: a short course series. Part 2: overview of deposit types, distribution, ages, settings, alteration facies, and ore deposit models: Geological Survey of Canada, Scientific Presentation 81, 154 p.

Corriveau, L., Montreuil, J.-F., Blein, O., Ehrig, K., Potter, E.G., Fabris, A., and Clark, J., 2022a, Mineral systems with IOCG and affiliated deposits: part 2 – geochemical footprints, *in* Corriveau, L., Potter, E.G. and Mumin, A.H., eds., Mineral systems with iron oxide copper-gold (IOCG) and affiliated deposits: Geological Association of Canada, Special Paper 52, p. 159-204.

Corriveau, L., Montreuil, J.-F., Potter, E.G., Blein, O., and De Toni, A.F., 2022b, Mineral systems with IOCG and affiliated deposits: part 3 – metal pathways and ore deposit model, *in* Corriveau, L., Potter, E.G. and Mumin, A.H., eds., Mineral systems with iron oxide copper-gold (IOCG) and affiliated deposits: Geological Association of Canada, Special Paper 52, p. 205-245.

Corriveau, L., Montreuil, J.-F., De Toni, A.F., Potter, E.G., and Percival, J.B., 2022c, Mapping mineral systems with IOCG and affiliated deposits: a facies approach, *in* Corriveau, L., Potter, E.G. and Mumin, A.H., eds., Mineral systems with iron oxide copper-gold (IOCG) and affiliated deposits: Geological Association of Canada, Special Paper 52, p. 69-111.

Corriveau, L., Montreuil, J.-F., Potter, E.G., Ehrig, K., Clark J., Mumin, A.H., and Williams, P.J., 2022d, Mineral systems with IOCG and affiliated deposits: part 1 – metasomatic footprints of alteration facies, *in* Corriveau, L., Potter, E.G. and Mumin, A.H., eds., Mineral systems with iron oxide copper-gold (IOCG) and affiliated deposits: Geological Association of Canada, Special Paper 52, p. 113-158.

Courage, D.C., 2013, A detailed geological, geochemical and mineralogical study of the Koorae prospect and the host rocks of the Topsails intrusive suite, Hinds Lake area, Newfoundland: Unpublished B.Sc. (Hons) thesis, Memorial University of Newfoundland, Canada, 154 p.

Couture, J.F., Cole, G., Zhang, B., Nilsson, J., Dance, A., Scott, C., and Vidal, M.I., 2017, Technical report for the Candelaria copper mining complex, Atacama Province, Region III, Chile [online]: Available at www.lundinmining.com.

Daliran, F., Stosch, H.-G., Williams, P.J., Jamali, H., and Dorri, M.-B., 2022, Early Cambrian IOA-REE, U-Th and Cu(Au)-Bi-Co-Ni-Ag-As-sulphide deposits of the Bafq district, East-central Iran, *in* Corriveau, L., Potter, E.G. and Mumin, A.H., eds., Mineral systems with iron oxide copper-gold (IOCG) and affiliated deposits: Geological Association of Canada, Special Paper 52, p. 409-424.

Davidson, G.J., Paterson, H., Meffre, S., and Berry, R.F., 2007, Characteristics and origin of the Oak Dam East breccia-hosted, iron oxide-Cu-U-(Au) deposit: Olympic Dam region, Gawler Craton, South Australia: Economic Geology, v. 102, p. 1471-1498.

Davis, W., Corriveau, L., van Breemen, O., Bleeker, W., Montreuil, J.-F., Potter, E.G., and Pelleter, E., 2011, Timing of IOCG mineralizing and alteration events within the Great Bear magmatic zone, *in* Fischer, B.J. and Watson, D.M., eds., 39th Annual Yellowknife Geoscience Forum Abstract Volume: Northwest Territories Geoscience Office, Abstracts Volume 2011 p. 97.

Day, W.C., Slack, J.F., Ayuso, R.A., and Seeger, C.M., 2016, Regional geologic and petrologic framework for iron oxide ± apatite ± rare earth element and iron oxide copper-gold deposits of the Mesoproterozoic St. Francois Mountains Terrane, Southeast Missouri, USA, *in* Slack, J., Corriveau, L. and Hitzman, M., eds., Proterozoic iron oxide-apatite (± REE) and iron oxide-copper-gold and affiliated deposits of Southeast Missouri, USA, and the Great Bear magmatic zone, Northwest Territories, Canada: Economic Geology, v. 111, p. 1825-1858.

De Haller, A., Corfu, F., Fontboté, L., Schaltegger, U., Barra, F., Chiaradia, M., Frank, M., and Alvarado, J.Z., 2006, Geology, geochronology, and Hf and Pb isotope data of the Raúl-Condestable iron oxide-copper-gold deposit, central coast of Perú; Economic Geology, v. 101, p. 281-310.

De Toni, A.F., 2016, Les paragénèses à magnétite des altérations associées aux systèmes à oxydes de fer et altérations en éléments alcalins, zone magmatique du Grand lac de l'Ours: Unpublished M.Sc. thesis, Institut national de la Recherche scientifique, 534 p.

Decrée, S., Marignac, C., De Putter, T., Yans, J., Clauer, N., Dermech, M., Aloui, K., and Baele, J.-M., 2013, The Oued Belif hematite-rich breccia: a Miocene iron oxide Cu-Au-(U-REE) deposit in the Nefza mining district, Tunisia: Economic Geology, v. 108, p. 1425-1457.

del Real, I., Thompson, J.F.H., and Carriedo, J., 2018, Lithological and structural controls on the genesis of the Candelaria-Punta del Cobre iron oxide copper gold district, Northern Chile: Ore Geology Reviews, v. 102, p. 106-153.

Dufréchou, G., Harris, L.B., Corriveau, L., and Antonoff, V., 2015, Regional and local controls on mineralization and pluton emplacement in the Bondy gneiss complex, Grenville Province, Canada interpreted from aeromagnetic and gravity data: Journal of Applied Geophysics, v. 116, p. 192-205.

Desrochers, J.-P., 2014, Technical report on the Sagar property, Romanet Horst, Labrador Trough, Québec, Canada (latitude, 56°22'N and longitude 68°00'W; NTS map sheets 24B/05 and 24C/08): National Instrument 43–101 Technical Report prepared for Honey Badger Exploration Inc., available at www.sedar.com.

Ehrig, K., McPhie, J., and Kamenetsky, V.S., 2012, Geology and mineralogical zonation of the Olympic Dam iron oxide Cu-U-Au-Ag deposit, South Australia, *in* Hedenquist, J.W., Harris, M. and Camus, F., eds., Geology and genesis of major copper deposits and districts of the world: a tribute to Richard H. Sillitoe: Economic Geology Special Publication 16, p. 237-267.

Ehrig, K., Kamenetsky, V.S., McPhie, J., Apukhtina, O., Ciobanu, C.L., Cook, N., Kontonikas-Charos, A., and Krneta, S., 2017, The IOCG-IOA Olympic Dam Cu-U-Au-Ag deposit and nearby prospects, South Australia: Proceedings of the 14th SGA Biennial Meeting, 20-23 August 2017, Québec City, p. 823-827.

Eilu, P., Rasilainen, K., Halkoaho, T., Huovinen, I., Kärkkäinen, N., Kontoniemi, O., Lepistö, K., Niiranen, T., and Sorjonen-Ward, P., 2015, Quantitative assessment of undiscovered resources in orogenic gold deposits in Finland: Geological Survey of Finland, Report of Investigation 216, 318 p.

Enkin, R.J., Corriveau, L., and Hayward, N., 2016, Metasomatic alteration control of petrophysical properties in the Great Bear magmatic zone (Northwest Territories, Canada), *in* Slack, J., Corriveau, L. and Hitzman, M., eds., Proterozoic iron oxide-apatite (± REE) and iron oxide-copper-gold and affiliated deposits of Southeast Missouri, USA, and the Great Bear magmatic zone, Northwest Territories, Canada: Economic Geology, v. 111, p. 2073-2085.

EXCO Resources Ltd, 2012, EXCO Resources Ltd information memorandum, Queensland Cloncurry copper project: Available at www.excoresources.com .

Fabris, A., 2022, Geochemical characteristics of IOCG deposits from the Olympic Copper-Gold Province, South Australia, *in* Corriveau, L., Potter, E.G. and Mumin, A.H., eds., Mineral systems with iron oxide copper-gold (IOCG) and affiliated deposits: Geological Association of Canada, Special Paper 52, p. 247-262.

Fabris, A., Katona, L., Gordon, G., Reed, G., Keeping, T., Gouthas, G., and Swain, G., 2018, Characterisation and mapping of Cu–Au skarn systems in the Punt Hill region, Olympic Cu–Au Province: MESA Journal, v. 87, p. 15-27.

Fan, H.R., Hu, F.F., Yang, K.F., Pirajno, F., Liu, X., and Wang, K.Y., 2014, Integrated U-Pb and Sm-Nd geochronology for a REE-rich carbonatite dyke at the giant Bayan Obo REE deposit, Northern China: Ore Geology Reviews, v. 63, p. 510-519.

Fan, H.R., Yang, K.F., Hu, F.F., Liu, S., and Wang, K.Y., 2015, The giant Bayan Obo REE-Nb-Fe deposit, China: controversy and ore genesis: Geoscience Frontiers, doi:10.1016/j.gsf.2015.11.005.

Ferreira Filho, C.F., Ferraz de Oliveira, M.M., Mansur, E.T., and Rosa, W.D., 2021, The Jaguar hydrothermal nickel sulfide deposit: evidence for a nickel-rich member of IOCG-type deposits in the Carajás Mineral Province, Brazil: Journal of South American Earth Sciences, v. 111, 103501.

Foose, M.P., and McLelland, J.M., 1995, Proterozoic low-Ti iron-oxide deposits in New York and New Jersey; relation to Fe-oxide (Cu-U-Au-rare earth element) deposits and tectonic implications: Geology, v. 23, p. 665-668.

Forslund, N., 2012, Alteration and fluid characterization of the Hamlin Lake IOCG occurrence, Northwestern Ontario, Canada: Unpublished M.Sc. Thesis, Lakehead University, Thunder Bay, 285 p.

Fortier, S.M., Nassar, N.T., Lederer, G.W., Brainard, J., Gambogi, J., and McCullough, E.A., 2019, Draft critical mineral list: summary of methodology and background information: U.S. Geological Survey technical input document in response to secretarial order No. 3359: U.S. Geological Survey, Open-File Report 2018–1021, 26 p.

Furic, R., and Jébrak, M., 2005, Archaean IOCG deposit in a fluidized dilational jog (Chibougamau, Abitibi, Canada): Geological Society of America, Abstracts with Programs, v. 37, No. 7, p. 516.

Gagnon, R., Buro, Y.A., Ibrango, S., Gagnon, D., Stapinsky, M., Del Carpio, S., and Larochelle, E., 2018, Projet de terres rares Kwyjibo: Rapport technique NI 43-101 révisé, 292 p., available at www.sedar.com.

Galicki, M., Marshall, D., Staples, R., Thorkelson, D., Downie, C., Gallagher, C., Enkin, R., and Davis, W., 2012, Iron oxide ± Cu ± Au deposits in the Iron Range, Purcell Basin, Southeastern British Columbia: Economic Geology, v. 107, p. 1293-1301.

Gandhi, S.S., 1978, Geological observations and exploration guides to uranium in the Bear and Slave structural provinces and the Nonacho Basin, District of Mackenzie: Geological Survey of Canada, Paper 78-1B, p. 141-150.

Gandhi, S.S., 1992, Polymetallic deposits of the southern Great Bear magmatic zone, in Canada-Northwest Territories Mineral Development Subsidiary Agreement 1987-1991: Geological Survey of Canada, Open File 2484, p. 135-139.

Gandhi, S.S., 1994, Geological setting and genetic aspects of mineral occurrences in the southern Great Bear magmatic zone, Northwest Territories, *in* Sinclair, W.D. and Richardson, D.G., eds., Studies of rare-metal deposits in the Northwest Territories: Geological Survey of Canada, Bulletin 475, p. 63-96.

Gandhi, S.S. (compiler), 2015, World Fe oxide +/- Cu-Au-U (IOCG) deposit database: world minerals geoscience database project: Geological Survey of Canada, Open File 7774, 9 p.

Gandhi, S.S., and Halliday, D., 1993, Gravity survey of the Sue-Dianne deposit, Northwest Territories: Geological Survey of Canada. Paper 93-1E, p. 231-238.

Gandhi, S.S., Prasad, N., and Charbonneau, B.W., 1996, Geological and geophysical signatures of a large polymetallic exploration target at Lou Lake, southern Great Bear Magmatic Zone, Northwest Territories: Geological Survey of Canada, Current Research Paper 1996-E, p. 147-158.

Gandhi, S.S., Mortensen, J.K., Prasad, N., and van Breemen, O., 2001, Magmatic evolution of the southern Great Bear continental arc, northwestern Canadian Shield: geochronological constraints: Canadian Journal of Earth Sciences, v. 38, p. 767-785.

Gandhi, S.S., Kerswill, J.A., and Lemkow, D., 2013, Potential for vein-hosted copper mineralization in the area of the proposed Thaidene Nene National Park, East Arm of Great Slave Lake, Chapter 17, *in* Wright, D.F., Kjarsgaard, B.A., Ambrose, E.J. and Bonham-Carter, G.F., eds., Mineral and energy resource assessment for the proposed Thaidene Nene National Park reserve, East Arm of Great Slave Lake, Northwest Territories: Geological Survey of Canada, Open File 7196, p. 437-461.

Gandhi, S.S., Montreuil, J.-F., and Corriveau, L., 2014, Geology and mineral occurrences, Mazenod Lake - Lou Lake area, Northwest Territories: Geological Survey of Canada, Canadian Geoscience Map 148, 1 map sheet.

Gandhi, S.S., Potter, E.G., and Fayek, M., 2018, New constraints on genesis of the polymetallic veins at Port Radium, Great Bear Lake, Northwest Canadian Shield: Ore Geology Reviews, v. 96, p. 28-47.

Garcia, V.B., Schutesky, M.E., Oliveira, C.G., Whitehouse, M.J., Huhn, S.R.B., and Augustin, C.T., 2020, The Neoarchean GT-34 Ni deposit, Carajás mineral Province, Brazil: an atypical IOCG-related Ni sulfide mineralization: Ore Geology Reviews, v. 127, 103773.

Gauthier, L., Hall, G., Stein, H., and Schaltegger, U., 2001, The Osborne deposit, Cloncurry district: a 1595 Ma Cu-Au skarn deposit, *in* Williams, P.J., ed., A hydrothermal odyssey, Extended Conference Abstracts, 17–19 May, James Cook University, Townsville: EGRU Contribution 59, p. 58-59.

Gauthier, M., Chartrand, F., Cayer, A., and David, J., 2004, The Kwyjibo Cu-REE-U-Au-Mo-F property, Quebec: a Mesoproterozoic polymetallic iron oxide deposit in the Northeastern Grenville Province: Economic Geology, v. 99, p. 1177-1196.

Gebert, J.S., Jackson, J.E., and O'Neil, C.E., 2007, Edailla area of interest non-renewable resources assessment (phase I) Great Bear Lake area, Northwest Territories Parts of NTS 86K, 86L, 86M, 86N and 96I: Northwest Territories Geoscience Office, NWT Open File 2007-06, 56 p.

Gelcich, S., Davis, D.W., and Spooner, E.T.C., 2005, Testing the apatite-magnetite geochronometer: U-Pb and $^{40}Ar/^{39}Ar$ geochronology of plutonic rocks, massive magnetite-apatite tabular bodies, and IOCG mineralization in Northern Chile: Geochimica et Cosmochimica Acta, v. 69, p. 3367-3384.

Glencore, 2020, Resources and reserves as at 31 December 2019: Available at https://www.glencore.com.

Goad, R.E., Mumin, A.H., Duke, N.A., Neale, K.L., Mulligan, D.L., and Camier, W.J., 2000, The NICO and Sue-Dianne Proterozoic, iron oxide-hosted, polymetallic deposits, Northwest Territories: application of the Olympic Dam model in exploration: Exploration and Mining Geology, v. 9, p. 123-140.

Groves, D.I., and Vielreicher, N.M., 2001, The Phalabowra (Palabora) carbonatite-hosted magnetite-copper sulfide deposit, South Africa: an endmember of the iron-oxide copper-gold-rare earth element deposit group?: Mineralium Deposita, v. 36, p. 189-194.

Groves, D.I., Bierlein, F.P., Meinert, L.D., and Hitzman, M.W., 2010, Iron oxide copper-gold (IOCG) deposits through Earth history. Implications for origin, lithospheric setting, and distinction from other epigenetic iron oxide deposits: Economic Geology, v. 105, p. 641-654.

Harlov, D.E., Wirth, R., and Förster, H.J., 2005, An experimental study of dissolution-reprecipitation in fluorapatite: fluid infiltration and the formation of monazite: Contributions to Mineralogy and Petrology, v. 150, p. 268-286.

Haynes, D.W., 2006, The Olympic Dam ore deposit discovery: a personal view: SEG Newsletter, v. 66, p. 8-17.

Haynes, D.W., Cross, K.C., Bills, R.T., and Reed, M.H., 1995, Olympic Dam ore genesis: a fluid mixing model: Economic Geology, v. 90, p. 281-307.

Hayward, N., Enkin, R.J., Corriveau, L., Montreuil, J.-F., and Kerswill, J., 2013, The application of rapid potential field methods for the targeting of IOCG mineralisation based on physical property data, Great Bear Magmatic Zone, Canada: Journal of Applied Geophysics, v. 94, p. 42-58.

Hayward, N., and Corriveau, L., 2014, Fault reconstructions using aeromagnetic data in the Great Bear magmatic zone, Northwest Territories, Canada: Canadian Journal of Earth Sciences, v. 51, p. 927-942.

Hayward, Na., Corriveau, L., Craven, J., and Enkin, R., 2016, Geophysical signature of the NICO Au-Co-Bi-Cu deposit and its iron oxide-alkali alteration system, Northwest Territories, Canada, *in* Slack, J., Corriveau, L. and Hitzman, M., eds., Proterozoic iron oxide-apatite (± REE) and iron oxide-copper-gold and affiliated deposits of Southeast Missouri, USA, and the Great Bear magmatic zone, Northwest Territories, Canada: Economic Geology, v. 111, p. 2087-2110.

Hennessey, B.T., and Puritch, E., 2008, A technical report on a mineral resource estimate for the Sue-Dianne deposit, Mazenod Lake area, Northwest Territories, Canada: Fortune Minerals Limited, Technical Report, 125 p. Available at www.sedar.com.

Hildebrand, R.S., 1984, Geology of the Rainy Lake-White Eagle Falls area district of Mackenzie: early Proterozoic cauldrons, stratovolcanoes and subvolcanic plutons: Geological Survey of Canada, Paper 83-20, 42 p., 1 map.

Hildebrand, R.S., 1986, Kiruna-type deposits: their origin and relationship to intermediate subvolcanic plutons in the Great Bear Magmatic Zone, northwest Canada: Economic Geology, v. 81, p. 640-659.

Hildebrand, R.S., 2011, Geological synthesis of Northern Wopmay/ Coppermine Homocline, Northwest Territories – Nunavut: Geological Survey of Canada, Open File 6390, and NTGO Open Report 2010-011.

Hildebrand, R.S., 2017, Precambrian geology, Leith Peninsula-Rivière Grandin area, Northwest Territories: Geological Survey of Canada, Canadian Geoscience Map 153, 1 map sheet.

Hildebrand, R.S., Hoffman, P.F., Housh, T., and Bowring, S.A., 2010, The nature of volcano-plutonic relations and shapes of epizonal plutons of continental arcs as revealed in the Great Bear magmatic zone, northwestern Canada: Geosphere, v. 6, p. 812-839.

Hildebrand, R.S., Bowring, S., and Pelleter, K.F., 2014, Calder River, map area: Geological Survey of Canada, Canadian Geoscience Map 154, NWT Open Report 2013-03, 1 map sheet.

Hinchey, A.M., and LaFlamme, C., 2009, The Paleoproterozoic volcano-sedimentary rocks of the Aillik Group and associated plutonic suites of the Aillik Domain, Makkovik Province, Labrador: Newfoundland and Labrador Department of Natural Resources, Geological Survey, Report 09-1, p. 159-182.

Hitzman, M.W., Oreskes, N., and Einaudi, M.T., 1992, Geological characteristics and tectonic setting of Proterozoic iron oxide (Cu-U-Au-LREE) deposits: Precambrian Research, v. 58, p. 241-287.

Hitzman, M.W., and Valenta, R.K., 2005, Uranium in iron oxide-copper-gold (IOCG) systems: Economic Geology, v. 100, p. 1657-1661.

Hofstra, A., Lisitsin, V., Corriveau, L., Paradis, S., Peter, J., Lauzière, K., Lawley, C., Gadd, M., Pilote, J., Honsberger, I., Bastrakov, E., Champion, D., Czarnota, K., Doublier, M., Huston, D., Raymond, O., VanDerWielen, S., Emsbo, P., Granitto, M., and Kreiner, D., 2021, Deposit classification scheme for the Critical Minerals Mapping Initiative Global Geochemical Database: U.S. Geological Survey Open-File Report 2021–1049, 60 p.

Hood, S.B., 2012, Mid-crustal Cu-Au mineralisation during episodic pluton emplacement, hydrothermal fluid flow, and ductile deformation at the Minto deposit, YT, Canada: Unpublished M.Sc. thesis, The University of British Columbia, 220 p.

Hu, H., Li, J.-W., Harlov, D.E., Lentz, D.R., McFarlane, C.R.M., and Yang, Y.-H., 2020, A genetic link between iron oxide-apatite and iron skarn mineralization in the Jinniu volcanic basin, Daye district, eastern China: evidence from magnetite geochemistry and multi-mineral U-Pb geochronology: GSA Bulletin, v. 132, p. 899-917.

Huang, X.-W., Qi, L., Gao, J.-F., and Zhou, M.-F., 2013, First reliable Re–Os ages of pyrite and stable isotope compositions of Fe(-Cu) deposits in the Hami region, Eastern Tianshan orogenic belt, NW China: Resource Geology, v. 63, p. 166-187.

Huang, X.-W., Beaudoin, G., De Toni, A.-F., Corriveau, L., Makvandi, S., and Boutroy, E., 2022, Iron-oxide trace element fingerprinting of iron oxide copper-gold and iron oxide-apatite deposits: a review, *in* Corriveau, L., Potter, E.G. and Mumin, A.H., eds., Mineral systems with iron oxide copper-gold (IOCG) and affiliated deposits: Geological Association of Canada, Special Paper 52, p. 347-364.

Hunt, J.A., Baker, T., and Thorkelson, D.J., 2010, Wernecke Breccia: Proterozoic IOCG mineralised breccia system, Yukon, Canada, *in* Porter, T.M., ed., Hydrothermal iron oxide copper-gold and related deposits: a global perspective, v. 4: PGC Publishing, Adelaide, p. 345-356.

Huston, D.L., Blewett, R.S., Skirrow, R., McQueen, A., Wang, J., Jaques, L., and Waters, D., 2012, Foundations of wealth—Australia's major mineral provinces, *in* Blewett, R. ed., Shaping a nation: a geology of Australia: Australian University Press, p. 381-481. http://doi.org/10.22459/SN.08.2012.

Ismail, R., Ciobanu, C.L., Cook, N.J., Giles, D., Schmidt-Mumm, A., and Wade, B., 2014, Rare earths and other trace elements in minerals from skarn assemblages, Hillside iron oxide–copper–gold deposit, Yorke Peninsula, South Australia: Lithos, v. 184-187, p. 456-477.

Jackson, V.A., and Ootes, L., 2012, Preliminary geologic map of the south-central Wopmay Orogen (parts of NTS 86B, 86C, and 86D); results from 2009 to 2011: NWT Geoscience Office, NWT Open Report 2012-004, 1 map, 1:100,000 scale.

Jébrak, M., 2022, Use of breccias in IOCG exploration: an update review, *in* Corriveau, L., Potter, E.G. and Mumin, A.H., eds., Mineral systems with iron oxide copper-gold (IOCG) and affiliated deposits: Geological Association of Canada, Special Paper 52, p. 315-324.

Katona, L., and Fabris, A., 2022, Defining geophysical signatures of IOCG deposits in the Olympic Copper-Gold Province, South Australia, *in* Corriveau, L., Potter, E.G. and Mumin, A.H., eds., Mineral systems with iron oxide copper-gold (IOCG) and affiliated deposits: Geological Association of Canada, Special Paper 52, p. 299-313.

Kish, L., and Cuney, M., 1981, Uraninite–albite veins from the Mistamisk valley of the Labrador Trough, Québec: Mineralogical Magazine, v. 44, p. 471-483.

Knight, J., Lowe, J., Joy, S., Cameron, J., Merrillees, J., Nag, S., Shah, N., Dua, G., and Jhala, K., 2002, The Khetri Copper Belt, Rajasthan: iron oxide copper-gold terrane in the Proterozoic of NW India, *in* Porter, T.M., eds., Hydrothermal iron oxide copper-gold and related deposits: a global perspective, v. 2: PGC Publishing, Adelaide, p. 321-341.

Knipping, J.L., Bilenker, L.D., Simon, A.C., Reich, M., Barra, F., Deditius, A.P., Lundstrom, C., Bindeman, I., and Munizaga, R., 2015, Giant Kiruna-type deposits form by efficient flotation of magmatic magnetite suspensions: Geology, v. 43, p. 591-594.

Kolb, J., Meyer, F.M., Vennemann, T., Sindern, S., Prantl, S., Böttcher, M.E., and Sakellaris, G.A., 2010, Characterisation of the hydrothermal fluids of the Guelb Moghrein iron oxide-Cu-Au-Co deposit, Mauritania: ore mineral chemistry, fluid inclusions and isotope geochemistry, *in* Porter, T.M., ed., Hydrothermal iron oxide copper-gold and related deposits: a global perspective, v. 4: PGC Publishing, Adelaide, p. 553-572.

Kontak, D.J., Archibald, D.A., Creaser, R.A., and Heaman, L.M., 2008, Dating hydrothermal alteration and IOCG mineralization along a terrane-bounding fault zone: the Copper Lake deposit, Nova Scotia: Atlantic Geology, v. 44, p. 146-166.

Kovacs, N., Allan, M.M., Crowley, J.L., Colpron, M., Hart, C.J.R., Zagorevski, A., and Creaser, R.A., 2020, Carmacks copper Cu-Au-Ag deposit: mineralization and postore migmatization of a Stikine Arc porphyry copper system in Yukon, Canada: Economic Geology, v. 115, p. 1413-1442.

Kreiner, D., and Barton, M.D., 2011, High-level alteration in iron-oxide (-Cu–Au) (IOCG) vein systems, examples near Copiapó, Chile: Proceedings of the 11th Biennial SGA meeting, Antofagasta, Chile, p. 497-499.

Kreiner, D., and Barton, M.D., 2017, Sulfur-poor intense acid hydrothermal alteration: a distinctive hydrothermal environment: Ore Geology Reviews, v. 88, p. 174-187.

Lentz, D., Steele-MacInnis, M., and Charlier, B., 2019, Carbonatitic to limestone syntectic decarbonation reactions in silicate magmas: $CO_2$ oxidant enhancing IOA liquid immiscibility: Geological Association of Canada-Mineralogical Association of Canada, Abstracts, v. 42, p. 130.

Li, W., Audétat, A., and Zhang, J., 2015, The role of evaporites in the formation of magnetite–apatite deposits along the Middle and Lower Yangtze River, China: evidence from LA-ICP-MS analysis of fluid inclusions: Ore Geology Reviews, v. 67, p. 264-278.

Liu, Y., Fan, Y., Zhou, T., Zhang, L., White, N.C., Hong, H., and Zhang, W., 2018, LA-ICP-MS titanite U-Pb dating and mineral chemistry of the Luohe magnetite-apatite (MA)-type deposit in the Lu-Zong volcanic basin, Eastern China: Ore Geology Reviews, v. 92, p. 284-296.

Lobato, L.M., Pimentel, M.M., Cruz, S.P.C., Machado, N., Noce, C.M., and Alkmim, F.F., 2015, U-Pb geochronology of the Lagoa Real uranium district, Brazil: implications for the age of the uranium mineralization: Journal of South American Earth Sciences, v. 58, p. 129-140.

Lulin, J.-M., Bissonnette, F., Delpech, E., Fortin, J., Pelletier, P.A., Philippin, M., and Wülser, P.A., 2010, Le Corridor de Rex: une nouvelle province minérale dans le Nord du Québec: Azimut Exploration web site as accessed February 2015, www.azimut-exploration.com/fr/presentations/-AZM_le_corridor_Rex_sept_2012.pdf.

MacDonald Mines Exploration Ltd., 2019, MacDonald Mines summarizes the potential of the Scadding mine: Press release, May 2, 2019.

MacHattie, T.G., and O'Reilly, G.A., 2009, Timing of iron oxide-copper-gold (IOCG) mineralization and alteration along the Cobequid-Chedabucto Fault Zone: Nova Scotia Department of Natural Resources, Mineral Resources Branch, Report ME 2009–1, p. 63-69.

Macmillan, E., Cook, N.J., Ehrig, K., Ciobanu, C.L., and Pring, A., 2016, Uraninite from the Olympic Dam IOCG-U-Ag deposit: linking textural and compositional variation to temporal evolution: American Mineralogist, v. 101, p. 1295-1320.

Magrina, B., Jébrak, M., and Cuney, M., 2005, Le magmatisme de la région de Kwyjibo, Province du Grenville (Canada): intérêt pour les minéralisations de type fer-oxydes associées: Canadian Journal of Earth Sciences, v. 42, p. 1849-1864.

Mao, J., Xie, G., Duan, C., Pirajno, F., Ishiyama, D., and Chen, Y., 2011, A tectono-genetic model for porphyry–skarn–stratabound Cu–Au–Mo–Fe and magnetite–apatite deposits along the Middle–Lower Yangtze River Valley, Eastern China: Ore Geology Reviews, v. 43, p. 294-314.

Mark, G., Oliver, N.H.S., Williams, P.J., Valenta, R.K., and Crookes, R.A., 2000, The evolution of the Ernest Henry Fe-oxide-(Cu–Au) hydrothermal system, *in* Porter, T.M., ed., Hydrothermal iron oxide copper–gold and related deposits: a global perspective, v. 1: PGC Publishing, Adelaide, p. 123-136.

Marschik, R., and Fontboté, L., 2001, The Candelaria–Punta del Cobre iron oxide Cu–Au (–Zn–Ag) deposits, Chile: Economic Geology, v. 96, p. 1799-1826.

Mathur, R., Marschik, R., Ruiz, J., Munizaga, F., Leveille, R.A., and Martin, W., 2002, Age of mineralization of the Candelaria Fe oxide Cu-Au deposit and the origin of the Chilean iron belt, based on Re-Os isotopes: Economic Geology, v. 97, p. 59-71.

McGloin, M., Tomkins, A.G., Webb, G.P., Spiers, K., MacRae, C.M., Paterson, D., and Ryna, C.G., 2016, Release of uranium from highly radiogenic zircon through metamictization: the source of orogenic uranium ores: Geology, v. 44, p. 15-18.

Melo, G.H.C., Monteiro, L.V.S., Xavier, R.P., Moreto, C.P.N., Santiago, E.S.B., Dufrane, S.A., Aires, B., and Santos, A.F.F., 2016, Temporal evolution of the giant Salobo IOCG deposit, Carajás Province (Brazil): constraints from paragenesis of hydrothermal alteration and U-Pb geochronology: Mineralium Deposita, v. 52, p. 709-732.

Mernagh, T.P., and Miezitis, Y., 2008, A review of the geochemical processes controlling the distribution of thorium in the Earth's crust and Australia's thorium resources: Geoscience Australia Record 2008/05, 48 p.

Meyer, G., Cosec, M., Grabowski, G.P.B., Guindon, D.L., Beauchamp, S., and Chaloux, E.C., 2003, Report of activities 2002, Resident Geologist Program, Kirkland Lake: Ontario Geological Survey, Open File Report 6114, 72 p.

Monteiro, L.V.S., Xavier, R.P., Carvalho, E.R., Hitzman, M.W., Johnson, C.A., Souza Filho, C.R., and Torresi, I., 2008, Space and temporal zoning of hydrothermal alteration and mineralization in the Sossego iron oxide-copper-gold deposit, Carajás Mineral Province, Brazil: paragenesis and stable isotope constraints: Mineralium Deposita, v. 43, p. 129-159.

Montreuil, J.-F., Corriveau, L., and Grunsky, E.C., 2013, Compositional data analysis of IOCG systems, Great Bear magmatic zone, Canada: to each alteration types its own geochemical signature: Geochemistry: Exploration, Environment, Analysis, v. 13, p. 229-247.

Montreuil, J.-F., Corriveau, L., and Potter, E.G., 2015, Formation of albitite-hosted uranium within IOCG systems: the Southern Breccia, Great Bear magmatic zone, Northwest Territories, Canada: Mineralium Deposita, v. 50, p. 293-325.

Montreuil, J.-F., Corriveau, L., and Davis, W., 2016a, Tectonomagmatic evolution of the southern Great Bear magmatic zone (Northwest Territories, Canada) – Implications on the genesis of iron oxide alkali-altered hydrothermal systems, *in* Slack, J., Corriveau, L. and Hitzman, M., eds., Proterozoic iron oxide-apatite (± REE) and iron oxide-copper-gold and affiliated deposits of Southeast Missouri, USA, and the Great Bear magmatic zone, Northwest Territories, Canada: Economic Geology, v. 111, p. 2111-2138.

Montreuil, J.-F., Corriveau, L., Potter, E.G., and De Toni, A.F., 2016b, On the relation between alteration facies and metal endowment of iron oxide–alkali-altered systems, southern Great Bear magmatic zone (Canada), *in* Slack, J., Corriveau, L. and Hitzman, M., eds., Proterozoic iron oxide-apatite (± REE) and iron oxide-copper-gold and affiliated deposits of Southeast Missouri, USA, and the Great Bear magmatic zone, Northwest Territories, Canada: Economic Geology, v. 111, p. 2139-2168.

Montreuil, J.-F., Potter, E.G., Corriveau, L., and Davis, W.J., 2016c, Element mobility patterns in magnetite-group IOCG systems: the Fab IOCG system, Northwest Territories, Canada: Ore Geology Reviews, v. 72, p. 562-584.

Moreto, C.P.N., Monteiro, L.V.S., Xavier, R.P., Creaser, R.A., DuFrane, S.A., and Melo, G.H.C., 2015, Timing of multiple hydrothermal events in the iron oxide–copper–gold deposits of the Southern Copper Belt, Carajás Province, Brazil: Mineralium Deposita, v. 50, p. 517-546.

Mudd, G.M., Jowitt, S.M., and Werner, T.T., 2017, The world's by-product and critical metal resources part I: uncertainties, current reporting practices, implications and grounds for optimism: Ore Geology Reviews, v. 86, p. 924-938.

Mukherjee, R., Venkatesh, A.S., and Fareeduddin, 2016, Albitite hosted gold-sulfide mineralization: an example from the Paleoproterozoic Aravalli supracrustal sequence, Bhukia area, Western India: Episodes, v. 39, p. 590-598.

Mumin, A.H., 2010, The Eden Lake rare metal (REE, Y, U, Th, phosphate) carbonatite complex, Manitoba, updated report: SEDAR, June 2010, 111 p.

Mumin, A.H. (ed.), 2015, Echo Bay IOCG thematic map series: geology, structure and hydrothermal alteration of a stratovolcano complex, Northwest Territories, Canada: Geological Survey of Canada, Open File 7807, 19 p., 18 sheets.

Mumin, A.H., and Trott, M., 2003, Hydrothermal iron-sulphide copper-graphite mineralization in the northern Kisseynew Domain, Trans-Hudson Orogen, Manitoba (NTS 63O and 64B): evidence for deep-seated IOCG (Olympic Dam)–style metal deposition?: Manitoba Geological Survey, Report of Activities 2003, p. 79-85.

Mumin, A.H., and Perrin, J.A., 2005, Scoping study for the hydrothermal iron-oxide copper-gold (IOCG) deposit type in Manitoba: summary of regional investigations: Manitoba Industry, Economic Development and Mines, Manitoba Geological Survey, Geoscientific Paper GP2005-2, 38 p.

Mumin, A.H., Corriveau, L., Somarin, A.K., and Ootes, L., 2007, Iron oxide copper-gold-type polymetallic mineralization in the Contact Lake Belt, Great Bear Magmatic Zone, Northwest Territories, Canada: Exploration and Mining Geology, v. 16, p. 187-208.

Mumin, A.H., Somarin, A.K., Jones, B., Corriveau, L., Ootes, L., and Camier, J., 2010, The IOCG-porphyry-epithermal continuum of deposits types in the Great Bear Magmatic Zone, Northwest Territories, Canada, *in* Corriveau, L. and Mumin, A.H., eds., Exploring for iron oxide copper-gold deposits: Canada and global analogues: Geological Association of Canada, Short Course Notes, No. 20, p. 59-78.

Nadeau, O., 2015, Ore metals beneath volcanoes: Nature Geoscience, v. 8, p. 168-170.

Nadeau, O., Stix, J., and Williams-Jones, A.E., 2013, The behavior of Cu, Zn and Pb during magmatic–hydrothermal activity at Merapi volcano, Indonesia: Chemical Geology, v. 342, p. 167-179.

Neymark, L.A., Holm-Denoma, C.S., Pietruszka, A.J., Aleinikoff, J.N., Fanning, C.M., Pillers, R.M., and Moscati, R.J., 2016, High spatial resolution U-Pb geochronology and Pb isotope geochemistry of magnetite-apatite ore from the Pea Ridge iron oxide-apatite deposit, St. Francois Mountains, Southeast Missouri, USA: Economic Geology, v. 111, p. 1915-1933.

New-Brunswick Department of Mines, 2003, New Brunswick deposit database, URN 590.

Nyström, J.O., and Henriquez, F., 1994, Magmatic features of iron ores of the Kiruna type in Chile and Sweden: ore textures and magnetite geochemistry: Economic Geology, v. 89, p. 820-839.

O'Driscoll, E.S.T., 1986, Observations of the lineament-ore relation: Philosophical Transactions of the Royal Society of London, v. A317, p. 195-218.

Oliver, N.H.S., Pearson, P.J., Holcombe, R.J., and Ord, A., 1999, Mary Kathleen metamorphic–hydrothermal uranium–rare-earth element deposit: ore genesis and numerical model of coupled deformation and fluid flow: Australian Journal of Earth Sciences, v. 46, p. 467-484.

Oliver, N.H.S., Mark, G., Pollard, P.J., Rubenach, M.J., Bastrakov, E., Williams, P.J., Marshall, L.C., Baker, T., and Nemchin, A.A., 2004, The role of sodic alteration in the genesis of iron oxide-copper-gold deposits: geochemistry and geochemical modelling of fluid-rock interaction in the Cloncurry district, Australia: Economic Geology, v. 99, p. 1145-1176.

Oliver, N.H.S., Butera, K.M., Rubenach, M.J., Marshall, L.J., Cleverley, J.S., Mark, G., Tullemans, F., and Esser, D., 2008, The protracted hydrothermal evolution of the Mount Isa Eastern Succession: a review and tectonic implications: Precambrian Research, v. 163, p. 108-130.

Ootes, L., Harris, J., Jackson, V.A., Azar, B., and Corriveau, L., 2013, Uranium-enriched bedrock in the central Wopmay Orogen: implications for uranium mineralization, *in* Potter, E.G., Quirt, D. and Jefferson, C.W., eds., Uranium in Canada: geological environments and exploration developments: Exploration and Mining Geology, v. 21, p. 85-103.

Ootes, L., Snyder, D., Davis, W.J., Acosta-Góngora, P., Corriveau, L., Mumin, A.H., Montreuil, J.-F., Gleeson, S.A., Samson, I.A., and Jackson, V.A., 2017, A Paleoproterozoic Andean-type iron oxide copper-gold environment, the Great Bear magmatic zone, Northwest Canada: Ore Geology Reviews, v. 81, p. 123-139.

Oreskes, N., and Einaudi, M.T., 1990, Origin of rare earth element-enriched hematite breccias at the Olympic Dam Cu-U-Au-Ag deposit, Roxby Downs, South Australia: Economic Geology, v. 85, p. 1-28.

OZ Minerals, 2014a, Initial 202 Mt at 0.6% copper resource for Khamsin: ASX Release 26 May 2014, 20 p.

OZ Minerals, 2014b, Annual resource and reserve update for Prominent Hill: ASX Release 20 November 2014, 50 p.

OZ Minerals, 2019, OZ Minerals 2019 annual and sustainability report: Available at ozminerals.com.

Pal, D.C., Barton, M.D., and Sarangi, A.K., 2009, Deciphering a multistage history affecting U–Cu(–Fe) mineralization in the Singhbhum Shear Zone, eastern India, using pyrite textures and compositions in the Turamdih U–Cu(–Fe) deposit: Mineralium Deposita, v. 44, p. 61-80.

Paladin Energy, 2015, Michelin deposit, geology and resources: Accessed at paladinenergy.com.au.

Pankka, H.S., and Vanhanen, E.J., 1992, Early Proterozoic Au-Co-U mineralization in the Kuusamo district, northeast Finland: Precambrian Research, v. 58, p. 387-400.

Perreault, S., and Lafrance, B., 2015, Kwyjibo, a REE-enriched iron oxides-copper-gold (IOCG) deposit, Grenville Province, Québec, *in* Simandl, G.J. and Neetz, M., eds., Symposium on strategic and critical materials proceedings, November 13-14, 2015, Victoria, British Columbia: British Columbia Ministry of Energy and Mines, British Columbia Geological Survey Paper 2015-3, p. 139-145.

Piette-Lauzière, N., Graziani, R., Larson, K.P., and Kellett, D.A., 2019, Reactivation of the Eastern Highlands shear zone, Cape Breton Island, Appalachian Orogen, *in* Rogers, N., ed., Targeted Geoscience Initiative: 2018 report of activities: Geological Survey of Canada, Open file 8549, p. 295-305.

Polito, P.A., Kyser, T.K., and Stanley, C., 2009, The Proterozoic, albitite-hosted, Valhalla uranium deposit, Queensland, Australia: a description of the alteration assemblage associated with uranium mineralization in diamond drill hole V39: Mineralium Deposita, v. 44, p. 11-40.

Porter, T.M., 2010, Current understanding of iron oxide associated-alkali altered mineralised systems. Part 1 - An overview, *in* Porter, T.M., ed., Hydrothermal iron oxide copper-gold and related deposits: a global perspective, v. 3: PGC Publishing, Adelaide, p. 5-32.

Potter, E.G., Corriveau, L., and Kerswill, J.K., 2013a, Potential for iron oxide-copper–gold and affiliated deposits in the proposed national park area of the East Arm, Northwest Territories: insights from the Great Bear magmatic zone and global analogs, *in* Wright, D.F., Kjarsgaard, B.A., Ambrose, E.J. and Bonham-Carter, G.F., eds., Mineral and energy resource assessment for the proposed Thaidene Nene National Park reserve, East Arm of Great Slave Lake, Northwest Territories: Geological Survey of Canada, Open File 7196, Chapter 19, p. 477-493.

Potter, E.G., Montreuil, J.-F., Corriveau, L., and De Toni, A., 2013b, Geology and hydrothermal alteration of the Fab Lake region, Northwest Territories: Geological Survey of Canada, Open File 7339, 26 p.

Potter, E.G., Corriveau, L., and Kjarsgaard, B., 2019a, Paleoproterozoic iron oxide apatite (IOA) and iron oxide-copper-gold (IOCG) mineralization in the East Arm Basin, Northwest Territories, Canada: Canadian Journal of Earth Sciences, v. 57, p. 167-183.

Potter, E.G., Montreuil, J.-F., Corriveau, L., and Davis, W.J., 2019b, The Southern Breccia metasomatic uranium system of the Great Bear magmatic zone, Canada: iron oxide-copper-gold (IOCG) and albitite-hosted uranium linkages, *in* Decrée, S. and Robb, L., eds., Ore deposits: origin, exploration, and exploitation: Geophysical Monograph 242, First Edition, American Geophysical Union, John Wiley & Sons, Inc., p. 109-130.

Potter, E.G., Acosta-Góngora, P., Corriveau, L., Montreuil, J.-F., and Yang, Z., 2022, Uranium enrichment processes in metasomatic iron oxide and alkali-calcic systems as revealed by uraninite trace element chemistry, *in* Corriveau, L., Potter, E.G. and Mumin, A.H., eds., Mineral systems with iron oxide copper-gold (IOCG) and affiliated deposits: Geological Association of Canada, Special Paper 52, p. 325-345.

Quin, S.P., and Mercer, B.J., 2008, The Minto copper-gold deposit - IOCG or what?: Geological Association of Canada, Québec 2008, Abstracts volume, v. 33, p. 140.

Ray, S.K., 1990, The albitite line of northern Rajasthan - A fossil intracontinental rift zone: Journal of the Geological Society of India, v. 86, p. 413-423.

Reeve, J.S., Cross, K.C., Smith, R.N., and Oreskes, N., 1990, The Olympic Dam copper-uranium-gold-silver deposit, South Australia, *in* Hughes, F., ed., Geology of mineral deposits of Australia and Papua New Guinea: Australian Institute of Mining and Metallurgy Monograph 14, p. 1009-1035.

Reid, A.J., 2019, The Olympic Cu-Au Province, Gawler Craton: a review of the lithospheric architecture, geodynamic setting, alteration systems, cover successions and prospectivity: Minerals, v. 9, 371.

Reid, A.J., Swain, G., Mason, D., and Maas, R., 2011, Nature and timing of Cu–Au–Zn–Pb mineralisation at Punt Hill, eastern Gawler Craton: MESA Journal, v. 60, p. 7-27.

Reischmann, T., 1995, Precise U/Th age determination with baddeleyite ($ZrO_2$), a case study from the Phalaborwa Igneous Complex, South Africa: South African Journal of Geology, v. 98, p. 1-4.

Rex Minerals Ltd., 2015, Hillside project, mineral resources and ore reserves: Available at www.rexminerals.com.au.

Richards, J.P., and Mumin A.H., 2013a, Lithospheric fertilization and mineralization by arc magmas: genetic links and secular differences between porphyry copper±molybdenum±gold and magmatic-hydrothermal iron oxide copper-gold deposits, *in* Colpron, M., Bissig, T., Rusk, B.G., and Thompson, J.F.H., eds., Tectonics, metallogeny, and discovery: the North American Cordillera and similar accretionary settings: Society of Economic Geologists, Special Publication 17, p. 277-299.

Richards, J.P., and Mumin A.H., 2013b, Magmatic-hydrothermal processes within an evolving Earth: iron oxide-copper-gold and porphyry Cu±Mo±Au deposits: Geology, v. 41, p. 767-770.

Richards, J.P., Lopez, G.P., Zhu, J., Creaser, R.A., Locock, A.J., and Mumin, A.H., 2017, Contrasting tectonic settings and sulfur contents of magmas associated with Cretaceous porphyry Cu-Au and intrusion-related iron oxide Cu-Au deposits in northern Chile: Economic Geology, v. 112, p. 295-318.

Roberts, D.E., and Hudson, G.R.T., 1983, The Olympic Dam copper-uranium-gold deposit, Roxby Downs, South Australia: Economic Geology, v. 78, p.799-822.

Robinson, B.W., and Ohmoto, H., 1973, Mineralogy, fluid inclusions, and stable isotopes of the Echo Bay U-Ni-Ag-Cu deposits, Northwest Territories, Canada: Economic Geology, v. 68, p. 635-656.

Rojas, P.A., Barra, F., Deditius, A., Reich, M., Simon, A., Roberts, M., and Rojo, M., 2018, New contributions to the understanding of Kiruna-type iron oxide-apatite deposits revealed by magnetite ore and gangue mineral geochemistry at the El Romeral deposit, Chile: Ore Geology Reviews, v. 93, p. 413-435.

Romer, R.L., Martinsson, O., and Perdahl, J.-A., 1994, Geochronology of the Kiruna iron ores and hydrothermal alterations: Economic Geology, v. 89, p. 1249-1261.

Rukhlov, A.S., 2011, Review of metallic mineralization in Alberta with emphasis on gold potential: Energy Resources Conservation Board, ERCB/AGS Open File Report 2011-01, 93 p.

Rusk, B., Oliver, N., Blenkinsop, T., Zhang, D., Williams, P., Cleverley, J., and Habermann, H., 2010, Physical and chemical characteristics of the Ernest Henry iron oxide copper gold deposit, Cloncurry, Queensland, Australia: implications for IOCG genesis, *in* Porter, T.M., ed., Hydrothermal iron oxide copper-gold and related deposits: a global perspective, v. 3: PGC Publishing, Adelaide, p. 201-218.

Salles, R.D.R., de Souza Filho, C.R., Cudahy, T., Vicente, L.E., and Monteiro, L.V.S., 2017, Hyperspectral remote sensing applied to uranium exploration: a case study at the Mary Kathleen metamorphic-hydrothermal U-REE deposit, NW, Queensland, Australia: Journal of Geochemical Exploration, v. 179, p. 36-50.

Sangster, P.J., LeBaron, P.S., Laidlaw, D.A., Wilson, A.C., Carter, T.R., and Fortner, L., 2011, Report of activities 2010, Resident geologist program, southern Ontario regional resident geologist report: southeastern and southwestern Ontario districts and petroleum resources centre: Ontario Geological Survey, Open File Report 6267, 65 p.

Sangster, P.J., Le Baron, P.S., Charbonneau, S.J., Laidlaw, D.A., Wilson, A.C., Carter, T.R., and Fortner, L., 2012, Report of activities 2011, resident geologist program, southern Ontario regional resident geologist report: Ontario Geological Survey, Open File Report 6277, 72 p.

Schandl, E.S., and Gorton, M.P., 2007, The Scadding gold mine, east of the Sudbury igneous complex, Ontario: an IOCG-type deposit?; The Canadian Mineralogist, v. 45, p. 1415-1441.

Schlegel, T.U., and Heinrich, C.A., 2015, Lithology and hydrothermal alteration control the distribution of copper grade in the Prominent Hill iron oxide-copper-gold deposit (Gawler Craton, South Australia): Economic Geology, v. 110, p. 1953-1994.

Schlegel, T.U., Wagner, T., Wälle, M., and Heinrich, C.A., 2018, Hematite breccia-hosted iron oxide copper-gold deposits require magmatic fluid components exposed to atmospheric oxidation: evidence from Prominent Hill, Gawler Craton, South Australia: Economic Geology, v. 113, p. 597-644.

Schofield, A. (ed.), 2012, An assessment of the uranium and geothermal prospectivity of the southern Northern Territory: Geoscience Australia, Record 2012/51, 214 p.

Schutesky, M.E., Oliveira, C., Hagemann, S.G., and Monteiro, V.S., 2020, A thematic issue dedicated to the 50$^{th}$ year of the discovery of the Carajás Mineral Province: Ore Geology Reviews, v. 129, 103819.

Selleck, B., McLelland, J., and Hamilton, M.A., 2004, Magmatic-hydrothermal leaching and origin of late- to post-tectonic quartz-rich rocks, Adirondack Highlands, New York, *in* Tollo, R.P., Corriveau, L., McLelland, J. and Bartholomew, M., eds., Proterozoic tectonic evolution of the Grenville Orogen in North America: Geological Society of America Memoir, No 197, p. 379-390.

Seo, S., Choi, S.G., Kima, D.W., Park, J.W., and Oh, C.W., 2015, A new genetic model for the Triassic Yangyang iron-oxide–apatite deposit, South Korea: constraints from in situ U–Pb and trace element analyses of accessory minerals: Ore Geology Reviews, v. 70, p. 110-135.

Setterfield, T., Chartrand, F., and Campbell, J., 2006, Report on work completed by Geovector Management between June and October 2006 on the Sagar property, Romanet Horst, Labrador Trough, Quebec, Canada: Geovector Managment Inc., p. 1-83.

Sillitoe, R.H., 2003, Iron oxide-copper-gold deposits: an Andean view: Mineralium Deposita, v. 38, p. 787-812.

Sillitoe, R.H., and Burrows, D.R., 2002, New field evidence bearing on the origin of the El Laco magnetite deposit, northern Chile: Economic Geology, v. 97, p. 1101-1109.

Sillitoe, R.H., Magaranov, G., Mladenov, V., and Creaser, R.A., 2020, Rosen, Bulgaria: a newly recognized iron oxide-copper-gold district: Economic Geology, v. 115, p. 481-488.

Simard, M., Beaudoin, G., Bernard, J., and Hupé, A., 2006, Metallogeny of the Mont-de-l'Aigle IOCG deposit, Gaspé Peninsula, Québec, Canada: Mineralium Deposita, v. 41, p. 607-636.

Simon, A.C., Knipping, J., Childress, T., La Cruz, N., Konecke, B., Reich, M., Barra, F., Palma, G., Deditius, A.P., Bilenker, L., Lundstrom, C., and Bindeman, I., 2017, A magmatic flotation model that genetically links iron oxide-apatite and iron oxide-copper-gold deposits: Proceedings of the 14$^{th}$ SGA Biennial Meeting, 20-23 August 2017, Québec City, p. 827-830.

Sinclair, W.D., 2007, Porphyry deposits, *in* Goodfellow, W.D., ed., Mineral deposits of Canada: a synthesis of major deposit-types, district metallogeny, the evolution of geological provinces, and exploration methods: Geological Association of Canada, Mineral Deposits Division, Special Publication No. 5, p. 223-243.

Skanderberg, B.N., 2001, A synopsis of iron oxide ± Cu ± Au ± P, F, REE deposits with emphasis on the geology, metallogenesis, and exploration potential of the Great Bear magmatic zone, Northwest Territories, Canada: Unpublished M.Sc. thesis, Rhodes University, South Africa, 87 p.

Skirrow, R.G., 2000, Gold-copper-bismuth deposits of the Tennant Creek district, Australia: a reappraisal of diverse high-grade systems, *in* Porter, T.M., ed., Hydrothermal iron oxide copper-gold and related deposits: a global perspective, v. 1: PGC Publishing, Adelaide, p. 149-160.

Skirrow, R.G., 2010, "Hematite-group" IOCG±U ore systems: tectonic settings, hydrothermal characteristics, and Cu-Au and U mineralizing processes, *in* Corriveau, L. and Mumin, A.H., eds., Exploring for iron oxide copper-gold deposits: Canada and global analogues: Geological Association of Canada, Short Course Notes, No. 20, p. 39-57.

Skirrow, R.G., 2022, Hematite-group IOCG ± U deposits: an update on their tectonic settings, hydrothermal characteristics, and Cu-Au-U mineralizing processes, *in* Corriveau, L., Potter, E.G. and Mumin, A.H., eds., Mineral systems with iron oxide copper-gold (IOCG) and affiliated deposits: Geological Association of Canada, Special Paper 52, p. 27-51.

Skirrow, R.G., and Davidson, G., 2007, A special issue devoted to Proterozoic iron oxide Cu-Au-(U) and gold mineral systems of the Gawler craton: preface: Economic Geology, v. 102, p. 1373-1375.

Skirrow, R.G., Bastrakov, E., Davidson, G.J., Raymond, O., and Heithersay, P., 2002, Geological framework, distribution and controls of Fe-oxide Cu-Au deposits in the Gawler Craton. Part II. Alteration and mineralization, *in* Porter, T.M., ed., Hydrothermal iron oxide copper-gold and related deposits: a global perspective v. 2: PGC Publishing, Adelaide, p. 33-47.

Skirrow, R.G., Schofield, A., and Connolly, D., 2011, Uranium-rich iron oxide-copper-gold, *in* Huston, D.L. and van der Wielen, S.E., eds., An assessment of the uranium and geothermal prospectivity of east-central South Australia: Geoscience Australia, Record, 2011/34, 229 p.

Skirrow, R.G., Huston, D.L., Mernagh, T.P., Thorne, J.P., Dulfer, H., and Senior, A.B., 2013, Critical commodities for a high-tech world: Australia's potential to supply global demand: Geoscience Australia, Canberra, 118 p.

Slack, J., 2013, Descriptive and geoenvironmental model for cobalt–copper–gold deposits in metasedimentary rocks: U.S. Geological Survey Scientific Investigations Report 2010–5070–G, 218 p.

Slack, J., Corriveau, L., and Hitzman, M., 2016, A special issue devoted to Proterozoic iron oxide-apatite (± REE) and iron oxide-copper-gold and affiliated deposits of Southeast Missouri, USA, and the Great Bear magmatic zone, Northwest Territories, Canada – preface, *in* Slack, J., Corriveau, L. and Hitzman, M., eds., Proterozoic iron oxide-apatite (± REE) and iron oxide-copper-gold and affiliated deposits of Southeast Missouri, USA, and the Great Bear magmatic zone, Northwest Territories, Canada: Economic Geology, v. 111, p. 1803-1814.

Smith, M., and Chengyu, W., 2000, The geology and genesis of the Bayan Obo Fe-REE-Nb deposit: a review, *in* Porter, T.M., ed., Hydrothermal iron oxide copper-gold and related deposits: a global perspective, v. 1: PGC Publishing, Adelaide, p. 271-281.

Somarin, A.K., and Mumin, A.H., 2012, The Paleoproterozoic high heat production Richardson granite, Great Bear magmatic zone, Northwest Territories, Canada: source of U for Port Radium?; Resources Geology, v. 62, p. 227-242.

Sparkes, G.W., 2017, Uranium mineralization within the Central Mineral Belt of Labrador: a summary of the diverse styles, settings and timing of mineralization: Government of Newfoundland and Labrador, Department of Natural Resources, Geological Survey, St. John's, Open File LAB/1684, 198 p.

Stosch, H.G., Romer, R.L., Daliran, F., and Rhede, D., 2011, Uranium–lead ages of apatite from iron oxide ores of the Bafq District, East-Central Iran: Mineralium Deposita, v. 46, p. 9-21.

Tallarico, F.H.B., McNaughton, N.J., Groves, D.I., Fletcher, I.R., Figueiredo, B.R., Carvolho, J.B., Rego, J.L., and Nunes, A.R., 2004, Geological and SHRIMP II U–Pb constraints on the age and origin of the Breves Cu-Au-(W-Bi-Sn) deposit, Carajás, Brazil: Mineralium Deposita, v. 39, p. 68-86.

Thorkelson, D.J., Mortensen, J.K., Creaser, R.A., Davidson, G.J., and Abbott, J.G., 2001, Early Proterozoic magmatism in Yukon, Canada: constraints on the evolution of northwestern Laurentia: Canadian Journal of Earth Sciences, v. 38, p. 1479-1494.

Tiddy, C.J., and Giles, D., 2020, Suprasubduction zone model for metal endowment at 1.60–1.57 Ga in eastern Australia: Ore Geology Reviews, v. 122, 103483.

Tornos, F., Velasco, F., and Hanchar, J.M., 2016, Iron-rich melts, magmatic magnetite, and superheated hydrothermal systems: the El Laco deposit, Chile: Geology, v. 44, p. 427-430.

Tornos, F., Velasco, F., and Hanchar, J.M., 2017, The magmatic to magmatic-hydrothermal evolution of the El Laco deposit (Chile) and its implications for the genesis of magnetite-apatite deposits: Economic Geology, v. 112, p. 1595-1628.

Torab, F.M., and Lehmann, B., 2007, Magnetite-apatite deposits of the Bafq district, Central Iran: apatite geochemistry and monazite geochronology: Mineralogical Magazine, v. 71, p. 347-363.

Tremblay, R.J., and Koziol, M., 2007, Report on Alto ventures Ltd Coldstream project 2006 diamond drilling and old core re-sampling programs, Shebandowan greenstone belt: June 1st, 2007, available at www.geologyontario.mndmf.gov.on.ca/mndmfiles.

Turner, D., 2012, Independent technical report on the Kiyuk Lake property, Nunavut Territory, Canada: National Instrument 43-101 report, available at www.sedar.com.

Valley, P.M., Hanchar, J.M., and Whitehouse, M.J., 2009, Direct dating of Fe oxide-(Cu-Au) mineralization by U/Pb zircon geochronology: Geology, v. 37, p. 223-226.

Valley, P.M., Hanchar, J.M., and Whitehouse, M.J., 2011, New insights on the evolution of the Lyon Mountain granite and associated Kiruna-type magnetite-apatite deposits, Adirondack Mountains, New York State: Geosphere, v. 7, p. 357-389.

Veloso, A.S.R., Monteiro, L.V.S., and Juliani, C., 2020, The link between hydrothermal nickel mineralization and an iron oxide-copper-gold (IOCG) system: constraints based on mineral chemistry in the Jatobá deposit, Carajás Province: Ore Geology Reviews, v. 121, 103555.

Verissimo, C.U.V., Santos, R.V., Parente, C.V., de Oliveira, C.G., Cavalcanti, J.A.D., and Neto, J.A.N., 2016, The Itataia phosphate-uranium deposit (Ceara, Brazil) new petrographic, geochemistry and isotope studies: Journal of South American Earth Sciences, v. 70, p. 115-144.

Wade, C.E., Payne, J.L., Barovich, K.M., and Reid, A.J., 2019, Heterogeneity of the sub-continental lithospheric mantle and 'non-juvenile' mantle additions to a Proterozoic silicic large igneous province: Lithos, v. 340-341, p. 87-107.

Wanhainen, C., Broman, C., and Martinsson, O., 2003, The Aitik Cu–Au–Ag deposit in northern Sweden: a product of high salinity fluids: Mineralium Deposita, v. 38, p. 715-726.

Watari, T., Nansai, K., and Nakajima, K., 2020, Review of critical metal dynamics to 2050 for 48 elements: Resources, Conservation & Recycling, v. 155, 104669.

Weatherston, A.J., Inglis, O.E., Gray, J., Busby, D., and Couture, B., 2016, Guide to authors: Geological Survey of Canada, Open file 8095, 219 p.

Wilde, A., 2013, Towards a model for albitite-type uranium: Minerals, v. 3, p. 36-48.

Williams, M.R., Holwell, D.A., Lilly, R.M., Case, G.N.D., and McDonald, I., 2015, Mineralogical and fluid characteristics of the fluorite-rich Monakoff and E1 Cu–Au deposits, Cloncurry region, Queensland, Australia: implications for regional F–Ba-rich IOCG mineralisation: Ore Geology Reviews, v. 64, p. 103-127.

Williams, P.J., 2010a, Classifying IOCG deposits, *in* Corriveau, L. and Mumin, A.H., eds., Exploring for iron oxide copper-gold deposits: Canada and global analogues: Geological Association of Canada, Short Course Notes, No. 20, p. 13-21.

Williams, P.J., 2010b, "Magnetite-group" IOCGs with special reference to Cloncurry and Northern Sweden: settings, alteration, deposit characteristics, fluid sources, and their relationship to apatite-rich iron ores, *in* Corriveau, L. and Mumin, A.H., eds., Exploring for iron oxide copper-gold deposits: Canada and global analogues: Geological Association of Canada, Short Course Notes, No. 20, p. 23-38.

Williams, P.J., 2022, Magnetite-group IOCGs with special reference to Cloncurry and Northern Sweden: settings, alteration, deposit characteristics, fluid sources, and their relationship to apatite-rich iron ores, *in* Corriveau, L., Potter, E.G. and Mumin, A.H., eds., Mineral systems with iron oxide copper-gold (IOCG) and affiliated deposits: Geological Association of Canada, Special Paper 52, p. 53-68.

Williams, P.J., and Skirrow, R.G., 2000, Overview of IOCG deposits in the Curnamona Province and Cloncurry district (eastern Mount Isa block), Australia, *in* Porter, T.M., ed., Hydrothermal iron oxide copper-gold and related deposits: a global perspective, v. 1: PGC Publishing, p. 105-122.

Williams, P.J., Barton, M.D., Johnson, D.A., Fontboté, L., de Haller, A., Mark, G., Oliver, N.H.S., and Marschik, R., 2005, Iron-oxide copper-gold deposits: geology, space-time distribution, and possible modes of origin: Economic Geology 100th Anniversary Volume, p. 371-405.

Xavier, R.P., Monteiro, L.V.S., de Souza Filho, C.R., Torresi, I., de Resende Carvalho, E., Dreher, A.M., Wiedenbeck, M., Trumbull, R.B., Pestilho, A.L.S., and Moreto, C.P.N., 2010, The iron oxide copper-gold deposits of the Carajás mineral province, Brazil: an updated and critical review, *in* Porter, T.M., ed., Hydrothermal iron oxide copper–gold and related deposits: a global perspective, v. 3: PGC Publishing, Adelaide, p. 285-306.

Xavier, R.P., Moreto, C.P.N., Monteiro, L.V.S., Melo, G.H.C., Toledo, P., Hunger, R.B., Delinardo da Silva, M., Previato, M., Jesus, S.S.G.P., and Huhn, S.B., 2017, Geology and metallogeny of Neoarchean and Paleoproterozoic copper systems of the Carajás domain, Amazonian Craton, Brazil: Proceedings of the 14th SGA Biennial Meeting, 20-23 August 2017, Québec City, p. 899-902.

Yilmazer, E., Güleç, N., Kuşcu, I., and Lentz, D.R., 2014, Geology, geochemistry, and geochronology of Fe-oxide Cu (±Au) mineralization associated with Şamli pluton, western Turkey: Ore Geology Reviews, v. 57, p. 191-215.

Yu, J., Chen, Y., Mao, J., Pirajno, F., and Duan, C., 2011, Review of geology, alteration and origin of iron oxide–apatite deposits in the Cretaceous Ningwu basin, Lower Yangtze River Valley, eastern China: implications for ore genesis and geodynamic setting: Ore Geology Reviews, v. 43, p. 170-181.

Zeng, L., 2020, Formation mechanism and genetic model of iron-oxide apatite deposits in the Ningwu district, China: Unpublished Ph.D. thesis, China University of Geosciences, Wuhan, 270 p.

Zeng, M., Zhang, D., Zhang, Z., Li, T., Li, C., and Wei, C., 2018, Structural controls on the Lala iron-copper deposit of the Kangdian metallogenic province, southwestern China: tectonic and metallogenic implications: Ore Geology Reviews, v. 97, p. 35-54.

Zeng, L.P., Zhao, X.F., Hammerli, J., and Spandler, C., 2020, Tracking fluid sources for skarn formation using scapolite geochemistry: an example from the Jinshandian iron skarn deposit, Eastern China: Mineralium Deposita, v. 55, p. 1029-1046.

Zhao, X.-F., Zeng, L.-P., Hu, H., and Li, X.-C., 2016, Iron-oxide apatite deposits in eastern China formed by accumulation of magmatic hydrosaline chloride liquids: 34th IGC abstract, Paper 2293, Cape Town.

Zhao, X.-F., Su, Z.-K., and Zeng, L.-P., 2017a, Genetic models of IOCG and IOA deposits from China: implications for ore genesis and their possible links: Proceedings of the 14th SGA Biennial Meeting, 20-23 August 2017, Québec City, p. 835-839.

Zhao, X.F., Zhou, M.F., Su, Z.K., Li, X.C., Chen, W.T., and Li, J.W., 2017b, Geology, geochronology, and geochemistry of the Dahongshan Fe-Cu-(Au-Ag) deposit, Southwest China: implications for the formation of iron oxide copper-gold deposits in intracratonic rift settings: Economic Geology, v. 112, p. 603-628.

Zhao, X.-F., Chen, H., Zhao, L., and Zhou, M.-F., 2022, Linkages among IOA, skarn, and magnetite-group IOCG deposits in China: from deposit studies to mineral potential assessment, *in* Corriveau, L., Potter, E.G. and Mumin, A.H., eds., Mineral systems with iron oxide copper-gold (IOCG) and affiliated deposits: Geological Association of Canada, Special Paper 52, p. 383-407.

Zhou, T., Fan, Y., Yuan, F., Zhang, L., Qian, B., Ma, L., and Yang, X., 2013, Geology and geochronology of magnetite–apatite deposits in the Ning-Wu volcanic basin, Eastern China: Journal of Asian Earth Sciences, v. 66, p. 90-107.

# Hematite-group IOCG ± U Deposits: An Update on their Tectonic Settings, Hydrothermal Characteristics, and Cu-Au-U Mineralizing Processes

**Roger G. Skirrow**
*Geoscience Australia*, Canberra, Australia*
**former affiliation*
*roger.skirrow@gmail.com*

*Recommended citation: Skirrow, R.G., 2022, Hematite-group IOCG ± U deposits: an update on their tectonic settings, hydrothermal characteristics, and Cu-Au-U mineralizing processes, in Corriveau, L., Potter, E.G. and Mumin, A.H., eds., Mineral systems with iron oxide-copper-gold (IOCG) and affiliated deposits: Geological Association of Canada, Special Paper 52, p. 27-51.*

## Abstract

Hematite-rich IOCG ± U deposits occur in several IOCG districts together with magnetite-dominated deposits. The Olympic Dam Cu-U-Au deposit in the Gawler Craton of South Australia is the world's largest IOCG deposit and uranium resource, and is the best known example of hematite-group IOCG deposits. Through comparison of this terrane with others hosting hematite-group deposits, two distinct processes are recognized in the formation of hematite-bearing IOCG ± U deposits: single-fluid-rock interaction, and two-fluid processes including mixing. The most important settings for hematite-group IOCG ± U deposit formation are those involving fluid mixing at shallow crustal levels, although mid-crustal examples are known from some terranes.

The following criteria are proposed for recognition of terranes with high potential for major hematite-group uranium-rich IOCG deposits:

- Syn- to post-subduction, syn- to post-orogenic, settings distal (several hundred kilometres) from continental margins, characterized by bimodal magmatism including voluminous uranium-rich (e.g. A-type) subaerial felsic volcanic and/or high-level felsic intrusive rocks. These terranes show evidence of a switch from compressive to extensional deformation coincident with crustal melting, possibly driven by mantle lithosphere removal (delamination or convective) in the case of the Gawler Craton;
- Crustal-scale structural pathways for magmas and fluids, e.g. shear zones in pre-IOCG orogenic belts at former cratonic margins or trans-crustal to trans-lithospheric boundaries within cratons;
- Mafic/ultramafic intrusive magmatism marking the loci of crustal-scale thermal anomalies and high geothermal gradients that resulted in regional-scale upper crustal fluid flow;
- Syn- to post-compressional district- to deposit-scale magnetite-rich alteration characterized by $Fe^{2+}$-K metasomatism and generally minor copper-gold mineralization (magnetite, K-feldspar or biotite, actinolite, quartz, apatite, pyrite, chalcopyrite). Albitic Na-Ca (Fe) alteration may be exposed in deeply exhumed areas;
- Exhumation of active upper crustal magnetite-forming hydrothermal regime, allowing interaction of this alteration with oxidized surface derived fluid, in extensional or transtensional settings;
- Hydrological settings such as basins or calderas in which large volumes of oxidized groundwaters or basinal waters were mobilized through uranium-rich host rocks to sites of fluid upflow associated with magnetite formation, allowing fluid mixing;
- Deposit-scale hydrothermal alteration zones in hematite-group IOCG (±U) deposits typically contain combinations of hematite, chlorite, sericite, carbonate, pyrite, gold, chalcopyrite, bornite, chalcocite, barite, fluorite and various REE, uranium and phosphate minerals; and
- Higher grade copper-gold mineralization generally forms within hematite-rich zones laterally or vertically adjacent to magnetite-bearing zones; higher grade uranium mineralization is generally associated with gold-rich and/or more oxidized mineral assemblages.

## Résumé

Des gîtes IOCG ± U riches en hématite sont présents dans plusieurs districts IOCG ainsi que des gîtes à dominance de magnétite. Le gisement de Cu-U-Au d'Olympic Dam dans le craton de Gawler, South Australia, est le plus gros gisement IOCG et la plus grosse ressource en uranium au monde; il est également l'exemple le mieux connu des gîtes IOCG à hématite. À l'aide de comparaisons de ce terrane avec d'autres contenant des gîtes à hématite, on peut reconnaître deux processus distincts dans la formation des gîtes IOCG ± U à hématite: l'interaction d'un seul fluide avec l'encaissant, et des processus à deux fluides, y compris par mélange de fluides. Les contextes les plus importants pour la formation de gîtes IOCG ± U à hématite sont ceux impliquant le mélange de fluides à un niveau crustal superficiel, bien que des exemples au niveau de croûte moyenne soient connus dans certains terranes.

Les critères suivants sont proposés pour reconnaitre les terranes à potentiel élevé pour de larges gîtes IOCG riches en uranium et en hématite :

- Contextes d'arrière-arc intracontinentaux ou distaux contenants de grands volumes de roches volcaniques felsiques subaériennes et (ou) de roches felsiques intrusives hypabyssales riches en uranium (p. ex. type A). Ces terranes montrent des évidences de transition entre une déformation en compression et une déformation en extension contemporaine à de

la fusion au niveau de la croûte, cette dernière potentiellement induite par l'élimination du manteau lithosphérique (par delamination ou convection) dans le cas du craton de Gawler.
- Structures d'échelle crustale servants de conduits pour les magmas et les fluides, p. ex. des zones de cisaillement dans des ceintures orogéniques pré-IOCG le long d'anciennes marges cratoniques ou des discontinuités trans-lithosphérique au sein de cratons.
- Magmatisme intrusif mafique-ultramafique soulignant les sites d'anomalies thermiques et de gradients géothermiques élevés qui ont mené à l'écoulement de fluides dans la croûte supérieure à l'échelle régionale.
- Altération riche en magnétite syn- à post-compression à l'échelle du district ou des gîtes, associée à un métasomatisme $Fe^{2+}$-K et une minéralisation cuivre-or généralement mineure (magnétite, feldspath potassique ou biotite, actinote, quartz, apatite, pyrite, chalcopyrite). Une altération Na-Ca (-Fe) albitique peut affleurer au sein de niveaux profonds exhumés.
- Exhumation d'un régime hydrothermal où la magnétite crystallise au sein de la croûte supérieure suivie d'une rééquilibration avec un fluide oxydé provenant de la surface, dans des contextes d'extension ou de transtension.
- Contextes hydrologiques tels que des bassins ou des calderas dans lesquels de grands volumes d'eau souterraine ou de bassin ont été mobilisés à travers des roches encaissantes riches en U vers des sites où les fluides associés à la crystallisation de magnétite remontent ce qui induit un mélange de fluides.
- Zones d'altération hydrothermale à hématite, chlorite, séricite, carbonate, pyrite, or, chalcopyrite, bornite, chalcocite, barite et minéraux divers à ETR et à phosphate au sein des gîtes IOCG (±U) à hématite.
- Teneurs en cuivre et en or plus élevées au sein des zones riches en hématite et à côté ou au dessus des zones à magnétite ; la minéralisation la plus uranifère est généralement associée à des assemblages minéralogiques riches en or et (ou) plus oxydés.

## Introduction

Hematite-rich IOCG deposits represent an economically important subtype in the spectrum of magnetite- to hematite-dominated IOCG deposits (Williams, 2010a). The Olympic Dam Cu-U-Au deposit in the Gawler Craton, South Australia, is the world's largest IOCG deposit and best-known example of the hematitic subtype. With a total resource of ~10.7 billion tonnes, Olympic Dam is the largest known uranium resource currently being mined on Earth (BHP, 2018). Other large hematite-rich IOCG deposits in the Gawler Craton include the Prominent Hill and Carrapateena deposits. In several other IOCG districts, hematite-rich IOCG deposits are present together with magnetite-dominated deposits. Examples include the Starra (Selwyn) deposit in the Cloncurry district, Gecko and other deposits in the Tennant Creek district, Mantoverde and Teresa de Colmo deposits in the Chilean Iron Belt, Portia deposit in the Curnamona Province of southern Australia, Sue Dianne deposit in the Great Bear magmatic zone, Canada, and Alvo 118 deposit in the Carajás district, Brazil. The hematite-group IOCG deposits represent attractive exploration targets due to commonly higher Au/Cu ratios and higher uranium contents than magnetite-dominated deposits in the same districts. Additionally, the presence of bornite ± chalcocite-rich high-grade copper zones in some hematite-group IOCG deposits may enhance the economics of very deeply buried hematitic deposits relative to lower grade magnetite-dominated deposits at equivalent depth. The Carrapateena deposit, currently being developed in South Australia, is an example where the bornite-chalcopyrite-chalcocite resource is at a depth of ~470 m and extends to ~1420 m below surface (Fairclough, 2005; OZ Minerals, 2019).

This contribution is an update of the review by Skirrow (2010), and compares hematite-group IOCG ± U ore systems in the Gawler Craton (Fig. 1) with other provinces hosting hematite-group IOCG deposits. Recent results are synthesized on the tectonic setting, timing, characteristics of mineralization and alteration, and genesis of hematite-group IOCG ± U ore systems. A revised model is presented for the tectonic setting and hydrothermal evolution of IOCG ± U ore systems in southern Australia that can account for the development of hematite- versus magnetite-dominated alteration and mineralization. Particular reference is made to uranium-rich members of the IOCG family, and the geological 'ingredients' important in formation of uranium-rich IOCG ore systems.

## Regional and Tectonic Settings of Hematite-group IOCG (U) Systems: Gawler Craton Case Study

Hitzman (2000) proposed that most IOCG deposits formed in three "end-member" tectonic settings where the following geodynamic processes were active: (a) anorogenic magmatism, (b) intracontinental "orogenic basin collapse," and (c) extension along subduction-related continental margins. The Olympic Dam deposit has been considered the archetypal example of IOCG deposits in anorogenic or intracontinental rift settings (e.g. Hitzman, 2000; Groves et al., 2005, 2010). However, this notion has been recently challenged, as evidence has emerged for compressive deformation and orogenesis in the Gawler Craton and Curnamona Province to the east around the time of Olympic Dam deposit formation. This tectonism has been attributed to the far-field effects of convergent margin plate tectonic processes, although no consensus has been reached on the position and polarity of subduction (Ferris et al., 2002a; Betts et al., 2003, 2009; Wade et al., 2006; Direen and Lyons, 2007). Within the proposed broad continental margin setting, it has been suggested that magmatism and IOCG systems occurred within a back-arc setting (Ferris et al., 2002a; Betts et al., 2003; Wade et al., 2006) or syntectonically in a foreland basin setting (Hand et al., 2007, 2008). The model of Betts et al. (2003, 2009) involved a mantle plume impinging on a continental margin. The anorogenic intracontinental models appear to be incompatible with recent syn-orogenic continental margin models for the tectonic setting of Olympic

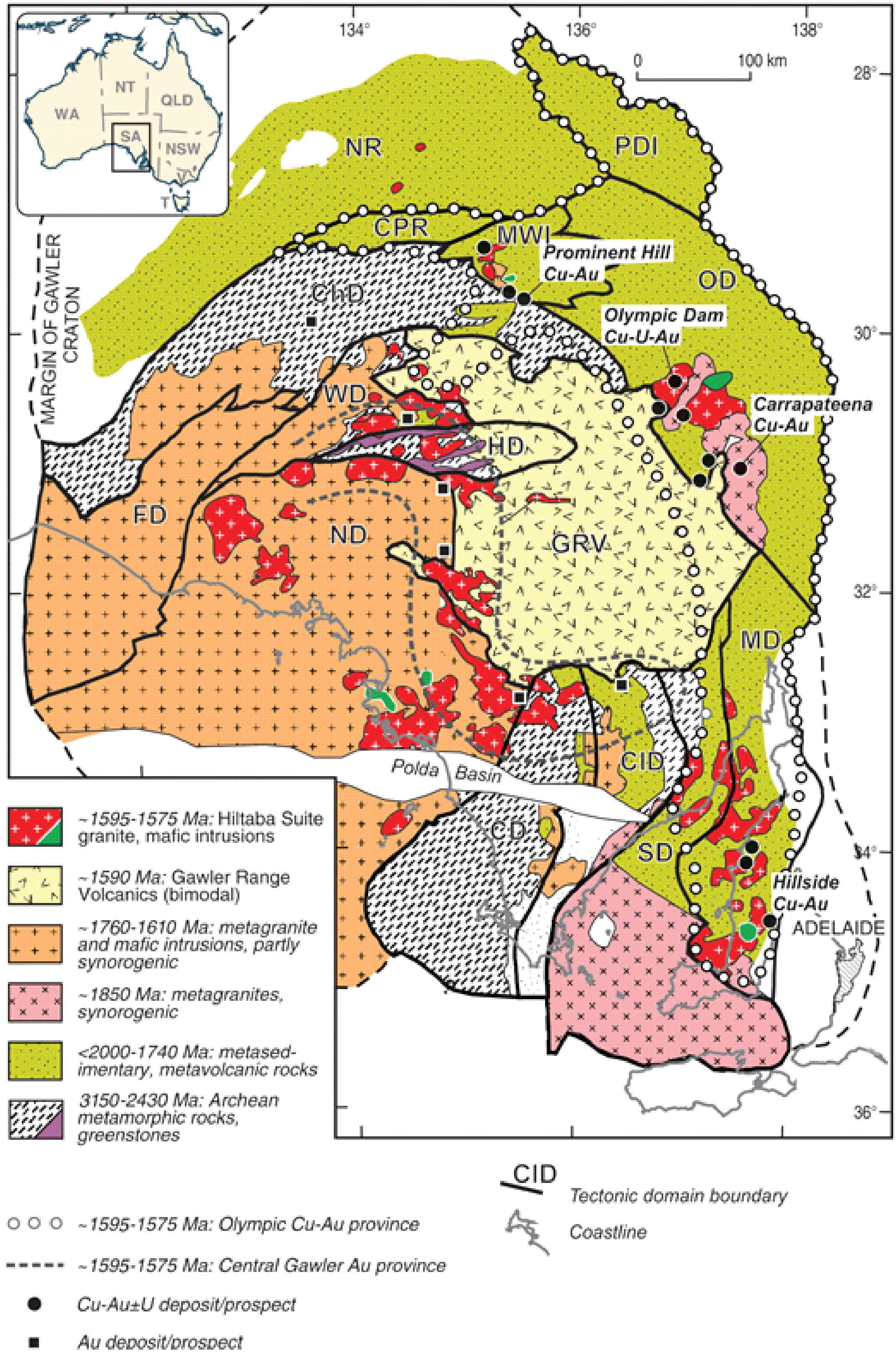


**FIGURE 1**. Geology of the Gawler Craton (pre-Neoproterozoic, excluding Mesoproterozoic Pandurra Formation), tectonic domains, and principal IOCG ± U and gold deposits and prospects in the Olympic Cu-Au (-U) province and central Gawler gold province. Tectono-stratigraphic domains: CD - Coulta, ChD - Christie, ClD - Cleve, CPR - Coober Pedy Ridge, FD - Fowler, GRV - Gawler Range Volcanics, HD - Harris, MD - Moonta, MWI - Mt. Woods Inlier, ND - Nuyts, NR - Nawa Ridge, OD - Olympic, PDI - Peake and Denison Inlier, SD - Spencer. Geology map based on Cowley (2008).

Dam. Moreover, none of the models consider in detail the timing and development of the IOCG ± U systems in both the Gawler Craton and Curnamona Province, nor satisfactorily account for the chemistry of large-volume A-type felsic and K-rich mafic magmatism (Hiltaba Suite and Gawler Range Volcanics (GRV)) that accompany IOCG ± U formation.

Here an alternative hypothesis is presented, updated from Skirrow (2010) and Hayward and Skirrow (2010), that attempts to reconcile the 'anorogenic' and 'orogenic' settings of IOCG systems, involving switching of tectonic style from dominantly compression to extension. Hematite- and magnetite-dominated IOCG deposit styles are placed into this tectonic context. It is suggested that compressional deformation and thickening of cratonic lithosphere were driven by accretion/collision at a distant plate margin. Large-volume bimodal magmatism and extension are viewed as consequences of removal of overthickened mantle lithosphere beneath the central and eastern Gawler Craton. The IOCG deposits are proposed to have formed in a post-collisional, post-subduction setting some hundreds of kilometres inboard of a previously active subduction zone (Skirrow et al., 2018).

Evidence in support of this hypothesis is presented in Figures 2 and 3, and discussed below for three time intervals (see details in Skirrow et al., 2018). These time-space and time-slice figures for the Gawler Craton and Curnamona Province synthesize available geochronology on magmatism, tectonism and IOCG ± U hydrothermal activity for the late Paleoproterozoic to early Mesoproterozoic. The Gawler Craton and Curnamona Province experienced broadly similar thermal, igneous and hydrothermal events between 1660 and 1540 Ma (Fig. 2). The similar A-type geochemistry and palaeomagnetic poles of 1590–1580 Ma volcanic rocks in both terranes (Drexel et al., 1993; M. Wingate, pers. comm., 2006; Wade et al., 2012) strongly suggest that the terranes were contiguous by this time, or even as early as 1730 Ma (Preiss, 2006). Separation of the Gawler Craton and Curnamona Province during Neoproterozoic rifting, and shortening during the Delamerian Orogeny (Cambrian) resulted in their present configuration.

*1630–1595 Ma Events and IOCG Systems*

Cessation of sedimentation in the Upper Willyama Supergroup after 1642 ± 5 Ma (Page et al., 2005) and the onset of the Olarian Orogeny in the southern Curnamona Province at 1610–1620 Ma (Forbes et al., 2005; Rutherford et al., 2007) marked the initial inversion of the Upper Willyama Supergroup basin (Figs. 2, 3). Regional-scale stratabound sodic (albitic) alteration occurred at ~1630 Ma in parts of the Curnamona Province (Teale and Fanning, 2000).

Magnetite-dominant and minor hematitic IOCG mineralization associated with K-Fe alteration, and high-temperature syn-tectonic Au (-Cu-Mo) mineralization (e.g. White Dam deposit), developed in the southern Curnamona Province possibly as early as 1612–1630 Ma (Skirrow et al., 2000; Williams and Skirrow, 2000). However, a slightly younger Re-Os age of ~1603 Ma was determined by re-analysis of a molybdenite sample previously dated at ~1612 Ma (Waukaloo deposit, R. Creaser and R. Skirrow, unpub. data). These results, relative timing and structural relationships of copper-gold mineralization suggest that the IOCG and related Au (-Cu-Mo) systems formed during the Olarian Orogeny crustal shortening and metamorphic event, which peaked at ~1600 Ma (Page and Laing, 1992; Page et al., 2005). The Portia IOCG deposit in the northern Olary Domain is the most hematite-rich and gold-rich of the larger deposits in the district, and occurs in lower metamorphic grade host rocks (upper greenschist facies; Teale and Fanning, 2000) than magnetite-dominant IOCG deposits further south (amphibolite to granulite facies; Clarke et al., 1987). Limited available data suggest that a northward-shallowing depth of crustal exposure broadly corresponds to increasing hematite content of the IOCG deposits (i.e. shallower levels of crust exposed in the north).

In the Gawler Craton, inversion of basin(s) partly age-equivalent with the Upper Willyama Supergroup (Tarcoola Formation) occurred in the period 1650–1590 Ma. Compressive deformation was also recorded in the St. Peter Suite in the Nuyts domain (Fig. 2) which has magmatic arc-like geochemical characteristics and was emplaced syntectonically at 1620–1608 Ma (Ferris et al., 2002a; Hand et al., 2007; Swain et al., 2008). Moreover, a small number of radiometric dates from widely separated locations across the Gawler Craton record low- to high-grade metamorphic events between ~1630 Ma and ~1576 Ma (Figs. 2, 3; e.g. Hand et al., 2007; Forbes et al., 2011 and references therein). Collectively, these observations suggest that tectonism coeval with the earliest stages of the Olarian Orogeny in the Curnamona Province also affected the Gawler Craton from as early as ~1630 Ma. The oldest ages for IOCG-related alteration in the Gawler Craton are ~1620 Ma, for monazite associated with syn-deformational magnetite-biotite alteration, and titanite in sodic-calcic alteration in the Moonta-Wallaroo district (Raymond et al., 2002; Skirrow et al., 2006, 2007; Conor et al., 2010).

The kinematics of the Olarian Orogeny in the Curnamona Province have received considerable attention. While many workers have suggested that D1, D2 and D3 of the Olarian Orogeny were roughly coaxial with northwest-directed tectonic transport, Gibson et al. (2004) proposed that D2 accompanied peak metamorphism at ~1600 Ma and involved northeast to southwest compression (as shown in Fig. 3, 1630–1595 Ma panel for Curnamona Province).

The kinematics in the Gawler Craton during the earliest stages of tectonism at 1630–1595 Ma are unclear. One scenario, extrapolating from the Gibson et al. (2004) model for Curnamona Province, may involve northeast-southwest-directed compression (as speculated in Fig. 3, see arrows for the Gawler Craton). This would be consistent with inferred thrusting on major northwest trending faults imaged in seismic data near the Olympic Dam deposit (Lyons and Goleby, 2005; Drummond et al., 2006), although the timing of this movement is not well constrained by the seismic data alone. In contrast, however, emerging evidence from the Moonta domain suggests that isoclinal folding (possibly at ~1610–1600 Ma) resulted from northwest-southeast-directed compression

(Conor et al., 2010; Brotodewo et al., 2018). This was overprinted by upright folding, shearing, Hiltaba Suite intrusion and calcsilicate-rich alteration, also within a regime of northwest-southeast-directed shortening (Brotodewo et al., 2018; see 1595–1585 Ma interval below).

*1595–1585 Ma Events and IOCG Systems*

By approximately 1595–1585 Ma (Fig. 3), compressive deformation in the Curnamona Province resulted in southeast to northwest tectonic transport, during the D3 final phase of the Olarian Orogeny (Gibson et al., 2004; Page et al., 2005; Preiss, 2006). Regional sodic-calcic alteration (albite-calc-silicate) accompanied D3 in the western parts of the Curnamona Province at ~1585 Ma (Skirrow et al., 2000).

In the Gawler Craton, deformation accompanied the earliest phases of the Hiltaba Suite at ~1595 Ma and possibly very locally affected the lower GRV and coeval sedimentary rocks (e.g. Conor, 1995; Direen and Lyons, 2007; Hand et al., 2007; Conor et al., 2010; Schlegel and Heinrich, 2015; Brotodewo et al., 2018). Stress directions for this early Hiltaba-aged deformation appear to have been similar to the northwest-directed compression documented for D3 in the Curnamona Province (McLean and Betts, 2003; Hand et al., 2007, 2008; Conor et al., 2010; Stewart and Betts, 2010; Brotodewo et al., 2018). This is indicated in Figure 3 by the arrow near the Curnamona Province indicating northwest-directed shortening, which probably also applies to the Gawler Craton.

The granitic host rocks to the Olympic Dam deposit were intruded at ~1595 Ma (Jagodzinski, 2005). By 1592–1587 Ma the voluminous felsic-dominated upper GRV was emplaced in the central and eastern Gawler Craton, and the Benagerie Volcanic Suite erupted in the northern Curnamona Province (Wade et al., 2012; Jagodzinski et al., 2016). The lack of significant deformation of the upper GRV may be due to cessation of compressional deformation with a switch to extension in this part of the Gawler Craton. An extensional tectonic regime in the Gawler Craton between ~1595 Ma and ~1585 Ma is also consistent with the upper crustal emplacement of mafic (in places high-K) and ultramafic intrusions in the Olympic Dam district, Moonta-Wallaroo district, Mt. Woods Inlier and central Gawler Craton (Johnson and Cross, 1995; Budd and Fraser, 2004; Jagodzinski, 2005; Skirrow et al., 2007; Zang et al., 2007; Wade, 2012; Huang et al., 2016). High temperature crustal melting at <30 km depth across much of the Gawler Craton, resulting in the Hiltaba Suite and GRV, is indicative of extraordinary heat transfer from mantle to crust (Creaser and White, 1991). While not definitive in itself, this melting in conjunction with mantle-derived

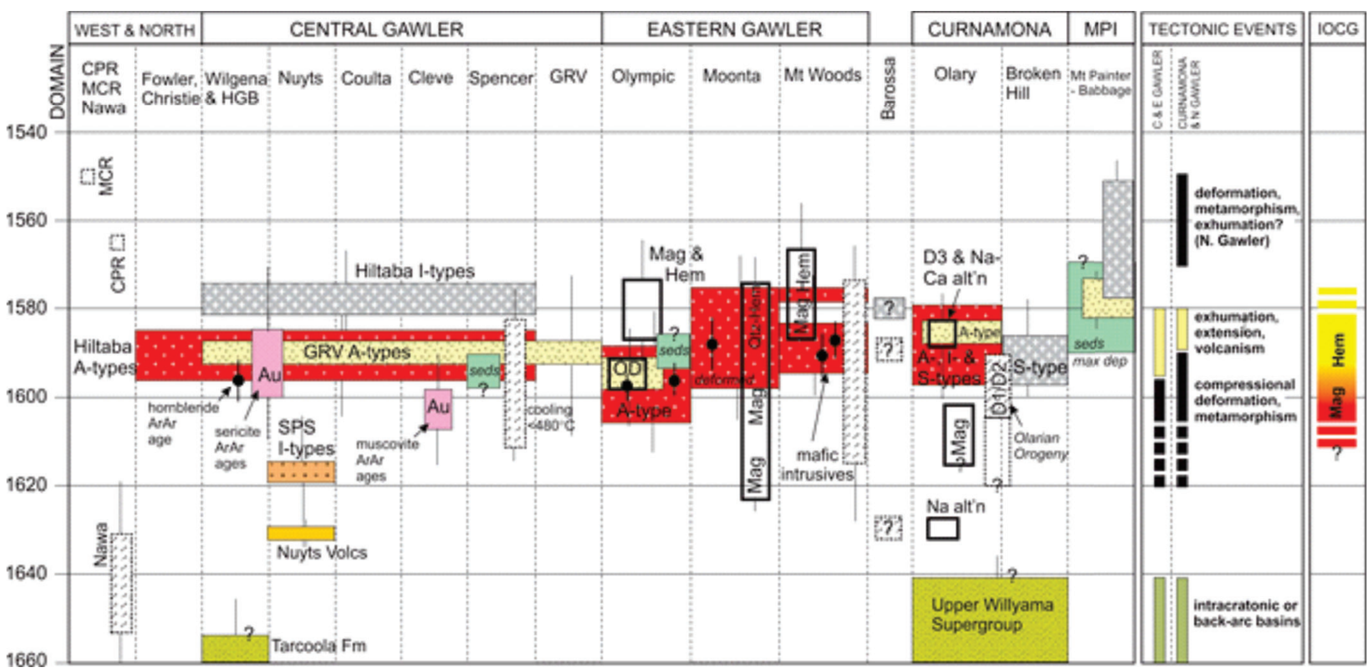


**Figure 2**. Time-space diagram of the Gawler Craton and Curnamona Province in the late Paleoproterozoic to early Mesoproterozoic (ages in Ma, left side), based on geochronological data for IOCG ± U and gold hydrothermal activity, magmatism and metamorphism / cooling events. Boxes with 'whiskers' represent ranges of radiometric ages (boxes) with error bars ('whiskers'). Age ranges of igneous, metamorphic and sedimentary rocks determined by U-Pb methods (mainly ion probe). Dashed boxes represent cooling events, determined from mainly $^{40}Ar/^{39}Ar$ dating. Boxes labelled 'Au' also determined from $^{40}Ar/^{39}Ar$ dating of hydrothermal white mica. Ages of IOCG-related alteration and mineralization determined by U-Pb, $^{40}Ar/^{39}Ar$ and Re-Os dating. A synthesis of interpreted tectonic and IOCG events (this study) is shown at right. Tectonic domains correspond to those in Figure 1. Age ranges for gold-only mineralization in the central Gawler Craton are from Budd and Fraser (2004) and Fraser et al. (2007) including the adjustments suggested by Fraser et al. (2006), and are within error of the Hiltaba-GRV magmatism (see text). Sources of other data: Neumann and Fraser (2007) and references therein, Williams and Skirrow (2000), Budd and Skirrow (2007), Fraser et al. (2007), Skirrow et al. (2006, 2007), Reid et al. (2013), Ciobanu et al. (2013), and Bowden et al. (2017).

magmatism is compatible with an extensional setting. Direct evidence of extension such as normal faulting or basin formation is not well documented, in part due to limited outcrop. Half-grabens filled by GRV have been interpreted in seismic reflection data to the south of the Carrapateena deposit (Carr et al., 2010), supporting the notion of syn-GRV extension. Additionally, several areas of sedimentary deposition at least partly synchronous GRV volcanism have been recognized in the Gawler Craton (Fig. 2, green rectangles labelled ‘seds’). One example is the Roopena area where flat-lying sedimentary units are intercalated with the lower GRV (Curtis et al., 2018). A second example is the ‘bedded clastic facies’ at the Olympic Dam deposit described most recently by Ehrig et al. (2012) and McPhie et al. (2011, 2016). Although previous workers attributed the bedded clastic rocks to volcanic maar-diatreme processes (e.g. Oreskes and Einaudi, 1990; Reeve et al., 1990; Haynes et al., 1995; Johnson and Cross, 1995), new observations led McPhie et al. (2011, 2016) to interpret these sedimentary rocks as remnants of a once-larger fault-controlled basin that was partly coeval with felsic volcanism and which largely post-dated the GRV. The maximum depositional age of the bedded clastic facies is constrained by the ~1590 Ma ages of the youngest detrital zircon populations (McPhie et al., 2016). Such a basin is consistent with at least local crustal extension at, or after, ~1590 Ma. Interpretation of the timing of this basin relative to the main ore-forming events is somewhat controversial, however (see below).

Magnetite-dominant IOCG alteration and mineralization in the Olympic copper-gold province formed initially during

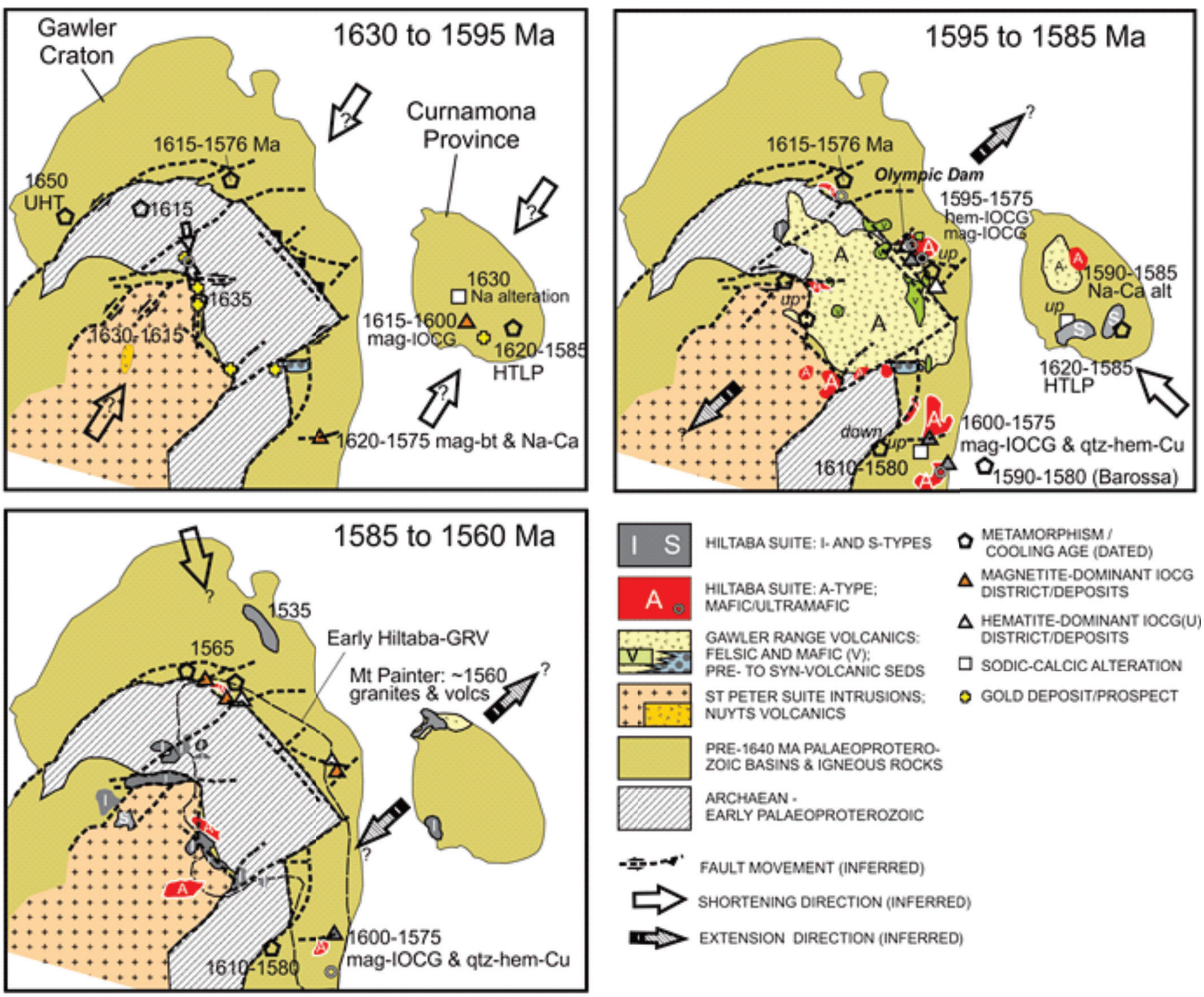


**Figure 3.** Time-slice interpretive maps of the Gawler Craton and Curnamona Province in the late Paleoproterozoic to early Mesoproterozoic, showing spatial and temporal distribution of IOCG±U and gold hydrothermal activity, magmatism, metamorphism / cooling ages, and inferred shortening and extension directions of tectonism. Abbreviations: HTLP - high-temperature low-pressure; UHT - ultra high-temperature metamorphism; mag - magnetite; bt - biotite; qz - quartz; hem - hematite.

ductile to brittle-ductile compressional deformation conditions, as also observed in the Curnamona Province (Fig. 4A, B, C). On the other hand, some magnetite alteration is undeformed and overprints GRV (e.g. Emmie Bluff drill hole SAE7, Bastrakov et al., 2007). Dating of magnetite-related alteration has revealed a spread of ages from ~1620 to ~1570 Ma in the Olympic Cu-Au(-U) province (Fig. 2; Raymond et al., 2002; Skirrow et al., 2006, 2007; Conor et al., 2010; Gregory et al., 2011; Bowden et al., 2017), consistent with relative timing relationships ranging from syn-deformational to post-deformational.

Direct dating of hematitic alteration in the Olympic copper-gold province is more limited, with reconnaissance ages between ~1575 Ma and ~1600 Ma reported by Skirrow et al. (2007). Relative timing relationships and U-Pb geochronology at Olympic Dam suggest that hematite and related Cu-U-Au mineralization developed within the Olympic Dam Breccia Complex (ODBC) at 1590–1595 Ma (Johnson and Cross, 1995; Jagodzinski, 2005). This is supported by dating of uranium bearing hematite in the ODBC by Pb-Pb isotopic methods (LA-ICPMS) which has yielded ages of 1590 ± 8 Ma and 1577 ± 5 Ma (Ciobanu et al., 2013). Elsewhere, further support for 1600–1575 Ma IOCG-related hematitic alteration is provided by a Re-Os age of 1586 ± 8 Ma for molybdenite within a hematite-copper sulphide hydrothermal assemblage at the Vulcan copper-gold prospect (Reid et al., 2013). Additionally, $^{40}Ar/^{39}Ar$ dating of hydrothermal white micas associated with hematite and sulphide mineralization at the Prominent Hill deposit yielded ages of 1575 ± 10 Ma and 1569 ± 10 Ma for the least isotopically disturbed samples, which are regarded as minimum ages of sericite alteration (Bowden et al., 2017).

Unlike paragenetically early magnetite-bearing alteration in the Olympic Cu-Au (-U) province, hematitic alteration shows no evidence of control by penetrative ductile deformation fabrics. Rather, brittle deformation was dominant during hematitic alteration (e.g. brecciation, brittle faulting, open space filling). Kinematics during this brittle deformation have been reported only for the Olympic Dam deposit, where early stages of ODBC formation were controlled by west-northwest-trending regional faults with dextral components of strike-slip movement (Drexel et al., 1993).

### *1585–1560 Ma and Later Thermal Events*

Most intrusions of the Hiltaba Suite younger than ~1585 Ma are of I-type rather than A-type composition, and most were emplaced in areas peripheral to the domain of early A-types, in the western and northern Gawler Craton and in the Curnamona Province (Ludwig and Cooper, 1984; Budd, 2006). In the period ~1575 to ~1560 Ma, magmatism and medium- to high-grade metamorphism appears to have been restricted mainly to the northern Gawler Craton and northern Curnamona Province within the Mt. Painter and Babbage inliers (Figs. 2, 3). The reasons for this changing space-time pattern of magmatism are unclear. However, I-type Hiltaba Suite granitoids yield lower zircon crystallization temperatures than the A-types (Budd, 2006). Their temporal and spatial distribution on the periphery of the earlier thermal anomaly represented by the A-types may reflect lower temperature crustal melting and/or different sources (Budd, 2006), which ultimately may relate to migration of the locus of lithospheric thinning (Skirrow et al., 2018). Hand et al. (2007) viewed the metamorphism in the northern and western Gawler Craton during 1570–1540 Ma as part of the Kararan Orogeny. They distinguish this event from earlier deformation associated with the Hiltaba Suite, which they considered to have been wholly compressional.

Gold-dominated shear-hosted mineralization in the central Gawler Craton appears to be spatially associated with the I-type Hiltaba Suite intrusions (Budd, 2006; Budd and Skirrow, 2007; Fraser et al., 2007). Initial studies indicated that minimum ages of sericite alteration associated with gold were ~1580 Ma (Budd and Fraser, 2004; Fraser et al., 2007), suggesting a temporal association with the I-type Hiltaba Suite granitoids. However, intercalibration of $^{40}Ar/^{39}Ar$ and U-Pb timescales and re-evaluation of $^{40}Ar/^{39}Ar$ ages for gold-related sericite alteration suggests that gold mineralization could have formed at ~1594 Ma (Fraser et al., 2006) with uncertainties of ±3 Ma (analytical + J-parameter) or ±6 Ma (total uncertainties; Fraser et al., 2006; Bowden et al., 2017). Formation of gold mineralization up to a few million years prior to the GRV, during the earliest stages of emplacement of the Hiltaba Suite and associated compressive deformation, would be consistent with relative and absolute timing constraints. Thus, gold mineralization in the central Gawler Craton could be similar in timing to some syn-tectonic magnetite-dominated alteration in the Olympic Cu-Au (-U) province to the east. Further work is required to better constrain the timing and origins of the gold-dominated shear-hosted systems in the central Gawler Craton.

There is growing evidence of modification of the 1595–1575 Ma IOCG hydrothermal systems in the Olympic copper-gold province. For example, in the Moonta-Wallaroo district, K-Ar data record ages from ~1550 to ~1430 Ma for biotite, muscovite and amphibole (Webb et al., 1986). Between the Olympic Dam and Prominent Hill deposits, sericite alteration and igneous K-feldspar in Neoarchean tonalite record $^{40}Ar/^{39}Ar$ ages of ~1600 and ~1565 Ma, respectively, which represent the timing of (hydro)thermal activity and/or cooling to closure temperatures (Reid et al., 2017). Hydrothermal monazite at the Oak Dam copper-gold deposit records an age of 1455 ± 20 Ma (U-Pb, LA-ICPMS), interpreted as a reset age by Davidson et al. (2007). At the Olympic Dam deposit, numerous post-1590 Ma ages have been reported. These include: a Re-Os isochron age of 1258 ± 28 Ma from whole-rock and mineral separates, which was regarded by McInnes et al. (2008) as a reset age; and Sm isotope data indicating substantial introduction or re-deposition of uranium and/or repeated fractionation of uranium and samarium isotopes since ~1590 Ma (Kirchenbaur et al., 2016). Moreover, sedimentary material has been recently reported from within the ODBC that was likely derived from the post-1590 Ma Pandurra Formation, which has ~1440 Ma diagenetic ages (Cherry et al., 2017). McPhie et al. (2011, 2016) argued that the ODBC and ore formation at Olympic Dam occurred after the formation of the bedded clastic facies. However, an alternative scenario consistent with the geology and geochronology is that most if not all of the 'bedded clastic facies' were deposited after the main hematitic brecciation and ore-forming event(s), and were subsequently down-faulted (along with parts of the Pandurra Formation) into the present positions within the ODBC. Minor quantities of sulphides and other hydrothermal minerals interstitial to framework grains in the bedded clastic facies (McPhie et al., 2016) could be explained by local redistribution of metals and sulphur within the ODBC during relatively minor hydrothermal activity post-dating the bedded clastic facies.

In summary, the available evidence supports a model in which the vast bulk of the iron oxides, copper, gold, REE and probably uranium were introduced during the formation of the ODBC at 1595–1590 Ma. Hydrothermal activity may have continued at least until ~1575 Ma, as documented elsewhere in the region, along with relatively local basin development. During this period and/or after deposition of the Pandurra

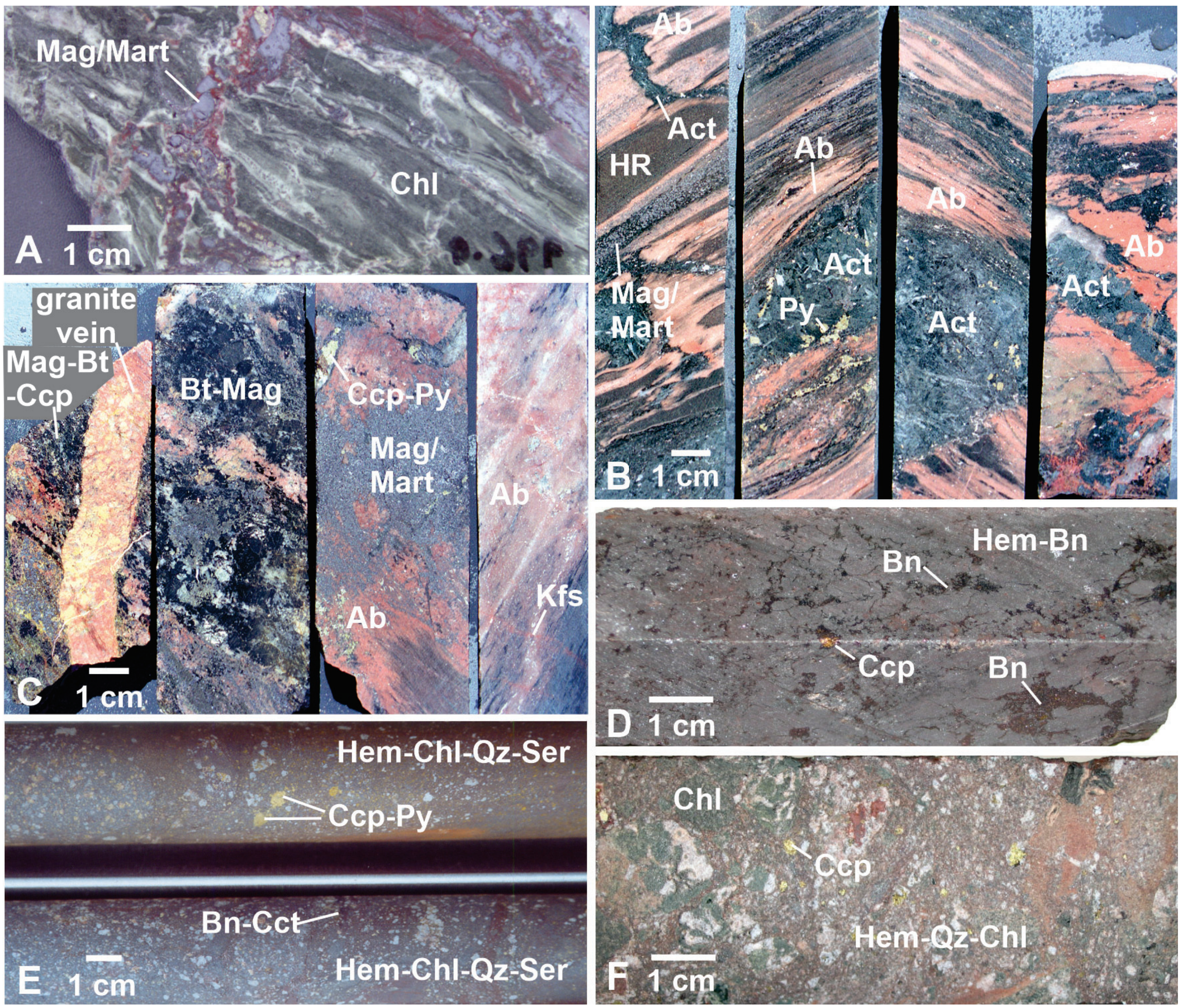


FIGURE 4. Drill cores from the Olympic Cu-Au (-U) province, Gawler Craton. Core diametre 4-5 cm. **A.** Folded syntectonic veins of magnetite replaced by martite, within chlorite-altered metasedimentary rocks; Emmie Bluff. **B.** Four pieces of drill core, showing syn- to post-tectonic actinolite veins and magnetite/martite replacements with albitic alteration aureoles; Moonta-Wallaroo district. **C.** Four pieces of drill core, showing magnetite and associated minor chalcopyrite and biotite-magnetite-chalcopyrite alteration cut by granite vein; late-stage thin K-feldspar veinlets shown in core at right; Moonta-Wallaroo district. **D.** Massive hematite rock with high-grade bornite and minor chalcopyrite mineralization; Carrapateena deposit, drillhole CAR002. Image with permission of OZ Minerals Pty Ltd. **E.** Olympic Dam mineralization, showing transition from chalcopyrite-pyrite mineralization to bornite-chalcocite mineralization within hematite-chlorite-quartz-sericite breccia. Image with permission of BHP. **F.** Breccia of chloritized quartz-bearing granitoid with abundant hematite and minor chalcopyrite; Carrapateena deposit, drillhole CAR002. Image with permission of OZ Minerals Ltd. Abbreviations: Act - actinolite; Ab- albite; Bn - bornite; Bt - biotite; Cc - chalcocite; Ccp - chalcopyrite; Chl - chlorite; Hem - hematite; HR - host rock; Kfs - K-feldspar; Mag/mart -magnetite/martite; Py - pyrite; Qz - quartz.

Formation, extensional faulting may have led to down-faulting of post-1590 Ma basinal rocks. Localized redistribution of copper, uranium and other metals appears to have continued within the ODBC during multiple events as late as the Delamerian Orogeny (Kirchenbaur et al., 2016).

*Exhumation and IOCG (U) Systems in Southern Australia*

In both the Gawler Craton and northern Curnamona Province there is fragmentary evidence for rapid exhumation around the periods of the switch in tectonic regime. In the eastern Gawler Craton, parts of the Burgoyne Batholith, which hosts the Olympic Dam Cu-U-Au deposit, were emplaced at depths of 4–8 km at 1595–1597 Ma (Creaser, 1996; Jagodzinski, 2005). Formation of the ODBC and associated IOCG mineralization at 1595–1590 Ma in a subvolcanic setting (Johnson and Cross, 1995; Jagodzinski, 2005; Skirrow et al., 2007) implies several kilometres of exhumation within a few million years. In the northwestern Curnamona Province, upper greenschist facies rocks metamorphosed during the Olarian Orogeny (1620–1585 Ma) were exhumed then unconformably overlain at 1585–1580 Ma by the Benagerie Volcanics (Fanning et al., 1998; Korsch et al., 2006; M. Wingate, pers. comm., 2006). This inferred exhumation may have been very significant for development of hematite- versus magnetite-dominated IOCG ± U systems (see Processes, below).

*Geodynamic Models – Southern Australia*

A number of geodynamic and tectonic models have been published over the past two decades for the Gawler Craton, within the context of the Australian Proterozoic. As noted earlier, most of these models place the Gawler Craton in a continental margin or back-arc plate tectonic setting in the late Paleoproterozoic – early Mesoproterozoic, with or without the influence of a mantle plume. Compressive deformation is attributed to accretion/collision of an island arc, oceanic plateau or crustal block(s) with the southwest margin of Gawler Craton at 1630–1600 Ma (Ferris et al., 2002a; Betts and Giles, 2006; Betts et al., 2009) or at the northern margin (Wade et al., 2006). In these models, the Hiltaba Suite and GRV were emplaced in a continental back-arc setting (Ferris et al., 2002a; Betts and Giles, 2006; Wade et al., 2006; Betts et al., 2009). A foreland basin model for the GRV was proposed by Hand et al. (2007, 2008), involving northwest-southeast shortening. Slab roll-back (over-riding a mantle plume) and extension of the continental margin were suggested by Betts et al. (2003, 2009) to have followed the shortening. However, mantle plumes in continental settings characteristically produce mafic-dominated and, in places, bimodal magmatism and generally are not associated with widespread and contemporaneous orogenesis. Furthermore, the A-type geochemistry, large volume, and non-arc-like spatial distribution of the GRV and Hiltaba Suite felsic and mafic intrusions are unlike typical igneous suites in magmatic arc or back-arc or foreland basin settings (Budd, 2006).

Ferris et al. (2002b) mentioned the notion of lithospheric thinning by delamination or slab breakoff, and recognized both compressive and extensional tectonism during Hiltaba Suite-GRV magmatism. A continental back-arc setting was proposed for this magmatism. In the 2010 version of the present contribution, this concept of lithospheric delamination was broadened to include the Curnamona Province, and the IOCG systems were placed within an intracontinental or 'far-field continental back-arc' setting, distal from active subduction. Subsequent work, involving integration of geological observations, geochemical and isotopic compositions of mafic igneous rocks, new magneto-telluric and seismic velocity data for the mantle lithosphere, and mantle-derived xenolith/xenocryst data, has revealed new insights on the tectonic and geodynamic setting of the IOCG deposits in the Gawler Craton and Curnamona Province (Skirrow et al., 2018). Accordingly, IOCG formation is now viewed as forming in a post-subduction, syn- to post-orogenic setting, several hundred kilometres inboard of the former active continental margin represented by the 1620–1610 Ma St. Peter Suite and ~1630 Ma Nuyts Volcanics (Fig. 5; Skirrow et al., 2018).

The trace element compositions of the mafic volcanic and intrusive rocks of GRV- and Hiltaba Suite-age appear to vary spatially from arc-like (e.g. high Th/Yb) compositions in the central Gawler Craton to less arc-like and more MORB-like compositions (e.g. lower Th/Yb) in areas peripheral to the central part of the craton (Skirrow et al., 2018). However, rather than a contemporary subduction-modified mantle source for the arc-like signatures in the central Gawler Craton, it is suggested that these compositions are the result of re-melting of previously metasomatized and refertilized lithospheric mantle. Such modification including hydration, which is inferred from the unusually high electrical conductivities and low seismic velocities in the central Gawler lithospheric mantle, was most likely related to subduction during possibly multiple events since the Archean (Skirrow et al., 2018). The trigger for re-melting of the metasomatized lithospheric mantle is proposed to have been a collision between an oceanic plateau (e.g. Betts et al., 2009), island arc, or microcontinent with the southwest margin of the Gawler Craton during and/or soon after the formation of the 1620–1610 Ma St. Peter Suite. This led to lithospheric thickening and shortening represented by the Olarian Orogeny in the Curnamona Province, peaking around ~1600 Ma. The locus of the shortening may have been lithosphere that was weakened or thinned by earlier subduction-related processes (e.g. Hyndman et al., 2005) and/or by radiogenic heating (McLaren et al., 2005). Previously refertilized and hence relatively dense lithospheric mantle, along with relatively weak hydrous-metasomatized lithospheric mantle, became gravitationally unstable during this event, and began to detach or founder (Fig. 5). Details of this process, and examples elsewhere in the world, are given by Skirrow et al. (2018).

As a consequence of asthenospheric upflow filling space formerly occupied by (foundered) lithosphere and decompressional partial melting, the sub-Gawler and sub-Curnamona lithospheric mantle and crust were invaded by melts with MORB-like compositions. Previously refertilized and metasomatized zones of lithosphere were particularly favourable for re-melting (via conductive heat transfer and/or decompression), yielding mafic volcanic rocks of the GRV and Hiltaba Suite-aged mafic intrusions in the central Gawler Craton with geochemical and isotopic signatures reflecting the subduction-modified mantle sources. Continued and extensive foundering or 'delamination' of mantle lithosphere resulted in enormous transfer of heat from the mantle to the base of the crust, where large-scale partial melting produced the Hiltaba Suite granitoids and GRV and BVS felsic volcanic rocks.

Although mild extension is a consequence of lithospheric removal, crustal thickness may not decrease significantly over the region of lithospheric detachment (Houseman and Molnar, 1991). Hence, crustal melting in this model does not require major amounts of crustal thinning (cf. Drummond et al., 2006). The lack of seismic reflection evidence for a lower-crustal mafic underplate beneath the Olympic Dam deposit was noted by Drummond et al. (2006). However, this is not inconsistent with a model of lithosphere detachment. For example, Schurr

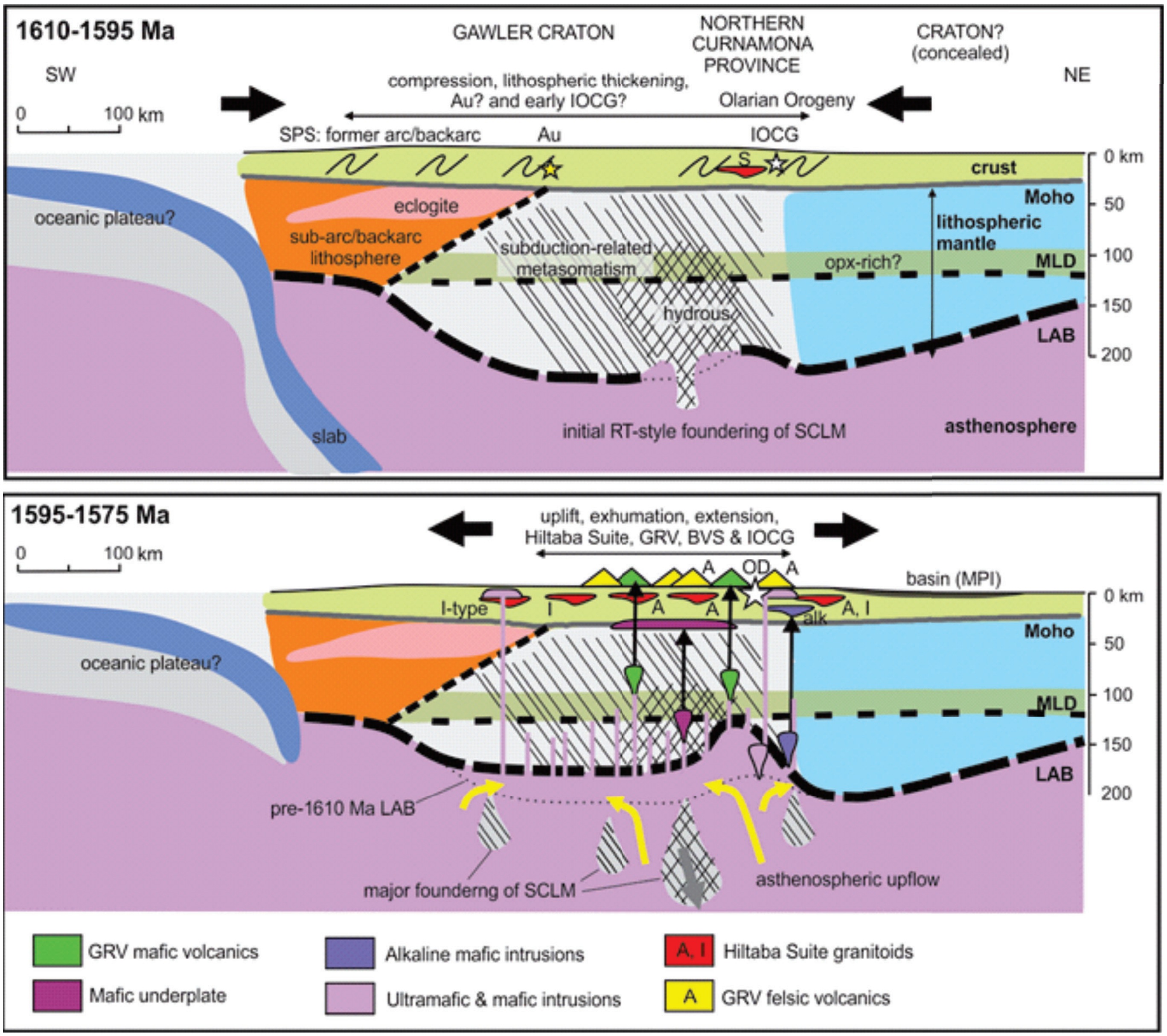


**Figure 5**. Schematic tectonic cross section of the Gawler Craton and Curnamona Province at 1610–1595 Ma and during the main IOCG ore-forming events at 1595–1575 Ma. A crude spatial zoning of A- and I-type Hiltaba Suite and GRV magmatism is indicated. Lower crustal melting to produce the Hiltaba Suite and GRV felsic volcanics was driven by mafic and ultramafic magmatism related to detachment and removal of mantle lithosphere. Synchronous lithospheric shortening at the margins of the orogen and mild crustal extension above the thinned lithosphere developed in an overall compressive setting, perhaps driven by accretion/collision at a continental margin to the southwest (present day coordinates). A post-subduction setting of IOCG ore formation distal from a former active continental margin is suggested (see text). Figure slightly modified from Figure 12 in Skirrow et al. (2018) with permission of Wiley Publishing.

et al. (2006) seismically imaged detached lithosphere and crustal melt zones in the back-arc of the central Andes, yet no lower-crustal mafic underplate is evident in seismic reflection data (ANCORP, 1999).

Other geological consequences of mantle lithosphere removal, in addition to crustal melting and high-K magmatism, include: uplift and exhumation; shortening followed by extension; and coeval crustal extension and compression in different parts of the tectonic system (e.g. Kay and Kay, 1993; Schott and Schmeling, 1998; Houseman and Molnar, 2001). The tectonic evolution outlined above for the Gawler Craton and Curnamona Province is consistent with lithosphere removal, whether by Rayleigh-Taylor type convective processes or 'delamination'.

Based on studies of the Gawler Craton, it is proposed that the post-subduction, syn- to post-orogenic setting is especially favourable for IOCG ore-forming systems because this setting permits the spatial and temporal coincidence of: (a) high geothermal gradients in the upper crust, capable of driving (b) widespread and deep circulation of hydrothermal fluids of diverse origins; (c) mixing of deep-sourced and shallow-sourced fluids; and (d) availability of favourable sources of Fe, Cu, Au and U (e.g. mafic and felsic igneous rocks) in the upper crust. Whether the iron and ore metals in the IOCG deposits are derived via leaching of host rocks or via direct transfer from magmas via magmatic-hydrothermal fluids to the ore deposits is a subject of continuing debate.

## Tectonic Settings of Other Hematite-group IOCG Ore Systems

The Gawler Craton appears to be unique among IOCG provinces in the dominance of hematite-rich over magnetite-rich IOCG deposits, and also in its endowment of Cu, Au and U. There are, however, hematite-rich IOCG deposits in several other IOCG provinces, including (from oldest to youngest): Great Bear magmatic zone, Northwest Territories, Canada; Tennant Creek district in the Northern Territory of Australia; Olary Domain in the Curnamona Province, South Australia; Cloncurry district in the Mt. Isa orogen of northwest Queensland; Chilean Iron Belt. The settings of these districts are briefly reviewed below.

The Paleoproterozoic Great Bear magmatic zone contains a wide range of iron oxide and alkali alteration systems which include several relatively small (as presently known) iron oxide-rich deposits of Au, Cu, Co and Bi (Goad et al., 2000; Mumin et al., 2010; Corriveau et al., 2016; Montreuil et al., 2016a, b). Two of the larger deposits are the NICO Au-Co-Bi deposit (33 Mt at 1.0 g/t Au, 0.11% Co, 0.14% Bi, 0.04% Cu, proven + probable reserves; Burgess et al., 2014) and the Sue Dianne Cu-Ag(-Au) deposit (8.4 Mt at 0.8% Cu, 0.07 g/t Au, 3.2 g/t Ag, indicated resource; Hennessey and Puritch, 2008).

The NICO deposit is magnetite-rich, arsenopyrite-bearing, and relatively reduced (with minor pyrrhotite, loellingite, native Bi). The earliest stages of the deposit formed during the waning stages of the Calderian orogeny at brittle-ductile deformation conditions (Montreuil et al., 2016a, b). Later stages of the NICO deposit, the magnetite-hematite breccia-hosted Sue Dianne deposit, and numerous IOCG occurrences are interpreted to have formed under brittle deformation conditions (Montreuil et al., 2016b). The change in mineralization style has been correlated with a switch from compressional to transtensional tectonism and a transition from dominantly syn-collisional magmatism at 1880–1873 Ma to volcanic arc magmatism at a continental margin at 1873–1866 Ma, and finally to K-rich magmatism with within-plate affinity at 1866–1855 Ma (Mumin et al., 2014; Montreuil et al., 2016a; Ootes et al., 2017).

In the Tennant Creek district, magnetite ironstones developed during compressional deformation at brittle-ductile mesothermal (greenschist facies) conditions, whereas later hematite alteration is associated generally with brittle deformation (Skirrow, 2000). The tectonic setting of the compressional deformation at 1850–1845 Ma is unclear, with intracontinental and distal back-arc settings proposed (Etheridge et al., 1987; Betts and Giles, 2006). It is notable that this orogenesis was followed closely by bimodal volcanism and sedimentation of the Ooradidgee Group, (1845 ± 7 to 1827 ± 9 Ma; Compston, 1995), which exhibits less deformation than the older rocks. Although further work is required, these relationships are consistent with a switch from a compressional to an extensional or transtensional setting. Hence, by analogy with the Gawler Craton, the Tennant Creek district may have potential for shallow-crustal hematite-rich IOCG ± U ore systems within volcanic rocks of the Ooradidgee Group (which post-dates the main 1850–1845 Ma deformation event).

The IOCG deposits of the Cloncurry district, including the hematite-rich Starra gold-copper deposit, are generally considered to have formed at >5 km depth during the Isan Orogeny (D2) at 1600–1590 Ma (e.g. Osborne) and also later in the Isan Orogeny (D4) between ~1540 and ~1500 Ma (e.g. Williams, 2010b; Duncan et al., 2011; Babo et al., 2017 and references therein). The second period of IOCG ore formation (during D4) was broadly coeval with the A-type Williams-Naraku Suite granitoids (see Babo et al., 2017, for summary of geochronology). There are some similarities in the evolution of the Mt. Isa orogen, Gawler Craton and Curnamona Province, including the presence of ~1850 Ma syn-orogenic granitoids, sedimentation terminating at 1660–1640 Ma, and major tectonothermal events at 1600–1590 Ma (Duncan et al., 2011; Fitzherbert and Downes, 2017; Reid, 2017). However, the Cloncurry district appears to lack high-volume magmatism during the 1600–1590 Ma D2 orogenesis, and the Gawler Craton and Curnamona Province appear to lack the high-volume 1540–1500 Ma felsic intrusive magmatism of the Eastern Succession in the Mt. Isa orogen. Notwithstanding, it is interesting to note that a possible switch from compressional to extensional regimes has been recorded locally in the Cloncurry district between ~1530 Ma (D4) and ≤1500 Ma (D5; Austin and Blenkinsop, 2010). The broader significance of this finding has yet to be determined, but this possible switch in tectonic style is remarkably similar to those associated with

IOCG deposit formation described above for the Gawler Craton, Great Bear magmatic zone and Tennant Creek district (Montreuil et al., 2016a).

The tectonic setting and evolution of major Cretaceous IOCG districts in the Andes appears to be somewhat different from the Australian and Canadian Proterozoic examples. Back-arc and intra-arc extensional settings have been proposed for the Late Jurassic to Early-Mid Cretaceous magnetite- and hematite-group IOCG systems of the Andean continental margin (e.g. Sillitoe, 2003; Richards and Mumin, 2013; Richards et al., 2017). IOCG mineralization in the Mantoverde district is thought to be related to transtension along the Atacama Fault Zone, with local dilation controlling the location of brecciation and mineralization (Benavides et al., 2007). Major inversion occurred in the Late Cretaceous, evidently postdating (rather than pre-dating) the larger magnetite- and hematite-group IOCG deposits. For the major IOCG deposits at least (e.g. Candelaria, Mantoverde, Raúl Condestable) this evolution appears to differ from the Australian Proterozoic provinces. In the latter, magnetite-group and some deeper hematite-group IOCG deposits are closely associated with compressional deformation, whereas shallow-crustal hematite-group IOCG deposits form where compression ceases and/or where there is a switch to extension (Skirrow, 2010). Nevertheless, in the Andes there are several small IOCG systems that developed in the Late Cretaceous during extension that immediately followed the major inversion event (Sillitoe, 2003), echoing the Gawler Craton-Curnamona Province scenario.

## Alteration and Mineralization Characteristics of Hematite-group IOCG (U) Ore Systems

Hematite and magnetite are present in IOCG ± U deposits in a continuum of ratios from magnetite-only through magnetite+hematite to hematite-only (Williams, 2010a). The timing of hematite relative to magnetite varies among IOCG systems; most commonly there is a sequential development of magnetite then hematite, but in some deposits the sequence is hematite-magnetite-hematite. This spectrum of hematite occurrence together with zoning of alteration and mineralization, provide important constraints on IOCG ± U genesis and exploration. The Olympic Cu-Au (-U) province in the eastern Gawler Craton is instructive in containing representatives of both magnetite- and hematite-group end-member deposit styles. Alteration and mineralization characteristics are described below and compared with other districts containing hematite-group IOCG ± U deposits.

*Gawler Craton*

The Olympic Cu-Au (-U) province comprises three known IOCG (U) districts, each with distinctive patterns of regional- and deposit-scale hydrothermal alteration and mineralization (Skirrow et al., 2002, 2007; Bastrakov et al., 2007). The Olympic Dam district contains the Olympic Dam Cu-U-Au deposit (10.73 Bt at 0.72% Cu, 0.30 g/t Au, 0.23 kg/t $U_3O_8$, 1.28 g/t Ag, measured + indicated + inferred resource, BHP, 2018), the Carrapateena copper-gold deposit (970 Mt at 0.5% Cu, 0.2 g/t Au, 3 g/t Ag, measured + indicated + inferred resource, OZ Minerals, 2019), and numerous subeconomic IOCG deposits and prospects. The recently discovered Fremantle Doctor hematite breccia-hosted deposit, located ~2 km northeast of Carrapateena, contains an inferred resource of 104 Mt at 0.7% Cu, 0.5 g/t Au and 3 g/t Ag (OZ Minerals, 2018). The Mt. Woods district, to the northwest of Olympic Dam, hosts the Prominent Hill copper-gold deposit (160 Mt at 1.0% Cu, 0.7 g/t Au, 3 g/t Ag, measured + indicated + inferred resources, OZ Minerals, 2017) immediately south of the Mt. Woods Inlier. The third IOCG district, Moonta-Wallaroo, has witnessed the discovery of the Hillside copper-gold deposit (Conor et al., 2010) since the 2010 version of this paper. This deposit contains 337 Mt at 0.60% Cu, 0.14 g/t Au (measured + indicated + inferred resources; Rex Minerals, 2015). The district also hosts several small copper-gold deposits that were mined up to the 1980s, some of which are IOCG-related whereas others are probably not. The Olympic Dam and Prominent Hill deposits are currently being mined, whereas the Carrapateena deposit is expected to commence production in 2019.

Three principal types of metasomatism are recognized in the Olympic Cu-Au (-U) province, each characterized by distinctive hydrothermal mineral assemblages (Table 1; Skirrow et al., 2002, 2007; Bastrakov et al., 2007). The three main assemblages and their sub-types are described briefly below.

The Na-Ca-Fe, $Fe^{2+}$-K and $Fe^{3+}$-$H_2O$-$CO_2$ metasomatic types are broadly equivalent to the sodic-calcic, potassic and hydrolytic alteration types, respectively, described in other IOCG provinces globally (e.g. Barton and Johnson, 1996; Hitzman, 2000; Williams et al., 2005; Corriveau et al., 2010, 2016; Williams, 2010a; Barton, 2014). The terminology used for the Gawler Craton is slightly modified from the generic terms used elsewhere, in order to accurately represent the major observed hydrothermal mineral assemblages, and corresponding element metasomatism. For example, ‘hydrolytic’ alteration in the Gawler Craton includes locally abundant hematite and carbonate, as well as hydrous phases. Hence the assemblage hematite-sericite-chlorite-carbonate, or $Fe^{3+}$-$H_2O$-$CO_2$ metasomatism, are used in preference to ‘hydrolytic’.

The Na-Ca-Fe metasomatism is represented in the Olympic Cu-Au (-U) province by assemblages of hydrothermal albite-calsilicate (actinolite and/or diopside) ± magnetite, commonly with minor titanite and scapolite. This alteration typically forms kilometre-scale regional alteration zones in both the Moonta-Wallaroo and Mt. Woods IOCG ± U districts, but sodic alteration is much less evident in the Olmpic Dam district. The rarely observed hydrothermal albite in this district may represent relicts of sodic metasomatism surviving after widespread K-feldspar overprinting (Bastrakov et al., 2007). At the granite-hosted Olympic Dam Cu-U-Au deposit, early albitization of plagioclase has been described at the periphery and deeper within the alteration system (Mauger et al., 2016; Kontonikas-Charos et al., 2017). However, mass-balance calculations indicate that there was little or no sodium addition at the scale of sampling (1 metre drill core samples), unlike regional albitic alteration zones in some other IOCG provinces (Kontonikas-Charos et al., 2017). In the Moonta-Wallaroo district, Na-Ca ± Fe metasomatism is characterized by pervasive albite-actinolite ± magnetite ± diopside regional alteration of metasedimentary and metavolcanic rocks (Conor, 1995; Raymond et al., 2002; Conor et al., 2010). The albite-actinolite/diopside ± magnetite alteration is strikingly similar to assemblages in the Cloncurry, Norbotten (northern Sweden) and Curnamona IOCG provinces (Conor, 1995; Raymond et al., 2002; Williams, 2010b).

Garnet-bearing, 'skarn'-like mineral assemblages are relatively uncommon in the Olympic Cu-Au (-U) province as a whole (e.g. Gow et al., 1994; Skirrow et al., 2002; Reid et al., 2011; Fabris et al., 2018), but are an important host to copper-gold mineralization at the Hillside deposit (Conor et al., 2010; Ismail et al., 2014). Here, copper-gold mineralization has been described as overprinting (with hematite) a range of 'skarn' types, which include combinations of: albite- and/or K-feldspar, pyroxene (hedenbergite-diopside), garnet (andradite-grossular), magnetite, allanite, titanite, clinozoisite and actinolite (Conor et al., 2010; Ismail et al., 2014). At the Emmie Bluff deposit in the southern part of the Olympic Dam district veins with clinopyroxene, garnet, magnetite, amphibole, allanite and other minerals cut GRV felsic volcanic rocks (Gow et al., 1994). At the Punt Hill prospect (~40 km south of Carrapateena) a texturally early assemblage of grossular-rich garnet and diopside replaced laminated metasedimentary rocks (probably Wallaroo Group), and was interpreted as a prograde skarn assemblage by Reid et al. (2011). These authors reported a Sm-Nd age of 1577 ± 7 Ma for garnet and clinopyroxene separates. The early assemblage was overprinted by a diverse group of hydrothermal minerals including andraditic garnet, calcite, quartz, K-feldspar, amphibole, Cu-Zn-Pb sulphides, gold, hematite, chlorite, fluorite, apatite, barite, anhydrite and tourmaline (Reid et al., 2011; Fabris et al., 2018). Hematitic breccias and veins of quartz-K-feldspar-chlorite-hematite are also present although magnetite is almost absent and overall iron oxide content is low. The best intersection at Punt Hill is 159 m at 0.47% Cu, 0.1 g/t Au, 5 g/t Ag, 0.48% Zn and 0.12% Pb; copper mineralization is represented by bornite, chalcocite and chalcopyrite. Reid et al. (2011) and Fabris et al. (2018) interpreted the Cu-Zn-Pb mineralization as part of a retrograde skarn assemblage, similar to those observed in 'oxidized copper-gold skarn' deposits worldwide. More broadly in the Olympic copper-gold province the origins of the skarn alteration assemblages and relationships with the IOCG hydrothermal systems remain unclear, although direct magmatic-hydrothermal processes were envisaged by Ismail et al. (2014) and implied by Reid et al. (2011). However, it is also possible that some of the skarn types are variants of the Na-Ca-Fe metasomatic assemblage described above. In any case, the earlier skarn assemblages appear to be largely barren and were locally overprinted by Cu-Au (-Zn-Pb) associated with hematite and in places chlorite.

**Table 1.** Alteration mineral assemblages in IOCG ± U districts of the Olympic Cu-Au (-U) province, Gawler Craton (see text for references).

| District | Metasomatism type, and minerals | | |
|---|---|---|---|
| | Na-Ca-Fe | $Fe^{2+}$-K | $Fe^{3+}$-$H_2O$-$CO_2$ |
| **Mt Woods Inlier (MWI) & Prominent Hill deposit** | MWI: Ab, Cpx, Act, Mag, Ttn, Scp | MWI: Mag, Bt, Phl, Kfs, locally Py, Ccp, Po, Ttn, Ap; Prom. Hill: Mag, Bt/Phl, Py, Kfs, Act, Chl, Tlc, Srp | MWI: Chl, Hem, Cb, Prom. Hill: Hem, Chl, Ser, Ccp, Bn, Cct, Ap, Fl, Brt, REE, Urn, Ap |
| **Olympic Dam district** | Ab rarely preserved | Mag, Kfs, Act, Ttn, Py, Ap, Cb, Qz, Ccp | Hem, Ser, Chl, Cb locally Py, Ccp, Bn, Cct, Brt, Fl, Urn, REE |
| **Moonta-Wallaroo** | Ab, Act, Mag, Dp, Ttn, Scp | Bt, Mag, Ab, locally Py, Ccp, Mnz, Ttn, Ap | Chl, Qz, Kfs, Cb, locally Py, Ccp, Mol |

Abbreviations: Ab – albite, Act – actinolite, Ap – apatite, Bn – bornite, Brt – barite, Bt – biotite, Cb – carbonate, Cct – chalcocite, Ccp – chalcopyrite, Chl – chlorite, Dp – diopside, Fl – fluorite, Hem – hematite, Kfs – K-feldspar, Mag – magnetite, Mnz – monazite, Mol – molybdenite, MWI – Mt. Woods Inlier, Phl – phlogopite, Po – pyrrhotite, Prom. Hill – Prominent Hill deposit, Py – pyrite, Qz – quartz, Scp – scapolite, Ser – sericite, Srp – serpentine, Tlc – talc, Ttn – titanite, Urn – uraninite.

The alteration products of $Fe^{2+}$-K metasomatism are primarily magnetite with either biotite or K-feldspar, depending upon the IOCG district and crustal level of preservation. The magnetite- and biotite-rich alteration subtype (with or without albite) is present in the Moonta-Wallaoo and Mt. Woods districts, which are both interpreted to expose deeper levels of the IOCG hydrothermal systems because a tectonic foliation is commonly present (Skirrow et al., 2002, 2007; Conor et al., 2010). In some biotite-magnetite alteration, minor quantities of chalcopyrite, pyrite and/or pyrrhotite are present along with minor titanite, monazite, allanite, apatite and fluorite (Fig. 4C). This type of sulphide mineralization, typified by some of the Wallaroo lodes and considered to be an early phase of IOCG mineralization, is distinct from the iron-copper sulphides introduced later with chlorite, quartz and K-feldspar (Skirrow et al., 2002, 2007; Conor et al., 2010). Conor (1995) and Conor et al. (2010) described a spatial association of biotite-magnetite alteration with Hiltaba Suite intrusive contacts and with shear zones. Mutually cross-cutting relationships between magnetite-biotite alteration and these granitic intrusions have also been noted (Fig. 4C; Conor, 1995; Raymond, 2003; Skirrow et al., 2007).

In contrast, in the Olympic Dam district, $Fe^{2+}$-K metasomatism is represented by the magnetite-K-feldspar alteration subtype, representing a high crustal level as inferred from the overprinting of undeformed GRV by this alteration. Such alteration also commonly contains actinolite, carbonate, apatite, quartz and pyrite but only minor or no copper sulphide mineralization.

The hematite-sericite-chlorite-carbonate ($Fe^{3+}$-K-$H_2O$-$CO_2$) assemblage occurs in all three districts. However, this alteration is most intense and widespread in the Olympic Dam district and at the Prominent Hill deposit in the Mt. Woods district. Economic Cu-Au-U mineralization is closely associated with hematitic alteration assemblages in the Gawler Craton (Fig. 4D, E, F), although barren hematite-rich alteration is also present (e.g. Titan prospect; Bastrakov et al., 2007).

Relative timing relationships indicate that albite-actinolite ± magnetite alteration is overprinted by biotite-magnetite alteration, which in turn is replaced and cut by hematite-sericite-chlorite-carbonate alteration. However, a caveat on this generalization is that all three assemblages are rarely present at a single location. Furthermore, Haynes et al. (1995) argued that magnetite and hematite at Olympic Dam formed more or less simultaneously in the ODBC, in multiple cycles. Albite or actinolite accompanying biotite-magnetite alteration in some places may represent transitional assemblages. Uncommon miarolitic scapolite appears to have formed early in the Na-Ca-Fe metasomatism, and is commonly overprinted by albite and biotite (Skirrow et al., 2007).

Reconnaissance geochronology of hydrothermal titanite and monazite has not yet resolved differences in the timing of albite-actinolite ± magnetite, biotite-magnetite, or magnetite-K-feldspar-calcsilicate alteration. As noted above, ion probe U-Pb ages between ~1620 and ~1570 Ma yield overlapping uncertainties at the 2-sigma level (Fig. 2; Raymond et al., 2002; Skirrow et al., 2006, 2007). The few available dates for minerals directly associated with hematitic alteration and copper-gold mineralization indicate ages of ~1600 to ~1575 Ma (molybdenite Re-Os, white mica $^{40}Ar/^{39}Ar$; Skirrow et al., 2007; Reid et al., 2013; Bowden et al., 2017). These ages encompass the age of the major introduction of Fe-Cu-Au-U and hematitic breccia formation at the Olympic Dam deposit (Johnson and Cross, 1995; Jagodzinski, 2005; Ciobanu et al., 2013). However, as discussed earlier, there is some evidence for redistribution or even addition of ore metals after this main ore-forming event.

Hematite-sericite-chlorite-carbonate alteration is interpreted to represent shallow crustal hydrothermal activity (150°–250°C), whereas magnetite-bearing assemblages formed mostly at deeper levels at 350°–450°C. This is based on temperature estimates from fluid inclusions, oxygen isotope geothermometry and mineral stabilities, and on structural styles accompanying alteration in the Olympic Cu-Au (-U) province (Bastrakov et al., 2007; Davidson et al., 2007).

Mineralization characteristics and geology of the Olympic Dam Cu-U-Au deposit have been described in detail elsewhere (Reeve et al., 1990; Oreskes and Einaudi, 1992; Haynes et al., 1995; Reynolds, 2000; Ehrig et al., 2012). In brief, zoned Cu-U-Au-REE mineralization is hosted by hematite- and granite-rich multi-stage breccias of diverse hydrothermal, phreatomagmatic and tectonic origin. Pyrite-chalcopyrite mineralization with lower grade gold and uranium occurs in the lower and outer parts of the deposit. A remarkably sharp transition upward and inward to bornite-chalcocite mineralization is located at a deposit-wide interface, above which most of the higher grade Cu, U and Au is mined. The so-called ‘barren hematite-quartz core’ contains significant LREE mineralization, and some of the higher grade gold and uranium mineralization occurs near its margins. Many textural varieties of hematite are present, including common fine- to medium-grained prismatic and specular hematite. Magnetite, on the other hand, is confined to several relatively small zones deeper in the deposit, in association with siderite (Reeve et al., 1990; Oreskes and Einaudi, 1992; Haynes et al., 1995; Ehrig et al., 2012) or with fluoroapatite, pyrite and quartz (Apukhtina et al., 2017). The significance of the deep magnetite-fluorapatite zone is not yet clear but it is notable that several of the weakly mineralized and barren iron oxide-rich alteration systems in the Olympic Dam district also contain minor apatite (up to a few volume percent, e.g. Acropolis prospect, Drexel et al., 1993; Skirrow et al., 2002, 2007; Bastrakov et al., 2007). Fluorapatite is also present at the Prominent Hill deposit and nearby prospects in both magnetite- and hematite-rich hydrothermal assemblages (Schlegel and Heinrich, 2015).

The Prominent Hill deposit is hosted by hematitic breccias within a diverse range of host rocks including essentially unmetamorphosed sedimentary rocks (argillite, carbonate, greywacke, sandstone) and younger mafic to intermediate volcanic rocks believed to be members of the lower GRV (Belperio et al., 2007; Freeman and Tomkinson, 2010; Schlegel and Heinrich, 2015). The hydrothermal system comprises a ~2 km long hematitic breccia body flanked to the north by copper-gold and separate gold ore zones hosted in the breccias (Belperio et al., 2007). Hematite content only weakly correlates with copper grades, and the alteration is zoned from hematite-quartz ± gold to transitional hematite-chlorite-sericite with copper-iron sulphides (Schlegel and Heinrich, 2015). The central hematite-quartz zones are flanked by bornite-chalcocite-rich zones, a feature that is very similar to the zoning at Olympic Dam. Prominent Hill mineralization also contains anomalous concentrations of uranium (uraninite, coffinite), REE (including monazite), fluorine (fluorite, fluorapatite) and barium (barite). A major north-dipping fault separates the overturned southern domain from largely barren, magnetite-phlogopite/biotite-amphibole-chlorite-pyrite-rich ‘skarn’ alteration to the north, where low metamorphic grade sedimentary rocks are also present. On the basis of geopetal structures in breccia matrix, Schlegel and Heinrich (2015) proposed that copper mineralization at Prominent Hill was introduced after steep tilting of the host GRV and older sedimentary host rocks. A range of mafic to felsic intrusive dykes with steep dips is also present within the deposit.

Although only brief descriptions of the Carrapateena copper-gold deposit are presently available, this information indicates that bornite-chalcopyrite mineralization is hosted by hematite-rich breccia, suggesting many similarities with the Olympic Dam and Prominent Hill deposits (Fairclough, 2005; Porter, 2010). The subvertical pipe-like breccia bodies are hosted by granitoids of the 1850–1860 Ma Donington Suite (Hand et al., 2007; Porter, 2010). Hydrothermal alteration of granitoid clasts and breccia matrix is dominated by chlorite, sericite and hematite, with lesser quartz, carbonate (siderite or ankerite), barite, monazite, magnetite, apatite, fluorite and zircon. Copper-iron sulphides are zoned within the breccia pipe, from three separate near-vertical bornite-rich central zones outwards through bornite-chalcopyrite and thence to chalcopyrite-pyrite outer zones (Porter, 2010). The discovery drill hole CAR002 comprised 178 m (from 476 m depth) at 1.83% Cu, 0.64 g/t Au, 0.21% La and 0.13% Ce (Fairclough, 2005).

The Hillside copper-gold deposit is magnetite-rich in comparison to the Olympic Dam, Prominent Hill and Carrapateena deposits, although copper sulphide mineralization is at least partly associated with a hematitic overprint on the magnetite-bearing skarn-like mineral assemblage (Conor et al., 2010; Ismail et al., 2014). Interestingly, available data suggest that the deposit also lacks the extensive brecciation, sericitic alteration, higher uranium contents and highly anomalous barium and fluorine contents of the three aforementioned hematite-rich deposits.

Sulphur isotope compositions of copper and iron sulphides vary widely in the Olympic Cu-Au (-U) province. Prior to the recent publication of results on the Prominent Hill deposit, the lowest reported values were from the Oak Dam East prospect ($\delta^{34}S_{chalcopyrite}$ values of -14 to -8‰, Davidson et al., 2007) and from the Olympic Dam deposit (e.g. average $\delta^{34}S_{chalcopyrite}$ values of -6‰; average $\delta^{34}S_{chalcocite}$ values of -10‰; Eldridge and Danti, 1994). A comprehensive data set from Prominent Hill shows a much wider variation for sulphides, from -33.5‰ to 29.9‰, with most bornite, chalcocite, digenite and idaite having $\delta^{34}S$ values of -16.2‰ to -4.6‰, and most pyrite and chalcopyrite in the hematite breccias having $\delta^{34}S$ values of -10.4‰ to -4.7‰ (Schlegel et al., 2017). Pyrite and chalcopyrite in the magnetite-rich 'skarns' have higher $\delta^{34}S$ values of -4.7‰ to -1.2‰. It is noteworthy that these three hydrothermal systems with low $\delta^{34}S$ values (Olympic Dam, Oak Dam, Prominent Hill) are some of the most uranium-rich in the metallogenic province. Elsewhere in the Olympic Cu-Au (-U) province, sulphur isotope values of chalcopyrite and pyrite fall into two groups: -4 to +4‰, and +5 to +12‰ (Bastrakov et al., 2007; Schlegel et al., 2017). Leached igneous and/or magmatic-hydrothermal sulphur sources are suggested for the former, with sulphur introduced by fluids of intermediate to reduced oxidation state with $\Sigma H_2S \geq \Sigma SO_4^{2-}$. The group of higher sulphur isotope values reflects contributions from leached metasedimentary sources and/or the Proterozoic hydrosphere, for example sulphate-rich evaporitic waters (Haynes et al., 1995; Bastrakov et al., 2007). The strongly negative values at Olympic Dam, Oak Dam East and Prominent Hill represent fractionation under more oxidized conditions with or without the effects of phase separation (Eldridge and Danti, 1994; Bastrakov et al., 2007; Davidson et al., 2007; Schlegel et al., 2017). At the Prominent Hill deposit, the very wide range of sulphur isotope values of sulphide and sulphate minerals were interpreted by Schlegel et al. (2017) as the products of a two-stage process involving ultimately 'magmatic-sourced' sulphur with a $\delta^{34}S$ value of ~4‰. The diversity of isotope values was explained in terms of differing reduced versus oxidized trajectories; the former producing sulphides in the paragenetic early magnetite 'skarns' and the latter yielding the extremely low $\delta^{34}S$ values in some of the copper-iron sulphides in the Prominent Hill mineralization.

*Other Districts with Hematite-group IOCG Deposits*

The Alvo 118 copper-gold deposit in the Carajás Mineral Province (Brazil) has been described as either a variant of an IOCG deposit (Torresi et al., 2012) or an intrusion-related Cu-Au (W-Sn-Bi-Mo) deposit (Grainger et al., 2008). Although the chalcopyrite ± bornite ± chalcocite mineralization is relatively quartz-rich and contains less iron oxides (20 vol % hematite, 10 vol % magnetite) than the well known IOCG deposits in the Carajás Mineral Province, Torresi et al. (2012) argue that the structural style, hydrothermal alteration zonation and geochemistry are sufficiently similar to the major IOCG deposits for Alvo 118 to be considered a shallow-crustal hematitic variant. However, available geochronology (1868 ± 7 Ma, 1869 ± 7 Ma, U-Pb xenotime ages; see summary of geochronology by Melo et al., 2017) indicates that Alvo 118 mineralization is part of a much younger (Paleoproterozoic) metallogenic event in comparison to the major Archean IOCG deposits such as the magnetite-rich Salobo, Sossego, Igarapé Bahia, Bacuba and Bacuri deposits (see Melo et al., 2017). A key conclusion from fluid inclusion and stable isotope studies at Alvo 118 is the recognition of two distinct fluids that may have mixed: a hot (>200°C) saline brine and a lower temperature (<200°C), low to intermediate salinity, fluid (Torresi et al., 2012). These and other isotopic and geochemical data for the Alvo 118 and other IOCG deposits of the Carajas Mineral Province have been used to propose involvement of both (evolved) meteoric fluids and highly saline fluids of hybrid origins (with variable magmatic and bittern brine contributions; see discussion by Torresi et al., 2012).

The Paleoproterozoic Tennant Creek district in northern Australia is characterized by a range of magnetite-dominant to hematite-rich IOCG deposits. Of the hundreds of iron oxide-rich epigenetic 'ironstone' bodies, only a few dozen are known to contain significant Au-Cu-Bi mineralization (Wedekind et al., 1989; Skirrow, 2000). Barren examples of both magnetite- and hematite-dominated ironstones are present in the district. In general, hematite postdates magnetite although the earliest iron oxides may have been iron-oxyhydroxides that were replaced by magnetite (Large, 1975). Deposits or zones with lower Au/Cu ratios generally are magnetite-dominated and contain chalcopyrite with minor pyrite, bismuth sulphosalts (commonly selenium-rich) and pyrrhotite in some cases. Examples include the Peko and West Peko deposits and parts of the Warrego deposit. Sulphides and gold are commonly associated with chlorite and muscovite in veinlets cutting the magnetite ironstones, and reduced silicates such as minnesotaite and stilpnomelane are present locally (Skirrow and Walshe, 2002). Hematite is rare or non-existent in mineralized zones of these relatively reduced deposits. Sulphur isotope compositions of sulphides in the reduced deposits cluster around 0–4‰ (Skirrow, 2000; R. Wedekind, pers. comm.).

Tennant Creek deposits or zones with higher Au/Cu ratios occur in both hematite- and magnetite-dominated ironstones. High-grade gold mineralization in the Juno, White Devil and TC8 Au (±Cu-Bi) deposits occurs in magnetite-dominated zones with very minor hematite, whereas the upper hematite-dominated zones at Juno and TC8 contain low metal grades. Sulphur isotope zoning in these deposits of intermediate redox state (magnetite ± pyrite ± hematite) shows a similar overall pattern: negative $\delta^{34}S_{sulphide}$ values in magnetite-veined zones beneath massive ironstone and/or in lower parts of ironstone, increasing upward within the ironstones (Large, 1975; Huston et al., 1993). Peripheral alteration zones have either higher $\delta^{34}S$ values (e.g. in chalcopyrite-hematite-bearing dolomite zone, Juno) or low values similar to those beneath ironstone (e.g. White Devil). Higher-grade gold zones are associated with either negative $\delta^{34}S_{sulphide}$ values (Juno; Large, 1975) or with positive values in the gradient of negative to positive $\delta^{34}S_{sulphide}$ compositions (White Devil; Huston et al., 1993).

In hematite-dominated ironstones, the strongly hematitic K44 orebody in the Gecko deposit has higher Au/Cu ratios and lower (negative) $\delta^{34}S_{sulphide}$ compositions compared to the underlying magnetite-dominant parts of the deposit (Huston et al., 1993). At the small Eldorado deposit, high-grade gold with minor bismuth mineralization is associated with both intensely hematized magnetite-rich ironstone and with very negative sulphur isotope values of bismuth sulphosalts and rare chalcopyrite (Skirrow, 2000; Skirrow and Walshe, 2002). In contrast to magnetite developed during brittle-ductile deformation, this late-stage hematite alteration is characteristically vuggy and associated with brittle fractures, veins and breccia.

The Starra deposit in the Cloncurry district is hosted by massive replacive ironstone lenses and breccias within Paleoproterozoic metasedimentary rocks. The magnetite-dominated ironstones were mineralized in places by later chalcopyrite-pyrite-hematite-carbonate assemblages in association with brittle and ductile structures (Williams, 1998; Rotherham et al., 1998). Hydrothermal mineral assemblages in most other IOCG deposits in the Cloncurry district are of generally reduced composition (e.g. pyrrhotite-bearing, Osborne and Eloise deposits) or of intermediate redox state (e.g. magnetite-pyrite-bearing, Ernest Henry deposit). As noted by Williams (2010b), copper-gold mineralization in the Ernest Henry deposit is closely associated with magnetite-pyrite deposition, although late-stage mineralized veins contain significant amounts of hematite in addition to magnetite (Mark et al., 2000). Sulphur isotope compositions of chalcopyrite at Starra, Ernest Henry and Osborne are broadly similar and range from approximately -4‰ to +4‰ (Mark et al., 2000, and references therein).

The Andean IOCG province in Chile and Peru is characterized by both magnetite-rich and hematitic IOCG deposits (Sillitoe, 2003), in some cases with both present in the same district. In general, hematitic alteration in the Andean IOCG province is associated with chlorite, sericite, carbonate ± albite or K-feldspar. Gold contents tend to be higher in the hematite-rich deposits, albeit overall much lower than in the Australian Proterozoic IOCG deposits (Sillitoe, 2003). The Mantoverde deposit is one of the larger examples of hematite-rich IOCG deposits in the province (Benavides et al., 2007; Rieger et al., 2010). Early district-scale magnetite and K-feldspar alteration resulted in barren to weakly copper-mineralized iron oxide bodies. This assemblage was overprinted in places by chlorite-sericite-quartz alteration and then hematite-rich chalcopyrite mineralization at Mantoverde. The Cretaceous IOCG hydrothermal activity in the district was associated with brecciation and stockwork formation at shallow crustal levels, with evidence for boiling in fluid inclusion data (Benavides et al., 2007). Albitization is rare in the district, unlike in many other Andean IOCG districts (Ullrich and Clark, 1999). At district- to deposit-scale, hematite alteration appears to have formed at shallower levels than hydrothermal magnetite (Benavides et al., 2007), a pattern repeated in the Candelaria-Punta del Cobre district (Marschik and Fontboté, 2001; Sillitoe, 2003). Notwithstanding the occurrence of mushketovite (Williams, 2010b), hematite-chlorite-sericite-carbonate alteration generally postdates the magnetite-calcsilicate-feldspar-biotite-apatite assemblages (Benavides et al., 2007; Sillitoe, 2003). There are clear parallels between these Andean systems and the Gawler Craton and other provinces with hematite-group IOCG deposits, not only in zoning patterns of hydrothermal mineral assemblages but also in relative timing relationships between the principal hydrothermal mineral assemblages. Benavides et al. (2007) reported sulphur isotope values of -7‰ to +11‰ for chalcopyrite and other sulphides at Mantoverde. As summarized by Barton (2014) and Chen (2013), high $\delta^{34}S$ values (e.g. $\delta^{34}S_{sulphide}$ >10‰) and very low values (e.g. $\delta^{34}S_{sulphide}$ <-5‰) are present in many of the Andean IOCG deposits, whether magnetite- or hematite-dominated. Zoning patterns of sulphur isotopes have not been reported in detail in the Andean IOCG deposits.

*Uranium Distribution*

Uranium is commonly anomalous in IOCG deposits, although it attains economic grade in very few deposits (Hitzman et al., 1992; Hitzman and Valenta, 2005). Uranium occurs in Olympic Dam principally as uraninite, coffinite and brannerite, and is distributed at low grades throughout the mineralized hematitic breccias (Reeve et al., 1990). Higher grades of uranium are weakly correlated with bornite-chalcocite zones (Reynolds, 2000). Higher-grade gold zones occur between the uraniferous bornite-chalcocite mineralization and the 'barren hematite-quartz' core of the deposit (Reynolds, 2000). By comparison, the Prominent Hill deposit in the northern Olympic copper-gold province is far less endowed with uranium, although narrow high-grade zones are present (e.g. up to 5000 ppm U; Belperio et al., 2007). Unlike at Olympic Dam, the higher-grade uranium is associated with chalcopyrite rather than bornite-chalcocite. Hitzman and Valenta (2005) noted the different host rocks at Prominent Hill (andesite; felsic and mafic dykes) compared to Olympic Dam (Hiltaba Suite granite). The sub-economic Oak Dam East Cu-U (-Au) deposit in the Olympic Dam district contains significant uranium enrichment within the main chalcopyrite-pyrite zone (Davidson et al., 2007). The granitic host rock at Oak Dam East is assigned to the ~1850 Ma Donington Suite, which is less uraniferous than the Hiltaba Suite (Creaser, 1989). Most other IOCG prospects in the Olympic Cu-Au (-U) province that are hosted by metasedimentary units have insignificant reported uranium, whether magnetite- or hematite-rich.

Uranium is locally enriched in some IOCG deposits of the Tennant Creek district (Stolz et al., 1994). Zoning of uranium has not been widely documented, although at the Juno Au-Bi (Cu) deposit, Large (1975) described uranium spatially overlapping with high-grade gold in the core of the magnetite-dominated ironstone, zoning outward and upward antipathetically to bismuth (not shown), then copper (Fig. 6).

Anomalous uranium is present in some magnetite-group deposits, including several in the Carajás district of Brazil and in the Cloncurry district (Hitzman and Valenta, 2005). Zoning of uranium distribution has not been reported.

In the Great Bear magmatic zone, uranium enrichment has been reported in the Sue Dianne deposit (Goad et al., 2000) as well as in numerous other occurrences (e.g. FAB, Potter et al., 2013; Montreuil et al., 2016c; Southern Breccia, Montreuil et al., 2015; Potter et al., 2019, 2022).

In the Andean IOCG province, uranium contents tend to be lower than in the Australian and Brazilian Precambrian IOCG deposits (Sillitoe, 2003). Nevertheless, hematite-rich deposits in the Andes generally have higher uranium contents than their magnetite-rich counterparts (Sillitoe, 2003).

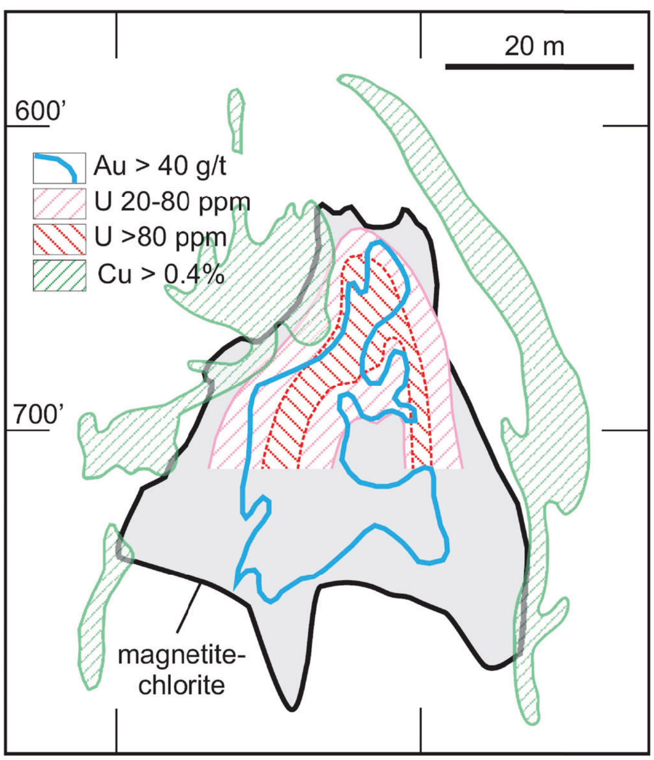


**Figure 6.** Cross section of uranium, gold and copper distribution, No. 2 orebody, Juno Au-Bi (-Cu) deposit, Tennant Creek district. Copper outside the magnetite-chlorite ironstone is hosted mainly by talc-magnetite and dolomite alteration zones (not shown). Redrawn from Large (1975).

### Processes of Hematite-group IOCG (U) Deposit Formation

Two distinct processes may account for hematite-bearing IOCG (U) deposits (Figs. 7, 8; see also Williams, 2010a): (1) single-fluid-rock interactions, and (2) two-fluid processes, including mixing. Where and how Cu-Au-U ore is best developed may reflect the interplay between the two processes. A key factor governing this interplay is crustal depth of IOCG deposit development, which in turn is influenced by tectonic processes of uplift and exhumation. Figure 8 schematically illustrates typical alteration zoning patterns and ore-forming processes in hematite-group IOCG hydrothermal systems. In general terms, the alteration zoning is similar to that described by Hitzman et al. (1992) and Williams et al. (2005), and the concept of fluid mixing is based on the models of Haynes et al. (1995) and Bastrakov et al. (2007).

*Single-fluid-rock Interaction*

The first process (Fig. 7, left panel; Fig. 8A) invokes evolution of a single deep-sourced or deeply-circulated fluid (A) ascending along an adiabatic pressure-temperature path, from magnetite-stable conditions at depth to hematite stability at shallower crustal levels. Fluid-rock buffering reactions along the flow paths result in partial to complete re-equilibration of fluid chemistry and isotope compositions, possibly disguising

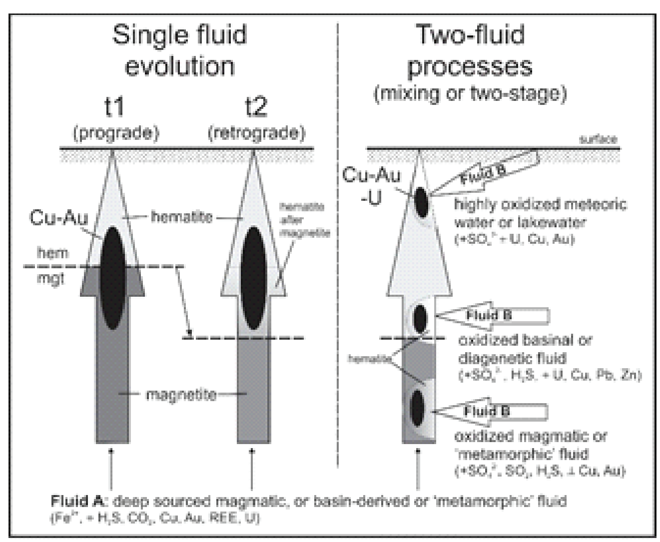


**Figure 7.** Cartoon sections representing formation of hematite-group IOCG deposits, by single-fluid evolution and two-fluid processes (see text). Stages in evolution are denoted by time 1 (t1) or time 2 (t2).

the isotopic and chemical signatures of the source rocks or magmas. Thermal collapse (retrogression, at time t2 in Fig. 7) of these single-fluid systems may cause overprinting of early magnetite and related alteration by hematite and associated lower temperature alteration. This may result in localized leaching, and/or remobilization and upgrading of copper, uranium and gold. The oxygen isotope composition of the fluid(s) involved in forming both magnetite- and hematite-related alteration is likely to be similar.

Deposition of significant Cu-Au-U mineralization is dependant not only on the metal content of the deep-sourced or deeply-circulated fluid but also on the presence of physico-chemical gradients capable of inducing saturation of the ore minerals. Based on the observed mineralogy of magnetite-Kfeldspar or magnetite-biotite ± pyrite ± actinolite and rare pyrrhotite, fluid A is inferred to be of intermediate to reduced oxidation state. This relatively high-temperature brine is therefore able to transport high concentrations of iron as $Fe^{2+}$ (e.g. aqueous $FeCl_2$, Crerar and Barnes, 1976; Seyfried and Ding, 1993) which will tend to limit the sulphur content ($H_2S >> \Sigma SO_4^{2-}$) to relatively low levels due to the stability of pyrrhotite and pyrite. Under these conditions near magnetite-pyrite-pyrotite stability, the Fe/Cu ratio in the fluids will be significantly higher than in fluids of higher oxidation state (e.g. hematite-magnetite-pyrite-stable; Seyfried and Ding, 1993). In deeper parts of the systems, $CO_2 \pm CH_4$ may be carried either in fluid A or in a coexisting low-density fluid (Pollard, 2000; Skirrow and Walshe, 2002). In the Gawler Craton these single-fluid systems generally result in barren to weakly mineralized magnetite-dominated IOCG systems with little or no zoning of iron- and copper-iron sulphide minerals or of sulphur isotopes (Fig. 8A). Examples of weakly copper-gold mineralized and barren magnetite-rich hydrothermal systems include the Acropolis, Titan, Torrens, Emmie Bluff and Murdie Murdie prospects (Bastrakov et al., 2007). Reconnaissance microbeam analysis (PIXE) of hypersaline high-temperature (>400ºC) fluids related to magnetite and associated minor copper mineralization in the Olympic Dam region indicates moderate to very high copper concentrations (>500 ppm to several wt% Cu, Bastrakov et al., 2007). The lack of significant Cu-Au-U mineralization in these magnetite-rich IOCG systems is attributed to undersaturation of copper minerals in the high-temperature brines, and/or limited supply of fluids and metals. Clearly the formation of major IOCG ± U deposits with ore-grade Cu-Au-U in the Gawler Craton involved different processes to solely single-fluid (A)-rock interaction. This requirement also appears to be the case in several of the better-studied magnetite-rich IOCG deposits such as Ernest Henry (see 'two-fluid processes' below) and deposits in the Carajás Mineral Province (e.g. Xavier et al., 2009; Barton, 2014).

The models of Large (1975) and Huston et al. (1993) for Au-Cu-Bi deposits in the Tennant Creek district may be other examples of process (1). However, fluid mixing also was important in some deposits (see next section).

*Two-fluid Processes*

The second process leading to formation of hematite-bearing IOCG (U) deposits involves two fluids either mixing or in two-stage interactions (Fig. 7, right panel; Fig. 8B). Several previous studies have invoked fluid mixing or two-stage processes in IOCG genesis (e.g. Gow et al., 1994; Haynes et al., 1995; Mark et al., 2000; Marschik and Fontboté, 2001; Skirrow and Walshe, 2002; Oliver et al., 2004; Williams et al., 2005; Torresi et al., 2012). Below, a general scheme is suggested with particular reference to hematite-group IOCG ± U ore systems. In process (2), a deep-sourced or deeply circulated fluid akin to fluid A in process (1) mixes with, or is succeeded by, an oxidized fluid (B) carrying sulphate and Cu-Au ± U. Process (2) results in diverse hematitic IOCG ± U deposits, ranging from deep-seated to shallow-crustal variants. The following examples are given from deeper to shallower settings.

In mesothermal crustal settings, mixing occurs between fluid A and a deep-sourced (e.g. metamorphic or magmatic) oxidized fluid (B), or by overprinting of fluid A-related alteration by fluid B (Fig. 7, right panel, lowermost of three mixing scenarios). Fluid mixing at >5 km depth has been proposed for IOCG deposits of the Cloncurry district, such as

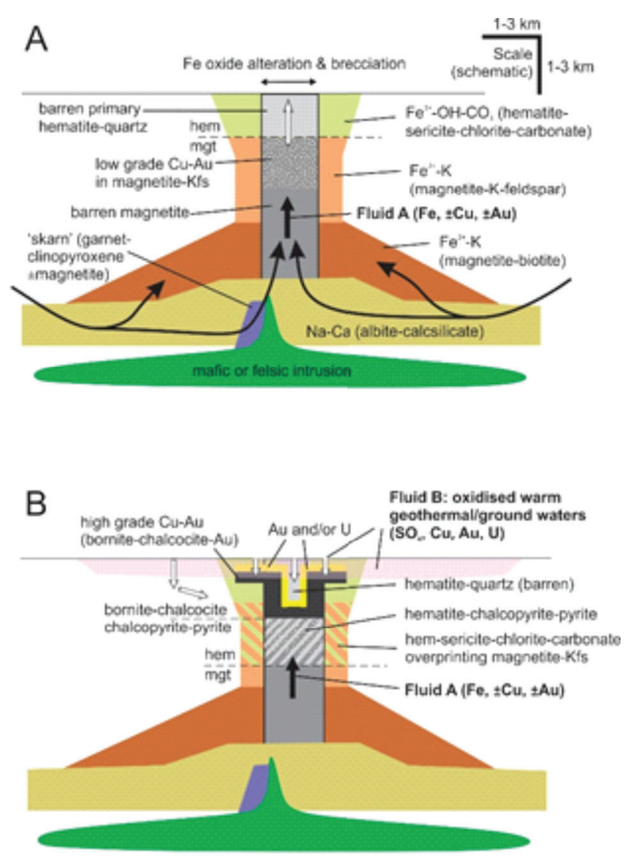


**Figure 8.** Schematic cross section of alteration zoning and ore-forming processes in the evolution of hematite-group IOCG systems of the Olympic Dam type. A. Early, single-fluid stage involving deep-sourced Fluid A. B. Later, two-fluid stage involving mixing of Fluids A and B or overprinting of early alteration by Fluid B.

the Ernest Henry deposit (Williams et al., 2001; Oliver et al., 2004). The Starra deposit is a possible example in which magnetite-bearing assemblages were overprinted by deep-sourced oxidized fluid B, or where this fluid mixed with the magnetite-forming fluid. Halogen compositions (Br, I, Cl) of hematite-stage fluid inclusions show evidence of more than one fluid, with contributions from magmatic-hydrothermal as well as non-magmatic sources (Williams et al., 2001, 2005; Kendrick et al., 2007; Williams, 2010b). The relatively enriched $\delta^{18}O$ values calculated for fluids in equilibrium with hematite assemblages at Starra (Rotherham et al., 1998; Williams et al., 2005) indicate insignificant direct involvement of surficial fluids (Williams, 2010b). Other less oxidized IOCG deposits in the Cloncurry district may have involved mixing of fluid A with variants of fluid B that were of reduced or intermediate redox state and with high ratios of reduced/oxidized sulphur. Oliver et al. (2004) suggested a mafic igneous source for some sulphur in IOCG deposits of the Cloncurry district.

Iron oxide Au-Bi-Cu deposits of the Tennant Creek district represent a generally higher crustal level of IOCG hydrothermal activity than the Cloncurry district, with formation at greenschist rather than amphibolite facies conditions (Davidson, 2002; Skirrow et al., 2002). This is represented in Figure 7 (right panel, middle of three scenarios). Fluid A either deposited magnetite-rich ironstones and evolved to a Au-Cu-Bi-bearing ore fluid (Large, 1975), or fluid A developed separately from the ironstone-forming fluid as a reduced (magnetite-pyrrhotite stable, $\Sigma H_2S >> \Sigma SO_4^{2-}$) to intermediate-redox (magnetite-pyrite stable) ore fluid (Skirrow and Walshe, 2002). In this model, fluid B is represented by oxidized (hematite stable) calcium-rich basinal brines. The patterns of sulphur isotope zoning and the spectrum of reduced to oxidized mineral assemblages are interpreted as the products of differing contributions of relatively reduced fluid A with oxidized fluid B during fluid mixing and fluid-rock reactions at the site of the ironstones (Skirrow, 1993; Skirrow and Walshe, 2002). Huston et al. (1993) envisaged mixing at deeper crustal levels prior to fluid reaction with ironstones. Hematite-rich deposits or zones with higher Au/Cu ratios and lower sulphur isotope values resulted where oxidized fluid B dominated over fluid A. Reconnaissance PIXE data for fluid inclusions suggest the calcic brines lack appreciable copper (Khin Zaw et al., 1994; R. Skirrow, unpub. data). The numerous hematite-altered yet largely barren ironstones in the Tennant Creek district may be examples in which the oxidized brine contained only low gold-copper concentrations and remained undersaturated with respect to copper and gold minerals. A further consequence is that the oxidized brines appear to have leached copper and produced extremely high gold grades in some deposits, perhaps by upgrading via dissolution and re-precipitation (e.g. Eldorado, 1 m intervals with >1000 g/t). Hydrothermal leaching by fluid B may also account for the vuggy textures of hematitic alteration zones in these deposits (Skirrow and Walshe, 2002) and as observed in the Olympic Cu-Au (-U) province (Bastrakov et al., 2007). In the reduced end-member deposits (e.g. West Peko, Warrego) gold deposition occurred partly in response to desulphidation of an $H_2S$-bearing ore fluid during reaction with magnetite-rich ironstone that formed earlier during deformation (Skirrow and Walshe, 2002). Alternatively, reduction of an oxidized magmatic-hydrothermal metalliferous brine led to ore deposition (Huston et al., 1993). Oxygen-hydrogen isotope compositions calculated for most fluids, whether related to iron oxides or mineralization, resemble those of sedimentary basin waters, although compositions of some samples approach magmatic water values (R. Wedekind and D. Huston, pers. comm.; Skirrow, 1993). However, sulphur isotope values for sulphides in reduced deposits in the Tennant Creek district indicate $\delta^{34}S_{fluid}$ compositions of ~3–4‰, consistent with a magmatic-hydrothermal or leached igneous rock source of sulphur (Huston et al., 1993; Skirrow, 2000).

Shallow crustal settings host the most important hematite-group and uranium-bearing IOCG deposits such as those in the Gawler Craton. Figure 7 (right panel, uppermost scenario) and Figure 8B illustrate a generalized model of these IOCG systems, including alteration zoning. In this subvolcanic to epithermal setting, process (2) involved mixing between ascending fluid A and shallow-sourced oxidized fluid B, or overprinting of fluid A mineral assemblages by minerals related to fluid B. In Figure 8B, the magnetite-rich system may evolve into the hematite-rich system as temperatures decline and fluid chemistry evolves through fluid-rock reactions. The key difference compared to previous examples of process (2) is the involvement of oxidized surface-derived or evolved surficial waters, for example meteoric water, lake water or connate brines. In the Olympic Cu-Au (-U) province, whereas fluid A was ubiquitous and led to consistent alteration assemblages and $Fe^{2+}$-K metasomatism in a large number of systems (Table 1: magnetite, K-feldspar or biotite, actinolite, quartz, carbonate, apatite, and minor chalcopyrite and pyrite), major contributions of fluid B were evidently very localized to the known large, hematite-rich, IOCG deposits. Subeconomic IOCG prospects elsewhere in the district do not generally record major input of surface derived waters, and fluids were mostly less oxidized than at Olympic Dam (Bastrakov et al., 2007). Where present in the sub-economic systems, fluid B appears to have post-dated (rather than mixed with) the pre-existing fluid A-related assemblages, leading to local leaching or upgrading of pre-existing copper-gold mineralization (Bastrakov et al., 2007).

Additional evidence for a second, shallow-sourced, fluid is provided by oxygen isotope data for the Olympic Dam deposit, which record the input of meteoric or evolved surficial waters (Oreskes and Einaudi, 1992). Haynes et al. (1995) numerically modelled mixing of oxidized, ~150°C, sulphate-bearing, evolved (basalt-reacted) playa lake waters with deep-sourced ~300°C, iron-rich relatively reduced fluid. The results are consistent with observed zoning in the deposit, from deeper magnetite-siderite and pyrite-chalcopyrite to shallower hematite and bornite-chalcocite-uraninite-gold. Recent detailed geological, geochemical, fluid inclusion and sulphur-isotope studies at the Prominent Hill deposit (Schlegel et al., 2012, 2017; Schlegel and Heinrich, 2015) supports the involvement of a sulphate-rich shallow-crustal fluid reservoir in IOCG ore formation. Whereas Bastrakov et al. (2007) invoked a non-magmatic contribution of sulphate (with modelled fluid $\delta^{34}S_{\Sigma S}$ = +13‰) in the groundwater/geothermal reservoir to explain (average) values of -10‰ for chalcocite at the Olympic Dam deposit, a magmatic source of sulphur in the sulphate reservoir (with fluid $\delta^{34}S_{\Sigma S}$ = ~4‰) was proposed by Schlegel et al. (2017) at Prominent Hill. This sulphate was envisaged to have formed by disproportionation reactions when GRV-derived, magmatic, sulphur-rich volatiles (and copper) dissolved in highly oxidized groundwaters. Whether the copper was transferred from magmas via magmatic-hydrothermal fluids and thence a groundwater reservoir into the IOCG deposits (Schlegel et al., 2017), or was leached from mafic GRV and other sources (Haynes et al., 1995), remains an open question. In any case it seems that at least two fluids were involved in ore formation at both deposits, and fluid mixing was very likely involved.

The Mantoverde hematite-group IOCG deposit in Chile may be an example in a subvolcanic setting where fluid B introduced sulphur from seawater and/or through dissolution of evaporites (Benavides et al., 2007). This also may be the case at the Mina Justa and Raul-Condestable Cu-Au deposits in the central Andes (Chen, 2013).

*Role of Exhumation*

Exhumation of terranes containing sub-volcanic or deeper magnetite-dominated IOCG systems may expose these relatively reduced hydrothermal systems to near-surface oxidized shallow-crustal fluids where steep geothermal gradients are also extant. The timing of exhumation influences whether fluid mixing versus two-stage fluid-rock reaction were important in hematite-rich IOCG ± U development (Fig. 7; Bastrakov et al., 2007; Skirrow, 2010). Exhumation during active magnetite-forming processes may have been conducive for fluid mixing, massive hematite formation and significant Cu-Au-U deposition. Olympic Dam is a possible example. Terranes exhumed well after cessation of magnetite-dominated alteration are likely to contain mainly magnetite-rich systems with local hematite replacement of magnetite (Bastrakov et al., 2007). However, in terranes where conditions favoured fluid mixing at depth and formation of magnetite-group IOCG deposits or deeper hematite-group IOCG deposits, it is this post-IOCG exhumation that allows such systems to be detected in the shallow subsurface by exploration techniques. Terranes not exhumed significantly since IOCG hydrothermal activity may be characterized by weak hematitic alteration in the shallow subsurface and magnetite-dominated IOCG systems at depth. Thus, the crustal depths, the tectonic settings and evolution of terranes favourable for hematite-group IOCG(U) ore systems are likely to be different from those with potential for detectable magnetite-group IOCG, due to differences in preservation.

## Summary: Criteria for Uranium-rich Hematite-group IOCG deposits

A conjunction of tectonic and geological factors or criteria is necessary for efficient large-scale copper, gold and uranium mass transfer in order to form major hematite-group IOCG (U) deposits (see also Skirrow et al., 2006):

1. Tectonic settings characterized by voluminous uranium-rich (e.g. A-type) subaerial felsic volcanic and/or high-level felsic intrusive rocks, and conducive to subsequent preservation of shallow crustal levels. Permissive settings include syn- to post-subduction settings that are distal (up to several hundred kilometres inboard) from continental margins, with evidence of a switch from compressive to extensional deformation (i.e. syn- to post-orogenic settings). Crustal melting was possibly driven by mantle lithosphere removal (convective, or delamination, etc.), which also may lead to exhumation.
2. Crustal-scale magma and fluid pathways, e.g. earlier orogenic belt and trans-crustal to trans-lithospheric discontinuities at cratonic margins or within cratons.
3. Pre-IOCG basins lacking major reduced sections (Haynes, 2000) and commonly showing evidence for evaporites.
4. High to extreme palaeogeothermal gradients resulting in regional-scale uppermost crustal fluid flow (fluid A, magnetite- and/or hematite-rich hydrothermal alteration zones); mafic/ultramafic intrusive magmatism may mark the locus of crustal-scale thermal anomalies, and may contribute ore metals or sulphur to IOCG systems.
5. Exhumation of an active magnetite-forming hydrothermal regime, allowing interactions between this alteration and oxidized surface-derived fluid B, and permitting fluid mixing.
6. Hydrological settings in which large volumes of oxidized groundwaters or basinal waters (fluid B) are mobilized to sites of fluid A upflow, e.g. basins related to tectonism, calderas or maar volcanic centres (Reeve et al., 1990; Haynes et al., 1995).
7. Exposure of uranium-rich source rocks to fluids migrating in this hydrological setting.
8. Reducing agents to facilitate precipitation of $U^{6+}$ as $U^{4+}$ minerals; e.g. mixing of fluids A and B or reaction of oxidized fluid B with $Fe^{2+}$- or $S^{2}$-bearing or reduced-C minerals. Variants of unconformity-related uranium deposits may exist in some IOCG (U) districts (Davidson et al., 2007).
9. Hydrothermal assemblages associated with uranium mineralization in IOCG deposits typically contain combinations of hematite, chlorite, sericite, carbonate, pyrite, chalcopyrite, bornite, chalcocite, barite, fluorite, apatite and various REE, uranium and phosphate minerals.
10. Higher-grade copper-gold mineralization generally forms within hematite-rich zones laterally or vertically adjacent to magnetite-bearing zones; higher-grade uranium mineralization is generally associated with gold-rich and/or more oxidized mineral assemblages.

## Acknowledgments

Colleagues at Geoscience Australia are thanked for their support, enthusiasm and stimulating discussions during the Gawler Craton Project. Staff at the Geological Survey of South Australia, the University of Adelaide, and in numerous companies provided valuable assistance during the period of Geoscience Australia's work in the Gawler Craton and Curnamona Province. I thank Louise Corriveau for the invitation to contribute this paper and for editorial efforts in producing this GAC Special Paper. Eric Potter and Anthony Reid are thanked for constructive and helpful reviews. Figure 8 is slightly modified from Figure 12 in Skirrow et al. (2018), an open-access publication of Wiley Publishing (licence CC BY-NC-ND, Crown Copyright on behalf of the Commonwealth of Australia). RGS publishes with the permission of the CEO, Geoscience Australia.

## References

ANCORP Working Group, 1999, Seismic reflection image revealing offset of Andean subduction-zone earthquake locations into oceanic mantle: Nature, v. 397, p. 341-344.

Apukhtina, O.B., Kamenetsky, V.S., Ehrig, K., Kamenetsky, M.B., Maas, R., Thompson, J., McPhie, J., Ciobanu, C.L., and Cook, N.J., 2017, Early, deep magnetite-fluorapatite mineralization at the Olympic Dam Cu-U-Au-Ag deposit, South Australia: Economic Geology, v. 112, p. 1531-1542.

Austin, J.R., and Blenkinsop, T.G., 2010, Cloncurry Fault Zone: strain partitioning and reactivation in a crustal-scale deformation zone, Mt Isa Inlier: Australian Journal of Earth Sciences, v. 57, p. 1-21.

Babo, J., Spandler, C., Oliver, N.H., Brown, M., Rubenach, M.J., and Creaser, R.A., 2017, The high-grade Mo-Re Merlin deposit, Cloncurry district, Australia: paragenesis and geochronology of hydrothermal alteration and ore formation: Economic Geology, v. 112, p. 397-422.

Barton, M.D., 2014, Iron oxide (-Cu-Au-REE-P-Ag-U-Co) systems, *in* Scott, S.D., ed., Treatise on Geochemistry, Second Edition: Elsevier Inc., p. 515-541.

Barton, M.D., and Johnson, D.A., 1996, Evaporitic source model for igneous-related Fe oxide–(REE-Cu-Au-U) mineralization: Geology, v. 24, p. 259-262.

Bastrakov, E.N., Skirrow, R.G., and Davidson, G.J., 2007, Fluids in sub-economic Fe-oxide Cu-Au systems of the Olympic Cu-Au-(U) province: Economic Geology, v. 102, p. 1415-1440.

Belperio, A.P., Flint, R., and Freeman, H., 2007, Prominent Hill – a hematite-dominated, iron oxide copper-gold system: Economic Geology, v. 102, p. 1499-1510.

Benavides, J., Kyser, T.K., Clark, A.H., Oates, C.J., Zamora, R., Tarnovschi, R., and Castillo, B., 2007, The Mantoverde iron oxide-copper-gold district, III Región, Chile: the role of regionally derived, nonmagmatic fluids in chalcopyrite mineralization: Economic Geology, v. 102, p. 415-440.

Betts, P.G., and Giles, D., 2006, The 1800-1100 Ma tectonic evolution of Australia: Precambrian Research, v. 144, p. 92-125.

Betts, P.G., Giles, D., and Lister, G.S., 2003, The Hiltaba Event – an example of hotspot related flat subduction?: Geological Society of Australia, Abstracts v. 72, p. 67.

Betts, P.G., Giles, D., Foden, J., Schaefer, B.F., Mark, G., Pankhurst, M.J., Forbes, C.J., Williams, H.A., Chalmers, N.C., and Hills, Q., 2009, Mesoproterozoic plume-modified orogenesis in eastern Precambrian Australia: Tectonics, v. 28, TC3006, doi:10.1029/2008TC002325.

BHP, 2018, BHP Billiton Limited annual report 2018, 300 p. Available at: www.bhp.com/investor-centre

Bowden, B., Fraser, G., Davidson, G.J., Meffre, S., Skirrow, R., Bull, S., and Thompson, J., 2017, Age constraints on the hydrothermal history of the Prominent Hill iron oxide copper-gold deposit, South Australia: Mineralium Deposita, v. 52, p. 863-881.

Brotodewo, A., Tiddy, C.J., Reid, A., Wade, C., and Conor, C., 2018, Relationships between magmatism and deformation in northern Yorke Peninsula and southeastern Proterozoic Australia: Australian Journal of Earth Sciences, v. 65, p. 619-641.

Budd, A.R., 2006, A- & I-type subdivision of the Gawler Ranges-Hiltaba volcano-plutonic association: Geochimica et Cosmochimica Acta, v. 70, Issue 18, p. A72-A72.

Budd, A.R., and Fraser, G.L., 2004, Geological relationships and Ar/Ar constraints on gold mineralization at Tarcoola, central Gawler gold province, South Australia: Australian Journal of Earth Sciences, v. 51, p. 685-699.

Budd, A.R., and Skirrow, R.G., 2007, The nature and origin of gold deposits of the Tarcoola goldfield and implications for the central Gawler gold province: Economic Geology, v. 102, p. 1541-1563.

Burgess, H., Gowans, R.M., Hennessey, B.T., Lattanzi, C.R., and Puritch, E., 2014, Technical report on the feasibility study for the NICO gold–cobalt–bismuth–copper deposit, Northwest Territories, Canada: Fortune Minerals Ltd., NI 43-101 Technical Report No. 1335, 385 p. Available at www.sedar.com

Carr, L.K., Korsch, R.J., Holzschuh, J., Costelloe, R.D., Meixner, A.J., Matthews, C., and Godsmark, B., 2010, Geological interpretation of seismic reflection lines 08GA-C1 and 09TE-01: Arrowie Basin, South Australia, *in* Korsch, R.J. and Kositcin, N., eds., South Australian seismic and MT workshop 2010, extended abstracts: Geoscience Australia Record 2010/10, 6 May 2010, Adelaide, p. 54-65.

Chen, H., 2013, External sulfur in IOCG mineralization: implications on definition and classification of the IOCG clan: Ore Geology Reviews, v. 51, p. 74-78.

Cherry, A.R., McPhie, J., Kamenetsky, V.S., Ehrig, K., Keeling, J.L., Kamenetsky, M.B., Meffre, S., and Apukhtina, O.B., 2017, Linking Olympic Dam and the Cariewerloo Basin: was a sedimentary basin involved in formation of the world's largest uranium deposit?: Precambrian Research, v. 300, p. 168-180.

Ciobanu, C.L., Wade, B.P., Cook, N.J., Mumm, A.S., and Giles, D., 2013, Uranium-bearing hematite from the Olympic Dam Cu–U–Au deposit, South Australia: a geochemical tracer and reconnaissance Pb–Pb geochronometer: Precambrian Research, v. 238, p. 129-147.

Clarke, G.L., Guiraud, M., Powell, R., and Burg, J.P., 1987, Metamorphism in the Olary Block, South Australia: compression with cooling in a Proterozoic fold belt: Journal of Metamorphic Petrology, v. 5, p. 291-306.

Compston, D.M., 1995, Time constraints on the evolution of the Tennant Creek block, northern Australia: Precambrian Research, v. 71, p. 107-129.

Conor, C.H.H., 1995, Moonta-Wallaroo region: an interpretation of the geology of the Maitland and Wallaroo 1:100 000 sheet areas: Mines and Energy South Australia, Open File Envelope 8886, DME 588/93.

Conor, C., Raymond, O., Baker, T., Teale, G., Say, P., and Lowe, G., 2010, Alteration and mineralization in the Moonta-wallaroo Cu-Au mining field region, Olympic domain, South Australia, *in* Porter, T.M., ed., Hydrothermal iron oxide copper-gold and related deposits: a global perspective, volume 3: PGC Publishing, Adelaide, p. 1-24.

Corriveau, L., Williams, P.J., and Mumin, H.A., 2010, Alteration vectors to IOCG mineralization – from uncharted terranes to deposits, *in* Corriveau, L. and Mumin, A.H., eds., Exploring for iron oxide copper-gold deposits: Canada and global analogues: Geological Association of Canada, Short Course Notes, No. 20, p. 89-110.

Corriveau, L., Montreuil, J.F., and Potter, E.G., 2016, Alteration facies linkages among iron oxide copper-gold, iron oxide-apatite, and affiliated deposits in the Great Bear magmatic zone, Northwest Territories, Canada, *in* Slack, J., Corriveau, L. and Hitzman, M., eds., Proterozoic iron oxide-apatite (± REE) and iron oxide-copper-gold and affiliated deposits of Southeast Missouri, USA, and the Great Bear magmatic zone, Northwest Territories, Canada: Economic Geology, v. 111, p. 2045-2072.

Cowley, W.M. (compiler), 2008, Solid geology of South Australia: Archaean to Early Mesoproterozoic time slice map: Geological Survey of South Australia.

Creaser, R.A., 1989, The geology and petrology of Middle Proterozoic felsic magmatism of the Stuart Shelf, South Australia: Unpublished Ph.D. thesis, Australia, La Trobe University, 434 p.

Creaser, R.A., 1996, Petrogenesis of a Mesoproterozoic quartz latite-granitoid suite from the Roxby Downs area, South Australia: Precambrian Research, v. 79, p. 371-394.

Creaser, R.A., and White, A.J.R., 1991, Yardea Dacite – large volume, high temperature felsic volcanism from the Middle Proterozoic of South Australia: Geology, v. 19, p. 48-51.

Crerar, D.A., and Barnes, H.L., 1976, Ore solution chemistry; V, Solubilities of chalcopyrite and chalcocite assemblages in hydrothermal solution at 200 degrees to 350 degrees C: Economic Geology, v. 71, p. 772-794.

Curtis, S., Wade, C., and Reid, A., 2018, Sedimentary basin formation associated with a silicic large igneous province: stratigraphy and provenance of the Mesoproterozoic Roopena Basin, Gawler Range Volcanics: Australian Journal of Earth Sciences, v. 65, p. 1-17.

Davidson, G.J., 2002, The shallow to mid-crustal family of iron oxide copper-gold deposits: size, alteration and mechanisms of formation, *in* Cooke, D.R. and Pongratz, J., eds., Giant ore deposits: characteristics, genesis and exploration: University of Tasmania, CODES Special Publication 4, p. 79-102.

Davidson, G.J., Paterson, H.L., Meffre, S., and Berry, R., 2007, Characteristics and origin of the breccia hosted, Cu-U-rich, Oak Dam East ironstone: Olympic Dam-like mineralization beneath the Stuart Shelf: Economic Geology, v. 102, p. 1471-1498.

Direen, N.G., and Lyons, P., 2007, Crustal setting of iron oxide Cu-Au mineral systems of the Olympic Dam district, South Australia: insights from potential field data: Economic Geology, v. 102, p. 1397-1414.

Drexel, J.F., Preiss, W.V., and Parker, A.J., 1993, The geology of South Australia: the Precambrian, volume 1: South Australia Geological Survey, Bulletin, v. 54, 242 p.

Drummond, B., Lyons, P., Goleby, B., and Jones, L., 2006, Constraining models of the tectonic setting of the giant Olympic Dam iron oxide-copper-gold deposit, South Australia, using deep seismic reflection data: Tectonophysics, v. 420, p. 91-103.

Duncan, R.J., Stein, H.J., Evans, K.A., Hitzman, M.W., Nelson, E.P., and Kirwin, D.J., 2011, A new geochronological framework for mineralization and alteration in the Selwyn-Mount Dore corridor, Eastern fold belt, Mount Isa inlier, Australia: genetic implications for iron oxide copper-gold deposits: Economic Geology, v. 106, p. 169-192.

Ehrig, K., McPhie, J., and Kamenetsky, V., 2012, Geology and mineralogical zonation of the Olympic Dam iron oxide Cu–U–Au–Ag deposit, South Australia, *in* Hedenquist, J.W., Harris, M. and Camus, F., eds., Geology and genesis of major copper deposits and districts of the world: a tribute to Richard H. Sillitoe: Economic Geology Special Publication, No. 16, p. 237-267.

Eldridge, C.S., and Danti, K., 1994, Low sulfur isotope ratios; high gold values - a closer look at the Olympic Dam deposit via SHRIMP: The Geological Society of America, Annual Meeting, Abstracts with Programs, Seattle, p. A-498-A-499.

Etheridge, M.A., Rutland, R.W.R., and Wyborn, L.A.I., 1987, Orogenesis and tectonic processes in the Early to Middle Proterozoic of northern Australia: American Geophysical Union, Geodynamic Series 17, p. 131-147.

Fabris, A., Katona, L., Gordon, G., Reed, G., Keeping, T., Gouthas, G., and Swain, G., 2018, Characterisation and mapping of Cu-Au skarn systems in the Punt Hill region, Olympic Cu-Au Province: MESA Journal, v. 87, p. 15-27.

Fairclough, M., 2005, Geological and metallogenic setting of the Carrapateena FeO-Cu-Au prospect—a PACE success story: MESA Journal, v. 38, p. 4-7.

Fanning, C.M., Ashley, P., Cook, N., Teale, G., and Conor, C., 1998, A geochronological perspective of crustal evolution in the Curnamona Province: Australian Geological Survey Organisation, Record 1998/25, p. 30-37.

Ferris, G.M., Schwarz, M.P., and Heithersay, P., 2002a, The geological framework, distribution and controls of Fe-oxide Cu-Au deposits in the Gawler Craton. Part I. Geological and tectonic framework, *in* Porter, T.M., ed., Hydrothermal iron oxide copper-gold and related deposits: a global perspective, volume 2: PGC Publishing, Adelaide, p. 9-31.

Ferris, G.M., Barovich, K., and Hand, M., 2002b, Putting the Hiltaba Suite into a tectonic context: Geological Society of Australia, Abstracts, v. 67, p. 63.

Fitzherbert, J.A., and Downes, P.M., 2017, Curnamona Province – geological history and mineral systems, *in* Phillips, G.N., ed., Australian ore deposits: The Australasian Institute of Mining and Metallurgy, Monograph 32, p. 635-640.

Forbes, C.J., Betts, P.G., Weinberg, R., and Buick, I.S., 2005, A structural metamorphic study of the Broken Hill Block, NSW, Australia: Journal of Metamorphic Geology, v. 23, p. 745-770.

Forbes, C.J., Giles, D., Hand, M., Betts, P.G., Suzuki, K., Chalmers, N., and Dutch, R., 2011, Using P–T paths to interpret the tectonothermal setting of prograde metamorphism: an example from the northeastern Gawler Craton, South Australia: Precambrian Research, v. 185, p. 65-85.

Fraser, G.L., Skirrow, R.G., and Budd, A.R., 2006, Geochronology of Mesoproterozoic gold mineralization in the Gawler Craton, and temporal links with the Gawler Range Volcanics: Geochimica et Cosmochimica Acta, v. 70, Issue 18, p. A185.

Fraser, G.L., Skirrow, R.G., Schmidt-Mumm, A., and Holm, O., 2007, Mesoproterozoic gold prospects in the central Gawler Craton, South Australia: geology, alteration, fluids and timing: Economic Geology, v. 102, p. 1511-1539.

Freeman, H., and Tomkinson, M., 2010, Geological setting of iron oxide related mineralization in the southern Mount Woods Domain, South Australia, *in* Porter, T.M., ed., Hydrothermal iron oxide copper-gold and related deposits: a global perspective, volume 3: PGC Publishing, Adelaide, p. 171-190.

Gibson, G.M., Peljo, M., and Chamberlain, T., 2004, Evidence and timing of crustal extension versus shortening in the early tectonothermal evolution of the Proterozoic continental rift sequence at Broken Hill, Australia: Tectonics, v. 23, TC5012, doi:10.1029/2003TC001552, 20 p.

Goad, R.E., Mumin, A.H., Duke, N.A., Neale, K.L., and Mulligan, D.L., 2000, Geology of the Proterozoic iron oxide-hosted NICO cobalt-gold-bismuth, and Sue Dianne copper-silver deposits, southern Great Bear magmatic zone, Northwest Territories, Canada, *in* Porter, T.M., ed., Hydrothermal iron oxide copper-gold and related deposits: a global perspective, volume 1: PGC Publishing, Adelaide, p. 249-267.

Gow, P.A., Wall, V.J., Oliver, N.H.S., and Valenta, R.K., 1994, Proterozoic iron oxide (Cu-U-Au-REE) deposits: further evidence of hydrothermal origins: Geology, v. 22, p. 633-636.

Grainger, C.J., Groves, D.I., Tallarico, F.H., and Fletcher, I.R., 2008, Metallogenesis of the Carajás mineral province, southern Amazon craton, Brazil: varying styles of Archean through Paleoproterozoic to Neoproterozoic base-and precious-metal mineralisation: Ore Geology Reviews, v. 33, p. 451-489.

Gregory, C.J., Reid, A.J., Say, P., and Teale, G.S., 2011, U–Pb geochronology of hydrothermal allanite and titanite and magmatic zircon from the Hillside Cu–Au deposit, Yorke Peninsula, *in* Reid, A.J. and Jagodzinski, E.A., eds., PACE geochronology: results of collaborative geochronology projects 2009–10 South Australia: Department of Primary Industries and Resources, Report Book 2011/00003, p. 95-126.

Groves, D.I., Condie, K.C., Goldfarb, R.J., Hronsky, J.M.A., and Vielreicher, R.M., 2005, Secular changes in global tectonic processes and their influence on the temporal distribution of gold-bearing mineral deposits: Economic Geology, v. 100, p. 203-224.

Groves, D.I., Bierlein, F.P., Meinert, L.D., and Hitzman, M.W., 2010, Iron oxide copper-gold (IOCG) deposits through Earth history: implications for origin, lithospheric setting, and distinction from other epigenetic iron oxide deposits: Economic Geology, v. 105, p. 641-654.

Hand, M., Reid, A., and Jagodzinski, E., 2007, Tectonic framework and evolution of the Gawler Craton, South Australia: Economic Geology, v. 102, p. 1377-1395.

Hand, M., Reid, A., Szpunar, M., Direen, N., Wade, B., Payne, J., and Barovich, K., 2008, Crustal architecture during the early Mesoproterozoic Hiltaba mineralization event: are the Gawler Range Volcanics a foreland basin fill?: MESA Journal, v. 51, p. 19-24.

Haynes, D.W., 2000, Iron oxide copper (-gold) deposits: their position in the ore deposit spectrum and modes of origin, *in* Porter, T.M., ed., Hydrothermal iron oxide copper-gold and related deposits: a global perspective, volume 1: PGC Publishing, Adelaide, p. 71-90.

Haynes, D.W., Cross, K.C., Bills, R.T., and Reed, M.H., 1995, Olympic Dam ore genesis: a fluid mixing model: Economic Geology, v. 90, p. 281-307.

Hayward, N., and Skirrow, R.G., 2010, Geodynamic setting and controls on iron oxide Cu-Au (±U) ore in the Gawler Craton, South Australia, *in* Porter, T.M., ed., Hydrothermal iron oxide copper-gold and related deposits: a global perspective, volume 3: PGC Publishing, Adelaide, p. 105-131.

Hennessey, B.T., and Puritch, E., 2008, A technical report on a mineral resource estimate for the Sue-Dianne deposit, Mazenod Lake area, Northwest Territories, Canada: Fortune Minerals Limited, Technical Report, 125 p. Available at www.sedar.com

Hitzman, M.W., 2000, Iron oxide-Cu-Au deposits: what, where, when and why, *in* Porter, T.M., ed., Hydrothermal iron oxide copper-gold and related deposits: a global perspective, volume 1: PGC Publishing, Adelaide, p. 9-25.

Hitzman, M.W., and Valenta, R.K., 2005, Uranium in iron oxide-copper-gold (IOCG) systems: Economic Geology, v. 100, p. 1657-1661.

Hitzman, M.W., Oreskes, N., and Einaudi, M.T., 1992, Geological characteristics and tectonic setting of Proterozoic iron oxide (Cu-U-Au-LREE) deposits: Precambrian Research, v. 58, p. 241-287.

Houseman, G., and Molnar, P., 2001, Mechanisms of lithospheric rejuvenation associated with continental orogeny, *in* Miller, J.A., Holdsworth, R.E., Buick, I.S. and Hand, M., eds., Continental reactivation and reworking: Geological Society of London, Special Publications, v. 184, p. 13-38.

Huang, Q., Kamenetsky, V.S., Ehrig, K., McPhie, J., Kamenetsky, M., Cross, K., Meffre, S., Agangi, A., Chambefort, I., Direen, N.G., and Maas, R., 2016, Olivine-phyric basalt in the Mesoproterozoic Gawler silicic large igneous province, South Australia: examples at the Olympic Dam iron oxide Cu–U–Au–Ag deposit and other localities: Precambrian Research, v. 281, p. 185-199.

Huston, D.L., Bolger, C., and Cozens, G., 1993, Comparison of mineral deposits at the Gecko and White Devil deposits: implications for ore genesis in the Tennant Creek district, Northern Territory, Australia: Economic Geology, v. 88, p. 1198-1225.

Hyndman, R.D., Currie, C.A., and Mazzotti, S.P., 2005, Subduction zone backarcs, mobile belts, and orogenic heat: GSA Today, v. 15, p. 4-10.

Ismail, R., Ciobanu, C.L., Cook, N.J., Teale, G.S., Giles, D., Mumm, A.S., and Wade, B., 2014, Rare earths and other trace elements in minerals from skarn assemblages, Hillside iron oxide–copper–gold deposit, Yorke Peninsula, South Australia: Lithos, v. 184, p. 456-477.

Jagodzinski, E.A., 2005, Compilation of SHRIMP U-Pb geochronological data, Olympic Domain, Gawler Craton, South Australia, 2001-2003: Geoscience Australia Record, v. 2005/20.

Jagodzinski, E.A., Reid, A., Crowley, J., McAvaney, S., and Wade, C., 2016, New CA-TIMS dates for the Gawler Range Volcanics: implications for the duration of volcanism: Geological Survey of South Australia, Report Book 2016/00032, p. 17-18.

Johnson, J.P., and Cross, K.C., 1995, U-Pb geochronological constraints on the genesis of the Olympic Dam Cu-U-Au-Ag deposit, South Australia: Economic Geology, v. 90, p. 1046-1063.

Kay, R.W., and Kay, S.M., 1993, Delamination and delamination magmatism: Tectonophysics, v. 219, p. 177-189.

Kendrick, M.A., Mark, G., and Phillips, D., 2007, Mid-crustal fluid mixing in a Proterozoic Fe oxide–Cu–Au deposit, Ernest Henry, Australia: evidence from Ar, Kr, Xe, Cl, Br, and I: Earth and Planetary Science Letters, v. 256, p. 328-343.

Khin Zaw, Huston, D.L., Large, R.R., Mernagh, T., and Hoffman, C., 1994, Microthermometry and geochemistry of fluid inclusions from the Tennant Creek gold-copper deposits, Northern Territory: implications for exploration of auriferous ironstones: Australian Institute of Mining and Metallurgy Annual Conference, Darwin, 5-9 August 1994, p. 185-188.

Kirchenbaur, M., Maas, R., Ehrig, K., Kamenetsky, V.S., Strub, E., Ballhaus, C., and Münker, C., 2016, Uranium and Sm isotope studies of the supergiant Olympic Dam Cu–Au–U–Ag deposit, South Australia: Geochimica et Cosmochimica Acta, v. 180, p. 15-32.

Kontonikas-Charos, A., Ciobanu, C.L., Cook, N.J., Ehrig, K., Krneta, S., and Kamenetsky, V.S., 2017, Feldspar evolution in the Roxby Downs Granite, host to Fe-oxide Cu-Au-(U) mineralization at Olympic Dam, South Australia: Ore Geology Reviews, v. 80, p. 838-859.

Korsch, R.J., Preiss, W.V., Conor, C.H.H., Goleby, B.R., Fomin, T., Robertson, R.R., and Burtt, A.C., 2006, Tectonic implications based on the deep seismic reflection data from the Curnamona Province, South Australia: Geoscience Australia Record 2006/12, p. 73-80.

Large, R.R., 1975, Zonation of hydrothermal minerals at the Juno Mine, Tennant Creek goldfield, Central Australia: Economic Geology, v. 70, p. 1387-1413.

Ludwig, K.R., and Cooper, J.A., 1984, Geochronology of Precambrian granites and associated U-Ti-Th mineralization, northern Olary province, South Australia: Contributions to Mineralogy and Petrology, v. 86, p. 298-308.

Lyons, P., and Goleby, B.R., 2005, The 2003 Gawler Craton Seismic survey: workshop notes from Gawler Craton State of Play conference, 2004: Geoscience Australia Record, v. 2005/19.

Mark, G., Oliver, N.H.S., Williams, P.J., Valenta, R.K., and Crookes, R.A., 2000, The evolution of the Ernest Henry Fe-oxide-(Cu-Au) hydrothermal system, *in* Porter, T.M., ed., Hydrothermal iron oxide copper-gold and related deposits: a global perspective, volume 1: PGC Publishing, Adelaide, p. 123-136.

Marschik, R., and Fontboté, L., 2001, The Candelaria-Punta del Cobre iron oxide Cu-Au(-Zn-Ag) deposits, Chile: Economic Geology, v. 96, p. 1799-1826.

Mauger, A.J., Ehrig, K., Kontonikas-Charos, A., Ciobanu, C.L., Cook, N.J., and Kamenetsky, V.S., 2016, Alteration at the Olympic Dam IOCG–U deposit: insights into distal to proximal feldspar and phyllosilicate chemistry from infrared reflectance spectroscopy: Australian Journal of Earth Sciences, v. 63, p. 959-972.

McInnes, B.I.A., Keays, R.R., Lambert, D.D., Hellstrom, J., and Allwood, J.S., 2008, Re–Os geochronology and isotope systematics of the Tanami, Tennant Creek and Olympic Dam Cu–Au deposits: Australian Journal of Earth Sciences, v. 55, p. 967-981.

McLaren, S., Sandiford, M., and Powell, R., 2005, Contrasting styles of Proterozoic crustal evolution: a hot-plate tectonic model for Australian terranes: Geology, v. 33, p. 673-676.

McLean, M.A., and Betts, P.G., 2003, Geophysical constraints of shear zones and geometry of Hiltaba Suite granites in the western Gawler Craton, Australia: Australian Journal of Earth Sciences, v. 50, p. 525-541.

McPhie, J., Kamenetsky, V.S., Chambefort, I., Ehrig, K., and Green, N., 2011, Origin of the supergiant Olympic Dam Cu-U-Au-Ag deposit, South Australia: was a sedimentary basin involved?: Geology, v. 39, p. 795-798.

McPhie, J., Orth, K., Kamenetsky, V., Kamenetsky, M., and Ehrig, K., 2016, Characteristics, origin and significance of Mesoproterozoic bedded clastic facies at the Olympic Dam Cu–U–Au–Ag deposit, South Australia: Precambrian Research, v. 276, p. 85-100.

Melo, G.H.C., Monteiro, L.V., Xavier, R.P., Moreto, C.P., Santiago, E.S., Dufrane, S.A., Aires, B., and Santos, A.F., 2017, Temporal evolution of the giant Salobo IOCG deposit, Carajás Province (Brazil): constraints from paragenesis of hydrothermal alteration and U-Pb geochronology: Mineralium Deposita, v. 52, p. 709-732.

Montreuil, J.-F., Corriveau, L., and Potter, E.G., 2015, Formation of albitite-hosted uranium within IOCG systems: the Southern Breccia, Great Bear magmatic zone, Northwest Territories, Canada: Mineralium Deposita, v. 50, p. 293-325.

Montreuil, J.-F., Corriveau, L., and Davis, W., 2016a, Tectonomagmatic evolution of the southern Great Bear magmatic zone (Northwest Territories, Canada) – Implications on the genesis of iron oxide alkali-altered hydrothermal systems, *in* Slack, J., Corriveau, L. and Hitzman, M., eds., Proterozoic iron oxide-apatite (± REE) and iron oxide-copper-gold and affiliated deposits of Southeast Missouri, USA, and the Great Bear magmatic zone, Northwest Territories, Canada: Economic Geology, v. 111, p. 2111-2138.

Montreuil, J.-F., Corriveau, L., Potter, E.G., and De Toni, A.F., 2016b, On the relation between alteration facies and metal endowment of iron oxide–alkali –altered systems, southern Great Bear Magmatic Zone (Canada), *in* Slack, J., Corriveau, L. and Hitzman, M., eds., Proterozoic iron oxide-apatite (± REE) and iron oxide-copper-gold and affiliated deposits of Southeast Missouri, USA, and the Great Bear magmatic zone, Northwest Territories, Canada: Economic Geology, v. 111, p. 2139-2168.

Montreuil, J.-F., Potter, E., Corriveau, L., and Davis, W.J., 2016c, Element mobility patterns in magnetite-group IOCG systems: the Fab IOCG system, Northwest Territories, Canada: Ore Geology Reviews, v. 72, p. 562-584.

Mumin, A.H., Somarin, A.K., Jones, B., Corriveau, L., Ootes, L., and Camier, J., 2010, The IOCG-porphyry-epithermal continuum of deposit types in the Great Bear magmatic zone, Northwest Territories, Canada, *in* Corriveau, L. and Mumin, H., eds., Exploring for iron oxide copper-gold deposits: Canada and global analogues: Geological Association of Canada Short Course Notes, No 20, p. 59-78.

Mumin, A.H., Phillips, A., Katsuragi, C.J., Mumin, A., and Ivanov, G., 2014, Geotectonic Interpretation of the Echo Bay Stratovolcano Complex, Northern Great Bear Magmatic Zone, Northwest Territories: Northwest Territories Geological Survey, Open File 2014-04.

Neumann, N.L., and Fraser, G.L. (eds.), 2007, Geochronological synthesis and time-space plots for Proterozoic Australia: Geoscience Australia Record 2007/06.

Oliver, N.H.S., Mark, G., Pollard, P.J., Rubenach, M.J., Bastrakov, E., Williams, P.J., Marshall, L.C., Baker, T., and Nemchin, A.A., 2004, The role of sodic alteration in the genesis of iron oxide-copper-gold deposits: geochemistry and geochemical modelling of fluid-rock intereaction in the Cloncurry district, Australia: Economic Geology, v. 99, p. 1145-1176.

Ootes, L., Snyder, D., Davis, W.J., Acosta-Góngora, P., Corriveau, L., Mumin, A.H., Gleeson, S.A., Samson, I.M., Montreuil, J.-F., Potter, E.G., and Jackson, V.A., 2017, A Paleoproterozoic Andean-type iron oxide copper-gold environment, the Great Bear magmatic zone, Northwest Canada: Ore Geology Reviews, v. 81, p. 123-139.

Oreskes, N., and Einaudi, M.T., 1990, Origin of rare earth element-enriched hematite breccias at the Olympic Dam Cu-U-Au-Ag deposit, Roxby Downs, South Australia: Economic Geology, v. 85, p. 1-28.

Oreskes, N., and Einaudi, M.T., 1992, Origin of hydrothermal fluids at Olympic Dam: preliminary results from fluid inclusions and stable isotopes: Economic Geology, v. 87, p. 64-90.

OZ Minerals, 2017, 2017 annual report: Available at https://www.ozminerals.com/-uploads/media/OZMinerals_2017_Annual_and_Sustainability_Report.pdf

OZ Minerals, 2018, Fremantle Doctor project mineral resource statement and explanatory notes: Available at https://www.ozminerals.com/media/fremantle-doctor-project-mineral-resource-statement-and-explanatory-notes-a/.

OZ Minerals, 2019, OZ Minerals 2018 Annual and sustainability report: Available at ozminerals.com.

Page, R.W., and Laing, W.P., 1992, Felsic metavolcanic rocks related to the Broken Hill Pb-Zn-Ag orebody, Australia: Economic Geology, v. 87, p. 2138-2168.

Page, R.W., Stevens, B.P.J., and Gibson, G.M., 2005, Geochronology of the sequence hosting the Broken Hill Pb-Zn-Ag orebody, Australia: Economic Geology, v. 100, p. 633-661.

Pollard, P.J., 2000, Evidence of a magmatic fluid and metal source for Fe-oxide Cu-Au mineralization, *in* Porter, T.M., ed., Hydrothermal iron oxide copper-gold and related deposits: a global perspective, volume 1: PGC Publishing, Adelaide, p. 27-41.

Porter, T.M., 2010, The Carrapateena iron oxide copper gold deposit, Gawler craton, South Australia: a review, *in* Porter, T.M., ed., Hydrothermal iron oxide copper-gold and related deposits: a global perspective, volume 3: PGC Publishing, Adelaide, p. 191-200.

Potter, E.G., Montreuil, J.-F., Corriveau, L., and De Toni, A., 2013, Geology and hydrothermal alteration of the Fab Lake region, Northwest Territories: Geological Survey of Canada, Open File 7339.

Potter, E.G., Montreuil, J.-F., Corriveau, L., and Davis, W., 2019, The Southern Breccia metasomatic uranium system of the Great Bear magmatic zone, Canada: iron oxide-copper-gold (IOCG) and albitite-hosted uranium linkages, *in* Decrée, S. and Robb, L., eds., Ore deposits: origin, exploration, and exploitation: Geophysical Monograph 242, First Edition, American Geophysical Union, John Wiley & Sons, Inc., p. 109-130.

Potter, E.G., Acosta-Góngora, P., Corriveau, L., Montreuil, J-F., and Yang, Z., 2022, Uranium enrichment processes in metasomatic iron oxide and alkali-calcic systems as revealed by uraninite trace element chemistry, *in* Corriveau, L., Potter, E.G. and Mumin, A.H., eds., Mineral systems with iron oxide copper-gold (IOCG) and affiliated deposits: Geological Association of Canada, Special Paper 52, p. 325-345.

Preiss, W.V., 2006, Tectonic overview of the Curnamona Province: Geoscience Australia Record 2006/21, p. 145-157.

Raymond, O.L., 2003, Moonta Subdomain (Yorke Peninsula), geophysical interpretation of basement geology, 1: 250 000 scale map (Second Edition): Geoscience Australia, Canberra.

Raymond, O.L., Fletcher, I., and McNaughton, N., 2002, Copper-gold mineral systems in the southeastern Gawler Craton - another Mt Isa Eastern Succession?, *in* Preiss, V.P., ed., Geoscience 2002: expanding horizons: 16th Australian Geological Convention, Adelaide, South Australia, Geological Society of Australia, Abstracts No. 67, p. 69.

Reeve, J.S., Cross, K.C., Smith, R.N., and Oreskes, N., 1990, Olympic Dam copper-uranium-gold-silver deposit, *in* Hughes, F.E., ed., Geology of the mineral deposits of Australia and Papua New Guinea: The Australasian Institute of Mining and Metallurgy, Monograph 14, p. 1009-1035.

Reid, A.J., 2017, Geology and metallogeny of the Gawler Craton, *in* Phillips, G.N., ed., Australian ore deposits: The Australasian Institute of Mining and Metallurgy, Monograph 32, p. 589-594.

Reid, A.J., Swain, G., Mason, D., and Maas, R., 2011, Project PGC01-02: nature and timing of Cu-Au-Zn-Pb mineralisation at Punt Hill, eastern Gawler Craton, *in* Reid, A.J. and Jagodzinski, E.A., eds., PACE geochronology: results of collaborative geochronology projects 2009–10: South Australia Department of Primary Industries and Resources, Report Book 2011/00003, p. 27-41.

Reid, A.J., Smith, R.N., Baker, T., Jagodzinski, E.A., Selby, D., Gregory, C.J., and Skirrow, R.G., 2013, Re-Os dating of molybdenite within hematite breccias from the Vulcan Cu-Au prospect, Olympic Cu-Au province, South Australia: Economic Geology, v. 108, p. 883-894.

Rex Minerals, 2015, Mineral resource & ore reserve for the Hillside deposit: Available at https://www.rexminerals.com.au/ resourceshillside.

Reynolds, L.J., 2000, Geology of the Olympic Dam Cu-U-Au-Ag-REE deposit, *in* Porter, T.M., ed., Hydrothermal iron oxide copper-gold and related deposits: a global perspective, volume 1: PGC Publishing, Adelaide, p. 93-104.

Richards, J.P., and Mumin, A.H., 2013, Magmatic-hydrothermal processes within an evolving Earth: iron oxide-copper-gold and porphyry Cu±Mo±Au deposits: Geology, v. 41, p. 767-770.

Richards, J.P., López, G.P., Zhu, J.J., Creaser, R.A., Locock, A.J., and Mumin, A.H., 2017, contrasting tectonic settings and sulfur contents of magmas associated with Cretaceous porphyry Cu±Mo±Au and intrusion-related iron oxide Cu-Au deposits in Northern Chile: Economic Geology, v. 112, p. 295-318.

Rieger, A.A., Marschik, R., Díaz, M., Hölzl, S., Chiaradia, M., Akker, B., and Spangenberg, J.E., 2010, The hypogene iron oxide copper-gold mineralization in the Mantoverde district, northern Chile: Economic Geology, v. 105, p. 1271-1299.

Rotherham, J.F., Blake, K.L., Cartwright, I., and Williams, P.J., 1998, Stable isotope evidence for the origin of the Mesoproterozoic Starra Au-Cu deposit, Cloncurry district, northwest Queensland: Economic Geology, v. 93, p. 1435-1449.

Rutherford, L., Hand, M., and Barovich, K., 2007, Timing of Proterozoic metamorphism in the southern Curnamona Province: implications for tectonic models and continental reconstructions: Australian Journal of Earth Sciences, v. 54, p. 65-81.

Schlegel, T.U., and Heinrich, C.A., 2015, Lithology and hydrothermal alteration control the distribution of copper grade in the Prominent Hill iron oxide-copper-gold deposit (Gawler craton, South Australia): Economic Geology, v. 110, p. 1953-1994.

Schlegel, T.U., Wälle, M., Steele-MacInnis, M., and Heinrich, C.A., 2012, Accurate and precise quantification of major and trace element compositions of calcic–sodic fluid inclusions by combined microthermometry and LA-ICPMS analysis: Chemical Geology, v. 334, p. 144-153.

Schlegel, T.U., Wagner, T., Boyce, A., and Heinrich, C.A., 2017, A magmatic source of hydrothermal sulfur for the Prominent Hill deposit and associated prospects in the Olympic iron oxide copper-gold (IOCG) province of South Australia: Ore Geology Reviews, v. 89, p. 1058-1090.

Schott, B., and Schmeling, H., 1998, Delamination and detachment of a lithospheric root: Tectonophysics, v. 296, p. 225-247.

Schurr, B., Rietbrock, A., Asch, G., Kind, R., and Oncken, O., 2006, Evidence for lithospheric detachment in the central Andes from local earthquake tomography: Tectonophysics, v. 415, p. 203-223.

Seyfried Jr, W.E., and Ding, K., 1993, The effect of redox on the relative solubilities of copper and iron in Cl-bearing aqueous fluids at elevated temperatures and pressures: an experimental study with application to subseafloor hydrothermal systems: Geochimica et Cosmochimica Acta, v. 57, p. 1905-1917.

Sillitoe, R.H., 2003, Iron oxide-copper-gold deposits: an Andean view: Mineralium Deposita, v. 38, p. 787-812.

Skirrow, R.G., 1993, The genesis of gold-copper-bismuth deposits, Tennant Creek, Northern Territory: Unpublished Ph.D. thesis, Canberra, Australian National University, 158 p.

Skirrow, R.G., 2000, Gold-copper-bismuth deposits of the Tennant Creek district, Australia: a reappraisal of diverse high-grade systems, *in* Porter, T.M., ed., Hydrothermal iron oxide copper-gold and related deposits: a global perspective, volume 1: PGC Publishing, Adelaide, p. 149-160.

Skirrow, R.G., 2010, 'Hematite-group' IOCG ±U ore systems: tectonic settings, hydrothermal characteristics, and Cu-Au and U mineralizing processes, *in* Corriveau, L. and Mumin, H., eds., Exploring for iron oxide copper-gold deposits: Canada and global analogues: Geological Association of Canada, Short Course Notes, No. 20, p. 39-59.

Skirrow, R.G., and Walshe, J.L., 2002, Reduced and oxidized Au-Cu-Bi iron oxide deposits of the Tennant Creek Inlier, Australia: an integrated geologic and chemical model: Economic Geology, v. 97, p. 1167-1202.

Skirrow, R.G., Ashley, P.M., Suzuki, K., and McNaughton, N.J., 2000, Time-space framework of Cu–Au(–Mo) and regional alteration systems in the Curnamona Province: AGSO Record, v. 10, p. 83-86.

Skirrow, R.G., Bastrakov, E., Davidson, G.J., Raymond, O., and Heithersay, P., 2002, Geological framework, distribution and controls of Fe-oxide Cu-Au deposits in the Gawler Craton. Part II. Alteration and mineralization, *in* Porter, T.M., ed., Hydrothermal iron oxide copper-gold and related deposits: a global perspective, volume 2: PGC Publishing, Adelaide, p. 33-47.

Skirrow, R.G., Fairclough, M.C., Budd, A.R., Lyons, P., Raymond, O., Milligan, P., Bastrakov, E., Fraser, G., Highet, L., Holm, O., and Williams, N., 2006, Iron oxide Cu-Au (-U) potential map of the Gawler Craton, South Australia (1st Edition), 1:500 000 scale map: Geoscience Australia, Canberra.

Skirrow, R.G., Bastrakov, E.N., Barovich, K, Fraser, G.L., Creaser, R.A., Fanning, C.M., Raymond, O.L., and Davidson, G.J., 2007, Timing of iron oxide Cu-Au-(U) hydrothermal activity and Nd isotopic constraints on metal sources in the Gawler Craton, South Australia: Economic Geology, v. 102, p. 1441-1470.

Skirrow, R.G., van der Wielen, S.E., Champion, D.C., Czarnota, K., and Thiel, S., 2018, Lithospheric architecture and mantle metasomatism linked to iron oxide Cu-Au ore formation: multidisciplinary evidence from the Olympic Dam region, South Australia: Geochemistry, Geophysics, Geosystems, v. 19, p. 2673-2705.

Stewart, J.R., and Betts, P.G., 2010, Late Paleo–Mesoproterozoic plate margin deformation in the southern Gawler Craton: insights from structural and aeromagnetic analysis: Precambrian Research, v. 177, p. 55-72.

Stolz, A.J., Large, R.R., Robinson, P., and Wedekind, R., 1994, Criteria for distinguishing between gold-bearing and barren ironstones at Tennant Creek, Northern Territory, Australia: Journal of Geochemical Exploration, v. 51, p. 247-264.

Swain, G., Barovich, K., Hand, M., Ferris, G., and Schwarz, M., 2008, Petrogenesis of the St Peter Suite, southern Australia: arc magmatism and Proterozoic crustal growth of the South Australian Craton: Precambrian Research, v. 166, p. 283-296.

Teale, G.S., and Fanning, C.M., 2000, The Portia-North Portia Cu-Au(-Mo) prospect, South Australia: timing of mineralization, albitisation and origin of ore fluid, *in* Porter, T.M., ed., Hydrothermal iron oxide copper-gold and related deposits: a global perspective, volume 1: PGC Publishing, Adelaide, p. 137-147.

Torresi, I., Xavier, R.P., Bortholoto, D.F., and Monteiro, L.V., 2012, Hydrothermal alteration, fluid inclusions and stable isotope systematics of the Alvo 118 iron oxide–copper–gold deposit, Carajás Mineral Province (Brazil): implications for ore genesis: Mineralium Deposita, v. 47, p. 299-323.

Ullrich, T.D., and Clark, A.H., 1999, The Candelaria copper-gold deposit, Region III, Chile: paragenesis, geochronology and fluid composition, *in* Stanley, C.J., ed., Mineral deposits: processes to processing: Balkema, Rotterdam, p. 201-204.

Wade, C.E., 2012, Geochemistry of pre-1570 Ma mafic magmatism within South Australia: implications for possible tectonic settings and timing of major mineralization events in South Australia: Department of State Development, South Australia, Adelaide, Report Book 2012/00019.

Wade, B.P., Barovich, K.M., Hand, M., Scrimgeour, I.R., and Close, D.F., 2006, Evidence for Early Mesoproterozoic arc magmatism in the Musgrave Block, central Australia: implications for Proterozoic crustal growth and tectonic reconstructions of Australia: The Journal of Geology, v. 114, p. 43-63.

Wade, C.E., Reid, A.J., Wingate, M.T., Jagodzinski, E.A., and Barovich, K., 2012, Geochemistry and geochronology of the c. 1585 Ma Benagerie Volcanic Suite, southern Australia: relationship to the Gawler Range Volcanics and implications for the petrogenesis of a Mesoproterozoic silicic large igneous province: Precambrian Research, v. 206, p. 17-35.

Webb, A.W., Thomson, B.P., Blissett, A.H., Daly, S.J., Flint, R.B., and Parker, A.J., 1986, Geochronology of the Gawler Craton, South Australia: Australian Journal of Earth Sciences, v. 33, p. 119-143.

Wedekind, M.R., Large, R.R., and Williams, B.T., 1989, Controls on high-grade gold mineralization at Tennant Creek, Northern Territory, Australia: Economic Geology, Monograph 6, p. 168-179.

Williams, P.J., 1998, An introduction to the metallogeny of the McArthur River-Mount Isa-Cloncurry minerals province: Economic Geology, v. 93, p. 1120-1131.

Williams, P.J., 2010a, Classifying IOCG Deposits, *in* Corriveau, L. and Mumin, A.H., eds., Exploring for iron oxide copper-gold deposits: Canada and global analogues: Geological Association of Canada, Short Course Notes, No. 20, p. 13-21.

Williams, P.J., 2010b, "Magnetite-group" IOCGs with special reference to Cloncurry and Northern Sweden: settings, alteration, deposit characteristics, fluid sources, and their relationship to apatite-rich iron ores, *in* Corriveau, L. and Mumin, A.H., eds., Exploring for iron oxide copper-gold deposits: Canada and global analogues: Geological Association of Canada, Short Course Notes, No. 20, p. 23-38.

Williams, P.J., and Skirrow, R.G., 2000, Overview of iron oxide-copper-gold deposits in the Curnamona Province and Cloncurry district (eastern Mount Isa Block), Australia, *in* Porter, T.M., ed., Hydrothermal iron oxide copper-gold and related deposits: a global perspective, volume 1: PGC Publishing, Adelaide, p. 105-122.

Williams, P.J., Guoyi Dong, Ryan, C.G., Pollard, P.J., Rotherham, J.F., Mernagh, T.P., and Chapman, L.H., 2001, Geochemistry of hypersaline fluid inclusions from the Starra (Fe oxide)-Au-Cu deposit, Cloncurry district, Queensland: Economic Geology, v. 96, p. 875-883.

Williams, P.J., Barton, M.D., Johnson, D.A., Fontboté, L., de Haller, A., Mark, G., Oliver, N.H.S., and Marschik, R., 2005, Iron oxide copper-gold deposits: geology, space-time distribution, and possible modes of origin: Economic Geology, v. 100, p. 371-405.

Xavier, R.P., Rusk, B., Emsbo, P., and Monteiro, L.V.S., 2009, Composition and source of salinity of ore-bearing fluids in Cu-Au systems of the Carajás Mineral Province, Brazil: Proceedings of the 10th Biennial Meeting of the SGA, 17-20 August 2009, Townsville, Australia, p. 272-274.

Zang, W.L., Fanning, C.M., Purvis, A.C., Raymond, R.L., and Both, R.A., 2007, Mesoproterozoic bimodal plutonism in the southeastern Gawler Craton, South Australia: Australian Journal of Earth Sciences, v. 54, p. 661-674.

# “Magnetite-group” IOCGs with Special Reference to Cloncurry (NW Queensland) and Northern Sweden: Settings, Alteration, Deposit Characteristics, Fluid Sources, and Their Relationship to Apatite-rich Iron Ores

**Patrick J. Williams**
**1957-2018**
*Formerly at Economic Geology Research Unit, School of Earth and Environmental Sciences,*
*James Cook University, Townsville 4811, Australia*
*Manuscript reproduced from the 2010 Geological Association of Canada Short Course Notes, No. 20*
***With Fond Memories***

*Recommended citation: Williams, P.J., 2022, "Magnetite-group" IOCGs with special reference to Cloncurry (NW Queensland) and northern Sweden: settings, alteration, deposit characteristics, fluid sources and their relationship to apatite-rich iron ores, in Corriveau, L., Potter, E.G. and Mumin, A.H., eds., Mineral systems with iron oxide-copper-gold (IOCG) and affiliated deposits: Geological Association of Canada, Special Paper 52, p. 53-68.*

## Abstract

Iron oxide-copper-gold (IOCG) and archetypical iron oxide-apatite (IOA) deposits in Norrbotten, Sweden are products of ca. 150 Ma evolution of a Palaeoproterozoic continental margin arc. The IOCG and affiliated deposits near Cloncurry in northwest Queensland formed during at least two separate metallogenic events in intracontinental, possibly distal subduction-related settings. Most Cloncurry IOCG deposits appear to have formed at 1540–1500 Ma in association with the emplacement of batholithic, predominantly potassic I-type (A-type) granitoids and the development of giant, dominantly sodic-calcic-type alteration systems. The principal wall rock alteration around Norrbotten IOA deposits and barren iron oxide accumulations in the Cloncurry district is sodic-calcic. Norrbotten IOA deposits mostly occur independently of economically significant copper and gold and where metal sulphides are hosted by IOA deposits they are part of a late stage paragenetic association. IOCG deposits in both districts are mostly associated with moderate to high temperature K-Fe-(Ba-Mn) silicate ± magnetite alteration, typically overprinting pre-existing sodic-calcic assemblages with abundant late-stage carbonates (predominantly calcite). The potassic alteration assemblages and magnetite association are reminiscent of porphyry-related copper-gold deposits but the mineralogy and geochemistry of the IOCG deposits are different in other ways and also rather more variable than in porphyry-related systems. Currently available data in the two described settings are inadequate to argue for or against a direct process link between IOA and IOCG deposits. Recent studies of IOCG fluid inclusion geochemistry suggest that IOCG deposits may have been formed in more than one fundamentally different type of hydrothermal system, some but not all of which were characterized by direct involvement of magmatic fluids.

## Résumé

Les gîtes d’oxydes de fer–cuivre–or (IOCG) et les gîtes d’oxydes de fer–apatite archétypiques (IOA) à Norrbotten, Suède, sont les produits de l’évolution, pendant environ 150 millions d’années, d’un arc de marge continentale paléoprotérozoïque. Les gîtes IOCG et affiliés près de Cloncurry dans le nord-ouest du Queensland se sont formés au cours d’au moins deux événements métallogéniques séparés dans des contextes intracontinentaux, peut-être distaux, reliés à une zone de subduction. La plupart des gîtes IOCG à Cloncurry semblent s’être formés à 1540–1500 Ma, pendant la mise en place de granitoïdes batholitiques surtout potassiques de type I (type A) et le développement de systèmes d’altération géants surtout de type sodicalcique. L’altération principale affectant les encaissants autour des gîtes IOA à Norrbotten et les accumulations d’oxydes de fer stériles dans le district de Cloncurry est sodique–calcique. Les gîtes IOA à Norrbotten sont majoritairement indépendants des gîtes de cuivre-or d’intérêt économique, et là où des sulfures à métaux sont encaissés dans des gîtes IOA, ces sulfures font partie d’une association paragénétique tardive. Les gîtes IOCG dans les deux districts sont majoritairement associés à une altération à silicates ± magnétite K–Fe (–Ba–Mn) de température modérée à élevée, laquelle se superpose sur des assemblages sodicalciques préexistants à carbonates tardifs abondants. Les assemblages de l’altération potassique et l’association à magnétite rappellent les gîtes de cuivre-or de type porphyre, mais la minéralogie et la géochimie des gîtes IOCG montrent des traits différents et plutôt variables par rapport aux systèmes reliés aux porphyres. Les données présentement disponibles provenant des deux contextes décrits sont inadéquates pour pouvoir argumenter pour ou contre un lien direct de processus entre les gîtes IOA et les gîtes IOCG. Des études récentes sur la géochimie des inclusions fluides dans des gîtes IOCG suggèrent que ces derniers ont pu se former à partir de plus d’un type de système hydrothermal, que ces systèmes étaient fondamentalement différents et que certains d’entre eux, mais pas tous, étaient caractérisés par l’implication directe de fluides magmatiques

## Introduction

The majority of economically-significant IOCG systems contain magnetite as the principal iron oxide (e.g. Williams et al., 2005). These are typically in districts that also contain barren or weakly copper-gold mineralized magnetite bodies, a situation that provides an immediate challenge to geophysics-based exploration. Some IOCG districts contain examples of the equally distinctive iron oxide-apatite ("IOA") deposits, commonly referred to as Kiruna-type iron ores. This has created much speculation about possible genetic relationships between these two deposit types (e.g. Hitzman, 2000).

This chapter reviews features of IOCG deposits in two key Proterozoic districts. Northern Norrbotten county in Sweden is one of the world's principal IOA districts and also contains a variety of magnetite-bearing copper-gold deposits, some of which can be readily classified as IOCGs whereas others are more problematical (Table 1; Carlon, 2000). The Cloncurry area in northwest Queensland, Australia contains several economically significant IOCG and affiliated deposits (Table 2) representing a number of different deposit styles, and to date has been the most intensively studied IOCG setting worldwide (Williams and Skirrow, 2000; Mark et al., 2006a). These districts provide important case studies in magnetite group IOCG alteration associations, deposit style diversity, distinctions between barren and copper-gold mineralized iron oxide accumulations, and the relationships between IOCG and IOA deposits.

## Geological Context and Copper-gold Deposit Styles

*Norrbotten*

IOA and IOCG deposits in northern Sweden and adjacent parts of Norway and Finland (Fig. 1) formed during the evolution of a Palaeoproterozoic continental margin arc from ca. 1.90 to 1.75 Ga (Juhlin et al., 2002). The age, tectonic context and metallogenic character in many respects resemble those of Great Bear magmatic zone in northern Canada (Mumin et al., 2010). The principal intrusive suites of the region were emplaced in two main phases, an older one from ca. 1.88–1.86 Ga that produced differentiated basic to felsic rocks (Haparanda and perthite-monzonite suites), and a younger phase of felsic granites and pegmatites (Lina granites; e.g. Bergman et al., 2001). Ore deposits are hosted both by juvenile arc rocks and by older Palaeoproterozoic volcanosedimentary sequences preserved from earlier rift events (Martinsson and Weihed, 1999).

Epigenetic copper-gold deposits are concentrated in the Kiruna-Gällivare area of Norrbotten which also hosts the most significant IOA deposits. The latter have a strong spatial association with intermediate to felsic metavolcanic rocks of the 1.91–1.88 Ga Porphyry Group (Bergman et al., 2001;

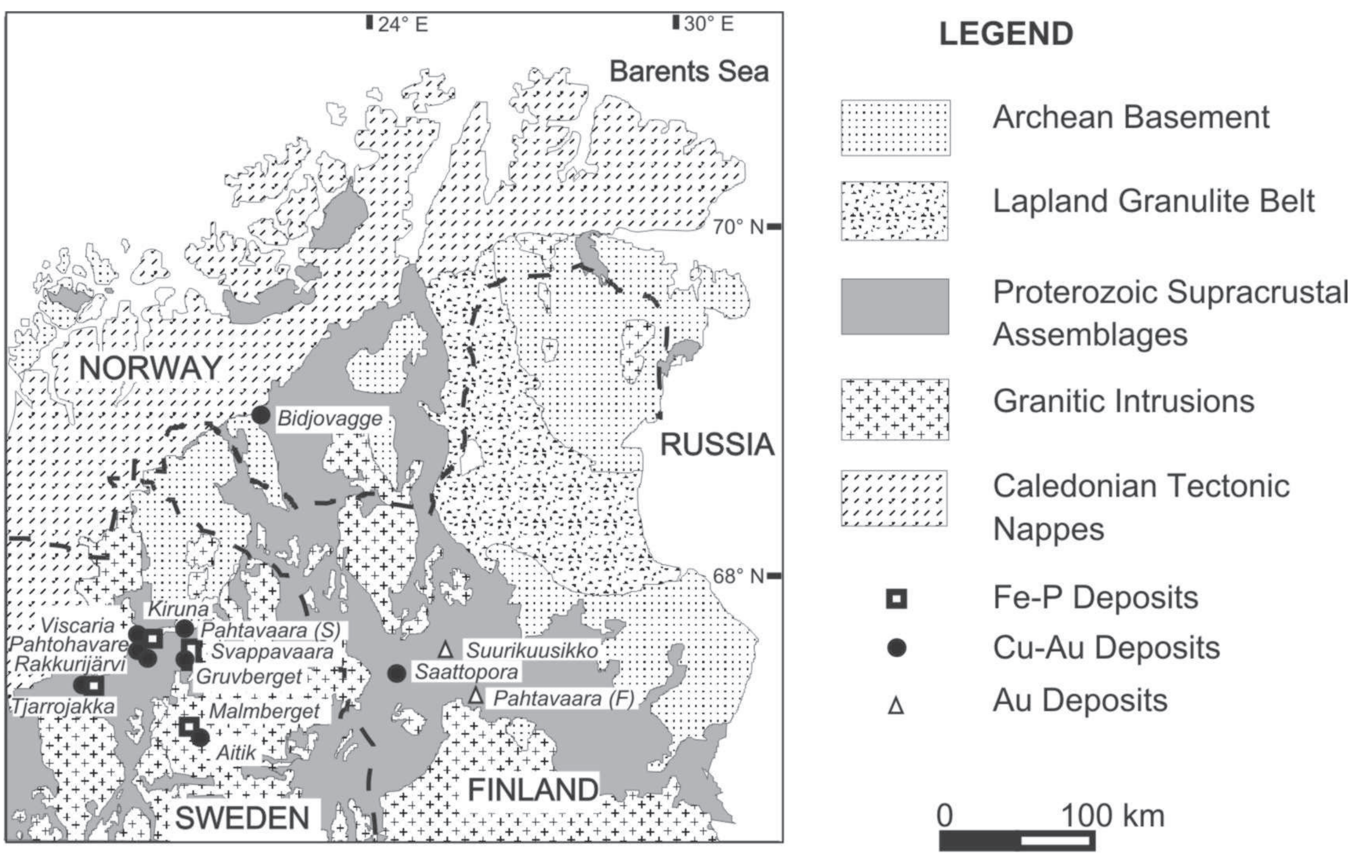


**Figure** 1. Geological map of the northern Fennoscandian Shield showing the location of selected copper and iron oxide apatite deposits (adapted from Ettner et al., 1994).

Edfelt et al., 2006; Fig. 1). The copper-gold deposits occur in different parts of the stratigraphic sequence and some are hosted by intrusions. At two places (i.e. Gruvberget and Tjårrojåkka; Fig. 1), significant copper-gold occurrences are closely associated, but not coincident with large iron oxide-apatite bodies (Lindskog, 2001; Edfelt et al., 2005). Some of the Norrbotten copper-gold deposits have strong IOCG affinities (e.g. Kiskamavaara, Nautanen, Pahtohavare, Rakkurijärvi, Tjårrojåkka copper; Table 1) whereas others such as the large deposit at Aitik and the Vaikijaur prospect have associations with intrusions and other characteristics consistent with a possible porphyry type origin (Wanhainen et al., 2003; Lundmark et al., 2005).

*Cloncurry*

The geology of the Cloncurry district (Fig. 2) is dominated by 1.85–1.60 Ga supracrustal sequences intruded by several generations of batholithic granitoids (e.g. Williams and Skirrow, 2000). There appear to have been two episodes of copper-gold metallogeny associated with discrete orogenic events at around 1.60 Ga and from 1.55 to 1.50 Ga (e.g. Betts et al., 2006). These rock systems have conventionally been interpreted as products of intracratonic basin development and orogeny (e.g. Etheridge et al., 1987). However, Betts et al. (2002, 2006) have recently proposed that the supracrustal sequences developed in distant subduction-related marginal basin settings and that deformation and granitoid emplacement (and by implication iron oxide-copper-gold mineralization) from around 1.60 Ga were associated with a destructive plate boundary east of the current Australian continent.

The Cloncurry copper-gold deposits display some striking similarities with those in Norrbotten. They have a range of host rocks and are distributed mainly within various parts of the regional supracrustal sequence although a giant hydrothermal magnetite deposit and copper-gold prospect at Lightning Creek is granitoid-hosted (Table 2). Regional sodic (-calcic) metasomatism is mainly represented by albite and actinolite though scapolitic rocks are also present locally (e.g. De Jong and Williams, 1995). As in Norrbotten, the copper-gold deposits have a more specific association with potassic alteration represented by biotite (-magnetite) and K-feldspar. Chalcopyrite and pyrite are again the most important sulphide minerals though some of the Cloncurry ores (e.g. Eloise; parts of the Osborne deposit) are pyrrhotite-rich. Syn- to post-mineralization carbonate minerals are present in all cases. The Lightning

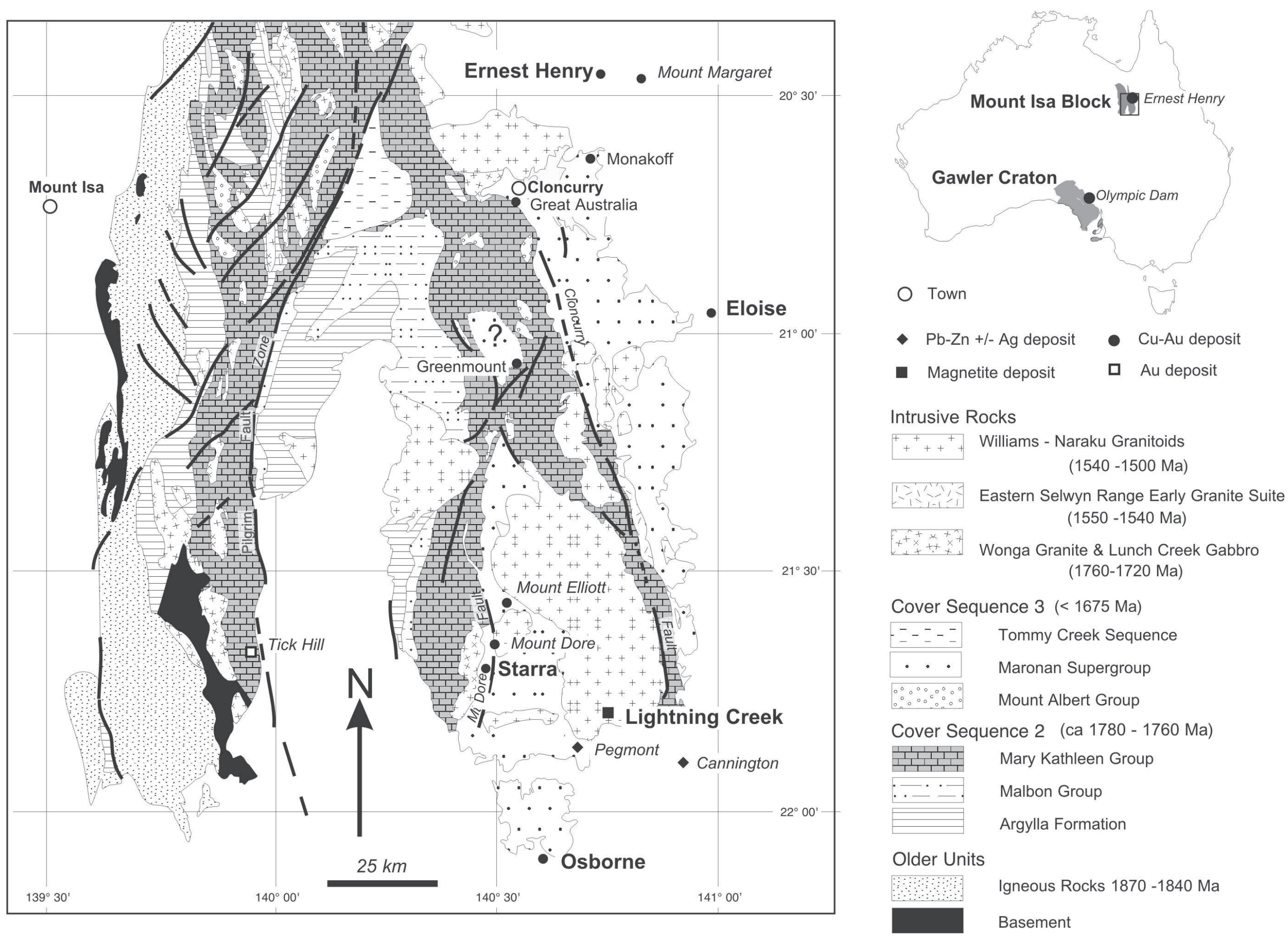


**FIGURE** 2. Geology and principal mineral deposits of the Cloncurry district (adapted from Williams, 1998).

TABLE 1. Characteristics of selected iron and copper deposits in Norrbotten, Sweden

| Deposit | Resource Principal Metals (Element Associations) | Structural Setting & Style | Principal Alteration & Paragenesis | References |
|---|---|---|---|---|
| **Gruvberget** | 74 Mt @ 41% Fe (P) (Cu sulphides in host rocks no resource) | Massive Mgt+Hem body | 1) Ab, Act, Scp, Mgt<br>2) Kfs-Ep-Ccp-Bn-Mgt, Cct | Frietsch (1966)<br>Lindskog (2001) |
| **Kiirunavaara** | 2000 Mt @ 60–68% Fe (P) (minor Fe-Cu sulphides | Massive Mgt+Hem body with marginal Mgt matrix breccias | 1) Ab, Act, Scp, Mgt<br>2) Hem<br>3) Py-Ccp-Cct | Frietsch (1978); Cliff et al. (1990); Blake (1992); Nyström and Henriquez (1994) |
| **Malmberget** | 660 Mt @ 51–61% Fe (P) | Massive Mgt and Hem lenses in a high grade metamorphic setting greatly intruded by synmetamorphic granites. | Ab, Kfs, Bt, Scp | Geijer (1930)<br>Grip and Frietsch (1973)<br>Bergman et al. (2001) |
| **Rektorn** | 2.5 Mt Fe, Ap | Ap-rich and Qtz-rich Mgt + Hem massive ore | Kfs, Ms, Chl<br>Late stage Py, Ccp, Cct | Giejer (1950)<br>Berman et al. ( 2001) |
| **Svappavaara-Leveaniemi** | 308 Mt @ 35–65% Fe (P) | Massive Mgt and Mgt matrix breccia in Bt schist | Ab, Amph, Mgt, Ap, Cct | Frietsch (1966); Hitzman et al. (1992); Bergman et al. (2001) |
| **Tjårrojåkka Fe** | 53 Mt @ 52% Fe, (P, minor Cu) | Massive Mgt and Mgt matrix breccia | 1) Ab, Scp, Mgt, Ap<br>2) Kfs, Amph Late stage Hem, Py, Ccp, Cct | Edfelt et al. (2005, 2006)<br>Sandrin and Elming (2007) |
| **Aitik** | 600 Mt @ 0.4% Cu, 0.2 g/t Au (Ba) | Shear zone hosted (?) IOCG or porphyry). Veins and disseminations | 1) Hbl, Kfs, Scp, Mgt<br>2) Grt, Bt, Ms, Qtz, Mgt, Ccp, Py, Cct | Zweifel (1976); Monro (1988) Wanhainen et al. (2003, 2005, 2006) |
| **Kiskamavaara** | 3.4 Mt @ 0.37% Cu (0.09% Co) | Sulphides and Fe oxides in breccia matrix | 1) Ab, Scp, 2) (Ba) Kfs<br>3) Mgt, Hem, Ccp, Py | Frietsch et al. (1997)<br>Bergman et al. (2001) |
| **Nautanen** | 0.6 Mt @ 2.4% Cu, 1.3 g/t Au, 11 g/t Ag | Shear zone hosted disseminated Ccp-Bn-Mgt | Amph, Alm/Sps, Bt, Mgt | Danielson (1985)<br>Frietsch et al. (1997) |
| **Pahtohavare** | 5.4 Mt @ 2.2% Cu, 1.3 g/t Au | Sulphide-Qtz-Ank veins in albitized carbonaceous schists | 1) Ab, Bt-Scp<br>2) Bt<br>3) Ccp-Py-Ank-Qtz | Carlson (1991)<br>Frietsch et al. (1997)<br>Martinsson (1997) |
| **Rakkurijärvi** | Cu, Au | Brecciated Mgt-Ap and metavolcanic rocks | 1) Ab, Mgt, Scp, Act, Ap<br>2) Scp, Bt, Kfs, Hem, 3) Chl, Ep Ccp, Py, Cct, Hem | Smith et al. (2007) |
| **Tjårrojåkka Cu** | 13.1 Mt @ 0.43% Cu (Mo) | Ap-Mgt-sulphide veins and disseminations | 1) Ab, Scp, Mgt, 2) Kfs, Hbl, Bt, Hem, Py, Ccp, 3) Cct | Edfelt et al. (2005, 2006)<br>Sandrin and Elming (2007) |
| **Vaikijaur** | Cu, Au (Mo) | Qtz-sulphide veins and disseminations | 1) Kfs, Bt, Qtz, Mgt, Py<br>2) Epi, Chl, Ms, Ccp, Mby | Lundmark et al. (2005) |
| **Viscaria** | 30 Mt @ 1.5% Cu (Zn, Ag, Au, Ba, P) | Stratabound Mgt-sulphide lenses in carbonaceous schist (? VHMS) | Ms, Bt, Kfs (alteration) Mgt, Po, Ccp, Cct, Brt (ore) | Martinsson (1997)<br>Carlon (2000) |

Mineral abbreviations (Tables 1 and 2): Act - actinolite; Ab - albite; Alm - almandine; Adr - andradite; Amph- amphibole (unspecified); Anh - anhydrite; Ap - apatite; Brt - barite; Bt - biotite; Bn - bornite; Cct - calcite; Cc - chalcocite; Cbt- cobaltite; Ccp - chalcopyrite; Chl - chlorite; Di - diopside; Dol - dolomite; Ep - Epidote; Fl - fluorite; Gn - galena; Hem - hematite; Hbl - hornblende; Hyl - hyalophane; Kfs - K-feldspar; Mgt - magnetite; Mby - Molybdenite; Ms - muscovite; Phl - phlogopite; Py - pyrite; Po - pyrrhotite; Qtz - quartz; Rds - rhodochrosite; Scp - scapolite; Sd - siderite; Sps - spessartine; Sp - sphalerite; Tur - tourmaline.

**Table 2.** Characteristics of selected iron and/or copper deposits in the Cloncurry District. Mineral abbreviations as in Table 1.

| Deposit | Resource Principal Metals (Element Associations) | Structural Setting & Style | Principal Alteration & Paragenesis | References |
|---|---|---|---|---|
| **Lightning Creek** | *Fe >2000 Mt Mgt (modelled from geophysics)* | Subhorizontal vein-dyke association in felsic pluton | 1) Ab-Di<br>2) Mgt-Di-Qtz | Perring et al. (2000, 2001) |
| **Eloise** | 3.7 Mt @ 4.1% Cu, 1.1 g/t Au (12g/t Ag, Co, Ni) | Shear zone hosted sulphide ± Qtz lenses | 1) Ab<br>2) Hbl-Bt-Qtz<br>3) Chl-Ms-Act-Cct-Mgt-Ccp-Po-Py | Brecianini et al. (1992); Baker (1998); Baker and Laing (1998); Baker et al. (2001)<br>Mudd (2007) |
| **Ernest Henry** | 167 Mt @ 1.1% Cu, 0.54 g/t Au (Co, As, Mo, Ba) | Mgt-sulphide matrix breccia body bounded by shear zones | 1) Ab-Di-Act-Mgt<br>2) Bt-Alm/Sps-Kfs-Mgt<br>3) Kfs/Hyl, 4) Bt-Qtz-Mgt-Ccp-Py-Cct-Brt-Fl; 5) Cct-Dol-Qtz | Webb and Rowston (1995)<br>Twyerould (1997)<br>Mark et al. (2006b) |
| **Mount Elliott** | 6.3 Mt @ 4.6% Cu, 1.8 g/t Au (Co, Ni) | Fault controlled, skarn hosted veins and breccia | 1) Ab; 2) Di-Act-Scp; 3) Adr-Mgt-Py-Ccp-Po; 4) Cct-Ap | Wang and Williams (2001)<br>Sleigh (2002) |
| **Osborne** | 15.5 Mt @ 3.0% Cu, 1.0 g/t Au (Co, Mo) | Qtz-sulphide lodes | 1) Ab-Bt (? metamorphic)<br>2) Bt/Phl-Qtz-Mgt; 3) Qtz-Mgt-Hem-Py-Po-Ccp; 4) Ms-Chl-Cct | Adshead (1995); Adshead et al. (1998); Gauthier et al. (2001); Mudd (2007) |
| **Starra** | 6.9 Mt @ 2.1% Cu, 4.6 g/t Au | Shear zone hosted ironstones with sulphide overprint | 1) Ab<br>2) Bt-Mgt<br>3) Ms-Chl-Hem-Cct-Anh-Py-Ccp-Bn-Cc | Davidson et al. (1989); Rotherham (1996); Adshead-Bell (1998); Rotherham et al. (1998); Sleigh (2002) |
| **Mount Dore** | 27 Mt @ 0.7% Cu (0.1 g/t Au, Zn) | Fault controlled breccia and veins | 1) Qtz, Bt, Kfs, Ms<br>2) Chl-Ap-Cct-Py-Ccp | Beardsmore (1992)<br>Sleigh (2002) |
| **Mount Cobalt** | 20 kt @ 4% Co (As, W, REE) | Shear zone-hosted sulph-arsenide veins | 1) Scp, Bt, Ab<br>2) Cbt | Nisbet et al. (1983) |

Creek occurrence is notable because it preserves evidence for large-scale magnetite precipitation from locally-derived magmatic fluids under transitional magmatic-hydrothermal conditions (Perring et al., 2000). Conditions of copper-gold mineralization as deduced from a combination of hydrothermal phase relationships, fluid inclusion evidence and stable isotope equilibration temperatures, seem to have differed from place-to-place (e.g. 350–450°C at Ernest Henry as opposed to 220–360°C at Starra; Rotherham et al., 1998; Mark et al., 2001).

## Timing of Mineralization in a Regional Context

*Norrbotten*

The Kiirunavaara IOA deposit has been shown to be older than 1880 ± 3 Ma based on the U-Pb zircon age of a cross-cutting granophyre dyke (Cliff et al., 1990). Titanites associated with magnetite near the northern extension of the deposit at Luossavaara have been dated at 1888 ± 6 Ma and 1876 ± 9 Ma (Romer et al., 1994). This suggests IOA ore emplacement near Kiruna was temporally associated with the Svecofennian volcanism and early intrusions at ca. 1885 Ma.

Several of the IOA deposits (e.g. Kiirunavaara, Gruvberget, Tjårrojåkka) contain, or are spatially associated with copper ± gold occurrences (Table 1). In such cases the sulphide parageneses invariably overprint the magnetite bodies (Fig. 3). Economically-significant copper occurrences hosted by IOA deposits are not known with the possible exception of the Rakkurijärvi prospect where a portion of the copper is hosted by brecciated magnetite rock (Smith et al., 2007). Age constraints on Norrbotten copper metallogeny suggest a temporal association with regional intrusive activity and a protracted evolutionary history. Two molybdenites from porphyry-style veins at the Vaikijaur prospect gave Re-Os ages of 1889 ± 10 Ma and 1868 ± 6 Ma (Lundmark et al., 2005). At Rakkurijärvi two molybdenites from the copper-bearing sulphide paragenesis yielded ages of 1853 ± 6 and 1862 ± 6 Ma (Smith et al., 2007). Replicate molybdenites from a deformed barite vein at Aitik gave ages of 1876 ± 10 and 1875 ± 6 Ma which are similar to that of a spatially associated quartz monzodiorite (1887 ± 8 Ma; Wanhainen et al., 2006) and interpreted to reflect the age of primary mineralization (Wanhainen et al., 2005, 2006). Molybdenites from a quartz-chalcopyrite vein and an older (deformed) pegmatite were constrained to 1856–1840 Ma and one from an undeformed pegmatite gave an age of 1728 ± 7 Ma. U-Pb dating of Aitik titanites from a variety of alteration associations and pegmatite gave a range of ages from ca. 1805 to 1750 Ma, which in conjunction with the other data led Wanhainen et al. (2005) to suggest that the deposit was significantly remobilized during that period. Thus

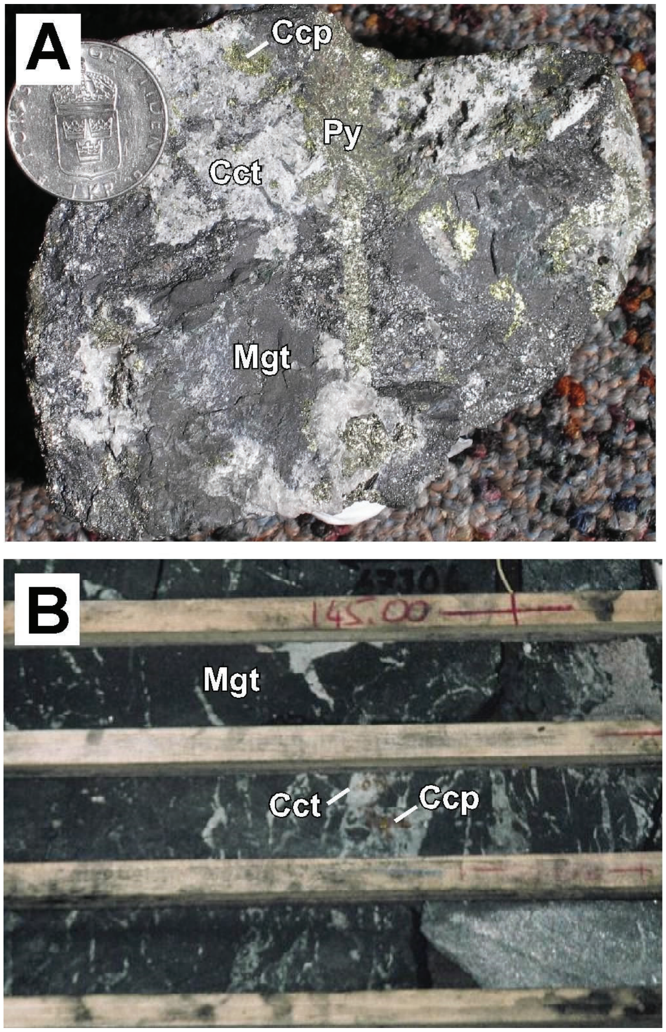


**FIGURE 3.** Examples of magnetite-sulphide relationships in Norrbotten IOA deposits. **A.** Hand sample from the Kiirunavaara deposit with brecciated fine-grained magnetite (Mgt) ore overprinted by pyrite (Py)-chalcopyrite (Ccp)-calcite (Cct). **B.** Drill core (3 cm diameter) from the Tjårrojåkka iron deposit showing magnetite overprinted by chalcopyrite (Ccp)-bearing calcite (Cct) veins.

while some of the Norrbotten copper deposits maybe the same age as the Kiirunavaara iron ores, others (e.g. Rakkurijärvi) appear to be significantly younger. Yet others (e.g. Aitik) could be younger by 10–15 m.y. within the constraints of the current dating.

*Cloncurry*

U-Pb ages of zircons and titanites from metamorphic rocks and synmetamorphic pegmatites imply there was a high grade metamorphic event at ca. 1600 Ma (Fig. 4). Re-Os dates of molybdenite from the Osborne deposit (Gauthier et al., 2001) imply there was a phase of IOCG formation at about this time (corresponding to the major IOCG-forming events in the Gawler craton and Curnamona province in southern Australia; Williams and Pollard, 2003). No major intrusions of this age are known in the Cloncurry district. $^{40}Ar/^{39}Ar$ ages of metamorphic amphiboles and biotites suggest resetting and cooling through blocking temperatures from ca. 1570 to 1540 Ma (Fig. 4), coincident in the later parts with the onset of granitoid emplacement and of regional sodic metasomatic breccia systems (Williams, 1994; De Jong and Williams, 1995; Oliver et al., 2004). Most geochronological data from other IOCG and affiliated mineralized systems in the district suggest these formed synchronously with granitoid intrusion and ongoing Na metasomatism from ca. 1540 to 1500 Ma.

In the case of Ernest Henry, U-Pb titanite dates of pre-ore alteration (Mark et al., 2006b), a U-Pb rutile date from ore breccia (Gunton, 1999), $^{40}Ar/^{39}Ar$ ages of metasomatic biotites (Twyerould, 1997) and several Re-Os ages of molybdenite from peripheral veins (Mark et al., 2004c) are all consistent with ore emplacement at ca. 1530 Ma. However, three replicate whole rock Re-Os ages from a single ore sample gave conflicting results close to 1670 Ma (Mark et al., 2004c). This discrepancy remains unexplained. $^{40}Ar/^{39}Ar$ ages of hydrothermal phyllosilicates and amphiboles from several other copper deposits in the district including Eloise, Mount Elliott and Starra are in the range 1530–1500 Ma (Pollard and Perkins, 1997; Perkins and Wyborn, 1998; Baker et al., 2001) and the large magmatic-hydrothermal magnetite deposit at Lightning Creek is constrained to 1520–1510 Ma from SHRIMP U-Pb zircon dating of the igneous hosts (Pollard and McNaughton, 1997).

## Alteration-mineralization Zoning and Paragenesis

*Regional-scale Alteration*

Bedrock is generally poorly exposed in Norrbotten owing to extensive cover of glacial till, peat and lakes. However, many of the outcrops that do exist, particularly in the supracrustal sequences, reveal evidence of sodium-chlorine metasomatism manifested in the development of scapolite (Frietsch et al., 1997). By contrast, large portions of the Cloncurry district are very well exposed and reveal the presence of a huge volume of brecciated and metasomatized rocks in which the main alteration is sodic-calcic and characterized principally by albitic plagioclase, actinolite and diopside with plentiful evidence for redistribution of iron and its localized concentration as magnetite. The altered rocks are concentrated along the flanks, and in the roof zones of the 1540–1500 Ma batholithic granitoid bodies. A wealth of field and geochronological data demonstrate a close temporal association between the alteration and these intrusions (Williams, 1994; De Jong and Williams, 1995; Mark, 1998; Mark and Foster, 2000; Mark et al., 2004c; Oliver et al., 2004, 2006; Marshall and Oliver, 2006; Austin and Blenkinsop, 2008). Systematic drilling of the greater area around the (concealed) Ernest Henry deposit has revealed extensive sodic-calcic alteration of the predominantly metavolcanic host rocks (Mark et al., 2006b; Corriveau et al., 2010).

*Deposit-related Alteration*

In Norrbotten, the principal alteration associated with IOA deposits is sodic-calcic in character (e.g. Fig. 5A; Frietsch et

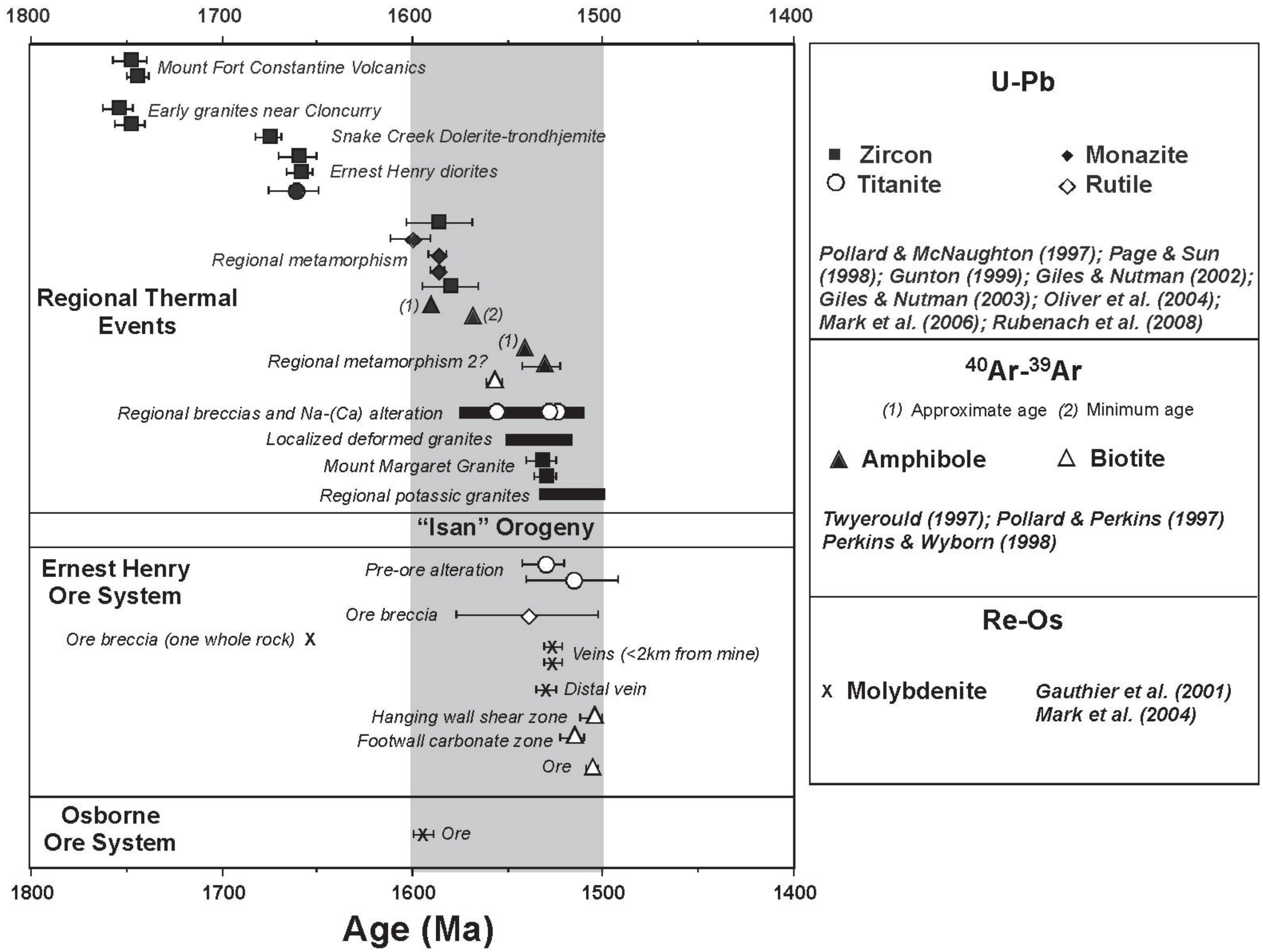


**FIGURE 4.** Geochronological constraints on intrusions, metamorphism, regional sodic-calcic alteration and the age of mineralization in the two principal IOCG deposits of the Cloncurry district.

al., 1997; Bergman et al., 2001) though some hematite-rich examples (e.g. Malmberget, Rektorn) have K-feldspar altered wall rocks along with biotite in higher grade metamorphic settings (Bergman et al., 2001). Sulphides in IOCG and possible IOCG deposits (e.g. Aitik) have medium to high temperature potassium-iron silicate ± magnetite alteration characterized by biotite, (Ba)-K-feldspar, muscovite and spessartine-almandine garnet (Table 1; Fig. 5B–D). Sulphide-related potassium-iron alteration overprinted sodium-(calcium) alteration in all cases where both types are documented (e.g. Kiskamavaara, Pahtohavare, Rakkurijärvi, Tjårrojåkka; Table 1; Fig. 5B). The ores typically contain carbonate that either formed synchronously with, or post-dates ore emplacement.

Similar relationships are observed in the Cloncurry district where barren metasomatic magnetite ironstones, including the large magnetite accumulation at Lightning Creek, several examples within a few km of the Ernest Henry mine and numerous magnetite accumulations in the extensively exposed regional alteration system are all associated with sodic-calcic alteration (Williams, 1994; Perring et al., 2000; Carew, 2004; Mark et al., 2006b). IOCG and IOCG-affiliated deposits (Williams, 2010) are mostly characterized by various K-Fe silicate ± magnetite assemblages that overprinted pre-existing sodic-calcic altered rocks (Table 2; Fig. 5E–G). Surface drilling around the Ernest Henry deposit has delineated a ~3 x 2 km potassium (+ Ba) anomaly accentuated by the contrast with the surrounding K potassic-depleted rocks with sodic-calcic alteration (Mark et al., 2006b; Corriveau et al., 2010). One economically significant deposit, namely Mount Elliott (Table 2) lacks potassic alteration and is characterized by diopside-magnetite skarn that also overprints earlier albitization. Some deposits that are hosted by carbonaceous pelites lack iron oxides and are referred to here as "IOCG-affiliated" (Williams, 2010; e.g. Mount Dore, Table 2; Lady Clayre prospect, Fig. 5F). As in Norrbotten, carbonates are typically abundant minerals in later paragenetic stages and display a strong paragenetic affinity with the sulphides.

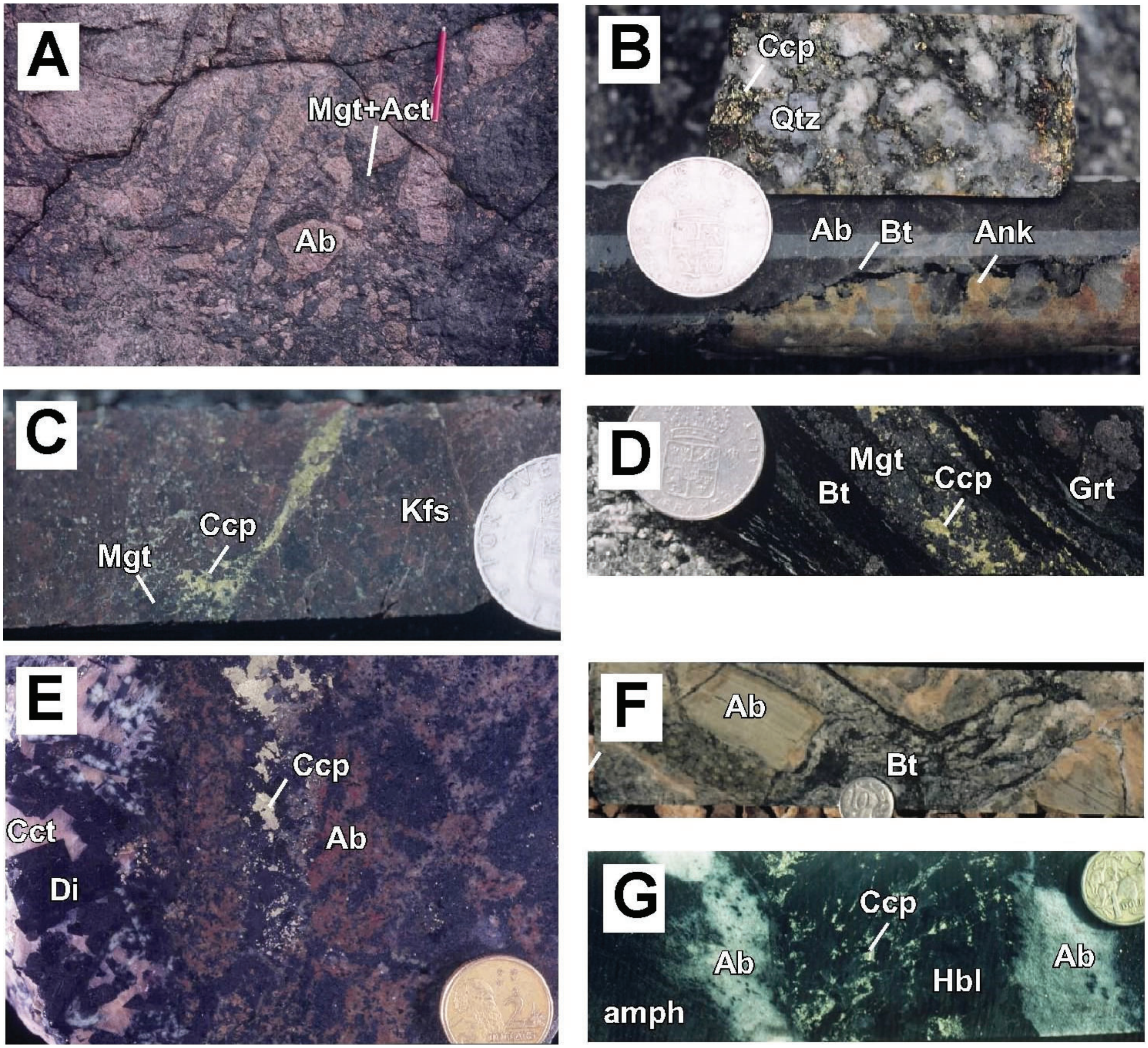


**Figure 5.** Examples of paragenetic relationships in IOA, IOCG and IOCG-affiliated deposits from Norrbotten and the Cloncurry district. **A.** Contact breccia at margin of the Kiirunavaara IOA deposit with clasts of albitized metavolcanic rocks (Ab) and magnetite (Mgt) + actinolite (Act) matrix. **B.** Samples from the Pahtahavre deposit showing albitized metasedimentary wall rock (Ab) cut by ankerite (Ank) + quartz (Qtz) + chalcopyrite (Ccp) veins with thin biotite (Bt) alteration selvages. **C.** Pervasively K-feldspar altered metavolcanic rock (Kfs) from the Kiskamavaara deposit overprinted by magnetite (Mgt) and chalcopyrite (Ccp). **D.** Sample from the Nautanen deposit with almandine-spessartine garnet (Grt) and biotite (Bt) overprinted by magnetite (Mgt) and chalcopyrite (Ccp).E. Albitized metasedimentary rock (Ab) overgrown and replaced by diopside (Di) which is partly replaced by chalcopyrite (Ccp) and infilled by calcite (Cct). **F.** Brecciated albitized metapelite (Ab) with biotite rich matrix (Bt), Lady Clayre prospect (a magnetite-absent deposit hosted by altered carbonaceous pelite in the Cloncurry district. **G.** Sample from the Eloise deposit illustrating amphibolite (amph) with hornblende (Hbl) vein in albitized (Ab) zone. The hornblende is partly overprinted by chalcopyrite (Ccp).

## Discussion

*Generalized Paragenetic Evolution of the IOCG Deposits*

The IOCG and affiliated deposits in Norrbotten and the Cloncurry district represent the higher temperature (magnetite-dominated) part of the IOCG spectrum contrasting with hematite group deposits such as Olympic Dam that are characterized by lower temperature phyllosilicate-dominated alteration (Williams, 2010). Williams (2001) argued a common mode of origin for the somewhat diverse magnetite group IOCG and affiliated deposits in the Cloncurry district and Curnamona province in southern Australia based on the shared features of their alteration zoning and paragenesis (Fig. 6). The Norrbotten copper-gold deposits conform with this view in that they share the common features of the other ore systems including one or more generations of sodic ± calcic alteration

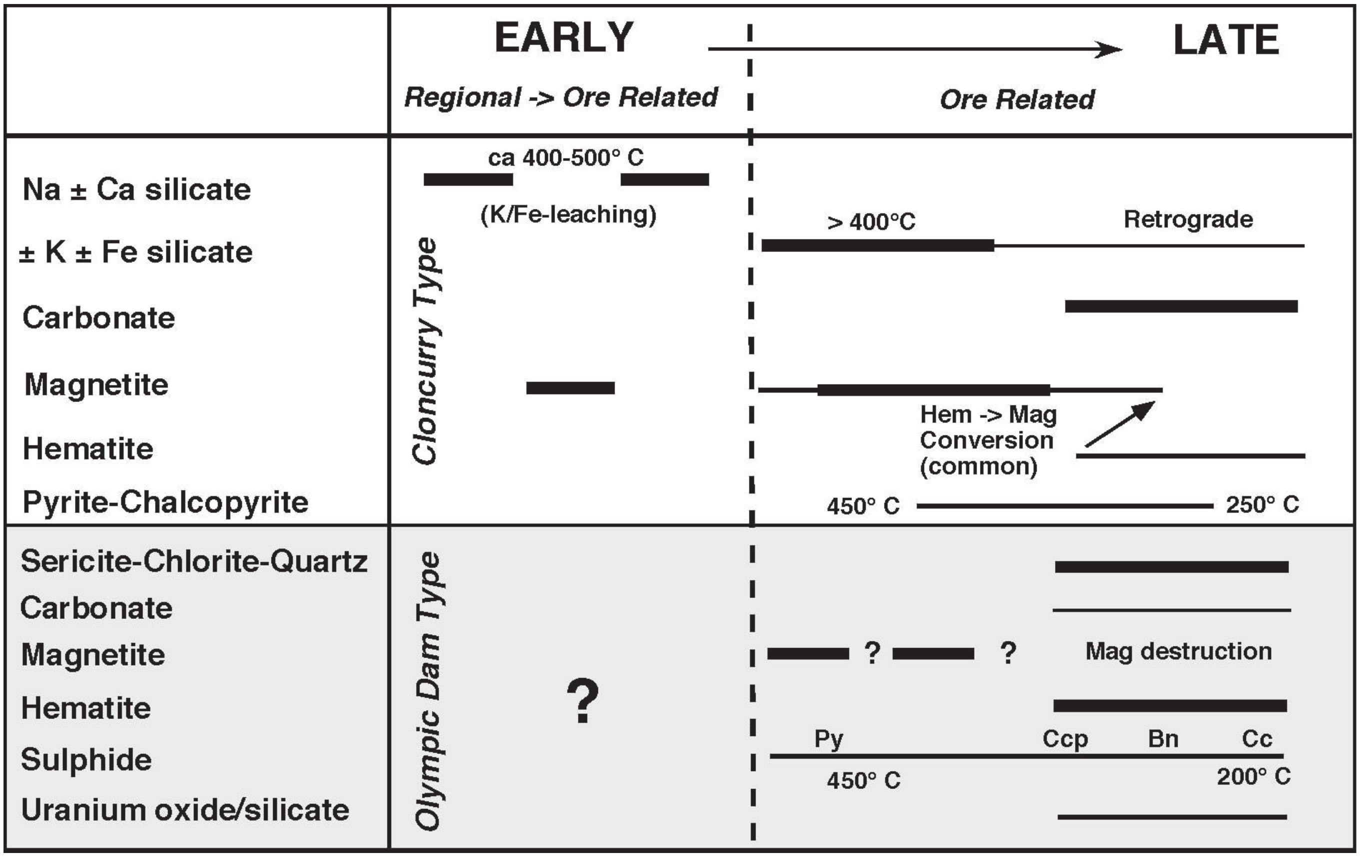


**FIGURE 6.** Generalized paragenetic sequence of "Cloncurry-type" (i.e. magnetite group) and "Olympic Dam-type" (i.e. hematite group) IOCG deposits.

overprinted by 300–500°C iron ± potassium metasomatism in the immediate ore environments. Copper-gold mineralization either overlapped with this iron ± potassium stage or with later carbonate deposition.

*Hematite to Magnetite Conversion*

Hematite is commonly noted as a phase of increasing importance in the later paragenetic stages of magnetite group IOCG deposits consistent with a general reduction of temperature over time (e.g. Rakkurijärvi, Tjårrojåkka, Ernest Henry, Starra; Tables 1 and 2, Fig. 6). A curious feature of some of these deposits is that late stage hematite is itself pseudomorphed by magnetite producing the texture that has been referred to as "mushketovite" (e.g. Marschik and Fontboté, 2001) as observed at Starra (Rotherham, 1997) and Ernest Henry (Mark et al., 2006b). This is normally interpreted to be a consequence of an inversion in the retrograde history affecting the $fO_2$ and temperature dependent equilbrium:

$$3Fe_2O_3 <=> 2Fe_3O_4 + 0.5O_2$$

However, an alternative mechanism for mushketovite-formation may be a pH control of iron oxide stability (Ohmoto, 2003) linked to the carbonic nature of late IOCG fluids. In many cases this nature is revealed by the presence of carbonates and by fluid inclusion data (e.g. Bin Fu et al., 2003; Williams et al., 2003). Thus mushketovite could be induced by $CO_2$ phase separation, a process that might be facilitated by rapid pressure drops related to fracturing and brecciation and that might cause magnetite to form at the expense of hematite by:

$$Fe_2O_3 + Fe^{2+} + HCO_3^- <=> Fe_3O_4 + CO_2 + H^+$$

Such a process might also be linked to sulphide deposition as $CO_2$ loss also has the effect of producing a net increase in fluid pH and reduces sulphide solubilities. Various authors have suggested this may have been an important ore-forming mechanism in the Cloncurry IOCG and related deposits (e.g. Beardsmore, 1992; Adshead, 1995; Xu and Pollard, 1999; Bin Fu et al., 2003).

*Origins of Fluids and Salinity in the IOA and IOCG Systems*

The origins of fluid, salinity and ore components in IOCG deposits have been widely debated in recent years (e.g. Williams, 1994; Barton and Johnson, 1996, 2000; Pollard, 2000, 2006; Williams et al., 2005). Magnetite-group IOCG deposits have some features in common with porphyry-related copper-gold deposits that are also typically magnetite-rich (e.g. Sillitoe, 1997). In particular, the porphyry-related deposits have similar alteration associations including K-silicate (K-feldspar, biotite, muscovite) and skarn (diopside, calcic garnet). There seems little doubt that the porphyry-related deposits are magmatic-hydrothermal with a mode of formation involving the separation of brines from the coeval and spatially associated, typically calc-alkaline to alkaline dioritic magmas (e.g. Ulrich et al., 1999). A similar (i.e. magmatic-hydrothermal) mode of origin might therefore be considered for IOCG deposits albeit in comparatively distal, and in some cases deep-seated settings (Pollard, 2000; cf. Fig. 7). However, IOCG and porphyry deposits also exhibit a number of differences, and in some cases the manifestations of these differences are quite variable (Table 3). This would appear to mean that IOCG deposits are products of more complex and variable hydrothermal systems than those that produce porphyry-related deposits. Notably some alkaline porphyry-related deposits share various IOCG characteristics including paucity of quartz, association with magnetite-apatite bodies and presence of carbonates in the ore parageneses (e.g. Lang et al., 1995).

Important questions arising from these similarities and differences include (1) which if any of the economically important metals in IOCG deposits were principally or significantly sourced from magmas, (2) were there fundamentally different processes leading to the creation of IOA and IOCG deposits, or were the two linked along a single genetic pathway (i.e. evolved IOA fluids create IOCG deposits), and (3) did the IOA deposits form by orthomagmatic (e.g. Nyström and Henriquez, 1994) or hydrothermal (e.g. Barton and Johnson, 1996) processes?

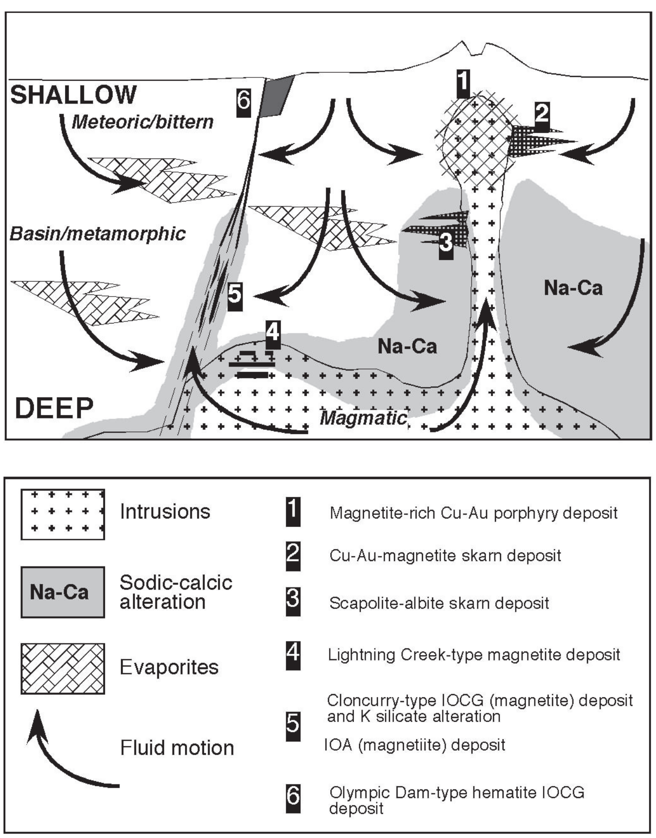


FIGURE 7. Conceptual cartoon comparing possible fluid sources in IOCG and porphyry-related hydrothermal systems.

Considerable recent effort has been invested in research aimed at addressing these questions in the two terrains considered here. Significant progress has been made in some respects though as yet there have been few comparative studies of IOCG, IOA and other affiliated deposits. There are also still very few radiogenic isotope (e.g. strontium, neodymium) data that might shed light on source components.

Fluid inclusion studies have been undertaken of most of the significant IOCG deposits in these districts (summarized in Williams et al., 2003; see also Mustard et al., 2003; Mark et al., 2005; Smith and Gleeson, 2005; Edfelt, 2007) and have very consistently revealed that the hydrothermal systems individually involved both complex hypersaline brines and relatively dilute $NaCl-CaCl_2$ fluids. Carbonic fluid inclusions are present in almost every example studied. Homogenization temperatures of mineralization stage inclusions range up to values greater than 400°C in almost all cases. The main iron oxide-apatite parageneses of the Norbbotten IOA deposits have generally not proven to be amenable to fluid inclusion studies. However, Edfelt (2007) has reported moderate salinity inclusions with liquid-vapour homogenization temperatures greater than 370°C in apatite from the Tjårrojåkka iron deposit.

Light (i.e. H, C, O) stable isotope data are available for most of the significant Cloncurry deposits (Beardsmore, 1992; Adshead, 1995; Twyerould, 1997; Rotherham et al., 1998; Perring et al., 2000; Baker et al., 2001; Wang and Williams, 2001; Williams and Pollard, 2003; Mark et al., 2005; Marshall et al., 2006). Some attention has also been paid to parts of the regional

TABLE 3. Comparison of mineral associations and geochemical features of IOCG and typical porphyry-related deposits in calc-alkaline magmatic arcs.

| | Typical calc-alkaline Cu-Au porphyry deposit | IOCG deposits |
|---|---|---|
| **Quartz** | Abundant in sulphide-related stockworks | Variable abundance, commonly minor |
| **Mn-rich garnet in K-silicate alteration** | No | In some cases (e.g. Ernest Henry, Nautanen) |
| **Carbonates in ore parageneses** | No | Common but not ubiquitous |
| **District association with IOA deposits** | Mostly not | Common but not in all cases |
| **Sulphates in ore parageneses** | Anhydrite common, barite absent | Barite or anhydrite may be present (generally not both) |
| **Element associations** | Ag, ± Mo | Ag, Co, ± B, ±F, ±P, ± Ni, ±As ±Mo, ±Ba, ± LREE, ±W, ± U |

alteration system (Mark et al., 2004a, b; Marshall and Oliver, 2006; Marshall et al., 2006). The data generally imply that the ore fluids either had a magmatic source or had equilibrated with igneous or metamorphic rocks at elevated temperatures. Actinolite δD data from the Mount Elliott deposit (Wang and Williams, 2001) and regional alteration associated with sodic igneous rocks and magmatic-hydrothermal veins (Mark et al., 2004a) display pronounced depletion trends that have been interpreted to be signatures of magmatic degassing (i.e. evidence of magmatic fluid input). In general the Cloncurry stable isotope data show no signs of the involvement of surficial waters except in late stage epithermal quartz-adularia veins that overprint, and may be much younger than the regional sodic-dominated alteration (Mark et al., 2004b; Marshall and Oliver, 2006).

Only a few light stable isotope studies have been undertaken in Norrbottem. O'Farrelly (1990) and Blake (1992) undertook detailed oxygen isotope studies of the Kiirunavaara IOA deposit and its host rocks that led to the conclusion that the ore system there was dominated by a high temperature ( >550°C) magmatic-hydrothermal fluid. Edfelt (2007) reported stable isotope data from the Tjårrojåkka IOA and IOCG deposits that are consistent with both having formed from magmatic fluids or fluids that had equilibrated with igneous rocks. Lower implied δ18O for fluids associated with late stage zeolite and carbonate-bearing veins provided the only indication of surficial fluid involvement. Edfelt (2007) also reported Sm-Nd isotopic data for six mineral separates from the Tjårrojåkka IOA deposit that imply some portion of the neodymium is derived from the Archean basement.

Several recent studies have used analyses of conservative fluid components in fluid inclusions such as halogens and noble gases to place constraints on the sources of fluids and salinity in these deposits. In contrast to stable isotopes, these components are little affected by fluid-rock interactions. Smith and Gleeson (2005) reported the results of bulk extraction Br/Cl and $\delta^{37}$Cl determinations from late stage quartz veins cutting Norrbotten IOA deposits and from several IOCG deposits including Pahtohavare, Nautanen and Gruvberget. The Br/Cl ratios were found to be similar to those expected in magmatic fluids and do not support the involvement of evaporite-related halogens in the deposits studied. The measured $\delta^{37}$Cl values are lower than those of any previously analyzed fluid inclusions and were interpreted to reflect chlorine isotope fractionation involving minerals such as scapolite and biotite. It is not thought this would have significantly affected the fluid Br/Cl ratios. An independent study of single high salinity fluid inclusions from the Pahtohavare deposit using PIXE confirms the magmatic like Br/Cl ratios of high salinity Fe-rich fluid inclusions thought to have been closely associated with mineralization (Fig. 8). However, PIXE data for ore stage inclusions from the Aitik deposit (Wanhainen et al., 2003) reveal highly elevated Br/Cl ratios that suggest the involvement of deeply circulated bittern brines (Fig. 8).

Fluid inclusions from several Cloncurry IOCG deposits and the Lightning Creek magnetite deposit have also been investigated using PIXE. Williams et al. (2001) found that high salinity inclusions from the magnetite and sulphide stages in the Starra deposit had rather variable Br/Cl ratios that cluster close to normal magmatic values but include several lower values (consistent with salinity derived from evaporitic halite dissolution) and one outlying value higher than the magmatic range. Pre- and syn-mineralization high salinity brine inclusions from Ernest Henry also have very variable Br/Cl ratios implying at least two sources of salinity, one magmatic-like and the other similar to evaporitic halite (Fig. 8; Mark et al., 2005). On the other hand, high salinity inclusions in hydrothermal quartz from the Lightning Creek magnetite deposit have typical magmatic Br/Cl ratios (Fig. 8) consistent with the transitional magmatic-hydrothermal context implied from textural and stable isotopic data (Perring et al., 2000). Baker et al. (2008) report a general correspondence of higher copper-content and higher (magmatic-like) Br/Cl ratios in compiled fluid inclusion PIXE analyses from the Cloncurry deposits.

The fluid inclusion chemistry of two Cloncurry IOCG deposits, Osborne and Ernest Henry, has recently been studied using a bulk extraction neutron activation technique that allows the simultaneous determination of noble gas isotopic and halogen ratios (Kendrick et al., 2007; Fisher and Kendrick, 2008). The same technique has also been applied to samples from the regional sodic-calcic alteration system (Kendrick et al., 2008). In the case of Ernest Henry the data are consistent with mixing of two brines. One of these was characterized by higher and typical magmatic Br/Cl and I/Cl (Fig. 8) along with high $^{40}$Ar/$^{36}$Ar ratios typical of I-type magmatic fluids. (Kendrick et al., 2008). The other brine had lower Br/Cl and I/Cl (Fig. 8) along with low $^{40}$Ar/$^{36}$Ar ratios suggesting halite dissolution by near surface sedimentary formation waters that are deduced to have been deeply circulated to the estimated 6–10 km depths of mineralization. The conservative noble gas isotope ratios therefore appear to reveal the presence of fluid components whose oxygen and hydrogen stable isotope signature has been obliterated by fluid-rock interaction. Application of the same technique at the Osborne deposit again revealed highly varied Br/Cl and I/Cl but in this case associated with uniformly low $^{40}$Ar/$^{36}$Ar ratios that provide no support for the involvement of A- or I-type magmatic fluids (Fisher and Kendrick, 2008). In this case the best interpretation seems to be that formation of the deposit involved mixing of fluids generated in the metamorphic setting and it is interesting to note that the Re-Os dating of Osborne mineralization suggests it took place at ca. 1600 Ma (Gauthier et al., 2001), some 50–60 million years before the onset of regional batholith emplacement.

Fluid inclusions from the regional sodic-calcic alteration system have characteristics that vary with location. Some are best interpreted as sedimentary formation waters derived from the upper crust that had acquired their variable to high salinities by dissolving halite or meta-evaporitic scapolite. Others have high $^{40}$Ar/$^{36}$Ar ratios and Br/Cl and I/Cl ratios indicative of a magmatic source (Kendrick et al., 2008).

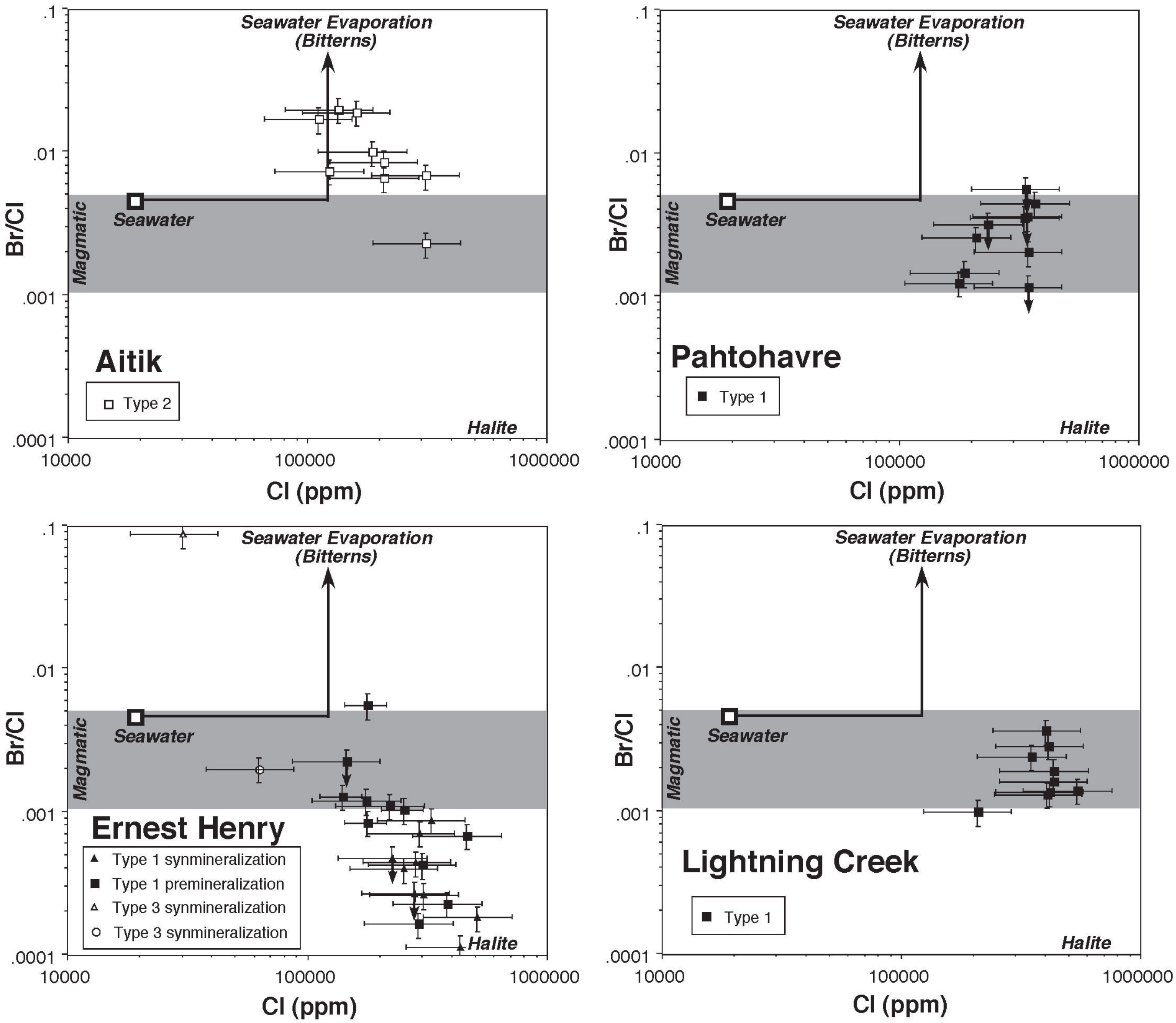


**Figure 8.** Bromine - chlorine relationships determined by proton induced X-ray excitation (PIXE) in single fluid inclusions from some Norrbotten and Cloncurry mineral deposits (P.J. Williams, G. Dong, G. Mark, O. Martinsson, C. Broman, C. Ryan unpublished data Perring et al., 2000; Williams et al., 2003; Mark et al., 2005). Br/Cl ratios suggest different mixed salinity sources with evaporate-related components at the Aitik (bittern component) and Ernest Henry (halite/meta-evaporite component) deposits. Br/Cl ratios in inclusions from the Pahtohavare Cu-Au and Lightning Creek magnetite deposits are compatible with magmatic sources of salinity.

## Summary

The main points from this review of magnetite-group IOCG deposits in two early Proterozoic settings are summarized as follows:

(1) IOCG and archetypical IOA deposits in Norrbotten, Sweden are products of ca. 150 Ma evolution of a Palaeoproterozoic continental margin arc. The largest IOA deposit at Kiruna formed in association with early arc volcanism whereas IOCG deposits could be more closely associated with younger intrusions.

(2) IOCG and possibly affiliated deposits in the Cloncurry district in northwest Queensland formed during at least two separate metallogenic events in an intracontinental setting with tectonic activity that may have been distally driven by subduction. One of these events at ca. 1600 Ma produced the second largest known IOCG deposit in the district, namely the Osborne deposit at a time when there was no known coeval A- or I-type magmatism. The largest IOCG deposit, Ernest Henry, along with a number of other examples and the very large Lightning Creek magmatic-hydrothermal magnetite deposit appear to have formed at 1540–1500 Ma in association with the emplacement of batholithic, predominantly potassic I-type (A-type) granitoids and the development of giant, dominantly sodic-calcic type alteration systems.

(3) The principal wall rock alteration around Norrbotten IOA deposits and barren iron oxide accumulations in the Cloncurry district (including Lightning Creek) is sodic-calcic in character and dominated by albitic plagioclase, scapolite, actinolite, diopside and magnetite.

(4) Norrbotten IOA deposits mostly occur independently of economically significant copper and gold. Where metal sulphides are hosted by IOA deposits they invariably form a late part of a late stage paragenetic association which could be much younger than the host.

(5) Economically significant IOCG deposits in both districts are mostly associated with moderate to high temperature K-Fe-(Ba-Mn) silicate alteration, typically overprinting pre-existing sodic-calcic assemblages and characterized by minerals such as K-(Ba) feldspar, muscovite, biotite and spessartine-almandine garnet, which may be accompanied by magnetite. Exceptions are provided by deposits such as Mount Elliott in the Cloncurry district which is dominated by diopside skarn and lacks potassic alteration. Carbonates are typically abundant in late stage syn- or post-mineralization parageneses. The only economically significant copper sulphide is chalcopyrite. Where present, hematite is subordinate to, and overprints magnetite. The ores in some deposits such as Eloise, Mount Elliott and Osborne in the Cloncurry district contain large quantities of pyrrhotite.

(6) Whereas the potassic alteration assemblages and magnetite association are reminiscent of porphyry-related copper-gold deposits, the mineralogy and geochemistry of the IOCG deposits is different in other ways and also rather more variable than in porphyry-related systems. Moreover the sodic-calcic and iron oxide alteration is significantly more extensive.

(7) Currently available data in the two described settings are inadequate to argue for or against a direct process link between IOA and IOCG deposits.

(8) Whereas stable isotope data are generally consistent with a magmatic fluid origin for both IOA and IOCG deposits, recent studies of fluid inclusion geochemistry of the latter have revealed clear evidence of the involvement of non magmatic fluids and sources of salinity. In the Cloncurry district these new data suggest that IOCG deposits may have been formed in fundamentally different types of hydrothermal systems including one that involved mixing of more than one type of deeply derived or circulated non magmatic fluid (Osborne) and another that involved mixing of a magmatic fluid and deeply circulated surface waters that had interacted with rocks containing evaporite-derived halogens (Ernest Henry).

## Acknowledgments

Studies in northern Sweden have been supported by the Georange foundation and facilitated by colleagues at the Luleå University of Technology, particularly Pär Wiehed and Olof Martinsson. Research in the Cloncurry District since 1990 has been supported by many agencies including, James Cook University, the Australian Research Council through its Strategic Partnerships with Industry and Linkage grant schemes and many mining companies, in part co-ordinated by the Australian Mineral Industries Research Association (AMIRA). This work has involved more than 70 colleagues and students amongst whom the contributions of Geordie Mark and Peter Pollard have been particularly important in establishing the state of knowledge reported here. Charlie Jefferson and John Kerswill are thanked for their comments on the manuscript.

## References

Adshead, N.D., 1995, Geology, alteration and geochemistry of the Osborne Cu-Au deposit, Cloncurry district, NW Queensland: Ph.D. thesis, James Cook University, Townsville, 382 p.

Adshead, N.D., Voulgaris, P., and Muscio, V.N., 1998, Osborne copper-gold deposit: Australasian Institute of Mining and Metallurgy Monograph 22, p. 793-798.

Adshead-Bell, N.A., 1998, Evolution of the Starra and Selwyn high strain zones, Eastern Fold Belt, Mount Isa Inlier: implications for Au-Cu mineralization: Economic Geology, v. 93, p. 1450-1462.

Austin, J.R., and Blenkinsop, T.G., 2008, The Cloncurry Lineament: geophysical and geological evidence for a deep crustal structure in the Eastern Succession of the Mount Isa Inlier: Precambrian Research, v. 163, p. 50-68.

Baker, T., 1998, Alteration, mineralization and fluid evolution at the Eloise Cu-Au deposit, Cloncurry district, NW Queensland: Economic Geology, v. 93, p. 1213-1236.

Baker T., and Laing W.P., 1998, The Eloise Cu-Au deposit, Mt Isa Block: structural environment and structural controls on ore: Australian Journal of Earth Sciences, v. 45, p. 429-444.

Baker, T., Perkins, C., Blake, K.L., and Williams, P.J., 2001, Isotopic constraints on the genesis of the Eloise Cu-Au deposit, Cloncurry district, NW Queensland, Australia: Economic Geology, v. 96, p. 723-742.

Baker, T., Mustard, R., Fu, B., Williams, P.J., Mark, G., and Ryan, C.G., 2008, Mixed messages in Proterozoic iron oxide-copper-gold systems: insights from PIXE analysis of halogens and copper: Mineralium Deposita, v. 43, p. 599-608.

Barton, M.D., and Johnson, D.A., 1996, Evaporitic source model for igneous-related Fe oxide-(REE-Cu-Au-U) mineralization: Geology, v. 24, p. 259-262.

Barton, M.D., and Johnson, D.A., 2000, Alternative brine sources for Fe-oxide (-Cu-Au) systems: implications for hydrothermal alteration and metals, *in* Porter, T.M., ed., Hydrothermal iron oxide copper-gold and related deposits: a global perspective, v. 1: PCG Publishing, Adelaide, p. 43-60.

Beardsmore, T.J., 1992, Petrogenesis of Mount Dore-style breccia-hosted copper ± gold mineralization in the Kuridala-Selwyn region of Northwestern Queensland: Ph.D. thesis, James Cook University, 292 p.

Bergman, S., Kübler, L., and Martinsson, O., 2001, Description of regional maps of northern Norrbotten County (east of the Caledonian Orogen): Sveriges Geologiska Undersökning Ba 56, 110 p.

Betts, P.G., Giles, D., Lister, G.S., and Frick, L.R., 2002, Evolution of the Australian lithosphere: Australian Journal of Earth Sciences, v. 49, p. 661-695.

Betts, P.G., Giles, D., Mark, G., Lister, G.S., Goleby, B.R., and Alliéres, L., 2006, Synthesis of the Proterozoic evolution of the Mt Isa Inlier: Australian Journal of Earth Sciences, v. 53, p. 187-211.

Bin Fu, Williams, P.J., Oliver, N.H.S., Guoyi Dong, Pollard, P.J., and Mark, G., 2003, Fluid mixing versus unmixing as an ore-forming process in the Cloncurry Fe oxide-Cu-Au district, NW Queensland, Australia: evidence from fluid inclusions: Journal of Geochemical Exploration, v. 78-79, p. 617-622.

Blake, K.L., 1992, The petrology, geochemistry and association to ore formation of the host rocks of the Kiirunavaara magnetite-apatite deposit northern Sweden: Ph.D. thesis, University of Wales College of Cardiff.

Brescianini, R.F., Asten, M.W., and McLean, N., 1992, Geophysical characteristics of the Eloise Cu-Au deposits, NW Queensland: Exploration Geophysics, v. 23, p. 33-42.

Carew, M.J., 2004, Controls on Cu-Au mineralisation and Fe oxide metasomatism in the Eastern Fold Belt, N.W. Queensland, Australia: Ph.D. thesis, James Cook University of North Queensland, 308 p.

Carlon, C.J., 2000, Iron oxide systems and base metal mineralisation in northern Sweden, *in* Porter, T.M., ed., Hydrothermal iron oxide copper-gold and related deposits: a global perspective, v. 1: PCG Publishing, Adelaide, p. 283-296.

Carlson, L., 1991, The Pahtohavare copper-gold prospect: Geologiska Foreningen i Stockholm Forhanlinger, v. 113, p. 45-46.

Cliff, R.A., Rickard, D., and Blake, K., 1990, Isotope systematics of the Kiruna magnetite ores, Sweden: part 1. The age of the ore: Economic Geology, v. 85, p. 1770-1776.

Corriveau, L., Williams, P.J., and Mumin, A.H., 2010, Alteration vectors to IOCG mineralization: from uncharted terranes to deposits, *in* Corriveau, L. and Mumin, A.H., eds., Exploring for iron oxide copper-gold deposits: Canada and global analogues: Geological Association of Canada, Short Course Notes, No. 20, p. 89-110.

Danielson, S., 1985, Nautanen, geologi och resultat av 1983 års diamantsborrning: Sveriges Geologigiska Undersökning, PRAP 85090, 15 p.

Davidson, G., Large, R., Kary, G., and Osborne, R., 1989, The BIF-hosted Starra and Trough Tank Au-Cu mineralization: a new stratiform association from the Proterozoic eastern succession of Mt. Isa, Australia: Economic Geology Monograph 6, p. 135-150.

De Jong, G., and Williams, P.J., 1995, Giant metasomatic system formed during exhumation of mid crustal Proterozoic rocks in the vicinity of the Cloncurry Fault, NW Queensland: Australian Journal of Earth Sciences, v. 42, p. 281-290.

Edfelt, Å., 2007, The Tjårrojåkka apatite-iron and Cu (-Au) deposits, northern Sweden – products of one ore-forming event: Doctoral thesis, Luleå University of Technology Publication 2007:17.

Edfelt, Å., Armstrong, R.N., Smith, M., and Martinsson, O., 2005, Alteration paragenesis and mineral chemistry of the Tjårrojåkka apatite-iron and Cu (-Au) occurrences, Kiruna area, northern Sweden: Mineralium Deposita, v. 40, p. 409-434.

Edfelt, Å., Sandrin, A., Evins, P., Jeffries, T., Storey, C., Elming, S-Å., and Martinsson, O., 2006, Stratigraphy and tectonic setting of the host rocks to the Tjårrojåkka Fe-oxide Cu-Au deposits, Kiruna area, northern Sweden: GFF, v. 128, p. 221-232.

Etheridge, M.A., Rutland, R.W.R., and Wyborn, L.A.I., 1987, Orogenesis and tectonic process in the Early to Middle Proterozoic of northern Australia, *in* Kröner, A., ed., Proterozoic lithosphere evolution: Geodynamics Series, 17, American Geophysical Union, Geological Society of America, p. 131-147.

Ettner, D.C., Bjolykke, A., and Andersen, T., 1994, A fluid inclusion and stable isotope study of the Proterozoic Bidjovagge Au-Cu deposit, Finnmark, northern Norway: Mineralium Deposita, v. 29, p. 16-29.

Fisher, L.A., and Kendrick, M.A., 2008, Metamorphic fluid origins in the Osborne Fe oxide-Cu-Au deposit, Australia: evidence from noble gases and halogens: Mineralium Deposita, v. 43, p. 483-497.

Frietsch, R., 1966, Berggrund och malmer i Svappavaarafältet, norra Sverige: Sveriges Geologigiska Undersökning, C760, 62 p.

Frietsch, R., 1978, On the magmatic origin of iron ores of the Kiruna type: Economic Geology, v. 73, p. 478-485.

Frietsch, R., 1997, The iron ore inventory programme 1963-1972 in Norrbotten County: Sveriges Geologigiska Undersökning Rapporter och Meddelanden, 92, 77 p.

Frietsch, R., Tuisku, P., Martinsson, O., and Perdahl, J.-A., 1997, Early Proterozoic Cu-(Au) and Fe ore deposits associated with regional Na-Cl metasomatism in northern Fennoscandia: Ore Geology Reviews, v. 12, p. 1-34.

Gauthier, L., Hall, G., Stein, H., and Schaltegger, U., 2001, The Osborne deposit, Cloncurry district: a 1595 Ma Cu-Au skarn deposit, *in* Williams, P.J., ed., A hydrothermal odyssey: Extended Conference Abstracts: Economic Geology Research Unit Contribution 59, p. 58-59.

Geijer, P., 1930, Gällivare malmfält, gologisk bescrivning: Sveriges Geologigiska Undersökning, Ca 22, 115 p.

Geijer, P., 1950, The Rektorn orebody at Kiruna: Sveriges Geologigiska Undersökning, C514, 18 p.

Giles, D., and Nutman, A.P., 2002, SHRIMP U-Pb monazite dating of 1600–1580 Ma amphibolite facies metamorphism in the southeastern Mt Isa Block, Australia: Australian Journal of Earth Sciences, v. 49, p. 455-465.

Giles, D., and Nutman, A.P., 2003, SHRIMP U-Pb dating of the host rocks of the Cannington Ag-Pb-Zn deposit, southeastern Mt Isa Block: Australian Journal of Earth Sciences, v. 50, p. 295-309.

Grip, E., and Frietsch, R., 1973, Malm i Serige 2, norra Sverige: Stockholm, Almqvist and Wiksell, 295 p.

Gunton, C.G., 1999, A study of molybdenum at the Ernest Henry Cu-Au deposit, northwest Queensland: B.Sc. Honours thesis, Australian National University, 68 p.

Hitzman, M.C., 2000, Iron oxide-Cu-Au deposits: what, where, when, and why?, *in* Porter, T.M., ed., Hydrothermal iron oxide copper-gold and related deposits: a global perspective, v. 1: PCG Publishing, Adelaide, p. 9-25.

Juhlin, C., Elming, S-Å., Mellqvist, C., Öhlander, B., Weihed, P., and Wikström, A., 2002, Crustal reflectivity near the Archaean-Proterozoic boundary in northern Sweden and the implications for the tectonic evolution of the area: Geophysical Journal International, v. 150, p. 180-197.

Kendrick, M.A., Mark, G., and Phillips, D., 2007, Mid-crustal fluid mixing in a Proterozoic Fe oxide-Cu-Au deposit, Ernest Henry, Australia: evidence from Ar, Kr, Xe, Cl, Br and I: Earth and Planetary Science Letters, v. 256, p. 328-343.

Kendrick, M.A., Baker, T., Fu, B., Phillips, D., and Williams, P.J., 2008, Noble gas and halogen constraints on regionally extensive mid-crustal Na–Ca metasomatism, the Proterozoic Eastern Mount Isa Block, Australia: Precambrian Research, v. 163, p. 131-150.

Lang, J.R., Lueck, B., Mortensen, J.K., Stanley, C.R., and Thompson, J.F.H., 1995, Triassic-Jurassic silica-undersaturated and silica-saturated alkalic intrusions in the Cordillera of British Columbia: implications for arc magmatism: Geology, v. 23, p. 451-454.

Lindskog, L., 2001, Relationships bewteen Fe-oxide Cu/Au deposits at Gruvberget – Kiruna district, northern Sweden: B.Sc. Honours thesis, Townsville, James Cook University, 123 p.

Lundmark, C., Stein, H., and Weihed, P., 2005, The geology and Re-Os geochronology of the Palaeoproterozoic Vaikijaur Cu-Au-(Mo) porphyry-style deposit in the Jokkmokk granitoid, northern Sweden: Mineralium Deposita, v. 40, p. 396-408.

Mark, G., 1998, Albitite formation by selective pervasive sodic alteration of tonalite plutons in the Cloncurry district, Queensland: Australian Journal of Earth Sciences, v. 45, p. 765-774.

Mark, G., and Foster, D.R.W., 2000, Magmatic-hydrothermal albite–actinolite–apatite-rich rocks from the Cloncurry district, NW Queensland, Australia: Lithos, v. 51, p. 223-245.

Mark, G., Williams, P., Ryan, C., and Mernagh, T., 2001, Fluid chemistry and ore-forming processes at the Ernest Henry Fe oxide-copper-gold deposit, NW Queensland: Townsville, James Cook University, Economic Geology Research Unit Contribution 59, p. 124-125.

Mark, G., Foster, D.W., Pollard, P.J., Williams, P.J., Tolman, J., and Darvall, M., 2004a, Magmatic fluid input during large-scale Na-Ca alteration in the Cloncurry Fe oxide-(Cu-Au) district, NW Queensland, Australia: Terra Nova, v. 16, p. 54-61.

Mark, G., Williams, P.J., and Boyce, A., 2004b, Low latitude meteoric fluid flow along the Cloncurry Fault, Cloncurry minerals province, NW Queensland, Australia: geodynamic and metallogenic implications: Chemical Geology, v. 207, p. 117-132.

Mark, G., Stein, H., and Salt, C., 2004c, Re-Os isotopic evidence for two periods of sulfide mineralisation in the vicinity of the Ernest Henry Cu-Au deposit, northwest Queensland, Australia: 17th Australian Geological Convention Abstracts, Geological Society of Australia, Melbourne, p. 96.

Mark, G., Williams, P.J., Oliver, N.H.S., Ryan, C.G., and Mernagh, T., 2005, Fluid inclusion and stable isotope geochemistry of the Ernest Henry iron oxide-copper-gold deposit, Queensland, Australia, *in* Mao, J. and Bierlien, F.P., eds., Mineral deposit research: meeting the global challenge: Springer, Berlin, p. 785-788.

Mark, G., Oliver, N.H.S., and Carew, M.J., 2006a, Insights into the genesis and diversity of epigenetic Cu–Au mineralisation in the Cloncurry district, Mt Isa Inlier, northwest Queensland: Australian Journal of Earth Sciences, v. 53, p. 109-124.

Mark, G., Oliver, N.H.S., and Williams, P.J., 2006b, Mineralogical and chemical evolution of the Ernest Henry Fe oxide-Cu-Au ore system, Cloncurry district, northwest Queensland, Australia: Mineralium Deposita, v. 40, p. 769-801.

Marschik, R., and Fontboté, L., 2001, The Candelaria-Punta del Cobre iron oxide Cu-Au (-Zn-Ag) deposits, Chile: Economic Geology, v. 96, p. 1799-1826.

Marshall, L.J., and Oliver, N.H.S., 2006, Monitoring fluid chemistry in iron oxide–copper–gold-related metasomatic processes, eastern Mt Isa Block, Australia: Geofluids, v. 6, p. 45-66.

Marshall, L.J., Oliver, N.H.S., and Davidson, G.J., 2006, Carbon and oxygen isotope constraints on fluid sources and fluid-wall rock interaction in regional alteration and iron-oxide-copper-gold mineralisation, eastern Mt Isa Block, Australia: Mineralium Deposita, v. 41, p. 429-452.

Martinsson, O., 1997, Tectonic setting and metallogeny of the Kiruna greenstones: Doctoral Thesis, Luleå University of Technology, 1997:19, 162 p.

Martinsson, O., and Weihed, P., 1999, Metallogeny of juvenile Palaeoproterozoic volcanic arcs and greenstone belts in rifted Archaean crust in the northern part of Sweden, Fennoscandian Shield, *in* Stanley, C.J. et al., eds., Mineral deposits: processes to processing: Balkema, Rotterdam, p. 1329-1332.

Monro, D., 1988, The geology and genesis of the Aitik Cu-Au deposit, Arctic Sweden: Ph.D. thesis, University of Wales College of Cardiff.

Mudd, G.M., 2007, An analysis of historic production trends in Australian base metal mining: Ore Geology Reviews, v. 32, p. 227-261.

Mumin, A.H., Somarin, A.K., Jones, B., Corriveau, L., Ootes, L., and Camier, J., 2010, The IOCG-porphyry-epithermal continuum of deposits types in the Great Bear magmatic zone, Northwest Territories, Canada, *in* Corriveau, L. and Mumin, A.H., eds., Exploring for iron oxide copper-gold deposits: Canada and global analogues: Geological Association of Canada, Short Course Notes, No. 20, p. 59-78.

Mustard, R., Baker, T., Williams, P., Ulrich, T., Mernagh, T., Ryan, C.G., Van Achterbergh, E., and Adshead, N., 2003, Cu-rich brines at the Osborne and Starra deposits: implications for immiscibility in Fe-oxide Cu-Au systems: Applied Earth Science Transactions of the Institutions of Mining and Metallurgy, Section B, v. 112, p. B189-191.

Nisbet, B.W., Devlin, S.P., and Joyce, P.J., 1983, Geology and suggested genesis of cobalt-tungsten mineralization at Mount Cobalt, northwestern Queensland: Proceedings of the Australasian Institute of Mining and Metallurgy, v. 287, p. 9-17.

Nyström, J.O., and Henriquez, F., 1994, Magmatic features of iron ores of the Kiruna-type in Chile and Sweden: ore textures and magnetite geochemistry: Economic Geology, v. 89, p. 820-839.

O'Farrelly, K.S., 1990, A stable isotope investigation of the origin and evolution of the Kiirunavaara iron mine, northern Sweden: Ph.D. thesis, University of Wales College of Cardiff.

Ohmoto, H., 2003, Non redox transformations of magnetite-hematite in hydrothermal systems: Economic Geology, v. 98, p. 157-162.

Oliver, N.H.S., Mark, G., Pollard, P.J., Rubenach, M.J., Bastrakov, E., Williams, P.J., Marshall, L.C., Baker, T., and Nemchin, A.A., 2004, The role of sodic alteration in the genesis of iron oxide-copper-gold deposits: geochemistry and geochemical modelling of fluid-rock interaction in the Cloncurry district, Australia: Economic Geology, v. 99, p. 1145-1176.

Oliver, N.H.S., Rubenach, M.J., Fu, B., Baker, T., Blenkinsop, T.G., Cleverley, J.S., Marshall, L.J., and Ridd, P.J., 2006, Granite-related fluid overpressure and volatile release in the mid crust: fluidized breccias from the Cloncurry district, Australia: Geofluids, v. 6, p. 1-13.

Page, R.W., and Sun, S-s., 1998, Aspects of geochronology and crustal evolution in the Eastern Fold Belt, Mt Isa Inlier: Australian Journal of Earth Sciences, v. 45, p. 343-361.

Perkins, C., and Wyborn, L., 1998, Age of Cu-Au mineralisation, Cloncurry district, Mount Isa Inlier, as determined by $^{40}Ar/^{39}Ar$ dating: Australian Journal of Earth Sciences, v. 45, p. 233-246.

Perring, C.S., Pollard, P.J., Dong, G., Nunn, A.J., and Blake, K.L., 2000, The Lightning Creek sill complex, Cloncurry district, northwest Queensland: a source of fluids for Fe-oxide- Cu-Au mineralization and sodic-calcic alteration: Economic Geology, v. 95, p. 1067-1069.

Perring, C.S., Pollard, P.J., and Nunn, A.J., 2001, Petrogenesis of the Squirrel Hills granite and associated magnetite-rich sill and vein complex: Lightning Creek prospect, Cloncurry district, northwest Queensland: Precambrian Research, v. 105, p. 213-238.

Pollard, P.J., 2000, Evidence of a magmatic fluid source for iron oxide-Cu-Au mineralisation, *in* Porter, T.M., ed., Hydrothermal iron oxide copper-gold and related deposits: a global perspective, v. 1: PCG Publishing, Adelaide, p. 27-41.

Pollard, P.J., 2006, An intrusion-related origin for Cu-Au mineralization in iron oxide-copper-gold (IOCG) provinces: Mineralium Deposita, v. 41, p. 179-187.

Pollard, P.J., and McNaughton, N.J., 1997, U/Pb geochronology and Sm/Nd isotope characterization of Proterozoic intrusive rocks in the Cloncurry district, Mount Isa inlier, Australia: AMIRA P438 Cloncurry Base Metals and Gold Final Report, Section 4, 19 p.

Pollard, P.J., and Perkins, C., 1997, $^{40}Ar/^{39}Ar$ geochronology of alteration and Cu-Au-Co mineralization in the Cloncurry district, Mount Isa Inlier: AMIRA P438 Cloncurry Base Metals and Gold Final Report, Section 3, 40 p.

Romer, R.L., Martinsson, O., and Perdahl, J.A., 1994, Geochronology of the Kiruna iron ores and hydrothermal alterations: Economic Geology, v. 89, p. 1249-1261.

Rotherham, J.F., 1997, A metasomatic origin for the iron-oxide Au-Cu Starra orebodies, Eastern Fold Belt, Mount Isa Inlier: Mineralium Deposita, v. 32, p. 205-218.

Rotherham, J.F., Blake, K.L., Cartwright, I., and Williams, P.J., 1998, Stable isotope evidence for the origin of the Mesoproterozoic Starra Au-Cu deposit, Cloncurry district, northwest Queensland: Economic Geology, v. 93, p. 1435-1449.

Rubenach, M.J., Foster, D.R.W., Evins, P.M., Blake, K.L., and Fanning, C.M., 2008, Age constraints on the tectonothermal evolution of the Selwyn zone, Eastern Fold Belt, Mount Isa inlier: Precambrian Research, v. 163, p. 81-107.

Sandrin, A., and Elming S-Å., 2006, Geophysical and petrophysical study of an iron oxide copper gold deposit in northern Sweden: Ore Geology Reviews, v. 29, p. 1-18.

Sillitoe, R.H., 1997, Characteristics and controls of the largest porphyry copper-gold and epithermal gold deposits in the circum-Pacific region: Australian Journal of Earth Sciences, v. 44, p. 373-388.

Sleigh, D., 2002, The Selwyn Line tabular iron-copper-gold mineralised system, Mount Isa Inlier, NW Queensland, Australia, *in* Porter, T.M., ed., Hydrothermal iron oxide copper-gold and related deposits: a global perspective, v. 2: PCG Publishing, Adelaide, p. 77-93.

Smith, M., and Gleeson, S.A., 2005, Constraints on the source and evolution of mineralising fluids in the Norrbotten Fe oxide-Cu-Au province, Sweden, *in* Mao, J. and Bierlien, F.P., eds., Mineral deposit research: meeting the global challenge: Springer, Berlin, p. 825-828.

Smith, M., Coppard, J., Herrington, R., and Stein, H., 2007, The geology of the Rakkurijärvi Cu-(Au) prospect, Norrbotten: a new iron oxide-copper-gold deposit in northern Sweden: Economic Geology, v. 102, p. 393-414.

Twyerould, S.C., 1997, The geology and genesis of the Ernest Henry Fe-Cu-Au deposit, NW Queensland, Australia: Ph.D. thesis, University of Oregon, 494 p.

Ulrich, T., Günther, D., and Heinrich, C.A., 1999, Gold concentrations of magmatic brines and the metal budget of porphyry copper deposits: Nature, v. 399, p. 676-679.

Wang, S., and Williams, P.J., 2001, Geochemistry and origin of Proterozoic skarns at the Mount Elliott Cu-Au(-Co-Ni) deposit, Cloncurry district, NW Queensland, Australia: Mineralium Deposita, v. 36, p. 109-124.

Wanhainen, C., Broman, C., and Martinsson, O., 2003, The Aitik Cu–Au–Ag deposit in northern Sweden: a product of high salinity fluids: Mineralium Deposita, v. 38, p. 715-726.

Wanhainen, C., Billström, K., Martinsson, O., Stein, H., and Nordin, R., 2005, 160 Ma of magmatic/hydrothermal and metamorphic activity in the Gällivare area: Re–Os dating of molybdenite and U–Pb dating of titanite from the Aitik Cu–Au–Ag deposit, northern Sweden: Mineralium Deposita, v. 40, p. 435-447.

Wanhainen, C., Billström, K., and Martinsson, O., 2006, Age, petrology and geochemistry of the porphyritic Aitik intrusion, and its relation to the disseminated Aitik Cu-Au-Ag deposit, northern Sweden: GFF, v. 128, p. 273-286.

Williams, P.J., 1994, Iron mobility during synmetamorphic alteration in the Selwyn Range area, NW Queensland: implications for the origin of ironstone-hosted Au-Cu deposits: Mineralium Deposita, v. 29, p. 250-260.

Williams, P.J., 1998, Metalliferous economic geology of the Mt Isa Eastern succession, northwest Queensland: Australian Journal of Earth Sciences, v. 45, p. 329-341.

Williams, P.J., 2001, Time-space relations of hydrothermal alteration and Fe-oxide-Cu-Au deposits in the Cloncurry and Curnamona regions, Australia: Geological Society of America 2001 Annual Meeting Abstracts, http://gsa.confex.com/gsa/2001AM/finalprogram/abstract_21591.htm

Williams, P.J., 2010, Classifying IOCG Deposits, *in* Corriveau, L. and Mumin, A.H., eds., Exploring for iron oxide copper-gold deposits: Canada and global analogues: Geological Association of Canada, Short Course Notes, No. 20, p. 13-21.

Williams, P.J., and Pollard, P.J., 2003, Australian Proterozoic iron oxide-Cu-Au deposits: an overview with new metallogenic and exploration data from the Cloncurry district, northwest Queensland: Exploration and Mining Geology, v. 10, p. 191-213.

Williams, P.J., and Skirrow, R.G., 2000, Overview of iron oxide-copper-gold deposits in the Curnamona Province and Cloncurry District (Eastern Mount Isa Block), Australia, *in* Porter, T.M., ed., Hydrothermal iron oxide copper-gold and related deposits: a global perspective, v. 1: PCG Publishing, Adelaide, p. 105-122.

Williams, P.J., Dong, G., Pollard, P.J., Broman, C., Martinsson, O., Wanhainen, C., Mark, G., Ryan, C.G., and Mernagh, T.P., 2003, The nature of iron oxide-copper-gold ore fluids: fluid inclusion evidence from Norrbotten (Sweden) and the Cloncurry district (Australia), *in* Eliopoulos, D.G. et al., eds., Mineral exploration and sustainable development: Millpress, Rotterdam, p. 1127-1130.

Williams, P.J., Barton, M.D., Johnson, D.A., Fontboté, L., de Haller, A., Mark, G., Oliver, N.H.S., and Marschik, R., 2005, Iron-oxide copper-gold deposits: geology, space-time distribution, and possible modes of origin: Economic Geology 100th Anniversary Volume, p. 371-405.

Xu, G., and Pollard, P.J., 1999, Origin of $CO_2$-rich fluid inclusions in synorogenic veins from the Eastern Mount Isa Fold Belt, NW Queensland, and their implications for mineralization: Mineralium Deposita, v. 34, p. 395-404.

Zwiefel, H., 1976, Aitik – geological documentation of a disseminated copper deposit: Sveriges Geologie Undersok C.720, 79 p.

# Mapping Mineral Systems with IOCG and Affiliated Deposits: A Facies Approach

**Louise Corriveau**
*Natural Resources Canada, Geological Survey of Canada, Québec, Canada*
*louise.corriveau@NRCan-RNCan.gc.ca*

**Jean-François Montreuil**
*Red Pine Exploration, Ontario, Canada*

**Anthony F. De Toni**
*SOQUEM Inc., Québec, Canada*

**Eric G. Potter and Jeanne B. Percival**
*Natural Resources Canada, Geological Survey of Canada, Ontario, Canada*

*Recommended citation: Corriveau, L., Montreuil, J.-F., De Toni, A.F., Potter, E.G., and Percival, J.B., 2022, Mapping mineral systems with IOCG and affiliated deposits: a facies approach, in Corriveau, L., Potter, E.G. and Mumin, A.H., eds., Mineral systems with iron oxide copper-gold (IOCG) and affiliated deposits: Geological Association of Canada, Special Paper 52, p. 69-111.*

## Abstract

Ore systems with regional-scale iron oxide and alkali-calcic metasomatism host iron oxide copper-gold, iron oxide-apatite, iron and polymetallic skarn, albitite-hosted uranium, and epithermal deposits. The deposits develop through prograde, retrograde, telescoped and cyclical metasomatic paths across diverse rocks types, leading to alteration zones with highly variable mineral assemblages, mineral contents, textures, structures and spatial distribution. Deciphering the evolution of these mineral systems through mapping alteration assemblages, veins and breccia is key to effective exploration, but can be hampered by the complexities of the systems and resemblance of some metasomatites to common sedimentary, volcanic, plutonic or metamorphic rocks. In the Great Bear magmatic zone in northern Canada, a series of well exposed and preserved mineralized systems were mapped from their sub-volcanic roots to their shallowest levels as well as along fault zones. The great complexity of the metasomatic rocks observed and described in this paper was resolved by applying a metamorphic petrology 'facies' approach to alteration mapping. This approach defines a given facies according to the spectrum of mineral assemblages that crystallized under similar physicochemical conditions and produced diagnostic bulk compositions. Rather than simply reflecting element enrichment or depletion, each alteration facies is a product of systematic elemental partitioning between fluid and rock, and the stability of the resultant mineral assemblages as the magmatic-hydrothermal systems evolve. This approach greatly simplifies the descriptive terminology and alteration mapping protocols for iron oxide and alkali-calcic alteration systems and their deposits.

## Résumé

Les systèmes minéralisés à altération alcali-calcique et à oxydes de fer donnent lieu à la formation de gîtes à oxydes de fer-cuivre-or, à oxydes de fer-apatite, à skarn ferrifère ou polymétallique, à uranium au sein d'albitite ou épithermaux. Ces gîtes se forment via des cheminements métasomatiques progrades, rétrogrades, télescopés ou cycliques au sein d'encaissants divers ce qui mènent à des assemblages minéralogiques, des proportions minérales, des textures, des structures et une distribution spatiale des zones d'altération qui varient fortement. Décoder l'évolution de ces systèmes par la cartographie des séquences d'altération, des veines et des brèches est essentiel au succès des programmes d'exploration. Toutefois le tout est souvent complexifié par la grande variabilité des systèmes et la ressemblance de certaines roches métasomatiques avec des roches sédimentaires, volcaniques, plutoniques ou métamorphiques. Dans la zone magmatique du Grand lac de l'Ours dans le nord du Canada, ce type de systèmes est très bien exposé et bien préservé et plusieurs ont été cartographiés de leur racines sub-volcaniques jusqu'à leurs niveaux superficiels ainsi que le long de zones de failles. Compte tenu du degré de complexité des roches métasomatiques observées et décrites dans cet article, une approche de cartographie d'altération par « faciès » empruntée à la pétrologie métamorphique a été retenue. Cette classification regroupe en faciès distincts les ensembles d'assemblages minéralogiques qui cristallisent sous de même conditions physicochimiques suivant des compositions diagnostiques. Plutôt que de refléter simplement l'enrichissement et l'appauvrissement des éléments, chaque faciès d'altération est la conséquence de la redistribution systématique des éléments entre le fluide et la roche, et de la stabilité des assemblages minéraux durant l'évolution des systèmes magmatiques-hydrothermaux. Cette approche simplifie grandement la terminologie descriptive et les protocoles de cartographie de l'altération pour les systèmes d'altération alcali-calcique et à oxydes de fer et leurs gîtes.

## Introduction

Iron oxide and alkali-calcic alteration systems (IOAA) form the largest high-temperature metasomatic systems in the exposed continental crust, featuring unparalleled, pervasively intense regional-scale alteration (see Marschik and Fontboté, 2001; Williams et al., 2005; Mark et al., 2006; Mumin et al., 2007, 2010; Monteiro et al., 2008; Porter, 2010). Fertile IOAA systems can host magnetite-, magnetite-hematite- and hematite-group iron-oxide copper-gold (IOCG) deposits, as well as iron oxide ± apatite (IOA) deposits, iron and polymetallic skarn deposits, iron oxide-uranium deposits, and albitite-hosted U, Au-Co-U and Mo-Re deposits (Corriveau et al., 2022a–d and references therein). The near-surface expression of these systems can lead to epithermal mineralization and associated alteration types (Mumin et al., 2010 and references therein).

The footprints of alteration and mineralization within IOAA systems include very diagnostic geological, geochemical and geophysical signatures that are detectable at regional and provincial scales (Montreuil et al., 2013; Enkin et al., 2016; Hayward et al., 2016; Acosta-Góngora et al., 2019; Skirrow et al., 2019; Katona and Fabris, 2022). However, the rugged physiography and lack of infrastructure typical of prospective areas in Canada have hampered the acquisition of detailed gravity, magnetotelluric and radiometric surveys at the scale of the metallogenic provinces. Conversely, the Quaternary glaciation has exposed extensive geological windows across these settings, making regional geological mapping a key exploration tool (Corriveau and Potter, in press). Over the last fifteen years, the Geological Survey of Canada and its provincial, territorial, First Nations, academic and private sector collaborators developed a geological ore deposit model that focused on geological exploration (Corriveau et al., 2016) and applied it to the Great Bear magmatic zone in the Northwest Territories (Fig. 1; Corriveau and Potter, in press), Romanet Horst in the Labrador Trough in Québec, and Central Mineral Belt in Labrador (see Fig. 2 in Corriveau et al., 2022d). With this tool came the need for optimizing mapping protocols and field description terminology of metasomatites.

Unlike many global IOA and IOCG districts that are poorly exposed, exposure of IOAA systems in the Great Bear magmatic zone (GBMZ; Fig. 1) permits recognition of the full extent of the systems from weak, cryptic alteration to intense, complete replacement of the host rocks and ultimately to mineralization. The 1.87–1.85 Ga volcanic sequences and intrusive rocks of the GBMZ were not affected by any significant orogenic reworking and regional metamorphism except for some post-1.87 Ga deformation along the Wopmay fault zone (Fig. 1; Hildebrand et al., 2010; Jackson et al., 2013; Montreuil et al., 2016a; Ootes et al., 2017), in contrast to some other prospective settings of the Canadian Shield (Corriveau et al., 2010a). Sub-arctic vegetation, extensive glacially-polished outcrops, tilting of supracrustal sequences, including during caldera collapse, and late-stage, broad arching of the belt provide exceptional exposures of entire IOAA systems from bottom to top, as well as laterally from metamorphosed

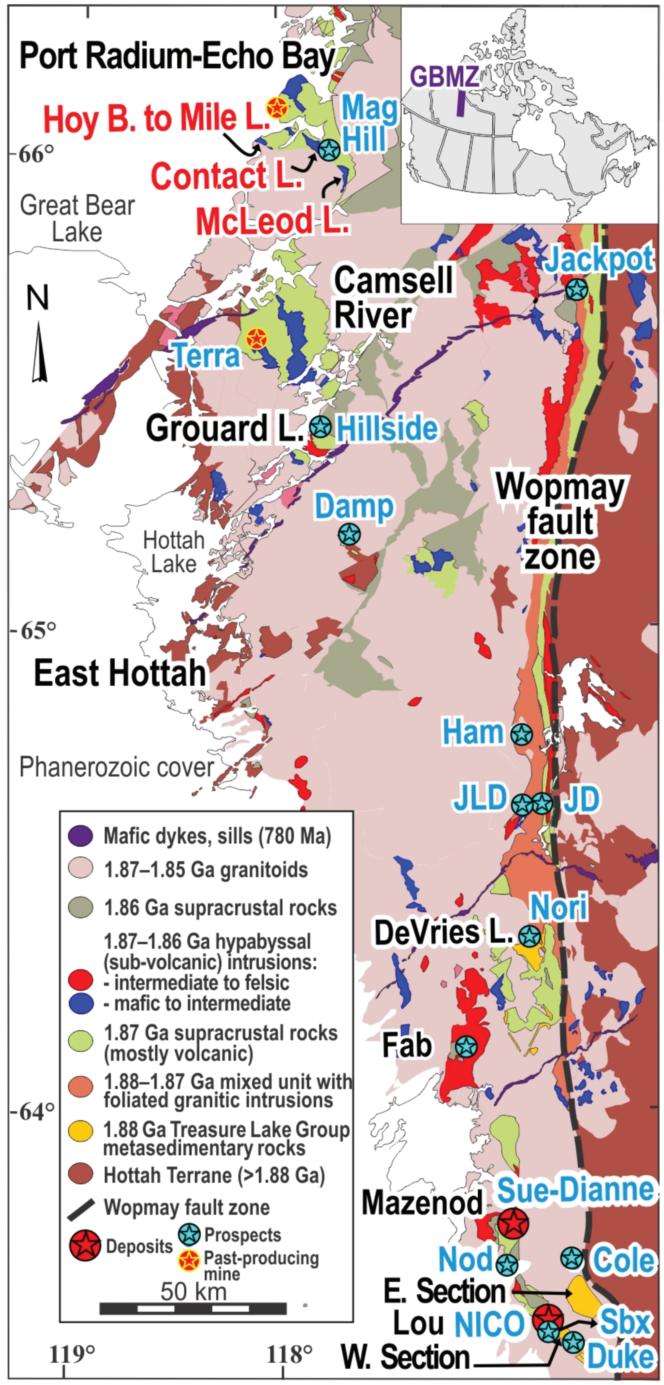


**Figure 1.** Location of selected IOAA systems and districts (labelled in black) and the main deposits and occurrences (labelled in red) in the part of the GBMZ investigated in this paper in the Northwest Territories, Canada (modified from Corriveau et al., 2016). The simplified geology highlights syn- and pre-1.87 Ga host units. The western section of the Treasure Lake Group extends from the Lou to the Duke systems, with the Lou system including the Au-Co-Bi-Cu NICO deposit, the Peanut Lake prospect and the albitite-hosted uranium mineralization of the Southern Breccia (SBx) albitite corridor. The Cole prospect occurs within the volcanic units north of the eastern section of the Treasure Lake Group (E. section). The Sue Dianne Cu-Ag deposit, Brooke prospect and Cat showing occur within the Mazenod system. Inset shows the location of the exposed part of the GBMZ in Canada. L: Lake.

basement host rocks, early sedimentary basins, and through sub-volcanic intrusions, volcanic sequences and paleo-surface epithermal caps (Fig. 1; Hildebrand, 1983, 1984a, b, 1986; Gandhi, 1994; Mumin et al., 2007, 2010, 2014). The IOAA metasomatites exhibit extreme variations in morphology (replacement zones, veins and breccia), mineral assemblages, modal abundances, intensity of replacement, density of veins, types of breccia and styles of mineralization. This variety complicates ore systems characterization and exploration.

To optimize exploration for IOAA systems, this paper 1) revisits the notions of metasomatic facies applied to mineral deposits (e.g. Burnham, 1962; Zharikov et al., 2007); 2) refines alteration mapping protocols; 3) provides a classification for alteration intensity; 4) illustrates and describes the megascopic attributes, mineral assemblages and regional to outcrop-scale space-time relationships of alteration facies across the GBMZ IOAA systems; and 5) reviews the resemblances of some metasomatites to more common rocks. Illustrations focus on the transformation of host rocks at regional scale using albitization as the main example, as well as alteration overprints, veins and breccia in albitized hosts. Mineralization and deposits are described in Mumin et al. (2007, 2010), Ootes et al. (2008, 2010, 2017), Acosta-Góngora et al. (2011, 2015), Montreuil et al. (2015, 2016b, c) and Potter et al. (2019, 2022).

## Geological Environments of the Great Bear Magmatic Zone Iron Oxide and Alkali-calcic Systems

Host rocks of the Great Bear IOAA systems consist largely of 1.87 Ga subaerial, porphyritic to amygdaloidal volcanic and volcaniclastic rocks of the Labine and Faber Groups that form intra-caldera and outflow sheets and subordinate debris flow breccia (Fig. 2A, B). Lacustrine-fluvial sedimentary rocks also occur within the volcanic sequence (Hildebrand et al., 1987, 2010), along with intra-caldera carbonate units that are locally stromatolitic, such as in the Grouard Lake system (Fig. 1).

The volcanic rocks in the southern GBMZ are unconformable on the 1.88 Ga Treasure Lake Group. Sub-volcanic sheet-like intrusions, and syn-volcanic sills, laccoliths and mafic to felsic dyke swarms intruded the volcanic sequences (e.g. dioritic intrusions at McLeod Lake, Contact Lake, Hoy Bay and Mile Lake intrusions; Figs. 1, 2C–E). These intrusions formed and were hydrothermally altered during the first pan-GBMZ volcanic event at ca. 1.87 Ga (Hildebrand, 1986; Mumin et al., 2007). For example, an 1.87 Ga diorite is albitized along its endocontact zone (left side of Fig. 2C) and sporadic potassic (K-feldspar) alteration is observed across most of the intrusion (Fig. 2C–E; Mumin et al., 2010).

At 1.87 Ga, some of the volcanic sequences, their coeval intrusions and their basement were variably tilted, differentially uplifted and locally deformed along faults and shear zones (Hildebrand et al., 2010; Enkin et al., 2012; Hayward et al., 2016; Montreuil et al., 2016a, b). This was followed by regional-scale deposition of an ignimbritic cover sequence at ca. 1.862 Ga and intrusion of 1.87–1.85 Ga granodiorite to monzogranite batholiths (Ootes et al., 2017). Regional geology and host rock descriptions are provided in Hildebrand et al. (1987, 2010), Gandhi et al. (2001), Jackson and Ootes (2012) and Montreuil et al. (2016a, c).

Basement rocks consist of the Hottah Terrane arc sequences and overlying sedimentary rocks of the 1.88 Ga Treasure Lake Group (Figs. 1, 2F–L; Gandhi and van Breemen, 2005). The Treasure Lake Group was metamorphosed to greenschist to lower-amphibolite facies (e.g. development of biotite assemblages, Fig. 2L) prior to the onset of IOAA metasomatism and intrusion of early 1.876 Ga granitic dykes coeval with albitization (Bennett et al., 2012). The Treasure Lake Group consists of several distinct sedimentary rock types, including, from bottom to top, units of siltstone-wacke, carbonates, and quartz arenite. The layering and structure of the best-preserved units at the type locality, the Treasure Lake section of Gandhi and van Breemen (2005), permitted mapping of the units along strike for 15 km beyond the zone of intense metasomatism (Fig. 2F–L; Gandhi et al., 2014). The quartz arenite unit is 300–500 m thick (Gandhi et al., 2014); it occurs as massive, centimetre- to decimetre-scale beds, but includes argillaceous siltstone beds up to 10 m thick. Graded bedding, cross-bedding, and ripple marks are diagnostic (Fig. 2F). Argillites are sparse. This unit marks the uppermost host to the NICO deposit ore zone (Fig. 1), where alteration intensity varies from weak to locally intense. The carbonate unit is 100 m thick and can be traced 15 km along strike (Gandhi et al., 2014). It consists of thinly-bedded limestone and dolomite metamorphosed to marble and interlayered with metasiltstone laminations (Fig. 2G). The unit is weakly altered at the type locality and locally in the eastern section. The siltstone-wacke unit is typically thin-bedded; bed thickness and megascopic changes in composition are fairly regular across a variety of inliers, making the unit easily recognizable even after metasomatism (Fig. 2H–L; Gandhi et al., 2014). Unaltered examples are rare.

After 1.87 Ga, the volcanic sequences, their intrusions and the basement were variably tilted and cut by transcurrent faults (Hildebrand et al., 2010), exposing deep basement roots across the belt. None of the post-1.87 Ga intrusive and volcanic units of the GBMZ host IOAA metasomatites, although they host vein-type mineralization, including mineralized giant quartz veins along a northeast-trending transform fault network (Gandhi et al., 2000; Somarin and Mumin, 2012; Hayward et al., 2013).

## Field Methods

Petrological mapping was conducted across known IOAA systems of the GBMZ in the Northwest Territories (i.e. excluding those in Nunavut). The various suites of alteration assemblages were classified according to alteration facies irrespective of textural and structural attributes, a protocol adapted from petrological mapping of metamorphic facies and bathozones (see Carmichael, 1969, 1978) and described in the following section. Element mobility across systems was empirically assessed in the field (similar to mapping of metamorphic reactions through recognition of isograds and bathograds in the field) using alteration assemblages and

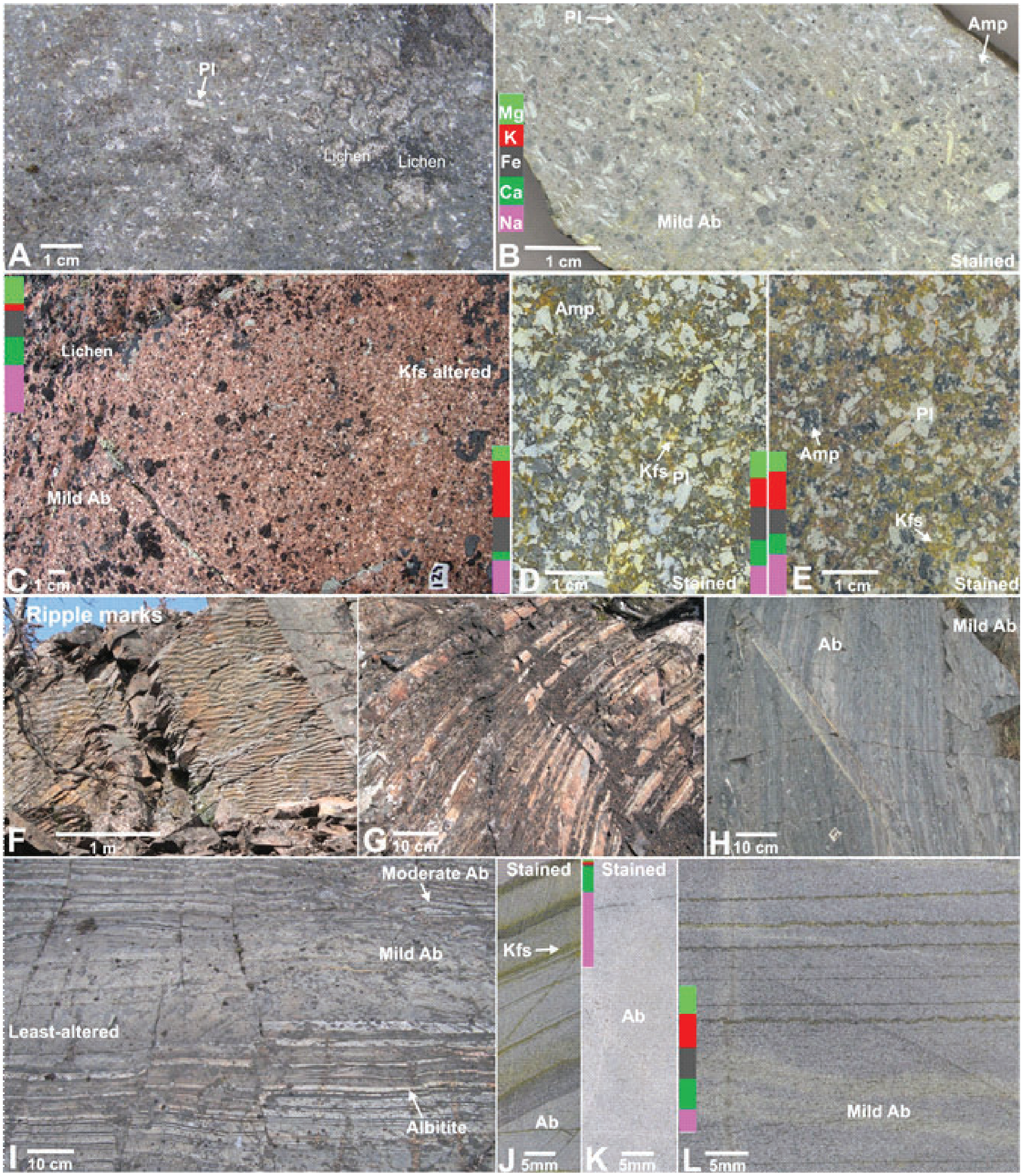


**Figure 2.** Field photographs and cobaltinitrite-stained rock slabs of 'least-altered' host rocks. Molar proportions of Na-Ca-K-Fe-Mg are shown as coloured bars (see Fig. 2B). In this and other figures, mineral abbreviations are from Whitney and Evans (2010), deposits and districts are shown in Figure 1, and Geological Survey of Canada field stations are provided (e.g. CQA-05-095). **A, B**. Porphyritic andesite, Port Radium-Echo Bay district (A: CQA-05-095; B: CQA-05-054A). **C–E.** Contact Lake monzodiorite (C: CQA-05-124; D: CQA-05-056A; E: CQA-05-125A; K-feldspar stains yellow in D and E). **F–H.** Treasure Lake Group upper siltstone, middle carbonate and lower siltstone units respectively in F, G and H, Duke system (F: 09CQA-0055; G: 09CQA-0053; H: 09-CQA-083). **I–L.** Lower siltstone unit (I–J: CQA-05-251; K: 05JY2249; L: CQA-05-239). Albitization of host rocks ranges from mild (paler grey tones of volcanic groundmass and sedimentary layers and albitization of phenocrysts; A–E, I, J, L) to locally intense (sharp white sedimentary layers in I, J and K). Darker layers are richer in biotite and, in K, albitization is pervasive across layers poorer in biotite and in part totally replaces fine laminations richer in biotite. Albitization is also intense along a set of parallel fractures in H, along a set of conjugate fractures in K and as stratabound splay-off haloes from fractures in H and along haloes of fractures in L. Albitization is associated with a change in bulk-rock molar proportions as shown in the coloured bars. (B) and (L) are least and (K) most sodic-altered, and C (right side) is most potassic-altered. NRCan photos 2020-458 to 2020-469.

combining the mineralogy of the mapped assemblages with their generic chemical formulae. These first order compositional variations helped infer metal pathways from some of the deposit sources, including: 1) where elements and metals were selectively leached by fluids as they dissolved least-altered host rocks and earlier metasomatites; 2) the fluid-metal pathways during fluid transport; and 3) the sites of element precipitation during development of the diagnostic sets of alteration facies and their affiliated mineralization. Geochemical data from more than 2000 representative samples support the major-element mobility interpreted megascopically (Corriveau et al., 2015; Montreuil et al., 2016b). Finally, field interpretation of metasomatism and brecciation was guided by global research on these processes (e.g. Barton et al., 1988; Ross et al., 2002; Oliver et al., 2004, 2006, 2008; Otake et al., 2010; Putnis and Austrheim, 2010, 2012; Harlov and Austrheim, 2012; Rubenach, 2012; Jébrak, 2022).

The geological database on the lithology of host sequences is extensive across the belt (see Hildebrand, 1983, 1984a, 2011, 2017; Hildebrand et al., 1987, 2010; Gandhi et al., 2001, 2014; Jackson et al., 2013; Montreuil et al., 2016a; Ootes et al., 2017). For this study, outcrop descriptions from ~65,000 localities, including unpublished data from R. Hildebrand, >18,000 field photographs of metasomatites and host rocks, and about 3,000 cobaltinitrite-stained and non-stained rock samples, accompany whole-rock analyses (this work; Hildebrand, 2011; Corriveau et al., 2015). Throughout this paper, outcrop numbers are labelled using GSC project leader identifier (CQA, PUA, KZ) or NTGS crew member identifier (JY, VB), year (05 to 11) and station number (e.g. CQA-05-054). In some cases, the unit is also identified by the addition of a letter to the station number (e.g. CQA-05-054A) (field database in preparation for publication).

Field descriptions of metasomatites and associated mineralization include: the style and intensity of metasomatism (replacement, veins, vein haloes, breccia infill and replacement haloes of breccia fragments), the stable alteration facies (each qualified by the suite of mineral assemblages present and their modal abundances), textures, relative proportion of rock types (protoliths and metasomatites) in the outcrop, spatial extent, breccia maturity (as classified in Jébrak, 2010) and transitional, overprinting, juxtaposing and crosscutting relationships. Pre-alteration attributes of the host rocks were also noted where protoliths were preserved and/or exposed (Fig. 2). Figure 3 provides a broad overview of how alteration varies in terms of mineral contents, assemblages and textures, and the challenge inherent in interpreting host rocks at outcrop scale without a regional stratigraphic framework.

Some outcrops display only a single alteration facies and mineral assemblage, whereas others record successive and pulsating alteration facies that overprinted but did not obliterate earlier ones. On a single outcrop, up to 40 distinct metasomatic rock types can be mapped, each of which is extremely varied in extent, alteration intensity, and mineral assemblages within each facies zone. Field photographs are accompanied by coloured bars representing whole-rock molar proportions (e.g. Fig. 2) where such analyses are available (see description of bars in the section 'Compositional Range of Metasomatites').

Alteration mapping was done in more detail along tilted or differentially uplifted sections (see Mumin et al., 2007, 2010; Somarin and Mumin, 2014; Mumin, 2015; Corriveau et al., 2016, 2022a–c; Montreuil et al., 2016a). In addition, Potter et al. (2013) produced a map of the Fab system, Mumin (2015) produced a series of maps from the Port Radium-Echo Bay district, and Bowdidge et al. (2014a, b) and Bowdidge and Dunford (2015) refined the alteration map of Hildebrand (1986) for the Camsell River district.

The field description of alteration is complemented by information from cobaltinitrite-stained rock slabs, petrography and 3D imaging of hand samples by computed tomography (CT) scanning, mineralogical assessment by X-ray diffraction, mineral chemistry by SEM/EPMA, magnetic susceptibility measurements (field and lab-based), density measurements, and geochemical data, including field analysis of equivalent *(e)* *e*U, *e*Th and K using a gamma-ray spectrometer (Corriveau et al., 2015, and work in progress; De Toni, 2016; Enkin et al., 2016; Percival et al., 2016; Normandeau et al., 2018).

Mineralized systems along the Wopmay fault zone (e.g. Ham, JLD, JD; Fig. 1) are commonly deformed and recrystallized at high temperature, which complicates interpretation (Jackson et al., 2013; Ootes et al., 2017; Corriveau et al., work in progress). This contrasts markedly with the metasomatic record from the rest of the GBMZ, which is relatively un-metamorphosed (sub-greenschist facies). As such, the IOAA systems of the Wopmay fault zone are not used as examples in this paper. Descriptive terms for metamorphosed IOAA systems are provided in Bonnet and Corriveau (2007) and Corriveau et al. (2018).

## An Alteration Facies Approach to Mapping

*Context*

Mapping protocols for metamorphic terranes have a long track record of defining and mapping metamorphic facies, isograds and bathograds. Interpretation of the mineral assemblages and reactions is based on the classic Gibbs phase rule, chemographic diagrams (to track how mineral assemblages and mineral contents change as a function of host-rock composition, temperature, and pressure), use of Schreinemaker's rule in phase diagrams, and P–T diagrams (Carmichael, 1978; Pattison et al., 2005 and references therein). The underlying assumption is that the megascopic attributes of rocks in outcrop exist at a scale optimal for extracting information on mineral assemblages, the isograds and metamorphic reactions they record, and their prograde metamorphic path, acknowledging that mineral assemblages are significantly refined by paragenetic assessment at microscopic scales (cf. Pattison et al., 2005 based on Carmichael, 1969, p. 244–245; Corriveau, 1982; Corriveau and Spry, 2014). This is also the case for the systematic, commonly depth-to-surface metasomatic progression of IOAA systems, but, in contrast to orogenic metamorphic terranes, this evolution is largely driven by declining temperatures and major changes in fluid chemistry that control the chemical composition of metasomatic rocks during regional-scale fluid-governed development of the system (e.g. Bardina and Popov, 1992).

*Petrological Mapping Protocol*

The petrological mapping protocol used for the studied IOAA systems focuses on mapping the succession of alteration facies observed at outcrop scale and their mineral assemblages, the stability of which is commonly best recorded at megascopic scale (Table 1). The assemblages are themselves defined by the minerals present, and each assemblage is described in terms of textures, field relationships with host lithotypes, structures, replacement-type alteration, veins, breccia, and alteration associated with veins and breccia.

The mapping strategy follows metamorphic petrological mapping protocols (Carmichael, 1969, 1978; Pattison et al., 2005), in that the mineral assemblages are the key building blocks (Table 1; Fig. 4). This protocol significantly differs from the mapping of individual minerals in hydrothermal alteration zones, a practice encouraged in economic geology and applied to trench and property maps, drill cores and ore deposits; in those cases, the direct mapping of alteration types is discouraged (Einaudi, 1997; Brimhall et al., 2006; Mumin, 2015; Cernuschi, 2017), although mapped minerals are then interpreted in terms of alteration types. This economic geology approach (commonly quoted as Anaconda-style mapping) could not be implemented for alteration mapping of the regional-scale IOAA systems because of the extreme variation in mineralogy, mineral assemblages, modal abundance (0 to 100 vol %), intensity of alteration, and degree of preservation of protolith textures even within a single outcrop.

Field attributes were key to developing the method:

1) The fine- to coarse-grained nature of the metasomatites allowed the assessment of which mineral assemblages were stable at megascopic scale (including the suite of minerals seen in breccia and vein infill and their haloes) and which suites of assemblages formed together (Table 1; Fig. 4). This was possible despite differences in host rocks both within outcrops and within and among systems ranging from volcanic, volcaniclastic, and sedimentary rocks (e.g. Port Radium-Echo Bay and Camsell River districts), metasiliciclastic and metacarbonate rocks (Southern Breccia, NICO, Carbonate Mountain, Duke and DeVries) and intrusive rocks (Fab, Southern Breccia).
2) Glacially polished and weakly weathered outcrops enhanced the discrimination of mineral attributes through colour and glassiness versus clay-rich weathered surfaces, differential weathering, etc.
3) The density of outcrops provided semi-continuous field exposures of the progressive alteration or brecciation of host rocks, from relatively unaltered or weakly fractured host rocks to intensely and pervasively metasomatized or brecciated rocks (Fig. 3).
4) Each alteration type identified (including gangue minerals of the associated mineralization) had a similar suite of mineral assemblages, and these suites, their composition, metal associations and crosscutting and overprinting relationships (Fig. 3C, D) were coherently repeated at mineral system scales despite differences in host rock types of the mineral systems mapped.

**Table 1.** Alteration facies from the GBMZ. Gangue minerals are listed in terms of abundance with the main minerals in bold, accessory to trace minerals in a normal font, and rare occurrences in italics. Common ore minerals are in a normal font while rare ones are in italics. Mineral abbreviations from Whitney and Evans (2010), except for bastnaesite (Bsn) and parisite (Pst) from Canadian Mineralogist (2018). Yttrialite: Ytt.

| Facies | Minerals in assemblages (alteration and gangue) | Mineralization |
|---|---|---|
| **Na** | **Ab, Cpx (Aug)**: Ttn, Rt, Zrn, Qz, *Cal* | |
| **Na-Ca-Fe** | **Ab, Amp (Act-Hbl), Mag, Ap, Cpx (Aug)***;* Ttn, Rt, Zrn, Qz*; Cal, Bt, Fl, Chl* | (La-Ce-Nd-Pr) Aln*; Mnz, Thr, (Ce-Nd) Pst, (Y-Ce-Nd) Urn* |
| **Skarn (i.e. HT Ca-Mg-Fe)** | **Cpx (Aug, Di), Grt (And, Grs), Cal, Ep, Ab, Mag, Ap**; Chl, Qz, Ttn | Py, Gn, Sp |
| **HT Ca-Fe** | **Amp (Act-Hbl-Cum), Mag, Ap, Aln**; Cpx, Grt (And), Ep, Ttn, Cal, Chl, Qz, Rt; *Fl, Sap, Fe-Ti oxides, Cld* | Po, Py, Sch, (Ce-La-Nd) Aln, (U-Y-Ce-Nd-Ir) Thr, (Nd-La-Ce-Pr) Pst, Y oxides; *Urn, Au, Skt* |
| **HT Fe** | **Mag, Ap;** Chl, Rt, Grt | Py, Mzn, Xtm, thorite*; Sp, Mol, Y-Nb oxides* |
| **HT Ca-K-Fe** | **Amp (Hbl-Act), Kfs, Mag, Bt, Cpx (Aug), Grt, Ap;** Chl, Pmp, Qz, Ttn; *Cal, Zrn, Fl, Fe-Ti oxides* | Py, Po, Apy, Mrc, sulpharsenides, Co-Bi sulphides, arsenides, (Y) Aln, Mnz, Xtm, (Ce-Nd-U-Y) Thr; *Urn, Cpy, Sp, Bsn* |
| **HT K-Fe** | **Bt, Kfs, Mag;** Ap, Ser, Ms, Zrn, Rt, Ttn, Fe-Ti-Mn oxides; *Chl, Ilm, Aln, Fl, Cal, odinite* | Py, Cpy, Co-Bi sulphides, Mol, Mnz, Xtm, Urn, Au; *(Y-Ce-La) Aln, Apy, Thr, Ytt, Gn, Pb-As-Ni sulphides, Th-U-Y-Zr oxides* |
| **LT K-Fe to LT Ca-Mg-Fe** | **Hem, Kfs, Ser, Chl, ± Ep, Brt, Fl, Sd, Dol, Cal, Ank, Mag, Qz** + up to other 90 minerals (Ehrig et al., 2012) | Cpy, Bn, Cct, Dg, djurelite, large variety of uranium and REE minerals see Ehrig et al. (2012) |

Mineral assemblages and their space-time relationships in the studied IOAA systems satisfy the definitions of metamorphic and metasomatic facies of Schmid et al. (2007) and Zharikov et al. (2007). Paraphrasing their definitions, each IOAA metasomatic facies corresponds to a systematic suite of mineral assemblages that are repeatedly associated in time and which appear to be related to a specific range in physicochemical conditions, in particular temperature. The entire suite of related facies reflects the petrogenetic processes that form the system.

The megascopic attributes of the metasomatic rocks best preserve the progressive development of the IOAA systems at

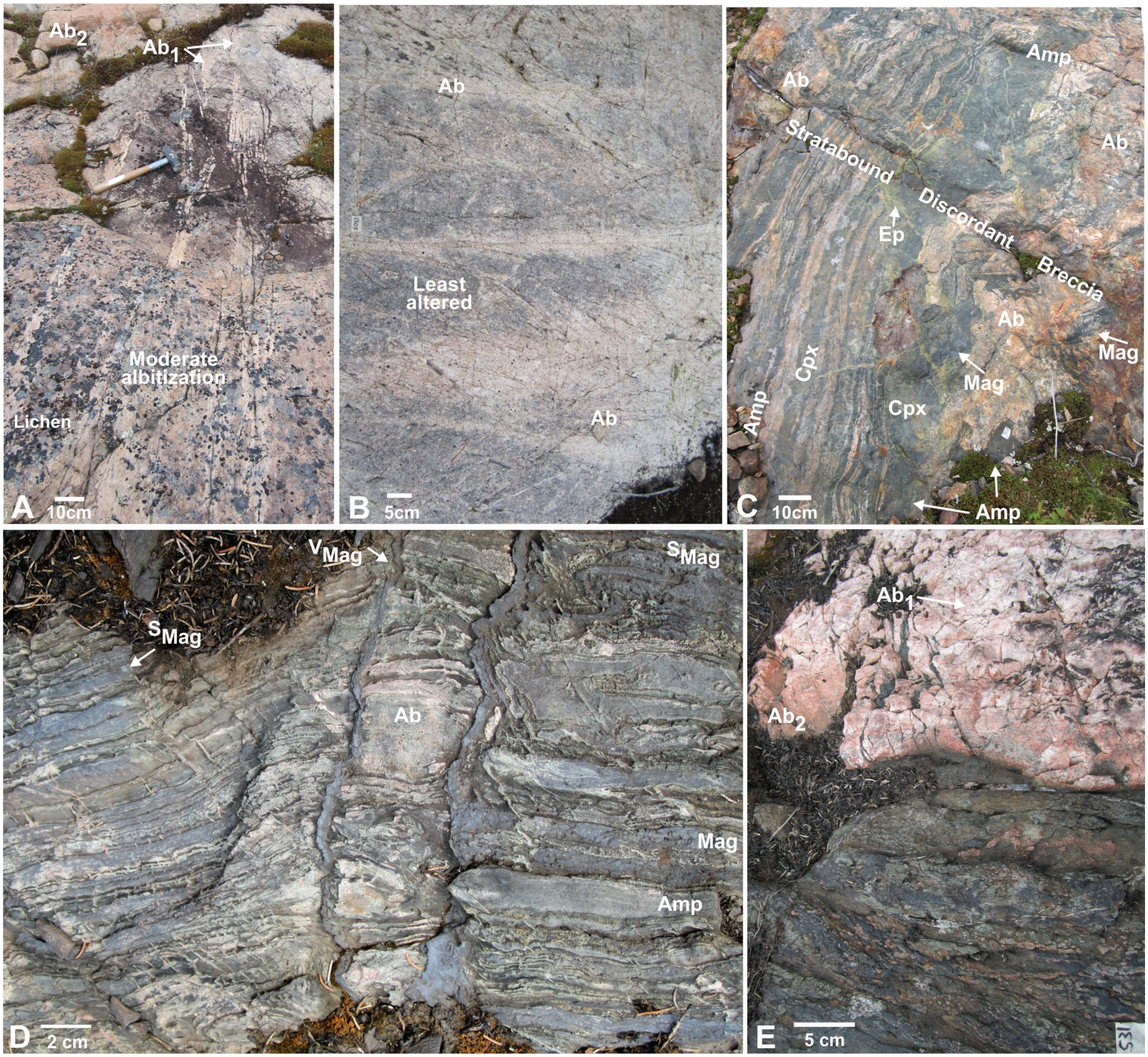


**Figure 3.** Variety in morphology, extent, types and intensity of alteration within volcanic and metasedimentary hosts, and linkages to fracturing and veining. **A.** Pervasive and moderate-to-strong albitization of a volcanic rock cut by fractures with albitite haloes (10CQA-0200). Both generations consist of white albite (grouped as Ab1) and are locally replaced by patches of pink Ab2 albite. **B.** Albitization haloes along fractures that coalesced into pervasive white albitite (10CQA-1305). **C.** Stratabound albite and skarn alteration of inferred interlayered clastic and carbonate sedimentary rocks (10CQA-302). The skarn layers are selectively and variably replaced by amphibole and, together with the albitite layers, are brecciated and infilled by amphibole and magnetite cement. High intensity amphibole replacement destroys primary (bedding) features. **D.** Selective, stratabound amphibole and magnetite replacement of a previously albitized metasiltstone unit cut by magnetite veins ($V^{Mag}$), and associated stratabound magnetite alteration ($S^{Mag}$) of albitized layers (11PUA-010). High intensity amphibole replacement destroys primary (bedding) features. **E.** Intense and selective stratabound albitization and amphibole alteration of a bedded unit, producing massive layers of albitite (white and pink) and amphibole (dark green) alteration resembling syenite and metamorphic amphibolite, respectively (11PUA-0531). As observed in A the earlier white albite ($Ab^1$) is in part replaced by patches of pink ($Ab^2$) albite. Veins of amphibole cut the albitite. Collectively, A to D illustrate the progression of regional-scale alteration facies in IOAA systems from Na (albitite) to skarn (i.e. HT Ca-Mg-Fe) to HT Ca-Fe (amphibole-dominant to magnetite-dominant) metasomatites. NRCan photos 2020-470 to 2020-474.

outcrop, deposit and regional scale, and from depth to surface. At microscopic scales, secondary, largely hydrolytic or carbonate-rich alteration obliterates or is intermixed so closely with original metasomatic assemblages (e.g. De Toni, 2016) that using microscopic information can lead to mixed assemblages and misleading information. Though a poor scale to define alteration facies, microscopic-scale information significantly helps refine field information and assess the retrograde part of the metasomatic paths within systems.

*Contexts for Terminology*

Labelling alteration types (facies) during mapping of IOAA systems was initially a challenge. Complex terminologies to which some IOAA alteration and metasomatic facies could be linked, such as alkaline metasomatites, aceite, gumbeite, secondary quartzite, beresite, fenite (Bardina and Popov, 1992; Zharikov et al., 2007) were avoided and a new scheme developed.

Gifkins et al. (2005) make a strong distinction between mineral-based alteration nomenclature and bulk-compositional alteration nomenclature. The former is said to be a field nomenclature that can be refined through petrography whereas the latter requires chemical analyses. This separation is unnecessary in IOAA system descriptions as the phaneritic grain size and limited numbers of mineral phases in IOAA metasomatites allow the characterization of the essential major element chemistry from the observed mineral assemblages and mineral abundances.

Another challenge faced was the application of existing zoning models and alteration nomenclature to the regional mapping of IOAA metasomatites. Combining gangue and iron-oxide mineralization into a single alteration assemblage (Fig. 4) shifted the focus from mineral zoning to the distinctive suites of mineral assemblages and their sequence of crystallization. This approach allowed a coherent suite of mineral assemblages to be consistently grouped into 'alteration facies', and labelled according to temperature of formation and the diagnostic major-element cation(s) in their index minerals (Fig. 4). The temperature ranges of alteration assemblages are based on thermometric studies of alteration from IOCG deposits worldwide and in the GBMZ, as well as similarities of these assemblages to well-characterized greenschist and amphibolite facies metamorphic rocks (as described in Corriveau et al., 2016). The mapping protocol adopted thus differs from those recommended for more 'normal' alteration systems by using the diagnostic cations of the dominant mineral phases within each suite of metasomatic mineral assemblages to name the alteration facies (Figs. 5, 6). This approach follows metamorphic petrology principles of phase equilibrium (e.g. Burnham, 1962), simplifies field mapping, and facilitates visualisation of bulk rock compositional variations while mapping, including using chemographic diagrams for metallogenic studies (e.g. Creasy, 1959).

As IOAA systems evolve and temperatures decline, mineral assemblages may have similar dominant cations but distinct mineralogy due to the different temperatures under which they form (Fig. 4; Table 1). This is taken into account by adding a 'high' or 'low' temperature qualifier to the facies. Consequently, each metasomatite incorporating calcic amphibole, magnetite, apatite, clinopyroxene or epidote was labelled as a Ca-Fe alteration facies (or Na-Ca-Fe facies if albite was also present). This Ca-Fe assemblage shares affinities with regional amphibolite-facies metamorphic rocks that form between 450°C and 700°C, i.e. a 'high' temperature. Another suite of Ca-Fe

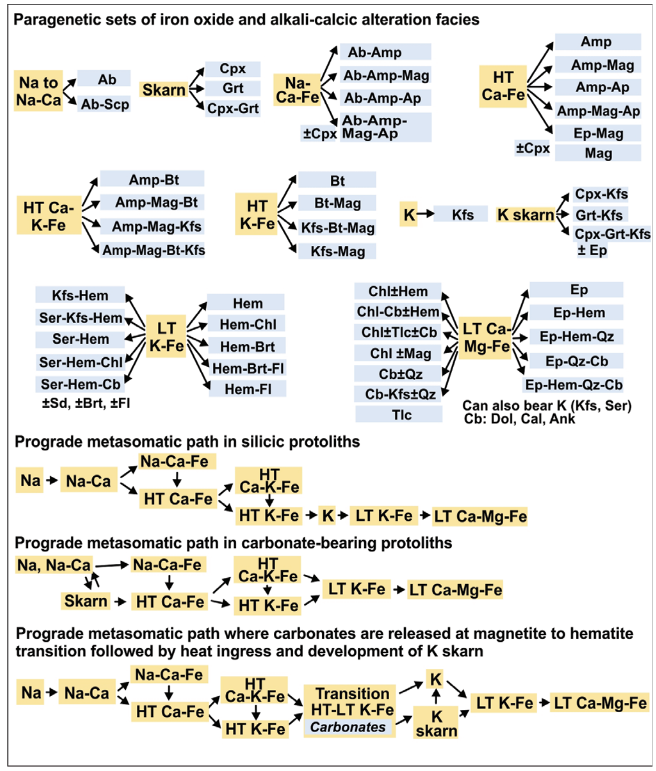


**FIGURE 4.** Alteration facies and sequences of crystallization based on depth-to-surface distribution and crosscutting relationships in IOAA systems in the GBMZ. Mineral abbreviations are from Whitney and Evans (2010). Prograde metasomatism is defined as the sequence of alteration facies from the roots of the system(s) to their shallowest levels, and reflects the consecutive metasomatic reactions observed, associated systematic element partitioning, and mineral stability as the magmatic-hydrothermal fluid plume rises toward surface (Corriveau et al., 2022b). Each facies may have end-members characterized by a single index cation. The LT Ca-Mg-Fe facies has multiple end-member assemblages, some of which may be prograde and others retrograde (Corriveau et al., 2022b).

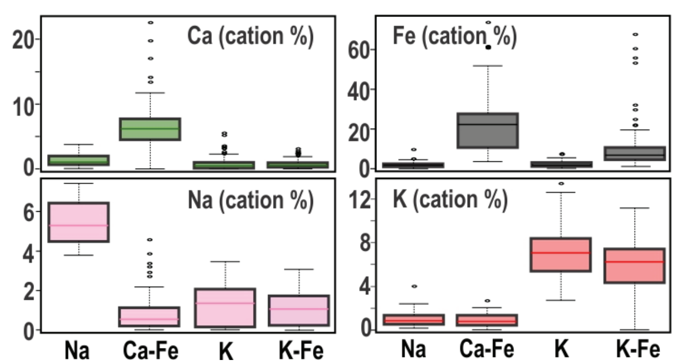


**FIGURE 5.** Molar proportions for the main IOAA facies of the GBMZ (n=386 samples; data from Corriveau et al., 2015). Average composition, one and three standard deviations are shown as bars, boxes and whiskers, respectively. Dots are outlying values. Colour reflects the diagnostic mineral for each element.

metasomatites contains epidote and variable modal proportions of calcic and iron/magnesium-rich minerals (chlorite, calcite, siderite, ankerite, ± hematite). These assemblages replace the amphibole-magnetite-bearing Ca-Fe assemblages or form independently from them; they are typical of greenschist facies rocks that form between 300°C and 450°C, i.e. a 'low' temperature. To discriminate these two sets of Ca-Fe (± Mg) alteration in the field, they were labelled high temperature (HT) Ca-Fe and low temperature (LT) Ca-Mg-Fe assemblages respectively. A few minerals (e.g. epidote) occur in both high- and low-temperature facies. Some metasomatites within IOAA systems have names that have been entrenched in the literature, such as albitite (>80 modal % albite) and skarn. Both terms were used instead of Na and HT Ca-Mg-Fe facies respectively.

*Alteration Facies Nomenclature*

From high to low temperature, the sequence of alteration facies and the names of their metasomatites are:

- Na metasomatites consisting of albite ± quartz and scapolite with accessory rutile, titanite and zircon. The most intense expression is albitite, which contains >80 modal % albite.
- Skarn with clinopyroxene ± garnet that forms in carbonate rocks and carbonate alteration.
- HT Na-Ca-Fe metasomatites in which field textures allow for recognition of co-crystallizing albite and amphibole, ± clinopyroxene, magnetite, scapolite.
- HT Ca-Fe metasomatites with calcic amphibole, magnetite, apatite ± clinopyroxene, epidote, REE-bearing minerals. Distinguishing clinopyroxene-dominant from amphibole-dominant assemblages allows for the discrimination between skarn and HT Ca-Fe alteration facies, respectively.
- HT Ca-K-Fe metasomatites with calcic amphibole, biotite, magnetite, ± arsenopyrite, pyrite, pyrrhotite, minor clinopyroxene.
- HT K-Fe metasomatites with magnetite, biotite and (or) K-feldspar ± chalcopyrite.
- K-skarn for K-feldspar-bearing skarn and K-felsite for K-feldspar dominated felsite.
- LT K-Fe metasomatites with hematite, K-feldspar or sericite, ± carbonate and chlorite, ± chalcopyrite, bornite, chalcocite, REE or U-bearing minerals (cf. hydrolytic alteration of Hitzman et al., 1992).
- LT Ca-Mg-Fe metasomatites with epidote, chlorite or carbonates ± allanite, other REE-bearing minerals and sulphides formed at an alteration intensity beyond that of typical propylitic alteration.

Breccia regularly forms in the HT to LT K-Fe, K-felsite and K-skarn facies. Skarn alteration was mapped separately from the transitional HT Na-Ca-Fe and the HT Ca-Fe facies as it has a distinct HT Ca-Mg-Fe mineral assemblage (clinopyroxene- or garnet-bearing) and physical properties (low magnetic susceptibility but high density), more magnesium, fewer hydrous minerals (i.e. amphibole or micas), and is regularly replaced by HT Ca-Fe facies (Corriveau et al., 2016, this work; Enkin et al., 2016). Furthermore, the IOAA systems commonly evolve to epithermal and vein systems, including widespread sericitic alteration, as well as to phyllic alteration. Orthomagmatic K-feldspar alteration is also common.

The metasomatic facies nomenclature presented here reduces the complexities of mapping metasomatic rocks without a major loss of information, and allows qualitative assessment of the chemical evolution and mineral potential of the systems while mapping. The merit of this nomenclature system has greatly simplified field data capture within corporate databases.

## Compositional Range of Metasomatites

The range in Na, Ca, K and Fe concentrations for the main alteration facies (Fig. 5) are a function of the type of facies, intensity of alteration, and (at weak to moderate alteration intensity) host rock types. Each facies has its own chemical signature and molar proportions of Na, Ca, Fe, K and Mg (or Si and Al) help identify facies and are useful proxies for their distinctive minerals. The molar proportions for each facies are so distinct that they provide true barcodes of alteration facies (Fig. 6). Where bulk rock composition is available, the Na-Ca-Fe-K-Mg barcode of the rock is reported on photos (e.g. Fig. 2), linking mineral assemblages to bulk rock compositions.

Plotting barcodes along drill cores, on maps and on chemical discriminant diagrams significantly helps to assess the mineral potential of a region, prognosticate fault zones (including sense of movements), indicate changes in host lithotypes (where alteration is mild to moderate), track alteration intensity, and interpret the evolution of systems at deposit- to regional-scales (e.g. Corriveau et al., 2016, 2022a, b; Montreuil et al., 2016b; Blein et al., 2022). The Na-Ca-Fe-K-Mg barcodes help distinguish IOAA facies within systems whereas the Na-Ca-Fe-K-[(Si+Al)/10] barcodes help differentiate IOAA systems

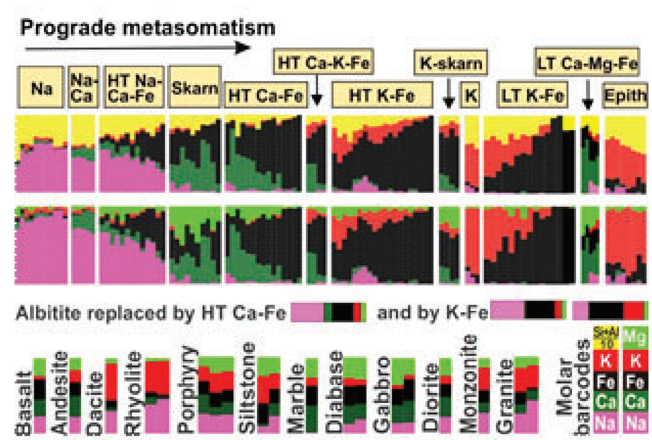


**Figure 6.** Molar proportions of Na, Ca, Fe, K and Mg or (Si-Al)/10 in bulk rocks of IOAA facies expressed as bars. Common sedimentary and igneous rocks have three to four main cations whereas intensely altered rocks have 1 or 2 main cations. The number of cations in altered rocks increases when overprinted (e.g. HT Ca-Fe overprint of albitite). Epith: epithermal alteration.

from associated epithermal caps and veins as well as from other mineral systems and deposit types (Corriveau et al., 2022a). Plotting the barcodes on the IOCG alteration (AIOCG) diagram of Montreuil et al. (2013) and the chlorite-carbonate-pyrite index (CCPI) box plot of Large et al. (2001) also helps discriminate the lithogeochemical footprints of volcanogenic massive sulphide, porphyry, epithermal and SEDEX ore systems from IOAA systems (Blein and Corriveau, 2017; Corriveau et al., 2018; Blein et al., 2022).

## IOAA Systems - Depth-to-surface Transects

Transects across tilted volcanic stratigraphy and basement at Mag Hill, Mile Lake, Grouard Lake and Camsell River provide 3D information on depth-to-surface evolution of IOAA systems across the GBMZ (Bowdidge et al., 2014a, b; Somarin and Mumin, 2014; Bowdidge and Dunford, 2015; Mumin, 2015; Corriveau et al., 2016, 2022a, c; De Toni, 2016). Differential uplift, exhumation and tilting combined with drill core data also provide depth to surface information across the Lou system, including on the NICO deposit and the Southern Breccia albitite corridor (Goad et al., 2000a, b; Montreuil et al., 2015, 2016a, b; Corriveau et al., 2016, 2022b, c; Potter et al., 2019). Intrusive relationships constrain the age of the Lou system to 1873–1868 Ma (Gandhi et al., 2001; Montreuil et al., 2016b).

The tilted Mag Hill cross-section transects the southeastern part of the Port Radium-Echo Bay IOAA system from bottom to top, across altered sub-volcanic diorite intrusion and overlying andesite, to the near-surface phyllic and epithermal lithocap. Albitite forms at the roof and within the intrusion and evolves upward to HT Na-Ca-Fe facies and IOA mineralization (Mag Hill prospect), and to the hematite-bearing Fe Zone and adjacent K-feldspar halo. The transect ends with the mineralized phyllic alteration of the Echo Bay Gossan with a paleodepth of less than 200 m (Somarin and Mumin, 2014). An overlying conglomerate includes clasts of IOAA metasomatites.

At Grouard Lake in the northern GBMZ, the system formed across a tilted volcanic pile where andesite from an earlier caldera is overlain by local stromatolitic carbonate and by volcanic rocks of a second caldera (Hildebrand et al., 2014). Major fault zones bound the system laterally. The stratigraphically deeper albitite zones display a transition up-stratigraphy to albitite breccia, skarn and abundant HT Ca-Fe alteration with local HT K-Fe alteration (Fig. 4C in Corriveau et al., 2022a). The basal section of the system hosts the Zn-Pb-Ag Hillside prospect and local copper mineralization among albitized and skarn-altered carbonate rocks (Knox, 1998).

The Sue-Dianne deposit evolves from an albitized intrusion to the hematite-rich cap, beginning at a vertical depth of 300 metres and terminating at what is interpreted to be the paleosurface. It is part of the regional-scale Mazenod system (Fig. 1). Epithermal veins were superimposed on the high-temperature alteration facies, and extend at depth into the underlying intrusion. Entire sequences of alteration facies are also well exposed at Mile Lake and Hoy Bay in the Port Radium-Echo Bay district, at DeVries Lake, and across the Duke system.

## Morphology of Metasomatites and Metasomatic Fronts

The morphology (replacement, vein, breccia) of the alteration facies, and textures shared among their constituent minerals, enable documentation of paragenetic sets and space-time relationships between metasomatites, intrusive bodies and structural features (faults, breccia zones, unconformities, etc.). Throughout the GBMZ IOAA systems, alteration is dominated by replacement-type textures (Table 2; Figs. 2H–L, 7, 8). The alteration fronts are best interpreted as interfaces of intense, coupled dissolution-reprecipitation processes that act at outcrop to district scales — a metasomatic process well characterized at microscopic scale (see Harlov and Austrheim, 2012), including for IOA deposits (Harlov et al., 2002, 2016).

Host-rock textures may be preserved (Figs. 2H–K, 8A–D) or destroyed (Figs. 7E, F, 8) by alteration. Intensity of alteration is classified as subtle (i.e. incipient), weak, moderate to strong, intense, and megascopically complete based on the degree to which host minerals and textures are preserved and new textures and minerals formed, the grain size to which metasomatites crystallize, and the spatial extent of the alteration. The intensity classification described in Table 3 is inspired from Gifkins et al. (2005).

Least- to most-altered sequences and interfaces between arrested fluid fronts and least-altered rocks were used to understand how alteration progressed (Figs. 2H, 7A, B, 8A), acknowledging that preservation is due to the inability of the fluid front to progress further. This field approach to understanding the evolution of IOAA systems is supported by striking similarities between observations of these interfaces, observations across *bona fide* zones of progressive alteration at the regional scale, and experimental results.

*Incipient to Strong Replacement*

At incipient stages, replacement occurs as haloes along fractures, veinlets (Figs. 2H, 9A, 11A) and localized alteration fronts, is selective and stratabound in bedded sedimentary or volcaniclastic rocks, and finger-like, patchy to variegated (i.e. interconnected irregular patches) in more isotropic hosts (e.g. volcanic rocks). Textures of the host are largely preserved (Figs. 2B, H–J, 8C, D), and hydrothermal minerals are typically very fine- to fine-grained (Fig. 2J–L). Alteration is characterized by multiple mineral phases and chemical components (low variance assemblage according to Gibbs' phase rule) and residual, refractory or stable host minerals such as biotite (commonly aphanitic) in metasedimentary units or plagioclase phenocrysts in volcanic and volcaniclastic rocks (Figs. 2A–E, L, 8B–D). Components of the fluids in strong disequilibrium with the host rocks induce neocrystallization, whereas some host minerals are pseudomorphed by metasomatic minerals.

At low to moderate intensity of alteration (e.g. albitization), the composition of the host can be significantly modified (Montreuil et al., 2015, 2016b) but many chemical components remain in the rock (e.g. Oliver et al., 2004; Rubenach, 2012). Alteration is interpreted to have formed under fluid-rock ratios between the pseudo-front and Khorzinskii-style front, which

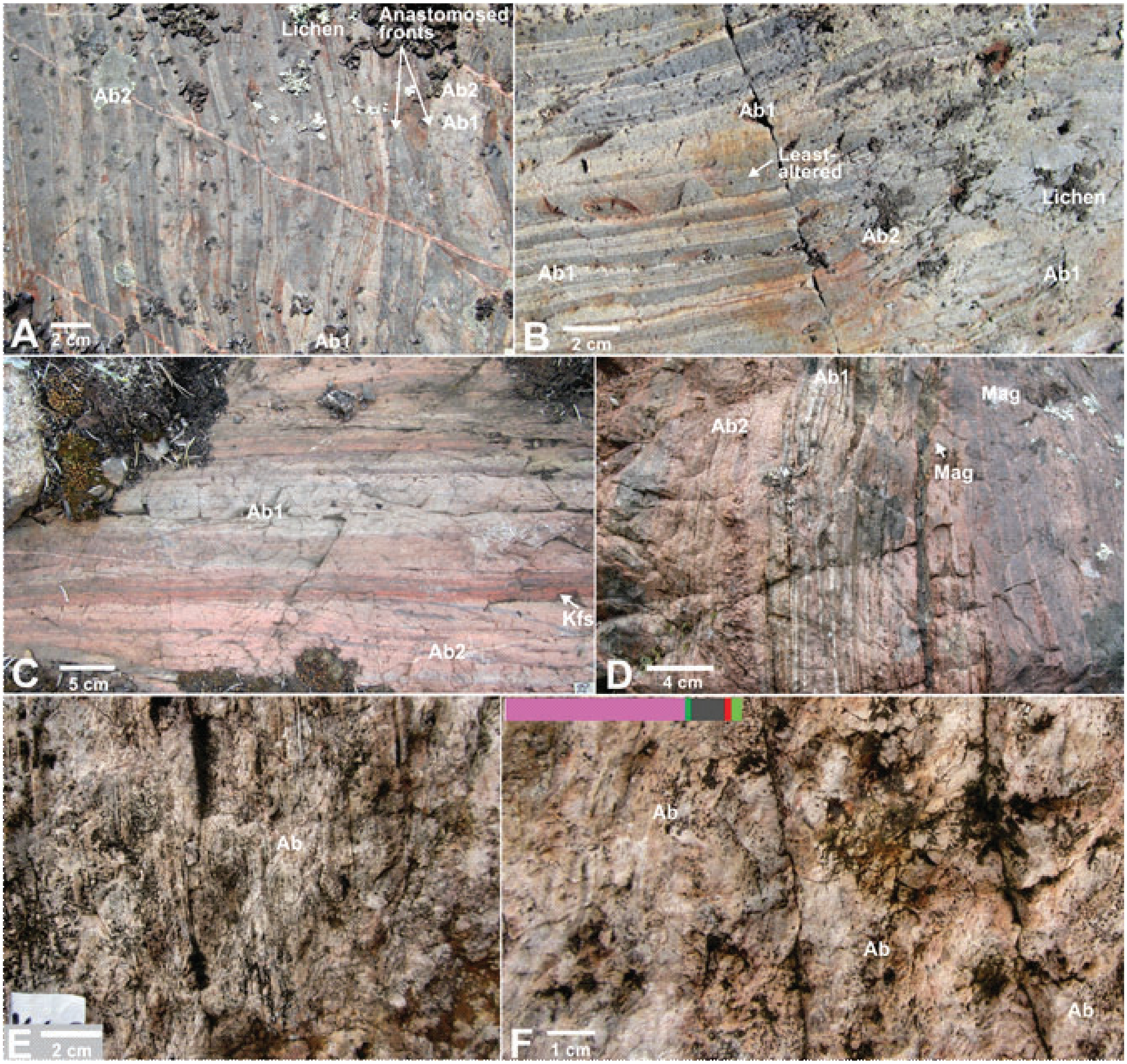


**Figure 7.** Albitization of metasiltstone south of the Au-Co-Bi-Cu NICO deposit. **A, B.** Selective stratabound albitization (Ab1: first generation of white albite) increasing in intensity to pervasive albitization (right), Southern Breccia albitite corridor (A–B: 11PUA-0517). A second generation of pink (earthy hematite-pigmented) albitization (Ab2) occurs as veins in A and as patches in B. **C.** Intense, selective albitization ranging from early white albite (Ab1) to pink albite (Ab2) (11PUA-0528). **D.** Local stratabound albitization (Ab1, Ab2) overprinted by pervasive, layer-preserving K-feldspar alteration and replaced by penetrative, texture-destructive magnetite alteration and magnetite veins and stockworks, Hump prospect (09-CQA-0039). Irregular veins and dyke of monzonite cut these alteration types, are locally emplaced parallel to layering, and are themselves locally replaced by propylitic alteration. **E, F.** Pervasive and intense, texture-destructive albitization through coalescence of alteration fronts along layering and fracture haloes, Southern Breccia (E, F: 10CQA-1665). NRCan photos 2020-475 to 2020-480.

Oliver et al. (2004) define as the interval between non-infiltrated, rock-buffered or least-altered host rocks and the infiltrated rocks across which alteration progresses.

In bedded or laminated hosts, weak to strong alteration is stratabound and varies in intensity across outcrops (Figs. 2H–J, 7A, 9A). The density of altered layers gradually increases (Figs. 2I, 7B, D, 9A–D) and contiguous layers may be selectively altered to distinct assemblages without megascopic evidence for crosscutting relationships among distinct alteration facies (Fig. 9A–C). This can lead, at strong intensity, to development of distinct layers of albitite, massive magnetite and massive hornblendite such as in metasedimentary rocks of the

**Table 2.** Terms used to describe alteration, modified from Gifkins et al. (2005; microscopic textural terms also used megascopically).

| | |
|---|---|
| Style | **Haloes**: alteration of host rocks along the margins of fractures (original fracture remains visible) or veins, within fractures of breccia fragments, along alteration fronts replacing host rocks, along breccia and clasts; and along stratigraphic and intrusive contacts and faults. Not to be confused with selvages as noted below. |
| | **Selective**<br>*Stratabound*: alteration that is layer- or lamination-bound in sedimentary or volcaniclastic rocks.<br>*Discordant planar-edged*: where replacement takes the aspect of a vein, a stockwork or a dyke in terms of extent and width, with sharp, largely parallel contacts. Haloes occur or are absent. These fronts may stem from damage zones or fractures that are concealed by alteration but which had sharp contacts or that were formed within a homogeneous, low-porosity host.<br>*Pseudomorph*: where alteration replaces and preserves the shape of pre-existing breccia fragments, sedimentary and volcaniclastic clasts, phenocrysts and other specific components of host rocks. Includes overgrowths on phenocrysts, clasts, and breccia fragments.<br>*Selective-pervasive* when the object is completely replaced; variegated when the object is selectively replaced; selective and restricted when the core or margin of the object is selectively replaced, or an overgrowth forms along the margins of the replaced object/grains, or along a main crystallographic axis of a mineral. |
| | **Pervasive**<br>*Variegated fronts*: irregular distribution and shapes (e.g. interconnected patches).<br>Finger-like, anastomosing (interconnected network), layered or laminated (irregular, parallel, concentric, oblique) or banded, amoeboid, zoned (concentric, irregular), patches, lenses, pods, spots, pseudorod (formed of microscopic neoblasts).<br>*Massive*: non-foliated alteration that forms across layering, groundmass, fragments, clasts, phenocrysts, and any other host textures. |
| | **Dissemination**: spotty, patchy, variegated distribution. |
| Distribution, contacts, aspects | **Extent**: regional, at deposit scale or local. |
| | **Relationship to host stratigraphy**: stratabound, semi-conformable, discordant, anastomosing, pipe. |
| | **Field relationships to original protolith**: earlier and subsequent alteration facies, intrusive rocks, stratigraphy, faults, extensional jogs, unconformities, etc.; cuts, overprints, grades to, is associated with, transitional to, cut by, overprinted by, evolves to, in, adjacent to, in sharp contact with, enclaved within, includes, etc. |
| | **Spatial association**<br>*Haloes*: externally along fractures, veins, breccia matrix; also forms at the scale of the system, an alteration facies and a breccia. Breccia matrix haloes form selvages along clasts.<br>*Selvages*: distinct marginal vein infills as well as internal replacement of fragment margins or phenocryst margins.<br>*Cores*: alteration of cores of breccia fragments, clasts or phenocrysts. |
| | **Occurrence**: rare, sporadic, irregular, common, regular, ubiquitous. |
| | **Contacts**: sharp, gradual, interdigitated. |
| | **Aspect**: homogeneous, heterogeneous, disseminated, patchy, spotty, mottled, vein or dyke-like, zoned, interconnected, anastomosing, corona, etc. |
| Textures | **Host**: preserved, relic, pseudomorphed, destroyed, recrystallized. |
| | **Intensity**: subtle/weak, incipient/mild, moderate, strong, intense, megascopically complete. |
| | **Grain size**: aphanitic, fine-, medium- to coarse-grained, pseudopegmatitic (coarse megascopically but consisting of mosaic of neoblasts internally), pegmatitic. |
| | Equidimensional, equigranular, heterogranular, hypidiomorphic granular, euhedral, subhedral, anhedral grains, zoned crystals, mineral layering, inward facing crystals. |

Grouard system (Fig. 9A–C) and in the Lou system distal from the intense to complete alteration envelope of the NICO deposit. With increasing intensity, stratabound alteration propagates to other layers along networks of bedding-destructive merging and anastomosing replacement fronts (Figs. 3C, D, 7A, 9C–E) that will ultimately coalesce into intense pervasive alteration and destruction of most primary bedding structures (Figs. 3E, 9E, F).

Pervasive, weak to strong alteration of sedimentary rocks may preserve primary sedimentary textures, e.g. the albitization and coupled selective albitization and actinolite (± clinopyroxene) stratabound alteration of cross-beds in the Port Radium-Echo Bay district (Fig. 9G, H). This can help trace stratigraphic units within systems and identify the nature of primary rock types.

An atypical outcrop of nodular albitite occurs within a corridor of massive albitite that replaced the otherwise weakly- to strongly-altered metasiltstone at DeVries Lake. Though original bedding has been destroyed across the albitite corridor, a series of outcrops containing albitite nodules display bedding structures defined by a chicken wire-textured amphibole matrix (Fig. 10A, B). These layers are intercalated with more homogeneous amphibole or albitite layers ranging from 2 to 10 cm in thickness and interpreted as replacing primary bedforms. For the most part, the diameter of the albitite nodules range from ~1 to 10 cm but locally the nodules form stringers of irregular and smaller nodules. Smaller nodules also form at the intersection of larger nodules. This bedded nodular unit contains inter-nodular carbonate, and resembles chicken-wire, nodular, and enterolithic anhydrite and intercalated carbonate formed during diagenesis of gypsum beds deposited in a sabkha environment (Fig. 9 in Zamannejad et al., 2013). This is the first robust evidence of evaporite units in the GBMZ. At DeVries, alteration of a particularly reactive saline unit may have been sufficient for pervasive albitization without extreme changes in host-rock textures.

Preservation of fine laminations during weak to strong magnetite alteration of albitized and recrystallized carbonate units has locally enhanced stromatolite structures, allowing the discovery of this (very localized) unit at the uppermost level of the first caldera in the Camsell River district (Fig. 10C–G). This provides potential evidence for a saline caldera lake; however, here and elsewhere within the same carbonate unit, early albitization and associated recrystallization of carbonates without subsequent magnetite alteration has significantly destroyed the primary laminations of stromatolites, leading to the development of homogeneous, white, recrystallized and albitized carbonates (Fig. 10E–G).

Selective stratabound alteration may also be accompanied by haloes, such as albite alteration or albitite haloes that accompany selective stratabound amphibole alteration of metasiltstone (Figs. 9A–E, 11A, B), and albitite layers displaying amphibole haloes (Fig. 9B). In most cases, as alteration intensifies, haloes coalesce (Figs. 9C, 11 B, C). Where haloes or altered layers are replaced by subsequent alteration, features such as bedding, fine laminations and alteration haloes fade progressively and a more homogeneous metasomatite forms (Figs. 9E, F, 11C). Fracture haloes and replaced damage zones may have sharp margins and resemble dykes, such as the albitite zone cutting bedding in Figure 11B.

In volcanic units and porphyritic intrusions, the main expression of weak to moderate alteration consists of altered phenocryst margins forming irregular selvages, selective replacement of phenocryst cores, or complete replacement of phenocrysts (Figs. 2A–E, 8B, D, 12A–F). Albite most commonly replaces phenocrysts (Fig. 12A–E), but in some cases replacement by K-feldspar, amphibole (De Toni, 2016) or

**Table 3.** Criteria for field assessment of alteration intensity.

| Alteration intensity | Preservation of host rock minerals | Distribution of alteration minerals | Preservation of host textures | New textures |
|---|---|---|---|---|
| **Subtle** | - <5% of fine to coarse-grained minerals altered.<br>- Incipient reaction rims around crystals, fragments and fractures in medium to coarse-grained minerals. | - Disseminated to penetrative replacement along the edges of crystals, fractures, laminae and beds.<br>- Disseminated replacement in groundmass.<br>- Volcanic glass is devitrified, cryptocrystalline and varies in colour on outcrop. | - Little modified and easily recognizable.<br>- Preservation of original textures and grain shape of the host. | - <5% new textures and minerals.<br>- Megascopically hard to distinguish but measurable (e.g. radiometric and magnetic susceptibility).<br>- Disseminated, irregular and heterogeneous.<br>- Microcrystalline. |
| **Weak** | - Feldspars partially replaced by other feldspars, amphiboles, micas, carbonates, epidote and/or iron oxides.<br>- Mafic minerals partially replaced by augite, hornblende, actinolite, iron oxides, sulphides, biotite, phlogopite, epidote or chlorite.<br>- Heterogeneous replacement of phenocrysts (e.g. rims, patches, spots). | - Sporadic penetrative replacement, irregular, selective or disseminated where new mineral phases replace or recrystallize minerals of the same group (e.g. plagioclase into albite) or sharing composition of key major elements (e.g. K-feldspar into biotite).<br>- Affects mainly the groundmass of porphyritic volcanic rocks.<br>- <1 cm alteration halo along veins and breccia selvages. | - Partial preservation of most primary textures. | - 5% to 25% new textures and/or minerals from alteration.<br>- Traces of dissolution or replacement at rim of crystals.<br>- Infiltration textures, inter-digitations and infilling.<br>- Weak replacement along cleavage) and corona or zonation development.<br>- Heterogeneous and irregular aspect. Variegated, spotted, disseminated and mottled.<br>- Microcrystalline to fine grained. |
| **Moderate to strong** | - Feldspars partially replaced or recrystallized with relics still visible. Igneous phenocrysts partially preserved and groundmass completely replaced. Alternatively, some phenocrysts are preferentially altered (e.g. plagioclase into amphibole or albite overgrowth).<br>- Mafic minerals mostly replaced with initial crystal morphology preserved (e.g. clinopyroxene replaced by amphibole or amphibole by epidote and/or chlorite). | - Stratabound to anastomosing alteration front, interdigitated, veins or shear zones. Forms lenses, patches and disseminated crystals commonly coarser-grained than the matrix.<br>- 1–10 cm alteration haloes along veins and breccia selvages. Haloes start coalescing where they intersect each other.<br>- Degree of replacement dependant of grain size, heterogeneity or composition of host rocks. Affects phenocrysts and groundmass of porphyritic volcanic rocks and distinct beds or laminae of sedimentary, volcaniclastic, metasedimentary and metavolcaniclastic. | - Delicate textures and textures of microcrystalline or fine grained host rocks substantially modified. Textures of coarser minerals are mainly preserved but locally destroyed or recrystallized.<br>- Primary textures control the aspect of new textures and influence grain size.<br>- Incipient pseudobrecciation of altered host through coalescence of anastomosing alteration fronts.<br>-Incipient corrosion of breccia clasts through replacement by matrix assemblages leading to pseudoclasts. | - 25% to 75% new textures and/or minerals from alteration.<br>- Heterogeneous and irregular aspects. Variegated, mottled and patchy. Occasionally, local development of pseudopegmatitic texture.<br>- Microcrystalline to coarse grained.<br>- Pseudobreccia and pseudoclasts. |
| **Intense** | - Host-rock minerals almost completely replaced and/or recrystallized.<br>- Phenocrysts shapes and mineral ghosts may occur. | - Pervasive replacement, including across host rock types and structures, homogeneous to heterogeneous with gradual or anastomosing/net-textured contacts between alteration zones.<br>- Extensive interconnecting and merging alteration haloes along veins and breccia selvages.<br>- Intensity of replacement largely independent of the compositional or textural heterogeneity of the host. | - Most primary textures destroyed.<br>- Scarce relics and mineral ghosts in zones less altered.<br>- Destruction of small scale or specific structures (e.g. laminae and fractures).<br>- Pseudobrecciation intensifies.<br>- Pronounced corrosion of breccia clasts through replacement by matrix assemblages leading to abundant pseudoclasts. | - 75% to 98% new textures and/or minerals from alteration.<br>- Gradual alteration front, generally equigranular.<br>- Predominant uniform aspect with scarce, less-altered relics.<br>- Extensive development of pseudopegmatitic texture and grain coarsening<br>- Microcrystalline to coarse grained.<br>- Pseudobreccia and pseudoclasts. |
| **Megascopically complete** | - Mineral assemblage completely distinct from host rocks in the field.<br>- Protolith hardly recognizable or cannot be recognized. | - Generalized replacement as uniform impregnation (e.g. paragenesis and modal mineralogy). Commonly massive on metre or greater scales, independent of the nature of host rock structures.<br>- Complete replacement with heterogeneities as function of the host rocks (e.g. stratabound alteration). | - Destruction of original textures or complete recrystallization.<br>- Local ghosts or pseudomorphs of phenocrysts. Some structures are preserved (e.g. discon-tinuities, bedding, breccias, etc.).<br>- Breccia clasts are largely replaced by matrix leading to highly mature breccia. | - >98% new textures and/or minerals from alteration.<br>- Massive, homogeneous or heterogeneous and regular aspects.<br>- Granular/mosaic texture with equigranular crystals.<br>- Microcrystalline to coarse grained.<br>- Matrix-dominant breccia and pseudobreccia. |

quartz (Fig. 12I) occurs. Alteration of groundmass remains weak or cryptic at first and gradually intensifies (Figs. 2B, C, 8B, D, 12).

Selective alteration of volcanic groundmass or volcaniclastic matrix may weakly preserve original phenocrysts, leaving a ghost texture in which both matrix and phenocrysts are altered (e.g. albitized; Fig. 12A, B). Alternatively, volcanic textures may be enhanced during iron oxide (especially magnetite) alteration (Fig. 12A–D, F). More intense alteration of a volcanic groundmass may produce patchy to pervasive alteration; in some cases, variably intense alteration can be traced as haloes to fracture or vein systems, likely infiltrating

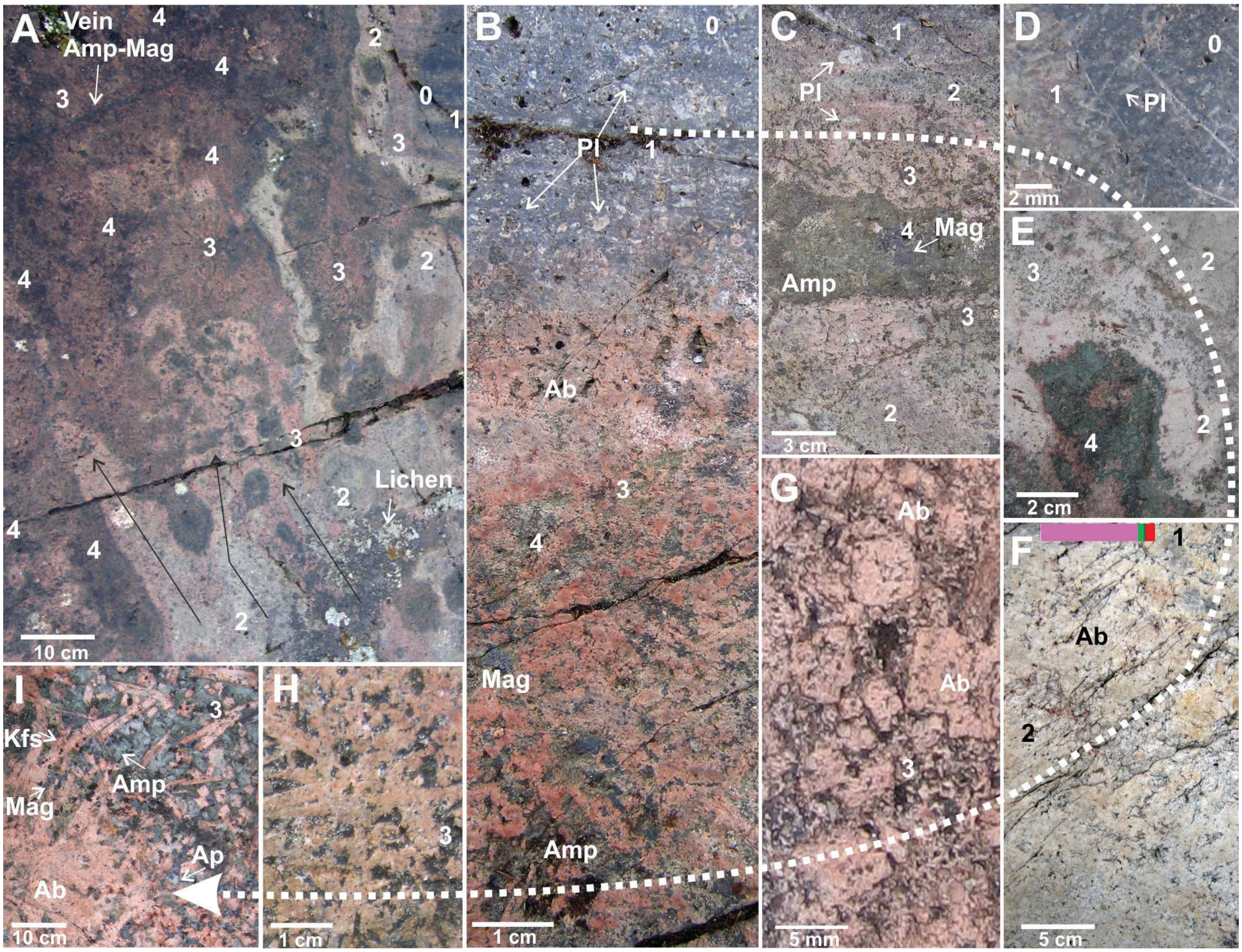


**Figure 8.** Albitization of plagioclase-phyric andesite to albitite and pegmatitic Na-Ca-Fe alteration facies (prograde path illustrated by the clockwise arrow; the 1 to 4 metasomatic sequence is described in the main text), Mag Hill. **A–E.** Incipient to intense albitization of the volcanic matrix and pseudomorphic replacement of plagioclase (Pl) phenocrysts by albite (A–D: CQA-05-095; E: CQA-05-105). In B, both amphibole and magnetite crystallize with albite in the pegmatitic HT Na-Ca-Fe alteration. In C, albitite evolves to amphibole-dominant HT Ca-Fe alteration. **F.** Massive albitite, similar to stage 2 albitization in A, forms an extensive corridor (> 100m thick) at the margin and above a 1.87 Ga diorite intrusion (CQA-05-208). **G–I.** Close-up of metasomatic textural reorganization of andesite to form pseudopegmatitic crystals of albite (consisting of microscopic seriate albite grains) and interstitial crystallization of amphibole ± magnetite-apatite assemblages (fine-grained at first in B and G, then medium- to coarse-grained in H and I) (G: CQA-05-131; H: CQA-05-095; I: CQA-05-104). Intensification of alteration decreases the amount of inclusions within the albite 'rods' from G through I, and increases the grain size of interstitial minerals. A mild K-feldspar overprint occurs along the margins of the albite crystals. NRCan photos 2020-481 to 2020-489.

associated damage zones with the coalescence of alteration haloes forming more homogeneous metasomatites (Figs. 8E, F, 11D–F, 12G; clasts in Fig. 12H). Similar processes are found within sedimentary units (Fig. 11 A–C).

In fragmental units (e.g. volcaniclastic rocks and albitite breccias), selective alteration of clasts may vary from weak to intense, patchy to pervasive, and core-selective or margin-selective (Figs. 12 G–H, 13). Core alteration is commonly pervasive (Fig. 13A, C–F) and weak to intense. Margin-selective alteration forms intra-clast selvages (Fig. 13A, B, F) and/or replacement haloes along clasts (Fig. 13E, F). Coeval alteration of matrix may be patchy to pervasive, weak to intense (Fig. 12G, H), or occur as stringers (Fig. 13B–E). Albite and magnetite alteration are the most common clast or matrix alteration (Figs. 12G–I, 13D–F), but amphibole (Fig. 13 A, C), K-feldspar (Fig. 13D), tourmaline, epidote and clinopyroxene also occur. Petrography indicates that replacement of fragment margins can occur after alteration of the cores (Fig. 13A, B, F). In Figure 13A–C, amphibole alteration of fragment cores and margins and groundmass is coeval with veining (Fig. 2F in Corriveau et al., 2022b). The endo- and exocontact alteration is intense and irregular, and characterized by small-scale apophyses in both the fragments and volcaniclastic matrix (Fig. 13A, B). Entire clasts may be replaced by amphibole only (Fig. 13A–C), or fragment cores may be altered to magnetite and coeval K-feldspar selvages and haloes (Fig. 13E, F). Selective alteration of fragments by magnetite may be incipient and pervasive (Fig. 13F) or locally very intense; it may affect only some fragments and not others, and also alter the matrix (Fig. 13D, E). Although locally the selective alteration is intense, the overall alteration is considered to be moderate, as only part of the host is altered.

Potassic and HT to LT K-Fe alteration of felsic intrusive rocks may be overlooked especially where it replaces igneous K-feldspar and plagioclase, rhyolite groundmass, and HT Ca-Fe metasomatites. Hydrothermal K-feldspar acquires a diagnostic reddish to intense brick-red hue in fresh leucocratic rocks, and a yellow colour in cobaltinitrite-stained rock slabs.

*Intense to Megascopically Complete Replacement*

As alteration intensifies, the number of mineral phases controlled by the major elements (the components of Gibbs' phase rule) decreases. Irregular patches and curvilinear or vein-shape replacement fronts prevail in homogeneous and massive hosts, whereas intense selective alteration (i.e. strata-bound, clast-selective or matrix-selective) prevails in bedded/laminated sedimentary rocks and in coarse fragmental rocks (Figs. 8A, 9B, C, 10D, 12G–I, 13C–F). Host textures are locally preserved (Figs. 7C, D, 8C, 9A–E, 11) but in general are destroyed where alteration is intense, e.g. where coalescence of alteration fronts and replacement of original textures occur (Figs. 3B, D, E, 7D–F, 8B, C, E–I, 9F). Some host rock minerals may be preserved, such as quartz grains where albitite replaced quartz-rich sedimentary rocks (De Toni, 2016). The weathered surface of such albitite (~ >80 modal % albite, <20% residual quartz) is particularly hard and distinct from that of the more common albitite (i.e. >90 modal % albite), which can be scratched with a hammer.

The transition from andesite to Na, Na-Ca-Fe and HT Ca-Fe alteration facies is locally preserved at outcrop scale along intense alteration fronts (Fig. 8A–C) that lead to well-defined pseudopegmatite (Fig. 8B, G–I). The black arrows in Figure 8A highlight the inferred pathways of saline fluid that albitized porphyritic andesite and dissolved, transported and re-precipitated selected elements (e.g. Ca, Fe and Mg from plagioclase phenocrysts and volcanic groundmass) to form faint to well-developed, pink, HT Na-Ca-Fe metasomatites (Fig. 8A–C, E, G–I). This record of progressive dissolution and reprecipitation at outcrop scale is interpreted to portray what likely happened at more regional scales. The different stages of alteration preserved in Figure 8 include:

1) Least-altered andesite with albitized plagioclase phenocrysts (Fig. 8A, B, D).
2) Incipient penetrative replacement of volcanic groundmass by very fine- to fine-grained equigranular albite along fronts, and replacement of plagioclase phenocrysts from margins to cores (Fig. 8A–D). Some fronts form haloes along fractures and lead to linear fronts similar to veins. Linear replacement zones may also have diffuse, millimetre- to metre-wide contacts with the host andesite, replacing host rocks pervasively or along anastomosing networks (Fig. 8A). These replacement zones are interpreted as representing channels for fluids along pre-existing damage zones associated with microcrack networks that increase porosity and permeability, a process described in detail in Oliver and Bons (2001), Montreuil et al. (2012) and Poulet et al. (2012). A close-up of an albitization interface with least-altered andesite (Fig. 8D) highlights a spike-like texture similar to the reaction interface in Figure 13B of Harlov et al. (2005). Figure 11D–F illustrates that the volcanic host that is cut by amphibole veins and their albitite haloes was first irregularly albitized. The early pervasive and largely uniform albitization is of moderate intensity, hence darker than the more albitized zones. Intensification of albitization leads to anastomosing stringers to very patchy and variegated replacement fronts of white albitite (Fig. 11D).
3) Finger-like to patchy zones of white albitite form (Fig. 8A, C, E) and grade outward to pink or white albitite. Isolated patches or more pervasive zones of interlocking rods of albite (very incipient stage 3) occur locally. Coalescence of albitization fronts may lead to irregular or concentric zoning across outcrops. Early zoning assemblages are ultimately destroyed where albitization is most intense, forming homogeneous and massive albitite at the scale of metres to hundreds of metres (Fig. 8F).
4) Pink, hematite-pigmented albitite with 1–10 cm long, rod-shaped albite crystals and interstitial amphibole ± magnetite and apatite form a pseudopegmatitic Na-Ca-Fe facies (Fig. 8A–C, E, G–I). These metasomatites form at the Na to HT Ca-Fe facies transition through metasomatic textural reorganization of andesite (Fig. 8B, H, I). The rod shape is typical of scapolite but no scapolite has been observed within this type of metasomatite in the GBMZ.
5) Crystallization of localized patches of medium-grained amphibole with minor magnetite and apatite (HT Ca-Fe alteration; Fig. 8A–C, E).

The incipient Na-Ca-Fe alteration forms patches, a few to tens of centimetres in length, of interlocking poikilitic albite crystals within albitite (Fig. 8G) and locally within least-altered rocks (Fig. 2A in Corriveau et al., 2010a). Rather than being well-formed crystals as expected from megascopic observation, the rods consist of microscopic seriate albite grains and were initially poikiloblastic, laden with inclusions, and commonly have diffuse margins. These ill-defined crystals are set within a groundmass consisting of very fine-grained interstitial magnetite and amphibole (Fig. 8G). Albite rosettes occur locally and at all scales (see matrix of albite crystals among the rod-shaped pseudo-coarse-grained albite crystals, Fig. 8G). Some of the crystals crystallized perpendicular to stage 2 albitite (not shown).

As metre-sized, isolated, variegated, anastomosing, or pervasive pegmatitic replacement zones form, the interlocking cm-long albite rods display sharper contacts and become homogeneous, i.e. devoid of megascopic inclusions, whereas interstitial amphibole and magnetite become coarser-grained and more euhedral (Fig. 8). The increased sharpness of the pseudopegmatitic, albite-rod texture and coupled increase in grain size of interstitial amphibole ± magnetite ± apatite (from very fine- to coarse-grained; Fig. 8) is also associated with an increase in the distribution and pervasiveness of this facies. Ultimately, metre- to kilometre-size alteration zones may form Mumin, 2015, displaying highly patchy or veined pegmatitic textures, some with very sharp contacts with host rock.

Figure 7 illustrates the incremental alteration of sedimentary rocks from selective stratabound replacement that preserves bedding but commonly destroys fine laminae (Fig. 7A–F), to texture-destructive replacement in massive and homogeneous alteration zones. Such styles of replacement typify Na, Na-Ca-Fe HT Ca-Fe and K (K-feldspar) alteration. The intensity of alteration varies from mild to intense but tends to be uniform along the same bed. The effect of this stratabound alteration is to reproduce bedding as a series of intercalated, weakly (Figs. 2I, 7A, B) to intensely altered layers containing distinct (Fig. 7C, D) or similar (e.g. albitite with distinct shades of white and pink; Fig. 7C, D) alteration assemblages. This contrasts with the most intense alteration, where the rocks commonly become homogeneous and massive. In Figures 2I and 7A, albitization is moderate: the least-altered grey layers (i.e. bedding) alternate with mildly albitized, slightly bleached layers and white, intensely albitized layers. Boundaries between layers vary from linear and sharp (Fig. 2I, J), to linear and diffuse, to very irregular networks of alteration that cross layers (Figs. 2H, 7A, B). In some cases, layers have sharp but cuspate boundaries (Fig. 7B). Similar textures occur where albitized layers are subsequently altered to amphibole or magnetite along or across layers (Figs. 9A–E, 11A–C), with or without albitized haloes.

Along the edges of intense, selective-type alteration zones, roll-front textures are locally observed (Fig. 22A in Corriveau et al., 2022c), and are interpreted as a megascopic record of coupled dissolution-reprecipitation processes taking place along specific layers (see Harlov et al., 2002); such observations were made across the metasedimentary sequences of the entire Treasure Lake Group. Distinct units of albitite, amphibolite-like metasomatic rock and ironstone formed through intense selective alteration (Figs. 7, 8C–F, 9F; Corriveau et al., 2022b, c). Selective replacement was also observed between different types of fragments, and between fragments and matrix in breccia, as described previously (Fig. 13D–F).

The transitions from incipient to intense alteration, and overprinting relationships across a variety of plutonic, volcanic and metasedimentary host rocks (Fig. 2), show that the original composition, porosity, permeability, and reactivity of the host rocks control selective alteration. As alteration intensity increases, the nature of the host rock has less influence on what is altered and how alteration proceeds. The most intense pervasive replacement was observed proximal to intrusions (i.e. heat sources), along fault zones, and along carbonate beds and their adjacent sedimentary rock units. These relationships record the effect of greater fluid volumes, higher temperatures, or more reactive fluids or host rocks (see Harlov and Austrheim, 2012). An empirical spatial relationship was also observed between the magnitude and intensity of the HT and LT K-Fe and K-skarn facies and the metal endowment of mineralization (Montreuil et al., 2016b).

*Veins and Haloes*

Veins and their haloes provide key indicators of the evolution of GBMZ IOAA systems and are described systematically (Table 4; Figs. 11A–C, 14–17). The lateral homogeneity of most veins, including across variably altered wall rocks, is typical of veins that crystallized from externally derived fluids (Oliver and Bons, 2001).

Many ‘veins’ display little or no evidence of filling a sharply defined open space. Instead, they are linear replacement zones whose development as haloes along fractures or their infiltration along linear damage zones may or may not be obvious (Figs. 11A, B, F, 15A, E–G, 16; Fig. 2 in Corriveau et al., 2010a). Veins, haloes and vein-shaped replacement zones may branch, follow offsets, form stockworks or parallel sets, and be linear, curved or very irregular (Figs. 11A, D, 16, 17). Their width may be fairly constant or highly variable along strike. At the extreme, parallel sets of such ‘veins’ may resemble stratabound alteration (Figs. 11A–C and 16 vs Fig. 9A–D).

The term ‘veins’ is favoured to describe linear replacement zones, as their morphologies, relationships to faults and fractures, and crosscutting relationships to host rocks mimic those of veins and that similar assemblages fill open space fractures in host rocks that are difficult to alter, such as plutonic rocks (Fig. 14F). The replacement veins can be interpreted as fault- or fracture-related replacements of hosts that are easily altered (i.e. reactive, porous and permeable), or as replacements of damage zones along poorly-defined faults and fractures. Thus, the definition of vein can be broadened to: *epigenetic tabular or sheet-like mineral filling or replacement zone that forms along a fault, fracture or damage zone in a host rock, with or without haloes replacing the host rock* (cf. vein definition in Neuendorf et al., 2005). Open-space filling or replacement may also produce discordant or stratabound series of lenses to strata; these were mapped as stringers rather than veins. Wispy replacement zones were mapped as schlieren.

Vein infills are largely fine- to medium-grained and equigranular (Figs. 11, 14–17). Sulphide, quartz, and carbonate veins, and locally HT Na-Ca-Fe and HT Ca-Fe veins, may be coarse-grained (Figs. 14A, D, E, 15B, D). Most veins are devoid of megascopic quartz except those formed in the later stages of IOAA systems (Fig. 14A, B, G vs. Figs. 11D–F, 14D–F, 15). The vein mineralogy is generally uniform along and across strike (Figs. 11D–F, 15C–H), although some jasper-quartz veins are zoned (Fig. 14B) and some veins show lateral variations in the proportions of amphibole and albite (Fig. 15A, B).

Internal vein selvages are rare (e.g. within amphibole-filled jogs with albite rims; Fig. 15A) except in late-stage quartz and hematite veins (Fig. 14B). Replacement haloes along veins are common, such as albite haloes along magnetite-amphibole veins (Figs. 11D–F, 15) or K-feldspar haloes along tourmaline veins (Fig. 14G). The haloes are fine-grained and typically 1–5 cm wide. Exceptions to this are thin (1–3 mm) veinlets with a very

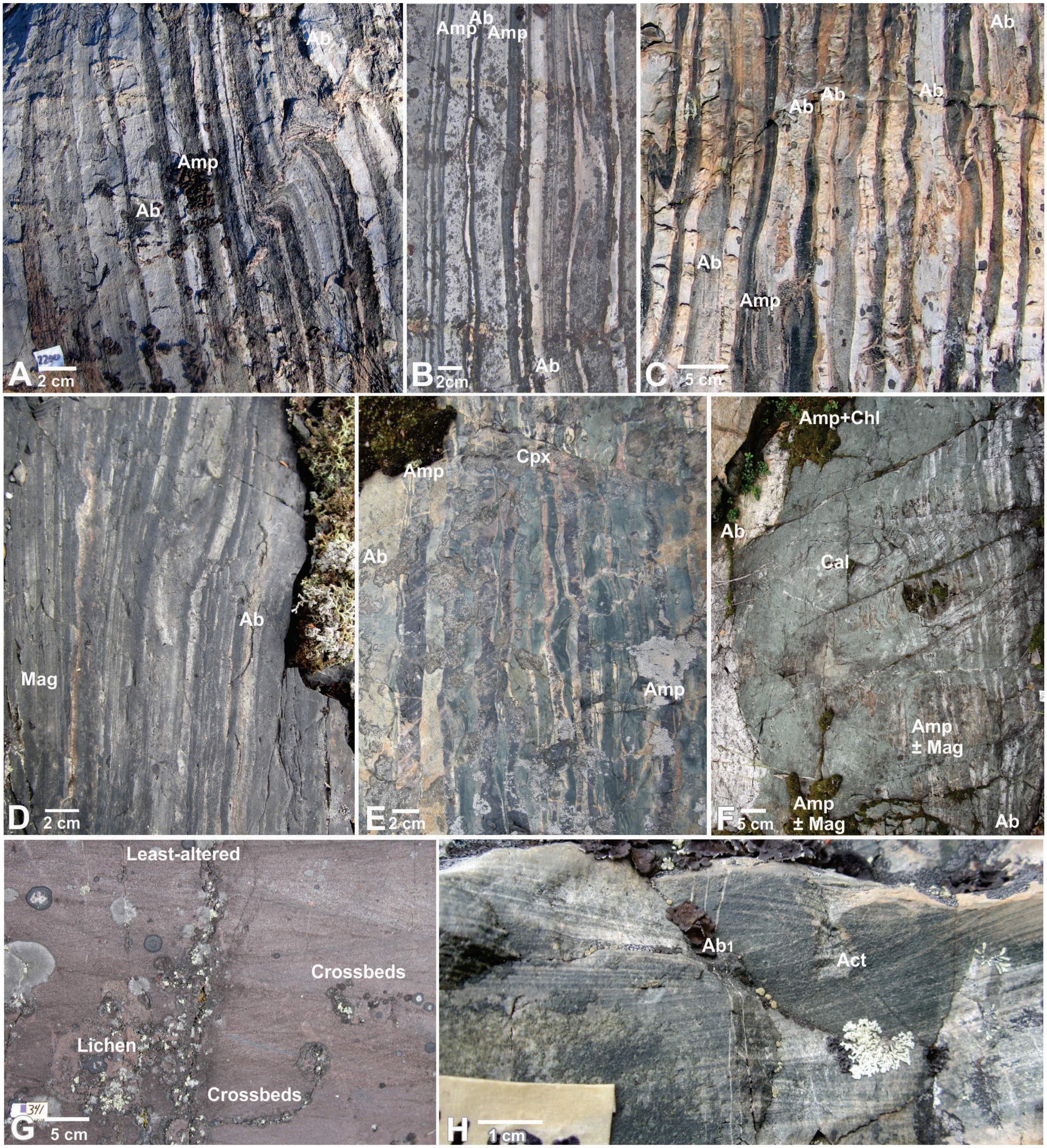


**FIGURE 9.** Stratabound albitization and Na-Ca-Fe alteration in sedimentary rocks. **A–C.** Weak to moderate (A–B) to locally strong (B–C) bedding-selective alteration with amphibole, albite or amphibole-albite assemblages, DeVries Lake (A: CQA-05-239; B–C: CQA-05-251). Stratabound alteration is uniform along layers and no crosscutting relationships are observed across layers. The albitite layers display haloes of amphibole, and the amphibole-dominant layers show haloes of albitite. These relationships are interpreted as evidence for the co-crystallization of albite (Na) and amphibole (Ca-Fe) within a Na-Ca-Fe facies. **D.** Stratabound magnetite alteration of albitized metasiltstone with varied intensity along layers and abundant overprint across layering (11PUA-010). **E, F.** Progressive, selective amphibole replacement (dull to dark green) of earlier skarn (blue-green layers), Grouard Lake (E: 10CQA-1602; F: 10CQA-301). In E, the earlier stratabound skarn alteration progressively transitions to a pervasive bedform-destructive skarn replacement of host unit and is heterogeneously replaced by amphibole. **G.** Weak and texture-preserving sodic alteration front in crossbedded sandstone, Port Radium-Echo Bay district (CQA-06-341). **H.** Moderate and texture-preserving HT Na-Ca-Fe alteration of crossbedded sandstone, Grouard Lake (10CQA-1495). NRCan photos 2020-490 to 2020-497.

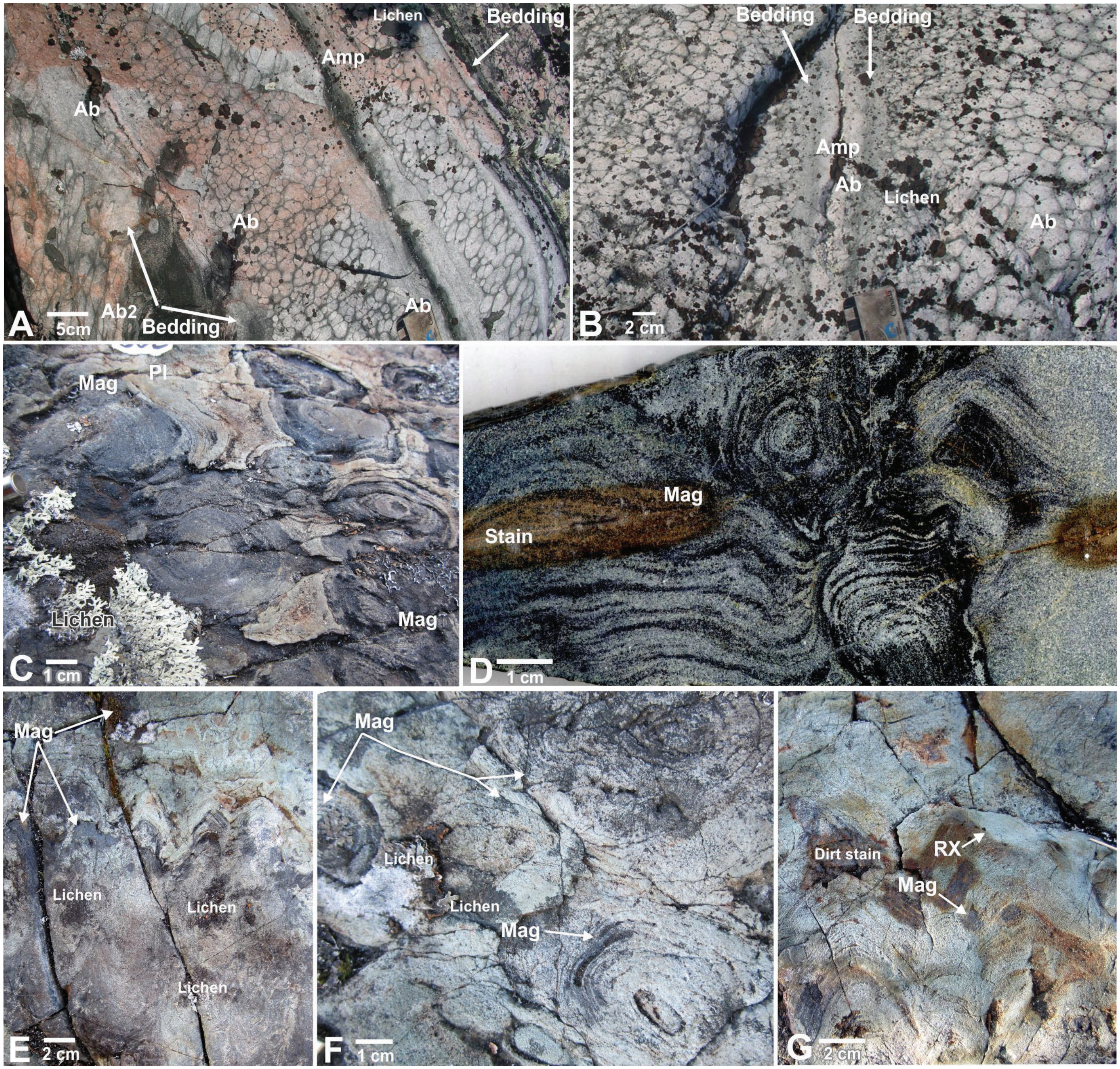


**FIGURE 10.** Field exposures of nodular albitite and metasomatized stromatolites. **A, B.** Layers of nodular albitite intercalated with albitite-dominant and amphibole-dominant layers and locally cut by amphibole veins with albite haloes. The layers of nodular albitite display a chicken-wire pattern made up of albitite nodules of variable size (in white) set within an amphibole matrix (in green). Internal laminations are locally recorded by amphibole. Textures are typical of evaporite beds with nodular anhydrite. At outcrop scale, some of the veins clearly cut former bedding, but in B the features also mimic zoned evaporite beds. Photo taken by V. Bennett; courtesy of the Northwest Territories Geological Survey. **C–G.** Selective magnetite replacement of stromatolite laminae enhances stromatolite structure subsequent to earlier albitization, weak skarn alteration and extensive recrystallization of carbonates (RX) that largely obscured the stromatolite structure, Grouard Lake (10-CQA-308; D: stained rock slab). C and F are plan view of stromatolite beds and D, E and F are sections. NRCan photos for C to G are 2020-498 to 2020-502.

fine-grained infill with very coarse-grained haloes of pseudopegmatitic albite-amphibole-magnetite alteration up to 25 cm wide.

Haloes typically form parallel to contacts (Figs. 11D–F, 15C), but some are very irregular and others coalesce into more pervasive alteration across the fracture network (Figs. 11, 14G, 15D–H). Lateral stratabound offshoots along haloes typically extend a few centimetres but can reach several metres locally. The most cryptic stratabound vein haloes consist of trains of centimetre-scale lenses of arsenopyrite spatially associated with veins cutting bedforms in the NICO deposit (Fig. 14E).

The mineral assemblages present and the intensity of replacement in vein haloes are fairly consistent along strike

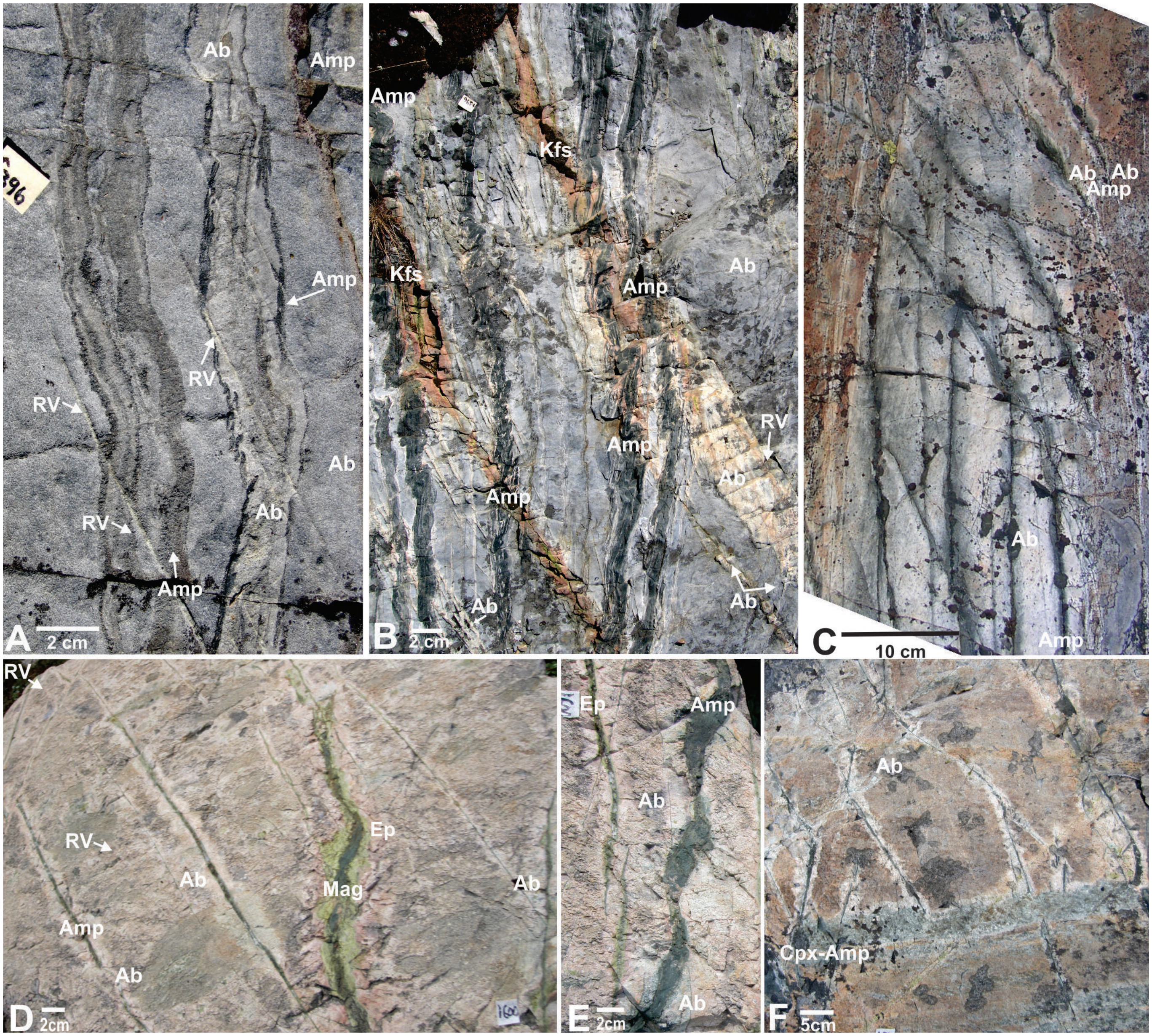


**Figure 11.** Variably albitized hosts replaced by Na-Ca-Fe alteration or cut by Na-Ca-Fe veins. **A, B.** Albitized metasiltstone interlayered with amphibole-altered layers. In B, the amphibole-altered layers display weak albitization haloes and are cut by fractures with sharp replacement haloes that resemble veins, DeVries Lake (A, B: CQA-05-396). RV: 'replacement vein'. Stratabound albitization from haloes varies in intensity along one such 'vein'. The more intense amphibole alteration follows both bedding and fractures and acts more as a 'vein' than as a simple stratabound alteration. In B, albitization along fractures locally reaches high intensity and forms albitite 'dykes/veins'. Contacts are sharp except for numerous spikes that extend as albitization fronts along transverse fracture networks. Along strike, the intensity of albitization within the 5 cm wide albitite zone decreases and the albitite fans out into a series of weakly albitized zones interpreted as highlighting the extent of damage zones along the fracture network. Later stage K-feldspar alteration is locally intense. **C.** Treasure Lake group metasiltstone intensely albitized (Na facies) and cut by two discordant sets of parallel veins of amphibole with albite haloes at DeVries Lake (HT Na-Ca-Fe facies) (from Jackson, 2008; photo courtesy of Northwest Territories Geological Survey). **D, E.** Sets of parallel amphibole veins with albite haloes cutting variably albitized andesite at Grouard Lake (10CQA-1600). Vein haloes have similar widths but the haloes locally branch into anastomosing replacements, transforming the albitized andesite into variegated albitite. The set of parallel veins is cut by veins with extension jog and more irregular albitite haloes discordant to the parallel veins. In D, epidote replaces both sets of veins preferentially to the albitite host. **F.** Sets of parallel amphibole veins with albite haloes form offshoots from a larger amphibole-clinopyroxene vein with albitite haloes, Grouard Lake (10CQA-1599). Albitite haloes are of highly irregular widths. NRCan photos for A and B are 2020-503 and 2020-504 and for D to F are 2020-505 to 2020-507.

(Figs. 11D–F, 15), although the vein infill may locally cut haloes (Fig. 15C). In most veins, aluminum-bearing minerals (e.g. albite or K-feldspar) preferentially crystallize in haloes, replacing silica- and aluminum-bearing minerals in the host

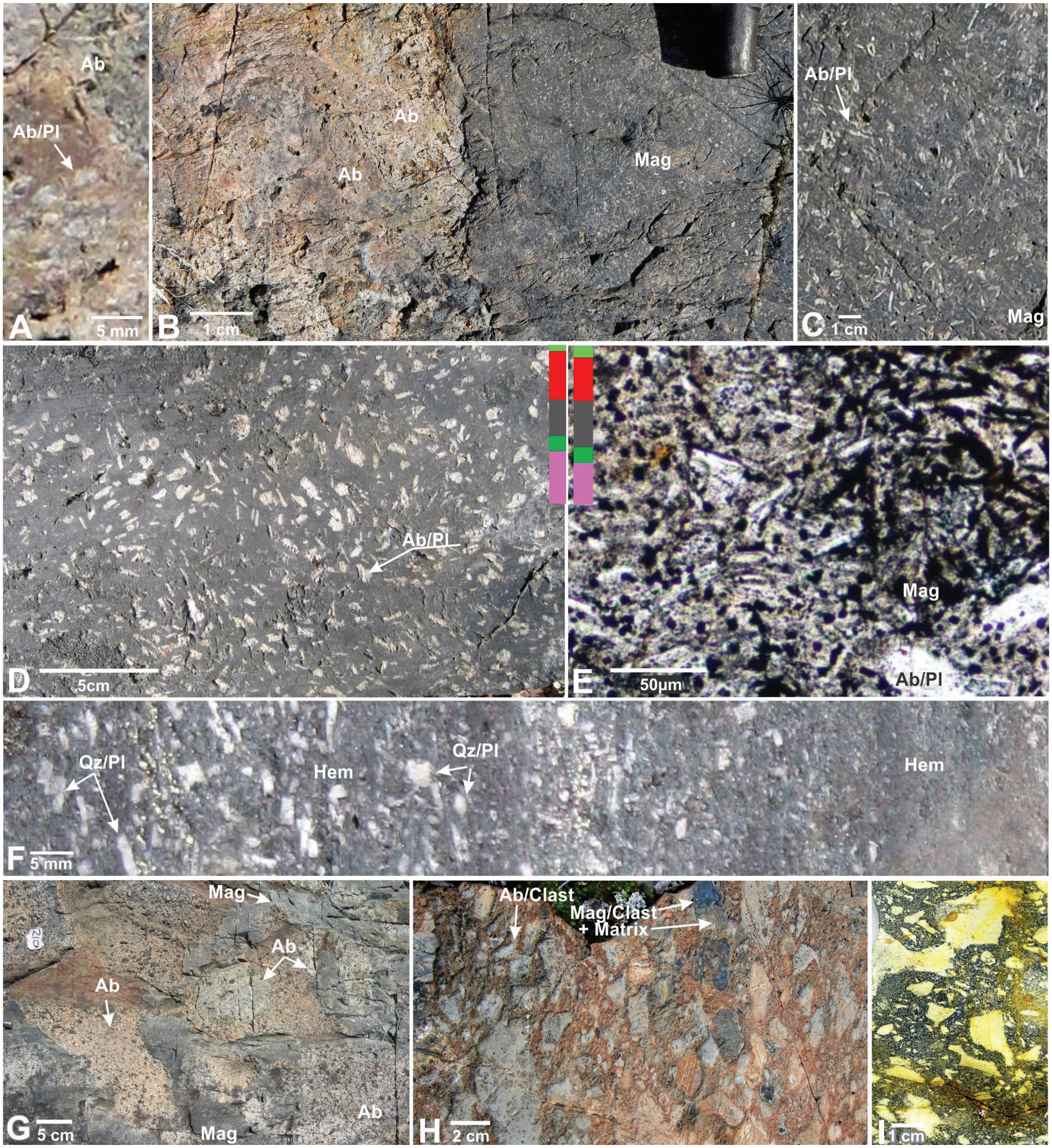


**FIGURE 12.** Field exposures of albite and magnetite alteration that preserved original textures of porphyritic andesite and volcaniclastic hosts. **A–C.** Albitized andesite showing selective replacement of the volcanic groundmass by magnetite that preserved the albitized plagioclase phenocrysts (Ab/Pl), southwest of Terra mine, Camsell River district (photos courtesy of DEMCo). **D, E.** Texture-enhancing alteration through selective replacement of porphyritic andesite groundmass by magnetite and preservation of albitized phenocrysts, Port-Radium-Echo Bay district (CQA-05-184; E: photomicrograph). **F.** Selective alteration of plagioclase phenocrysts by quartz (Qz/Pl) and of volcanic groundmass by hematite within porphyritic andesite in the Fe Zone, structurally above the Mag Hill IOA prospect, Port Radium-Echo Bay district (CQA-05-0273). **G–I.** Albitized volcaniclastic rocks shows selective replacement of matrix by magnetite in G and of clasts by magnetite in H and coeval weak replacement of matrix by magnetite in H, Grouard Lake (G: 10CQA-210; H–I: 10CQA-306; I: stained rock slabs). In the stained slab in I, magnetite preferentially replaced matrix but locally it incipiently replaced albitized clasts. A subsequent K-feldspar overprint is highlighted by the yellow cobaltinitrite stain. NRCan photos for D to I are 2020-508 to 2020-513.

rocks, whereas magnetite, amphibole (largely actinolite and hornblende) and apatite preferentially crystallize within the vein. This mineralogical association between veins and haloes is too consistent to be formed through coincidental emplacement of amphibole or magnetite veins within earlier feldspar veins hence this alternative was discarded. The contrast in alteration mineralogy of veins and haloes is interpreted to relate in part to the availability of constituent elements (e.g. aluminum for the crystallization of feldspar). As such, the diagnostic minerals and index cations of both vein infill and haloes define the alteration facies of the veins. Hence, in Figures 11D–F and 15, the veins belong to the HT Na-Ca-Fe facies in the same way as albite haloes along stratabound amphibole alteration or amphibole haloes along stratabound albite alteration (Figs. 9B–E, 11A). Some alteration zones are not regular enough to interpret them as coeval haloes to vein infill, or are distinctly cut by veins (Fig. 16). For example, amphibole-infilled veins with albitite haloes cut by, or evolving to, amphibole veins that sharply cut the albite haloes mark the transition from the HT Na-Ca-Fe facies to the HT Ca-Fe facies (e.g. Fab prospect; Fig. 15C). Across systems, the alteration facies defined by vein infills and associated haloes provide essential empirical information on facies evolution as metasomatism progresses.

In carbonate rocks, magnetite-dominant veins with sharp contacts may have magnetite haloes of uniform width; this contrasts with most other veins, in which the mineralogy of infills and haloes are distinct. The presence of magnetite haloes in carbonate rocks supports the interpretation that aluminum-bearing hosts are needed to precipitate feldspars from fluids through coupled dissolution-reprecipitation processes. Magnetite haloes also occur along a magnetite-infilled shear zone in metasiltstone near Peanut Lake south of the NICO deposit. The haloes formed very irregular replacement fronts that preferentially advanced along some layers. Alteration is weak to moderate. The very irregular fronts may indicate magnetite infiltration along damage zones linked to the shear zone.

Veins may be fault-bounded, lens-shaped, offset during emplacement, or display jogs typical of crack-normal extension (or shear displacement coupled with crack-normal extension) (Figs. 11D, E, 15A). They may display minor undulation (Fig. 14D) to pinch-and-swell structures, retaining continuity with narrow-to-wide necks and short-to-long swell separations (Figs. 14A, E, 15F, H, 16A), or with regular undulations and wide necks (Fig. 15G) (see Gardner et al., 2015). In boudinaged veins, boudins are typically rounded to locally angular, equant to elongate in shape, and may or may not display local continuity between fragments (Figs. 15G, 16). The geometry of boudins may be diverse (see Goscombe et al., 2004); Boudins commonly lie parallel to the veins; some are rotated (Fig. 15H). Some veins are both boudinaged and folded (Figs. 15H, 16B), whereas adjacent markers may show no such structures or be deformed more smoothly because of competency contrasts and strain partitioning (Figs. 11A, B, 15, 16A, B; Corriveau et al., 2016; Montreuil et al., 2016b). This brittle-ductile to ductile fabric is systematically associated with high-temperature veins formed in the HT Ca-Fe alteration facies. For example, amphibole veins cutting a zone of albitite in the DeVries IOAA system form a set of parallel veins that record coeval ductile deformation comprising internal folds, pinch-and-swell structures, and boudins (Figs. 15H, 16A, B). In addition, an amphibole-filled albitite breccia parallel to this vein set is characterized by ductile deformation that stretches the albitite fragments, forms an amphibole lineation, and locally develops shear zones (Fig. 18A–E). In Figure 15F and Figure 15G, stratabound magnetite alteration with diffuse contacts and amphibole alteration with sharp contacts and albite haloes are boudinaged. Albite crystallized as haloes along the boudin necks, whereas the crosscutting amphibole vein with haloes displays jogs parallel to the elongation (boudinage) of the stratabound alteration. These metasomatites record syn-metasomatic ductile and brittle-ductile deformation.

Veins may be sparse, form local to extensive stockworks (Figs. 14A, 15D, 17A), or anastomose into lens-shaped stockworks (Corriveau et al., 2022c). Stockworks in turn evolve to breccia or replacement zones (Fig. 17B). Higher-density vein networks are commonly indicative of an increase in the intensity of the associated alteration facies. Vein orientations may be random (Fig. 15A), parallel (Figs. 11B–D, F, 15C, D, G, H, 16), or at an angle typical of conjugate shears (Fig. 14E; Corriveau et al., 2022c). In extreme cases, sheeted veining may form a dense array of parallel veins that resemble stratabound-altered sedimentary rocks (Figs. 11A–C, 16; Corriveau et al., 2022c), even where veining is oblique to sedimentary layering (e.g. albite veins in Fig. 11A–C; amphibole vein in Fig. 16).

**Table 4.** Descriptive framework for veins modified from Gifkins et al. (2005)

| | |
|---|---|
| **Types** | Infill (including internal selvages) only, with haloes, (alteration facies of veins is defined by both the infill and halo assemblages). |
| **Contact** | Diffuse, sharp, gradational, with selvages or haloes. |
| **Mineral assemblages** | Groups of cogenetic minerals within vein, haloes, breccia matrix and fragments; representative alteration facies should be defined by combining infill and halo minerals including where breccia clasts have been thoroughly replaced as the matrix material precipitated. |
| **Texture** | Uniform (massive), composite, layered, laminated, incomplete, brecciated, cockade, colloform, comb, drusy, crustiform, fractured, pseudo-acicular, mesh, saccharoidal, zoned, mosaic, radial, fan-like, acicular, botryoidal, felted, nested, homogeneous, heterogeneous, fibrous, prismatic, spherulitic, vuggy. |
| **Fabric** | Massive (isotropic), foliated, foliated parallel to vein, foliated-oblique to vein contacts, foliated-perpendicular to vein contacts, with swell and neck textures and boudins of variable geometry. |
| **Network** | Single vein, stockwork, parallel veining, interconnected, anastomosing, crosscutting. |
| **Halo** | See replacement textures above, width, uniform front or irregular, selective stratabound incursion (splay). |
| **Variations** | Variations of mineral assemblages with respect to host rocks. |
| **Grain** | Size: aphanitic, fine-, medium- to coarse-grained, pseudopegmatitic (coarse megascopically but consisting of mosaic of neoblasts internally), pegmatitic. |
| | Texture: equant, equidimensional, equigranular, heterogranular, hypidiomorphic granular, euhedral, subhedral, anhedral grains, zoned crystals, mineral layering, inward facing crystals. |

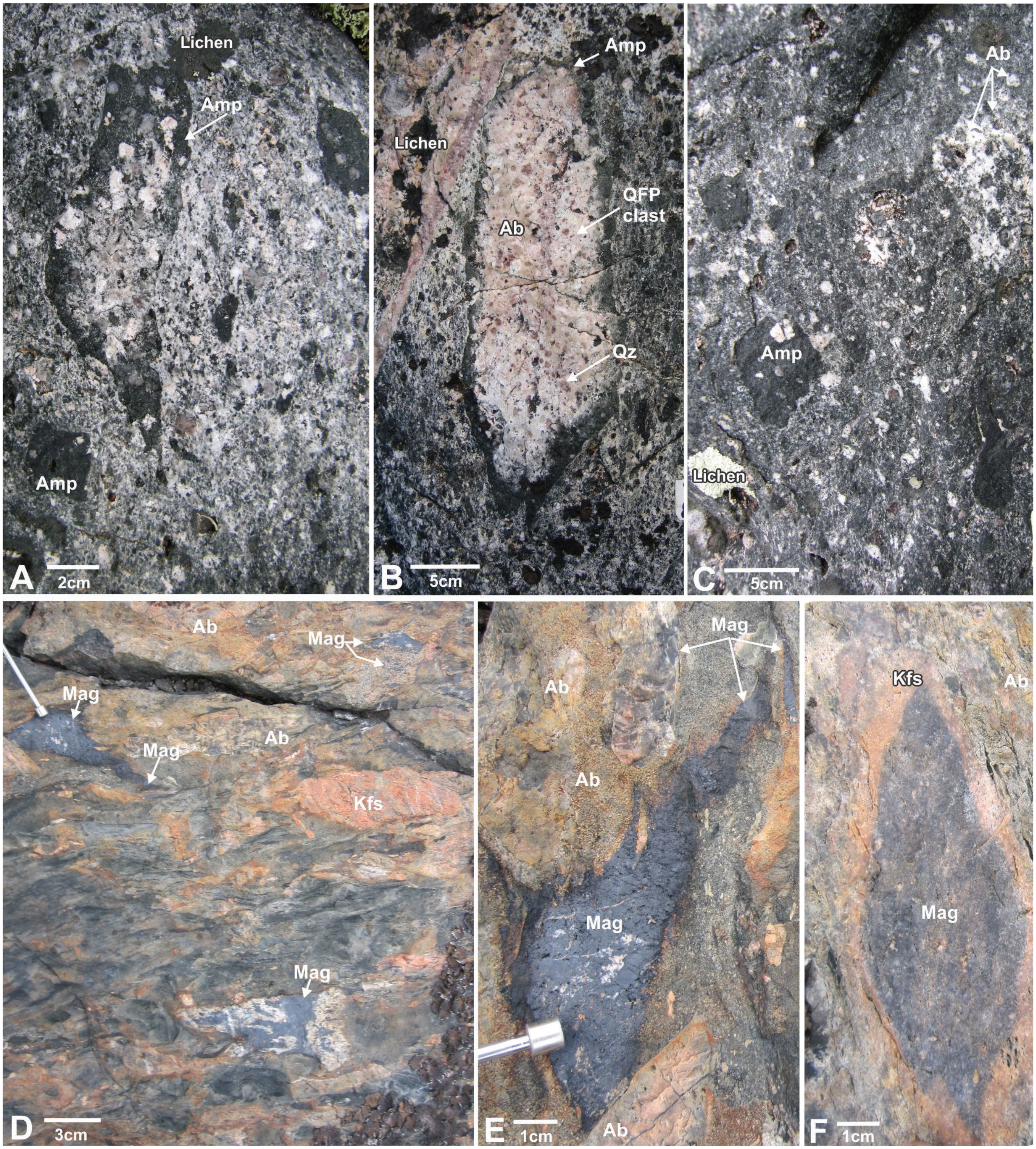


**FIGURE 13.** Selective alteration in fragmental rocks. **A–C.** Alteration of weakly to moderately albitized, fragmental volcaniclastic rocks with quartz-feldspar phyric felsic volcanic clasts (A–C: CQA-05-271). Some albitized fragments are selectively yet pervasively amphibole-altered, preserving some of the phenocrysts. Other fragments are fringed by intense amphibole alteration that defines thin (mm to cm), continuous to discontinuous haloes with sharp boundaries and apophyses cutting fragments and groundmass. Variegated amphibole alteration of the matrix varies in intensity, forming well-defined schlieren or diffuse patches (CQA-05-271). **D–F.** Selective magnetite alteration of an albitite breccia from the Southern Breccia corridor (D–F: 10CQA-1644). Magnetite locally alters the matrix, forming ill- to well-defined schlieren, and partially to completely replaces some albitite fragments. Some albitite fragments are partly to pervasively K-feldspar-altered (pink), whereas some magnetite-altered fragments have a K-feldspar halo — a regular occurrence interpreted as defining a single HT K-Fe facies. NRCan photos 2020-514 to 2020-519.

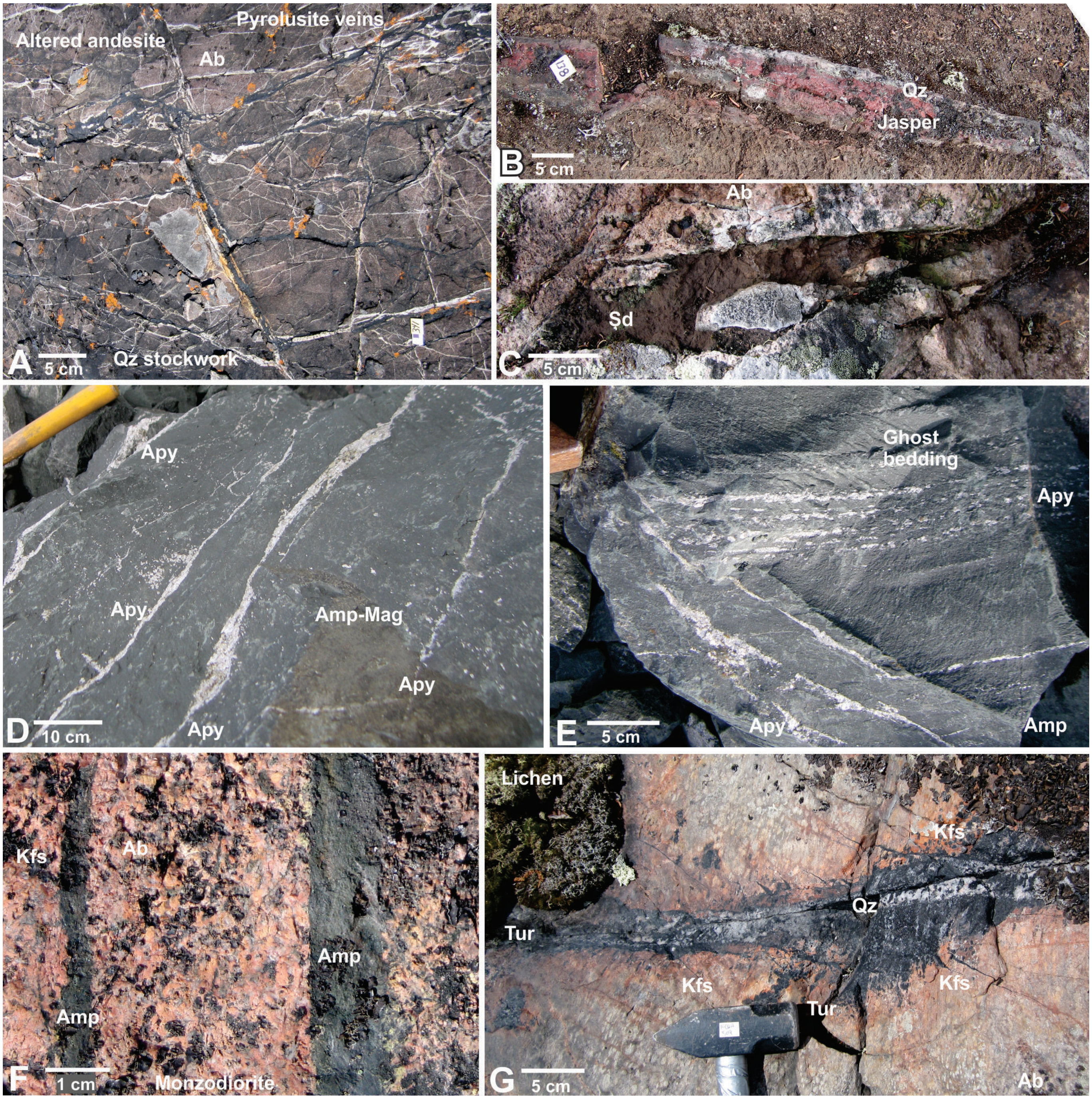


**Figure 14.** Vein morphologies. **A–C.** Late stage quartz and pyrolusite (A), jasper-quartz-hematite (B) and siderite (C) veins (A: CQA-06-341; B: CQA-05-138; C: CQA-05-129). The siderite vein displays apophyses, whereas the jasper vein is zoned with quartz selvages and a core of quartz ± specular hematite. **D, E.** Cobalt-rich arsenopyrite veins that cut metasiltstones pervasively amphibole-magnetite altered at the HT Ca-Fe facies within the ore zone of the Au-Co-Bi-Cu NICO deposit (D: CQA-08-551; E: CQA-08-550). In D, the veins display extensional jogs and apophyses and local pinch and swell structures. In E, the arsenopyrite veins follow two main orientations, one along the former bedding plane where the veins are either continuous with sharp contacts or are more irregular and formed of trains of stratabound arsenopyrite lenses of irregular length. **F.** Amphibole veins with both sharp and diffuse contacts in strongly albitized diorite of the Contact Lake pluton, Port Radium-Echo Bay district (CQA-06-381). **G.** Tourmaline-quartz vein with a K-feldspar halo, south of the Lou system at Burke Lake (10CQA-509). The tourmaline fills open spaces and replaces the albitized host. NRCan photos 2020-520 to 2020-526.

In the Southern Breccia corridor, albitite vein and fracture-halo networks are so well developed that they locally resemble stratabound albitite in sedimentary rocks.

*Breccia Zones*

Through alteration mapping of the GBMZ IOAA systems, magmatic-hydrothermal and structural breccia zones have been

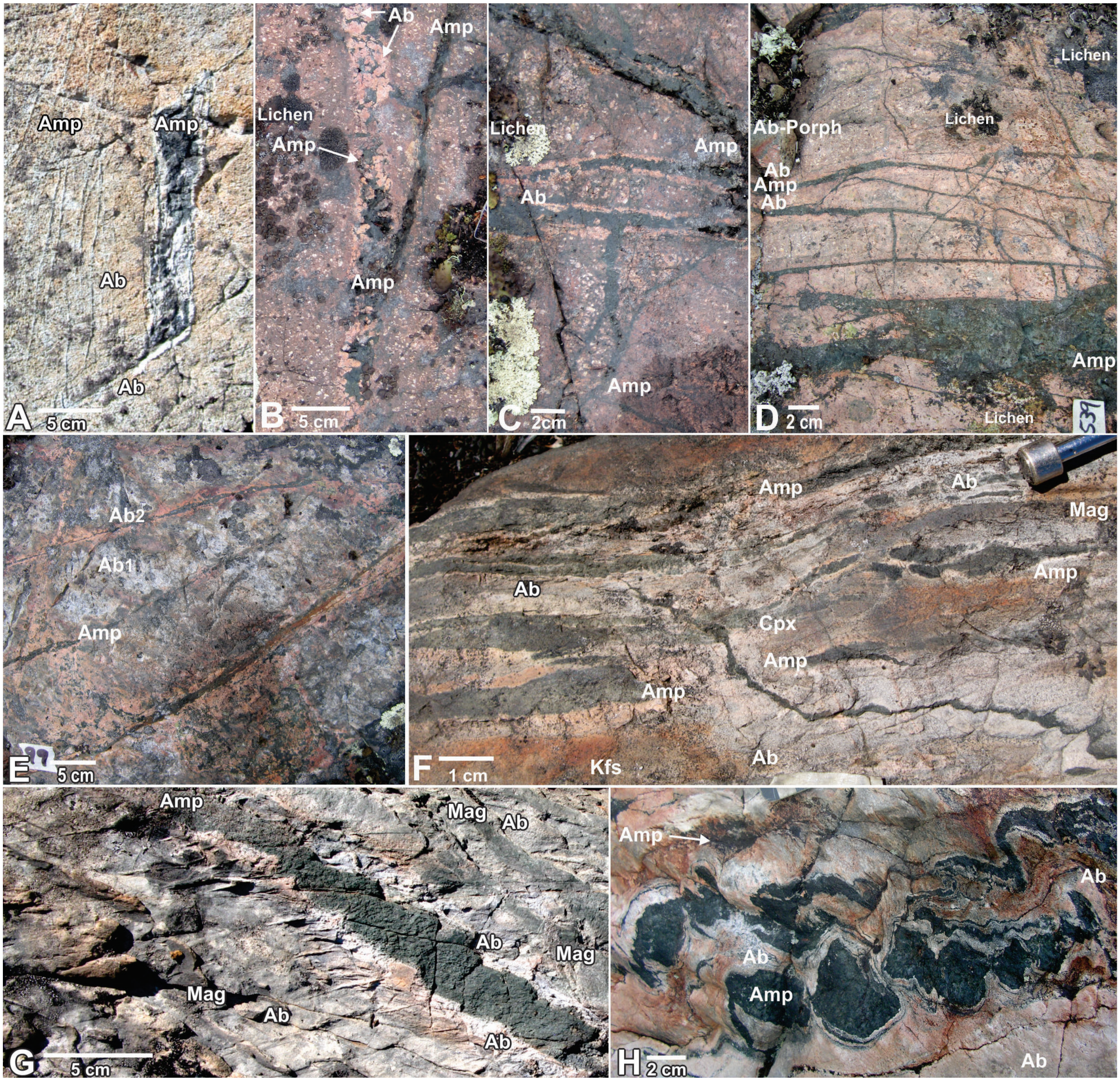


**Figure 15.** Vein haloes and selvages defining a Na-Ca-Fe facies. **A.** Albitite cut by parallel fractures with albite haloes, and subsequently cut by a vein with a tension gash comprising an amphibole core and an albite selvage, Grouard Lake (10CQA-1598). **B–D.** Amphibole veins with albite haloes or selvages cutting an albitized porphyritic intrusion (Ab-porph), Fab system (B, C: CQA-06-435; D: 11PUA539). In B, vein selvages consist of coarse-grained, subhedral albite, have irregular widths and may have crystallized within an open space. In C, the albitite crystallized along haloes and locally grew inwardly within the vein. These veins form a network that grades into irregular patches of coarse- to medium-grained amphibole, which replaces the porphyritic host and the albite haloes. These veins branch into an amphibole vein that cuts the albitite halo and marks a transition from HT Na-Ca-Fe facies to HT Ca-Fe facies. **E.** Thin amphibole veins with large albite haloes that coalesce into more pervasive albitization zones at vein intersections, Port Radium-Echo Bay district (CQA05-099). The veins cut earlier white albitization of the andesite host above the Contact Lake diorite. The second generation albitite is commonly pink. Grey patches are lichen. **F–H.** Amphibole veins with white albite haloes cutting moderately albitized metasiltstone units and earlier stratabound magnetite-amphibole alteration with albite haloes (F, G: Duke system, 09CQA-053; H: DeVries Lake near CQA-06-406 in Figure 16; photo by V. Bennett, courtesy of Northwest Territories Geological Survey, outcrop 05JYL2249). The discordant veins are linear in G, with pinch and swell structures and local infill of offsets (H). The haloes in F to H are also deformed. In H, the boudins show continuity at the neck or are segmented and the vein is folded. Where segmented, the albitite haloes are folded or form a continuous margin along the fragments. These boudinaged and folded veins occur within an albitite corridor where other amphibole veins (not shown) remain undeformed, highlighting severe strain partitioning within the alteration zones. NRCan photos for A to G are 2020-527 to 2020-533.

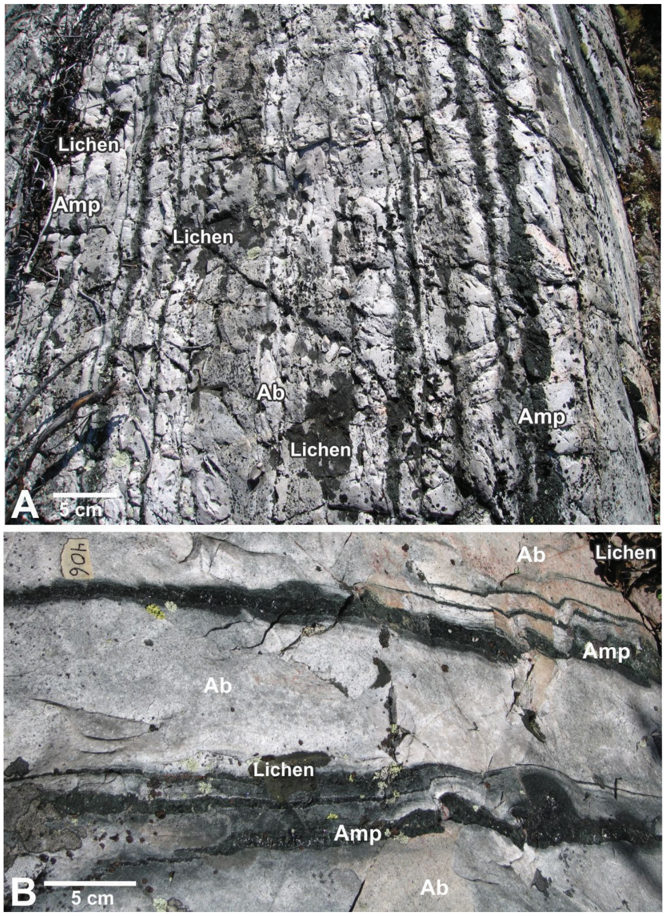


**Figure 16.** Network of parallel amphibole veins within intensely albitized metasiltstone, DeVries Lake. **A.** The veins have sharp to gradational contacts with the albitite, pinch and swell textures, segmented boudins, and minor folds (CQA-06-0407). Albitization of the metasiltstone varies in intensity, suggesting that it does not necessarily constitute haloes. **B.** Strong albitization observed along and discordant to amphibole veins (CQA-06-0406). The veins are interpreted as cutting bedding based on rare preservation of albitized bedding structures, and similar veins cutting the inferred sedimentary layering of the nodular albitite in Figure 10. NRCan photos 2020-534 and 2020-535.

classified in term of types, space-time relationships of alteration facies, and assemblages of associated mineralization (Table 5; Goad et al., 2000a, b; Mumin et al., 2007, 2010; Corriveau et al., 2010b, 2022b, c; Montreuil et al., 2015, 2016b; Mumin, 2015). The progressive development of breccia (Fig. 18), the nature of clast and infill assemblages, the clast-infill relationships (Fig. 19), and the selective/partial to pervasive replacement of breccia clasts and infill (Fig. 18) have been described following the terms in Table 5.

The most common hosts to IOAA-related breccia zones are least-altered to intensely albitized (meta)sedimentary, volcanic and porphyritic intrusive rocks, including volcaniclastic breccia, and albitite (Fig. 20). Breccia zones also regularly occur where HT K-Fe alteration is intense (Fig. 21E, F) and within K-felsite adjacent to HT K-Fe breccia. The following examples collectively record the variety of breccia types that form through evolution of IOAA systems (Corriveau et al., 2010b, 2016, 2022b, c). The Cole and Sue Dianne breccias form approximately circular bodies within and along the contact of porphyritic intrusions (Montreuil et al., 2016b). In contrast, the Mile Breccia hosting the Mile prospect extends regionally along stratigraphy in a generally arcuate shape as far as Hoy Bay and Port Radium (Mumin, 2015). The Southern Breccia corridor developed along an albitized fault zone, in part adjacent to a sub-volcanic granitic intrusion (Montreuil et al., 2015). All these breccia zones feature multiple stages of brecciation formed through a variety of processes.

At the Mile Breccia, stratabound structural-hydrothermal breccia forms adjacent to more intensely albitized beds, leading to parallel zones of breccia (Fig. 19C, D). Along this breccia complex and its extension at Hoy Bay, both formed at the contact of a sub-volcanic intrusion, albitite breccia is infilled by skarn and can evolve to K-skarn, HT K-Fe (magnetite-K-feldspar), K-felsite and LT K-Fe (hematite-K-feldspar) breccias (Corriveau et al., 2022c).

The Southern Breccia corridor initially experienced several generations of albitization, followed by several phases of brecciation related to tourmaline and HT K-Fe (K-feldspar-magnetite) alteration, the latter of which is associated with U, Cu and Mo mineralization (Montreuil et al., 2015; Hayward et al., 2016; Potter et al., 2019, 2022). Evidence for progressive *in situ* brecciation of albitite is common in well-bedded metasiltstone (Fig. 20). The elongate shape of the fragments (Figs. 19A, 20D, E) likely results from a combination of anisotropy in the bedded host and development of sets of bedding-parallel fractures. Where incipient, brecciation is most pronounced along an array of discontinuous shear zones oblique to bedding (Fig. 20A, C–E). Mosaic to chaotic breccias form along shears but commonly evolve to fluidized breccias in which fragments are aligned roughly parallel to relict bedding, pre-IOAA foliation, and the orientation of the breccia corridor (Figs. 19A, 20F). The breccia corridor is locally cut by pink albitite (Fig. 20A–D) or K-feldspar alteration, and rhyolite dykes that were progressively boudinaged during syn-tectonic magma emplacement. The overlying volcanic rocks are also locally weakly brecciated. During later stages of brecciation, tourmaline alteration replaces the albitite breccia (Fig. 20), and the breccia hosts pink fragments brecciated and aligned among the albitite fragments. The fabric is interpreted as resulting from flow, but such flow would have to be localized considering the common relics of bedding among the breccia. In Figure 20, the pale to darker grey replacement of fragments and bedding was originally mapped as least-altered metasiltstone. Discovery of incremental tourmalinization of the albitite breccia (Fig. 22A, B) suggests that all the pale grey components of the albitite clasts nearby reflect tourmalinization of albitized metasiltstone. Elsewhere, along the Southern Breccia, pervasive tourmaline alteration of albitized rocks leads to zones of tourmalinite several metres in width and in length with locally a weak foliation.

Crackle breccia transitions to mosaic breccia zones which are matrix-supported to locally clast-supported (Figs. 18, 19).

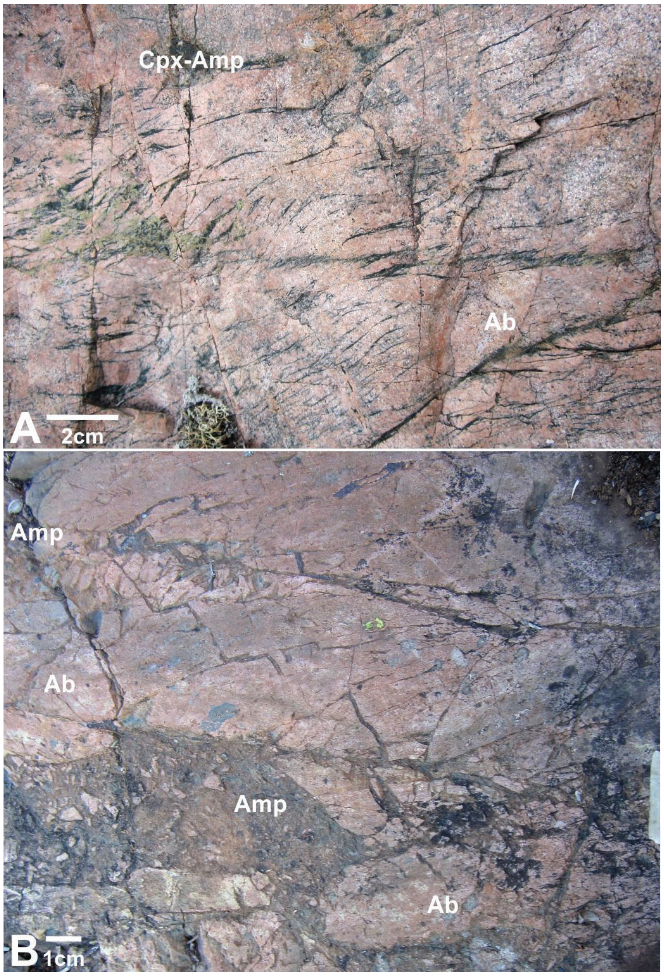


**Figure 17.** Vein networks at Grouard Lake. **A.** Curved clinopyroxene-amphibole veins in albitized volcanic rocks (10CQA-0201). **B.** Orthogonal set of amphibole veins in albitized host, forming crackle, mosaic and chaotic breccias (10CQA-1277). NRCan photos 2020-536 and 2020-537.

**Table 5.** Descriptive framework for breccia modified from Gifkins et al. (2005) and used during GBMZ alteration mapping. See also Jébrak (2022) and Corbett (2018).

| | |
|---|---|
| **Type** | Magmatic, volcanic, hydrothermal, structural, sedimentary, monomictic, polymictic, clast supported, matrix supported. |
| **Composition** | Infill, matrix (crushed, hydrothermal, magmatic, non to weakly hydrothermally altered), unaltered fragments, altered fragments. |
| **Geometric parameters** | Shape of clasts including rounding, aspect ratios (length to width) varying from equidimensional to elongate, complexity (i.e. boundary fractal dimension), dilatation ratios. |
| **Rounding** | Rounded, sub-rounded, sub-angular, angular, elongate, elongated/stretched, flattened. |
| **Matrix/infill** | < 20%, 20 – 40%, 40 – 60%, 60 – 80%, > 80%. |
| **Alteration** | Subtle/weak, incipient/mild, moderate, strong, intense, megascopically complete. |
| **Fabric** | Massive, fragment orientation (systematically oriented, preferential orientation, randomly oriented, jigsaw fit, imbricated like shingles and tiles), foliated matrix, foliated vein parallel, foliated-oblique to vein contacts, foliated-perpendicular to vein contacts, other. |
| **Network** | Single vein, stockwork, parallel veining, interconnected, anastomosing, crosscutting. |
| **Halo** | See replacement textures in Table 2. Selvages along clasts (i.e. halo along breccia matrix) can be breached, replaced and fragmented. |
| **Variations** | Lateral variation in composition relative to host rocks. |
| **Grain** | Size: aphanitic, fine-, medium- to coarse-grained, pseudopegmatitic (coarse megascopically but consisting of mosaic of neoblasts internally), pegmatitic. |
| | Texture: equant, equidimensional, equigranular, heterogranular, hypidiomorphic granular, euhedral, subhedral, anhedral grains, zoned crystals, mineral layering, inward facing crystals. |
| **Particle arrangement** | Chaotic, poorly sorted, moderately sorted, well sorted, imbricated (shingle), mosaic, crackle (jigsaw) breccia. |
| **Fragment contours** | Straight, embayment (corroded), lobate, cuspate, indented, diffuse (through replacement). |
| **Fragment cores** | Selectively replaced, corroded, poikiloblastic, homogeneous, heterogeneously altered. |
| **Particle size distribution** | Uniform, graded, gap-graded, uniform-graded. |
| **Process** | Comminution, collapse, hydraulic, explosion, fluidization, dissolution, replacement (corrosion, pseudobrecciation). Fluidization: see McCallum (1985). |
| **Maturity** | Immature, moderately mature, mature. |
| **'Pseudotextures'** | Pseudobreccia (due to dissolution and replacement), false polymictic textures due to a variety of selective alteration of fragments, false coherent texture due to pervasive selective alteration of fragments that regularly get interpreted as early with respect to brecciation (see also Gifkins et al., 2005, p. 63). |
| **Location** | Within breccia, at the margin of breccia. |
| **Field relationships** | With respect to stratigraphic units, alteration facies, fault zones, intrusive bodies. |

Shingle breccias with imbricate, tabular fragments are rare (Fig. 18F). Matrix-supported chaotic breccias (Fig. 19) and dissolution breccias occur locally (Corriveau et al., 2022c). Breccia infill consists commonly of HT Ca-Fe alteration assemblages of amphibole (actinolite, hornblende) ± apatite and magnetite, magnetite, skarn assemblages (clinopyroxene and garnet), and tourmaline, hematite, epidote or quartz (Figs. 18, 19). Infills are largely fine- to very fine-grained. One biotite-rich breccia was found at DeVries Lake and the biotite was randomly-oriented and medium-grained.

The morphology of clasts varies in terms of aspect ratios (length to width), roundness, complexity of contours and distribution. The mosaic breccias have angular clasts with fairly equant to rectangular shapes and were most common in albitite (Figs. 18, 19B, E). Chaotic and dissolution breccias have rounded fragments with sharp or irregular contours, including embayment in dissolution breccia. Breccia with significant dissolution/chemical corrosion is define as mature (Jébrak, 2010). An example of incipient dissolution of fragments can be found in Figure 19B. In Figure 21A, pseudobrecciation of albitite is induced by amphibole replacement. Evidence for dissolution breccia of albitite by amphibole preceded by hydraulic or tectonic fragmentation is locally found at Grouard Lake (Fig. 21B, C), within the dissolution breccia west and east of Mag Hill (Corriveau et al., 2022c), at Terra, and at Fab (Montreuil et al., 2016c). The in-situ progressive replacement leading to pseudoclasts provide conclusive evidence for dissolution breccia.

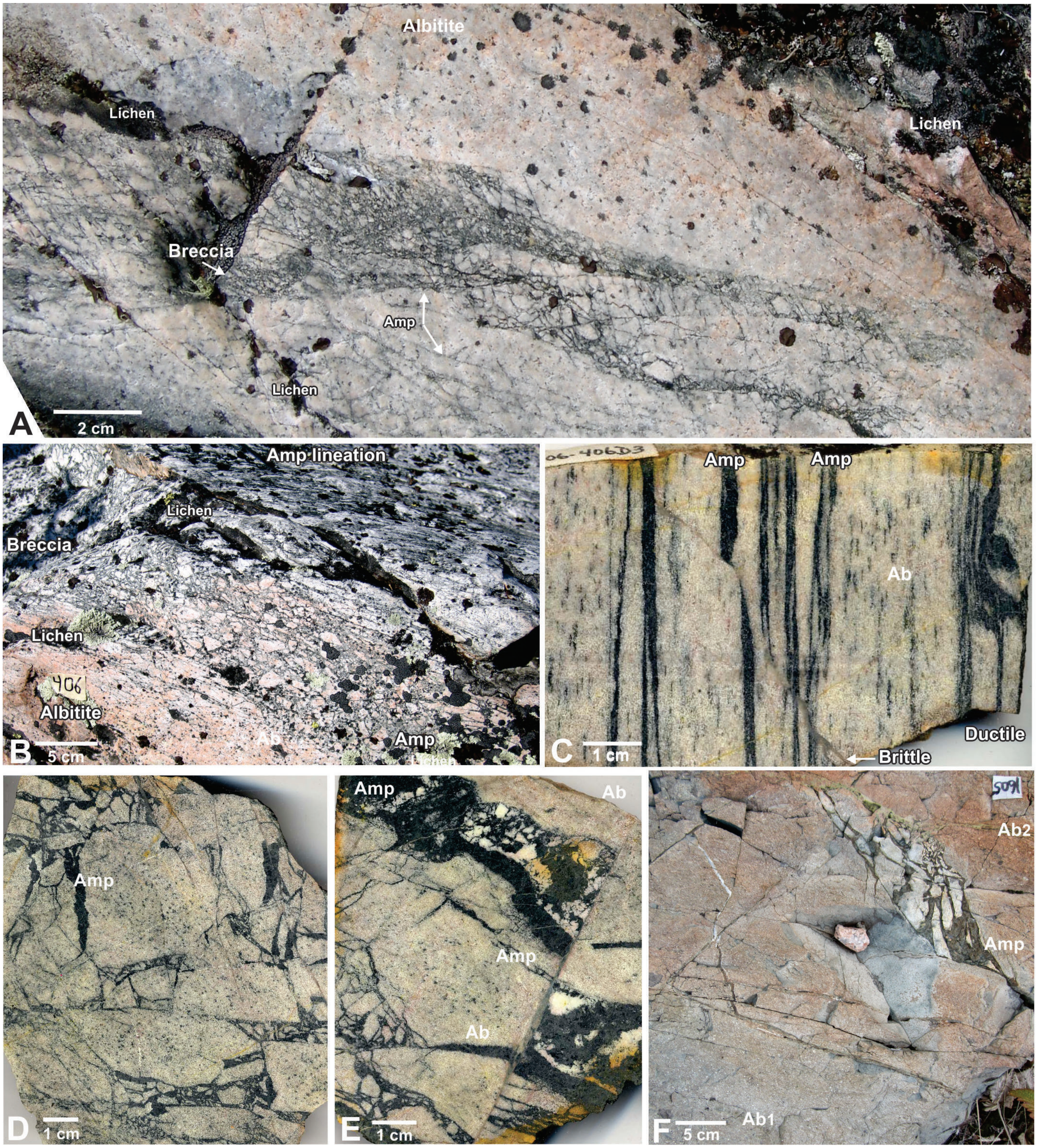


**FIGURE 18.** Brecciation of albitite in the HT Ca-Fe facies. **A–E.** Localized albitite breccia with amphibole breccia-filling proximal to a fault zone; DeVries Lake (A–E: CQA-06-406). The breccia zone preferentially extends along a well-developed set of parallel fractures with initial fragmentation along the fairly continuous fracture set and a conjugate set of discontinuous fractures; both sets are infilled by amphibole. Fragments are incipiently (D) to extensively (E) replaced by disseminated amphibole and along margins. In B and C, ductile deformation forms a strong lineation defined by the amphibole clots that replace fragments and by the amphibole infill. The elongation of the fragments perpendicular to this lineation is interpreted to be a result of parallel fracturing of the albitite and not of parallel fracturing along bedding planes of the sedimentary host or elongation due to deformation. **F.** Albitite shingle breccia with imbricated clasts and amphibole infill within a crackle breccia displaying orthogonal, parallel-sheeted and oblique fractures; Grouard Lake (10CQA-1605). Note that the orientation of the shingled clasts is parallel to the set of fractures oblique to the sheeted fractures. NRCan photos 2020-538 to 2020-543.

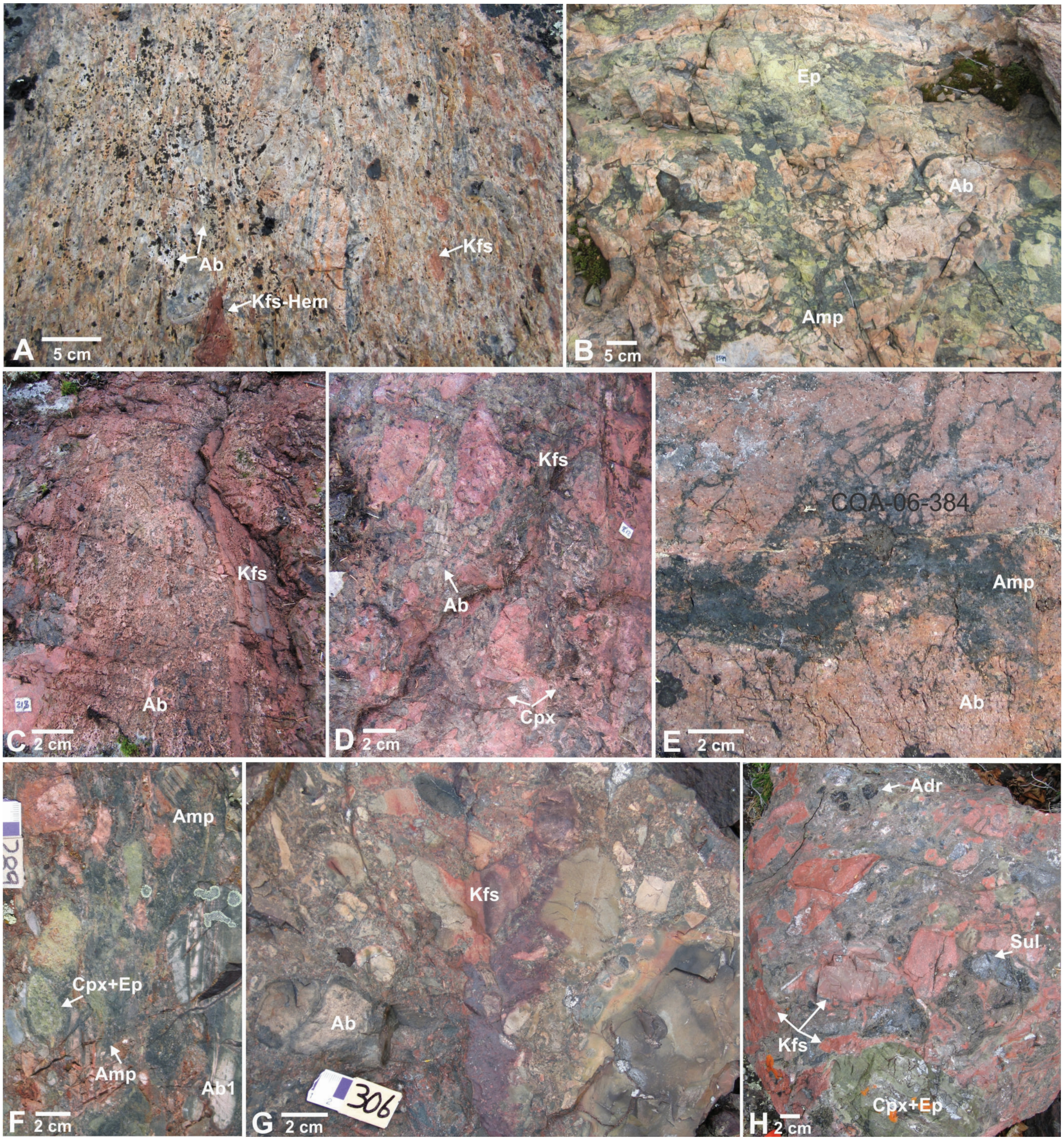


**Figure 19.** Brecciation of albitite and albitized volcaniclastic breccias. **A.** Albitite breccia with a well-defined planar fabric and some K-feldspar-rich clasts of uncertain origin, Southern Breccia albitite corridor (10CQA-1622). The fragmentation of a K-felsite or of K-feldspar altered rhyolite dykes are potential protoliths for the pink fragments within the breccia. **B.** Progressive brecciation of an albitite; breccia infilling by amphibole was followed by selective epidotization of the amphibole matrix and some albitite fragments, in association with carbonate and K-feldspar in the LT Ca-Mg-Fe alteration facies, Grouard Lake (10CQA-1599). A volcaniclastic host is possible. **C, D.** Stratabound brecciation of an albitite that replaced a volcaniclastic breccia featuring intense albitization, fragmentation of the albitized bedded unit parallel to layering, skarn replacement of the matrix, possible fluidization along bedding, and K-feldspar overprint, Mile Breccia (C, D: CQA-05-0218). **E.** Incipient brecciation of an albitite, infilled and locally extensively replaced by amphibole (CQA-06-384). **F–H.** Sequential and selective alteration of albitized fragments and infill by skarn (andradite and clinopyroxene), epidote, and K-feldspar in the chaotic breccia sector of the Mile Breccia (F–H: CQA-06-306). The K-feldspar-altered skarn is mineralized with copper sulphides (Mumin et al., 2010). NRCan photos 2020-544 to 551.

Conclusive evidence of fluidized breccia occurs locally. The most convincing examples include the fluidized magnetite-apatite breccia that cuts albitite in the Camsell River district (Bowdidge et al., 2014a; Bowdidge and Dunford, 2015; Corriveau et al., 2016, 2022b). It is also possible that the well-defined clast orientation in the Southern Breccia corridor and at the Mile prospect (Fig. 19A, C, D) is due to local fluidization. Fluidized breccias can have angular elongate fragments or fragments with very irregular contours (Oliver et al., 2006; Corriveau et al., 2022b). Rounding of fragments due to abrasion between fragments in fluidized breccia pipes (McCallum, 1985; Ross et al., 2002) would be hard to demonstrate as replacement of matrix material (e.g. rock flour) is generally pervasive and fragments are frequently replaced by alteration assemblages.

Breccia zones are commonly ‘monomictic’ in that the brecciated fragments are of the same composition. In some cases, varied hosts have been intensely albitized prior to brecciation, masking the original composition of the fragments (e.g. albitite breccias of the Southern Breccia corridor). Some of the hydrothermal and structural breccias are polymictic because of brecciation of polymictic volcaniclastic or sedimentary hosts (e.g. a volcaniclastic breccia, debris flow or conglomerate) such as the East Hottah system, Mile and Cole breccia bodies. Brecciation of variably altered host rocks may also lead to polymictic breccias (Fig. 21C), a common occurrence in the Grouard Lake area and Cole breccia (Corriveau et al., 2010b; Montreuil et al., 2015, 2016b).

Polymictic breccias may result from repeated alteration during or after brecciation, and from selective replacement of fragments. The most spectacular examples are observed at the Mile Breccia (Fig. 19F–H), within K-feldspar, magnetite or tourmaline-altered albitite breccia of the Southern Breccia corridor (Figs. 13D–F, 20) and in a magnetite-altered volcaniclastic breccia (Fig. 22). At the Mile Breccia, brecciation of an albitized fragmental volcaniclastic host (Fig. 19F) was followed by skarn and epidote alteration of clasts and matrix (Fig. 19C, D, G, H; Corriveau et al., 2010b). Early skarn (garnet-clinopyroxene, vesuvianite) was brecciated by Cu-Pb-Zn sulphide-mineralized K-skarn, forming black garnet clasts, skarn-altered fragments, skarn matrix, and interconnected brick-red K-feldspar alteration across the matrix, and along clast margins and sedimentary layering within clasts (Fig. 19C, D, F–H).

Breccia formed at the transition from HT K-Fe to LT K-Fe alteration facies, including at the K-skarn facies, are typically characterized by infilling of matrix by skarn assemblages or iron oxides, and replacement of fragments by K-feldspar. Such breccias commonly contain sulphides disseminated in the matrix or as veins or veinlets cutting the matrix. All three components (matrix, clast replacement and sulphide disseminations or veinlets) display a regular sequence of coeval crystallization with respect to the earlier or subsequent facies, supporting the interpretation that they represent a single facies, and are not an artefact of coincidental spatial association nor of selective ground preparation (Corriveau et al., 2016, 2022b). While mapping, all breccia components including their haloes were taken into account to define the alteration facies of the breccia. The K-feldspar alteration that commonly forms K-felsite haloes surrounding the iron oxide breccia is interpreted as a replacement front preceding the iron oxide breccia front. This is most extreme where iron oxides are particularly abundant and replace breccia fragments, suggesting that potassium was dissolved and entrained upwardly or laterally by the fluids.

As described for veins, the metasomatic fronts (haloes) originating from the breccia matrix may extend several metres into host rocks (Fig. 19E) and internally partially or thoroughly replace breccia fragments (Figs. 19B, 21F). Along veins, the haloes form sharp, bilateral alteration fronts largely parallel to the vein-host contacts. In breccia and pseudobreccia, the alteration fronts are very irregular (Figs. 19E, 21A–C, F). This is interpreted to reflect the distribution of enhanced permeability along damage zones (cf. Engvik et al., 2009). Coalescence of haloes from adjacent breccia zones forms zones of K-felsite tens of metres in diameter (Corriveau et al., 2022b). Without documenting the transition from non-brecciated material into the breccia zones, altered fragments and breccia haloes may be misinterpreted as previously altered hosts (Figs. 13D, 19H; Corriveau et al., 2016, 2022b).

Based on the diversity of breccia types, several fragmentation processes must be considered (e.g. hydraulic fracturing, tectonic fragmentation, chemical dissolution of fragments; see Jébrak, 2010). Despite the possibility of several processes, K-feldspar-rich K-Fe alteration is regularly accompanied by brecciation, along with precipitation of sulphides in veinlets and disseminations within the breccia matrix (Corriveau et al., 2016, 2022b).

## Resemblance of Metasomatites to Other Rock Types

A key question regarding IOCG and affiliated deposits is how to identify them and explore them efficiently. Previous sections have provided multiple examples of field attributes of the broad-scale haloes of intensely altered rocks that host these deposits. Some rocks are altered beyond recognition, an attribute typical of IOAA systems. In other cases, alteration enhanced primary rock textures, obscured timing relationships, or transformed a host into a rock resembling another lithotype entirely. For example, ‘amphibolite’, magnetite- or biotite-rich ‘amphibolite and schist’, laterally heterogeneous ‘banded iron formation’, and heterogeneous ‘syenite’ could fit the mineralogy and textures of some HT Ca-Fe metasomatites, albitites or K-felsites in an IOAA system.

### *Sodic Metasomatites versus Hornfels, Silicification Zones and Igneous Rocks*

Albitite was mapped as hornfels in the Camsell River and Nod districts (Hildebrand, 1984a; North, 1995) or as silicification zones in other districts (e.g. Romanet Horst of northeastern Canada as discussed in Corriveau et al., 2014). Because of the presence of microcrystalline quartz (residual in nature), aphanitic, white to light grey albitite outcrops are very hard, with glassy surfaces similar to silicification zones; this contrasts with the more typical

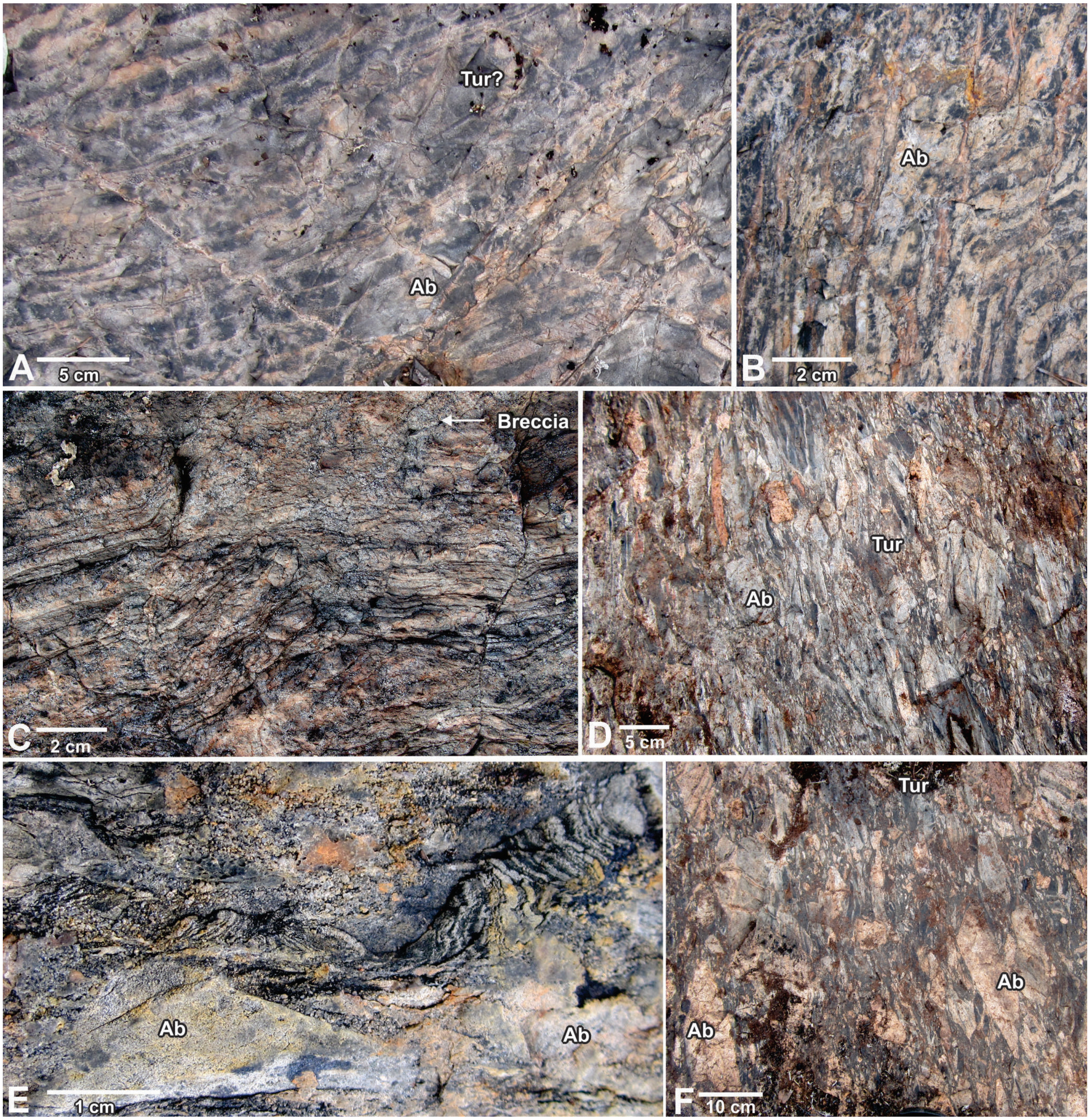


**FIGURE 20.** Progressive brecciation of albitite along fault zones. **A, B.** Incipient brecciation of stratabound albitite (white layers) and albitized metasiltstone (grey layers) cut in (A) by a set of orthogonal fractures oblique to bedding, Southern Breccia (A, B: 10CQA-1637). White albitite haloes form along fractures and albitized fractures and breccia zones are weakly overprinted by a pink K-feldspar alteration. In B, the albitized metasiltstone is folded and is cut by a set of parallel fractures with pink albitite. The albitized grey layers are increasingly altered by tourmaline leading to black patches of tourmalinite. In the field, incipient tourmaline alteration is difficult to distinguish from weakly albitized siltstone layers. **C.** Incipient brecciation of intensely albitized metasiltstone along a fault discordant to bedding in the Duke system (09CQA-0054). Albitite breccia fragments originally have a high aspect ratio due to fracturing of the stratabound albitite along bedding planes. **D.** Albitite breccia with a strong fabric defined by the preferred orientation of the larger fragments, Southern Breccia (10CQA-1640). Breccia infill and smaller fragments display chaotic breccia textures, local shingle textures, or a flow fabric parallel to the preferred orientation of the larger fragments. These textures record fluidization. **E.** Internal deformation of a breccia fragment and folding of layering within the larger albitite fragments (Southern Breccia; 09CQA-1674). **F.** Intense tourmaline alteration of the albitite breccia matrix and clasts in the same outcrop as D and Figure 22A, B. Early white albitite haloes along fractures cut by pink albitite are preserved within some larger fragments. NRCan photos 2020-552 to 2020-557.

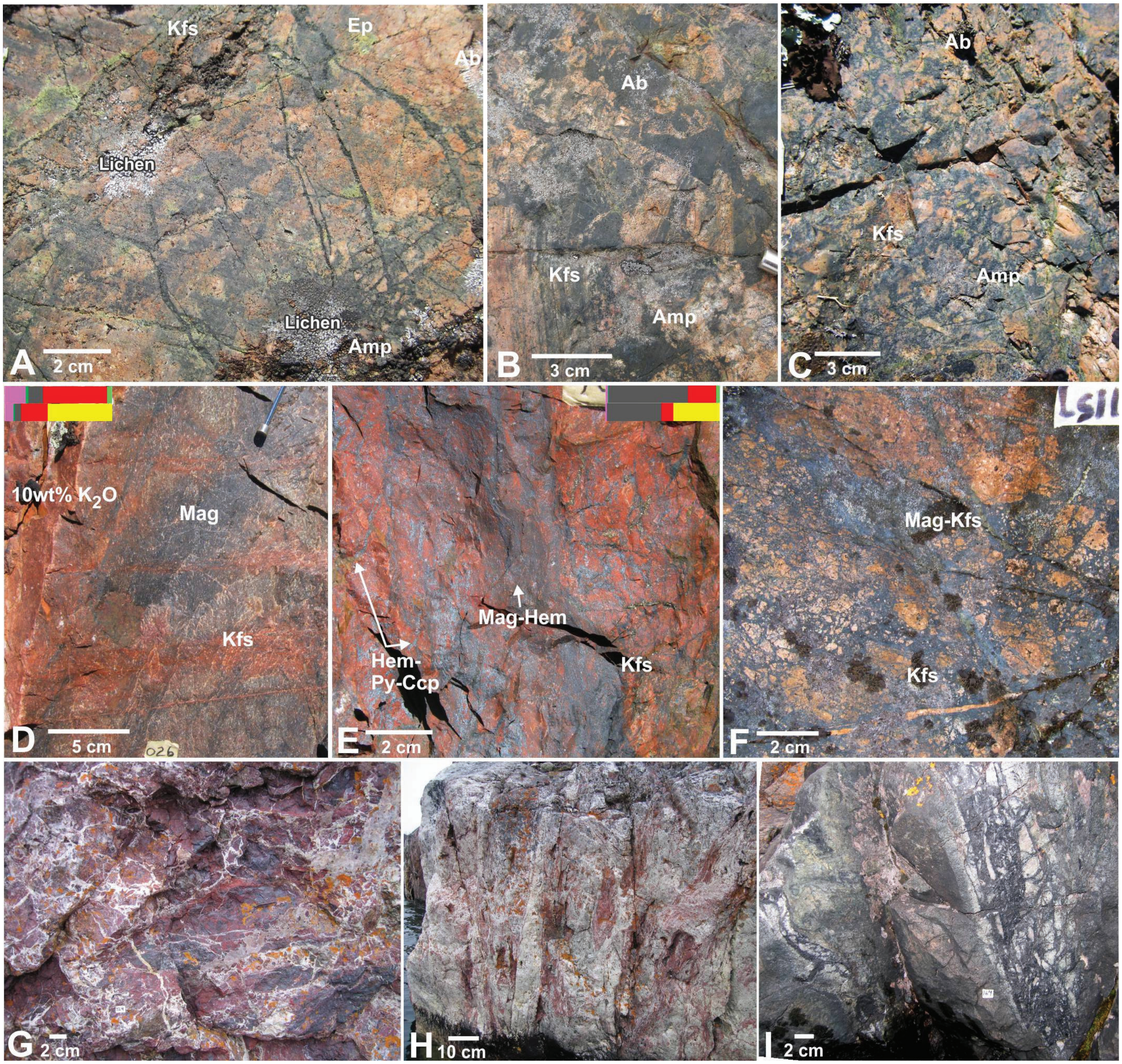


**FIGURE 21.** Evolution from replacement textures to mechanical brecciation to dissolution breccia and development of pseudobreccia by replacement. **A–C.** Incipient dissolution breccia formed by coalescing amphibole and amphibole-magnetite replacement of a differentially albitized host, Grouard Lake (A: 111PUA-1018; B, C: 10-CQA-0302). In A, the breccia is cut by amphibole veins. In C, the amphibole-magnetite replacement of former fragments is more intense than in B and leads to pervasive pseudobreccia textures having an apparent polymictic nature. **D, E.** Progressive K-feldspar replacement of a weak, patchy magnetite alteration in volcanic rocks at the Brooke prospect (D, E: 09CQA-026). This alteration evolves to K-felsite (not shown), to magnetite veins with K-feldspar haloes, and to mineralized breccia with magnetite infill and K-feldspar alteration of clasts. Disseminated pyrite and chalcopyrite are associated with magnetite in the breccia matrix, forming a copper-mineralized HT K-Fe facies. Hematite replaces magnetite. **F.** Mineralized HT K-Fe breccia with more intense K-feldspar alteration of clasts in areas of greater magnetite infill, Fab prospect (CQA09-1157). **G, H.** Late-stage breccia zone showing increasing brecciation and cementation by quartz, Port Radium-Echo Bay district (G, H: CQA-05-224). **I.** Tourmaline-quartz breccia cutting altered andesite that hosts veins of hematite and quartz (not shown), Port Radium-Echo Bay district (CQA05-164). NRCan photos 2020-558 to 2020-566.

chalky weathered surface of quartz-poor albitite, which is easily scratched by a hammer. For example, the fine-grained white host to the tourmaline vein in Figure 21I is typical of both albitite and silicification zones. Portable XRF, cobaltinitrite staining and geochemistry help identify such zones. Hence, historic reports of 'hornfels' and silicification zones, in view of regional albitite alteration and diverse polymetallic prospects, should be re-examined to assess potential for IOAA systems.

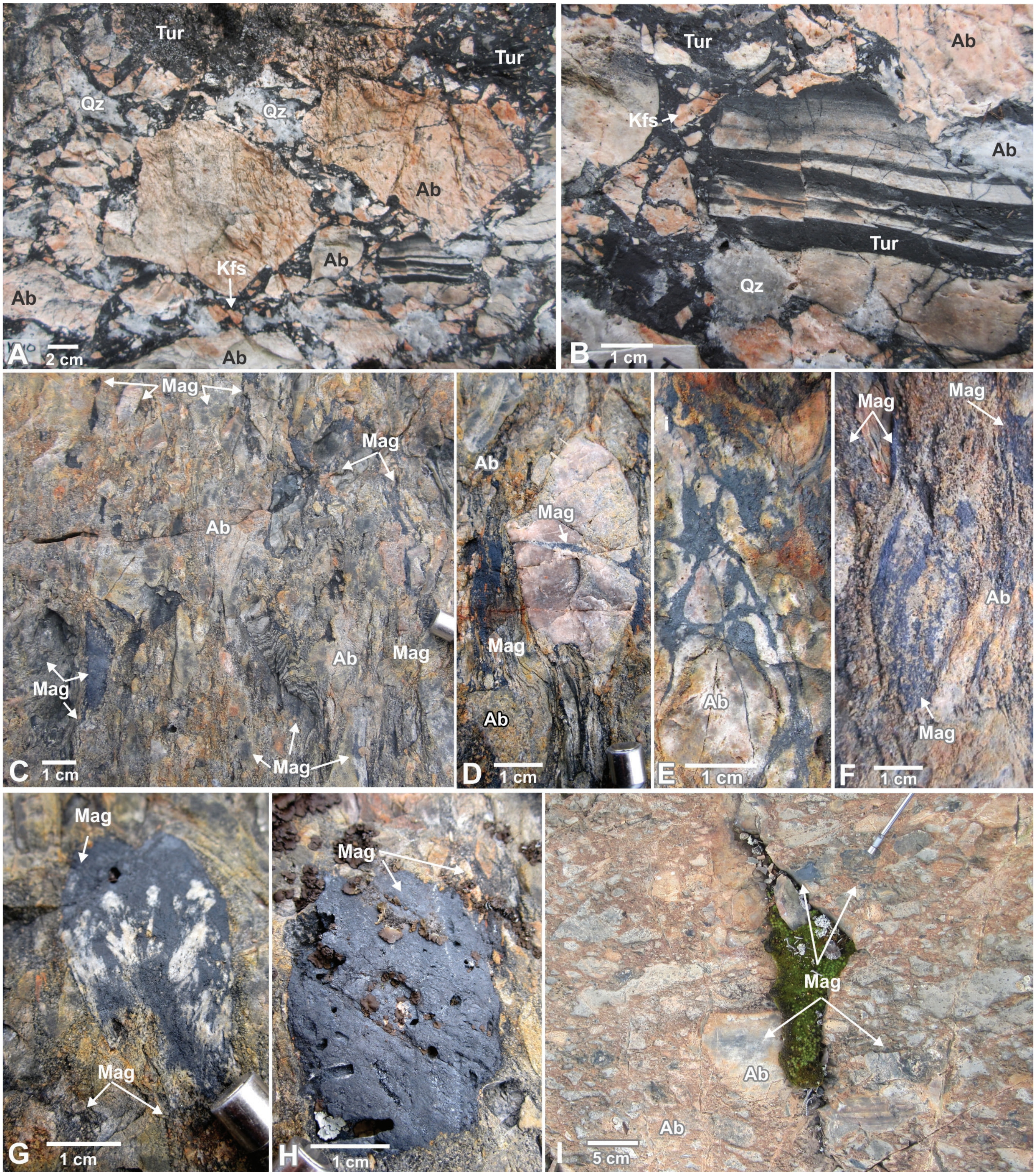


**FIGURE 22.** Selective replacement of breccia clasts. **A, B.** Albitite breccia replaced by tourmaline, K-feldspar and then quartz, Southern Breccia albitite corridor (A, B: 10CQA-1640). The tourmaline replaces fragments and matrix and infills fractures within fragments. The stratabound replacement of clasts by tourmaline enhances the original bedding planes of the albitized metasiltstone. K-feldspar overprints have a brick red colour. **C–H.** Magnetite alteration of an albitite breccia showing magnetite alteration fronts locally replacing and infilling the matrix and selectively replacing some of the fragments, Southern Breccia albitite corridor (C–H: CQA09-1674). Incremental replacement of fragments and small-scale extension of replacement into the matrix conclusively demonstrate that magnetite alteration postdates albitization and brecciation. **I.** Volcaniclastic breccia in which albitized lapilli and matrix are replaced locally by magnetite, Grouard Lake (10CQA-0306). Magnetite alteration postdates volcanism and albitization; it variably alters clasts or selectively alters clast cores. NRCan photos 2020-567 to 2020-575.

Coarse-grained, hypidiomorphic granular albitite containing light grey or purplish plagioclase locally occurs along the contacts of sub-volcanic intrusions and resembles the lilac and grey varieties of massif-type anorthosite; if metamorphosed, albitite resembles recrystallized equigranular anorthosite or tonalitic gneiss (see Fig. 2.2 in Corriveau et al., 2018). Similarly, pink or white albitite commonly resembles syenite (Figs. 3E, 7E). Light pink albitization may resemble K-feldspar alteration (Figs. 7, 8, 17–19 vs Fig. 13D–F) and be misinterpreted as a potential exploration target, especially in zones where later-stage mineralized veins occur (Damp and Nod prospects; North, 1995). Most often, K-feldspar alteration has a distinctive brick-red or orange-red hue (Figs. 19H, 21D, E), whereas moderate-to-intense earthy hematite alteration has a brownish hue (Fig. 11C). Albitite may acquire the reddish hue of K-felsite when pigmented by earthy hematite or overprinted by weak K-feldspar alteration (e.g. Southern Breccia; Montreuil et al., 2015, 2016b; Potter et al., 2019). However, portable gamma-ray spectrometry can distinguish K-feldspar alteration from pink to red-coloured albitite because of their different potassium contents (see also Shives, 2015).

Albitization of porphyritic volcanic and intrusive rocks may generate albite pseudophenocrysts, as described by Pelleter et al. (2010). In a global context, albitite 'dykes' and hypidiomorphic-granular albitite zones are commonly interpreted as igneous in origin and labelled 'albitophyre'. In the GBMZ, incremental albitization supports an epigenetic origin of the albitite, even for the most linear and sharp-edged end-members such as the 10 cm-wide, fine-grained, megascopically homogeneous, albitite replacement vein that cuts metasiltstone at DeVries in Figure 11B. A similar replacement vein in the Southern Breccia even has a regular, internal fracture pattern developed perpendicular to the walls. Two interpretations arise for the fractures: 1) the vein is actually a rapidly-cooled albitophyre dyke; or 2) fracturing perpendicular to the vein walls is the result of rheology contrasts within the deformation corridor. Taking into consideration all the epigenetic attributes observed for albitite in the GBMZ, and the fact that these 'veins' are hosted in albitite breccia or albitized sedimentary rocks, our preferred interpretation is that they demonstrate how focused, intense albitization along fractures and damage zones may produce igneous-looking rocks such as the vein studied by Rubenach and Lewthwaite (2002).

*High-temperature Ca-Fe Metasomatites versus Iron Formation, Amphibolite, and Iron Oxide Magmas*

In sedimentary and volcanic rocks, amphibole and magnetite alteration in the HT Ca-Fe facies is extremely efficient at preserving the textures and structures of the host rocks, to the point that such metasomatites may resemble syngenetic magnetite iron formation, amphibole- or magnetite-rich metasedimentary rocks, amphibolite (as a product of regional metamorphism of mafic rocks), metamorphosed marl, iron oxide lava flows, or intrusive bodies crystallized from iron oxide magmas (Figs. 3D, 9E, 12B–E, 14D, 23, 24; cf. Lee and Stout, 1989 vs. contrasting interpretation of Choi et al., 2011; Badham and Morton, 1976 vs Hildebrand, 1984a, 1986; Sidor, 2000 and Gandhi and van Breemen, 2005 vs. this work; Andersson, 2013; Day et al., 2017 vs. Nold et al., 2013, 2014). All examples of such rocks in the GBMZ developed through incremental alteration of sedimentary, volcanic, volcaniclastic or high-level porphyritic intrusive host rocks. Cobaltinitrite staining of cut rock slabs significantly aided in testing the origin of rock types by highlighting alteration in rocks that megascopically appeared unaltered or weakly altered.

In Figures 11B–E, 23H and 23I, pseudo-iron oxide volcanic rocks containing pseudo-albite phenocrysts represent magnetite-altered groundmass and albitized plagioclase phenocrysts, respectively, in rocks that grade into weakly-altered 1.87 Ga porphyritic andesite and sub-volcanic porphyritic intrusions. Locally, magnetite also selectively replaces amygdules and phenocrysts. Where most selective and intense (i.e. in the HT Ca-Fe and HT K-Fe facies), this alteration produces attributes resembling those interpreted as immiscible iron oxide magmas (cf. Andersson, 2013). Where most intense, magnetite replacement during the process of IOA mineralization results in textures that resemble igneous rocks (see also Hildebrand, 1986, p. 650; Mumin et al., 2007, 2010; Corriveau et al., 2010a, b, 2016, 2022a). Such rocks form structurally above albitite zones in simple vertical prograde sections (Mag Hill in the Port Radium-Echo Bay district), or cut albitite (Terra mine region in the Camsell River district) in the GBMZ (see field relationships described in Corriveau et al., 2022c). The metasomatic precipitation of magnetite following extensive leaching of iron through albitization is in line with field observation of timing relationships between albitite development and IOA mineralization in the GBMZ and globally.

In laminated and bedded sedimentary or volcaniclastic rocks, texture-preserving HT Ca-Fe alteration produces a well-layered ironstone (20 to nearly 100 wt% $Fe^2O^3$) and melanocratic layers of calcic amphibole (actinolite, hornblende) ± biotite and magnetite, or clinopyroxene ± garnet similar to some types of amphibolite, calc-silicate metasedimentary rocks, or banded iron formations (Figs. 3D, E, 9D–F, 16, 24C; Fig. 46 in Hildebrand, 1984a). In most cases, the stratabound alteration can be traced to irregular replacement zones that cut layering or to least-altered host rocks (Figs. 3D, 15F, G, 24, B, G). Through replacement, stratabound alteration evolves to discordant and more pervasive zones, including massive magnetite bodies, magnetite haloes formed along magnetite veins within carbonate rocks, and fracture-filling magnetite veins transitional to massive magnetite zones (Fig. 23A–F).

Previous studies in the GBMZ interpreted many stratabound ironstone units as sedimentary iron formations (Vivian, 1991; Gandhi, 1992) and calc-silicate rocks replaced by amphibole as marls (Sidor, 2000). However, field work clearly indicates that the ironstone, magnetite-rich sedimentary layers and amphibole-rich layers observed in the Treasure Lake Group are formed during epigenetic, stratabound magnetite and/or amphibole replacement. Even in incipient stages, such replacements may be perfectly stratabound, pervasive and laterally homogeneous along layers for tens of metres, such as the extensive hematitite lens replacing andesite in the Port Radium-Echo Bay district or the interlayered magnetite, albitite and locally albitite overprinted by earthy hematite layers in the Peanut Lake area (Mumin et al., 2007, 2010; Corriveau et al., 2010b, 2022c). Ironstone of this type that formed in the HT Ca-Fe facies, or pre-existing ironstone, may serve as reactive units in trapping metals associated with the more fertile alteration facies (see Williams, 1994).

In rare cases, fine laminations in sedimentary rocks are selectively replaced yet preserved, as observed in the Port Radium-Echo Bay district. Selective alteration of laminations may preserve host rock textures so strikingly that it can lead to misinterpretation of the rock origin. Albite or amphibole alteration of crossbeds is relatively easy to interpret as they are not heavy minerals that accumulate in crossbeds in sedimentary rocks (Fig. 9G, H). However, magnetite replacement in crossbed laminations has locally been interpreted to be detrital magnetite; such an interpretation may overlook metasomatism and obscure the timing relationships between host rocks and metasomatism. Similar replacement of fine laminations by magnetite is observed in stromatolites at Grouard Lake (Fig. 10C, D).

Locally, pervasive replacement across laminations forms more massive magnetite zones. In these cases, the discontinuity of magnetite laminations provides further insights on the origin of lamination-selective alteration. Selective replacement of fragments within volcanic, magmatic-hydrothermal, or structural breccias is also common, and may hamper recognition of amphibole, K-feldspar or magnetite alteration that postdates brecciation (Figs. 12H, 13, 22).

Iron oxide replacement zones have been mapped as sedimentary banded iron formations not only in the GBMZ but also in the Monakoff deposit of the Cloncurry district, Australia (Williams et al., 2015), in the Bafq district of Iran (Fig. 6 in Daliran et al., 2022), and in the Dahongshan deposit, Kangdian district, China (Figs. 4, 5 in Zhao et al., 2022). However, some examples in the Cloncurry district have been interpreted as metasomatic in origin (Williams, 1994). Some zones of the Bayan Obo deposit (Inner Mongolia, China) are also typical of stratabound iron oxide alteration (Fig. 10 in Smith et al., 2015), although true banded iron formation appears to be also present in the deposit (Fig. 9 in Chao et al., 1997; see also Huang et al., 2022). The absence of quartz, jasper, and siliceous iron minerals, the presence of layers rich in amphibole (actinolite, hornblende), clinopyroxene, albite or biotite, the occurrence of stratabound magnetite haloes along magnetite veins (Corriveau et al., 2022b, c), and geochemical signatures in ironstone such as elevated Ca, Hf, Mg, Nb, REE, Ta, Th, Ti, V, U, and Zr, are all signs of iron-rich IOAA alteration (see footprint of HT Ca-Fe alteration in Corriveau et al., 2022a).

*Potassic (K-feldspar) Metasomatites versus Rhyolites*

Potassic (K-feldspar) alteration of albitite and least-altered hosts commonly produces a homogeneous felsite that resembles rhyolite. The most striking and confusing examples are from the Southern Breccia district. At this locality, bona fide rhyolite flows of the Lou assemblage unconformably overlie steeply-dipping metasiltstone and metawacke beds of the Treasure Lake Group; some of these beds are pervasively albitized to such an extent that bedding is destroyed. In many outcrops, the unconformity is completely obliterated by very fine-grained, pervasive and intense potassic (K-feldspar) alteration that imparts a reddish-pink colour to the rocks. The intensity of alteration gradually decreases away from the unconformity, where host rocks are either sodic- or weakly-altered metasedimentary rocks. The significant differences in host-rock transformation to K-felsite highlights how K-feldspar-dominant potassic alteration is texture destructive. In places, the weathered surface of the K-feldspar alteration has lost its reddish hue and resembles albitite. These areas were affected by a recent forest fire, further illustrating the importance of carrying a gamma-ray spectrometer in the field for systematic measurement of potassium contents.

The southern GBMZ is underlain by abundant rhyolite units, in contrast to the northern GBMZ, where andesite is dominant. In parallel, sodic and HT Ca-Fe alteration is more dominant in the north and potassic and K-Fe alteration more prevalent in the south. However, a thorough re-investigation of rhyolites across the GBMZ has revealed that some of the previously mapped rhyolites in the southern GBMZ are in fact potassic-altered andesitic rocks (Montreuil et al., 2016a; Ootes et al., 2017).

*Orogenic Metamorphic Rocks versus Metasomatites*

Ductile deformation is common within HT Ca-Fe alteration zones of the GBMZ, a feature common to IOAA systems worldwide (Corriveau et al., 2022c). Ductile deformation may lead to misinterpretation of syn-tectonic metasomatites as orogenic metamorphic rocks that pre- or postdate metasomatism in areas where rocks are poorly exposed or relationships are not constrained (Corriveau et al., 2016). In the GBMZ, regional mapping revealed that intensely deformed, folded, boudinaged and schistose rocks are systematically associated with HT Ca-Fe facies metasomatites, and locally with albitized beds interlayered with stratabound HT Ca-Fe alteration (Fig. 24F, G). Brittle deformation, in contrast, is expressed by fracture networks with albitite or K-feldspar haloes in least-altered hosts or infilled by veins (Figs. 17–20), breccia within earlier albitite, and breccia associated with HT and LT K-Fe metasomatites, K-felsite breccia and K-skarn, as well as late-stage quartz, carbonate or tourmaline breccia and veins (Fig. 21E–I). In boudinaged, stratabound albitite units within HT Ca-Fe metasomatites, subsequent HT K-Fe alteration forms along fracture networks and brecciates the albitite, highlighting that the host rocks cooled rapidly enough for brittle deformation to occur (Fig. 24G, H). The ductile (and brittle-ductile) deformation in the HT Ca-Fe facies illustrates the changes in rheology associated with the ingress of high-temperature fluids needed to form this alteration facies, and the strain partitioning that high-temperature fluid flow induces within systems (see Corriveau et al., 2022c).

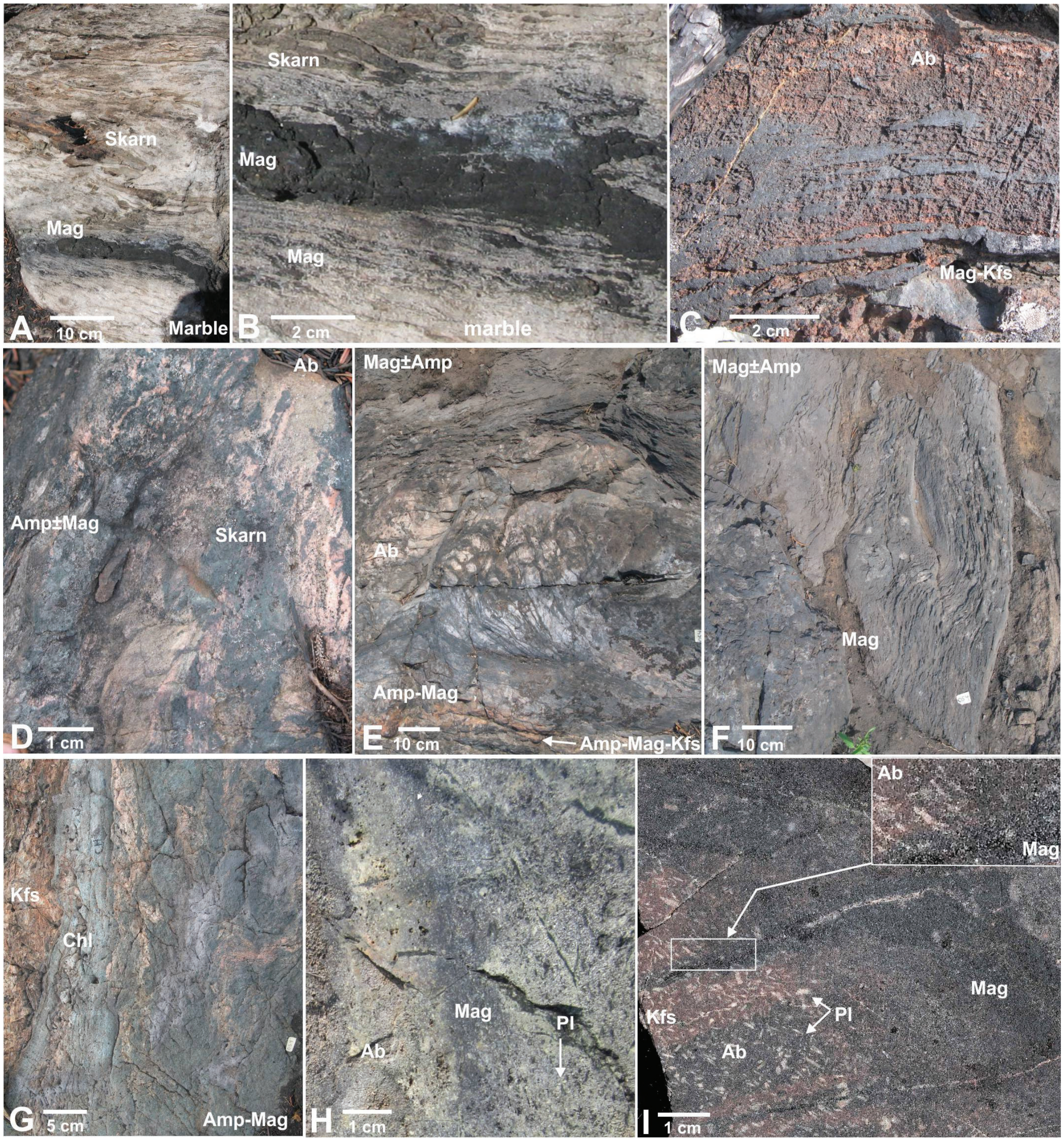


**Figure 23.** Progressive HT Ca-Fe and HT K-Fe alteration within supracrustal rocks. **A–G.** Amphibole to magnetite-dominant HT Ca-Fe facies within weakly altered marble and albitized metasiltstone at the Duke system (A, B: 09-CQA-053; C: 09-CQA-054; D: 09-CQA-1114; E–G: 09-CQA-054). In A and B, a magnetite vein with magnetite haloes cuts across layering in weakly altered marble. The vein displays intense replacement textures along contacts and apophyses. Vein haloes are as wide as the vein, of weak to moderate intensity, and displaying varied internal, stratabound to patchy morphologies. Discontinuities in the stratabound alteration along haloes lead to the development of trains of magnetite clots along bedding. The magnetite vein also cuts local patches of earlier stratabound alteration. In C, magnetite alteration propagated as diffuse to intense discordant alteration fronts, stratabound replacement veins, and sharp stratabound veins within a siltstone bed. The haloes of magnetite parallel to veining in the marble are more irregular than the sharp and straight veins resulting from stratabound ingress in siltstone. In D, patchy skarn alteration of albitized metasiltstone is irregularly replaced by HT Ca-Fa amphibole-dominant alteration. In E, amphibole-magnetite HT Ca-Fe alteration evolves to magnetite-dominant alteration of albitized metasiltstone along fracture networks. Coalescence of alteration across the fracture network and stratabound alteration produced magnetite-dominant ironstone layers. In F, the faint laminations within ironstone are folded, marking the transition from early brittle fracturing preserved in E to the ductile behaviour of the HT Ca-Fe alteration as intensity (and heat) increases during syntectonic metasomatism. In G, stratabound amphibole and amphibole-magnetite (HT Ca-Fe) alteration replaces albitized metasedimentary rock and is subsequently chloritized, whereas preserved albitized zones experienced K-feldspar alteration. **H.** Weak to moderate magnetite-dominant alteration that preserves the original porphyritic texture of albitized host andesite at Grouard Lake (09CQA-1097). Plagioclase phenocrysts (Pl) are albitized. **I.** Moderate magnetite-dominant HT K-Fe alteration, showing a K-feldspar halo (lower left) that preserves the original porphyritic texture of albitized host andesite at the Cat showing within the Mazenod system. NRCan photos 2020-576 to 2020-584.

## Defining Prograde and Retrograde Metasomatism

The excellent exposure and preservation of the GBMZ IOAA systems, from oldest to youngest and deep to shallow facies, permits characterization of prograde and retrograde metasomatic paths defining the regular sequence of crosscutting and overprinting relationships among alteration facies. The systematic evolution of IOAA systems is best observed megascopically because metasomatites of each alteration facies are commonly retrograded by microscopic hydrous or carbonate assemblages, irrespective of the metasomatic path of the entire system (De Toni, 2016). The widespread nature of retrograde assemblages highlights the need to differentiate the prograde evolution of these systems from the multitude of retrogression events that subsequently affect each alteration facies.

In ore deposit studies, 'prograde' alteration generally refers to progressively higher-temperature assemblages superimposed on lower-temperature assemblages during a 'heating up' cycle of the system, whereas 'retrograde' alteration consists of lower-temperature alteration assemblages superimposed on higher-temperature assemblages. In IOAA systems, the application of such a definition is not straightforward and can be misleading. Consequently, various definitions have been proposed for prograde and retrograde pathways in systems that host IOCG deposits. Williams et al. (2005, p. 390) consider IOCG mineralization as a retrograde process as it occurs in the low-temperature stages of an alteration sequence evolving from high to low temperature. On the other hand, Skirrow (2010, 2022) defines the prograde pathway as the original and unidirectional footprint from high temperature at depth to lower temperature toward surface, and the retrograde stages as those associated with thermal collapse of the system, where low-temperature alteration overprints high-temperature alteration. In the latter scenario, in situ, captured fluids replace earlier alteration, or in association with uplift (and exhumation), low-temperature fluids infiltrate as per the two-stage model of Skirrow (2010) and Hayward and Skirrow (2010).

A simplified analogy is a chain reaction which, once triggered by the collection, heating, and ascent of hypersaline fluids, will induce a series of self-sustained fluid-rock reactions driven by the high disequilibrium between the physical and chemical properties of the fluid plume(s), and those of host rocks as the plume ascends toward surface. To best capture this fluid-rock chain reaction, the prograde metasomatic path is defined as the sequence of alteration facies that developed in the system — from oldest to youngest, from depth to surface, and through overall declining temperatures. The prograde path is marked by extensive chemical changes in host rock composition. At each step, fluids captured within early alteration zones will cool and retrogress their host metasomatites. Early alteration facies may also be retrograded by lower-temperature overprints common in these tectonically active environments. The metasomatic rocks formed through the prograde path differ markedly from the most common retrograde overprints, in which lower temperature, hydrous, hydrolytic or carbonate-bearing alteration largely isochemically replaces higher temperature assemblages — except for the addition of volatiles, K, Mg and Si (Blein et al., 2022; Corriveau et al., 2022a).

Systems reach peak temperatures (e.g. 800°C) during HT Ca-Fe facies alteration after albitization. A possible explanation for these higher temperatures is that fluids captured by albitite served to raise the temperature of the host rocks regionally at the onset of metasomatism (Corriveau et al., 2022b). Fluids trapped and preserved by albitite are thus potentially cooler than the original fluids due to cooling by the host rocks. As the hot saline to hypersaline fluid column passes through early, porous albitite, it may remain at high temperatures, leading to recrystallization of albitite to the medium- to coarse-grained hypidiomorphic and the pegmatitic textures observed along some sub-volcanic intrusions in the northern GBMZ (Fig. 8; Corriveau et al., 2022c). Repeated emplacement of magmas (dykes, sills, intrusions) as the system evolves will also sustain and re-energize high-temperature regimes, as illustrated by the numerous dyke swarms and generations of HT Ca-Fe facies at the NICO deposit (Figs. 22, 23 in Corriveau et al., 2022c). Conversely, if albitite zones are uplifted prior to pervasive re-equilibration of the isotherms to the highest fluid temperatures, if they form along fault zones laterally away from the main fluid plume path or both, they remain fine-grained and porous, as observed in the Southern Breccia corridor. In such cases, the albitite zones are expected to record lower temperatures than most HT Ca-Fe alteration zones formed within the main pathway of the fluid plume.

As the fluid plumes cool, low-temperature facies form within IOAA systems and are commonly more spatially extensive but less intense than high-temperature facies. However, deposits within the Olympic Copper-Gold Province and epithermal caps of IOAA systems within the GBMZ demonstrate that LT K-Fe to LT Ca-Mg-Fe, and LT Si-K-Al-Fe alteration may also be very intense and extensive (see also the extent of phyllic to advanced argillic alteration at the Olympic Dam deposit in Ehrig et al., 2012).

Faulting and ingress of fluids with physicochemical conditions distinct from those of the evolving fluid column may lead to telescoping or repetition of alteration facies, and local disruption of the prograde sequence (Corriveau et al., 2022b). Overprinting effects may become complex as these systems pulse over time, but a dominant sequence that can be attributed to either a prograde or retrograde sequence is usually preserved. How the reactions prograde, retrograde, are telescoped or repeated ultimately impacts the type of deposit(s) formed (Corriveau et al., 2016, 2022b, c; Hayward et al., 2016). In addition, overprinting (e.g. early HT Ca-Fe alteration overprinted by HT Ca-K-Fe and HT K-Fe alteration; Figs. 22, 23 in Corriveau et al., 2022c) may lead to a combination of barren and mineralized alteration zones that complicate the interpretation of large geochemical databases, which may encompass a variety of alteration facies (cf. Dmitrijeva et al., 2019). It may also complicate the interpretation of mineral composition (e.g. magnetite; cf. Huang et al., 2022) as vectors

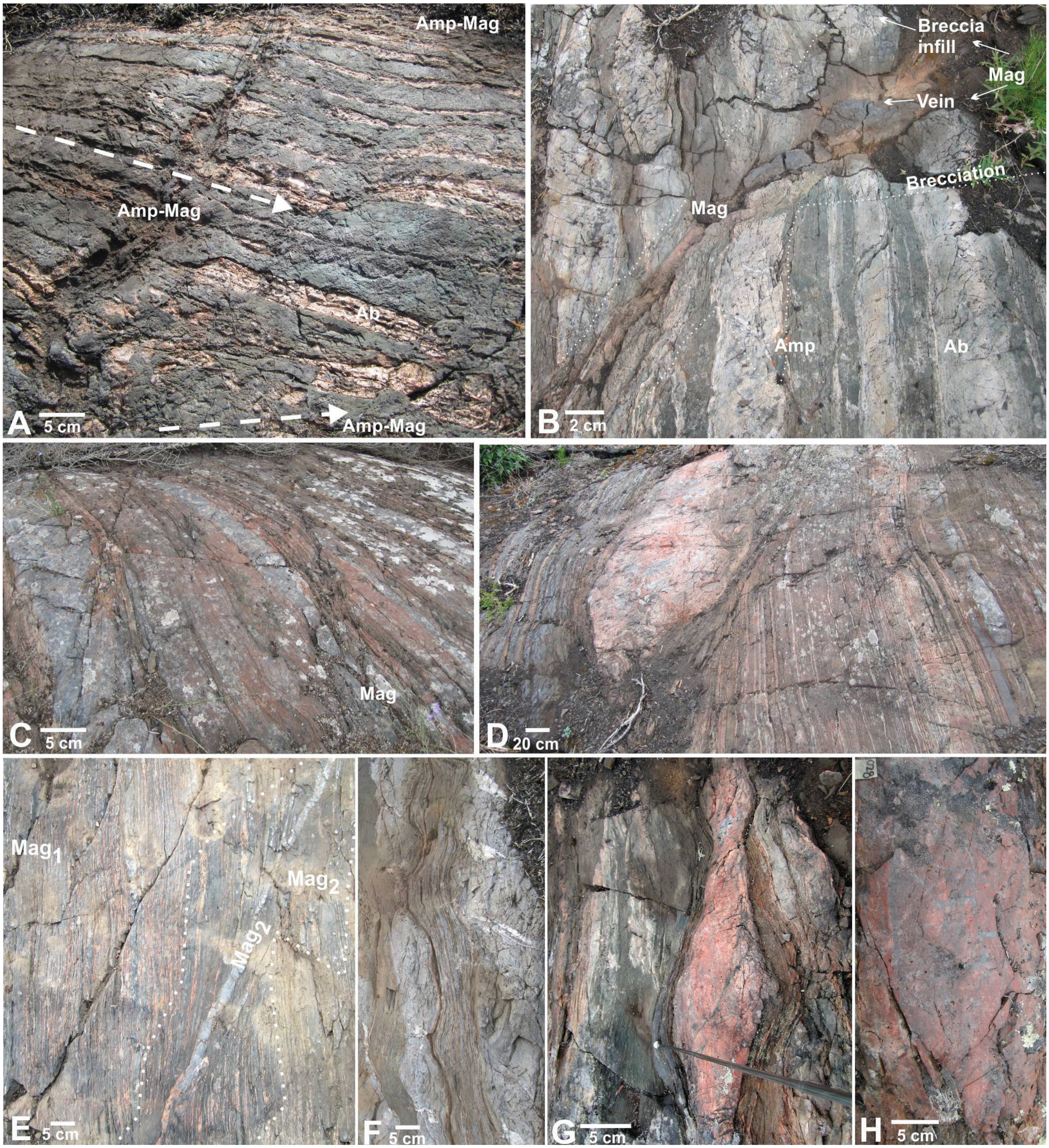


**Figure 24.** Development of ironstone and ductile deformation in HT Ca-Fe facies. **A, B.** Stratabound to slightly discordant amphibole-dominant alteration of albitized metasiltstone and metawacke unit (A: 11PUA-0506) with stratabound albitite (B: 11PUA-028). In B, C and E, shear zones oblique to layering are infilled by magnetite. **C.** Stratabound magnetite alteration leading to layered ironstones (C: 11PUA-028). **D.** Stratabound magnetite-altered layers are uniformly deformed whereas an albitite layer (pink) is boudinaged (D: 11PUA-028). **E.** Stratabound magnetite alteration (Mag1), irregular along albitized layers, is cut by a magnetite vein emplaced along a shear zone (Mag2) (E: 11PUA-028). Magnetite alteration haloes along the vein increase the stratabound alteration of the host. **F, G.** Syntectonic amphibole-dominant HT Ca-Fe alteration marked by foliation and warped along the swells and neck of boudinaged, stratabound magnetite-altered layers in (F) and an albitite layer in (G) (F, G: 11PUA-028). The albitite is K-feldspar altered, brecciated and infilled by magnetite associated with a HT K-Fe facies. **H.** Detail of the HT K-Fe breccia within albite layer in G (H: 11PUA-028). NRCan photos 2020-585 to 2020-592.

to mineralization. Furthermore, the generation of in situ inclusions (e.g. monazite or other minerals used for geochronology; Fig. 5G in Corriveau et al., 2022b) through dissolution-reprecipitation mechanisms may lead to misleading interpretations of mineralization ages. In the field, a gamma-ray spectrometer helps identify increasing concentrations of potassium (e.g. Shives, 2015) and the sometimes cryptic transition to HT Ca-K-Fe, K and K-Fe alteration (such as in amphibole or magnetite-dominant alteration zones). These field measurements help decipher overprinting relationships and help avoid chasing mineralization in regional, largely barren albite-amphibole-magnetite alteration zones.

## Concluding Remarks

Mapping IOAA systems at times defies our imagination. Within a single outcrop, alteration may vary from monomineralic to polymineralic; cryptic to pervasive, intense and extensive; texture-pseudomorphing to texture-destructive; fine-grained to pegmatitic; variegated to homogeneous; and alteration relationships from stratabound to clearly crosscutting. The extent and spatial distribution of alteration facies can vary gradually to abruptly, overlap over metres to hundreds of metres, or be displaced by faulting. The fine- to coarse-grained textural range facilitates representative sampling and documentation of mineral assemblages in the field. Consistency in the identification of mineral assemblages permits the mapping of alteration facies across systems. This mapping protocol refines those presented in alteration atlases of ore deposits and geological field manuals for metamorphic terrains and ore deposits, as none have dealt with the intrinsic, extreme, megascopic complexities of metasomatites in IOAA systems (Passchier et al., 1990; Einaudi, 1997; Thompson and Thompson, 1996; Marshall et al., 2004; Gifkins et al., 2005; Brimhall et al., 2006; Bonnet and Corriveau, 2007). Paraphrasing the Zharikov et al. (2007) definition of metasomatic facies, the IOAA facies concept provides a consistent means of describing the spectrum of rock types of the entire system without any terminology gaps or ambiguity. This approach simplifies field mapping by capturing the essence of the metasomatic system despite complex field relationships, varied host rock types, and extremely diverse textures, mineral assemblages and mineral contents of the metasomatites.

The metasomatic rock types are named by the alteration facies, namely albitite (i.e. Na), skarn (i.e. HT Ca-Fe-Mg), HT Na-Ca-Fe, HT Ca-Fe, HT Ca-K-Fe, HT K-Fe, LT K-Fe and LT Ca-Fe-Mg. In using diagnostic index cations as rock names for alteration, we provide continuity with Hitzman et al. (1992), Hitzman (2000), Marschik and Fontboté (2001), Skirrow (2010) and those who have built upon these works to describe IOAA systems. Entering information in a field database is thus greatly simplified, as the rocks have simple names that are transferable between districts. The metasomatites are then qualified by morphology (alteration, vein, breccia, haloes, etc.), mineral assemblages, textures, structures, host rocks (where identifiable), intensity and distribution of alteration, mineral contents, and relationships to hosts, igneous intrusions, deformation corridors, other alteration facies, breccia clasts, bedding, etc.

The resemblance of the IOAA metasomatites to more common rocks highlights the need for field mapping from least to most altered rocks (where possible). Additionally, the observation of atypical mineral assemblages or modal contents that are a key to recognizing these systems may be aided by portable XRF and gamma-ray spectrometers where metasomatites are fine-grained, and supported by geochemistry. As documented in the GBMZ, historic field and mineral exploration reports containing descriptions of banded iron formation, amphibolite, syenite, rhyolite, and white, very fine-grained silicification zones associated with seemingly disparate mineral showings, in terms of metal associations and proposed deposit types, should be re-evaluated in terms of IOAA potential. In Canada, under-developed prospects abound and the re-examination of their mineral systems may lead to the discoveries needed to renew mineral resources for the 21st century.

## Acknowledgments

This paper is a product of the Targeted Geoscience Initiative (TGI) and Geomapping for Energy and Minerals (GEM) programs of Natural Resources Canada (contribution 20200398) undertaken by the Geological Survey of Canada under collaborative agreements with the Northwest Territories Geological Survey, the Community Government of Gamètì and Fortune Minerals Limited. We thank all project participants, in particular the field crew, K. Lauzière (NRCan), V. Jackson (retired from NTGS) and GEM and TGI managers, administrative and technical teams. Close collaboration with territorial, Tłı̨chǫ and Sahtu governments, academia and private sector, in particular Fortune Minerals, Alberta Star Limited, Diamonds North, Cooper Minerals and the Denendeh Exploration and Mining Company (DEMCo) is also acknowledged. DEMCo kindly provided unpublished reports on the Camsell River district authored by C. Bowdidge, E.C. Walker and A. Dunford with permission of D. Beaulieu, CEO. We thank NTGS for permission to publish Figures 10A, B, 11C and 15H and V. Bennett for sharing these and other photos that led to the recognition of the potential nodular anhydrite at DeVries Lake. In addition, we could not have focused on alteration mapping without the superb quality of host lithological maps by R. Hildebrand, V. Jackson, S. Gandhi and P. Hoffman. Field work was permitted under the Aurora Research Institute Scientific Research licences 14548 and 14649, Wek'èezhìi Land and Water Board land use permits, Polar Continental Shelf Program and the Government of the Northwest Territories archaeological sites database agreements. The authors gratefully acknowledge the reviews of Anne-Aurélie Sappin and Raphaël Quentin de Gromard, the thorough edition of the manuscript prior to publication by Reginald Wilson, editor of the Geological Association of Canada, and previous internal reviews by I. McMartin, S. Simard, P.-S. Ross, C. Lawley and R. Enkin and JFM PhD examiners, G. Beaudoin, J. Franklin and R. Skirrow that led to this and companion papers.

## References


Acosta-Góngora, P., Gleeson, S., Ootes, L., Jackson, V.A., Lee, M., and Samson, I., 2011, Preliminary observations on the IOCG mineralization at the DAMP, Fab, and Nori showings and Terra-Norex Mines, Great Bear Magmatic Zone: Northwest Territories Geoscience Office, NWT Open Report 2011-001, 11 p.

Acosta-Góngora, P., Gleeson, S., Samson, I., Corriveau, L., Ootes, L., Taylor, B.E., Creaser, R.A., and Muehlenbachs, K., 2015, Genesis of the Paleoproterozoic NICO iron-oxide-cobalt-gold-bismuth deposit, Northwest Territories, Canada: evidence from isotope geochemistry and fluid inclusions: Precambrian Research, v. 268, p. 168-193.

Acosta-Góngora, P., Potter, E.G., Corriveau, L., Lawley, C.J.M., and Sparkes, G.W., 2019, Geochemistry of U±Cu±Mo±V mineralization, Central Mineral Belt, Labrador: differentiating between mineralization styles using a principal component analysis approach, *in* Rogers, N., ed., Targeted Geoscience Initiative: 2018 report of activities: Geological Survey of Canada, Open File 8549, p. 381-391.

Andersson, U.B., 2013, Coeval iron oxide and silicate magmas; structural evidence for immiscibility and mingling at Kiirunavaara and Luossavaara, Sweden: Society for Geology Applied to Mineral Deposits, 12th, Sweden, Extended Abstracts, p. 1633-1638.

Badham, J.P.N., and Morton, R.D., 1976, Magnetite-apatite intrusions and calc-alkaline magmatism, Camsell River, N.W.T: Canadian Journal of Earth Sciences, v. 13, p. 348-354.

Bardina, N.Y., and Popov, V.S., 1992, Classification of metasomatic rocks and facies of shallow metasomatism: International Geology Review, v. 34, p. 187-196.

Barton, M.D., Battles, D.A., Bebout, G.E., Capo, R.C., Christensen, J.N., Davis, S.R., Hanson, R.B., Michelsen, C.J., and Trim, H.E., 1988, Mesozoic contact metamorphism in the western United States, *in* Ernst, W.G., ed., Metamorphism and crustal evolution: Western conterminous United States, Rubey Volume VII, Prentice-Hall, Englewood Cliffs, New Jersey, p. 110-178.

Bennett, V., Rivers, T., and Jackson, V., 2012, A compilation of U-Pb zircon preliminary crystallization and depositional ages from the Paleoproterozoic southern Wopmay orogen, Northwest Territories: Northwest Territories Geoscience Office, NWT Open Report 2012-003, 172 p.

Blein, O., and Corriveau, L., 2017, Recognizing IOCG alteration facies at granulite facies in the Bondy Gneiss Complex of the Grenville Province: Proceedings of the 14th SGA Biennial Meeting, 20-23 August 2017, Québec City, p. 907-911.

Blein, O., Corriveau, L., Montreuil, J.-F., Ehrig, K., Fabris, A., Reid, A., and Pal, D., 2022, Geochemical signatures of metasomatic ore systems hosting IOCG, IOA, albite-hosted uranium and affiliated deposits: a tool for process studies and mineral exploration, *in* Corriveau, L., Potter, E.G. and Mumin, A.H., eds., Mineral systems with iron oxide copper-gold (IOCG) and affiliated deposits: Geological Association of Canada, Special Paper 52, p. 263-298.

Bonnet, A.-L., and Corriveau, L., 2007, Atlas et outils de reconnaissance de systèmes hydrothermaux métamorphisés dans les terranes gneissiques, *in* Goodfellow, W.D., ed., Mineral deposits of Canada: a synthesis of major deposit-types, district metallogeny, the evolution of geological provinces, and exploration methods: Geological Association of Canada, Mineral Deposits Division, Special Publication 5, DVD, 95 p.

Bowdidge, C., and Dunford, A., 2015, Camsell River property, Northwest Territories 86E09 and 86F12: Northwest Territories Geological Survey, Assessment Report 033952, 73 p.

Bowdidge, C., Walker, E.C., and Dunford, A., 2014a, DEMCo LTD. report on 2014 exploration Camsell River property, NTS 86E09, 86F12, Northwest Territories, 117°55'18" to 118°09'44" West, 65°33'34" to 65°38'33" North: Northwest Territories Geological Survey, Assessment Report 033596, 110 p.

Bowdidge, C., Walker, E.C., and Dunford, A., 2014b, IOCG style alteration and mineralization in a Proterozoic caldera, Camsell River, NWT, *in* Irwin, D. and Normandeau, P.X., compilers, 42nd Annual Yellowknife Geoscience Forum abstracts: Northwest Territories Geoscience Office, Yellowknife, NWT, YKGSF Abstracts Volume 2014, p. 18-19.

Brimhall, G.H., Dilles, J.H., and Proffett, J.M., 2006, The role of geologic mapping in mineral exploration: Society of Economic Geologists, Special Publication 12, p. 221-241.

Burnham, C.W., 1962, Facies and types of hydrothermal alteration: Economic Geology, v. 57, p. 768-784.

Canadian Mineralogist, 2018, The Canadian Mineralogist list of symbols for rock- and ore-forming minerals (September 30, 2018): Available at www.mineralogicalassociation.ca/index.php?p=116.

Carmichael, D., 1969, On the mechanism of prograde metamorphic reactions in quartz-bearing pelitic rocks: Contributions to Mineralogy and Petrology, v. 20, p. 244-267.

Carmichael, D., 1978, Metamorphic bathozones and bathograds: a measure of the depth of post-metamorphic uplift and erosion on the regional scale: American Journal of Science, v. 278, p. 769-797.

Cernuschi, F., 2017, Integrated interpretation of Anaconda-style mapping and core logging, trace element geochemistry and short wave infrared spectroscopy for the exploration of porphyry copper deposits: Decennial Minerals Exploration Conferences (DMEC), Geochemical and Infrared Spectral Mineralogical Data Integration for Mineral Exploration workshop, October 27, Toronto, Canada, available at dmec.ca.

Chao, E.C.T., Back, J.M., Minkin, J.A., Tatsumoto, M., Wang, J., Conrad, J.E., McKee, E.H., Hou, Z., Meng, Q., and Huang, S., 1997, The sedimentary carbonate-hosted giant Bayan Obo REE-Fe-Nb ore deposit of lnner Mongolia, China: a cornerstone example for giant polymetallic ore deposits of hydrothermal origin: US Geological Survey Bulletin 2143, 65 p.

Choi, S.G., Seo, J., Kim, D.W., Park, J.W., and Oh, C.W., 2011, Iron oxide-apatite (IOA)-type mineralization, Republic of Korea: the Yangyang magnetite deposit: Society for Geology Applied to Mineral Deposits, 11th, Antofagasta, Chile, Extended Abstracts, p. 506-508.

Corbett, G., 2018, Epithermal gold-silver and porphyry copper-gold exploration—Short course manual: Available at corbettgeology.com.

Corriveau, L., 1982, Physical conditions of the regional and retrograde metamorphism of the Chicoutimi area, Québec: Unpublished M.Sc. thesis, Queen's University, 264 p.

Corriveau, L., and Potter, E.G., in press, Advancing exploration for iron oxide-copper-gold and affiliated deposits in Canada: context, scientific overview, outcomes and impacts, *in* Pehrsson, S., Wodicka, N., Rogers, N. and Percival, J., eds., Canada's northern shield: new perspectives from the Geo-Mapping for Energy and Minerals Program: Geological Survey of Canada, Bulletin 612.

Corriveau, L., and Spry, P., 2014, Metamorphosed hydrothermal ore deposits, *in* Holland, H.D. and Turekian, K.K., eds., Treatise on Geochemistry, Second Edition, v. 13: Elsevier, p. 175-194.

Corriveau, L., Mumin, A.H., and Setterfield, T., 2010a, IOCG environments in Canada: characteristics, geological vectors to ore and challenges, *in* Porter, T.M., ed., Hydrothermal iron oxide copper-gold and related deposits: a global perspective, v. 4: PGC Publishing, Adelaide, p. 311-344.

Corriveau, L., Williams, P.J., and Mumin, A.H., 2010b, Alteration vectors to IOCG mineralisation - from uncharted terranes to deposits, *in* Corriveau, L. and Mumin, A.H., eds., Exploring for iron oxide copper-gold deposits: Canada and global analogues: Geological Association of Canada, Short Course Notes, No. 20, p. 89-110.

Corriveau, L., Nadeau, O., Montreuil, J.-F., and Desrochers, J.-P., 2014, Report of activities for the Core Zone: strategic geomapping and geoscience to assess the mineral potential of the Labrador Trough for multiple metals IOCG and affiliated deposits, Canada: Geological Survey of Canada, Open File 7714.

Corriveau, L., Lauzière, K., Montreuil, J.-F., Potter, E., Prémont, S., and Hanes, R., 2015, Dataset of new lithogeochemical analysis in the Great Bear magmatic zone, Northwest Territories, Canada: Geological Survey of Canada, Open File 7643, 19 p.

Corriveau, L., Montreuil, J.-F., and Potter, E.G., 2016, Alteration facies linkages among IOCG, IOA and affiliated deposits in the Great Bear magmatic zone, Canada, *in* Slack, J., Corriveau, L. and Hitzman, M., eds., Proterozoic iron oxide-apatite (± REE) and iron oxide-copper-gold and affiliated deposits of Southeast Missouri, USA, and the Great Bear magmatic zone, Northwest Territories, Canada: Economic Geology, v. 111, p. 2045-2072.

Corriveau, L., Blein, O., Gervais, F., Trapy, P.H., De Souza, S., and Fafard, D., 2018, Iron-oxide and alkali-calcic alteration, skarn, and epithermal mineralizing systems of the Grenville Province: the Bondy gneiss complex in the Central Metasedimentary Belt of Quebec as a case example - a field trip to the 14th Society for Geology Applied to Mineral Deposits (SGA) biennial meeting: Geological Survey of Canada, Open File 8349, 125 p.

Corriveau, L., Montreuil, J.-F., Blein, O., Ehrig, K., Potter, E.G., Fabris, A., and Clark, J., 2022a, Mineral systems with IOCG and affiliated deposits: part 2–geochemical footprints, *in* Corriveau, L., Potter, E.G. and Mumin, A.H., eds., Mineral systems with iron oxide copper-gold (IOCG) and affiliated deposits: Geological Association of Canada, Special Paper 52, p. 159-204.

Corriveau, L., Montreuil, J.-F., Potter, E.G., Blein, O., and De Toni, A.F., 2022b, Mineral systems with IOCG and affiliated deposits: part 3 – metal pathways and ore deposit model, *in* Corriveau, L., Potter, E.G. and Mumin, A.H., eds., Mineral systems with iron oxide copper-gold (IOCG) and affiliated deposits: Geological Association of Canada, Special Paper 52, p. 205-245.

Corriveau, L., Montreuil, J.-F., Potter, E.G., Ehrig, K., Clark, J., Mumin, A.H., and Williams, P.J., 2022c, Mineral systems with IOCG and affiliated deposits: part 1–metasomatic footprints of alteration facies, *in* Corriveau, L., Potter, E.G. and Mumin, A.H., eds., Mineral systems with iron oxide copper-gold (IOCG) and affiliated deposits: Geological Association of Canada, Special Paper 52, p. 113-158.

Corriveau, L., Mumin, A.H., and Potter, E.G., 2022d, Iron oxide copper-gold (Ag-Bi-Co-U-REE) and affiliated deposits: introduction and overview, *in* Corriveau, L., Potter, E.G. and Mumin, A.H., eds., Mineral systems with iron oxide copper-gold (IOCG) and affiliated deposits: Geological Association of Canada, Special Paper 52, p. 1-26.

Creasy, S.C., 1959, Some phase relations in the hydrothermally altered rocks of porphyry copper deposits: Economic Geology, v. 54, p. 351-373.

Daliran, F., Stosch, H.-G., Williams, P.J., Jamali, H., and Dorri, M.-B., 2022, Early Cambrian IOA-REE, U-Th and Cu(Au)-Bi-Co-Ni-Ag-As-sulphide deposits of the Bafq district, East-Central Iran, *in* Corriveau, L., Potter, E.G. and Mumin, A.H., eds., Mineral systems with iron oxide copper-gold (IOCG) and affiliated deposits: Geological Association of Canada, Special Paper 52, p. 409-424.

Day, W.C., Aleinikoff, J.N., du Bray, E., and Ayuso, R.A., 2017, Constraints on age of magmatism and iron oxide-apatite (IOA) and iron oxide copper-gold (IOCG) mineral deposit formation in the Mesoproterozoic St. Francois Mountains terrane of southeast Missouri, USA: Proceedings of the 14th SGA Biennial Meeting, 20-23 August 2017, Québec City, p. 855-857.

De Toni, A.F., 2016, Les paragénèses à magnétite des altérations associées aux systèmes à oxydes de fer et altérations en éléments alcalins, zone magmatique du Grand lac de l'Ours: Unpublished M.Sc. thesis, Institut national de la Recherche scientifique, 534 p.

Dmitrijeva, M., Ehrig, K.J., Ciobanu, C.L., Cook, N.J., Verdugo-Ihla, M.R., and Metcalfe, A.V., 2019, Defining IOCG signatures through compositional data analysis: a case study of lithogeochemical zoning from the Olympic Dam deposit, South Australia: Ore Geology Reviews, v. 105, p. 86-101.

Ehrig, K., McPhie, J., and Kamenetsky, V.S., 2012, Geology and mineralogical zonation of the Olympic Dam iron oxide Cu-U-Au-Ag deposit, South Australia, *in* Hedenquist, J.W., Harris, M. and Camus, F., eds., Geology and genesis of major copper deposits and districts of the world: a tribute to Richard H. Sillitoe: Economic Geology Special Publication 16, p. 237-267.

Einaudi, M.T., 1997, Mapping altered and mineralized rocks: an introduction to the Anaconda method: Unpublished report, Stanford, California, Department of Geological and Environmental Sciences, Stanford University, 16 p., available at researchgate.net.

Engvik, L., Stöckhert, B., and Engvik, A.K., 2009, Fluid infiltration, heat transport, and healing of microcracks in the damage zone of magmatic veins: numerical modeling: Journal of Geophysical Research, v. 114, B05203, doi:10.1029/2008JB005880.

Enkin, R.J., Montreuil, J.F., and Corriveau, L., 2012, Differential exhumation and concurrent fluid flow at the NICO Au–Co–Bi–Cu deposit and Southern Breccia U–Th–REE–Mo anomaly, Great Bear magmatic zone, NWT - A paleomagnetic and structural record: Geological Association of Canada – Mineralogical Association Canada, Joint Annual Meeting, Program with Abstracts, v. 35, p. 41.

Enkin, R.J., Corriveau, L., and Hayward, N., 2016, Metasomatic alteration control of petrophysical properties in the Great Bear magmatic zone (Northwest Territories, Canada): Economic Geology, v. 111, p. 2073-2085.

Gandhi, S.S., 1992, Magnetite deposits in metasiltstones of the Snare Group at Hump Lake, Northwest Territories: Geological Survey of Canada, Paper 92-1C, p. 225-235.

Gandhi, S.S., 1994, Geological setting and genetic aspects of mineral occurrences in the southern Great Bear Magmatic Zone, Northwest Territories, *in* Sinclair, W.D. and Richardson, D.G., eds., Studies of rare-metal deposits in the Northwest Territories: Geological Survey of Canada, Bulletin 475, p. 63-96.

Gandhi, S.S., and van Breemen, O., 2005, SHRIMP U-Pb geochronology of detrital zircons from the Treasure Lake Group; new evidence for Paleoproterozoic collisional tectonics in the southern Hottah Terrane, northwestern Canadian Shield: Canadian Journal of Earth Sciences, v. 42, p. 833-845.

Gandhi, S.S., Carrière, J.J., and Prasad, N., 2000, Implications of a preliminary fluid-inclusion study of giant quartz veins of the southern Great Bear magmatic zone, Northwest Territories: Geological Survey of Canada Paper 2000-1C, 13 p.

Gandhi, S.S., Mortensen, J.K., Prasad, N., and van Breemen, O., 2001, Magmatic evolution of the southern Great Bear continental arc, northwestern Canadian Shield: geochronological constraints: Canadian Journal of Earth Sciences, v. 38, p. 767-785.

Gandhi, S.S., Montreuil, J-F., and Corriveau, L., 2014, Geology and mineral occurrences, Mazenod Lake - Lou Lake area, Northwest Territories: Geological Survey of Canada, Canadian Geoscience Map 148, (ed. prelim.), 1 sheet.

Gardner, R.L., Piazolo, S., and Daczko, N.R., 2015, Pinch and swell structures: evidence for strain localisation by brittle–viscous behaviour in the middle crust: Solid Earth, v. 6, p. 1045-1061.

Gifkins, C., Herrmann, W., and Large, R., 2005, Altered volcanic rocks – A guide to description and interpretation: Centre for Ore Deposit Research, University of Tasmania, 275 p.

Goad, R.E., Mumin, A.H., Duke, N.A., Neale, K.L., and Mulligan, D.L., 2000a, Geology of the Proterozoic iron oxide-hosted, NICO cobalt-gold-bismuth, and Sue Dianne copper-silver deposits, southern Great Bear magmatic zone, Northwest Territories, Canada, *in* Porter, T.M., ed., Hydrothermal iron oxide copper-gold and related deposits. a global perspective, v. 1: PGC Publishing, Adelaide, p. 249-267.

Goad, R.E., Mumin, A.H., Duke, N.A., Neale, K.L., Mulligan, D.L., and Camier, W.J., 2000b, The NICO and Sue-Dianne Proterozoic, iron oxide-hosted, polymetallic deposits, Northwest Territories. Application of the Olympic Dam model in exploration: Exploration Mining Geology, v. 9, p. 123-140.

Goscombe, B.D., Passchier, C.W., and Hand, M., 2004, Boudinage classification: end-member boudin types and modified boudin structures: Journal of Structural Geology, v. 26, p. 739-763.

Harlov, D.E., and Austrheim, H., 2012, Metasomatism and the chemical transformation of rock: Lecture Notes in Earth System Sciences, 789 p.

Harlov, D.E., Andersson, U.B., Förster, H.-J., Nyström, J.O., Dulski, P., and Broman, C., 2002, Apatite–monazite relations in the Kiirunavaara magnetite–apatite ore, northern Sweden: Chemical Geology, v. 191, p. 47-72.

Harlov, D.E., Wirth, R., and Förster, H.-J., 2005, An experimental study of dissolution–reprecipitation in fluorapatite: fluid infiltration and the formation of monazite: Contributions to Mineralogy and Petrology, v. 150, p. 268-286.

Harlov, D.E., Meighan, C.J., Kerr, I.D., and Samson, I.M., 2016, Mineralogy, chemistry, and fluid-aided evolution of the Pea Ridge Fe oxide- (Y + REE) deposit, southeast Missouri, USA, *in* Slack, J., Corriveau, L. and Hitzman, M., eds., Proterozoic iron oxide-apatite (± REE) and iron oxide-copper-gold and affiliated deposits of Southeast Missouri, USA, and the Great Bear magmatic zone, Northwest Territories, Canada: Economic Geology, v. 111, p. 1963-1984.

Hayward, Na., Enkin, R.J., Corriveau, L., Montreuil, J-F., and Kerswill, J., 2013, The application of rapid potential field methods for the targeting of IOCG mineralisation based on physical property data, Great Bear magmatic zone, Canada: Journal of Applied Geophysics, v. 94, p. 42-58.

Hayward, Na., Corriveau, L., Craven, J.A., and Enkin, R.J., 2016, Geophysical signature of the NICO Au-Co-Bi-Cu deposit and its iron oxide-alkali alteration system, Northwest Territories, Canada, *in* Slack, J., Corriveau, L. and Hitzman, M., eds., Proterozoic iron oxide-apatite (± REE) and iron oxide-copper-gold and affiliated deposits of Southeast Missouri, USA, and the Great Bear magmatic zone, Northwest Territories, Canada: Economic Geology, v. 111, p. 2087-2110.

Hayward, Ni., and Skirrow, R.G., 2010, Geodynamic setting and controls on iron oxide Cu-Au (±U) ore in the Gawler craton, South Australia, in Porter, T.M., ed., Hydrothermal iron oxide copper-gold and related deposits: a global perspective, v. 3: PGC Publishing, Adelaide, p. 119-146.

Hildebrand, R.S., 1983, Geology - Echo Bay-MacAlpine Channel area, district of Mackenzie, Northwest Territories: Geological Survey of Canada, Map 1546A, scale 1:50 000.

Hildebrand, R.S., 1984a, Geology of the Rainy Lake-White Eagle Falls area, District of Mackenzie: Early Proterozoic cauldrons, stratovolcanoes and subvolcanic plutons: Geological Survey of Canada, Paper 83-20, 42 p., 1 map.

Hildebrand, R.S., 1984b, Folded cauldrons of the early Proterozoic LaBine Group, northwestern Canadian shield: Journal of Geophysical Research, v. 89, p. 8429-8440.

Hildebrand, R.S., 1986, Kiruna-type deposits: their origin and relationship to intermediate subvolcanic plutons in the Great Bear magmatic zone, Northwestern Canada: Economic Geology, v. 81, p. 640-659.

Hildebrand, R.S., 2011, Geological synthesis of Northern Wopmay Orogen / Coppermine Homocline, Northwest Territories – Nunavut: Geological Survey of Canada, Open File 6390, Northwest Territories Geoscience Office, Open Report 2010-011, 1 map, scale 1:500 000.

Hildebrand, R.S., 2017, Precambrian geology, Leith Peninsula-Rivière Grandin area, Northwest Territories: Geological Survey of Canada, Canadian Geoscience Map 153, (ed. prelim.), 1 sheet.

Hildebrand, R.S., Hoffman, P.F., and Bowring, S.A., 1987, Tectono-magmatic evolution of the 1.9 Ga Great Bear magmatic zone, Wopmay Orogen, Northwestern Canada: Journal of Volcanology and Geothermal Research, v. 32, p. 99-118.

Hildebrand, R.S., Hoffman, P.F., Housh, T., and Bowring, S.A., 2010, The nature of volcano-plutonic relations and shapes of epizonal plutons of continental arcs as revealed in the Great Bear magmatic zone, northwestern Canada: Geosphere, v. 6, p. 812-839.

Hildebrand, R.S., Bowring, S., and Pelleter, K.F., 2014, Calder River, map area: Geological Survey of Canada, Canadian Geoscience Map Series, CGM 154/ NWT Open Report 2013-03, 1 map sheet.

Hitzman, M.C., 2000, Iron oxide-Cu-Au deposits. What, where, when, and why?, *in* Porter, T.M., ed., Hydrothermal iron oxide copper-gold and related deposits. A global perspective, v. 1: PGC Publishing, Adelaide, p. 9-25.

Hitzman, M.C., Oreskes, N., and Einaudi, M.T., 1992, Geological characteristics and tectonic setting of Proterozoic iron oxide (Cu-U-Au-REE) deposits: Precambrian Research, v. 58, p. 241-287.

Huang, X.-W., Beaudoin, G., De Toni, A.-F., Corriveau, L., Makvandi, S., and Boutroy, E., 2022, Iron-oxide trace element fingerprinting of iron oxide copper-gold and iron oxide-apatite deposits: a review, *in* Corriveau, L., Potter, E.G. and Mumin, A.H., eds., Mineral systems with iron oxide copper-gold (IOCG) and affiliated deposits: Geological Association of Canada, Special Paper 52, p. 347-364.

Jackson, V.A., 2008, Preliminary geologic map of part of the southern Wopmay Orogen (parts of NTS 86B and 86C; 2007 updates; descriptive notes to accompany 1:100,000 scale map: Northwest Territories Geoscience Office, NWT Open Report 2008-007, 51 p.

Jackson, V.A., and Ootes, L., 2012, Preliminary geologic map of the south-central Wopmay Orogen (parts of NTS 86B, 86C, and 86D); results from 2009 to 2011: NWT Geoscience Office, NWT Open Report 2012-004, 1 map, 1:100,000 scale.

Jackson, V.A., van Breemen, O., Ootes, L., Bleeker, W., Bennett, V., Davis, W.D., Ketchum, J., and Smar, L., 2013, Ages of basement and intrusive phases East of the Wopmay fault zone, south-central Wopmay Orogen, NWT: a field-based U–Pb zircon study: Canadian Journal of Earth Sciences, v. 50, p. 979-1006.

Jébrak, M., 2010, Use of breccias in IOCG(U) exploration, *in* Corriveau, L. and Mumin, A.H., eds., Exploring for iron oxide copper–gold deposits: Canada and global analogues: Geological Association of Canada, Short Course Notes, No. 20, p. 79-88.

Jébrak, M., 2022, Use of breccias in IOCG exploration: an updated review, *in* Corriveau, L., Potter, E.G. and Mumin, A.H., eds., Mineral systems with iron oxide copper-gold (IOCG) and affiliated deposits: Geological Association of Canada, Special Paper 52, p. 315-324.

Katona, L., and Fabris, A., 2022, Defining geophysical signatures of IOCG deposits in the Olympic Copper-Gold province, South Australia, using geophysics, GIS and spatial statistics, *in* Corriveau, L., Potter, E.G. and Mumin, A.H., eds., Mineral systems with iron oxide copper-gold (IOCG) and affiliated deposits: Geological Association of Canada, Special Paper 52, p. 299-313.

Knox, A.W., 1998, Geological report on the Hillside zinc–lead–silver showing, Grouard Lake property: Northwest Territories Geoscience Office, Assessment Report 084043, 32 p.

Large, R.R., Gemmell, J.B., Paulick, H., and Huston, D.L., 2001, The alteration box plot-A simple approach to understanding the relationship between alteration mineralogy and lithogeochemistry associated with volcanic-hosted massive sulfide deposits: Economic Geology, v. 96, p. 957-971.

Lee, S.H., and Stout, J.H., 1989, Phase equilibria of coexisting minerals from amphibolites and syenitic rocks in the Yangyang magnetite deposits, Korea. Journal of the Geological Society of Korea, v. 25, p. 365-380.

Mark, G., Oliver, N.H.S., and Williams, P.J., 2006, Mineralogical and chemical evolution of the Ernest Henry Fe oxide-Cu-Au ore system, Cloncurry district, northwest Queensland, Australia: Mineralium Deposita, v. 40, p. 769-801.

Marschik, R., and Fontboté, L., 2001, The Candelaria–Punta del Cobre iron oxide Cu–Au (–Zn–Ag) deposits, Chile: Economic Geology, v. 96, p. 1799-1826.

Marshall, D., Anglin, C.D., and Mumin, A.H., 2004, Ore mineral atlas: Geological Association of Canada, Mineral Deposits Division, 112 p.

McCallum, M.E., 1985, Experimental evidence for fluidization processes in breccia pipe formation: Economic Geology, v. 80, p. 1523-1543.

Monteiro, L.V.S., Xavier, R.P., Carvalho, E.R., Hitzman, M.W., Johnson, C.A., Souza Filho, C.R., and Torresi, I., 2008, Space and temporal zoning of hydrothermal alteration and mineralization in the Sossego iron oxide-copper-gold deposit, Carajás Mineral Province, Brazil: paragenesis and stable isotope constraints: Mineralium Deposita, v. 43, p. 129-159.

Montreuil, J.-F., Corriveau, L., and Long, B., 2012, Porosity in albitites and the development of albitite-hosted U deposits: insights from X-ray computed tomography: CT Scan workshop, Development on non-medical environment, Québec, INRS, p. 5.

Montreuil, J.-F., Corriveau, L., and Grunsky, E.C., 2013, Compositional data analysis of IOCG systems, Great Bear magmatic zone, Canada: to each alteration types its own geochemical signature: Geochemistry: Exploration, Environment, Analysis, v. 13, p. 229-247.

Montreuil, J.-F., Corriveau, L., and Potter, E.G., 2015, Formation of albitite-hosted uranium within IOCG systems: the Southern Breccia, Great Bear magmatic zone, Northwest Territories, Canada: Mineralium Deposita, v. 50, p. 293-325.

Montreuil, J.-F., Corriveau, L., and Davis, W.J., 2016a, Tectonomagmatic evolution of the southern Great Bear magmatic zone (Northwest Territories, Canada) – Implications on the genesis of iron oxide alkali-altered hydrothermal systems, *in* Slack, J., Corriveau, L. and Hitzman, M., eds., Proterozoic iron oxide-apatite (± REE) and iron oxide-copper-gold and affiliated deposits of Southeast Missouri, USA, and the Great Bear magmatic zone, Northwest Territories, Canada: Economic Geology, v. 111, p. 2111-2138.

Montreuil, J.-F., Corriveau, L., Potter, E.G., and De Toni, A.F., 2016b, On the relation between alteration facies and metal endowment of iron oxide–alkali-altered systems, southern Great Bear Magmatic Zone (Canada), *in* Slack, J., Corriveau, L. and Hitzman, M., eds., Proterozoic iron oxide-apatite (± REE) and iron oxide-copper-gold and affiliated deposits of Southeast Missouri, USA, and the Great Bear magmatic zone, Northwest Territories, Canada: Economic Geology, v. 111, p. 2139-2168.

Montreuil, J.-F., Potter, E.G., Corriveau, L., and Davis, W.J., 2016c, Element mobility patterns in magnetite-group IOCG systems: the Fab IOCG system, Northwest Territories, Canada: Ore Geology Reviews, v. 72, p. 562-584.

Mumin, A.H. (ed.), 2015, Echo Bay IOCG thematic map series: geology, structure and hydrothermal alteration of a stratovolcano complex, Northwest Territories, Canada: Geological Survey of Canada, Open File 7807, 19 p., 18 sheets.

Mumin, A.H., Corriveau, L., Somarin, A.K., and Ootes, L., 2007, Iron oxide copper-gold-type polymetallic mineralisation in the Contact Lake Belt, Great Bear Magmatic Zone, Northwest Territories, Canada: Exploration and Mining Geology, v. 16, p. 187-208.

Mumin, A.H., Somarin, A.K., Jones, B., Corriveau, L., Ootes, L., and Camier, J., 2010, The IOCG-porphyry-epithermal continuum of deposits types in the Great Bear magmatic zone, Northwest Territories, Canada, *in* Corriveau, L. and Mumin, A.H., eds., Exploring for iron oxide copper-gold deposits: Canada and global analogues: Geological Association of Canada, Short Course Notes, No. 20, p. 59-78.

Mumin, A.H., Phillips, A., Katsuragi, C.J., Mumin, A., and Ivanov, G., 2014, Geotectonic interpretation of the Echo Bay stratovolcano complex, northern Great Bear magmatic zone, NWT, Canada: Northwest Territories Geoscience Office, NWT Open File 2014, 44 p.

Neuendorf, K.K.E., Mehl, J.P. Jr, and Jackson, J.A., 2005, Glossary of geology: American Geological Institute, Fifth Edition, 779 p.

Nold, J.L., Davidson, P., and Dudley, M.A., 2013, The Pilot Knob magnetite deposit in the Proterozoic St. Francois Mountains Terrane, southeast Missouri, USA: a magmatic and hydrothermal replacement iron deposit: Ore Geology Reviews, v. 53, p. 446-469.

Nold, J.L., Dudley, M.A., and Davidson, P., 2014, The Southeast Missouri (USA) Proterozoic iron metallogenic province—Types of deposits and genetic relationships to magnetite–apatite and iron oxide–copper–gold deposits: Ore Geology Reviews, v. 57, p. 154-171.

Normandeau, P.X., Harlov, D.E., Corriveau, L., Paquette, J., and McMartin, I., 2018, Characterization of fluorapatite within iron oxide alkali-calcic alteration systems of the Great Bear magmatic zone: a potential metasomatic process record: The Canadian Mineralogist, v. 56, p. 1-21.

North, J., 1995, Report on geological reconnaissance, prospecting, lithogeochemical sampling, steam sediment sampling, and interpretation of the Squirrel Lake property, Great Bear magmatic zone, district of Mackenzie, Northwest Territories: Northwest Territories Geoscience Office, Assessment Report 083647, 198 p.

Oliver, N.H.S., and Bons, P.D., 2001, Mechanisms of fluid flow and fluid–rock interaction in fossil metamorphic hydrothermal systems inferred from vein–wallrock patterns, geometry and microstructure: Geofluids, v. 1, p. 137-162.

Oliver, N.H.S., Mark, G., Pollard, P.J., Rubenach, M.J., Bastrakov, E., Williams, P.J., Marshall, L.C., Baker, T., and Nemchin, A.A., 2004, The role of sodic alteration in the genesis of iron oxide-copper–gold deposits: geochemistry and geochemical modelling of fluid-rock interaction in the Cloncurry district, Australia: Economic Geology, v. 99, p. 1145-1176.

Oliver, N.H.S., Rubenach, M.J., Baker, B.F., Blenkinsop, T.G., Cleverley, J.S., Marshall, L.J., and Ridd, P.J., 2006, Granite-related overpressure and volatile release in the mid crust: fluidized breccias from the Cloncurry district, Australia: Geofluids, v. 6, p. 346-358.

Oliver, N.H.S., Butera, K.M., Rubenach, M.J., Marshall, L.J., Cleverley, J.S., Mark, G., Tullemans, F., and Esser, D., 2008, The protracted hydrothermal evolution of the Mount Isa Eastern Succession: a review and tectonic implications: Precambrian Research, v. 163, p. 108-130.

Ootes, L., Jackson, V.A., and Corriveau, L., 2008, Assay results from the South Wopmay bedrock mapping project (2006–2007 field seasons): Northwest Territories Geoscience Office, NWT Open Report 2008-008, 13 p.

Ootes, L., Goff, S., Jackson, V., Gleeson, S., Creaser, R., Samson, I.M., Evensen, N., Corriveau, L., and Mumin, A.H., 2010, Timing and thermochemical constraints on multi-element mineralization at the Nori/RA Cu–Mo–U prospect, Great Bear magmatic zone, Northwest Territories, Canada: Mineralium Deposita, v. 45, p. 549-566.

Ootes, L., Snyder, D., Davis, W.J., Acosta-Góngora, P., Corriveau, L., Mumin, A.H., Montreuil, J.-F., Gleeson, S.A., Samson, I.A., and Jackson, V.A., 2017, A Paleoproterozoic Andean-type iron oxide copper-gold environment, the Great Bear magmatic zone, Northwest Canada: Ore Geology Reviews, v. 81, p. 123-139.

Otake, T., Wesolowski, D.J., Anovitz, L.M., Allard, L.F., and Ohmoto, H., 2010, Mechanisms of iron oxide transformations in hydrothermal systems: Geochimica et Cosmochimica Acta, v. 74, p. 6141-6156.

Passchier, C.W., Myers, J.S., and Kröner, A., 1990, Field geology of high-grade gneiss terrains: Springer Verlag, Germany, 150 p.

Pattison, D.R.M., St-Onge, M.R., and Bégin, N.J., 2005, Preface, *in* Pattison, D.R.M., St-Onge, M.R., Bégin, N.J. and Martin, R.F., eds., Truth and beauty in metamorphism: a tribute to Dugald M. Carmichael: The Canadian Mineralogist, v. 43, p. 1-10.

Pelleter, E., Gasquet, D., Cheilletz, A., and Mouttaqi, A., 2010, Alteration processes and impacts on regional-scale element mobility and geochronology, Tamlalt–Menhouhou deposit, Morocco, *in* Corriveau, L. and Mumin, A.H., eds., Exploring for iron oxide copper–gold deposits: Canada and global analogues: Geological Association of Canada, Short Course Notes, No. 20, p. 177-185.

Percival, J.B., Potter, E.G., Lauzière, K., Ijewliw, O., Bilot, I., Hunt, P., English, M.L.R., Olejarz, A.D., Laudadio, A.B., Enright, A., Robillard, K.-L., and Corriveau, L., 2016, Mineralogy, petrography and autoradiography of selected samples from the Contact Lake and NICO areas, Great Bear Magmatic Zone, Northwest Territories (IOCG-GEM Project): Geological Survey of Canada, Open File 7755, 48 p.

Porter, T.M., 2010, Current understanding of iron oxide associated-alkali altered mineralised systems. Part 1 - An overview, *in* Porter, T.M., ed., Hydrothermal iron oxide copper-gold and related deposits. A global perspective, v. 3: PGC Publishing, Adelaide, p. 5-32.

Potter, E.G., Montreuil, J.-F., Corriveau, L., and De Toni, A., 2013, Geology and hydrothermal alteration of the Fab Lake region, Northwest Territories: Geological Survey of Canada, Open File 7339, 26 p.

Potter, E.G., Montreuil, J.-F., Corriveau, L., and Davis, W., 2019, The Southern Breccia metasomatic uranium system of the Great Bear magmatic zone, Canada: iron oxide-copper-gold (IOCG) and albitite-hosted uranium linkages, *in* Decrée, S. and Robb, L., eds., Ore deposits: origin, exploration, and exploitation: Geophysical Monograph 242, First Edition, American Geophysical Union, John Wiley & Sons, Inc., p. 109-130.

Potter, E.G., Acosta-Góngora, P., Corriveau, L., Montreuil, J-F., and Yang, Z., 2022, Uranium enrichment processes in iron oxide and alkali-calcic alteration systems as revealed by uraninite trace element chemistry, *in* Corriveau, L., Potter, E.G. and Mumin, A.H., eds., Iron oxide copper-gold (Ag-Bi-Co-U-REE) and affiliated deposits: Geological Association of Canada, Special Paper 52, p. 325-345.

Poulet, T., Karrech, A., Regenauer-Lieb, K., Fisher, L., and Schaubs, P., 2012, Thermal–hydraulic–mechanical–chemical coupling with damage mechanics using ESCRIPTRT and ABAQUS: Tectonophysics, v. 526-529, p. 124-132.

Putnis, A., and Austrheim, H., 2010, Fluid-induced processes: metasomatism and metamorphism: Geofluids, v. 10, p. 254-269.

Putnis A., and Austrheim, H., 2012, Mechanisms of metasomatism and metamorphism on the local mineral scale: the role of dissolution-reprecipitation during mineral reequilibration, *in* Harlov, D.E. and Austrheim, H., eds., Metasomatism and the chemical transformation of rock: Lecture Notes in Earth System Sciences, p. 139-167.

Ross, P.S., Jébrak, M., and Walker, B.M., 2002, Discharge of hydrothermal fluids from a magma chamber and concomitant formation of a stratified breccia zone at the Questa porphyry molybdenum deposit, New Mexico: Economic Geology, v. 97, p. 1679-1699.

Rubenach, M.J., 2012, Structural controls of metasomatism on a regional scale, *in* Harlov, D.E. and Austrheim, H., eds., Metasomatism and the chemical transformation of rock: Lecture Notes in Earth System Sciences, Springer, p. 93-140.

Rubenach, M.J., and Lewthwaite, K.A., 2002, Metasomatic albitites and related biotite-rich schists from a low-pressure polymetamorphic terrane, Snake Creek Anticline, Mount Isa Inlier, north-eastern Australia: microstructures and P-T-d paths: Journal of Metamorphic Geology, v. 20, p. 191-202.

Schmid, R., Fettes, D., Harte, B., Davis, E., and Desmons, J., 2007, How to name a metamorphic rock. Recommendations by the IUGS Subcommission on the Systematics of Metamorphic Rocks: Web version 01/02/07 at www.bgs.ac.uk/scmr/home.html.

Shives, R.B.K., 2015, Using gamma ray spectrometry to find rare metals, *in* Simandl, G.J. and Neetz, M., eds., Symposium on strategic and critical materials proceedings, November 13-14, 2015, Victoria, British Columbia: British Columbia Ministry of Energy and Mines, British Columbia Geological Survey Paper 2015-3, p. 199-209.

Sidor, M., 2000, The origin of black rock alteration overprinting iron-rich sediments and its genetic relationship to disseminated polymetallic sulphide ores, Lou Lake, Northwest Territories, Canada: Unpublished M.Sc. Thesis, London, Canada, University of Western Ontario, 243 p.

Skirrow, R., 2010, "Hematite-group" IOCG±U ore systems. Tectonic settings, hydrothermal characteristics, and Cu-Au and U mineralizing processes, *in* Corriveau, L. and Mumin, A.H., eds., Exploring for iron oxide copper-gold deposits: Canada and global analogues: Geological Association of Canada, Short Course Notes, No. 20, p. 39-58.

Skirrow, R.G., 2022, Hematite-group IOCG ± U deposits: an update on their tectonic settings, hydrothermal characteristics, and Cu-Au-U mineralizing processes, *in* Corriveau, L., Potter, E.G. and Mumin, A.H., eds., Mineral systems with iron oxide copper-gold (IOCG) and affiliated deposits: Geological Association of Canada, Special Paper 52, p. 27-51.

Skirrow, S.G., Murr, J., Schofield, A., Huston, D.L., van der Wielen, S., Czarnota, K., Coghlan, R., Highet, L.M., Connolly, D., Doublier, M., and Duan, J., 2019, Mapping iron oxide Cu-Au (IOCG) mineral potential in Australia using a knowledge-driven mineral systems-based approach: Ore Geology Reviews, v. 113, 103011.

Smith, M.P., Campbell, L.S., and Kynicky, J., 2015, A review of the genesis of the world class Bayan Obo Fe–REE–Nb deposits, Inner Mongolia, China: multistage processes and outstanding questions: Ore Geology Reviews, v. 64, p. 459-476.

Somarin, A.K., and Mumin, A.H., 2012, The Paleoproterozoic high heat production Richardson granite, Great Bear magmatic zone, Northwest Territories, Canada: source of U for Port Radium?: Resources Geology, v. 62, p. 227-242.

Somarin, A.K., and Mumin, A.H., 2014, P–T-composition and evolution of paleofluids in the Paleoproterozoic Mag Hill IOCG hydrothermal system, Contact Lake belt, Northwest Territories, Canada: Mineralium Deposita, v. 49, p. 199-215.

Thompson, A.J.B., and Thompson, J.F.H., 1996, A field and petrographic guide to hydrothermal alteration minerals: Geological Association of Canada, Mineral Deposits Division, 119 p.

Vivian, G., 1991, Aber Resources Limited: report on 1991 geological and geophysical programme, DeVries Lake project: Northwest Territories Geological Survey, Assessment Report 083158, 60 p., 1 map.

Whitney, D.L., and Evans, B.W., 2010, Abbreviations for names of rock-forming minerals: American Mineralogist, v. 95, p. 185-187.

Williams, M.R., Holwell, D.A., Lilly, R.M., Case, G.N.D., and McDonald, I., 2015, Mineralogical and fluid characteristics of the fluorite-rich Monakoff and E1 Cu–Au deposits, Cloncurry region, Queensland, Australia: implications for regional F–Ba-rich IOCG mineralisation: Ore Geology Reviews, v. 64, p. 103-127.

Williams, P.J., 1994, Iron mobility during synmetamorphic alteration in the Selwyn Range area, NW Queensland: implications for the origin of ironstone-hosted Au-Cu deposits: Mineralium Deposita, v. 29, p. 250-260.

Williams, P.J., Barton, M.D., Johnson, D.A., Fontboté, L., de Haller, A., Mark, G., Oliver, N.H.S., and Marschik, R., 2005, Iron oxide copper-gold deposits; geology, space-time distribution, and possible modes of origin: Economic Geology 100th Anniversary Volume, p. 371-405.

Zamannejad, A., Jahani, D., Lotfpour, M., and Movahed, B., 2013, Mixed evaporite/carbonate characteristics of the Triassic Kangan Formation, offshore area, Persian Gulf: Revista Mexicana de Ciencias Geológicas, v. 30, p. 540-551.

Zhao, X.-F., Chen, H., Zhao, L., and Zhou, M.-F., 2022, Linkages among IOA, skarn, and magnetite-group IOCG deposits in China: from deposit studies to mineral potential assessment, *in* Corriveau, L., Potter, E.G. and Mumin, A.H., eds., Mineral systems with iron oxide copper-gold (IOCG) and affiliated deposits: Geological Association of Canada, Special Paper 52, p. 383-407.

Zharikov, V.A., Pertsev, F.N., Rusinov, V.L., Callegari, E., and Fettes, D.J., 2007, Metasomatism and metasomatic rocks: Recommendations by the IUGS Subcommission on the Systematics of Metamorphic Rocks, Web version 01.02.07 at www.bgs.ac.uk/scmr/home.html.

# Mineral Systems with IOCG and Affiliated Deposits: Part 1 – Metasomatic Footprints of Alteration Facies


**Louise Corriveau**
*Natural Resources Canada, Geological Survey of Canada, Québec, Canada*
*louise.corriveau@NRCan-RNCan.gc.ca*

**Jean-Francois Montreuil**
*Red Pine Exploration, Ontario, Canada*

**Eric Potter**
*Natural Resources Canada, Geological Survey of Canada, Ontario, Canada*

**Kathy Ehrig, Jesse M. Clark**
*BHP-Olympic Dam, Adelaide, Australia*

**A. Hamid Mumin**
*Department of Geology, Brandon University, Manitoba, Canada*

**Patrick J. Williams**
*In memoriam*



*Recommended citation: Corriveau, L., Montreuil, J.-F., Potter, E.G., Ehrig, K., Clark, J.M., Mumin, A.H., and Williams, P.J., 2022, Mineral systems with IOCG and affiliated deposits: part 1 – metasomatic footprints of alteration facies, in Corriveau, L., Potter, E.G. and Mumin, A.H., eds., Mineral systems with iron oxide copper-gold (IOCG) and affiliated deposits: Geological Association of Canada, Special Paper 52, p. 113-158.*



## Abstract

Metasomatic mineral systems with iron oxide and alkali-calcic hydrothermal alteration chemically and texturally transform significant volumes of the upper crust and produce iron oxide copper-gold (IOCG), iron oxide-apatite (IOA) and affiliated critical metal deposits. By combining the silicate, carbonate and phosphate alteration assemblages with iron oxides, a diagnostic set of alteration 'facies' emerges. A systematic sequence of crosscutting relationships amongst these facies, and spatial zoning relative to depth and heat sources, are illustrated using examples from the Great Bear magmatic zone in Canada, and the Ernest Henry copper-gold and Cu-U-Au-Ag Olympic Dam IOCG deposits in Australia. Facies 1 Na (albite, minor scapolite, residual quartz) is the earliest, most extensive and commonly deepest facies. It forms albitite (composed of >80 modal % albite) corridors up to tens of kilometres long, either at the roots of the systems above intrusions or along major fault zones where the albitite becomes extensively brecciated. The Na facies transitions through Na-Ca (albite-scapolite) and high-temperature Na-Ca-Fe (albite, amphibole, magnetite) assemblages to Facies 2, which is defined by high-temperature Ca-Fe mineral assemblages (amphibole, magnetite, apatite) that replace, vein and cement breccias within albitite zones and least-altered host rocks. The largest footprint of this Ca-Fe facies occurs in carbonate-bearing sedimentary sequences where skarn (clinopyroxene, garnet) may form early, pre to syn albitite, but is progressively replaced by the high-temperature Ca-Fe assemblages. Facies 1 to 2 delineate areas of interest at the regional scale, and also host magnetite skarn and iron oxide-apatite (IOA) deposits. Systems that evolve to Facies 3 high-temperature K-Fe (magnetite-K-feldspar/biotite), Facies 4a K-skarn (clinopyroxene, garnet, K-feldspar), Facies 4b K-felsite (K-feldspar), and Facies 5 lower-temperature K-Fe ± Ca, Mg, $H^+$, $CO_2$, Si and Ba (sericite, K-feldspar, hematite, chlorite, carbonate, epidote) have the capacity to produce extensive breccia zones and significant IOCG deposits. Facies 6 low-temperature K, Si, Al ± Ba, Fe comprises vein systems, phyllic alteration and epithermal lithocaps. The well-constrained relationships among iron oxide and alkali-calcic alteration facies and their distribution within the Australian and Canadian case studies provide a robust framework to interpret fluid pathways and system development globally.

## Résumé

Les systèmes minéralisateurs métasomatiques à altération hydrothermale alcali-calcique et à oxydes de fer transforment chimiquement et texturalement d'importants volumes de la croûte supérieure et produisent des gîtes à oxydes de fer cuivre-or (IOCG), oxydes de fer-apatite (IOA) et gîtes à métaux critiques affiliés. En combinant les oxydes de fer aux assemblages d'altération à silicates, carbonates et phosphates, un ensemble diagnostique de " faciès " d'altération émerge. La cristallisation et la bréchification régulière des faciès de la racine des systèmes à la surface et latéralement, distales à proximales des sources de chaleur, définissent le cheminement métasomatique prograde des systèmes. Ces faciès présentent une séquence de cristallisation régulière qui définit le cheminement prograde de ces systèmes minéralisateurs. Cet article décrit et illustre les faciès d'altération alcali-calcique et à oxydes de fer au sein des systèmes de la zone magmatique du Grand lac de l'Ours et les compare à ceux des gîtes IOCG d'Ernest Henry (cuivre-or) et d'Olympic Dam (Cu-U-Au-Ag ) en Australie pour mieux cadrer l'interprétation de ces systèmes à l'échelle mondiale. Le Faciès 1 Na (albite, scapolite occasionnelle et quartz résiduel) est le faciès le plus précoce, étendu et généralement profond et mène à la formation de corridors d'albitite (>80 % d'albite) de dizaines de kilomètres de long soit le long de zones de failles majeures où l'albitite se fait bréchifiée ou à la racine des systèmes au-dessus d'intrusions. Le Faciès 1 Na transite par de l'altération à assemblages à Na-Ca (albite, scapolite) et Na-Ca-Fe de haute température (albite, amphibole, magnétite) vers le Faciès 2 à assemblages à Ca-Fe de haute température (amphibole, magnétite, apatite) et ses zones de remplacement, veines et remplissage de brèches au sein d'albitite ou roches peu altérées. La plus large empreinte de ce faciès à Ca-Fe est dans les séquences sédimentaires carbonatées où du skarn (clinopyroxène, grenat) précoce y est progressivement remplacé par des assemblages à Ca-Fe de haute température. Les faciès 1 à 2 délimitent les zones d'intérêt à l'échelle régionale et forment les encaissants immédiats de skarn à magnétite et de gîtes à oxydes de fer-apatite (IOA). Les systèmes qui évoluent jusqu'au Faciès 3 K-Fe de haute température (magnétite, feldspath potassique ou biotite), au Faciès 4a skarn-K (skarn à feldspath potassique), au Faciès 4b felsite potassique (feldspath potassique) et au Faciès 5 K-Fe à Ca-Mg ± $H^+$, $CO_2$, Si et Ba de basse température (séricite, feldspath potassique, hématite, chlorite, carbonate, épidote) ont la capacité de produire de vastes brèches et d'importants gisements IOCG. Le Facies 6 à K, Si, Al ± Ba, Fe forme des systèmes de veines, des zones d'altération phyllique et des lithocaps épithermaux. Les relations bien définies entre les faciès d'altération à oxydes de fer et alcali-calcique et leur distribution au sein des cas d'étude australiens et canadiens utilisés dans cet article cadre le parcours des fluides et le développement des systèmes à l'échelle globale.

## Introduction

Ore deposits that form within regional-scale metasomatic iron oxide and alkali-calcic alteration (IOAA) systems include iron oxide-copper-gold (IOCG) and iron oxide-apatite (IOA) deposits, their critical metal-bearing variants, and deposits with variable iron oxide contents such as skarn, Mo-Re, and albitite-hosted uranium and Au-Co-U (Porter, 2010a; Williams, 2010a; Corriveau et al., 2016, 2022a–d; Babo et al., 2017: Hofstra et al., 2021). Similarities in province- to deposit-scale alteration facies and sequences of alteration and brecciation are observed in IOAA systems worldwide. Studies of such deposits without an understanding of the metasomatic evolution of the broader mineralizing system and its host rocks can lead to confusion about terminology and scope of IOCG and affiliated deposits. Refinements to earlier deposit models are required to best portray and classify the variety of deposits observed, including variations among systems and their impacts on deposit types formed.

Understanding how IOAA systems produce such a large variety of deposit types first requires documentation and recognition of successive suites of metasomatic rocks (alteration facies) whose development was triggered by the ascent of upper crustal fluid plumes that ultimately formed the deposits. This (Part 1) paper describes and illustrates the alteration facies formed within IOAA systems using three case study areas. The copper-gold Ernest Henry magnetite-group IOCG deposit (Cloncurry district) has resources of 166 Mt at 1.1% Cu, and 0.54 g/t Au (pre-mining; Lilly et al., 2017) and 87.1 Mt at 1.17% Cu, 0.62 g/t Au (underground; Glencore, 2020). The Cu-U-Au-Ag Olympic Dam hematite-group IOCG deposit (Olympic Copper-Gold Province) in Australia has resources of 10,070 Mt at 0.62% Cu, 0.21 kg/t $U^3O^8$, 0.27 g/t Au, and 1.0 g/t Ag as open cut and 1,041 Mt at 1.68% Cu, 0.47 kg/t $U^3O^8$, 0.63 g/t Au, and 3 g/t Ag as underground ore (BHP, 2020). Systems from the Great Bear magmatic zone (GBMZ) in Canada include the Au-Co-Bi-Cu NICO deposit, a critical metal IOCG variant with reserves of 33 Mt at 1.02 g/t Au, 0.12% Co, 0.14% Bi and 0.04% Cu (Fig. 1; Burgess et al., 2014).

Part 2 (Corriveau et al., 2022a) to this paper documents the composition and metal associations of each alteration facies and illustrates the geochemical footprints of systems that evolve simply as well as of systems with telescoped alteration facies. Part 3 (Corriveau et al., 2022c) synthesizes the sequence of crosscutting relationships amongst the facies, their spatial zoning relative to depth and heat sources, and their impact on ore deposit models. It also highlights the variety of deposits with critical and strategic metals in IOAA systems. The Part 1 to Part 3 papers are meant to provide a robust baseline to assess the geological and geochemical footprints of IOAA systems, metasomatic fluid pathways to ore, and ore deposit models.

Each mineral system hosting the deposits examined herein is associated with voluminous magmatism, but the main host rock of each deposit is largely uniform (e.g. volcanic at Ernest Henry, plutonic at Olympic Dam and meta-sedimentary at NICO; Mumin et al., 2010; Rusk et al., 2010;

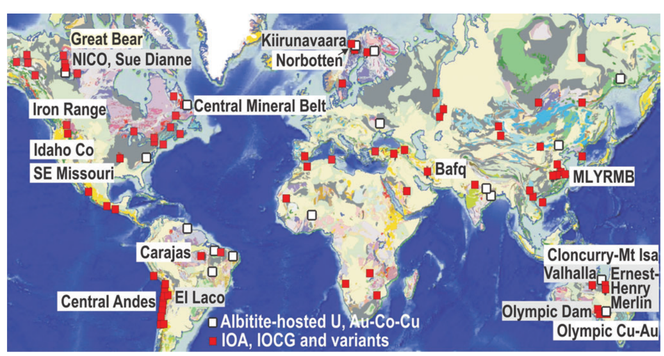


**Figure 1.** Location of IOAA systems and deposits cited in text using as background the geological map of the world by Chorlton (2007). Additional districts are labelled in Corriveau et al. (2022d). MLYRMB is Middle-Lower Yangtze River metallogenic belt.

Skirrow, 2010; Richards and Mumin, 2013a, b; Montreuil et al., 2016a). The relative homogeneity of the host rocks within each study area allows characterization of the mineralogical, chemical and textural alteration of the host rocks (Fig. 2) without the increased complexity arising from variable host-rock composition, or lithological controls on alteration assemblages.

Diagnostic sets of mineral assemblages or 'facies' account for the variety of alteration types observed when petrologic and chemical information are combined and iron oxides are included within the mineral assemblages of the alteration facies ("the IOAA facies approach"; Corriveau et al., 2016, 2022b). Inclusion of iron oxides avoids confusion introduced by terms such as 'potassic' alteration for rocks that have 10–50% iron oxides or iron-rich ferromagnesian minerals such as amphiboles and micas, making the distinctive character of IOAA facies more obvious (Corriveau et al., 2016). The facies approach also allows use of compositional proxies representing the dominant minerals and cations of each facies within IOAA systems (Fig. 2; Montreuil et al., 2015, 2016b; Corriveau et al., 2016, 2022a; Blein et al., 2022). Each facies can include assemblages that encompass an extensive mineralogical and compositional range as a result of the physicochemical conditions of fluids, intensity of alteration, and host rock types.

Figure 2 summarizes the sequence of alteration facies and mineral assemblages using a prograde, depth-to-surface metasomatic path as mapped in many parts of the Great Bear magmatic zone (GBMZ). Notwithstanding faulting, Facies 1 Na, transitional Facies 1–2 high-temperature (HT) Na-Ca-Fe (including skarn in carbonate sequences), and Facies 2 HT Ca-Fe alteration form in the deeper parts of the mineral systems. Facies 2 is the immediate host to IOA deposits. Transitional Facies 2–3 (HT Ca-K-Fe) alteration hosts cobalt-rich variants of IOCG deposits that have variable iron oxide and copper contents and an array of critical metals. Facies 3–5 are immediate hosts to IOCG deposits: Facies 3 consists of HT K-Fe, Facies 4 of K and K-skarn alteration. Facies 5 (LT K-Fe and LT Ca-Fe-Mg) has several end-members dominated by iron, notably LT K-Fe and LT Ca-Fe-Mg alteration. This facies includes variants with quartz, barite, fluorite, and carbonates, hence the $H^+$, $CO_2$, Ba, F, and Si added to the historical labels used for this facies (e.g. Hitzman et al., 1992; Skirrow, 2010). Facies 6 has many end-members, including quartz or carbonate-rich veins, phyllic (sericite-quartz-pyrite) to sericite-dominant hydrolytic alteration, and silicification. Metal associations vary at each facies as discussed in Part 2 (Corriveau et al., 2022a).

Using alteration footprints as vectors to IOCG mineralization requires looking beyond iron oxide breccia zones and veins, to recognize weak to intense and even megascopically complete alteration in the field or drill cores to establish the sequence of alteration (Corriveau et al., 2022b). Veins and breccia zones further refine the relative timing of alteration and record the extent of hydraulic or tectonically controlled fracturing (Corriveau et al., 2022b). Laboratory hydrofluoric etching and cobaltinitrite staining of rock slabs help refine timing relationships among alteration facies and visualize metasomatic processes: K-feldspar stains yellow, whereas biotite, carbonate, and amphibole stain various shades of green, grey and white. Staining also allows porous metasomatic K-feldspar to be distinguished from igneous K-feldspar, as the latter is typically more resistant to etching and staining.

### Case Study 1 – Ernest Henry, Cloncurry District

The IOAA systems of the Cloncurry district, Australia are located within the eastern half of the Mount Isa Inlier (Fig. 3). These systems host magnetite-group IOCG (e.g. Ernest Henry, Monakoff, Starra, Osborne), cobalt-rich (Mount Cobalt), iron sulphide-dominant copper-gold (e.g. Eloise), and iron oxide-poor Au–Cu, Cu–Au–Mo, Mo–Re and Pb–Zn (Mount Dore, Merlin, Lanham's Shaft) deposits and prospects (Figs. 3, 4). The western half of the Mount Isa Inlier hosts IOAA systems in which U, Th and REE dominate as commodities, such as the Valhalla albitite-hosted uranium deposit and the Mary Kathleen skarn-hosted U-Th-REE deposit (Fig. 3; Oliver et al., 1999; McGloin et al., 2013; Wilde et al., 2013).

The 1530 Ma Ernest Henry copper-gold deposit consists of a K-feldspar and iron oxide breccia ore body composed of

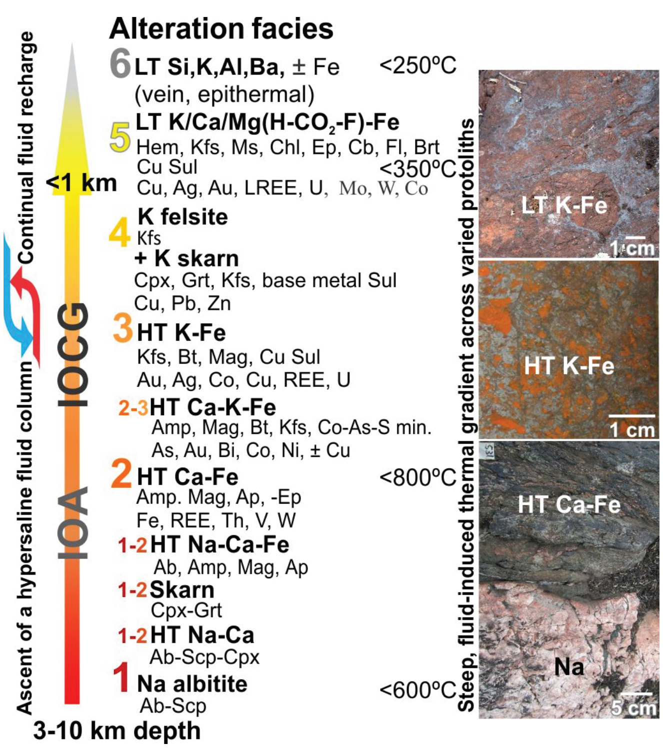


**Figure 2.** Prograde sequence of IOAA facies and minerals within assemblages (modified from Corriveau et al., 2016). Mineral abbreviations in all figures are from Whitney and Evans (2010); Sul: sulphides; As-S min: arsenides and sulpharsenides. NRCan photos: 2020-474, 2020-673, 2020-674.

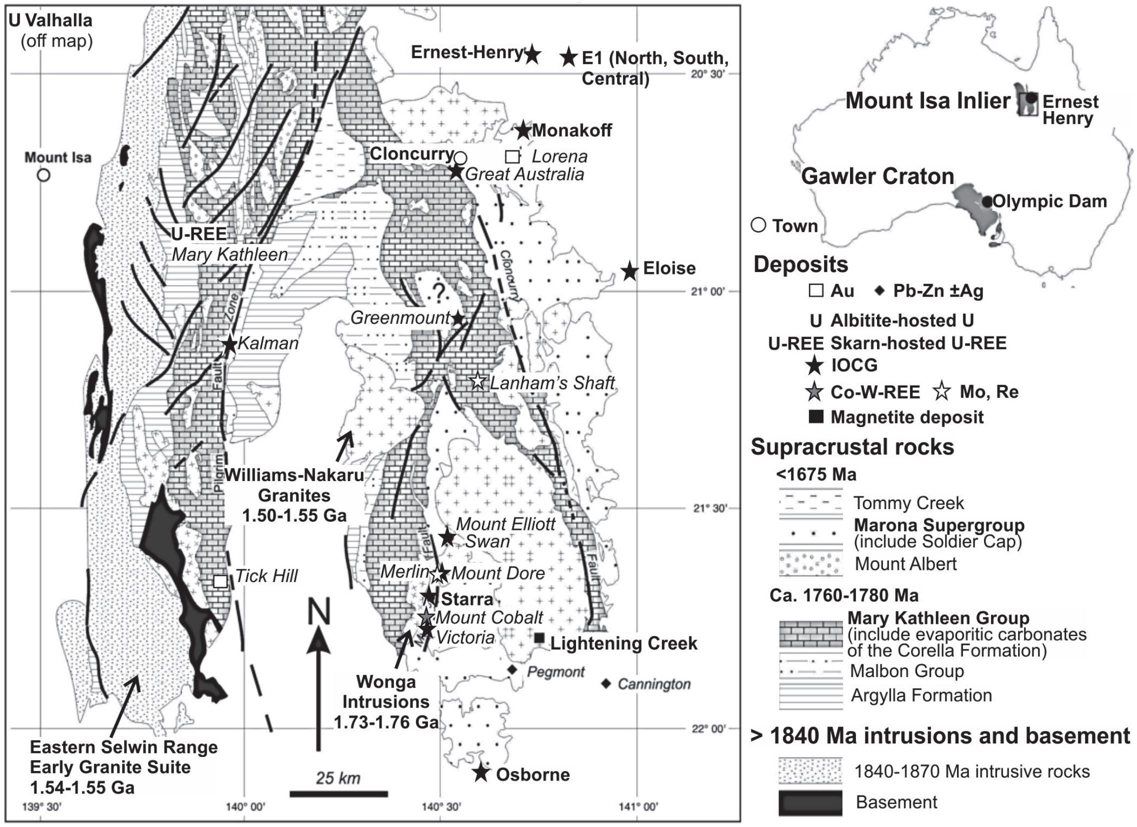


**FIGURE 3.** Geology and ore deposits of the Cloncurry district in the Mount Isa Inlier (adapted from Williams, 1998 and Williams, 2010b). Cover sequences are in white. Albitite corridors (not shown) occur throughout the Mount Isa province.

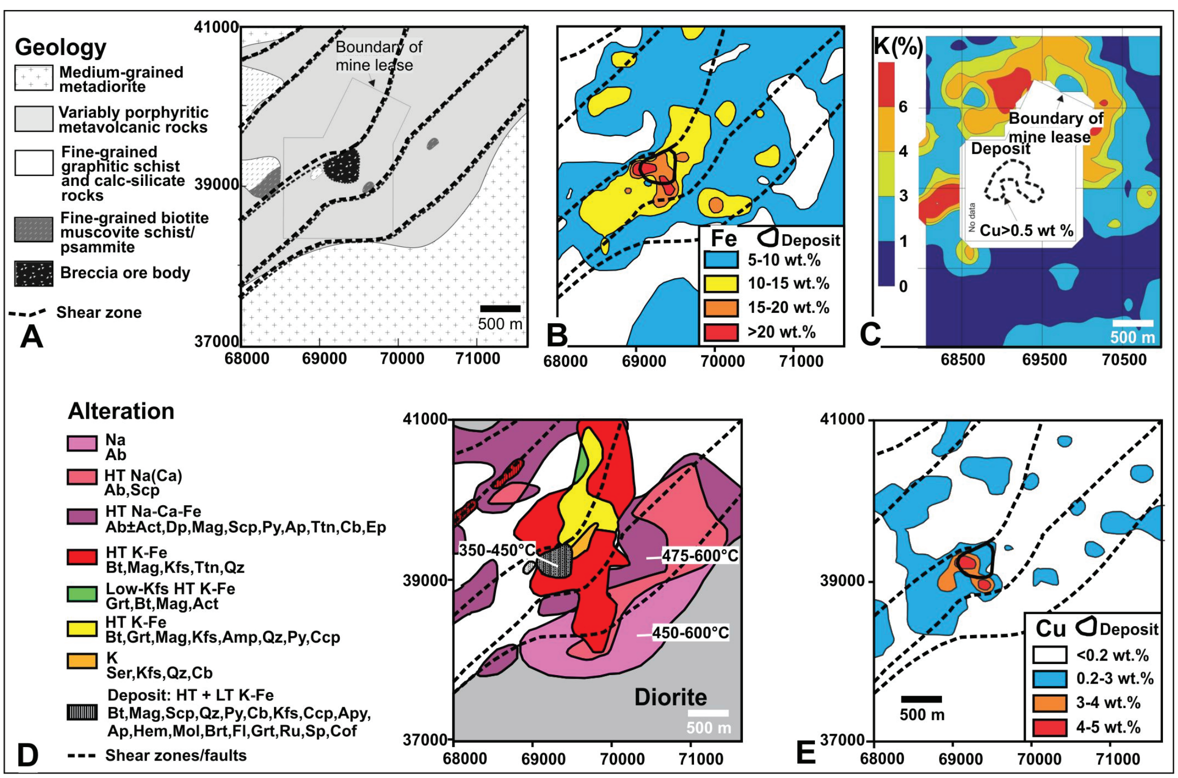


**FIGURE 4.** Geology and chemical haloes of the Ernest Henry deposit at ~200 m below surface, interpreted from borehole geology (adapted from Mark et al., 2006 and Oliver et al., 2004). **A.** Map of host rocks. **B, C.** Contoured K and Fe contents of altered rocks. **D.** Distribution of alteration facies and mineral assemblages. **E.** Copper contents of altered and mineralized rocks.

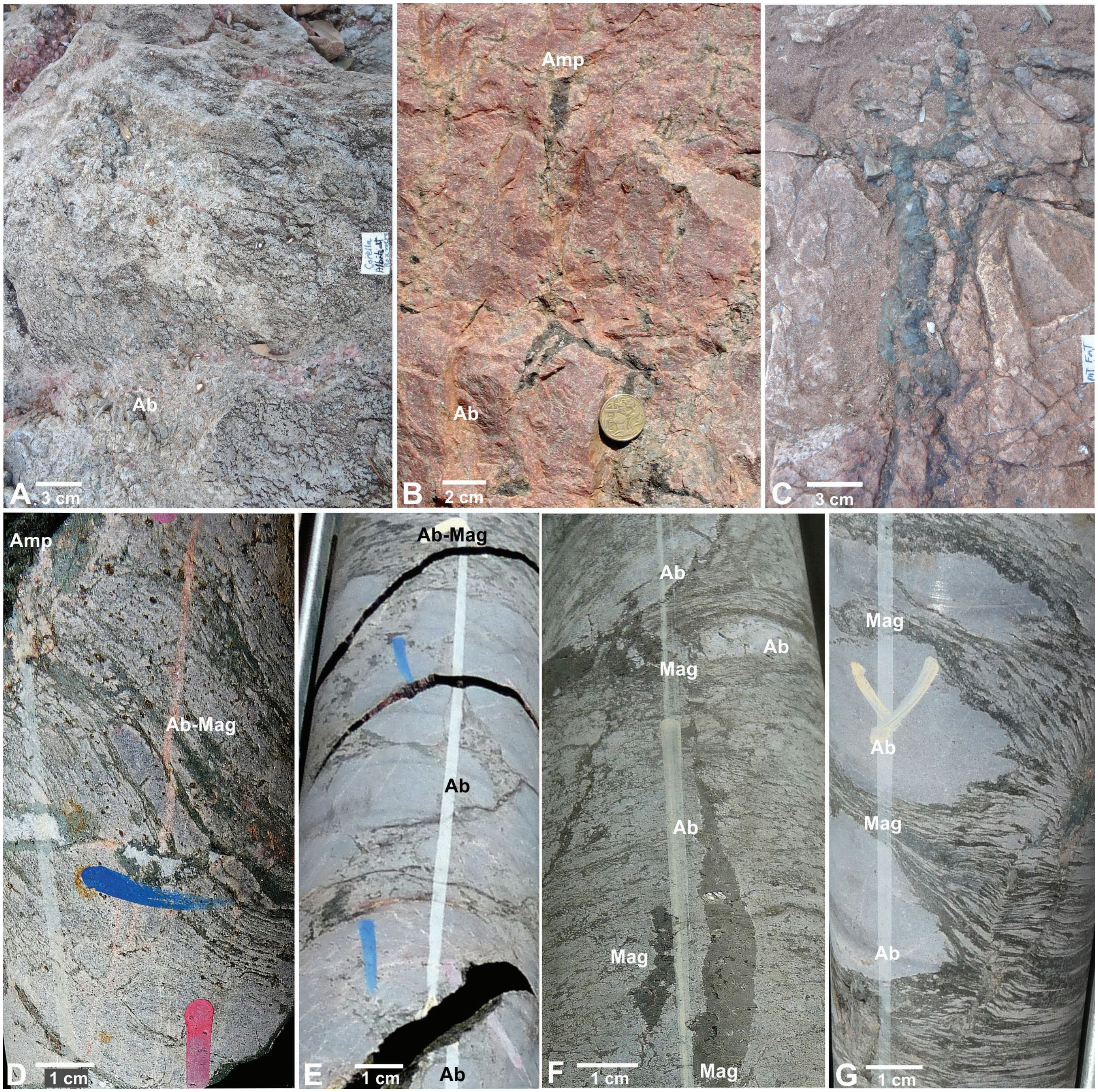


**FIGURE 5.** Albitite breccia and incipient HT Ca-Fe alteration in the Cloncurry district. **A.** Brecciated albitite replacing meta-evaporitic carbonate rocks at Roxmere Waterhole (~75 km south of the Ernest Henry deposit). **B.** Pervasively albitized felsic metavolcanic rock with irregular actinolite veins at Mount Fort Constantine (nearest natural exposures of the host sequence, ~10 km from the Ernest Henry deposit). **C.** Albitite breccia cut by amphibole-rich veins typical of the early stages of the HT Ca-Fe facies (Mount Fort Constantine). **D–G.** Albitite replacing volcanic host rocks within the Ernest Henry deposit is in turn replaced by magnetite and cut by actinolite veins (drill hole EH691). Note the development of a set of parallel fractures increasingly infilled by magnetite and forming an albitite breccia (D) that evolves to chaotic albitite breccia (E, F); the transition from brittle (D–F) to ductile (G) deformation is accompanied by dissolution of albitite fragments, as recorded by their ragged contours (G). B: photo from Corriveau et al. (2010b); A, C–G: NRCan photos 2020-675 to 2020-680.

magnetite, arsenian and cobaltian pyrite, chalcopyrite, native gold, electrum, and rare tellurides (Figs. 3, 4; Mark et al., 2000, 2006; Williams and Skirrow, 2000; Foster et al., 2007; Rusk et al., 2010). Cobalt is significantly enriched within the deposit but is not included in the resource estimates.

*Regional-scale Albitization*

Regional-scale albitization of metamorphosed evaporitic carbonate rocks affected several 100 km$^2$ of exposed Proterozoic basement rocks in the Cloncurry district (Fig. 5; De Jong and Williams, 1995; Marshall and Oliver, 2008).

Scapolite, commonly taken as an indication of the presence of evaporite or highly saline brines in the host sequences, crystallized early during metamorphism and was subsequently replaced by metasomatic albite (Morrissey and Tomkins, 2020). Metasomatic scapolite also precipitated with albite in albitite corridors and constitutes a transitional Na-Ca facies (Oliver et al., 2004).

In the Cloncurry district, albitite corridors are brecciated; breccias are locally infilled by amphibole or carbonate, and cut by amphibole veins (Fig. 5A–C). Albitization is strongest along lithological contacts and calcite-poor units, regional faults, and above the roof zones of a batholith coeval with the host IOAA system (Oliver et al., 2004; Mark et al., 2006). The distribution of albitization is interpreted as lithologically controlled due to preferential strain and fluid flow along calcite-poor units that are more susceptible to fracturing and brecciation than the interlayered marble layers (Marshall and Oliver, 2008).

*Deposit-scale Alteration*

Hydrothermal alteration at the Ernest Henry deposit has produced a pronounced, kilometre-scale zoning (Figs. 4–7) that can be described using the metasomatic facies approach, complementing the detailed description of Mark et al. (2006). Host rocks in the alteration halo of the deposit are dominantly basaltic-dacitic metavolcanic rocks intruded by (meta)diorite (Mark et al., 2006). Relics of volcanic plagioclase phenocrysts are locally preserved within breccia clasts in the ore zone (Fig. 7A). Below the ore zone, a hydrothermally-altered sedimentary host-rock that was metamorphosed at 1.58 Ga has an apatite-calcite-quartz-garnet assemblage distinct from those

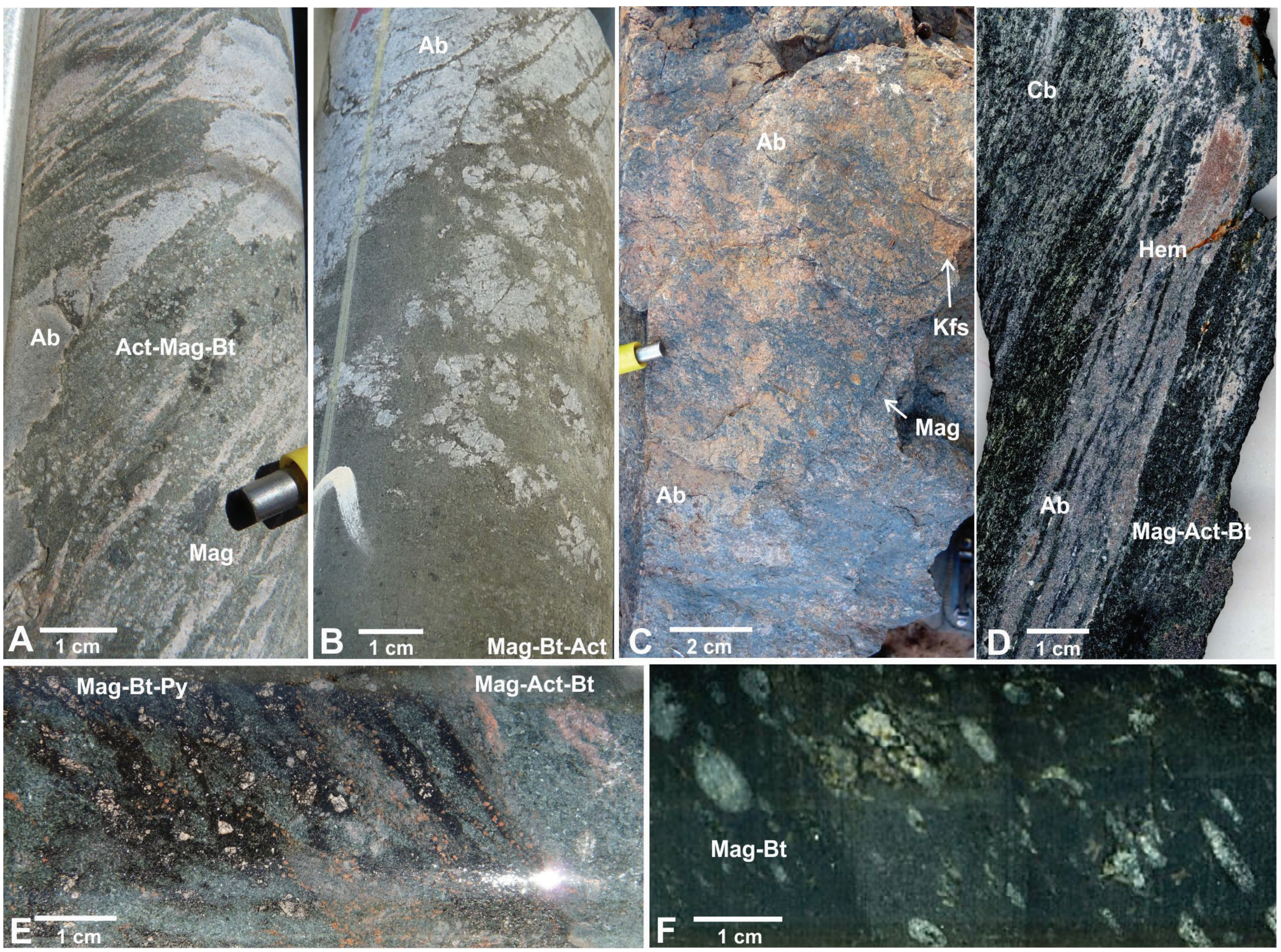


**FIGURE 6.** Development of HT Ca-Fe, HT Ca-K-Fe and biotite-dominant HT K-Fe alteration facies after albitization. **A.** Ductile to brittle-ductile deformation of albitite clasts within a magnetite-actinolite-biotite matrix in the HT Ca-K-Fe facies (Ernest Henry deposit, drill hole EH691). Larger fragments are fractured, brecciated and display dissolution textures along margins. **B.** Albitite cut and brecciated by magnetite, and re-brecciated and dissolved by magnetite-biotite ± actinolite matrix (Ernest Henry deposit. drill hole EH691). **C.** Albitite cut, brecciated and replaced by magnetite ± actinolite (Mount Fort Constantine). **D.** Foliated HT Ca-K-Fe alteration facies replacing albitized host rock and replaced by later carbonate alteration (waste pile, Ernest Henry deposit). **E.** Zones of magnetite-biotite-pyrite alteration replaced by magnetite, actinolite and biotite alteration (Ernest Henry deposit, drill hole EH691). **F.** Deformed metavolcanic rock with relict amygdaloidal texture and strong biotite-magnetite alteration of the groundmass (drill core from ~500 m northeast (along strike) of the Ernest Henry deposit. F: photo from Corriveau et al. (2010b); A–E: NRCan photos 2020-681 to 2020-685.

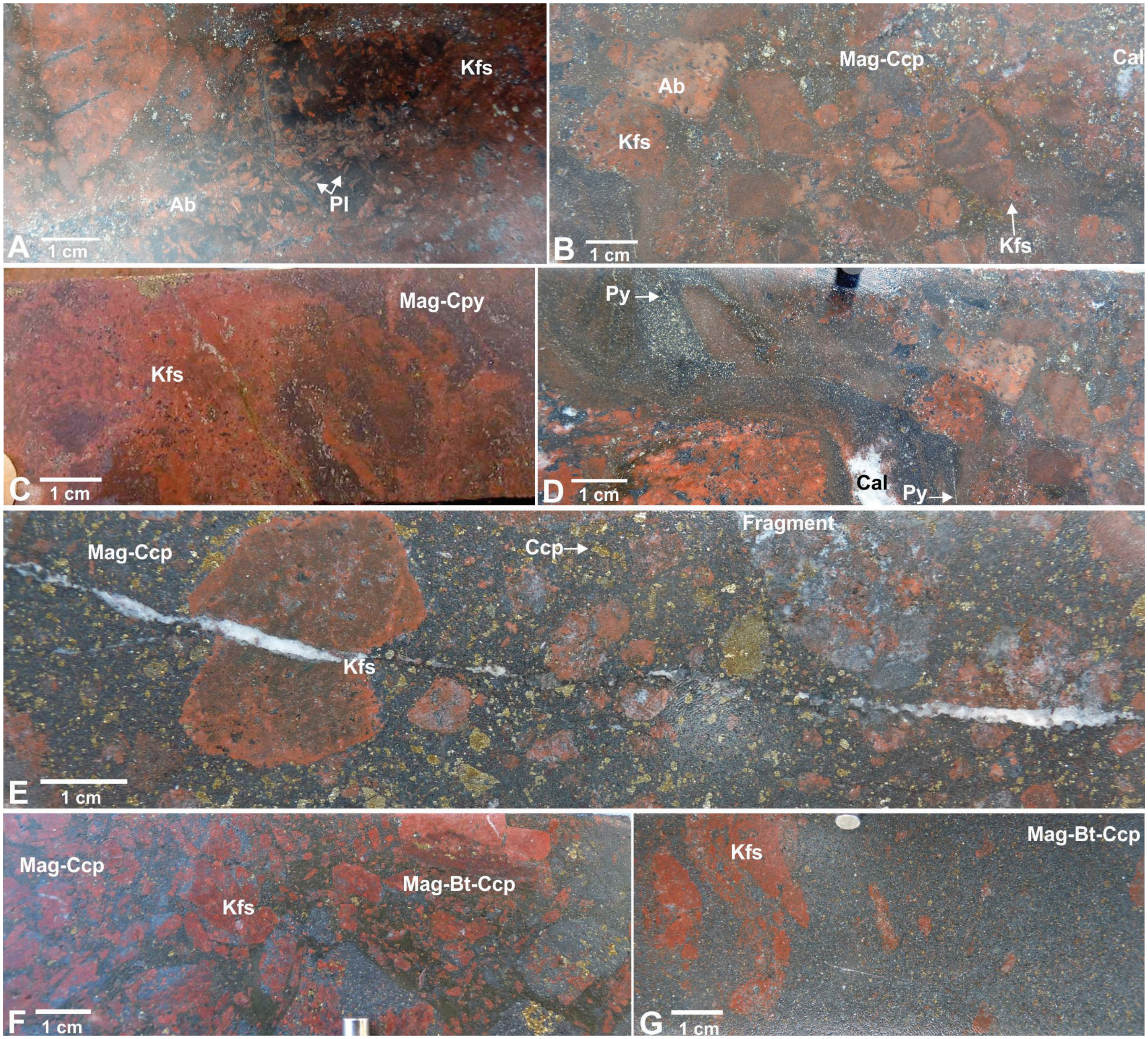


**Figure 7.** Replacement and brecciation of metavolcanic rocks by HT K-Fe alteration at the Ernest Henry deposit (Australia). **A.** Plagioclase-phyric andesite variably albitized, forming pseudoclasts subsequently fractured, infilled and replaced by K-feldspar and magnetite. Plagioclase phenocrysts (Pl) are texturally preserved but albitized and K-feldspar altered. The altered rocks and zones of pseudoclasts are brecciated, infilled and extensively replaced by a pyrite-chalcopyrite-magnetite assemblage. **B.** More intense K-feldspar alteration along and across clasts compared to A, with extensive dissolution of clasts along fractures and replacement of clasts by a pyrite-chalcopyrite-magnetite assemblage. K-feldspar haloes develop along fractures and clasts margins. Some marginal haloes are discontinuous and embayed and are interpreted as fragmented through renewed brecciation of clasts and additional replacement by matrix magnetite-pyrite ± chalcopyrite assemblages. Potential rotation of clasts through brecciation is also observed. These textures illustrate that fracturing intensified during brecciation coeval with extensive replacement of clasts and pseudoclast formation (i.e. clasts formed through in situ interconnected replacement fronts). **C.** The halo of K-feldspar-rich alteration that envelops the deposit is cut and replaced by biotite-magnetite alteration (drill core sample tens of metres outside of the ore breccia). **D.** Localized orientation of clasts among a matrix with trains of pyrite, a texture typical of fluidization whereas most of the matrix displays textures typical of in situ replacement of clasts. The red halo along fragment rims is typical of incipient, in situ K-feldspar alteration of clasts. **E–G.** Ore breccia where the K-feldspar alteration of clasts and combined infill and replacement of breccia matrix as well as clasts by magnetite defines a HT K-Fe breccia with both clasts and pseudoclasts. In E, breccia includes clasts of the main ore zone (fragment labelled) that illustrate both replacement and physical brecciation. In F, the ore breccia with a steely magnetite-chalcopyrite matrix and associated K-feldspar altered clasts are re-brecciated and locally replaced by a darker magnetite-biotite-chalcopyrite assemblage (drill core EH665). The new clasts have largely straight (i.e. non-dissolved, non-replaced) margins. This is a well-preserved example of the several generations of brecciation at the HT K-Fe facies in the deposit. In G, clasts and pseudoclasts are largely replaced by the magnetite-biotite-chalcopyrite matrix. C: photo from Corriveau et al. (2010b); A, B, D–G: NRCan photos 2020-686 to 2020-691.

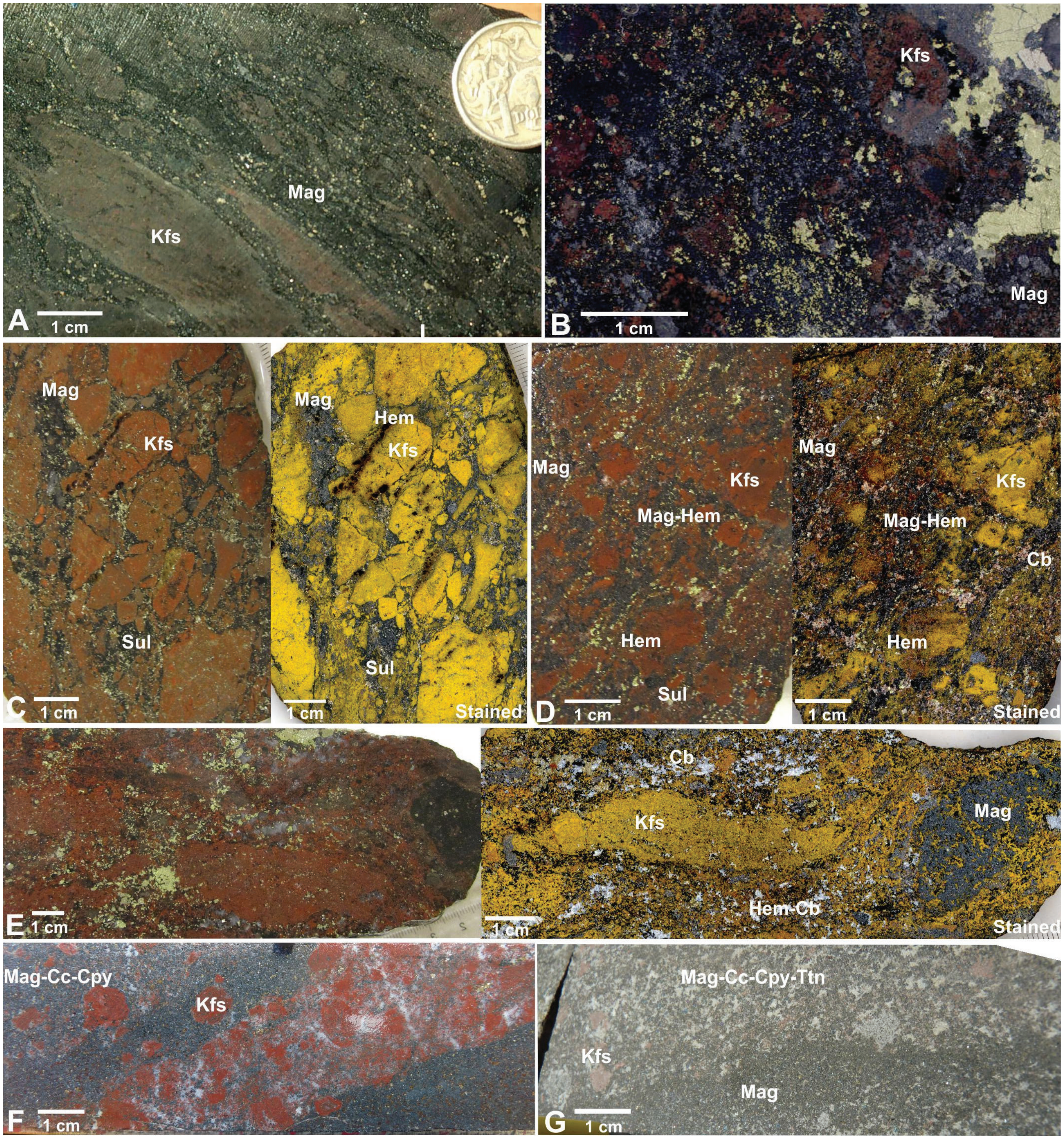


**Figure 8.** Copper-sulphide mineralization associated with HT K-Fe alteration at the Ernest Henry deposit. **A.** Hanging wall shear zone with elongate K-feldspar altered clasts and magnetite-rich matrix. **B.** High-grade ore breccia. **C–E.** Breccia with K-feldspar-altered clasts and magnetite-pyrite matrix in C, and magnetite-pyrite-calcite matrix in D and E (from 2009 waste pile). K-feldspar with a deeper red hue is pigmented by hematite. Hematite alteration overprints both matrix and clasts, notably where calcite becomes more abundant such as in D and E. The fairly isotropic matrix suggests that clast elongation may result from fragmentation along parallel fractures such as those illustrated in Figure 5D. Stained = hydrofluoric etching and cobaltinitrite staining where K-feldspar stains yellow, calcite stains white and hematite stains brown. **F, G.** Series of brecciation and mineralization events associated with precipitation of calcite (drill hole EH 691, Ernest Henry deposit). In F, early magnetite-calcite-chalcopyrite breccia with K-feldspar-altered clasts is cut and replaced by calcite, then re-fragmented and entrained in a magnetite-rich breccia matrix, as illustrated by the sharp contacts of calcite replacement and veins within clasts. In G, calcite-rich breccia with magnetite and local titanite is mineralized with chalcopyrite and displays crystal sorting typical of fluidization textures. A, B: photos from Corriveau et al. (2010b); C–G: NRCan photos 2020-692 to 2020-699.

described in this paper for IOAA systems (Inter-lens of Cave et al., 2018). The contact zone between these metasedimentary rocks and the volcanic rocks may have played a role in the distribution of subsequent pre-ore biotite-magnetite-Mn garnet ± K-feldspar alteration, and syn-ore K-feldspar-rich, magnetite-biotite alteration at 1.53 Ga (Fig. 8; Cave et al., 2018).

Regional-scale albitite and amphibole- to magnetite-altered albitized units also occur within the deposit (Figs. 4, 5D–G). These zones are variably veined and brecciated with actinolite, diopside and magnetite infill, typical of Facies 2 HT Ca-Fe alteration (Figs. 5D–G, 6). Fracture-parallel to chaotic breccia in albitite are infilled with actinolite-bearing assemblages (Fig. 5D), and where this actinolite-dominant alteration evolves to magnetite-rich alteration, brittle-ductile deformation and development of a mineral foliation is observed (Figs. 5G, 6A, D; e.g. lens-shaped, wispy albitized volcanic clasts within an albite-magnetite matrix).

A ~2 x 3 km area featuring HT Ca-K-Fe and HT K-Fe facies alteration is centred on the deposit and displays a southwest-northeast elongation parallel to the local structural fabric. Whole-rock potassium and iron contents provide a general view of alteration distribution due to the uniformly meta-igneous and plagioclase-rich nature of the hosts (Fig. 4B, C; Mark et al., 2006; Corriveau et al., 2010b). The ore zone is bounded by two northeast-trending ductile shear zones that have a moderate dip of 45° to the south-southeast. Along the hanging-wall shear zone, the metavolcanic rocks are altered to HT Ca-K-Fe facies characterized by a biotite-magnetite-actinolite assemblage (Rusk et al., 2010). This assemblage cuts earlier albitite in drill cores and evolves to cobaltian pyrite-magnetite-biotite alteration (Fig. 6). Some shear zones also host pre-ore biotite-magnetite ± garnet (spessartine to almandine) alteration succeeded by pink to red K-feldspar alteration with variable barium contents, forming a HT K-Fe (± Mn, Ba) facies (Figs. 7, 8; Twyerould, 1997). The K-feldspar-altered volcanic rocks form a halo to the mineralized magnetite-K-feldspar-dominant breccia core (see Fig. 4 in Rusk et al., 2010). K-feldspar preferentially replaces clasts in the ore breccia (Fig. 7). Magnetite, biotite, chalcopyrite and locally garnet precipitated within the breccia matrix and veins and record, with the K-feldspar-altered clasts, a Facies 3 HT K-Fe alteration in the ore breccia. Early magnetite-K-feldspar-chalcopyrite breccia is locally re-brecciated by a biotite-magnetite-K-feldspar-chalcopyrite assemblage (Fig. 7F). These assemblages evolved to a magnetite and chalcopyrite-stable pyrite-gold-fluorite-barite-calcite assemblage, with minor hematization (Figs. 7, 8).

The breccia zones examined in this study comprise multiple generations of breccia, characterized by repeated dissolution and replacement of K-feldspar-altered breccia clasts by the magnetite-rich matrix, leading to very irregular and embayed clast contours and gradual contacts (Figs. 7, 8), as well as to clast rounding typical of very mature breccias (see Jébrak, 2022). Fluidization (i.e. high-energy flow of the fluid-clast mixtures) textures are also preserved (Figs. 7D, 8G; cf. Oliver et al., 2006; Rusk et al., 2010).

The sequence of hydrothermal alteration at Ernest Henry evolved from Na through Na-Ca-Fe, HT Ca-Fe, and mineralized HT Ca-K-Fe and HT K-Fe facies, with local LT K-Fe overprints and local mineralized LT Ca-Fe (magnetite-calcite) alteration of volcanic rocks between and along fault zones. In situ brecciation occurs within albitized zones in the deposit but was most intense during the development of the HT K-Fe alteration facies. As noted from extensive field observations in the GBMZ mineral systems, K-Fe alteration facies is instrumental in the development of breccia in these systems (see also Corriveau et al., 2010b, 2016).

## Case Study 2 – Olympic Dam Deposit

*Regional Context*

The hematite-group Olympic Dam Cu-U-Au-Ag deposit occurs within the Olympic Copper-Gold Province of South Australia. The wide range of polymetallic IOAA deposits in this province include other hematite-group IOCG deposits such as Prominent Hill (Cu-Au-Ag), Fremantle Doctor (Cu-Au-Ag), Carrapateena (Cu-Au-Ag) and Khamsin (Cu-Au-Ag-U) (Fig. 9; Schlegel and Heinrich, 2015; Porter, 2010b; Skirrow, 2022) as well as magnetite-to-hematite group IOCG mineralization at the Oak Dam East prospect (Davidson et al., 2007),

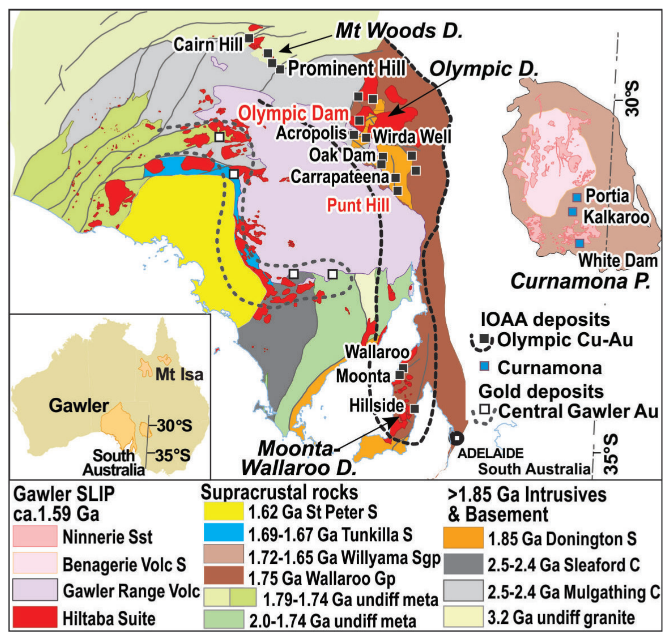


**Figure 9.** Schematic map of lithotypes in the Gawler Craton (after Reid, 2019). The Benagerie Volcanic Suite and granitoids of the Ninnerie Supersuite in the Curnamona Province are considered largely equivalent to the Gawler Range Volcanics and Hiltaba Suite of the Olympic Copper-Gold Province, respectively. The basement rocks to the Hiltaba Suite include older volcanic and sedimentary rocks (St Peter Suite, Tunkillia Suite, Willyama Supergroup, Wallaroo Group), intrusive rocks (Donington Suite), and a series of undifferentiated meta-igneous and metasedimentary rocks (undiff meta), granite and granitic gneiss (undiff granite) and basement complexes with granitic intrusions, orthogneisses and supracrustal sequences (Reid, 2019). *C*: complex; *Sst*: Supersuite; *S*: Suite; *Sgp*: Supergroup; *Gp*: Group; *Volc*: volcanic.

magnetite-dominant IOCG to IOA mineralization below 2 km depth at Olympic Dam, and IOA mineralization at Cairn Hill (Clark, 2014). Recent discoveries in the region (e.g. new zones at Oak Dam west; BHP, 2018) reinforce the high IOCG and IOA potential of the region. Potassic-skarn and magnetite-dominant breccia occur at the Hillside Cu-Au deposit (Conor et al., 2010; Ismail et al., 2014). The Punt Hill deposit in the southern part of the province has polymetallic copper-gold mineralization typical of LT Ca-Fe-Mg and K-skarn associated with IOCG deposits, but in contrast to Hillside, there is no known iron oxide breccia (Reid et al., 2011; Fabris et al., 2018; Blein et al., 2022).

Host rocks to IOCG and affiliated deposits in the Olympic Copper-Gold Province include the Donington Suite, the lower Gawler Range Volcanics and some granite intrusions of the Hiltaba Suite (Fabris, 2022; Skirrow, 2022). Alteration facies span the entire range of IOAA systems (Fig. 2). Albitization is observed in the Olympic Dam, Oak Dam, Mount Woods Inlier and Moonta-Wallaroo districts (Davidson et al., 2007; Freeman and Tomkinson, 2010; Clark, 2014; Skirrow, 2022). Magnetite-apatite ± amphibole HT Ca-Fe alteration occurs in deeper parts of the Olympic Dam deposit (Ehrig et al., 2017a, b) and in the Cairn Hill deposit, and is locally overprinted by structurally controlled HT K-Fe (magnetite-biotite-K-feldspar ± copper-gold) alteration. Magnetite-amphibole assemblages (HT Ca-Fe facies) replace breccia clasts of Donington Suite granite in the Oak Dam East prospect, and are overprinted by chlorite (LT Ca-Mg-Fe facies) (Davidson et al., 2007).

The LT K-Fe facies, typically hematite-sericite alteration associated with copper-gold (± REE ± uranium) ore, ranges to hematite-dominant variations in breccia matrix and veins at the Olympic Dam, Prominent Hill and Carrapateena deposits (Ehrig et al., 2012, 2017a, b; Schlegel and Heinrich, 2015). In these deposits, the LT K-Fe facies is hosted by large breccia complexes in which varying degrees of mechanical and chemical/dissolution brecciation (i.e. fragmentation and replacement) led development of 'mature' breccia (as described by Schlegel and Heinrich, 2015; Jébrak, 2022). The pervasive hematite-sericite alteration evolved to a hematite-dominant facies with hematite-quartz and either carbonate or barite-rich variants, and locally to advanced argillic alteration (Ehrig et al., 2012). In carbonate units, K-skarn alteration also occurs (e.g. Punt Hill deposit; Reid et al., 2011; Fabris et al., 2018).

The exceptional metal endowment of the Olympic Copper-Gold Province (see Table 1 in Corriveau et al., 2022a) can be traced to multiple sources of metals and fluids (Skirrow et al., 2018), and efficient transfer of high-temperature magmas and fluids along trans-lithospheric faults from a metasomatized sub-continental lithospheric mantle (Skirrow and Davidson, 2007; Hayward and Skirrow, 2010; Skirrow, 2010, 2022; Skirrow et al., 2011, 2018; Reid and Fabris, 2015; Fabris, 2022). Interpretation of the geodynamic settings suggests foundering of the lithospheric mantle inboard from a continental magmatic arc that partially destroyed the lithospheric root of an Archean-Proterozoic craton. These events induced a switch from a compressional to extensional regime that favoured mixing of shallow and deep crustal fluids, and optimized metal precipitation (Skirrow, 2010, 2022; Skirrow et al., 2018).

The mafic to felsic rocks of the Gawler Range Volcanics, including alkaline basalts, were deposited above a sedimentary basin succession interpreted to contain formation waters (Reid and Fabris, 2015). They were intruded by mafic to ultramafic dykes and sills and oxidized high-temperature A-type granitic intrusions (Hiltaba Suite; 760–910°C; Ferguson et al., 2020), and locally overlain by sedimentary rocks in a restricted basin (McPhie et al., 2011, 2016; Ehrig et al., 2017b). The supracrustal units, Hiltaba Suite granitic rocks, and earlier intrusive rocks (e.g. Donington granitoids) were altered by hydrothermal fluids and constitute some of the metal sources for the deposits (Skirrow et al., 2018).

*Host Rocks of the Olympic Dam Deposit*

The Olympic Dam deposit consists of successive tectonic-magmatic-hydrothermal breccias infilled and increasingly replaced upwardly and inwardly by hematite-dominant assemblages that collectively form the Olympic Dam Breccia Complex (Haynes et al., 1995; Reynolds, 2000). Alteration and breccia footprint is ~50 km$^2$ in area and buried under about 350 m of younger rocks. The current ore zone is ~6 km long by 3 km wide and at least 800 m deep (Fig. 10). The deepest drillhole intersected mineralization at more than 2 km below the surface.

The deposit is entirely hosted by the 1593.87 ± 0.21 Ma Roxby Downs Granite, which is part of the ca. 1598–1583 Ma Hiltaba Suite (Fig. 10). Subordinate host lithotypes include: 1) 1595–1590 Ma felsic lavas of the lower Gawler Range Volcanics that mostly predated the Roxby Downs Granite, and a subvolcanic quartz-phyric rhyolite that intruded the breccia complex; 2) ca. 1590 Ma (alkaline) mafic-ultramafic lavas, dykes and sills; and 3) ca. 1590 Ma bedded clastic sedimentary and volcaniclastic rocks (Figs. 10, 11; Ehrig et al., 2012, 2017b and references therein; Jagodzinski, 2014). Older sedimentary hosts to the Hiltaba-aged plutons, preserved at Wirrda Well, Acropolis and Oak Dam, have not been identified in the Olympic Dam region (Cherry et al., 2017, 2018).

The ca. 1590 Ma Bedded Clastic Facies was deposited above the deposit in a fault-bounded basin, likely controlled by major ENE and NNW regional faults (Fig. 10). The dominant preserved facies are beds of laminated mudstone and graded sandstone typical of a below-wave base subaqueous setting (Fig. 11; McPhie et al., 2011). Conglomerate beds were likely deposited from high-concentration gravity currents (debris flows and turbidity currents). The primary source of detritus (zircon and quartz) is the Hiltaba Suite granites (possibly the Roxby Downs Granite; HS-RDG in Fig. 11). Less abundant detrital chromite grains with varying compositions imply single or multiple sources of ~1590 Ma alkaline mafic-ultramafic lavas. Minor volcanic quartz, as well as shards and crystal fragments typical of ash fall deposits, are likely sourced from felsic Gawler Range Volcanics units and their depositional sites tens to hundreds of kilometres away

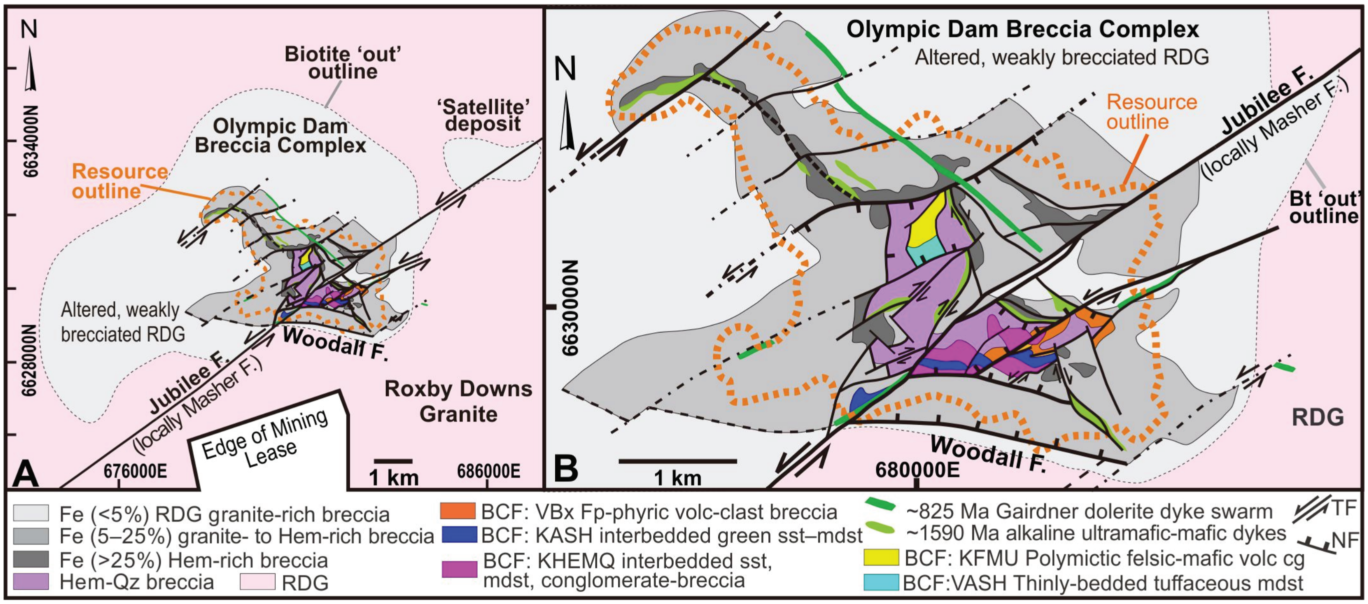


**Figure 10.** Simplified geology map of the Olympic Dam deposit at 350 m below sea level, showing the extent of the Olympic Dam Breccia Complex (ODBC), host lithotypes, deposit-scale structural architecture, and resource outline (modified after Ehrig et al., 2012 and Clark et al., 2018). **A.** The biotite 'out' outline refers to the area where the igneous biotite of the host Roxby Downs Granite (RDG) is pervasively altered. The geology of the area has recently been refined; the biotite-out outline delimits the Olympic Dam Breccia Complex (ODBC) and a satellite deposit to the east. **B.** Close-up of the ODBC. Within the ODBC, the regional-scale Jubilee fault is locally mapped as the Masher fault. The Woodall fault is a normal fault where altered rocks of the sedimentary basin are in sharp contact with the Roxby Downs Granite. The Bedded Clastic Facies (BCF) consists of a basal unit of interbedded hematite mudstone and quartz-rich sandstone (KHEMQ), a unit of polymictic volcaniclastic breccia with felsic and mafic clasts of Gawler Range Volcanics (VBx), interbedded chlorite-rich sandstone and mudstone rich in detrital chromite (KASH), thinly bedded, tuffaceous mudstone (VASH) and polymictic conglomerate with felsic and mafic clasts of Gawler Range Volcanics (KFMU). *Volc*: volcanic; *cg*: conglomerate; *sst*: sandstone; *mdst*: mudstone; *F*: fault; *TF*: transcurrent fault; *NF*: normal fault. Lithotypes and their abbreviations are illustrated and further described and defined in Figure 11.

(McPhie et al., 2016). Exhalative chemical precipitates and sub-surface boiling textures in the deposit indicate the system evolved to <1–2 km depth and interacted with the overlying active basin. The lowest preserved stratigraphic unit within the basin (KHEMQ, Fig. 10) records hydrothermal activity at a disconformable basin contact and is broadly mineralized, though subeconomic (usually <1 wt % Cu). However, a down-faulted block of brecciated KHEMQ with a minor granite component is significantly mineralized (>2 wt% Cu and 1.5 ppm Au) at depth in the second-deepest drillhole (RD1988) of the deposit, which ended at 1.89 km depth in 1.6% Cu, 290 ppm $U_3O_8$, 1.16 ppm Au, 10 ppm Ag, and 310 ppm Mo (Ehrig et al., 2012).

Deposition of the Bedded Clastic Facies has been tightly constrained to 1590.97 ± 0.58 Ma (CA-TIMS geochronology on a tuffaceous mudstone in the thin-bedded green and red mudstone facies association of the northern domain of the Bedded Clastic Facies; Cherry et al., 2018), indicating a dynamic but brief, ~3 million-year period of Roxby Downs Granite intrusion, cooling and crystallization, uplift and exhumation, basin development and deposition.

*Structural Framework of the Olympic Dam Deposit*

The deposit is structurally controlled, in that mafic dyke intrusion, brecciation and hydrothermal fluid flow were initially focused at intersections of major ENE-NNW regional faults, creating local zones of dilation and contraction. First-order, trans-lithospheric, NNW-SSE-trending structures are interpreted to represent early, pre-mineral basement architecture that strongly influenced the overall orientation of resultant IOAA deposits, including Olympic Dam. This underlying structural control is scale-invariant; i.e. the majority of local-scale (tens to hundreds of metres), high-grade, intensely hematized breccia bodies display sub-vertical NNW-SSE-oriented geometries, particularly in the northern parts of the Olympic Dam deposit, where they are interpreted to represent preserved segments of 'blind' NNW-SSE structural expressions. Syn-mineralization ENE-WSW structures — including the regionally continuous Jubilee Fault, which is an important deposit-scale fault zone at Olympic Dam — are major domain-bounding fault zones that preserve a complex tectonothermal history with evidence for repeated post-mineral reactivation. Their intersection with the older NNW-SSE structures likely controlled regional Gawler Range felsic and mafic volcanism, rhombic-shaped Hiltaba Suite plutons and batholiths, and sedimentary basins.

The Bedded Clastic Facies (BCF in Fig. 10) is preserved in fault-bounded blocks within the Olympic Dam Breccia Complex, chiefly controlled by the Woodall Fault and the Jubilee Fault (Fig. 10; Clark et al., 2018). These rocks were not subjected to the same intensity of brecciation or alteration as the main breccia complex, and were initially tilted and down-faulted into the complex during the extensive metasomatism. The preserved sections suggest that the uncompacted sediment thickness was >500 m, indicating an extensive deep, subaqueous depositional environment (McPhie et al., 2011).

The deposit has experienced multiple post-mineralization brittle deformation events leading to the preservation and dismemberment of the breccia complex and incorporation of blocks of the Bedded Clastic Facies, shallower alteration facies and younger units (Clark et al., 2018). A down-faulted, ca. 1450 Ma sedimentary unit that postdates breccia formation (not shown in Fig. 10) records renewed hydrothermal alteration and uranium remobilization and reactivation of the breccia complex (Cherry et al., 2017, 2018; Clark and Ehrig, 2019).

The recognition of pre- and syn-mineralization faults is difficult due to intense brecciation and dissolution of primary host rocks (Fig. 12). Lithological contacts and/or early fault

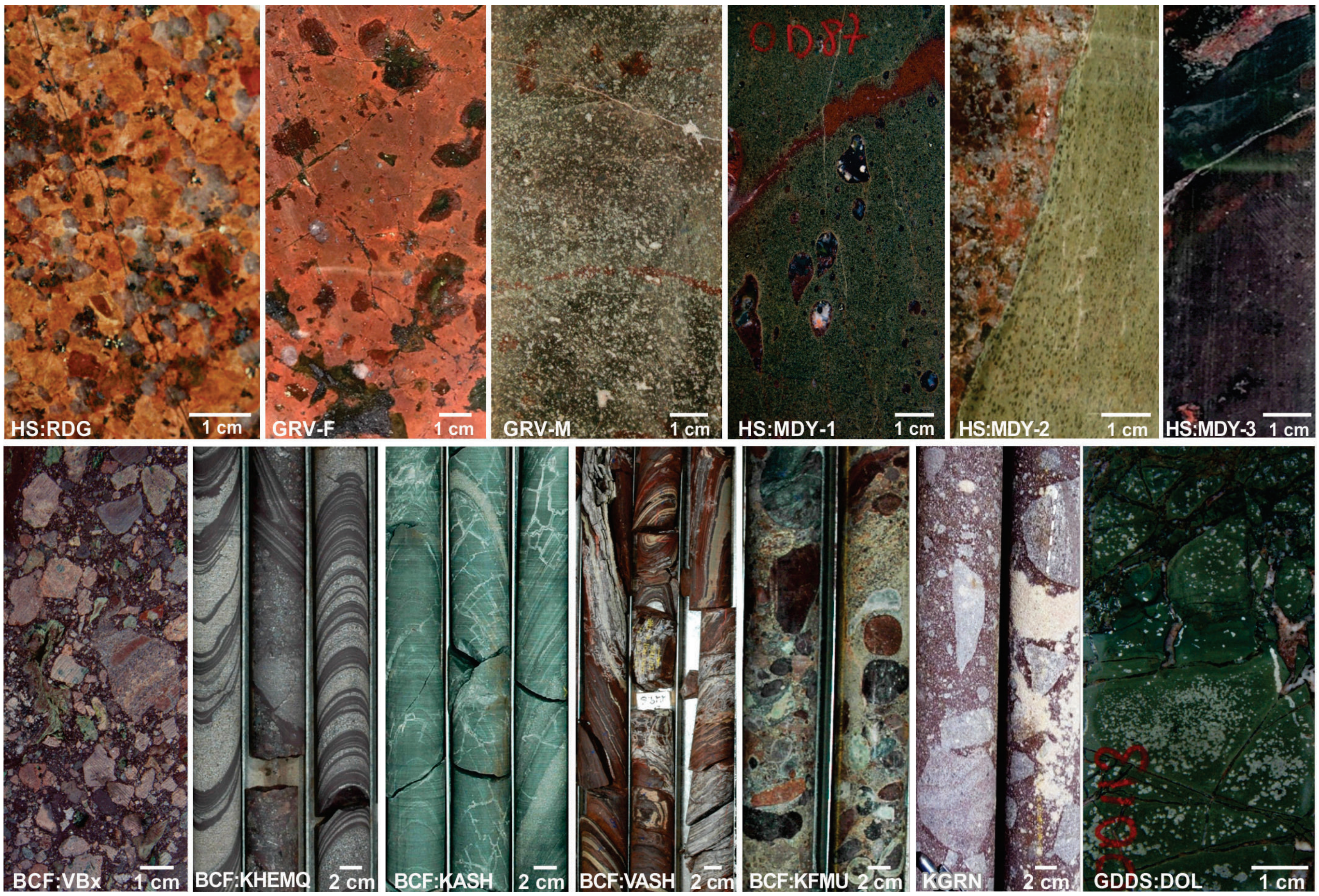


**Figure 11.** Diversity of felsic, mafic-ultramafic and sedimentary host rocks at the Olympic Dam deposit. HS: Hiltaba Suite; RDG: Roxby Downs Granite; MDY: mafic-ultramafic dyke; GRV: Gawler Range Volcanics; F: felsic; M: mafic-ultramafic; BCF: Bedded Clastic Facies; VBx: volcaniclastic breccia; KHEMQ: interbedded hematite mudstones with quartz-rich sandstones; KASH: interbedded chlorite-rich sandstone and mudstone rich in detrital chromite; VASH: thinly bedded, tuffaceous mudstone; KFMU: polymictic felsic and mafic GRV-clast conglomerate; KGRN: quartz-rich sandstone; **HS:RDG**: Minimal fracturing of the granite host rock. The reddish to reddish-brown alteration forms a patchy network of albite-K-feldspar alteration (Kontonikas-Charos et al., 2017). **GRV-F**. Pervasive potassic alteration replacing the aphanitic groundmass, in which the reddish to pinkish hue represents K-feldspar alteration or intense sericitic alteration. **GRV-M**. This sample is amygdaloidal and has a porphyritic texture defined by relict olivine and pyroxene phenocrysts. The amygdules are filled by magnesium-carbonate ± chlorite, silica and apatite. A faint beige hue is the result of magnesium-carbonate alteration, which is cut by hematite veins. Chlorite-sericite alteration of phenocrysts is typical, as well as intense alteration of the microlitic groundmass with variable quantities of hematite. **HS:MDY-1**. Chlorite-altered porphyritic and amygdaloidal mafic dyke. Amygdules are filled with a quartz-carbonate-chlorite ± fluorite-chalcopyrite assemblage. The microlitic groundmass is intensely altered by chlorite-sericite, cut by hematite ± chalcopyrite veins. **HS:MDY-2**. Olivine-phyric ultramafic dyke with a sharp, 3 mm-wide quenched contact with incipiently brecciated granite. The groundmass is altered by sericite-chlorite and magnesium-carbonate with total replacement of olivine phenocrysts by sericite ± silica-apatite. **HS:MDY-3**. Intensely chlorite-sericite-hematite altered alkaline ultramafic dyke with a well-developed quenched margin defined by sericite-chlorite alteration. Minor carbonate and barite veins cut the altered dyke. **BCF:VBx**. Fragmented, sericite-altered porphyritic dacite (GRV-F) clasts predominate with minor wispy, sericite-chlorite-altered mafic-ultramafic (picritic) clasts in an intensely hematized matrix. **BCF**. The Bedded Clastic Facies includes polymictic felsic and mafic GRV-clast volcaniclastic breccia (VBX), several sedimentary units (KASH, VASH and KFMU) and a basal, mineralized KHEMQ unit. **KGRN**: ~1450 Ma, well-sorted quartz-rich sandstone (breccia) is correlated with the regionally-extensive Pandurra Formation, which postdates the Olympic Dam deposit. **GDDS: DOL**: ~825 Ma Gairdner dolerite (to basaltic) dyke swarm.

zones are typically obscured by faulting and brecciation; sharp boundaries indicate either a fault contact or a dyke or vein that has intruded the breccia (Fig. 12F). The sustained heat ingress associated with syn-metasomatism felsic and mafic-ultramafic magma emplacement across the province, and the geodynamic environment from which magmas and fluids were derived, allowed the system to mature to a giant polymetallic IOCG deposit (Ehrig et al., 2017b).

*Alteration Facies and Mineralogical Zoning in the Olympic Dam Deposit*

The distinctive host rocks of the Olympic Dam deposit help to assess progressive alteration, brecciation and mineralization that led to ore formation. The host Roxby Downs Granite displays an alteration continuum from a relatively coherent 'facies', to irregular, polymictic and chaotic polyphase breccias, reflecting increasing intensity of alteration and brecciation that obliterated primary textures (Fig. 12). Several mineralogical zonation patterns are recognized inwards and upwards from the margins of the breccia complex (Reeve et al., 1990; Oreskes and Einaudi, 1992; Ehrig et al., 2012, 2017a, b; Dmitrijeva et al., 2019), although original patterns are disrupted by faulting (Ehrig and Clark, 2019). Because of multiple precipitation and dissolution events, bona fide mineral assemblages are difficult to assess in detail, and spatially associated minerals are best referred to as mineral associations or alteration zones (see Apukhtina et al., 2020). This mineralogical zoning frames the lower-temperature evolution of IOAA systems and associated patterns of mineralization.

From the margins of the breccia complex inwards and upwards (Figs. 12–16), alteration of the granitic host rock produced (1) an orthoclase-sericite-hematite zone (spatially associated with siderite) that evolved to, (2) hematite-sericite alteration accompanied by complete destruction of K-feldspar and precipitation of fluorite and economic sulphides (Cu, U, Au and Ag), and eventually (3) a barren hematite, quartz, barite, sericite, and illite ± hematite alteration at the centre of the deposit (e.g. HEMQ; Figs. 13, 15). Early reduced magnetite-apatite-bearing alteration with variable chlorite, calcite, siderite, pyrite, chalcopyrite or fluorocarbonates is present at the margins and in the deeper parts of the deposit (Fig. 14A–E; Apukhtina et al., 2017, 2020). This early alteration is best ascribed to the development of an iron-rich HT Ca-Fe alteration (i.e. an early IOA mineralization) that evolved to high $fCO_2$ conditions, low calcium contents and crystallization of siderite and chlorite (Fig. 14). Although the texturally destructive nature of the later hematite-sericite alteration overprint likely obscures the full extent of the early, deep HT Ca-Fe alteration facies, there is a clear redox control whereby earlier magnetite-apatite alteration associated with calcite is overprinted by a predominantly $Fe^{2+}$-stable hematite-siderite-chlorite alteration association (Fig. 14). These relatively reduced alteration facies are classified as 'footwall' alteration assemblages (Fig. 13A).

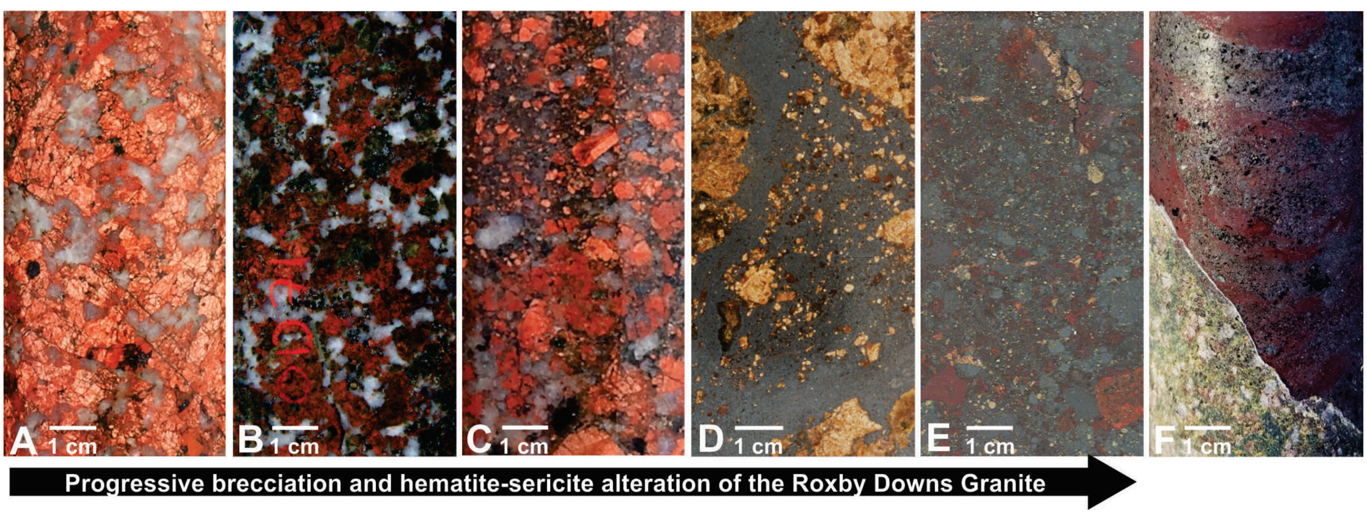


**Figure 12.** Progressive LT K-Fe alteration and brecciation of the Roxby Downs Granite host rock. **A.** Onset of alteration and brecciation of the Roxby Downs Granite, showing extensive development of fracture sets with reddish alteration haloes and coalescence of haloes into more pervasive alteration. Post-magmatic coarsening processes during albite-K-feldspar alteration resulted in minor feldspar dissolution and quartz precipitation and led to the unique, 'connected' quartz crystals texture. **B.** Increased chloritization-sericitization and hematization of mafic minerals and primary feldspars, which have a distinctive 'reddish' hue due to micro-inclusions of hematite in the feldspar. **C.** Increased brecciation intensity is evidenced by variably fragmented, altered feldspars that locally become matrix-supported (hematite-altered matrix). At this stage, the fragments are enriched in potassium and strongly depleted in sodium. **D.** Matrix-supported hematite breccia dominated by altered granite fragments of various sizes. Note: the granite clasts are sub-rounded to rounded, indicating chemical dissolution processes. **E.** Total textural destruction of the granite host to a hematite matrix-supported polyphase breccia with variable sulphide precipitation. **F.** Classic example of a polyphase breccia at Olympic Dam, displaying a sharp contact between variably brecciated and altered, granite clast-supported breccia (lower left), and an intensely hematite-altered, matrix-supported, multi-generational breccia containing high concentrations of steely hematite-fluorite-chalcocite-bornite mineralization. Photos courtesy of BHP-Olympic Dam.

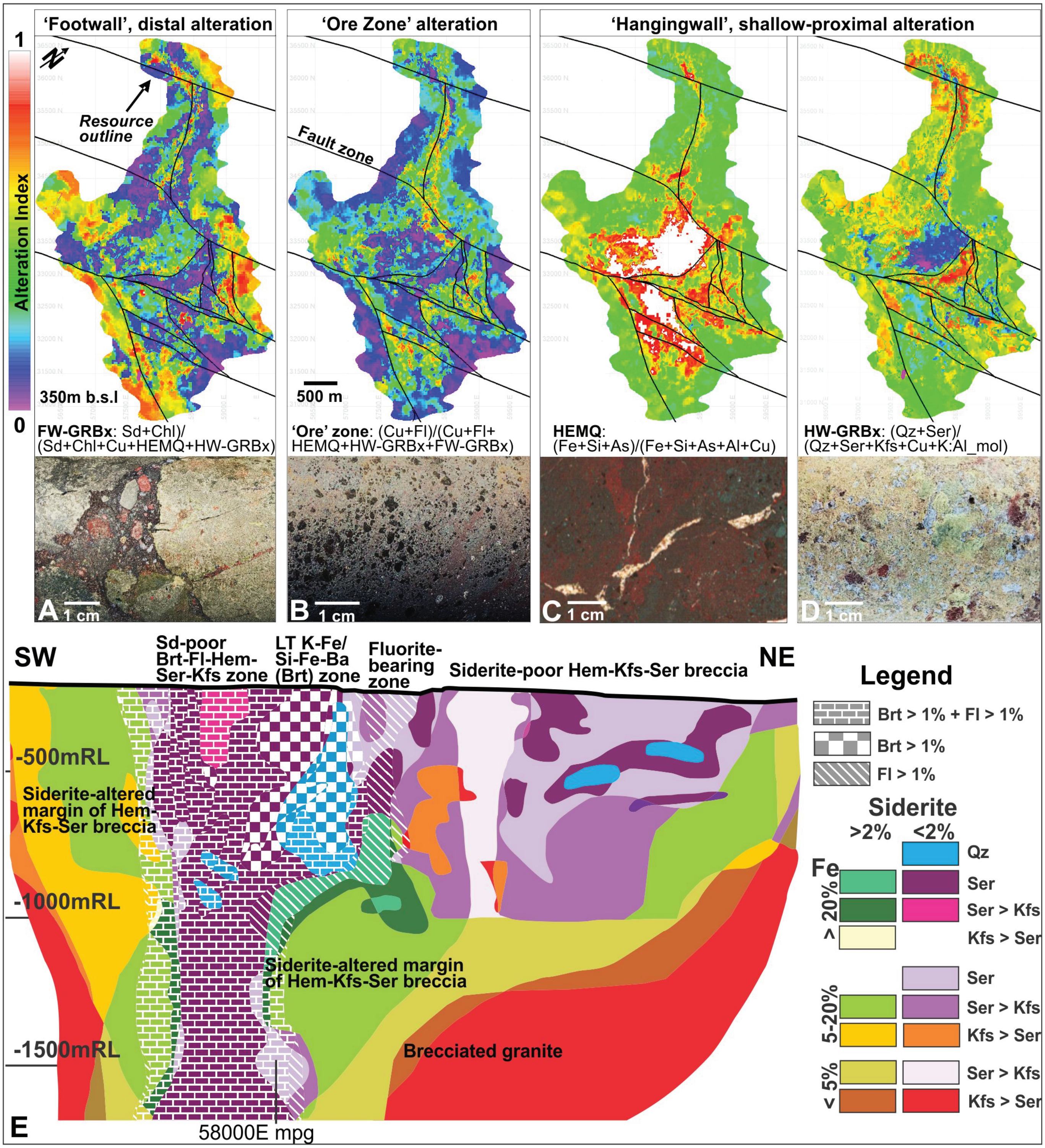


**FIGURE 13.** Alteration assemblages across the Olympic Dam deposit. **Top**. Various alteration indices mapping out 'footwall' and 'hangingwall' alteration facies relative to the economic orebody. Paragenetically early and relatively higher-temperature alteration assemblages are overprinted/superimposed and obliterated by later, lower-temperature assemblages reflecting a complex, dynamic spatiotemporal evolution of IOA through to LT facies at Olympic Dam. Therefore, these mapped alteration facies embody the present geometry and whole-rock geochemical signature of preserved and exposed alteration types. Places where the alteration index exceeds 0.8 (up to 1) represent the zones of most intense development of the respective alteration facies. **A.** Iron-rich HT to LT K-Fe-$CO_2$ alteration characterized by a hematite (replacing magnetite)-siderite-pyrite ± relict magnetite-chalcopyrite-sericite breccia (footwall granite breccia: 'FW-GRBx') that is interpreted to represent a deeper/peripheral, high-temperature and relatively reduced alteration facies. Within this

alteration type, relict zones of high-temperature IOA are preserved and overprinted by iron-rich HT K-Fe (-$CO_2$) alteration, characterized by magnetite-apatite-quartz-chlorite ± siderite-pyrite-chalcopyrite and magnetite-siderite ± pyrite assemblages. 350m b.s.l.: 350 m below sea level. **B.** Iron-rich LT K-Fe (-F, ± $CO_2$) facies, characterized by typically polyphase hematite-fluorite breccia with minor sericite; siderite, represents the primary host to the economic orebody, a chalcocite-bornite and bornite-chalcopyrite-rich hematite breccia. Overall, these intensely altered breccia bodies show discrete geometries controlled by the underlying pre- to syn-mineral structural architecture, and likely reflects the highest permeability and fluid-rock interaction zones. As the iron-rich HT K-Fe (-$CO_2$) facies evolved in space and time towards LT K-Fe ± Si facies, localized high-fluid flux in highly-permeable fault zones — that channeled the flow of fluid, energy and mafic-ultramafic dyke injection — caused intense brecciation and favourable physicochemical conditions for iron-rich LT F-Fe (-K ± $CO_2$) alteration. Note: all alteration facies, especially the 'hangingwall' facies, have been greatly affected and dislocated by post-mineralization structural and locally hydrothermal disruption. **C.** Iron-rich LT Si-Ba-Fe alteration is characterized by a texturally destructive hematite-quartz assemblage commonly accompanied by barite ± carbonate veins ('HEMQ' alteration); here, alteration is so intense that it displays textural 'inversion', i.e. protoliths are texturally and geochemically unresolvable. This alteration type is an 'end-member', shallow-proximal alteration type representing the hydrothermal fluid 'outflow' zones that largely interacted with the overlying, active sedimentary basin. HEMQ alteration is interpreted to form as a direct, exhalative precipitant and as a near-surface replacement of (predominately) sedimentary rocks of the Bedded Clastic Facies, and represents the variably 'acidic' outflow zones of the broader hydrothermal system. Note: the HEMQ alteration is spatially associated with the fault-bounded Bedded Clastic Facies (a shallow facies marker) and similarly retains anomalous abundances of elements typical of the deposit. **D.** LT K-Al ± Fe, Si alteration characterized by sericite-illite ± quartz-hematite breccia (hangingwall granite breccia: 'HW-GRBx'), and localized occurrences of advanced argillic alteration. Similar to HEMQ, this alteration type is also interpreted to represent a shallow alteration facies and relatively 'acidic' outflow zones of the broader hydrothermal system. However, this alteration is spatially extensive, reflecting a strong lateral component to hydrothermal outflow and leading to widespread distal alteration of predominantly the Roxby Downs Granite. Although texturally destructive, the fluid was buffered by the strongly alkaline Roxby Downs Granite, therefore preserving the granite texture and relict granite clasts. Advanced argillic alteration is restricted to discrete zones. **Bottom**. As an alternative to alteration indices, normative-calculated mineralogy calculated from the extensive whole-rock geochemical (drillhole) database is used to characterize a range of alteration types, conditional to specific, quantitative mineralogy. **E.** Cross-section of the Olympic Dam deposit modified from Ehrig et al. (2012) to portray the evolution of the LT K-Fe facies as hematite becomes dominant, that quartz, carbonate, fluorite and barite variants form and the system transitions to localized sericite-rich alteration types. The distribution of alteration types in the chalcopyrite-pyrite, chalcopyrite-bornite, bornite-chalcocite and non-sulphide zones across the deposit is shown in Figure 14 of Ehrig et al. (2012). Iron is in wt% Fe; K-feldspar and sericite proportions are derived from their respective weight per cent content based on mineral liberation analysis of modal mineralogy from scanning electron microscope data (Gu, 2003). Photos courtesy of BHP-Olympic Dam.

The transition from $Fe^{2+}$-stable 'footwall' alteration to the $Fe^{3+}$-stable LT K-Fe and LT Ca-Fe facies characterized by hematite-sericite-fluorite zones is typically sharp and associated with a marked increase in sulphide content, including bornite-chalcocite mineralization. Above these facies, LT Ba-Si-Fe and LT Si-Fe facies 'hanging wall'-type alteration is typical, and is interpreted to represent the relatively acidic 'outflow' hydrothermal zones located in a shallow-proximal position relative to the main breccia complex (Figs. 13C, D, 15).

An inner marginal zone of sericite, illite ± hematite ± fluorite alteration is enriched in gold and lead, which represents later, post-mineralization remobilization spatially controlled by second- and third-order structures in favourable alteration-protolith sites. The central parts of the breccia complex consist of hematite-quartz alteration, with abundant barite veins and metal enrichments consisting of As, Mo and Sb (Corriveau et al., 2022a). Sericite-dominant (sericitization largely devoid of hematite) and advanced argillic alteration (paragonite, illite, quartz, zunyite, diaspore and kaolinite; Ehrig et al., 2017b) also occur locally within the hanging wall alteration assemblage (Fig. 13D).

The paragenetic sequence of sulphide precipitation is sphalerite → galena → pyrite → chalcopyrite → bornite → chalcocite. Sphalerite and galena occur in trace amounts, but sphalerite contents are locally up to 2 wt% in distal breccia (Ehrig et al., 2012). Late-stage veinlets of galena occur within the hematite-quartz-barite breccia. Uranium precipitated largely as uraninite, coffinite and brannerite in complex intergrowths; the proportion of uraninite increases with increasing iron contents (Ehrig et al., 2012). Geochemically anomalous, but sub-economic, Mo-W-Sn-As-Sb mineralization occurs in the southern part of the deposit, which defines a shallow-proximal to distal, paragenetically early zonation pattern of base metal-poor (Mo-W-Sn-As-Sb) minerals → base metal-rich (Cu-Pb-Zn) minerals → sulphide barren (hematite-quartz-barite breccia).

Distal, satellite mineralization occurs approximately four km northeast of the Olympic Dam deposit (Fig. 10A). The distal deposit (approximately 2 km in length, 0.5 km in width and 0.8 km in depth) lies on a broadly coincident gravity and magnetic geophysical anomaly down-strike from the regional Jubilee Fault. Alteration mineralogy and geochemistry are comparable to that seen at the margins of the Olympic Dam Breccia Complex. Alteration consists of hematite-sericite altered Roxby Downs Granite exhibiting red-stained K-feldspar, which occurs in association with sparse copper-(iron)-sulphide mineralization rarely exceeding 1 wt% Cu (Kontonikas-Charos et al., 2017). Relict magnetite-apatite-quartz (IOA) alteration is overprinted by hematite-sericite alteration; however, a broad magnetic susceptibility anomaly is observed throughout the satellite deposit, likely representing deeper, peripheral alteration linked to the broader Olympic Dam mineral system.

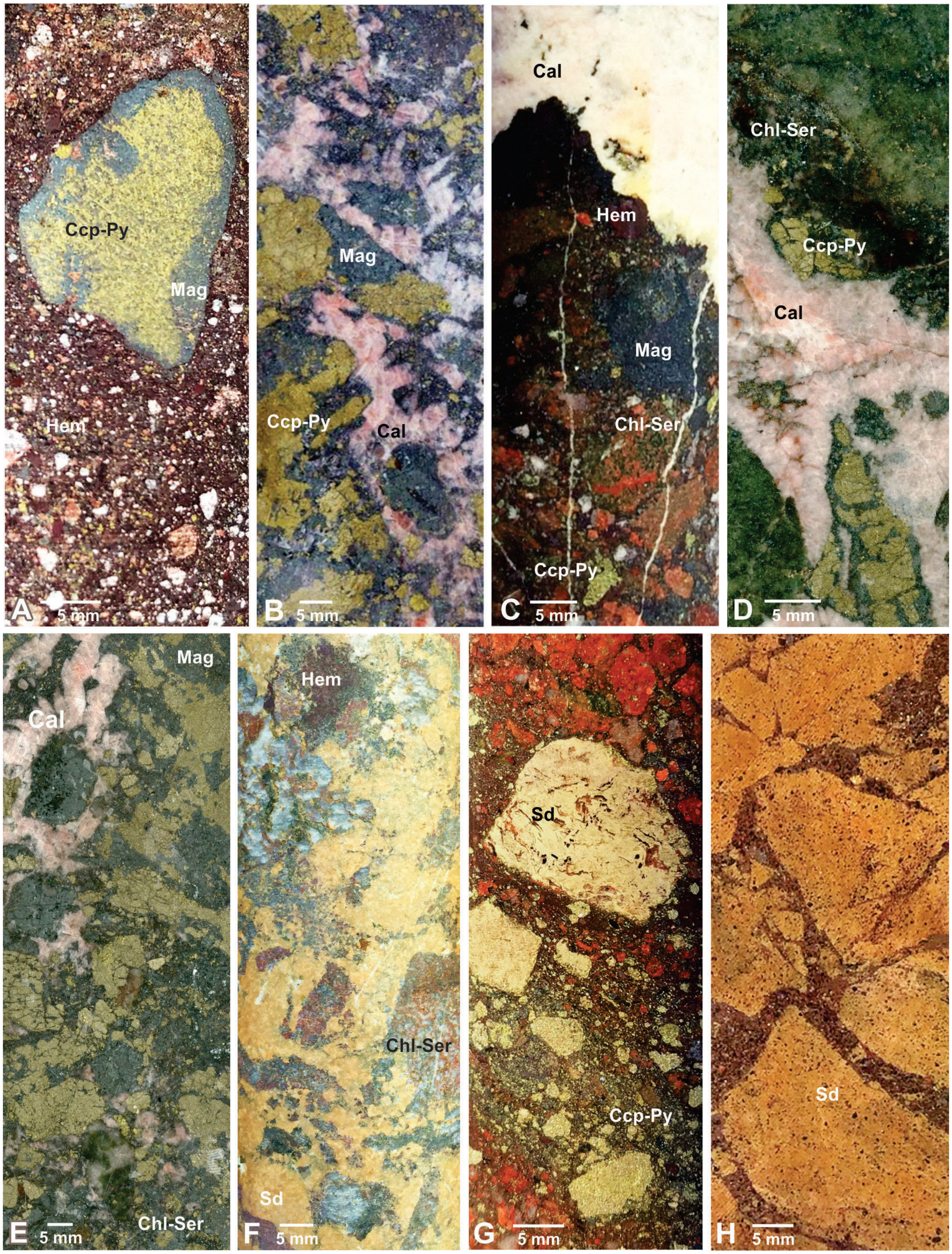


**Figure 14.** Overview of magnetite-rich and carbonate-rich alteration at Olympic Dam. **A.** Clasts of early magnetite alteration overprinted by chalcopyrite ± pyrite mineralization and preserved within a LT K-Fe altered granite breccia. The large clast is interpreted to have been transported vertically upwards and incorporated into parts of the shallower alteration facies. **B–E.** Early HT Ca-Fe magnetite-apatite alteration cut in B by chalcopyrite-pyrite mineralization and subsequently brecciated and infilled by calcite while being cut by chlorite-sericite-chalcopyrite and pyrite in C and D. In E, the series of alterations observed in B are replaced by chlorite-sericite alteration. The relationships are preserved in the deeper, peripheral part of the Olympic Dam Breccia Complex. **F–H.** Siderite-hematite (formerly magnetite)-chalcopyrite-pyrite mineral assemblage formed as the hydrothermal system evolved and overprinted earlier HT Ca-Fe facies. Hyper-saturation of $CO_2$ led to an influx of siderite-stable alteration, accompanied by hematite alteration of earlier HT Ca-Fe facies and deeper calcite alteration. H. Siderite also occurs as hydrothermal infill and cement within syn-mineralization fault zones and represents an excellent structural marker. Photos courtesy of BHP-Olympic Dam.

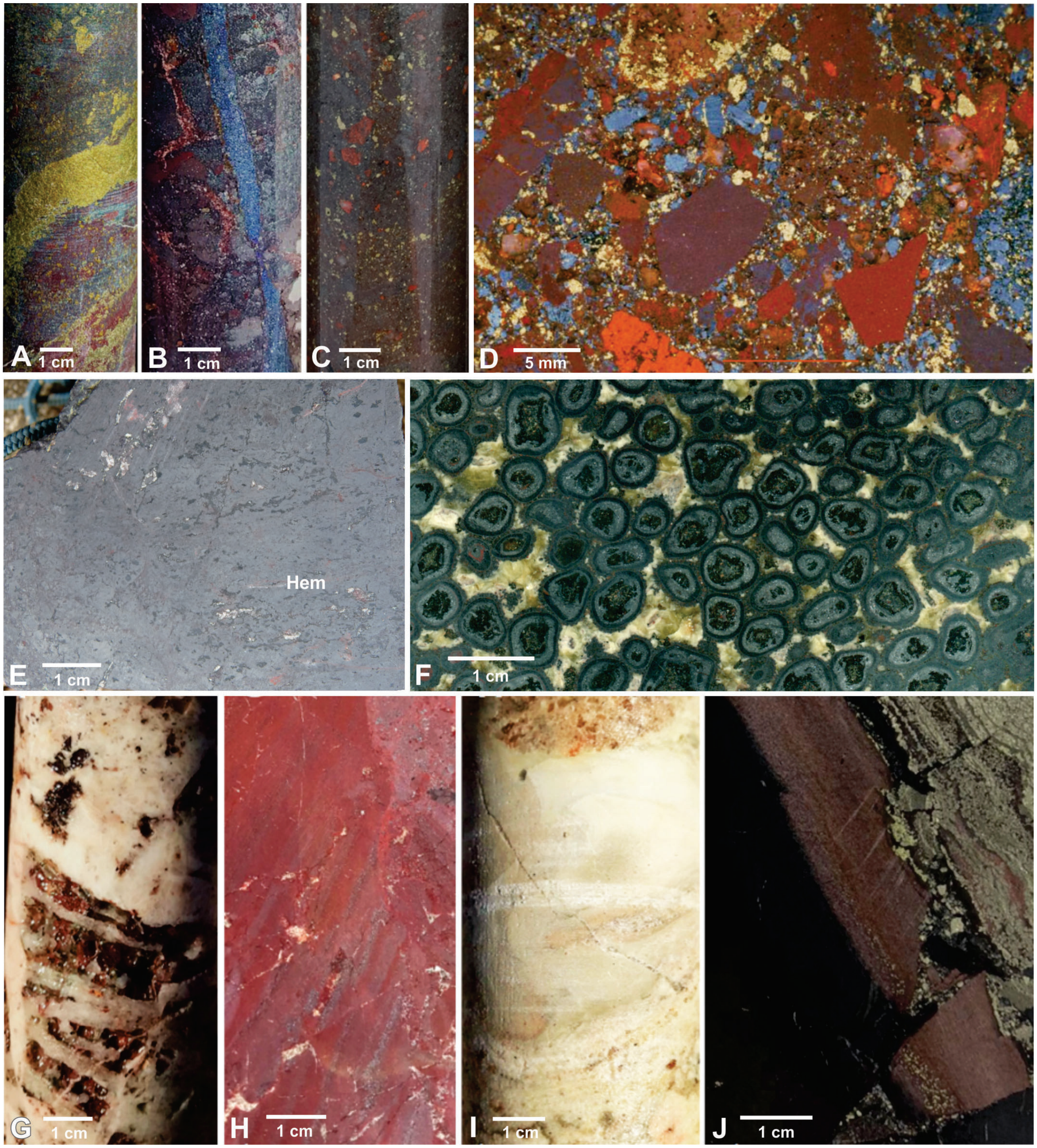


**Figure 15.** Overview of LT K-Fe facies and LT Si-Ba-Fe facies at the Olympic Dam deposit. **A–D.** Hematite-dominant LT K-Fe alteration with variable chalcopyrite- or bornite-chalcocite-dominant sulphide assemblages hosted in polyphase matrix-supported hematite breccias. Minor relict clasts of granite represent almost full textural 'inversion' of the protolith via intense brecciation-alteration textures. **E.** Sample of steely hematite alteration. **F.** Hematite-fluorite-sulphide 'pisoliths' supported by a hydrothermal siderite cement, interpreted to represent sub-surface hydrothermal boiling textures whereby the vugs are infilled from the outside in. **G.** Low-temperature 'epithermal' quartz veins, distal to the Olympic Dam deposit, represent near-surface alteration. The vein morphologies are usually chaotic. **H.** Typical hematite-quartz ± barite alteration with rare preservation of relict protoliths (volcaniclastic facies). This sample is located within the allochthonous Bedded Clastic Facies fault block, suggesting this alteration occurred in-situ near the paleo-surface as a shallow-proximal alteration. This is supported by an element signature typical of the deposit (Corriveau et al., 2022a). **I.** Sericite-illite-Al-OH-quartz altered granite breccia representing a good example of localized advanced argillic alteration at Olympic Dam. **J.** Possible preserved remnants of exhalative horizons from the overlying basin-lake floor. The red zones are barite chemical precipitate interlayered with very fine-grained hematite and chalcopyrite. Photos courtesy of BHP-Olympic Dam.

## Case study 3 – Great Bear Magmatic Zone

*Regional Geological Setting*

The GBMZ is a ca. 1876–1855 Ma silicic large igneous province (SLIP) formed within a suprasubduction zone setting (Fig. 16A; Ootes et al., 2017). Detailed geological investigations, alteration mapping and mineral exploration provide a wealth of information on this IOAA province (Fig. 16B–D; Hildebrand, 1983, 1984, 2011, 2017; Goad et al., 2000; Mumin et al., 2007, 2010; Corriveau et al., 2010a, b, 2016; Jackson and Ootes, 2012; Potter et al., 2013; Gandhi et al., 2014; Hildebrand et al., 2014; Montreuil et al., 2015, 2016a, b, c; Mumin, 2015; Corriveau and Potter, in press). The pre-, syn- and post-mineralization history of volcanic and plutonic events, as well as the spatial distribution, deposit-scale evolution and relative timing of IOA, IOCG, skarn, albitite-hosted uranium and five-element vein mineralization, are discussed herein.

Onset of SLIP magmatism consists of rare 1.88–1.87 Ga granitic dykes and intrusions emplaced after inversion of a slightly older (1.88 Ga) sedimentary basin, i.e. Treasure Lake Group that formed on an earlier continental magmatic arc (active from 2.0 to 1.97 Ga and from 1.93 to 1.89 Ga) (Gandhi et al., 2001; Corriveau et al., 2007; Ootes et al., 2017). This arc was accreted to the Archean Slave Craton during the Calderian orogeny that lasted between 1882.5 ± 0.9 to 1876.4 ± 2.4 Ma (Hoffman et al., 2011; Jackson et al., 2013). The Wopmay fault zone accommodated most of the collision between the Hottah terrane and the Slave craton. This collision occurred at a time of dramatic geodynamic changes in the subduction zone process that led to renewed magmatic flare-up at 1876 Ma within an active margin extension setting following a period of magmatic quiescence (collision of an oceanic plateau?) during a ca. 150 million year subduction-related system. Renewed arc magmatism comprised discrete 1.87 Ga high-K calc-alkaline to shoshonitic volcanic centres unconformable on the 1.88 Ga metasedimentary rocks and coeval subvolcanic intrusions, dominantly intermediate in composition in the north, and felsic (locally A-type) composition in the south (Ootes et al., 2013, 2017). Detailed stratigraphy of the associated stratovolcanoes and caldera collapse events, clastic infill and resurgent intrusive events are described in Hildebrand et al. (2010, and references therein).

Widespread IOAA metasomatism between 1873 and 1866 Ma was associated with the 1.87 Ga volcanic activity (Montreuil et al., 2016a, c; Ootes et al., 2017). Volcanic rocks and coeval yet underlying (1.88 Ga Treasure Lake Group) sedimentary rocks were preferentially altered and mineralized, but in some cases mineralization is hosted by spatially and/or genetically associated intrusions (Somarin and Mumin, 2014; Montreuil et al., 2015, 2016a, c). Coeval with metasomatism, host rocks were variably tilted, differentially uplifted and locally deformed along faults and shear zones (Enkin et al., 2012; Hayward et al., 2016; Montreuil et al., 2016a; Corriveau et al., 2022b). Subsequently, the 1.87 Ga volcanic edifices and IOAA systems were capped by a belt-scale, ca. 1862 Ma rhyolite and ignimbrite sequence while being intruded at depth by a multi-phase, 1869–1855 Ma granodiorite to granitic batholith. Most of these plutonic rocks were emplaced between ca. 1867 and 1860 Ma (Gandhi et al., 2001; Hildebrand et al., 2010; Ootes et al., 2017). The SLIP magmatism ended with intrusion of low magnetic susceptibility, high heat-generating rapakivi granite plutons locally enriched in uranium that were emplaced ca. 1860 to 1855 Ma (Gandhi et al., 2001; Hildebrand et al., 2010; Somarin and Mumin, 2012; Hayward and Corriveau, 2014; Montreuil et al., 2016a; Ootes et al., 2017).

Crustal- to deposit-scale faults were active before, during and after the development of the IOAA systems; these include the Wopmay fault, which separates the GBMZ continental magmatic arc from mostly older plutonic and metamorphic rocks that are, in part, reworked rocks of the Archean Slave Craton to the east (Fig. 16; Jackson et al., 2013; Mumin et al., 2014; Montreuil et al., 2016a). Only one major tectonomagmatic event affected the GBMZ, i.e. the 1.87–1.85 Ga magmatism (Ootes et al., 2017). Hence, the 1.87 Ga and younger units, including the IOAA systems, were not affected by any significant metamorphism except for those along the Wopmay fault zone. Remobilization of metals is limited to quartz and carbonate veins associated with local mafic sills and dykes, or with plutonic activity at 1.85 Ga (Hildebrand et al., 2010; Davis et al., 2011; Gandhi et al., 2018).

The formation of spatially discrete 1.87 Ga volcanic centres and coeval IOAA systems during a brief hiatus in continental arc magmatism along an Archean craton in the GBMZ is similar to the suprasubduction zone settings of the lower Gawler Range Volcanics in the Olympic Copper-Gold Province and both share basements of older sedimentary and arc magmatic rocks (see model and discussions in Tiddy and Giles, 2020). Even the post-IOAA system ignimbrite flare-up in the GBMZ mimics the temporal sequence of the upper Gawler Range Volcanic activity – including the age ranges of the Hiltaba Suite and the GBMZ batholith that are both the product of SLIP magmatism. As such, the distribution of GBMZ IOAA systems within fertile volcanic centres and subvolcanic intrusions, and their position as inliers among post-IOAA, largely barren (± uranium enriched) intrusions, can provide insights on the settings of mineral systems in the Olympic Copper-Gold Province (Mumin et al., 2007; Hildebrand et al., 2010; Montreuil et al., 2015, 2016a, c).

The suprasubduction environment of the GBMZ and the major change in tectonic regime during IOAA metasomatism are features also similar to Andean-type IOCG mineralization (Chen and Zhao, 2022). Furthermore, the GBMZ also has many geotectonic, architectural and chemical similarities with Phanerozoic porphyry copper systems (Mumin et al., 2010; Richards and Mumin, 2013a, b).

*Host Settings of the Mineral Systems*

The metasomatic systems of the Port Radium-Echo Bay, Camsell River, Mazenod, Cole and Lou districts (Fig. 16) feature altered and mineralized 1.87 to 1.865 Ga volcanic

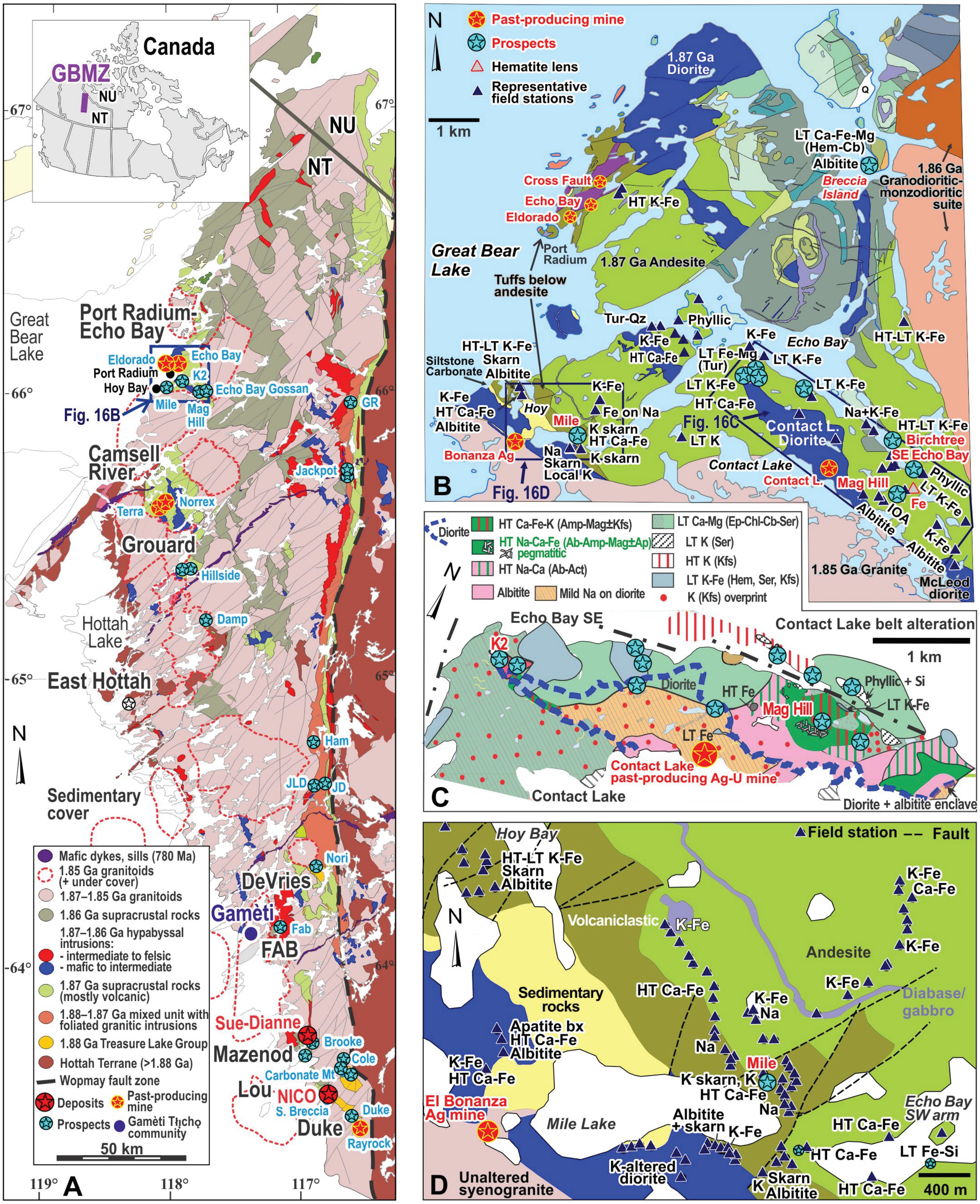


**FIGURE 16.** Geology of GBMZ exposures in the Northwest Territories (NT) and Nunavut (NU), showing the mineral systems and occurrences examined in this study (modified from Corriveau et al., 2016). **A.** Province-scale geology. For simplicity, the individual plutonic phases of the 1.87–1.85 Ga granodioritic to granitic batholith are grouped (the plutons and their phases are detailed in Hildebrand, 2011; Jackson and Ootes, 2012; Gandhi et al., 2014). The distribution of 1.85 Ga low-magnetic susceptibility rapakivi granite outlined in red defines a north-northwesterly trend front oblique to the earlier, largely north-south-trending 1.87–1.85 Ga batholith (Hayward and Corriveau, 2014). Inset shows the location of the belt in Canada. **B.** Port Radium-Echo Bay district geology and alteration (Hildebrand, 1983; Mumin, 2015). Location is shown in A. **C.** Alteration facies above the roof of the 1.87 Ga Contact Lake diorite intrusion (see Mumin et al., 2010); volcanic and intrusive rocks are tilted moderately to the northeast (Hildebrand, 1983). Location is shown in B. **D.** Geology and alteration of the Mile Lake-Hoy Bay region in the Port Radium-Echo Bay district. Location is shown in B.

sequences that were deposited above a series of coeval subvolcanic intrusions. The alteration systems also replaced carbonate-altered, thin-bedded volcaniclastic rocks at the Mile prospect (Fig. 16D; Mumin et al., 2010), and volcanic, volcaniclastic and carbonate rocks at the Grouard system (Fig. 2 in Corriveau et al., 2022a) and historic Terra mine (Hildebrand, 1984).

Available age data confirms synchronous metasomatism, volcanism and plutonism across the GBMZ at 1.87 Ga (Davis et al., 2011; Montreuil et al., 2016a, c). In the southern GBMZ, the Lou (host to the NICO deposit), Duke, DeVries and Carbonate Mountain IOAA systems are largely hosted by 1.88 Ga metasedimentary rocks of the Treasure Lake Group, which underlies the 1.87 Ga volcanic rocks (Gandhi and van Breemen, 2005; Ootes et al., 2017). The volcanic rocks and subvolcanic intrusions host the Cole albitite-hosted uranium prospect as well as the IOCG Cu-Au-Ag Sue Dianne deposit and Brooke prospect (Fig. 16A).

Subvolcanic intrusions across the belt are albitized, replaced and veined by amphibole-bearing assemblages and K-feldspar alteration (Fig. 16C, D); they locally host albitite enclaves, indicating that magmatism was coeval with metasomatism. In contrast, conglomerates overlying the Port Radium-Echo Bay and Camsell River ore systems contain volcanic rocks that are minimally altered and include clasts of metasomatic rock types such as jaspilite that formed in the upper part of the system (Mumin et al., 2010; Bowdidge et al., 2014; Bowdidge and Dunford, 2015). These conglomerates constitute part of the infill of major caldera collapse structures, and mark the end of IOAA metasomatism. Stromatolite-bearing carbonate rocks at the base of and within the 1.87 Ga volcanic sequence may reflect collapse of the arc and inundation by saline waters, although development of a saline crater lake may be a more likely origin as they were deposited after a caldera event.

The Southern Breccia zone, a three kilometre-long U (± Mo, Cu) mineralized albitite corridor south of the NICO deposit (Fig. 16), and the presence of a large conductive body below the known NICO ore zones (~500 metres) (Hayward et al., 2016) indicate that this region has potential for additional economic discoveries (Montreuil et al., 2016b; Fortune Minerals, 2019; Potter et al., 2022). Copper, Ag, Au, Zn and Pb mineralization, anomalous Au, Pt, As, P and Bi concentrations, and enrichment in REE have also been discovered in the region of the past-producing Terra mine in the Camsell River district (Bowdidge et al., 2014; Bowdidge and Dunford, 2015; Fig. 16; Fig. 2 in Corriveau et al., 2022a).

*Facies 1 Na Alteration and Albitite*

Sodic (± Ca) alteration (Facies 1 in Fig. 2) is most pervasive and intense along regional to local discontinuities (intrusive contacts, roof zones of subvolcanic intrusions, faults and deformation zones). Where albitization is intense, irregular or stratabound, albitization fronts coalesce into massive albitite irrespective of the host rock type (Figs. 17, 18). Albite dominates, and residual quartz along with apatite, calcite, titanite, rutile, zircon and monazite constitute the main accessory minerals (Hildebrand, 1986; Acosta-Góngora et al., 2015b; De Toni, 2016, Percival et al., 2016).

Though scapolite is present in many albitite zones worldwide and interpreted as evidence for the presence of evaporite within host sequences (Oliver et al., 2004; Pelleter et al., 2010; Yardley, 2012; Zhao et al., 2022), scapolite is rare within the GBMZ, and albite, not scapolite, replaces a possible evaporite unit in the DeVries system (i.e. chicken-wire textured layers of albitite interpreted as nodular anhydrite beds; Fig. 9G, H in Corriveau et al., 2022b).

Albitization typically occurs as corridors of massive to semi-continuous albitite (Figs. 12B, 13, 14); it forms earlier and commonly at deeper levels than HT Ca-Fe and HT-LT K-Fe facies alteration and sulphide mineralization. Relics of albitization occur in some deposits (e.g. the NICO deposit) within zones of HT Ca-Fe and HT Ca-K-Fe alteration (De Toni, 2016). Intense and pervasive albitization in andesite above subvolcanic intrusions forms albitite corridors a few kilometres in length in the Port Radium-Echo Bay and Camsell River districts (e.g. McLeod Lake and Mile Lake intrusions; Figs. 16B–D, 17), and in andesite and carbonates above a diorite in the Grouard system (Fig. 18A, B). The albitite is fine to coarse-grained, and white, creamy, pinkish or purplish in colour. Local homogeneous, medium-grained, pseudo-igneous textures mimic the hypidiomorphic texture of syenite or massive anorthosite (Fig. 17D–F, H, L; Corriveau et al., 2022b).

Albitization of sedimentary and volcaniclastic rocks along fault zones and away from intrusions tends to be initially layer-selective and stratabound, and increasingly discordant and pervasive as the intensity of alteration increases (see Corriveau et al., 2022b). These albitized rocks and albitites remain largely fine-grained, a possible indicator that temperatures remained lower than in albitites formed within volcanic rocks above sub-volcanic intrusions. Where quartz-rich siliciclastic units are albitized, some of the quartz grains can be preserved, leading to very competent and hard albitite that is resistant to weathering.

White albitite predates pink albitite (Figs. 17C, H, I, 18) and may be selectively preserved, such as in the albitized lapilli within a volcaniclastic unit south of Hoy Bay (Fig. 17C); both pink and white albitite can be pervasive and the dominant albitite type at outcrop scale (Figs. 18C–20D). Selective albitization of specific layers in sedimentary rocks, and more intense albitization of plagioclase phenocrysts in volcanic rocks, are both common (Figs. 19A, B, 20D). Subordinate, patchy, reddish K-feldspar alteration replaces albitite locally to pervasively, such as in the Southern Breccia corridor and the Port Radium-Echo Bay district (Fig. 17H–J). Extensive pink albitization and K-feldspar overprints enhance the resemblance of albitite to syenite (Fig. 17E).

*Albitite Breccia*

Increasing intensity of albitization results in the development of albitite corridors; however, brecciation is not linked to the intensity of albitization (in marked contrast to correlation between brecciation and intense K-Fe alteration;

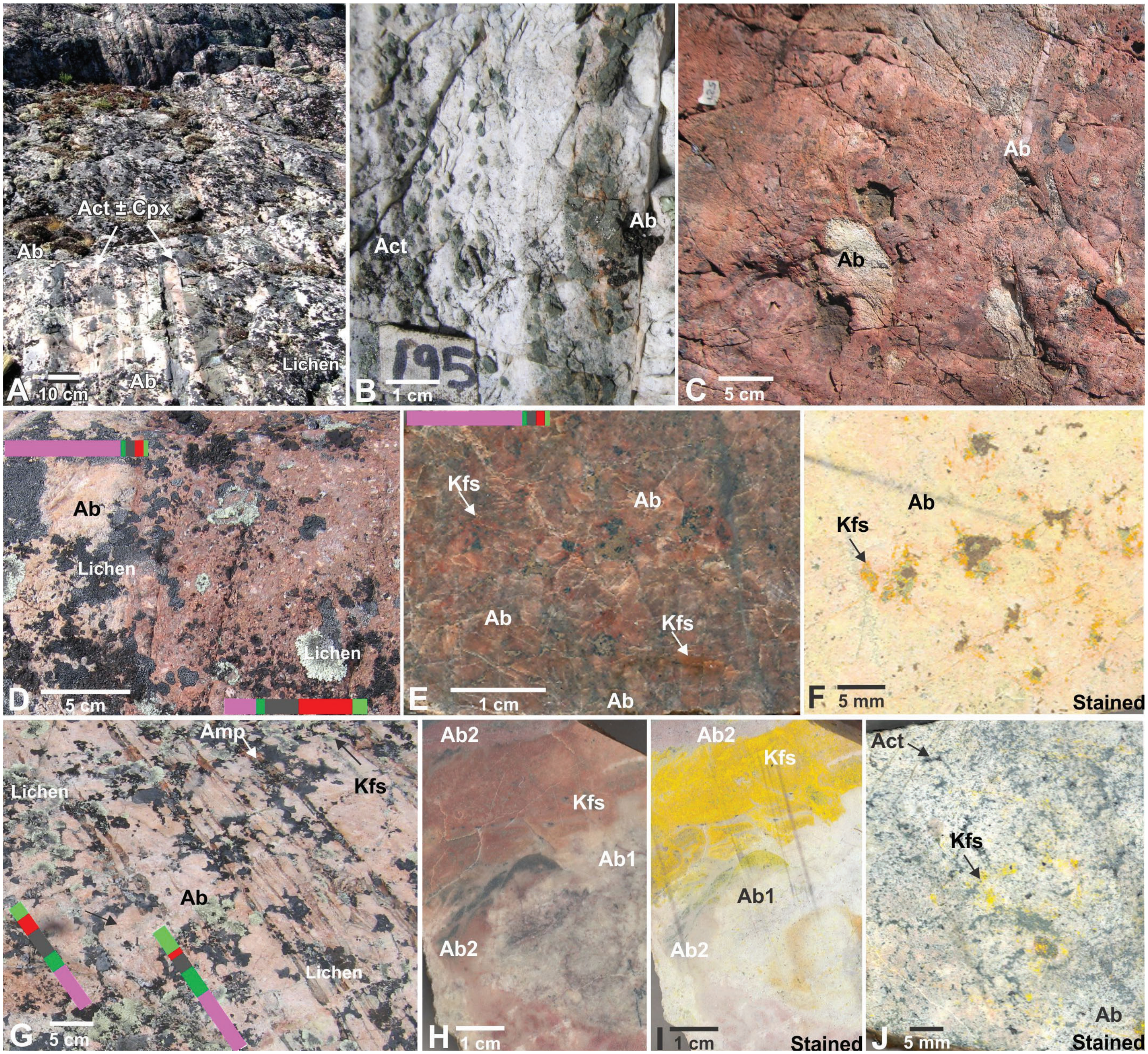


**FIGURE 17.** Albitite from the Port Radium-Echo Bay district. **A, B.** Stratabound white albitization and albite-clinopyroxene-actinolite alteration of sedimentary rocks west of the McLeod diorite (A: CQA-06-0330; B: CQA-05-0195). **C.** Lapilli tuff with early white albitization of lapilli and pink albitization of matrix south of Hoy Bay (CQA-07-0528). **D–F.** Endocontact albitite of the Contact Lake intrusion (Fig. 16B; CQA-05-0124). In these and other figures, Na-Ca-Fe-K-Mg molar barcodes provide linkages with Part 2 (Corriveau et al., 2022a). **G–J.** Albitite at the contact with the 1.87 Ga McLeod Lake intrusion (Fig. 16B, C; CQA-05-0195). The darker layers consist of stratabound albite-actinolite ± clinopyroxene alteration of the sedimentary or volcaniclastic host rocks as well as of alteration fronts and veins emplaced along or cutting across layering. A second generation of pink albitite overprints the white albitite in H and I. Disseminated actinolite and clinopyroxene are locally present (stains green in J), and K-feldspar alteration (stains yellow in I and J) of the albitite is common (abundant in H and I, minor in J). Stained = hydrofluoric etching followed by cobaltinitrite staining. NRCan photos 2020-700 to 2020-709.

Corriveau et al., 2016). Hence, metasomatic albitization does not lead to hydrothermal brecciation. Rather, albitite forms haloes along fractures and permeates damage zones, progressively replacing host rocks; such processes are most extensive along or near fault zones. However, corridors of early albitite are often extensively brecciated syn- to post albitization (e.g. Southern Breccia, Mile, DeVries, Grouard, Cole and Fab (Figs. 16A, 18B–D). Albitite clasts, breccia matrix, and massive albitite replaced by a second generation of albitite, i.e. the pink albitite (Fig. 18C, D) can be accompanied by moderate degrees of tectonic disruption.

Albitite along fault zones and zones of albitite breccia are regularly infilled and replaced by subsequent alteration assemblages. Examples include clinopyroxene-dominant skarn

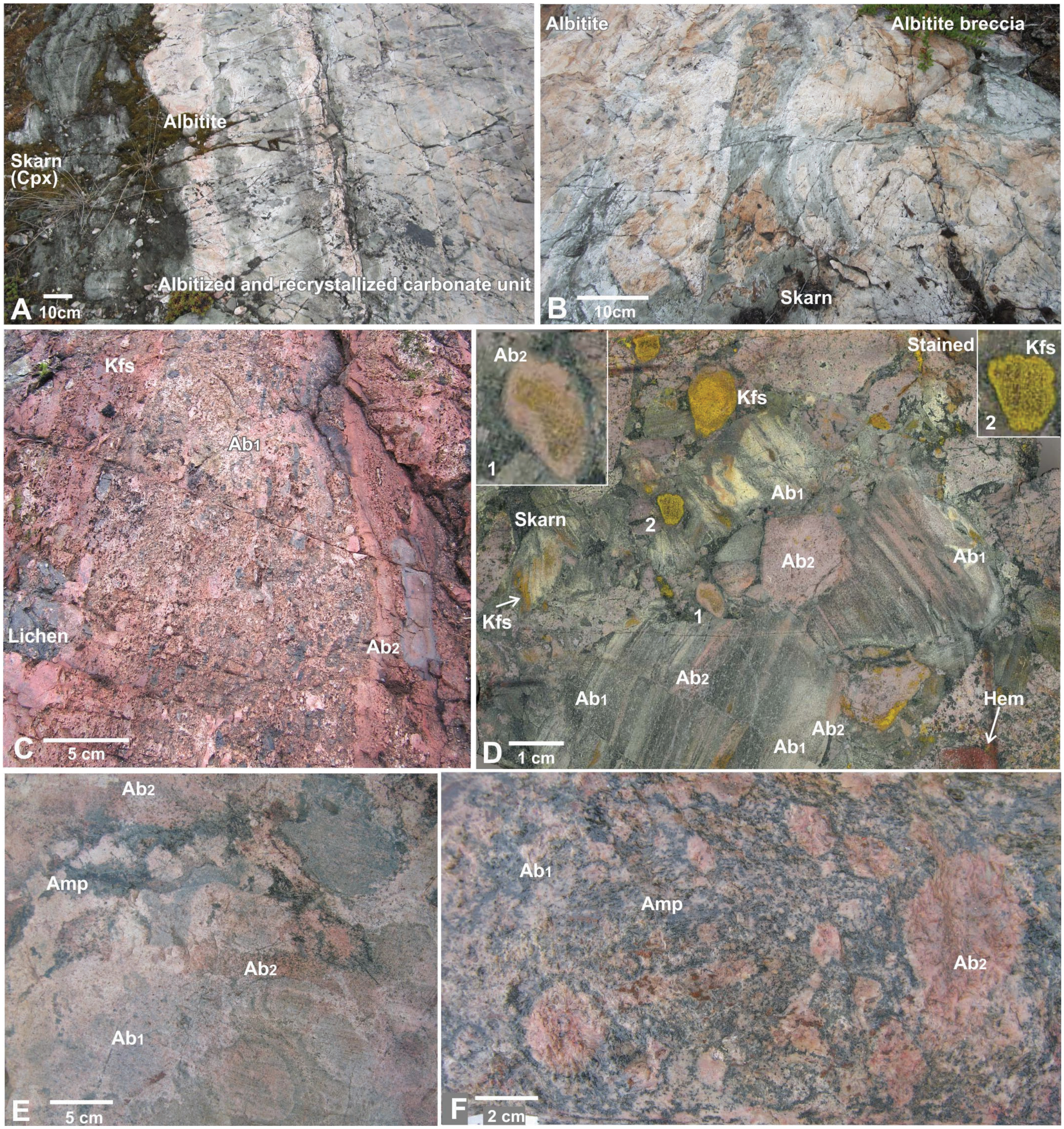


**Figure 18.** Albitite, skarn and albitite breccia in 1.87 Ga volcanic and sedimentary rocks in the GBMZ. **A, B.** Outcrop with stratabound skarn and albitite layers within an albitized carbonate unit (A) that evolves to brecciated albitite cut by skarn in B, Grouard system (10CQA-0202). **C, D.** Brecciated albitized volcaniclastic rocks above the 1.87 Ga Mile Lake diorite, Port Radium-Echo Bay district (C: CQA-05-0218; D: CQA-06-0356). Early stratabound to pervasive white albitite (Ab1) is brecciated and the albitite breccias are overprinted by pink albite (Ab2) along alteration fronts crossing clasts and matrix, along bedforms within clasts, and at clast margins (inset 1 in D). Fine-grained skarn assemblages fill the breccia matrix and weakly to strongly replace some fragments. A subsequent K-feldspar alteration extends across clasts and matrix, along bedforms in C, and is clast-selective in D (yellow stain from hydrofluoric etching and cobaltinitrite staining). The increased intensity of alteration along fragment margins provides conclusive evidence that this alteration postdates brecciation. In C, brecciation is stratabound and clasts align parallel to former bedding. **E, F.** Heterogeneous albitite with zoned patches stemming from incremental albitization (CQA-05-0105). Some albitite displays radial rods of albite in E, where a brecciated zone is infilled by an amphibole-bearing assemblage, whereas most zones of albitite have been dissolved, producing a dissolution breccia that could be misinterpreted as a diatreme in F. NRCan photos 2020-710 to 2020-715.

(Fig. 18C, D), HT Ca-Fe alteration (with amphibole- to magnetite-, or even apatite-dominant assemblages; Figs. 5, 6, 20), tourmaline (Kelly et al., 2020; Corriveau et al., 2022b), K-felsite, K-skarn, HT to LT K-Fe (Montreuil et al., 2015), LT Ca-Fe-Mg (Corriveau et al., 2022c), and phyllic to sericitic alteration and associated mineralization (Ag, Au, Co, Cu, Mo, REE, U; e.g. Damp, Southern Breccia and Cole; Montreuil et al., 2015, 2016b).

The Southern Breccia albitite corridor is bound to the northeast by a geophysical discontinuity that reaches the mantle and is interpreted as a thrust fault that juxtaposed the deeper albitite breccia corridor against the HT Ca-Fe and HT Ca-K-Fe metasomatic rocks and Au-Co-Bi-Cu ore of the NICO deposit during K and HT to LT K-Fe alteration (Craven et al., 2013; Corriveau et al., 2016; Hayward et al., 2016). A series of faults orthogonal to bedding and the inferred bounding thrust fault have segmented the corridor and exposed a broad range of alteration zones from different crustal levels across the Lou system (e.g. HT K-Fe facies with U-Cu-Mo mineralization, and shallower crustal levels with uranium-bearing LT K-Fe alteration; Fig. 11 in Corriveau et al., 2022c; Enkin et al., 2012; Montreuil et al., 2015; Potter et al., 2019). Multiple brittle-ductile shear zones and breccia bodies, parallel or discordant to the sedimentary layering, host the post-albitization alteration and record syn-metasomatic tectonic activity across the system (Montreuil et al., 2016b).

An extensive crater lake-volcaniclastic breccia complex is intensely albitized above subvolcanic diorite intrusions from Mile Lake to Hoy Bay (Figs. 16D, 18C, D; Mumin et al., 2010; Mumin, 2015). The presence of kink folds in breccia fragments suggests a tectonic control on brecciation of albitite in the Mile Lake area. Away from fault zones, crackle breccia occurs along zones of stratabound albitization interlayered with less altered tuffaceous beds south of Mile Lake. Close to fault zones and along geological contacts with contrasting rheology, large, layered to chaotic albitite breccia ± skarn occur to the south and southeast of Mile Lake (Fig. 18C, D). Breccia fragments are angular, 2 to >10 cm in diameter, and bedding in sedimentary clasts is locally internally kinked. Minor to extensive, fine-grained, poorly crystalline skarn assemblages infill the breccia matrix and form veinlets (Fig. 18C, D). Elongate clasts may be aligned parallel to bedding (Fig. 18C), but the origin of the alignment remains uncertain as local shingle breccia textures suggest that displacement of fragments occurred. Structurally above the albitized units, the volcaniclastic units were altered to skarn, moderate amphibole- to epidote-dominant HT Ca-Fe facies, K-skarn, and K-felsite, and include associated polymetallic mineralization and late hematite-quartz veins (Corriveau et al., 2010b; Mumin et al., 2010).

*Skarn and Iron Skarn Associated with Facies 1–2*

Carbonate units and carbonate-altered hosts are replaced by clinopyroxene-dominant skarn containing variable proportions of garnet prior to, during or after albitization, commonly distal to intrusive bodies. Skarn occurs as stratabound replacements within and adjacent to carbonate units at Grouard (Fig. 18A), and as irregular alteration fronts, veins or breccia-infill within albitite breccia at Grouard and south of Mile Lake (Fig. 18B–D). In the Eastern Treasure Lake system, stratabound to variably textured skarn hosts the Ron, Hump and Carbonate Mountain prospects (Mumin et al., 2010; Montreuil et al., 2016b). Skarn is commonly weakly to completely replaced by HT Ca-Fe alteration facies, such as across the Lou and Duke systems hosting the NICO deposit and Duke prospect, as well as at Fab and Grouard (Corriveau et al., 2016; Montreuil et al., 2016b).

Skarn within albitite, and least-altered units lacking potassic minerals such as biotite and K-feldspar are generally devoid of base or precious metal mineralization, such as the skarn within albitite to the southeast of Mile Lake (Fig. 18C). Barren skarn contrasts with skarn containing potassic minerals and K-skarn hosting polymetallic mineralization. Notable examples include the Mile Lake K-skarn prospect, which is significantly enriched in Zn, Cu, Pb, Ag, Mo and W, and the Carbonate Mountain skarn prospect (including skarn with a pyroxene and K-feldspar assemblage), which is mineralized in Zn, Cu and Pb (Mumin et al., 1996). At Grouard Lake, the Hillside prospect hosts Pb-Zn-Ag mineralization (galena, sphalerite, pyrite) in epidote-bearing clinopyroxene skarn that was partly replaced by actinolite ± K-feldspar (HT Ca-K-Fe) (Hughes, 1997; Knox, 1998). Chalcopyrite is locally present. High-grade Pb-Zn mineralization is also enriched in Bi (≤ 0.15%), Cd (≤ 791 ppm) and W (≤ 0.20%).

*Transitional Na-Ca-Fe Alteration Facies*

Increasing amphibole and magnetite contents marks the transition from the Na to the HT Na-Ca-Fe facies (Figs. 17J, 18F, 19). Within sedimentary and volcaniclastic hosts, both facies can coexist as distinct stratabound alteration zones consisting of albitite interlayered with albite-amphibole ± clinopyroxene alteration, such as west of the McLeod Lake pluton (Fig. 17A, G) where sedimentary structures (including local cross-lamination) and host rock lithological variations are preserved (Corriveau et al., 2022b). At DeVries Lake, albitized layers coexist with amphibole-dominant and with magnetite-dominant layers, collectively forming a Na-Ca-Fe facies assemblage. In addition to stratabound alteration, layer-concordant veins also form (Fig. 17G), suggesting that a combination of porosity, permeability and compositional differences between layers accounts for the development of the Na-Ca-Fe alteration along specific layers.

Intense grain coarsening and textural changes may occur at the HT Na-Ca-Fe facies, characterized by the development of pegmatitic textures consisting of coarse-grained elongate crystals of albite (internally consisting of microcrystalline albite) within a coarse-grained magnetite, actinolite and apatite groundmass (Fig. 19; Corriveau et al., 2022b). Accessory minerals include augite, titanite, rutile and zircon (De Toni, 2016). Such rocks form decimetre-sized patches, veins or stockworks within albitite units (Figs. 18E within zones of Ab2), ranging to kilometre-long bodies in albitized andesite (Camsell River and Port Radium-Echo Bay districts; Fig. 19), albitized porphyritic intrusions (Fab prospect; Corriveau et al., 2010b), and albitized metasedimentary rocks (Dennis prospect; Montreuil et al., 2016b). The largest body (1 km in length) lies above the Contact Lake pluton and associated albitite corridor (Fig. 16C; Mumin et al., 2007; Corriveau et al., 2010b), within a formerly homogeneous, 2 km-thick, porphyritic andesite sequence (Hildebrand, 1983). Here, a pervasive rosette texture dominates (Fig. 19D, E), but locally, interlocking fractures up to 15 m long, enveloped by haloes of comb-textured, decimetre-long albite crystals, occur over tens of metres, forming some of the most spectacular outcrops observed in the GBMZ. Outcrops of relict albitized porphyritic andesite occur sporadically throughout the body. At the exposed upper contact of the body, the host andesite is replaced by coarse-grained HT Na-Ca-Fe alteration (Fig. 19A–C). Texturally, this alteration progresses from interlocking poikilitic albite crystals with 'fuzzy' crystal margins, abundant inclusions, and interstices filled with very fine-grained magnetite and amphibole (Fig. 19B), to increasingly well-formed albite rods in a mosaic-textured matrix of coarser-grained interstitial amphibole, amphibole-magnetite and amphibole, magnetite and apatite (Fig. 19C–E; Somarin and Mumin, 2014; see also Corriveau et al., 2010a, b, 2016, 2022b).

*Facies 2 (HT Ca-Fe) and IOA Mineralization*

The HT Ca-Fe alteration facies consists of mineral assemblages with amphibole, magnetite, apatite and locally epidote. In siliciclastic rocks, amphibole-dominant assemblages tend to be early and followed by magnetite-dominant assemblages (Figs. 18D–F vs. 18G–I and 19A vs 19B). The transitions from HT Na-Ca-Fe to HT Ca-Fe facies in such rocks are well exposed structurally above the McLeod, Mile and Contact lakes plutons (Fig. 16B–D). In volcanic rocks, albitite bodies that evolved to pseudo-pegmatitic HT Na-Ca-Fe metasomatites are cut by amphibole and magnetite-amphibole ± apatite veins and stockworks ± albite haloes (Fig. 20). At hand sample or outcrop scales, amphibole infills the fractures in albitite crackle breccia (HT Ca-Fe; Figs. 18E, 20F, G), or forms a dissolution breccia that may resemble a diatreme, featuring albitite clasts replaced by amphibole (Fig. 18F).

In sequences with carbonate rocks, Na evolves to HT Ca-Fe facies through skarn (± magnetite-skarn), amphibole-dominant, mixed amphibole-magnetite-dominant or locally epidote-magnetite-dominant, and finally to magnetite-dominant assemblages and IOA mineralization (Figs. 18A, B, 21, 22; Acosta-Góngora et al., 2015b; Montreuil et al., 2016a, b; Corriveau et al., 2022b). West of Mile Lake (Fig. 20C), an apatite-dominant assemblage forms the matrix of an albitite breccia with an amphibole-dominant breccia halo. Replacement,

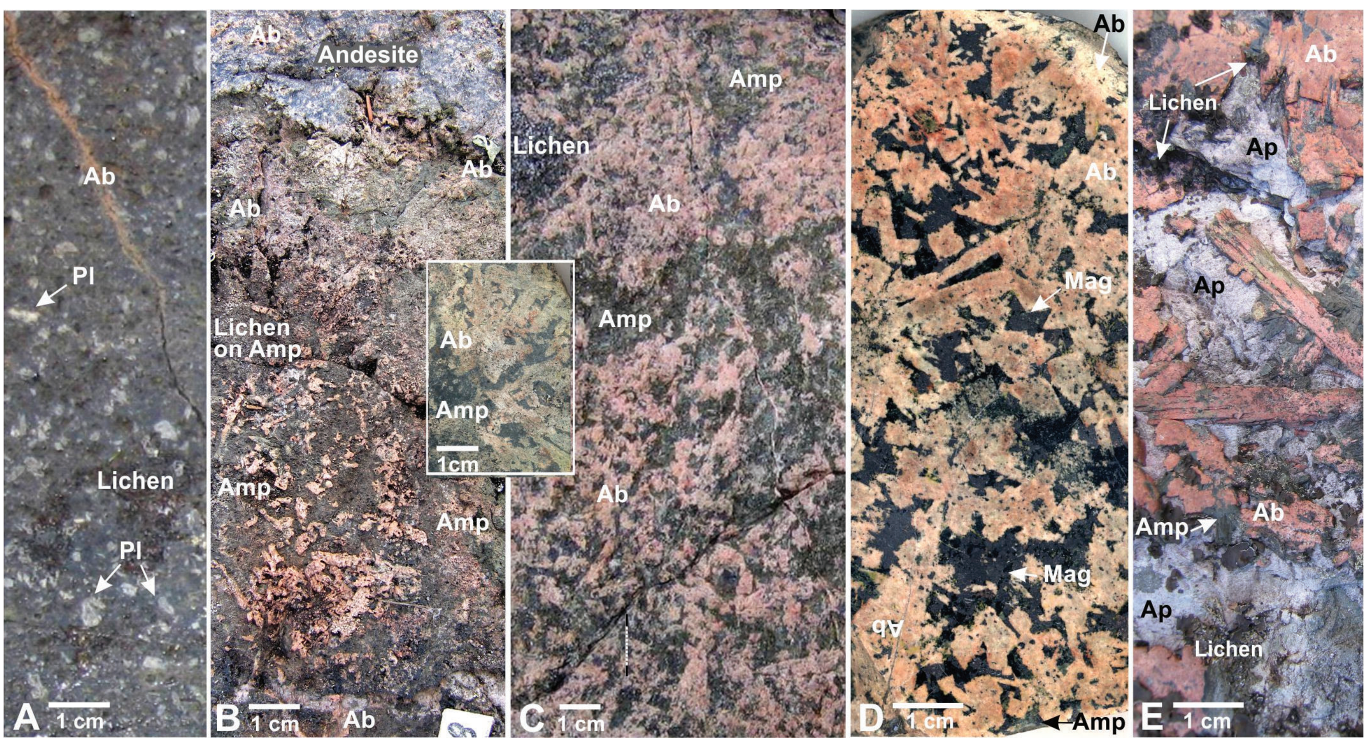


**FIGURE 19.** Incremental texture-destructive HT Na-Ca-Fe alteration of albitized porphyritic andesite, Mag Hill prospect area (Fig. 16C). **A.** Least-altered andesite with plagioclase phenocrysts partly to locally pervasively albitized (CQA-05-0095). **B.** Porphyritic andesite albitized and progressively replaced by randomly oriented, metasomatic, poikiloblastic, rod-shape albite crystals and interstitial fine-grained amphibole. **C.** Porphyritic andesite pervasively replaced by albite and amphibole displaying poorly-formed crystals compared to D and E (CQA-05-0095). These zones have gradual contacts with the porphyritic andesite of A. **D, E.** Pegmatitic, randomly oriented, megascopically euhedral albite crystals (light pink), interstitial amphibole and magnetite (in D) and apatite (in E) (CQA-05-0113). Microscopically, the albite crystals consist of albite neoblasts. NRCan photos 2020-716 to 2020-720.

veining and breccia infilling by HT Ca-Fe assemblages occur within or structurally above Na alteration zones (Fig. 20). Within intense HT Ca-Fe alteration zones, relics of albite and clinopyroxene are locally present (De Toni, 2016), but where HT Ca-Fe alteration is incipient to strong, relics of albitized hosts and albitite are common (Figs. 20D–G, 21A–C, 22A) and relics of skarn occur locally (Mile prospect, NICO to South Duke, Fab; De Toni, 2016).

Replacive HT Ca-Fe alteration produces a great variety of mineral assemblages, mineral proportions and textures (Figs. 20–22). Selective alteration consists of preferential replacement of volcanic matrix by amphibole (Fig. 18D) or magnetite (Corriveau et al., 2022b), amygdales by magnetite within volcanic rocks, laminations by magnetite in stromatolites (Grouard), and sedimentary cross laminations by actinolite (McLeod Lake) and magnetite (Camsell River district), as illustrated by Corriveau et al. (2022b). Stratabound alteration is also frequently very selective, and mineral proportions vary significantly from one layer to another. Stratabound HT Ca-Fe alteration is typically weak at Mile Lake, where it postdates skarn alteration, but it is intense at Port Radium (Fig. 20E) and in the area of the NICO deposit (Fig. 22). In many cases, preservation of fine sedimentary lamination and bedding structures creates a metasomatite that resembles sedimentary iron formation (Figs. 21A–C, 22B, C), whereas pervasive and intense amphibole alteration can produce rocks that resemble a (metamorphic) amphibolite (Corriveau et al., 2022b). Metasomatites can also resemble marl and volcanic lavas.

Veins tend to follow the metasomatic evolution of the HT Ca-Fe facies, as early amphibole-dominant assemblages evolve toward more magnetite-dominant assemblages (Figs. 20A, B, 21). Amphibole-dominant veins commonly cut albitite, and magnetite-dominant veins cut HT Ca-Fe-altered units (± earlier albitite), but the prograde sequence can be disrupted by renewed HT Ca-Fe alteration in the form of amphibole veins cutting the HT Ca-Fe and HT Ca-K-Fe assemblages (Figs. 20A, B, E, 21C). Magnetite veins locally have diffuse contacts (e.g. in carbonate rocks; Corriveau et al., 2022b), and stratabound offshoots within clastic sedimentary units occur locally (Fig. 21B).

Within andesitic volcanic rocks, HT Ca-Fe alteration is most intense where it evolves to IOA mineralization (e.g. Port Radium, Mag Hill, Terra; Figs. 20, 21D, E). Within sedimentary rocks, this facies can be very extensive, especially where carbonate rocks are present (e.g. the Lou, Duke, and Grouard systems; Montreuil et al., 2016b; Corriveau et al., 2022b). The HT Ca-Fe facies is also associated with a series of IOA zones along the Wopmay Fault, some of which contain REE mineralization (Corriveau et al., 2015, 2016, 2022a; Montreuil et al., 2016b). Replacive HT Ca-Fe metasomatites and IOA mineralization may be brecciated, with clasts and matrix having varied amphibole, amphibole-magnetite, and amphibole-magnetite-apatite assemblages (Fig. 21H, I).

Fluidized IOA breccia zones showing clast alignment diagnostic of clast transport (i.e. fluidization; Jébrak, 2022) form bodies up to a metre wide that sharply cut albitite. Flow textures in fluidized breccia zones resemble xenolith transport in dykes. These breccias occur without in situ development of amphibole- to magnetite-rich HT Ca-Fe replacement zones and are most common in the Camsell River district (Fig. 21D, E; southwest of Terra mine; Bowdidge et al., 2014; Bowdidge and Dunford, 2015; Corriveau et al., 2016). Magnetite-rich alteration and veins also cut albitite in the Southern Breccia corridor but have no spatial association with amphibole-rich HT Ca-Fe facies (the latter prevailing on the opposite side of the fault zone that separates the Southern Breccia corridor from the NICO deposit; Montreuil et al., 2015, 2016b).

In the Peanut Lake area and across the Duke system (Fig. 16A), domains with strong brittle-ductile deformation and local folding extend from a few metres to hundreds of metres in length and a few tens of centimetres to a few metres in thickness (Fig. 21C). Collectively, they define narrow deformation zones up to 1 km in length (Montreuil et al., 2016a, b). Features like amphibolite layers containing red (almandine) garnet porphyroblasts, which could be interpreted as the products of regional (orogenic) metamorphism (Corriveau and Spry, 2014), occur in higher-strain domains within the HT Ca-Fe facies in stratigraphic contact with least-altered sedimentary rocks that have preserved ripple marks (Duke system).

*Facies 2-3 (HT Ca-K-Fe) and Au-Co-Bi Deposits*

A transitional HT Ca-K-Fe assemblage (between the HT Ca-Fe and HT K-Fe alteration facies) is common in carbonate-rich sedimentary rocks, and commonly hosts cobalt and Co-Au-Bi mineralization (Figs. 22E, F, 23). In siliciclastic rocks, the spatial footprint of this facies tends to be more restricted. The transitional HT Ca-K-Fe facies also occurs as veins and replacements in HT Ca-Fe facies rocks, as observed in the Port Radium IOA prospect (Corriveau et al., 2022c) and NICO deposit (Mumin et al., 2010; Corriveau et al., 2016). Mineral assemblages consist of combinations of amphibole, magnetite, biotite, K-feldspar, tourmaline and iron- or cobalt-sulphides, arsenides, native bismuth, bismuthinite, bismuth tellurides, emplectite, native gold, gold tellurides, chalcopyrite, pyrite, pyrrhotite, scheelite and various Au-Bi-Sb-Te minerals (Figs. 22E, F, 23; Goad et al., 2000; Acosta-Góngora et al., 2015b; Montreuil et al., 2015, 2016b).

In albitized rocks or geological units with elevated feldspar contents, the transitional HT Ca-K-Fe facies initially consists of 1) K-feldspar haloes associated with magnetite-amphibole ± apatite veins, stockworks and breccias in albitite (Figs. 22E, 24A, B) or albitized rocks (Fig. 24C, D); and 2) K-feldspar replacement of albite crystals in equilibrium with interstitial amphibole and magnetite in pegmatitic Na-Ca-Fe metasomatite. In geological units rich in ferromagnesian minerals, overprinting of biotite (± K-feldspar) on earlier amphibole and amphibole-magnetite is characteristic of the HT Ca-K-Fe alteration facies (Figs. 22, 23).

Biotite-rich HT Ca-K-Fe alteration is largely replacive and stratabound (Fig. 22), locally foliated or brecciated; at the

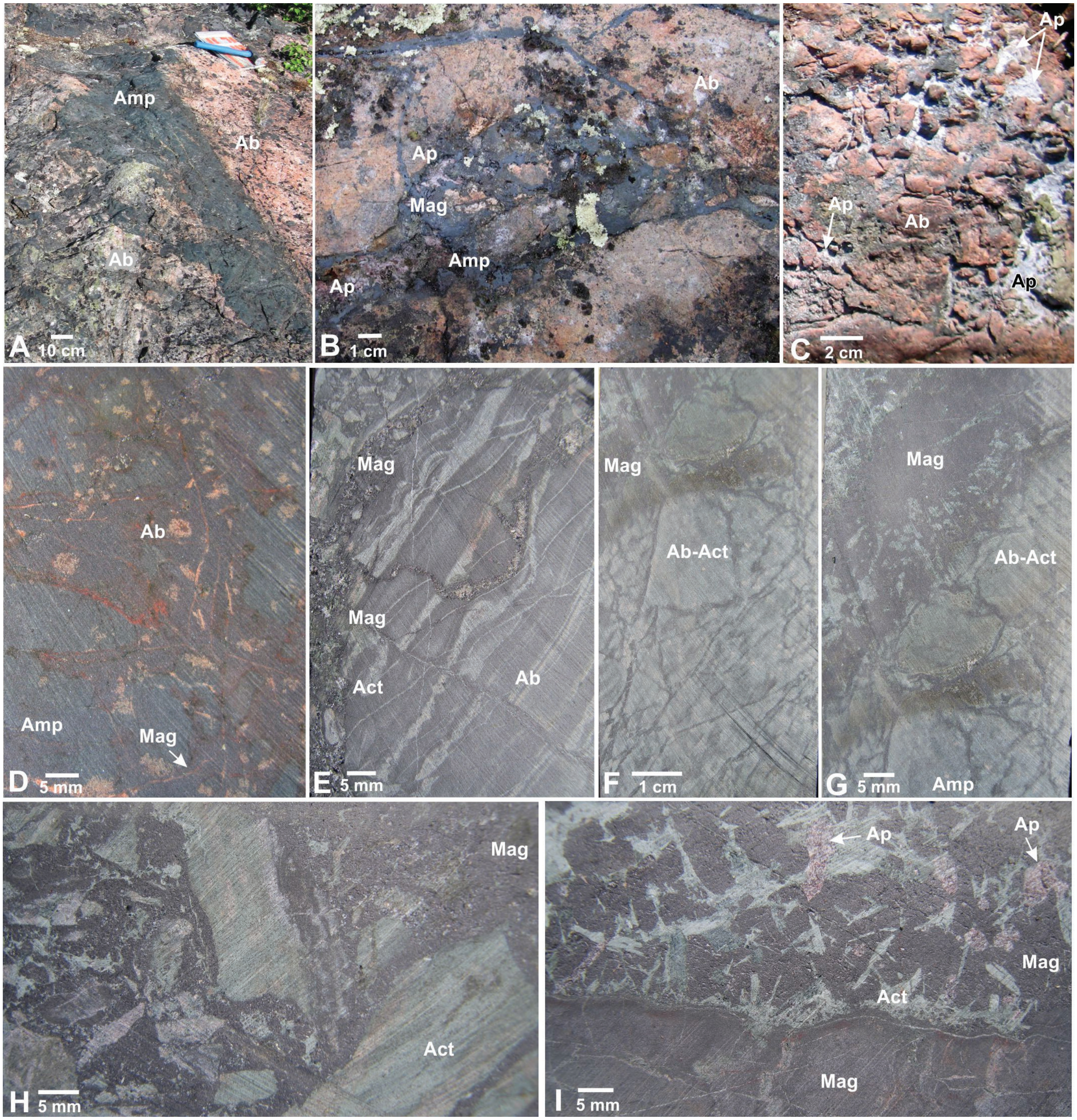


**Figure 20.** High-temperature Ca-Fe alteration. **A.** Amphibole-dominant alteration that ranges from a sharp and linear vein morphology to a replacement front within an albitized porphyritic intrusion, Fab system (CQA-06-0384). **B.** Magnetite-dominant veins with amphibole and apatite, transitioning to breccia within albitized andesite, Port Radium-Echo Bay district (CQA-05-0100). **C.** Brecciated albitite infilled with apatite, west of Mile Lake (CQA-07-0534). **D, E.** Amphibole-magnetite replacement in andesite (in D) and sedimentary rock (in E) in the Port Radium IOA prospect. In D, plagioclase phenocrysts are preferentially albitized and the volcanic matrix altered to amphibole. In E, stratabound amphibole, magnetite and albite alteration is cut by a magnetite vein. **F, G.** Brecciated albitized host infilled and replaced by amphibole, cut by a magnetite vein (in F), and replaced extensively by magnetite (in G) (Port Radium). **H.** Amphibole-altered host brecciated and infilled by magnetite (Port Radium). **I.** Zones of magnetite replacement intersected by drilling at Port Radium are cut by an actinolite-magnetite-apatite assemblage. NRCan photos 2020-721 to 2020-729.

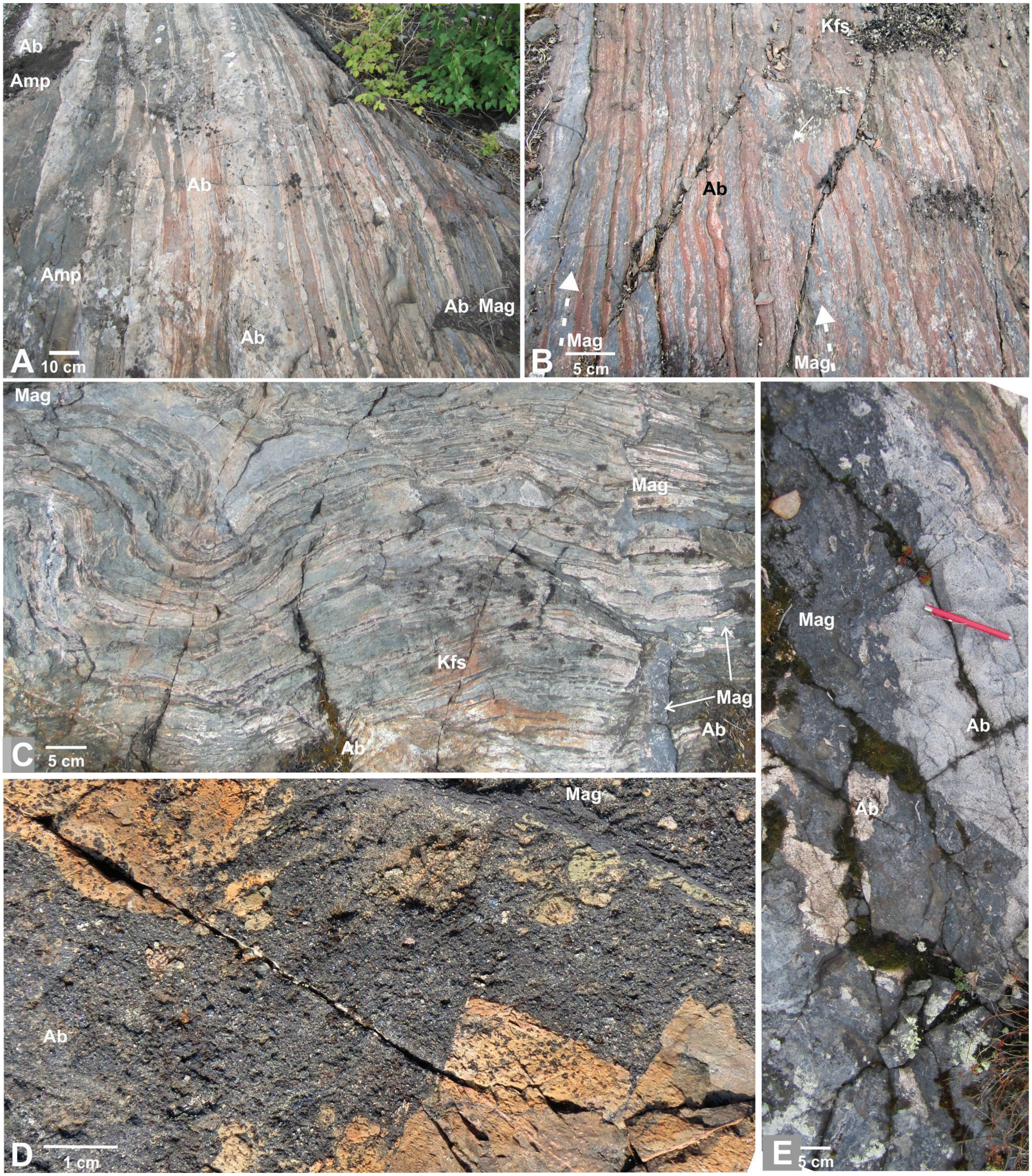


**Figure 21.** High-temperature Ca-Fe alteration and IOA mineralization. **A–C.** Albitized siltstone replaced by stratabound amphibole- to magnetite-dominant alteration, at Peanut Lake southeast of the NICO deposit (11PUA-028). Ductile deformation is coeval with magnetite alteration and leads to boudinage of albitized layers in B and folding of magnetite-rich layers in C. In B, some layers are not fully replaced by magnetite, highlighting the progression of alteration fronts along bedding and ruling out a sedimentary origin for the magnetite layers. Stratabound K-feldspar alteration replaces albitized layers and is accompanied by hematization, enhancing the resemblance of the metasomatic rock to a banded iron formation. **D, E.** Fluidized magnetite breccia (i.e. with transport of breccia clasts) within albitite, in which fluidization is recorded by the preferred orientation of albitite fragments (in E) along a flow foliation parallel to the magnetite contact. D, E: photos courtesy of DEMCo Ltd; A–C: NRCan photos 2020-730 to 2020-732.

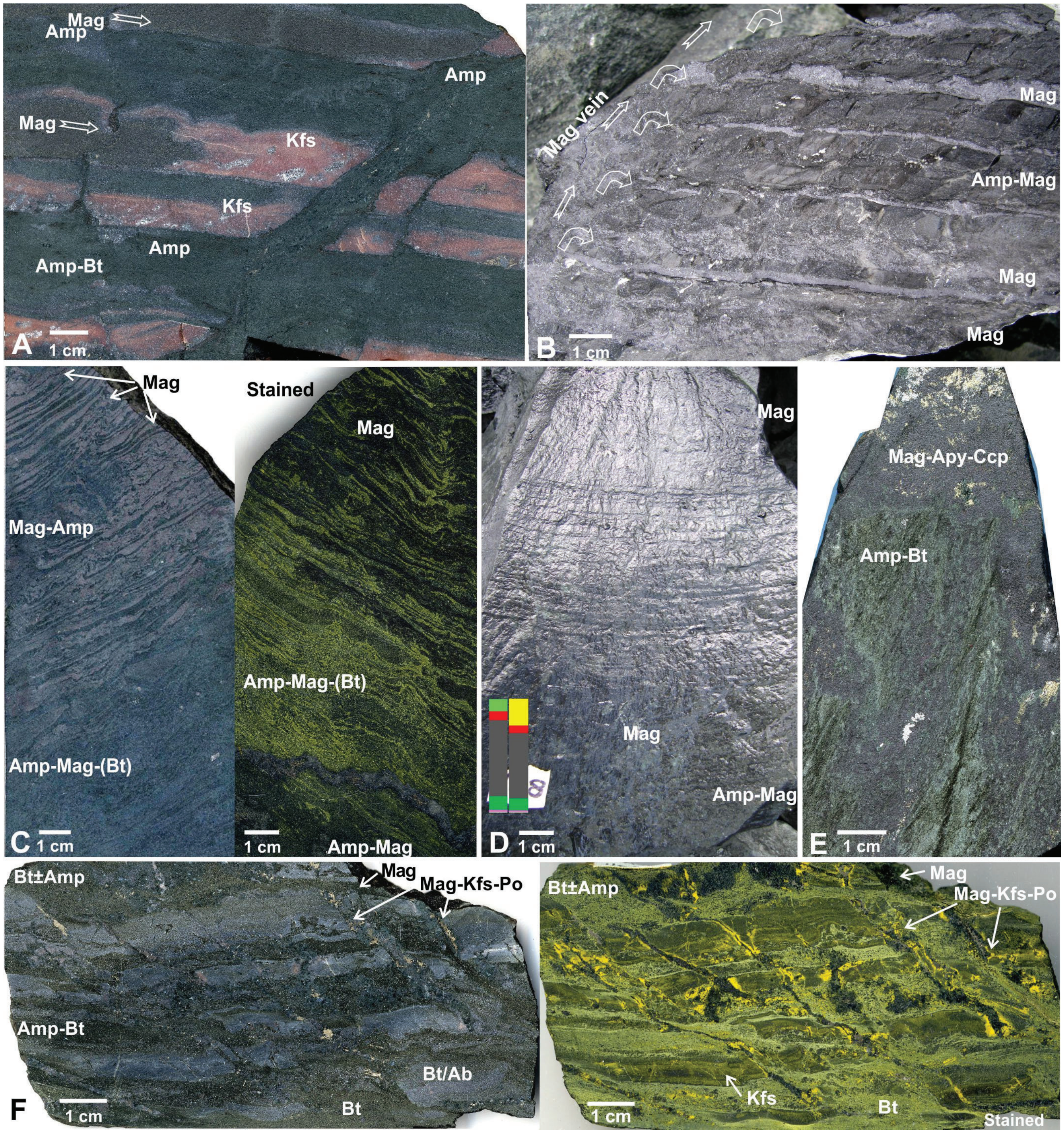


FIGURE 22. Repeated pulses of HT Ca-Fe and HT Ca-K-Fe alteration and veining of metasiltstone within the NICO deposit. **A.** Relics of albitized siltstone are selectively replaced by stratabound amphibole, amphibole-magnetite, magnetite, amphibole-biotite and K-feldspar alteration (CQA-07-0480). Magnetite alteration fronts (arrows) replacing K-feldspar-altered layers are preserved. Amphibole veins crossing the stratabound alteration record renewed HT Ca-Fe facies. **B–D.** Preferential replacement of wacke layers by magnetite and of siltstone layers by amphibole-magnetite (± biotite) assemblages (B: CQA-07-0460; C: CQA-07-0469; D: CQA-07-0468). In B, the stratabound magnetite alteration represents multi-phase haloes of a magnetite vein. In C (right), magnetite remains black whereas amphibole-magnetite and accessory biotite stains green. Renewed amphibole-magnetite-biotite alteration leads to destruction of bedforms. In D, molar barcodes are Na-Ca-Fe-K-Mg (left) and Na-Ca-Fe-K-(Si/3) (right). **E.** Weakly foliated, stratabound amphibole-biotite alteration cut by irregular fronts of amphibole-magnetite alteration and sharply cut by a magnetite-arsenopyrite-chalcopyrite vein with amphibole haloes (CQA-08-0552). **F.** Stratabound amphibole alteration and stratabound albite alteration replaced by K-feldspar and by stratabound to discordant biotite-rich alteration fronts (CQA-07-0486E). Faults cutting the multiple phases of stratabound alteration are infilled by a set of parallel magnetite and pyrrhotite veins with K-feldspar haloes, defining a HT K-Fe mineral assemblage. NRCan photos 2020-733 to 2020-740.

NICO deposit and in the Duke system, it hosts As-Fe-Co-rich sulpharsenides and sulphides (e.g. cobalt-rich arsenopyrite ± pyrite and pyrrhotite) either as disseminations, veins or veinlets (Figs. 22, 23; Acosta-Góngora et al., 2015a, b; Montreuil et al., 2016b). In contrast, intense K-feldspar-rich amphibole-magnetite alteration is typically brecciated and mineralized with chalcopyrite (Fig. 24C, D; discussed further in next section) in addition to arsenopyrite. At the NICO deposit, the HT Ca-K-Fe assemblages (magnetite, hornblende, biotite, ± tourmaline ± K-feldspar) form replacive alteration fronts, veins and rare breccia zones that pervasively overprint or cut each other within massive or stratabound amphibole- to magnetite-altered metasedimentary rocks (Figs. 21, 22). Faulting of stratabound HT Ca-Fe and Ca-K-Fe alteration was coeval with renewed amphibole or HT Ca-K-Fe veining with or without sulphides and sulpharsenides (arsenopyrite and pyrrhotite dominant), pyrite and chalcopyrite (Fig. 23). The distribution of arsenopyrite and other sulpharsenides occurs as veins, and as stratabound disseminations that typically originate in veins (Fig. 23A). Discordant dissemination trains of arsenopyrite parallel to the brittle fault network are interpreted as incipient veining along structurally damaged zones.

Brecciation of stratabound HT Ca-Fe and HT Ca-K-Fe metasomatites and mineralized zones is rare and largely cryptic across the NICO deposit. However, in one case an ore breccia displays clasts of stratabound hornblende-actinolite-magnetite alteration in a matrix of fibrous and radial actinolite (Corriveau et al., 2010b). This radial texture in actinolite crystals is also observed in alteration fronts that cut HT Ca-K-Fe and earlier HT Ca-Fe stratabound alteration, where it forms diffuse stockworks or infills fault zones, including a fault that cuts a rhyolite dyke and juxtaposes it against brecciated, stratabound HT Ca-Fe alteration (Fig. 23F). The biotite-amphibole-magnetite-arsenopyrite assemblage along the fault provides evidence of syn-metasomatic faulting. Other breccia zones consist of clasts of amphibole-rich metasomatites within a K-feldspar-altered amphibole- and amphibole-magnetite matrix, signalling prograde evolution to the more K-feldspar-rich HT Ca-K-Fe facies. A breccia infilled by magnetite-calcite-chalcopyrite bears similarities to the later-stage mineralization assemblage of the Ernest Henry deposit (Fig. 23G).

*Facies 3 (HT K-Fe)*

The HT K-Fe alteration facies shows two distinct end-member assemblages biotite and magnetite with variable amounts of K-feldspar, chalcopyrite, pyrite and arsenopyrite; and K-feldspar and magnetite with variable amounts of biotite, chalcopyrite, bornite and pyrite (Mumin et al., 2007, 2019; Montreuil et al., 2016b, c). The biotite-rich facies (1) generally forms earlier than the K-feldspar-rich assemblage; (2) is most common in sedimentary and mafic host rocks and in earlier HT Ca-Fe and HT Ca-K-Fe alteration zones; (3) is largely stratabound in sedimentary hosts; and (4) locally displays a mineral foliation at the NICO deposit (Fig. 22E, F) and in DeVries system (Ootes et al., 2013; Kelly et al., 2020). Biotite-magnetite alteration also replaces albitite within sedimentary rocks at the Southern Breccia. Within the HT K-Fe facies of the DeVries system, zones of intense magnetite-biotite replacement and local biotite breccia evolve to magnetite-K-feldspar and tourmaline alteration, breccia and associated sulphide mineralization (Ootes et al., 2010; Kelly et al., 2020).

The K-feldspar-magnetite end-member is most common in least-altered to potassic-altered felsic to intermediate volcanic and porphyritic intrusive rocks (Fig. 24E–G). Where weak to moderate in intensity, this alteration initially produces a variegated K-feldspar-magnetite alteration (e.g. to the north of the NICO deposit and at Brooke; Fig. 24E). Increased intensity of K-feldspar-magnetite alteration leads to brecciation. Altered host rocks evolve from stockworks to breccia bodies; magnetite preferentially crystallizes within the breccia matrix, and K-feldspar replaces fragments and forms haloes along the iron oxide breccia zones. Although alteration styles and mineralogy differ between matrix and clasts, the overall alteration assemblage includes both K-feldspar and magnetite. Chalcopyrite, local bornite, bismuthinite, pyrite, fluorite, gold, molybdenite or uraninite precipitate as disseminations within the matrix or as narrow veinlets across breccia. The transition from least-altered volcanic rocks to mineralized breccia is particularly well exposed at the Chalco and Summit Peak copper prospects above the NICO deposit, the Cu-Au-Ag Sue Dianne deposit, and the Fab and Brooke prospects (Fig. 23C–G; Mumin et al., 2007, 2010; Corriveau et al., 2010b, 2022c; Montreuil et al., 2016a, b, c). At the Southern Breccia, the HT K-Fe breccia is enriched in uranium (Montreuil et al., 2015; Potter et al., 2019, 2022). As magnetite contents increase, matrix magnetite and associated mineralization replaces the K-feldspar-altered fragments, breaching earlier K-feldspar altered clast margins (Fig. 24G), as observed in the Ernest Henry deposit (Fig. 7B).

Adjacent to amphibole-rich replacive alteration zones and veins, K-feldspar-magnetite breccia may also include amphibole in the matrix as part of a transition from the HT Ca-Fe facies to HT Ca-Fe-K facies (Fig. 24C, D). Sulphide mineralization tends to crystallize in veins and veinlets as well as disseminations within the breccia matrix.

At Peanut Lake, east of the NICO deposit, a HT K-Fe breccia zone tens of centimetres to metres wide cuts folded and boudinaged stratabound HT Ca-Fe metasomatites, recording the transition from ductile behavior during HT Ca-Fe alteration to brittle behaviour during HT K-Fe alteration (Corriveau et al., 2022b). At the Duke prospect, an atypical epidote-bearing HT K-Fe assemblage (K-feldspar–epidote ± magnetite) replaces earlier HT Ca-Fe and Ca-Fe-K alteration zones and evolves to a LT Ca-Fe-Mg alteration (Montreuil et al., 2016b).

*Facies 4a (K-skarn Breccia)*

Potassic skarn, consisting of skarn intimately associated with K-feldspar alteration, hosts polymetallic Zn-, Pb-, Cu-sulphide mineralization within the Mile Lake breccia complex (Fig. 25; Mumin et al., 2010). The K-feldspar-bearing skarn is distinct from simple K-feldspar alteration of earlier skarn in its timing and spatial relationships to other alteration facies.

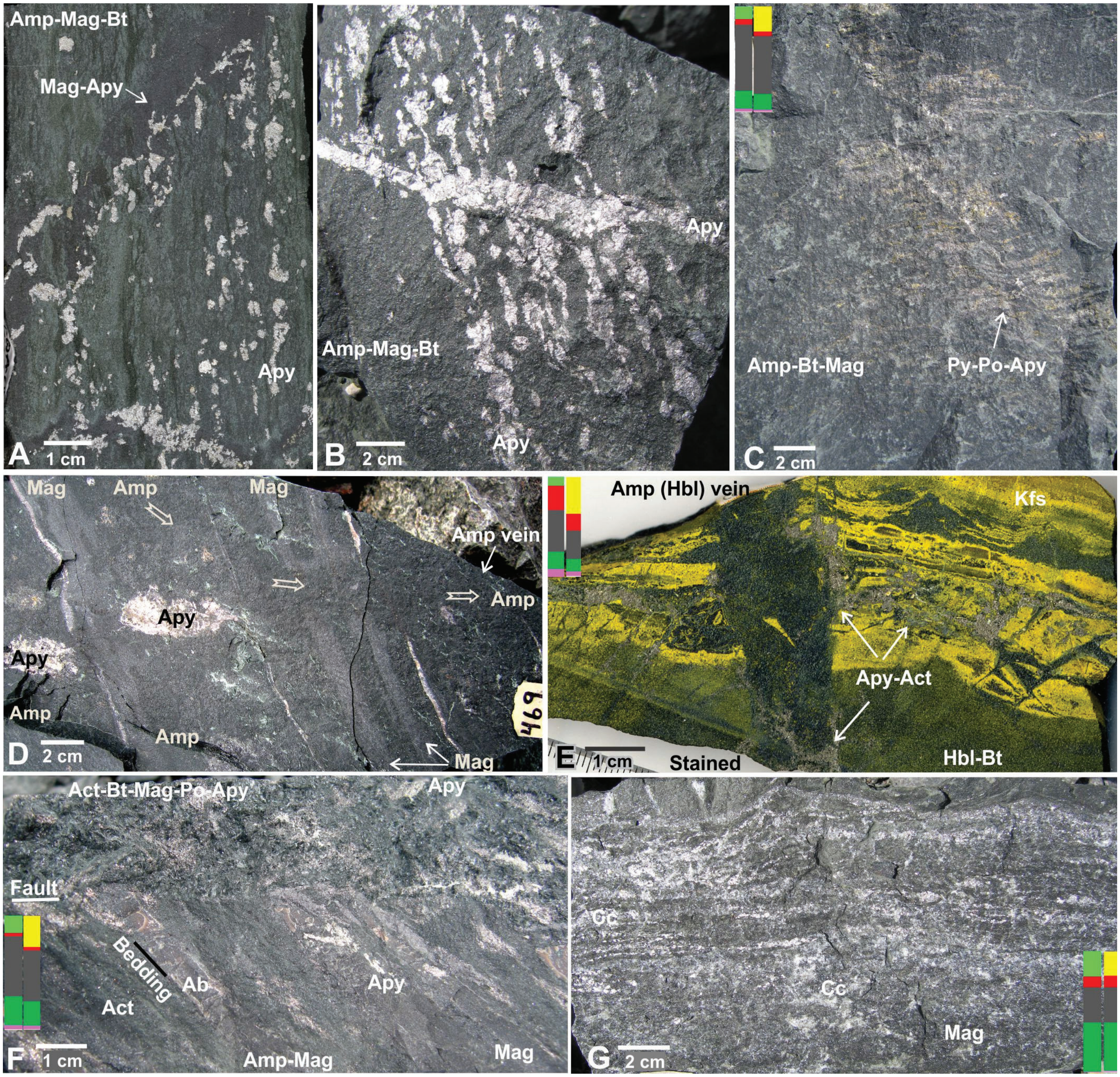


**Figure 23.** Cyclical HT Ca-Fe and HT Ca-K-Fe alteration within the NICO Au-Co-Bi-Cu ore zone. **A.** Stratabound HT Ca-Fe magnetite-amphibole alteration overprinted by biotite-rich stratabound stockworks and cut by veins of arsenopyrite-magnetite (CQA-08-0552). Stratabound offshoots along the veins formed discontinuous trains of arsenopyrite lenses along bedforms. **B.** Stratabound magnetite-amphibole alteration overprinted by discontinuous trains of arsenopyrite and cut sharply by veins of arsenopyrite (CQA-08-0552). **C**. Intense texture-destructive amphibole-magnetite-biotite alteration of siltstone, which is cut by a series of sigmoidal lenses of pyrrhotite, pyrite and arsenopyrite forming stratabound offshoots from a discordant vein (CA-07-0465). **D.** Discontinuous train of arsenopyrite clots cutting interlayered, stratabound amphibole-magnetite and magnetite-dominant alteration at a high angle (CQA-07-0469). The discordant train of clots and the stratabound alteration are both cut by a very diffuse vein with slightly coarser-grained and randomly oriented amphibole. This sample is in stratigraphic continuity with the finely laminated magnetite alteration of Figure 22C. **E.** Cobaltinitrite-stained rock slab of stratabound, amphibole-altered layers and brecciated, K-feldspar-altered layers cut by an amphibole vein and veined by arsenopyrite (CQA-07-0480J). **F.** Fault zone infilled by HT Ca-K-Fe alteration that cuts stratabound magnetite, amphibole and arsenopyrite-altered siltstone, and is cut in turn by carbonate veinlets (CQA-07-0484). **G.** Amphibole-magnetite-altered siltstone, fractured and infilled by stratabound to discordant calcite-magnetite alteration and associated arsenopyrite (CQA-07-0466). NRCan photos 2020-741 to 2020-747.

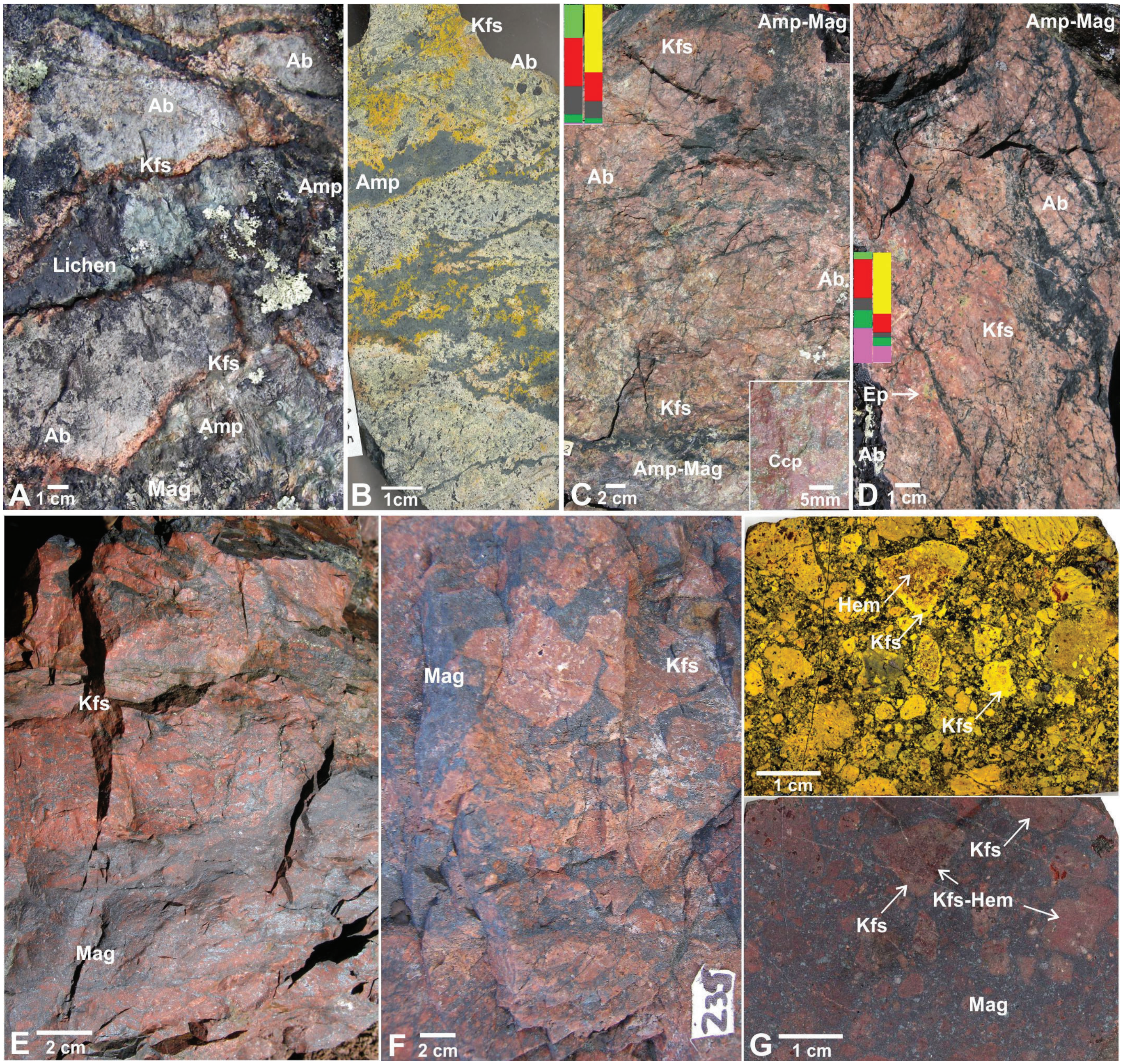


**FIGURE 24.** Progressive development of HT K-Fe alteration within volcanic rocks and porphyritic intrusions. **A, B.** Amphibole-magnetite vein with an early albite halo that evolved to and was replaced by a K-feldspar halo, which also overprinted albitized porphyritic andesite structurally above the McLeod Lake intrusion in the Port Radium-Echo Bay district (CQA-05-0201; from Corriveau et al., 2010b). **C, D.** K-feldspar-amphibole-magnetite alteration with coeval brecciation in the Fab system (C: CQA-06-0392; D: CQA-06-0384). Amphibole-magnetite and chalcopyrite infill the matrix, whereas K-feldspar replaces fragments. **E.** Magnetite-K-feldspar breccia at the Brooke prospect, showing intense K-feldspar alteration of host and clasts that was coeval with brecciation (09CQA-0026). **F, G.** Magnetite breccia with K-feldspar-altered clasts at the Sue Dianne deposit (CQA-05-0235). On the cobaltinitrite-stained rock slab, some clast margins display K-feldspar-altered selvages, whereas most clasts are pervasively altered by K-feldspar and fine disseminations of earthy hematite. NRCan photos 2020-748 to 2020-755.

Early skarn is replaced by amphibole-dominant HT Ca-Fe alteration and upwardly evolves to K-feldspar-skarn breccia that is cut by hematite-bearing alteration (Corriveau et al., 2010a). Protracted alteration and overprinting of multiple alteration facies produce a mineral assemblage comprising andradite, grossular, vesuvianite, diopside and epidote in various combinations with K-feldspar, chlorite, bright red hematite, specular hematite, actinolite, albite, tremolite, and calcite (Fig. 25A–D; May, 2007). Faulting along a fault system mapped by Hildebrand (1983) juxtaposed the K-skarn breccia against and structurally above the barren albitite breccia of Figure 18C located south of Mile Lake (Fig. 16D).

*Facies 4b (K-felsite Breccia)*

Intense K-feldspar alteration commonly forms laterally from, structurally above, or directly at the transition from Facies 3 HT K-Fe through to Facies 5 LT K-Fe alteration (Goad et al., 2000; Corriveau et al., 2010b, 2016; Mumin et al., 2010). Brecciation synchronous with K-feldspar alteration can be progressive, and zones of K-felsite breccia and alteration locally define haloes of variable width between least-altered host and mineralized iron oxide breccias. The brecciated nature of K-felsite is commonly cryptic (Fig. 25E, F). The transition from K-felsite to copper-sulphide and/or arsenide-bearing breccia and iron oxide breccia was observed at the Echo Bay mine, Birchtree showing (Contact Lake belt), Sue Dianne deposit, Brooke prospect, and Summit Peak showing. Within this transition, the K-felsite zones are progressively fractured within K-feldspar alteration haloes, and the fracture system grades into crackle breccia and chaotic, clast-supported K-felsite breccia (Fig. 25F–J; Corriveau et al., 2010a).

Chaotic breccia grades into clast- to matrix-supported iron oxide breccia, accompanied by increased K-feldspar alteration of clasts and precipitation of copper sulphides. Increasing iron oxide contents results in replacement of clasts by magnetite and precipitation of copper sulphides (Fig. 24E, F; e.g. in hydrothermally altered, fractured and brecciated structural corridors at the Fab Lake prospect and Sue Dianne deposit; Ootes et al., 2008; Montreuil et al., 2016c). In contrast, the increase in K-feldspar alteration that forms the K-felsite is not associated with coeval sulphide precipitation (though it is a preferred host for late-stage sulphide veins).

Although K-feldspar alteration of albitite is common, K-felsite brecciation of albitized units or albitite is not. Other types of intense K-feldspar alteration can form across IOAA systems but they are not always brecciated or mineralized (Corriveau et al., 2016). Such K-felsite alters volcanic rocks over an area of 1.5 km by 4 km above the NICO deposit (Goad et al., 2000; Shives et al., 2000), the Southern Breccia albitite, and the unconformity between the metasiltstone host and the overlying volcanic rocks. These K-felsite zones are linked to the development of K-Fe alteration, which contrasts with orthomagmatic K-feldspar alteration associated with subvolcanic intrusions. The latter is less intense and more irregularly distributed based on mapping of the reddish colouration typical of K-feldspar alteration.

Unravelling the timing of K-feldspar alteration in breccia zones can be complex, as moderate to intense K-feldspar alteration of earlier facies and least-altered rocks is common during the formation of K-felsite, K-skarn and K-Fe alteration. For example, in Figure 18D, the albitite breccia at Mile Lake contains K-feldspar-altered fragments (stained yellow) among clasts of albitized laminated tuffs and a breccia matrix devoid of K-feldspar alteration. Pervasively K-feldspar-altered clasts of this kind have been interpreted as evidence of a phase of K-feldspar alteration predating albitization and brecciation (Corriveau et al., 2010b). Additional studies revealed that several clasts experienced K-feldspar alteration along their margins, and that the breccia matrix was locally replaced by K-feldspar. These textures illustrate that K-feldspar selectively replaced porous albitite after brecciation (Fig. 18D).

*Facies 5 (LT Fe–K/Ca/Mg) and Late-stage Alteration*

The LT Fe–K/Ca/Mg alteration facies comprises two end-members, the LT K-Fe and LT Ca-Fe-Mg facies, each evolving to iron-dominant assemblages. Morphology of the alteration varies from replacement of least-altered rocks, and overprints that can be traced and distinguished from earlier alteration, to veins and breccias.

The LT K-Fe alteration facies consists of mineral assemblages composed of hematite (including earthy, crystalline with a dull patina and specular varieties), K-feldspar, white mica (sericite), ± tourmaline, quartz, chlorite, epidote, fluorite, barite and carbonate (Figs. 26, 27). The LT K-Fe facies evolves from a hematite-K-feldspar assemblage (Figs. 26A, D, 27A, B, E) to a hematite-white mica (sericite) assemblage (Fig. 27C, D), hematite-dominant assemblages (Figs. 26B, C, E, 27F, G), and to barite (Fig. 27H), carbonate (Fig. 26F), jasper or quartz (Fig. 27G), and fluorite-bearing assemblages.

The LT Ca-Fe-Mg alteration facies, comprising epidote, chlorite, carbonates (calcite, dolomite, siderite), quartz, fluorite, allanite and locally K-feldspar, is coeval with or post-dates the LT K-Fe facies. Iron- to magnesium-dominant carbonate veins, replacements, and breccia zones are commonly coeval with chloritization. The LT Ca-Fe-Mg metasomatites are locally mineralized in REE (Montreuil et al., 2016b), but in districts worldwide, they may host gold mineralization (e.g. at the Scadding Au-(Co-Cu-Ni) deposit and the Au-Cu-Bi deposits of the Tennant Creek Inlier; Skirrow and Walshe, 2002; Schandl and Gorton, 2007; Macdonald Mines Ltd, 2020). In the GBMZ, local but intense chlorite alteration of albitite occurs in the Southern Breccia and as overprints of the HT Ca-Fe alteration in the South Duke system. The late chlorite-earthy hematite veins cutting the Southern Breccia parallel to the normal fault network that cut across the system are enriched in U, Au, Bi, La, and Ce (2 ppm Au, 1490 ppm Bi, 93 ppm La, and 340 ppm Ce; Gandhi and Lentz, 1990).

Low-temperature K-Fe alteration is moderate to locally intense, and generally associated with brecciation and copper-sulphide mineralization at Sue Dianne, K2, Port Radium, Echo Bay Gossan, Damp and Mile Lake (Camier, 2002; Mumin et al., 2007, 2010, 2014; Acosta-Góngora et al., 2014, 2015b; Somarin and Mumin, 2014; Mumin, 2015; Montreuil et al., 2016b). More hematite veins and hematite-K-feldspar breccia form locally, notably north of the NICO deposit and in the Southern Breccia. Hematite also occurs with chalcopyrite, arsenopyrite, bismuthinite and emplectite as part of a distinct, later stage of mineralization at NICO that postdates magnetite-bearing mineralization (Acosta-Góngora et al., 2015b). In most examples of the GBMZ, however, the LT K-Fe facies replaces earlier magnetite-K-feldspar assemblages within breccia zones. Field observation (diagnostic reddish hue of hematite-pigmented hydrothermal K-feldspar) and staining (haloes

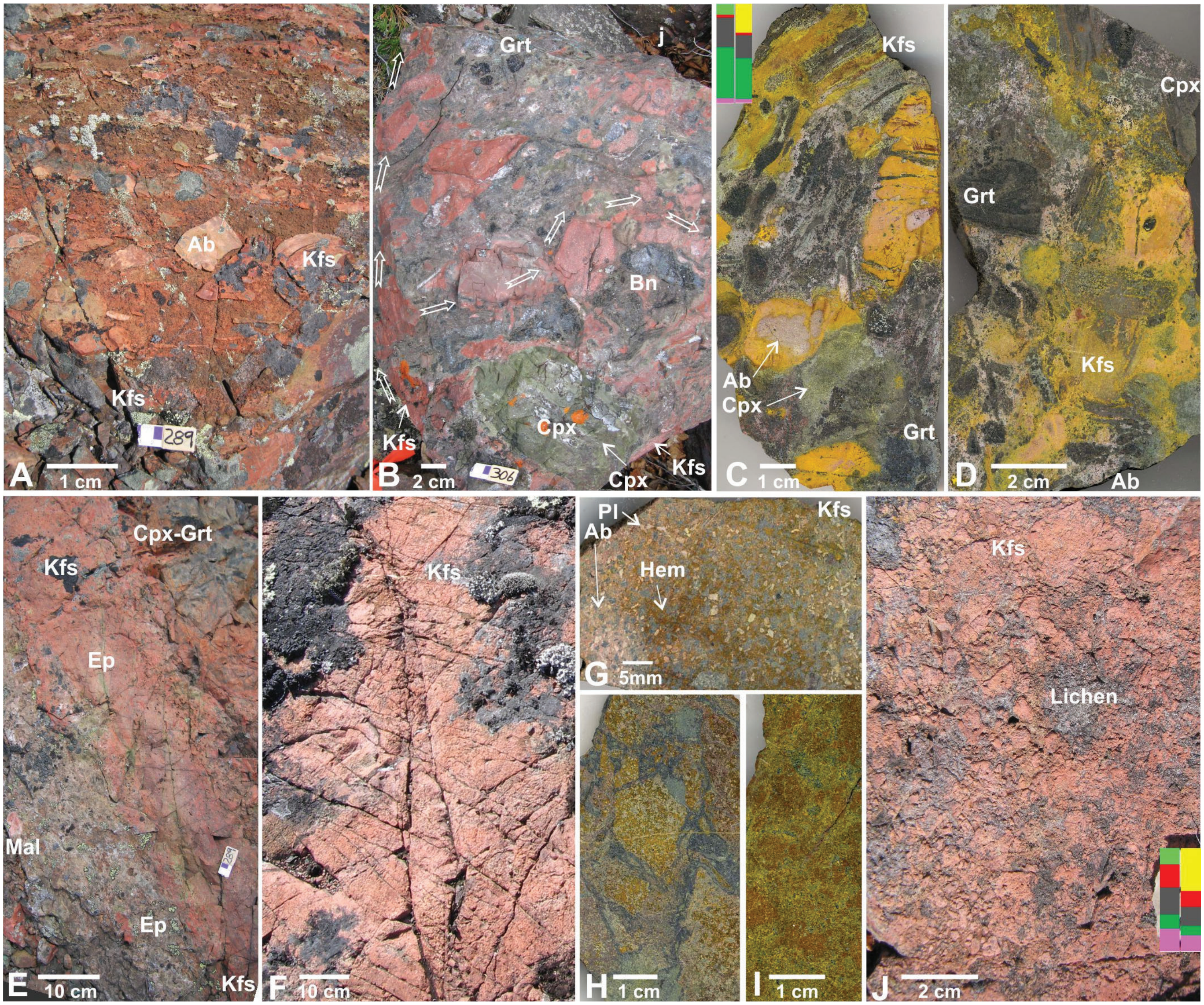


**Figure 25.** Mile breccia and breccias in the Hoy Bay area (Fig. 16B), illustrating K-skarn and K-felsite breccia within volcaniclastic rocks. **A.** Volcaniclastic breccia replaced by skarn and stratabound K-feldspar alteration (red hue) that overprints the skarn matrix and fragments (CQA-06-0289). **B.** Re-brecciated volcaniclastic breccia with medium- to coarse-grained skarn matrix mineralized in copper sulphides and replaced by K-feldspar. The K-feldspar alteration forms faint alteration fronts that replace matrix, clast margins and entire clasts. The most intense K-feldspar alteration fronts have a darker pink to red hue whereas the darker red hue corresponds to hematite-stained K-feldspar (CQA-06-0306). **C, D.** Cobaltinitrite-stained rock slab of Mile Lake breccia, where skarn assemblages infill breccia matrix and K-feldspar alteration (yellow stain) replaces some components of the breccia matrix and clasts (CQA-06-0289). Alteration of clasts is pervasive or selective, forming a selvage along clast margins and infiltrating fractures within clasts. The yellow-stained K-feldspar in C and D correspond to the darker pink to red alteration on weathered and fresh surfaces in A and B. Hematite-stained K-feldspar has an orange to reddish brown colour. **E.** Early, fine-grained skarn pervasively replaced by a K-felsite and cut by epidote (CQA-06-0289). **F–H.** Outcrop of K-felsite breccia due north of Mile Lake, where it replaces albitized porphyritic andesite (CQA-06-0296). Matrix amphibole within crackle breccia is only obvious on stained slabs in H. **I, J.** Crackle breccia of K-felsite in a former albitite at Hoy Bay (CQA-07-0527). NRCan photos 2020-756 to 2020-765.

stained yellow) provide evidence that K-feldspar precipitated coeval with hematite at the LT K-Fe facies.

At the Sue Dianne deposit, hematite-sericite replaces magnetite-K-feldspar within the matrix of the upper part of the breccia (Figs. 24F, G, 26A; Camier, 2002; Mumin et al., 2010). At the Damp prospect, the overprint consists of hematite, K-feldspar, quartz and disseminated chalcopyrite, replaced by covellite, carrollite ($CuCo_2S_4$), bornite, and uraninite (Acosta-Góngora et al., 2014). A darker red selvage along clasts is typical of renewed K-feldspar alteration during hematization. Field evidence of low intensity LT K-Fe facies includes widespread relics of earlier albitization in K-feldspar-altered clasts at the Damp prospect and in the Hoy Bay area (e.g. supported by high Na contents of the breccia in Fig. 26D), and a lack of additional brecciation coeval with hematite alteration at Hoy Bay (Fig. 26D, E). The moderate intensity of alteration preserves the alteration sequence from albitization (Fig. 17C), to magnetite-clinopyroxene-epidote and K-feldspar-magnetite crackle to chaotic breccia, K-felsite breccia (Fig. 25I, J), and hematite-K-feldspar overprints on K-feldspar-magnetite breccia (Fig. 26D, E).

A hematite-dominant variant of the LT K-Fe facies consists of bright, crystalline hematite with a steely patina ± silicification or specular hematite (e.g. compare the bright patches of hematite in Fig. 27C to the crystalline but dull hematite in Fig. 26E). This variant evolves to zones of silicification ± hematization. At East Hottah (Fig. 16A), it forms extensive hematite breccias and veins among K-feldspar- or clay-altered hosts (Fig. 27). These breccia bodies are decametres long and a few metres wide. They are clast-to-matrix supported, with abundant specular hematite in the matrix and replacing clasts. The host system is cut by extensive quartz-hematite, quartz-hematite-carbonate, jasper-hematite and quartz stockworks, as well as by local barite veins (Fig. 27H). The earlier clay alteration evolves to a very fine-grained, black end-member. Enrichment in Ba, F, W, REE and Y occurs in the hematite-rich and clay-rich assemblages (e.g. 1120 ppm Y; Corriveau et al., 2015).

At the Fe Zone, structurally above the Mag Hill IOA prospect (Fig. 16C), intense and pervasive steely hematite alteration replaced porphyritic andesite in a 200 m long by up to 10 m-thick lens (Fig. 26B, C). Replacement has largely destroyed the original porphyritic texture of the host andesite, and transformed the host into a massive or faintly layered hematitite (Fig. 26C). Locally, the porphyritic texture of the host is preserved through selective silicification of the former plagioclase phenocrysts (Fig. 26B). A K-feldspar halo surrounds the hematitic lens. The brilliant, steely nature of the specular hematite in these examples contrasts with the commonly dull specular hematite in IOCG breccias containing copper sulphides. However, it resembles the barren post-ore hematite alteration at Olympic Dam (Fig. 15E) and the gold-bearing hematite-silica breccia of the Prominent Hill deposit, where the breccia is devoid of copper (Belperio et al., 2007; Schlegel, 2015).

A largely barren albitite breccia cemented by hematite and carbonates grades into silicified breccia at Breccia Island in the Port Radium-Echo Bay district (Fig. 26F, G; Mumin et al., 2010). Crystallization of microscopic hematite commonly accompanies K-feldspar alteration and albitization (Figs. 17, 18, 24–26), but an intense brick red colour may also result from silicification (due to hematite dusting) and/or hematization of albitite (Fig. 26G). Intense hematite alteration and silicification can produce jasper veins ± quartz and hematite (Fig. 27G; Mumin et al., 2010).

The LT K-Fe facies evolves to hematite-bearing veins and breccia containing quartz, jasper, barite or carbonates (mainly calcite or siderite) in the area of the K2 IOCG prospect of the Port Radium-Echo Bay district. Barite veins are common at the NICO deposit and at Hottah (Fig. 27H).

The IOAA systems evolves at low temperatures to extensive quartz and carbonate veining (e.g. NICO, Sue Dianne; Mumin et al., 2010; Montreuil et al., 2016b), phyllic alteration (quartz-sericite-pyrite; e.g. Echo Bay Gossan; Mumin et al., 2010) and epithermal type alteration, which form the distinct end-members of the extremely diverse Facies 6 LT Si-K-Al-Ba assemblages. Phyllic alteration intermixed with sericite-dominant alteration has led to the formation of numerous gossanous outcrops in the northern GBMZ, some of which are mineralized (Gossan Island and Echo Bay Gossan along the Contact Lake Belt; Mumin et al., 2007, 2010; Somarin and Mumin, 2014; Mumin, 2015). Epithermal veins, including quartz ± carbonate ± sulpharsenides, commonly cut all preceding alteration facies (Mumin et al., 2010).

Tourmaline alteration is common within IOAA systems of the GBMZ and produces tourmaline veins and breccias in association with magnetite or quartz and K-feldspar (Mumin et al., 2007, 2010; Kelly et al., 2020). However, tourmaline veins cut and are cut by a variety of alteration facies (Kelly et al., 2020) and do not form at a specific time within IOAA system evolution. In contrast, emplacement of granitic veins was commonly coeval with IOAA metasomatism, and the presence of tourmaline may be linked to fluid ingress during magma emplacement rather than the IOAA fluid plume per se; hence, it was not included in the deposit model of Corriveau et al. (2016).

### Syn-metasomatic Ductile to Brittle Deformation

Brecciation, fracturing, faulting and ductile deformation in large magmatic-hydrothermal systems, including IOAA systems, are a function of: 1) inflation and stoping during magmatism; 2) tectonic load; 3) tectono-hydrothermal effects including hydrofracturing, over- and under-pressurization and fluid flow; and 4) mineralogy, permeability, porosity and textures that control competency. Consequently, understanding the nature and origin of tectonic features is complicated. One consistent feature in IOAA systems is the development of ductile to brittle-ductile deformation within HT Ca-Fe facies (Fig. 21C; Corriveau et al., 2022b). Such ductile deformation may relate to regional orogenic events in IOAA districts, but also as more localized syn-metasomatic deformation (e.g. shear zones related to intrusion emplacement), which may complicate interpretation of alteration systems.

In the GBMZ, cross-cutting relationships between alteration facies and 1873–1868 Ma dykes from the NICO deposit, Peanut deformation corridor, Southern Breccia and Duke system indicate that: (1) Facies 1 albitite is brecciated prior to and during the onset of the HT Ca-Fe facies (brittle behaviour observed throughout the GBMZ); (2) HT Ca-Fe, HT Ca-K-Fe, and biotite-rich HT K-Fe facies display brittle-ductile deformation, including ductile folding, boudinage and foliation (Figs. 21B, C, 22E; 'BAM schist' of Goad et al., 2000; Acosta-Góngora et al., 2015a); and (3) subsequent HT K-Fe facies is coeval with formation of angular breccia, including breccia that cuts foliated amphibole-dominant alteration (Figs. 23E, 24; Corriveau et al., 2022b). At NICO, veins that cut the stratabound-altered sedimentary host sequence are not

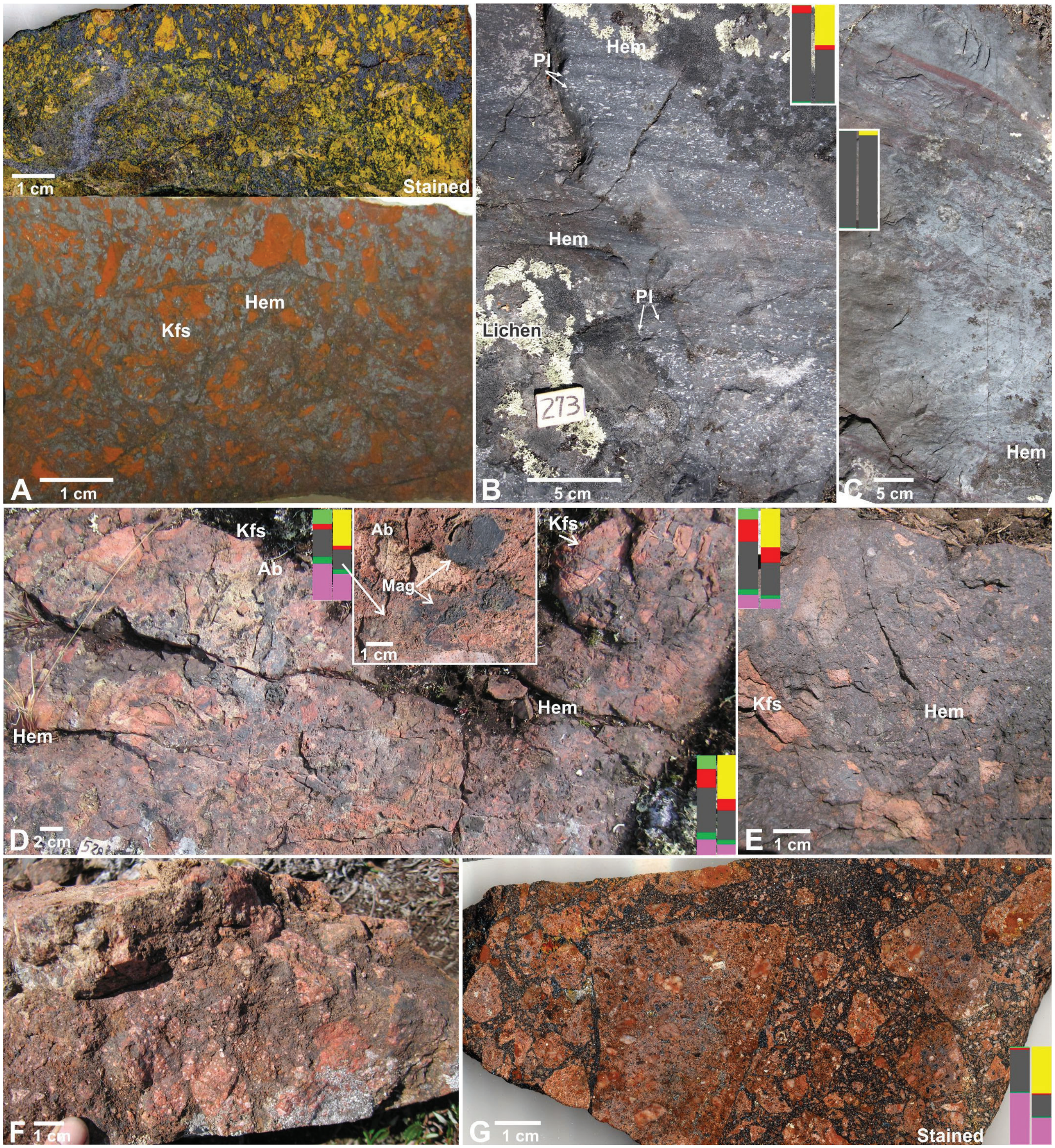


**FIGURE 26.** Low temperature K-Fe facies. **A.** Hematite-dominant breccia with K-feldspar alteration of clasts and relics of quartz from the host at the Sue Dianne deposit. This unit is mineralized in chalcopyrite, bornite, chalcocite, covellite, uraninite, magnetite, gold, molybdenite, bismuthinite and fluorite. **B, C.** Replacive hematite alteration of porphyritic andesite. In B, layers with local preservation of plagioclase phenocrysts (altered to quartz) within a pervasively hematite-altered groundmass, are intercalated with porphyritic andesite that is also pervasively altered to hematite. In C, hematite alteration completely destroyed the porphyritic texture and developed locally irregular laminations that may stem from original compositional (flow?) layering in a massive, hematite-dominant metasomatite (CQA-06-0273). **D, E.** Hematite alteration of a magnetite-altered and albitized pyroclastic breccia preserves most of the breccia texture in D but is generally texture destructive in E; Hoy Bay (CQA-07-0528). Inset in D: magnetite clasts and other types of clasts are overprinted by specular hematite. **F, G.** Breccia with clasts of albitized volcanic rocks and hematite-carbonate infill at Breccia Island (CQA-07-0519). NRCan photos 2020-674, 2020-767 to 2020-774.

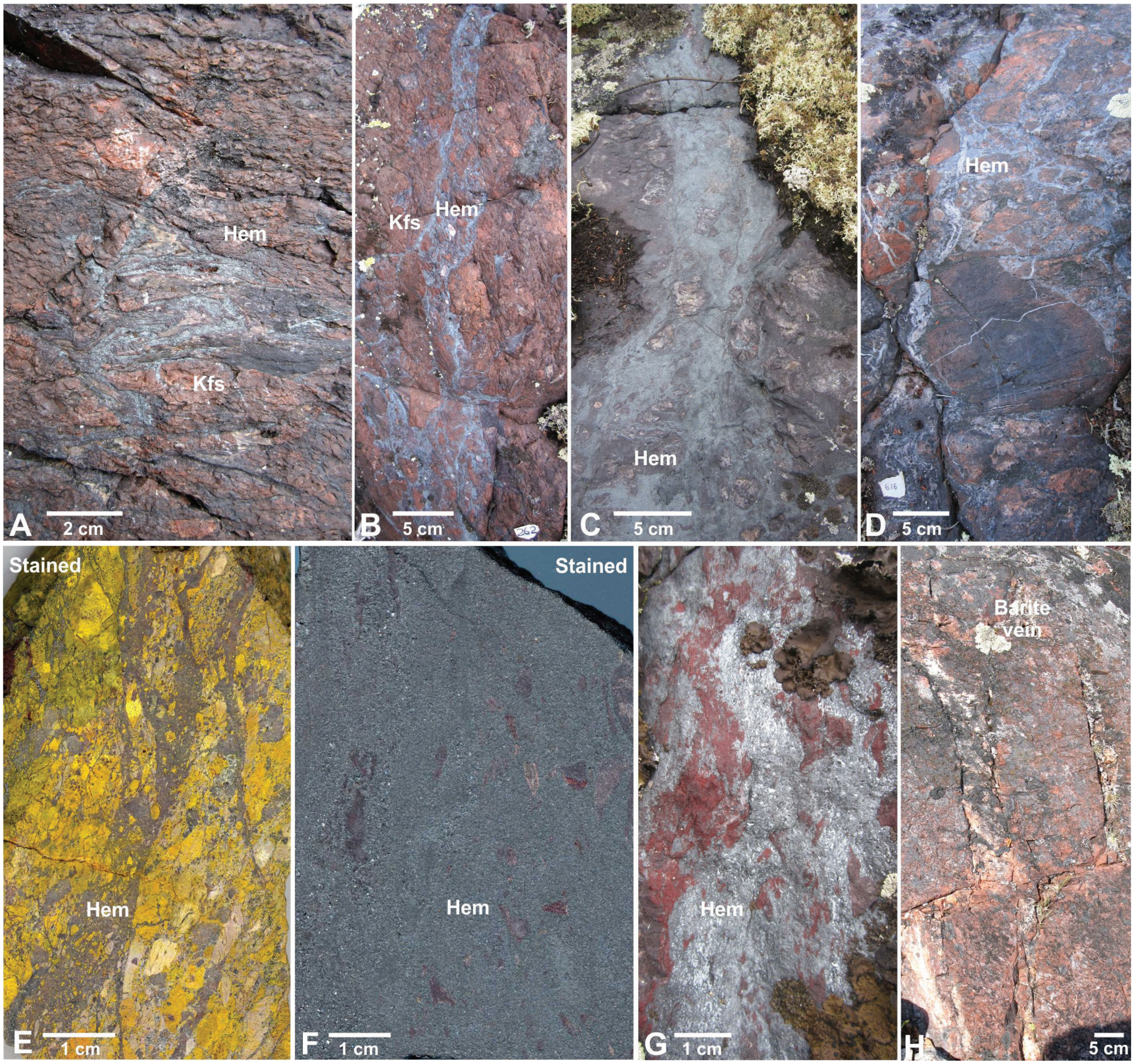


**FIGURE 27.** Breccia with Facies 5 LT K-Fe alteration, Fe-Si variants and barite veins at the East Hottah system. **A, B.** Hematite breccia within an intensely K-feldspar altered host (10CQA-0262). **C, D.** Hematite breccia within dark, clay-altered host (C: 10CQA-1546; D: 10CQA-0616). **E.** Hematite breccia cutting a K-feldspar-altered breccia (10CQA-0284E). In many such rocks, clay alteration stains white and is difficult to discriminate from albitization. Timing relationships between hematite infilling and K-feldspar alteration of clasts is uncertain, as clear K-feldspar haloes are not observed along the hematite infills and K-feldspar alteration is widespread throughout the region. **F.** Hematite breccia with hematized and silicified clasts (10CQA-1552A). **G.** Particularly bright, steely specular hematite breccia within a hematized and silicified zone (bright red patina similar to some clasts in F), at the same outcrop as in D (10CQA-1546). **H.** Barite veins (09CQA-1195). NRCan photos 2020-775 to 2020-782.

deformed away from zones of brittle-ductile deformation. Furthermore, crystals of biotite and amphibole are commonly randomly oriented in replacement zones, veins and breccia matrix where they may cut foliated stratabound amphibole-magnetite alteration. The HT Ca-Fe metasomatites are cut by or give way structurally upwardly to undeformed K-Fe breccia and veins (e.g. Summit Peak and Chalco prospect within volcanic rocks above the NICO deposit). These textures indicate that ductile deformation and associated recrystallization of metasomatites were localized. Combined with the absence of penetrative (ductile) tectonic fabrics across the IOAA systems and overlying volcanic rocks of the GBMZ, it is clear that there was no post-metasomatic regional metamorphism and deformation. The higher temperatures recorded during HT Ca-Fe facies alteration, driven by syn-deformation magma emplacement as noted at the Southern Breccia corridor and DeVries system, may foster the development of syn-metasomatic ductile deformation instead of brecciation (Corriveau et al., 2007; Montreuil et al., 2016a).

Brittle-ductile to brittle deformation was also observed at the Ernest Henry deposit in Australia. Albitite within the deposit and throughout the district — as in the GBMZ and many other settings globally — is brecciated and infilled by skarn or HT Ca-Fe assemblages (Figs. 5A–F, 6A, B, 18B–E). Elongate breccia fragments may form where sets of parallel fractures develop as illustrated in Figure 5D. Elongate fragments in subsequent HT K-Fe breccia (Fig. 8A, E) may then reflect this parallel fracturing, and are not evidence of ductile deformation. However, albitite clasts become flattened and foliation develops where magnetite-dominant HT Ca-Fe alteration forms (Fig. 5G). Globally, many HT Ca-Fe metasomatites exhibit similar ductile fabrics, in marked contrast to the brittle behaviour of subsequent HT K-Fe ore breccias (Figs. 7, 8). Brittle-ductile to ductile deformation at the HT Ca-Fe facies also appears to be common at the Guelb Moghrein deposit in Mauritania (Kirschbaum and Hitzman, 2016) and across the Cloncurry district in Australia. Such observations are most compatible with development of syn-metasomatic ductile deformation as an intrinsic response to high-temperature conditions during HT Ca-Fe facies alteration. Further work is required to understand the relationships between ductile deformation and IOAA metasomatism, but fluid flow is known to increase deformation rates in ductile fault zones by driving ‘softening’ reactions and/or increasing ambient temperatures within the fault zone (Dipple and Ferry, 1992). Development of a strong planar fabric also induces weakening, strain localization, and softening reactions along shear zones (Maggi et al., 2014), particularly where phyllosilicates (biotite) replace stronger framework and chain silicates (Wintsch et al., 1995). Understanding these relationships would preclude the interpretation of foliated HT Ca-Fe or biotite-rich HT Ca-K-Fe and K-Fe-altered rocks as evidence for post-metasomatic orogenesis.

## Mineral System Development and Fluid Pathways

The sequence of iron oxide and alkali-calcic alteration illustrated herein (Fig. 28) represents a first-order documentation of the spatial and mineralogical-chemical transformations of host rocks associated with the ascent of a regional-scale fluid plume across the upper crust. The distribution of the alteration facies also records zones of enhanced permeability and the main fluid pathways across systems.

*Structural and Fluid Pressure-induced Fluid Pathways*

Alteration zones such as albitite corridors develop along major discontinuities (e.g. fault zones, volcanic-plutonic contacts, and sedimentary units of contrasting competency (Figs. 17, 18; Oliver et al., 2004; Marshall and Oliver, 2008; Montreuil et al., 2015; Corriveau et al., 2022b). Hydrofracturing associated with strain partitioning along and between shear zones and among lithological units (Ernest Henry deposit; Twyerould, 1997; Cave et al., 2018; Marshall and Oliver, 2008), dilation and brecciation between shear zones (Mark et al., 2006), and clast transport by over-pressured fluids during explosive brecciation (Oliver et al., 2006) can focus and enhance fluid flow. Along major fault systems, splay faults and transverse faults can divert fluids from the more regional-scale fault zones (McLaughlin et al., 2016; del Real et al., 2018). Albitization of sedimentary rocks along fault zones develops parallel to bedding planes and along fracture networks. Strain partitioning can promote delamination of the differentially altered beds to form elongate fragments with a strong preferred orientation (Corriveau et al., 2022b). Parallel fracturing of albitite can also lead to elongate fragments with a strong preferred orientation (Fig. 5C, D). Breccia fabric can be accentuated by subsequent tectonic deformation (including transient ductile behaviour at the HT Ca-Fe facies; Figs. 5G, 6D), or by fluid-mediated mass transport of metasomatic mush and fragments (Fig. 21E). Although rounded fragments are commonly taken as indicative of comminution during fragment transport (i.e. milling), the examples provided herein, in Corriveau et al., 2022b) and Schlegel and Heinrich (2015), demonstrate that the intense dissolution-reprecipitation processes taking place as matrix replaces breccia fragments or as fluid fronts replace host rocks is another means of generating equidimensional and even spherical breccia fragments and pseudo clasts in metasomatites (Figs. 7B, E, 12E, 18F). Conclusive evidence of explosive breccia or fluidization is rare in the GBMZ, at Prominent Hill, and in the examples provided herein for the Ernest Henry deposit and Cloncurry district, but fluidization has been interpreted to occur in the Cloncurry district and at Olympic Dam (Oliver et al., 2006; Rusk et al., 2010).

As brecciation wanes in IOAA systems, extensional fractures form perpendicular to the breccia fabric and are infilled by hydrothermal veins (e.g. Figure 5F from the Ernest Henry deposit) or by granitic magma (Southern Breccia; Montreuil et al., 2016a). The orientation of the extension fractures could reflect evolution from ductile to brittle deformation or a change in the stress field from compressional to extensional. A switch between compressional, extensional or transtensional stress regime during metasomatism and mineralization aligns with regional geodynamic settings and compositional changes in intrusions proposed by several authors (Williams et al., 2005; Skirrow et al., 2007; Groves et al., 2010; Montreuil et al., 2016a; Tiddy and Giles, 2020; Skirrow, 2022).

Montreuil et al. (2016b) also demonstrated that magmas can be emplaced parallel to the breccia fabric, and that the consequent higher temperature regime favours crystallization of magnetite-dominant assemblages and ductile deformation (Fig. 11 in Corriveau et al., 2022c). Because the temperature rise is transient, the system returns to brittle deformation and localized emplacement of magmas within extensional jogs.

Similarly, fluids infiltrating along deformation zones can reach high temperatures typical of the HT Ca-Fe facies and lead to transient syn-metasomatic ductile deformation, as discussed in the previous section.

Breccias provide insights on the impact of tectonics and hydrothermal activity in the creation of permeability, whereas extensive dissolution and replacement of breccia clasts (increasing the volume of the apparent matrix) and of host rocks along fracture networks (leading to pseudoclasts and pseudobreccia) highlight the importance of fractures, damage zones and progressive fluid-host and fluid-clast disequilibrium in focusing intense alteration (Schlegel and Heinrich, 2015; Jébrak, 2022; Skirrow, 2022). Brecciation and replacement leading to pseudobreccia textures both provide ideal fluid pathways; ultimately, identifying structural sets that host alteration facies helps to define fluid pathways that can guide mineral exploration along or across structures (Schlegel and Heinrich, 2015; Hayward et al., 2016; Clark et al., 2018; Corriveau et al., 2022c).

*Fluid Pathways Induced through Fluid-rock Reactions*

The pervasiveness, intensity and scale of replacement illustrated in this paper at outcrop- to district-scales imply that fluid circulation is not simply structurally controlled by fault and breccia corridors. Evidence shows that major parts of these alteration systems must also form via fluid infiltration of porous, permeable or reactive hosts, as well as through coupled dissolution-reprecipitation reactions between fluids and hosts. Porosity and permeability can be modified by syn-metasomatic fracturing and brecciation or through transient, grain-scale remobilization of elements during fluid-rock reactions, and vary according to the host rock type (Clark et al., 2006; Harlov and Austrheim, 2012; Poulet et al., 2012; Kontonikas-Charos et al., 2018). Porosity is created during albitization (Montreuil et al., 2012) and by dissolution of carbonate units to form skarn, HT Ca-Fe alteration (e.g. GBMZ) or hematite alteration (Prominent Hill; Schlegel and Heinrich, 2015).

Metasomatic reactions can be very selective. In sedimentary rocks, stratabound alteration fronts feature mineral assemblages and mineral contents that are distinct from layer to layer, while preserving the original sedimentary bedding (this work; Corriveau et al., 2022b). Although local lithological control can govern mineral assemblages and mineral proportions at each facies (see Harlov et al., 2016), the regular sequence of alteration facies documented in systems with distinct host rock types demonstrates that the overall IOAA facies generally form regardless of host rock composition.

*Other Pathways*

Some fluid pathways are difficult to recognize because of the scale of the system and poorly understood geological controls. Palinspastic reconstructions by Hayward and Corriveau (2014), prior to extensive northeast-trending transcurrent faulting and after IOAA metasomatism, demonstrate that the most endowed IOAA systems are located at the edge of a belt-scale front of large A-type granite intrusions emplaced ca. 20 million years after development of IOAA systems, and at the edge of a subsequent sedimentary basin (see also Hoggard et al., 2020). Geodynamic controls and lithospheric-scale architecture most likely controlled this distribution, and potential roles of geodynamic controls are observed in many IOCG districts (Skirrow et al., 2018).

Understanding the multi-dimensional nature of the lithospheric, structural and lithological controls on the distribution of IOAA systems, as well as the geometry and distribution of alteration and mineralization zones, are essential in planning exploration programs. Explorers must consider that the geological continuity of mineralized zones can vary considerably at the scale of mineral occurrences and deposits, as fluid flow is not solely constrained by linear tectonic discontinuities or breccia zones but evolves regionally from depth to surface in response to distance from the source(s) of heat. Although such systems develop into extensive districts, they do not all evolve through the same temperature gradients, which can greatly influence the intensity of alteration facies and their development.

*System Evolution*

Labelling alteration facies according to the index cations of the diagnostic minerals (themselves an intrinsic result of distinctive bulk rock compositions; see Corriveau et al., 2022a) provides a simple means to represent the chemical and mineralogical changes induced by the consecutive reactions within the system. The reporting of alteration facies on maps and in drill cores is therefore a means to portray fluid pathways at regional to deposit scales. It is also a means to assess if system evolution was simple or if it was disrupted through tectonics, magmatism and external ingress of fluids, as discussed in Corriveau et al. (2022c). As the distribution of alteration facies may also provide vectors to mineralization, (Fig. 28), it also serves as a predictive tool for mineral potential (Potter et al., 2020).

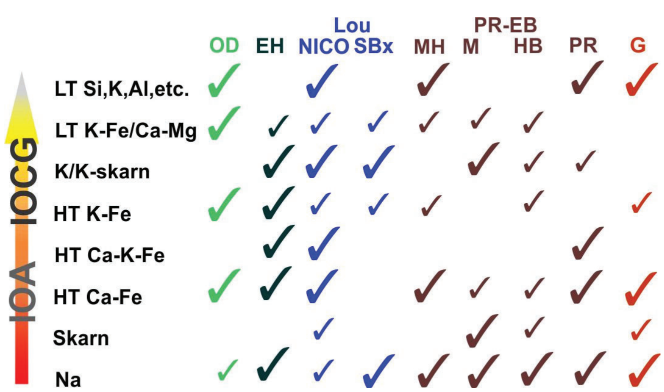


**Figure 28.** Summary of IOAA facies in the case examples discussed in this paper. OD: Olympic Dam deposit; EH: Ernest Henry deposit; SBx: Southern Breccia corridor; PR-EB: Port Radium-Echo Bay district; MH: Mag Hill prospect; M: Mile Lake prospect; HB: Hoy Bay sector; PR: Port Radium; G: Guelb Moghrein. Line weight of checkmark reflects the abundance and intensity of the alteration facies.

At regional scales, Na and HT Na-Ca-Fe alteration zones are distal to mineralization, and proximal to associated intrusive heat sources and fault zones (e.g. DeVries Lake SE; Jackson, 2008). These facies are normally barren and develop deep in the core of the system or along fault zones. They can be subjected to tectonic fracturing, brecciation and thrusting into the field of fertile alteration. Where overprinted by HT Ca-K-Fe (Au, Co, Bi, Cu) and the HT to LT K-Fe (Cu and multiple metals) facies, albitite may be an ore host.

Prior to renewed mapping, a lack of Na, Na-Ca and Na-Ca-Fe facies was reported at the NICO deposit (Corriveau et al., 2011), and in the Missouri district (Day et al., 2016). However, albitization and albitite have been shown to occur, based on additional regional exploration and mapping (e.g. Montreuil et al., 2015), and more extensive geophysical surveys (e.g. Southeast Missouri district; McCafferty et al., 2019). Here, albitite is interpreted to be inherent to the development of IOAA systems.

Because of the elevated temperature of the fluid plume, skarn develops within carbonate sedimentary hosts or previously carbonate-altered hosts irrespective of the presence of a proximal intrusion. Skarn has a consistent spatial association with albitite; skarn may coexist with albitite in distinct host rock types (Fig. 18A), overprint albitite-altered zones, or fill albitite breccia matrix (Fig. 18B–D). As the system evolves, skarn is in turn overprinted and replaced by HT Ca-Fe facies, including magnetite-dominant alteration that can produce iron skarn or IOA deposits (Corriveau et al., 2022b).

Where HT Ca-Fe (and Na-Ca-Fe) alteration is incipient to moderate, a lithological control, and corresponding host-rock compositional or permeability control, is locally observed on alteration products, especially in terms of mineral content but also in mineral assemblages. Selective alteration is common, such as the selective replacement of some volcanic fragments by amphibole-dominant or magnetite-dominant alteration (Corriveau et al., 2022c). Field evidence also includes the selective and decoupled replacement of host sedimentary layers by amphibole, magnetite or epidote (and in some cases albite) leading to amphibole-, magnetite-, or epidote-dominant (locally albite-dominant) layers during HT Ca-Fe facies and HT Na-Ca-Fe alteration (Figs. 17A, G, 20E, 21A–C, 22; Corriveau et al., 2022c). Subsequent alteration can further enhance layer-selective alteration types, with the result that later-stage alteration facies form preferentially within some layers (Figs. 21A–C, 22).

Within sedimentary and volcanic rocks, iron oxide metasomatism associated with HT Ca-Fe facies can be efficient at preserving some host textures and structures. Stratabound metasomatic banded ironstones are recognized in the GBMZ and Cloncurry district (Williams, 1994; Williams et al., 2015), but in some cases stratabound iron oxide replacement zones are still interpreted as sedimentary banded iron formations.

During HT and LT K-Fe alteration, brecciation is associated with increasing K-feldspar alteration, forming fractured to brecciated K-feldspar-rich haloes to iron oxide breccia, and to iron oxide breccia with K-feldspar-altered clasts (pervasive or increasing in intensity from clast margins to core). Such brecciation is an intrinsic consequence of the intensification of alteration at these facies. It can be aided by faulting and magma emplacement, explaining the increase in brecciation along faults and mafic to ultramafic intrusions at the Olympic Dam deposit (Ehrig et al., 2017b). Sericitization is abundant at the LT K-Fe facies and is well documented at Sue Dianne in the GBMZ and in the hematite-group IOCG deposits (Ehrig et al., 2012; Schlegel and Heinrich, 2015). Sericite alteration could not be easily detected during regional mapping in the GBMZ and may be under-represented in the literature.

During brecciation, breccia clasts are commonly sub-equant and evolve from sharp boundaries to increasingly ragged boundaries. Although these textures can be generated by several mechanisms (cf. Jébrak, 2022), the textures observed in this study support replacement of K-feldspar-altered clasts by iron oxides and associated copper-sulphide mineralization (Fig. 24G). Ore breccias that formed at HT and LT K-Fe facies display similar megascopic attributes at the Olympic Dam, Ernest Henry and Sue Dianne deposits (Figs. 7, 8, 12, 24F, G, 26A). Aside from local fluidization textures observed within some ore breccia zones, ore breccia textures at the Ernest Henry deposit are typical of in situ brecciation and extensive dissolution and replacement along clast margins, fractures and damage zones associated with the development of the HT K-Fe facies. Similar replacement features were mapped in the GBMZ, where their impact on chemistry was tested by analysis of least-altered rocks in the Fab system. Mass balance and immobile element signatures of HT K-Fe alteration from this system (Montreuil et al., 2016c) indicate that the prevalent dissolution and replacement reactions, coupled with a slight volume gain related to brecciation, led to dilution of typically immobile elements (e.g. Ti, Al, Zr, Hf). Thus dissolution-reprecipitation mechanisms created dilution signatures or mixing lines similar to those seen in breccias where proportions of breccia cement increases as the breccias evolve from mosaic to chaotic types (e.g. Mort and Woodcock, 2008). This study reinforces the importance of field, drill core and stained rock slab observation in assessing the role of replacement in creating breccia-type textures (see also Jébrak, 2022).

At the HT K-Fe to LT K-Fe transition, carbonate alteration may occur. Cooling may drive the system to acidic conditions, at which point carbonate can no longer precipitate and existing carbonate may break down (Richards and Mumin, 2013a, b). Renewed fluid ingress will transform such carbonate alteration into skarn that is closely related to and stable with K-feldspar alteration, thus forming a K-skarn facies. At this stage, K-feldspar-dominant K-felsite breccia also forms. The presence of carbonate alteration overprinted by K-skarn at the magnetite-to-hematite transition at the Mile breccia provides evidence that IOAA system fluids can generate their own skarn facies.

The K-feldspar-dominant haloes that surround or are adjacent to iron oxide breccia bodies occur at local to deposit scales and are typically brecciated, such as the ten metre-wide K-felsite breccia at Mile Lake and the K-feldspar halo around the Ernest Henry and Sue Dianne deposits. In contrast, the moderate to intense K-feldspar alteration haloes above the NICO deposit, as well as phyllic alteration (Echo Bay Gossan, Port Radium-Echo Bay district), may extend for several kilometres in length/diameter. In these cases, the altered rocks remain relatively intact, with minimal brecciation. Extensive texture-preserving alteration is common, even though the alteration may totally obliterate and replace the primary mineralogy. In areas without significant overburden, extensive zones of K enrichment and K/eTh anomalies associated with IOAA systems can be captured by airborne radiometric surveys (e.g. the NICO and Sue Dianne deposits of the GBMZ; Richardson et al., 1973; Gandhi et al., 1996; Shives et al., 2000).

Ultimately, IOAA systems are responsible for chemical, mineralogical, textural and even structural changes in large volumes of upper crust: field exposures of such systems extend over hundreds of $km^2$. The descriptions and photos provided in this paper further illustrate that GBMZ IOAA systems share attributes with archetypal IOA, magnetite-group and hematite-group IOCG deposits, as well as with Co-rich IOCG variants. Parts 2 and 3 (Corriveau et al., 2022a, c) discuss these points further, whereas Corriveau et al. (2022b) summarize descriptive terminology and address the importance of recognizing these alteration facies and their relationships to deformation while mapping and core logging. These mapping and lithogeochemical tools are also applicable where IOAA systems have been metamorphosed, including metamorphism to upper amphibolite and granulite facies (Corriveau et al., 2018).

## Conclusions

Metasomatism within iron oxide and alkali-calcic alteration systems leading to generation of IOA, IOCG and affiliated critical metal deposits is intense, extensive and globally unmatched by any other ore system. The various metasomatic mineral assemblages and alteration types containing silicate, carbonate, oxide, sulphide, arsenide, and phosphate minerals, correspond to distinct and diagnostic alteration facies. Using the facies approach, a consistent depth-to-surface and time sequence emerges as alteration progresses. The regional Facies 1 Na alteration and local skarn (i.e. HT Ca-Mg-Fe) evolve to Facies 2 HT Ca-Fe and IOA mineralization through the transitional Facies 1–2 Na-Ca and HT Na-Ca-Fe, and give way to the transitional Facies 2–3 HT Ca-K-Fe and their Au-Co-Bi IOCG variants. IOCG mineralization forms within Facies 3 HT K-Fe through Facies 4 HT K and HT K-skarn to Facies 5 LT K-Fe (and local LT Ca-Mg-Fe end-members). Finally, Facies 6 encompasses all later-stages alteration and veining, including phyllic alteration, epithermal lithocaps, silicification, and quartz ± carbonate veins.

The Au-Co-Bi-Cu NICO deposit, where ore precipitates at the HT Ca-K-Fe facies, is rich in biotite, Au, Co and Bi, but is less enriched in Cu than typical magnetite-group IOCG deposits. In contrast, the ore at the magnetite-group Ernest Henry deposit precipitated at the biotite to K-feldspar transition of the HT K-Fe facies and then within a carbonate-magnetite assemblage, and is rich in Cu, Au and Co. The U, Au, Cu and Ag ore and REE mineralization of the Olympic Dam hematite-group IOCG deposit precipitated as the K-feldspar-stable assemblages transitioned to sericite-rich LT K-Fe facies and its hematite-dominant variants.

The combined chemical- and mineral-based approach to grouping mineral assemblages into facies allows alteration mapping to be a proxy for the IOAA fluid pathways from sources to ore, independently of tectonic disruption. Alteration facies evolve systematically from depth to surface and laterally away from heat sources, and serve as excellent vectors towards IOCG and affiliated deposits. Alteration facies can also be repeated or telescoped, creating complex prograde, retrograde and crosscutting relationships and zones with overprinting of alteration types, as observed at many deposits. Overprinting of alteration facies occurs at the waning stages of each major hydrothermal facies, but can also occur by telescoping of alteration facies during rapid exhumation or faulting, or through changes in fluid source and composition as these dynamic magmatic-hydrothermal systems evolve. As a result, parts of the sequence may be missing or not preserved at any given location, although the successive stages of alteration and overprinting fall within the framework discussed in this paper.

## Acknowledgments

This paper is Natural Resources Canada, Land and Minerals Sector contribution 20190065. The research was conducted under the uranium ore systems subproject of the Targeted Geoscience Initiative (TGI) and furthers earlier research within the TGI Deep Search project and the Great Bear-IOCG project of the Geomapping for Energy and Minerals program. Fieldwork was conducted in collaboration with the Northwest Territories Geoscience Office South Wopmay Bedrock Mapping project, Alberta Star Development Corporation, Fortune Minerals Limited, graduate and undergraduate students, and industry, university and government colleagues from across Canada who generously contributed time, effort, knowledge, logistical infrastructures or funding for the projects.

Research in the Cloncurry district by P.J. Williams for the original paper (Corriveau et al., 2010b) has been supported by many agencies including, James Cook University, the Australian Research Council through its Strategic Partnerships with Industry and Linkage grant schemes and many mining companies, in part co-ordinated by the Australian Mineral Industries Research Association (AMIRA). Insights on the district were enabled by Nick Oliver and colleagues through their fieldtrip in the Cloncurry district (Oliver et al., 2009) and the fantastic collaborations they have had with Ernest Henry Mining. Permission to publish photos from the mine was granted by Brad Miller, Senior Mine Geologist.

The authors thank BHP Olympic Dam for approval to contribute to this volume and funding the research at Olympic Dam presented in this paper. We also thank reviewers Dawn Kellett, Crystal Laflamme, Tobias Schlegel, Nick Oliver and Robin Goad for their valued comments and suggested edits of the original manuscript. The insightful comments of Dr. Schlegel were also instrumental to revisions of the complementary contributions to this paper in this volume.

## References


Acosta-Góngora, P., Gleeson, S.A., Samson, I., Ootes, L., and Corriveau, L., 2014, Trace element geochemistry of magnetite and its relationship to mineralization in the Great Bear magmatic zone, NWT, Canada: Economic Geology, v. 109, p. 1901-1928.

Acosta-Góngora, G.P., Gleeson, S.A., Samson, I., Ootes, L., and Corriveau, L., 2015a, Gold refining by bismuth melts in the iron oxide-dominated NICO Au-Co-Bi (±Cu±W) deposit, NWT, Canada: Economic Geology, v. 110, p. 291-314.

Acosta-Góngora, P., Gleeson, S., Samson, I., Corriveau, L., Ootes, L., Taylor, B.E., Creaser, R.A., and Muehlenbachs, K., 2015b, Genesis of the Paleoproterozoic NICO iron-oxide-cobalt-gold-bismuth deposit, Northwest Territories, Canada: evidence from isotope geochemistry and fluid inclusions: Precambrian Research, v. 268, p. 168-193.

Apukhtina, O.B., Kamenetsky, V.S., Ehrig, K., Kamenetsky, M.B., Maas, R., Thompson, J., McPhie, J., Ciobanu, C.L., and Cook, N.J., 2017, Early, deep magnetite-fluorapatite mineralization at the Olympic Dam Cu-U-Au-Ag deposit, South Australia: Economic Geology, v. 112, p. 1531-1542.

Apukhtina, O.B., Ehrig, K., Kamenetsky, V.S., Kamenetsky, M.B., Goemann, K., Maas, R., McPhie, J., Cook, N.J., and Ciobanu C.L., 2020, Carbonates at the supergiant Olympic Dam Cu-U-Au-Ag deposit, South Australia. Part 1: distribution, textures, associations and stable isotope (C, O) signatures: Ore Geology Reviews, v. 126, 103775.

Babo, J., Spandler, C., Oliver, N., Brown, M., Rubenach, M., and Creaser, R.A., 2017, The high-grade Mo-Re Merlin deposit, Cloncurry District, Australia: paragenesis and geochronology of hydrothermal alteration and ore formation: Economic Geology, v. 112, p. 397-422.

Belperio, A., Flint, R., and Freeman, H., 2007, Prominent Hill: a hematite-dominated, iron oxide copper-gold system: Economic Geology, v. 102, p. 1499-1510.

BHP, 2018, BHP copper exploration program update: Press release on November 27th, 2018.

BHP, 2020, Annual report 2020: available at www.bhp.com

Blein, O., Corriveau, L., Montreuil, J.-F., Ehrig, K., Fabris, A., Reid, A., and Pal, D., 2022, Geochemical signatures of metasomatic ore systems hosting IOCG, IOA, albite-hosted uranium and affiliated deposits: a tool for process studies and mineral exploration, *in* Corriveau, L., Potter, E.G. and Mumin, A.H., eds., Mineral systems with iron oxide copper-gold (IOCG) and affiliated deposits: Geological Association of Canada, Special Paper 52, p. 263-298.

Bowdidge, C., and Dunford, A., 2015, Camsell River property, Northwest Territories 86E09 and 86F12: Northwest Territories Geological Survey, Assessment Report 033952, 73 p.

Bowdidge, C., Walker, E.C., and Dunford, A., 2014, DEMCo LTD. report on 2014 exploration Camsell River property, NTS 86E09, 86F12, Northwest Territories, 117°55'18" to 118°09'44" West, 65°33'34" to 65°38'33" North: Northwest Territories Geological Survey, Assessment Report 033596, 110 p.

Burgess, H., Gowans, R.M., Hennessey, B.T., Lattanzi, C.R., and Puritch, E., 2014, Technical report on the feasibility study for the NICO gold–cobalt–bismuth–copper deposit, Northwest Territories, Canada: Fortune Minerals Ltd., NI 43-101 Technical Report No. 1335, 385 p. Available at www.sedar.com.

Camier, J., 2002, The Sue-Dianne Fe-oxide Cu-Ag-Au breccia complex, southern Great Bear Magmatic Zone, Northwest Territories, Canada: Unpublished M.Sc. thesis, University of Western Ontario, London, Ontario, 210 p.

Cave, B.W., Lilly, R., Glorie, S., and Gillespie, J., 2018, Geology, apatite geochronology, and geochemistry of the Ernest Henry inter-lens: implications for a re-examined deposit model: Minerals, v. 8, 405.

Chen, H., and Zhao, L., 2022, Iron oxide copper-gold mineralization in the Central Andes: ore deposit geology and modelling, *in* Corriveau, L., Potter, E.G. and Mumin, A.H., eds., Mineral systems with iron oxide copper-gold (IOCG) and affiliated deposits: Geological Association of Canada, Special Paper 52, p. 365-381.

Cherry, A., Kamenetsky, V., McPhie, J., Kamenetsky, M., Ehrig, K., and Keeling, J., 2017, Post-1590 Ma modification of the supergiant Olympic Dam deposit: links with regional tectonothermal events: Proceedings of the 14th SGA Biennial Meeting, 20-23 August 2017, Québec City, p. 847-850.

Cherry, A., Ehrig, K., Kamenetsky, V.S., McPhie, J., Crowley, J., and Kamenetsky, M., 2018, Precise geochronological constraints on the origin, setting and incorporation of ca. 1.59 Ga surficial facies into the Olympic Dam Breccia Complex, South Australia: Precambrian Research, v. 315, p. 162-168.

Chorlton, L.B. (compiler), 2007, Generalized geology of the world: bedrock domains and major faults in GIS format: Geological Survey of Canada, Open File 5529, 1 CD-ROM.

Clark, C., Schmidt-Mumm, A., and Collins, A.S., 2006, A coupled micro- and macrostructural approach to the analysis of fluid induced brecciation, Curnamona Province, South Australia: Journal of Structural Geology, v. 28, p. 745-761.

Clark, J.M., 2014, Defining the style of mineralisation at the Cairn Hill magnetite-sulphide deposit, Mount Woods Inlier, Gawler Craton, South Australia: Unpublished B.Sc. (Hons.) thesis, University of Adelaide, 69 p.

Clark, J.M., and Ehrig, K., 2019, What controls high-grade copper mineralisation at Olympic Dam?: The Australasian Institute of Mining and Metallurgy: Melbourne, Proceedings Mining Geology 2019, p. 222-236.

Clark, J.M., Ehrig, K., Poznik, N., Cherry, A., McPhie, J., and Kamenetsky, V., 2018, Syn- to post-mineralisation structural dismemberment of the Olympic Dam Fe-oxide Cu-U-Au-Ag deposit: Society of Economic Geologists Annual Conference Proceedings - Metals, Mining and Society, Denver, Colorado.

Conor, C., Raymond, O., Baker, T., Teale, G., Say, P., and Lowe, G., 2010, Alteration and mineralisation in the Moonta-Wallaroo copper-gold mining field region, Olympic Domain, South Australia, *in* Porter, T.M., ed., Hydrothermal iron oxide copper-gold and related deposits: a global perspective, v. 3: PGC Publishing, Adelaide, p. 147-170.

Corriveau, L., and Potter, E.G., in press, Advancing exploration for iron oxide-copper-gold and affiliated deposits in Canada: context, scientific overview, outcomes and impacts, *in* Pehrsson, S., Wodicka. N., Rogers, N. and Percival, J., eds., Canada's northern shield: new perspectives from the Geo-Mapping for Energy and Minerals Program: Geological Survey of Canada, Bulletin 612.

Corriveau, L., and Spry, P., 2014, Metamorphosed hydrothermal ore deposits, *in* Holland, H.D. and Turekian, K.K., eds., Treatise on geochemistry, second edition: Elsevier, v. 13, p. 175-194.

Corriveau, L., Ootes, L., Mumin, A.H., Jackson, V., Bennett, V., Cremer, J.-F., Rivard, B., McMartin, I., and Beaudoin, G., 2007, Alteration vectoring to IOCG(U) deposits in frontier volcano-plutonic terrains, Canada, *in* Milkereit, B., ed., Proceedings of Exploration 07: Fifth Decennial International Conference on Mineral Exploration, p. 1171-1177.

Corriveau, L., Mumin, A.H., and Setterfield, T., 2010a, IOCG environments in Canada: characteristics, geological vectors to ore and challenges, *in* Porter, T.M., ed., Hydrothermal iron oxide copper-gold and related deposits: a global perspective, v. 4: PGC Publishing, Adelaide, p. 311-344.

Corriveau, L., Williams, P.J., and Mumin, A.H., 2010b, Alteration vectors to IOCG mineralization – from uncharted terranes to deposits, *in* Corriveau, L. and Mumin, A.H., eds., Exploring for iron oxide copper-gold deposits: Canada and global analogues: Geological Association of Canada, Short Course Notes, No. 20, p. 89-110.

Corriveau, L., Mumin, A.H., and Montreuil, J.-F., 2011, The Great Bear magmatic zone (Canada): the IOCG spectrum and related deposit types: Society for Geology Applied to Mineral Deposits, 11th, Antofagasta, Chile, Extended Abstracts, p. 524-526.

Corriveau, L., Lauzière, K., Montreuil, J.-F., Potter, E.G., Hanes, R., and Prémont, S., 2015, Dataset of geochemical data from iron oxide alkali-altered mineralizing systems of the Great Bear magmatic zone (NWT): Geological Survey of Canada, Open File 7643, 19 p., 6 geochemical datasets.

Corriveau, L., Montreuil, J.-F., and Potter, E.G., 2016, Alteration facies linkages among IOCG, IOA and affiliated deposits in the Great Bear magmatic zone, Canada, *in* Slack, J., Corriveau, L. and Hitzman, M., eds., Proterozoic iron oxide-apatite (± REE) and iron oxide-copper-gold and affiliated deposits of Southeast Missouri, USA, and the Great Bear magmatic zone, Northwest Territories, Canada: Economic Geology, v. 111, p. 2045-2072.

Corriveau, L., Blein, O., Gervais, F., Trapy, P.H., De Souza, S., and Fafard, D., 2018, Iron-oxide and alkali-calcic alteration, skarn and epithermal mineralizing systems of the Grenville Province: the Bondy gneiss complex in the Central Metasedimentary Belt of Quebec as a case example - a field trip to the 14th Society for Geology Applied to Mineral Deposits (SGA) biennial meeting: Geological Survey of Canada, Open File 8349, 136 p.

Corriveau, L., Montreuil, J.-F., Blein, O., Ehrig, K., Potter, E.G., Fabris, A., and Clark, J., 2022a, Mineral systems with IOCG and affiliated deposits: part 2 – geochemical footprint, *in* Corriveau, L., Potter, E.G. and Mumin, A.H., eds., Mineral systems with iron oxide copper-gold (IOCG) and affiliated deposits: Geological Association of Canada, Special Paper 52, p. 159-204.

Corriveau, L., Montreuil, J.-F., De Toni, A.F., Potter, E.G., and Percival, J.B., 2022b, Mapping mineral systems with IOCG and affiliated deposits: a facies approach, *in* Corriveau, L., Potter, E.G. and Mumin, A.H., eds., Mineral systems with iron oxide copper-gold (IOCG) and affiliated deposits: Geological Association of Canada, Special Paper 52, p. 69-111.

Corriveau, L., Montreuil, J.-F., Potter, E.G., Blein, O., and De Toni, A.F., 2022c, Mineral systems with IOCG and affiliated deposits: part 3 – metal pathways and ore deposit model, *in* Corriveau, L., Potter, E.G. and Mumin, A.H., eds., Mineral systems with iron oxide copper-gold (IOCG) and affiliated deposits: Geological Association of Canada, Special Paper 52, p. 205-245.

Corriveau, L., Mumin, A.H., and Potter, E.G., 2022d, Mineral systems with iron oxide copper-gold (Ag-Bi-Co-U-REE) and affiliated deposits: introduction and overview, *in* Corriveau, L., Potter, E.G. and Mumin, A.H., eds., Mineral systems with iron oxide copper-gold (IOCG) and affiliated deposits: Geological Association of Canada, Special Paper 52, p. 1-26.

Craven, J.A., Roberts, B., Hayward, N., Stefanescu, M., and Corriveau, L., 2013, A magnetotelluric survey and preliminary geophysical inversion and visualization of the NICO IOCG deposit, NWT: Geological Survey of Canada, Open File 7465, 26 p.

Davidson, G.J., Paterson, H., Meffre, S., and Berry, R.F., 2007, Characteristics and origin of the Oak Dam East breccia-hosted, iron oxide-Cu-U-(Au) deposit: Olympic Dam region, Gawler Craton, South Australia: Economic Geology, v. 102, p. 1471-1498.

Davis, W.J., Corriveau, L., van Breemen, O., Bleeker, W., Montreuil, J.-F., Potter, E.G., and Pelleter, E., 2011, Timing of IOCG mineralizing and alteration events within the Great Bear magmatic zone, *in* Fischer, B.J. and Watson, D.M., eds., 39th Annual Yellowknife Geoscience Forum Abstract Volume: Northwest Territories Geoscience Office, p. 97.

Day, W.C., Slack, J.F., Ayuso, R.A., and Seeger, C.M., 2016, Regional geologic and petrologic framework for iron oxide ± apatite ± rare earth element and iron oxide copper-gold deposits of the Mesoproterozoic St. Francois Mountains Terrane, Southeast Missouri, USA, *in* Slack, J., Corriveau, L. and Hitzman, M., eds., Proterozoic iron oxide-apatite (± REE) and iron oxide-copper-gold and affiliated deposits of Southeast Missouri, USA, and the Great Bear magmatic zone, Northwest Territories, Canada: Economic Geology, v. 111, p. 1825-1858.

De Jong, G., and Williams, P.J., 1995, Giant metasomatic system formed during exhumation of mid crustal Proterozoic rocks in the vicinity of the Cloncurry Fault, NW Queensland: Australian Journal of Earth Sciences, v. 42, p. 281-290.

De Toni, A.F., 2016, Les paragénèses à magnétite des altérations associées aux systèmes à oxydes de fer et altérations en éléments alcalins, zone magmatique du Grand lac de l'Ours: Unpublished M.Sc. thesis, Institut national de la Recherche Scientifique, 534 p.

del Real, I., Thompson, J.F.H., and Carriedo, J., 2018, Lithological and structural controls on the genesis of the Candelaria-Punta del Cobre iron oxide copper gold district, Northern Chile: Ore Geology Reviews, v. 102, p. 106-153.

Dipple, G.M., and Ferry, J.M., 1992, Metasomatism and fluid flow in ductile fault zones: Contributions to Mineralogy and Petrology, v. 112, p. 149-164.

Dmitrijeva, M., Ehrig, K.J., Ciobanu, C.L., Cook, N.J., Verdugo-Ihl, M.R., and Metcalfe, A.V., 2019, Defining IOCG signatures through compositional data analysis: a case study of lithogeochemical zoning from the Olympic Dam deposit, South Australia: Ore Geology Reviews, v. 105, p. 86-101.

Ehrig, K., and Clark, J., 2019, Insights into the structural evolution of Olympic Dam — the not so boring billion…: South Australian Exploration and Mining Conference, November 2019, available at saemc.com.au/archive/2019/2019_19_ehrig.pdf.

Ehrig, K., McPhie, J., and Kamenetsky, V.S., 2012, Geology and mineralogical zonation of the Olympic Dam iron oxide Cu-U-Au-Ag deposit, South Australia, *in* Hedenquist, J.W., Harris, M., and Camus, F., eds., Geology and genesis of major copper deposits and districts of the world: a tribute to Richard H. Sillitoe: Economic Geology Special Publication 16, p. 237-267.

Ehrig, K., Kamenetsky, V.S., McPhie, J., Apukhtina, O., Ciobanu, C.L., Cook, N., Kontonikas-Charos, A., and Krneta, S., 2017a, The IOCG-IOA Olympic Dam Cu-U-Au-Ag deposit and nearby prospects, South Australia: Proceedings of the 14th SGA Biennial Meeting, 20-23 August 2017, Québec City, p. 823-827.

Ehrig, K., Kamenetsky, V.S., McPhie, J., Apukhtina, O., Cook, N., and Ciobanu, C.L., 2017b, Olympic Dam iron oxide Cu-U-Au-Ag deposit, *in* Phillips, G.N., ed., Australian ore deposits: The Australasian Institute of Mining and Metallurgy, Melbourne, p. 601-610.

Enkin, R.J., Montreuil, J.F., and Corriveau, L., 2012, Differential exhumation and concurrent fluid flow at the NICO Au–Co–Bi–Cu deposit and Southern Breccia U–Th–REE–Mo anomaly, Great Bear magmatic zone, NWT — A paleomagnetic and structural record: Geological Association of Canada – Mineralogical Association Canada, Joint Annual Meeting, Program with Abstracts, v. 35, p. 41.

Fabris, A., 2022, Geochemical characteristics of IOCG deposits from the Olympic Copper-Gold Province, South Australia, *in* Corriveau, L., Potter, E.G. and Mumin, A.H., eds., Mineral systems with iron oxide copper-gold (IOCG) and affiliated deposits: Geological Association of Canada, Special Paper 52, p. 247-262.

Fabris, A., Katona, L., Gordon, G., Reed, G., Keeping, T., Gouthas, G., and Swain, G., 2018, Characterisation and mapping of Cu–Au skarn systems in the Punt Hill region, Olympic Cu–Au Province: MESA Journal, v. 87, p. 15-27.

Ferguson, M.R.M., Ehrig, K., Meffre, S., and Cherry, A.R., 2020, Associations between zircon and Fe–Ti oxides in Hiltaba event magmatic rocks, South Australia: atomic- or pluton-scale processes?: Australian Journal of Earth Sciences, v. 67, p. 201-220.

Fortune Minerals, 2019, Fortune Minerals announces new discovery at NICO: July 18th 2019 press release, available at fortuneminerals.com.

Foster, A.R., Williams, P.J., and Ryan, C.G., 2007, Distribution of gold in hypogene ore at the Ernest Henry iron oxide copper-gold deposit, Cloncurry district, NW Queensland: Exploration and Mining Geology, v. 16, p. 125-143.

Freeman, H., and Tomkinson, M., 2010, Geological setting of iron oxide related mineralisation in the southern Mount Woods Domain, South Australia, *in* Porter, T.M., ed., Hydrothermal iron oxide copper-gold and related deposits: a global perspective, v. 3: PGC Publishing, Adelaide, p. 171-191.

Gandhi, S.S., and Lentz, D.R., 1990, Bi–Co–Cu–Au–As and U occurrences in the Snare Group metasediments and felsic volcanics of the southern Great Bear magmatic zone, Lou Lake, Northwest Territories: Geological Survey of Canada, Paper 90-1C, p. 239-253.

Gandhi, S.S., and van Breemen, O., 2005, SHRIMP U–Pb geochronology of detrital zircons from the Treasure Lake Group — new evidence for Paleoproterozoic collisional tectonics in the southern Hottah terrane, northwestern Canadian Shield: Canadian Journal of Earth Sciences, v. 42, p. 833-845.

Gandhi, S.S., Prasad, N., and Charbonneau, B.W., 1996, Geological and geophysical signatures of a large polymetallic exploration target at Lou Lake, southern Great Bear Magmatic Zone, Northwest Territories: Geological Survey of Canada, Current Research Paper 1996-E, p. 147-158.

Gandhi, S.S., Mortensen, J.K., Prasad, N., and van Breemen, O., 2001, Magmatic evolution of the southern Great Bear continental arc, northwestern Canadian Shield: geochronological constraints: Canadian Journal of Earth Sciences, v. 38, p. 767-785.

Gandhi, S.S., Montreuil, J-F., and Corriveau, L., 2014, Geology and mineral occurrences, Mazenod Lake - Lou Lake area, Northwest Territories: Geological Survey of Canada, Canadian Geoscience Map 148, 1 sheet.

Gandhi, S.S., Potter, E.G., and Fayek, M., 2018, New constraints on genesis of the polymetallic veins at Port Radium, Great Bear Lake, Northwest Canadian Shield: Ore Geology Reviews, v. 96, p. 28-47.

Glencore, 2020, Resources and reserves as at 31 December 2019: Available at https://www.glencore.com/.

Goad, R.E., Mumin, A.H., Duke, N.A., Neale, K.L., and Mulligan, D.L., 2000, Geology of the Proterozoic iron oxide-hosted NICO cobalt-gold-bismuth, and Sue-Dianne copper-silver deposits, southern Great Bear Magmatic Zone, Northwest Territories, Canada, *in* Porter, T.M., ed., Hydrothermal iron oxide copper-gold and related deposits: a global perspective, v. 1: PGC Publishing, Adelaide, p. 249-267.

Groves, D.I., Bierlein, F.P., Meinert, L.D., and Hitzman, M.W., 2010, Iron oxide copper-gold (IOCG) deposits through Earth history. Implications for origin, lithospheric setting, and distinction from other epigenetic iron oxide deposits: Economic Geology, v. 105, p. 641-654.

Gu, Y., 2003, Automated scanning electron microscope based mineral liberation analysis: Journal of Minerals and Materials Characterization and Engineering, v. 2, p. 33-41.

Harlov, D.E., and Austrheim, H., 2012, Metasomatism and the chemical transformation of rock: Lecture Notes in Earth System Sciences, 789 p.

Harlov, D.E., Meighan, C.J., Kerr, I.D., and Samson, I.M., 2016, Mineralogy, chemistry, and fluid-aided evolution of the Pea Ridge Fe oxide- (Y + REE) deposit, Southeast Missouri, USA: Economic Geology, v. 111, p. 1963-1984.

Haynes, D.W., Cross, K.C., Bills, R.T., and Reed, M.H., 1995, Olympic Dam ore genesis: a fluid mixing model: Economic Geology, v. 90, p. 281-307.

Hayward, N., and Corriveau, L., 2014, Fault reconstructions using aeromagnetic data in the Great Bear magmatic zone, Northwest Territories, Canada: Canadian Journal of Earth Sciences, v. 51, p. 927-942.

Hayward, N., Corriveau, L., Craven, J.A., and Enkin, R.J., 2016, Geophysical signature of alteration and mineralisation envelope at the Au-Co-Bi-Cu NICO deposit, NT, Canada, *in* Slack, J., Corriveau, L. and Hitzman, M., eds., Proterozoic iron oxide-apatite (± REE) and iron oxide-copper-gold and affiliated deposits of Southeast Missouri, USA, and the Great Bear magmatic zone, Northwest Territories, Canada: Economic Geology, v. 111, p. 2087-2110.

Hayward, Ni., and Skirrow, R.G., 2010, Geodynamic setting and controls on iron oxide Cu-Au (±U) ore in the Gawler craton, South Australia, *in* Porter, T.M., ed., Hydrothermal iron oxide copper-gold and related deposits: a global perspective, v. 3: PGC Publishing, Adelaide, p. 119-146.

Hildebrand, R.S., 1983, Geology – Echo Bay-MacAlpine Channel area, district of Mackenzie, Northwest Territories: Geological Survey Canada, Map 1546A, scale 1:50,000.

Hildebrand, R.S., 1984, Geology of the Rainy Lake-White Eagle Falls area district of Mackenzie: early Proterozoic cauldrons, stratovolcanoes and subvolcanic plutons: Geological Survey of Canada, Paper 83-20, 42 p.

Hildebrand, R.S., 1986, Kiruna-type deposits: their origin and relationship to intermediate subvolcanic plutons in the Great Bear Magmatic Zone, northwest Canada: Economic Geology, v. 81, p. 640-659.

Hildebrand, R.S., 2011, Geological synthesis of Northern Wopmay Orogen / Coppermine Homocline, Northwest Territories – Nunavut: Geological Survey of Canada, Open File 6390, Northwest Territories Geoscience Office, Open Report 2010-011, 1 map sheet, scale 1:500 000.

Hildebrand, R.S., 2017, Precambrian geology, Leith Peninsula-Rivière Grandin area, Northwest Territories: Geological Survey of Canada, Canadian Geoscience Map 153, 1 sheet.

Hildebrand, R.S., Hoffman, P.F., Housh, T., and Bowring, S.A., 2010, The nature of volcano-plutonic relations and shapes of epizonal plutons of continental arcs as revealed in the Great Bear magmatic zone, northwestern Canada: Geosphere, v. 6, p. 812-839.

Hildebrand, R.S., Bowring, S., and Pelleter, K.F., 2014, Calder River, map area: Geological Survey of Canada, Canadian Geoscience Map Series, CGM 154/ Northwest Territories Geoscience Office, Open Report 2013-03, 1 map sheet.

Hitzman, M.W., Oreskes, N., and Einaudi, M.T., 1992, Geological characteristics and tectonic setting of Proterozoic iron oxide (Cu-U-Au-LREE) deposits: Precambrian Research, v. 58, p. 241-287.

Hoffman, P.F., Bowring, S.A., Buchwaldt, R., and Hildebrand, R.S., 2011, Birthdate for the Coronation paleocean: age of initial rifting in Wopmay orogen, Canada: Canadian Journal of Earth Sciences, v. 48, p. 281-293.

Hofstra, A., Lisitsin, V., Corriveau, L., Paradis, S., Peter, J., Lauzière, K., Lawley, C., Gadd, M., Pilote, J., Honsberger, I., Bastrakov, E., Champion, D., Czarnota, K., Doublier, M., Huston, D., Raymond, O., Van Der Wielen, S., Emsbo, P., Granitto, M., and Kreiner, D., 2021, Deposit classification scheme for the Critical Minerals Mapping Initiative Global Geochemical Database: U.S. Geological Survey Open-File Report 2021–1049, 60 p.

Hoggard, M.J., Czarnota, K., Richards, F.D., Huston, D., Jaques, L., and Ghelichkhan, S., 2020, Global distribution of sediment-hosted metals controlled by craton edge stability: Nature Geoscience, v. 13, p. 504-510.

Hughes, T.N.J., 1997, Geological report of the Grouard Lake property, Grouard Lake, NT - Phelps Dodge Corporation of Canada limited: Northwest Territories Geoscience Office, Assessment Report 084042, 47 p.

Ismail, R., Ciobanu, C.L., Cook, N.J., Giles, D., Schmidt-Mumm, A., and Wade, B., 2014, Rare earths and other trace elements in minerals from skarn assemblages, Hillside iron oxide–copper–gold deposit, Yorke Peninsula, South Australia: Lithos, v. 184-187, p. 456-477.

Jackson, V.A., 2008, Preliminary geologic map of part of the southern Wopmay Orogen (parts of NTS 86B and 86C; 2007 updates); descriptive notes to accompany 1:100,000 scale map: Northwest Territories Geoscience Office, NWT Open Report 2008-007, 51 p.

Jackson, V.A., and Ootes, L., 2012, Preliminary geologic map of the south-central Wopmay Orogen (parts of NTS 86B, 86C, and 86D); results from 2009 to 2011: Northwest Territories Geoscience Office, Open Report 2012-004, 1 map, 1:100,000 scale.

Jackson, V.A., van Breemen, O., Ootes, L., Bleeker, W., Bennett, V., Davis, W.D., Ketchum, J., and Smar, L., 2013, Ages of basement and intrusive phases East of the Wopmay fault zone, south-central Wopmay Orogen, NWT: a field-based U–Pb zircon study: Canadian Journal of Earth Sciences, v. 50, p. 979-1006.

Jagodzinski, E.A., 2014, The age of magmatic and hydrothermal zircon at Olympic Dam: Australian Earth Sciences Convention, Proceedings, v. 110, p. 260 (Geological Society of Australia, Sydney).

Jébrak, M., 2022, Use of breccias in IOCG exploration: an updated review, *in* Corriveau, L., Mumin, A.H. and Potter, E.G., eds., Mineral systems with iron oxide copper-gold (IOCG) and affiliated deposits: Geological Association of Canada, Special Paper 52, p. 315-324.

Kelly, C.J., Davis, W.J., Potter, E.G., and Corriveau, L., 2020, Geochemistry of hydrothermal tourmaline from IOCG occurrences in the Great Bear magmatic zone: implications for fluid source(s) and fluid composition evolution: Ore Geology Reviews, v. 118, 103329.

Kirschbaum, M.J., and Hitzman, M.W., 2016, Guelb Moghrein: an unusual carbonate-hosted iron oxide copper-gold deposit in Mauritania, northwest Africa: Economic Geology, v. 111, p. 763-770.

Knox, A.W., 1998, Geological report on the Hillside zinc–lead–silver showing, Grouard Lake property: Northwest Territories Geoscience Office, Assessment Report 084043, 32 p.

Kontonikas-Charos, K., Ciobanu, C.L., Cook, N.J., Ehrig, K., Krneta, S., and Kamenetsky, V.S., 2017, Feldspar evolution in the Roxby Downs Granite, host to Fe-oxide Cu-Au-(U) mineralisation at Olympic Dam, South Australia: Ore Geology Reviews, v. 80, p. 838-859.

Kontonikas-Charos, A., Ciobanu, C., Cook, N., Ehrig, K., Ismail, R., Krneta, S., and Basak, A., 2018, Feldspar mineralogy and rare-earth element (re)mobilization in iron-oxide copper gold systems from South Australia: a nanoscale study: Mineralogical Magazine, v. 82, p. 173-197.

Lilly, R., Case, G., and Miller, B., 2017, Ernest Henry iron oxide copper-gold deposit, *in* Phillips, N., ed., Australian ore deposits, 6th edition: The Australasian Institute of Mining and Metallurgy, Monograph 32, p. 1-6.

Macdonald Mines Ltd., 2020, SPJ Project high-grade gold deposit in an emerging polymetallic gold district, March 2020: Available at macdonaldmines.com/wp-content/uploads/2020/03/BMK_PPT-March-2020.pdf.

Maggi, M., Rossetti, F., Ranalli, G., and Theye. T., 2014, Feedback between fluid infiltration and rheology along a regional ductile-to-brittle shear zone: the East Tenda Shear Zone (Alpine Corsica): Tectonics, v. 33, p. 253-280.

Mark, G., Oliver, N.H.S., Williams, P.J., Valenta, R.K., and Crookes, R.A., 2000, The evolution of the Ernest Henry Fe-oxide-(Cu-Au) hydrothermal system, *in* Porter, T.M., ed., Hydrothermal iron oxide copper-gold and related deposits: a global perspective, v. 1: PGC Publishing, Adelaide, p. 123-136.

Mark, G., Oliver, N.H.S., and Williams, P.J., 2006, Mineralogical and chemical evolution of the Ernest Henry Fe oxide-Cu-Au ore system, Cloncurry district, northwest Queensland, Australia: Mineralium Deposita, v. 40, p. 769-801.

Marshall, L.J., and Oliver, N.H.S., 2008, Constraints on hydrothermal fluid pathways within Mary Kathleen Group stratigraphy of the Cloncurry iron-oxide–copper–gold District, Australia: Precambrian Research, v. 163, p. 151-158.

May, L.H., 2007, Petrography of the Mile Lake breccia, Great Bear Magmatic Zone, N.W.T.: Unpublished B.Sc. Honors thesis, Brandon University, 77 p.

McCafferty, A.E., Phillips, J.D., Hofstra, A.H., and Day, W.C., 2019, Crustal architecture beneath the southern Midcontinent (USA) and controls on Mesoproterozoic iron-oxide mineralization from 3D geophysical models: Ore Geology Reviews, v. 111, 102966.

McGloin, M., Tomkins, A., and Weinberg, R., 2013, Isan U and Th mobility and related ore mineralisation: Proceedings of the 12th Biennial SGA meeting, Upsala, Sweden, 4 p.

McLaughlin, B., Montreuil, J.-F., and Desrochers, J.-P., 2016, Exploration report (summer and fall 2014 drill program) on the Sagar Property, Romanet Horst, Labrador Trough, Québec, Canada: Ministère de l'Énergie et des Ressources naturelles Québec, GM 69734, 65 p.

McPhie, J., Kamenetsky, V.S., Chambefort, I., Ehrig, K., and Green, N., 2011, Origin of the supergiant Olympic Dam Cu–U–Au–Ag deposit, South Australia: was a sedimentary basin involved?: Geology, v. 39, p. 795-798.

McPhie, J., Orth, K., Kamenetsky, V., Kamenetsky, M., and Ehrig, K., 2016, Characteristics, origin and significance of Mesoproterozoic bedded clastic facies at the Olympic Dam Cu–U–Au–Ag deposit, South Australia: Precambrian Research, v. 276, p. 85-100.

Montreuil, J.-F., Corriveau, L., and Long, B., 2012, Porosity in albitites and the development of albitite-hosted U deposits: insights from X-ray computed tomography: CT Scan workshop, Development on non-medical environment, Québec, INRS.

Montreuil, J.-F., Corriveau, L., and Potter, E.G., 2015, Formation of albitite-hosted uranium within IOCG systems: the Southern Breccia, Great Bear magmatic zone, Northwest Territories, Canada: Mineralium Deposita, v. 50, p. 293-325.

Montreuil, J.-F., Corriveau, L., and Davis, W., 2016a, Tectonomagmatic evolution of the southern Great Bear magmatic zone (Northwest Territories, Canada) – Implications on the genesis of iron oxide alkali-altered hydrothermal systems, *in* Slack, J., Corriveau, L. and Hitzman, M., eds., Proterozoic iron oxide-apatite (± REE) and iron oxide-copper-gold and affiliated deposits of Southeast Missouri, USA, and the Great Bear magmatic zone, Northwest Territories, Canada: Economic Geology, v. 111, p. 2111-2138.

Montreuil, J.-F., Corriveau, L., Potter, E.G., and De Toni, A.F., 2016b, On the relation between alteration facies and metal endowment of iron oxide–alkali-altered systems, southern Great Bear Magmatic Zone (Canada), *in* Slack, J., Corriveau, L. and Hitzman, M., eds., Proterozoic iron oxide-apatite (± REE) and iron oxide-copper-gold and affiliated deposits of Southeast Missouri, USA, and the Great Bear magmatic zone, Northwest Territories, Canada: Economic Geology, v. 111, p. 2139-2168.

Montreuil, J.-F., Potter, E.G., Corriveau, L., and Davis, W.J., 2016c, Element mobility patterns in magnetite-group IOCG systems: the Fab IOCG system, Northwest Territories, Canada: Ore Geology Reviews, v. 72, p. 562-584.

Morrissey, L.J., and Tomkins, A.G., 2020, Evaporite-bearing orogenic belts produce ligand-rich and diverse metamorphic fluids: Geochimica et Cosmochimica Acta, v. 275, p. 163-187.

Mort, K., and Woodcock, N.H., 2008, Quantifying fault breccia geometry: Dent Fault, NW England: Journal of Structural Geology, v. 30, p. 701-709.

Mumin, A.H. (ed.), 2015, Echo Bay IOCG thematic map series: geology, structure and hydrothermal alteration of a stratovolcano complex, Northwest Territories, Canada: Geological Survey of Canada, Open File 7807, 19 p., 18 sheets.

Mumin, A.H., Goad, R.E., and Mulligan, D.L., 1996, A report on the geology of the Treasure (F49508), Island 1 (F51395), Island 2 (F51396), Island 3 (F51397), and Island 4 (F49511) claims, Marian River area, Mackenzie (south) district, Northwest Territories, Canada: Northwest Territories Geoscience Office, Assessment Report 083776, 69 p.

Mumin, A.H., Corriveau, L., Somarin, A.K., and Ootes, L., 2007, Iron oxide copper-gold-type polymetallic mineralisation in the Contact Lake Belt, Great Bear Magmatic Zone, Northwest Territories, Canada: Exploration and Mining Geology, v. 16, p. 187-208.

Mumin, A.H., Somarin, A.K., Jones, B., Corriveau, L., Ootes, L., and Camier, J., 2010, The IOCG-porphyry-epithermal continuum of deposits types in the Great Bear Magmatic Zone, Northwest Territories, Canada, *in* Corriveau, L. and Mumin, A.H., eds., Exploring for iron oxide copper-gold deposits: Canada and global analogues: Geological Association of Canada, Short Course Notes, No. 20, p. 59-78.

Mumin, A.H., Phillips, A., Katsuragi, C.J., Mumin, A., and Ivanov, G., 2014, Geotectonic interpretation of the Echo Bay stratovolcano complex, northern Great Bear magmatic zone, NWT, Canada: Northwest Territories Geoscience Office, Open File 2014-04, 44 p.

Oliver, N.H.S., Pearson, P.J., Holcombe, R.J., and Ord, A., 1999, Mary Kathleen metamorphic–hydrothermal uranium–rare-earth element deposit: ore genesis and numerical model of coupled deformation and fluid flow: Australian Journal of Earth Sciences, v. 46, p. 467-484.

Oliver, N.H.S., Mark, G., Pollard, P.J., Rubenach, M.J., Bastrakov, E., Williams, P.J., Marshall, L.C., Baker, T., and Nemchin, A.A., 2004, The role of sodic alteration in the genesis of iron oxide-copper-gold deposits: geochemistry and geochemical modelling of fluid-rock interaction in the Cloncurry district, Australia: Economic Geology, v. 99, p. 1145-1176.

Oliver, N.H.S., Rubenach, M.J., Baker, B.F., Blenkinsop, T.G., Cleverley, J.S., Marshall, L.J., and Ridd, P.J., 2006, Granite-related overpressure and volatile release in the mid crust: fluidized breccias from the Cloncurry district, Australia: Geofluids, v. 6, p. 346-358.

Oliver, N.H.S., Rusk, B.G., Long, R., and Zhang, D., 2009, Copper- and iron-oxide-Cu-Au deposits, and their associated alteration and brecciation, Mount Isa block: SGA post-conference trip field guide: Mt Isa Cu, IOCG and breccias. EGRU/JCU, 40 p.

Ootes, L., Jackson, V.A., and Corriveau, L., 2008, Assay results from the South Wopmay Bedrock Mapping Project (2006 – 2007 field seasons): Northwest Territories Geoscience Office, Open Report 2008-008, 13 p.

Ootes, L., Goff, S., Jackson, V.A., Gleeson, S.A., Creaser, R.A., Samson, I.M.S., Evensen, N., Corriveau, L., and Mumin, A.H., 2010, Timing and thermo-chemical constraints on multi-element mineralization at the Nori/RA Cu–Mo–U prospect, Great Bear magmatic zone, Northwest Territories, Canada: Mineralium Deposita, v. 45, p. 549-566.

Ootes, L., Harris, J., Jackson, V.A., Azar, B., and Corriveau, L., 2013, Uranium-enriched bedrock in the central Wopmay orogen: implications for uranium mineralization, *in* Potter, E.G., Quirt, D. and Jefferson, C.W., eds., Uranium in Canada: geological environments and exploration developments: Exploration and Mining Geology, v. 21, p. 85-103.

Ootes, L., Snyder, D., Davis, W.J., Acosta-Góngora, P., Corriveau, L., Mumin, A.H., Gleeson, S.A., Samson, I.A., Montreuil, J.-F., Potter, E.G., and Jackson, V.A., 2017, A Paleoproterozoic Andean-type iron oxide copper-gold environment, the Great Bear magmatic zone, Northwest Canada: Ore Geology Reviews, v. 81, p. 123-139.

Oreskes, N., and Einaudi, M.T., 1992, Origin of hydrothermal fluids at Olympic Dam; preliminary results from fluid inclusions and stable isotopes: Economic Geology, v. 87, p. 64-90.

Pelleter, E., Gasquet, D., Cheilletz, A., and Mouttaqi, A., 2010, Alteration processes and impacts on regional-scale element mobility and geochronology, Tamlalt-Menhouhou deposit, Morocco, *in* Corriveau, L. and Mumin, A.H., eds., Exploring for iron oxide copper-gold deposits: Canada and global analogues: Geological Association of Canada, Short Course Notes, No. 20, p. 177-185.

Percival, J.B., Potter, E.G., Lauzière, K., Ijewliw, O., Bilot, I., Hunt, P., English, M.L.R., Olejarz, A.D., Laudadio, A.B., Enright, A., Robillard, K.-L., and Corriveau, L., 2016, Mineralogy, petrography and autoradiography of selected samples from the Contact Lake and NICO areas, Great Bear Magmatic Zone, Northwest Territories (IOCG-GEM Project): Geological Survey of Canada, Open File 7755, 48 p.

Porter, T.M., 2010a, Current understanding of iron oxide associated-alkali altered mineralised systems. Part 1 - An overview, *in* Porter, T.M., ed., Hydrothermal iron oxide copper-gold and related deposits: a global perspective, v. 3: PGC Publishing, Adelaide, p. 5-32.

Porter, T.M., 2010b, The Carrapateena iron oxide copper gold deposit, Gawler Craton, South Australia: a review, *in* Porter, T.M., ed., Hydrothermal iron oxide copper-gold and related deposits: a global perspective, v. 3: PGC Publishing, Adelaide, p. 191-200.

Potter, E.G., Montreuil, J.-F., Corriveau, L., and De Toni, A., 2013, Geology and hydrothermal alteration of the Fab Lake region, Northwest Territories: Geological Survey of Canada, Open File 7339, 26 p.

Potter, E.G., Montreuil, J.-F., Corriveau, L., and Davis, W., 2019, The Southern Breccia metasomatic uranium system of the Great Bear magmatic zone, Canada: iron oxide-copper-gold (IOCG) and albitite-hosted uranium linkages, *in* Decrée, S. and Robb, L., eds., Ore deposits: origin, exploration, and exploitation: Geophysical Monograph 242, American Geophysical Union, John Wiley & Sons, Inc., p. 109-130.

Potter, E.G., Corriveau, L., and Kjarsgaard, B., 2020, Paleoproterozoic iron oxide apatite (IOA) and iron oxide-copper-gold (IOCG) mineralization in the East Arm Basin, Northwest Territories, Canada: Canadian Journal of Earth Sciences, v. 57, p. 167-183.

Potter, E.G., Acosta-Góngora, P., Corriveau, L., Montreuil, J-F., and Yang, Z., 2022, Uranium enrichment processes in iron oxide and alkali-calcic alteration systems as revealed by trace element signatures of uraninite, *in* Corriveau, L., Potter, E.G. and Mumin, A.H., eds., Mineral systems with iron oxide copper-gold (IOCG) and affiliated deposits: Geological Association of Canada, Special Paper 52, p. 325-345.

Poulet, T., Karrech, A., Regenauer-Lieb, K., Fisher, L., and Schaubs, P., 2012, Thermal–hydraulic–mechanical–chemical coupling with damage mechanics using ESCRIPTRT and ABAQUS: Tectonophysics, v. 526-529, p. 124-132.

Reeve, J.S., Cross, K.C., Smith, R.N., and Oreskes, N., 1990, The Olympic Dam copper-uranium-gold-silver deposit, South Australia, *in* Hughes, F., ed., Geology of mineral deposits of Australia and Papua New Guinea: Australian Institute of Mining and Metallurgy, Monograph 14, p. 1009-1035.

Reid, A., 2019, The Olympic Cu-Au Province, Gawler Craton: a review of the lithospheric architecture, geodynamic setting, alteration systems, cover successions and prospectivity: Minerals, v. 9, 371.

Reid, A.J., and Fabris, A., 2015, Influence of pre-existing low metamorphic grade sedimentary successions on the distribution of iron oxide copper-gold mineralisation in the Olympic Cu-Au Province, Gawler Craton: Economic Geology, v. 110, p. 2147-2157.

Reid, A.J., Swain, G., Mason, D., and Maas, R., 2011, Nature and timing of Cu–Au–Zn–Pb mineralisation at Punt Hill, eastern Gawler Craton: MESA Journal, v. 60, p. 7-27.

Reynolds, L.J., 2000, Geology of the Olympic Dam Cu-U-Au-Ag-REE deposit, *in* Porter, T.M., ed., Hydrothermal iron oxide copper-gold and related deposits: a global perspective, v. 1: PGC Publishing, Adelaide, p. 93-104.

Richards, J.P., and Mumin, A.H., 2013a, Lithospheric fertilization and mineralization by arc magmas: genetic links and secular differences between porphyry copper±molybdenum±gold and magmatic-hydrothermal iron oxide copper-gold deposits, *in* Colpron, M., Bissig, T., Rusk, B.G. and Thompson, J.F.H., eds., Tectonics, metallogeny, and discovery: the North American Cordillera and similar accretionary settings: Society of Economic Geologists, Special Publication 17, p. 277-299.

Richards, J.P., and Mumin, A.H., 2013b, Magmatic-hydrothermal processes within an evolving Earth: iron oxide-copper-gold and porphyry Cu±Mo±Au deposits: Geology, v. 41, p. 767-770.

Richardson, K.A., Holman, P.B., Elliott, B., Charbonneau, B.W., and McGlynn, J.C., 1973, Gamma-ray spectrometer maps and profiles, District of Mackenzie, Northwest Territories, (NTS 86A, B, C, F, G, H): Geological Survey of Canada, Open File 140, 8 maps, scale 1:250 000.

Rusk, B., Oliver, N., Blenkinsop, T., Zhang, D., Williams, P., Cleverley, J., and Habermann, H., 2010, Physical and chemical characteristics of the Ernest Henry iron oxide copper gold deposit, Cloncurry, Queensland, Australia; Implications for IOCG genesis, *in* Porter, T.M., ed., Hydrothermal iron oxide copper-gold and related deposits: a global perspective, v. 3: PGC Publishing, Adelaide, p. 201-218.

Schandl, E.S., and Gorton, M.P., 2007, The Scadding gold mine, east of the Sudbury Igneous Complex, Ontario: an IOCG-type deposit?: The Canadian Mineralogist, v. 45, p. 1415-1441.

Schlegel, T.U., 2015, The Prominent Hill iron oxide-Cu Au deposit in South Australia – a deposit formation model based on geology, geochemistry, stable isotopes and fluid inclusions: Unpublished Ph.D. thesis, ETH Zurich, Dissertation-No 22485, 290 p.

Schlegel, T.U., and Heinrich, C.A., 2015, Lithology and hydrothermal alteration control the distribution of copper grade in the Prominent Hill iron oxide-copper-gold deposit (Gawler Craton, South Australia): Economic Geology, v. 110, p. 1953-1994.

Shives, R.B.K., Charbonneau, B.W., and Ford, K.L., 2000, The detection of potassic alteration by gamma-ray spectrometry – Recognition of alteration related to mineralization: Geophysics, v. 65, p. 2001-2011.

Skirrow, R., 2010, “Hematite-group” IOCG ± U ore systems: tectonic settings, hydrothermal characteristics, and Cu-Au and U mineralizing processes, *in* Corriveau, L. and Mumin, A.H., eds., Exploring for iron oxide copper-gold deposits: Canada and global analogues: Geological Association of Canada, Short Course Notes, No. 20, p. 39-57.

Skirrow, R.G., 2022, Hematite-group IOCG ± U deposits: an update on their tectonic settings, hydrothermal characteristics, and Cu-Au-U mineralizing processes, *in* Corriveau, L., Potter, E.G. and Mumin, A.H., eds., Mineral systems with iron oxide copper-gold (IOCG) and affiliated deposits: Geological Association of Canada, Special Paper 52, p. 27-51.

Skirrow, R.G., and Davidson, G., 2007, A special issue devoted to Proterozoic iron oxide Cu-Au-(U) and gold mineral systems of the Gawler craton: preface: Economic Geology, v. 102, p. 1373-1375.

Skirrow, R.G., and Walshe, J.L., 2002, Reduced and oxidized Au-Cu-Bi iron oxide deposits of the Tennant Creek inlier, Australia: an integrated geologic and chemical model: Economic Geology, v. 97, p. 1167-1202.

Skirrow, R.G., Schofield, A., and Connolly, D., 2011, Uranium-rich iron oxide-copper-gold, *in* Huston, D.L. and van der Wielen, S.E., eds., An assessment of the uranium and geothermal prospectivity of east-central South Australia: Geoscience Australia, Record, 2011/34, 229 p.

Skirrow, R.G., van der Wielen, S.E., Champion, D.C., Czarnota, K., and Thiel, S., 2018, Lithospheric architecture and mantle metasomatism linked to iron oxide Cu-Au ore formation: multidisciplinary evidence from the Olympic Dam region, South Australia: Geochemistry, Geophysics, Geosystems, v. 19, p. 2673-2705.

Somarin, A.K., and Mumin, A.H., 2012, The Paleo-Proterozoic high heat production Richardson granite, Great Bear magmatic zone, Northwest Territories, Canada: source of U for Port Radium?: Resources Geology, v. 62, p. 227-242.

Somarin, A.K., and Mumin, A.H., 2014, P–T-composition and evolution of paleofluids in the Paleoproterozoic Mag Hill IOCG hydrothermal system, Contact Lake belt, Northwest Territories, Canada: Mineralium Deposita, v. 49, p. 199-215.

Tiddy, C.J., and Giles, D., 2020, Suprasubduction zone model for metal endowment at 1.60–1.57 Ga in eastern Australia: Ore Geology Reviews, v. 122, 103483.

Twyerould, S.C., 1997, The geology and genesis of the Ernest Henry Fe-Cu-Au deposit, NW Queensland, Australia: Unpublished Ph.D. Thesis, University of Oregon, 494 p.

Whitney, D.L., and Evans, B.W., 2010, Abbreviations for names of rock-forming minerals: American Mineralogist, v. 95, p. 185-187.

Wilde, A., Otto, A., Jory, J., MacRae, C., Pownceby, M., Wilson, N., and Torpy, A., 2013, Geology and mineralogy of uranium deposits from Mount Isa, Australia: implications for albitite uranium deposit models: Minerals, v. 3, p. 258-283.

Williams, P.J., 1994, Iron mobility during synmetamorphic alteration in the Selwyn Range area, NW Queensland: implications for the origin of ironstone-hosted Au-Cu deposits: Mineralium Deposita, v. 29, p. 250-260.

Williams, P.J., 1998, Metalliferous economic geology of the Mt. Isa Eastern Succession, northwest Queensland: Australian Journal of Earth Sciences, v. 45, p. 329-341.

Williams, P.J., 2010a, Classifying IOCG deposits, *in* Corriveau, L. and Mumin, A.H., eds., Exploring for iron oxide copper-gold deposits: Canada and global analogues: Geological Association of Canada, Short Course Notes, No. 20, p. 13-21.

Williams, P.J., 2010b, “Magnetite-group” IOCGs with special reference to Cloncurry and Northern Sweden: settings, alteration, deposit characteristics, fluid sources, and their relationship to apatite-rich iron ores, *in* Corriveau, L. and Mumin, A.H., eds., Exploring for iron oxide copper-gold deposits: Canada and global analogues: Geological Association of Canada, Short Course Notes, No. 20, p. 23-38.

Williams, P.J., and Skirrow, R.G., 2000, Overview of iron oxide-copper-gold deposits in the Curnamona Province and Cloncurry District (Eastern Mount Isa Block), Australia, *in* Porter, T.M., ed., Hydrothermal iron oxide copper-gold and related deposits: a global perspective, v. 1: PGC Publishing, Adelaide, p. 105-122.

Williams, P.J., Barton, M.D., Johnson, D.A., Fontboté, L., de Haller, A., Mark, G., Oliver, N.H.S., and Marschik, R., 2005, Iron-oxide copper-gold deposits: geology, space-time distribution, and possible modes of origin: Economic Geology 100th Anniversary Volume, p. 371-405.

Wintsch, R.P., Christoffersen, R., and Kronenberg, A.K., 1995, Fluid-rock reaction weakening of fault zones: Journal of Geophysical Research: Solid Earth, v. 100, p. 13021-13032.

Yardley, B.W.D., 2012, The chemical composition of metasomatic fluids in the crust, *in* Harlov, D.E. and Austrheim, H., eds., Metasomatism and the chemical transformation of rock: Lecture Notes in Earth System Sciences, p. 17-51.

Zhao, X.-F., Chen, H., Zhao, L., and Zhou, M.-F., 2022, Linkages among IOA, skarn, and magnetite-group IOCG deposits in China: from deposit studies to mineral potential assessment, *in* Corriveau, L., Potter, E.G. and Mumin, A.H., eds., Mineral systems with iron oxide copper-gold (IOCG) and affiliated deposits: Geological Association of Canada, Special Paper 52, p. 383-407.

# Mineral Systems with IOCG and Affiliated Deposits: Part 2 – Geochemical Footprints


**Louise Corriveau**
*Natural Resources Canada, Geological Survey of Canada, Québec, Canada*
*louise.corriveau@NRCan-RNCan.gc.ca*

**Jean-Francois Montreuil**
*Red Pine Exploration, Ontario, Canada*

**Olivier Blein**
*Bureau de recherches géologiques et minières, Orléans, France*

**Kathy Ehrig**
*BHP-Olympic Dam, Adelaide, Australia*

**Eric G. Potter**
*Natural Resources Canada, Geological Survey of Canada, Ontario, Canada*

**Adrian Fabris**
*Geological Survey of South Australia, Adelaide, Australia*

**Jesse Clark**
*BHP-Olympic Dam, Adelaide, Australia*



*Recommended citation: Corriveau, L., Montreuil, J.-F., Blein, O., Ehrig, K., Potter, E.G., Fabris. A., and Clark, J., 2022, Mineral systems with IOCG and affiliated deposits: part 2 – geochemical footprints, in Corriveau, L., Potter, E.G. and Mumin, A.H., eds., Mineral systems with iron oxide copper-gold (IOCG) and affiliated deposits: Geological Association of Canada, Special Paper 52, p. 159-204.*



## Abstract

Regional iron oxide and alkali-calcic alteration systems generate a wide variety of ore deposits, including iron oxide-apatite (IOA), iron oxide copper-gold (IOCG), iron oxide Co, Bi, REE or U, skarn, and albitite-hosted uranium and Au-Co ± U deposits. The Great Bear magmatic zone (Canada), Cloncurry district and Olympic Copper-Gold Province (Australia) are used as examples to illustrate the lithogeochemical footprints of these mineralizing hydrothermal systems. Plotting metal contents on a diagram that discriminates the iron oxide and alkali-calcic alteration facies (AIOCG plot) highlights the coupling of V, Sc, Ni ± Pb ± Zn with Ca and Fe, as Facies 1 (Na) alteration evolves to Facies 2 (high-temperature Ca-Fe) alteration and IOA mineralization. In metasedimentary rocks, propagation of fluid-rock reactions towards Facies 3 forms a transitional Facies 2–3 (high-temperature Ca-K-Fe) alteration that is marked by enrichment in cobalt and gold and onset of copper precipitation. Au-Co-Bi ± Cu deposits with iron-rich end-members are associated with the precipitation of As, Bi and W (e.g. NICO deposit, Great Bear). Facies 3 (high-temperature K-Fe) alteration containing biotite may also be rich in cobalt and arsenic (Ernest Henry, Cloncurry), whereas Facies 3 alteration in which K-feldspar prevails over biotite is associated with precipitation of Ag, Au, Bi, Cu, Mo, REE, ± U and locally Ni. Facies 4 (K-felsite) alteration is either barren or locally enriched in thorium. Alternatively, in carbonate units and carbonate-altered units, zones of K-skarn may form and host polymetallic mineralization. Facies 5 (low-temperature K-Fe to Ca-Mg-Fe) alteration is associated with the formation of mineralized zones containing variable proportions of Ag, Au, Cd, Cu, Mo, Pb, REE, U and Zn. The sequence of alteration facies records the pathways followed by metals during deposit formation within the system. The resulting footprints provide mappable criteria in outcrop and drill core for mineral potential assessments and facilitate vectoring to IOCG and affiliated mineralization, including variants enriched in critical metals.

## Résumé

Les systèmes régionaux à altération alcali-calcique et à oxydes de fer génèrent une grande diversité de types de gîtes, incluant à oxydes de fer-apatite (IOA), oxydes de fer cuivre-or (IOCG), oxydes de fer Co/Bi/ETR/U, skarn et U et Au-Co± U au sein d'albitite. La zone magmatique du Grand lac de l'Ours (Canada), le district de Cloncurry et la province Cuivre-Or d'Olympic (Australie) illustrent l'empreinte lithogéochimique de ces systèmes minéralisateurs. En reportant leurs métaux sur un diagramme discriminant des faciès d'altération alcali-calcique et à oxydes de fer (diagramme AIOCG), on y observe un couplage du V, Sc, Ni, ± Pb, ± Zn avec Ca+Fe lorsque le Faciès d'altération1 évolue au Faciès d'altération 2, et la minéralisation à IOA. Dans des séquences sédimentaires, la transition vers le Facies 3 consiste en un Facies d'altération

2–3 à Ca-K-Fe à haute température marqué par un enrichissement en cobalt et en or, un début de précipitation du cuivre. À l'atteinte des pôles plus riches en fer, un enrichissement en As, Bi et W donne lieu aux gîtes à Au-Co-Bi ±Cu (p. ex. gîte de NICO, Province de l'Ours). Le Faciès d'altération 3 (K-Fe à haute température) riche en biotite peut être enrichi en cobalt et arsenic (p. ex. Ernest Henry, Cloncurry) alors que le Faciès 3 avec feldspath potassique est marqué par la précipitation d'Ag, Bi, Cu, Mo, ETR, ±U, ± Ni. Le Faciès 4 inclue des brèches de felsite potassique largement stérile ou localement enrichie en thorium ou, au sein de séquences carbonatées, du skarn potassique à minéralisation polymétallique. Le Faciès d'altération 5 (K-Fe à Ca-Mg-Fe à basse température) est associé à des enrichissements en Ag, Au, Bi, Cd, Cu, ETR, Mo, Pb, U et Zn. La séquence de faciès d'altération enregistre le parcours des métaux vers les gîtes alors que leurs empreintes lithogéochimiques fournissent des critères cartographiables pour l'évaluation du potentiel minéral et facilitent l'élaboration de stratégies d'exploration pour la vectorisation vers les gîtes IOCG et affiliés, y compris de nombreuses variantes enrichies en métaux critiques.

## Introduction

Metasomatic iron oxide and alkali-calcic alteration (IOAA) systems generate iron oxide-apatite (IOA), iron oxide copper-gold (IOCG), and a vast array of critical metal deposits (Fig. 1; Williams, 2010; Corriveau et al., 2016, 2022a–d; Hofstra et al., 2021). This Part 2 of three contributions documents the geochemical footprints of alteration facies and mineralization types formed through the ascent, infiltration and physicochemical evolution of voluminous, super-heated, saline to hypersaline fluid plumes through the upper crust. Case studies include those described in Part 1 (mineral systems from the Great Bear magmatic zone, Canada and the Ernest Henry and Olympic Dam deposits, Australia; Corriveau et al., 2022c) with additional information from the Punt Hill deposit in the Olympic Copper-Gold Province (Australia), and various deposits of the Kwyjibo (Canada), Southeast Missouri (USA), Romanet Horst (Canada), Wanapitei (Canada) and Middle-Lower Yangtze River Metallogenic Belt districts (China; Fig. 1).

Part 1 case studies illustrate the geological footprints and space-time relationships amongst the consecutive alteration facies formed in metasomatic IOAA systems (Corriveau et al. (2022c). Part 3 (Corriveau et al., 2022b) summarizes the field relationships of each alteration facies documented in Part 1, describes the associated mineralization, and links both with the metal associations documented in this paper. Together, Parts 1 to 3 link deposit types formed through the consecutive fluid plume discharge and recharge of metals as IOAA systems evolve towards surface. Thirty of the fifty-one metals listed as critical by the Canadian, United States, European, Japan and Australian governments are economic and potential commodities in IOAA systems (Al, Ag, Au, As, Ba, Bi, Co, Cu, F, Mo, Nb, Ni, PGE (Pd, Pt), Rb, Re, REE (LREE, HREE and Y), Sb, Sc, Sn, Sr, Ta, Te, U, V, W, Zn and Zr in addition to non critical Fe and Cd (lists in Fortier et al., 2019; Austrade, 2020; Emsbo et al., 2021; Natural Resources Canada, 2021).

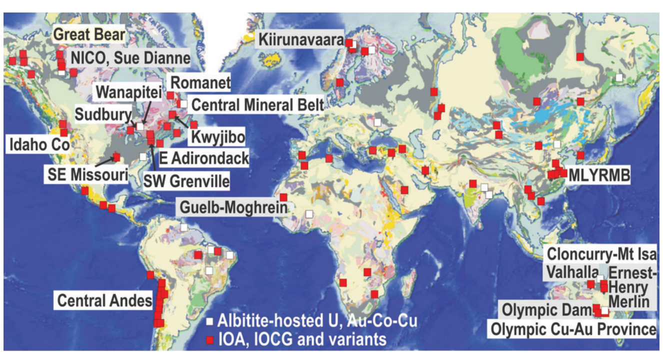


**Figure 1.** Location of case studies, deposits and districts cited in text (a larger and more detailed figure is available in Corriveau et al., 2022d). The Curnamona Province lies to the east of the Olympic Copper-Gold Province in the Gawler Craton. Deposits in the Mount Isa Province and Cloncurry district are shown in Figure 3 of Part 1 (Corriveau et al., 2022c). The Wanapitei district includes the Scadding Au-(Co-Cu-Ni) deposit (Schandl and Gorton, 2007; Corriveau et al., 2022b, c). MLYRMB: Middle-Lower Yangtze River Metallogenic Belt. A description of these deposits can be found in Porter GeoConsultancy (2021).

## Principles, Geochemical Tools and Data

*Alteration Facies*

Following Corriveau et al. (2016, 2022a) and Parts 1 and 3 (Corriveau et al., 2022b, c), metasomatic mineral assemblages and compositional modifications to host rocks in IOAA systems are grouped into six distinct alteration facies (Table 1). Each facies is defined by a specific suite of stable mineral assemblages whose precipitation controls the whole-rock compositions of the metasomatites. The spatial and temporal relationships amongst the consecutive alteration facies reflect the evolution of physicochemical conditions of fluid-rock reactions across the system (e.g. changes in temperature, composition, eH and pH of the fluid plume). Following the field-based timeline of facies and their high-temperature (HT) to low temperature (LT) conditions of crystallization, Facies 1 is 'Na' alteration, Facies 2 is 'HT Ca-Fe' alteration, Facies 3 is 'HT K-Fe' alteration, Facies 4 is 'K-felsite' and/or 'K-skarn' alteration, and Facies 5 is 'LT K-Fe' and/or 'LT Ca-Mg-Fe' alteration (with Si, Ba, $CO_2$ and F-rich variants). Facies 6 (not detailed in table 1)combines epithermal systems, silicification and carbonate alteration, and later vein systems. Transitional Facies 1–2 comprises HT Na-Ca-Fe and skarn alteration, and Facies 2–3 consists of HT Ca-K-Fe alteration.

The temperature ranges for each alteration facies are empirically established using their stable mineral assemblages (supported by global fluid inclusion studies; see Corriveau et al., 2016, 2022b). 'Low-temperature' is used to refer to mineral assemblages that formed below 375°C, whereas 'high-temperature' refers to mineral assemblages that formed above 375°C. Sericite is used as a general term for fine-grained

**Table 1.** Main alteration facies (i.e. 1 to 5) and examples from districts discussed in text. Deposits and districts are located in Figure 1.

| Facies | | Minerals | | | | Elements added or relatively enriched | | | Elements removed | Examples |
|---|---|---|---|---|---|---|---|---|---|---|
| | | Major | Accessory to major | Accessory to traces | Ore Mineralogy | Resource/ reserve | Economic potential | Others | | |
| Facies 5 | LT Ca-Mg-$Fe^{2+}$ | Chl, Mag | Ab, Amp (Mns, Stp), Ank, Fe-Dol | Ap, Bas, Gad, Mnz, Rt, Syn | Ccp, Native Au, Po, Py | Au, Cu | Bi, Co, U | Fe, LREE, Na, Ni | | Wanapitei (Scadding) |
| | LT Ca-Mg-$Fe^{3+}$ | Act, Adr, Aln, Chl, Ep, Hem, Hst | Ank, Brt, Cal, Kfs, Ms | Fl, Mnz | Brn, Ccp, Cct, Gn, Py, Sp | Ag, Au, Cu, Pb, U, Zn | LREE | Ba, F, Fe, S, K, Mn, Sb, Sn, Sr, Te, W | | Gawler (Hillside, Punt Hill) |
| | LT Fe-Si | Hem, Qz | Aln, Ank, Brt, Cal, Fl, Sid | Mnz, Ms | Ccp, Native Au, Py | Au, Cu, Fe | LREE, U | Ba, Fe, Si | | Gawler (Olympic Dam, Prominent Hill), GBMZ (East Hottah) |
| | LT K-Fe | Chl, Hem, Ms, Sd | Aln, Ank, Brt, Cal, Dol, Ep, Fl, Kfs, Qz | See Ehrig et al., 2012 | Brn, Ccp, Cct, Hem, Native Au, LREE minerals, Py, Urn | Ag, Au, Cu, Fe, U | Co, LREE, Mo, Pb, Re, W, Zn | As, Ba, C, Cd, F, K, Mn, P, S, Sb, Se, Sn, Te, W | Most where intense | Gawler (Olympic Dam, Prominent Hill), GBMZ (Sue Dianne, K2) |
| Facies 4 | K-skarn | Aln, Cpx (Adr-Grs), Ep, Kfs | Ank, Cal, Dol, Mag | Ap, Rt, Ttn | Ccp, Gn, Mol, Py, Sp | None | Cu, Mo, Pb, Zn | K, Th, U | | Gawler (Hillside, Punt Hill), GBMZ (Mile) |
| | K felsite | Kfs | | Brt, Hem, Mag | | None | None | Ba, K, Rb, Th | Ca, Fe, Mg, Na, Sr | Cloncurry (Ernest Henry), GBMZ |
| Facies 3 | HT K-Fe (Kfs) | Kfs, Mag | Bt, Cal, Chl | Aln, Ap, Fl, Ilm, Ttn, Zrn | Ccp, Mol, Native Au, Py, Urn | Ag, Au, Cu, Fe, U | Mo | Ba, C, F, K, Rb, Mn, P, REE, Sb, Te, Th, V, Zr | Ca, Mg, Na, Sr | Cloncurry (Ernest Henry), GBMZ (Fab, Southern Breccia, Sue Dianne, Summit Peak) |
| | HT K-Fe (Bt) | Bt, Mag | Amp (Gru, Hbl), Grt, Kfs | Aln, Ilm, Mnz, Xtm | Brn, Ccp, Native Au, Urn, Po, Py | Ag, Au, Co, Cu, Fe, U | Mo, Pd, Pt | Ba, C, F, K, Rb, Mn, P, REE, Sb, Te, Th, V, Zr | Ca, Mg, Na, Sr | Cloncurry (Ernest Henry) |
| Facies 2–3 | HT Ca-K-Fe | Amp (Act, Hbl), Bt, Kfs, Mag | Ap, Cpx (Aug-Hd), Grt, Sid | Fl, Qz, Thr, Ttn, Zrn | Apy, Bism, Car, Co-Apy, Ccp, Co-Loe, Co-Py, Cob, Gers, Lin, Po, Py, Saf, Sch, Sieg, Sku, Sma, Urn | Au, Bi, Co, Cu | Ag, As, Mo, Ni, Sb, Se, Te, W | Ba, Ca, K, P, Rb, REE, S, Th, U, Y | Mg, Na, Sr | GBMZ (Cole, NICO, Port Radium) |
| Facies 2 | HT Ca-Fe | Amp (Act, Cum, Hbl), Mag | Aln, Ap, Cpx (Dp-Hd, Aug), Ep, Qz | Bas, Cal, Ttn, Thr, Zrn | Mag, Po, Pn, REE minerals (e.g. Adr, Ap, Bas, Bri, Fl, Gad, Kai, Kei, Mnz, Syn), Sch | Fe, REE, P | Co, Ni, V, W | Ca, Mg, P, Th, U | K, Mg, Rb, Sr | GBMZ (Mag Hill, K2, Port Radium, Terra, Ham, JLD, Duke, Peanut Lake, NICO), Olympic Dam, Kwyjibo (Josette), SE Missouri (Pea Ridge) |
| Facies 1–2 | Fe-skarn | Cpx (Dp-Hd), Grt (Adr-Grs), Mag | Amp (Hbl, Tr), Qz | Ap, Ttn | Mag, Sch | Fe, W | REE, Co, Ni, V | P, Th, U | C, Ca or Mg, Sr | GBMZ (Duke, Hump, NICO) |
| | Skarn | Cpx (Aug, Dp-Hd), Grt (Adr-Grs, Alm) | Aln, Amp (Hbl, Tr), Cal, Chl, Dol, Mag, Phl | Ap, Ttn | Sch | | W | Fe | C | GBMZ (Duke, Hump, NICO) |
| | HT Na-Ca-Fe | Ab, Amp (Act, Hbl), Mag | Ap, Cpx (Aug) | Fl, Mnz, Ttn, Zrn | | None | Fe, REE, V | Na, Ca, P, Th | Metals, most elements | GBMZ (Mag Hill, DeVries) |
| Facies 1 | Na and Na-Ca | Ab, Scp (residual Qz) | Amp (Act, Hbl), Cpx (Aug) Mag | Rt, Ttn, Zrn | None | None | None | Al, Ga, Na, Nb, Ta, Ti, Zr | Metals, most elements | GBMZ, Cloncurry |

Mineral abbreviations from Whitney and Evans (2010) when available. Bas: bastnaesite [(Ce,La)$CO_3$(OH,F)]; Bism: bismuthinite ($Bi_2S_3$); Bri: britholite [$(Ce,Ca)_5(SiO_4)_3OH$]; Car: carrollite ($CuCo_2S_4$); Cob: cobaltite (CoAsS); Co-Apy: cobaltian arsenopyrite [(Fe,Co)AsS]; Gad: gadolinite ($Y_2Fe^{2+}Be_2Si_2O_{10}$); Gers: gersdorffite (NiAsS); Kai: kainosite [$Ca_2$(Y,Ce) $SiO_4O_{12}(CO_3)(H_2O)$]; Kei: keilhauite [(Ca,Ti)($Al_2$,$Fe_2$,$Y_2$)$SiO_5$]; Loe: loellingite [(Fe,Co)AsS]; Lin: linnaeite ($Co^{2+}Co^{3+}2S_4$); Saf: safflorite ($CoAs_2$); Sieg: siegenite [$(Ni,Co)_3S_4$]; Sku: skutterudite ($CoAs_3$); Sma: smaltite [$(Co,Fe,Ni)As_2$]; Syn: synchysite [Ca(Ce,La) $(CO_3)_2F$]. Pyrite is commonly cobalt-bearing in the HT Ca-K-Fe alteration facies. REE-bearing minerals in HT Ca-Fe assemblages may result from in situ remobilization.

phyllosilicates of the paragonite-muscovite-celadonite series, which are present in variable quantities in alteration zones formed at Facies 5. This follows an approach taken by Ehrig et al. (2012) for the fine-grained muscovite, illite, phengite and paragonite assemblages at the Olympic Dam deposit.

*Sample Selection and Geochemical Data*

Geochemical data processing methods follow Montreuil et al. (2013) and Blein et al. (2022) and use large geochemical datasets from the Great Bear magmatic zone (GBMZ) (Corriveau et al., 2015) and Olympic Copper-Gold Province, including the Olympic Dam deposit (Appendix 1; Ehrig et al., 2012, 2017a, b; Dmitrijeva et al., 2019; South Australian Resources Information Gateway; BHP-Olympic Dam, unpub. data, 2018). Additional datasets include those of the Southeast Missouri IOA and IOCG district (USA) and the Canadian Kwyjibo IOA and IOCG district of the Grenville Province, which hosts the Josette IOA-REE deposit (Fig. 1; Appendix 2; Magrina et al., 2005; Perreault and Artinian, 2013; Day et al., 2016a, b). Geochemical sampling and analytical methods are provided in the references cited for each case study above.

Intensely altered metasomatites representative of the distinct alteration facies and their least-altered protoliths were preferentially sampled to populate the GBMZ geochemical dataset (Corriveau et al., 2015). Moderately altered rocks, overprints of multiple facies and mixtures of veins and hosts were avoided in collecting samples for geochemical analysis. These samples consists of rock chips from the most homogeneous outcrop components of metasomatites (sampled by hammer or rock saw) bagged after removing veins, fracture haloes, less altered components and other impurities. Breccias were also analyzed where field relationships to other alteration types demonstrated the coeval nature of pervasive clast alteration, precipitation of matrix material, and associated mineralized veinlets with respect to the sequence of alteration facies. Exceptions are samples from mineralization zones hosted by albitite breccia in which alteration of host albitite clasts was in some cases limited and the sample composition reflects that of both host rock and overprints. Veins commonly contain metals remobilized from pre-existing alteration facies or mineralization, and were avoided unless shown to be coeval with the replacement-type alteration. In contrast to samples selected for geochemistry, hand samples were selected to best reveal crosscutting relationships amongst metasomatites, intrusive rocks and protoliths. The detailed description of sampling protocols for Great Bear metasomatic rocks, guidelines on how to handle overprints, veining, breccia, sample submission size versus grain size, and the analytical methods used and tested (e.g. best versus problematical methods for minerals resistive to dissolution) are provided in Corriveau et al. (2015).

The metal associations for each alteration facies are derived from the composition of GBMZ metasomatites rather than subsequent vein material. Samples from the global datasets provide geochemical trends that reinforce and complement the trends defined by GBMZ data.

*Identification and Visualization Tools for Alteration Facies*

The composition of alteration facies characteristic of an IOAA system and their chemical evolution can be visualized using a molar barcode system and the AIOCG diagram of Montreuil et al. (2013) (Fig. 2; Montreuil et al., 2015, 2016b; Corriveau et al., 2016, 2017; Blein et al., 2022). The barcodes consist of the molar proportions of index cations for the six alteration facies. The weight percent oxides from whole-rock geochemical analyses are divided by atomic mass of the oxide and multiplied by the number of cations in the oxide to calculate the molar proportion of each cation. Through time, optimization of barcodes to fingerprint alteration facies has led to two main type of barcodes: Na-Ca-Fe-K-Mg barcodes that optimize the fingerprinting of alteration facies and their overprints and Na-Ca-Fe-K-([Si+Al]/10) barcodes that optimize the distinction between IOAA systems and systems with other deposit types as well as between IOAA and quartz and carbonate veins (see discussions in the section *Comparison of IOAA Systems with Other Types of Systems*).

The compositions of least-altered sedimentary and igneous rocks are typically represented by three to four dominant cations, whereas intensely altered rocks are dominated by one, two, and occasionally three cations because of the restricted number of mineral phases they contain and the typically high volume-percent of one or two dominant metasomatic minerals (Fig. 2). Exceptions exist. Rhyolite has two dominant cations (potassium and sodium) in the Na-Ca-Fe-K-Mg barcodes. Potassic-alkaline syenite may have barcodes somewhat similar to biotite-rich HT K-Fe alteration facies (e.g. Kensington-Skootamatta syenite of the southwest Grenville Province in Figure A3; Appendix 3; Corriveau et al., 1990; Corriveau, 2013). Trondhjemite shares the sodium-dominant barcodes of albitite but remains distinct because of its diagnostic higher proportions of calcium and potassium (Fig. 2).

The AIOCG discriminant boxplot of Montreuil et al. (2013), which was developed using geochemical data from the most intense alteration zones of the GBMZ, is based on two alteration indices (Fig. 3). The $K/(K+Na+0.5Ca)_{molar}$ index along the y-axis discriminates Na from K alteration and is a variant of the Madeisky (1996) index. The $(2Ca+5Fe+2Mn)/(2Ca+5Fe+2Mn+Mg+Si)_{molar}$ index along the x-axis discriminates alkali (Na-K) alteration from Ca-Fe, K-Fe and Fe alteration. The combination of barcodes and the AIOCG diagram provides an effective, visual first-order tool to classify alteration facies and interpret the evolution of IOAA systems (this work; Blein et al., 2022). The distinct molar proportions of the major cations for each alteration facies compared to common sedimentary, volcanic and plutonic rocks allow an assessment to be made of the alteration facies present, and a determination of whether systems are evolving simply (i.e. prograding linearly), or if they have cyclical or disrupted evolutionary paths, as discussed in the metasomatic path section of Part 3 (Corriveau et al., 2022b; Figs. 2, 3A–D; see also Corriveau et al., 2016, 2018a, b, 2020; Blein et al., 2022).

Least-altered mafic to felsic igneous and siliciclastic sedimentary rocks, such as those of the GBMZ, fall within a very restricted field in the AIOCG diagram (Fig. 3A). Shoshonitic to ultrapotassic suites plot in the upper part of the least-altered field; some samples also trend towards the K-Fe, Ca-K-Fe and Ca-Fe fields (Fig. A3; Appendix 3). Trondhjemite plots within the Na field (Blein et al., 2022). Melanocratic mafic rocks and ultramafic rocks may plot in the Na-Ca-Fe fields, and sedimentary banded iron formations may plot in the Fe-rich Ca-Fe or Ca-Fe fields, depending on the $(Fe/Si)_{molar}$ ratios of the rocks (Blein et al., 2022).

Facies 1 to 4 (Na, HT Na-Ca-Fe, HT Ca-Fe, HT Ca-K-Fe, HT K-Fe and HT K) metasomatites are well represented by the GBMZ datasets and fill their respective fields of the diagram (Fig. 3B–E). Samples of Facies 5 LT K-Fe to LT Ca-Mg-Fe alteration are scarce, and overlap with the HT Ca-Fe,

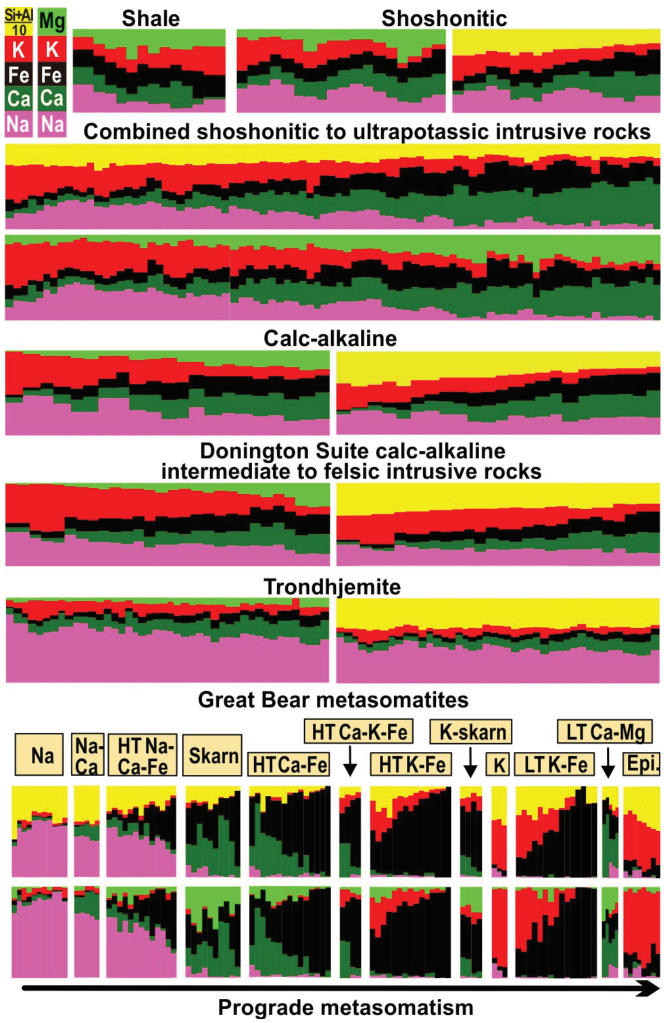


**FIGURE 2**. Molar barcodes displaying whole-rock compositions of IOAA systems contrasted with those of common sedimentary and igneous rocks, and atypical intrusive rocks such as trondhjemite from tonalite-trondhjemite and granodiorite suites, and felsic to ultramafic intrusive rocks of the shoshonitic to potassic-alkaline and ultrapotassic rocks of the Kensington-Skootamatta intrusive suite (Gromet et al., 1984; Corriveau, 1989; GEOROC database at http://georoc.mpch-mainz.gwdg.de). Barcodes are grouped to represent the variation seen in each facies and rock-type.

HT Ca-K-Fe and HT K-Fe fields (Fig. 3F, G). Within each field, barcodes of high-temperature and low-temperature alteration may or may not be similar, but the overall barcode trends defined by a suite of samples help to assess alteration intensity and types, as illustrated in Figure 3D (see intensity ranges in Corriveau et al., 2022a). Working hypotheses must be validated by field and drill core observations.

Compositional differences related to late-stage alteration, host rock types and facies variants require further discrimination (e.g. plotting $CO_2$ contents). Carbonates and altered rocks rich in calcite plot along the transition from the Na-Ca-Fe to Ca-Fe fields (Fig. 3G). Dolomite-rich rocks fall closer to the Na field, and siderite falls within the Fe-rich HT Ca-Fe alteration field. Analyses of mineralized drill core samples that are rich in late-stage carbonate alteration or veins unrelated to the primary alteration facies must be removed from datasets to better link mineralization types with alteration facies. Where carbonates are part of the alteration facies, patterns of mineralized rocks on the AIOCG diagram will not change dramatically from the overall pattern by removing samples with high $CO_2$ contents, as displayed in Appendix 4 (Fig. A4).

Trends of increasing alteration intensity or overprinting transect multiple fields (Fig. 3G). As alteration increases in intensity from weak to strong, sample plots migrate from the least-altered field to the field defined by a given alteration facies; in the process, some metasomatites may plot in an 'incorrect' facies field (Fig. 3D, G). Mixed facies compositions arise where an earlier alteration facies is significantly overprinted by a later alteration facies (e.g. albitite replaced by HT K-Fe alteration in Figure 3D). Such samples may also plot in an incorrect facies field or within the least-altered field of the AIOCG diagram (Fig. 3G).

Barcodes help identify increasing alteration intensity (as the proportions of one or two cations gradually increase with respect to the others) as well as overprints (e.g. atypical Na-Ca-Fe-K-Mg barcodes). For example, albitization that replaces all primary minerals results in decreasing Ca-K-Fe-Mg proportions and increasing sodium proportions in the barcodes. An iron and sodium-dominant barcode cannot reflect albitization of a common rock type, as albitization destroys magnetite, resulting in iron-poor and sodium-dominant barcodes. In contrast, increasing magnetite-biotite or K-feldspar-magnetite HT K-Fe alteration of albitite produces sodium and iron-dominant barcodes, as illustrated by the lower-right and upper-left white dashed lines in Figure 3D (samples from the Southern Breccia albitite corridor, GBMZ, Canada; Montreuil et al., 2015; Potter et al., 2019; Corriveau et al., 2022b). For these samples, an interpretation involving LT Ca-Mg-Fe alteration (e.g. chlorite or carbonate alteration) can be discarded as it would result in high proportions of iron and magnesium in the sodium-dominant barcodes of the albitite. An amphibole-bearing alteration is also less likely because of the lack of calcium in the barcodes, and can be conclusively discarded by field observation of alteration assemblages. Hematite alteration is a possible means of increasing the iron proportion, but hematite-bearing breccia is

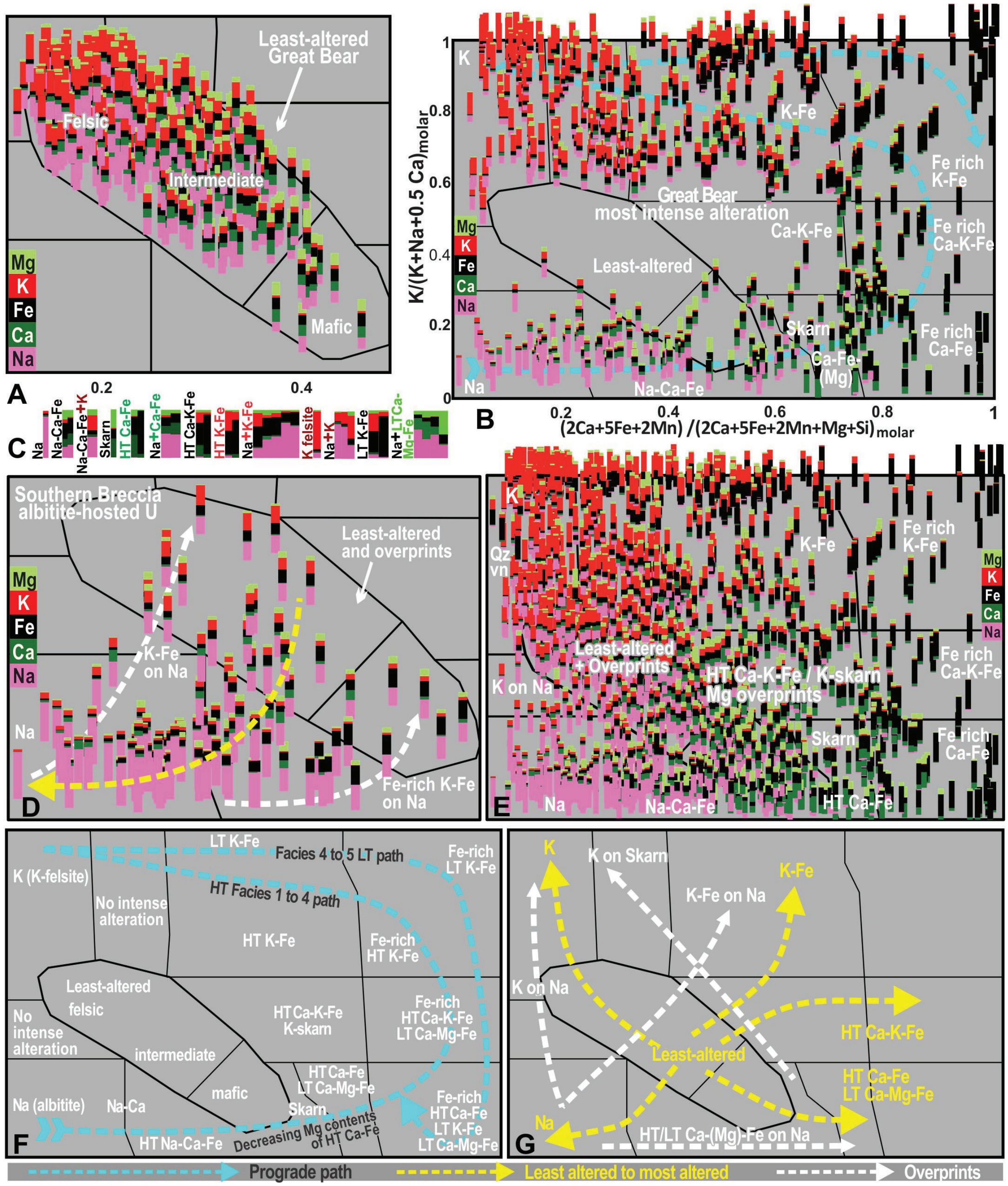


**FIGURE 3.** Lithogeochemical footprints of least-altered rocks, metasomatites and mineralized samples from IOAA systems of the GBMZ illustrated by plotting Na-Ca-Fe-K-Mg barcodes on the AIOCG diagram of Montreuil et al. (2013). Diagram axes and least-altered field in A and D are defined in B, and key examples of barcodes for each alteration facies are shown in C and Figure 2. **A.** Distribution of least-altered mafic to felsic and siliciclastic sedimentary rocks. **B.** Distribution of metasomatites with the most intense alteration, defining the prograde metasomatic path (blue arrow); each alteration facies is labelled in white. **C.** Examples of barcodes for albitite overprinted by HT Ca-Fe, HT or LT K-Fe, K and LT Ca-Mg-Fe alteration facies, compared with representative barcodes for each facies and of K-altered Na-Ca-Fe metasomatites. Colour changes to text are simply to highlight a facies and their overprints. Most of these overprints are observed in D. **D.** Lithogeochemical trends of increasing albitization from least-altered hosts to albitite (Na-dominant barcodes, yellow path) and of increasing K-feldspar dominant and magnetite-dominant K-Fe alteration of albitite (white paths). **E.** Compilation of rock samples from the GBMZ IOAA systems, including least altered to intensely altered samples. **F.** Trend of prograde metasomatism (blue path) and types of alteration observed in each field from high-temperature to lower-temperature alteration facies. **G.** Examples of trends defined by the progression of alteration from least altered to most altered rocks for a variety of facies (yellow paths), and from least-overprinted alteration facies to intense overprinting by a distinct alteration facies (white paths). Combinations of these multiple paths control the distribution of samples in E. Qz vn: Quartz veins.

rare in this case study. Where potassic alteration of albitite is moderate to intense, Na-Ca-Fe-K-Mg barcodes may be similar to those of rhyolite and shoshonitic syenite. It may also result in proportions of sodium and potassium that are similar to those of a trondhjemite if the overprint is weak to moderate, but the proportions of calcium in trondhjemite are significantly greater. These examples illustrate that plotting chemical data from metasomatized rocks on the AIOCG diagram to derive alteration facies without reference to barcodes may lead to misinterpretation. The processes described also explain why complete coverage of the AIOCG diagram with data points is common when plotting large lithogeochemical datasets from a geological province in which all IOAA facies and the intensity of alteration varies (Fig. 3E).

## Great Bear Magmatic Zone, Canada

The Great Bear magmatic zone (GBMZ) is currently the best documented IOAA district in Canada, with a large variety of alteration facies and mineralization types exposed at surface (Corriveau et al., 2022c). The belt includes IOA (± REE), IOCG, Co-Au-Bi IOCG variants, Pb-Zn skarn, polymetallic K-skarn, albitite-hosted uranium mineralization, and polymetallic mineralization associated with phyllic and epithermal-type alteration and veins (Mumin et al., 2010; Corriveau et al., 2016; Montreuil et al., 2016a–c). Two deposits are known, the NICO iron oxide-rich Au-Co-Bi-Cu deposit, overprinted and overlain by magnetite-to-hematite-group IOCG mineralization, and the Cu-Au-Ag Sue Dianne magnetite-to-hematite-group IOCG deposit (Fig. 4; Appendix 2; Corriveau et al., 2022b, c).

### *Geological Context of Great Bear IOAA Systems*

The GBMZ developed within a postcollisional Andean-type continental arc along the Archean Slave craton of the northern Canadian Shield (Figs. 1, 4A). Great Bear arc magmatism started in the latter stages of the 1.88 Ga Calderian orogeny, which metamorphosed the 1.88 Ga sedimentary rocks of the Treasure Lake Group overlying the Hottah terrane (Bennett and Rivers, 2006). Early calc-alkaline to shoshonitic magmatism (1878 to 1869 Ma) was responsible for the formation of a series of volcanic centres and sub-volcanic intrusions associated with local siliciclastic and carbonate sedimentary rocks (i.e. the 1.87 Ga supracrustal rocks of Fig. 4A; Hildebrand et al., 1987, 2010; Gandhi et al., 2001; Mumin et al., 2010; Bowdidge et al., 2014; Bowdidge and Dunford, 2015; Ootes et al., 2015, 2017; Montreuil et al., 2016a–c). The volcanic centres are extensively metasomatized and mineralized (Hildebrand, 1986; Mumin et al., 2007, 2010; Corriveau et al., 2010a, b, 2016, 2022c).

The metasomatic IOAA systems of the GBMZ formed in a very narrow time interval (largely between 1875–1866 Ma), although subsequent metal remobilization produced younger mineralized veins; Davis et al., 2011; Montreuil et al., 2016a, c; Gandhi et al., 2018; Trottier, 2019). After IOAA metasomatism, a voluminous ignimbritic eruption at ca. 1862 Ma formed an extensive volcaniclastic blanket over earlier volcanic and basement rocks, and multiphase granodioritic to monzonitic batholiths intruded the belt between ca. 1873 and 1855 Ma (Hildebrand et al., 1987, 2010; Hayward and Corriveau, 2014; Mumin et al., 2014; Montreuil et al., 2016a, c; Ootes et al., 2017). Subsequent 1.85 Ga A-type rapakivi granite plutons are aligned in a northwest-southeast direction, oblique to the main trend of the belt (Hayward and Corriveau, 2014; Ootes et al., 2017), and rare syenite bodies intruded at ca. 1845 Ma (Ootes et al., 2017).

The IOAA systems of the GBMZ postdate peak deformation associated with the Calderian orogeny, except along the Wopmay fault zone at the eastern boundary of the belt (Fig. 4A), where syn-GBMZ tectonic reactivation of the fault occurred. This led to variable recrystallization of IOAA systems, particularly REE-mineralized IOA mineralization (Jackson et al., 2013; Corriveau et al., 2015; De Toni, 2016). The GBMZ shares key characteristics with the Olympic Copper-Gold Province, notably the pre- to syn-metasomatic timing of early volcanism (i.e. Lower Gawler Range Volcanics), the short-lived IOAA metasomatism, and the post-IOAA voluminous ignimbrite flare-up (upper Gawler Range Volcanics) and batholith emplacement (Reid and Fabris, 2015; Jagodzinski et al., 2016; Reid et al., 2019). A suprasubduction zone environment is proposed for both the GBMZ and the Olympic Copper-Gold Province (Hildebrand et al., 2010; Montreuil et al., 2016a; Ootes et al., 2017; Tiddy and Giles, 2020).

Metal-bearing fluids in 1.87 Ga rocks have largely a magmatic signature (Somarin and Mumin, 2014; Acosta-Góngora et al., 2015). Boron isotope signatures in tourmaline stem either from a magmatic fluid or from scavenging of boron from basement igneous rocks (Kelly et al., 2020). Potential additional fluid sources include coeval saline fluids, based on 1) the presence of stromatolite-bearing carbonates in the Camsell River district that may have precipitated in an intra-caldera lake during IOAA metasomatism (Fig. 10C, D in Corriveau et al., 2022a); and 2) devolatilization of earlier evaporites, as inferred by pseudomorphic albite and amphibole replacement of textures typical of nodular anhydrites at DeVries Lake (Fig. 10A, B in Corriveau et al., 2022a). As the syn-metasomatic sub-volcanic intrusions at the root of the GBMZ IOAA systems were extensively albitized, the magmatic fluid sources are interpreted to be the underlying magma chambers, not the sub-volcanic intrusions themselves. Deeper fluid sources are also inferred based on transcrustal corridors of low reflectivity and low resistivity in the GBMZ and the Olympic Copper-Gold Province (e.g. Spratt et al., 2009; Wise and Thiel, 2020).

### *Alteration Facies in the Great Bear IOAA Systems*

The IOAA systems of the GBMZ display extensive and intense alteration of host rocks. Most of the systems feature preserved depth-to-surface profiles as a result of tectonic tilting, thrusting, normal faulting or differential uplift (Mumin et al., 2007; Hildebrand et al., 2010; Bowdidge et al., 2014; Bowdidge and Dunford, 2015; Ootes et al., 2017). Tilted profiles include the Mag Hill and Mile sections in the Port Radium-Echo Bay district (Fig. 4E, F), and the Grouard Lake and Camsell River

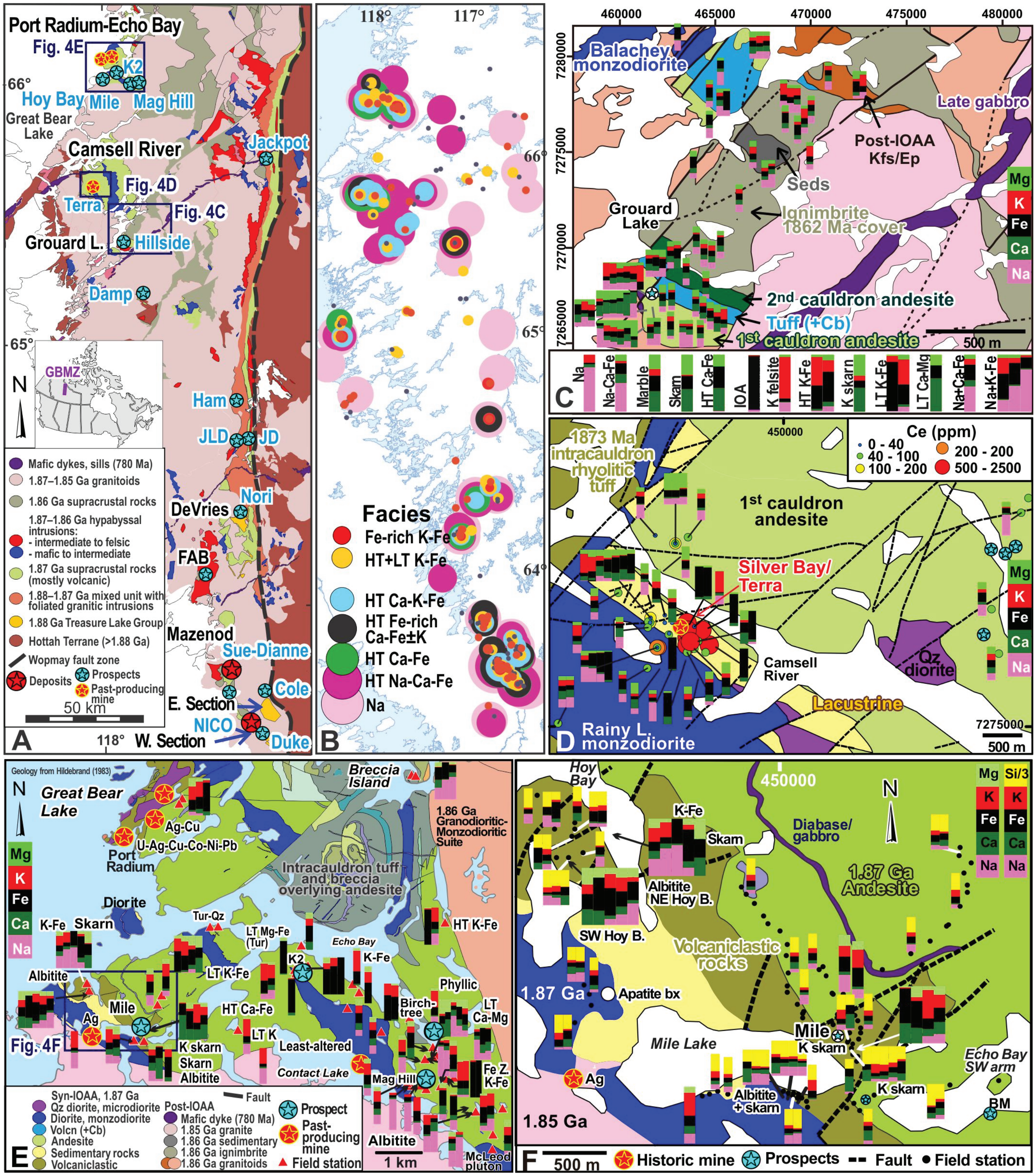


**FIGURE 4.** Synoptic geological and chemical maps of selected GBMZ IOAA systems. **A.** Geology and location of systems; inset shows the location of GBMZ exposures in Canada (modified from Corriveau et al., 2016). **B.** Distribution of alteration facies; earlier to later footprints is ranked from greater to smaller radius. **C, D.** Geology and Na-Ca-Fe-K-Mg barcodes of alteration in the Grouard Lake and Terra regions of the Camsell River district. Geological map from Hildebrand et al. (2014). High REE values (portrayed by cerium contents in D) are spatially associated to HT K-Fe alteration (potassium-iron-dominant barcodes). Representative barcodes of GBMZ systems are shown in C. Geochemical data from Corriveau et al. (2015) and DEMCo Limited (unpub. data). **E, F.** Geology and Na-Ca-Fe-K-Mg barcodes (E and F) and Na-Ca-Fe-K-Si/3 barcodes (F) of alteration in the Port Radium-Echo Bay district with details in F for the Mile Lake to Hoy Bay sector in the southwestern part of the district. Areas with skarn have barcodes dominated by Ca, Fe and Mg. In E, Fe Z = Fe Zone (Hem-Qz).

sections in the Camsell River district, which hosts the past-producing Terra vein-type silver mine (Figs. 4A, C, D, 5).

The tilted sections above sub-volcanic intrusions in the Port Radium-Echo Bay and Camsell River districts, combined with sections that expose different depth profiles across the Lou and Duke systems, record evolution of the GBMZ IOAA systems. Early alteration consists of Facies 1 Na alteration (albite; Fig. 5A), which evolves to Facies 1–2 skarn and HT Na-Ca-Fe alteration (albite-amphibole-magnetite ± apatite), then to Facies 2 HT Ca-Fe alteration (amphibole-magnetite ± apatite; Fig. 5B) and IOA mineralization, some of which carries significant REE contents. Facies 2 can transition through HT Ca-K-Fe alteration (amphibole-biotite-K-feldspar-magnetite) and Au-Co-Bi-(Cu) mineralization (Facies 2–3) within sedimentary host rocks, or else evolves directly to Facies 3 HT K-Fe alteration (magnetite-biotite-K-feldspar; Fig. 5C) in volcanic sequences associated with magnetite-group IOCG mineralization. The development of extensive zones of HT Ca-K-Fe alteration near and within the carbonate-rich units of the GBMZ illustrates a host-rock compositional control on the development of this particular alteration facies, in marked contrast to other facies in which host-rock compositions control the mineral content of alteration assemblages but not the development of the facies itself.

Facies 4 K-felsite alteration (K-feldspar; Fig. 5D), accompanied by localized zones of K-skarn alteration (skarn with K-feldspar), marks the magnetite-to-hematite transition. Facies 5 consists of LT K-Fe and LT Ca-Mg-Fe alteration and their Si, Ba, F and $CO_2$ variants. Collectively, the mineral assemblages may include K-feldspar, sericite, hematite, chlorite, carbonates, barite, and fluorite (Fig. 5E–G). Facies 6 encompasses all late-stage, low-temperature veins, breccias and replacement overprints (e.g. quartz, Fe-Mg-Mn carbonates, epidote, barite and jasper), as well as phyllic, sericitic, and argillic to advanced argillic alteration associated with the formation of gossans and epithermal lithocaps (Mumin et al., 2010).

Transitional assemblages of minerals occur between each of the main alteration facies. In the NICO deposit, and the Mile and Grouard Lake systems, within and adjacent to carbonate and carbonate-altered units, skarn (clinopyroxene-garnet) occurs in zones of albitite and represents a transitional facies between Facies 1 and 2 (Fig. 4C, E; Corriveau et al., 2022c). At the past-producing Terra mine, epidote-magnetite alteration occurs within amphibole- to magnetite-dominant HT Ca-Fe alteration zones; it is cut by magnetite veins and intensifies to IOA mineralization (Figs. 4, 5B–H in Part 3, Corriveau et al., 2022b). Facies 5 LT K-Fe alteration transitions to a LT Fe-Si facies east of Mag Hill, where it forms a hematite-rich zone with accessory quartz (Fig. 26B, E in Part 1, Corriveau et al., 2022c), and near the K2 IOCG prospect and East Hottah system, where it forms jasper and quartz-hematite-jasper veins (Fig. 27G in Part 1, Corriveau et al., 2022c). At Terra, Facies 5 alteration occurs as a LT Ca-Mg-Fe chlorite-rich chalcopyrite-bearing alteration zone that overprints K-felsite (Fig. 5G). Brecciated albitite corridors of Facies 1 Na are preferential hosts for subsequent uranium mineralization.

Typical GBMZ surface exposures have no secondary iron oxide staining associated with sulphide mineralization (Fig. 5G). Recognizing the alteration facies that commonly host mineralization, as well as typically barren alteration facies proximal to the mineralized host rocks is key to effective exploration (Corriveau et al., 2018b, 2020, 2022b).

## Ernest Henry Deposit, Cloncurry District, Australia

*Systems within Mount Isa Province*

In the Cloncurry district (eastern half of the Mount Isa Province), deposits within IOAA systems and associated metasomatic iron oxide-poor to iron-poor alkali-calcic systems

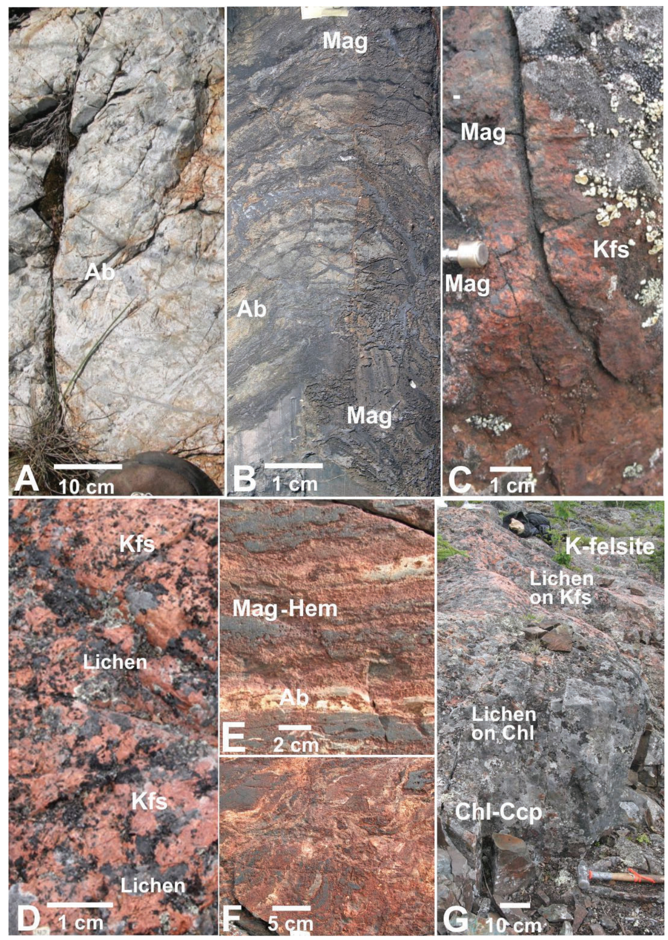


**Figure 5.** Alteration facies at Terra, GBMZ. **A.** Brecciated albitite typical of Facies 1 Na (outcrop 09CQA-0135). **B.** Stratabound magnetite alteration and stockwork replacing and cutting albitized host and recording Facies 2 HT Ca-Fe alteration (09CQA-0144). **C.** Magnetite-K-feldspar breccia in which the K-feldspar alteration of the clasts and coeval precipitation of magnetite in the matrix jointly record Facies 3 K-Fe alteration (09CQA-0142). **D.** Pervasive K-feldspar felsite breccia typical of Facies 4 K alteration (09CQA-0142). Grey is lichen. **E, F.** Stratabound K-feldspar-hematite alteration at Facies 5 LT K-Fe replacing stratabound albitization and magnetite alteration in E and transitioning to a breccia in F (09CQA-0141). **G.** Chlorite alteration with disseminated chalcopyrite, recording a Facies 5 LT Ca-Mg-Fe alteration (09CQA-0142).

range from IOCG (Ernest Henry, Monakoff) to cobalt-rich (Mt. Cobalt) or iron oxide-poor Au-Cu, Cu-Pb-Zn or Mo-Re (Mount Dore/Merlin, Lanham's Shaft) deposits (Fig. 3 in Part 1, Corriveau et al., 2022c). In the western half of the Mount Isa Province, systems are poorer in iron oxides; they host the Valhalla albitite-hosted uranium deposit and the Mary Kathleen skarn-hosted U-Th-REE deposit (Oliver et al., 1999; McGloin et al., 2013; Wilde et al., 2013). Both sectors feature corridors of albitite and a variety of polymetallic prospects (e.g. Figs. 3–5 in Part 1, Corriveau et al., 2022c). Chalcopyrite and pyrite are the most common sulphides; cobalt is positively correlated with copper and gold enrichment in IOCG ores, whereas other deposits have pyrrhotite-rich (e.g. Osborne, Eloise) or arsenopyrite-rich (Lorena) ores (Williams and Pollard, 2001). Discovery dates for deposits range from 1880–2008 for Mt Elliot-SWAN, 1990 for Ernest Henry, 2006 for Rocklands, and 2008 for Merlin (Table 2).

The cation barcodes of samples from representative deposits are shown in Figure 6, and the total resources for the deposits are reported in Table 2. The cation barcodes of selected samples from the Cloncurry district define a prograde IOAA path; six samples are numbered to highlight nuances in their geochemistry. The samples labelled 1 to 4 on Figure 6 display barcodes typical of albitite replaced by subsequent IOAA facies. The iron-rich and iron-magnesium-rich barcodes of these samples have sodium proportions typical of albitite paired with iron only or with iron and magnesium, in contrast to normal host rocks that also contain significant calcium and potassium. Samples 5 and 6 have Ca-Fe-K-Mg proportions comparable to intermediate igneous rocks and are typical of samples affected by moderate albitization.

*Overview of Ernest Henry Deposit*

The 1530 Ma Ernest Henry deposit is a structurally controlled magnetite-group IOCG deposit enriched in cobalt (average of 500 ppm Co, up to >3000 ppm), molybdenum (mean of 180 ppm Mo), uranium (mean of 50 ppm U) and arsenic (≤5000 ppm with an average of 350 ppm As) (Foster et al., 2007; Rusk et al., 2010). The deposit is hosted by a zoned, kilometre-scale alteration system that evolved from regional albitization to localized HT Ca-Fe and HT Ca-K-Fe alteration, then to HT K-Fe and LT Ca-Mg-Fe alteration facies, forming a ~ 2 x 3 km potassium-iron anomaly centred on the deposit (Corriveau et al., 2022c). Extensive zones of albitite replaced nearly all the original protolith minerals, including metamorphic scapolite (Morrissey and Tomkins, 2020), while forming albite and minor secondary scapolite in a transitional Na-Ca facies (Oliver et al., 2004). This replacement resulted in extensive metal leaching, which could have contributed to the metal endowment of the fluid plume (Oliver et al., 2008).

Two HT K-Fe alteration types are present in the Ernest Henry deposit. Early HT K-Fe alteration is rich in biotite, and contains variable magnetite and pyrite along with accessory to minor chalcopyrite. The pyrite is enriched in arsenic, cobalt, and nickel, and may have contributed to the elevated cobalt content of the deposit and to the positive correlation of arsenic, cobalt, and nickel with copper in chalcopyrite-bearing ore zones (Rusk et al., 2010). However biotite-rich HT K-Fe alteration did not significantly contribute to copper-gold mineralization.

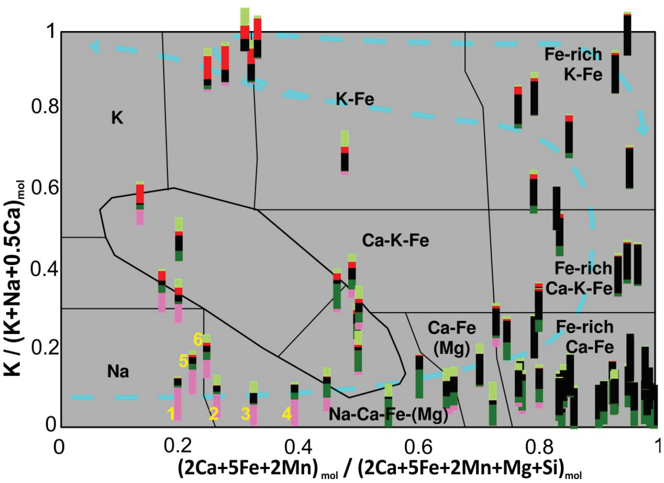


**Figure 6.** Composition of metasomatites and mineralization from the Cloncurry district plotted as Na-Ca-Fe-K-Mg barcodes on the AIOCG diagram (geochemical dataset from Patterson et al., 2016). Data points plot mainly along the prograde path of the GBMZ IOAA systems (in blue). Samples 1 to 6 are discussed in text.

**Table 2.** Total resources for selected deposits in the Mount Isa Province of Australia.

| Deposits | Resources |
|---|---|
| **Ernest Henry** | 166 Mt at 1.1 wt% Cu, 0.54 g/t Au (pre-mining resource): 87.1 Mt at 1.17 wt% Cu, 0.62 g/t Au (2020 underground resource) |
| **Mt Dore** | 111 Mt at 0.53 wt% Cu, 0.09 g/t Au, 0.06 wt% Pb, 0.31 wt% Zn |
| **Mt Elliot-SWAN** | 353.7 Mt at 0.6 wt% Cu, 0.35 g/t Au |
| **Merlin** | 6.4 Mt at 1.5 wt% Mo, 26 g/t Re |
| **Rocklands** | 55.4 Mt at 0.64 wt% Cu, 290 ppm Co, 0.15 ppm Au, 5.1 wt% Mag + 227 Mt at 16 wt% Mag |
| **Osborne** | 12 Mt at 1.4 wt% Cu, 0.88 g/t Au |
| **Monakoff** | 2.4 Mt at 0.95 wt% Cu, 0.3 g/t Au (112 ppm $U_3O_8$) |
| **E1** | 10 Mt at 0.7 wt% Cu, 0.22 g/t Au |
| **Valhalla** | 34.7 Mt at 830 ppm $U_3O_8$ |
| **Mary Kathleen, Elaine 1, Elaine-Dorothy** | 9.5 Mt at 1300 ppm $U_3O_8$ |
| | 0.83 Mt at 280 ppm $U_3O_8$, 3200 ppm TREE |
| | 26.1 Mt at 0.56 wt% Cu, 0.09 g/t Au |

Chinalco Yunnan Copper Resources (2010, 2012a, b); Chinova Resources (2014a, b, 2017); Cudeco (2017); Lilly et al. (2017); Glencore (2020); Porter Geoconsultancy (2021).

K-feldspar-dominant HT K-Fe alteration contains abundant magnetite, overprints the early biotite-rich HT K-Fe alteration, and evolves to a carbonate-magnetite alteration in turn cut by renewed biotite-rich HT K-Fe alteration (Fig. 7 in Corriveau et al., 2022c). All these alteration assemblages are closely associated with extensive brecciation and magnetite-group IOCG mineralization and described in detail in Mark et al. (2006). Copper-gold mineralization associated with K-feldspar-rich HT K-Fe alteration develops within magnetite-K-feldspar-biotite-chalcopyrite breccia, in which K-feldspar selectively altered the host-rock clasts, and biotite, magnetite (with high Mn/Ti ratios) and chalcopyrite constitute the breccia matrix.

Magnetite-carbonate alteration associated with copper-gold mineralization may represent a subtype of Facies 5 LT Ca-Mg-Fe alteration. It consists of carbonate, magnetite and chalcopyrite that replace K-feldspar-altered clasts and matrix of breccia zones within the deposit. Chalcopyrite, native gold and electrum are the main ore minerals; other minerals with economic potential include arsenian and cobaltian pyrite, rare tellurides, and accessory molybdenite, arsenopyrite, sphalerite, galena, coffinite, and cobaltite. Actinolite, garnet, apatite, fluorite, rutile, monazite, barite and quartz occur as accessory to minor minerals in the breccia zones (Figs. 7, 8 in Part 1, Corriveau et al., 2022c; Mark et al., 2000, 2006; Williams and Skirrow, 2000; Foster et al., 2007; Rusk et al., 2010). Magnetite of Facies 3 and 5 is locally and weakly replaced by hematite in ore breccias (Corriveau et al., 2022c).

The zones of magnetite-group IOCG mineralization are enriched in F, Mn, Co, As, Mo, Ba, and W (e.g. Mark et al., 2006), which may represent a suite of elements deposited at different alteration facies but were later mobilized and concentrated in the deposit.

## Olympic Copper-Gold Province, Australia

The Olympic Copper-Gold Province hosts a wide range of IOCG deposits (Olympic Dam, Prominent Hill, Oak Dam, Carrapateena, Hillside, Khamsin, Acropolis, Wirrda Well and Fremantle Doctor IOCG deposits), as well as the skarn-hosted Punt Hill deposit. The geological setting and deposit characteristics of this metallogenic province are reviewed in Skirrow (2022), whereas the geochemical attributes are characterized by Fabris (2022); an overview of the deposit with plan view and cross-section of alteration is provided in Part 1 (Corriveau et al., 2022c).

*Olympic Dam Deposit Reserves, Resources, Critical Elements*

The Olympic Dam deposit is largely hosted by the 1.59 Ga Roxby Downs granite (RDG) of the Hiltaba Suite. Mineralization is circumscribed by the fault-bounded Olympic Dam Breccia Complex (ODBC; Figs. 7, 8). Total reserves are currently of 537 Mt at 1.87 wt% Cu, 0.57 kg/t $U_3O_8$, 0.71 g/t Au and 4 g/t Ag, with a reserve life of 54 years and a metallurgical recovery of 94% for copper, 69% for $U_3O_8$, 69% for gold, and 64% for silver (BHP, 2019). Cobalt resources are at least 650 Mt at 0.02 wt% Co (Williams and Pollard, 2001; Slack et al., 2017). The deposit open-pit ore resources are estimated at 10,070 Mt at 0.62% Cu, 0.21 kg/t $U_3O_8$, 0.27 g/t Au, and 1.0 g/t Ag in addition to underground resources of 1,041 Mt at 1.68% Cu, 0.47 kg/t $U_3O_8$, 0.63 g/t Au, and 3 g/t Ag (+ ~0.3 wt% LREE, 0.01 wt% HREE) (Corriveau et al., 2018b; BHP, 2020). Recovered commodities include Cu, Au, Ag and U.

Abundances of REEs are significant in the Olympic Dam deposit (Fig. 7D) but REE recovery is not currently economic. Within the dataset used in this study, 43% of the samples have total REE > 2000 ppm, 20% are > 5000 ppm, 10% are > 7000 ppm and 2% are > 10000 ppm. Among these, the 5% richest HREE contents have 30–256 ppm Dy, 15–145 ppm Er, 53–151 ppm Gd, and 122–725 ppm Y. The HREE are strongly correlated with $P_2O_5$ contents; 5% of the analyses richest in HREE have average 0.54 wt% $P_2O_5$ (0.55% median value) in contrast to the entire dataset mean of 0.21 wt% $P_2O_5$ and median of 0.18 wt% $P_2O_5$ resulting in a 150% increase in $P_2O_5$ contents for the HREE-rich samples. There is also a 50% increase in $CO_2$ for the 5% analyses richest in HREE from the overall mean of 1.6 wt% $CO_2$ and median of 0.45 wt% to a mean of 2.51 wt% $CO_2$ and median of 0.75 wt% $CO_2$.

*Olympic Dam Deposit Geology*

In the outer rim of the ODBC, the Roxby Downs granite is increasingly brecciated and the breccia clasts sericitized and replaced by abundant hematite and siderite (Fig. 7C; Ehrig et al., 2017b; Blein et al., 2022). The geochemical signature is significantly different from its precursor as illustrated by the marked changes in barcode signatures from least-altered granite (drill core RD2495) to the sericitized and hematized granite (Fig. 8; Ehrig et al., 2012).

The intermediate zone of the ODBC is the most mineralized. Sericite-hematite alteration variably preserves earlier K-feldspar whereas the fluorite to siderite ratio tends to increase inward and upward (Fig. 7; Fig. 13 in Part 1, Corriveau et al., 2022c; Fig. 5 in Ehrig et al., 2017b). The iron oxide content sharply increases as Facies 5 alteration intensifies; the K-feldspar and sericite content decreases proportionally as they are replaced by hematite (Figs. 7A, C, 8). The core of the ODBC is composed of a hematite-quartz-barite (HEMQ) alteration assemblage, representing the LT Fe-Si component of Facies 5 (Figs. 7A–C, 8). The transition between the intermediate zone and the HEMQ core of the ODBC features the highest sericite content of the ODBC, variable hematite and fluorite, and abundant gold associated with bornite-chalcopyrite mineralization (Fig. 7C, D). This is illustrated by the distribution of alteration minerals and metal contents on the 350 m level plan of a mineral resource block model (Fig. 7D).

Within the ODBC, Facies 5 LT K-Fe alteration variably overprints earlier magnetite ± apatite, chlorite, quartz and siderite, as well as deeper and peripheral magnetite-apatite assemblages that are cut by calcite veins or enclosed in calcite breccia cement (Apukhtina et al., 2017; Ehrig et al., 2017b; Corriveau et al., 2022c). Pyrite that precipitated as part of a

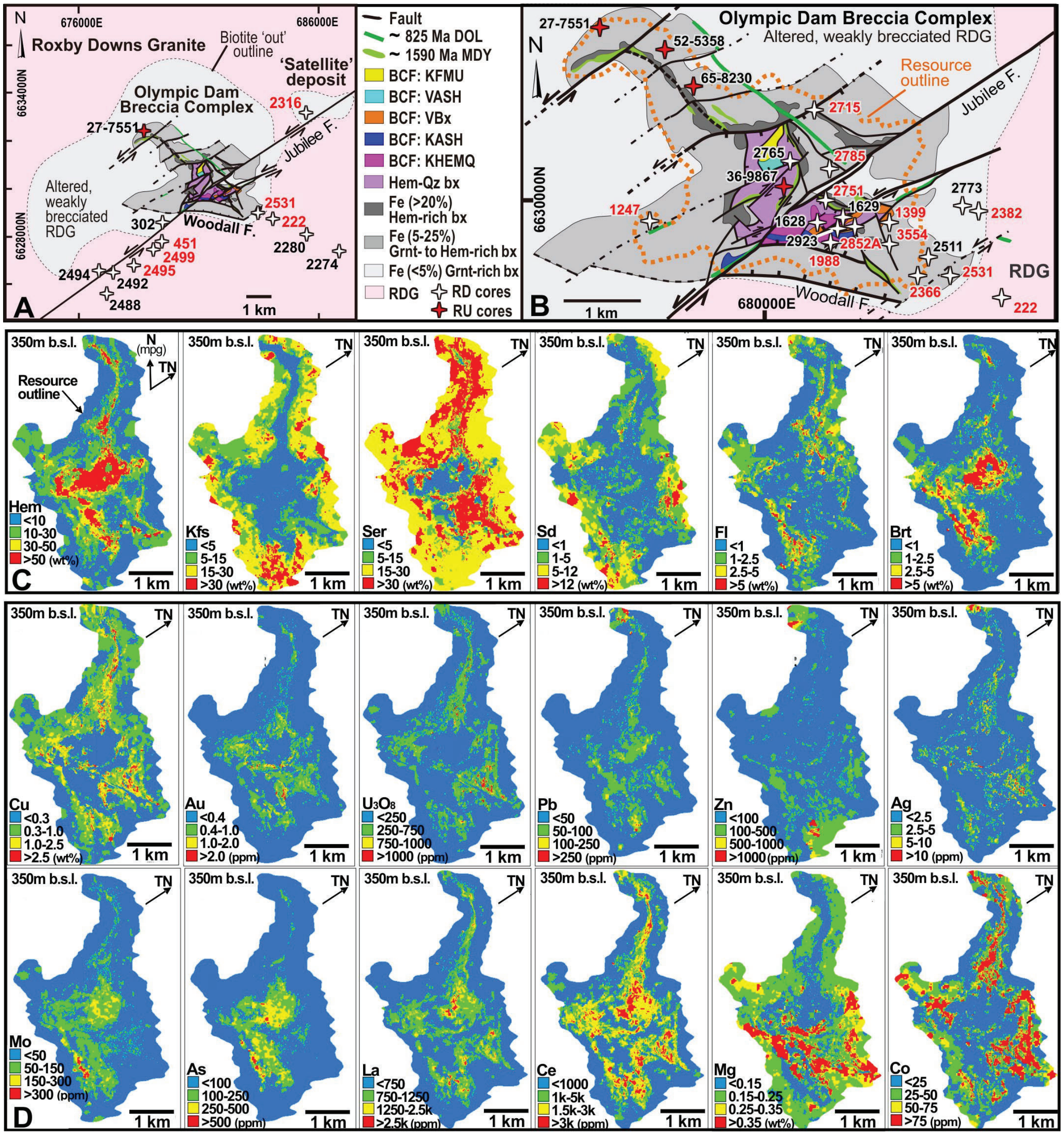


**FIGURE 7.** Alteration mineralogy and metal contents at the Olympic Dam deposit in plan view at level 350 m near the eroded paleosurface (~350–360 m below sea level). **A, B.** Simplified deposit geology map at 350 m below sea level showing the areal extent of the Olympic Dam Breccia Complex (ODBC), host lithotypes, deposit-scale structural architecture and resource outline (modified after Ehrig et al., 2012 and Clark et al., 2018). Also shown is the distribution of drill cores from the RD and RU series within and adjacent to the ODBC (Corriveau et al., 2022b). The biotite 'out' outline of the ODBC refers to the area where the igneous biotite of the host Roxby Downs Granite (RDG) is pervasively altered. A similar outline marks the limit of a satellite deposit, the characteristics of which are described in Part 1 (Corriveau et al., 2022c) and the footprint shown in Figure 8. Zoning in terms of iron contents is at the map level but iron contents vary greatly with depth, as shown by the variations in iron proportions of barcodes in Figure 8. The RDG and the Bedded Clastic Facies (BCF) with its basal interbedded hematite mudstone and quartz-rich sandstone unit (KHEMQ), polymictic volcaniclastic breccia unit with felsic and mafic clasts of Gawler Range Volcanics (VBx), interbedded chlorite-rich sandstone and mudstone rich in detrital chromite (KASH), thinly bedded, tuffaceous mudstone (VASH) and polymictic conglomerate with felsic and mafic clasts of Gawler Range Volcanics (KFMU), are intruded by mafic-ultramafic dykes (MDY). The DOL unit corresponds to the ~825 Ma Gairdner doleritic (to basaltic) dyke swarm. The extent of satellite mineralization along the regionally continuous Jubilee Fault is illustrated in A. Alteration mineralogy and whole-rock composition of the satellite deposit are comparable to the margins of the ODBC. Drill core numbers in red indicate those used in Figure 8. **C.** Distribution of key minerals in the LT K-Fe (hematite breccia in which K-feldspar is initially stable and then transitions to sericitic white mica as the dominant potassic phase), Fe-$CO_2$ (hematite ± magnetite with siderite), LT Fe ± Ca-K (hematite ± fluorite and sericite) and LT Fe-Ba (hematite breccia with barite veins) alteration facies. **D.** Distribution of metals at the same level, updated from Ehrig et al. (2012) using a 2020 deposit model (this work; BHP-Olympic Dam, unpub. data, 2018).

magnetite-siderite assemblage in an Olympic Dam satellite deposit is locally rich in As, Au, Bi, Co, Ni, Se and Te, a signature typical of the HT Ca-K-Fe assemblage of the NICO deposit in the GBMZ (Clark, J., unpub. data, 2017). Variably preserved relics of magnetite are also observed within sericite-hematite alteration to vertical depths >2 km, and proximal-to-distal to the hematite-quartz-barite core of the breccia complex (based on magnetic susceptibility data: Ehrig et al., 2012; BHP-Olympic Dam, unpub. data, 2018). Among the sulphide species, pyrite and chalcopyrite, with subsidiary zones of bornite and chalcopyrite, are preferentially associated with the muscovite-hematite assemblage, along with siderite and variable quantities of fluorite. The sulphide assemblage of bornite, chalcocite, and local chalcopyrite is constrained to the muscovite-hematite-fluorite alteration zones, which lack siderite (Ehrig et al., 2012).

In the ODBC, relics of an early sodic alteration exist at depth and along the Jubilee Fault in borehole 2316 below a satellite deposit (Fig. 7A, B; Kontonikas-Charos et al., 2017). Regionally in the Olympic Copper-Gold Province, sodic alteration is documented at the Emmie Bluff, Murdie Murdi and Titan prospects, the Oak Dam deposit, and in the Mount Woods Inlier and Moonta-Wallaroo districts (Davidson et al., 2007; Freeman and Tomkinson, 2010; Clark, 2014; Blein et al., 2022; Skirrow, 2022).

*Olympic Dam Deposit Geochemical Footprint*

On the AIOCG diagram, increasing alteration of the Roxby Downs Granite from the margins to the core of the ODBC defines a clockwise path from the least-altered field through the K, K-Fe, Ca-K-Fe and Ca-Fe alteration fields and iron-rich equivalents (Figs. 9, 10). This trend is indicated by a light blue arrow on Figure 10A. The onset of this path is marked by an increase in the proportions of K-feldspar and sericite at the expense of plagioclase, i.e. a decrease in sodium and calcium and increase in the proportions of potassium and iron in altered samples. This alteration defines a path from the least-altered field to the K-Fe field (Figs. 9A, B, 10A–C). Though some samples plot in the least-altered field, where alteration is less intense (yellow path in Figure 10A), the altered samples can be discriminated from least-altered granitoids by the lack of calcium in their barcodes (see Donington Suite samples that fall in the same area of the least-altered field but have calcium in their barcodes in Figure 10D). As alteration intensifies and the proportion of iron-rich minerals (hematite and siderite) increases, the altered samples initially migrate towards the Fe-rich K-Fe field of the diagram, and then into the Fe-rich Ca-K-Fe and Fe-rich Ca-Fe fields (Figs. 9 A–D, H–J, 10A–C). This trend illustrates increasing iron enrichment with intensifying and evolving Facies 5 alteration associated with the progressive destruction of sericite and K-feldspar by hematite, local siderite, and fluorite.

The data from borehole RD2366 suggests that intensifying magnetite-bearing alteration in the ODBC forms a compositional trend sub-parallel to hematite-bearing Facies 5 alteration on the AIOCG diagram (Fig. 9E–G; see Fig. 32 in Blein et al., 2022). The samples containing high proportions of iron in molar barcodes (Fig. 9F) are characterized by high magnetic susceptibilities compared to most of the hematite-rich altered samples in the Ehrig et al. (2012) dataset, supporting the presence of abundant magnetite. Elevated $CO_2$ (Fig. 8), Co, and S, and low Ca suggest the presence of siderite and pyrite, possibly indicating that these samples represent variably preserved relics of a magnetite-siderite-pyrite assemblage.

In boreholes sampling a hematite-fluorite assemblage, the trend defined by intensifying Facies 5 alteration shifts slightly to the left compared to the trend of intensifying Facies 5 alteration without fluorite, because of increasing Ca/Fe ratios (Fig. 9 C, D, H–J). Plotting the relationship between molar concentrations of calcium and $CO_2$ helps to determine whether fluorite or calcite is the main calcium repository in altered samples. In boreholes sampling zones with elevated calcite contents, a positive covariation exists between the molar proportions of calcium and $CO_2$ contents. Perturbations of the positive covariation between molar concentrations of calcium and fluorine in boreholes sampling zones with abundant fluorite can also indicate the presence of calcite or other calcium-bearing minerals. The relationship between the presence of some metals and the precipitation of fluorite, without interference from precipitation of carbonate, can be assessed by removing $CO_2$-rich analyses, as done in Appendix 4 (Fig. A4).

Late-stage calcite ± barite and fluorite veins and barite-siderite-fluorite veins generate barcode outliers that are not part of the main sequence of metal deposition in the deposit and have to be considered separately.

In the HEMQ core of the ODBC, samples with low-silica contents plot in the Fe-rich K-Fe to Fe-rich Ca-Fe fields; with increasing quartz content and Si/Fe ratios, the sample plot shifts to the left on the x axis of the AIOCG diagram, and may plot in the Ca-Fe-(Mg) field (e.g. borehole RD2751; Figs. 7, 9H–J, 10A, B).

The sparse relic of early albitization is observed in the few samples trending towards the sodic alteration field (Fig. 10A–C). However, albitized rocks are detected in boreholes located southeast of Olympic Dam (Fig. 10E, F), a region underlain by the Donington Suite intrusion, the least-altered composition of which is plotted in Figure 10D. The barcodes with a high proportion of sodium in Figure 10E and F can be distinguished from trondhjemite (barcodes in Fig. 10D) because of their lack of calcium, simplifying interpretation of the metasomatic signature.

Mafic and ultramafic dykes coeval with IOCG mineralization are extensively altered and brecciated, and display a wide range of metasomatic compositions on the AIOCG diagram (Fig. 10C). In contrast, sedimentary units, though altered and interpreted to be coeval (in part) with brecciation in the ODBC (Cherry et al., 2019; Clark and Ehrig, 2019), as well as the later Gairdner diabase dykes, plot in clustered groups of samples, typical of none-to-weak alteration overprints (Figs. 9H, 10A–C). The weak trend observed in

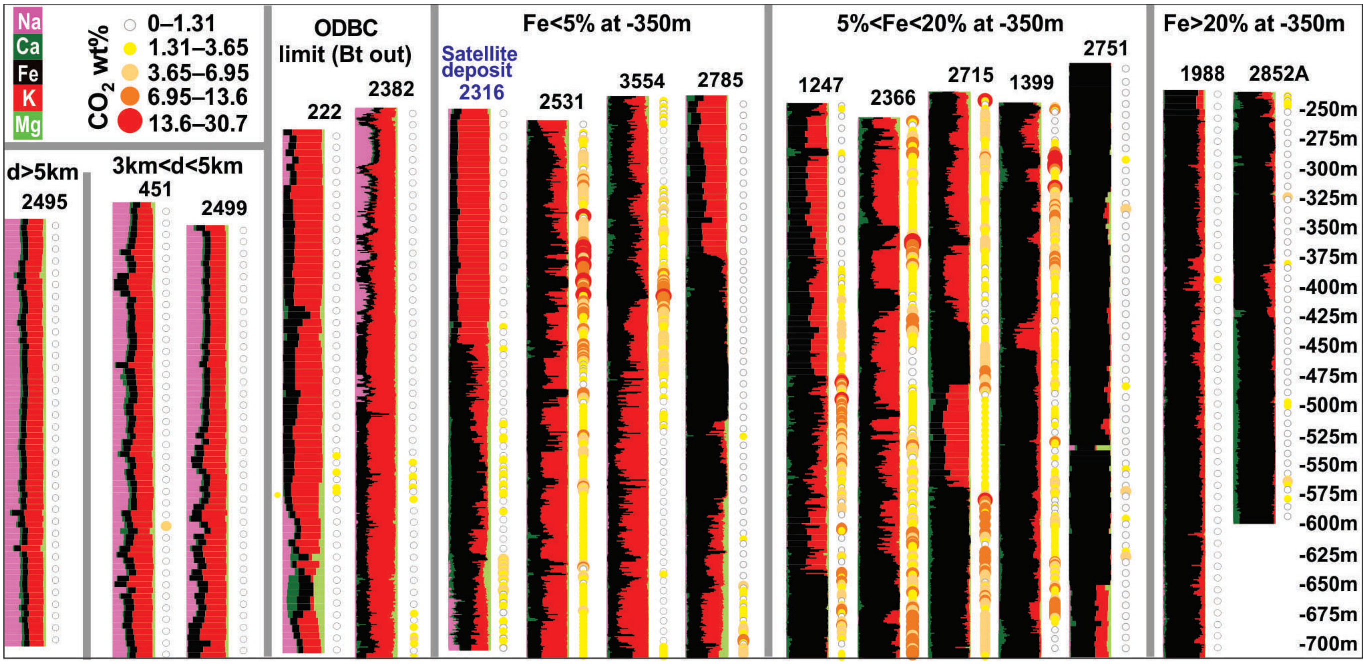


**Figure 8.** An overview of the compositional evolution of alteration outside of the ODBC and of alteration and mineralization within the ODBC is provided by this cross-section truncated at the -700 m level. Alteration is displayed using molar proportion barcodes along representative boreholes, paired to $CO_2$ contents in wt%. Drillhole numbers are labelled at the top of each core. From left to right, the boreholes are arranged from most distal to most proximal to the core of the ODBC (Figs. 7, A1). Intervals of low $CO_2$ contents are shown with lower density of point data for simplicity. Borehole 2316 also illustrates the footprint of the Olympic Dam satellite deposit along the Jubilee Fault (see Fig. 7A).

Gairdner dyke samples towards Ca-Fe alteration represents local replacement by or veining with chlorite, magnetite, carbonates and apatite, despite the dykes postdating the main IOAA metasomatism (Fig. 10A, C; Huang et al., 2017).

*Punt Hill Deposit Geology and Geochemical Footprint*

The Punt Hill polymetallic skarn deposit (Cu-Au-Ag-Zn-Pb-REE) was selected by the Geological Survey of South Australia as a case study to characterize regional-to-deposit scale alteration in the Olympic Copper-Gold Province through integration of geology, petrology, geochemistry, geochronology, HyLogger-3™ hyperspectral scans, and measurements of magnetic susceptibility and specific gravity from drill cores and regional geophysical (magnetic and gravity) inversion models (Reid et al., 2011; Fabris et al., 2018a, b; South Australia Geodata Database, 2020). Blein et al. (2022) contrast the AIOCG-diagram footprints proximal and distal to mineralization, whereas this contribution uses the Punt Hill deposit to illustrate the overall evolution of metal associations within IOAA systems. Detailed information on metal endowment and geochemical and mineralogical footprints is available in Fabris et al. (2018b).

The Punt Hill deposit is hosted by 1.76 Ga carbonate-bearing metasedimentary rocks that were intensely replaced by 1.58 Ga early stratabound Facies 1–2 skarn assemblages dominated by garnet and clinopyroxene (diopside with minor augite and hedenbergite). Skarn assemblages are variably overprinted by Facies 4 K-feldspar (microcline) alteration, forming laminae of K-felsite within the skarn. The K-feldspar-altered skarn is subsequently veined and weakly to moderately replaced by 1.58 Ga copper-sulphide mineralization associated with Facies 5 LT Ca-Mg-Fe assemblages. Elevated copper values are associated with more hematite-altered rocks.

Strong potassic alteration extends into the overlying volcaniclastic felsic rocks of the 1.59 Ga Gawler Range Volcanics. Here, K-feldspar and sericite are associated with variable chlorite, carbonate, hematite, epidote and gypsum. Local skarn (garnet, pyroxene, serpentine, amphibole, epidote, talc) is also present and may be intensely hematized. The 1.85 Ga Donington Suite granitic rocks that underlie the skarn-altered carbonate-bearing metasedimentary units are only weakly altered to chlorite, hematite, carbonate and sericite, recording a LT Ca-Mg-Fe (-K) alteration. To date, only minor copper mineralization has been intersected within the underlying Donington Suite granite or overlying Gawler Range Volcanics.

Although sodic alteration has not been directly documented at Punt Hill, proximal multi-kilometre scale gravity lows in residual images, currently interpreted as potential Hiltaba Suite granite intrusions (Fabris et al., 2018b), may consist of albitite zones, such as along the Southern Breccia albitite corridor of the GBMZ, which is located south of the NICO deposit (Hayward et al., 2016).

The geochemical trends characteristic of the Punt Hill deposit are summarized on the AIOCG diagram (Fig. 11A–C) and further discussed in Blein et al. (2022). Early skarn assemblages straddle the Na-Ca-Fe and Ca-Fe (Mg) fields and trend towards the K field induced by K-feldspar alteration of the skarn (and the stability of K-feldspar-altered skarn). The alteration path of felsic rocks evolves from the least-altered to the K and K-Fe fields. The weakly potassic and LT Ca-Mg-Fe-altered Donington granitoids largely plot within the least-altered field. The intensely potassic-altered skarn occupies fields similar to those of potassium-altered and potassium-iron-altered felsic rocks of the Gawler Range Volcanics; the barcodes indicate that magnesium is preserved in chloritized and skarn assemblages (Fig. 11B).

## Case Examples of IOA Deposits with Heavy Rare Earth Element Mineralization

Iron oxide-apatite deposits contain 30–60 wt% Fe and may host significant REE and HREE mineralization such as the two case examples used in this paper. These deposits are largely

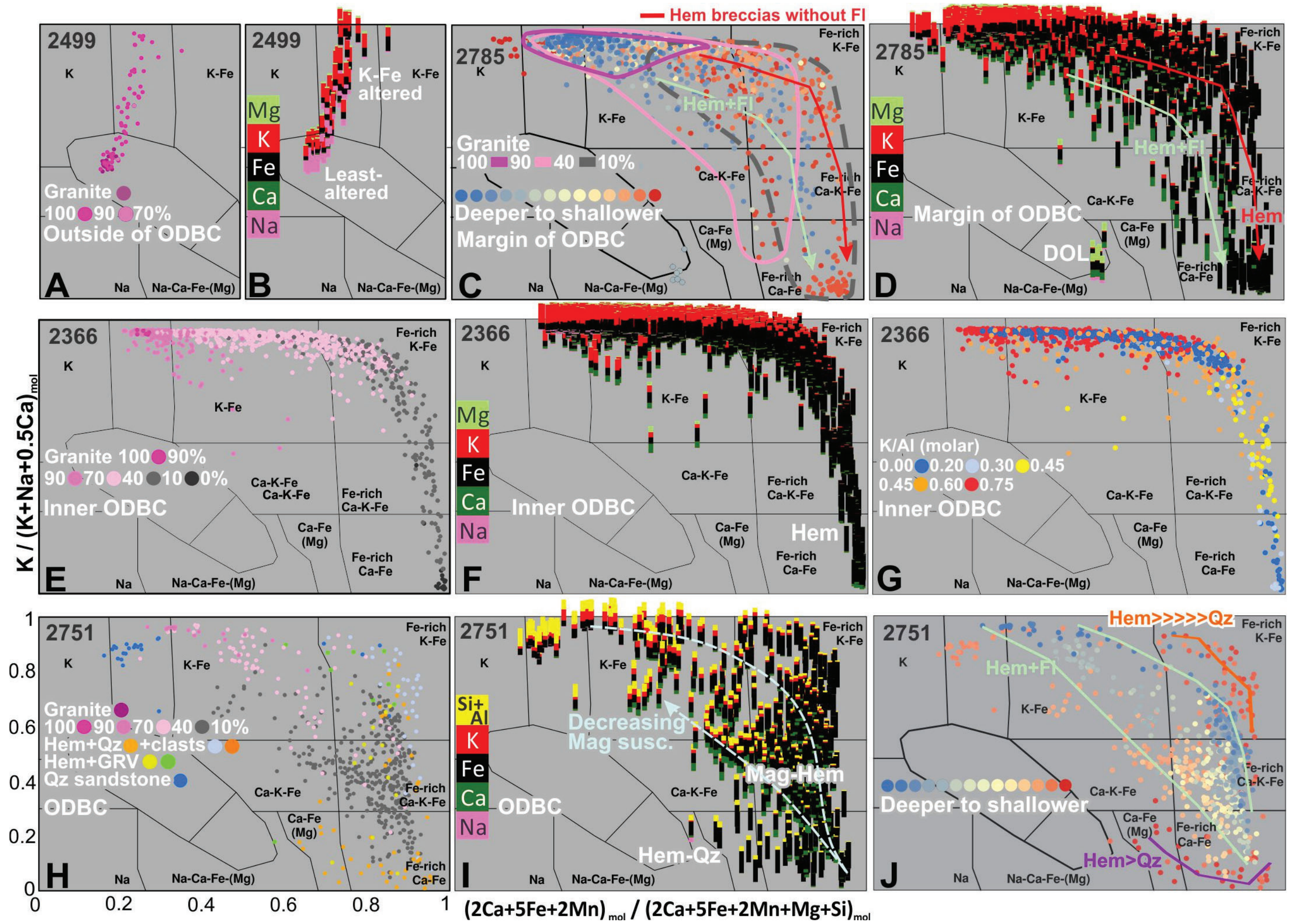


**FIGURE 9.** Diagnostic trends of the lithogeochemical evolution of the Olympic Dam Breccia Complex (ODBC) based on samples from representative boreholes plotted on the AIOCG diagram of Montreuil et al. (2013). Numbers in top left of each plot refer to the boreholes in Figure 8; depth of samples reach 1150 m. Rock types have been classified across the deposit based on the proportion of granitic clasts preserved amongst the hematite-dominant alteration assemblages and breccia infill. Host granite composition is only preserved in (A). **A, B.** Trend of increasing intensity of LT K-Fe alteration of Hiltaba Suite granite outside of the breccia complex (A); barcodes are shown in B. The increasing proportion of potassium over sodium in barcodes reflects the increasing proportion of K-feldspar and sericite compared to plagioclase. **C, D.** Patterns of increasing intensity of Facies 5 hematite-sericite alteration (red trend) and hematite-fluorite (pale green trend) alteration in brecciated granite as the proportion of granite clasts decreases and alteration of clasts to hematite-dominant breccia increases. Clast content intervals of samples are marked by purple, pink and grey fields. Colours of dots refer to depth of samples. The hematite-fluorite path is shifted towards the left of the diagram at comparable iron contents and is largely sub-parallel to the trend defined by increasing hematite alteration along the hematite-sericite trend in red. The weakly altered Gairdner diabase dykes (DOL: dolerite) plot in a discrete cluster close to the unaltered sample field. **E–G.** Iron-oxide alteration trend defined by intensifying magnetite-bearing alteration in addition to hematite-bearing alteration along the same path as the hematite alteration without fluorite in D, based on samples from borehole 2366. **H–J**. Alteration paths formed by fluorite-bearing hematite alteration (pale green trend), hematite-dominant hematite-sericite alteration (orange trend) and increasing quartz contents in the HEMQ core of the ODBC (purple trend), based on samples from borehole 2751. Increasing silica in the hematite-quartz assemblage gradually shifts the projections of HEMQ samples towards the left of the diagram. Decreasing magnetic susceptibility of samples is shown by a pale blue arrow in I.

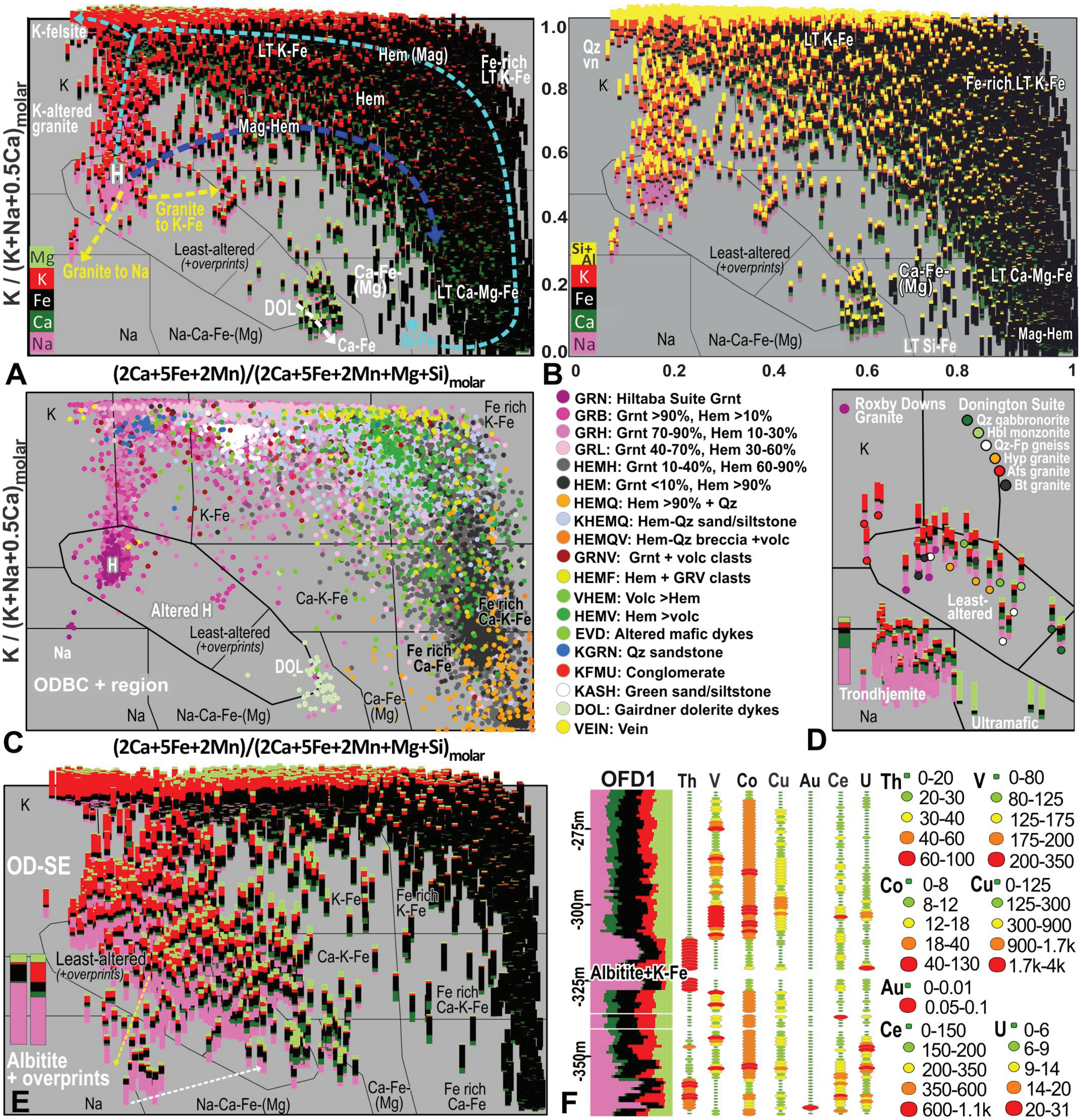


**Figure 10.** Lithogeochemical footprints of alteration facies and least-altered rocks in the region of the Olympic Dam deposit illustrated on the AIOCG diagram of Montreuil et al. (2013). Diagram axes defined in A and B. **A.** Trends of increasing alteration of Hiltaba Suite granite through albitization (lower left yellow line), and magnetite and hematite-bearing alteration (respectively the dark and pale blue arrows interpreted from the magnetic susceptibility data). In the least-altered field, felsic rocks belong to the Hiltaba Suite (H) and Gawler Range Volcanics, and mafic rocks are Gairdner diabase dykes (DOL). The least-altered field also includes some moderately altered granitoids. The base of the Na-Ca-Fe-K-Mg barcodes corresponds to where samples plot in the diagram. **B.** Samples in A are represented by the (Si+Al)/10 barcodes to discriminate hematite-quartz breccia and quartz veins from other alteration types. **C.** Distribution of rock types of the Olympic Dam Breccia Complex (ODBC) subdivided according to breccia components as per Ehrig et al. (2012) and BHP-Olympic Dam (unpub. data, 2018) datasets. Each breccia type spans several alteration fields due to increasing intensity of alteration and evolving mineral assemblages. GRN is least-altered Roxby Downs Granite outside the ODBC. Breccia units with granitic clasts are subdivided into units dominated by altered granite (grnt) clasts (GRB, GRH, GRL) to those dominated by hematite (HEMH, HEM). Hematite+quartz+barite breccia is HEMQ, or HEMQV if volcanic clasts are present. Barite veins are common within HEMQ (Clark et al., 2019). Units derived from sedimentary rocks include KHEMQ (well-bedded, hematite-rich

sandstone, mudstone and conglomerate-breccia), KFMU (polymictic volcanic conglomerate), and KASH (chlorite-bearing, laminated sandstone and mudstone). GRNV, HEMF, VHEM and HEMV are breccia units containing porphyritic felsic to mafic volcanic clasts and variably hematite-dominant assemblages. The KGRN unit consists of ~1450 Ma well-sorted quartz-rich sandstone (breccia) correlated with the regionally-extensive Pandurra Formation, which postdates the deposit. EVD refers to pre- to syn-mineralization altered mafic dykes, and DOL to post-brecciation plagioclase-pyroxene-phyric diabase dykes (Gairdner dykes). **D.** Least-altered granite outside of the ODBC (drillhole RD-2495) and least-altered mafic to felsic rocks of the Donington Suite. Examples of trondhjemite and ultramafic rocks (derived from the GEOROC database) are shown to highlight differences in barcode proportions compared to albitized rocks and mafic rocks. **E.** Barcodes of samples from boreholes southeast of Olympic Dam (OD-SE) located in Figure A1, including OFD1 drillholes in F. **F.** Weakly to moderately altered granitic rocks southeast of the Olympic Dam deposit from drillholes OFD1 (Fig. A1), including localized zones with extensive albitization (high Na proportions in barcodes around the -325 m level) associated with low metal contents and relative enrichment in very immobile elements (e.g. thorium). Elevated Co, V and Cu contents are more pronounced in barcodes with higher proportions of Ca-Mg-Fe (i.e. a LT Ca-Mg-Fe or a HT Ca-Fe alteration). Low Cu, Bi and U contents are typical of alteration zones lacking high proportions of K and Fe (i.e. intense LT K-Fe alteration, see barcodes of Fig. 2 for K-Fe facies). Copper contents above 1700 ppm (red disk) are found in parts of the drill cores not shown in F.

devoid of sulphides (see Corriveau et al., 2022d; Daliran et al., 2022; Huang et al., 2022; Zhao et al., 2022); the Jaguar IOA-nickel deposit with mineral reserves of 58.6 Mt at 0.95 wt% Ni being a notable exception (Centaurus Metals Limited, 2021; Ferreira Filho et al., 2021).

*Pea Ridge Deposit, Southeast Missouri District, USA*

The Southeast Missouri district (USA; Fig. 1) hosts several IOA deposits, one IOCG deposit, and significant historic iron mines within Mesoproterozoic volcanoplutonic rocks (Day et al., 2016b; Starkey and Seeger, 2016). This section summarizes the geological attributes of the Pea Ridge IOA deposit, which is used as a case example for heavy REE mineralization in IOAA systems (Fig. 11D, E).

The Pea Ridge IOA deposit (ca. 1.47 Ga) is hosted by ash-flow tuff and high-silica lava flows (Aleinikoff et al., 2016). The iron ore zone (~ 2 km long, 0.75 km wide; 60–90% magnetite; 47–55 wt% Fe) consists of massive magnetite locally altered to hematite and associated with fluoroapatite, quartz, and variable actinolite, phlogopite, pyrite, and chalcopyrite. Talc, barite, calcite and synchysite also occur. The magnetite core transitions to a peripheral zone of magnetite-cemented breccias containing rhyolite clasts and amphibole-quartz-altered clasts. Alteration haloes include zones of: 1) amphibole-quartz-apatite assemblages (veins, breccias and replacements); 2) silicification (overprinting magnetite, amphibole and hematite, and associated with quartz veins and quartz-K-feldspar veins); and 3) hematite (see Fig. 2 in Harlov et al., 2016). Specular hematite is associated with apatite, quartz, and accessory chalcopyrite, pyrite, monazite and xenotime.

Breccia pipes rich in REE, Y and Th were emplaced as fluidized breccias across the Pea Ridge IOA deposit and footwall rocks, and include fragments representative of all the alteration zones (Nuelle et al., 1992; Harlov et al., 2016). Emplacement postdates the IOA mineralization by 5 to 10 Ma (Neymark et al., 2016). Breccia filling consists of quartz, carbonate (calcite, dolomite), allanite, barite, chlorite, fluoroapatite, hematite, K-feldspar, monazite, synchysite and xenotime in variable proportions, along with minor pyrite, chalcopyrite, molybdenite, bastnaesite, electrum, cassiterite, epidote and galena (Harlov et al., 2016). Minor to accessory thorite and rutile are present in variable amounts, intergrown with monazite and xenotime.

*Josette REE Deposit, Kwyjibo District, Québec, Canada*

The Kwyjibo district in the northeastern part of the Proterozoic Grenville Province in Canada hosts a wide range of IOAA mineral assemblages and IOA to IOCG mineralization types, including the IOA-REE Josette deposit (Fig. 1; Appendix 2; Clark et al., 2005, 2010; Perreault, 2015). Alteration assemblages of the IOAA system replace a variably deformed and recrystallized 1.17 Ga leucogranite (albitized at the periphery of the system; Magrina et al., 2005) and older host rocks, including a possible felsic lapilli tuff (Perreault, 2015). Metasomatites are themselves variably deformed and recrystallized; local primary breccia textures and gneissic fabrics are preserved (Clark et al., 2010; Perreault, 2015).

Field relationships constrain the primary IOAA systems of the district to 1.17 Ga (Corriveau et al., 2010b), i.e. a co-mingled, mafic-felsic dyke diagnostic of the regional 1.17 Ga dyke suite (Wodicka et al., 2003) cuts a slightly deformed magnetite breccia in a 1.17 Ga leucogranite. As per other systems globally, renewed intrusive and tectonic activities (i.e. at 0.98 Ga) led to in-situ REE remobilization and formation of the REE mineralized veins at the Josette deposit at ca. 0.98 Ga (cf. Gauthier et al., 2004; Clark et al., 2005; Perreault, 2015; Perreault and Lafrance 2015; Sappin and Perreault, 2021).

The Josette deposit, used in this contribution as a case example for HREE-bearing IOA mineralization, is the largest zone of mineralization currently defined in the Kwyjibo district (Perreault, 2015; Perreault and Lafrance, 2015; Gagnon et al., 2018). Resources are of 6.92 Mt at 2.72 wt% $REE_2O_3$, 53 wt% $Fe_2O_3$ (measured + indicated) +1.33 Mt at 3.64 wt% $REE_2O_3$, 48 wt% $Fe_2O_3$ (inferred) (Appendix 2). The distribution of the 2.72 wt% $REE_2O_3$ is as follow: the LREE account for 1.83 wt% and the HREE including yttrium for 0.89 wt% whereas, in terms of potential products, the $Nd_2O_3$ + $Pr_2O_3$ grade is of 0.55 wt%, $Dy_2O_3$ is of 0.09 wt%, and other REO + $Y_2O_3$ are of 2.08 wt% (Gagnon et al., 2018).

Metasomatic mineral assemblages, including those recrystallized to upper amphibolite facies are described in Clark (2003), Clark et al. (2005, 2010) and Perreault (2015). These assemblages are diagnostic of Facies 1 (Na with albite; most common outside of the deposit), Facies 1–2 (Na-Ca-Fe-bearing plagioclase and scapolite, and skarn bearing andradite, clinopyroxene and (or) fluorite), Facies 2 (HT Ca-Fe with magnetite, apatite, clinopyroxene), Facies 2–3 (HT Ca-K-Fe

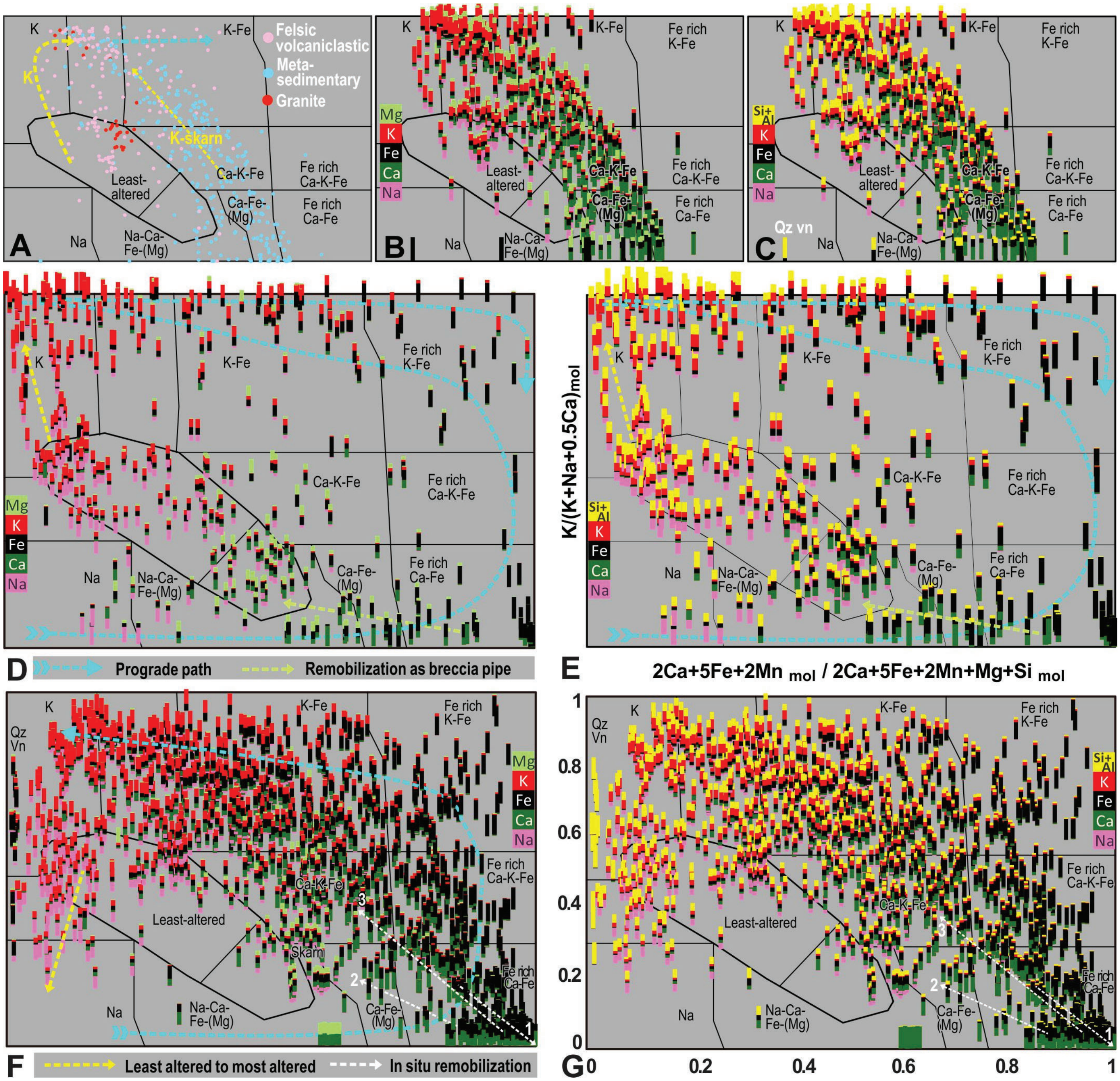


**FIGURE 11.** Lithogeochemical footprints of metasomatites and least-altered host rocks of the Punt Hill deposit in the Olympic Copper-Gold Province (Australia), Southeast Missouri (USA), and Kwyjibo (Canada) districts, illustrated by plotting Na-Ca-Fe-K-Mg and Na-Ca-Fe-K-([Si+Al]/10) barcodes on the AIOCG diagram of Montreuil et al. (2013). **A–C.** Skarn at the Punt Hill deposit straddles the Ca-Fe (Mg) and Fe-rich Ca-Fe boundary of the diagram. Skarn that is overprinted by LT Ca-Mg-Fe alteration is displaced to the left due to higher magnesium contents, whereas skarn overprinted by K-feldspar alteration is displaced towards the K to K-Fe field. K-feldspar-altered Gawler Range Volcanic units (felsic volcaniclastic samples) plot in the K to K-Fe field. Samples of weakly K and LT Ca-Mg-Fe (chlorite-hematite-carbonate)-altered Donington granitoids straddle the boundary between the least-altered and K-Fe fields. Data compiled from the Geological Survey of South Australia (https://map.sarig.sa.gov.au/). **D, E.** Mineral systems hosting IOA and IOCG deposits in the Southeast Missouri district, based on the dataset of Day et al. (2016a). The trend of most intense alteration is in blue. The trend defined by REE mineralization (largely within breccia pipes that cut the IOA Pea Ridge deposit) is in pale green. **F, G.** The Kwyjibo district data from Magrina et al. (2005) and Perreault and Artinian (2013). The trend for albitization of host rocks is in yellow. The trends defined by REE-mineralized samples are shown by white arrows 1 to 3 and their distinct mineral associations are discussed in text.

with biotite, hornblende) and Facies 3 (HT K-Fe with magnetite, microcline, biotite) alteration (Fig. 11F, G). Local Facies 5 hematite alteration and muscovite-bearing alteration also occur.

Mineralized zones consist of fine-grained, massive to brecciated bodies of magnetite (>50% by volume) that are cut by magnetite veins and by REE-mineralized stockworks of apatite-britholite-allanite veins containing variable kainosite, andradite, hornblende, titanite and, locally, clinopyroxene, scapolite, plagioclase, siderite, calcite and quartz (Sappin and Perreault, 2021). The density of veins is highly variable and can reach 90% in some zones. Allanite, apatite, britholite and titanite are the main hosts of REE. Kainosite, monazite, bastnaesite, gadolinite, synchysite and keilhauite are accessory REE-bearing minerals (Table 1). Locally, andradite may contain up to 15% of the total REE content of the mineralized zones (Perreault and Lafrance, 2015). Veins of pyrrhotite-pyrite locally mineralized in chalcopyrite and veins of secondary magnetite also cut the magnetite-rich alteration (Gagnon et al., 2018).

Compositional variations in REE-mineralized samples follow three main trends on the AIOCG diagram (Fig. 11F, G). Veins with second generation magnetite and REE-minerals or sulphides plot along trend 1. Veins rich in britholite, andradite, or fluorite that have calcium-dominant barcodes with silica-aluminum components in Figure 11G occur along trend 2, whereas REE-rich veins containing apatite, magnetite, allanite, or hosted by biotite-hornblende gneisses comprising an assemblage typical of the HT Ca-K-Fe alteration facies, mostly fall along trend 3.

### Facies 1 and Transition to Facies 2: Metal Leaching

*Facies 1 – Na Alteration*

Regionally pervasive and commonly intense Na alteration is the earliest alteration facies to develop within IOAA systems. Sodium alteration generates regional-scale corridors with abundant albitite, defined herein as consisting of >80% modal albite; sodium is dominant in barcodes (Figs. 2, 3, 4B–F, 5A, 6). Albitization occurs in metasedimentary rocks in the Southern Breccia and Cloncurry districts (Figs. 3D, 6), in igneous intrusions in the Olympic Dam (Fig. 10A, E, F), Southeast Missouri and Kwyjibo districts (Fig. 11D–G), felsic volcanic rocks in the Southeast Missouri district (Fig. 11D), and intermediate igneous rocks in the GBMZ (Figs. 2, 3A, D, 4D, E). In all cases, albitization defines a trend from the least-altered field directly towards the Na field in the AIOCG diagram. Albitized mafic or carbonate-bearing rocks evolve from the least-altered field through the Na-Ca-Fe field and then towards the Na field (e.g. Romanet Horst in Corriveau et al., 2014; Blein et al., 2022). Albitization leads to an increase in the proportion of sodium in barcodes, whereas host rock Ca, Fe, K and Mg contents decrease and their original proportions remain largely unchanged as their decreases occur with respect to the proportion of sodium (e.g. barcodes 5 and 6, Fig. 6; yellow trend, Fig. 3D). The preservation of original Ca, Fe, K and Mg proportions enables the ability to distinguish albitization of least-altered host rocks from most alteration overprints of albitite and from trondhjemite (Figs. 10D, E, 12).

Most elements (e.g. Ca, Fe, K, Mg, Cu, Co, Sc and V) are depleted relative to least-altered rocks during albitization; others, e.g. Zr, Al, Ta, Th, Ti and Na, remain immobile or are enriched (Fig. 12; Oliver et al., 2004; Montreuil et al., 2016a). Albitization progresses from initial leaching of Ca, K, Fe, and Mg to leaching of virtually all elements, including immobile elements (e.g. REEs).

Overprinting of albitite by other alteration facies results in addition of cations to the sodium-dominant albitite barcodes, such as calcium and iron (HT Ca-Fe alteration), and potassium and iron (HT and LT K-Fe alteration) (Fig. 12A–C). Overprints of LT Ca-Mg-Fe alteration on albitite produce sodium-dominant barcodes with calcium and magnesium and plot from the Na field towards and through the Na-Ca-Fe field (e.g. in 'first cauldron andesite', Fig. 4C, D; Fig. 28 of Blein et al., 2022). Based on barcode signatures, albitization is interpreted to have been locally significant southeast of the Olympic Dam deposit, where it was overprinted by moderate K-Fe alteration (barcodes at the -315 to -325 m and the ~360 m depth sections, Fig. 10F; barcodes along the yellow arrows, Figs. 10E, 12B).

*Facies 1–2 Skarn*

Skarn assemblages (clinopyroxene- to garnet-dominant) and calc-silicate rocks form slightly before, during, or slightly after Facies 1 Na alteration within carbonate-rich units (e.g., GBMZ and Cloncurry district; Fig. 18A–D in Part 1, Corriveau et al., 2022c; Oliver et al., 2004; Montreuil et al., 2016b). Such skarn is a rare example of strong compositional control by host rocks on the type of alteration to develop. Carbonate rocks can also be albitized without the development of skarn (e.g. Romanet Horst; Corriveau et al., 2014). Skarn is generally replaced by HT Ca-Fe alteration (NICO deposit, Canada), and in some cases by iron-skarn rich in magnetite or IOA mineralization (e.g. Middle-Lower Yangtze River Metallogenic Belt; Zhao et al., 2022). Extensive replacement of skarn (Ca-Mg-Fe barcodes) by HT Ca-Fe alteration (calcium-iron-dominant barcodes) commonly obliterates its distinctive geochemical footprint (Figs. 3B, 12A). Preservation of skarn at the Punt Hill deposit in Australia allows first-order discrimination between the lithogeochemical footprint and metal association of skarn and HT Ca-Fe alteration on the AIOCG diagram (Figs. 11, 13).

Skarn is low in sodium, has calcium-dominant and calcium-iron barcodes with magnesium, and plots at the transition from the Na-Ca-Fe to Ca-Fe fields on the AIOCG diagram (Figs. 3D, 11B, 13; Fig. 24 of Blein et al., 2022). A lack of sodium is common in the barcodes even where skarn is associated with albitite (Fig. 12A). Calcium or magnesium remain dominant over iron where skarn has not been replaced by later alteration facies, and the proportion of cations in the carbonate protoliths may be preserved (e.g. NICO deposit early skarn assemblages with diopsidic clinopyroxene and garnet; Montreuil et al., 2015, 2016b).

Tungsten precipitation in Facies 1–2 skarn is recorded by the presence of scheelite at Punt Hill and in GBMZ skarn assemblages, including inclusions in early magnetite of the NICO deposit (De Toni, 2016). At Punt Hill, samples with barcodes characteristic of skarn alteration (particularly where

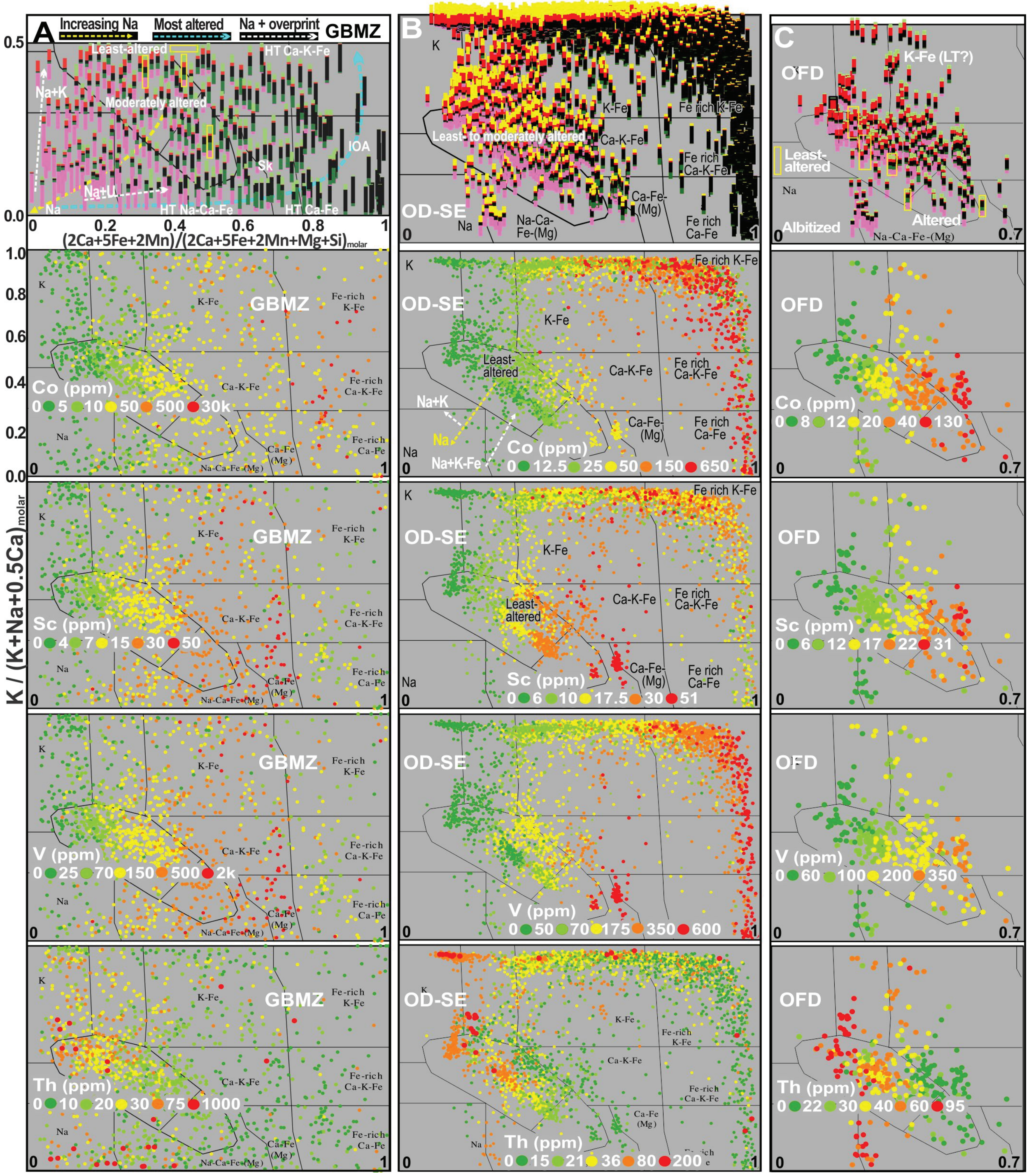

**FIGURE 12.** Lithogeochemical footprints of Co, Sc, V and Th for least-altered to intensely altered rocks of the Great Bear magmatic zone (Canada) and the southeast region of the Olympic Dam deposit (Australia) plotted on the AIOCG diagram of Montreuil et al. (2013). Metal contents below 17.3 ppm Co, 14 ppm Sc, 97 ppm V, and 10 ppm Th are lower than those of average continental crust (Hu and Gao, 2008; Rudnick and Gao, 2014) and likely reflect leaching during metasomatism. Trends are best interpreted by comparing the metal contents with the variations in Na-Ca-Fe-K-Mg and Na-Ca-Fe-K-([Si+Al]/10) barcodes (Figs. 3, 10) to assess the geochemical differences in alteration types. **A.** Examples from the Great Bear magmatic zone. The top diagram (with the Na-Ca-Fe-K-Mg barcodes) displays representative samples that illustrate the incremental changes in cation proportions related to increasing alteration. Samples with barcodes typical of least-altered rocks are highlighted by a yellow frame. Only the lower half of the AIOCG diagram is shown in order to focus on variations induced by increasing albitization of host rocks to albitite and subsequent overprints. The yellow arrow represents the multiple albitization trends that populate the Na field from and across the field of least-altered rocks. Along these paths, Ca, Fe, K and Mg contents of least-altered rocks decrease and barcodes become sodium-dominant through albitization. Comparison of Co, Sc, V and Th endowment along this yellow trend illustrates that intensely albitized samples without overprints (without significant iron and potassium in the sodium-dominant barcodes) have the lowest Co, Sc and V, whereas Th is variable.

The blue arrow represents samples with the highest intensity of alteration and increasing Co, Sc and V in calcium-iron to iron-dominant barcodes parallel to the X axis. Two samples from the Great Bear magmatic zones in the Corriveau et al. (2015) dataset have scandium values above 50 ppm (101 ppm and 224 ppm Sc) and were excluded from the upper 10% field as being anomalous. Three fields have high thorium contents (Na, Na-Ca-Fe, and K). Across the Na to Na-Ca-Fe field, sodium-dominant barcodes with subsidiary iron enrichment represent albitized rocks overprinted by a K-Fe alteration. The Na + U white arrow illustrates the path of albitite that is variably replaced by HT to LT K-Fe and LT Ca-Mg-Fe alteration and commonly mineralized in uranium. Along this path, the low concentrations of Co, Sc and V in albitite are variably increased by the metal endowment of overprinting alteration, leading to highly variable metal contents in the lower part of the Na field. Skarn (Sk) samples plot at the transition from the Na-Ca-Fe to Ca-Fe fields. The Na+K white arrow represents albitite increasingly replaced by K-feldspar (a path along which Co, Sc and V contents remain low). **B.** Samples from the region southeast of Olympic Dam (OD-SE), including drillholes OFD1-3 shown in C. Many samples in the least-altered field have sodium-iron-dominant barcodes with increasing potassium, potentially reflecting albitized host rocks overprinted by iron oxide alteration. The yellow arrow in the cobalt diagram is typical of increasing albitization. The Na+K white arrow is a potential path of increasing potassic alteration and iron oxide overprinting of albitized rocks. The Na+K-Fe arrow is a potential path of increasing K-Fe alteration of albitized samples. Contents of Co, V and Sc in LT K-Fe and Ca-Mg-Fe alteration zones in the region also increase with increasing iron contents but are not as enriched as at the HT Ca-K-Fe facies in the GBMZ (in A). **C.** Inset illustrating the enrichment and depletion within a subset (OFD drill cores) of the dataset in B.

garnet-rich) are enriched in In, Sn, W and Y (Fig. 13, barcodes in Fig. 11B, C).

Increasing proportions of iron with respect to calcium or magnesium (Fig. 3B) lead to the formation of iron-skarn (hedenbergitic clinopyroxene, magnetite) and HT Ca-Fe alteration (iron-amphibole and iron-amphibole-magnetite; Montreuil et al., 2016b). At Punt Hill, the scarcity of samples with iron-rich barcodes (Fig. 11B; Blein et al., 2022; Corriveau et al., 2022c) suggests that zones of intense iron alteration, typically associated with significant polymetallic mineralization in the IOAA systems of the Gawler Craton, are absent, or that zones of high magnetic response have not been drilled.

*Facies 1–2 Na to Na-Ca-Fe*

Albitite and Na-Ca (albite-scapolite; Table 1) alteration give way to Na-Ca-Fe metasomatites; barcodes may be similar to those of least-altered andesite (Fig. 3C). As Na-Ca-Fe alteration increases in intensity or evolves towards the HT Ca-Fe facies, magnesium decreases and Na, Ca and Fe contents increase (barcodes in Figs. 3D, F, 12A). At first, amphibole prevails over magnetite, but magnetite can locally become more abundant than amphibole, creating barcodes dominated by sodium and iron that are difficult to distinguish from albitite replaced by magnetite-bearing alteration (e.g. Southern Breccia, Fig. 3D).

### Facies 2: HT Ca-Fe Alteration Facies and REE-rich Metal Associations and Deposits

Albitite and Na-Ca-Fe facies transition to HT Ca-Fe amphibole, apatite and/or magnetite-bearing assemblages (± titanite, allanite; Table 1). Strong HT Ca-Fe alteration creates calcium-iron to iron dominant barcodes (Figs. 3B, E, 4C, 11D–G, 12A, 14A). Sodium, K, Ba and Sr are depleted and Ca, Fe, Mg, Co, Ni, V, Sn, and in some cases W, Th and REE are enriched relative to host rocks (Figs. 14A, B, 15; Montreuil et al., 2016a; Blein et al., 2022). The coeval depletion in Sr and enrichment in Ca during HT Ca-Fe alteration results in a significant decoupling between these two elements (Fig. 15). Magnesium contents gradually decrease relative to iron and calcium as HT Ca-Fe alteration increases in intensity and the proportion of iron oxide or iron-rich amphibole increases in the alteration assemblages (Fig. 3F; see barcodes in Figs. 2, 3B,C, 4C, D, 11D–G). Overprinting of skarn by Facies 2 HT Ca-Fe and Facies 2–3 HT Ca-K-Fe alteration (De Toni, 2016; Montreuil et al., 2016b) may remobilize tungsten in scheelite-bearing skarn and lead to enrichment such as the tungsten mineralization at the NICO deposit (average of 0.02 wt% with grades up to 2 wt% over 2 m of drill core; Goad et al., 2000).

The HT Ca-Fe alteration facies may evolve to generate IOA deposits with iron ores and/or significant enrichment in critical metals such as vanadium, REE and nickel (Figs. 14, 15; Mumin et al., 2010; Gagnon et al., 2018; Corriveau et al., 2022b; Ferreira Filho et al., 2021). In general, IOA mineralization with significant REE endowment occurs in IOAA systems that have evolved to potassium-bearing alteration facies. The potassic-altered zones are typically spatially decoupled from, and occur as proximal to distal alteration envelopes to IOA mineralization. This is portrayed by molar barcodes and REE contents for the Terra mine region (Figs. 3D, 14A) and on the AIOCG discriminant plots from the Southeast Missouri and Kwyjibo districts (Figs. 11D, G, 14C, D), where both iron dominant barcodes of IOA mineralization and iron and potassium-dominant barcodes of HT K-Fe alteration occur within the host system. The REE and HREE (Er, Tm, Yb, Lu) contents in IOA-mineralized rocks and IOAA facies within systems are fairly similar in the Kwyjibo and Southeast Missouri districts except for the high-grade REE mineralization that differs in terms of morphology, degree of remobilization from the host IOA deposit and trends in the AIOCG diagram.

High-grade heavy to light REE mineralization in IOA deposits occurs as veins, replacement zones and breccia pipes that cut or overprint IOA mineralization. In some cases, total rare earth oxide grades exceed 1 wt% (e.g. resources grade of 2.72 wt% $REE_2O_3$ at Josette, Appendix 2; historic resource grade of 12 wt% $REE_2O_3$ for the Pea Ridge breccia pipes, Seeger, 2000; Fig. 14C, D).

At the Josette deposit of the Kwyjibo district, REE mineralization occurs in veins derived from in situ remobilization of REE from the host IOA deposit, i.e. without extensive transport of REE outside zones of IOA mineralization

(Sappin and Perreault, 2021). The chemical signature of veins hosting high-grade REE mineralization does not strongly differ from the host IOA mineralization in terms of molar barcodes or position in the AIOCG diagram (Fig. 14D). An exception in the Kwyjibo district comes from samples with high REE contents, low $P_2O_5$, and much higher calcium proportions in their barcodes. This may relate to the association of REE with fluorite-bearing assemblages in certain zones of mineralization.

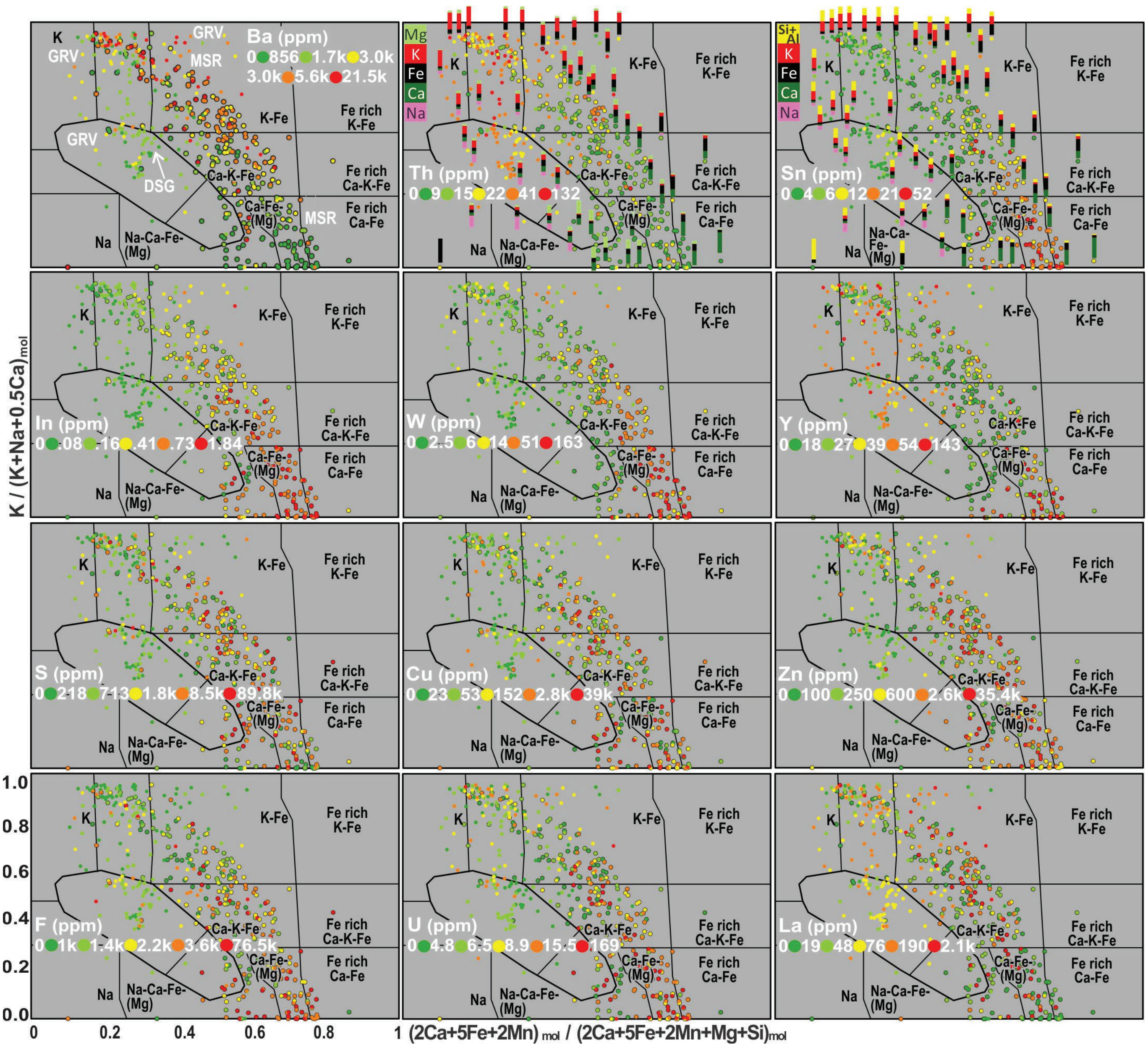


**FIGURE 13.** Distribution of host rock types, barcodes and metal contents of altered rocks from the Punt Hill deposit in Australia plotted on the AIOCG diagram of Montreuil et al. (2013). Symbols for skarn-altered, carbonate-bearing metasedimentary rocks have black outlines. Metal contents greater than 628 ppm Ba, 28 ppm Cu, 527 ppm F, 0.056 ppm In, 31 ppm La, 621 ppm S, 10.5 ppm Th, 2.1 ppm Sn, 2.7 ppm U, 1.9 ppm W, 21 ppm Y, and 67 ppm Zn are above those of continental crust values (Hu and Gao, 2008; Rudnick and Gao, 2014) (except for lanthanum, which ranges from 48–76 ppm in the host rocks). Enrichments in Sn, In, Y and W are mainly restricted to the Ca-Fe (Mg) field. Most metal contents significantly above continental crustal values are distributed across the Ca-Fe to K-Fe fields. Data compiled from the Geological Survey of South Australia (https://map.sarig.sa.gov.au/). The colours in the respective elemental plots (dark green to red) are determined by the 0–25; 25–50, 50–70, 70–90, 90–100 percentile distribution for that element from the datasets. Other metals not shown in the figure that have 70–100 percentile contents significantly above continental crust values include Ag (1–53 ppm), Au (32–440 ppb), Bi (3–163 ppm), Cd (0.8–66 ppm), Co (19–397 ppm), Cr (60–1120 ppm), Cs (8–106 ppm), Li (75–482 ppm), MgO (5–19 wt%), MnO (0.9–11.7 wt%), Mo (2–73 ppm), Ni (37–412 ppm), Pb (56–5098 ppm), Sc (13–40 ppm), Ta (1–7 ppm), $TiO_2$ (0.6–3.8 wt%), and V (89–359 ppm). GRV: Gawler Range Volcanics; DSG: Donington Suite granite; MSR: metasedimentary rocks.

In the Southeast Missouri district, high-grade REE mineralization occurs as fluidized breccia pipes that cut the Pea Ridge IOA deposit (Fig. 11D, E). As such, the pipes are a lot more remobilized from the IOA host than the Josette REE-mineralized veins. Samples of the Pea Ridge IOA deposit with >50 wt% $Fe_2O_3$ that have been analyzed for REE reveal total REE contents between 45 and 2017 ppm (average 951 ppm); La/Yb ranges from 0.25 to 34.7 (average 14.5). An outlier sample rich in apatite (15.69 wt% $P_2O_5$), excluded from the previous average, contains 10,868 ppm REE and has a La/Yb value of 25.4. The REE contents of the magnetite-altered core relate closely to the volume of apatite (Harlov et al., 2016).

In the breccia pipes of the Pea Ridge deposit, the REE contents of the high-grade REE mineralization in the Day et al. (2016a) dataset range from 17,145 ppm to 299,541 ppm (average 167,406 ppm) total REE, with La/Yb ratios ranging from 20.2 to 93.0 (average 30.6, excluding an outlier at 93.0). The average La/Yb ratio for these samples is of 30.6, somewhat higher than the 19.8 La/Yb ratio in samples from the magnetite core that have >0.5 wt% $P_2O_5$. Examination of the apatite indicates that REE were concentrated in the breccia pipes as a result of REE remobilization from apatite in the magnetite core (Harlov et al., 2016). The La/Yb ratio suggests minimal decoupling between LREE and HREE during remobilization. Contents of Si, Mg, and Mn are higher, and iron is lower than the precursor IOA mineralization (Fig. 11D, E); on an AIOCG diagram, they plot outside of the Fe-rich Ca-Fe field of the IOA deposit (Figs. 11D, 14C). This is consistent with REE remobilization by post-IOAA hydrothermal activity (Harlov et al., 2016).

### Facies 2–3 transition: HT Ca-K-Fe Alteration Facies and Cobalt-rich Metal Associations and Deposits

The HT Ca-K-Fe facies (actinolite, biotite, magnetite ± garnet ± K-feldspar) evolves from biotite- to K-feldspar-bearing and amphibole to magnetite dominant and is genetically related to Au, Bi, Co, Ni, and REE mineralization accompanied by sulpharsenides, arsenides and sulphides (Table 1; Fig. 15). In calcium-iron-dominant barcodes (Figs. 3B, 12A), i.e. amphibole-magnetite assemblages, scandium and vanadium contents increase with potassium from the HT Ca-Fe to HT Ca-K-Fe facies, and strontium remains decoupled from calcium including through the transition to iron-dominant barcodes (commonly magnetite-rich assemblages); zirconium is not as consistently depleted (Figs. 12A, 15). Copper contents largely remain <1000 ppm.

As alteration assemblages become iron-dominant (magnetite-dominant in the studied case examples) and plot in the Fe-rich HT Ca-K-Fe field of the AIOCG diagram, As, Bi, Co and W contents increase with increasing proportions of potassium (Figs. 12A, 15). The result is the formation of cobalt- and iron-rich deposits in which Au, Bi, Cu, Ni, REE and W also have economic potential. Examples can have amphibole, biotite or magnetite as iron-dominant mineral species and include the Au-Bi-Co-Cu ± Te-Se-Sb-W NICO deposit, Co-Cu-Au-Bi-Y-REE deposits of the Idaho Cobalt Belt and the Cu-Au-Co ± Ni-Bi-Te-Ag Guelb Moghrein deposit in Mauritania (Goad et al., 2000; Skirrow and Walshe, 2002; McMartin et al., 2011; Slack, 2013; Acosta-Góngora et al., 2015; Kirschbaum and Hitzman, 2016).

In the GBMZ dataset, lead and zinc enrichments observed in the Ca-Fe and Ca-K-Fe fields of the AIOCG diagram are not to be interpreted as part of a transition from HT Ca-Fe to HT Ca-K-Fe alteration, as they are related to overprints on carbonate-bearing host rocks. Furthermore, many transitions involving increasing intensity of alteration and alteration overprints may overlap the Ca-K-Fe field and should be interpreted with caution.

### Facies 3 HT K-Fe Alteration and Brecciation: Metal Associations in Magnetite-group IOCG Deposits

The HT K-Fe alteration facies marks the onset of significant chalcopyrite precipitation and may initially manifest as a biotite-magnetite assemblage (with variable K-feldspar) in mafic host rocks, sedimentary units, or where the HT Ca-K-Fe facies replaces an earlier HT Ca-Fe or HT Ca-K-Fe alteration facies rich in amphibole (GBMZ; Corriveau et al., 2016; Montreuil et al., 2016b; Idaho Cobalt Belt; Slack, 2013). In felsic to intermediate rocks, K-feldspar-magnetite assemblages with accessory to minor biotite are typical of the facies. This assemblage may also overprint and replace the biotite-rich assemblages as HT K-Fe alteration intensifies and evolves (e.g. Ernest Henry deposit in Part 1, Corriveau et al., 2022c).

HT K-Fe alteration of least-altered rocks is marked by increasingly potassium- and iron-dominant barcodes and trends that transition from the least-altered field to the K-Fe field (Fig. 3E, G), or from the Ca-K-Fe and iron-rich Ca-K-Fe fields towards the K-Fe field (Fig. 3B, D) (see also Blein et al., 2022). Breccias in zones of magnetite-group IOCG mineralization with magnetite ± biotite and copper-gold mineralization in the matrix, and coeval K-feldspar alteration of clasts commonly fall within the K-Fe field. With increasing abundance of iron oxides (and progressive replacement of clasts by iron oxides), the sample plots migrate into the iron-rich K-Fe field (Figs. 3B, 6). On the AIOCG diagram, the path of albitite that has been overprinted by K-Fe alteration first passes through the Na and least-altered fields prior to entering the K-Fe field (Figs. 3D, 12A, B). Figure 15 illustrates some of the notable enrichments in Cu, Ag, REE, Mo and U at this facies in the GBMZ. At the Ernest Henry deposit, the variety of HT K-Fe alteration assemblages are enriched in As, Au, Ba, Co, Cu, F, Mn, Mo, and W (e.g. Mark et al., 2006)

### Facies 4 K-felsite and K-skarn Breccia

The transition between the HT and LT K-Fe facies commonly involves the formation of barren K-felsite (K-feldspar) breccia; these potassium-dominant rocks plot in the K field of the AIOCG diagram (K-felsite barcodes, Fig. 3B, C). K-felsite breccias with K-dominant barcodes also occur as

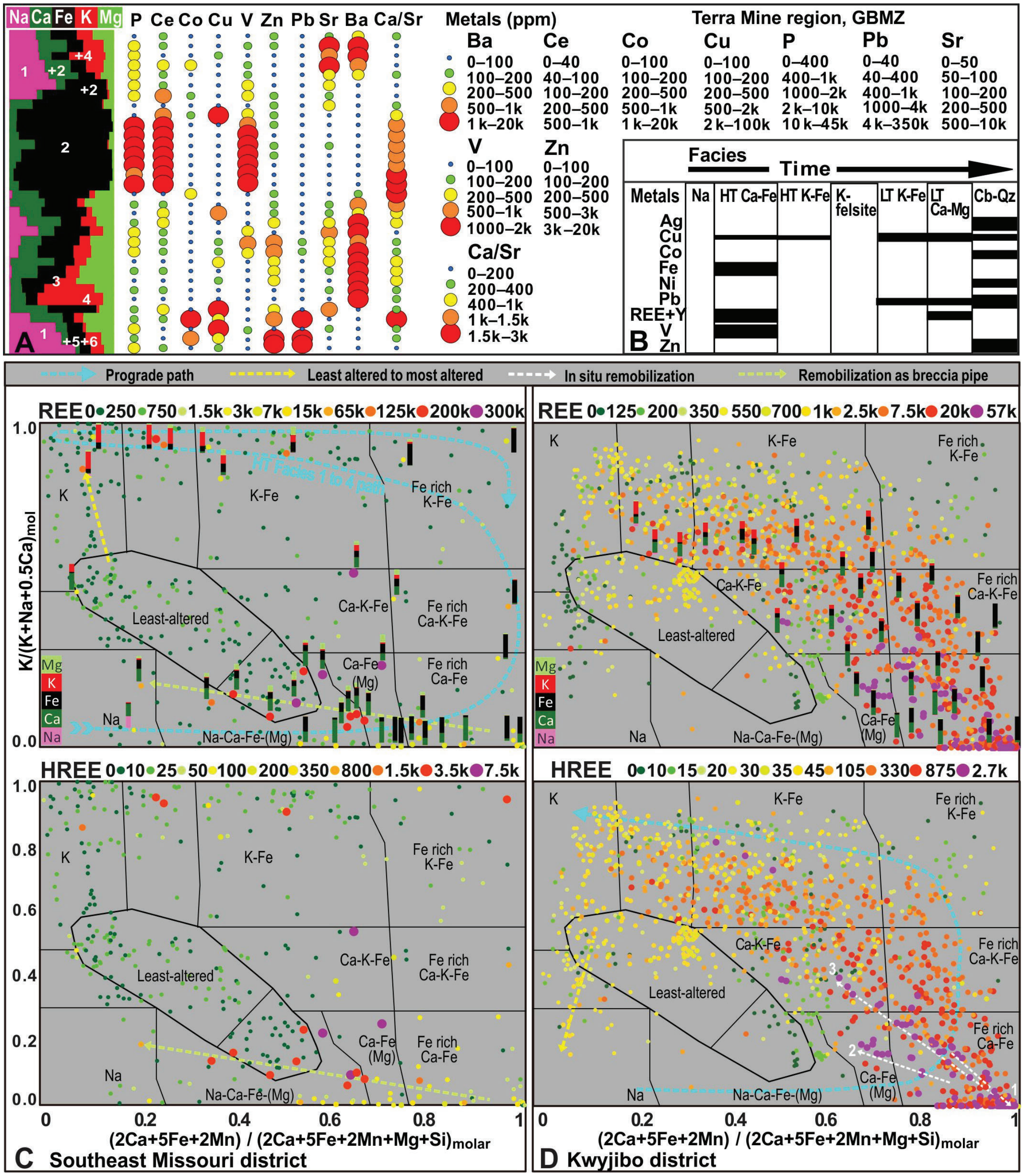


**FIGURE 14.** Representative total REE and HREE contents (in ppm) of metasomatites and least-altered host rocks from systems with IOA mineralization. The data are plotted on the AIOCG diagram of Montreuil et al. (2013) as a series of cation barcodes in A and B, and as metal contents in C and D. Representative Na-Ca-Fe-K-Mg barcodes and alteration paths in B to D are extracted from Figure 11 and plotted to help guide interpretation of metal endowment as alteration and alteration overprints evolve. **A.** Representative composition of metasomatites from grab samples collected during regional mapping, expressed as Na-Ca-Fe-K-Mg molar barcodes and metal contents in the Terra mine region, GBMZ. The samples are grouped by compositional signature to highlight the varied metal associations for each alteration facies. 1: Early Facies 1 albitite, host to subsequent overprinting (+); 2: Facies 2 HT Ca-Fe dominant barcodes and IOA mineralization with high P, Ce, V and Ca/Sr; +2: amphibole to magnetite-dominant overprint on albitized host rocks; 3: Facies 3 HT K-Fe barcodes rich in barium overprinting epidote-rich HT Ca-Fe alteration; 4: Facies 4 K-felsite with high barium and potassium-dominant barcode; +4: K-feldspar alteration overprint on host rock (monzonite); +5+6: Facies 1 albitite overprinted by Facies 5 LT K-Fe and Facies 6 zinc- and lead-bearing carbonate veins. **B.** Synopsis of alteration facies and their associated metals in the Terra mine region. **C.** Southeast Missouri IOAA district data from Day et al. (2016a), including the REE-mineralized breccia pipes that cut the Pea Ridge IOA deposit along the REE mineralization trend in pale green. **D.** The Kwyjibo IOAA district from Magrina et al. (2005) and Perreault and Artinian (2013), including the REE-mineralized veins among their host IOA mineralization at the Josette REE deposit.

haloes at the margins of magnetite or hematite breccias (e.g. Sue Dianne deposit, GBMZ and Ernest Henry deposit, Australia; Corriveau et al., 2022c). Where telescoping alteration leads to overprinting of earlier albitite by K-felsite facies, sodium commonly remains in the resulting barcodes (Na+K barcodes, Fig. 3C).

At the magnetite to hematite transition, the ascent of high-temperature fluids into skarn or units containing abundant carbonates of sedimentary or hydrothermal origin may lead to the formation of the K-skarn facies (calc-silicate minerals with K-feldspar) without proximal intrusive rocks. In particular, transient carbonate alteration that precipitates at the transition from HT to LT K-Fe alteration (likely at the cooler head of the fluid plume) is subsequently transformed into K-skarn (likely through extensive reheating of the host by the main corpus of the fluid plume). Within the K-skarn facies, incipient to moderate polymetallic mineralization may occur, consisting of bornite, chalcocite, chalcopyrite, sphalerite, galena, molybdenite and pyrite, as at the Mile prospect of the GBMZ (Mumin et al., 2010; Fig. 25B–D in Part 1, Corriveau et al., 2022c).

At the Punt Hill Cu, Au ± Ag, Zn, Pb deposit, Australia, K-felsite and K-skarn assemblages overprinted early skarn and evolved to LT Ca-Mg-Fe alteration and mineralization (Fabris et al., 2018a, b). Samples of the potassic-altered skarn plot in AIOCG fields similar to those of overlying K- and K-Fe-altered felsic rocks of the Gawler Range Volcanics, but have molar barcodes with higher proportions of magnesium (Figs. 11A, B, 13). Early skarn has very low Al, Ba, Ti, Tl, Th and Zr (Al, Ti, Tl and Zr not shown in Fig. 13) and high Ca (highest percentile in the 22–41 wt% range) compared to K-altered and K-skarn-altered rocks and mineralization associated with LT Ca-Mg-Fe facies veins and replacements. Enrichments in Ca, Sn, In, Y and W are mainly restricted to the Ca-Fe (Mg) field of the AIOCG diagram (Fig. 13). Other metals significantly above average continental crustal values (above the $70^{th}$ percentile for each element) are distributed across the Ca-Fe to K-Fe fields (Fig. 13), including Ag, Au, Bi, Cd, Co, Li, MnO, Mo, Ni, Pb, $TiO_2$ and V (not shown in Fig. 13). In contrast, the highest Cr and Sc values plot within the Ca-K-Fe to K-Fe field, the highest Ta in the K-Fe to K fields, and highest Cs and MgO in the Na-Ca-Fe to K fields of the AIOCG diagram (not shown in Fig. 13).

## Facies 5: Hematite-group IOCG and Variant Deposits

Facies 5 consists of two end-members: LT K-Fe (± Ca-F, $CO_2$) and LT Ca-Mg-Fe (± K, $CO_2$). Metal enrichments include Ag, Au, Bi, Co, Cu, Fe, LREE, Mo, Pb, Re, U and Zn (Figs. 7, 16–19; Skirrow and Walshe, 2002; Ehrig et al., 2012; Rex Minerals Ltd, 2015; Babo et al., 2017; BHP, 2020; OZ Minerals, 2020). Mineralization typical of the LT K-Fe end-member comprises breccia-hosted copper sulphides with hematite and sericitic white mica. In contrast, the LT Ca-Mg-Fe end-member is characterized by Au-Co-U mineralization with carbonates, epidote, chlorite and hematite (e.g. albitite-hosted Au-Co-U deposits).

*Geochemical Footprint of the Olympic Dam Deposit*

Brecciation has produced very distinctive rock units in the ODBC (Fig. 7A, B; 55 non-breccia/breccia rock types; Ehrig et al., 2019), but alteration facies and metal content variations form relatively simple trends across the K-Fe, Fe-rich K-Fe and Ca-Fe fields of the AIOCG diagram. These simple trends are also present in a plan view of the deposit, regardless of the breccia type or breccia clast proportions (Figs. 7, 16–19). Figures 16 to 19 illustrate groups of elements that display similar trends on the AIOCG diagram. On these figures, analyses of sedimentary units (KRGN, KFMU, KASH), dolerite dykes (DOL) and veins (Vein) were omitted to focus on alteration trends for the main host rock types.

In Figure 16, the selected elements show a systematic decrease in abundance from the K- to Fe-rich Ca-Fe fields. Conversely, selected elements in Figure 17 show a systematic increase in abundance from the K- to Fe-rich Ca-Fe fields, and form a cluster at the boundary of the Fe-rich Ca-Fe and Fe-rich Ca-K-Fe fields. These samples tend to occur at relatively shallow depths (Fig. 17); they have distinctive calcium-iron-dominant and potassium-poor barcodes (Fig. 19) and K/Al ratios between 0.6 and 0.75 (Fig. 18). In Figure 18, selected elements are distributed along the V-shape trend of decreasing magnetic susceptibility (Fig. 9I) and form a small cluster at the lower part of the Fe-rich Ca-Fe field. Elements with variable trends are illustrated in Figure 19 along with diagrams highlighting similar zones defined by depth, location or the hematite-quartz (Fe+Si)/(Fe+Si+Al) alteration index (HMSI). This index was developed by Schlegel and Heinrich (2015) for the Prominent Hill deposit, where HMSI inversely correlates with copper content and economic copper grades have K/Al (molar) between 0.34 and 0.40, K/Na (molar) of 20–36, and HMSI <0.98. At the Olympic Dam deposit, element contents, K/Al ratios and HMSI indices vary slightly from those at Prominent Hill, and higher copper grades are more closely related to the distribution of fluorite and its spatial association with bornite-chalcocite mineralized zones (Figs. 7, 17–19).

In the Olympic Dam AIOCG diagrams, samples that plot in the Ca-Fe field largely reflect the presence of fluorite and the complete destruction and replacement of sericite and K-feldspar by hematite, magnetite and iron carbonate. The calcium content is typically not related to LT Ca-Mg-Fe calcite, dolomite, ankerite or HT Ca-Fe apatite, as calcium is decoupled from both $CO_2$ and $P_2O_5$ contents in the AIOCG diagram (Fig. 18). Zones of K-felsite with intense sericitization of granitic clasts are preferentially developed in the upper part of the deposit (Fig. 8); localized intense sericitic alteration and advanced argillic alteration are also present (low K/Al ratios in Figs. 9G, 18; Ehrig et al., 2012).

*Low-temperature K-Fe Alteration*

The LT K-Fe (± Ca-F, $CO_2$) facies typically develops within felsic to intermediate igneous rocks and progresses from: 1) K-feldspar-stable assemblages comprising hematite (commonly replacing earlier HT K-Fe facies), variable siderite, and minor to moderate sericite overprints, with

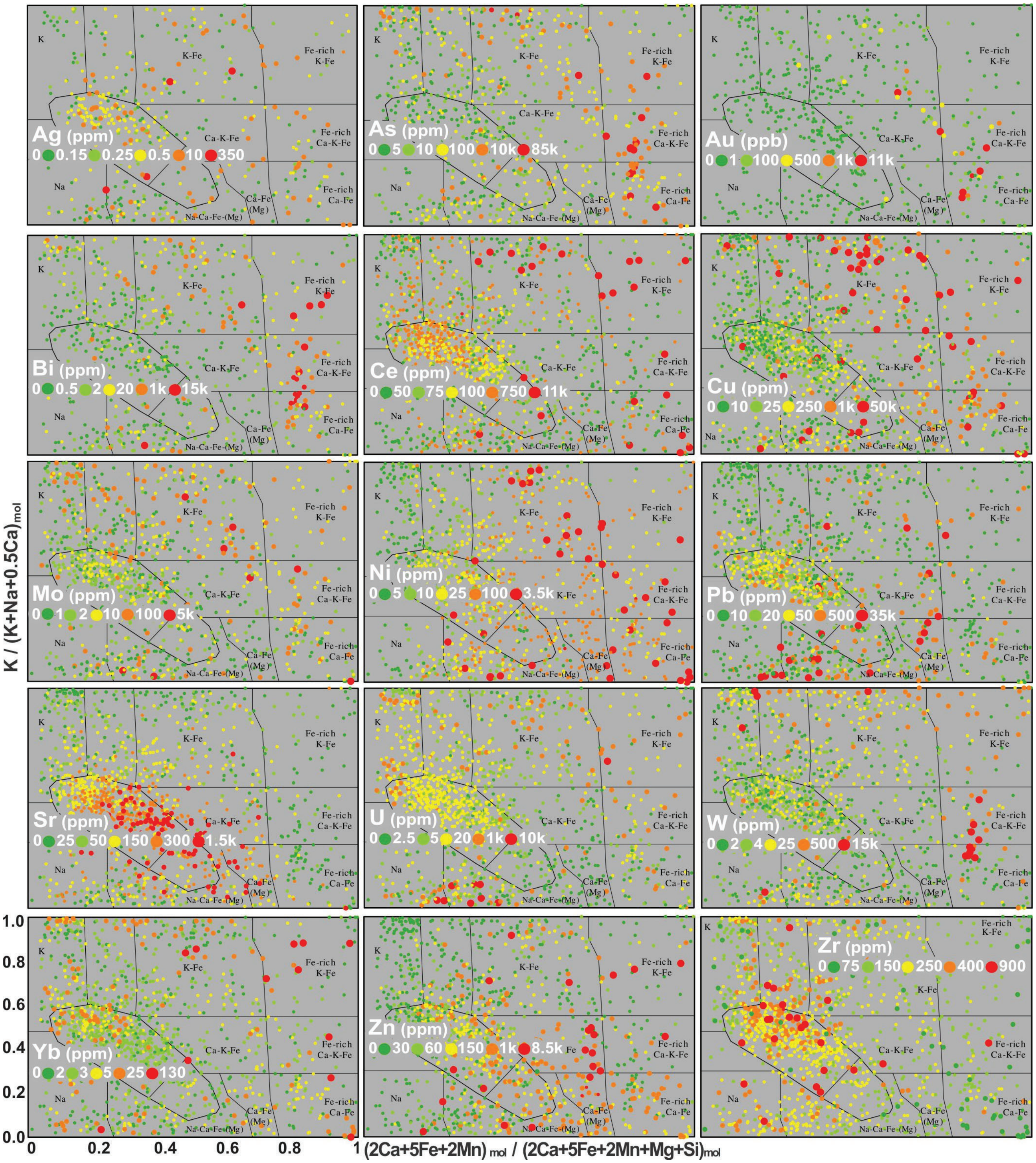


**FIGURE 15.** Variations in metal contents (in ppm except gold in ppb) in IOAA systems of the Great Bear magmatic zone (Canada). Gold is not reported for samples analyzed by ICP-MS (Corriveau et al., 2015). The Co, Sc, V and Th contents are shown in Fig. 12. Metal contents below 63 ppm Ce, 28 ppm Cu, 1.1 ppm Mo, 47 ppm Ni, 17 ppm Pb, 320 ppm Sr, 2.7 ppm U, 1.9 ppm W, 1.96 ppm Yb, 67 ppm Zn, and 193 ppm Zr are lower than those of average continental crust (Hu and Gao, 2008; Rudnick and Gao, 2014), and likely reflect leaching during metasomatism. Alteration facies control on metal trends is best interpreted through variations in Na-Ca-Fe-K-Mg and Na-Ca-Fe-K-([Si+Al]/10) barcodes (Figs. 3, 12A). Samples of albitite-hosted uranium mineralization plot in the Na and Na-Ca-Fe fields because albitite is overprinted by LT Ca-Mg-Fe alteration, and does not imply that mineralization precipitates at Facies 1. The range in element contents follows a percentile distribution, illustrated in five colours ranging from dark green to red (0–25; 25–50, 50–70, 70–90, 90–100). Other metals (not shown in the figure) with 90–100 percentile contents significantly above average continental crust include (in wt%) $Al_2O_3$ (17–35) and $Fe_2O_3$ (32–100), and in ppm, Ba (1.5k–10.6k), Cs (10–64), In (2.5–11), Nd (65–2845), Rb (350–1070), Sb (15–125), Sr (300–1.5k), Ta (2–162), Te (2–26), and Y (63–1.7k).

potassium-iron-dominant barcodes and high K/Al; to 2) sericite-rich, hematite-dominant assemblages containing variable fluorite and siderite, iron-dominant barcodes with potassium and/or calcium, and lower K/Al (Figs. 7C, 9G, 19; Ehrig et al., 2012; Barton, 2014; Schlegel and Heinrich, 2015; Corriveau et al., 2016, 2022c). Chlorite, epidote, quartz, calcite, siderite, barite, fluorite and allanite may occur in minor to major quantities (Fig. 7). In the later stages of the LT K-Fe facies, extreme iron enrichment is associated with precipitation of silica and forms hematite-quartz zones that are either barren (Olympic Dam deposit; Fe Zone occurrence in the GBMZ; Fig. 4E) or gold-bearing (Prominent Hill deposit). The iron-dominant barcodes straddle the Fe-rich Ca-Fe and the Ca-Fe (Mg) fields of the AIOCG diagram (Fig. 9H–J).

At Olympic Dam, the increasing intensity of hematite-rich alteration at Facies 5 defines two main element associations, depending on whether granite clasts or early magnetite, hematite, siderite, barite, fluorite and quartz breccia matrix material are being replaced (Figs. 16–19). In breccias where the proportion of granitic fragments to metasomatic cements exceeds 1, the compositional influence of the granitic fragments generates higher alkali contents, such as Na, K, Rb and Cs (stable in K-feldspar and sericite; Fig. 16). The relatively immobile high-field-strength elements, particularly, Zr, Hf and Ti, as well as Al and Ga, follow the same distribution, and are likely to represent, at least in part, residual signatures of the granite (Fig. 16; see Group 1 non-mineralized rocks signature of Dmitrijeva et al., 2019). Along this trend, K/Al ratios are typically greater than 0.6, indicating that K-feldspar and muscovite are both present and that the K-feldspar to muscovite ratio exceeds 1 in certain samples (Fig. 18). Based on the path from the least-altered granite, the trend can be interpreted to progress through similar K/Na+Ca ratios (i.e. horizontally), towards either the iron-rich K-Fe or the K field, depending on the amount of iron added to the matrix of the breccias and the percentage of matrix (Fig. 16).

Enrichments in Li, Ta and Zn generally cluster where granitic rocks are preserved (Figs. 16, 18, 19); however, the distribution of highest values is more variable and their control is not obvious using the AIOCG diagram alone.

As iron oxide (hematite>>magnetite) content increases and K-feldspar, sericite and granitic clasts are progressively replaced by iron-bearing minerals (siderite, magnetite, hematite), a series of distinct metal associations forms a trend from the K-Fe field towards the Fe-rich K-Fe, then vertically across the Fe-rich Ca-K-Fe and Fe-rich Ca-Fe fields (Fig. 18). Along this trend, K/Al ratios decrease to a range of 0.3 to 0.45 through progressive replacement of K-feldspar by sericite as iron alteration intensifies, and then further decreases to between 0.2 and 0.0, forming a cluster of samples at the bottom right of the Fe-rich Ca-Fe field where the potassic minerals have been completely replaced. Element associations along this trend can be further subdivided into distinct groups.

High concentrations of chalcophile elements (e.g. Ag, Bi, Cu) and sulphur occur in the field of Ca-K-Fe alteration and extend from the K-Fe field through to Fe-rich fields as hematization increases. The main cluster straddles the Fe-rich Ca-K-Fe and Fe-rich Ca-Fe fields (Fig. 17), along with As, Au, Ba, CaO, LREE, Mo, Sb, Sn, Sr, W and Te. Precipitation of these elements primarily in sericite- and hematite rich alteration zone with low to high abundances of fluorite is supported by 1) the association of this cluster with samples having low to high calcium contents; 2) K/Al ratios in the range of 0.30 to 0.45 (muscovite greater than K-feldspar; Fig. 18; see also zones of calcium-rich barcodes in Fig. 19); 3) the lack of a complementary cluster in the $CO_2$ and $P_2O_5$ diagrams (Fig. 18); 4) HMSI index values between 0.93 to 0.98; and 5) the location at the core of the breccia complex (white dots in the location diagram, Fig. 19). This grouping is similar to the Au-W-Mo-As-Sb signature of Dmitrijeva et al. (2019).

Clusters of samples rich in the middle to heavy REE, U and Se coincide with samples having a HMSI index greater than 0.9 that plot in the iron-rich Ca-Fe to K-Fe fields (Fig. 19). The U and Se association is supported by the grouping of U-Cu-S-Se documented in Dmitrijeva et al. (2019), although in the AIOCG diagram, Cu and S tend to be most enriched in the Fe-rich Ca-Fe to Ca-Fe-K facies, whereas enrichment in uranium spans all the iron-rich facies (Ca-Fe to K-Fe). The Dmitrijeva et al. (2019) dataset does not include REE, but HREE and MREE exhibit trends similar to uranium and selenium, whereas the LREE mimic the behaviour of Au-W-Mo-As (Figs. 17, 18). Finally, a group of elements, including Nb, Co, Ta and P (Fig. 18) form a small cluster at very low K/Al ratios, high magnetic susceptibilities and high CaO, $CO_2$, $P_2O_5$ and S contents in the most iron-rich and potassium-poor corner of the iron-rich HT Ca-Fe field; this is consistent with the distinct chemical footprint of pyrite-magnetite-siderite-apatite assemblages.

*LT Ca-Mg-$Fe^{3+}$ Alteration*

Mineralization at the LT Ca-Mg-Fe facies occurs at the Scadding mine (Canada) within chlorite-rich zones of albitite breccia and within skarn and K-skarn at the Punt Hill deposit in Australia (Table 1). At the Cu-Au (± Ag-Zn-Pb) Punt Hill deposit, chalcocite, bornite, chalcopyrite, sphalerite, galena and pyrite precipitated within veins and replacement zones interstitial to early skarn clinopyroxene and garnet at the LT Ca-Mg-Fe facies (Fig. 13; Fabris et al., 2018a, b). The chalcopyrite is positively correlated with chlorite, and bornite and rare gold with hematite (Fabris et al., 2018a, b). On the AIOCG diagrams, this translates into the presence of intermixed Ca-Fe-Mg-dominant barcodes from LT Ca-Mg-Fe facies and HT skarn alteration, and mixed metal associations (Fig. 11B–G). In contrast to the early skarn, which is associated with high Sn, In, Y and W, and is restricted to the Ca-Fe (Mg) field, later-stage mineralization is distributed across several alteration facies, is associated with enrichment in Cu, F, La, U, and Zn (Fig. 13) along with Co, total REE, and Yb (not shown in Fig. 13), and follows the distribution of sulphur.

*LT Ca-Mg-$Fe^{2+}$ Alteration*

In IOAA systems with abundant Ca-, Fe-, and Mg-rich host rocks or albitite, and under reduced conditions, a LT Ca-Mg-$Fe^{2+}$-($CO_2$) facies forms, comprising assemblages of chlorite (with or without iron sulphides), magnetite, carbonates (siderite, dolomite, ankerite), iron phyllosilicates (e.g. stilpnomelane) and minor biotite (Fe ± K).

On the AIOCG diagram, samples affected by LT Ca-Mg-$Fe^{2+}$-($CO_2$) facies alteration progressively trend towards the Fe-rich Ca-Fe and Fe-rich Ca-K-Fe fields through decreasing potassium contents. Host rock composition exhibits a significant control on the chemical signatures of this alteration type. As LT $Fe^{2+}$-Mg-$CO_2$ alteration intensifies, the Fe/Mg ratio generally increases but the magnesium content in the altered host rocks depends on the ability of the system to crystallize chlorite. For example, in the gold-mineralized Scadding deposit in Ontario, residual magnesium from the host rock remains in the prograde LT Mg-$CO_2$-$Fe^{2+}$ alteration facies as magnesium was accommodated in chlorite. Samples containing chlorite-hosted magnesium tend to plot or are deflected towards the Ca-Fe field of the diagram.

In contrast to prograde LT Ca-Mg-Fe-(K, $CO_2$) alteration, retrograde alteration does not precipitate significant iron-rich mineralization, but may instead lead to a marked increase in the proportion of magnesium in barcodes.

*Iron-poor Mineralization*

Following extensive iron-bearing alteration, polymetallic mineralization at Facies 5 and subsequent vein-type mineralization may be iron-poor in IOAA systems or in iron-poor environments as observed at the Mount Dore and Merlin deposits in Australia (Williams et al., 2005; Babo et al., 2017; Hofstra et al., 2021).

## Distinctiveness of IOAA Systems Geochemical Footprints and Metal Associations

*Geochemical Footprints of IOAA Systems*

Except for sodic alteration, IOAA facies develops significant and diagnostic enrichments in iron, calcium, and/or potassium, as well as localized enrichments in Mg, Na or Si. In most altered samples, the combined silica-aluminum proportions in Na-Ca-Fe-K-[(Si+Al)/10] barcodes are lower than those of least-altered host rocks except for samples trending towards the K field in the AIOCG diagram (Figs. 10B, 11E, G, 12B). In typical IOAA systems, the spectrum of least-altered to most-altered rocks completely covers the AIOCG diagram (e.g. GBMZ, Fig. 3E–G). In contrast, sampling focused on deposits commonly leads to partial coverage of the diagram (e.g. dataset for the Olympic Dam and Punt Hill deposits; Figs. 10, 11). Sampling of albitite-hosted mineralization (Fig. 3D) or systems where this mineralization type prevails (e.g. Romanet Horst and Central Mineral Belt, Canada; Acosta-Góngora and Potter, 2018; Blein et al., 2022), generate plots dominated by the Na to K, Na-Ca-Fe, or least-altered fields.

Iron enrichment is diagnostic of IOAA systems but the trends on the AIOCG diagram may vary depending of the iron minerals precipitated (a function of host rocks and fluid physicochemical conditions as discussed in Corriveau et al., 2022b). For example, the high $CO_{2-}$ trend decoupled from CaO-rich samples in the AIOCG diagrams of the Olympic Dam deposit helps identify the distribution of siderite-rich samples and contrast it to iron oxide-rich ones with lesser siderite (Figs. 17, 18).

*Comparison of Metal Associations amongst Facies*

Early Facies 1 Na alteration is accompanied by extensive leaching of the altered rocks, enrichment in sodium, and variable enrichments in Al, Ga, Nb, Ta, Ti, Th and Zr relative to the original composition of the host. Elements such as Ag, Co, Cu, LREE (e.g. Ce), Ni, Pb, Sc, Sr, Yb and Zn are variably leached and mobilized in the fluid column (Table 1; Figs. 12, 15). Facies 1–2 (Na-Ca-(Fe)) alteration is also an important leaching stage (e.g. Fab system of the GBMZ; Montreuil et al., 2016c), but locally, Ca, Fe, and P (± REE and V) are slightly to moderately enriched (e.g. Mag Hill sector, GBMZ; analyses in Corriveau et al., 2015).

The first important stage of iron enrichment occurs during Facies 1–2 iron-skarn mineralization and Facies 2 HT Ca-Fe alteration. In skarn, iron contents gradually increase at the expense of magnesium, leading to more iron-rich clinopyroxene, followed by precipitation of magnetite or replacement of the skarn assemblage by HT Ca-Fe alteration. In HT Ca-Fe alteration zones, especially in ferromagnesian host sequences, amphibole-dominant alteration is followed by iron oxide precipitation as the iron component of the HT Ca-Fe facies intensifies. These trends result in calcium- and iron-dominant barcodes, with variable magnesium, that progressively evolve towards iron-dominant barcodes (Figs. 2–4, 12, 15). Sodium, K, Ba, and Sr are depleted or remain in the fluids, whereas Ca, Co, Fe, Mg, Ni, P, V, Sn, and in some cases W, Th, U and REE precipitate in HT Ca-Fe alteration zones (Figs. 2, 3, 15; Montreuil et al., 2016b, c; Blein et al., 2022).

Iron-rich end-members of the HT Ca-Fe alteration facies may lead to IOA deposits with iron ores and precipitate F, P and REE in magnetite ± phosphate and REE-minerals (Figs. 2, 3, 12, 14, 15, 20A, B). Cobalt enrichment is rare, nickel enrichment varies but can lead to nickel deposits (see Corriveau et al., 2022b), and significant vanadium enrichment may occur in IOA mineralized zones (Table 1; Figs. 12, 15; Mumin et al., 2010).

The HREE contents of the HT Ca-Fe alteration facies, IOA deposits and REE mineralization are on average greater than those of other IOAA facies (Figs. 14C, D, 20C–F). In IOA deposits, such as the Josette and Pea Ridge deposits, the metasomatites most enriched in REE are characterized by slight LREE fractionated patterns and HREE contents greater than those of carbonatites (e.g. Mountain Pass, Asharm and Weishan deposits) and laterite derived from them (e.g. Mt Weld deposit) that are generally enriched in LREE (Fig. 20A; Jones et al., 2013) as well as greater than the average HREE contents of the Olympic Dam IOCG deposit (Fig. 20A).

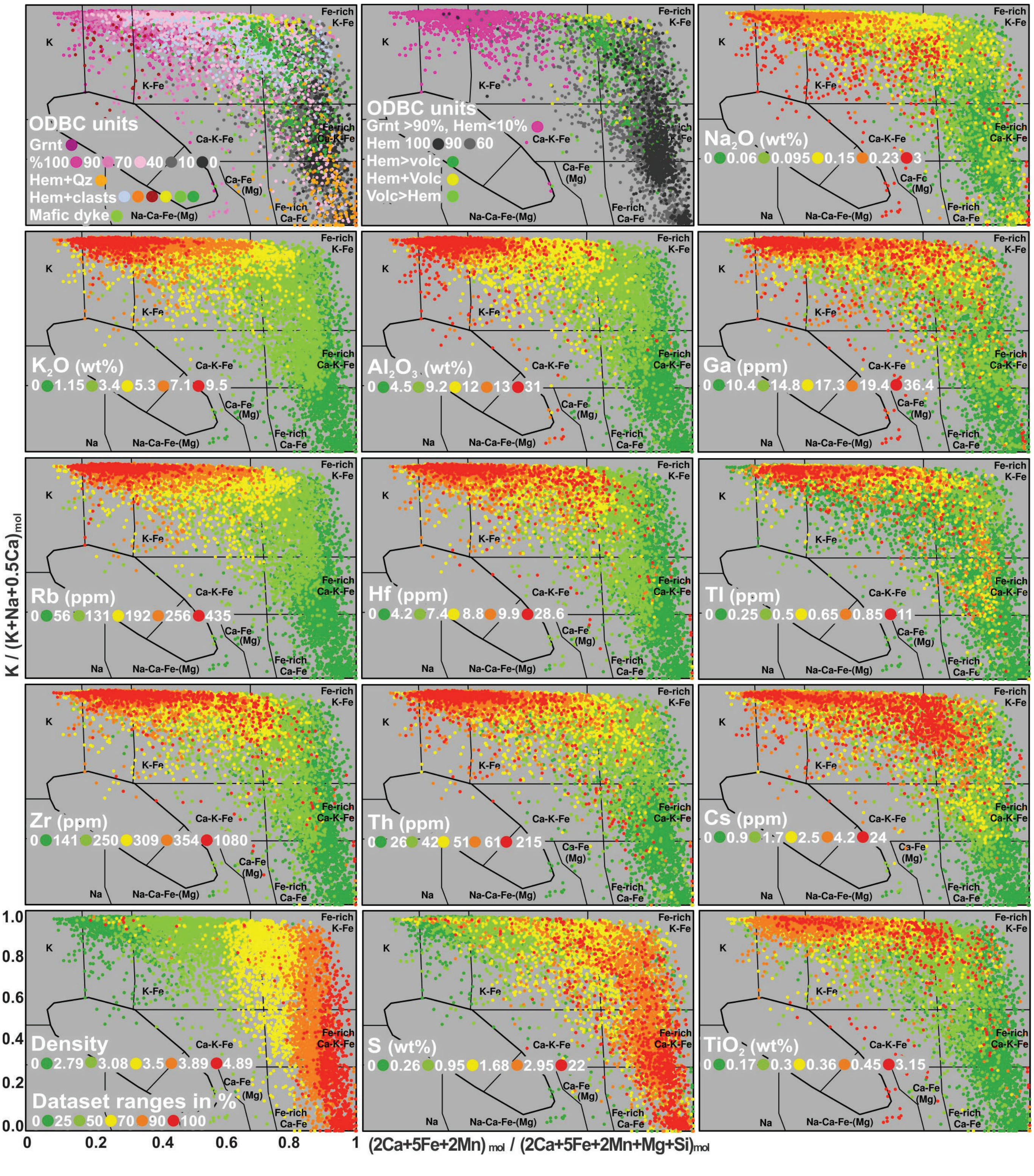


**FIGURE 16.** Contents of $Al_2O_3$, Cs, Ga, Hf, $K_2O$, $Na_2O$, Rb, S, Th, $TiO_2$, Tl, and Zr, distribution of units, and density of samples from lithological units of the Olympic Dam Breccia Complex (listed in Figure 10) except for KRGN, KFMU, KASH, DOL and Vein. The diagrams group elements particularly enriched in altered granite and depleted in the hematite-dominant samples. The element contents are plotted on the AIOCG diagram of Montreuil et al. (2013). The sulphur and density distributions illustrate that high-density and sulphide-bearing ores significantly overlap with hematite-dominant metasomatites. Hiltaba Suite granite and Gawler Range Volcanics are extensively altered even where hematite is minor; they define a trend across the K, K-Fe and Fe-rich K-Fe and Ca-Fe alteration fields via progressive K-feldspar (minor) and white mica alteration, increasing hematite precipitation, and increasing fluorite precipitation within hematite-rich breccia. Element contents are plotted dark green to red following a percentile distribution (0–25; 25–50, 50–70, 70–90, 90–100).

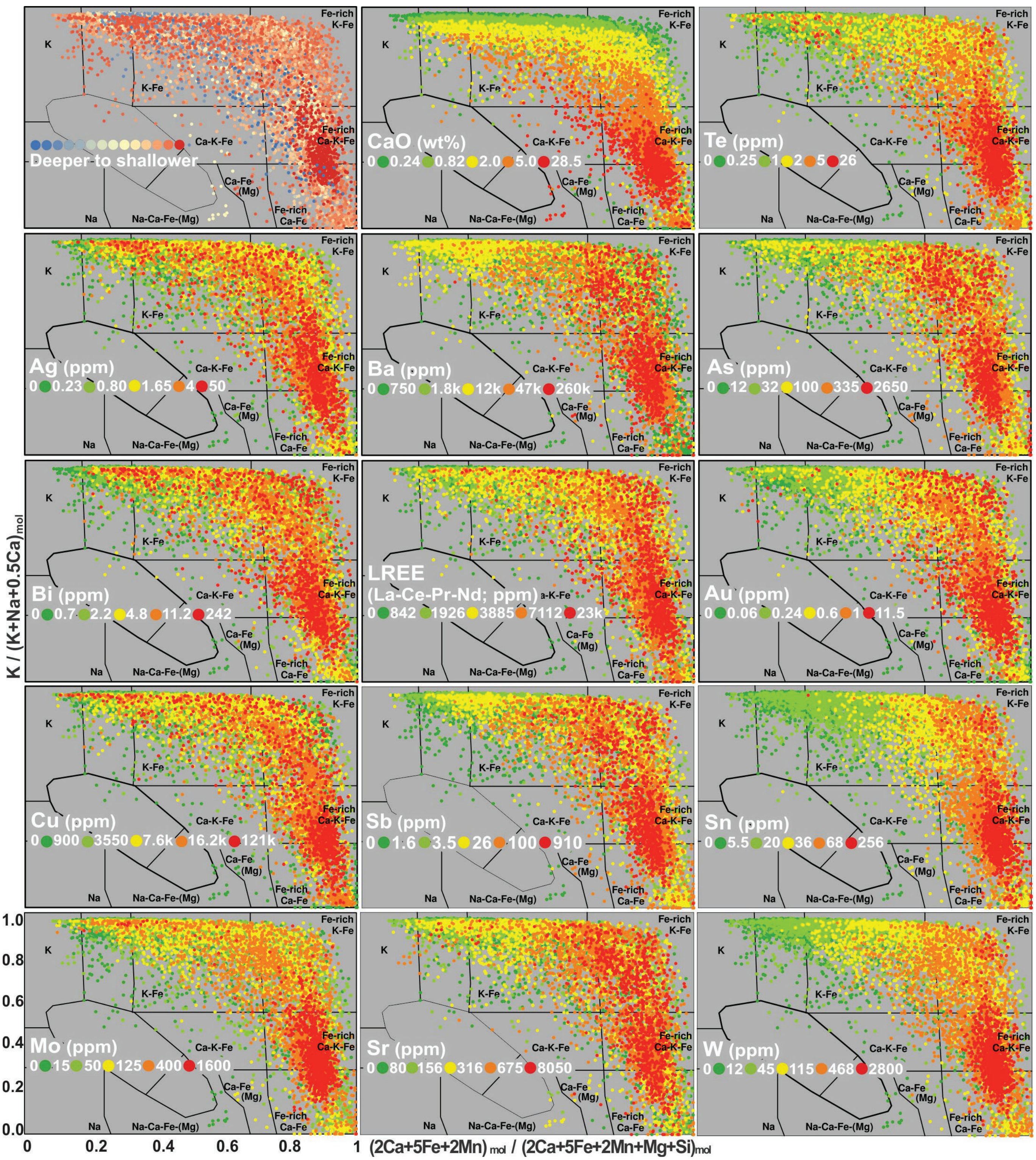


**Figure 17.** Distribution of sample depths and of Ag, Au, As, Ba, Bi, CaO, Cu, LREE, Mo, Sb, Sn, Sr, Te, and W contents in the ODBC. The data are plotted on the AIOCG diagram of Montreuil et al. (2013). Element contents mostly exceed average upper crustal values, even in their lowest range (upper crust contents in ppm: Ag, 0.053; As, 4.8; Au, 0.0015; Ba, 628; Bi, 0.16; Ca, 25661; Cu, 28; Mo, 1.1; Sb, 0.4; Sn, 2.1; Sr, 320; Te, 0.027; W, 1.9; Hu and Gao, 2008; Rudnick and Gao, 2014). Metal-rich samples that plot in the Fe-rich Ca-Fe field largely reflect the presence of fluorite, not carbonate or HT Ca-Fe alteration; however, fluorine content was not available in the processed dataset. Element contents are plotted dark green to red following a percentile distribution (0–25; 25–50, 50–70, 70–90, 90–100).

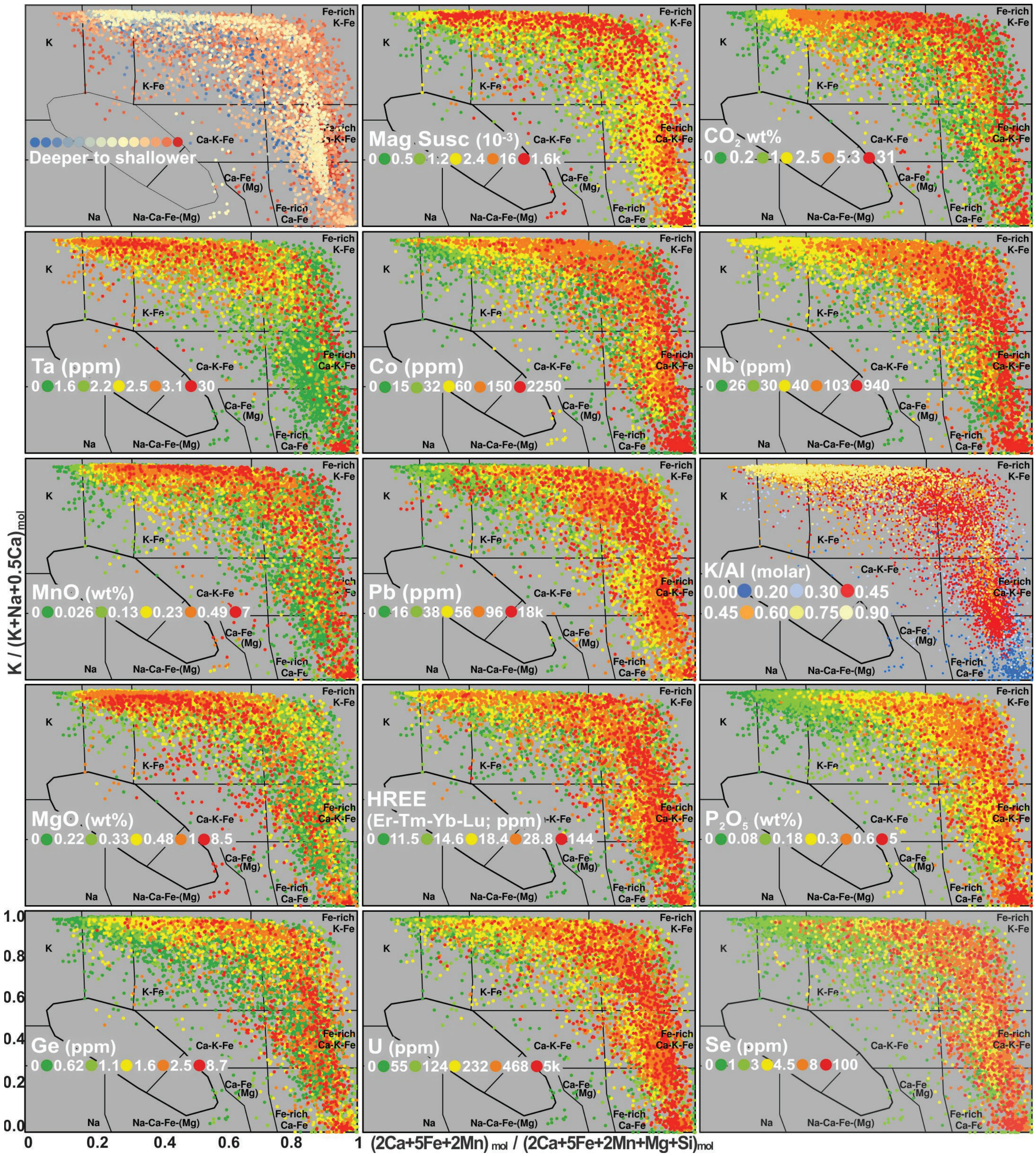


**FIGURE 18.** Distribution of Co, $CO_2$, Ge, HREE, MgO, MnO, Nb, $P_2O_5$, Pb, Se, Ta, and U contents, depths, K/Al ratios and magnetic susceptibilities in the ODBC. The data are plotted on the AIOCG diagram of Montreuil et al. (2013). Mid-depth samples are highlighted to illustrate that the most magnetite-rich samples (high susceptibility samples) occur at depth to mid-depth in the deposit. Most element contents exceed average upper crustal values except for their lowest ranges (average upper crust contents in ppm: C, 940; Co, 17.3; Ge, 1.4; Nb, 12; Pb, 17; Se, 0.09; Ta, 0.9; U, 2.7; Hu and Gao, 2008; Rudnick and Gao, 2014). Element contents are plotted dark green to red following a percentile distribution (0–25; 25–50, 50–70, 70–90, 90–100).

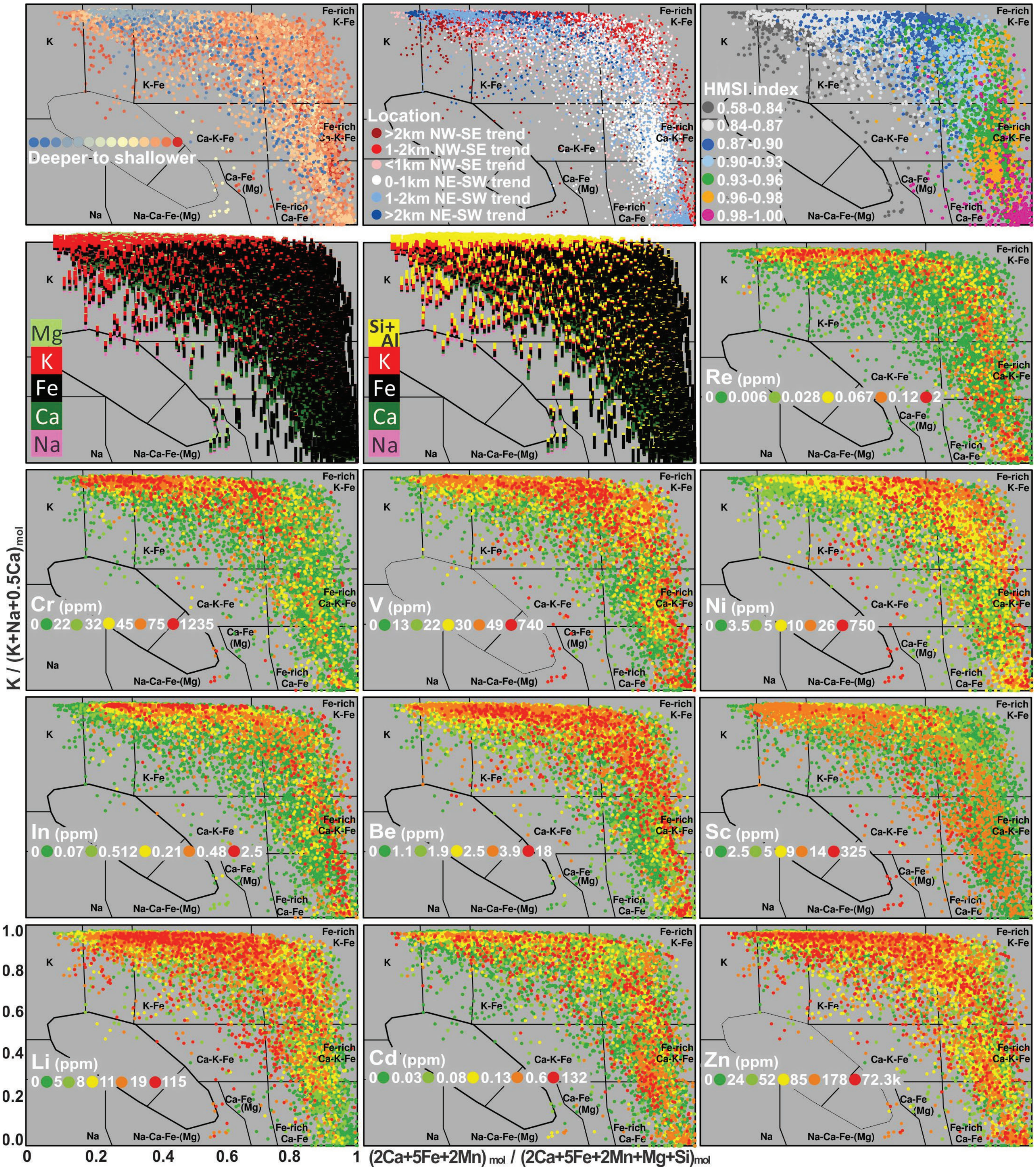


**FIGURE 19.** Distribution of Be, Cd, Cr, In, Li, Ni, Re, Sc, V, and Zn contents, depth, location and HMSI index (= (Fe+Si)/(Fe+Si +Al)) of samples from the ODBC. The element contents are plotted on the AIOCG diagram of Montreuil et al. (2013). The abundance of many elements is mostly below average upper crustal values except for Re (average upper crust contents in ppm: Be, 2.1; Cd, 0.09; Cr, 92; In, 0.056; Li, 24; Ni, 47; Re, 0.000198; Sc, 14; V, 97; Zn, 67; Hu and Gao, 2008; Rudnick and Gao, 2014). Element contents are plotted dark green to red following a percentile distribution (0–25; 25–50, 50–70, 70–90, 90–100).

The rare earth elements substitute for other elements within phosphate and carbonate minerals such as in apatite, bastnaesite, monazite and xenotime (Fig. 20B). These two mineral groups represent the main carriers of REE within igneous (carbonatite, alkaline complex, pegmatite), hydrothermal (IOCG, skarn), or secondary/sedimentary (heavy metal sands, laterite, tailings, shale-hosted, alluvial/placer) REE deposits (Weng et al., 2013). Bastnaesite from the Weishan and Mountain Pass deposits are characterized by highly fractionated REE patterns, with a high enrichment in LREE (Fig. 20B). Apatite from the IOA Minneville and Cheever deposits in the Eastern Adirondack Mountain district of the Grenville Province (USA) share the slightly fractionated REE pattern of IOA deposits but display highly variable REE contents (Fig. 20A, B).

The metasomatic evolution of the host IOAA system seems to play an important role in REE precipitation within IOA deposits. The consecutive alteration facies of GBMZ and Kwyjibo IOAA systems display regular relative enrichments or depletions with respect to least-altered rocks and earlier or subsequent alteration facies while commonly sharing a similar pattern. Samples of the HT Ca-Fe facies are systematically the most enriched. Samples that plot within the HT Ca-K-Fe field of the AIOCG diagram follow but include many composite samples of HT Ca-Fe alteration and potassium-bearing overprints that plot within the HT Ca-K-Fe field (Fig. 20E). Composite samples reflecting a mixture of host and REE-mineralized veins at Kwyjibo (Fig. 20D) are more enriched than true HT Ca-K-Fe altered rocks from the GBMZ (Fig. 20F). The HT K and HT K-Fe alteration are slightly

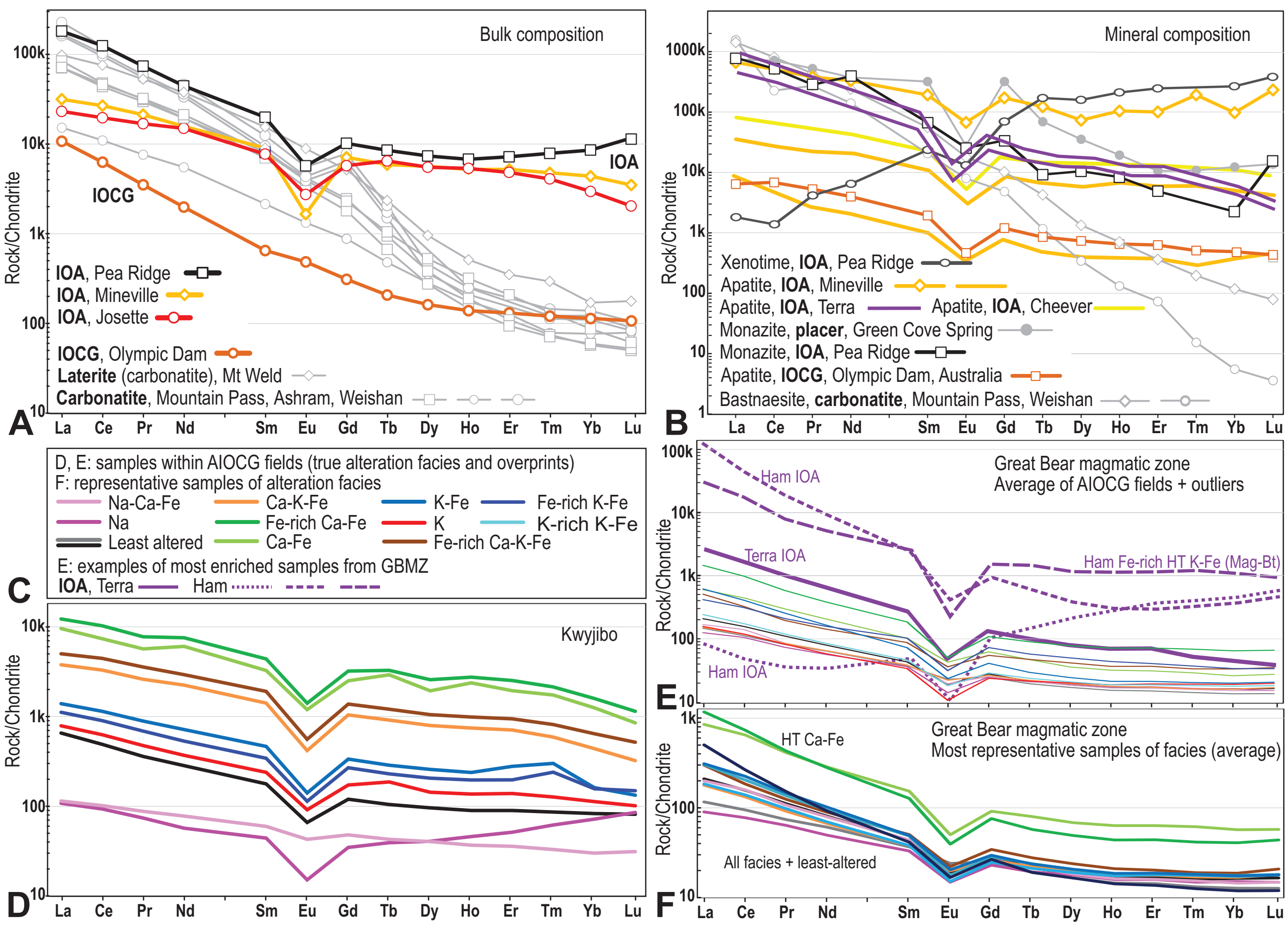


**Figure 20.** Rare earth element patterns of representative REE deposits, alteration facies and REE-bearing minerals within REE deposits. **A.** Comparison between the REE patterns of the Josette (Canada; Magrina et al., 2005; Perreault and Artinian, 2013), Pea Ridge (USA; Day et al., 2016a), Mineville (USA) IOA deposits, Olympic Dam (Australia) IOCG deposit, the Mountain Pass (USA), Asharm (Canada) and Weishan (China) carbonatite deposits and the Mt Weld (Australia) laterite deposit derived from carbonatite (Weng et al., 2013; Taylor et al., 2019). **B.** Comparison between the REE patterns of apatite from the Mineville and Cheever IOA deposit, USA (Roedder et al., 1987; Castor, 2008; Lupulescu et al., 2017), monazite from the Green Cove Spring placer deposit, USA (Hedrick, 2003), bastnaesite from the Mountain Pass (USA) and Weishan (China) carbonatite deposits (Castor, 1986; Olinger, 2019; Wang et al., 2019; Jia and Liu, 2020) and apatite from the Olympic Dam deposit (Krneta et al., 2018) and the Terra mine in the GBMZ (Normandeau, 2018). **C–F.** Comparison of REE patterns for each alteration facies (Kwyjibo district and GBMZ systems; data from Perreault and Artinian, 2013; Corriveau et al., 2015). Legend for D to F is in C. In D and E the patterns are derived from averages of samples within AIOCG diagrams and as such also include samples with overprints. In F, least-altered volcanic rocks with mafic compositions and with intermediate and felsic compositions are plotted in grey and black respectively.

enriched relative to least-altered rocks but less enriched than HT Ca-Fe alteration and IOA deposits (Fig. 20C–F). Sodic altered rocks are depleted in REE relative to least-altered rocks (Fig. 20D–F).

Samples from recrystallized IOA mineralization at the Ham IOA prospect and other prospects along the reactivated eastern margin of the GBMZ systematically show significant HREE enrichment with variable REE patterns with respect to the average most intense HT Ca-Fe altered samples from the GBMZ whereas the non metamorphosed Terra mine IOA mineralization is enriched with respect to average HT Ca-Fe and shares a similar pattern (Fig. 20E).

As systems evolve, iron becomes increasingly associated with potassium, forming Facies 2–3 HT Ca-K-Fe alteration. Critical metals (Co and variable As, Au, Bi, Ni and Cu contents; Table 1; Figs. 12, 15) may precipitate up to one or two orders of magnitude greater than values observed in other facies, as illustrated by the NICO deposit (Fig. 21A; Blein et al., 2022). The REE, including HREE, Sb, Se, Te and W are also variably enriched (Fig. 21A). At the NICO deposit, Sb, Se and Te are enriched in bismuth leach residues (R. Goad, pers. comm., 2021).

At Facies 3 HT K-Fe alteration, potassium becomes the main cation associated with iron (±remaining calcium) and copper precipitates to form magnetite-group IOCG mineralization. Other variants include uranium-rich or cobalt-rich mineralization with or without abundant copper and precious metals. Enrichments are observed in Ag, Au, Co, Cu, Pd, Pt, and U and to a lesser extent in Ba, Bi, C, Cl, F, Fe, K, Mo, Mn, P, Rb, REE including variable HREE, S, Sb, Te, Th, V, and W.

As the system progresses to Facies 5 LT K-Fe and LT Ca-Mg-Fe-(K) alteration, iron, potassium and variable calcium and magnesium precipitates. Potassium-iron dominant assemblages lead to copper-sulphide mineralization within hematite-group IOCG deposits and iron-oxide poor variants. Iron-dominant assemblages can form gold-, gold-cobalt- or uranium-rich mineralization with or without other metals like copper. Mineralization includes variable concentrations of Ag, Au, Bi, Co, Cu, LREE, Mo, Pb, Re, U and Zn and lesser As, Ba, C, Cd, F, Fe, K, Mn, P, S, Sb, Sn, Te and W contents (Figs. 16–19, 21B). Atypical iron-poor polymetallic mineralization significantly enriched in gold or critical metals forms in some systems (e.g. Mount Dore, Merlin and Tick Hill deposits in Australia; Babo et al., 2017; Williams et al., 2005). Subsequent fluid circulation within IOAA systems can enrich the original metal endowment as illustrated by Ehrig et al. (2021) for the uranium mineralization at the Olympic Dam deposit.

*Comparison of IOAA Systems with Other Types of Systems*

Chemical differences exist between alteration facies characteristic of IOAA systems and those formed in VMS, SEDEX, epithermal or porphyry systems (Figs. 22, 23). Some of these differences are diagnostic of IOAA systems and can be used to discriminate them from systems forming other deposit types when interpreting large lithogeochemical datasets. Publically available analytical data for representative metasomatites from VMS, porphyry, epithermal, IOAA and SEDEX hydrothermal systems are plotted on the Large et al. (2001) 'alteration box plot' diagram and on the Montreuil et al. (2013) AIOCG diagram (Figs. 22, 23). Each sample is represented by its Na-Ca-Fe-Mg and Na-Ca-Fe-K-([Si+Al]/10) barcodes on the alteration plots to aid the interpretation of chemical trends and the cationic signature of each alteration system.

The 'alteration box plot' of Large et al. (2001) uses the Ishikawa alteration index (AI; Ishikawa et al., 1976) on the horizontal axis and the chlorite-carbonate-pyrite index or CCPI (Large et al., 2001) on the vertical axis (AI and CCPI are defined in Fig. 22). The alteration index calibrates the intensity of sericitic and chloritic alteration of magmatic rocks based on the premise that the major-element composition of altered volcanic and plutonic rocks reflects the degree of alteration and is a useful guide to the proximity of ore. In the AIOCG diagram of Montreuil et al. (2013), the vertical axis discriminates between sodic and potassic alteration facies, whereas the horizontal axis discriminates alkali and silica-rich alteration from Ca-Fe, K-Fe, and Fe-rich alteration facies (Fig. 23). The distinct indices in the diagrams thus provide a large spectrum of information from geochemical datasets.

These diagrams illustrate the extensive iron enrichment and relative absence of silica in the iron-rich alteration facies of IOAA systems (Figs. 10A, B, 22, 23; Blein et al., 2022). The prevalence, diversity and spatiotemporal abundance of iron-dominant alteration facies with low silica contents is the most striking difference between alteration in IOAA systems and alteration in VMS, SEDEX, epithermal and porphyry systems, and is diagnostic of IOAA systems. Although late-stage quartz veins may overprint IOAA facies and artificially inflate the proportion of silica in barcodes (if sampling has not avoided such veins), the barcodes are generally diagnostic and can be interpreted separately, as done in Figures 3, 10 and 11.

Iron-rich alteration in IOAA systems may be genetically associated with polymetallic mineralization but can be spatially coupled or decoupled from such mineralization. In IOAA systems such as the GBMZ, high $Fe_2O_{3t}$ contents ($Fe_2O_{3t}$ contents >20 wt%) are restricted to CCPI values >80, with no specific AI values (Fig. 22). In VMS, porphyry and epithermal deposits, iron-dominant alteration facies are minor to absent, except in mineralized zones in which iron-rich alteration is commonly associated with silica addition. In felsic- and mafic-$Fe_2O_{3t}$ contents >20 wt% are restricted to AI values >40, and CCPI values >90 (Fig. 22). Unlike IOAA systems, typical porphyry and epithermal deposits lack $Fe_2O_{3t}$ contents >20 wt% (Fig. 22).

On the AIOCG diagram, large lithogeochemical datasets from IOAA systems (magnetite- or hematite-group IOCG) include numerous samples that plot in the iron-rich K-Fe, Ca-K-Fe and Ca-Fe fields (Figs. 10A, B, 23). Intense alteration of the ODBC defines a prograde metasomatic path from K, K-Fe to iron-rich facies alteration (Fig. 10A, B). Such prograde metasomatic paths associated with significant iron

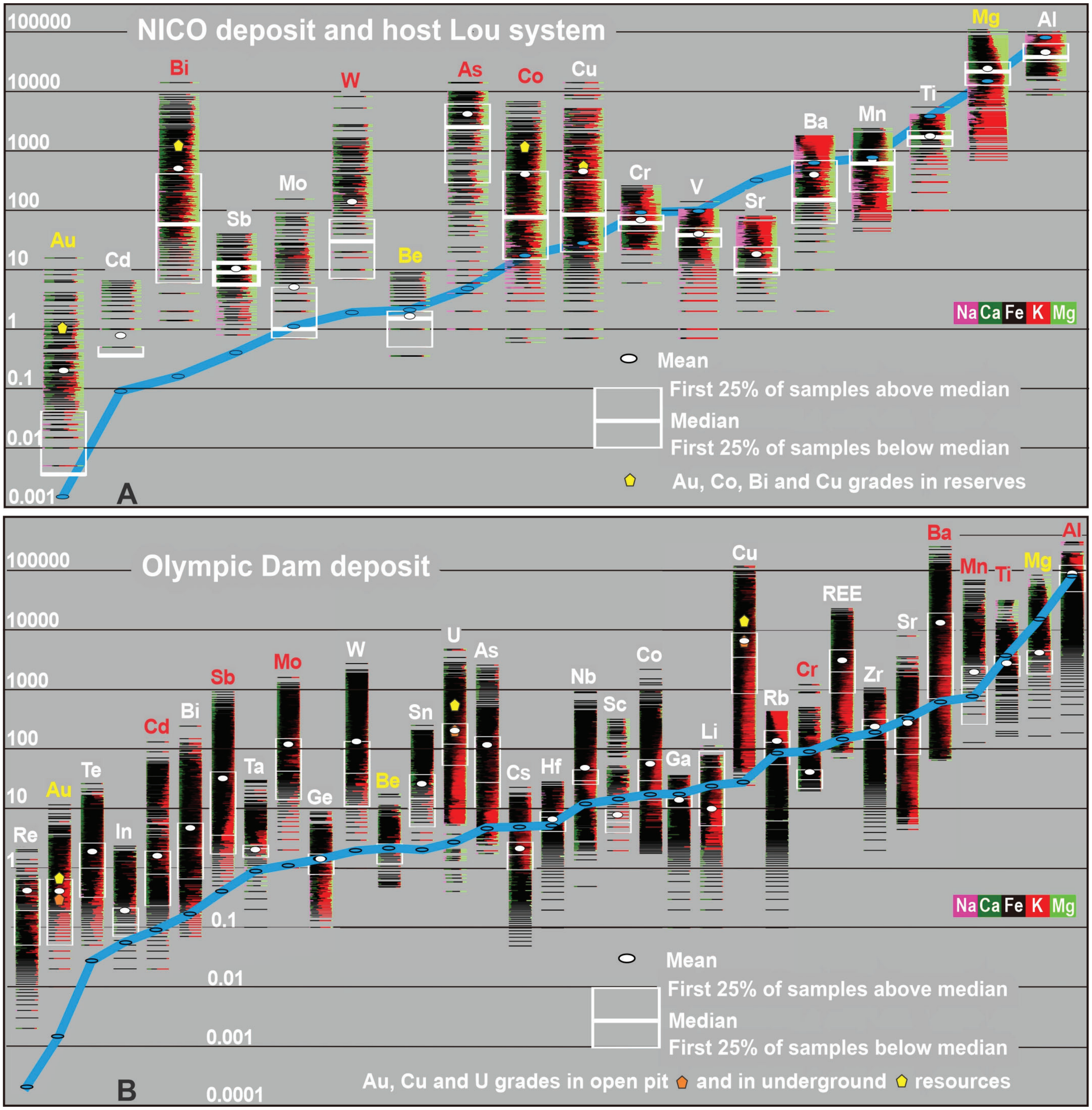


**FIGURE 21.** Metal contents (in ppm) of a suite of samples from the Lou IOAA system, including the NICO deposit, and the Olympic Dam deposits compared to bulk continental crust (blue line; Hu and Gao, 2008; Rudnick and Gao, 2014) following a USGS methodology (A. Hofstra, pers. comm., 2021). **A.** Samples of metasomatites and mineralized zones from the Lou IOAA system, including from the Au-Co-Bi-Cu NICO deposit, the albitite-hosted uranium mineralization of the Southern Breccia, the Chalco and Summit Peak IOCG prospects and non mineralized outcrops across the system. Data is compiled from Corriveau et al. (2015) and Mumin (1997). For the NICO deposit, the dataset includes 1996 drill cores (96-01–06, 96-11, 96-13, 96-16, 96-17, 96-24, 96-25, 96-30) and representative geochemical samples selected from the muck piles across the ore zone. The mean and the median is representative of the entire system and is thus not representative of the metal contents in the NICO deposit alone. **B.** Samples from the Olympic Dam deposit. Elements highlighted in red, yellow and white are those significantly enriched compared to bulk continental crust but those in red are much more enriched in one of the two deposits and those in yellow are enriched in both deposits. The molar Na-Ca-Fe-K-Mg barcode is shown for each sample below each element to highlight how metal contents and metal associations evolve from one facies to the next. Resources in Burgess et al. (2014) and BHP (2020). In A, tungsten is in red as Goad et al. (2000) report an early indicated tungsten resource of 0.02% and up to 2% W over 2 m in drill cores.

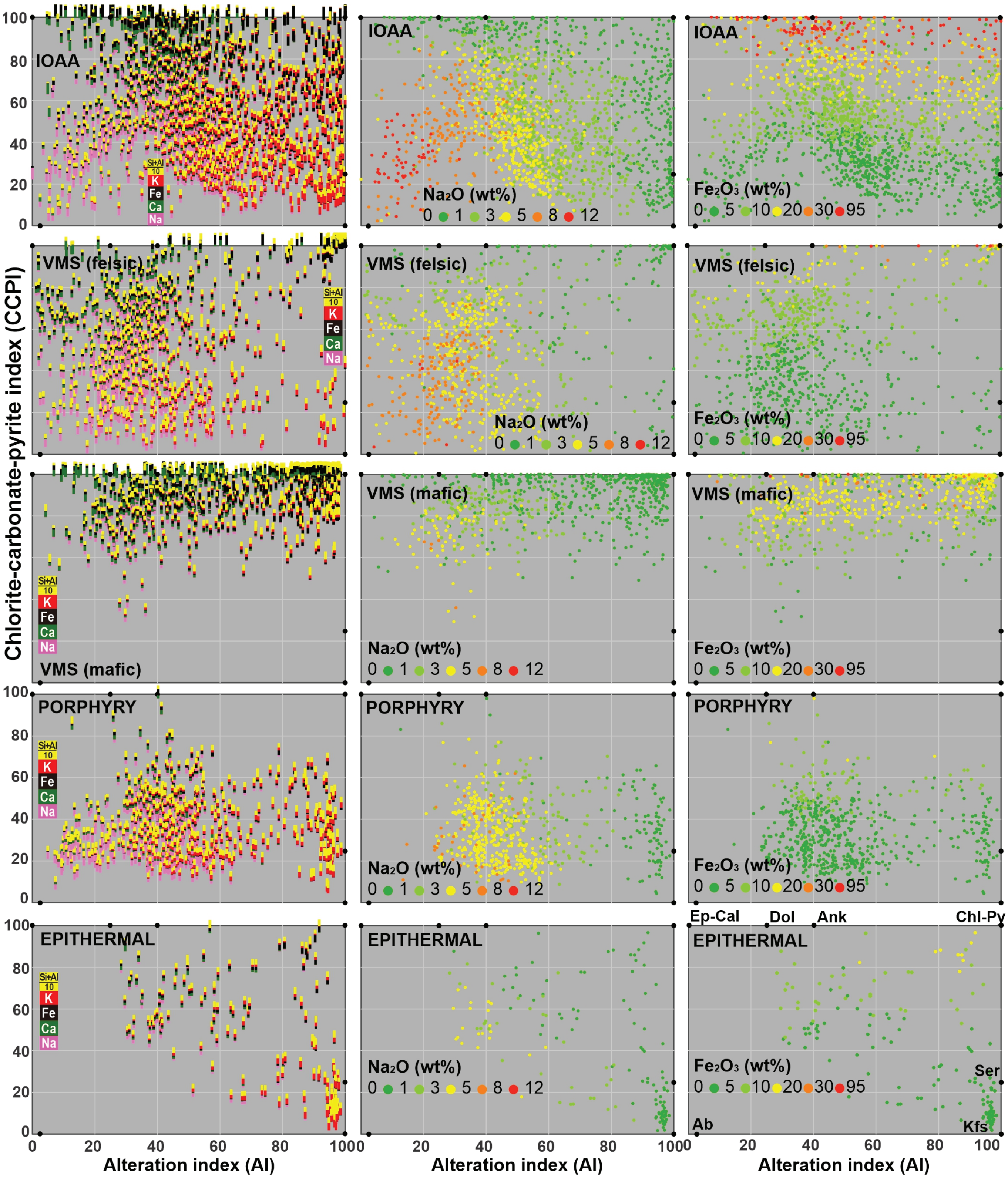


**Figure 22.** Chemical footprint of alteration zones from selected deposit types and host systems on the AI versus CCPI diagram of Large et al. (2001). The left column portrays the Na-Ca-Fe-K-([Si+Al]/10) molar barcodes, whereas the central and right-hand columns illustrate sample distributions based on $Na_2O$ and $Fe_2O_3$ contents, respectively. IOAA: iron oxide and alkali-calcic alteration systems using the Great Bear magmatic zone dataset (Corriveau et al., 2015). VMS (felsic): Archean VMS from Australia (Hollis et al., 2015). VMS (mafic): Paleoproterozoic Lalor VMS (Caté et al., 2017). Porphyry: Dilles et al. (2000) and Du Bray et al. (2007). Epithermal: Warren et al. (2007). AI = 100($K_2O$+MgO) / ($K_2O$+MgO+$Na_2O$+CaO). CCPI = 100(MgO+FeO) / (MgO+FeO+$Na_2O$+$K_2O$).

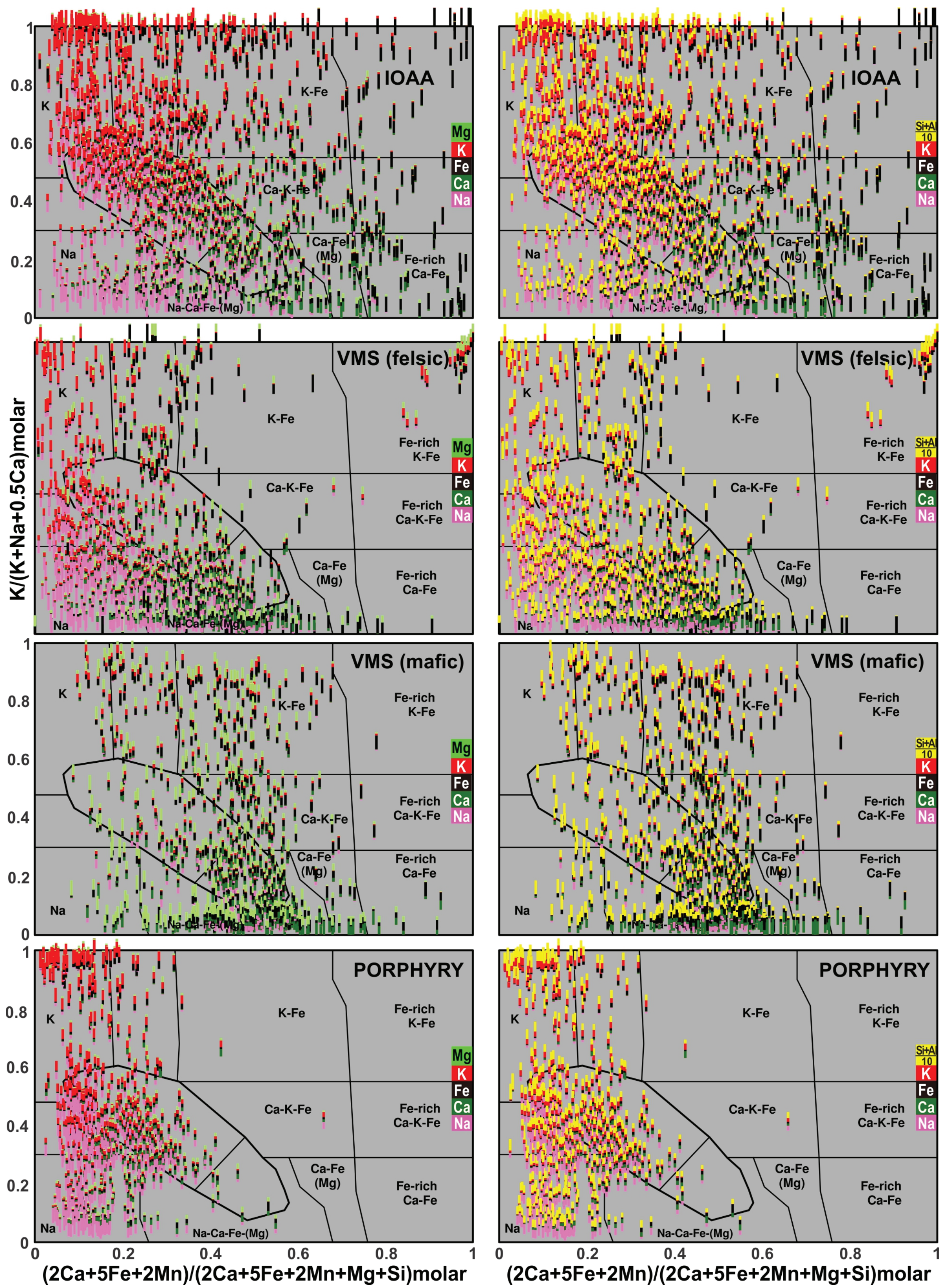


**FIGURE 23.** Chemical footprints of VMS, porphyry and IOAA systems on the AIOCG diagram of Montreuil et al. (2013). Plots on the left side, represented by the Na-Ca-Fe-K-Mg barcodes, highlight the coupled Fe and K enrichment in IOAA systems and the higher proportions of Mg in VMS and porphyry systems. Plots on the right side, represented by the Na-Ca-Fe-K-([Si+Al]/10) barcodes, highlight the higher proportions of Si in VMS and porphyry systems. Differences between VMS, porphyry and IOAA systems are further illustrated by comparing them with the footprint of the Olympic Dam deposit in Figure 10A, B. Sources of data listed in Figure 22.

enrichment are not observed in VMS, porphyry and epithermal systems. Rather, in these hydrothermal systems, altered facies are restricted to the left side of the AIOCG diagram, and exhibit large proportions of Mg, Si, Al and K in their barcodes due to chloritization, silicification, and potassic alteration, respectively (Fig. 23).

Albitization is common and regional in scale in some VMS and orogenic gold systems, and is common at depth in porphyry systems (Witt, 1992; Brauhart et al., 1998; Alt, 1999; Lipske and Dilles, 2000; Eilu et al., 2007). Samples plot within the Na field but the $Na_2O$ content of the most altered host rocks (e.g. Archean felsic-hosted VMS deposits) rarely exceeds 8 wt% (Fig. 23). Albitite is absent in Paleoproterozoic mafic-hosted VMS deposits (Fig. 23). In contrast to VMS, porphyry, epithermal and orogenic gold systems, IOAA systems form regional-scale corridors of albitite in which host rocks are intensely sodic-altered regardless of their composition and mineralogy (e.g. mafic to felsic rocks or siliciclastic to impure carbonate units). In such rocks, the albitite (also called ‘albitophyre’ in some papers) commonly contains 8 to 12 wt% $Na_2O$ (Fig. 22; Marschik et al., 1997; Oliver et al., 2004; Cuney et al., 2012; Corriveau et al., 2015; Sparkes, 2017).

The molar barcodes of samples in the respective datasets demonstrate that cation associations in potassic and silica-aluminum bearing alteration facies of IOAA systems are also distinct from typical VMS, epithermal or porphyry deposits (Fig. 22). In the Large et al. (2001) alteration index diagram, intensely potassic-altered rocks in VMS, epithermal and porphyry deposits are characterized by Na-Ca-Fe-K-[(Si+Al)/10] barcodes with high silica-aluminum proportions (Fig. 22). In IOAA systems, potassic alteration is not typically associated with silicification, but rather with iron enrichment, although the Si+Al component within the barcodes may locally attain similar high values (Fig. 23). Barcodes with (Si + Al)/10 in lieu of Mg molar proportions also help identify samples containing mineralized quartz, carbonate and fluorite veins, and to assess the proper alteration facies of the mineralization.

## Conclusions

Large geochemical datasets from the GBMZ and Australian case studies (Cloncurry district, Olympic Dam deposit and Punt Hill deposit) have been processed using the Montreuil et al. (2013) AIOCG diagram and interpreted within the IOAA framework of Corriveau et al. (2010b, 2016, 2022b) and Blein et al. (2022). The distribution of major and trace elements on the AIOCG diagram illustrates the element depletion and enrichment patterns of each alteration facies and associated mineralization within IOAA mineral systems. This visual lithogeochemical method employing regional geochemical datasets helps assess the IOAA potential of a district. In addition, the critical metal contents of higher- versus lower-temperature deposit types were contrasted by comparing the metal endowment of the NICO and Olympic Dam deposits with average continental crustal values. This comparison provides further insights into the exceptional critical-metal endowments of IOAA systems, as described by Skirrow et al. (2013).

Early and commonly deep-seated Na to Na-Ca-Fe alteration leads to precipitation of sodium in albite and leaching of most other elements, although Th, Ti and Zr may be variably enriched. High-temperature Ca-Fe alteration (or skarn development within carbonate units) may be enriched in Ca, Co, Fe, Mg, Ni, P, V, Sn, and in some cases W, Th, U and REE. As the system evolves to the HT Ca-K-Fe facies, As, Au and Co are regularly enriched whereas Bi, Cu, Ni, REE and W are variably enriched. At the HT K-Fe facies, polymetallic mineralization with copper sulphides may include enrichments in many elements, although Ag, Au, Co, Cu, Pd, Pt, and U are most enriched compared to bulk continental crustal values. The K-skarn facies is characterized by local mineralized zones containing variable Cu, Zn, Pb, Ag, Mo and W, as observed at the Mile Lake prospect in the GBMZ. As alteration systems evolve to the LT K-Fe and LT Ca-Mg-Fe facies, mineralized zones again include variable enrichment in many elements; however, Ag, Au, Ba, Bi, Co, Cu, F, LREE, Mo, Pb, Re, U, and Zn are most enriched compared to bulk continental crust.

Plotting the molar proportion barcodes on the AIOCG diagram also provides a clear visual means of distinguishing IOAA systems from other ore systems. Although the IOAA data from the Great Bear magmatic zone overlaps other deposit types on the AI versus CCPI diagram of Large et al. (2001) (Fig. 22), IOAA systems are distinct on the AIOCG diagram (Fig. 23). Characteristic features include extreme enrichment in iron and to a lesser degree in potassium, whereas alteration associated with VMS deposits hosted by felsic rocks lack Ca-Fe and K-rich alteration and also have higher proportions of silica. VMS deposits associated with mafic rocks lack potassium- and sodium-rich alteration, while containing greater proportions of magnesium and silica. Finally, porphyry systems lack the extreme iron enrichment and Ca-Fe alteration, and exhibit molar barcodes with greater proportions of silica and potassium.

## Acknowledgments

This research of the Hydrothermal Ore System project of the Targeted Geoscience Initiative (Natural Resources Canada) furthers earlier research under the Geomapping for Energy and Minerals (Great Bear-IOCG project). Fieldwork in the Northwest Territories that supported the acquisition of the vast geochemical dataset for the GBMZ was conducted in collaboration with the Northwest Territories Geological Survey, Fortune Minerals Limited, Alberta Star Development Corporation, Hunter Bay Minerals, Diamonds North, Tłı̨chǫ Government with particular thanks to E. Erasmus, B. Black and K. Garner, Sahtu Government, Déline̜ Land Corporation, Déline̜ Renewable Resource Council with a particular thank-you to Edward Reeves, Wek’èezhìi Land and Water Board, Polar Continental Shelf Program and Community Government of Gamèti with particular thanks to E. Williah, D. Apple, C. Gon, C. Arrowmaker and J. Mantla. Many graduate and undergraduate students, and industry, university and government colleagues from across Canada generously contributed time, effort, logistical infrastructures or funding for this research, in particular GBMZ field crew graduate and undergraduate students, including P. Acosta-Góngora, V. Boulanger-Martel, A. De Toni, C. Fontaine, L.-P. Gélinas, M. Lee, P. Normandeau, G. Robinson, and S. Simard.

The authors thank Erin Adlakha, Paul Duuring, Michael Gadd, Vladimir Lisitsin and Nicolas Piette-Lauzière for their thorough review of the manuscript and Reginald Wilson, editor of the Geological Association of Canada, for his thorough editing of the manuscript prior to publication. The authors also thank BHP-Olympic Dam for providing geochemical data from the Olympic Dam deposit and some prospects and deposits from the region to publish this research. Datasets from DEMCo, the Denendeh Exploration and Mining Company, also contributed to our understanding of the geochemical footprints of the mineral systems in the Camsell River district (NWT, Canada) and to the dataset of Figure 4d. We thank Darrell Beaulieu and Colin Bowdidge for providing us with DEMCo's datasets and Roman Hanes for processing and conducting the QA-QC of the geochemical data for Figure 4d. This is NRCan/EMS contribution 20200578.

## References

Acosta-Góngora, P., and Potter, E.G., 2018, Preliminary geochemical characterization of the Central Mineral Belt uranium geochemistry database, *in* Rogers, N., ed., Targeted Geoscience Initiative: 2017 report of activities: Geological Survey of Canada, Open File 8373, p. 57-63.

Acosta-Góngora, P., Gleeson, S., Samson, I., Corriveau, L., Ootes, L., Taylor, B.E., Creaser, R.A., and Muehlenbachs, K., 2015, Genesis of the Paleoproterozoic NICO iron-oxide-cobalt-gold-bismuth deposit, Northwest Territories, Canada: evidence from isotope geochemistry and fluid inclusions: Precambrian Research, v. 268, p. 168-193.

Aleinikoff, J.N., Selby, D., Slack, J.F., Day, W.C., Pillers, R.M., Cosca, M.A., Seeger, C.M., Fanning, C.M., and Samson, I.M., 2016, U-Pb, Re-Os, and Ar/Ar geochronology of REE-rich breccia pipes and associated host rocks from the Mesoproterozoic Pea Ridge Fe-REE-Au deposit, St. Francois Mountains, Missouri, *in* Slack, J., Corriveau, L. and Hitzman, M., eds., Proterozoic iron oxide-apatite (± REE) and iron oxide-copper-gold and affiliated deposits of Southeast Missouri, USA, and the Great Bear magmatic zone, Northwest Territories, Canada: Economic Geology, v. 111, p. 1883-1914.

Alt, J.C., 1999, Hydrothermal alteration and mineralization of oceanic crust: mineralogy, geochemistry and processes: Reviews in Economic Geology, v. 8, p. 133-155.

Apukhtina, O.B., Kamenetsky, V.S., Ehrig, K., Kamenetsky, M.B., Maas, R., Thompson, J., McPhie, J., Ciobanu, C.L., and Cook, N.J., 2017, Early, deep magnetite-fluorapatite mineralization at the Olympic Dam Cu-U-Au-Ag deposit, South Australia: Economic Geology, v. 112, p. 1531-1542.

Austrade, 2020, Australian critical minerals prospectus: Australian Trade and Investment Commission (Austrade), available at www.austrade.gov.au.

Babo, J., Spandler, C., Oliver, N., Brown, M., Rubenach, M., and Creaser, R.A., 2017, The high-grade Mo-Re Merlin deposit, Cloncurry district, Australia: paragenesis and geochronology of hydrothermal alteration and ore formation: Economic Geology, v. 112, p. 397-422.

Barton, M.D., 2014, Iron oxide(–Cu–Au–REE–P–Ag–U–Co) systems, *in* Holland, H.D. and Turekian, K.K., eds., Treatise on geochemistry, second edition, v. 13: Elsevier, p. 515-541.

Bennett, V., and Rivers, T., 2006, U-Pb ages of zircon primary crystallization and inheritance for magmatic rocks of the southern Wopmay Orogen, Northwest Territories: Northwest Territories Geoscience Office, NWT Open Report 2006-006, 64 p.

BHP, 2019, Annual report 2019: available at www.bhp.com

BHP, 2020, Annual report 2020: available at www.bhp.com

Blein, O., Corriveau, L., Montreuil, J.-F., Ehrig, K., Fabris, A., Reid, A., and Pal, D., 2022, Geochemical signatures of metasomatic ore systems hosting IOCG, IOA, albite-hosted uranium and affiliated deposits: a tool for process studies and mineral exploration, *in* Corriveau, L., Potter, E.G. and Mumin, A.H., eds., Mineral systems with iron oxide copper-gold (IOCG) and affiliated deposits: Geological Association of Canada, Special Paper 52, p. 263-298.

Bowdidge, C., and Dunford, A., 2015, Camsell River property, Northwest Territories, 86E09 and 86F12: Northwest Territories Geological Survey, Assessment Report 033952, 73 p.

Bowdidge, C., Walker, E.C., and Dunford, A., 2014, DEMCo LTD. report on 2014 exploration Camsell River property, NTS 86E09, 86F12, Northwest Territories: Northwest Territories Geological Survey, Assessment Report 033596, 110 p.

Brauhart, C.W., Groves, D.L., and Morant, P., 1998, Regional alteration systems associated with volcanogenic massive sulfide mineralization at Panorma, Pilbara, Western Australia: Economic Geology, v. 93, p. 292-302.

Burgess, H., Gowans, R.M., Hennessey, B.T., Lattanzi, C.R., and Puritch, E., 2014, Technical report on the feasibility study for the NICO gold–cobalt–bismuth–copper deposit, Northwest Territories, Canada: Fortune Minerals Ltd., NI 43-101 Technical Report No. 1335, 385 p., available at www.sedar.com.

Castor, S.B., 1986, Mountain Pass bastnasite: some new data: Technical Report, Mountain Pass, Molycorp, CA, 6 p.

Castor, S., 2008, Rare earth deposits of North America: Resource Geology, v. 58, p. 337-347.

Caté, A., Mercier-Langevin, P., Ross, P.S., Bécu, V., Lauzière, K., Hannington, M., and Dubé, B., 2017, Whole-rock lithogeochemistry of the Lalor auriferous VMS deposit, Manitoba, Canada: Geological Survey of Canada, Open File 8107, 3 p.

Centaurus Metals Limited, 2021, The Jaguar nickel sulphide project value-add scoping study, executive summary, May 2021, available at www.centaurus.com.au.

Cherry, A., Ehrig, K., Kamenetsky, V.S., McPhie, J., Crowley, J., and Kamenetsky, M., 2018, Precise geochronological constraints on the origin, setting and incorporation of ca. 1.59 Ga surficial facies into the Olympic Dam Breccia Complex, South Australia: Precambrian Research, v. 315, p. 162-168.

Chinalco Yunnan Copper Resources, 2010, Inferred resource estimate – Elaine-Dorothy uranium – rare earth element (REE): ASX/Media Announcement 24 March 2010.

Chinalco Yunnan Copper Resources, 2012a, 26.1 Mt inferred JORC resource estimate Elaine 1 copper-gold deposit: ASX/Media Announcement 29 June 2012.

Chinalco Yunnan Copper Resources, 2012b, CYU and GSE update on high grade uranium in NW Queensland: ASX/Media Announcement 25 October 2012.

Chinova Resources, 2014a, Merlin molybdenum / rhenium project, 2014, available at www.chinovaresources.com.

Chinova Resources, 2014b, Mount Dore copper deposit, resource estimate: as at September, 2014: Technical report prepared by Chinova Resources, 110 p., available at www.chinovaresources.com.

Chinova Resources, 2017, Mount Elliott Swan resource estimation update summary, available at www.chinovaresources.com.

Clark, J.M., 2014, Defining the style of mineralisation at the Cairn Hill magnetite-sulphide deposit, Mount Woods Inlier, Gawler Craton, South Australia: Unpublished B.Sc. (Hons.) thesis, University of Adelaide, 69 p.

Clark, J.M., and Ehrig, K., 2019, What controls high-grade copper mineralisation at Olympic Dam?: The Australasian Institute of Mining and Metallurgy: Melbourne, 11th International Mining Geology Conference 2019 Proceedings, p. 222-236.

Clark, J.M., Ehrig, K., Poznik, N., Cherry, A., McPhie, J., and Kamenetsky, V.S., 2018, Syn to post mineralization structural dismemberment of the Olympic Dam Fe oxide Cu-U-Au-Ag deposit: Society of Economic Geologist Conference Poster, Denver Co, available at https://www.researchgate.net/publication/338169039.

Clark, J.M., Passmore, M., and Poznik, N., 2019, Olympic Dam rock quality designation model – an integrated approach: AusIMM Tenth International Mining Geology conference proceedings, September 20, 2017.

Clark, T., 2003, Métallogénie des métaux usuels, précieux et énergétiques, et des éléments des terres rares, région de Manitou-Wakeham, Moyenne-Côte-Nord, *in* Brisebois, D. and Clark, T., Synthèse géologique et métallogénique de la partie est de la Province de Grenville: Ministère des Ressources naturelles, Québec, DV 2002-03, p. 269-326.

Clark, T., Gobeil, A., and David, J., 2005, Iron oxide-Cu-Au-type and related mineralization in the Manitou Lake area, Grenville Province, Quebec: variations in composition and alteration style, *in* Corriveau, L. and Clark, T., eds., The Grenville Province: a geological and mineral resources perspective derived from government and academic research initiatives: Canadian Journal of Earth Sciences, v. 42, p. 1829-1847.

Clark, T., Gobeil, A., and Chevé, S., 2010, Alterations in IOCG-type and related deposits in the Manitou Lake area, Eastern Grenville Province, Québec, *in* Corriveau, L. and Mumin, A.H., eds., Exploring for iron oxide copper–gold deposits: Canada and global analogues: Geological Association of Canada, Short Course Notes, No. 20, p. 127-146.

Corriveau, L., 1989, Potassic alkaline plutonism in the southwestern Grenville Province: Unpublished Ph.D. thesis, McGill University, 263 p.

Corriveau, L., 2013, Architecture de la ceinture métasédimentaire centrale au Québec, Province de Grenville : un exemple de l'analyse de terrains de métamorphisme élevé: Geological Survey of Canada, Bulletin 586, 264 p.

Corriveau, L., Heaman, L.M., Marcantonio, F., and van Breemen, O., 1990, 1.1 Ga K-rich alkaline plutonism in the southwestern Grenville Province - U-Pb constraints for the timing of subduction-related magmatism: Contributions to Mineralogy and Petrology, v. 105, p. 473-485.

Corriveau, L., Mumin, A.H., and Setterfield, T., 2010a, IOCG environments in Canada: characteristics, geological vectors to ore and challenges, *in* Porter, T.M., ed., Hydrothermal iron oxide copper-gold and related deposits: a global perspective, v. 4: PGC Publishing, Adelaide, p. 311-344.

Corriveau, L., Williams, P.J., and Mumin, A.H., 2010b, Alteration vectors to IOCG mineralization – from uncharted terranes to deposits, *in* Corriveau, L. and Mumin, A.H., eds., Exploring for iron oxide copper-gold deposits: Canada and global analogues: Geological Association of Canada, Short Course Notes, No. 20, p. 89-110.

Corriveau, L., Nadeau, O., Montreuil, J.-F., and Desrochers, J.-P., 2014, Report of activities for the Core Zone: strategic geomapping and geoscience to assess the mineral potential of the Labrador Trough for multiple metals IOCG and affiliated deposits, Canada: Geological Survey of Canada, Open File 7714, 12 p.

Corriveau, L., Lauzière, K., Montreuil, J.-F., Potter, E.G., Hanes, R., and Prémont, S., 2015, Dataset of geochemical data from iron oxide alkali-altered mineralizing systems of the Great Bear magmatic zone (NWT): Geological Survey of Canada, Open File 7643, 19 p., 6 geochemical datasets.

Corriveau, L., Montreuil, J.-F., and Potter, E.G., 2016, Alteration facies linkages among IOCG, IOA and affiliated deposits in the Great Bear magmatic zone, Canada, *in* Slack, J., Corriveau, L. and Hitzman, M., eds., Proterozoic iron oxide-apatite (± REE) and iron oxide-copper-gold and affiliated deposits of Southeast Missouri, USA, and the Great Bear magmatic zone, Northwest Territories, Canada: Economic Geology, v. 111, p. 2045-2072.

Corriveau, L., Potter, E., Acosta-Góngora, P., Blein, O., Montreuil, J.-F., De Toni, A.F., Day, W.C., Slack, J.F., and Ayuso, R.A., 2017, Petrological mapping and chemical discrimination of alteration facies as vectors to IOA, IOCG, and affiliated deposits within Laurentia and beyond: Proceedings of the 14th SGA Biennial Meeting, 20-23 August 2017, Québec City, p. 851-855.

Corriveau, L., Blein, O., Gervais, F., Trapy, P.H., De Souza, S., and Fafard, D., 2018a, Iron-oxide and alkali-calcic alteration, skarn and epithermal mineralizing systems of the Grenville Province: the Bondy gneiss complex in the Central Metasedimentary Belt of Quebec as a case example - a field trip to the 14th Society for Geology Applied to Mineral Deposits (SGA) biennial meeting: Geological Survey of Canada, Open File 8349, 136 p. doi.org/10.4095/311230.

Corriveau, L., Potter, E.G., Montreuil, J.-F., Blein, O., Ehrig, K., and De Toni, A., 2018b, Iron-oxide and alkali-calcic alteration ore systems and their polymetallic IOA, IOCG, skarn, albitite-hosted U±Au±Co, and affiliated deposits: a short course series. Part 2: overview of deposit types, distribution, ages, settings, alteration facies, and ore deposit models: Geological Survey of Canada, Scientific Presentation 81, 154 p. doi.org/10.4095/306560.

Corriveau, L., Potter, E.G., Montreuil, J.-F., Blein, O., Ehrig, K., and Fabris, A., 2020, Alteration facies of IOA, IOCG and affiliated deposits: understanding the similarities, recognising the diversity in these ore systems. Geological Survey of South Australia, GSSA Iron Oxide - Copper-Gold Mineral Systems Workshop 2019, 77 p. http://www.energymining.sa.gov.au/__data/assets/pdf_file/0004/358708/REDCorriveau_IOCGworkshop_Alteration_Final.pdf.

Corriveau, L., Montreuil, J.-F., De Toni, A.F., Potter, E.G., and Percival, J.B., 2022a, Mapping mineral systems with IOCG and affiliated deposits: a facies approach, *in* Corriveau, L., Potter, E.G. and Mumin, A.H., eds., Mineral systems with iron oxide copper-gold (IOCG) and affiliated deposits: Geological Association of Canada, Special Paper 52, p. 69-111.

Corriveau, L., Montreuil, J.-F., Potter, E.G., Blein, O., and De Toni, A.F., 2022b, Mineral systems with IOCG and affiliated deposits: part 3 – metal pathways and ore deposit model, *in* Corriveau, L., Potter, E.G. and Mumin, A.H., eds., Mineral systems with iron oxide copper-gold (IOCG) and affiliated deposits: Geological Association of Canada, Special Paper 52, p. 205-245.

Corriveau, L., Montreuil, J.-F., Potter, E.G., Ehrig, K., Clark, J., Mumin, A.H., and Williams, P.J., 2022c, Mineral systems with IOCG and affiliated deposits: part 1 – metasomatic footprints of alteration facies, *in* Corriveau, L., Potter, E.G. and Mumin, A.H., eds., Mineral systems with iron oxide copper-gold (IOCG) and affiliated deposits: Geological Association of Canada, Special Paper 52, p. 113-158.

Corriveau, L., Mumin, A.H., and Potter, E.G., 2022d, Mineral systems with iron oxide copper-gold (Ag-Bi-Co-U-REE) and affiliated deposits: introduction and overview, *in* Corriveau, L., Potter, E.G. and Mumin, A.H., eds., Mineral systems with iron oxide copper-gold (IOCG) and affiliated deposits: Geological Association of Canada, Special Paper 52, p. 1-26

Creaser, R.A., 1989, The geology and petrology of Middle Proterozoic felsic magmatism of the Stuart Shelf, South Australia: Unpublished Ph.D. thesis, La Trobe University, Melbourne, Australia.

Cudeco, 2017, 2017 annual report, available at www.cudeco.com.au.

Cuney, M., Emetz, A., Mercadier, J., Mykchaylov, V., Shunko, V., and Yuslenko, A., 2012, Uranium deposits associated with Na-metasomatism from central Ukraine: a review of some of the major deposits and genetic constraints: Ore Geology Reviews, v. 44, p. 82-106.

Daliran, F., Stosch, H.-G., Williams, P.J., Jamali, H., and Dorri, M.-B., 2022, Early Cambrian IOA-REE, U-Th and Cu(Au)-Bi-Co-Ni-Ag-As-sulphide deposits of the Bafq district, East-Central Iran, *in* Corriveau, L., Potter, E.G. and Mumin, A.H., eds., Mineral systems with iron oxide copper-gold (IOCG) and affiliated deposits: Geological Association of Canada, Special Paper 52, p. 409-424.

Davidson, G.J., Paterson, H., Meffre, S., and Berry, R.F., 2007, Characteristics and origin of the Oak Dam East breccia-hosted, iron oxide-Cu-U-(Au) deposit: Olympic Dam region, Gawler Craton, South Australia: Economic Geology, v. 102, p. 1471-1498.

Davis, W.J., Corriveau, L., van Breemen, O., Bleeker, W., Montreuil, J.-F., Potter, E.G., and Pelleter, E., 2011, Timing of IOCG mineralizing and alteration events within the Great Bear magmatic zone, *in* Fischer, B.J. and Watson, D.M., compilers, 39th annual Yellowknife Geoscience Forum: Northwest Territories Geoscience Office, Abstract Volume 2011, p. 97.

Day, W.C., Granitto, M., Slack, J.F., and Ayuso, R.A., 2016a, Geochemical data and classification scheme for outcrop and drill core samples from Mesoproterozoic rocks and iron-oxide deposits and prospects of Southeast Missouri: U.S. Geological Survey Data Release, ScienceBase, available at: http://dx.doi.org/10.5066/F7P26W67.

Day, W.C., Slack, J.F., Ayuso, R.A., and Seeger, C.M., 2016b, Regional geologic and petrologic framework for iron oxide ± apatite ± rare earth element and iron oxide copper-gold deposits of the Mesoproterozoic St. Francois Mountains Terrane, Southeast Missouri, USA, *in* Slack, J., Corriveau, L. and Hitzman, M., eds., Proterozoic iron oxide-apatite (± REE) and iron oxide-copper-gold and affiliated deposits of Southeast Missouri, USA, and the Great Bear magmatic zone, Northwest Territories, Canada: Economic Geology, v. 111, p. 1825-1858.

De Toni, A.F., 2016, Les paragénèses à magnétite des altérations associées aux systèmes à oxydes de fer et altérations en éléments alcalins, zone magmatique du Grand lac de l'Ours: Unpublished M.Sc. thesis, Institut national de la Recherche scientifique, 534 p.

Dilles, J.H., Einaudi, M.T., Proffett, J., and Barton, M.D., 2000, Overview of the Yerington porphyry copper district: magmatic to nonmagmatic sources of hydrothermal fluids, their flow paths, alteration affects on rocks, and Cu-Mo-Fe-Au ores, *in* Dilles, J.H., Barton, M.D., Johnson, D.A., Proffett, J., Einaudi, M.T. and Crafford, E.J., eds., Part I. Contrasting styles of intrusion-associated hydrothermal systems; part II. Geology & gold deposits of the Getchell region: Society of Economic Geologists Guidebook Series, v. 32, p. 55-66.

Dmitrijeva, M., Ehrig, K.J., Ciobanu, C.L., Cook, N.J., Verdugo-Ihl, M.R., and Metcalfe, A.V., 2019, Defining IOCG signatures through compositional data analysis: a case study of lithogeochemical zoning from the Olympic Dam deposit, South Australia: Ore Geology Reviews, v. 105, p. 86-101.

Du Bray, E.A., Ressel, M.W., and Barnes, C.G., 2007, Geochemical database of intrusive rocks of north-central and northeastern Nevada: USGS, Data Series 244.

Ehrig, K., McPhie, J., and Kamenetsky, V.S., 2012, Geology and mineralogical zonation of the Olympic Dam iron oxide Cu-U-Au-Ag deposit, South Australia, *in* Hedenquist, J.W., Harris, M. and Camus, F., eds., Geology and genesis of major copper deposits and districts of the world: a tribute to Richard H. Sillitoe: Economic Geology Special Publication 16, p. 237-267.

Ehrig, K., Kamenetsky, V.S., McPhie, J., Apukhtina, O., Ciobanu, C.L., Cook, N., Kontonikas-Charos, A., and Krneta, S., 2017a, The IOCG-IOA Olympic Dam Cu-U-Au-Ag deposit and nearby prospects, South Australia: Proceedings of the 14th SGA Biennial Meeting, 20-23 August 2017, Québec City, p. 823-827.

Ehrig, K., Kamenetsky, V.S., McPhie, J., Apukhtina, O., Cook, N., and Ciobanu, C.L., 2017b, Olympic Dam iron oxide Cu-U-Au-Ag deposit, *in* Phillips, G.N., ed., Australian ore deposits: The Australasian Institute of Mining and Metallurgy, v. 32, Melbourne, p. 601-610.

Ehrig, K., Kamenetsky, V.S., McPhie, J., Macmillan, E., Thompson, J., Kamenetsky, M., and Maas, R., 2021, Staged formation of the supergiant Olympic Dam uranium deposit, Australia: Geology, v. 49, doi.org/10.1130/G48930.1.

Eilu, P., Pankka, H., Keinänen, V., Kortelainen, V., Niiranen, T., and Pulkkinen, E., 2007, Characteristics of gold mineralization in the greenstone belts of northern Finland: Geological Survey of Finland, Special Paper 44, p. 57-106.

Emsbo, P., Lawley, C., and Czarnota, K., 2021, Geological surveys unite to improve critical mineral security: Eos, 102.

Fabris, A., 2022, Geochemical characteristics of IOCG deposits from the Olympic Copper-Gold Province, South Australia, *in* Corriveau, L., Potter, E.G. and Mumin, A.H., eds., Mineral systems with iron oxide copper-gold (IOCG) and affiliated deposits: Geological Association of Canada, Special Paper 52, p. 247-262.

Fabris, A., Katona, L., Gordon, G., Reed, G., Keeping, T., Gouthas, G., and Swain, G., 2018a, Characterisation and mapping of Cu–Au skarn systems in the Punt Hill region, Olympic Cu–Au Province: MESA Journal, v. 87, p. 15-27.

Fabris, A., Katona, L., Gordon, G., Reed, G., Keeping, T., Gouthas, G., and Swain, G., 2018b, Characterising and mapping alteration in the Punt Hill region: a data integration project: Department of the Premier and Cabinet, South Australia, Adelaide, Report Book 2018/00010, 604 p.

Ferguson, M.R.M., Ehrig, K., Meffre, S., and Cherry, A.R., 2020, Associations between zircon and Fe–Ti oxides in Hiltaba event magmatic rocks, South Australia: atomic- or pluton-scale processes?: Australian Journal of Earth Sciences, v. 67, p. 201-220.

Ferreira Filho, C.F., Ferraz de Oliveira, M.M., Mansur, E.T., and Rosa, W.D., 2021, The Jaguar hydrothermal nickel sulfide deposit: evidence for a nickel-rich member of IOCG-type deposits in the Carajás Mineral Province, Brazil: Journal of South American Earth Sciences, v. 111, 103501.

Fortier, S.M., Nassar, N.T., Lederer, G.W., Brainard, J., Gambogi, J., and McCullough, E.A., 2019, Draft critical mineral list—summary of methodology and background information—U.S. Geological Survey technical input document in response to secretarial order No. 3359: U.S. Geological Survey, Open-File Report 2018–1021, 26 p.

Foster, A.R., Williams, P.J., and Ryan, C.G., 2007, Distribution of gold in hypogene ore at the Ernest Henry iron oxide copper-gold deposit, Cloncurry district, NW Queensland: Exploration and Mining Geology, v. 16, p. 125-143.

Fraser, R.D., and Giroux, G.H., 2009, The Anna Lake uranium project, Central Mineral Belt, Labrador, Canada: NI 43-101 Technical Report, 94 p.

Freeman, H., and Tomkinson, M., 2010, geological setting of iron oxide related mineralisation in the Southern Mount Woods Domain, South Australia, *in* Porter, T.M., ed., Hydrothermal iron oxide copper-gold and related deposits: a global perspective, v. 3: PGC Publishing, Adelaide, p. 171-191.

Gagnon, R., Buro, Y.A., Ibrango, S., Gagnon, D., Stapinsky, M., Del Carpio, S., and Larochelle, E., 2018, Projet de terres rares Kwyjibo: Rapport technique NI 43-101 révisé, 292 p.

Gandhi, S.S., Mortensen, J.K., Prasad, N., and van Breemen, O., 2001, Magmatic evolution of the southern Great Bear continental arc, northwestern Canadian Shield: geochronological constraints: Canadian Journal of Earth Sciences, v. 38, p. 767-785.

Gandhi, S.S., Potter, E.G., and Fayek, M., 2018, New constraints on genesis of the polymetallic veins at Port Radium, Great Bear Lake, Northwest Canadian Shield: Ore Geology Reviews, v. 96, p. 28-47.

Gauthier, M., Chartrand, F., Cayer, A., and David, J., 2004, The Kwyjibo Cu-REE-U-Au-Mo-F property, Quebec: a Mesoproterozoic polymetallic iron oxide deposit in the Northeastern Grenville Province: Economic Geology, v. 99, p. 1177-1196.

Glencore, 2020, Resources and reserves as at 31 December 2019, available at https://www.glencore.com/

Goad, R.E., Mumin, A.H., Duke, N.A., Neale, K.L., and Mulligan, D.L., 2000, Geology of the Proterozoic iron oxide-hosted NICO cobalt-gold-bismuth, and Sue-Dianne copper-silver deposits, southern Great Bear Magmatic Zone, Northwest Territories, Canada, *in* Porter, T.M., ed., Hydrothermal iron oxide copper-gold and related deposits: a global perspective, v. 1: PGC Publishing, Adelaide, p. 249-267.

Gromet, L.P., Haskin, L.A., Korotev, R.L., and Dymek, R.F., 1984, The North American shale composite: its compilation, major and trace element characteristics: Geochimica et Cosmochimica Acta, v. 48, p. 2469-2482.

Harlov, D.E., Meighan, C.J., Kerr, I.D., and Samson, I.M., 2016, Mineralogy, chemistry, and fluid-aided evolution of the Pea Ridge Fe oxide- (Y + REE) deposit, Southeast Missouri, USA: Economic Geology, v. 111, p. 1963-1984.

Hayward, N., and Corriveau, L., 2014, Fault reconstructions using aeromagnetic data in the Great Bear magmatic zone, Northwest Territories, Canada: Canadian Journal of Earth Sciences, v. 51 p. 1-16.

Hayward, N., Corriveau, L., Craven, J.A., and Enkin, R.J., 2016, Geophysical signature of alteration and mineralisation envelope at the Au-Co-Bi-Cu NICO deposit, NT, Canada, *in* Slack, J., Corriveau, L. and Hitzman, M., eds., Proterozoic iron oxide-apatite (± REE) and iron oxide-copper-gold and affiliated deposits of Southeast Missouri, USA, and the Great Bear magmatic zone, Northwest Territories, Canada: Economic Geology, v. 111, p. 2087-2110.

Hedrick, J.B., 2003, Rare earths: US Geological Survey, Minerals Yearbook 2003, p. 60.1-60.15.

Hennessey, B.T., and Puritch, E., 2008, A technical report on a mineral resource estimate for the Sue-Dianne deposit, Mazenod Lake area, Northwest Territories, Canada: Fortune Minerals Limited, NI 43-101 Technical Report, 125 p., available at www.sedar.com.

Hildebrand, R.S., 1986, Kiruna-type deposits: their origin and relationship to intermediate subvolcanic plutons in the Great Bear Magmatic Zone, northwest Canada: Economic Geology, v. 81, p. 640-659.

Hildebrand, R.S., Hoffman, P.F., and Bowring, S.A., 1987, Tectonomagmatic evolution of the 1.9 Ga Great Bear Magmatic Zone, Wopmay Orogen, northwestern Canada: Journal of Volcanology and Geothermal Research, v. 32, p. 99-118.

Hildebrand, R.S., Hoffman, P.F., Housh, T., and Bowring, S.A., 2010, The nature of volcano-plutonic relations and shapes of epizonal plutons of continental arcs as revealed in the Great Bear magmatic zone, northwestern Canada: Geosphere, v. 6, p. 812-839.

Hildebrand, R.S., Bowring, S., and Pelleter, K.F., 2014, Calder River, map area: Geological Survey of Canada: Canadian Geoscience Map 154/ NWT Open Report 2013-03, 1 map sheet.

Hofstra, A., Lisitsin, V., Corriveau, L., Paradis, S., Peter, J., Lauzière, K., Lawley, C., Gadd, M., Pilote, J., Honsberger, I., Bastrakov, E., Champion, D., Czarnota, K., Doublier, M., Huston, D., Raymond, O., Van Der Wielen, S., Emsbo, P., Granitto, M., and Kreiner, D., 2021, Deposit classification scheme for the Critical Minerals Mapping Initiative Global Geochemical Database: U.S. Geological Survey Open-File Report 2021–1049, 60 p.

Hollis, S.P., Yeats, C.J., Wyche, S., Barnes, S.J., Ivanic, T.J., Belford, S.M., Davidson, G.J., Roache, A.J., and Wingate, M.T.D., 2015, A review of volcanic-hosted massive sulfide (VHMS) mineralization in the Archean Yilgarn Craton, Western Australia: tectonic, stratigraphic and geochemical associations: Precambrian Research, v. 260, p. 113-135.

Hu, Z., and Gao, S., 2008, Upper crustal abundances of trace elements: a revision and update: Chemical Geology, v. 253, p. 205-221.

Huang, Q., Kamenetsky, V.S., Ehrig, K., McPhie, J., Kamenetsky, M., Apukhtina, O., and Chambefort, I., 2017, Effects of hydrothermal alteration on mafic lithologies at the Olympic Dam Cu-U-Au-Ag deposit: Precambrian Research, v. 292, p. 305-322.

Huang, X.-W., Beaudoin, G., De Toni, A.-F., Corriveau, L., Makvandi, S., and Boutroy, E., 2022, Iron-oxide trace element fingerprinting of iron oxide copper-gold and iron oxide-apatite deposits: a review, *in* Corriveau, L., Potter, E.G. and Mumin, A.H., eds., Mineral systems with iron oxide copper-gold (IOCG) and affiliated deposits: Geological Association of Canada, Special Paper 52, p. 347-364.

Ishikawa, Y., Sawaguchi, T., Iwaya, S., and Horiuchi, M., 1976, Delineation of prospecting targets for Kuroko deposits based on modes of volcanism of underlying dacite and alteration haloes: Mining Geology, v. 26, p. 105-117.

Jackson, V.A., van Breemen, O., Ootes, L., Bleeker, W., Bennett, V., Davis, W.J., Ketchum, J., and Smar, L., 2013, Ages of basement and intrusive phases East of the Wopmay fault zone, south-central Wopmay Orogen, NWT: a field-based U–Pb zircon study: Canadian Journal of Earth Sciences, v. 50, p. 979-1006.

Jagodzinski, E.A., Reid, A., Crowley, J., McAvaney, S., and Wade, C., 2016, New CA-TIMS dates for the Gawler Range Volcanics: implications for the duration of volcanism: Geological Survey of South Australia, Report Book 2016/00032, p. 17-18.

Jia, Y.-H., and Liu, Y., 2020, REE enrichment during magmatic-hydrothermal processes in carbonatite-related REE deposits: a case study of the Weishan REE deposit, China: Minerals, v. 10, 25.

Jones, A.P., Genge, M., and Carmody, L., 2013, Carbonate melts and carbonatites: Review of Mineralogy and Geochemistry, v. 5, p. 289-322.

Kelly, C.J., Davis, W.J., Potter, E.G., and Corriveau, L., 2020, Geochemistry of hydrothermal tourmaline from IOCG occurrences in the Great Bear magmatic zone: implications for fluid source(s) and fluid composition evolution: Ore Geology Reviews, v. 118, 103329.

Kirschbaum, M.J., and Hitzman, M.W., 2016, Guelb Moghrein: an unusual carbonate-hosted iron oxide copper-gold deposit in Mauritania, northwest Africa: Economic Geology, v. 111, p. 763-770.

Kontonikas-Charos, K., Ciobanu, C.L., Cook, N.J., Ehrig, K., Krneta, S., and Kamenetsky, V.S., 2017, Feldspar evolution in the Roxby Downs Granite, host to Fe-oxide Cu-Au-(U) mineralisation at Olympic Dam, South Australia: Ore Geology Reviews, v. 80, p. 838-859.

Krneta, S., Ciobanu, C.L., Cook, N.J., and Ehrig, K.J., 2018, Numerical modeling of REE fractionation patterns in fluoroapatite from the Olympic Dam deposit (South Australia): Minerals, v. 8, 342.

Large, R.R., Gemmel, J.B., Paulick, H., and Huston, D.L., 2001, The alteration box plot: a simple approach to understanding the relationship between alteration mineralogy and lithogeochemistry associated with volcanic-hosted massive sulphide deposits: Economic Geology, v. 96, p. 957-971.

Lilly, R., Case, G., and Miller, B., 2017, Ernest Henry iron oxide copper-gold deposit, *in* Phillips, G.N., ed., Australian ore deposits, 6th edition: The Australasian Institute of Mining and Metallurgy, Monograph 32, p. 1-6.

Lipske, J.L., and Dilles, J.H., 2000, Advanced argillic and sericitic alteration in the subvolcanic environment of the Yerington porphyry copper district, Buckskin Range, Nevada: Society of Economic Geologists Guidebook Series 32, p. 91-99.

Lupulescu, M.V., Hughes, J.M., Chiarenzelli, J.R., and Bailey, D.G., 2017, Texture, crystal structure, and composition of fluorapatites from iron oxide-apatite (IOA) deposits, Eastern Adirondack Mountains, New York: The Canadian Mineralogist, v. 55, p. 399-417.

Madeisky, H.E., 1996, A lithogeochemical and radiometric study of hydrothermal alteration and metal zoning at the Cinola epithermal gold deposit, Queen Charlotte Islands, British Columbia, *in* Coyner, A.R. and Fahey, P.L., eds., Geology and ore deposits of the American Cordillera: Geological Society of Nevada, USA, v. 3, p. 1153-1185.

Magrina, B., Jébrak, M., and Cuney, M., 2005, Le magmatisme de la région de Kwyjibo, Province du Grenville (Canada): intérêt pour les minéralisations de type fer-oxydes associées, *in* Corriveau, L. and Clark, T., eds., The Grenville Province: a geological and mineral resources perspective derived from government and academic research initiatives: Canadian Journal Earth Science, v. 42, p. 1849-1864.

Magyarosi, Z., Baker, J., and MacKenzie, J., 2012, Data compilation and interpretation report, Fostung project, Ontario, Canada, available at http://www.geologyontario.mndm.gov.on.ca/mndmfiles/afri/data/imaging/20000008530/20013274.pdf

Mark, G., Oliver, N.H.S., Williams, P.J., Valenta, R.K., and Crookes, R.A., 2000, The evolution of the Ernest Henry Fe-oxide-(Cu-Au) hydrothermal system, *in* Porter, T.M., ed., Hydrothermal iron oxide copper-gold and related deposits: a global perspective, v. 1: PGC Publishing, Adelaide, p. 123-136.

Mark, G., Oliver, N.H.S., and Williams, P.J., 2006, Mineralogical and chemical evolution of the Ernest Henry Fe oxide-Cu-Au ore system, Cloncurry district, northwest Queensland, Australia: Mineralium Deposita, v. 40, p. 769-801.

Marschik, R., Singer, B.S., Munizaga, F., Tassinari, C., Moritz, R., and Fontboté, L., 1997, Age of Cu(-Fe)-Au mineralization and thermal evolution of the Punta del Cobre district, Chile: Mineralium Deposita, v. 32, p. 531-546.

Mauger, A.J., Ehrig, K., Kontonikas-Charos, A., Ciobanu, C.L., Cook, N.J., and Kamenetsky, V.S., 2016, Alteration at the Olympic Dam IOCG–U deposit: insights into distal to proximal feldspar and phyllosilicate chemistry from infrared reflectance spectroscopy: Australian Journal of Earth Sciences, v. 63, p. 959-972.

McGloin, M., Tomkins, A., and Weinberg, R., 2013, Isan U and Th mobility and related ore mineralisation: Proceedings of the 12th Biennial SGA meeting, Upsala, Sweden, 4 p.

McMartin, I., Corriveau, L., and Beaudoin, G., 2011, An orientation study of the heavy mineral signature of the NICO Co-Au-Bi deposit, Great Bear magmatic zone, Northwest Territories, Canada: Geochemistry: Exploration, Environment, Analysis, v. 11, p. 293-307.

Montreuil, J.-F., Corriveau, L., and Grunsky, E.C., 2013, Compositional data analysis of IOCG systems, Great Bear magmatic zone, Canada: to each alteration types its own geochemical signature: Geochemistry: Exploration, Environment, Analysis, v. 13, p. 229-247.

Montreuil, J.-F., Corriveau, L., and Potter, E.G., 2015, Formation of albitite-hosted uranium within IOCG systems: the Southern Breccia, Great Bear magmatic zone, Northwest Territories, Canada: Mineralium Deposita, v. 50, p. 293-325.

Montreuil, J.-F., Corriveau, L., and Davis, W., 2016a, Tectonomagmatic evolution of the southern Great Bear magmatic zone (Northwest Territories, Canada) – Implications on the genesis of iron oxide alkali-altered hydrothermal systems, *in* Slack, J., Corriveau, L. and Hitzman, M., eds., Proterozoic iron oxide-apatite (± REE) and iron oxide-copper-gold and affiliated deposits of Southeast Missouri, USA, and the Great Bear magmatic zone, Northwest Territories, Canada: Economic Geology, v. 111, p. 2111-2138.

Montreuil, J.-F., Corriveau, L., Potter, E.G., and De Toni, A.F., 2016b, On the relation between alteration facies and metal endowment of iron oxide–alkali-altered systems, southern Great Bear magmatic zone (Canada), *in* Slack, J., Corriveau, L. and Hitzman, M., eds., Proterozoic iron oxide-apatite (± REE) and iron oxide-copper-gold and affiliated deposits of Southeast Missouri, USA, and the Great Bear magmatic zone, Northwest Territories, Canada: Economic Geology, v. 111, p. 2139-2168.

Montreuil, J.-F., Potter, E., Corriveau, L., and Davis, W.J., 2016c, Element mobility patterns in magnetite-group IOCG systems: the Fab IOCG system, Northwest Territories, Canada: Ore Geology Reviews, v. 72, p. 562-584.

Morgan, J.A., and Giroux, G.H., 2008, Form 43-101 technical report on the Central Mineral Belt (CMB) uranium project, Labrador, Canada: NI 43-101 Technical report, 237 p.

Morrissey, L.J., and Tomkins, A.G., 2020, Evaporite-bearing orogenic belts produce ligand-rich and diverse metamorphic fluids: Geochimica et Cosmochimica Acta, v. 275, p. 163-187.

Mumin, A.H., 1997, A qualifying report on the geology and mineralization of the NICO 1 (F28905), NICO 2 (F28906), NICO 3 (F50933), NICO 4 (F18965), NICO 5 (F18966), NICO 6 (F50155), NICO 7 (F50156), NICO 8 (F50157), NICO 9 (F50158), NICO 10 (F50159), NICO 11 (F51389), NICO 12 (F51390) claims, Marian River area, Mackenzie (South) District, Northwest Territories, Canada: Northwest Territories Geoscience Office, Assessment Report 084202, 61 p.

Mumin, A.H., Corriveau, L., Somarin, A.K., and Ootes, L., 2007, Iron oxide copper-gold-type polymetallic mineralisation in the Contact Lake Belt, Great Bear magmatic zone, Northwest Territories, Canada: Exploration and Mining Geology, v. 16, p. 187-208.

Mumin, A.H., Somarin, A.K., Jones, B., Corriveau, L., Ootes, L., and Camier, J., 2010, The IOCG-porphyry-epithermal continuum of deposits types in the Great Bear Magmatic Zone, Northwest Territories, Canada, *in* Corriveau, L. and Mumin, A.H., eds., Exploring for iron oxide copper-gold deposits: Canada and global analogues: Geological Association of Canada, Short Course Notes, No. 20, p. 59-78.

Mumin, A.H., Phillips, A., Katsuragi, C.J., Mumin, A., and Ivanov, G., 2014, Geotectonic interpretation of the Echo Bay stratovolcano complex, northern Great Bear magmatic zone, NWT, Canada: Northwest Territories Geoscience Office, NWT Open File 2014-04.

Natural Resources Canada, 2021, Canada's list of critical minerals, available at https://www.nrcan.gc.ca/criticalminerals.

Neymark, L.A., Holm-Denoma, C.S., Pietruszka, A.J., Aleinikoff, J.N., Fanning, C.M., Pillers, R.M., and Moscati, R.J., 2016, High spatial resolution U-Pb geochronology and Pb isotope geochemistry of magnetite-apatite ore from the Pea Ridge iron oxide-apatite deposit, St. Francois Mountains, southeast Missouri, USA, *in* Slack, J., Corriveau, L. and Hitzman, M., eds., Proterozoic iron oxide-apatite (± REE) and iron oxide-copper-gold and affiliated deposits of Southeast Missouri, USA, and the Great Bear magmatic zone, Northwest Territories, Canada: Economic Geology, v. 111, p. 1915-1933.

Normandeau, P., 2018, Drift prospecting applied to iron oxide alkali-altered systems and iron oxide copper-gold deposits in the Great Bear magmatic zone, Northwest Territories, Canada: Unpublished Ph.D. thesis, McGill University, Montréal, 226 p.

Nuelle, L.M., Day, W.C., Sidder, G.B., and Seeger, C.M., 1992, Geology and mineral paragenesis of the Pea Ridge iron ore mine, Washington County, Missouri — origin of the rare-earth-element- and gold-bearing breccia pipes, *in* Day, W.C. and Lane, D.E., eds., Strategic and critical minerals in the Midcontinent region: U.S. Geological Survey Bulletin 1989-a, p. A1-A11.

Olinger, D.A., 2019, Carbonatite whole-rock and calcite geochemistry from the Bear Lodge alkaline complex, Wyoming and Mountain Pass mine, California: U.S. Geological Survey data release, available at https://doi.org/10.5066/P9634NRU.

Oliver, N.H.S., Pearson, P.J., Holcombe, R.J., and Ord, A., 1999, Mary Kathleen metamorphic–hydrothermal uranium–rare-earth element deposit: ore genesis and numerical model of coupled deformation and fluid flow: Australian Journal of Earth Sciences, v. 46, p. 467-484.

Oliver, N.H.S., Mark, G., Pollard, P.J., Rubenach, M.J., Bastrakov, E., Williams, P.J., Marshall, L.C., Baker, T., and Nemchin, A.A., 2004, The role of sodic alteration in the genesis of iron oxide-copper-gold deposits: geochemistry and geochemical modelling of fluid-rock intereaction in the Cloncurry district, Australia: Economic Geology, v. 99, p. 1145-1176.

Oliver, N.H.S., Butera, K.M., Rubenach, M.J., Marshall, L.J., Cleverley, J.S., Mark, G., Tullemans, F., and Esser, D., 2008, The protracted hydrothermal evolution of the Mount Isa Eastern Succession: a review and tectonic implications: Precambrian Research, v. 163, p. 108-130.

Ootes, L., Davis, W.J., Jackson, V.A., and van Breemen, O., 2015, Chronostratigraphy of the Hottah terrane and Great Bear magmatic zone of Wopmay Orogen, Canada, and exploration of a terrane translation model: Canadian Journal of Earth Sciences, v. 52, p. 1062-1092.

Ootes, L., Snyder, D., Davis, W.J., Acosta-Góngora, P., Corriveau, L., Mumin, A.H., Montreuil, J.-F., Gleeson, S.A., Samson, I.A., and Jackson, V.A., 2017, A Paleoproterozoic Andean-type iron oxide copper-gold environment, the Great Bear magmatic zone, Northwest Canada: Ore Geology Reviews, v. 81, p. 123-139.

OZ Minerals Limited, 2020, Carrapateena 2020 mineral resources and ore reserves statement and explanatory notes as at 30 June 2020, available at www.ozminerals.com

Paladin Energy, 2019, Michelin Project, Labrador Canada: Paladin Energy Ltd., available http://www.paladinenergy.com.au/project/michelin-canada, accessed on September 1, 2019.

Patterson, B., LeGras, M., Gazley, M., Austin, J., Godel, B., Walshe, J., Hawkins, S., Sisson, M., and Birchall, R., 2016, Uncover Cloncurry data pack, v1: CSIRO data collection, doi.org/10.4225/08/5806a55f5797f.

Perreault, S., 2015, Rapport d'exploration des campagnes de terrain de 2012 et 2013 et sommaire des résultats des essais métallurgiques de 2013 et 2014, Propriété Kwyjibo (1088-5), SNRC 22P03: Ministère des Ressources naturelles du Québec, GM 69518, 85 p.

Perreault, S., and Artinian, B., 2013, Rapport technique sur les travaux d'exploration de 2010 et de la campagne de forage de 2011, projet Kwyjibo (1088-5): Ministère des Ressources naturelles du Québec, GM 67330, 47 p.

Perreault, S., and Lafrance, B., 2015, Kwyjibo, a REE-enriched iron oxides-copper-gold (IOCG) deposit, Grenville Province, Québec, *in* Simandl, G.J. and Neetz, M., eds., Symposium on strategic and critical materials proceedings, November 13-14, 2015, Victoria, British Columbia: British Columbia Ministry of Energy and Mines, British Columbia Geological Survey Paper 2015-3, p. 139-145.

Porter GeoConsultancy, 2021, A geological database of the world's important mineral deposits, available at http://www.portergeo.com.au.

Potter, E.G., Montreuil, J.-F., Corriveau, L., and Davis, W.J., 2019, The Southern Breccia metasomatic uranium system of the Great Bear magmatic zone, Canada: iron oxide-copper-gold (IOCG) and albitite-hosted uranium linkages, *in* Decrée, S. and Robb, L., eds., Ore deposits: origin, exploration, and exploitation: American Geophysical Union, Geophysical Monograph 242, John Wiley & Sons, Inc., p. 109-130.

Reid, A.J., 2019, The Olympic Cu-Au Province, Gawler Craton: a review of the lithospheric architecture, geodynamic setting, alteration systems, cover successions and prospectivity: Minerals, v. 9, 371.

Reid, A.J., and Fabris, A.J., 2015, Influence of pre-existing low metamorphic grade sedimentary successions on the distribution of iron oxide copper-gold mineralisation in the Olympic Cu-Au- Province, Gawler Craton: Economic Geology, v. 110, p. 2147-2157.

Reid, A.J., Swain, G., Mason, D., and Mass, R., 2011, Nature and timing of Cu–Au–Zn–Pb mineralisation at Punt Hill, eastern Gawler Craton: MESA Journal, v. 60, p. 7-17.

Rex Minerals Ltd., 2015, Hillside project, mineral resources and ore reserves, available at www.rexminerals.com.au.

Roeder, P.K., MacArthur, D., Ma, X., Palmer, G.R., and Mariano, J.N., 1987, Cathodoluminescence and microprobe study of rare earth elements in apatite: American Mineralogist, v. 72, p. 801-811.

Ross, D.A., 2009, Technical report on the CMBNW property, Labrador, Canada: NI 43-101 Technical report, available at sedar.com.

Rudnick, R.L., and Gao, S., 2014, Composition of the continental crust, *in* Holland, H.D. and Turekian, K.K., eds., Treatise on geochemistry, second edition, v. 3: Elsevier, p. 1-64.

Rusk, B., Oliver, N., Blenkinsop, T., Zhang, D., Williams, P., Cleverley, J., and Habermann, H., 2010, Physical and chemical characteristics of the Ernest Henry iron oxide copper gold deposit, Cloncurry, Queensland, Australia; Implications for IOCG genesis, *in* Porter, T.M., ed., Hydrothermal iron oxide copper-gold and related deposits: a global perspective, v. 3: PGC Publishing, Adelaide, p. 201-218.

Sangster, P.J., Le Baron, P.S., Charbonneau, S.J., Laidlaw, D.A., Wilson, A.C., Carter, T.R., and Fortner, L., 2012, Report of activities 2011, resident geologist program, southern Ontario regional resident geologist report: Southeastern and Southwestern Ontario Districts and Petroleum Resources Centre, Ontario Geological Survey, Open File Report 6277, 72 p.

Sappin, A.-A., and Perreault, S., 2021, Drill core pictures and description of samples collected from the REE Kwyjibo deposit (SOQUEM warehouse, Val d'Or, QC - October 2015): Geological Survey of Canada, Open File 8794, 14 p.

Schandl, E.S., and Gorton, M.P., 2007, The Scadding gold mine, east of the Sudbury Igneous Complex, Ontario: an IOCG-type deposit?: The Canadian Mineralogist, v. 45, p. 1415-1441.

Schlegel, T.U., and Heinrich, C.A., 2015, Lithology and hydrothermal alteration control the distribution of copper grade in the Prominent Hill iron oxide-copper-gold deposit (Gawler Craton, South Australia): Economic Geology, v. 110, p. 1953-1994.

Seeger, C.M., 2000, Southeast Missouri iron metallogenic province: characteristics and general chemistry, *in* Porter, T.M., ed., Hydrothermal iron oxide copper-gold and related deposits: a global perspective, v. 1: PGC Publishing, Adelaide, p. 237-248.

Skirrow, R.G., 2022, Hematite-group IOCG ± U deposits: an update on their tectonic settings, hydrothermal characteristics, and Cu-Au-U mineralizing processes, *in* Corriveau, L., Potter, E.G. and Mumin, A.H., eds., Mineral systems with iron oxide copper-gold (IOCG) and affiliated deposits: Geological Association of Canada, Special Paper 52, p. 27-51.

Skirrow, R.G., and Walshe, J.L., 2002, Reduced and oxidized Au-Cu-Bi iron oxide deposits of the Tennant Creek inlier, Australia: an integrated geologic and chemical model: Economic Geology, v. 97, p. 1167-1202.

Skirrow, R.G., Huston, D.L., Mernagh, T.P., Thorne, J.P., Dulfer, H., and Senior, A.B., 2013, Critical commodities for a high-tech world: Australia's potential to supply global demand: Geoscience Australia, Canberra, 118 p.

Slack, J., 2013, Descriptive and geoenvironmental model for cobalt–copper–gold deposits in metasedimentary rocks: U.S. Geological Survey Scientific Investigations Report 2010–5070–G, 218 p.

Slack, J.F., Kimball, B.E., and Shedd, K.B., 2017, Cobalt, *in* Schulz, K.J., DeYoung, J.H., Jr., Seal, R.R., II and Bradley, D.C., eds., Critical mineral resources of the United States—Economic and environmental geology and prospects for future supply: U.S. Geological Survey Professional Paper 1802, p. F1-F40.

Somarin, A.K., and Mumin, A.H., 2014, P–T-composition and evolution of paleofluids in the Paleoproterozoic Mag Hill IOCG hydrothermal system, Contact Lake belt, Northwest Territories, Canada: Mineralium Deposita, v. 49, p. 199-215.

South Australia Geodata Database, 2020, Olympic Dam HyLogger data release, available at http://www.energymining.sa.gov.au/minerals/geoscience/geoscientific_data/hylogger/olympic_dam_hylogger_data_release.

Sparkes, G.W., 2017, Uranium mineralization within the Central Mineral Belt of Labrador: a summary of the diverse styles, settings and timing of mineralization: Government of Newfoundland and Labrador, Department of Natural Resources, Geological Survey, St. John's, Open File LAB/1684, 198 p.

Spratt, J.E., Jones, A.G., Jackson, V.A., Collins, L., and Avdeeva, A., 2009, Lithospheric geometry of the Wopmay Orogen from a Slave craton to Bear Province magnetotelluric transect: Journal of Geophysical Research, v. 114, 18 p.

Starkey, M.A., and Seeger, C.M., 2016, Mining and exploration history of the southeast Missouri iron metallogenic province, *in* Slack, J., Corriveau, L. and Hitzman, M., eds., Proterozoic iron oxide-apatite (± REE) and iron oxide-copper-gold and affiliated deposits of Southeast Missouri, USA, and the Great Bear magmatic zone, Northwest Territories, Canada: Economic Geology, v. 111, p. 1815-1823.

Taylor, R.D., Shah, A.K., Walsh, G.J., and Taylor, C.D., 2019, Geochemistry and geophysics of Iron Oxide-Apatite deposits and associated waste piles with implications for potential rare earth element resources from ore and historical mine waste in the Eastern Adirondack Highlands, New York, USA: Economic Geology, v. 114, p. 1569-1598.

Tiddy, C.J., and Giles, D., 2020, Suprasubduction zone model for metal endowment at 1.60–1.57 Ga in eastern Australia: Ore Geology Reviews, v. 122, 103483.

Trottier, C.R.M., 2019, Fluid inclusion, stable and radiogenic isotope, and geochronological investigation of the polymetallic "five-element" vein deposit at the Eldorado Mine, Port Radium, Northwest Territories, Canada: Unpublished M.Sc. thesis, Saint Mary's University, 186 p.

Wallis, C.S., Sparkes, B.A., and Giroux, G.H., 2011, Technical report on the Central Mineral Belt (CMB) uranium-vanadium project, Labrador, Canada: NI 43-101 Technical Report, 94 p.

Wang, C., Liu, J., Zhang, H., Zhang, X., Zhang, D., Xi, Z., and Wang, Z., 2019, Geochronology and mineralogy of the Weishan carbonatite in Shandong province, eastern China: Geoscience Frontiers, v. 10, p. 769-785.

Warren, I., Simmons, S.F., and Mauk, J.L., 2007, Whole-rock geochemical techniques for evaluating hydrothermal alteration, mass changes, and compositional gradients associated with epithermal Au-Ag mineralization: Economic Geology, v. 102, p. 923-948.

Weng, Z.H., Jowitt, S.M., Mudd, G.M., and Haque, N., 2013, Assessing rare earth element mineral deposit types and links to environmental impacts: Applied Earth Science (Transactions of the Institution of Mining and Metallurgy), v. 122, p. 83-96.

Whitney, D.L., and Evans, B.W., 2010, Abbreviations for names of rock-forming minerals: American Mineralogist, v. 95, p. 185-187.

Wilde, A., Otto, A., Jory, J., MacRae, C., Pownceby, M., Wilson, N., and Torpy, A., 2013, Geology and mineralogy of uranium deposits from Mount Isa, Australia: implications for albitite uranium deposit models: Minerals, v. 3, p. 258-283.

Williams, P.J., 2010, Classifying IOCG deposits, *in* Corriveau, L. and Mumin, A.H., eds., Exploring for iron oxide copper-gold deposits: Canada and global analogues: Geological Association of Canada, Short Course Notes, No. 20, p. 13-21.

Williams, P.J., and Pollard, P.J., 2001, Australian Proterozoic iron oxide-Cu-Au deposits: an overview with new metallogenic and exploration data from the Cloncurry district, northwest Queensland: Exploration and Mining Geology, v. 10, p. 191-213.

Williams, P.J., and Skirrow, R.G., 2000, Overview of iron oxide-copper-gold deposits in the Curnamona Province and Cloncurry District (Eastern Mount Isa Block), Australia, *in* Porter, T.M., ed., Hydrothermal iron oxide copper-gold and related deposits: a global perspective, v. 1: PGC Publishing, Adelaide, p. 105-122.

Williams, P.J., Barton, M.D., Johnson, D.A., Fontboté, L., de Haller, A., Mark, G., Oliver, N.H.S., and Marschik, R., 2005, Iron-oxide copper-gold deposits: geology, space-time distribution, and possible modes of origin: Economic Geology 100th Anniversary Volume, p. 371-405.

Wise, T., and Thiel, S., 2020, Proterozoic tectonothermal processes imaged with magnetotellurics and seismic reflection in southern Australia: Geoscience Frontiers, v. 11, p. 885-893.

Witt, W.K., 1992, Porphyry intrusions and albitites in the Barboc-Kalgoree area, western Australia, and their role in Archean epigenetic gold mineralization: Canadian Journal of Earth Sciences, v. 29, p. 1609-1622.

Wodicka, N., David, J., Parent, M., Gobeil, A., and Verpaelst, P., 2003, Géochronologie U–Pb et Pb–Pb de la région de Sept-Îles-Natashquan, Province de Grenville, moyenne Côte-Nord, *in* Brisebois, D. and Clark, T., eds., Géologie et ressources minérales de la partie est de la Province de Grenville: Ministère des Ressources naturelles, de la Faune et des Parcs, Québec, DV 2002-03, p. 59-117.

Zhao, X.-F., Chen, H., Zhao, L., and Zhou, M.-F., 2022, Linkages among IOA, skarn, and magnetite-group IOCG deposits in China: from deposit studies to mineral potential assessment, *in* Corriveau, L., Potter, E.G. and Mumin, A.H., eds., Mineral systems with iron oxide copper-gold (IOCG) and affiliated deposits: Geological Association of Canada, Special Paper 52, p. 383-407.

## Appendix 1: Data Sources and location

For the Olympic Dam deposit and adjacent regions, geochemical trends are based on drill cores RD 222, 302, 451, 1247, 1399, 1628, 1629, 1988, 2274, 2280, 2316, 2366, 2382, 2488, 2492, 2494, 2495, 2499, 2511, 2531, 2715, 2751, 2765, 2773, 2785, 2852A, 2923 and 3554 and drill cores RU 27-7551, RU36-9867-9867W1, RU52-5358 and RU65-8230 (Fig. 7A, B). The ODF-1, 2 and 3 drill cores located southeast of the Olympic Dam deposit (Fig. A1) were also used to illustrate systems with less intense alteration (BHP-Olympic Dam, unpub. data, 2018). Images and HyLogger™ mineralogy of drill cores with numbers in bold can be accessed using the South Australian Resource Information Gateway and the results discussed in Mauger et al. (2016). Analytical methods are described in Dmitrijeva et al. (2019) and Blein et al. (2022).

For the Punt Hill deposit AIOCG diagrams, the datasets from the EC21, GHDD1, GHDD2, GHDD3, GHDD4, GHDD5, GHDD6, GHDD7, HL002, PRL21/SAR8, PRL23/SAR9, PY4, WHD1, WPPD2, WWDD01 drill cores were used. Data compiled from the Geological Survey of South Australia, via South Australian Resources Information Gateway (https://map.sarig.sa.gov.au/).

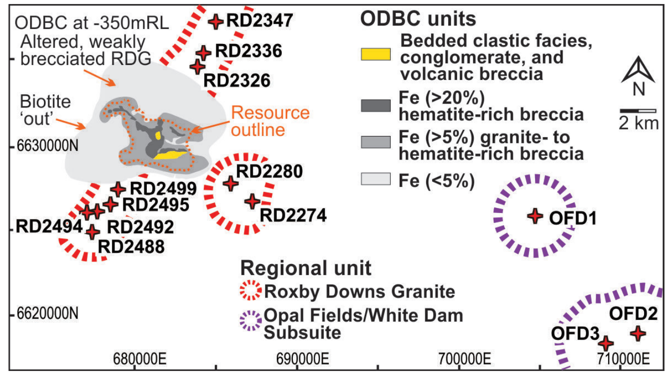


**Figure A1.** Distribution of drill cores from the RD and OFD series within the region of the Olympic Dam deposits and outside the Olympic Dam Breccia Complex (ODBC). The White Dam and Opal Fields Subsuites of the Hiltaba Suite are named after nearby prospects (Creaser, 1989; Ferguson et al., 2020). Figure modified from Ferguson et al. (2020).

## Appendix 2: Total Canadian IOCG and affiliated resources

| | | |
|---|---|---|
| **NICO** | **reserves GBMZ** | 33 Mt at 1.02 g/t Au, 0.12 wt% Co, 0.14 wt% Bi, 0.04 wt% Cu |
| **Sue Dianne** | **GBMZ** | 8.4 Mt at 0.80 wt% Cu, 0.07 g/t Au, 3.2 g/t Ag |
| **Michelin** | **Central Mineral Belt** | 42.7 Mt at 0.098 wt% $U_3O_8$ |
| **Moran Lake** | **Central Mineral Belt** | 6.92 Mt at 0.034 wt% $U_3O_8$, 0.078 wt% $V_2O_5$ (indicated) + 5.3 Mt at 0.024 wt% $U_3O_8$, 0.089 wt% $V_2O_5$ (inferred) 7.79 Mt at 0.18 wt% $V_2O_5$ (indicated) + 21.6 Mt at 0.17 wt% $V_2O_5$ (inferred) outside uranium mineralization zone |
| **Anna Lake** | **Central Mineral Belt** | 7.3 Mt at 0.037 wt% $U_3O_8$ |
| **Two-Time** | **Central Mineral Belt** | 1.8 Mt at 0.058 wt% $U_3O_8$ |
| **Josette** | **Grenville Province** | 6.92 Mt at 2.72 wt% $REE_2O_3$, 53 wt% $Fe_2O_3$ (measured + indicated) +1.33 Mt at 3.64 wt% $REE_2O_3$, 48 wt% $Fe_2O_3$ (inferred) |
| **Fostung** | **Sudbury district** | 12.4 Mt at 0.2 wt% $WO_3$ |
| **Marmoraton** | **Grenville Province** | 28 Mt at 42 wt% Fe |

Hennessey and Puritch (2008); Morgan and Giroux (2008); Fraser and Giroux (2009); Ross (2009); Wallis et al. (2011); Magyarosi et al. (2012), Sangster et al. (2012); Burgess et al. (2014); Paladin Energy (2019); Gagnon et al. (2018)

## Appendix 3: Footprint of shoshonitic, potassic alkaline and ultrapotassic intrusive rocks

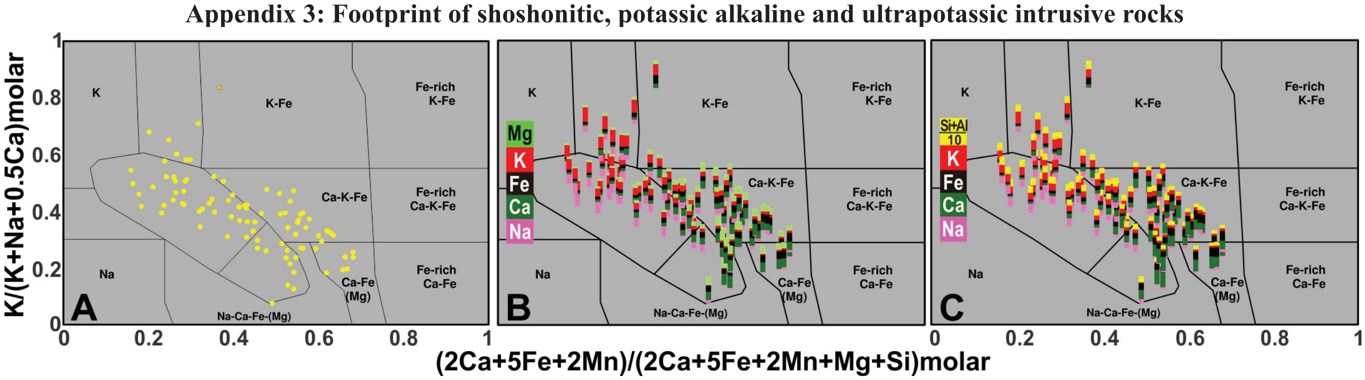


**Figure A3.** Molar barcodes of representative whole rock compositions of the Kensington-Skootamatta intrusive suite, Grenville Province, Canada. Samples are from the Baskatong, Cameron, Gracefield, Kensington, Loranger, Sainte Véronique plutons emplaced between 1089 and 1076 Ma along a 400-km-long plutonic belt (Corriveau et al., 1990). B. Na-Ca-Fe-K-Mg molar barcodes. C. Na-Ca-Fe-K-([Si+Al]/10) molar barcodes. Geochemical data in Corriveau (1989)

## Appendix 4: Variations of metals in samples containing less than 0.3 wt% $CO_2$ at the Olympic Dam deposit

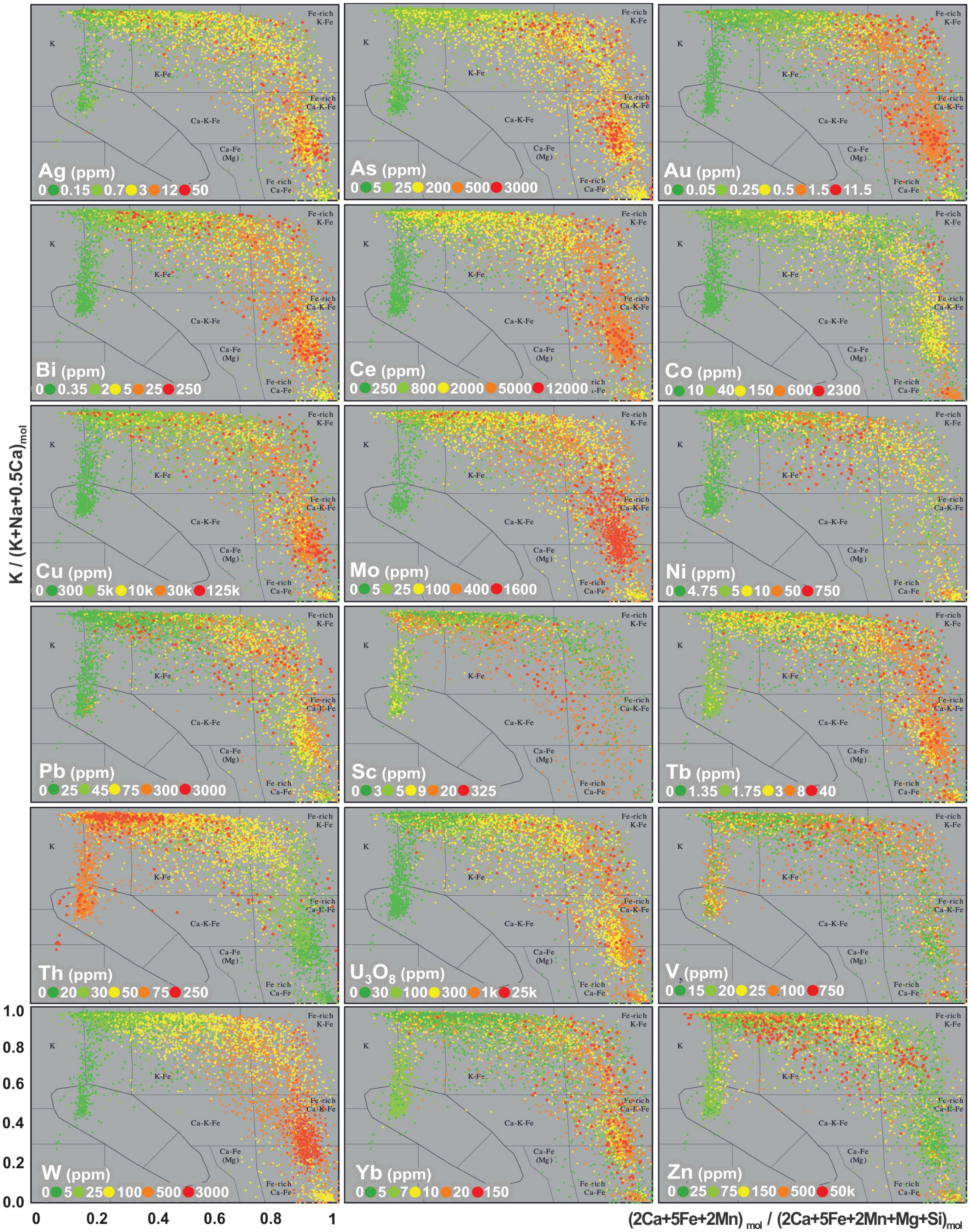


**Figure A4.** Variations in metal contents in the LT K-Fe through LT Fe-Si and LT Ca-Mg-Fe (carbonates, fluorite) alteration of the Olympic Dam deposit using samples containing less than 0.3 wt% $CO_2$. Removing all carbonates helps distinguish alteration related to carbonates versus alteration associated with iron oxides and fluorite. Compare with Figures 16–19, in which carbonate-bearing samples are included.

# Mineral Systems with IOCG and Affiliated Deposits: Part 3 – Metal Pathways and Ore Deposit Model


**Louise Corriveau**
*Natural Resources Canada, Geological Survey of Canada, Québec, Canada*
*louise.corriveau@NRCan-RNCan.gc.ca*

**Jean-Francois Montreuil**
*Red Pine Exploration, Ontario, Canada*

**Eric Potter**
*Natural Resources Canada, Geological Survey of Canada, Ontario, Canada*

**Olivier Blein**
*Bureau de recherches géologiques et minières, Orléans, France*

**Anthony De toni**
*SOQUEM Inc., Québec, Canada*



*Recommended citation: Corriveau, L., Montreuil, J.-F., Potter, E.G, Blein, O., and De Toni, A.F., 2022, Mineral systems with IOCG and affiliated deposits: part 3 – metal pathways and ore deposit model, in Corriveau, L., Potter, E.G. and Mumin, A.H., eds., Mineral systems with iron oxide copper-gold (IOCG) and affiliated deposits: Geological Association of Canada, Special Paper 52, p. 205-245.*



## Abstract

Metasomatic iron-oxide and alkali-calcic alteration systems form a wide range of iron-oxide copper-gold (IOCG), iron oxide-apatite (IOA) and primary critical metal deposits. Economic resources include Ag, Au, Bi, Co, Cu, F, Fe, Mo, Nb, Ni, Pb, Pd, Pt, Re, rare earth elements (both heavy and light REE), U, V, W and Zn. Metal enrichments or byproducts include: Al, As, Ba, Cd, Rb, Sb, Sc, Se, Sn, Sr, Ta, Te, Th, Y and Zr. The ascent of voluminous saline to hypersaline fluid plumes in tectonically and magmatically active continental upper crust triggers these metasomatic systems. High disequilibrium between fluids and host rocks drives metasomatism and self-sustains the formation of consecutive iron-oxide and alkali-calcic alteration facies, each having distinct mineral assemblages and deposit types. This paper links alteration facies to the spectrum of deposit types using examples from the global districts examined in the companion Parts 1 and 2 papers and other contributions from this volume.

The ascent of a metal-laden hypersaline fluid plume first triggers regional-scale albitization in the upper crust (Facies 1 with Na alteration and transitional Facies 1–2 with Na-Ca-Fe alteration). Barren albitite corridors develop above sub-volcanic intrusions and along fault zones, and skarn forms amongst albitite in the presence of carbonate rocks. These steps recharge the fluid plume with metals, volatiles and other elements through extensive decarbonation and dissolution of minerals from host rocks. Proximal to the thermal cores of the systems, metal-rich fluids outflowing from Facies 1 trigger the onset Facies 2 (high-temperature Ca-Fe) alteration under very high temperatures, reaching 800 to 900°C in the presence of coeval intrusions. Iron skarn (e.g. Middle-Lower Yangtze River Metallogenic Belt in China), IOA deposits (e.g. Southeast Missouri district, US) and their Fe-REE ± P, F, Nb or Fe-Ni variants also form at this stage, including REE ores formed through subsequent remobilization of primary REE endowment (e.g. Josette REE deposit, Québec). Crosscutting relationships between iron mineralization and albitite indicate that albitite precipitates first and is not linked to magnetite precipitation (e.g. Great Bear magmatic zone in Canada and the Middle-Lower Yangtze River Metallogenic Belt in China).

Fluids outflowing from Facies 2 form a transitional Facies 2–3 HT Ca-K-Fe alteration. Precipitation of Co, Bi, Au (± Cu, Ni) may form cobalt-bismuth deposits rich in iron silicates, iron sulphides or iron oxides. Tungsten, initially deposited in earlier skarn, can be remobilized to form additional mineralized zones in which Sb, Se, and Te are potential byproducts (e.g. NICO deposit in Canada). In most systems, Facies 2 directly evolves to Facies 3 (high-temperature K-Fe), which marks the onset of extensive brecciation and formation of magnetite-group IOCG deposits (Ernest Henry copper-gold deposit in Australia, Sue Dianne Cu-Au-Ag deposit in Canada). Palladium and platinum are enriched in some biotite-rich magnetite-group IOCG deposits (Dahongshan Fe-Cu-Au-Ag-Co-Pd-Pt deposit in China). Facies 4 alteration consists of locally mineralized K-skarn and barren K-felsite breccia (commonly as haloes around IOCG breccias or within K-skarn). These alteration types may subsequently host polymetallic deposits (Punt Hill in Australia) or form components of magnetite-to-hematite group IOCG deposits (e.g. Candelaria Cu-Au-Ag deposit, Chile). Facies 5 alteration zones (low-temperature K-Fe and Ca-Mg-Fe and their Ca-F-Fe and Si-Fe ± Ba variants) host a wide range of polymetallic deposits, including 1) hematite-group IOCG deposits with Ag, Au, Cu and U resources and LREE mineralization (e.g. Olympic Dam Cu-U-Au-Ag deposit in Australia), and 2) an emerging group of iron oxide- to iron-poor deposits, including Au-Co, Mo-Re ± Cu ± Au and Au-Pb-Zn (e.g. Merlin, Mount Dore and Tick Hill deposits in Australia; Scadding deposit in Canada). Facies 6 (K, Si, Al) comprises epithermal mineralization and polymetallic vein systems (including late-stage ones).

Syn-metasomatic magma emplacement, tectonic and volcanic activity, and mixing of external fluids with the main fluid plume can induce a cyclical build-up or telescoping of alteration facies as well as retrogression of higher temperature mineral assemblages. The overprinting of albitite corridors by Facies 3 and Facies 5 fluids may generate albitite-hosted U and Au-Co ± U deposits (e.g. Southern Breccia albitite corridor in Canada; Valhalla in Australia). Reactivation of systems via renewed fluid circulation driven by orogenesis, magmatism or burial periodically remobilize early metal endowments into mineralized veins and breccias; five-element (Ag, As, Bi, Co, Ni, ± U) veins are an example of such processes. The paragenetic ore system model presented herein provides a framework to classify the variety of ore deposits encountered in these systems while providing effective and predictive mapping and exploration tools for IOCG and affiliated deposits, including their primary critical metal deposits. It also enables to better frame alteration facies and mineralization that are low in iron oxides but rich in iron silicates, iron carbonates and iron sulphides as well as those poor in iron within metasomatic iron and alkali-calcic (MIAC) systems.

## Résumé

Les systèmes métasomatiques à altération alcali-calcique et à oxydes de fer forment un large éventail de gîtes primaires à métaux de base, critiques et précieux dont ceux à oxydes de fer-cuivre-or (IOCG), à oxydes de fer-apatite (IOA) et à métaux critiques. Ces gîtes contiennent des ressources économiques en Ag, Au, Bi, Co, Cu, éléments des terres rares (légères et lourdes), F, Fe, Mo, Nb, Ni, Pb, Pd, Pt, Re, U, V, W et Zn. Des enrichissements significatifs ou des sous-produits en Al, As, Ba, Cd, Rb, Sb, Sc, Se, Sn, Sr, Ta, Te, Th, Y et Zr sont aussi présents. L'ascension de volumineux panaches de fluides salins ou hypersalins dans des environnements continentaux à tectonique et magmatisme actifs déclenche les systèmes. Un déséquilibre important et persistant entre les fluides et l'encaissant provoque le métasomatisme et forme des séries successives de faciès d'altération alcali-calcique et à oxydes de fer. Chaque faciès précipite ses propres assemblages de minéraux et types de gîtes. Cet article relie le tout en utilisant les exemples de districts mondiaux examinés dans les Parties 1 et 2, dans cet article et dans les autres contributions de ce volume.

L'ascension d'un panache de fluides hypersalins chargés de métaux provoque d'abord une albitisation régionale dans la croûte supérieure (l'altération du Faciès 1 avec Na et du Faciès transitionnel 1–2 avec Na-Ca-Fe). Des couloirs d'albitite stérile se forment au-dessus des intrusions sub-volcaniques et le long des zones de failles. Du skarn se forme parmi l'albitite en présence de roches carbonatées. Ces étapes rechargent le panache de fluide en métaux, volatiles et autres éléments par la dissolution massive des minéraux des encaissants et leur décarbonation. Près des noyaux thermiques du système, les fluides sortants déclenchent une altération au Faciès 2 (Ca-Fe de haute température) à des températures très élevées, atteignant 800 à 900°C en présence d'intrusions syn-métasomatiques. Ce faciès donne lieu à des gîtes de skarn ferrifère (p. ex. ceinture métallogénique du fleuve Yangtsé moyen inférieur en Chine), à des IOA (p. ex. le district du sud-est du Missouri aux États-Unis) et de leurs variantes à Fe-ETR-(±P, F, Nb) ou Fe-Ni résultant d'une remobilisation de l'enrichissement primaire en ETR (p. ex. le gîte à ETR Josette au Québec). Les relations de recoupement entre la minéralisation à fer et les couloirs d'albitite (p. ex. la zone magmatique du Grand lac de l'Ours au Canada et la ceinture métallogénique du fleuve Yangtsé moyen inférieur en Chine) indiquant que l'albitite se forme en premier et n'est pas une conséquence de la précipitation des oxydes de fer.

Dans les panaches où le potassium est disponible, les fluides s'échappant du Faciès 2 au sein de séquences sédimentaires forment une altération transitionnelle (Faciès 2–3 Ca-K-Fe à haute température). Le Co, Bi, Au (± Cu, Ni) y précipitent et peuvent former des gîtes de cobalt et bismuth à silicates, sulfures ou oxydes de fer. Le tungstène, ayant précipité dans du skarn, peut être remobilisé été enrichi tandis que Sb, Se et Te sont des sous-produits potentiels (p. ex. le gisement NICO au Canada). Dans la plupart des systèmes, le Faciès 2 évolue directement vers le Faciès 3 (K-Fe de haute température), une bréchification extensive et la formation de gîtes IOCG du groupe à magnétite (le gîte Ernest Henry en Australie et Sue Dianne au Canada). Des ressources de palladium et de platine sont connues au sein de gîtes IOCG du groupe à magnétite riches en biotite (p. ex. le gîte de Dahongshan en Chine). Le Faciès 4 est constitué de skarn potassique localement minéralisé et de brèche de felsite potassique stérile (généralement sous forme de halos autour de brèches IOCG ou dans du skarn potassique). Ces types d'altération peuvent encaisser des gîtes polymétalliques (Punt Hill en Australie) ou constituer des composantes de gîtes IOCG du groupe à magnétite vers hématite (p. ex. Candelaria au Chili). Le Faciès 5 (K-Fe et Ca-Mg-Fe de basse température ainsi que leurs variantes Ca-F-Fe et Si-Fe ± Ba) précipitent un large éventail de gîtes polymétalliques. Cela comprend les gisements IOCG du groupe à hématite avec des ressources en Ag, Au, Cu et U et une minéralisation en ETR légères (p. ex. le gisement Olympic Dam en Australie), et un groupe émergent de gisements pauvres en oxyde de fer à pauvres en fer, y compris des gisements à Au-Co, Mo-Re±Cu±Au et Au-Pb-Zn (p. ex les gisements Merlin, Mount Dore et Tick Hill en Australie; le gisement Scadding au Canada). Le Faciès 6 (K, Si, Al) comprend une minéralisation épithermale et des systèmes de veines polymétalliques, certaines tardives et issues de la remobilisation des métaux des systèmes mêmes.

La mise en place de magmas ou du tectonisme et volcanisme syn-métasomatiques ainsi que le mélange de fluides externes avec le panache de fluide principal peuvent induire une cyclicité dans la précipitation des faciès d'altération ou leur télescopage ainsi qu'une rétrogradation des assemblages de minéraux de plus haute température. La circulation de fluides aux conditions des Faciès 3 et Faciès 5 dans des couloirs d'albitite peut conduire à la formation de gîtes d'uranium ou à Au-Co±U encaissés dans de l'albitite (p. ex. les indices du corridor d'albitite de la Southern Breccia au Canada et le gîte de Valhalla en Australie). La réactivation des systèmes, via de nouveaux épisodes de circulation de fluides lors d'orogénèses ou de mises en place de magmas, remobilise périodiquement les métaux des systèmes dans de nouvelles zones minéralisées. Des veines à cinq éléments (Ag, As, Bi, Co, Ni, ± U) sont un exemple de tels processus. Le modèle métallogénique basé sur les faciès d'altération cadre la variété de gîtes minéraux rencontrés dans ces systèmes tout en fournissant des outils de cartographie et d'exploration efficaces et prédictifs pour les gisements IOCG et affiliés, y compris leurs variantes à métaux critiques. Le modèle permet aussi de mieux cadrer les faciès d'altération et les types de minéralisation pauvres en oxydes de fer mais riches en silicates de fer, carbonates de fer et sulfures de fer ainsi que ceux pauvres en fer au sein de système métasomatiques alcali-calciques et à fer.

## Introduction

Regional-scale metasomatic iron oxide and alkali-calcic alteration (IOAA) systems include a range of epigenetic, structurally-controlled, hydrothermal deposits in which Ag, Au, Bi, Co, Cu, F, Fe, Mo, Ni, P, Pb, Re, REE (light and heavy), U, and Zn are primary economic commodities (Fig. 1; Tables 1, 2; Porter, 2010a; Williams, 2010a; Corriveau et al., 2016; Hofstra et al., 2021). Iron oxide copper-gold (IOCG) and iron oxide ± apatite (IOA) deposits are the most common deposit types (Williams et al., 2005; Porter, 2010a). These systems also form rare earth element (REE) IOA variants, iron and polymetallic skarn, albitite-hosted U, Au and Co, and iron-rich to iron-poor Ag, Au, Bi, Co, Cu, Mo, Re and U deposits (Table 1; Hitzman and Valenta, 2005; Porter, 2010a, b; Williams, 2010a; Slack, 2013; Montreuil et al., 2015; Corriveau et al., 2016; Day et al., 2016; Babo et al., 2017; Gagnon et al., 2018; Potter et al., 2020a; Hofstra et al., 2021).

Deposits associated with IOAA systems contain 30 of the 51 critical metals defined by the USA, Australia, Europe, Japan and Canada ('critical metals' lists provided in Emsbo et al., 2021; Natural Resources Canada, 2021). As the systems are capable of generating deposits where critical metals are primary commodities not simply by-products or minor commodities, the discovery and development of deposits such as the REE-rich Josette and the NICO Au-Co-Bi-Cu deposits in Canada (Fig. 1; Table 2), is a key step in securing supply of economically important minerals globally. Economic deposits containing Ag, Au, Bi, Co, Cu, F, Fe, Mo, Nb, Ni, Pb, Pd, Pt, Re, U, V, W, Zn, and REE, both light REE (LREE: La–Sm) and heavy REE (HREE: Eu–Lu), and potential resources of Al, As, Ba, Cd, Rb, Sb, Sc, Se, Sn, Sr, Ta, Te, Th, Y and Zr are known (Slack et al., 2017; Corriveau et al., 2018b, 2022b; Veloso et al., 2020;

**Table 1.** Resources contained in selected IOCG and affiliated deposits, Olympic Copper-Gold Province, Australia.

| Deposit | Disco-vered | Ressources |
|---|---|---|
| **Olympic Dam** | 1975 | 10,070 Mt at 0.62% Cu, 0.21 kg/t $U_3O_8$, 0.27 g/t Au, 1.0 g/t Ag, open cut; 1,041 Mt at 1.68% Cu, 0.47 kg/t $U_3O_8$, 0.63 g/t Au, 3 g/t Ag, underground ore (+ ~0.3% LREE, 0.01% HREE) |
| **Prominent Hill** | 2001 | 210 Mt at 1.2% Cu, 0.5 g/t Au, 2.8 g/t Ag + 31 Mt at 0.1% Cu, 1.5 g/t Au, 1.1 g/t Ag (+U, + REE) |
| **Carrapateena** | 2005 | 970 Mt at 0.5% Cu, 0.2 g/t Au, 3 g/t Ag (+U) |
| **Hillside** | 2009 | 337 Mt at 0.6% Cu, 0.14 g/t Au, 15.7% Fe (+Ag, U) |
| **Khamsin** | 2012 | 202 Mt at 0.6% Cu, 0.1 g/t Au, 1.7 g/t Ag, 86 ppm U |
| **Oak Dam East** | 1976 | ~560 Mt at 41–56% Fe, 0.2% Cu, 690 ppm U |
| **Oak Dam West** | 2018 | Intersection of 425m @ 3.04% Cu, 0.6 g/t Au and 6 g/t Ag; drilling for resources estimate in progress |
| **Fremantle Doctor** | 2013 | 104 Mt at 0.7% Cu, 0.5 g/t Au, 3 g/t Ag |

References: Belperio et al. (2007); Davidson et al. (2007); OZ Minerals (2013a, b, 2019); Rex Minerals Ltd. (2015); BHP Limited (2018, 2020); Williams et al. (2017).

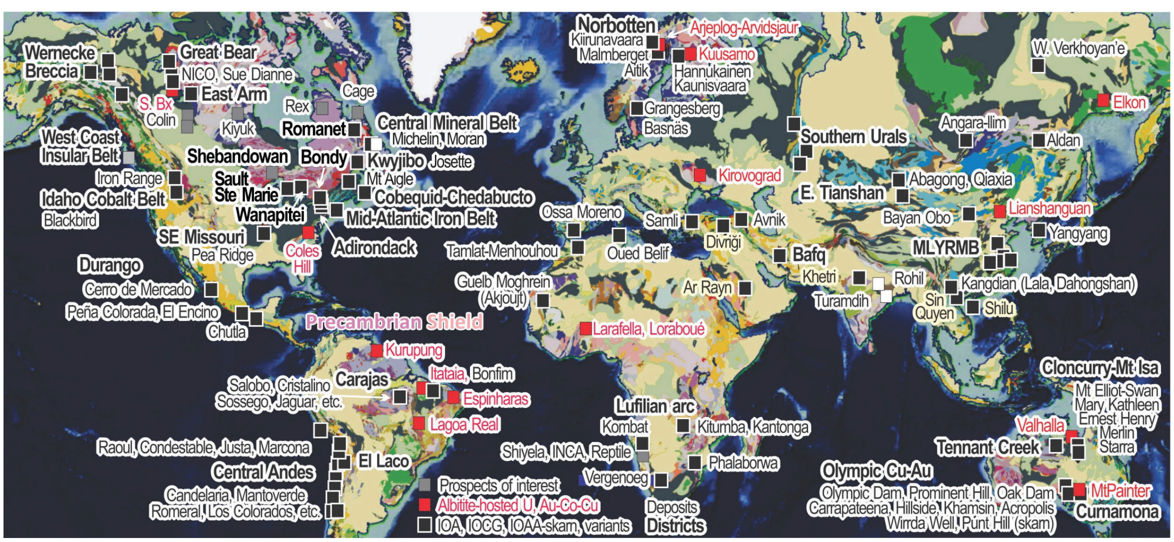


**Figure 1.** Location of IOCG and affiliated critical metal deposits (see overview of deposits in Porter GeoConsultancy, 2021; geological map: Chorlton, 2007). In Canada, the Wanapitei district includes the Scadding Au-(Co-Cu-Ni) deposit and to the south the Sudbury district includes the Fostung tungsten deposit; the Romanet Horst includes the Delhi Pacific Cu-Au-Ag prospect. The Middle-Lower Yangtze River Metallogenic Belt (MLYRMB) in China includes the IOA deposits of the Ningwu, Daye and Luzong districts (Zhao et al., 2022). The Rajasthan district in India includes the Khetri IOCG deposit and albitite-hosted uranium deposits (Ray, 1990; Pandey et al., 2016).

**Table 2.** Metals in the main alteration facies of IOAA systems and global examples (locations in Figure 1). Continued on next page.

| Facies | | Minerals | | | Element enrichment | | | Examples | |
|---|---|---|---|---|---|---|---|---|---|
| | | Major | Accessory to major | Mineralization | Major commodity | Economic potential | Others | Lou system (GBMZ) | Districts (Deposits) Dominant primary mineralization |
| Facies 5 | LT Ca/ Mg/Na/K Si/H+/ $CO^2$ | Qz, Cb (Dol, Cal), Chl, Ab, Kfs, Ms | | Ccp, Brn, Cct, Co-Py, Co-As, Gn, Mol, Native Au, Sp, Urn | Au, Co, Cu, Mo, Re, U, Zn | | | | Cloncurry[1,2] (Merlin, Mount Dore, Mary Kathleen, Tick Hill), Others[3–7] (Michelin, Lagoa Real, Romanet Horst, Kuusamo, Wanapitei) |
| Facies 5 | LT Ca-Mg-$Fe^{2+}$ | Chl, Mag | Ab, Amp (Mns, Stp), Ank, Dol | Ccp, Native Au, Po, Py, Apy | Au, Cu | Bi, Co, U | Fe, LREE, Na, Ni | | Wanapitei[7,8] (Scadding) |
| Facies 5 | LT Ca-Mg-$Fe^{3+}$ -(±F) | Act, Adr, Aln, Chl, Ep, Hem, Hst | Ank, Brt, Cal, Fl, Kfs, Ms | Brn, Ccp, Cct, Gn, Py, Sp, LREE minerals, Urn | Ag, Au, Cu, Pb, U, Zn | LREE | Ba, F, Fe, S, K, Mn, Sb, Sn, Sr, Te, W | | Olympic Cu-Au[7,9,10] (Hillside, Punt Hill, Mt Dore), Central Mineral Belt[11] (Michelin) |
| Facies 5 | LT Si-Fe-(±Ba) | Hem, Qz | Aln, Ank, Brt, Cal, Fl, Sid | Ccp, Native Au, LREE minerals, Py, Urn | Au, Cu, Fe | LREE, U | Ba, Fe, Si | | Olympic Cu-Au[10,12,13] (Olympic Dam, Prominent Hill, Oak Dam West), GBMZ[7] (East Hottah, Fe zone) |
| Facies 5 | LT K-Fe | Chl, Hem, Ms, Sd | Aln, Ank, Brt, Cal, Dol, Ep, Fl, Kfs, Qz | Brn, Ccp, Cct, Hem, Native Au, LREE minerals, Py, Urn | Ag, Au, Cu, Fe, U | Co, LREE, Mo, Pb, Re, W, Zn | As, Ba, C, Cd, F, K, Mn, P, S, Sb, Se, Sn, Te, W | In volcanic rocks above NICO; overprints on HT K-Fe + mineralized veins at NICO | Olympic Cu-Au[10, 12–14] (Olympic Dam, Oak Dam West, Prominent Hill, Carrapateena), SE Missouri[15] (Boss-Bixby), GBMZ7 (Sue Dianne, K2), Kangdian[16] (Xikuang-shan), Central Andes[17] (Mantoverde) |
| Facies 4 | K-skarn | Aln, Cpx (Adr-Grs), Ep, Kfs | Ank, Cal, Dol, Mag | Bn, Ccp, Cv, Gn, Mol, Py, Sp | None | Cu, Mo, Pb, Zn | K, Th, U | Exobreccia along felsic dykes | Olympic Cu-Au[7,9,10] (Hillside, Punt Hill), GBMZ[7] (Mile Lake) |
| Facies 4 | K felsite | Kfs | | | None | None | Ba, K, Rb, Th | In volcanic rocks above NICO; overprints on Southern Breccia albitite; breccia along felsic dykes | Cloncurry (Ernest Henry[7,18]), GBMZ[7] (Sue Dianne, Mile Lake) |
| Facies 3 | HT K-Fe (Kfs) | Kfs, Mag | Bt, Cal, Chl | Ccp, Mol, Native Au, Py, Urn | Ag, Au, Cu, Fe, U | Mo | Ba, C, F, K, Rb, Mn, P, REE, Sb, Te, Th, V, Zr | Iron oxide breccia with Kfs-altered clasts in volcanic rocks above NICO and in albitite at Southern Breccia | Olympic Cu-Au[10] (Olympic Dam, Mag relics at Oak Dam West[12]), Cloncurry[7] (Ernest Henry[18]), GBMZ[7,19] (Sue Dianne, Summit Peak, Fab, Southern Breccia), Central Andes[17] (Candelaria) |
| Facies 3 | HT K-Fe (Bt) | Bt, Mag | Amp (Gru, Hbl), Grt, Kfs | Brn, Ccp, Native Au, Urn, Po, Py | Ag, Au, Co, Cu, Fe, U | Mo, Pd, Pt | Ba, C, F, K, Rb, Mn, P, REE, Sb, Te, Th, V, Zr | Stratabound Bt-dominant overprint on HT Ca-K-Fe at NICO; Mag-Bt patches in Southern Breccia | Olympic Cu-Au[10] (Cairn Hill[19], Manxman[20], Moonta-Wallaroo[21]), Cloncurry[7] (Ernest Henry[18], Eloise[22]), Kangdian[16] (Dahongshan, Yinachang, Lala), Carajás[23] (Salobo), Guelb Morghein[24], NICO (Cu)[25] |

Centaurus Metals Limited, 2021). Yet, the full spectrum of IOCG and affiliated critical metal deposits is significantly under-represented in districts globally, and linkages amongst the diverse deposit types within the broader metasomatic systems can be misunderstood or not recognized.

The variety of deposit types is an outcome of the physico-chemical evolution of voluminous saline to hypersaline fluid plumes that ascend through and infiltrate the upper crust (Table 2; Corriveau et al., 2016; this work). Fluid-rock interactions trigger a chain of mineral reactions and element mobilizations that drive and self-sustain the precipitation of consecutive and compositionally distinct alteration facies, and control metal precipitation along the fluid pathways. The geological-geochemical space-time analysis of metasomatic IOAA systems undertaken in Parts 1 and 2 (Corriveau et al., 2022b, c) provides insights on the feedback mechanisms between fluid plume evolution and alteration facies formed. This paper unravels the role of fluid plume evolution in forming the distinct deposit types and metal associations that characterize each alteration facies. Facies definition, description, occurrences, paragenetic transitions and space-time relationships are detailed in Corriveau et al. (2022a–c); the figures and examples provided therein complement those in this paper.

The main case examples used in this paper include systems and deposits from the Great Bear magmatic zone (GBMZ) and the Kwyjibo, Romanet Horst, and Wanapitei districts in Canada, the Ernest Henry, Olympic Dam and Punt Hill deposits in Australia, the Missouri district in the central USA, and the Middle-Lower Yangtze River metallogenic belt in China (Fig. 1).

**Table 2 (continued).** Metals in the main alteration facies of IOAA systems and global examples (locations in Figure 1).

| Facies | | Minerals | | | Element enrichment | | | Examples | |
|---|---|---|---|---|---|---|---|---|---|
| | | **Major** | **Accessory to major** | **Mineralization** | **Major commodity** | **Economic potential** | **Others** | **Lou system (GBMZ)** | **Districts (Deposits) Dominant primary mineralization** |
| **Facies 2–3** | **HT Ca-K-Fe** | Amp (Act, Hbl), Bt, Kfs, Mag | Ap, Cpx (Aug-Hd), Grt, Sid | Apy, Bism, Co-Apy, Ccp, Co-Loe, Co-Py, Cob, Gers, Lin, Po, Py, Saf, Sch, Sieg, Sku, Urn | Au, Bi, Co, Cu, Ni | Ag, As, Mo, Sb, Se, Te, W | Ba, Ca, K, P, Rb, REE, S, Th, U, Y | Stratabound Bt-Amp-Mag overprints of HT Ca-Fe with Apy stringers and veins at NICO; patches in Southern Breccia | Olympic Cu-Au[7,10] (Acropolis-IOA[26], Oak Dam East[27]), GBMZ[7] (NICO Au-Co-Bi, Port Radium, Cole), Guelb Morghein[24], Sin Quyen[28], Carajás[29] (Jatobá, Jaguar, GT-34) |
| **Facies 2** | **HT Ca-Fe** | Amp (Act, Cum, Hbl), Mag | Aln, Ap, Cpx (Dp-Hd, Aug), Ep, Qz | Mag, Mlr, Po, Pn, Py, REE minerals (e.g. Ap, Mnz, Adr, Fl), Sch | Fe, Ni, P, REE | Co, V, W | Ca, Mg, Th, U | Stratabound Amp to Mag in clastic and carbonate units; Amp to Mag veins cutting HT Ca-K-Fe at NICO recording repetition of facies; patches and veins in Southern Breccia | Olympic Cu-Au[10,12] (Olympic Dam, Oak Dam East[27]), GBMZ[7] (Mag Hill, Port Radium, Terra, JLD), Kwyjibo (Josette[30,31], Lac Marmont[30]), SW Grenville (Marmoraton[35], Bondy[36]), MLYRMB[32] (Washan), Carajás[29] (Jatobá, Jaguar), Andes[17] (El Laco, Los Colorados, Marcona), Norrbotten (Kiirunavaara, Grängesberg), Adirondack Mtns[33], SE Missouri[15,34] (Pea Ridge, Pilot Knob). |
| **Facies 1–2** | **Fe-skarn** | Cpx (Dp-Hd), Grt (Adr-Grs), Mag | Amp (Hbl, Tr), Qz | Mag, Sch | Fe, W | REE, Co, Ni, V | P, Th, U | | Olympic Cu-Au[10] (Hillside[37]), GBMZ[7] (Duke, Hump, NICO), MLYRMB[32] (Longqiao, Hemushan, Wangbaoshan), Eastern Tianshan[32], Norrbotten[38] |
| | **Skarn** | Cpx (Aug, Dp-Hd), Grt (Adr-Grs) | Aln, Amp (Hbl, Tr), Cal, Chl, Dol, Mag, Phl | Sch | | W | Fe | Relics in Amp HT Ca-Fe of carbonate unit at NICO | Olympic Cu-Au[9,10] (Punt Hill), GBMZ[7] (Duke, Hump, NICO W zone[25]), Sudbury (Fostung)[39] |
| | **HT Na-Ca-Fe** | Ab, Amp (Act, Hbl), Mag | Ap, Cpx (Aug) | | None | Fe, REE, V | Na, Ca, P, Th | Rare | Olympic Cu-Au[10] (Oak Dam East[12], Cairn Hill[19], Manxman[20]), GBMZ[7] (Mag Hill, DeVries), Sin Quyen[27], Bafq[40] |
| **Facies 1** | **Na and Na-Ca** | Ab, Scp (residual Qz) | Amp (Act, Hbl), Cpx (Aug) | None | None | Al | Ga, Na, Nb, Ta, Ti, Zr | Southern Breccia albitite corridor; relics at NICO | Cloncurry[2,7,18,37], Curnamona[41], GBMZ[7], Kangdian[16], MLYRMB[32], Bafq[40], Norrbotten[38] |

Mineral abbreviations in this table (and in figures) are from Whitney and Evans (2010). Additional abbreviations are Bas: bastnaesite; Bism: bismuthinite; Cob: cobaltite; Gad: gadolinite; Gers: gersdorffite; Loe: loellingite; Lin: linnaeite; Saf: safflorite; Sieg: siegenite; Sku: skutterudite; Syn: synchysite. Major commodities are derived from mineral resources information and metals of economic potential from global databases and listed references including Corriveau et al. (2015, 2022b). References: 1: Babo et al. (2017); 2: Oliver et al. (1999); 3: Acosta-Góngora et al. (2018, 2019); 4:Cuney et al. (2012); 5: Corriveau et al. (2014), Montreuil et al. (2014); 6: Dragon Mining Limited (2014); 7: Corriveau et al. (2022a, b, this work); 8: Schandl and Gorton (2007); 9: Fabris et al. (2018); 10: Williams and Pollard (2001), Skirrow (2022), Fabris (2022); 11: Hicks (2015), Sparkes (2017); 12: Ehrig et al. (2012), King (2019); 13: Schlegel and Heinrich (2015); 14: Porter (2010a, b); 15: Day et al. (2016); 16: Zhao et al. (2022); 17: Chen and Zhao (2022); 18: Mark et al. (2006); 19: Clark (2014); 20: Hampton (1997); 21: Skirrow et al. (2007); 22: Baker (1998); 23: Melo et al. (2017); 24: Kirschbaum and Hitzman (2016); 25: Montreuil et al. (2016b); 26: Krneta et al. (2017); 27: Davidson et al. (2007); 28: Ngo et al. (2020); 29: Oliveira (2017), Garcia et al. (2020), Veloso et al. (2020), Ferreira Filho et al. (2021); 30: Clark et al. (2010); 31: Perreault and Lafrance (2015), Gagnon et al. (2018); 32: Yu et al. (2011), Zeng (2020), Zhao et al. (2022); 33: Taylor et al. (2019); 34: Harlov et al. (2016); 35: Carter (1984); 36: Corriveau et al. (2018a); 37: Teale (2019); 38: Williams (2010b); 39: Stryhas and More (2007); 40: Daliran et al. (2022); 41: Williams and Skirrow (2000).

## System Overview and Definitions

### *Alteration Facies*

Each IOAA facies is defined by the stability of a specific series of mineral assemblages and has distinct metal associations (Table 2; Corriveau et al., 2010a, b, 2016, 2022a–d); the sequence of alteration facies is regular in IOAA systems worldwide at system-scale (this work; Corriveau et al., 2020, 2022c). In contrast, the spatial extent, mineralogy of the assemblages, mineral contents and metal endowment of each alteration facies can vary significantly within a single system and between IOAA systems.

Facies 1 — Na alteration — produces albitite. The transition from Facies 1 to 2 includes albite-dominant Na-Ca and Na-Ca-Fe alteration and clinopyroxene-dominant skarn (Ca-Mg-Fe) alteration. Facies 2 — high-temperature (HT) Ca-Fe alteration — is largely amphibole- to magnetite-dominant and generates IOA and IOA-heavy REE or Ni deposits. The transition between Facies 2 and 3 is represented by HT Ca-K-Fe alteration, which is most common in sedimentary rocks and dominated by amphibole, magnetite, and biotite. Facies 3 comprises HT K-Fe alteration, characterized by biotite, K-feldspar or other potassic minerals in association with magnetite. Facies 4 comprises K-felsite (K-feldspar-dominant) and K-skarn alteration, whereas

Facies 5 consists of low-temperature (LT) K-Fe and LT Ca-Mg-Fe alteration, including their many Si, Ba, $CO_2$, F, and $Fe^{2+}$ versus $Fe^{3+}$ variants. Facies 6 encompasses epithermal alteration, silicification, quartz, carbonate, barite and/or fluorite veins, and associated mineralization.

Iron is commonly the dominant cation in HT Ca-Fe, HT Ca-K-Fe, HT K-Fe, and LT K-Fe and LT Ca-Mg-Fe variants, in which alteration becomes most intense and mature. All iron-dominant facies are identified and qualified by index cations (K, Ca, etc.) to emphasize the facies type (but not the weight per cent content of the diagnostic cations). For example, where most intense at the Olympic Dam deposit, the LT K-Fe alteration facies is a hematite-dominant alteration with subordinate K-bearing white mica. "Low-temperature" is used to qualify mineral assemblages that formed largely below ~400°C (i.e. in the temperature range of the metamorphic greenschist facies and lower). "High-temperature" is used to qualify mineral assemblages that formed largely above ~400°C (i.e. in the temperature range of the metamorphic amphibolite facies and higher).

*Metasomatic Paths*

The sequential development of alteration facies records consecutive and self-propagating chemical fluid-rock reactions driven by extreme physicochemical disequilibrium between the ascending fluid plume and host rocks. The progression of metasomatism from Facies 1 to Facies 6 alteration and associated metal precipitation is defined as the prograde metasomatic path (Corriveau et al., 2022a). A simple path does not imply that the fluids came from a single source, but rather that incorporation of external fluids did not disrupt the prograding alteration facies sequence during the evolution of the main fluid plume.

Retrograde alteration in IOAA systems is defined as replacement of earlier IOAA facies by assemblages not directly related to the prograding chemical reactions characteristic of the evolution of the main fluid plume. Retrograde alteration can result from the cooling of metasomatic pore fluids captured by the metasomatites or by infiltration of external low-temperature fluids after or during ascent of the original fluid plume. Retrogression may or may not induce major chemical changes in earlier metasomatic rocks aside from the addition of volatiles (e.g. hydration reaction of minerals) and oxidation of iron. Additionally, it is not typically associated with significant influx of metals, in contrast to prograde low-temperature alteration (see sections on Facies 5 and 6), which may be accompanied by significant mineralization.

The definition of prograde IOAA metasomatism differs from the definition of prograde orogenic metamorphism in that the consecutive metasomatic mineralogical and textural transformation of protoliths occurs largely through declining temperatures. In both cases, retrogression takes place following a break in the defined prograding sequence, via lower-temperature overprints of higher-temperature assemblages.

Defining the prograde path of consecutive alteration facies in IOAA systems also differs from normal practice in economic geology. However, it portrays the depth-to-surface evolution of the system (where simple) and help best interpret variations induced by pulsating and disrupted metasomatic sequences. These variations are related to ingress of external fluids from basinal brines, meteoric water, caldera lake fluids, or renewed magma emplacement and/or active tectonism during the evolution of the main fluid plume (Williams et al., 2005, 2010; Barton, 2014; Melo et al., 2019; Schlegel et al., 2020). Telescoped metasomatic paths occur where earlier alteration facies are exposed out-of-sequence to subsequent facies conditions, and are typically associated with active tectonics, syn-metasomatic thrusting, or "sudden" ingress of voluminous amounts of low-temperature fluids. A cyclical path is defined by the recurrence of an alteration facies through ingress of high-temperature fluids recharged by syn-metasomatic magma emplacement.

## Facies 1 and Transition to Facies 2: Na, Na-Ca-Fe and Skarn Alteration

*Na Alteration: Definition, Occurrences and Localities*

Facies 1 is the early and pervasive Na alteration that leads to formation of regional-scale corridors of albitite having bulk sodium contents in the range of 8 to 12 wt% $Na_2O$. Along regional discontinuities and through coupled dissolution and reprecipitation processes, the albite-dominant assemblages (Table 2) replace all host rocks and original mineralogy, leaving behind a highly porous, fragile albitite of low density and magnetic susceptibility (Oliver et al., 2004; Montreuil et al., 2012; Putnis, 2015; Enkin et al., 2016). This facies is a fundamental and intrinsic first stage in the development of IOAA systems (Parts 1, 2; Williams et al., 2005; Porter, 2010a, b).

Albitization progresses most readily along contacts between units, within permeable or chemically reactive units (e.g. carbonate-bearing), or along faults, deformation zones and roof zones of sub-volcanic intrusions. Albitite corridors can extend tens of kilometres along strike and a few kilometres in width (Figs. 2, 3; Figs. 17, 18A, B, 24A in Corriveau et al., 2022c; Hildebrand, 1986; Williams et al., 2005; Marshall and Oliver, 2008; Porter, 2010a, b; Montreuil et al., 2012; McLaughlin et al., 2016; Zhao et al., 2022). Albitization may be weak to moderate within zones of lower fluid flow and at albitization fronts where the intensity of alteration decreases. In such zones, albitization forms haloes along fractures; it is stratabound and layer-selective in sedimentary rocks, but forms varitextured patches or sharp alteration fronts in volcanic rocks (Corriveau et al., 2022a). Albitite zones progressively merge across layers, fracture networks and metasomatic fronts. At the roof zones of hot intrusions, such as the subvolcanic diorite intrusions of the northern GBMZ, fine-grained albitite may recrystallize to a massive, medium- to coarse-grained hypidiomorphic texture (Fig. 17 in Corriveau et al., 2022c). Progressive albitization of sedimentary and igneous host rocks confirms the metasomatic origin of the albitite and rules out an igneous origin (Figs. 2, 3A, B, 4A, B; Figs. 5, 17–19 in Corriveau et al., 2022c), despite the fact that metasomatic albitite may

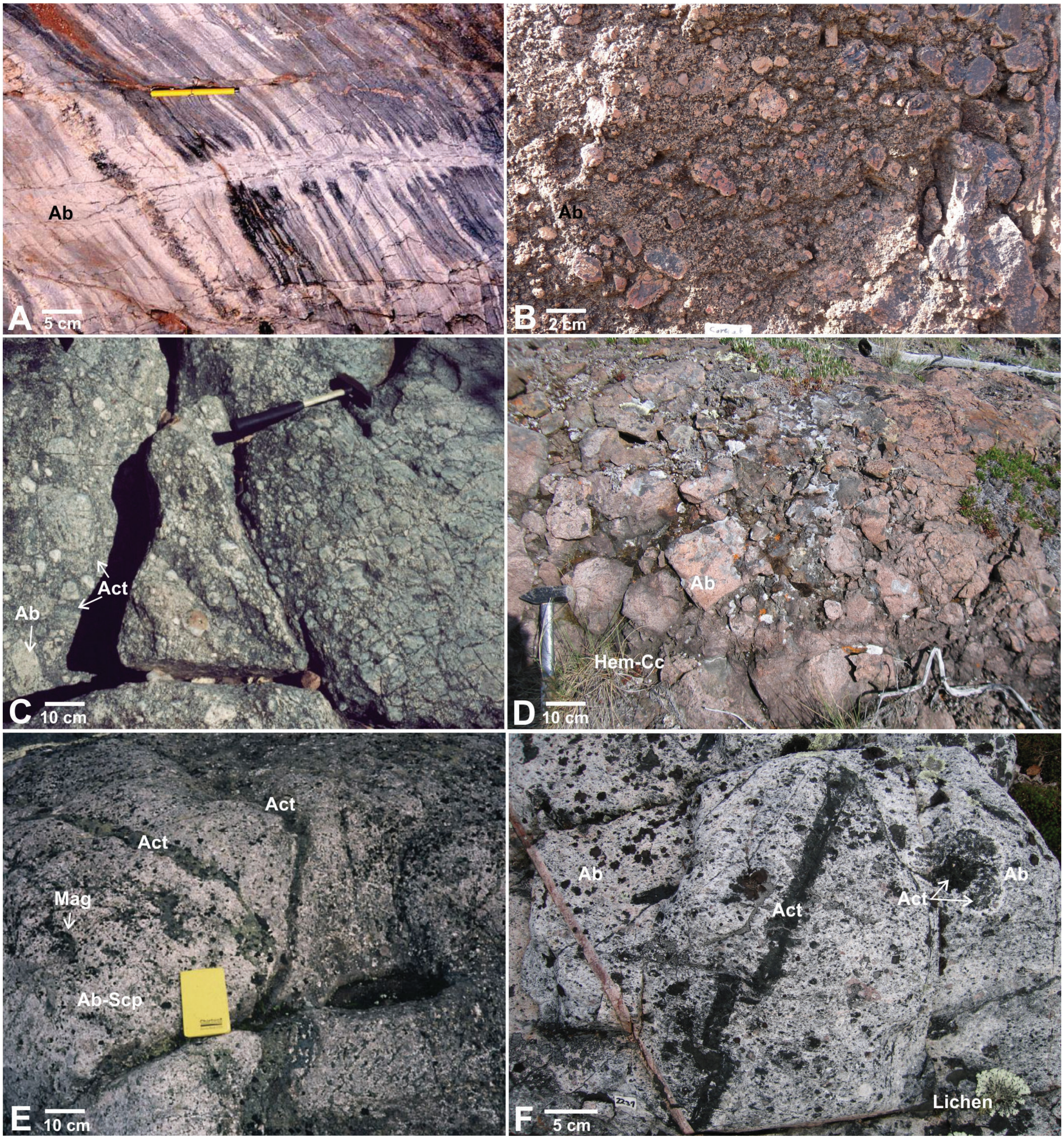


Figure 2. Facies 1 and transitions to Facies 2 illustrating commonalities in Na and HT Ca-Fe alteration amongst Canadian and Australian IOAA systems. **A.** Zones of metasedimentary rocks (dark) replaced by texture-destructive albitization (white) parallel to strata and fractures from the Walparuta prospect (Olary Domain, Curnamona Province, South Australia). **B.** Carbonate-altered breccia with clasts of albitized, metamorphosed evaporitic carbonate rocks (Corella Formation) in the Cloncurry district, Australia (Oliver et al., 2009). **C.** Contact zone of a breccia composed of pervasively albitized metasedimentary rocks cut by actinolite veins (left), which transitions to a breccia of rounded albitite clasts in an actinolite-rich matrix (Cloncurry district, Australia; De Jong and Williams, 1995). **D.** Breccia with albitized andesitic clasts and a carbonate-rich matrix near the hematite breccia of Figure 26G in Corriveau et al. (2022c), Contact Lake belt, GBMZ, Canada (CQA-07-520). **E.** Scapolite-albite-altered metavolcanic rocks with actinolite veins and spotty (black) magnetite alteration, host to the Gruvberget IOA deposit, northern Sweden. **F.** Pervasively albitized volcaniclastic unit between the Fab and DeVries systems veined and altered by an amphibole-dominant mineral assemblage, GBMZ, Canada (CQA-05-0271). Clasts of volcanic and porphyritic intrusive rocks are selectively altered to amphibole (± albitite selvages). A, C and E: photos from Corriveau et al. (2010b); B, D, F: NRCan photos 2020-790 to 2020-792.

display hypidiomorphic granular textures and resemble syenitic or anorthositic intrusive rocks (Fig. 17E, F in Corriveau et al., 2022c).

Sodic alteration and albitite corridors are best exposed where the original depth to surface (vertical) profile of a system has been disturbed by syn-metasomatic or subsequent volcanic activity, tectonism or orogenesis, e.g. at the GBMZ, Wanapitei district, and Central Mineral Belt in Canada (Gates, 1991; Hildebrand et al., 2010; Mumin et al., 2010; Hayward et al., 2016; Acosta-Góngora et al., 2019; Yarie and Wray, 2019). At the regional scale, districts featuring extensive exploration drilling (e.g. Ernest Henry deposit in Australia; Mark et al., 2006), or geophysical surveys (Southeast Missouri district in US, McCafferty et al., 2019; NICO deposit, Canada; Hayward et al., 2016), or those with exposed vertical sections (Montreuil et al., 2015), all reveal broad zones of sodic alteration in the form of albitite corridors.

Phanerozoic settings with albitite corridors include the Middle-Lower Yangtze River Metallogenic Belt (Ningwu Research Group, 1978; Zhao et al., 2022), the Bafq district in Iran (Daliran et al., 2022) and the Telmalt-Menhoulou deposit in Morocco (Pelleter et al., 2010). Neoproterozoic albitite corridors occur in the Lufilian arc in Africa (Lobo-Guerrero, 2010). Paleo- to Mesoproterozoic albitite corridors are most extensively exposed and include those of the Canadian GBMZ and Wanapitei districts, Australian Cloncurry district and Curnamona Province, Indian Rajasthan district and Ukrainian Kirovograd district (Figs. 1, 3, 4; Hildebrand, 1986; Teale and Fanning, 2000; Oliver et al., 2004; Schandl and Gorton, 2007; Cuney et al., 2012; Wilde et al., 2013; Montreuil et al., 2015, 2016b; Mumin, 2015; Yadav et al., 2015; Yarie and Wray, 2019).

*Albite-dominant Alteration as a Metal Source*

During intense albitization, most of the elements forming the host-rock minerals are not compatible with the albite and accessory minerals (e.g. rutile, titanite and zircon which can be dated) that replaces them (Oliver et al., 2004; Pelleter et al., 2010; Davis et al., 2011; Montreuil et al., 2016a, c). During albitization, these incompatible elements (e.g. Ca, Fe, K, Mg, Cu, Co), including normally immobile (REE) and volatile elements, are transferred to the fluid plume, forming a metasomatite principally composed of Al, Si and Na (ibid.). Some trace elements, e.g. Zr, Hf, Ga, Nb, Ta, Th and Ti, are compatible with accessory minerals in the albitite and may become relatively enriched during albitization compared to compositions of the protoliths (Oliver et al., 2004; Montreuil et al., 2016a). Some zones contain residual quartz, resulting in high silica as well as sodium contents (e.g. 73–82 wt% $SiO_2$; Corriveau et al., 2015). In certain IOAA systems, mass balance calculations suggest that regional sodic metasomatism can account for the metal budget in spatially associated mineral deposits (Pelleter et al., 2010).

The abundance of accessory actinolite, diopside and scapolite increases at the transition from Na to Na-Ca and Na-Ca-Fe facies alteration, although albite remains dominant (Figs. 5, 17F, J, 18, 19 in Corriveau et al., 2022c). In the meta-evaporite-bearing sequences of the Cloncurry district, albite replaced metamorphic scapolite during the formation of albitite then co-crystallized with metasomatic scapolite as part of a Na-Ca facies alteration (Fig. 2E; Oliver et al., 2004; Morrissey and Tomkins, 2020). In the GBMZ, scapolite-absent albite-amphibole Na-Ca alteration preserves bedding and nodular anhydrite textures typical of evaporite units (Corriveau et al., 2022a). Within volcanic, volcaniclastic and siliciclastic sedimentary units, albitite commonly lacks scapolite.

Above subvolcanic intrusions, albitite, ± Na-Ca (albite-scapolite) alteration transition upward to albite-dominant Na-Ca-Fe alteration composed of actinolite, apatite and local clinopyroxene, epidote or magnetite, such as in the GBMZ (Fig. 2F). At this stage, oligoclase may crystallize instead of albite (Kreiner and Barton, 2017). The original minerals of the host rocks react out, increasing the metal content in the outgoing fluids, whereas Al, Ca, Sr, V and Na precipitate or remain in the altered rocks (Table 2; e.g. Montreuil et al., 2016c). As Na-Ca-Fe alteration intensifies and evolves to the HT Ca-Fe facies, sodium and then magnesium contents decrease while calcium and iron contents increase. At first, clinopyroxene and amphibole dominate over magnetite but as alteration progresses magnetite becomes more abundant than the ferromagnesian silicates (Corriveau et al., 2022c).

*Textural Insights on Magmatic Heat Ingress*

The Na-Ca-Fe facies alteration can be very intense, forming pegmatitic replacement zones (pervasive up to 1 km across) or veins consisting of albite-amphibole ± apatite ± magnetite, especially above subvolcanic intrusions (Fig. 19 in Corriveau et al., 2022c; Daliran et al., 2022). Scapolite or anhydrite may also form (e.g. El Laco deposit in Chile and IOA deposits of the Middle-Lower Yangtze River Metallogenic Belt in China; Fig. 3B in Tornos et al., 2017; Fig. 2E, F in Li et al., 2015, pers. comm., 2017; Zhao et al., 2022). Along fault zones and other discontinuities away from intrusions, albite-amphibole (± magnetite, apatite) pegmatitic and hypidiomorphic, medium-grained albitite zones are sparse and very patchy (< 1 m). The typical fine-grained nature of the albitite and the variable intensity of albitization provide empirical field evidence that heat ingress is not as sustained along fault zones as it is above subvolcanic intrusions (e.g. Southern Breccia corridor and Romanet Horst albitite observed along fault zones).

*Albitite Corridors: Ground Preparation for Mineralization*

Sodic and Na-Ca alteration zones and albitite corridors are barren during metasomatism. Along faults, shear zones and stratigraphic units with distinct rheologies and reactivities, syn- to post-albitization partitioning of brittle and brittle-ductile deformation induces extensive fracturing and brecciation of the porous and brittle albitite corridors, including microfractured damage zones. Crustal permeability and fluid flow are enhanced, allowing the albitite corridors to become preferential hosts for subsequent mineralization

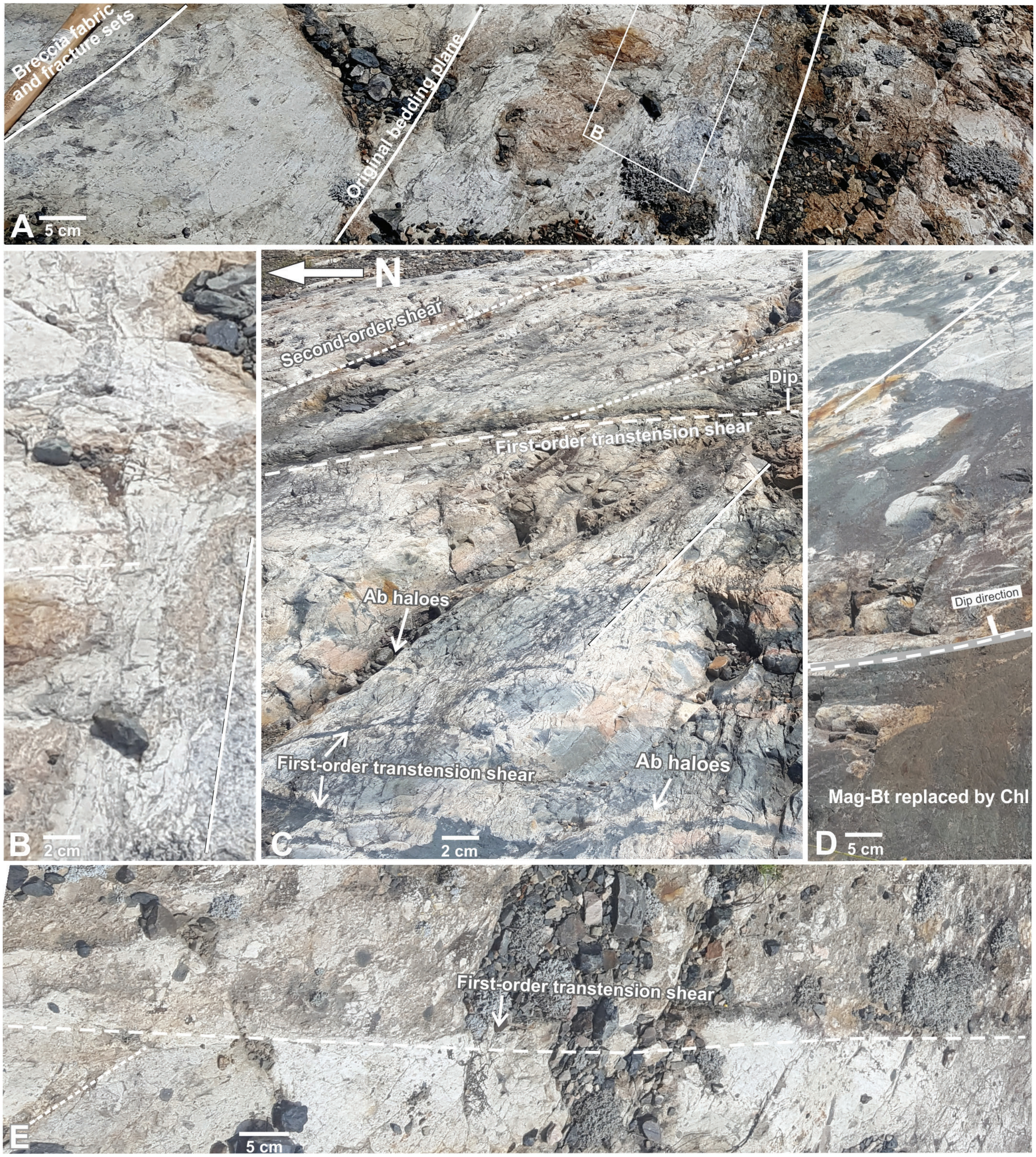


**FIGURE 3.** Albitite corridor in Paleoproterozoic Huronian-Group sedimentary rocks, in which intense albitization and brecciation serve as ground preparation for chlorite-dominant LT Ca-Mg-Fe gold mineralization at the past-producing Scadding gold-cobalt mine, Wanapitei district, Canada (Yarie and Wray, 2019). **A.** Transect across albitite breccia developed parallel to sedimentary bedding planes. **B, C.** Brittle to brittle-ductile transtensional faults and splay shear zones serve as first- and second-order pathways for mineralizing fluids, respectively, at high angles to and along the original bedding planes of the host. Chlorite-dominant gold mineralization infills the faults, whereas albitite crystallizes as haloes and coalesces into extensive replacement zones. **D.** Extensive replacement zones and infill of albitite breccia by chlorite-dominant assemblages replacing a magnetite-biotite assemblage. At the scale of individual gold zones, the splay shear zones and associated breccias can be the primary control on the geometry of mineralization. **E.** Albitite breccia showing renewed albitization following brecciation along bedding planes. Such renewed albitization within regional-scale albitite corridors occurs in other global districts (e.g. Tennant Creek, Skirrow and Walshe, 2002). Photos courtesy of MacDonald Mines Exploration Ltd.

(Figs. 2–4; Figs. 5, 6, 20, 21D, 26F, G in Corriveau et al., 2022c; Marshall and Oliver, 2008; Oliver et al., 2009; Montreuil et al., 2012, 2015, 2016b; Poulet et al., 2012). Mineralization processes are well illustrated by field relationships between albitite and networks of mineralized veins and alteration zones in the Southern Breccia (U, Cu, Mo) of the GBMZ (Montreuil et al., 2015; Potter et al., 2019), the Scadding and Norstar deposits (Au, Ag, Cu) of the Wanapitei district (Fig. 3; Schandl and Gorton, 2007; Yarie and Wray, 2019), Romanet Horst (U, Ag, Au, Co, Cu) in Quebec (Kish and Cuney, 1981; Montreuil et al., 2014; McLaughlin et al., 2016), the uraniferous Central Mineral Belt in Labrador (Sparkes, 2017; Acosta-Góngora et al., 2019), and the Kuusamo (Au, U, Co) deposit in Finland (Dragon Mining, 2014).

Along faults and lithological discontinuities, albitite corridors transition laterally or upward into, are in faulted contact with or overprinted by, HT Ca-Fe or subsequent alteration facies and associated mineralization. Exploring laterally or deeper beyond the albitite zones can lead to discovery of mineralization in favourable chemical or structural traps. In such contexts, especially where tectonically- or volcanically-induced structural disruption occurs, interpreting albitite as simply the deep, barren roots of the system could result in mineralized zones being overlooked during exploration. The presence of subsequent alteration facies, such as the Na-Ca-Fe and HT Ca-Fe facies, represent vectors to potential mineralization at depth or beyond the albitite zones.

*Albitite-associated Skarn: Mappable Criteria for IOAA Systems*

Within carbonate-rich units, high temperature IOAA systems develop skarn assemblages (and calc-silicate rocks) before, during, or slightly after sodic alteration (GBMZ and Cloncurry district; Fig. 18A, B in Corriveau et al., 2022c; Oliver et al., 2004; Montreuil et al., 2016b; Hu et al., 2019). The skarn facies typically evolves to iron-rich compositions, occasionally progresses to magnetite-rich skarn assemblages, and is frequently replaced by HT Ca-Fe alteration. The timing and spatial association between albitite, skarn, magnetite-rich skarn, HT Ca-Fe facies, and the absence of intrusions linked to skarn development help to distinguish skarn alteration and mineralization formed in IOAA systems from typical intrusion-related skarn deposits.

The intense development of magnetite-rich skarn alteration can lead to iron-skarn deposits such as in the GBMZ in Canada, the eastern Adirondack Highlands in USA and the Middle-Lower Yangtze River Metallogenic Belt of China (Leonard and Buddington, 1964; Corriveau et al., 2010b, 2022c; Taylor et al., 2018, 2019; Hu et al., 2019; Zhao et al., 2022). In the Middle-Lower Yangtze River Metallogenic Belt, ca. 130 Ma iron-skarn deposits are coeval with IOA deposits (e.g. Fig. 8 in Zhao et al., 2022), whereas most intrusion-related skarn deposits (i.e. skarn developed along intrusive contacts without a spatial relationship to albitite or HT Ca-Fe alteration at regional scale) predate the development of IOAA systems.

Skarn alteration occurs amongst IOAA systems of the Central Andes (Chen and Zhao, 2022), and Eastern Tianshan and Eastern Junggar districts in China (Zhao et al., 2022). Skarn assemblages replace albitized intrusions and andesite and are subsequently replaced by HT Ca-Fe alteration at the Fab prospect, GBMZ, and Cerro Negro Norte deposit in the Central Andes (Montreuil et al., 2016c; Tornos et al., 2021). The Punt Hill and Hillside deposits in Australia are characterized by skarn facies that host large zones of polymetallic mineralization in later-stage alteration facies: Facies 4 K-skarn, and Facies 5 LT Ca-Mg-Fe alteration (Figs. 11A–C, 13 in Corriveau et al., 2022b; Fabris et al., 2018; Blein et al., 2022; Fabris, 2022).

Skarn does not form in all IOAA systems that have carbonate-rich rocks. In the Romanet Horst and Central Mineral Belt (Canada), carbonate hosts are instead albitized, exhibit localized sulphate alteration, and are hematite-altered. Basalt and fine-grained gabbro in these districts, along with other host rock types, are extensively albitized or meta-somatized to albitite (Corriveau et al., 2014; McLaughlin et al., 2016; Sparkes, 2017; Acosta-Góngora et al., 2019; Blein et al., 2022).

*Polymetallic Mineralization within Skarn Alteration*

The stability of scheelite during skarn alteration of carbonate rocks led to primary tungsten enrichment in the NICO deposit in Canada and Punt Hill deposit in Australia (Corriveau et al., 2022b) that was remobilized and concentrated during subsequent alteration (Goad et al., 2000; De Toni, 2016; Montreuil et al., 2016b). In the NICO deposit, this process resulted in significant tungsten mineralization, with average grades of 0.02% W (as indicated in early estimates of the NICO mineral resource), and up to 2% W over 2 m in drill core (Goad et al., 2000). Within skarn alteration zones at Punt Hill, In, Sn, W, Y and HREE are enriched several orders of magnitude above their average crustal contents but still significantly lower than typical ore grades for these metals (Corriveau et al., 2022b; cf. Lokanc et al., 2015; Liu, 2017). These elements are directly related to the skarn alteration and display a distribution within the Montreuil et al. (2013) AIOCG diagram that is distinct from the Au, Cu and S enrichments associated with lower temperature overprints (Fig. 13 in Corriveau et al., 2022b).

**Facies 2: HT Ca-Fe Alteration and IOA (± REE) Deposits**

*HT Ca-Fe Alteration: Definition, Occurrences and Localities*

Facies 2 HT Ca-Fe alteration consists of mineral assemblages having variable modal proportions of amphibole, apatite and magnetite (± allanite, epidote, titanite). If HT Ca-Fe metasomatites are recrystallized (e.g. during deformation), garnet (almandine) can occur within the mineral assemblage. Amphibole-dominant alteration evolves to magnetite-dominant and rarely to apatite-dominant alteration, irrespective of host composition. Host textures are locally preserved but in most cases they are destroyed. Zones of HT Ca-Fe alteration are

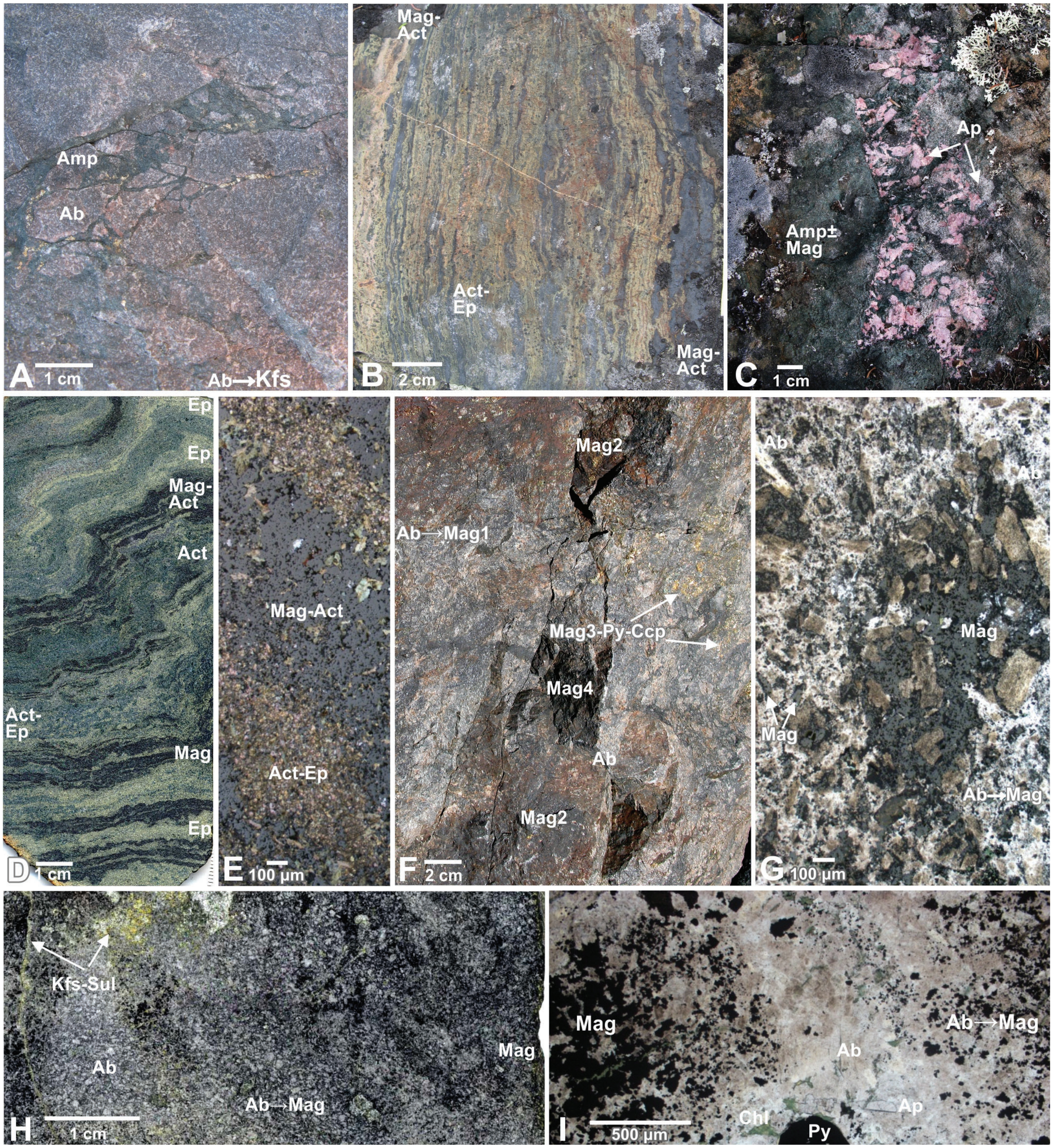


FIGURE 4. Facies 2 HT Ca-Fe alteration, Camsell River district, GBMZ, Canada. **A.** Albitized andesite cut by HT Ca-Fe amphibole veins and replaced by patches of LT Ca-Mg-Fe chlorite-epidote alteration assemblages and local weak K-feldspar alteration (Northrim; outcrop 09CQA-0139). **B, D, E.** Stratabound to anastomosing magnetite, actinolite-epidote and epidote alteration in sedimentary rocks (Terra; outcrop 09CQA-144). **C.** Coarse-grained amphibole and apatite veins cutting stratabound, amphibole-altered sedimentary rocks (Terra; outcrop 09CQA-0134). **F–I.** Albitized fragmental volcanic rocks replaced by anastomosing fronts of disseminated microcrystalline to fine magnetite (Ab to Mag1) and, in F, cut by irregular veins of magnetite (Mag2 locally porous and enclosing scheelite; De Toni, 2016) and accessory allanite, apatite and titanite (Northrim mine, mineralized block and outcrop 09CQA-0139). In F, H and I, early HT Ca-Fe alteration zones are cut by LT Ca-Mg-Fe veins and stockworks consisting of calcite, magnetite, sulphides, chlorite, epidote and quartz, and locally displaying K-feldspar haloes (yellow in the cobaltinitrite-stained slab shown in H). Magnetite 1 alteration is most abundant between albitized plagioclase phenocrysts (white / beige in G and I) and volcanic fragments, as rims on fragments (H right side) or within fragment cores (I). Some strongly albitized fragment margins are less altered by magnetite (H and I). Photomicrographs under transmitted and reflected light (E and G) and transmitted light (I) (De Toni, 2016). A–D, F and H: NRCan photos 2020-793 to 2020-798.

extensively documented in the Bafq district (Iran), GBMZ (Canada), Middle-Lower Yangtze River Metallogenic Belt (China) and in the Cloncurry district (Australia; Figs. 2E, F, 4; Figs. 6, 20–22 in Corriveau et al., 2022c; De Toni, 2016a; Daliran et al., 2022; Zhao et al., 2022). Magnetite-dominant end-members form iron oxide-apatite deposits and variants with heavy and light REE as primary commodities (Fig. 4B, 5; Figs. 20, 21 in Corriveau et al., 2022c).

In HT Ca-Fe alteration zones, Na, K, Ba, and Sr are depleted, whereas Ca, Fe, Mg, Co, Ni, V, Sn and, in some cases, Th, V, W and REE are enriched relative to protolith concentrations (Figs. 11D–G, 14 in Corriveau et al., 2022b; Montreuil et al., 2016a; Blein et al., 2022). The facies forms veins, patches and disseminations within albitite (e.g. Southern Breccia in the GBMZ), and replacement zones above albitite and Na-Ca-Fe alteration zones upward from heat sources and inward toward the thermal core of the system (e.g. Mag Hill in the GBMZ). It is a common infill of albitite breccia. The HT Ca-Fe facies generates large spatial footprints in carbonate-bearing sequences; for example, earlier skarn (if present) is systematically and progressively replaced by HT Ca-Fe assemblages (e.g. Grouard and Lou systems and NICO deposit in the GBMZ; Fig. 4B–E; De Toni, 2016; Montreuil et al., 2016a; Corriveau et al., 2022c). Decarbonation of the host supracrustal sequence can be intense to near-complete, and furthers the decarbonation process initiated during regional albitization. This leads to skarn alteration of carbonate rocks and $CO_2$ recharge to the fluid plume.

In zones of strong magnetite enrichment within the HT Ca-Fe facies, fluidized breccia zones consisting of magnetite or magnetite-apatite form; they occur as discrete telescoped zones, sharply crosscutting earlier alteration facies (e.g. Fig. 5B–H; Fig. 21D, E in Corriveau et al., 2022c from Camsell River in Canada; Bafq district in Iran, Daliran et al., 2022; IOA-Ni Jaguar deposit in Brazil; Ferreira Filho et al., 2021). Magnetite breccia pipes and dykes hosting albitized clasts occur in the Cloncurry district and have been interpreted as the products of high-energy fluidization (see Fig. 3A in Rusk et al., 2010). Apatite veins and breccias occur locally (e.g. GBMZ and Bafq district; Fig. 20C in Corriveau et al., 2022c; Daliran et al., 2022).

*IOA Deposits*

IOA deposits and apatite-poor variants are most common within high-temperature systems spatially associated with dioritic intrusions where extensive Na to HT Ca-Fe facies have evolved to epithermal mineralization-related alteration without first evolving to extensive/intense Facies 3 to 5 alteration (i.e. formed proximal to surface). Examples include IOA deposits in the GBMZ, Middle-Lower Yangtze River Metallogenic Belt in China, Central Andes in Chile and Peru (Hildebrand, 1986; Mumin et al., 2010; Tornos et al., 2021; Zhao et al., 2022).

The archetypal IOA deposits are Kiruna in the Norrbotten district in Sweden and El Laco in the High Andes of Chile (Figs. 1, 5I). Other well-characterized districts hosting IOA deposits include the Middle-Lower Yangtze River Metallogenic Belt in China, Southeast Missouri and eastern Adirondack Highlands in USA, Bafq in Iran, Chilean and Peruvian iron belts of the Central Andes, and GBMZ in Canada (Fig. 5; Leonard and Buddington, 1964; Ningwu Research Group, 1978; Hildebrand, 1986; Friehauf et al., 2002; Yu et al., 2011; Chen, 2013; Day et al., 2016; Tornos et al., 2017, 2021; Simon et al., 2018; Taylor et al., 2019; Daliran et al., 2022; Zhao et al., 2022).

In the field, the transition from Na to HT Ca-Fe alteration, IOA deposits and apatite-poor IOA variants occurs via progressive changes from albite-dominant Na, Na-Ca and Na-Ca-Fe alteration to amphibole- and then magnetite-dominant HT Ca-Fe alteration. This is particularly well illustrated in the Mag Hill prospect of the GBMZ and is also observed in other prospects of the GBMZ and Bafq districts (Fig. 5A, B, J, I; Fig. 20 in Corriveau et al., 2022c; Mumin et al., 2007, 2010; Corriveau et al., 2016; Daliran et al., 2022). At the El Laco deposit in Chile, an andesite breccia is progressively replaced by magnetite-dominant HT Ca-Fe alteration, and evolves to massive IOA mineralization (Fig. 5I). Elsewhere, IOA mineralization and apatite-poor variants sharply cut or replace albitite, skarn and iron-skarn alteration (e.g. Middle-Lower Yangtze River Metallogenic Belt and Camsell River district of the GBMZ; Fig. 5C; Fig. 21D, E in Corriveau et al., 2022c; Hildebrand, 1986; Bowdidge et al., 2014, Zhao et al., 2022).

*IOA-REE Deposits*

Iron oxide-apatite mineralization may be either barren or host to significant quantities of critical metals such as nickel, vanadium and REE (Mumin et al., 2010; Gagnon et al., 2018; Ngo et al., 2020; Ferreira Filho et al., 2021). Endowment of REE in IOA mineralization is most pronounced in systems that show evidence for incipient to moderate K-Fe facies alteration. Apatite largely controls the primary REE endowment in IOA mineralized zones; allanite, bastnaesite, britholite, monazite, synchysite, xenotime and some REE-rich fluorocarbonates are subsidiary REE minerals (Lypaczewski et al., 2013; Aleinikoff et al., 2016; De Toni, 2016; Montreuil et al., 2016b; Normandeau et al., 2018). The subsidiary REE minerals are largely derived from dissolution-reprecipitation reactions between apatite formed at the HT Ca-Fe facies and subsequent lower-temperature fluids (e.g. Montreuil et al., 2016c; Normandeau et al., 2018; Corriveau et al., 2022b), or by post-IOAA fluids (e.g. Pea Ridge deposit in US; Harlov et al., 2016). The REE remobilization can lead to deposits with HREE as primary commodities (e.g. Josette deposit; Gagnon et al., 2018).

The evolution of REE-endowed IOA deposits to potassium-bearing alteration (e.g. K-Fe alteration) is observed at the system scale and not necessarily within the boundaries of IOA and REE mineralized zones themselves. Zones of REE-endowed IOA mineralization at the Mag Hill prospect in the GBMZ are structurally overlain by K-feldspar-bearing alteration zones. In the Terra Mine area of the northern GBMZ, REE-rich IOA mineralization evolves to zones of HT Ca-K-Fe alteration and K-felsite (Figs. 4D, 5, 14A, B in Corriveau et al., 2022b).

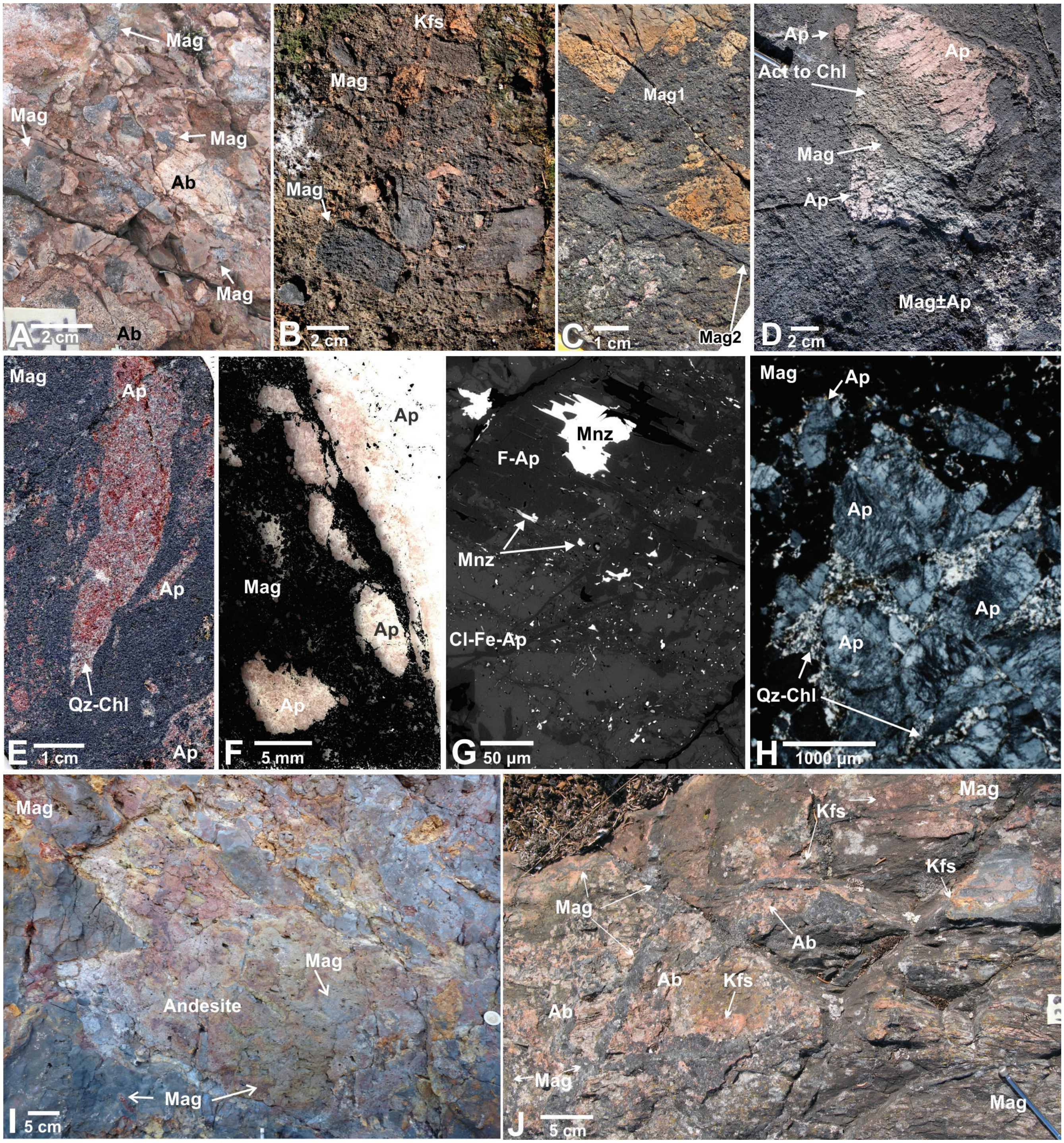


**FIGURE 5.** Transition from HT Ca-Fe alteration to IOA mineralization (A–H, J: Terra Mine, GBMZ; I: El Laco, Chile). **A.** Albitized fragmental volcanic rocks replaced by disseminated magnetite along anastomosing fronts within matrix, within cores of fragments with intensely albitized rims, or across entire clasts (09-CQA-0134). **B–H.** Incremental magnetite alteration of a fragmental volcanic rock (09CQA-0128). Incipient alteration selectively alters some fragments (B). More intense alteration completely replaces the matrix (C) and evolves to pervasive REE-bearing IOA mineralization (reaching 2000 ppm total REE; Corriveau et al., 2015) in which host rocks are completely replaced by magnetite and apatite. Local, very coarse-grained apatite (D) was subsequently brecciated and locally fluidized amongst a magnetite "mush" to define by and defines a flow foliation. Such apatite grains are cut by actinolite and chloritized (D–H). Fluorapatite grains with higher initial chlorine (paler grey in G) are replaced along an array of fractures to fluorapatite having lower iron and chlorine contents (darker grey) and disseminated monazite crystals (white). Back-scattered electron image in G. Plane and crosspolarized photomicrographs in F and H. **I.** Progressive magnetite alteration of andesite breccia, El Laco IOA deposit, Chile. **J.** Re-brecciation and magnetite infill of the altered fragmental volcanic rock shown in B. A weak K-feldspar overprint is stable with magnetite and may relate to the event that recrystallized the REE-bearing apatite to the fluorapatite-monazite assemblage. A–E, I and J: NRCan photos 2020-799 to 2020-804.

The Josette REE-rich IOA deposit in Québec, Canada, occurs in an area of the Kwyjibo district that has evolved to K-Fe alteration and IOCG mineralization. To the south of the Kwyjibo district, IOA mineralization in the Lac Marmont deposit is devoid of REE endowment, and the host system has no known IOCG mineralization (Clark et al., 2010). The Southeast Missouri district (USA) hosts the Boss-Bixby IOCG deposit, as well as the REE-endowed Pea Ridge and other IOA deposits such as Pilot Knob and Kratz Spring (Day et al., 2016). Alteration at Pea Ridge evolved from HT Ca-Fe alteration composed of magnetite and amphibole-bearing assemblages, to magnetite and hematite-rich zones that include K-Fe alteration (iron oxides, K-feldspar, and biotite or phlogopite). In contrast, the Pilot Knob and Kratz Spring deposits, dominated by HT Ca-Fe alteration, are not enriched in REE (Day et al., 2016).

In IOA deposits that mature to Facies 3, 5 or 6 (e.g. Pea Ridge and Josette), high-grade REE mineralization occurs in veins and breccia pipes that cut IOA mineralization but remain within or at the margin of the related IOA deposit (Sappin and Perreault, 2021). Remobilization of REE from apatite and other minerals that precipitated at the HT Ca-Fe facies appears necessary to form REE mineralization reaching average total rare-earth oxide ($REE_2O_3$) grades greater than 1 wt%. The breccia pipes that cut the Pea Ridge IOA deposit (Southeast Missouri, USA) contain 0.2 Mt at 12% $REE_2O_3$ (resource not classified; Nuelle et al., 1992; Aleinikoff et al., 2016; Day et al., 2016). The mineralized veins within the Josette IOA deposit contain a resource of 6.92 Mt grading 2.72% $REE_2O_3$, 53.12% $Fe_2O_3$ and 4.44% $P_2O_5$ (measured + indicated), plus 1.33 Mt of 3.64% $REE_2O_3$ 48.28 $Fe_2O_3$ and 5.62 $P_2O_5$ (inferred) (Gagnon et al., 2018). The HREE plus yttrium account for 0.89 wt% of the 2.72 wt% $REE_2O_3$ grades (i.e. 32.7% of the REE resource) and potential products include $Dy_2O_3$ which make HREE a primary commodity (Gagnon et al., 2018).

Extensive REE ores also form in magnetite bodies in association with carbonatite intrusions, whose host metasomatic systems generate most of the IOAA facies including hematite-bearing ones (e.g. Bayan Obo in China; Chao et al., 1997; Huang et al., 2022).

### Facies 2–3: HT Ca-K-Fe Alteration and Polymetallic Cobalt-iron Deposits

*HT Ca-K-Fe Alteration: Definition, Occurrences and Localities*

The HT Ca-K-Fe facies comprises assemblages of actinolite, biotite, magnetite, ± garnet ± K-feldspar that evolve from amphibole or magnetite-dominant to biotite-rich and locally biotite-dominant assemblages. The facies most commonly evolves from and overprints earlier HT Ca-Fe alteration and occurs as stratabound alteration, discordant lenses, veins and local breccias (Fig. 6; NICO to Duke in the GBMZ, Figs. 22C, E, F, 23A–E in Corriveau et al., 2022c; Dahongshan deposit in China; Zhao et al., 2017, 2019; Idaho Cobalt Belt, USA; Slack, 2013).

Intense and spatially extensive HT Ca-K-Fe alteration is most common in sedimentary sequences rich in carbonate rocks, mafic-ultramafic rocks, earlier HT Ca-Fe metasomatites, and IOA mineralization. The increased availability of calcium and magnesium promotes amphibole crystallization in the presence of biotite, K-feldspar and magnetite. In felsic to intermediate volcanic rocks, HT Ca-K-Fe alteration is absent or only locally developed, and the HT Ca-Fe facies commonly progresses directly to the HT K-Fe facies (e.g. GBMZ Fab system, and Summit Peak prospect overlying the NICO deposit; Montreuil et al., 2016b, c). Where the HT Ca-K-Fe facies is well-developed, it typically evolves to or alternates with a biotite-rich variant of the HT K-Fe facies that contains variable contents of magnetite (Fig. 6; Montreuil et al., 2016b).

*Critical and Precious Metal-rich Cobalt-Iron Deposits*

The HT Ca-K-Fe facies and certain zones at the biotite-rich HT K-Fe facies, can form iron oxide-rich to iron oxide-poor cobalt-rich deposits with diverse critical and precious metal associations, and variable base metals as primary commodities in addition to a vast array of by-products with economic potential. Examples include the Au-Bi-Co-Cu ore (±Te-Sb-Se; ±W) in the NICO deposit of Canada, Co-Cu-Au-Bi-Y-REE in the deposits of the Idaho Cobalt Belt in USA (e.g. Blackbird deposit) and Cu-Au-Co (± Ni-Bi-Te-Ag) at the Guelb Moghrein deposit in Mauritania (Goad et al., 2000; Slack, 2013; Kirschbaum and Hitzman, 2016; R. Goad, pers. comm., 2020).

Iron-bearing minerals in the cobalt-rich mineralized zones include variable proportions of magnetite, iron-bearing silicates (amphibole, biotite, localized garnet), iron sulphides (pyrite and pyrrhotite), and siderite. In certain cobalt-rich deposits or mineralized zones, iron oxides are absent from the gangue mineral assemblages and iron sulphides, iron-rich silicates and iron-rich carbonates are the main iron-bearing minerals.

At the NICO deposit, the highest grade Au-Bi-Co mineralization is associated with several pulses of HT Ca-K-Fe alteration that formed stratabound replacement lenses within a carbonate sequence altered to skarn, HT Ca-Fe and HT Ca-K-Fe facies (Fig. 6F–H; Figs. 22E, F, 23A–F in Corriveau et al., 2022c; De Toni, 2016; Montreuil et al., 2016b). Cobaltite, loellingite, and cobalt-rich arsenopyrite with accessory bismuthinite precipitated along with magnetite, biotite, amphibole, minor pyrrhotite and pyrite, native gold and unidentified bismuth phases associated with the sulpharsenides (cobalt-rich loellingite and cobaltite) and silicates (Sidor, 2000; Burgess et al., 2014; Acosta-Góngora et al., 2015b; Corriveau et al., 2022c). Potential mining by-products include Te, Sb and Se from the bismuth leach residue, whereas tungsten in isolated pods of scheelite, associated with pyrite, chalcopyrite and bismuthinite in arsenopyrite veins, is currently not economic (Acosta-Góngora et al., 2015b; R. Goad, pers. comm., 2020).

At the Guelb Moghrein deposit (Mauritania), a calcite-rich metacarbonate unit was hydrothermally altered to siderite. High-temperature Ca-K-Fe alteration then converted the siderite unit into assemblages containing grunerite-cummingtonite, biotite, magnetite, siderite, chlorite, and graphite. Cobalt mineralization

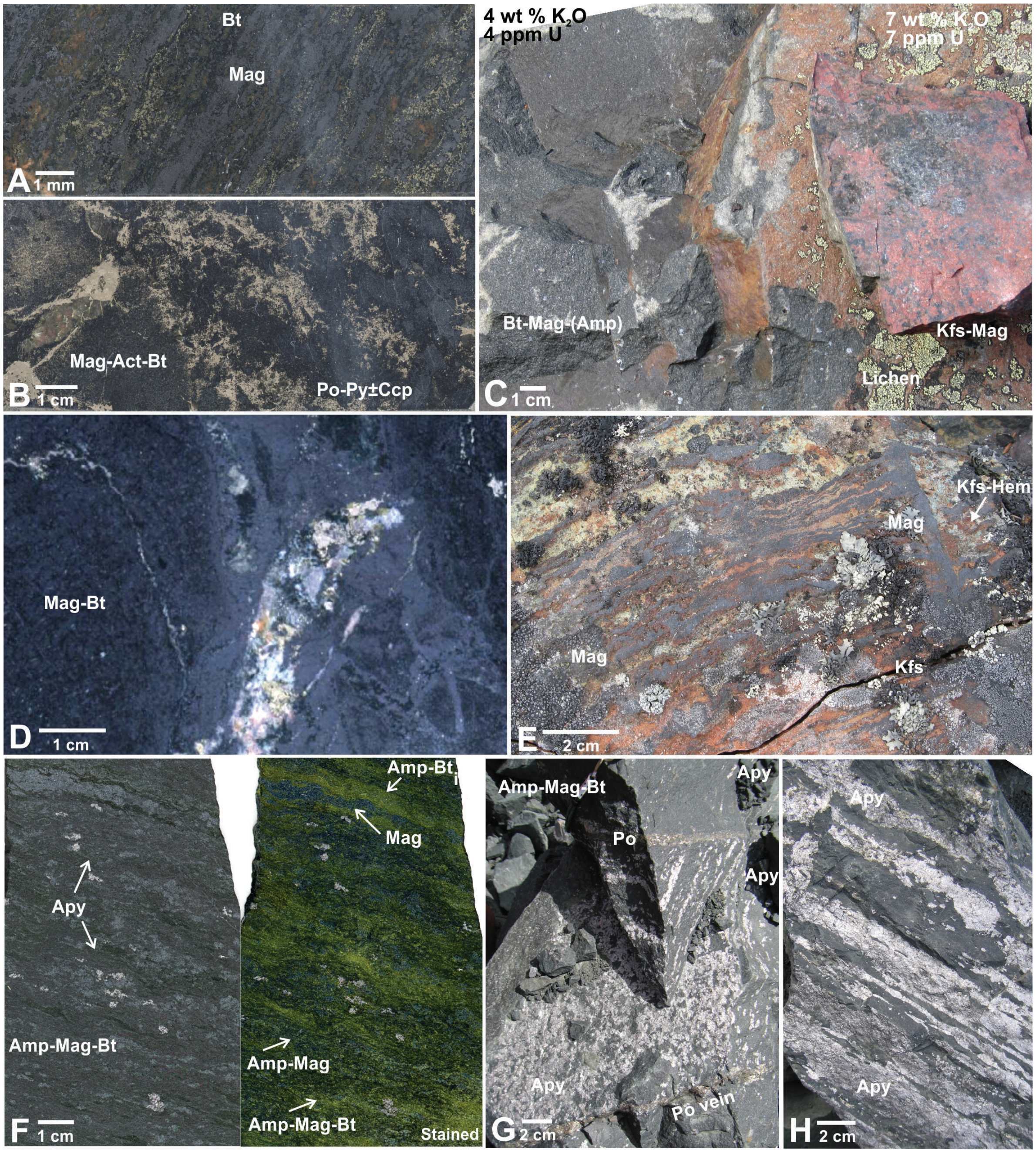


**Figure 6.** Transitions from HT Ca-Fe through HT Ca-K-Fe to HT K-Fe alteration facies. **A, B.** Magnetite-actinolite-biotite HT Ca-K-Fe assemblages replacing IOA mineralization at Port Radium, northern GBMZ, Canada. In A, pyrite is the dominant sulphide within drill core PR-06-02 (532.8'); in B, pyrrhotite is associated with minor pyrite, chalcopyrite, sphalerite, galena and Ni-Co bearing sulpharsenides in drill core PR-06-02 (811.6'). **C.** Magnetite-amphibole-biotite and K-feldspar-magnetite alteration of an andesite, Echo Bay mine area, northern GBMZ, Canada (outcrop CQA-06-0372). From Corriveau et al. (2010b). **D.** Pervasive magnetite-biotite alteration of andesite displaying increased magnetite alteration near sulphide-bearing veins, Candelaria deposit, Chile. **E.** Magnetite vein with extensive stratabound magnetite haloes and diffuse K-feldspar alteration within sedimentary rocks at the Terra Mine, northern GBMZ, Canada (outcrop 09CQA-144). This second generation of magnetite cuts and replaces magnetite-actinolite and epidote alteration and albitization of Figure 4B and D. **F.** Cyclical HT Ca-Fe and HT Ca-K-Fe alteration within the NICO deposit ore zone, GBMZ, Canada (CQA-07-0458). Stratabound amphibole-magnetite HT Ca-Fe alteration is overprinted by stratabound to discordant amphibole-magnetite-biotite HT Ca-K-Fe alteration, and subsequently cut by trains of arsenopyrite clots along and oblique to former sedimentary bedding. A magnetite HT Ca-Fe vein cuts all previous alteration. **G, H.** Stratabound cobalt-rich arsenopyrite ore with accessory fine-grained magnetite cuts fine-grained amphibole-magnetite-biotite metasomatites that replace pervasively and intensely metasedimentary rocks at the NICO deposit. In G, two parallel pyrrhotite-dominant veins with subsidiary magnetite and arsenopyrite sharply cut the stratabound arsenopyrite mineralization that is shown in 3D (CQA-08-552F from mullock piles M2319450 to M231951). A and B: photos courtesy of A.H. Mumin and Alberta Star; D: photo courtesy of Peter Pollard; from Corriveau et al. (2010b); C and E–H: NRCan photos 2020-805 to 2020-810.

(cobaltite, clinosafflorite, gersdorffite and pyrrhotite) associated with HT Ca-K-Fe alteration was overprinted by iron- and copper-rich mineralization (chalcopyrite and pyrrhotite), along with native gold, maldonite ($Au^2Bi$) and bismuth-gold tellurides (Kirschbaum and Hitzman, 2016).

In the Blackbird deposit of the Idaho Cobalt Belt (USA), cobalt-rich mineralization is associated with biotite-rich HT K-Fe facies alteration, and iron oxides are absent from mineralized zones (Slack, 2013). In the Iron Creek cobalt-copper deposit (USA), cobalt-rich mineralization and iron alteration are locally associated with a pyrite-pyrrhotite assemblage containing subsidiary magnetite; sulphides are the main iron minerals (Ristorcelli and Schlitt, 2019).

### Facies 3: HT K-Fe Alteration and Magnetite-group IOCG Deposits and Uranium Mineralization

*HT K-Fe Alteration: Definition, Occurrences and Localities*

The HT K-Fe alteration facies typically consists of a K-feldspar-magnetite assemblage with accessory to minor biotite in felsic to intermediate igneous rocks, intensely albitized rocks, and siliciclastic sedimentary rocks (Fig. 6C, E). In mafic or ultramafic igneous rocks, sedimentary units rich in clay or carbonate, or earlier HT Ca-Fe or HT Ca-K-Fe alteration zones rich in ferromagnesian minerals, the HT K-Fe alteration consists of assemblages rich in biotite, with abundant to absent magnetite, accessory amphibole and accessory to absent K-feldspar (e.g. Salobo in Brazil, Candelaria in Chile, and NICO and Duke in the GBMZ; Corriveau et al., 2016; Montreuil et al., 2016b; Idaho Cobalt Belt in the United States; Slack, 2013).

Biotite-rich members of the HT K-Fe facies assemblages form replacement zones, vein networks, stockworks, and (very locally) breccia zones. Replacement is stratabound or forms anastomosing networks along layers in sedimentary rocks. In contrast, K-feldspar-rich HT K-Fe alteration is typically associated with tectonic, hydraulic and dissolution breccias in a positive feedback loop (Corriveau et al., 2022c). In such breccia zones, K-feldspar preferentially replaces host rock fragments, whereas magnetite variably infills open spaces, replaces milled and pulverized rock fragments in the breccia matrix, and replaces breccia fragments (Corriveau et al., 2022c). As the facies evolves, magnetite may become dominant, and the breccias mature to a magnetite-rich dissolution breccia, as illustrated in Corriveau et al. (2022c).

Observations from the NICO deposit indicate that copper-rich mineralization postdates and may spatially overprint cobalt-rich mineralization (Montreuil et al., 2016b). Biotite-magnetite-K-feldspar-bearing HT K-Fe alteration and minor LT K-Fe alteration associated with magnetite-group IOCG mineralization remobilized earlier-formed Au, Bi, and Co, and contributed copper to the metal assemblages of the deposit (Montreuil et al., 2016b). Native bismuth, bismuth tellurides, emplectite, native gold, gold tellurides, chalcopyrite, pyrite and various Au-Bi-Sb-Te minerals also precipitated (Goad et al., 2000; McMartin et al., 2011; Acosta-Góngora et al., 2015b).

*Magnetite-group IOCG Deposits*

The HT K-Fe alteration facies marks the onset of significant copper precipitation in IOAA systems, as well as formation of large iron oxide breccia zones mineralized in Cu, Au and Ag, forming magnetite-group IOCG deposits with variable Co, Mo, REE and U (Marschik and Fontboté, 2001; Mark et al., 2006; Montreuil et al., 2016b; Melo et al., 2017). The archetypal deposit is Ernest Henry in the Cloncurry district of Australia. In the GBMZ, the Summit Peak prospect above the NICO deposit, the Brooke prospect, and the Sue Dianne deposit are good examples of early-stage HT K-Fe alteration being progressively veined and brecciated (Fig. 7A, B) to form variably mature breccia zones. Magnetite precipitates as breccia cement and replaces fragments (Fig. 7C–E). Pyrite and chalcopyrite precipitate as disseminations within the breccia cement and as veinlets that cut the breccia matrix. Potassium feldspar alters breccia fragments and forms haloes along magnetite-bearing veins and breccias. The systematic development of hematite rims around magnetite suggests progressively more oxidized conditions marking the transition to alteration Facies 5.

At the Ernest Henry deposit, magnetite-group IOCG mineralization formed in the HT K-Fe facies and the transition to a magnetite-carbonate assemblage comprising pyrite, chalcopyrite, K-feldspar, magnetite, biotite, specular hematite, muscovite, barite, fluorite and apatite (Fig. 7F, G; Figs. 7, 8 in Corriveau et al., 2022c; Mark et al., 2006; O'Brien, 2016). These relationships indicate that mineralization at Ernest Henry formed as the IOAA system evolved from Facies 3 to Facies 5 LT Ca-Mg-Fe-(K) alteration. In the magnetite-rich breccia zones of the deposit, mineralization first precipitated as veins and disseminations within the magnetite-dominant breccia cement, then formed disseminations within magnetite-rich replacement zones of K-feldspar-altered clasts (Fig. 7F, G).

At the Salobo deposit (Brazil), magnetite-group IOCG mineralization comprising bornite, chalcocite, and accessory chalcopyrite, molybdenite, cobaltite and safflorite occurs in a biotite-rich HT K-Fe alteration assemblage that evolved to a stilpnomelane, chamosite, greenalite, and iron-pyrosmalite Facies 5 LT Ca-Mg-Fe assemblages (Melo et al., 2017). At Candelaria, magnetite-group IOCG mineralization is associated with biotite-magnetite-K-feldspar-amphibole alteration (Fig. 6D; del Real et al., 2018). In the Port Radium-Echo Bay district in the northern GBMZ, biotite-rich HT Ca-K-Fe facies evolves to K-feldspar-rich K-Fe alteration, and is either barren (Fig. 6C) or mineralized with sphalerite, galena, chalcopyrite and sulpharsenides intergrown with pyrite and pyrrhotite, and enrichments in Co, Ni, and As (Fig. 6A, B; Mumin et al., 2010).

Gold precipitation in magnetite-group IOCG mineralization is closely associated with copper deposition. At the Ernest Henry deposit, native gold (electrum) precipitated with and slightly preceded chalcopyrite (Foster et al., 2007). In the Candelaria deposit, Marschik and Fontboté (2001) described native gold as micron-sized inclusions in chalcopyrite and fracture fillings in pyrite. At the Salobo deposit, gold predominantly occurs as inclusions in copper sulphides and magnetite, and is also associated with arsenides and sulpharsenides, suggesting a coeval precipitation with cobalt and copper (Melo et al., 2017).

*Uranium Mineralization*

The Southern Breccia albitite corridor is overprinted by uranium-rich mineralization having low base metal contents. Uraninite precipitated at the HT K-Fe facies with magnetite, K-feldspar and biotite, and accessory to minor pyrite, molybdenite, chalcopyrite, apatite, ilmenite, titanite, xenotime, zircon, barite, different varieties of aeschynite, and unidentified minerals containing variable Ca, Fe, Nb, REE (Nd, Dy, Ce), Ti, U, and Y (De Toni, 2016; Montreuil et al., 2016b; Potter et al., 2019, 2022). Uraninite in the HT K-Fe assemblages has elevated concentrations of thorium and REE, which tend to be preserved during later dissolution and precipitation reactions, and indicate mineralization

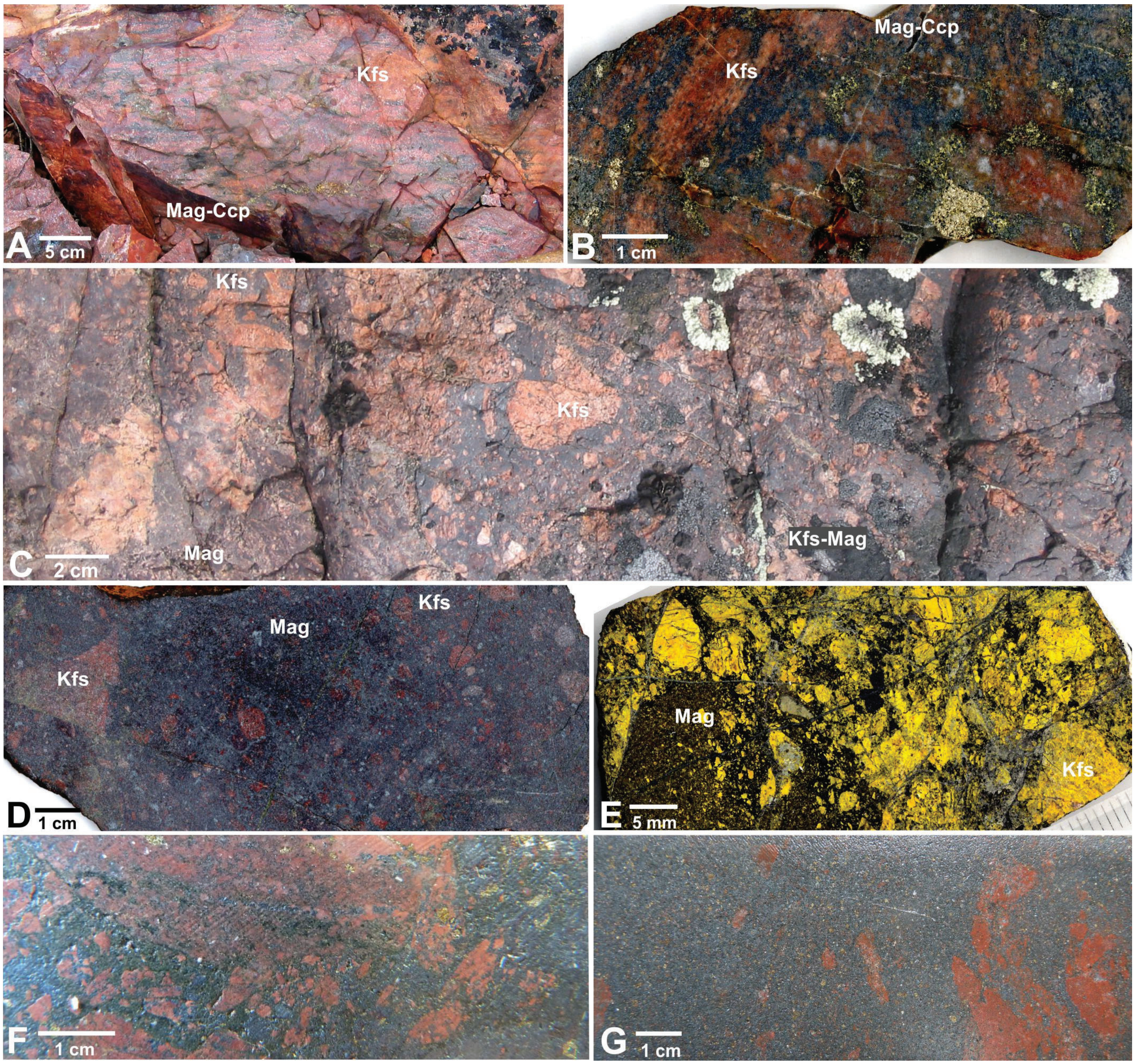


**Figure 7.** High-temperature K-Fe facies. **A, B.** Summit Peak K-felsite that has been brecciated, infilled and replaced by a chalcopyrite and magnetite matrix above the NICO deposit, GBMZ, Canada (KZ-09-SP-4). **C–E.** Ore breccia with magnetite-rich matrix and K-feldspar altered clasts at the Sue Dianne deposit, GBMZ, Canada. Clasts are progressively replaced by the chalcopyrite-magnetite matrix (C: 09CQA-1027; D: KZ-09-SD-7-1; E: KZ-09-SD-7-2). **F, G.** Ernest Henry ore zone (Cloncurry district, Australia) with K-feldspar-altered clasts intensely replaced by magnetite-calcite-chalcopyrite forming the matrix. A–G: NRCan photos: 2020-811 to 2020-817. Sample in E is cobaltinitrite stained.

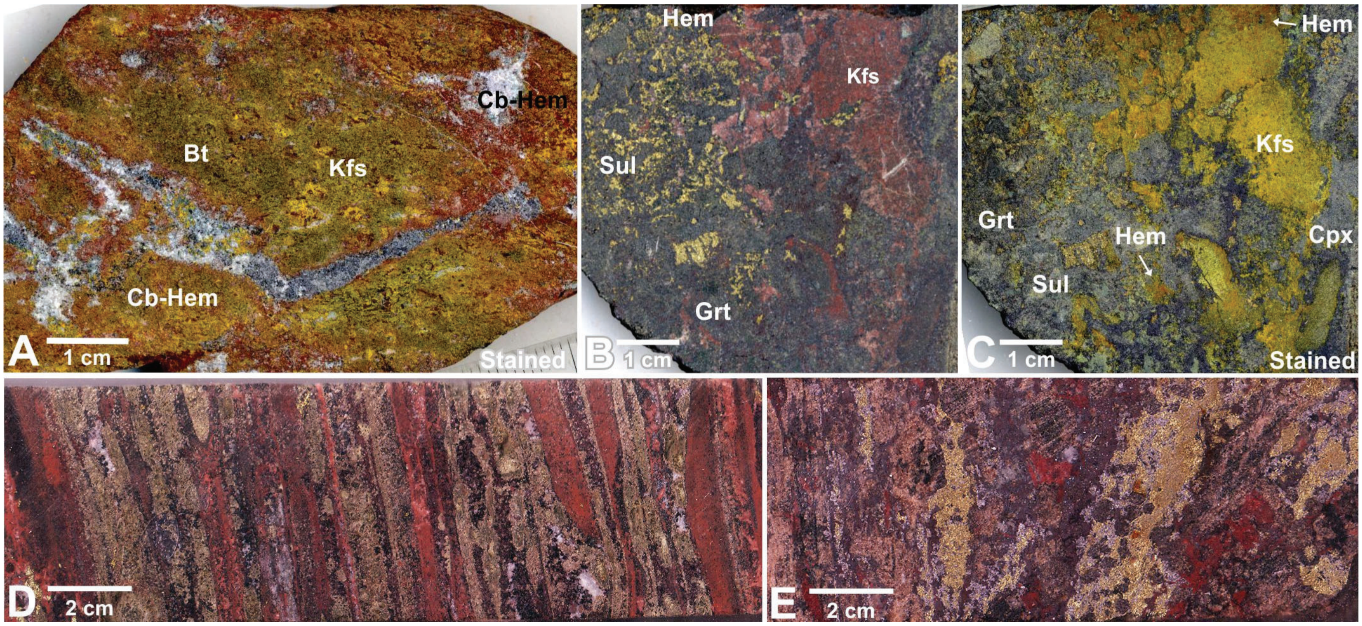


**Figure 8.** Potassic skarn facies. **A.** Cobaltinitrite-stained rock slab of magnetite-calcite vein with disseminated earthy hematite cutting across biotite-magnetite-K-feldspar alteration at the Ernest Henry ore zone (Cloncurry district, Australia). **B, C.** Polished (B) and cobaltinitrite-stained (C) rock slab from the Mile Lake prospect (GBMZ, Canada; CQA-06-0289). Early skarn and volcaniclastic host rocks are replaced by K-skarn consisting of K-feldspar that precipitated with a new generation of clinopyroxene, garnet and sulphides (pyrite, chalcopyrite, galena, bornite). **D, E.** Mixed assemblages of garnet, K-feldspar, chlorite, sulphide and hematite, recording K-skarn alteration overprinted by LT Ca-Mg-Fe alteration at the Groundhog prospect (Punt Hill deposit, Australia; drill hole GHDD1, at 886 m in D and at 854 m in E). The K-feldspar preferentially alters feldspathic layers of the sedimentary host rock. A–C: NRCan photos 2020-818 to 2020-820; D and E: photos courtesy of Monax Mining.

temperatures above 450°C (Potter et al., 2022). In contrast, uraninite in late, lower-temperature veins has low Th and HREE concentrations (Montreuil et al., 2016b; Potter et al., 2019, 2022). In order to precipitate in HT K-Fe facies (Fig. 6C), uranium is interpreted to have been transported as chloride and fluoride complexes by high-temperature, reduced, and possibly acidic fluids (Montreuil et al., 2016b; Timofeev et al., 2018; Potter et al., 2022). The temperature-dependent chemistry of uraninite in IOAA systems help to identify the conditions and timing of primary uranium mineralization in a deposit.

### Facies 4: K-felsite and Polymetallic K-skarn

The prograde evolution of IOAA systems is marked by the development of two main types of metasomatites, K-skarn and K-felsite, at the magnetite to hematite transition between the HT to LT K-Fe alteration. Both types of metasomatites have very localized spatial distribution and are marked by brecciation.

*Polymetallic K-skarn Breccia*

The K-skarn end-member of Facies 4 consists of clinopyroxene (diopside, hedenbergite), garnet (andradite, grossular), K-feldspar, biotite, vesuvianite, amphibole (hornblende, actinolite) and epidote-allanite (e.g. Mount Elliot, Hillside and Punt Hill in Australia and Mile Lake in the GBMZ; Fig. 8; Wang and Williams, 2001; Mumin et al., 2010; Ismail et al., 2014; Fabris et al., 2018). Accessory to minor scapolite, magnetite, hematite and abundant to minor sulphides also occur. Biotite and K-feldspar are minor to very abundant and K-feldspar preferentially replaces feldspathic components of host rocks (Fig. 8B–E).

In the northern GBMZ, localized K-skarn breccia occurs at the Mile Lake prospect within a volcaniclastic unit stratigraphically above HT Ca-Fe alteration. The K-skarn is cut by hematite veinlets (Fig. 8B, C; Fig. 25A–D in Corriveau et al., 2022c). Between Facies 3 and 5, carbonate alteration occurs (e.g. Ernest Henry deposit; Fig. 8A) and may explain why K-skarn can form in any lithotype as part of the normal IOAA alteration process, if such carbonate precipitation is transient and overprinted by high-temperature fluids (Fig. 8B, C).

A critical ingredient to the development of extensive K-skarn is the presence of carbonate-bearing sedimentary rocks (rich in calcium and/or magnesium) and derived skarn, such as observed at the Hillside and the Punt Hill deposits in the Olympic Copper-Gold Province (Fig. 8D, E; Fabris et al., 2018). A proximal intrusion is not required (Wang and Williams, 2001; Corriveau et al., 2016). Potassic skarn alteration is proximal to polymetallic mineralization at Hillside and Punt Hill in Australia (Fig. 8C–E; Fabris et al., 2018) and to magnetite-group IOCG deposits at Candelaria in Chile; Marschik and Fontboté, 2001). Locally it is the main host of polymetallic Cu-Pb-Zn mineralization consisting of bornite, chalcopyrite, sphalerite and galena (Mile Lake prospect; Mumin et al., 2010).

*Potassic-felsite Breccia*

In least-altered host rocks, albitite or K-skarn, the HT to LT K-Fe facies transition consists of K-felsite breccia dominated by K-feldspar. Such K-felsite breccias also form extensive haloes at the front and the sides of iron oxide breccias and are a striking field marker of proximity to IOCG-related mineralization.

Though barren at the time of crystallization, K-felsite breccias are commonly mineralized by later processes. For example, at the Birchtree occurrences in the GBMZ, a K-felsite breccia with zones of HT K-Fe alteration mineralized in chalcopyrite is cut by quartz-hematite veins (Fig. 9A; Mumin et al., 2007; Corriveau et al., 2015). At the Mile Lake prospect, K-skarn is locally progressively replaced by K-feldspar, producing zones of K-felsite (Fig. 25E in Corriveau et al., 2022c). A K-felsite zone also surrounds IOCG breccias at the Sue Dianne, Candelaria and Ernest Henry deposits (Marschik and Fontboté, 2001; Mark et al., 2006; Corriveau et al., 2016).

## Facies 5: Hematite-group IOCG Deposits and Cu-, Au-, and U-rich Mineralization

*LT K-Fe and LT Ca-Mg-Fe-(K) Alteration: Definition*

At temperatures between 375°C and 250°C, a wide range of physicochemical conditions leads to generation of extremely varied alteration assemblages, metal associations and deposit types which are herein grouped under Facies 5. Two main end-member facies form, LT K-Fe and LT Ca-Mg-Fe. The LT K-Fe alteration consists of hematite, sericitic white mica, and variable chlorite, fluorite, and carbonates (see mineralogy in Ehrig et al., 2012). Variants of the LT K-Fe facies include hematite-dominant LT Fe alteration, LT Ca-Fe alteration with hematite ± epidote or fluorite, and LT Si-Fe ± Ba alteration with hematite, quartz and variable barite.

The LT Ca-Mg-Fe ± K end-member includes two main subtypes that can be defined by one or more minerals containing variable quantities of Ca, Fe and Mg: 1) assemblages rich in chlorite, chlorite-magnetite, siderite, dolomite and ankerite, which represent a more reduced assemblage than LT K-Fe facies formed in host rocks rich in Ca, Mg and Fe; and 2) assemblages rich in epidote or chlorite with variable hematite, garnet, amphibole and carbonate, which typically represent a compositional counterpart to the LT K-Fe facies, but formed in host rocks rich in Ca, Mg and Fe. An emerging group of mineralization and deposit types is associated with iron-poor LT Ca-Mg ± K alteration. These are best denoted as iron-poor variants of the LT Ca-Mg-Fe ± K facies (e.g. Mount Dore copper-gold, Merlin molybdenum-rhenium and Tick Hill gold deposits in the Cloncurry district of Australia; Babo et al., 2017). The description of the varied quartz, carbonate, albite, K-feldspar, muscovite and chlorite alteration assemblages and classification of the deposits are, however, beyond the scope of this contribution.

*LT K-Fe Facies and Variants: Occurrences and Localities*

The LT K-Fe facies is best developed in geological environments where felsic-intermediate igneous rocks and siliciclastic sedimentary rocks predominate. At the onset, K-feldspar is stable with hematite where earlier K-feldspar-bearing HT K-Fe facies is replaced (Fig. 10A; Fig. 26D, E in Corriveau et al., 2022c). Precipitation of siderite and minor to moderate replacement of feldspars by sericite (i.e. fine-grained muscovite, illite, phengite and paragonite; Ehrig et al., 2012) is indicative of initial acid-neutral conditions. Intensification of alteration produces sericite-bearing and hematite-dominant assemblages containing variable fluorite and siderite (± K-feldspar relics), indicative of increasingly acidic (hydrolitic) conditions (Fig. 10B; Figs. 12D–F, 13, 26A, D, E in Corriveau et al., 2022c; Hitzman et al., 1992; Ehrig et al., 2012; Barton, 2014; Schlegel and Heinrich, 2015). At the extreme, hematite-fluorite assemblages define an oxidized LT Ca-Fe facies. Chlorite, epidote, quartz, calcite, siderite, barite, fluorite and allanite may all be minor to important phases.

Throughout the development of the LT K-Fe facies, iron contents of alteration zones are significantly greater than potassium contents, and hematite is the dominant iron mineral. It can range in appearance from an earthy reddish-brown variety to a steely, high-crystallinity variety, and to specular hematite (Figs. 9A, B, 10A–C; Figs. 12, 15, 26, 27A–F in Corriveau et al., 2022c). Economic minerals occur as disseminations at replacement fronts, in networks of multidirectional to parallel veins, and as disseminations in major breccia zones, as observed at the Carrapateena, Hillside, Olympic Dam and Prominent Hill deposits in Australia and the Mantoverde deposit in Chile (Fig. 10B; Benavides et al., 2007; Corriveau et al., 2010b, 2022c; Skirrow, 2010, 2022; Ehrig et al., 2012; Schlegel and Heinrich, 2015; Chen and Zhao, 2022).

In the later stages of the LT K-Fe facies alteration and commonly at the apex of known deposits, extreme iron enrichment forms zones of hematite-dominant LT Si-Fe ± Ba alteration comprising hematite, quartz, and barite (commonly as veinlets). This alteration is either barren or barren in base metals but mineralized in gold or LREE (e.g. upper central part of the Olympic Dam deposit, within the Prominent Hill and Oak Dam West deposits in Australia, and more locally in the East Hottah hematite breccia corridor and Fe Zone near Mag Hill in the GBMZ; Fig. 10C; Figs. 13A, E, 15H, 26B, C, 27B–D in Corriveau et al., 2022c; Davidson et al., 2007; Ehrig et al., 2012; Schlegel and Heinrich, 2015; King, 2019). In the GBMZ, jasper-quartz-hematite veins and barite veins also form during the later stages of Facies 5 alteration (Fig. 27G, H in Corriveau et al., 2022c).

The morphology of the LT K-Fe alteration facies includes pervasive-to-selective replacement zones, veins and breccias (Figs. 12–15, 26, 27 in Corriveau et al., 2022c). At the Olympic Dam deposit, intense LT K-Fe alteration, combined with brecciation of the host Roxby Downs Granite, led to extensive replacement of clasts by hematite-sericite-dominant assemblages, re-brecciation accompanied by siderite, barite and fluorite cement, and renewed dissolution of granitic and altered breccia clasts (Fig. 12 in Corriveau et al., 2022c; Ehrig et al., 2017). These processes resulted in an increase in density and hematite content toward the core of

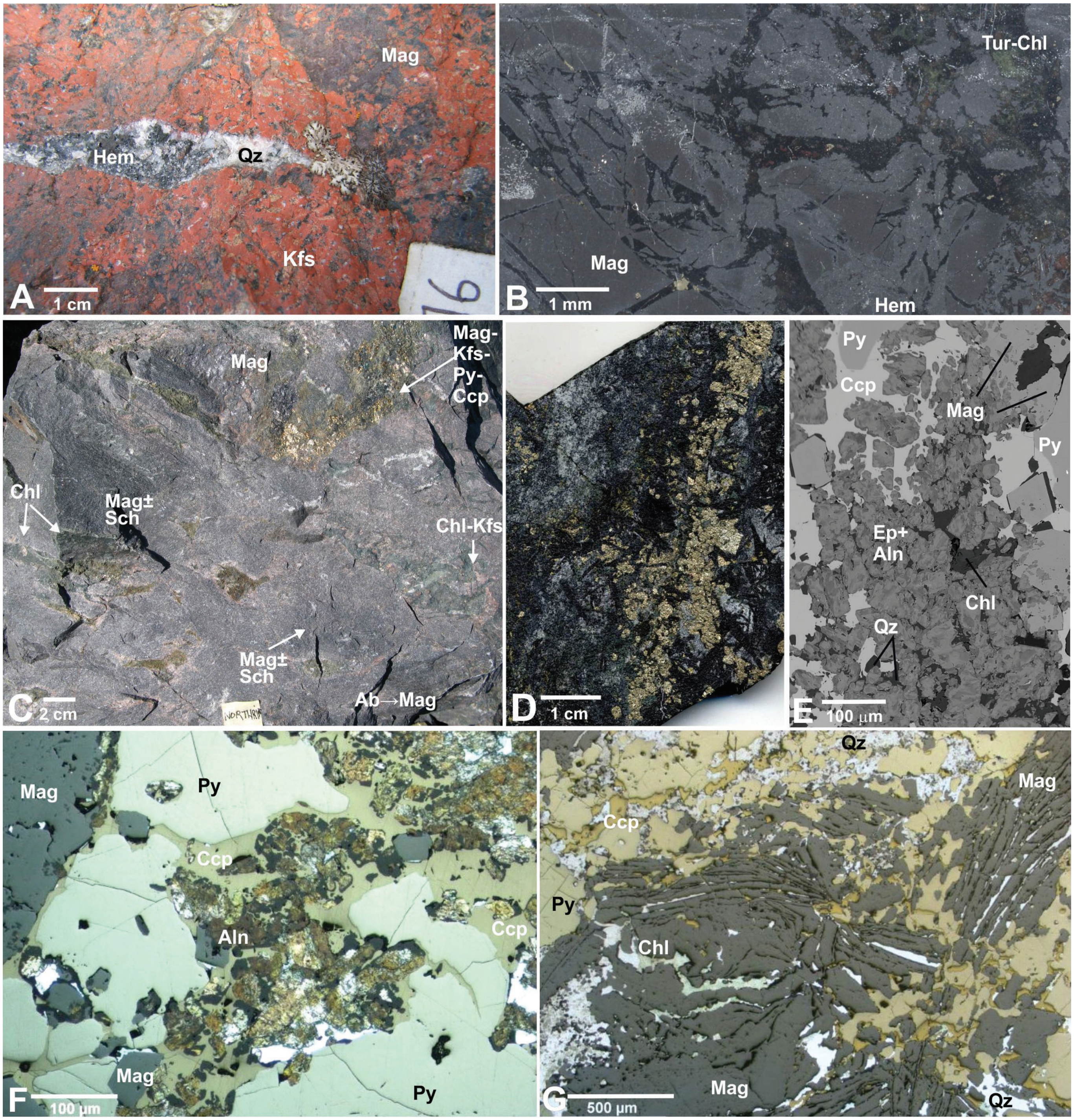


**FIGURE 9.** Images of the transition from HT to LT K-Fe facies. **A.** A zone of intense K-feldspar alteration brecciated, infilled with magnetite, and cut by fine stockworks of specular hematite, pyrite-chalcopyrite veins, and quartz-hematite veins; Birchtree showing, Contact Lake belt, GBMZ, Canada (CQA-05-0076). **B.** Hematite (lighter grey) replacement of magnetite (darker grey), and haloes of tourmaline-chlorite alteration within the Port Radium IOA prospect (PR-06-02, 60.7'). **C–G.** Porphyritic andesite pervasively albitized, replaced by moderate to intense magnetite alteration, and cut by scheelite-bearing, magnetite-dominant HT Ca-Fe alteration fronts and irregular veins. The veins contain accessory allanite, apatite and titanite (close-up in E), and are subsequently cut by stockworks filled with calcite, magnetite, sulphides, chlorite, epidote and quartz (close-up in D, E and G) (mineralized block of the Northrim mine at station 09CQA-0139, Camsell River district, Canada). In D, a vein of calcite, magnetite (mushketovite, see G), sulphides (pyrite and chalcopyrite), chlorite, epidote and quartz indicates a LT Ca-Mg-Fe alteration paragenesis in which hematite is subsequently replaced by magnetite that is possibly stabilized by high $fCO_2$ and alkalinity. This vein cuts all alteration types in C. In F, allanite and magnetite are cut by a pyrite, chalcopyrite, quartz, calcite and chlorite assemblage. Photomicrographs in F and G are under reflected and transmitted light, thin section 09CQA-0139B01. B: photo courtesy of A.H. Mumin and Alberta Star; A, C and D: NRCan photos 2020-821 to 2020-823.

the deposit (Figs. 12, 13 in Corriveau et al., 2022c; Reeve et al., 1990; Ehrig et al., 2012, 2017).

Repeated brecciation and associated replacement events during LT K-Fe to LT Ca-Fe and LT Fe-Si ± Ba alteration create complex relationships amongst minerals within Facies 5 metasomatites, and result in remobilization and concentration of metals such as Au, Co, Cu, REE and U that precipitated during earlier alteration (Benavides et al., 2007; Skirrow, 2010; Schlegel and Heinrich, 2015). Subsequent fluid circulation events may produce mineralized veins similar to those formed during the low-temperature stages of IOAA metasomatism (Ehrig et al., 2012, 2017; Ciobanu et al., 2013, 2017; Schlegel and Heinrich, 2015; Macmillan et al., 2016; Schmandt et al., 2017, 2019; Verdugo Ihl et al., 2017, 2019; Apukhtina et al., 2020; Maas et al., 2020; Schlegel et al., 2020). The chemical footprints of the facies (Corriveau et al., 2022b) are thus the sum of many processes related to repeated ingress of fluids having varied compositions (Dmitrijeva et al., 2019; Maas et al., 2020). These footprints may include the overprinting of earlier HT Ca-Fe and HT K-Fe facies rocks (Apukhtina et al., 2017, 2020; Corriveau et al., 2020, 2022c).

*LT Ca-Mg-Fe-(K) Facies: Occurrences and Localities*

Iron-rich LT Ca-Mg-Fe-(K) alteration precipitates metasomatic mineral assemblages rich in ferromagnesian minerals such as amphiboles, phyllosilicates and carbonates, potassic aluminosilicates and abundant to no iron oxides. Under high $fO_2$ conditions, mineral assemblages rich in andradite, epidote and amphibole with $Fe^{3+} > Fe^{2+}$ can also form. This is consistent with the low-temperature stability of andradite, which can form experimentally in the 250º to 350ºC range and below 200ºC in nature (Taylor and Liou, 1978; Gutzmer et al., 2001). In contrast, iron-rich LT Ca-Mg-Fe-(K) alteration under reduced conditions forms mineral assemblages rich in carbonates, chlorite, amphiboles, phyllosilicates and magnetite. In both facies, iron oxides precipitate when the amount of iron (as $Fe^{3+}$ and $Fe^{2+}$) in the system exceeds the ability of the ferromagnesian silicate and carbonate minerals to accommodate it.

The LT Ca-Mg-Fe-(K) facies is most common in Ca, Fe and Mg-rich host sequences (e.g. mafic to ultramafic rocks, carbonate rocks, skarn, HT Ca-Fe metasomatites), or where assemblages precipitated under reduced conditions. If multiple fluid sources are involved in the formation of the LT Ca-Mg-Fe-(K) facies, the mineralization types and metal associations are more diverse than those formed within the LT K-Fe facies. This variability likely reflects a greater range in the physicochemical conditions of the fluids forming the LT Ca-Mg-Fe-(K) facies, and chemical buffering capabilities of the host rocks.

*Copper Mineralization and Hematite-group IOCG Deposits*

Typical hematite-group IOCG deposits contain abundant hematite coeval with copper-gold mineralization; they are associated with the prograde development of LT K-Fe facies under increasing $fO_2$ conditions, when potassic aluminosilicate-bearing mineral assemblages become stable, iron contents increase and pH decreases (Hitzman et al., 1992; Barton, 2014; Schlegel and Heinrich, 2015; Skirrow, 2022). At the Olympic Dam deposit (Australia), sulphides evolved from sphalerite to galena, then pyrite followed by chalcopyrite, bornite and finally chalcocite (Ehrig et al., 2012, 2017).

At the Prominent Hill deposit (Australia), the main Cu-Au-(U-LREE) mineralization consists of copper sulphides intergrown with hematite, chlorite, muscovite, and variable siderite, ankerite, kaolinite, barite, fluorite, fluorapatite, REE minerals, and uraninite (Schlegel and Heinrich, 2015). The main copper sulphide species are chalcocite, bornite, digenite ($Cu_9S_5$), idaite ($Cu_5FeS_6$), and chalcopyrite (Belperio et al., 2007; Schlegel and Heinrich, 2015). Successive cycles of copper sulphide deposition are recorded in the deposit; all copper sulphides overprint pyrite deposited in the early stages of hematite-chlorite-sericite alteration. Peak gold (± copper) mineralization accompanies the formation of a hematite-quartz assemblage containing accessory to minor fluorapatite, barite, fluorite and REE minerals (Schlegel and Heinrich, 2015).

At the Carrapateena deposit, the main copper-gold mineralization relates to the formation of a hematite-chlorite-muscovite alteration assemblage that includes variable siderite, ankerite, quartz, and accessory barite, monazite, anatase, magnetite, fluorite, apatite and zircon (Porter GeoConsultancy, 2021). Chalcopyrite, associated with pyrite, is the main copper sulphide, and chalcocite, digenite and covellite occur as secondary copper sulphides. Gold-enriched mineralization also occurs among hematite zones with low copper (OZ Minerals, 2019).

At the Mantoverde deposit (Chile), the main Cu-(Au) mineralization occurred with specular hematite, calcite, muscovite, K-feldspar and chlorite, with accessory to minor tourmaline, titanite and scapolite (Rieger et al., 2010). Chalcopyrite is the main copper sulphide in the hypogene zone of the deposit; it co-precipitated with pyrite and is locally overprinted by digenite and bornite (Rieger et al., 2010).

As alteration evolves through multiple cycles of brecciation and replacement, the sequence of metal enrichment, depletion and remobilization generates a temporal and spatial zoning of metals within deposits, as illustrated by the distribution of metals and mineralization in plan views and cross sections of the Olympic Dam deposit (Corriveau et al., 2022b, c; see also Ehrig et al., 2012, 2017; Dmitrijeva et al., 2019).

At the LT Ca-Mg-Fe-(K) facies in Ca, Fe and Mg-rich hosts, copper-rich mineralization occurs without significant hematite under progressively increasing $fO_2$ conditions and decreasing pH – comparable to hematite-group IOCG mineralization formed at the LT K-Fe facies. At the Sossego deposit (Brazil), the main copper-gold mineralization with subsidiary Ag, Mo, Ni, Co and U is associated with the prograde development of LT Ca-Mg-Fe-(K) alteration that initially consisted of chlorite, epidote and calcite, followed by chlorite, quartz, hematite and muscovite (Monteiro et al., 2008). Similarly, at the Hillside copper-gold deposit (Olympic Copper-Gold Province), LT Ca-Mg-Fe-(K) alteration

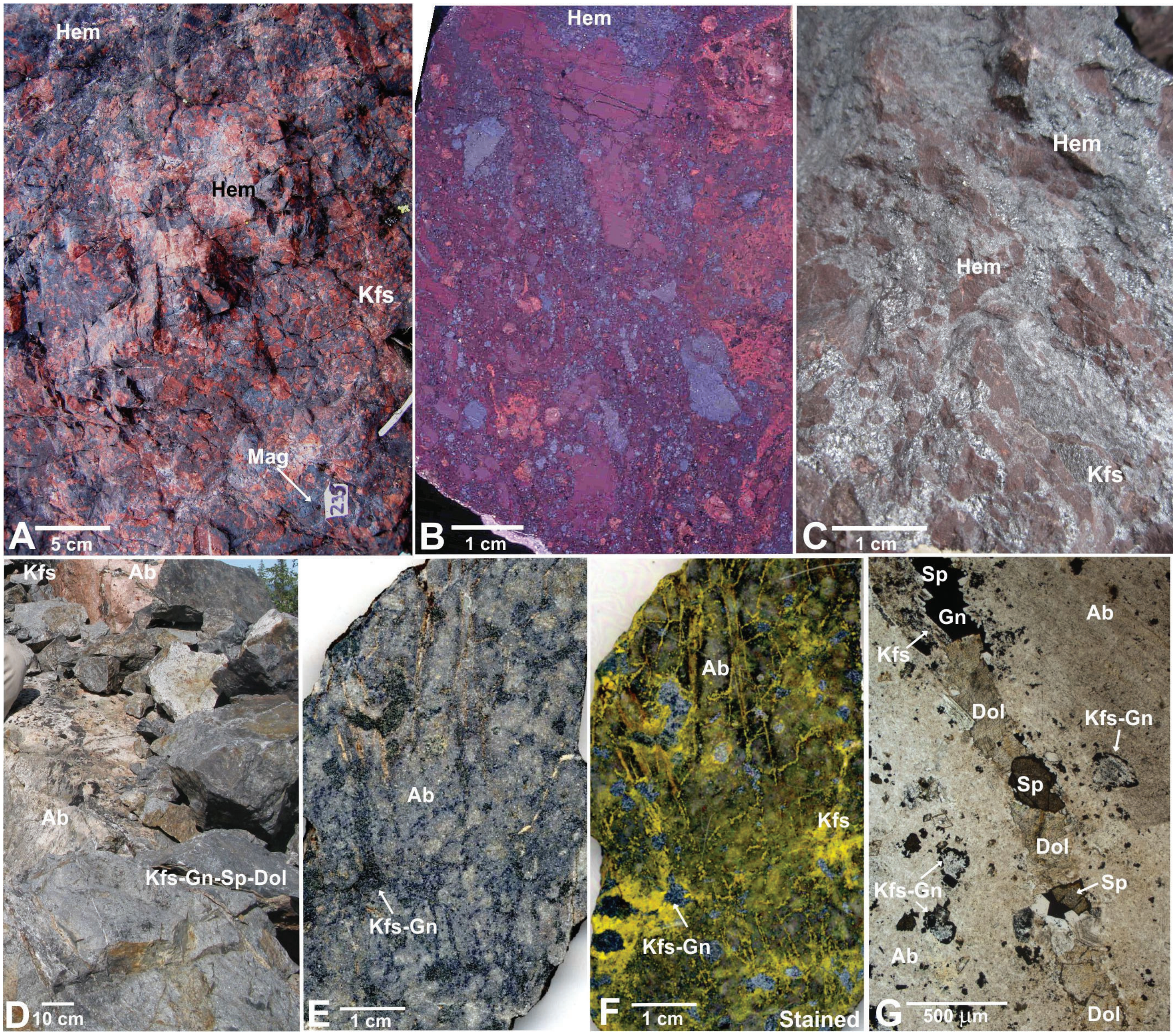


**Figure 10.** LT K-Fe alteration and vein-type mineralization. **A.** Magnetite-to-hematite breccia and K-feldspar-altered clasts at the Sue Dianne deposit, GBMZ, Canada (CQA-05-235). **B.** Multiphase hematite-sericite alteration in breccia from the Olympic Dam mine in South Australia. Texture-preserved quartz-bearing granite clasts are present, along with clasts dominantly replaced by hematite in both red and steel grey varieties. **C.** East Hottah (GBMZ) steely specular hematite breccia cutting K-feldspar altered host (10CQA-0263). **D–G.** Dolomite, sphalerite, and galena (± chlorite, tourmaline and quartz) veins and alteration patches with K-feldspar haloes within a brecciated intensely albitized porphyritic intrusion in the Camsell River district, GBMZ (09CQA-0135). F is the same sample as E, but cobaltinitrite-stained to highlight the presence of K-feldspar overprint (bright yellow). G: transmitted light photomicrograph of sample E. A–F: NRCan photos 2020-824 to 2020-828.

overprints earlier skarn and K-skarn alteration and is associated with copper-gold mineralization (Conor et al., 2010); this represents a skarn-hosted variant of hematite-group IOCG mineralization. Mineralization consists of pyrite and chalcopyrite, and subsidiary gold, electrum, silver-gold tellurides, cobaltite and molybdenite. Gangue minerals comprise andradite, diverse amphiboles, chlorite, epidote, hematite, K-feldspar and carbonates, in varying proportions (Ismail et al., 2014; Ismail, 2015; Teale, 2019).

In the Punt Hill area (Olympic Copper-Gold Province), Cu-Au-Zn-Pb mineralization is part of a LT Ca-Mg-Fe-(K) alteration assemblage that replaces large zones of skarn and K-skarn alteration (Fabris et al., 2018; Corriveau et al., 2022b). Chlorite correlates positively with chalcopyrite, and hematite with bornite and gold (Fabris et al., 2018).

At the Mount Elliot Cu-Au-(Co-Ni) deposit in Australia, zones of skarn alteration developed in carbonate-bearing metapelite, metagreywacke and metabasite. The main mineralization occurred during LT Ca-Mg-Fe-(K) alteration at temperatures around 350°C (Wang and Williams, 2001). The syn-mineralization assemblages include actinolite, magnetite, andradite, allanite and tourmaline, with minor biotite, K-feldspar and chlorite. Mineral assemblages containing magnetite, andradite and actinolite suggest intermediate conditions between the reduced and oxidized end members of the LT Ca-Mg-Fe-(K) facies.

In the Romanet Horst district (Canada), the Delhi Pacific Cu-Au-Ag prospect formed at the contact between sulphide-rich graphitic sedimentary rocks and intensely albitized flows. Copper-Au-Ag mineralization consists of pyrrhotite-pyrite-chalcopyrite and accessory bornite formed at the LT Ca-Mg-Fe-(K) alteration facies under reduced-intermediate (pyrrhotite-pyrite stable instead of iron oxides) and acidic conditions. Gangue minerals include carbonate, chlorite, quartz, and accessory muscovite (Desrochers, 2014).

*Gold Mineralization and Hematite-group IOCG Deposits*

Gold-rich mineralization, with or without base and critical metals, occur in certain LT K-Fe and LT Ca-Mg-Fe alteration zones. Significant gold mineralization formed under oxidized conditions in hematite- and quartz-dominant alteration zones of the LT K-Fe facies at the Prominent Hill deposit (Schlegel and Heinrich, 2015). At Olympic Dam, gold mineralization occurs in copper sulphide zones within the LT K-Fe alteration facies and is most enriched along the outer margin of the LT Si-Fe-(Ba) hematite-quartz-barite core (Ehrig et al., 2012). At Prominent Hill, the main zones of gold mineralization occur at the transition between hematite-chlorite-sericite and hematite-quartz alteration (Schlegel and Heinrich, 2015). Early-stage magnetite-phlogopite and magnetite-K-feldspar-pyrite with accessory chalcopyrite, pyrrhotite, apatite, titanite and monazite occur as variably preserved relics in some mineralized zones, as well as in satellite alteration zones around the main mineralized zones (Schlegel and Heinrich, 2015).

At the Scadding Au-(Co-Cu-Ni) deposit in Canada and some of the Au-Cu-Bi mineralized zones of the Tennant Creek Inlier in Australia, gold mineralization occurs under reduced to oxidized conditions in LT Ca-Mg-Fe alteration zones in which chlorite, minnesotaite, magnetite, quartz and hematite are present in variable quantities (Skirrow and Walshe, 2002; Schandl and Gorton, 2007; Yarie and Wray, 2019).

*Uranium-rich Mineralization*

Uranium commonly precipitates during Facies 5 alteration in IOCG deposits (Potter et al., 2022). At Olympic Dam, uranium precipitated largely as uraninite, coffinite and brannerite in association with hematite and chalcopyrite, with a first generation uraninite at Facies 5 (Ehrig et al., 2012, 2021). At Oak Dam East, fine-grained uraninite occurs in association with florencite ($CeAl_3(PO_4)_2(OH)_6$), monazite, and xenotime within chalcopyrite-bearing hematite-dominated breccia adjacent to sericite-illite and chlorite alteration zones (Davidson et al., 2007).

### Facies 6 - Vein-type Deposits, Epithermal Mineralization and Metal Remobilization and Addition

Facies 6 comprises all alteration and mineralization events that follow the development of Facies 5 during the prograde evolution of an IOAA system and afterwards. The development of Facies 6 generates a variety of vein systems, epithermal mineralization, and associated alteration types. In certain IOAA systems, the final stages of prograde evolution of the fluid plume produces mineralized quartz, barite, fluorite or carbonate-rich veins hosted by phyllic or other epithermal-style alteration zones. This occurs as a consequence of the increased silica, barium and carbon load, and decreasing pH of the ascending fluid plume.

Zones of epithermal mineralization and alteration (e.g. advanced argillic alteration assemblages) located in the near-surface or peripheral parts of IOAA systems have been reported in the GBMZ in Canada, the Andes (Chile), the Middle-Lower Yangtze River district (China), and the Olympic Copper-Gold Province (Australia) (Ningwu Research Group, 1978; Mumin et al., 2010; Ehrig et al., 2012; Li et al., 2015; Kreiner and Barton, 2017; Zhao et al., 2022). For example, some sericite-dominant and advanced argillic alteration formed locally at the Olympic Dam deposit (Fig. 13D in Corriveau et al., 2022c; Ehrig et al., 2017). In the GBMZ, examples of phyllic alteration and polymetallic vein-type mineralization occur at Gossan Island and the Echo Bay Gossan in the Port Radium-Echo Bay district (Mumin et al., 2010). Furthermore, barite-bearing veins (± quartz) postdate LT K-Fe facies in the NICO, K2 and East Hottah regions of the GBMZ (Fig. 27H in Corriveau et al., 2022c).

The veins form through renewed fluid circulation related to subsequent intrusive, volcanic or tectonic activity (orogenesis). The veins may host mineralization, such as the F-Ba-U-REE veins at the Monakoff and E1 prospects near the Ernest Henry deposit in the Cloncurry district (Williams et al., 2015), and U-REE-bearing veins at Mary Kathleen and other parts of the Mount Isa Province (Oliver et al., 1999; McGloin et al., 2013; Williams et al., 2015).

In many systems, the late veins commonly contain metal associations that reflect the metal enrichments of the host IOAA system (e.g. GBMZ and Central Mineral Belt; Mumin et al., 2010; Corriveau et al., 2016; Sparkes, 2017; Gandhi et al., 2018; Blein et al., 2022; this study). For example, at NICO in the GBMZ, a ca.1850 Ma calcite-magnetite-titanite-chalcopyrite vein cuts the ca. 1870 Ma NICO deposit, and contains an assemblage similar to IOAA-related stratabound calcite-magnetite alteration that cuts HT Ca-K-Fe alteration. The vein is coeval with the final stage of batholith intrusion in the GBMZ (Davis et al., 2011); its contained metal is interpreted to have been sourced in the NICO ore system and remobilized through renewed fluid circulation during batholith emplacement. This example is one of many in which dating such mineralized veins would provide no information on the timing of the mineralization related to development of the IOAA system (see also Corriveau et al., 2010a).

Uranium-rich and silver-rich variants of five-element (Ag, As, Bi, Co, Ni) vein systems are observed in the Port Radium-Echo Bay district and at the past-producing Northrim and Terra mines in the Camsell River district of the GBMZ (Fig. 9D–G; Mumin et al., 2010). At the past-producing Eldorado mine in the Port Radium-Echo Bay district, the five-element veins described by Kissin (1992) and Gandhi et al. (2018) were dated at 1442 ± 36 Ma (U-Pb date from hydrothermal xenotime; Trottier, 2019), whereas the host IOAA system formed at 1.87 Ga (Davis et al., 2011). The mineralizing fluids for the five-element veins in the northern GBMZ must have been derived, in part, from the lower Dismal Lakes Group (Re-Os model age of 1438 ± 8 Ma; Rainbird et al., 2020) of the Hornby Bay basin, which currently overlies the northwestern GBMZ. Nevertheless, as the metal assemblages in the five-element veins reflect the metal enrichments in the host IOAA system (see Mumin et al., 2010), the vein mineralization is interpreted to have been sourced from earlier IOAA mineralization during renewed fluid circulation. Addition is also possible as illustrated by the significant enrichment in uranium at the Olympic Dam deposit (Australia) nearly 1 billion years after the precipitation of the first generation of uranium precipitation at Facies 5 LT K-Fe alteration (Ehrig et al., 2021).

At the 1470 Ma Pea Ridge IOA deposit in the Southeast Missouri district, 1464 Ma, post-deposit breccia pipes hosting barite, dolomite, calcite, synchysite (Ca-Ce-(Y + REE) carbonate), K-feldspar, quartz, fluorapatite, monazite, xenotime, allanite, rutile, chlorite, and hematite display mineral assemblages similar to earlier alteration within zones of IOA mineralization (Aleinikoff et al., 2016; Harlov et al., 2016; Neymark et al., 2016). The similarity in alteration assemblages between post-IOAA veins and earlier IOAA facies illustrates that fluid recirculation can take place under physicochemical conditions similar to the host IOAA system.

Following high-grade metamorphism, local metal remobilization within mineralized IOAA systems can lead to formation of magnetite-pyrite-chalcopyrite-bornite-chalcocite-bearing veins as illustrated by the Bondy gneiss complex IOAA system that was metamorphosed to granulite facies (Corriveau and Spry, 2014; Dufréchou et al., 2015; Corriveau et al., 2018a). Provinces characterized by IOAA systems may also host giant quartz-hematite ± uraninite veins and pods, such as in the GBMZ, where the vein systems can extend for tens of kilometres, or quartz pods such as in the Lufilian arc in Africa (Lobo-Guerrero, 2010; Mumin et al., 2010). Many of these examples illustrate that post-IOAA remobilization can produce assemblages closely resembling those of the IOAA systems themselves, complicating interpretations of relative timing between IOAA alteration and mineralization.

## Rising Geotherms, Magma Emplacement, Cooling, Tectonics, and their Impacts on Deposit Types

Along fluid flow paths with elevated temperature gradients, pressure gradients exert only minor control on metasomatic reactions (Dipple and Ferry, 1992). Hence, temperature changes in the fluid plume during its evolution are interpreted as key to the development of the distinct metasomatic IOAA facies. At regional scales, the high temperatures achieved during metasomatism are best interpreted as a result of heat transfer from large volumes of high-temperature fluids, without the need for orogenic metamorphism. This is illustrated by geological provinces in which some of the host rocks are not metamorphosed beyond sub-greenschist facies (e.g. GBMZ, Canada). The original heat of the fluid plume can be transferred by exsolution of magmatic fluids and heating of mid-to-upper crustal fluids by large magma chambers, aided by the emplacement of subvolcanic intrusions and/or dykes during the ascent of the fluid plume. In the case of the Southern Breccia albitite-hosted uranium prospect, fluids have albitized the rocks adjacent to a fault zone structurally above a subvolcanic intrusion, and porphyritic dykes have intruded the albitite breccias during late stages of brecciation (Corriveau et al., 2022c). At the Olympic Dam deposit, emplacement of ultramafic dykes was coeval with IOAA metasomatism (Ehrig et al., 2012).

*Regional Heat Transfer – Sodic to Skarn Alteration*

Albitization occurs under a wide range of temperatures, from as low as >65°C for albitization of K-feldspar, to >110°C for albitization of plagioclase, to >550°C (Boles, 1982; Cathelineau, 1986; Aagaard et al., 1990; McCaig et al., 1990). In IOAA systems, fluid inclusions record temperatures from 450°C to 600°C within Na to Na-Ca and Na-Ca-Fe alteration zones (De Jong and Williams, 1995; Pollard, 2001; Oliver et al., 2006; Davidson et al., 2007; Williams et al., 2010; Somarin and Mumin, 2014). The maximum temperature is, however, uncertain. Close to the thermal core(s) of the system(s) and in zones of maximum fluid circulation, sodic alteration developed above ~400–550°C to form: 1) coeval skarn in carbonate rocks with peak temperatures of 900°C in the Middle-Lower Yangtze River Metallogenic Belt (Zeng, 2020); 2) scapolite in gabbro (e.g. 600–700°C; Engvik et al., 2017); 3) hypidiomorphic textures typical of plutonic rocks in albitite; and 4) coarse-grained amphibole-magnetite-apatite in Na-Ca-Fe pegmatites (e.g. Fig. 19 in Corriveau et al., 2022c; Corriveau et al., 2022a).

Metamorphic phase equilibria modeling of a variety of albitite samples from the GBMZ indicates that albite in calcium-bearing rocks is stable up to about 625°C, then reacts to produce more calcic plagioclase at higher temperatures (Trapy, 2018). This is important considering that oligoclase, not albite, is the most common plagioclase observed in Na-Ca alteration zones in some settings (Kreiner and Barton, 2017).

Sodium may be sourced from dilute aqueous fluids, or from saline and hypersaline brines and salt melts of different origins in a variety of geological settings (Dilles and Einaudi, 1992; Mark and Foster, 2000; Boulvais et al., 2007; Yardley, 2013; Engvik et al., 2017; Zeng, 2020; Zhao et al., 2022). In IOAA systems, regional-scale albitite corridors form not only within sedimentary sequences — in which high porosity allows retention of saline fluids through much of their geological history (Yardley and Bodnar, 2014; Montreuil et al., 2015;

Morrissey and Tomkins, 2020), but also in volcanic sequences and intrusive rocks of variable compositions, including basalts (e.g. Port Radium-Echo Bay and Camsell River districts, GBMZ; Romanet Horst; Corriveau et al., 2014; McLaughlin et al., 2016). Significant chemical modifications are required to transform host rocks into albitite with 10 to 12 wt % $Na_2O$,

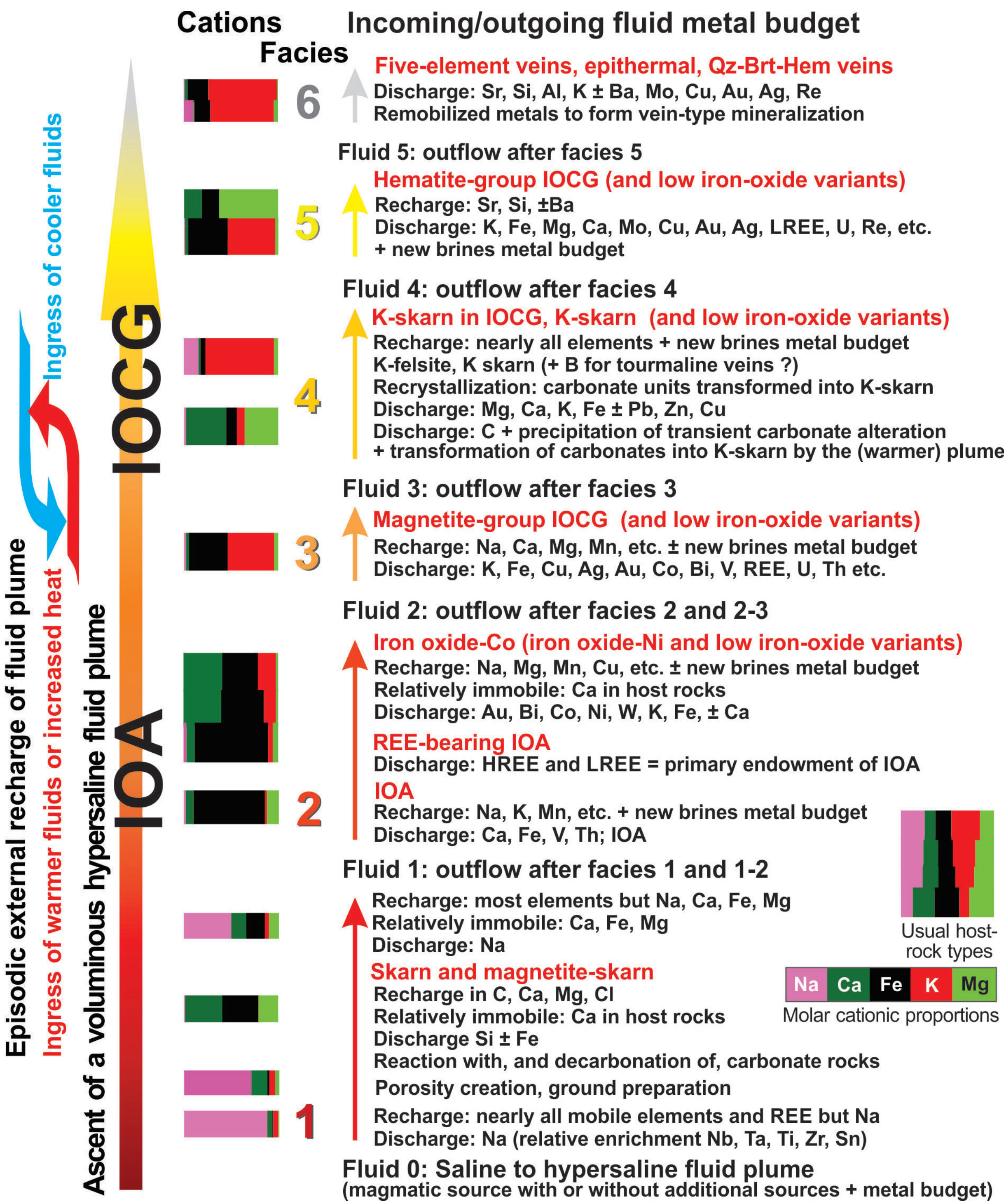


**FIGURE 11.** Alteration facies record the sequential recharge and discharge of elements and stable mineral assemblages as fluid conditions and metal of the main fluid plume evolves through metasomatic reactions. The large arrow represents the main fluid plume evolution whereas the coupled blue and red arrows represent the potential recharge of the main fluid plume with fluids from different sources and temperatures. At the upper crustal level, as observed through field work in the GBMZ and other systems globally the hypersaline fluid plume is driven by heat from the underlying magma chamber, re-energized by ultramafic to felsic magmatism, and channelled through fault zones and other discontinuities. However, magnetotelluric data suggest that fluid sources may be as deep as the mantle (Wise and Thiel, 2020). Modified from Corriveau et al. (2010b, 2016).

such as in the Southern Breccia albitite corridor, GBMZ (Fig. 11; Corriveau et al., 2015, 2022b). The regionally intense sodic alteration in IOAA systems must be triggered by a particularly voluminous, saline to hypersaline fluid plume at temperatures high enough to raise the regional geothermal gradient through reactions with host rocks.

Hot saline to hypersaline fluid plumes ascend into cool rocks, heating them and increasing the regional geothermal gradient. Early sodic alteration is thus expected to occur, in part, at lower temperatures than those in the core of the fluid plume. In contrast, the highest fluid temperatures during albitization and associated pervasive recrystallization of albitite are likely achieved above coeval intrusions. In such settings, zones of skarn are spatially associated with albitite if carbonate hosts are present (e.g. Grouard Lake and Mile Lake prospect in the GBMZ; Figs. 4C, F, 12A in Corriveau et al., 2022b; Fig. 18A, B in Corriveau et al., 2022c; Zhao et al., 2022). Under these contrasting settings, pervasive albitization and albitite corridors form under a wide range of temperatures along the main fluid pathways. A consequence is that, within lower-temperature systems, carbonate units are not necessarily transformed into skarn, such as in the albitite corridors along fault zones of the Romanet Horst in Canada and carbonate units in the Cloncurry district, Australia. Such corridors preserve porous albitite that can better trap metals if subsequently overprinted by mineralizing fluids (e.g. Romanet Horst Delhi Pacific Cu-Au-Ag prospect; McLaughlin et al., 2016).

*Peak Temperature – HT Ca-Fe Facies and IOA Deposits*

A systematic temporal and spatial association of IOA mineralization with coeval intermediate (andesitic) magmatism is observed from the Proterozoic to Recent (Badham and Morton, 1976; Ningwu Research Group, 1978; Hildebrand, 1986; Sillitoe, 2003; Mumin et al., 2007; Yu et al., 2011; Tornos et al., 2017; Zhao et al., 2022). In some cases, magmatism is more felsic, such as in the Southeast Missouri district (Day et al., 2016). Close to regional heat sources and where large volumes of fluids are circulating along structures, temperatures in IOAA systems peak from 600°C to above 800°C in zones of skarn and in HT Ca-Fe facies assemblages during IOA mineralization. For example, hypersaline fluid inclusions from garnet record temperatures between 799° and 904°C, with an average value of 865°C, in the Meishan IOA deposit of the Middle-Lower Yangtze River Metallogenic Belt; (Zeng, 2020). These temperatures approach or are comparable to those of igneous rocks (see Huang et al., 2022). They provide an approximation of the peak temperatures achieved by the original saline to hypersaline fluid plume, and illustrate the importance of syn-alteration emplacement of intermediate magmas during IOAA metasomatism to form IOA mineralization. Iron skarn mineralization may form during the transition from Na and skarn alteration to HT Ca-Fe alteration; this occurs prior to extensive replacement of skarn clinopyroxene by amphibole as magnetite crystallizes at the HT Ca-Fe facies.

*Declining Temperatures – From HT Ca-K-Fe to Epithermal Alteration and Polymetallic Mineralization*

As temperatures decline from more than 800°C at the HT Ca-Fe facies to 350–500°C through the HT Ca-K-Fe and HT K-Fe alteration facies, cobalt-rich and then copper-rich mineralization precipitates (Bastrakov and Skirrow, 2007; Baker et al., 2008; Skirrow, 2010; Williams, 2010b). Further decreases in temperature (170–375°C) stabilize the LT K-Fe, LT Ca-Mg-Fe and epithermal alteration facies (Marschik and Fontboté, 2001; Skirrow and Walshe, 2002; Davidson et al., 2007; Schandl and Gorton, 2007; Skirrow, 2010; Williams, 2010b).

Cooling of the fluid plume at the transition from HT Ca-Fe to HT Ca-K-Fe and HT K-Fe alteration facies may be abrupt, owing to the influx of externally derived low-temperature fluids or by tectonic telescoping of deeper and earlier-formed alteration zones to higher crustal levels where lower temperature alteration facies develop. Progressive cooling corresponds to a single-stage model, whereas more rapid cooling due to ingress of low-temperature fluids corresponds to a two-stage model, as discussed by Skirrow (2010, 2022) for IOCG deposits.

## Integrated Mineral Deposit Model

Metasomatic IOAA mineral systems form a wide range of deposit types that host economic resources of critical, base and precious metals, including iron oxide apatite (IOA) and iron oxide copper-gold (IOCG) deposits. However, reduced environments, or those rich in carbonate, graphite, calcium or magnesium, may favour the genesis of deposits containing iron silicates, iron sulphides and iron carbonates instead of iron oxides (e.g. iron sulphide copper-gold or cobalt-gold deposits). Iron-poor environments and conditions during the waning stages of IOAA and affiliated alteration systems also favour the precipitation of iron-poor metasomatites and deposits. To encompass IOAA variants poor in iron oxides the term metasomatic iron and alkali-calcic (MIAC) system is proposed. This section summarizes the evolution of MIAC systems with a focus on the iron oxide-bearing, IOAA, systems that generate IOCG and affiliated critical metal deposits, based on field geology and geochemical footprints (Figs. 11, 12; see Corriveau et al., 2022b, c; this work and references therein; and other contributions from this volume).

*Host Geological Environment*

Iron oxide and alkali-calcic alteration systems are triggered by the ascent, infiltration and percolation of large-volume, saline-to-hypersaline fluid plumes through the upper crust in environments experiencing concurrent tectonic deformation and most commonly magmatism (Fig. 11). The primary systems form within a short time frame (ca. 5 Ma; GBMZ and Olympic Dam deposit), but periodic reactivation of systems through renewed orogenesis, magmatism or burial can extend their lifetime (e.g. Olympic Dam and the past-producing Eldorado mine in the GBMZ; Gandhi et al., 2001, 2018; Trottier, 2019; Maas et al., 2020; Ehrig et al., 2021).

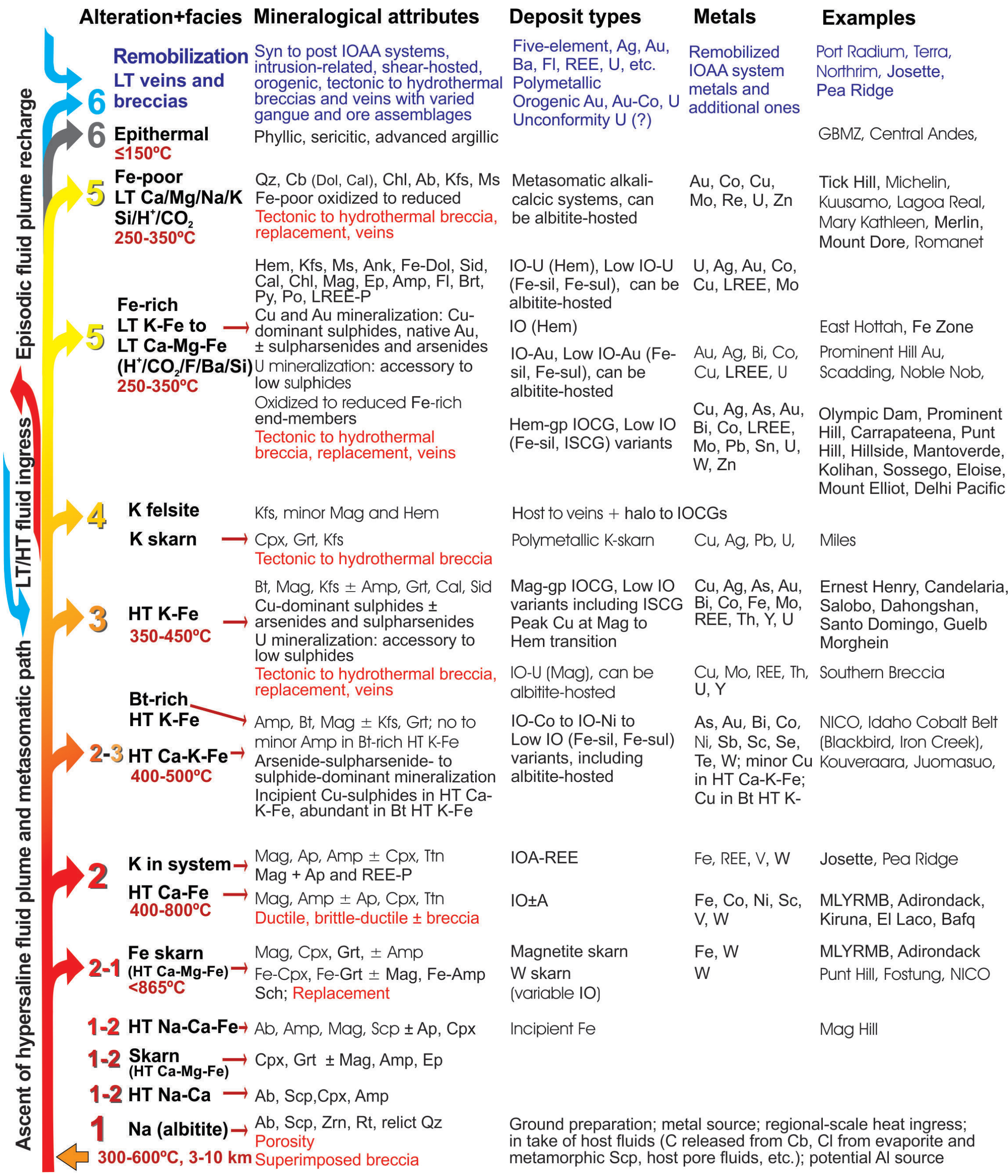


**Figure 12.** Mineral assemblages, corresponding alteration facies and style of deformation associated with the evolution of IOAA systems and variants poor in iron oxides that define the metasomatic iron and alkali-calcic (MIAC) system model (modified from Corriveau et al., 2010b, 2016). Additional deposits for each facies are listed in Table 2. The original fluid plume and its metal endowment may stem from fluids from multiple sources. The large arrow represents the main fluid plume evolution, largely from higher (HT) to lower (LT) temperatures, through interaction with cooler host rocks at regional scales. The coupled blue and red arrows represent potential fluid recharge to the main fluid plume from distinct sources, at different time and at different temperatures. Magmatic heat ingress and recharge with hot fluids stabilize the higher-temperature facies; ingress of lower temperature fluids stabilizes lower-temperature facies. Such ingress can lead to disruption and repetition of facies. Impacts of syn-metasomatic tectonics on depth to surface profile illustrated in Figures 3 and 13. IOAA: iron oxide and alkali-calcic alteration; IOA: iron oxide-apatite; IO-Co and IO-Ni: polymetallic iron-cobalt or iron-nickel mineralization in which iron oxides can, in some cases, be spatially decoupled from mineralization; Low IO: mineralization low in iron oxides but with Fe-sil (iron silicates) or Fe-sul (iron sulphides), can be rich in uranium (Low IO-U) or gold (Low IO-Au); Mag-gp: magnetite-group; ISCG = iron sulphide copper-gold; Hem-gp: hematite-group; IO-U (Mag) and IO-U (Hem): polymetallic iron oxide-uranium mineralization in which magnetite or hematite is the dominant iron oxide; MAC: metasomatic alkali-calcic end-member of IOAA systems that are poor in iron (may predominate, with albitite, across lower-temperature systems). MLYRMB= Middle-Lower Yangtze River Metallogenic Belt, China. Kuusamo district: Konttiaho, Juomasuo, Hangaslampi deposits. Structural attributes are shown in red font; late-stage remobilization during or subsequent to the evolution of IOAA systems is shown in blue font. Mineral abbreviations from Whitney and Evans (2010); LREE-P: phosphate rich in light REE; Fe-Dol: iron-rich dolomite. Deposit resources in Corriveau et al. (2018b) and Table 2.

Host rocks range from mafic to felsic volcanic rocks, ultramafic to felsic intrusive rocks, clastic to chemical sedimentary rocks, and their metamorphic derivatives. Environments dominated by clastic sedimentary rocks and felsic to intermediate volcanic and intrusive rocks are the most common hosts for IOCG mineralization (e.g. Olympic Copper-Gold Province and the immediate host rocks of the Ernest Henry deposit in the Cloncurry district, Australia, and Great Bear magmatic zone in Gandhi et al., 2001; Skirrow, 2010, 2022; Williams, 2010b; Wade et al., 2019; Corriveau et al., 2022c). Carbonate rocks dominate (with subsidiary mafic intrusive and volcanic rocks) in the Romanet Horst, and are abundant in the clastic sedimentary sequence in the Cloncurry district and the host sequence to the NICO deposit in the Great Bear magmatic zone (Marshall and Oliver, 2008; Corriveau et al., 2014, 2022c). Evaporites are common, either within older host rocks or coeval with metasomatism (Barton, 2014; Corriveau et al., 2022a; Zhao et al., 2022). Ultramafic and mafic rocks are abundant in the Carajás district in Brazil (Oliveira, 2017; Veloso et al., 2020).

Coeval magmatism represents an important heat and fluid source and provides insights on the geodynamic settings and evolution of host environments. Magma compositions range over much of the igneous spectrum (ultramafic to felsic, including carbonatites, with calc-alkaline to shoshonitic to alkaline affinities; Hildebrand, 1986; Ehrig et al., 2012; Barton, 2014; Wade et al., 2019; Huang et al., 2022). Magmas associated with IOCG mineralization generally crystallize magnetite, hence are oxidized (Barton, 2014).

IOAA systems typically develop in suprasubduction zone settings (Ootes et al., 2017; Tiddy and Giles, 2020; Tornos et al., 2021). Although batholiths are present in areas with IOCG, IOA and affiliated critical metal deposits, the main stages of batholith emplacement typically occur after the development of IOAA systems (Marschik et al., 1997; Montreuil et al., 2016a, c; Ootes et al., 2017; Wade et al., 2019; Tiddy and Giles, 2020). In the GBMZ and the Olympic Copper-Gold Province, peak IOAA metasomatic and mineralization events are demonstrably coeval with formation of discrete volcanic centers (including their associated subvolcanic intrusions and dyke swarms) that feature a wide range of magma compositions. Voluminous ignimbritic eruptions and emplacement of batholiths postdate the IOAA systems but contribute to remobilization of primary metals and extensive veining (Davis et al., 2011; Apukhtina et al., 2020; Maas et al., 2020).

*Fluid Plume Sources, Evolution and Metasomatic Footprints*

Globally, fluids that contribute to IOAA metasomatism range in origin from magmatic to meteoric, and include basinal brines, sea water, and saline caldera lake waters (Baker et al., 2008; Williams et al., 2010; Barton, 2014; Johnson et al., 2016; Schlegel et al., 2018, 2020; Chen and Zhao, 2022; Huang et al., 2022). In addition, metamorphic fluids can be derived via metamorphism of evaporite-bearing units or metasomatism of metamorphic scapolite (e.g. Barton, 2014; Morrissey and Tomkins, 2020). Fluid plumes may also comprise hypersaline fluids (also called hydrosaline melt or salt melt; Zeng, 2020; Zhao et al., 2022). Magmatic fluids are dominant in a large variety of IOAA deposit types, especially within early alteration facies (Pollard, 2001; Somarin and Mumin, 2014; Palma et al., 2020; Rodriguez-Mustafa et al., 2020).

The field geology of well-exposed regions indicates that IOAA systems reach lengths of 30–35 km and widths of 15 km (Mumin et al., 2007), whereas magnetic, gravity and magnetotelluric 3-D inversion models suggest that the vertical extent of their magnetic, dense and conductive components can be up to 7–10 km (Hayward, 2013; Hayward et al., 2016; McCafferty et al., 2019). For example, the low-magnetic and low-density footprint of sodic alteration (i.e. albitite and albitized hosts) has been imaged at depths up to ~10 km beneath calderas in the southeast Missouri district, USA (McCafferty et al., 2019). Sodic alteration at depth in this district is supported by the presence of an albitized granite intrusion in the more uplifted/exhumed sections of the district (Plymate et al., 1992). Pooling of fluids (from multiple sources) must take place below subvolcanic intrusions, as the intrusions and their volcanic or metasedimentary basement hosts are albitized (Corriveau et al., 2010b, 2022c). However, these fluids overlie the entire magma chambers (see model of Hildebrand et al., 2010), to account for the continuous alteration between subvolcanic intrusions (e.g. Corriveau et al., 2022c).

IOAA systems form extensive metallogenic districts in provinces along the edge of deep lithosphere roots (Groves et al., 2010; Skirrow et al., 2018; Wise and Thiel, 2020). This setting is also conducive to alkaline magmatism, emplacement of high radiogenic heat-producing granitic batholiths and development of sedimentary basins hosting SEDEX and uranium mineralization or deposits (e.g. southwest Grenville Province in Canada and Olympic Copper-Gold and Mt. Isa provinces; Corriveau et al., 2007; Adetunji et al., 2014; Hoggard et al., 2020; Wise and Thiel, 2020). Upper crustal systems extend at depth along a discrete, ~10 km-thick, trans-crustal corridor of low reflectivity and low resistivity (i.e. conductive) that transects Moho offsets (Wise and Thiel, 2020). Such corridors are interpreted as fossil mantle-to-crust conduits for magma and fluids that destroyed pre-existing fabrics in the lower crust and precipitated minor conductive minerals (Wise and Thiel, 2020). Examples include the southwest Grenville Province in Canada, the Olympic Copper-Gold Province in Australia and the Great Bear magmatic zone (Spratt et al., 2009; Craven et al., 2013; Skirrow et al., 2018; Wise and Thiel, 2020; Tornos et al., 2021); they represent important metallotects for IOCG, IOA and affiliated critical metal deposits, including for Canadian settings (Mumin and Corriveau, 2004; Corriveau, 2007; Corriveau et al., 2007, 2010a).

A high and self-sustained disequilibrium between the fluid plume and host rocks drives metasomatism. Dissolved elements and volatiles, such as those released by decarbonation of carbonate host rocks, as well as pore fluids, recharge the fluid plume and significantly change its composition (Fig. 11). Hence, an original highly reactive *Fluid 0* reacts with host rocks and forms *Alteration Facies 1*, and outflow during this stage creates

*Fluid 1*. *Fluid 1* remains highly reactive, and may cool down due to fluid-rock reactions during ascent into cooler rocks; alternatively, coeval magma emplacement and associated ingress of hot fluids may raise temperatures or help sustain high-temperature conditions. In both cases, the highly reactive *Fluid 1* is in disequilibrium with the host rocks and self-sustains the development of the system. Outgoing *Fluid 1* rises and reacts with *Host 1* or locally *Alteration Facies 1* to form *Alteration Facies 2*. Again, *Fluid 2* is compositionally distinct from *Fluid 1*, remains in high disequilibrium with host rocks, and reacts with *Host 2* or locally *Alteration Facies 1* or *2* to form *Alteration Facies 3* and outgoing *Fluid 3*, etc. (Figs. 11, 12).

Each alteration facies is associated with the selective dissolution (leaching) or deposition of specific assemblages of metals. Without significant tectonic or magmatic disruption or voluminous ingress of external fluids, the sequence consists of Na → Na-Ca-Fe → HT Ca-Fe → HT K-Fe → K-felsite → LT K-Fe/LT Ca-Mg-Fe alteration facies (± skarn alteration, including Fe-skarn deposits and K-skarn alteration). This sequence is defined as the prograde path of the iron oxide alkali-calcic systems (Table 2; Figs. 11, 12), and provides the framework for interpreting the metasomatic processes that lead to IOCG, IOA and affiliated critical metal deposits. As the fluid plume reaches near-surface, epithermal and vein systems develop.

In most IOAA systems, especially those hosting significant mineral deposits, the alteration sequence is marked by repetition of alteration facies through intake of pore fluids from metasomatized host rocks, renewed magma emplacement and heat, multiple cycles of tectonic burial and uplift, and introduction of externally derived, low-temperature surficial (meteoric, basinal, caldera lake) fluids (Barton, 2014; Su et al., 2016; Skirrow, 2022; Zhao et al., 2022). Synchronous metasomatic, tectonic and magmatic activities create new fluid pathways, increase interconnectivity of existing pathways, and support fluid mixing from varied sources (Figs. 11–13). Changes in regional to orogen-scale kinematics (e.g. a switch from compression to extension, or basin inversion following rifting and basin development) facilitate mixing between deep and shallow crustal fluid reservoirs that can lead to the formation of deposits (Oliver et al., 2004; Chen et al., 2013; Montreuil et al., 2016a; Skirrow et al., 2018). Factors that control metal precipitation include: 1) the evolving physicochemical conditions of the fluid plume; 2) the timing, composition, volume, and time of intrusion of coeval magmas that provide heat and fluids; 3) structural and lithological discontinuities and active faulting to channel large volumes of fluids from different sources in spatially restricted areas of the crust, aided by pressure changes related to deformation; and 4) the regional geology and availability of chemical (lithological) traps.

*Metasomatism: Supplementary Metal Sources and Porosity Enhancement*

Dissolution of minerals at depth and along major discontinuities and incremental recharge of the fluid metal load are most intense during regional-scale Na to Na-Ca-Fe alteration (Figs. 11, 12). Albitization induces particularly pronounced leaching of Ag, Co, LREE (e.g. Ce), Ni, Pb, Sc, Sr, Yb and Zn, whereas Th remains immobile (Corriveau et al., 2022b). Uranium-rich mineralization commonly occurs in regions where uranium-rich host rocks have been extensively albitized (Hitzman and Valenta, 2005; Ootes et al., 2013; Montreuil et al., 2015; Potter et al., 2019, 2022). Leaching of metals (e.g. copper) from mafic sources is interpreted to have enhanced the fertility of IOAA systems in the Olympic Copper-Gold Province (Skirrow et al., 2018). The large spectrum of metals added to the fluid due to the diversity of host rocks metasomatized during Facies 1 inevitably induces variations in isotopic and metal source signatures in mineral deposits (see Yardley and Bodnar, 2014).

Decarbonation of carbonate units during their transformation to skarn (e.g. Yardley and Lloyd, 1995), albitite or HT Ca-Fe alteration (e.g. NICO deposit) leads to transient porosity enhancement. Infiltration metasomatism within carbonate rocks thus increases permeability and fluid flow and must release large amounts of C, Ca and Mg into the fluid column (Corriveau et al., 2022b; this volume). The development of all alteration facies contribute to change the original composition and isotopic signature of the main fluid plume.

*Albitite-hosted Mineralization*

Although the Facies 1 Na, and Facies 1–2 Na-Ca and HT Na-Ca-Fe alteration zones are not mineralized during primary metasomatism, they can serve as fluid pathways and metal traps in which albitite is overprinted by fertile Facies 3 to 6 alteration (Figs. 3, 12; Montreuil et al., 2015; Potter et al., 2019). Deposits hosted by albitite include IOCG, albitite-hosted uranium, and polymetallic (e.g. Au, Co, U, ± Cu-sulphide) deposits. Examples include the Ernest Henry (Australia), Mantoverde (Chile), Tjårrojåkka (Sweden) and Kuusamo (Finland) deposits, the Southern Breccia (U-Mo-Cu), Damp and Cole (uranium) prospects in the GBMZ, the IOA to IOCG prospects of the Iron Range district (British Columbia, Canada), the IOCG Two Time and Croteau prospects, albitite-hosted Michelin uranium deposit and Kitts prospect of the Central Mineral Belt, the Scadding gold-cobalt deposit in the Wanapitei district, and the albitite-hosted uranium-gold and Cu-Au-Ag prospects of the Romanet Horst in Canada (Kish and Cuney, 1981; Clark and Wares, 2002; Edfelt et al., 2005; Benavides et al., 2007; Schandl and Gorton, 2007; Staples et al., 2008; Potter, 2009; Mumin et al., 2010; Galicki et al., 2012; Wilde, 2013; Corriveau et al., 2014; Montreuil et al., 2015, 2016b; O'Brien, 2016; Sparkes, 2017; Potter et al., 2019; Yarie and Wray, 2019).

*REE Deposits at the HT Ca-Fe Facies*

Leaching of Na, K, Ba, and Sr, and precipitation of Ca, Co, Fe, Mg, Ni, P, V, Sc, Sn, and in some cases W, Th, U and REE, occur at the HT Na-Ca-Fe and HT Ca-Fe alteration facies (Figs. 4D, 12, 14, 15 in Corriveau et al., 2022b; Montreuil et al., 2016b, c; Blein et al., 2022). Scandium, nickel, vanadium and REE can also be significantly

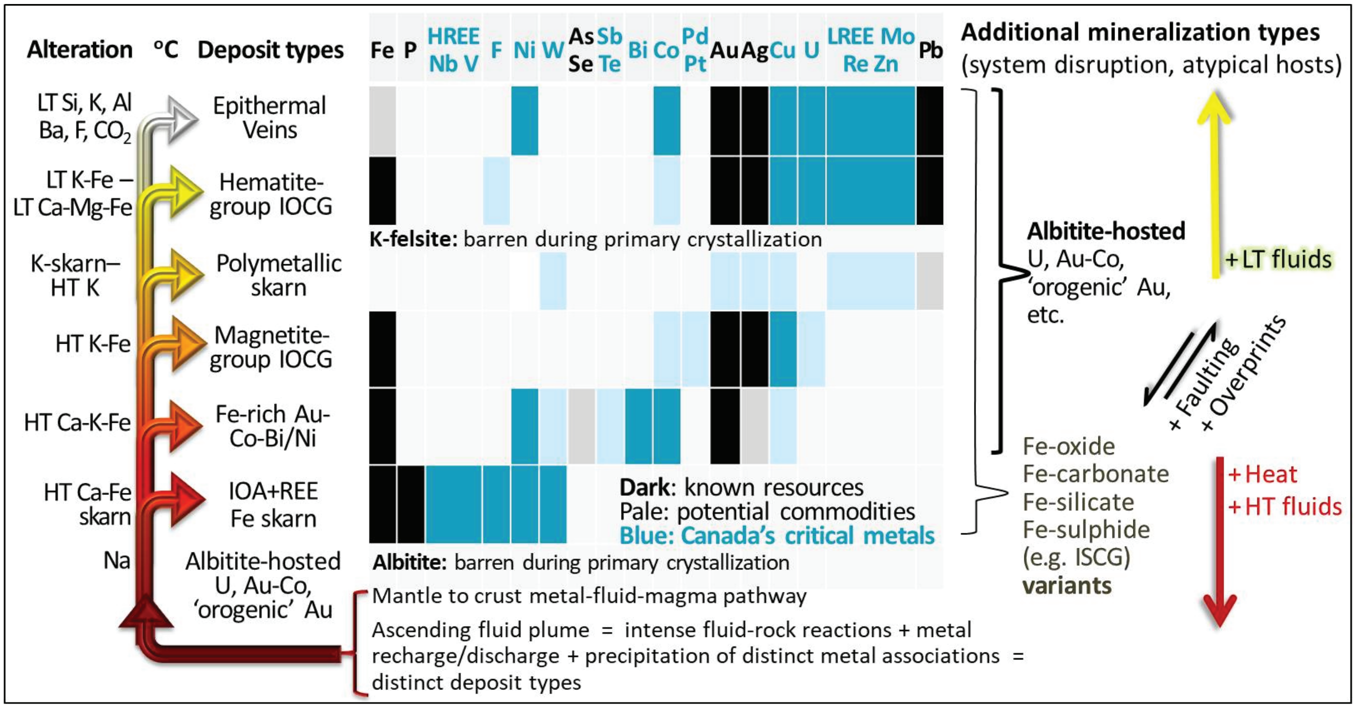


**Figure 13.** Metasomatic iron oxide and alkali-calcic (IOAA) systems and potential deposit types and resources, with Canada's critical metals highlighted in blue (Natural Resources Canada, 2021; see additional critical metals for the USA, Australia, Europe and Japan in Emsbo et al., 2021). Active tectonics disrupt the simple depth to surface alteration sequence, especially where deposits formed. Additional mineralization types can form through system disruption by fluid and heat ingress and in iron oxide-poor systems as noted on the far right. Collectively, the metasomatic IOAA systems and variants poor in iron oxides define MIAC systems (Fig. 12). Classification of deposit types based on this diagram can be found in Hofstra et al. (2021). Resource figures for IOCG, IOA and affiliated critical metal deposits are listed in Corriveau et al. (2018b) and additional references can be found in Table 1. Bayan Obo resources provided by Fan et al. (2016) are 57.4 Mt at 6 wt% $REE_2O_3$, 2.2 Mt at 0.13% $Nb_2O_5$, 1500 Mt at 35% Fe. Current underground resources at the Ernest Henry deposit are 87.1 Mt at 1.17% Cu and 0.62 g/t Au (Glencore, 2020). Nickel resources occur at the Jaguar deposit in the Carajás district (59 Mt @ 0.96% Ni; Centaurus Metals Limited, 2021). Examples of deposits for Facies 1 to 5 are listed in Table 1. Facies 6 case examples include the vein-type mineralization at the Merlin Mo-Re deposit (Australia; Babo et al., 2017) and the past-producing vein-type Echo Bay (Ag, Cu), Eldorado (U, Ag, Cu, Co, Ni, Pb), Contact Lake (Ag, U), El Bonanza (Ag), Terra (Ag), Norex (Ag) and Rayrock (U) mines in the Great Bear magmatic zone (Mumin et al., 2010; Trottier, 2019). Based on the upper 10% concentrations in the Olympic Dam (AU) and Great Bear magmatic (CA) datasets of Corriveau et al. (2015, 2022b), additional potential critical metal resources or by-products using the list of Emsbo et al. (2021) range from (in ppm), As:10k–85k; Ba: 47k–260k; Rb: 256–435; Sb: 100–910; Sc: 14–325; Se: 8–100; Sn: 68–256; Sr: 675–8k; Ta: 3–30; Te: 5–26; Th: 75–1k; V: 500–2k; Y: 137–710; Zr: 354–1k; and $Al_2O_3$: 17–35 wt%.

concentrated at this stage (Fig. 13). Within systems that sustained very high-temperature regimes, such as those above intermediate subvolcanic intrusions, magnetite-skarn and IOA mineralization commonly form (Figs. 4, 5, 13; Corriveau et al., 2022c; Zhao et al., 2022). A close spatial association of IOA mineralization with carbonate rocks is also common (Fig. 4A–E, Terra mine area, GBMZ; MLYRB in China, Zhao et al., 2021; Bayan Obo in China, Fan et al., 2016).

IOA deposits forming in IOAA systems that evolve to potassium-bearing facies may contain significant REE and evolve to deposits with LREE and HREE resources (Fig. 13; Fig. 20 in Corriveau et al., 2022b). The REE contents of the IOA deposit per se generally remain sub-economic unless REE are remobilized and re-concentrated through renewed fluid circulation as observed in the Josette (Canada) and Pea Ridge (USA) deposits (Table 2; Fig. 12; Figs. 14 and 20 in Corriveau et al., 2022b). In view of the close spatial association of IOAA deposits with a broad compositional range of coeval intrusions, magnetite-dominant REE deposits forming in association with carbonatite (e.g. Bayan Obo, Fan et al., 2016) are also included within the IOA spectrum.

*Precipitation of Polymetallic Mineralization at the HT Ca-K-Fe, HT K-Fe, K-skarn and LT K-Fe Facies*

Settings that foster the development of the transitional Facies 2–3, and Facies 3 to 5 (Fig. 12) can form polymetallic cobalt-rich, copper-rich, gold-rich or uranium-rich mineralization (Figs. 11–13). Distinct mineralization types are possible at each facies (including transitional facies), but complex coupling and decoupling of metals and irregular metal zoning may occur in mineralized zones because of repetition or telescoping of facies. Periodic remobilization of metals occurs as new alteration assemblages overprint earlier ones or form veins (Corriveau et al., 2022b).

Though mineralization is typically associated with iron oxides, the presence of graphitic, reduced (pyrrhotite-bearing), carbonate-bearing, or other calcium-magnesium-rich host rocks can supress the formation of iron oxides and instead favour formation of iron silicates, notably clinopyroxene (diopside-hedenbergite), amphiboles (e.g. actinolite, cummingtonite, grunerite, hornblende, hastingsite), ferromagnesian phyllosilicates (biotite, stilpnomelane), fayalite, garnet (almandine, andradite-grossular), chlorite, epidote, iron carbonates (siderite, ankerite, ferroan dolomite), and iron sulphides (pyrrhotite, pyrite) (Williams et al., 2005 and references therein). Prospects and deposits in the Tennant Creek district and Mount Isa Province (Australia), the Romanet Horst, Central Mineral Belt, and Wanapitei district (Canada), and in the Idaho Cobalt Belt (USA) are examples of mineralization zones in which iron sulphides and iron silicates are more abundant than iron oxides (Fig. 12; e.g. Skirrow and Walshe, 2002; Mumin and Trott, 2003; Slack, 2013; McLauchlin et al., 2016; Austin et al., 2017; Sparkes, 2017; Yarie and Wray, 2019).

Mineralized zones within overlapping Facies 2–3 HT Ca-K-Fe and Facies 3 biotite-rich HT K-Fe are typically enriched in critical metals such as As, Au, Co, and variably enriched in Bi, Cu, In, Ni, REE including HREE, Sb, Se, Te and W (e.g. NICO Au-Co-Bi-Cu deposit, Canada; Co-Cu-Au deposits of the Idaho Cobalt Belt, United States; Cu-Co-Au Guelb Moghrein IOCG deposit, Mauritania). Such mineralization is principally hosted by sedimentary sequences (e.g. a carbonate unit at NICO, Sidor, 2000; Montreuil et al., 2016b), and is associated with iron-rich alteration consisting of amphibole, biotite, iron sulphides and magnetite. Alteration and mineralization occur at high temperatures (>400–470°C at NICO; Sidor, 2000; Acosta-Góngora et al., 2015a) and typically under reduced conditions, as indicated by the precipitation of pyrrhotite or the presence of graphite in some mineralized zones.

At the HT Ca-K-Fe facies, the As, Bi, Co, Ni and W endowment of mineralized zones is greater than at the HT and LT K-Fe facies (Table 1; Corriveau et al., 2022b). Significant copper mineralization forms at the onset of HT K-Fe alteration and is generally decoupled from cobalt-rich mineralization; both locally overlap spatially. Gold may be enriched in parallel with cobalt and copper (Corriveau et al., 2022b). The timing of cobalt-rich and copper-rich mineralization is exemplified by the NICO deposit, where copper-bearing, HT K-Fe facies, magnetite-group IOCG mineralization overprints iron oxide Au-Bi-Co mineralization associated with the HT Ca-K-Fe facies. Temperatures above 400°C do not favour the destabilization of aqueous copper-chloride complexes (Liu and McPhail, 2005) and could be the main impediment to significant copper mineralization during HT Ca-K-Fe facies. Therefore, significant copper mineralization during HT K-Fe facies alteration is likely triggered by the cooling of fluids to below ~400°C (Liu and McPhail, 2005).

Facies 3 HT K-Fe alteration marks the onset of significant copper mineralization, formation of large breccia zones, and initiation of magnetite-group IOCG mineralization (Figs. 6, 7; Figs. 6, 15 in Corriveau et al., 2022b). Diverse metal enrichments in As, Ag, Au, Ba, Bi, C, Cl, Co, Cu, F, Fe, K, Mo, Mn, P, Rb, REE including variable HREE, S, Sb, Te, Th, V, U and W are all possible. Silver, Au, Co, Cu, and U may be particularly enriched. The main iron minerals are magnetite, biotite and locally siderite, in variable proportions.

Facies 4 K-skarn alteration can locally generate mineralized zones containing variable Cu, Zn, Pb, Ag, Mo and W (e.g. Mile Lake and Punt Hill; Figs. 13, 15 in Corriveau et al., 2022b; Mumin et al., 2010). However, in many cases, metal endowment in skarn facies is related to the LT Ca-Mg-Fe-(K) facies, such as the S-F-Cu-La-U-Zn trends at Punt Hill (Fig. 13 in Corriveau et al., 2022b) and the Ag-Au-Cu mineralization at Hillside (Teale, 2019).

As systems progress to Facies 5 LT K-Fe and LT Ca-Mg-Fe-(K) alteration, the wide range of conditions and fluid compositions considerably expands the number of stable mineral assemblages and possible metal associations (Figs. 9, 10, 12; Figs. 15–21 in Corriveau et al., 2022b). Mineralized zones incorporate enrichments in many elements, including Ag, As, Au, Ba, Bi, C, Cd, Co, Cu, F, Fe, K, LREE, Mn, Mo, P, Pb, S, Sb, Sn, Re, Te, U, W and Zn. Silver, Au, Bi, Co, Cu, LREE, Mo, Pb, Re, U and Zn may be particularly enriched (Fig. 13). The main types of deposits that form at Facies 5 comprise hematite-group IOCG mineralization (e.g. Olympic Dam, Mantoverde), including variants poor in iron oxides yet rich in iron silicates (e.g. Punt Hill in Australia, Sossego in Brazil) or iron sulphides (Delhi Pacific in Canada, Kolihan deposit in India), as well as iron-rich gold mineralization (e.g. Scadding in Canada, Prominent Hill gold-rich zones, deposits of the Tennant Creek district in Australia).

Copper-rich and uranium-rich mineralization types are regularly associated with potassic aluminosilicates (e.g. sericite, K-feldspar)-bearing alteration, whereas gold-rich and cobalt-rich mineralization types are regularly associated with alteration zones containing variable quantities of potassium in both the LT K-Fe and LT Ca-Mg-Fe facies. Uranium may be present in almost every IOAA facies and style of mineralization as a result of primary metasomatic enrichment, overprints (e.g. external fluid ingress), or remobilization (Ehrig et al., 2021; Fabris, 2022; Potter et al., 2022).

### Vectors to IOCG and Affiliated Critical Metal Deposits

In IOAA systems, deposits cluster within a large volume of rocks roughly 35 km long, 15 km wide and 10 km deep. Systems are spaced every 30–50 km along metallogenic provinces up to 1500 km in extent. A series of consecutive alteration facies are distinctive and diagnostic form (e.g. Na, HT Ca-Fe, HT K-Fe, LT Ca-Mg-Fe). The facies can be iron oxide-rich or poor but rich in iron silicates, iron sulphides and iron carbonates or poor in iron. Iron-oxide poor and iron-poor alteration facies can form throughout or late in the evolution of typical IOAA systems or occur in systems where iron oxides are deficient throughout. In parallel, IOAA facies can form in systems where iron oxide-poor and iron-poor alteration dominates. Collectively, all facies and associated mineralization types form regional metasomatic iron and alkali-calcic (MIAC) systems (Figs. 12, 13).

If an IOAA (or MIAC) affinity is not recognized in a mineral district, prospects are normally assigned to a deposit type based on host rocks and metal associations, e.g. VMS, SEDEX, volcanic-, vein-, or unconformity-hosted uranium or intrusion-related deposit types including carbonatite-related (Corriveau, 2007; Corriveau and Mumin, 2010; Potter et al., 2020a). The potential for IOA, IOCG, albitite-hosted uranium and Au-Co-U, or other IOAA-related (and MIAC-related) deposit types, including the large variety of deposit types with critical metals as primary commodities can then be overlooked. Finding and identifying IOCG, IOA and affiliated mineralization or reassessing known prospects in the context of IOAA (and the larger umbrella MIAC) systems may reveal the potential for a vast range of mineral deposit types, many with critical metals, and provides a more robust geoscience baseline for mineral potential and environmental assessments (Corriveau and Potter, in press). Moreover, IOAA/MIAC-related prospects open large geographic regions to exploration and their host alteration facies provide regional vectors for the entire range of potential deposits within the host systems. An example is the NICO Au-Co-Bi-Cu deposit for which the lack of albitite in historical maps triggered renewed mapping and the discovery of albitite-hosted U-Th ± Cu-Mo-sulphide mineralization of the Southern Breccia (Corriveau et al., 2011; Montreuil et al., 2015; Potter et al., 2019).

*Caveats in the Interpretation of Available Geoscience Data*

Alteration facies provide road maps to mineralization if they can be identified and mapped. Historically, many metasomatites have been overlooked as they may resemble common (unaltered) rocks (Corriveau et al., 2010b, 2016, 2022a), notably: 1) pink to red albitite, K-felsite and K-feldspar-altered clasts of iron oxide breccia may be interpreted as syenite, rhyolite, or clasts derived from same; 2) white albitite may be interpreted as recrystallized anorthosite, metatonalite, chert, zones of silicification, or their metamorphic derivatives; 3) amphibole-dominant HT Ca-Fe as marl, amphibolite, or metamorphosed mafic-derived clastic sedimentary rocks; 4) magnetite-dominant HT Ca-Fe alteration of sedimentary rocks as banded iron formation, and interlayered stratabound albitite as chert layers (subsequent hematization may also redden some layers); 5) biotite-rich HT Ca-K-Fe and HT K-Fe as biotite schist; 6) K-feldspar-altered clastic sedimentary rocks as arkose; and 7) tectono-hydrothermal breccia as agglomerate. However, skarn in IOAA systems can be distinguished from intrusion-related skarn by being spatially associated with extensive albitite (if exposure at regional scale is available).

Other types of alteration/mineralization are also susceptible to misinterpretation. The extensive LT Ca-Mg-Fe-(K) facies of IOAA systems may be interpreted as chloritic alteration or as veins commonly observed in many deposit types. Remobilization of primary metal endowments into late-stage veins can be interpreted as the system being long-lived or, conversely, much younger. Magnetite-altered volcanic rocks could be interpreted as a natural example of iron oxide magma if the replacement of the volcanic matrix by magnetite is not recognized. Fluorite and REE-rich mineralization are commonly attributed to alkaline magmatism, although fluorite showings are known in IOAA systems such as in the Kwyjibo district in Canada (Clark et al., 2010). A general solution is to define working hypotheses based on atypical rock-type associations, deposit-type diversity and metal associations within a region, and compare known features with the geological and geochemical fingerprints of IOAA systems.

*Lithogeochemical Mapping and Exploration Tools*

The distinct geological, mineralogical, geochemical and geophysical footprints of IOAA systems, including where metamorphosed to high-grade, are amenable to artificial intelligence-based exploration and help refine geoscience mapping and exploration strategies and mineral potential assessment (Corriveau et al., 2010a; Montreuil et al., 2016a–c; Fabris et al., 2018; Blein et al., 2022). Each facies comprises a distinctive series of mineral assemblages (with varied mineral proportions and contents) that correspond to distinct ranges in 1) bulk rock chemical composition (Blein et al., 2022; Corriveau et al., 2022b; Fabris, 2022), 2) mineral chemistry (Normandeau et al., 2018; Huang et al., 2022), 3) rock physical properties (Enkin et al., 2016, 2020) and 4) geophysical footprints (Hayward et al., 2016; Katona and Fabris, 2022).

Geochemical datasets provide a means for drafting chemical maps at deposit to province scales (e.g. using molar proportion barcodes) and the AIOCG alteration facies discriminant diagram of Montreuil et al. (2013) help in assessing the maturity and potential fertility of a system (see Blein et al., 2022; Corriveau et al., 2022b). Sample barcodes derived from Na-Ca-Fe-K-Mg molar proportions on the AIOCG diagram helps to identify 1) host-rock alteration at varying intensities, and 2) alteration overprints that combine two facies. Barcodes that use (Si + Al)/10 in lieu of Mg molar proportions best discriminate IOAA systems from systems that generate epithermal, porphyry, VMS and SEDEX deposits (Corriveau et al., 2022b). Alteration facies lithogeochemistry and field data are therefore key to machine learning and exploration aided by artificial intelligence, if alteration zones have been identified and sampled.

*Polymetallic Veins as a Probe of Metals in IOAA Systems*

Polymetallic veins associated with regional IOAA systems provide clues to the primary metal endowment of host systems (e.g. DeVries Lake, Gandhi, 1994; East Arm Basin, Potter et al., 2020a; Corriveau et al., 2022c; Daliran et al., 2022). At the past-producing Eldorado mine in the GBMZ and in the East Arm basin in Canada, metals from the “basement” of their IOAA systems were captured by fluids originating in overlying sedimentary rocks, and precipitated in five-element veins within and at the periphery of the IOAA systems (e.g. Trottier, 2019).

*Uranium as One of Many IOAA Element Metallotects*

The high mobility of uranium in response to periodic reactivation of crustal- to system-scale structures plays a major role in the generation of late-stage uranium-bearing mineralization, such as the Olympic Dam deposit in Australia (Apukhtina et al., 2020; Ehrig et al., 2021). Such faults control the geometry of cover sequences (Olympic Dam deposit, Corriveau et al., 2022c) and facilitate the migration of uranium and formation of uranium prospects at regional scales.

Uranium pathways can be efficiently detected by airborne radiometric surveys in geological environments without extensive overburden, by lake sediment geochemical surveys, and by field mapping with a scintillometer or gamma-ray spectrometer. As such, uranium prospects represent a key vector to potential IOAA systems in zones of polymetallic mineralization or albitite. It also highlights the IOAA potential of basement rocks underlying unconformity uranium deposits. For example, the Athabasca Basin is proximal to IOAA prospects (Colin and Marguerite River region of interest in the southwest and Nonacho basin to the North; Fig. 4 in Corriveau et al., 2022d). In addition, the presence of high-heat producing granites in the basement, and a major crustal-scale discontinuity below the Athabasca Basin, both induced high geothermal heat flow (cf. Potter et al., 2020b; Tschirhart et al., 2020). This setting shares the characteristics of environments favourable for the development of IOAA systems, and is similar to other IOAA metallogenic provinces such as the GBMZ (Somarin and Mumin, 2012; Craven et al., 2013), which may expand the perceived mineral potential of the basement rocks.

## Conclusion

The ascent, infiltration and percolation of voluminous saline to hypersaline fluid plumes through the upper crust leads to a chain of self-propagating fluid-rock reactions and the formation of consecutive diagnostic alteration facies [Na, skarn, HT Ca-Fe, HT Ca-K-Fe, HT K-Fe, K-skarn, K-felsite and LT K-Fe and LT Ca-Mg-Fe-(K)]. A consistent depth-to-surface sequence of facies defines the prograde metasomatic path of IOAA systems and associated deposit types from iron skarn, IOA, IOA-REE, and critical metals deposits with Au, Bi, Co, Sb, Se, Te, and W but without significant copper, followed by copper sulphide-bearing magnetite to hematite-group IOCG deposits, and their many variants. This path is commonly disrupted tectonically, as well by multiple ingresses of fluids from different sources and temperatures, and syn-metasomatic magma emplacement. These factors may generate additional deposit types such as albitite-hosted U/Au-Co-Cu deposits.

Host-rock compositions and geological environments vary. Nevertheless, each alteration facies comprises specific mineral assemblages associated with distinct ranges of bulk-rock compositions, rock physical properties and metal associations. The deposit types formed at each facies are all linked through the metasomatic evolution of the system at regional, upper-crustal scales. During development of sequential alteration facies, unstable host-rock minerals are dissolved, liberating metals and other elements and volatiles, which recharge the fluid plume and change its original chemical and isotopic composition as a function of the host sequences. The IOAA facies remain consistent across systems globally, but the extent to which facies develop, the quantity of specific minerals within facies assemblages, and metal endowments will vary. Some primary alteration types are barren but, at later stages become preferential traps for mineralization because of their inherited chemical reactivity or enhanced porosity or rheological weakness.

System propagation, upwards and laterally from primary heat and fluid plume sources, takes place in active geological environments. Metasomatism creates transient porosity and permeability at local scales through coupled dissolution and reprecipitation mineral reactions. In parallel, syn-metasomatic deformation contributes to the development or reactivation of shear zones, fault networks and breccia zones that enhance permeability, circulation, trapping and pooling of fluids in spatially constrained parts of the crust. Syn-metasomatic magma emplacement impacts the temperature and metal budget of the fluid plume, but IOAA systems form independently of magma types, which may be ultramafic to felsic, with calc-alkaline, shoshonitic, or alkaline (e.g. carbonatite) affinities.

Syn-metasomatic magmatism, tectonic telescoping and collapse as stress regimes change, and influx of fluids from different sources, can foster multiple pulses of alteration and mineralization in the active areas of these systems. This results in complex overprints of alteration assemblages and mineral deposits with diverse assemblages of metals. Mineral deposits are located in favourable structural or chemical traps in areas of maximum fluid flow within IOAA systems. In these dynamic metasomatic (magmatic-hydrothermal) systems affected by periodic reactivation, younger fluids can mobilize and concentrate metals deposited during earlier stages, and form mineral deposits with diverse and atypical metal assemblages; hence atypical deposit types should be prognosticated as a normal outcome of the evolution of IOAA systems. If one system is identified, it is likely that others occur in the same region, irrespective of host rock sequences, magma types, timing of faults, or terrane boundaries. However, applying the system-scale IOAA mineral deposit model based on the main alteration facies and metal assemblages is effective in predicting and vectoring to mineralization.

## Acknowledgments

This research was carried out under the Targeted Geoscience Initiative (Natural Resources Canada; LMS contribution 20210061) and furthers earlier research under the Geomapping for Energy and Minerals in the Great Bear magmatic zone (Great Bear-IOCG project) and in the Romanet Horst (Hudson-Ungava project). Fieldwork was conducted in collaboration with the Northwest Territories Geoscience Office South Wopmay Bedrock Mapping project, Alberta Star

Development Corporation, Fortune Minerals Limited, Honey Badger Exploration Inc., Energizer Resources Inc., DEMCo, graduate and undergraduate students, and industry, university and government colleagues from across Canada who generously contributed time, effort, logistical infrastructures or funding for this research. We thank BHP-Olympic Dam for providing the data and the support to publish Parts 1 and 2 which has broadened the scope of this TGI research. We also acknowledge organizations who granted access to their mines, prospects and drill cores and to SGA and SEG fieldtrip leaders, including Nick Oliver and Glencore at Ernest Henry, Patrick Williams and Ivanhoe at Merlin and Starra, Fernando Tornos and Compañía Minera del Pacífico at El Laco, and Bill Chavez and Erich Petersen at Candelaria and Mantoverde. We also acknowledge colleagues who share their knowledge during a workshop at the Geological Survey of South Australia (GSSA) core library, in particular Kathy Ehrig, Tobias Schlegel and Adrian Fabris. Finally, we thank Adrian Fabris, Suzanne Paradis, Xin-Fu Zhao, Vladimir Lisitsin and Jim Craven and Geological Association of Canada book editor, Reginald Wilson, for their thorough and insightful reviews of this paper.

## References

Aagaard, P., Egeberg, P.K., Saigal, G.C., Morad, S., and Bjorlykke, K., 1990, Diagenetic albitization of detrital K-feldspars in Jurassic, Lower Cretaceous, and Tertiary clastic reservoir rocks from offshore Norway. II. Formation water chemistry and kinetic considerations: Journal of Sedimentary Petrology, v. 60, p. 575-581.

Acosta-Góngora, G.P., Gleeson, S.A., Samson, I., Ootes, L., and Corriveau, L., 2015a, Gold refining by bismuth melts in the iron oxide-dominated NICO Au-Co-Bi (±Cu±W) deposit, NWT, Canada: Economic Geology, v. 110, p. 291-314.

Acosta-Góngora, P., Gleeson, S., Samson, I., Corriveau, L., Ootes, L., Taylor, B.E., Creaser, R.A., and Muehlenbachs, K., 2015b, Genesis of the Paleoproterozoic NICO iron-oxide-cobalt-gold-bismuth deposit, Northwest Territories, Canada: evidence from isotope geochemistry and fluid inclusions: Precambrian Research, v. 268, p. 168-193.

Acosta-Góngora, P., Duffet, C., Sparkes, G.W., and Potter, E.G., 2018, Central Mineral Belt uranium geochemistry database, Newfoundland and Labrador: Geological Survey of Canada, Open File 8352, 8 p.

Acosta-Góngora, P., Potter, E.G., Corriveau, L., Lawley, C.J.M., and Sparkes, G.W., 2019, Geochemistry of U±Cu±Mo±V mineralization, Central Mineral Belt, Labrador: differentiating between mineralization styles using a principal component analysis approach, *in* Rogers, N., ed., Targeted Geoscience Initiative: 2018 report of activities: Geological Survey of Canada, Open File 8549, p. 381-391.

Adetunji, A.Q., Ferguson, I.J., and Jones, A.G., 2014, Crustal and lithospheric scale structures of the Precambrian Superior-Grenville margin: Tectonophysics, v. 614, p. 146-149.

Aleinikoff, J.N., Selby, D., Slack, J.F., Day, W.C., Pillers, R.M., Cosca, M.A., Seeger, C.M., Fanning, C.M., and Samson, I.M., 2016, U-Pb, Re-Os, and Ar/Ar geochronology of REE-rich breccia pipes and associated host rocks from the Mesoproterozoic Pea Ridge Fe-REE-Au deposit, St. Francois Mountains, Missouri: Economic Geology, v. 111, p. 1883-1914.

Apukhtina, O.B., Kamenetsky, V.S., Ehrig, K., Kamenetsky, M.B., Maas, R., Thompson, J., McPhie, J., Ciobanu, C.L., and Cook, N.J., 2017, Early, deep magnetite-fluorapatite mineralization at the Olympic Dam Cu-U-Au-Ag deposit, South Australia: Economic Geology, v. 112, p. 1531-1542.

Apukhtina, O.B., Ehrig, K., Kamenetsky, V.S., Kamenetsky, M.B., Goemann, K., Maas, R., McPhie, J., Cook, N.J., and Ciobanu, C.L., 2020, Carbonates at the supergiant Olympic Dam Cu-U-Au-Ag deposit, South Australia. Part 1: distribution, textures, associations and stable isotope (C, O) signatures: Ore Geology Reviews, 103775.

Austin, J., Patterson, B., LeGras, M., Birchall, R., and Walshe, J., 2017, Geophysical Signatures of IOCG and Sedex style mineralization in the Mount Isa Eastern Succession, Queensland, Australia, in Exploration 17: 6th Decennial International Conference on Mineral Exploration, 16 p.

Babo, J., Spandler, C., Oliver, N., Brown, M., Rubenach, M., and Creaser, R.A., 2017, The high-grade Mo-Re Merlin deposit, Cloncurry District, Australia: paragenesis and geochronology of hydrothermal alteration and ore formation: Economic Geology, v. 112, p. 397-422.

Badham, J.P.N., and Morton, R.D., 1976, Magnetite-apatite intrusions and calc-alkaline magmatism, Camsell River, N.W.T.: Canadian Journal of Earth Sciences, v. 13, p. 348-354.

Baker, T., 1998, Alteration, mineralisation and fluid evolution at the Eloise Cu-Au deposit, Cloncurry district, NW Queensland: Economic Geology, v. 93, p. 1213-1236.

Baker, T., Mustard, R., Fu, B., Williams, P.J., Dong, G., Fisher, L., Mark, G., and Ryan, C.G., 2008, Mixed messages in iron oxide–copper–gold systems of the Cloncurry district, Australia: insights from PIXE analysis of halogens and copper in fluid inclusions: Mineralium Deposita, v. 43, p. 599-608.

Barton, M.D., 2014, Iron oxide(–Cu–Au–REE–P–Ag–U–Co) systems, *in* Holland, H.D. and Turekian, K.K., eds., Treatise on geochemistry, second edition, volume 13: Elsevier, p. 515-541.

Bastrakov, E.N., and Skirrow, R.G., 2007, Fluid evolution and origins of iron oxide–Cu–Au prospects in the Olympic Dam district, Gawler Craton, South Australia: Economic Geology, v. 102, p. 1415-1440.

Belperio, A., Flint, R., and Freeman, H., 2007, Prominent Hill: a hematite-dominated, iron oxide copper-gold system: Economic Geology, v. 102, p. 1499-1510.

Benavides, J., Kyser, T.K., Clark, A.H., Oates, C., Zamora, R., Tarnovschi, R., and Castillo, B., 2007, The Mantoverde iron oxide-copper-gold district, III Región, Chile: the role of regionally-derived, non-magmatic fluid contributions to chalcopyrite mineralization: Economic Geology, v. 102, p. 415-440.

BHP Limited, 2018, BHP copper exploration program update: Press release on November 27th, 2018, available at www.bhp.com.

BHP Limited, 2020, Annual report 2020: Available at bhp.com.

Blein, O., Corriveau, L., Montreuil, J.-F., Ehrig, K., Fabris, A., Reid, A., and Pal, D., 2022, Geochemical signatures of metasomatic ore systems hosting IOCG, IOA, albite-hosted uranium and affiliated deposits: a tool for process studies and mineral exploration, *in* Corriveau, L., Potter, E.G. and Mumin, A.H., eds., Mineral systems with iron oxide copper-gold (IOCG) and affiliated deposits: Geological Association of Canada, Special Paper 52, p. 263-298.

Boles, J.R., 1982, Active albitization of plagioclase, Gulf Coast Tertiary: American Journal of Sciences, v. 282, p. 165-180.

Boulvais, P., Ruffet, G., Cornichet, J., and Mermet, M., 2007, Cretaceous albitization and dequartzification of Hercynian peraluminous granite in the Salvezines Massif (French Pyrenees): Lithos, v. 93, p. 89-106.

Bowdidge, C., Walker, E.C., and Dunford, A., 2014, DEMCo LTD. report on 2014 exploration Camsell River property, NTS 86E09, 86F12, Northwest Territories: Northwest Territories Geological Survey, Assessment Report 033596, 110 p.

Burgess, H., Gowans, R.M., Hennessey, B.T., Lattanzi, C.R., and Puritch, E., 2014, Technical report on the feasibility study for the NICO gold–cobalt–bismuth–copper deposit, Northwest Territories, Canada: Fortune Minerals Ltd., NI 43-10 Technical Report No. 1335, 385 p. Available at www.sedar.com.

Carter, T.R., 1984, Metallogeny of the Grenville Province, Southeastern Ontario: Ontario Geological Survey, Open File Report 5515, 470 p.

Cathelineau, M., 1986, The hydrothermal alkali metasomatism effects on granitic rocks: quartz dissolution and related subsolidus changes: Journal of Petrology, v. 27, p. 945-965.

Centaurus Metals Limited, 2021, The Jaguar nickel sulphide project value-add scoping study, executive summary, May 2021: Available at www.centaurus.com.au.

Chao, E.C.T., Back, J.M., Minkin, J.A., Tatsumoto, M., Wang, J., Conrad, J.E., McKee, E.H., Hou, Z., Meng, Q., and Huang, S., 1997, The sedimentary carbonate-hosted giant Bayan Obo REE-Fe-Nb ore deposit of lnner Mongolia, China: a cornerstone example for giant polymetallic ore deposits of hydrothermal origin: US Geological Survey, Bulletin 2143, 65 p.

Chen, H., 2013, External sulphur in IOCG mineralization: implications on definition and classification of the IOCG clan: Ore Geology Reviews, v. 51, p. 74-78.

Chen, H., and Zhao, L., 2022, Iron oxide copper-gold mineralization in the Central Andes: ore deposit geology and modelling, *in* Corriveau, L., Potter, E.G. and Mumin, A.H., eds., Mineral systems with iron oxide copper-gold (IOCG) and affiliated deposits: Geological Association of Canada, Special Paper 52, p. 365-381.

Chen, H., Cooke, D.R., and Baker, M.J., 2013, Mesozoic iron oxide copper-gold mineralization in the central Andes and the Gondwana supercontinent breakup: Economic Geology, v. 108, p. 37-44.

Chorlton, L.B. (compiler), 2007, Generalized geology of the world: bedrock domains and major faults in GIS format: Geological Survey of Canada, Open File 5529, 48 p.

Ciobanu, C.L., Wade, B.P., Cook, N.J., Schmidt-Mumm, A., and Giles, D., 2013, Uranium-bearing hematite from the Olympic Dam Cu-U-Au deposit, South Australia: a geochemical tracer and reconnaissance Pb-Pb geochronometer: Precambrian Research, v. 238, p. 129-147.

Ciobanu, C., Cook, N., and Ehrig, K., 2017, Ore minerals down to the nanoscale: Cu-(Fe)-sulphides from the iron oxide copper gold deposit at Olympic Dam, South Australia: Ore Geology Reviews, v. 81, p. 1218-1235.

Clark, J.M., 2014, Defining the style of mineralisation at the Cairn Hill magnetite-sulphide deposit, Mount Woods Inlier, Gawler Craton, South Australia: Unpublished H.B.Sc. thesis, University of Adelaide, 69 p.

Clark, T., and Wares, R., 2004, Synthèse lithotectonique et métallogénique de l'Orogène du Nouveau-Québec (Fosse du Labrador): Ministère des Ressources naturelles et de la Faune, Québec, MM 2004-01, 177 p.

Clark, T., Gobeil, A., and Chevé, S., 2010, Alterations in IOCG-type and related deposits in the Manitou Lake area, Eastern Grenville Province, Québec, *in* Corriveau, L. and Mumin, A.H., eds., Exploring for iron oxide copper–gold deposits: Canada and global analogues: Geological Association of Canada, Short Course Notes, No. 20, p. 127-146.

Conor, C., Raymond, O., Baker, T., Teale, G., Say, P., and Lowe, G., 2010, Alteration and mineralisation in the Moonta-Wallaroo Cu–Au mining field region, Olympic domain, South Australia, *in* Porter, M., ed., Hydrothermal iron oxide copper-gold and related deposits: a global perspective, v. 3: PGC Publishing, Adelaide, p. 147-170.

Corriveau, L., 2007, Iron oxide copper–gold deposits: a Canadian perspective, *in* Goodfellow, W.D., ed., Mineral deposits of Canada: a synthesis of major deposit-types, district metallogeny, the evolution of geological provinces and exploration methods: Geological Association of Canada, Mineral Deposits Division, Special Publication, v. 5, p. 307-328.

Corriveau, L., and Mumin, A.H., 2010, Exploring for iron oxide copper–gold deposits: the need for case studies, classifications and exploration vectors, *in* Corriveau, L. and Mumin, A.H., eds., Exploring for iron oxide copper-gold deposits: Canada and global analogues: Geological Association of Canada, Short Course Notes, No. 20, p. 1-12.

Corriveau, L., and Potter, E.G., in press, Advancing exploration for iron oxide-copper-gold and affiliated deposits in Canada: context, scientific overview, outcomes and impacts, *in* Pehrsson, S., Wodicka. N., Rogers, N. and Percival, J., eds., Canada's northern shield: new perspectives from the Geo-Mapping for Energy and Minerals Program: Geological Survey of Canada, Bulletin 612.

Corriveau, L., and Spry, P., 2014, Metamorphosed hydrothermal ore deposits, *in* Holland, H.D. and Turekian, K.K., eds., Treatise on geochemistry, second edition: Elsevier, v. 13, p. 175-194.

Corriveau, L., Perreault, S., and Davidson, A., 2007, Prospectivity of the Grenville Province: a perspective, *in* Goodfellow, W., ed., Mineral deposits of Canada: a synthesis of major deposit-types, district metallogeny, the evolution of geological provinces, and exploration methods: Geological Association of Canada, Special Volume 5, p. 819-848.

Corriveau, L., Mumin, A.H., and Setterfield, T., 2010a, IOCG environments in Canada: characteristics, geological vectors to ore and challenges, *in* Porter, T.M., ed., Hydrothermal iron oxide copper-gold and related deposits: a global perspective, v. 4: PGC Publishing, Adelaide, p. 311-344.

Corriveau, L., Williams, P.J., and Mumin, A.H., 2010b, Alteration vectors to IOCG mineralization – from uncharted terranes to deposits, *in* Corriveau, L. and Mumin, A.H., eds., Exploring for iron oxide copper-gold deposits: Canada and global analogues: Geological Association of Canada, Short Course Notes, No. 20, p. 89-110.

Corriveau, L., Mumin, A.H., and Montreuil, J.-F., 2011, The Great Bear magmatic zone (Canada): the IOCG spectrum and related deposit types: Society for Geology Applied to Mineral Deposits, 11th, Antofagasta, Chile, Extended Abstracts, p. 524-526.

Corriveau, L., Nadeau, O., Montreuil, J.-F., and Desrochers, J.-P., 2014, Report of activities for the Core Zone: strategic geomapping and geoscience to assess the mineral potential of the Labrador Trough for multiple metals IOCG and affiliated deposits, Canada: Geological Survey of Canada, Open File 7714, 12 p.

Corriveau, L., Lauzière, K., Montreuil, J.-F., Potter, E.G., Hanes, R., and Prémont, S., 2015, Dataset of geochemical data from iron oxide alkali-altered mineralizing systems of the Great Bear magmatic zone (NWT): Geological Survey of Canada, Open File 7643, 19 p., 6 geochemical datasets.

Corriveau, L., Montreuil, J.-F., and Potter, E.G., 2016, Alteration facies linkages among IOCG, IOA and affiliated deposits in the Great Bear magmatic zone, Canada, *in* Slack, J., Corriveau, L. and Hitzman, M., eds., Proterozoic iron oxide-apatite (± REE) and iron oxide-copper-gold and affiliated deposits of Southeast Missouri, USA, and the Great Bear magmatic zone, Northwest Territories, Canada: Economic Geology, v. 111, p. 2045-2072.

Corriveau, L., Blein, O., Gervais, F., Trapy, P.H., De Souza, S., and Fafard, D., 2018a, Iron-oxide and alkali-calcic alteration, skarn and epithermal mineralizing systems of the Grenville Province: the Bondy gneiss complex in the Central Metasedimentary Belt of Quebec as a case example - a field trip to the 14th Society for Geology Applied to Mineral Deposits (SGA) biennial meeting: Geological Survey of Canada, Open File 8349, 136 p.

Corriveau, L., Potter, E.G., Montreuil, J.-F., Blein, O., Ehrig, K., and De Toni, A., 2018b, Iron-oxide and alkali-calcic alteration ore systems and their polymetallic IOA, IOCG, skarn, albitite-hosted U±Au±Co, and affiliated deposits: a short course series. Part 2: overview of deposit types, distribution, ages, settings, alteration facies, and ore deposit models: Geological Survey of Canada, Scientific Presentation 81, 154 p.

Corriveau, L., Potter, E.G., Montreuil, J.-F., Blein, O., Ehrig, K., and Fabris, A., 2020, Alteration facies of IOA, IOCG and affiliated deposits: understanding the similarities, recognising the diversity in these ore systems: Geological Survey of South Australia, GSSA Iron Oxide - Copper-Gold Mineral Systems Workshop 2019, 77 p.

Corriveau, L., Montreuil, J.-F., De Toni, A.F., Potter, E.G., and Percival, J.B., 2022a, Mapping mineral systems with IOCG and affiliated deposits: a facies approach, *in* Corriveau, L., Potter, E.G. and Mumin, A.H., eds., Mineral systems with iron oxide copper-gold (IOCG) and affiliated deposits: Geological Association of Canada, Special Paper 52, p. 69-111.

Corriveau, L., Montreuil, J.-F., Blein, O., Ehrig, K., and Potter, E.G., 2022b, Mineral systems with IOCG and affiliated deposits: part 2 – geochemical footprints, *in* Corriveau, L., Potter, E.G. and Mumin, A.H., eds., Mineral systems with iron oxide copper-gold (IOCG) and affiliated deposits: Geological Association of Canada, Special Paper 52, p. 159-204.

Corriveau, L., Montreuil, J.-F., Potter, E.G., Ehrig, K., Mumin, A.H., and Williams, P.J., 2022c, Mineral systems with IOCG and affiliated deposits: part 1 – alteration facies, *in* Corriveau, L., Potter, E.G. and Mumin, A.H., eds., Mineral systems with iron oxide copper-gold (IOCG) and affiliated deposits: Geological Association of Canada, Special Paper 52, p. 113-158.

Corriveau, L., Mumin, A.H., and Potter, E.G., 2022d, Mineral systems with iron oxide copper-gold (Ag-Bi-Co-U-REE) and affiliated deposits: introduction and overview, *in* Corriveau, L., Potter, E.G. and Mumin, A.H., eds., Mineral systems with iron oxide copper-gold (IOCG) and affiliated deposits: Geological Association of Canada, Special Paper 52, p. 1-26.

Craven, J.A., Roberts, B., Hayward, N., Stefanescu, M., and Corriveau, L., 2013, A magnetotelluric survey and preliminary geophysical inversion and visualization of the NICO IOCG deposit, NWT: Geological Survey of Canada, Open File 7465, 26 p.

Cuney, M., Emetz, A., Mercadier, J., Mykchaylov, V., Shunko, V., and Yuslenko, A., 2012, Uranium deposits associated with Na-metasomatism from central Ukraine: a review of some of the major deposits and genetic constraints: Ore Geology Reviews, v. 44, p. 82-106.

Daliran, F., Stosch, H.-G., Williams, P.J., Jamali, H., and Dorri, M.-B., 2022, Early Cambrian IOA-REE, U-Th and Cu(Au)-Bi-Co-Ni-Ag-As-sulphide deposits of the Bafq district, East-central Iran, *in* Corriveau, L., Potter, E.G. and Mumin, A.H., eds, Mineral systems with iron oxide copper-gold (IOCG) and affiliated deposits: Geological Association of Canada, Special Paper 52, p. 409-424.

Davidson, G.J., Paterson, H., Meffre, S., and Berry, R.F., 2007, Characteristics and origin of the Oak Dam East breccia-hosted, iron oxide-Cu-U-(Au) deposit: Olympic Dam region, Gawler Craton, South Australia: Economic Geology, v. 102, p. 1471-1498.

Davis, W.J., Corriveau, L., van Breemen, O., Bleeker, W., Montreuil, J.-F., Potter, E.G., and Pelleter, E., 2011, Timing of IOCG mineralizing and alteration events within the Great Bear magmatic zone, *in* Fischer, B.J. and Watson, D.M., eds., 39th Annual Yellowknife Geoscience Forum Abstract Volume: NWT Geoscience Office, p. 97.

Day, W.C., Slack, J.F., Ayuso, R.A., and Seeger, C.M., 2016, Regional geologic and petrologic framework for iron oxide ± apatite ± rare earth element and iron oxide copper-gold deposits of the Mesoproterozoic St. Francois Mountains Terrane, Southeast Missouri, USA, *in* Slack, J., Corriveau, L. and Hitzman, M., eds., Proterozoic iron oxide-apatite (± REE) and iron oxide-copper-gold and affiliated deposits of Southeast Missouri, USA, and the Great Bear magmatic zone, Northwest Territories, Canada: Economic Geology, v. 111, p. 1825-1858.

De Jong, G., and Williams, P.J., 1995, Giant metasomatic system formed during exhumation of mid crustal Proterozoic rocks in the vicinity of the Cloncurry Fault, NW Queensland: Australian Journal of Earth Sciences, v. 42, p. 281-290.

De Toni, A.F., 2016, Les paragénèses à magnétite des altérations associées aux systèmes à oxydes de fer et altérations en éléments alcalins, zone magmatique du Grand lac de l'Ours: Unpublished M.Sc. thesis, Institut national de la Recherche scientifique, 534 p.

del Real, I., Thompson, J.F.H., and Carriedo, J., 2018, Lithological and structural controls on the genesis of the Candelaria-Punta del Cobre iron oxide copper gold district, Northern Chile: Ore Geology Reviews, v. 102, p. 106-153.

Desrochers, J.-P., 2014, Technical report on the Sagar property, Romanet Horst, Labrador Trough, Québec, Canada (latitude, 56°22'N and longitude 68°00'W; NTS map sheets 24B/05 and 24C/08): National Instrument 43–101 Technical Report prepared for Honey Badger Exploration Inc., available at www.sedar.com.

Dilles, J.H., and Einaudi, M.T., 1992, Wall-rock alteration and hydrothermal flow paths about the Ann-Mason porphyry copper deposit, Nevada – A 6-km vertical reconstruction: Economic Geology, v. 87, p. 1963-2001.

Dipple, G.M., and Ferry, J.M., 1992, Metasomatism and fluid flow in ductile shear zones: Contributions to Mineralogy and Petrology, v. 112, p. 149-164.

Dmitrijeva, M., Ehrig, K.J., Ciobanu, C.L., Cook, N.J., Verdugo-Ihla, M.R., and Metcalfe, A.V., 2019, Defining IOCG signatures through compositional data analysis: a case study of lithogeochemical zoning from the Olympic Dam deposit, South Australia: Ore Geology Reviews, v. 105, p. 86-101.

Dragon Mining Limited, 2014, Resource updates lift Kuusamo ounces: ASX announcement, March 11th 2014, available at https://www.dragonmining.com.

Dufréchou, G., Harris, L.B., Corriveau, L., and Antonoff, V., 2015, Regional and local controls on mineralization and pluton emplacement in the Bondy gneiss complex, Grenville Province, Canada interpreted from aeromagnetic and gravity data: Journal of Applied Geophysics, v. 116, p. 192-205.

Edfelt, Å., Armstrong, R.N., Smith, M., and Martinsson, O., 2005, Alteration paragenesis and mineral chemistry of the Tjårrojåkka apatite–iron and Cu (-Au) occurrences, Kiruna area, northern Sweden: Mineralium Deposita, v. 40, p. 409-434.

Ehrig, K., McPhie, J., and Kamenetsky, V.S., 2012, Geology and mineralogical zonation of the Olympic Dam iron oxide Cu-U-Au-Ag deposit, South Australia, *in* Hedenquist, J.W., Harris, M. and Camus, F., eds., Geology and genesis of major copper deposits and districts of the world: a tribute to Richard H. Sillitoe: Economic Geology, Special Publication 16, p. 237-267.

Ehrig, K., Kamenetsky, V.S., McPhie, J., Apukhtina, O., Cook, N., and Ciobanu, C.L., 2017, Olympic Dam iron oxide Cu-U-Au-Ag deposit, *in* Phillips, G.N., ed., Australian ore deposits: The Australasian Institute of Mining and Metallurgy, v. 32, Melbourne, p. 601-610.

Ehrig, K., Kamenetsky, V.S., McPhie, J., Macmillan, E., Thompson, J., Kamenetsky, M., and Maas, R., 2021, Staged formation of the supergiant Olympic Dam uranium deposit, Australia: Geology, v. 49, doi.org/10.1130/G48930.1

Emsbo, P., Lawley, C., and Czarnota, K., 2021, Geological surveys unite to improve critical mineral security: Eos, 102.

Engvik, A.K., Corfu, F., Solli, A., and Austrheim, H., 2017, Sequence and timing of mineral replacement reactions during albitisation in the high-grade Bamble lithotectonic domain, S-Norway: Precambrian Research, v. 291, p. 1-16.

Enkin, R.J., Corriveau, L., and Hayward, N., 2016, Metasomatic alteration control of petrophysical properties in the Great Bear magmatic zone (Northwest Territories, Canada), *in* Slack, J., Corriveau, L. and Hitzman, M., eds., Proterozoic iron oxide-apatite (± REE) and iron oxide-copper-gold and affiliated deposits of Southeast Missouri, USA, and the Great Bear magmatic zone, Northwest Territories, Canada: Economic Geology, v. 111, p. 2073-2085.

Enkin, R.J., Hamilton, T.S., and Morris, W.A., 2020, The Henkel petrophysical plot: mineralogy and lithology from physical properties: Geochemistry, Geophysics, Geosystems, v. 20, 2019GC008818.

Fabris, A., 2022, Geochemical characteristics of IOCG deposits from the Olympic Copper-Gold Province, South Australia, *in* Corriveau, L., Potter, E.G. and Mumin, A.H., eds., Mineral systems with iron oxide copper-gold (IOCG) and affiliated deposits: Geological Association of Canada, Special Paper 52, p. 237-252.

Fabris, A., Katona, L., Gordon, G., Reed, G., Keeping, T., Gouthas, G., and Swain, G., 2018, Characterising and mapping alteration in the Punt Hill region: a data integration project: Department of the Premier and Cabinet, South Australia, Adelaide, Report Book 2018/00010, 604 p.

Fan, H.R., Yang, K.F., Hu, F.F., Liu, S., and Wang, K.Y., 2016, The giant Bayan Obo REE-Nb-Fe deposit, China: controversy and ore genesis: Geoscience Frontiers, v. 7, p. 335-344.

Ferreira Filho, C.F., Ferraz de Oliveira, M.M., Mansur, E.T., and Rosa, W.D., 2021, The Jaguar hydrothermal nickel sulfide deposit: evidence for a nickel-rich member of IOCG-type deposits in the Carajás Mineral Province, Brazil: Journal of South American Earth Sciences, v. 111, 103501.

Foster, A.R., Williams, P.J., and Ryan, C.G., 2007, Distribution of gold in hypogene ore at the Ernest Henry iron oxide copper-gold deposit, Cloncurry district, NW Queensland: Exploration and Mining Geology, v. 16, p. 125-143.

Friehauf, K.C., Smith, R.C., and Volkert, R.A., 2002, Comparison of the geology of Proterozoic iron oxide deposits in the Adirondack and mid-Atlantic Belt of Pennsylvania, New Jersey and New York, *in* Porter, T.M., ed., Hydrothermal iron oxide copper-gold and related deposits: a global perspective, v. 2: PGC Publishing, Adelaide, p. 247-252.

Gagnon, R., Buro, Y.A., Ibrango, S., Gagnon, D., Stapinsky, M., Del Carpio, S., and Larochelle, E., 2018, Projet de terres rares Kwyjibo: Rapport technique NI 43-101 révisé, 292 p., available at https://www.sedar.com.

Galicki, M., Marshall, D., Staples, R., Thorkelson, D., Downie, C., Gallagher, C., Enkin, R., and Davis, W., 2012, Iron oxide ± Cu ± Au deposits in the Iron Range, Purcell Basin, Southeastern British Columbia: Economic Geology, v. 10, p. 1293-1301.

Gandhi, S.S., 1994, Geological setting and genetic aspects of mineral occurrences in the southern Great Bear magmatic zone, Northwest Territories, *in* Sinclair, W.D. and Richardson, D.G., eds., Studies of rare-metal deposits in the Northwest Territories: Geological Survey of Canada, Bulletin 475, p. 63-96.

Gandhi, S.S., Mortensen, J.K., Prasad, N., and van Breemen, O., 2001, Magmatic evolution of the southern Great Bear continental arc, northwestern Canadian Shield: geochronological constraints: Canadian Journal of Earth Sciences, v. 38, p. 767-785.

Gandhi, S.S., Potter, E.G., and Fayek, M., 2018, New constraints on genesis of the polymetallic veins at Port Radium, Great Bear Lake, Northwest Canadian Shield: Ore Geology Reviews, v. 96, p. 28-47.

Garcia, V.B., Schutesky, M.E., Oliveira, C.G., Whitehouse, M.J., Huhn, S.R.B., and Augustin, C.T., 2020, The Neoarchean GT-34 Ni deposit, Carajás mineral Province, Brazil: an atypical IOCG-related Ni sulfide mineralization: Ore Geology Reviews, v. 127, 103773.

Gates, B.I., 1991, Sudbury mineral occurrence study: Ontario Geological Survey, Open File Report 5771, 289 p.

Glencore, 2020, Resources and reserves as at 31 December 2019: Available at https://www.glencore.com/

Goad, R.E., Mumin, A.H., Duke, N.A., Neale, K.L., and Mulligan, D.L., 2000, Geology of the Proterozoic iron oxide-hosted NICO cobalt-gold-bismuth, and Sue-Dianne copper-silver deposits, southern Great Bear Magmatic Zone, Northwest Territories, Canada, *in* Porter, T.M., ed., Hydrothermal iron oxide copper-gold and related deposits: a global perspective, v. 1: PGC Publishing, Adelaide, p. 249-267.

Groves, D.I., Bierlein, F.P., Meinert, L.D., and Hitzman, M.W., 2010, Iron oxide copper-gold (IOCG) deposits through Earth history. Implications for origin, lithospheric setting, and distinction from other epigenetic iron oxide deposits: Economic Geology, v. 105, p. 641-654.

Gutzmer, J., Pack, A., Lüders, V., Wilkinson, J.J., Beukes, N.J., and van Niekerk, H.S., 2001, Formation of jasper and andradite during low-temperature hydrothermal seafloor metamorphism, Ongeluk Formation, South Africa: Contributions to Mineralogy and Petrology, v. 142, p. 27-42.

Hampton, S., 1997, A study of the paragenesis and controls on Proterozoic (Cu-Fe-Au-REE) mineralisation at the Manxman A1 and Joes Dam South prospects, Mount Woods Inlier, South Australia: Unpublished H.B.Sc. thesis, James Cook University, 146 p.

Harlov, D.E., Meighan, C.J., Kerr, I.D., and Samson, I.M., 2016, Mineralogy, chemistry, and fluid-aided evolution of the Pea Ridge Fe oxide-(Y + REE) deposit, Southeast Missouri, USA: Economic Geology, v. 111, p. 1963-1984.

Hayward, N., 2013, 3D magnetic inversion of mineral prospects in the Great Bear magmatic zone, NT, Canada: Geological Survey of Canada, Open File 7421.

Hayward, N., Corriveau, L., Craven, J.A., and Enkin, R.J., 2016, Geophysical signature of the NICO Au-Co-Bi-Cu deposit and its iron oxide-alkali alteration system, Northwest Territories, Canada, *in* Slack, J., Corriveau, L. and Hitzman, M., eds., Proterozoic iron oxide-apatite (± REE) and iron oxide-copper-gold and affiliated deposits of Southeast Missouri, USA, and the Great Bear magmatic zone, Northwest Territories, Canada: Economic Geology, v. 111, p. 2087-2110.

Hicks, C., 2015, Petrological and geochemical investigations of the Michelin uranium deposit, Central Mineral Belt, Labrador: Unpublished M.Sc. thesis, Memorial University, St John's, 466 p.

Hildebrand, R.S., 1986, Kiruna-type deposits: their origin and relationship to intermediate subvolcanic plutons in the Great Bear Magmatic Zone, northwest Canada: Economic Geology, v. 81, p. 640-659.

Hildebrand, R.S., Hoffman, P.F., Housh, T., and Bowring, S.A., 2010, The nature of volcano-plutonic relations and shapes of epizonal plutons of continental arcs as revealed in the Great Bear magmatic zone, northwestern Canada: Geosphere, v. 6, p. 812-839.

Hitzman, M.W., and Valenta, R.K., 2005, Uranium in iron oxide-copper-gold (IOCG) systems: Economic Geology, v. 100, p. 1657-1661.

Hitzman, M.C., Oreskes, N., and Einaudi, M.T., 1992, Geological characteristics and tectonic setting of Proterozoic iron oxide (Cu-U-Au-REE) deposits: Precambrian Research, v. 58, p. 241-287.

Hofstra, A., Lisitsin, V., Corriveau, L., Paradis, S., Peter, J., Lauzière, K., Lawley, C., Gadd, M., Pilote, J., Honsberger, I., Bastrakov, E., Champion, D., Czarnota, K., Doublier, M., Huston, D., Raymond, O., VanDerWielen, S., Emsbo, P., Granitto, M., and Kreiner, D., 2021, Deposit classification scheme for the Critical Minerals Mapping Initiative Global Geochemical Database: U.S. Geological Survey Open-File Report 2021–1049, 60 p., https://doi.org/ 10.3133/ ofr20211049.

Hoggard, M.J., Czarnota, K., Richards, F.D., Huston, D., Jaques, L., and Ghelichkhan, S., 2020, Global distribution of sediment-hosted metals controlled by craton edge stability: Nature Geoscience, v. 13, p. 504-510.

Hu, H., Li, J.W., Harlov, D.E., Lentz, D.R., McFarlane, C.R.M., and Yang, Y.-H., 2019, A genetic link between iron oxide-apatite and iron skarn mineralization in the Jinniu volcanic basin, Daye district, eastern China: evidence from magnetite geochemistry and multi-mineral U-Pb geochronology: GSA Bulletin, v. 132, p. 899-917.

Huang, X.-W., Beaudoin, G., De Toni, A.-F., Corriveau, L., Makvandi, S., and Boutroy, E., 2022, Iron-oxide trace element fingerprinting of iron oxide copper-gold and iron oxide-apatite deposits: a review, *in* Corriveau, L., Potter, E.G. and Mumin, A.H., eds., Mineral systems with iron oxide copper-gold (IOCG) and affiliated deposits: Geological Association of Canada, Special Paper 52, p. 347-364.

Ismail, R., 2015, Spatial-temporal evolution of skarn alteration in IOCG systems: evidence from petrography, mineral trace element signatures and fluid inclusions studies at Hillside, Yorke Peninsula, South Australia: Unpublished Ph.D. thesis, The University of Adelaide, 352 p.

Ismail, R., Ciobanu, C.L., Cook, N.J., Giles, D., Schmidt-Mumm, A., and Wade, B., 2014, Rare earths and other trace elements in minerals from skarn assemblages, Hillside iron oxide–copper–gold deposit, Yorke Peninsula, South Australia: Lithos, v. 184-187, p. 456-477.

Johnson, C.A., Day, W.C., and Rye, R.O., 2016, Oxygen, hydrogen, sulfur, and carbon isotopes in the Pea Ridge magnetite-apatite deposit, southeast Missouri, and sulfur isotope comparisons to other iron deposits in the region, *in* Slack, J., Corriveau, L. and Hitzman, M., eds., Proterozoic iron oxide-apatite (± REE) and iron oxide-copper-gold and affiliated deposits of Southeast Missouri, USA, and the Great Bear magmatic zone, Northwest Territories, Canada: Economic Geology, v. 111, p. 2017-2032.

Katona, L., and Fabris, A., 2022, Defining geophysical signatures of IOCG deposits in the Olympic Copper-Gold province, South Australia, using geophysics, GIS and spatial statistics, *in* Corriveau, L., Potter, E.G. and Mumin, A.H., eds., Mineral systems with iron oxide copper-gold (IOCG) and affiliated deposits: Geological Association of Canada, Special Paper 52, p. 299-313.

King, J., 2019, Oak Dam - An early exploration opportunity, in South Australian Exploration and Mining Conference, Adelaide Convention Centre, Friday 27 November 2020: SAEMC Online Proceedings Archive, http://saemc.com.au/archive/2019/2019_03_king.pdf, 13 p.

Kirschbaum, M.J., and Hitzman, M.W., 2016, Guelb Moghrein: an unusual carbonate-hosted iron oxide copper-gold deposit in Mauritania, northwest Africa: Economic Geology, v. 111, p. 763-770.

Kish, L., and Cuney, M., 1981, Uraninite–albite veins from the Mistamisk valley of the Labrador Trough, Québec: Mineralogical Magazine, v. 44, p. 471-483.

Kissin, S.A., 1992, Five-element (Ni-Co-Ag-As-Bi) veins: Geoscience Canada, v. 19, p. 113-124.

Kreiner, D., and Barton, M.D., 2017, Sulfur-poor intense acid hydrothermal alteration: a distinctive hydrothermal environment: Ore Geology Reviews, v. 88, p. 174-187.

Krneta, S., Cook, N.J., Ciobanu, C.L., Ehrig, K., and Kontonikas-Charos, A., 2017, The Wirrda Well and Acropolis prospects, Gawler Craton, South Australia: insights into evolving fluid conditions through apatite chemistry: Journal of Geochemical Exploration, v. 181, p. 276-291.

Leonard, B.F., and Buddington, A.F., 1964, Ore deposits of the St. Lawrence county magnetite district Northwest Adirondacks New York: U.S. Geological Survey, Professional Paper 377, 275 p.

Li, W., Audétat, A., and Zhang, J., 2015, The role of evaporites in the formation of magnetite–apatite deposits along the Middle and Lower Yangtze River, China: evidence from LA-ICP-MS analysis of fluid inclusions: Ore Geology Reviews, v. 67, p. 264-278.

Liu, J., 2017, Indium mineralization in a Sn-poor skarn deposit: a case study of the Qibaoshan deposit, South China: Minerals, v. 7, 76.

Liu, W., and McPhail, D.C., 2005, Thermodynamic properties of copper chloride complexes and copper transport in magmatic-hydrothermal solutions: Chemical Geology, v. 221, p. 21-39.

Lobo-Guerrero, S.A., 2010, Iron oxide-copper-gold mineralization in the Greater Lufilian Arc, Africa, *in* Corriveau, L. and Mumin, A.H., eds., Exploring for iron oxide copper-gold deposits: Canada and global analogues: Geological Association of Canada, Short Course Notes, No. 20, p. 161-175.

Lokanc, M., Eggert, R., and Redlinger, M., 2015, The availability of indium: the present, medium term, and long term: National Renewable Energy Laboratory, 79 p., available at www.nrel.gov/publications.

Lypaczewski, P., Normandeau, P.X., Paquette, J., and McMartin, I., 2013, Petrographic and cathodoluminescence characterization of apatite from the Sue Dianne and Brooke IOCG mineralization systems, Great Bear magmatic zone, Northwest Territories, Canada: Geological Survey of Canada, Open File 7319, 18 p.

Maas, R., Apukhtina, O.B., Kamenetsky, V.S., Ehrig, K., and Sprung, P., 2020, Carbonates at the supergiant Olympic Dam U-Cu-Au deposit, South Australia, Part 2: Sm-Nd, Lu-Hf and Sr-Pb isotope constraints on the chronology of carbonate deposition: Ore Geology Reviews, 103745.

Macmillan, E., Cook, N.J., Ehrig, K., Ciobanu, C.L., and Pring, A., 2016, Uraninite from the Olympic Dam IOCG-U-Ag deposit: linking textural and compositional variation to temporal evolution: American Mineralogist, v. 101, p. 1295-1320.

Mark, G., and Foster, D.R.W., 2000, Magmatic–hydrothermal albite–actinolite–apatite-rich rocks from the Cloncurry district, NW Queensland, Australia: Lithos, v. 51, p. 223-245.

Mark, G., Oliver, N.H.S., and Williams, P.J., 2006, Mineralogical and chemical evolution of the Ernest Henry Fe oxide-Cu-Au ore system, Cloncurry district, northwest Queensland, Australia: Mineralium Deposita, v. 40, p. 769-801.

Marschik, R., and Fontboté, L., 2001, The Candelaria-Punta del Cobre iron oxide Cu-Au (-Zn-Ag) deposits, Chile: Economic Geology, v. 96, p. 1799-1826.

Marschik, R., Singer, B.S., Munizaga, F., Tassinari, C., Moritz, R., and Fontboté, L., 1997, Age of Cu(-Fe)-Au mineralization and thermal evolution of the Punta del Cobre district, Chile: Mineralium Deposita, v. 32, p. 531-546.

Marshall, L.J., and Oliver, N.H.S., 2008, Constraints on hydrothermal fluid pathways within Mary Kathleen Group stratigraphy of the Cloncurry iron-oxide–copper–gold district, Australia: Precambrian Research, v. 163, p. 151-158.

McCafferty, A.E., Phillips, J.D., Hofstra, A.H., and Day, W.C., 2019, Crustal architecture beneath the southern Midcontinent (USA) and controls on Mesoproterozoic iron-oxide mineralization from 3D geophysical models: Ore Geology Reviews, v. 111, 102966.

McCaig, A.M., Wickham, S.M., and Taylor, H.P., 1990, Deep fluid circulation in alpine shear zones, Pyrenees, France: field and oxygen isotope studies: Contribution to Mineralogy and Petrology, v. 106, p. 41-60.

McGloin, M., Tomkins, A., and Weinberg, R., 2013, Isan U and Th mobility and related ore mineralisation: Proceedings of the 12th Biennial SGA meeting, Upsala, Sweden, 4 p.

McLaughlin, B., Montreuil, J.-F., and Desrochers, J.-P., 2016, Exploration report (summer and fall 2014 drill program) on the Sagar Property, Romanet Horst, Labrador Trough, Québec, Canada: Ministère de l'Énergie et des Ressources naturelles, Québec, GM 69734, 65 p.

McMartin, I., Corriveau, L., and Beaudoin, G., 2011, An orientation study of the heavy mineral signature of the NICO Co-Au-Bi deposit, Great Bear magmatic zone, Northwest Territories, Canada: Geochemistry: Exploration, Environment, Analysis, v. 11, p. 293-307.

Melo, G.H.C., Monteiro, L.V.S., Xavier, R.P., Moreto, C.P.N., Santiago, E.S.B., Dufrane, S.A., Aires, B., and Santos, A.F.F., 2017, Temporal evolution of the giant Salobo IOCG deposit, Carajás Province (Brazil): constraints from paragenesis of hydrothermal alteration and U-Pb geochronology: Mineralium Deposita, v. 52, p. 709-732.

Melo, G.H.C., Monteiro, L.V.S., Xavier, R.P., Moreto, C.P.N., and Santiago, E., 2019, Tracing fluid sources for the Salobo and Igarapé Bahia deposits: implications for the genesis of the iron oxide copper-gold deposits in the Carajás Province, Brazil: Economic Geology, v. 114, p. 697-718.

Monteiro, L.V.S., Xavier, R.P., Carvalho, E.R., Hitzman, M.W., Johnson, C.A., Souza Filho, C.R., and Torresi, I., 2008, Spatial and temporal zoning of hydrothermal alteration and mineralization in the Sossego iron oxidecopper-gold deposit, Carajás Mineral Province, Brazil: paragenesis and stable isotope constraints: Mineralium Deposita, v. 43, p. 129-159.

Montreuil, J.-F., Corriveau, L., and Long, B., 2012, Porosity in albitites and the development of albitite-hosted U deposits: insights from x-ray computed tomography: CT Scan workshop, Development on non-medical environment, Québec, INRS-ETE, Quebec City, Program, p. 5.

Montreuil, J.-F., Corriveau, L., and Grunsky, E.C., 2013, Compositional data analysis of IOCG systems, Great Bear magmatic zone, Canada: to each alteration types its own geochemical signature: Geochemistry: Exploration, Environment, Analysis, v. 13, p. 229-247.

Montreuil, J.-F., Desrochers, J.-P., and Masters, J., 2014, Exploration report (July and August 2013 program) on the Sagar Property, Romanet Horst, Labrador Trough, Québec, Canada: Ministère de l'Énergie et des Ressources naturelles, Québec, GM 68408, 80 p.

Montreuil, J.-F., Corriveau, L., and Potter, E.G., 2015, Formation of albitite-hosted uranium within IOCG systems: the Southern Breccia, Great Bear magmatic zone, Northwest Territories, Canada: Mineralium Deposita, v. 50, p. 293-325.

Montreuil, J.-F., Corriveau, L., and Davis, W., 2016a, Tectonomagmatic evolution of the southern Great Bear magmatic zone (Northwest Territories, Canada) – Implications on the genesis of iron oxide alkali-altered hydrothermal systems, *in* Slack, J., Corriveau, L. and Hitzman, M., eds., Proterozoic iron oxide-apatite (± REE) and iron oxide-copper-gold and affiliated deposits of Southeast Missouri, USA, and the Great Bear magmatic zone, Northwest Territories, Canada: Economic Geology, v. 111, p. 2111-2138.

Montreuil, J.-F., Corriveau, L., Potter, E.G., and De Toni, A.F., 2016b, On the relation between alteration facies and metal endowment of iron oxide–alkali-altered systems, southern Great Bear magmatic zone (Canada), *in* Slack, J., Corriveau, L. and Hitzman, M., eds., Proterozoic iron oxide-apatite (± REE) and iron oxide-copper-gold and affiliated deposits of Southeast Missouri, USA, and the Great Bear magmatic zone, Northwest Territories, Canada: Economic Geology, v. 111, p. 2139-2168.

Montreuil, J.-F., Potter, E.G., Corriveau, L., and Davis, W.J., 2016c, Element mobility patterns in magnetite-group IOCG systems: the Fab IOCG system, Northwest Territories, Canada: Ore Geology Reviews, v. 72, p. 562-584.

Morrissey, L.J., and Tomkins, A.G., 2020, Evaporite-bearing orogenic belts produce ligand-rich and diverse metamorphic fluids: Geochimica et Cosmochimica Acta, v. 275, p. 163-187.

Mumin, A.H. (ed.), 2015, Echo Bay IOCG thematic map series: geology, structure and hydrothermal alteration of a stratovolcano complex, Northwest Territories, Canada: Geological Survey of Canada, Open File 7807, 19 p., 18 sheets.

Mumin, A.H., and Trott, M., 2003, Hydrothermal iron-sulphide copper-graphite mineralization in the northern Kisseynew Domain, Trans-Hudson Orogen, Manitoba (NTS 63O and 64B): evidence for deep-seated IOCG (Olympic Dam)–style metal deposition?: Manitoba Industry, Trade and Mines, Manitoba Geological Survey, Report of Activities 2003, p. 79-85.

Mumin, A.H. and Corriveau, L., 2004, The Eden deformation corridor and polymetallic mineral belt: Trans Hudson Orogen, Leaf Rapids District, Manitoba: Manitoba Geological Survey, Report of Activities 2004, p. 69-91.

Mumin, A.H., Corriveau, L., Somarin, A.K., and Ootes, L., 2007, Iron oxide copper-gold-type polymetallic mineralisation in the Contact Lake Belt, Great Bear magmatic zone, Northwest Territories, Canada: Exploration and Mining Geology, v. 16, p. 187-208.

Mumin, A.H., Somarin, A.K., Jones, B., Corriveau, L., Ootes, L., and Camier, J., 2010, The IOCG-porphyry-epithermal continuum of deposits types in the Great Bear Magmatic Zone, Northwest Territories, Canada, *in* Corriveau, L. and Mumin, A.H., eds., Exploring for iron oxide copper-gold deposits: Canada and global analogues: Geological Association of Canada, Short Course Notes, No. 20, p. 59-78.

Natural Resources Canada, 2021, Canada's list of critical minerals: Available at https://www.nrcan.gc.ca/criticalminerals.

Neymark, L.A., Holm-Denoma, C.S., Pietruszka, A.J., Aleinikoff, J.N., Fanning, C.M., Pillers, R.M., and Moscati, R.J., 2016, High spatial resolution U-Pb geochronology and Pb isotope geochemistry of magnetite-apatite ore from the Pea Ridge iron oxide-apatite deposit, St. Francois Mountains, southeast Missouri, USA: Economic Geology, v. 111, p. 1915-1933.

Ngo, X.D., Zhao, X.-F., Tran, T.H., Deng, X.D., and Li, J.W., 2020, Two episodes of REEs mineralization at the Sin Quyen IOCG deposit, NW Vietnam: Ore Geology Reviews, v. 125, 103676.

Ningwu Research Group, 1978, Ningwu porphyry iron ore deposits: Geological Publishing House, Beijing. (in Chinese), 196 p.

Normandeau, P.X., Harlov, D.E., Corriveau, L., Paquette, J., and McMartin, I., 2018, Characterization of fluorapatite within iron oxide alkali-calcic alteration systems of the Great Bear magmatic zone: a potential metasomatic process record: The Canadian Mineralogist, v. 56, p. 1-21.

Nuelle, L.M., Day, W.C., Sidder, G.B., and Seeger, C.M., 1992, Geology and mineral paragenesis of the Pea Ridge iron ore mine, Washington County, Missouri — origin of the rare-earth-element- and gold-bearing breccia pipes, *in* Day, W.C. and Lane, D.E., eds., Strategic and critical minerals in the Midcontinent region: U.S. Geological Survey Bulletin 1989-a, p. A1-A11.

O'Brien, S.P., 2016, Structural and mineralogical controls on the formation of the 'Inter-lens' at the Ernest Henry deposit, Queensland: Unpublished H.B.Sc. thesis, University of Adelaide, 137 p.

Oliveira, M.M.F., 2017, Caracterização e metalogênese do depósito de Ni do Jaguar, Província Mineral de Carajás: Unpublished M.Sc. Thesis, Universidade de Brasília, 115 p.

Oliver, N.H.S., Pearson, P.J., Holcombe, R.J., and Ord, A., 1999, Mary Kathleen metamorphic–hydrothermal uranium–rare-earth element deposit: ore genesis and numerical model of coupled deformation and fluid flow: Australian Journal of Earth Sciences, v. 46, p. 467-484.

Oliver, N.H.S., Mark, G., Pollard, P.J., Rubenach, M.J., Bastrakov, E., Williams, P.J., Marshall, L.C., Baker, T., and Nemchin, A.A., 2004, The role of sodic alteration in the genesis of iron oxide-copper-gold deposits: geochemistry and geochemical modelling of fluid-rock interaction in the Cloncurry district, Australia: Economic Geology, v. 99, p. 1145-1176.

Oliver, N.H.S., Rubenach, M.J., Baker, B.F., Blenkinsop, T.G., Cleverley, J.S., Marshall, L.J., and Ridd, P.J., 2006, Granite-related overpressure and volatile release in the mid crust: fluidized breccias from the Cloncurry district, Australia: Geofluids, v. 6, p. 346-358.

Oliver, N.H.S., Rusk, B.G., Long, R., and Zhang, D., 2009, Copper- and iron-oxide-Cu-Au deposits, and their associated alteration and brecciation, Mount Isa Block: SGA post-conference trip field guide, EGRU/JCU, 40 p.

Ootes, L., Harris, J., Jackson, V.A., Azar, B., and Corriveau, L., 2013, Uranium-enriched bedrock in the central Wopmay orogen: implications for uranium mineralization, *in* Potter, E.G., Quirt, D. and Jefferson, C.W., eds., Uranium in Canada: geological environments and exploration developments: Exploration and Mining Geology, v. 21, p. 85-103.

Ootes, L., Snyder, D., Davis, W.J., Acosta-Góngora, P., Corriveau, L., Mumin, A.H., Montreuil, J.-F., Gleeson, S.A., Samson, I.A., and Jackson, V.A., 2017, A Paleoproterozoic Andean-type iron oxide copper-gold environment, the Great Bear magmatic zone, Northwest Canada: Ore Geology Reviews, v. 81, p. 123-139.

OZ Minerals, 2013a, Carrapateena project, mineral resource explanatory notes as at 30 June 2013: Available at https://www.ozminerals.com.

OZ Minerals, 2013b, OZ minerals quarterly report for the three months ended 31 December 2012, 11 p. Published online 24 January 2013, https://www.ozminerals.com/media/oz-minerals-december-2012-quarterly-report.

OZ Minerals, 2019, OZ Minerals 2018 annual and sustainability report: Available at https://www.ozminerals.com.

Palma, G., Barra, F., Reich, M., Simon, A.C., and Romero, R., 2020, Magnetite geochemistry of Andean iron oxide-apatite (IOA) deposits: a review: Ore Geology Reviews, v. 126, 103748.

Pandey, U.K., Aravind, S.L., Panchal, P.K., Venkatesh, A.S., Sahoo, P.R., Chaturvedi, A.K., Rai, A.K., and Parihar, P.S., 2016, U-Pb, Pb-Pb and Sm-Nd ages of davidite within albitite zone from Bichun, Jaipur district, Rajasthan, India: possible link between uranium mineralization and Grenvillian Orogeny: Current Sciences, v. 111, p. 907-913.

Pelleter, E., Gasquet, D., Cheilletz, A., and Mouttaqi, A., 2010, Alteration processes and impacts on regional-scale element mobility and geochronology, Tamlalt-Menhouhou deposit, Morocco, *in* Corriveau, L. and Mumin, A.H., eds., Exploring for iron oxide copper-gold deposits: Canada and global analogues: Geological Association of Canada, Short Course Notes, No. 20, p. 177-185.

Perreault, S., and Lafrance, B., 2015, Kwyjibo, a REE-enriched iron oxides-copper-gold (IOCG) deposit, Grenville Province, Québec, *in* Simandl, G.J. and Neetz, M., eds., Symposium on strategic and critical materials proceedings, November 13-14, 2015, Victoria, British Columbia: British Columbia Ministry of Energy and Mines, British Columbia Geological Survey Paper 2015-3, p. 139-145.

Plymate, T.G., Daniel, C.G., and Cavaleri, M.E., 1992, Structural state of the K-feldspar in the Butler Hill-Breadtray granite, St Francois Mountains, southeastern Missouri: The Canadian Mineralogist, v. 30, p. 367-376.

Pollard, P.J., 2001, Sodic (-calcic) alteration in Fe-oxide Cu–Au districts: an origin via unmixing of magmatic $H_2O$–$CO_2$–NaCl ± $CaCl_2$–KCl fluids: Mineralium Deposita, v. 36, p. 93-100.

Porter, T.M., 2010a, Current understanding of iron oxide associated-alkali altered mineralised systems. Part 1 - An overview, *in* Porter, T.M., ed., Hydrothermal iron oxide copper-gold and related deposits: a global perspective, v. 3: PGC Publishing, Adelaide, p. 5-32.

Porter, T.M., 2010b, Current understanding of iron oxide associated-alkali altered mineralised systems. Part II, a review, *in* Porter, T.M., ed., Hydrothermal iron oxide copper-gold and related deposits: a global perspective, v. 3: PGC Publishing, Adelaide, p. 33-106.

Porter GeoConsultancy, 2021, A geological database of the world's important mineral deposits: Available at http://www.portergeo.com.au.

Potter, E.G., 2009, Genesis of polymetallic mineralization and the metallogeny of the Paleoproterozoic Cobalt Embayment, northern Ontario: Unpublished Ph.D. thesis, Carleton University, Ottawa, Ontario, 368 p.

Potter, E.G., Montreuil, J.-F., Corriveau, L., and Davis, W., 2019, The Southern Breccia metasomatic uranium system of the Great Bear magmatic zone, Canada: iron oxide-copper-gold (IOCG) and albitite-hosted uranium linkages, *in* Decrée, S. and Robb, L., eds., Ore deposits: origin, exploration, and exploitation: Geophysical Monograph 242: American Geophysical Union, John Wiley & Sons, Inc., p. 109-130.

Potter, E.G., Corriveau, L., and Kjarsgaard, B., 2020a, Paleoproterozoic iron oxide apatite (IOA) and iron oxide-copper-gold (IOCG) mineralization in the East Arm Basin, Northwest Territories, Canada: Canadian Journal of Earth Sciences, v. 57, p. 167-183.

Potter, E.G., Tschirhart, V., Powell, J.W., Kelly, C.J., Rabiei, M., Johnstone, D., Craven, J.A., Davis, W.J., Pehrsson, S., Mount, S.M., Chi, G., and Bethune, K.M., 2020b, Targeted Geoscience Initiative 5: integrated multidisciplinary studies of unconformity-related uranium deposits from the Patterson Lake corridor, northern Saskatchewan: Geological Survey of Canada, Bulletin 615, 37 p.

Potter, E.G., Acosta-Góngora, P., Corriveau, L., Montreuil, J.-F., and Yang, Z., 2022, Uranium enrichment processes in iron oxide and alkali-calcic alteration systems as revealed by trace element signatures of uraninite, *in* Corriveau, L., Potter, E.G. and Mumin, A.H., eds., Mineral systems with iron oxide copper-gold (IOCG) and affiliated deposits: Geological Association of Canada, Special Paper 52, p. 325-345.

Poulet, T., Karrech, A., Regenauer-Lieb, K., Fisher, L., and Schaubs, P., 2012, Thermal–hydraulic–mechanical–chemical coupling with damage mechanics using ESCRIPTRT and ABAQUS: Tectonophysics, v. 526-529, p. 124-132.

Putnis, A., 2015, Transient porosity resulting from fluid–mineral interaction and its consequences: Reviews in Mineralogy & Geochemistry, v. 80, p. 1-23.

Rainbird, R., Rooney, A.D., Creaser, R.A., Skulski, T., 2020, Shale and pyrite Re-Os ages from the Hornby Bay and Amundsen basins provide new chronological markers for Mesoproterozoic stratigraphic successions of northern Canada: Earth and Planetary Science Letters, v. 548, 116492.

Ray, S.K., 1990, The albitite line of northern Rajasthan – A fossil intracontinental rift zone: Journal of the Geological Society of India, v. 86, p. 413-423.

Reeve, J.S., Cross, K.C., Smith, R.N., and Oreskes, N., 1990, Olympic Dam copper-uranium-gold-silver deposit, *in* Hughes, F.E., ed., Geology of the mineral deposits of Australia and Papua New Guinea: The Australasian Institute of Mining and Metallurgy, Melbourne, p 1009-1035.

Rex Minerals Limited, 2015, Hillside project, mineral resources and ore reserves: Available at www.rexminerals.com.au.

Rieger, A.A., Marschik, R., and Díaz, M., 2010, The Mantoverde district, northern Chile: an example of distal portions of zoned IOCG systems, *in* Porter, T.M., ed., Hydrothermal iron oxide copper-gold and related deposits: a global perspective, v. 3: PGC Publishing, Adelaide, p. 273-284.

Ristorcelli, S.J., and Schlitt, J., 2019, Technical report with updated estimate of mineral resources for the Iron Creek cobalt-copper project, Lemhi County, Idaho, USA: 43-101 report prepared for First Cobalt, 124 p.

Rodriguez-Mustafa, M.A., Simon, A.C., del Real, I., Thompson, J.F.H., Bilenker, L.D., Barra, F., Bindeman, I., and Cadwell, D., 2020, A continuum from iron oxide copper-gold to iron oxide-apatite deposits: evidence from Fe and O stable isotopes and trace element chemistry of magnetite: Economic Geology, v. 115, p. 1443-1459.

Rusk, B., Oliver, N., Blenkinsop, T., Zhang, D., Williams, P., Cleverley, J., and Habermann, H., 2010, Physical and chemical characteristics of the Ernest Henry iron oxide copper gold deposit, Cloncurry, Queensland, Australia; implications for IOCG genesis, *in* Porter, T.M., ed., Hydrothermal iron oxide copper-gold and related deposits: a global perspective, v. 3: PGC Publishing, Adelaide, p. 201-218.

Sappin, A.-A., and Perreault, S., 2021, Drill core pictures and description of samples collected from the REE Kwyjibo deposit (SOQUEM warehouse, Val d'Or, QC - October 2015): Geological Survey of Canada, Open File 8794, 14 p.

Schandl, E.S., and Gorton, M.P., 2007, The Scadding gold mine, east of the Sudbury Igneous Complex, Ontario: an IOCG-type deposit?: The Canadian Mineralogist, v. 45, p. 1415-1441.

Schlegel, T.U., and Heinrich, C.A., 2015, Lithology and hydrothermal alteration control the distribution of copper grade in the Prominent Hill iron oxide-copper-gold deposit (Gawler Craton, South Australia): Economic Geology, v. 110, p. 1953-1994.

Schlegel, T.U., Wagner, T., Wälle, M., and Heinrich, C.A., 2018, Hematite breccia-hosted iron oxide copper-gold deposits require magmatic fluid components exposed to atmospheric oxidation: evidence from Prominent Hill, Gawler Craton, South Australia: Economic Geology, v. 113, p. 597-644.

Schlegel, T.U., Wagner, T., and Fusswinkel, T., 2020, Fluorite as indicator mineral in iron oxide-copper-gold systems: explaining the IOCG deposit diversity: Chemical Geology, v. 548, 119674.

Schmandt, D.S., Cook, N.J., Ciobanu, C.L., Ehrig, K., Wade, B.P., Gilbert, S., and Kamenetsky, V.S., 2017, Rare earth element fluorocarbonate minerals from the Olympic Dam Cu-U-Au-Ag deposit, South Australia: Minerals, v. 7, 202.

Schmandt, D.S., Cook, N.J., Ciobanu, C.L., Ehrig, K., Wade, B.P., Gilbert, S., and Kamenetsky, V.S., 2019, Rare earth element phosphate minerals from the Olympic Dam Cu-U-Au-Ag deposit, South Australia: recognizing temporal-spatial controls on REE mineralogy in an evolved IOCG system: The Canadian Mineralogist, v. 57, p. 3-24.

Sidor, M., 2000, The origin of black rock alteration overprinting iron-rich sediments and its genetic relationship to disseminated polymetallic ores, Lou Lake, Northwest Territories, Canada: Unpublished M.Sc. thesis, University of Western Ontario, London, Ontario, 243 p.

Sillitoe, R.H., 2003, Iron oxide-copper-gold deposits: an Andean view: Mineralium Deposita, v. 38, p. 787-812.

Simon, A.C., Knipping, J., Reich, M., Barra, F., Deditius, A.P., Bilenker, L., and Childress, T., 2018, Chapter 6, Kiruna-type iron oxide-apatite (IOA) and iron oxide copper-gold (IOCG) deposits form by a combination of igneous and magmatic-hydrothermal processes: evidence from the Chilean iron belt, *in* Arribas R., A.M. and Mauk, J.L., eds., Metals, minerals, and society: Society of Economic Geologists, Special Publication, No. 21, p. 89-114.

Skirrow, R., 2010, "Hematite-group" IOCG ± U ore systems: tectonic settings, hydrothermal characteristics, and Cu-Au and U mineralizing processes, *in* Corriveau, L. and Mumin, A.H., eds., Exploring for iron oxide copper-gold deposits: Canada and global analogues: Geological Association of Canada, Short Course Notes, No. 20, p. 39-57.

Skirrow, R., 2022, Hematite-group IOCG ± U deposits: an update on their tectonic settings, hydrothermal characteristics, and Cu-Au-U mineralizing processes, *in* Corriveau, L., Potter, E.G. and Mumin, A.H., eds., Mineral systems with iron oxide copper-gold (IOCG) and affiliated deposits: Geological Association of Canada, Special Paper 52, p. 27-51.

Skirrow, R.G., and Walshe, J.L., 2002, Reduced and oxidized Au-Cu-Bi iron oxide deposits of the Tennant Creek inlier, Australia: an integrated geologic and chemical model: Economic Geology, v. 97, p. 1167-1202.

Skirrow, R.G., Bastrakov, E.N., Barovich, K., Fraser, G.L., Creaser, R.A., Fanning, C.M., Raymond, O.L., and Davidson, G.J., 2007, Timing of iron oxide Cu-Au-(U) hydrothermal activity and Nd isotope constraints on metal sources in the Gawler craton, South Australia: Economic Geology, v. 102, p. 1441-1470.

Skirrow, R.G., van der Wielen, S.E., Champion, D.C., Czarnota, K., and Thiel, S., 2018, Lithospheric architecture and mantle metasomatism linked to iron oxide Cu-Au ore formation: multidisciplinary evidence from the Olympic Dam region, South Australia: Geochemistry, Geophysics, Geosystems, v. 19, p. 2673-2705.

Slack, J., 2013, Descriptive and geoenvironmental model for cobalt–copper–gold deposits in metasedimentary rocks: U.S. Geological Survey, Scientific Investigations Report 2010–5070–G, 218 p.

Slack, J.F., Kimball, B.E., and Shedd, K.B., 2017, Cobalt, *in* Schulz, K.J., DeYoung, J.H., Jr., Seal, R.R., II and Bradley, D.C., eds., Critical mineral resources of the United States—Economic and environmental geology and prospects for future supply: U.S. Geological Survey Professional Paper 1802, p. F1–F40.

Somarin, A.K., and Mumin, A.H., 2012, The Paleoproterozoic high heat production Richardson granite, Great Bear magmatic zone, Northwest Territories, Canada: source of U for Port Radium?: Resources Geology, v. 62, p. 227-242.

Somarin, A.K., and Mumin, A.H., 2014, P–T-composition and evolution of paleofluids in the Paleoproterozoic Mag Hill IOCG hydrothermal system, Contact Lake belt, Northwest Territories, Canada: Mineralium Deposita, v. 49, p. 199-215.

Sparkes, G.W., 2017, Uranium mineralization within the Central Mineral Belt of Labrador: a summary of the diverse styles, settings and timing of mineralization: Government of Newfoundland and Labrador, Department of Natural Resources, Geological Survey, St. John's, Open File LAB/1684, 198 p.

Spratt, J.E., Jones, A.G., Jackson, V.A., Collins, L., and Avdeeva, A., 2009, Lithospheric geometry of the Wopmay orogen Orogen from a Slave craton to Bear Province magnetotelluric transect: Journal of Geophysical Research, v. 114, 18 p.

Staples, R.D., Marshall, D., Fecova, K., Downie, C.C., Thorkelson, D.J., and Loughrey, L., 2008, Structurally-controlled iron oxide mineralization in the Iron Range Mountain and Mount Thompson region, British Columbia: Geological Survey of Canada, Current Research Paper 2008-15, 12 p.

Stryhas, B., and More, S.W., 2007, Ni 43-101 technical report on Resources Golden Predation Mines, Inc. Fostung project, Foster Township, Ontario, Canada: Available at https://www.sedar.com.

Su, Z.-K., Zhao, X.-F., Li, X.-C., and Zhou, M.-F., 2016, Using elemental and boron isotopic compositions of tourmaline to trace fluid evolutions of IOCG systems: the worldclass Dahongshan Fe-Cu deposit in SW China: Chemical Geology, v. 441, p. 265-279.

Taylor, B.E., and Liou, J.G., 1978, The low-temperature stability of andradite in C-O-H fluids: American Mineralogist, v. 63, p. 378-393.

Taylor, R.D., Taylor, C.D., Walsh, G.J., and Shah, A.K., 2018, Geochemistry of ore, host rock, and mine waste pile samples of iron oxide-apatite (IOA) deposits of the eastern Adirondack Highlands, New York, in relation to potential rare earth elements resources: U.S. Geological Survey Data Release, https://doi.org/10.5066/P9EEXCKI.

Taylor, R.D., Shah, A.K., Walsh, G.J., and Taylor, C.D., 2019, Geochemistry and geophysics of iron oxide-apatite deposits and associated waste piles with implications for potential rare earth element resources from ore and historical mine waste in the eastern Adirondack Highlands, New York, USA: Economic Geology, v. 114, p. 1569-1598.

Teale, G.S., 2019, The Hillside Cu Cu-Au deposit: geological model and alteration paragenesis: Geological Survey of South Australia, Iron oxide-copper-gold mineral systems workshop, 2nd-3rd December 2019, available at http://www.energymining.sa.gov.au/__data/assets/pdf_file/0010/354997/10_GrahamTeale.pdf

Teale, G.S., and Fanning, C.M., 2000, The Portia–North Portia Cu-Au(-Mo) prospect, South Australia: timing of mineralisation, albitisation and origin of ore fluid, *in* Porter, T.M., ed., Hydrothermal iron oxide copper-gold and related deposits: a global perspective, v. 1: PGC Publishing, Adelaide, p. 137-147.

Tiddy, C.J., and Giles, D., 2020, Suprasubduction zone model for metal endowment at 1.60–1.57 Ga in eastern Australia: Ore Geology Reviews, v. 122, 103483.

Timofeev, A., Migdisov, A.A., Williams-Jones, A.E., Roback, R., Nelson, A.T., and Xu, H., 2018, Uranium transport in acidic brines under reducing conditions: Nature Communications, v. 9, 1469.

Tornos, F., Velasco, F., and Hanchar, J.M., 2017, The magmatic to magmatic-hydrothermal evolution of the El Laco deposit (Chile) and its implications for the genesis of magnetite-apatite deposits: Economic Geology, v. 112, p. 1595-1628.

Tornos, F., Hanchar, J.M., Munizaga, R., Velasco, F., and Galindo, C., 2021, The role of the subducting slab and melt crystallization in the formation of magnetite-(apatite) systems, Coastal Cordillera of Chile: Mineralium Deposita, v. 56, p. 253-278.

Trapy, P.-H., 2018, Modélisation d'équilibre de phase prédictive des faciès d'altération associés aux gîtes à oxydes de fer-cuivre-or dans les terrains de hauts grades métamorphiques: Unpublished M.Sc. thesis, École Polytechnique de Montréal, 138 p.

Trottier, C.R.M., 2019, Fluid inclusion, stable and radiogenic isotope, and geochronological investigation of the polymetallic "five-element" vein deposit at the Eldorado Mine, Port Radium, Northwest Territories, Canada: Unpublished Ph.D. thesis, Saint-Mary's University, Halifax, 186 p.

Tschirhart, V., Pehrsson, S., Card, C., Potter, E.G., Powell, J., and Panã, D., 2020, Interpretation of buried basement in the southwestern Athabasca Basin, Canada, from integrated geophysical and geological datasets: Geochemistry: Exploration, Environment, Analysis, v. 21, 2019-061.

Veloso, A.S.R., Monteiro, L.V.S., and Juliani, C., 2020, The link between hydrothermal nickel mineralization and an iron oxidecopper–gold (IOCG) system: Constraints based on mineral chemistry in the Jatobá deposit, Carajás Province: Ore Geology Reviews, v. 121, 103555.

Verdugo-Ihl, M., Ciobanu, C., Cook, N., Ehrig, K., Courtney-Davies, L., and Gilbert, S., 2017, Textures and U-W-Sn-Mo signatures in hematite from the Olympic Dam Cu-U-Au-Ag deposit, South Australia: defining the archetype for IOCG deposits: Ore Geology Reviews, v. 91, p. 173-195.

Verdugo Ihl, M., Ciobanu, C.L., Slattery, A., Cook, N.J., Ehrig, K., and Courtney-Davies, L., 2019, Copper-arsenic nanoparticles in hematite: fingerprinting fluid-mineral interaction: Minerals, v. 9, 388.

Wade, C.E., Payne, J.L., Barovich, K.M., and Reid, A.J., 2019, Heterogeneity of the sub-continental lithospheric mantle and 'non-juvenile' mantle additions to a Proterozoic silicic large igneous province: Lithos, v. 340-341, p. 87-107.

Wang, S., and Williams, P.J., 2001, Geochemistry and origin of Proterozoic skarns at the Mount Elliott Cu–Au(–Co–Ni) deposit, Cloncurry district, NW Queensland, Australia: Mineralium Deposita, v. 36, p. 109-124.

Whitney, D.L., and Evans, B.W., 2010, Abbreviations for names of rock-forming minerals: American Mineralogist, v. 95, p. 185-187.

Wilde, A., 2013, Towards a model for albitite-type uranium: Minerals, v. 3, p. 36-48.

Wilde, A., Otto, A., Jory, J., MacRae, C., Pownceby, M., Wilson, N., and Torpy, A., 2013, Geology and mineralogy of uranium deposits from Mount Isa, Australia: implications for albitite uranium deposit models: Minerals, v. 3, p. 258-283.

Williams, M.R., Holwell, D.A., Lilly, R.M., Case, G.N.D., and McDonald, I., 2015, Mineralogical and fluid characteristics of the fluorite-rich Monakoff and E1 Cu–Au deposits, Cloncurry region, Queensland, Australia: implications for regional F–Ba-rich IOCG mineralisation: Ore Geology Reviews, v. 64, p. 103-127.

Williams, P.J., 2010a, Classifying IOCG deposits, *in* Corriveau, L. and Mumin, A.H., eds., Exploring for iron oxide copper-gold deposits: Canada and global analogues: Geological Association of Canada, Short Course Notes, No. 20, p. 13-21.

Williams, P.J., 2010b, "Magnetite-group" IOCGs with special reference to Cloncurry and Northern Sweden: settings, alteration, deposit characteristics, fluid sources, and their relationship to apatite-rich iron ores, *in* Corriveau, L. and Mumin, A.H., eds., Exploring for iron oxide copper-gold deposits: Canada and global analogues: Geological Association of Canada, Short Course Notes, No. 20, p. 23-38.

Williams, P.J., and Pollard, P.J., 2001, Australian Proterozoic iron oxide-Cu-Au deposits: an overview with new metallogenic and exploration data from the Cloncurry district, northwest Queensland: Exploration and Mining Geology, v. 10, p. 191-213.

Williams, P.J., and Skirrow, R.G., 2000, Overview of iron oxide-copper-gold deposits in the Curnamona Province and Cloncurry District (eastern Mount Isa Block), Australia, *in* Porter, T.M., ed., Hydrothermal iron oxide copper-gold and related deposits: a global perspective, v. 1: PGC Publishing, Adelaide, p. 105-122.

Williams, P.J., Barton, M.D., Johnson, D.A., Fontboté, L., de Haller, A., Mark, G., Oliver, N.H.S., and Marschik, R., 2005, Iron-oxide copper-gold deposits: geology, space-time distribution, and possible modes of origin: Economic Geology 100th Anniversary Volume, p. 371-405.

Williams, P.J., Kendrick, M., and Xavier, R.P., 2010, Sources of ore fluid components in IOCG deposits, *in* Porter, T.M., ed., Hydrothermal iron oxide copper–gold and related deposits: a global perspective, v. 3: PGC Publishing, Adelaide, p. 107-116.

Williams, P.J., Benavides, J., Sadikin, P., Schlegel, T., and OZ Minerals Prominent Hill Geology Team, 2017, Metallogenic significance of altered volcanic rocks near the Prominent Hill IOCG deposit, South Australia: Proceedings of the 14th SGA Biennial Meeting, 20-23 August 2017, Québec City, p. 895-899.

Wise, T., and Thiel, S., 2020, Proterozoic tectonothermal processes imaged with magnetotellurics and seismic reflection in southern Australia: Geoscience Frontiers, v. 11, p. 885-893.

Yadav, G.S., Muthamilselvan, A., Shaji, T.J., Nanda, L.K., and Rai, A.K., 2015, Recognition of a new albitite zone in northern Rajasthan: its implications on uranium mineralization: Current Science, v. 108, p. 1994-1998.

Yardley, B.W.D., 2013, The chemical composition of metamorphic fluids in the crust, *in* Harlov, D.E. and Austrheim, H., eds., Metasomatism and the chemical transformation of rock: Springer-Verlag, Berlin, Hiedelberg, p. 17-51.

Yardley, B.W.D., and Lloyd, G.E., 1995, Why metasomatic fronts are really metasomatic sides: Geology, v. 23, p. 53-56.

Yardley, B.W.D., and Bodnar, R.J., 2014, Fluids in the continental crust: Geochemical Perspective, v. 3, 127 p.

Yarie, Q., and Wray, N., 2019, National Instrument 43-101 technical report for the SPJ project, Macdonald Mines: Available at https://www.sedar.com.

Yu, J., Chen, Y., Mao, J., Pirajno, F., and Duan, C., 2011, Review of geology, alteration and origin of iron oxide–apatite deposits in the Cretaceous Ningwu basin, Lower Yangtze River Valley, eastern China: implications for ore genesis and geodynamic setting: Ore Geology Reviews, v. 43, p. 170-181.

Zeng, L., 2020, Formation mechanism and genetic model of iron-oxide apatite deposits in the Ningwu district, China: Unpublished Ph.D. thesis, China University of Geosciences, Wuhan, 270 p.

Zhao, X.F., Zhou, M.F., Su, Z.K., Li, X.C., Chen, W.T., and Li, J.W., 2017, Geology, geochronology, and geochemistry of the Dahongshan Fe-Cu-(Au-Ag) deposit, Southwest China: implications for the formation of iron oxide copper-gold deposits in intracratonic rift settings: Economic Geology, v. 112, p. 603-628.

Zhao, X.-F., Chen, W.-T., Li, X.-C., and Zhou, M.-F., 2019, Iron oxide copper-gold deposits in China: a review and perspectives on ore genesis, *in* Goldfarb, R. and Chang, Z., eds., Mineral deposits of China: SEG Special Publication, v. 22, p. 553-580.

Zhao, X.-F., Chen, H., Zhao, L., and Zhou, M.-F., 2022, Linkages among IOA, skarn, and magnetite-group IOCG deposits in China: from deposit studies to mineral potential assessment, *in* Corriveau, L., Potter, E.G. and Mumin, A.H., eds., Mineral systems with iron oxide copper-gold (IOCG) and affiliated deposits: Geological Association of Canada, Special Paper 52, p. 383-407.

# Geochemical Characteristics of IOCG Deposits from the Olympic Copper-Gold Province, South Australia

**Adrian Fabris**
*Geological Survey of South Australia, Department For Energy and Mining, Australia.*
*Adrian.Fabris@sa.gov.au*

*Recommended citation: Fabris, A., 2022, Geochemical characteristics of IOCG deposits from the Olympic Copper-Gold Province, South Australia, in Corriveau, L., Potter, E.G. and Mumin, A.H., eds., Mineral systems with iron oxide copper-gold (IOCG) and affiliated deposits: Geological Association of Canada, Special Paper 52, p. 247-262.*

## Abstract

The eastern margin of the Gawler Craton in South Australia is host to globally significant iron oxide-copper-gold deposits (IOCG) that include Olympic Dam, Prominent Hill and Carrapateena. These formed during a phase of widespread hydrothermal fluid-flow that caused extensive alteration and partial to complete replacement of host rocks. Subsequent differences in erosional levels preserved throughout the province have resulted in a spectrum of IOCG occurrences. These can be sub-divided into those dominated by hematite, and those dominated by magnetite. While alteration associated with many known prospects has been described, relatively few studies include a full suite of chemical data with which to assess common element characteristics of IOCG deposits. This contribution uses new geochemical data acquired on publically available drill core held in storage by the Geological Survey of South Australia from across the Olympic Copper-Gold Province to define geochemical characteristics of hematite-group and magnetite-group IOCG deposits. Public data from Olympic Dam are then compared to deposit samples acquired in this study to identify distinct geochemical characteristics of highly mineralized systems.

Both magnetite- and hematite-dominated IOCG deposits are significantly enriched in Cu, Au, S, Se, Sn, Te, Th, Tl, U and LREE (La, Ce, Pr, Nd, Sm), and depleted in Cr, Ni, Pd, Pt, Sc, Sr and V relative to bulk continental crust. While not necessarily enriched compared to bulk continental crustal values, the additional elements Ag, Co, Ni, Pb and Re are progressively enriched with increasing copper mineralization and are therefore also considered key elements for recognizing these mineral systems. Hematite-dominated deposits contain enrichment trends not observed in magnetite-dominated deposits. These involve the chalcophile elements As, Bi, In, Mo, Sb, Zn and minor elements F, Mn and W. The different element associations between magnetite- and hematite-dominated deposits is interpreted to relate to varying temperature and oxidation state of the ore system and implies that enrichment and depletion trends in these elements can be used to map the passage of hydrothermal fluids from high to lower temperatures, and to increasingly oxidized parts of the ore system. Analysis of samples from economic deposits indicate significantly higher values of Au, Ba, F, Mo, Te, U and LREE's. In particular, enrichment of Ce, La and Pr to >10 times bulk continental crustal values, even in weakly mineralized zones, provide the most reliable indicator that a significant system has developed.

## Résumé

La marge orientale du craton de Gawler, en Australie méridionale, abrite des gîtes à oxydes de fer-cuivre-or (IOCG) d'importance mondiale, dont Olympic Dam, Prominent Hill et Carrapateena. Ces gisements se sont formés pendant une phase d'écoulement de fluides hydrothermaux généralisé qui a entraîné une altération importante et un remplacement partiel ou complet des roches hôtes. Des différences dans le niveau d'érosion préservé au sein de la province ont donné lieu à un éventail de gîtes IOCG. Ces derniers peuvent être subdivisés comme soit dominés par l'hématite ou soit par la magnétite. Bien que l'altération associée à de nombreuses zones d'intérêt ait été décrite, relativement peu d'études comprennent une série complète de données géochimiques permettant d'évaluer les caractéristiques des éléments communs des gîtes IOCG. La présente contribution définie les caractéristiques géochimiques des gîtes IOCG à hématite et à magnétite à partir de nouvelles données géochimiques acquises sur des carottes de forage accessibles au public et conservées par la Geological Survey of South Australia dans l'ensemble de la province à cuivre-or d'Olympic. Les données publiques d'Olympic Dam sont ensuite comparées aux échantillons de gîtes acquis dans le cadre de cette étude afin de définir les caractéristiques géochimiques distinctes des systèmes fortement minéralisés.

Les gisements IOCG à dominance de magnétite et d'hématite sont enrichis en Cu, Au, S, Se, Sn, Te, Tl, U et ETR légères (La, Ce, Pr, Nd, Sm) et appauvris en Cr, Ni, Pd, Pt, Sc, Sr et V par rapport à la croûte continentale globale. Bien que les éléments suivants Ag, Co, Ni, Pb et Re ne soient pas toujours enrichis par rapport aux valeurs de la croûte continentale global, leur enrichissement progressif par rapport à celui de la minéralisation cuprifère en font eux aussi des éléments clés pour la reconnaissance de ces systèmes métallifères. Les gisements dominés par l'hématite présentent des tendances d'enrichissement qui ne sont pas observées dans les gisements dominés par la magnétite dont celles des éléments chalcophiles As, Bi, In, Mo, Sb, Zn et des éléments mineurs F, Mn et W. Les différentes associations d'éléments entre les gisements dominés par la magnétite et l'hématite sont interprétées comme étant liées aux variations de température et d'état d'oxydation des systèmes minéralisés et impliquent que les tendances d'enrichissement et d'appauvrissement de ces éléments peuvent être utilisées pour cartographier le passage des fluides hydrothermaux de leurs températures élevées à plus basses, et au sein des composantes de plus en plus oxydées de ces systèmes. L'analyse d'échantillons provenant de gisements économiques indique des valeurs significativement plus élevées en Au, Ba, F, Mo, Te, U et ETR légères. En particulier, l'enrichissement en Ce, La et Pr jusqu'à >10 fois les valeurs moyennes de la croûte continentale, même dans les zones faiblement minéralisées, constitue l'indicateur le plus fiable du développement d'un système important.

## Introduction

The Olympic Copper-Gold Province (Skirrow et al., 2002, 2007) of the Gawler Craton is host to Olympic Dam, the type example of breccia-hosted, hematite-rich iron oxide copper-gold (IOCG) deposits (e.g. Hitzman, 2000; Groves et al., 2005, 2010). In addition to the world-class Olympic Dam deposit (resource of 9 880 Mt at 0.63% Cu, 0.21 kg/t $U_3O_8$, 0.28 g/t Au and 1 g/t Ag; BHP, 2019), the province hosts occurrences that range in economic significance, and vary with respect to host rock, depth of formation and dominant alteration products (e.g. Gow et al., 1994; Hampton, 1997; Davidson, 2002; Skirrow et al., 2002, 2007; Davidson et al., 2007; Fig. 1). While all currently economic deposits in the Olympic Copper-Gold Province are dominated by hematite, the region hosts prospects with all the established alteration assemblages synonymous with the diversity of deposits within the IOCG and iron oxide-apatite (IOA) class (Skirrow et al., 2002; Skirrow et al., 2007; Williams, 2010; Corriveau et al., 2016). Numerous studies have focused on alteration mineralogy and paragenesis (e.g. Gow et al., 1994; Hampton, 1997; Skirrow et al., 2002, 2007; Conor et al., 2010), demonstrating a variety of both high- and low-temperature alteration assemblages and partial to complete alteration across a range of host rocks. These observations provide evidence of significant fluid-flow and capacity for multi-element mobilization across a range of temperatures and chemical conditions. This is supported by the broad range of elements reported to be associated with IOCG deposits (e.g. Williams et al., 2005; Ehrig et al., 2012; Montreuil et al., 2013, 2016; Barton, 2014; Dmitrijeva et al., 2019). However, while IOCG deposits are known to be associated with enrichment in a wide range of trace elements, relatively few deposit studies include a full suite of chemical data with which to assess common element characteristics of IOCG deposits (Williams et al., 2005). In this contribution, new whole-rock geochemical data acquired on legacy drill core from several mineralized systems that range in style, host rock and size from the Olympic Copper-Gold Province are used to define geochemical characteristics of both hematite- and magnetite-group IOCG deposits. Furthermore, this study investigates whether economic deposits have distinct geochemical characteristics compared to sub-economic prospects in the Olympic Copper-Gold Province.

## Geological Setting

The Olympic Copper-Gold Province is an arcuate belt along the eastern margin of the Mesoarchean-Mesoproterozoic Gawler Craton, South Australia (Fig. 1; Skirrow et al., 2002, 2007). The oldest known units of the Olympic Copper-Gold Province are Neoarchean orthogneisses, metasedimentary and meta-volcanic rocks of the Mulgathing Complex (Reid et al., 2014). These form basement and host to predominantly felsic intrusive units of the ca. 1850 Ma Donington Suite (Reid et al., 2008). Deposition of arenaceous sandstones and calcareous sandstones to siltstones of the Wallaroo Group followed during the period 1790–1740 Ma (Cowley et al., 2003; Jagodzinski, 2005). Sedimentation was terminated by the 1730–1690 Ma Kimban Orogeny, which resulted in amphibolite-granulite facies metamorphism across much of the Gawler Craton (e.g. Hand et al., 2007; Dutch et al., 2008). Notably, the effect of the Kimban Orogeny in the eastern Gawler Craton was more variable, with much of the Wallaroo Group remaining at low metamorphic grade (Fig. 1; Reid and Fabris, 2015).

The period 1600–1575 Ma saw the emplacement of extensive felsic and mafic units of the Hiltaba Suite (Flint et al., 1993) and eruption of the Gawler Range Volcanics (GRV; Blissett et al., 1993; Allen et al., 2003). Broadly synchronous with these magmatic events, the craton underwent localized deformation and high temperature metamorphism associated with the Kararan Orogeny (e.g. Cutts et al., 2011; Forbes et al., 2011). The effect of this major tectono-thermal event was widespread across the Gawler Craton and is linked to extensive mineralization and alteration that includes IOCG deposits of the Olympic Copper-Gold Province (Johnson, 1993; Johnson and Cross, 1995; Skirrow et al., 2002, 2007; Jagodzinski et al., 2007; Ciobanu et al., 2013; Reid et al., 2013). While there is debate about the tectonic setting for this event, one recent model suggests a process of melting of metasomatized mantle following lithospheric delamination (Skirrow, 2010, 2022; Skirrow et al., 2018).

Following extrusion of the GRV, a sequence of redbed sandstones (Pandurra Formation) was deposited within an intracratonic basin that covers much of the eastern Gawler Craton (Cowley and Flint, 1993; Beyer et al., 2018).

Opening of a rifting centre on the eastern flank of the Gawler Craton accommodated basinal sequences of the Adelaide Rift Complex during the period 840–500 Ma (Preiss, 1987; Wingate et al., 1998). Over the Olympic Copper-Gold Province, this rift process resulted in deposition of platform sediments of the Stuart Shelf. Permian and Mesozoic basins of thin or limited extent also cover the Olympic Copper-Gold Province, along with Plio-Pleistocene aeolian sand dunes.

## District Geology, Alteration and Mineralization

The Olympic Copper-Gold Province can be roughly subdivided into 3 districts, representing regions with distinct tectonic histories (Fig. 1). In the north, much of the Mount Woods Inlier is interpreted to have been buried beyond 10 km depth during the Hiltaba-GRV mineralizing event, and thus records high-temperature alteration developed in the mid-crust (Forbes et al., 2011). District alteration is dominated by early albite±pyroxene, magnetite and lesser biotite and amphibole (Hampton, 1997; Skirrow et al., 2002). Of the numerous prospects in the region, magnetite and skarn assemblages dominate although minor K-feldspar, hematite and pyrrhotite are common (Fig. 2A–D; Hampton, 1997; Freeman and Tomkinson, 2010).

The majority of magnetite-dominant copper-gold occurrences in the Olympic Copper-Gold Province lie within the Mount Woods Inlier (Fig. 1). Examples include the Manxman series of prospects, Joes Dam and Cairn Hill (Freeman and Tomkinson, 2010; Clark, 2014).

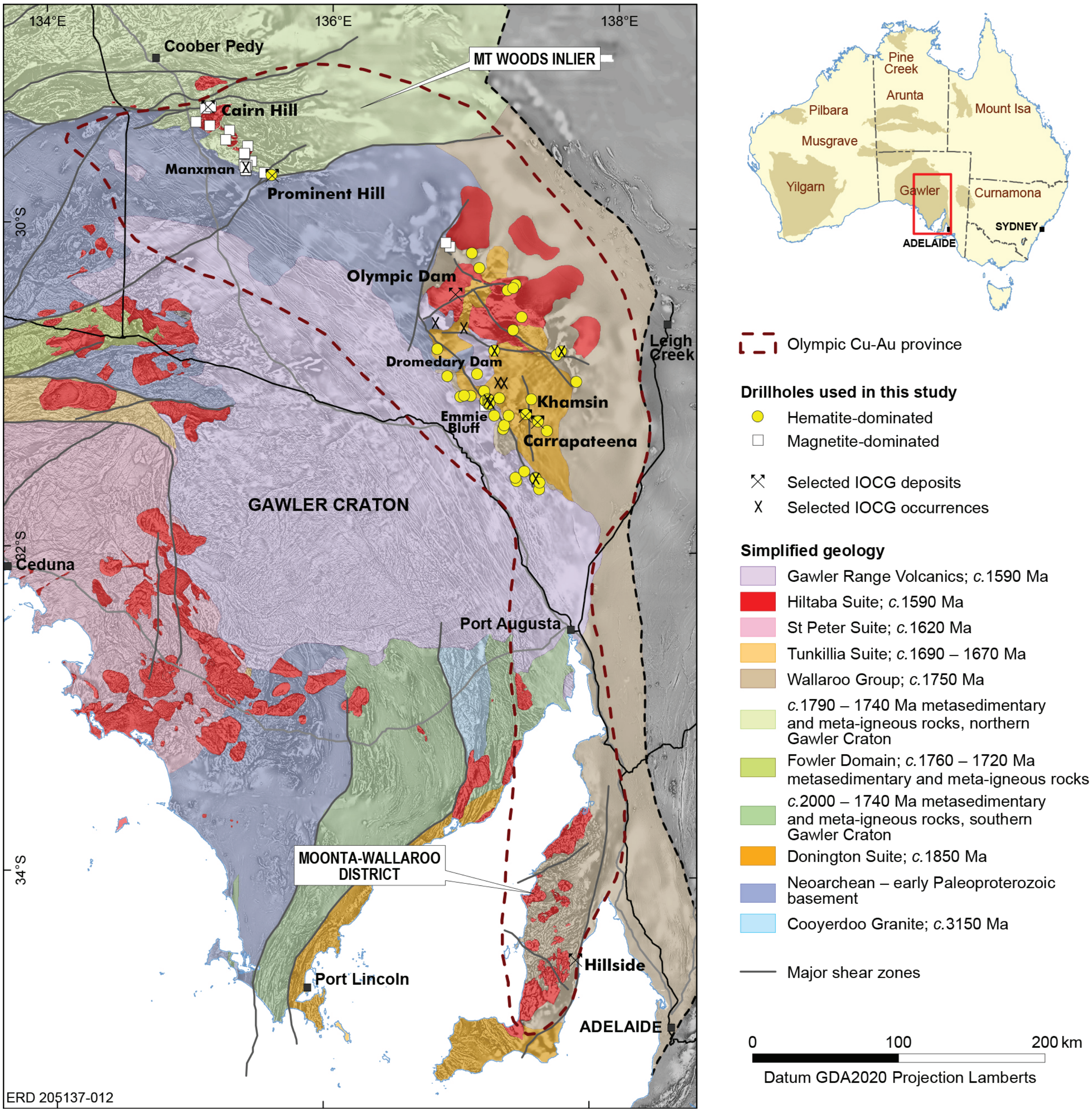


FIGURE 1. Simplified Gawler Craton geology showing the location of sampled drill holes and selected IOCG occurrences of the Olympic Copper-Gold Province, South Australia.

The central Olympic Copper-Gold Province encompasses the hematite-dominated deposits of Prominent Hill (130 Mt @ 1.1% Cu, 0.6 g/t Au and 3 g/t Ag; OZ Minerals, 2018), Carrapateena (587 Mt (sub-level and block cave) at 0.7% Cu, 0.3 g/t Au, 2.9 g/t Ag; OZ Minerals, 2019) and Olympic Dam (Fig. 1). While the host rocks to each of these deposits differ, alteration and mineralization characteristics are similar (Fig. 2E–J; Skirrow, 2022). Notably, although Prominent Hill is located in close vicinity to magnetite-dominated prospects of the Mount Woods Inlier, it is located south of a major thrust fault that tectonically separates it from higher metamorphic grade rocks to the north (Betts et al., 2003). The lack of high-grade metamorphism observed in the Olympic Dam district is evidence that it experienced a different metamorphic/tectonic history than the Mount Woods and Moonta-Wallaroo districts (Reid and Fabris, 2015).

The Moonta-Wallaroo district is exposed on the Yorke Peninsula and is situated in the southern Olympic Copper-Gold Province (Fig. 1). Although there is a rich history of mining that dates back to 1862, many copper-gold occurrences

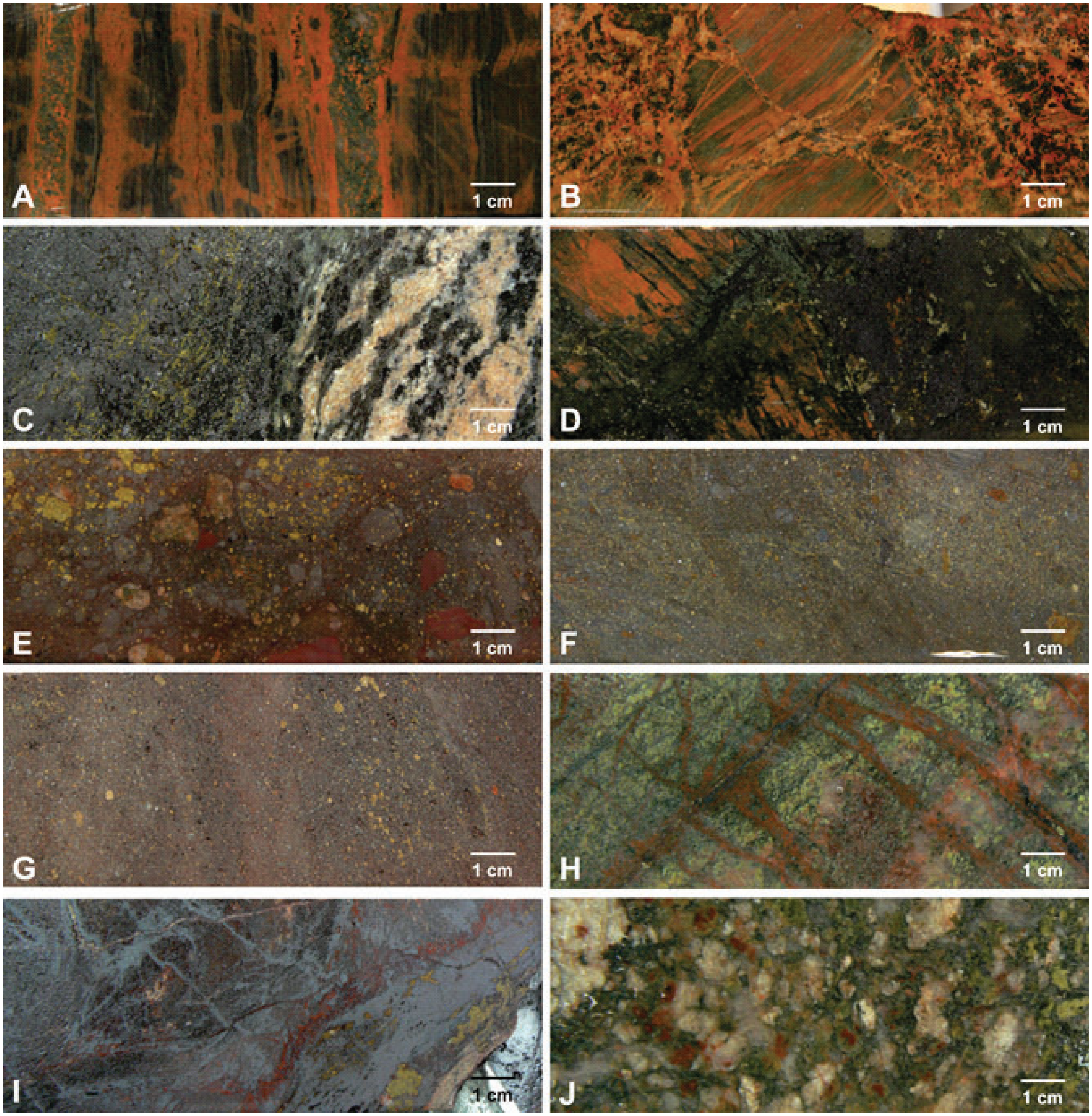


FIGURE 2. Examples of alteration and mineralization within the Mount Woods Inlier (A-D) and Olympic Dam district (E-J). **A**. Strongly albite-altered, finely-laminated metasedimentary rocks with pyroxene-albite-rich bands. Red albite alteration occurs along sedimentary layering and within cross-cutting veins. Manxman A1 prospect, drill hole DD86EN25, 165.6 m. **B**. Highly altered matrix-dominated breccia of sedimentary protolith, where remnant sedimentary layering can be observed in larger clasts. Metasomatic matrix composed of albite, oligoclase and pyroxene, Manxman A1 prospect, drill hole DD86EN25, 277.5 m. **C**. Magnetite-chalcopyrite mineralization developed within magnetite-rich orthogneiss, Cairn Hill deposit, drill hole CHDCU001, 289 m. Weak copper mineralization is typically associated with pyroxene±apatite-rich zones. **D**. Highly-altered breccia with magnetite-dominant matrix. Clasts with strong albite alteration. Matrix includes sulphides and pyroxene. Manxman A1 prospect, drill hole DD86EN25, 160 m. **E**. Re-brecciated, mineralized breccia, Olympic Dam deposit, underground drill hole RU39 5371, 73.7 m. **F**. Sulphide-rich hematite breccia, Prominent Hill deposit, drill hole DDHURAN 1, 460.6 m. **G**. Hematite breccia with common disseminated chalcopyrite, Carrapateena deposit, drill hole CAR02, 648.6 m. **H**. Intensely sericite-, chlorite-, hematite-, K-feldspar-altered foliated granite containing chlorite-hematite-sulphide veins, Dromedary Dam prospect, drill hole DRD1, 1186 m. **I**. Hematite-chlorite-altered metasedimentary rocks containing sulphide along bedding planes and within vein networks, Emmie Bluff prospect, drill hole SAE6, 984 m. **J**. Sericite-chlorite-hematite-altered granite intersected distal to the Khamsin prospect, drill hole PSC 4 SASC 2, 346.2 m.

such as Moonta, Wallaroo and Poona do not fit clearly within the IOCG class (Conor et al., 2010). Nevertheless, the district displays alteration trends typical of IOCG terranes such as Na and Na-Ca alteration (albite ± actinolite, diopside), and more localized magnetite-rich K-Fe (K-feldspar and biotite) alteration followed by later hematite-sericite chlorite ± carbonate alteration (Skirrow et al., 2002, 2007; Conor et al., 2010). The more recently discovered Hillside copper-gold deposit (Conor et al., 2010; Ismail et al., 2014) occurs along a major transtensional fault and provides an example of IOCG mineralization associated with a high temperature magnetite-rich skarn within and surrounding felsic and mafic Hiltaba Suite intrusions into Wallaroo Group metasedimentary rocks. More generally, mineralization in the Moonta-Wallaroo district is focused within shear zones and surrounding Hiltaba Suite intrusions (Conor et al., 2010; Conor, 2016).

## Sampling Approach and Methodology

Sample analysis was conducted on publically available drill core held at the South Australian Drill Core Reference Library. Motivation for new data collection followed a realization that most publically available lithogeochemical data for the region consisted only of elements of economic interest, using a range of methods that in many cases hindered comparison, and sample intervals that crossed geological boundaries. Drill hole selection aimed to achieve a broad coverage and representative samples of the range of alteration and mineralization styles known in the region (Fig. 1). Individual 1 m samples were taken every ~10 m down hole within basement; each sample best represented the lithology and mineralogy within the adjacent core trays. This paper presents results from 2032 samples from 77 drill holes, including samples collected from drill holes either intersecting or within 10 km of known copper-gold mineralization within hematite-dominated and magnetite-dominated IOCG occurrences (Fig. 1). Either quarter-core or core fillets were submitted to the lab for multi-element whole-rock analysis. Chemical analysis methodology was chosen to achieve both low detection limits and total digestion of all minerals.

## Analytical Methods

Geochemical analyses were undertaken by Intertek, Adelaide (www.intertek.com/minerals/a-to-z). Each sample was crushed, pulverized and analyzed for a 65 element suite by inductively coupled plasma mass spectrometry and optical emission spectrometry, fire assay or selective ion electrode, as indicated in Table 1. Major elements, rare earth elements (REE) and refractory minor elements were reported following a lithium borate fusion. Fluorine was determined following a carbonate fusion. A 25 g lead collection fire assay was used for gold and platinum-group elements. Remaining trace elements were determined following a four-acid digestion.

Standards and duplicates were included in each laboratory submission at a rate of approximately one every 20 samples.

TABLE 1. Drill core were analyzed for a 65 element suite using methods to ensure a total digest and achieve low detection limits.

| Method | Elements |
|---|---|
| Lead collection fire assay on 25 g sample | Au, Pt, Pd |
| 4 acid (ICP-OES) | Cu, Li, Ni, Pb, S, Zn |
| 4 acid (ICP-MS) | Ag, As, Bi, Cd, Co, Cs, Ge, In, Mo, Nb, Re, Sb, Se, Te, Tl |
| Carbonate fusion/SIE | F |
| Lithium borate fusion (ICP-OES) | $Al_2O_3$, CaO, Cr, $Fe_2O_3$, $K_2O$, MgO, MnO, $Na_2O$, $P_2O_5$, $SiO_2$, Sc, $TiO_2$, V |
| Lithium borate fusion (ICP-MS) | Ba, Be, Ce, Dy, Er, Eu, Ga, Gd, Hf, Ho, La, Lu, Nd, Pr, Rb, Sm, Sn, Sr, Ta, Tb, Th, Tm, U, W, Y, Yb, Zr |

The geochemical data can be downloaded from the Government of South Australia Department for Energy and Mining online portal: http://energymining.sa.gov.au/minerals/online_tools/free_data_delivery_and_publication_downloads/digital_maps_and_data.

## Geochemical Comparison

For the purpose of displaying and comparing geochemical data, multi-element diagrams have been used. Geochemical data were normalized to the bulk composition of the continental crust as defined in Rudnick and Gao (2003). The bulk continental crust rather than geochemical data from specific lithotypes was used due to the great variety of rock types in the dataset, and difficulty in distinguishing lithology in highly altered samples. Although the geochemical values of regional background and specific lithotypes may differ from average crustal abundance, the degree of enrichment and depletion in IOCG systems far exceeds that caused by these other factors, and was not considered to materially affect trends in the results (e.g. Montreuil et al., 2013).

In cases where values reported were less than the limits of detection, values of half the detection limit for the particular element have been used. Exceptions to this include where the detection limit was greater than the value of bulk continental crust (BCC; Rudnick and Gao, 2003), in which case, bulk crustal values were used (e.g. Re, Se).

Geochemical data were derived from unaltered to highly altered and mineralized samples. Median values are used to describe trends relative to BCC and both median and mean values are used to describe the effect of copper mineralization on the behaviour of minor and trace elements. To enable these comparisons, data were categorized based on copper concentration where samples containing <100 ppm Cu are regarded as unmineralized or background, 100–300 ppm Cu as anomalous values, 300–1000 ppm Cu as weakly mineralized, 1000–3000 ppm Cu as moderately mineralized, and >3000 ppm Cu indicate significantly mineralized samples. These categories enable observations of minor element behavior with relation to copper mineralization and were also chosen so that comparison could be made with published data from the Olympic Dam deposit (Ehrig et al., 2012).

## Results: Geochemical Trends

Median values provide a useful guide to typical values in hematite- and magnetite-dominated IOCG ore systems of the Olympic Copper-Gold Province. Median rather than mean values are the best indication of typical threshold levels as they are not skewed by extreme compositions. Table 2 summarizes median element values for samples containing >300 ppm Cu (part of copper mineralized systems) and provides a comparison of magnitude relative to bulk continental crust (Rudnick and Gao, 2003). These values provide a useful guide for mapping enrichment and depletion patterns within the mineral system (Figs. 3, 4).

*Minor and REE Trends in Magnetite-dominated IOCG Occurrences of the Olympic Copper-Gold Province*

The majority of samples from magnetite-dominated IOCG occurrences come from prospects of the Mount Woods Inlier (Fig. 1). Median, mean and ranges for the geochemical data collected in this study are listed in Appendix 1.

Minor and rare earth element values vary with respect to the average composition of the continental crust (Rudnick and Gao, 2003) and with increasing copper abundance (Table 2; Fig. 3). Elements that are significantly enriched (mineralized samples of >2 times BCC) include Au, Co, S, Se, Sn, Te, Th, Tl, U and LREE (Fig. 3A, C; Table 2). With the exception of thallium, values for these elements consistently increase with increasing copper content, demonstrating an association with copper mineralization (Fig. 3A, C). While thallium is significantly enriched compared to BCC, it shows a trend of decreasing value with increasing copper content. The elements Ag, Ni, Pb and Re increase with increasing copper mineralization although values are not consistently enriched compared to BCC. In addition, molybdenum becomes significantly enriched in mineralized samples with respect to mean but not to median values, due to outlier values as indicated in the ranges listed in Appendix 1.

Rare earth elements are enriched compared to BCC with a significantly greater LREE enrichment relative to the HREEs (Fig. 3C). Light REE enrichment consistently increases with increasing copper content. Rare earth element trends include a negative europium anomaly.

Compared to the composition of the BCC, median values indicate that magnetite-dominated IOCG occurrences of the Olympic Copper-Gold Province commonly have low Ba, Bi, Cd, Cr, Cs, Ge, Li, Ni, Pd, Pt, Rb, Sc, Sr, V, W and Zn values (<0.5 BCC; Table 2). Elements that decrease with increasing copper mineralization in both median and mean values include Ba, Cs, Ga, Hf, Mn, Rb, Ta, Tl and Zr, with a less consistent but overall decrease also in Be, Bi, Cd, Cr, Li, Sc, Sr, V and Zn (Fig. 3). Median tungsten abundances are negatively skewed by values below the detection limit, so the consistent depletion

TABLE 2. Median minor and trace element values of samples containing >300 ppm Cu from hematite- and magnetite-dominated IOCG occurrences from the Olympic Copper-Gold Province, relative to bulk continental crustal values of Rudnick and Gao (2003).

| | | | Hematite-dominated | | Magnetite-dominated | |
|---|---|---|---|---|---|---|
| | Unit | Continental crust | Median | Multiple of continental crust | Median | Multiple of continental crust |
| Au | ppm | 0.0013 | 0.0225 | 17.3 | 0.025 | 19.2 |
| Ag | ppm | 0.056 | 0.51 | 9.1 | 0.08 | 1.4 |
| As | ppm | 2.5 | 29.65 | 11.9 | 4.4 | 1.8 |
| Ba | ppm | 456 | 879 | 1.9 | 166.5 | 0.4 |
| Be | ppm | 1.9 | 2.775 | 1.5 | 1.6 | 0.8 |
| Bi | ppm | 0.18 | 2.11 | 11.7 | 0.06 | 0.3 |
| Cd | ppm | 0.08 | 0.1 | 1.3 | 0.03 | 0.4 |
| Co | ppm | 26.6 | 33.7 | 1.3 | 94.15 | 3.5 |
| Cr | ppm | 135 | 23 | 0.2 | 27.5 | 0.2 |
| Cs | ppm | 2 | 1.5 | 0.8 | 0.535 | 0.3 |
| F | ppm | 553 | 1437.5 | 2.6 | 520 | 0.9 |
| Ga | ppm | 16 | 16.3 | 1 | 9.85 | 0.6 |
| Ge | ppm | 1.3 | 1.12 | 0.9 | 0.67 | 0.5 |
| Hf | ppm | 3.7 | 3.2 | 0.9 | 2.6 | 0.7 |
| In | ppm | 0.05 | 0.3595 | 7.2 | 0.063 | 1.3 |
| Li | ppm | 17 | 26.45 | 1.6 | 8.9 | 0.5 |
| Mn | ppm | 774 | 2011.2 | 2.6 | 464.7 | 0.6 |
| Mo | ppm | 0.8 | 2.6 | 3.3 | 1.25 | 1.6 |
| Nb | ppm | 8 | 9.95 | 1.2 | 10.97 | 1.4 |
| Ni | ppm | 59 | 24.5 | 0.4 | 20 | 0.3 |
| Pb | ppm | 11 | 17.95 | 1.6 | 9 | 0.8 |
| Pd | ppm | 0.0015 | 0.0005 | 0.3 | 0.0005 | 0.3 |
| Pt | ppm | 0.0015 | 0.0005 | 0.3 | 0.0005 | 0.3 |
| Rb | ppm | 49 | 100 | 2 | 20 | 0.4 |
| Re | ppm | 0.005 | 0.004 | 0.8 | 0.006 | 1.2 |
| S | ppm | 404 | 4800 | 11.9 | 12987.5 | 32.1 |
| Sb | ppm | 0.2 | 2.3 | 11.5 | 0.2 | 1 |
| Sc | ppm | 21.9 | 7 | 0.3 | 5 | 0.2 |
| Se | ppm | 0.13 | 1.9 | 14.6 | 1.4 | 10.8 |
| Sn | ppm | 1.7 | 6 | 3.5 | 5 | 2.9 |
| Sr | ppm | 320 | 45 | 0.1 | 80.7 | 0.3 |
| Ta | ppm | 0.7 | 0.7 | 1 | 0.4 | 0.6 |
| Te | ppm | 0.01 | 0.17 | 17 | 0.385 | 38.5 |
| Th | ppm | 5.6 | 12.56 | 2.2 | 19.62 | 3.5 |
| Tl | ppm | 0.05 | 0.505 | 10.1 | 0.135 | 2.7 |
| U | ppm | 1.3 | 7.515 | 5.8 | 13.505 | 10.4 |
| V | ppm | 138 | 63 | 0.5 | 39.5 | 0.3 |
| W | ppm | 1 | 10 | 10 | 0.5 | 0.5 |
| Zn | ppm | 72 | 171 | 2.4 | 26 | 0.4 |
| Zr | ppm | 132 | 118 | 0.9 | 94.5 | 0.7 |
| La | ppm | 20 | 38.95 | 1.9 | 75.75 | 3.8 |
| Ce | ppm | 43 | 74.5 | 1.7 | 172.5 | 4 |
| Pr | ppm | 4.9 | 8.355 | 1.7 | 19.085 | 3.9 |
| Nd | ppm | 20 | 30.85 | 1.5 | 61.4 | 3.1 |
| Sm | ppm | 3.9 | 6.1 | 1.6 | 8.6 | 2.2 |
| Eu | ppm | 1.1 | 1.6 | 1.5 | 1.285 | 1.2 |
| Gd | ppm | 3.7 | 5.79 | 1.6 | 5.58 | 1.5 |
| Tb | ppm | 0.6 | 0.875 | 1.5 | 0.76 | 1.3 |
| Dy | ppm | 3.6 | 5.1 | 1.4 | 4.195 | 1.2 |
| Ho | ppm | 0.77 | 1 | 1.3 | 0.815 | 1.1 |
| Er | ppm | 2.1 | 2.7 | 1.3 | 2.285 | 1.1 |
| Tm | ppm | 0.28 | 0.395 | 1.4 | 0.34 | 1.2 |
| Yb | ppm | 1.9 | 2.665 | 1.4 | 2.315 | 1.2 |
| Lu | ppm | 0.3 | 0.41 | 1.4 | 0.365 | 1.2 |
| Y | ppm | 19 | 27.25 | 1.4 | 24.05 | 1.3 |

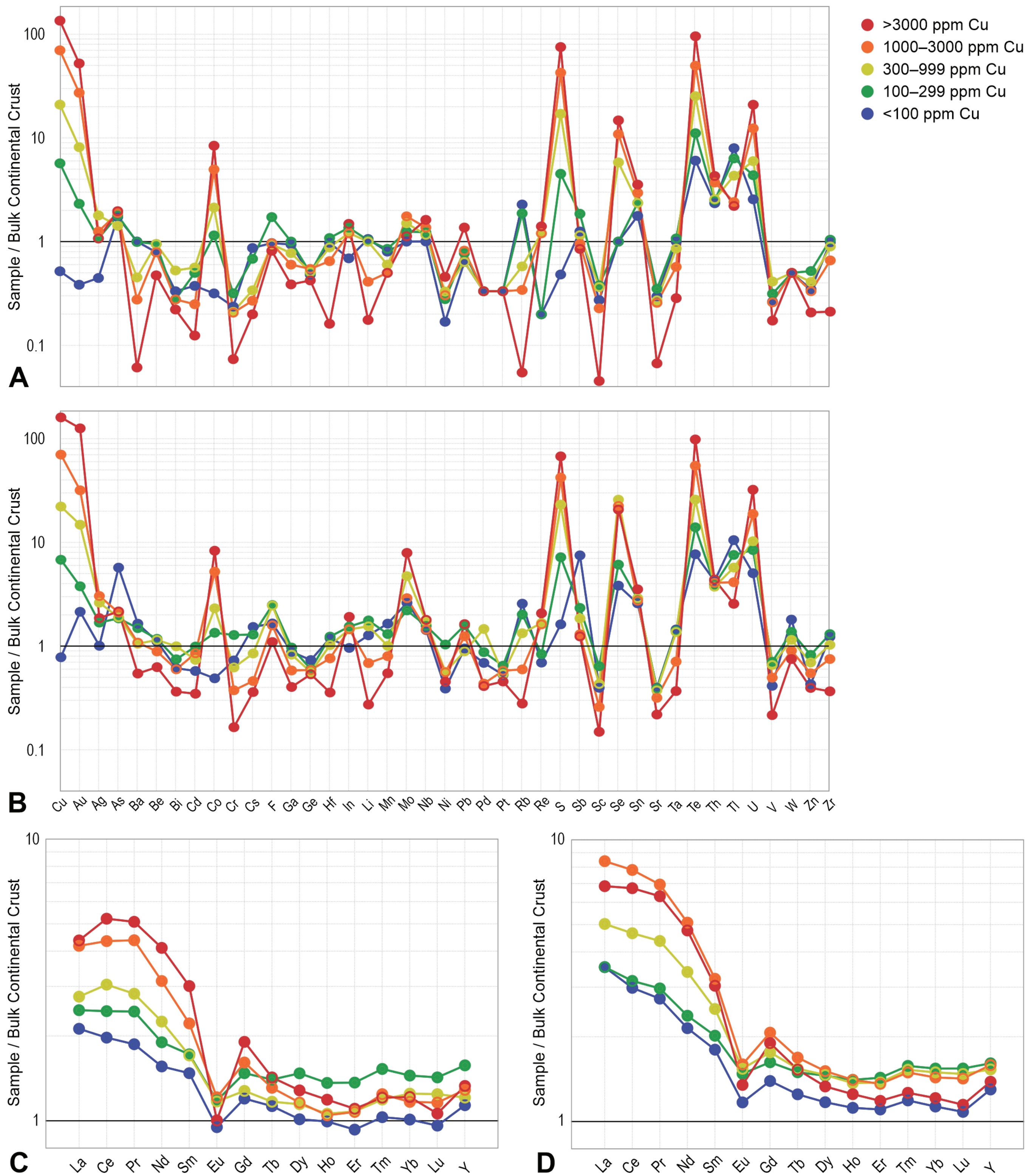


**Figure 3.** Multi-element diagrams depicting element concentrations relative to bulk continental crust of Rudnick and Gao (2003) within magnetite-dominated IOCG occurrences from the Olympic Copper-Gold Province (n=529). Geochemical data have been categorized by copper concentration, representing unmineralized (<100 ppm Cu; n=311), anomalous (100–299 ppm Cu; n=58), weakly mineralized (300–999 ppm Cu; n=64), moderately mineralized (1000–3000 ppm Cu; n=73) and significantly mineralized (>3000 ppm Cu; n=23) samples. **A**. Median minor element values. **B**. Mean minor element values. **C**. Median REE values. **D**. Mean REE values.

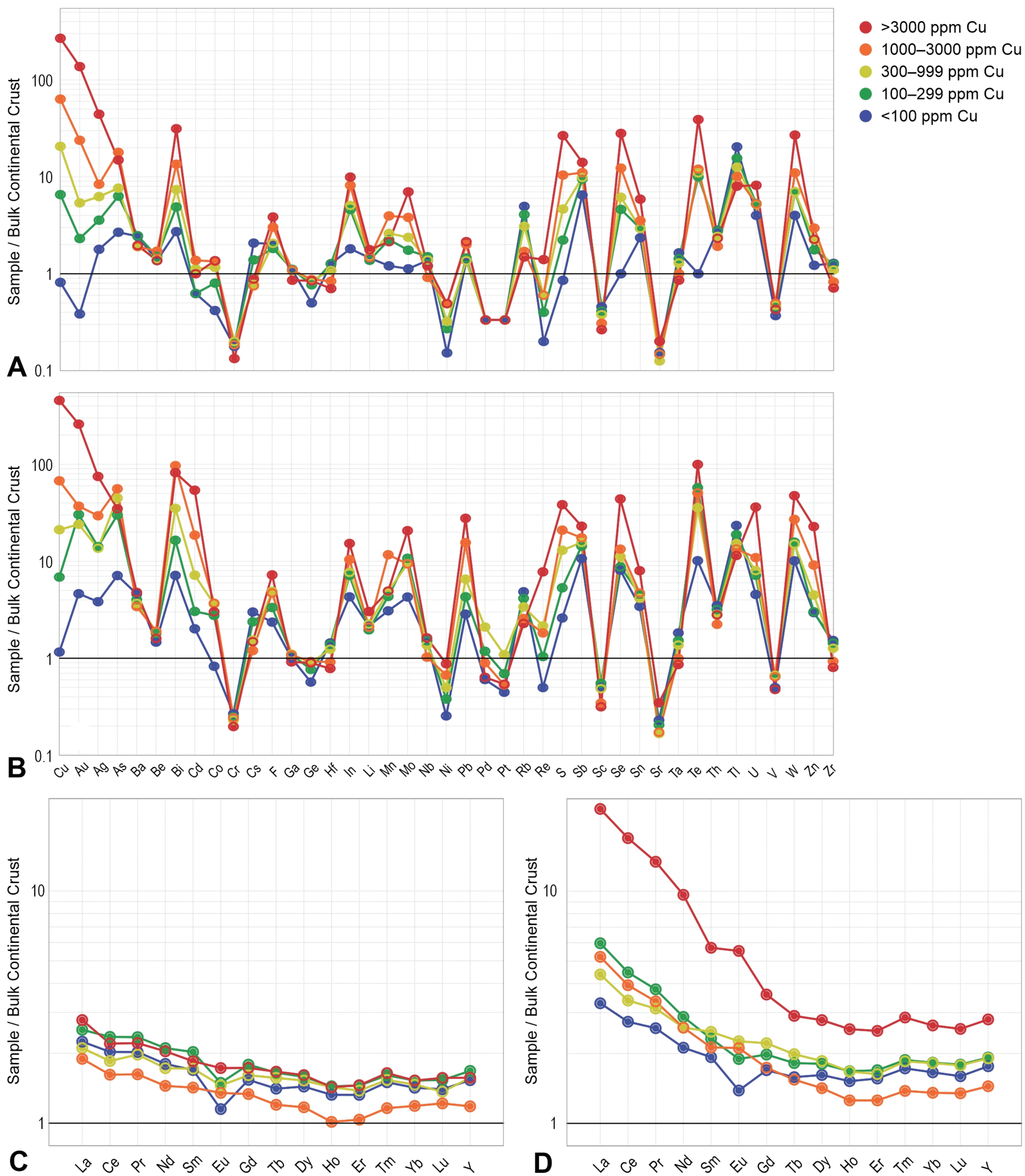


**FIGURE 4.** Multi-element diagrams depicting element concentrations relative to bulk continental crust of Rudnick and Gao (2003) within hematite-rich IOCG occurrences from the Olympic Copper-Gold Province (n=1503). Geochemical data has been categorized by copper concentration, representing unmineralized (<100 ppm Cu; n=740), anomalous (100–299 ppm Cu; n=253), weakly mineralized (300–999 ppm Cu; n=238), moderately mineralized (1000–3000 ppm Cu; n=131) and significantly mineralized (>3000 ppm Cu; n=141) samples. **A.** Median minor element values. **B.** Mean minor element values. **C.** Median REE values. **D.** Mean REE values.

trend displayed in mean values is regarded as significant (Fig. 3B). Many of the elements showing depletion trends are lithophile elements and can be attributed to dilution associated with increasing alteration and mineralization.

*Minor Elements and REE Trends in Hematite-dominated IOCG Occurrences of the Olympic Copper-Gold Province*

Drill holes sampled with respect to hematite-dominated IOCG ore systems encompass proximal to distal parts of both sub-economic and economic occurrences (Fig. 1). Median, mean and ranges for the geochemical data used in this assessment are given in Appendix 2.

Minor element values associated with hematite-dominated IOCG deposits are enriched compared to BCC for most elements (Fig. 4; Table 2). Significant enrichment (>2 times BCC) is evident in Ag, Au, As, Bi, F, In, Mn, Mo, Rb, S, Sb, Se, Te, Th, Tl, U, W and Zn. While elements depleted relative to BCC are similar to those from magnetite-dominated deposits in the region (e.g. Cr, Ni, Pd, Pt, Sc, Sr, V), hematite-dominated deposits have far greater Ag, As, Bi, F, In, Mn, Mo, Pb, Sb, W and Zn abundances. Rare earth elements are enriched compared to continental crust, with a greater LREE enrichment relative to the HREEs (Fig. 4B).

With increasing copper content, samples from hematite-dominated IOCG ore systems in the Olympic Copper-Gold Province become increasingly enriched in Ag, As, Au, Bi, Cd, Co, F, In, Mn, Mo, Ni, Pb, Re, S, Sb, Se, Sn, Te, U, W and Zn (Fig. 4). The overall trend of REEs remains similar for background through to mineralized samples, although with increasing copper content, europium anomalies range from strongly negative to weakly positive (Fig. 4C, D). Mean values from strongly mineralized samples (>3000 ppm Cu) show distinct enrichment, particularly in LREEs, relative to other categories (Fig. 4C). The discrepancy between mean and median values in this category indicate the influence of extreme abundances, many of which come from the Prominent Hill and Carrapateena deposits.

As with magnetite-dominated occurrences, although thallium is enriched relative to bulk continental crust, values decrease with increasing copper concentration. Other relative element depletion trends include Cs, Hf, Rb, Ta, Th and Zr. Comparative enrichment and depletion trends with increasing copper mineralization for both magnetite- and hematite-dominated deposits are listed in Table 3.

## Geochemical Trends in Highly Mineralized Ore Systems

Drill core samples taken from two significant hematite-rich copper-gold deposits, Prominent Hill and Carrapateena, were categorized by copper concentration to enable comparison with published data from Olympic Dam (Ehrig et al., 2012; Fig. 5). To appreciate the effect of the mineralizing system, background samples of comparative lithostratigraphic units to those hosting each deposit have been selected and plotted (Figs. 6–8). Comparative samples were chosen from unmineralized, nearby drill holes that were determined to be relatively unaltered based on Na/Al:K/Al values of ~1, demonstrating a lack of significant Na or K-Fe alteration (Fig. 9).

Several consistent trends emerge from the three deposits. In all three examples, REE trends in samples from the deposits show considerably higher REE values than those from the unmineralized, distal but comparable host-rock. Deposit samples show distinct LREE enrichment and positive europium anomalies, albeit weak in mineralized samples from the Carrapateena deposit. This pattern is evident in unmineralized

**Table 3.** Minor element associations with increasing copper mineralization within IOCG occurrences of the Olympic Copper-Gold Province. Elements in bold indicate those that show an increased abundance within copper mineralized samples of at least 10x those in unmineralized samples (<100 ppm Cu; Rudnick and Gao, 2003). Asterisk denotes elements that show inconsistent trends from unmineralized through to mineralized samples.

| | Hematite-dominated systems | Magnetite-dominated systems |
|---|---|---|
| Increase | **Ag**, As, **Au**, **Bi**, *Cd, Co, Eu, F, In, Mn, Mo, Ni, Pb, Re, **S**, Sb, **Se**, Sn, **Te**, U, W, Zn. | *Ag, **Au**, Ce, **Co**, La, *Ni, Nd, *Pb, Pr, *Re, **S**, **Se**, Sm, Sn, **Te**, Th, U. |
| Decrease | Cs, Hf, Rb, Ta, Th, Tl and Zr. | Ba, *Be, *Bi, *Cd, *Cr, Cs, Ga, Hf, *Li, Mn, Rb, *Sc, *Sr, Ta, Tl, *V, W, *Zn, Zr. |

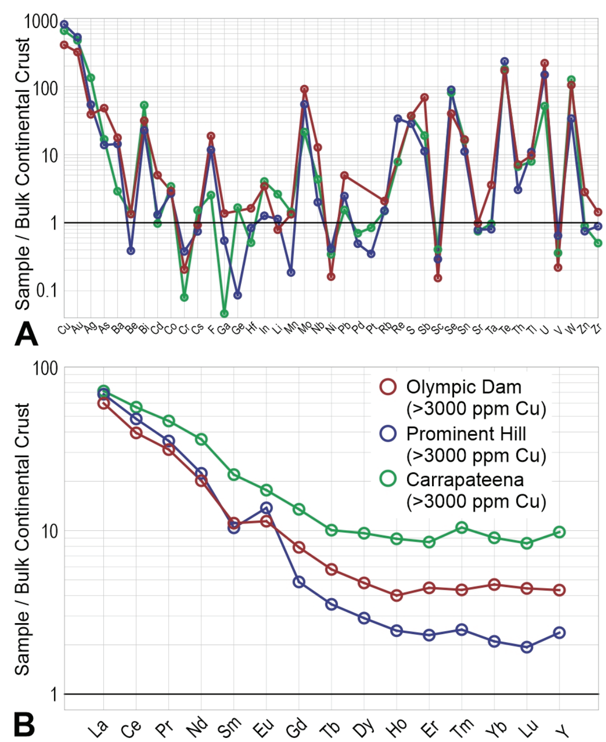


**Figure 5.** Multi-element diagram of mean values normalized by bulk continental crust (Rudnick and Gao, 2003) for significantly mineralized samples (>3000 ppm Cu) from Olympic Dam (Ehrig et al., 2012), Prominent Hill and Carrapateena deposits. **A.** Minor elements. **B.** REE. Note that Olympic Dam is missing values for Ge, Re, Pt and Pd in (A).

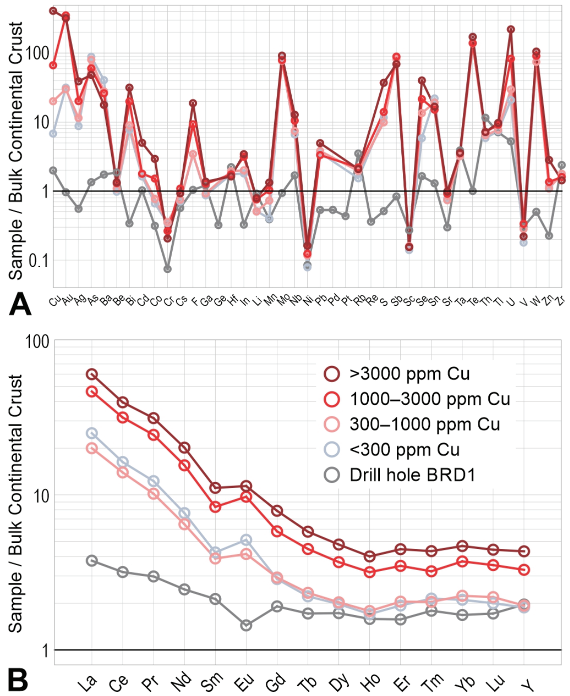


**FIGURE 6.** Multi-element diagram of mean values normalized by bulk continental crust (Rudnick and Gao, 2003) for data from the Olympic Dam deposit (Ehrig et al., 2012) categorized by copper content. Comparative background samples come from Hiltaba Suite granite intersected by drill hole BRD1 (n=10). **A**. Minor elements. **B**. REE.

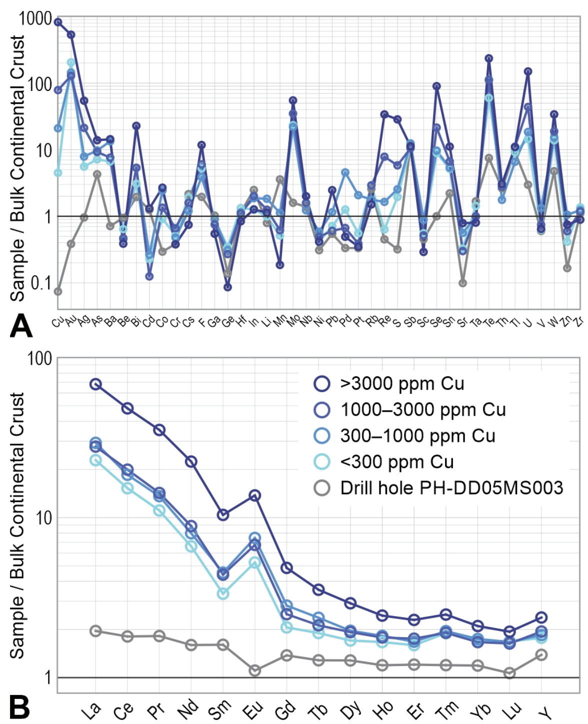


**FIGURE 7**. Multi-element diagram of mean values normalized by bulk continental crust (Rudnick and Gao, 2003) for data from the Prominent Hill deposit categorized by copper content. Comparative background samples come from Wallaroo Group metasedimentary rocks intersected by drill hole PH-DD05MS003 (n=4). **A**. Minor elements. **B**. REE.

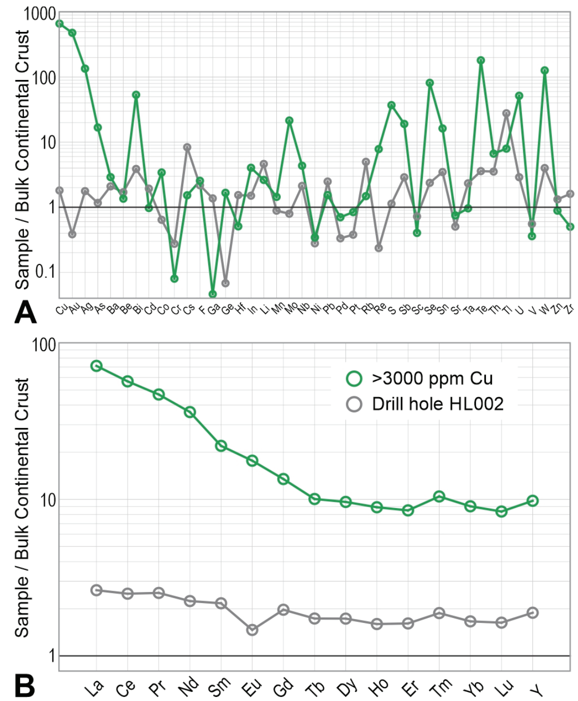


**FIGURE 8.** Multi-element diagram of mean values normalized by bulk continental crust (Rudnick and Gao, 2003) for data from the Carrapateena deposit categorized by copper content. Note that all samples contained >3000 ppm Cu. Comparative background samples come from Donington Suite granite intersected by drill hole HL002 (n=22). **A**. Minor elements. **B**. REE.

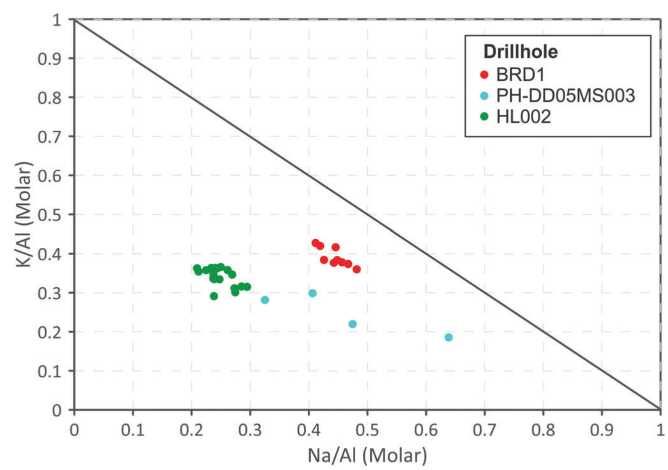


**FIGURE 9.** Feldspar element ratio diagram (Stanley and Madeisky, 1996) of selected unaltered, unmineralized samples from the drill holes BRD1, PH-DD05MS003 and HL002, which intersected comparable lithostratigraphic units to those at the Olympic Dam, Prominent Hill and Carrapateena deposits respectively.

through to mineralized samples from Olympic Dam and Prominent Hill (Figs. 6, 7).

Although the magnitudes vary, multi-element diagrams for the three deposits illustrate that similar groups of elements are either enriched or depleted in each deposit (Fig. 5). Notable divergence between deposits consists of depletion in Be, Ge

**TABLE 4.** Minor and rare earth element enrichment at Olympic Dam, Prominent Hill and Carrapateena relative to the barren equivalent host rock at each deposit. Elements underlined are unique to a particular deposit.

| | Olympic Dam | Prominent Hill | Carrapateena | Common elements |
|---|---|---|---|---|
| Enrichment of >5 times barren samples | Ag, As, Au, Ba, Bi, <u>Cd</u>, Co, Cu, F, <u>In</u>, Mo, <u>Nb</u>, <u>Pb</u>, S, Sb, Se, Sn, Te, U, W, <u>Zn</u>, REE | Ag, As, Au, Ba, Bi, Co, Cu, F, Mo, Re, S, Se, Sn, Te, U, W, REE | Ag, As, Au, Bi, Co, <u>Ge</u>, Mo, Re, S, Sb, Se, Sn, Te, U, W, REE | Ag, As, Au, Bi, Co, Cu, Mo, Re, S, Se, Sn, Te, U, W, REE |

and Mn and significantly higher Re values in samples from Prominent Hill; lower Ba, F and Ga values in Carrapateena samples; and considerably higher As, Cd, Mo, Nb, Sb and Ta values in samples from Olympic Dam. In data from Olympic Dam and Prominent Hill, the overall enrichment and depletion trends are also evident in unmineralized samples from each deposit (Figs. 6, 7). This is in contrast to geochemical data from the background samples, in which minor element values are much closer to the bulk continental crust and depletion and enrichment trends are generally different (Figs. 6–8). This demonstrates that mineralized systems have characteristic minor and REE chemistry (Table 4).

## Discussion

*Geochemical Characteristics of IOCG Deposits from the Olympic Copper-Gold Province, South Australia*

Whole-rock geochemical analysis is a routine method for assessing the economic significance of exploration samples. However, while target metals provide a direct indication of economic significance, recognition of proximity to a mineralizing system is enhanced by considering a multi-element suite. Analysis of a 65 element suite across a range of IOCG occurrences, including major deposits in the Olympic Copper-Gold Province, has demonstrated that these are true multi-element systems, with both magnetite- and hematite-rich occurrences showing multi-element enrichment or depletion trends (Tables 2 and 3). The results indicate that the IOCG-related hydrothermal fluids were able to mobilize a large range of elements. Both magnetite- and hematite-dominated occurrences have significantly enriched values (>2 times BCC) of Au, Cu, S, Se, Sn, Te, Th, Tl and U relative to BCC. Furthermore, the additional elements Ag, Co, Ni, Pb, Re and LREEs are progressively enriched with copper mineralization. These common geochemical trends are characteristics of IOCG deposits within the broader hydrothermal systems, and are therefore considered key elements for recognizing these mineral systems.

Distinct characteristics of hematite-dominated deposits are a greater enrichment in Ag, As, In and Mo, and enrichment in Ba, Be, Bi, Cd, F, Li, Mn, Pb, Rb, Sb, W and Zn. Magnetite-dominated deposits commonly contain higher cobalt and LREE values. In addition to higher relative median values, REE enrichment trends with increasing copper concentration are far more consistent in magnetite-dominated deposits, indicating systematic enrichment with copper mineralization. In contrast, relatively similar median REE values relative to copper concentration suggests that hematite-dominated systems do not share the same coupled enrichment with copper. Significantly higher mean REE values in highly mineralized samples (>3000 ppm Cu) from hematite-dominated occurrences compared to median values (Fig. 4D), indicate the presence of extreme REE enrichment, a characteristic of samples from economic deposits in the sample set.

*Geochemical Evidence for an Evolving Fluid*

Drilling in the Olympic Copper-Gold Province has identified widespread alteration and numerous drill hole intersections of copper-gold mineralization associated with iron oxides. While in detail each copper-gold occurrence generally displays spatial mineralogical variations, a useful broad classification is based on the dominant association of copper-gold with either magnetite or hematite, as described in Williams (2010), Skirrow (2010) and Skirrow et al. (2002, 2007). Magnetite-rich deposits of the Olympic Copper-Gold Province are dominated by Na and Na-Ca alteration, or by biotite or K-feldspar-bearing alteration assemblages, with both the Na and K-Fe alteration occurring paragenetically earlier than sericitic and chloritic (hydrolytic) alteration associated with hematite-rich deposits (Skirrow et al., 2002, 2007). Corriveau et al. (2016) proposed that although fluids within these mineralizing systems are affected by country rock (e.g. carbonate-rich units result in a dominance of skarn mineralogy), a common set of alteration minerals are recognized, and are the result of a cooling and evolving fluid. In this sense, higher temperature magnetite-rich IOCG deposits are considered to form generally earlier and deeper in the evolution of the hydrothermal system, compared to lower temperature and more oxidized hematite-rich IOCG deposits (Skirrow et al., 2002, 2007; Skirrow, 2010, 2022; Corriveau et al., 2016, 2022; Montreuil et al., 2016; Potter et al., 2022). Geochemical data collected in this study show that both hematite- and magnetite-dominated deposits share many common enrichment and depletion trends compared to BCC, supporting, at least in part, their early addition into these deposits. For example, uranium enrichment in samples from magnetite-dominated occurrences is commonly of a similar or greater magnitude than values in hematite-dominated occurrences, indicating that uranium mineralization occurs early in the development of these ore systems. This corroborates with uraninite trace element signatures that indicate primary precipitation during high-temperature, magnetite-bearing alteration (Potter et al., 2022). Similarly, of the other elements common to both magnetite- and hematite-dominated deposits, the magnitude of Au, Se, Sn and Te enrichment is similar, even though magnetite-dominated occurrences sampled were relatively small and economically insignificant.

There are several elements that are exclusively or more significantly enriched in hematite-dominated deposits (e.g. Ag, As, Bi, F, In, Mn, Mo, Sb, W and Zn). Several of these same elements are progressively depleted with increasing copper mineralization in magnetite-dominated deposits (e.g. Bi, Mn and W). In particular, Bi and W are commonly enriched to at least 10 times BCC in hematite-dominated deposits while getting progressively more depleted in magnetite-dominated deposits. This is tentatively interpreted to indicate that these elements are mobilized during high-temperature metasomatism of the country rock, and are precipitated in cooler, hematite-stable conditions. From a practical perspective, it indicates that the spatial enrichment and depletion patterns of these elements can be used to map the passage of hydrothermal fluids from high to lower temperatures, and to increasingly oxidized parts of the system.

*Are Large Ore Systems Unique?*

A considerable challenge to mineral exploration is distinguishing large from small ore systems based on relatively few drill holes. While minor element trends in data from Olympic Dam (Ehrig et al., 2012), Prominent Hill and Carrapateena show element associations that are generally similar to samples collected from prospects across the Olympic Copper-Gold Province, they commonly contain significantly higher values for Au, Ba, F, Mo, Re, Te, U and LREE. A characteristic feature of the minor element and REE chemistry from Olympic Dam (Ehrig et al., 2012), and supported by data from the Prominent Hill deposit collected in this study, is that highly elevated values of Au, Ba, F, Mo, Te, U and LREE occur even in samples with relatively low copper abundances (i.e. <300 ppm Cu). One of the most distinctive geochemical features is the significant elevation in REE abundances. In particular, samples from Olympic Dam and Prominent Hill have more than ten times bulk continental crustal values in the LREEs La, Ce and Pr, even in weakly mineralized samples. In comparison, in regional samples and other prospects analyzed, La, Ce and Pr values are typically <5 times bulk continental crustal abundance in all but the most copper mineralized samples from both hematite- and magnetite-dominated deposits. In addition, REE patterns from the Olympic Dam, Prominent Hill and Carrapateena deposits display a distinct positive europium anomaly, not generally evident in prospect samples. Similar positive europium anomalies have been attributed to highly oxidized hydrothermal fluids at the Monakoff IOCG deposit of the Cloncurry district, Queensland (Williams et al., 2015). This indicates that highly oxidized conditions are favorable for generating a significantly mineralized hematite-rich IOCG deposit.

## Conclusions

Large parts of the Olympic Copper-Gold Province are covered by more than 300 m of post-mineralization cover, and this has significantly hampered exploration and the assessment of many prospects. As a result, no surface exposure and relatively few drill holes are available to identify and map a potentially economic system. A significant finding of this study is that while the magnitude of enrichment or depletion may vary depending on proximity to mineralized zones, minor element and REE trends are generally consistent. This enables recognition of a mineralizing system, even when the most mineralized parts of the system have not yet been discovered. Both hematite- and magnetite-dominated IOCG deposits are significantly enriched compared to bulk continental crust in Cu, Au, S, Se, Sn, Te, Th, Tl and U. Minor and trace element comparisons relative to increasing copper content indicate that the additional elements Ag, Co, Ni, Pb, Re and LREEs are progressively enriched and therefore also associated with copper mineralization. Distinct characteristics of hematite-dominated deposits are far greater enrichment in Ag, As, In and Mo, and enrichment in Ba, Be, Bi, Cd, F, Li, Mn, Pb, Rb, Sb, W and Zn. Magnetite-dominated deposits commonly contain higher cobalt and LREE values. The elements bismuth and tungsten are progressively enriched to over 10 times BCC in hematite-dominated deposits but depleted in magnetite-dominated deposits and are therefore key elements for mapping the lower temperature and more oxidized part of the ore system.

A considerable challenge to mineral exploration is to distinguish large from small ore systems on the basis of relatively few drill holes. Analysis of minor element and REE trends in samples from the Prominent Hill and Carrapateena deposits were consistent with extensive geochemical data available from the Olympic Dam deposit (Ehrig et al., 2012). These indicate that while Olympic Dam is unique in terms of size and tonnage, with respect to geochemical associations, it is similar to other economic, hematite-dominated deposits in the region. This indicates there are similarities in terms of the fluid composition and chemical and physical conditions for the precipitation of metals across the Olympic Copper-Gold Province. Analysis of samples from economic deposits indicate that larger systems contain significantly higher values of Au, Ba, F, Mo, Re, Te, U and LREEs. In particular, enrichment in Ce, La and Pr greater than 10 times average continental crustal values provide the most reliable indicator that a significant system is present. Positive europium anomalies within REE patterns indicate hydrothermal fluids that were highly oxidized, and is a characteristic of large hematite-dominated IOCG deposits.

## Acknowledgments

Staff of the South Australian Drill Core Reference Library provided valuable logistical support for this project. Anthony Reid provided comments on an earlier version of this paper. Reviews of Olivier Blein and Eric Potter together with comments by Roger Skirrow are gratefully acknowledged. This paper is published with permission of the Director, Geological Survey of South Australia.

## References

Allen, S.R., McPhie, J., Ferris, G., and Cadd, A.G., 2008, Evolution and architecture of a large felsic igneous province in western Laurentia: the 1.6 Ga Gawler Range Volcanics South Australia: Journal of Volcanology and Geothermal Research, v. 172, p. 132-147.

Barton, M.D., 2014, Iron oxide (–Cu–Au–REE–P–Ag–U–Co) systems, *in* Holland, H.D. and Turekian, K.K., eds., Treatise on Geochemistry, second edition: Elsevier, Oxford, p. 515-541.

Betts, P.G., Valenta, R.K., and Finlay, J., 2003, Evolution of the Mount Woods Inlier, northern Gawler Craton, Southern Australia: an integrated structural and aeromagnetic analysis: Tectonophysics v. 366, p. 83-111.

Beyer, S.R., Kyser, K., Polito P.A., and Fraser, G.L., 2018, Mesoproterozoic rift sedimentation, fluid events and uranium prospectivity in the Cariewerloo Basin, Gawler Craton, South Australia: Australian Journal of Earth Sciences, v. 65, p. 409-426.

BHP, 2019, BHP Billiton Limited annual report 2019, 318 p. Available on: www.bhp.com/investor-centre.

Blissett, A.H., Creaser, R.A., Daly, S., Flint, D.J., and Parker, A.J., 1993, Gawler Range volcanics, *in* Drexel, J.F., Preiss, W.V. and Parker, A.J., eds., The geology of South Australia: the Precambrian, volume 1: South Australia Geological Survey, Bulletin 54, p. 107-131.

Ciobanu, C.L., Wade, B.P., Cook, N.J., Mumm, A.S., and Giles, D., 2013, Uranium-bearing hematite from the Olympic Dam Cu–U–Au deposit, South Australia: a geochemical tracer and reconnaissance Pb–Pb geochronometer: Precambrian Research, v. 238, p. 129-147.

Clark, J.M., 2014, Defining the style of mineralisation at the Cairn Hill magnetite-sulphide deposit, Mount Woods Inlier, Gawler Craton, South Australia: Unpublished H.B.Sc. thesis, University of Adelaide, 69 p.

Conor, C., 2016, Geological field excursion guide — IOCGs – where it all began: the Moonta-Wallaroo region of the eastern Gawler Craton: Department of State Development, South Australia and Geological Society of Australia, South Australian Division, Report Book 2016/00009.

Conor, C.C.H., Raymond, O., Baker, T., Teale, G.S., Say, P., and Lowe, G., 2010, Alteration and mineralisation in the Moonta-Wallaroo copper-gold mining field region, Olympic Domain, South Australia, *in* Porter, T.M., ed., Hydrothermal iron oxide copper-gold & related deposits: a global perspective, volume 3: PGC Publishing, Adelaide, p. 1-24.

Corriveau, L., Montreuil, J.F., and Potter, E.G., 2016, Alteration facies linkages among iron oxide copper-gold, iron oxide-apatite, and affiliated deposits in the Great Bear magmatic zone, Northwest Territories, Canada, *in* Slack, J., Corriveau, L. and Hitzman, M., eds., Proterozoic iron oxide-apatite (± REE) and iron oxide-copper-gold and affiliated deposits of Southeast Missouri, USA, and the Great Bear magmatic zone, Northwest Territories, Canada: Economic Geology, v. 111, p. 2045-2072.

Corriveau, L., Montreuil, J.-F., Blein, O., Ehrig, K., Potter, E.G., and De Toni, A.F., 2022, Mineral systems with IOCG and affiliated deposits: part 3 – metal pathways and ore deposit model, *in* Corriveau, L., Potter, E.G. and Mumin, A.H., eds., Mineral systems with iron oxide copper-gold (IOCG) and affiliated deposits: Geological Association of Canada, Special Paper 52, p. 205-245.

Cowley, W.M., and Flint, R.B., 1993, Epicratonic igneous rocks and sediments *in* Drexel, J.F., Preiss, W.V. and Parker, A.J., eds., The geology of South Australia: the Precambrian, volume 1: South Australia Geological Survey, Bulletin 54, p. 142-149.

Cowley, W.M., Conor, C.H.H., and Zang, W., 2003, New and revised Proterozoic stratigraphic units on northern Yorke Peninsula: MESA Journal, v. 29, p. 46-58.

Cutts, K., Hand, M., and Kelsey, D.E., 2011, Evidence for early Mesoproterozoic (ca. 1590 Ma) ultrahigh-temperature metamorphism in southern Australia: Lithos, v. 124, p. 1-16.

Davidson, G.J., 2002, The shallow to mid-crustal family of iron oxide copper-gold deposits: size, alteration and mechanisms of formation, *in* Cooke, D.R. and Pongratz, J., eds., Giant ore deposits: characteristics, genesis and exploration: CODES Special Publication 4, University of Tasmania, p. 79-102.

Davidson, G.J., Paterson, H.L., Meffre, S., and Berry, R., 2007, Characteristics and origin of the breccia hosted, Cu-U-rich, Oak Dam East ironstone: Olympic Dam-like mineralization beneath the Stuart Shelf: Economic Geology, v. 102, p. 1471-1498.

Dmitrijeva, M., Ehrig, K.J., Ciobanu, C.L., Cook, N.J., Verdugo-Ihl, M.R., and Metcalfe, A.V., 2019, Defining IOCG signatures through compositional data analysis: a case study of lithogeochemical zoning from the Olympic Dam deposit, South Australia: Ore Geology Reviews, v.105, p. 86-101.

Dutch, R., Hand, M., and Kinny, P.D., 2008, High-grade Paleoproterozoic reworking in the southeastern Gawler Craton, South Australia: Australian Journal of Earth Sciences, v. 55, p. 1063-1081.

Ehrig, K., McPhie, J., and Kamenetsky, V., 2012, Geology and mineralogical zonation of the Olympic Dam iron oxide Cu-U-Au-Ag deposit, South Australia, *in* Hedenquist, J.W., Harris, M. and Camus, F., eds., Geology and genesis of major copper deposits and districts of the world: a tribute to Richard H. Sillitoe: Society of Economic Geologists Special Publication 16, p. 237-267.

Flint, R.B., Blissett, A.H., Conor, C.H.H., Cowley, W.M., Cross, K.C., Creaser, R.A., Daly, S.J., Krieg, G.W., Major, R.B., Teale, G.S., and Parker, A.J., 1993, Mesoproterozoic, *in* Drexel, J.F., Preiss, W.V. and Parker, A.J., eds., The geology of South Australia: the Precambrian, volume 1: South Australia Geological Survey, Bulletin 54, p. 106-169.

Forbes, C.J., Giles, D., Hand, M., Betts, P.G., Suzuki, K., Chalmers, N., and Dutch, R., 2011, Using P–T paths to interpret the tectonothermal setting of prograde metamorphism: an example from the northeastern Gawler Craton, South Australia: Precambrian Research, v. 185, p.65-85.

Freeman, H., and Tomkinson, M., 2010, Geological setting of iron oxide related mineralization in the southern Mount Woods Domain, South Australia, *in* Porter, T.M., ed., Hydrothermal iron oxide copper-gold and related deposits: a global perspective, volume 3: PGC Publishing, Adelaide, p. 171-190.

Gow, P., Wall, V.I, Oliver, N.H.S., and Valenta, R.K., 1994, Proterozoic iron oxide (Cu-U-Au-REE) deposits: further evidence of hydrothermal origins: Geology, v. 22, p. 633-636.

Groves, D.I., Condie, K.C., Goldfarb, R.J., Hronsky, J.M.A., and Vielreicher, R.M., 2005, Secular changes in global tectonic processes and their influence on the temporal distribution of gold-bearing mineral deposits: Economic Geology, v. 100, p. 203-224.

Groves, D.I., Bierlein, F.P., Meinert, L.D., and Hitzman, M.W., 2010, Iron oxide copper-gold (IOCG) deposits through Earth history: implications for origin, lithospheric setting, and distinction from other epigenetic iron oxide deposits: Economic Geology, v. 105, p. 641-654.

Hampton, S., 1997, A study of the paragenesis and controls on Proterozoic (Cu-Fe-Au-REE) mineralisation at the Manxman A1 and Joes Dam South prospects, Mount Woods Inlier, South Australia: Unpublished H.B.Sc. thesis, James Cook University, 146 p.

Hand, M., Reid, A., and Jagodzinski, E., 2007, Tectonic framework and evolution of the Gawler Craton, South Australia: Economic Geology, v. 102, p. 1377-1395.

Hitzman, M.W., 2000, Iron oxide-Cu-Au deposits: what, where, when and why, *in* Porter, T.M., ed., Hydrothermal iron oxide copper-gold and related deposits: a global perspective, volume 1: PGC Publishing, Adelaide, p. 9-25.

Ismail, R., Ciobanu, C.L., Cook, N.J., Teale, G.S., Giles, D., Mumm, A.S., and Wade, B., 2014, Rare earths and other trace elements in minerals from skarn assemblages, Hillside iron oxide-copper-gold deposit, Yorke Peninsula, South Australia: Lithos 184-187, p. 456-477.

Jagodzinski, E.A., 2005, Compilation of SHRIMP U-Pb geochronological data, Olympic Domain, Gawler Craton, South Australia, 2001-2003: Geoscience Australia Record 2005/20, p. 211.

Jagodzinski, E.A., Reid, A.J., Chalmers, N.C., Swain, G., Frew, R.A., and Foudoulis, C., 2007, Compilation of SHRIMP U-Pb geochronological data for the Gawler craton, South Australia, 2007: South Australia, Department of Primary Industries and Resources Report Book 2007/21, p. 93.

Johnson, J.P., 1993, The geochronology and radiogenic isotope systematics of the Olympic Dam copper-uranium-gold-silver deposit, South Australia: Unpublished Ph.D. thesis, The Australian National University, 251 p.

Johnson, J.P., and Cross, K.C., 1995, U-Pb geochronological constraints on the genesis of the Olympic Dam Cu-U-Au-Ag deposit, South Australia: Economic Geology, v. 90, p. 1046-1063.

Montreuil, J.F., Corriveau, L., and Grunsky, E.C., 2013, Compositional data analysis of hydrothermal alteration in IOCG systems, Great Bear magmatic zone, Canada: to each alteration type its own geochemical signature: Geochemistry: Exploration, Environment, Analysis v. 13, p. 229-247.

Montreuil, J.-F., Corriveau, L., Potter, E.G., and De Toni, A.F., 2016, On the relation between alteration facies and metal endowment of iron oxide–alkali-altered systems, southern Great Bear magmatic zone (Canada), *in* Slack, J., Corriveau, L. and Hitzman, M., eds., Proterozoic iron oxide-apatite (± REE) and iron oxide-copper-gold and affiliated deposits of Southeast Missouri, USA, and the Great Bear magmatic zone, Northwest Territories, Canada: Economic Geology, v. 111, p. 2139-2168.

OZ Minerals, 2018, 2018 mineral resource and ore reserve statement and explanatory notes, 30 June 2018: Available at https://www.ozminerals.com/uploads/media/181112_Prominent_Hill_Mineral_Resource_and_Ore_Reserve_Statement_as_at_30_June_2018.pdf.

OZ Minerals, 2019, Mineral resource statement and explanatory notes as at 6 March 2019: Available at https://www.ozminerals.com/uploads/media/190306_ASX_Release_Carrapateena_Mineral_Resource_Statement.pdf.

Potter, E.G., Acosta-Góngora, P., Corriveau, L., Montreuil, J-F., and Yang, Z., 2022, Uranium enrichment processes in iron oxide and alkali-calcic alteration systems as revealed by trace element signatures of uraninite, *in* Corriveau, L., Potter, E.G. and Mumin, A.H., eds., Mineral systems with iron oxide copper-gold (IOCG) and affiliated deposits: Geological Association of Canada, Special Paper 52, p. 325-345.

Preiss, W.V. (compiler), 1987, The Adelaide Geosyncline—late Proterozoic stratigraphy, sedimentation, paleontology and tectonics: Bulletin of the Geological Survey of South Australia, v. 53, 438 p.

Reid, A.J., and Fabris, A.J., 2015, Influence of pre-existing low metamorphic grade sedimentary successions on the distribution of iron oxide copper-gold mineralisation in the Olympic Cu-Au Province, Gawler Craton: Economic Geology, v. 110, p. 2147-2157.

Reid, A., Hand, M., Jagodzinski, E., Kelsey, D., and Pearson, N.J., 2008, Palaeoproterozoic orogenesis within the southeastern Gawler Craton: South Australia Australian Journal of Earth Sciences, v. 55, p. 449-471.

Reid, A., Smith, R.N., Baker, T., Jagodzinski, E.A., Selby, D., Gregory, C.J., and Skirrow, R.G., 2013, Re-Os dating of molybdenite within hematite breccias from the Vulcan Cu-Au prospect, Olympic Cu-Au province, South Australia: Economic Geology, v. 108, p. 883-894.

Reid, A.J., Jagodzinski, E.A., Fraser, G.L., and Pawley, M.J., 2014, SHRIMP U-Pb zircon constraints on the tectonics of the Neoarchaean to early Palaeoproterozoic transition within the Mulgathing Complex, Gawler Craton, South Australia: Precambrian Research. v. 250, p. 27-49.

Rudnick, R.L., and Gao, S., 2003, Composition of the continental crust, *in* Rudnick, R.L., Holland, H.D. and Turekian, K.K., eds., Treatise on Geochemistry: Elsevier, v. 3, p. 1-64.

Skirrow, R.G., 2010, "Hematite-group" IOCG±U ore systems: tectonic settings, hydrothermal characteristics, and Cu-Au and U mineralizing processes, *in* Corriveau, L. and Mumin, A.H., eds., Exploring for iron oxide copper-gold deposits: Canada and global analogues: Geological Association of Canada, Short Course Notes, No. 20, p. 39-57.

Skirrow, R.G., 2022, Hematite-group IOCG ± U deposits: an update on their tectonic settings, hydrothermal characteristics, and Cu-Au-U mineralizing processes, *in* Corriveau, L., Potter, E.G. and Mumin, A.H., eds., Mineral systems with iron oxide copper-gold (IOCG) and affiliated deposits: Geological Association of Canada, Special Paper 52, p. 27-51.

Skirrow, R.G., Bastrakov, E., Davidson, G., Raymond, O.L., and Heithersay, P., 2002, The geological framework, distribution and controls of Fe-oxide and related alteration, and Cu-Au mineralisation in the Gawler Craton, South Australia. Part II: alteration and mineralisation, *in* Porter, T.M, ed., Hydrothermal iron oxide copper-gold and related deposits: a global perspective: PGC Publishing, Adelaide, p. 33-47.

Skirrow, R.G., Bastrakov, E.N., Barovich, K., Fraser, G.L., Creaser, R.A., Fanning, C.M., Raymond, O.L., and Davidson, G.J., 2007, Timing of iron oxide Cu-Au-(U) hydrothermal activity and Nd isotope constraints on metal sources in the Gawler Craton, South Australia: Economic Geology v. 102, p. 1441-1470.

Skirrow, R.G., van der Wielen, S.E., Champion, D.C., Czarnota, K., and Thiel, S., 2018, Lithospheric architecture and mantle metasomatism linked to iron oxide Cu-Au ore formation: multidisciplinary evidence from the Olympic Dam region, South Australia: Geochemistry, Geophysics, Geosystems, v. 19, p. 2673-2705.

Stanley, C.R., and Madeisky, H.E., 1996, Lithogeochemical exploration for metasomatic zones associated with hydrothermal mineral deposits using molar element ratio analysis: introduction, Lithogeochemical Exploration Research Project: Mineral Deposit Research Unit, University of British Columbia, Short Course Notes, 200 p.

Williams, M.R., Holwell, D.A., Lilly, R.M., Case, G.N.D., and McDonald, I., 2015, Mineralogical and fluid characteristics of the fluorite-rich Monakoff and E1 Cu-Au deposits, Cloncurry Region, Queensland, Australia: implications for regional F-Ba-rich IOCG mineralisation: Ore Geology Reviews, v. 64, p. 103-127.

Williams, P., 2010, Classifying IOCG deposits, *in* Corriveau, L. and Mumin, A.H., eds., Exploring for iron oxide copper-gold deposits: Canada and global analogues: Geological Association of Canada, Short Course Notes, No. 20, p. 13-21.

Williams, P.J., Barton, M.D., Johnson, D.A., Fontbote, L., de Haller, A., Mark, G., Oliver, N.H.S., and Marschik, R., 2005, Iron oxide copper-gold deposits: geology, space-time distribution and possible modes of origin, *in* Hedenquist, J.W., Thompson, J.F.H., Goldfarb, R.J. and Richards, J.P., eds., Economic Geology 100th Anniversary Volume: Society of Economic Geologists, p. 371-405.

Wingate, M.T., Campbell, I.H., Compston, W., and Gibson, G.M., 1998, Ion microprobe U–Pb ages for Neoproterozoic basaltic magmatism in south-central Australia and implications for the breakup of Rodinia: Precambrian Research, v. 87, p. 135-159.

**Appendix 1.** Summary geochemical data for magnetite-dominated IOCG samples analyed in this study. Asterisk denotes values below the limit of detection.

| | | Unmineralized <100 ppm Cu n=311 | | | Anomalous 100–299 ppm Cu n=58 | | | Weakly mineralised 300–999 ppm Cu n=64 | | | Moderately mineralized 1000–3000 ppm Cu n=73 | | | Mineralized >3000 ppm Cu n=23 | | |
|---|---|---|---|---|---|---|---|---|---|---|---|---|---|---|---|---|
| | | Median | Mean | Range | Median | Mean | Range | Median | Mean | Range | Median | Mean | Range | Median | Mean | Range |
| Cu | ppm | 14 | 20.8 | 0.5*-99.0 | 152.5 | 181 | 104.0-298 | 560 | 590 | 301.0-963 | 1860 | 1870 | 1023-2968 | 3585 | 4274 | 3004-8710 |
| Au | ppb | 0.5 | 2.74 | 0.5*-142.0 | 3 | 4.83 | 0.5*-34.0 | 10.5 | 19 | 0.5*-174.0 | 35 | 40.8 | 3.0-183.0 | 67 | 161 | 14.0-811 |
| Ag | ppm | 0.025 | 0.056 | 0.025*-1.15 | 0.06 | 0.093 | 0.025*-0.66 | 0.1 | 0.15 | 0.025*-0.49 | 0.07 | 0.17 | 0.025*-1.12 | 0.06 | 0.1 | 0.025*-0.71 |
| As | ppm | 4.3 | 14.1 | 0.25*-2052 | 4.45 | 4.57 | 0.25*-14.2 | 3.55 | 4.67 | 0.25*-19.0 | 4.7 | 5.19 | 0.25*-19.0 | 4.9 | 5.3 | 0.25*-17.4 |
| Ba | ppm | 456.5 | 739.4 | 3.5-10180 | 452.1 | 670 | 6.7-6336 | 206.6 | 473.8 | 0.25*-5023 | 126.3 | 485.7 | 3.1-9153 | 28.1 | 244.4 | 1.5-2840 |
| Be | ppm | 1.5 | 2.1 | 0.25*-18.8 | 1.8 | 2.2 | 0.25*-7.4 | 1.8 | 2.15 | 0.25*-5.4 | 1.5 | 1.66 | 0.25*-5.0 | 0.9 | 1.17 | 0.25*-3.9 |
| Bi | ppm | 0.06 | 0.1 | 0.005*-1.23 | 0.05 | 0.13 | 0.005*-1.52 | 0.1 | 0.18 | 0.005*-1.6 | 0.05 | 0.1 | 0.005*-0.71 | 0.04 | 0.06 | 0.005*-0.34 |
| Cd | ppm | 0.03 | 0.045 | 0.01*-0.68 | 0.04 | 0.078 | 0.01*-1.24 | 0.045 | 0.058 | 0.01*-0.44 | 0.02 | 0.07 | 0.01*-1.28 | 0.01 | 0.027 | 0.01*-0.13 |
| Co | ppm | 8.5 | 12.8 | 0.5-172.0 | 30.5 | 35.3 | 4.1-150.0 | 56.5 | 60.7 | 7.5-148.4 | 131.2 | 137 | 26.5-346 | 221.9 | 217.9 | 39.7-352.3 |
| Cr | ppm | 32 | 96.8 | 10.0-1681 | 43 | 170 | 10.0-1972 | 28.5 | 82.8 | 10.0-2061 | 28 | 50 | 10.0-1362 | 10 | 22 | 10.0-69.0 |
| Cs | ppm | 1.7 | 3 | 0.025*-23.0 | 1.37 | 2.55 | 0.08-12.4 | 0.68 | 1.67 | 0.07-10.1 | 0.54 | 0.91 | 0.025*-12.5 | 0.4 | 0.71 | 0.025*-7.29 |
| F | ppm | 535 | 901 | 25.0*-14338 | 951 | 1356 | 25.0*-7476 | 519 | 1342 | 99.0-13883 | 532 | 865 | 25.0*-9177 | 451 | 597 | 88.0-2508 |
| Ga | ppm | 15 | 13.9 | 0.5-43.4 | 16 | 15.3 | 0.9-29.2 | 12.4 | 13 | 1.4-35.6 | 9.6 | 9.18 | 0.4-20.9 | 6.2 | 6.37 | 1.1-11.7 |
| Ge | ppm | 0.625 | 0.94 | 0.025*-7.92 | 0.65 | 0.77 | 0.25-4.88 | 0.67 | 0.72 | 0.025*-2.2 | 0.71 | 0.75 | 0.07-2.38 | 0.55 | 0.69 | 0.23-1.57 |
| Hf | ppm | 3.6 | 4.4 | 0.05*-19.5 | 4 | 4.5 | 0.05*-12.1 | 3.25 | 3.73 | 0.5-10.3 | 2.4 | 2.78 | 0.05*-10.3 | 0.6 | 1.3 | 0.05*-4.6 |
| In | ppm | 0.035 | 0.047 | 0.0025*-0.33 | 0.07 | 0.08 | 0.013-0.277 | 0.06 | 0.07 | 0.02-0.297 | 0.06 | 0.07 | 0.015-0.16 | 0.07 | 0.09 | 0.03-0.38 |
| Li | ppm | 18 | 21.3 | 0.5*-86.4 | 17.5 | 29.6 | 1.0-143.0 | 17 | 26 | 2.0-264.0 | 7 | 11.5 | 0.5*-60.0 | 3 | 4.6 | 0.5*-29.8 |
| Mn | ppm | 619.6 | 1257 | 77.5*-20600 | 658 | 999 | 77.5*-3950 | 465 | 767 | 77.5*-2711 | 387 | 610 | 155.0-3717 | 387 | 418 | 77.5*-1394 |
| Mo | ppm | 0.8 | 2.1 | 0.05*-116.2 | 1 | 1.74 | 0.05*-14.4 | 1.2 | 3.73 | 0.4-43.3 | 1.4 | 2.29 | 0.3-21.0 | 0.9 | 6.25 | 0.1-105.8 |
| Nb | ppm | 8 | 11.25 | 0.1-299.0 | 9.8 | 12.4 | 0.78-65.8 | 9.3 | 13.56 | 0.8-81.0 | 10.9 | 11.38 | 1.5-40.24 | 12.9 | 14.1 | 1.9-41.7 |
| Ni | ppm | 10 | 22.65 | 0.5*-417 | 16.5 | 60.2 | 0.5*-568 | 19.5 | 32.8 | 0.5*-258 | 18 | 32.6 | 3.0-571 | 27 | 26.4 | 0.5*-62.0 |
| Pb | ppm | 7 | 10.3 | 2.5*-62.0 | 8.5 | 17.2 | 2.5*-240.0 | 7 | 9.7 | 2.5*-46.0 | 9 | 13.5 | 2.5*-108.0 | 15 | 17.7 | 2.5*-57.0 |
| Pd | ppb | 0.5 | 1 | 0.5*-20.0 | 0.5 | 1.3 | 0.5*-18.0 | 0.5 | 2.16 | 0.5*-90.0 | 0.5 | 0.64 | 0.5*-3.0 | 0.5 | 0.61 | 0.5*-2.0 |
| Pt | ppb | 0.5 | 0.78 | 0.5*-8.0 | 0.5 | 0.96 | 0.5*-8.0 | 0.5 | 0.8 | 0.5*-9.0 | 0.5 | 0.86 | 0.5*-8.0 | 0.5 | 0.67 | 0.5*-2.0 |
| Rb | ppm | 111.3 | 124 | 0.05*-587.5 | 91.6 | 97.5 | 0.4-295.0 | 28.3 | 64 | 1.2-414.0 | 16.8 | 28.8 | 0.4-211.0 | 2.7 | 13.49 | 0.2-139.3 |
| Re | ppm | 0.001 | 0.003 | 0.001*-0.06 | 0.001 | 0.004 | 0.001*-0.25 | 0.006 | 0.008 | 0.001*-0.05 | 0.006 | 0.008 | 0.001*-0.025 | 0.007 | 0.01 | 0.001*-0.045 |
| S | ppm | 195 | 646 | 25.0*-28124 | 1810 | 2864 | 25.0*-16739 | 6830 | 9230 | 509-112900 | 16968 | 16826 | 165.0-44454 | 29925 | 26924 | 5581-41366 |
| Sb | ppm | 0.25 | 1.48 | 0.025*-117.5 | 0.37 | 0.46 | 0.025*-1.2 | 0.23 | 0.37 | 0.025*-1.7 | 0.19 | 0.26 | 0.025*-1.0 | 0.17 | 0.245 | 0.025*-0.8 |
| Sc | ppm | 6 | 8.56 | 0.05*-52.4 | 8.3 | 13.8 | 0.05*-45.7 | 8 | 9.3 | 1.0-37.1 | 5 | 5.6 | 0.05*-29.2 | 1 | 3.2 | 0.05*-14.3 |
| Se | ppm | 0.13* | 0.49 | 0.13*-5.3 | 0.13* | 0.78 | 0.13*-8.7 | 0.75 | 3.3 | 0.13*-89.0 | 1.4 | 2.88 | 0.13*-32.1 | 1.9 | 2.66 | 0.13*-15.3 |
| Sn | ppm | 3 | 4.3 | 0.5*-20.0 | 4 | 4.8 | 0.5*-27.0 | 4 | 4.87 | 0.5*-15.0 | 5 | 4.6 | 1.0-9.0 | 6 | 5.91 | 3.0-8.0 |
| Sr | ppm | 95 | 125 | 1.2-4034 | 112.5 | 123.2 | 2.2-411.0 | 87.1 | 118.2 | 11.0-644 | 82.5 | 100 | 3.8-380.0 | 21.6 | 69 | 3.8-477.3 |
| Ta | ppm | 0.7 | 1 | 0.05*-41.5 | 0.75 | 0.97 | 0.05*-9.0 | 0.6 | 0.94 | 0.05*-6.7 | 0.4 | 0.49 | 0.05*-2.4 | 0.2 | 0.25 | 0.05*-1.1 |
| Te | ppm | 0.06 | 0.08 | 0.01*-1.71 | 0.11 | 0.14 | 0.01*-0.56 | 0.25 | 0.26 | 0.01*-0.89 | 0.49 | 0.54 | 0.09-1.6 | 0.94 | 0.97 | 0.36-1.48 |
| Th | ppm | 13.1 | 23.5 | 0.4-364.7 | 14 | 21.6 | 0.4-292.0 | 14.3 | 20.7 | 1.4-206.0 | 20.7 | 22.5 | 1.3-86.0 | 23.9 | 24.2 | 10.0-49.3 |
| Tl | ppm | 0.4 | 0.5 | 0.01*-1.83 | 0.32 | 0.37 | 0.01*-1.16 | 0.22 | 0.28 | 0.01*-1.6 | 0.12 | 0.2 | 0.01*-1.51 | 0.11 | 0.13 | 0.01*-0.35 |
| U | ppm | 3.31 | 6.5 | 0.025*-124.0 | 5.6 | 10.8 | 0.27-104.0 | 7.7 | 13.2 | 0.8-90.6 | 15.9 | 24.1 | 2.4-252.0 | 26.9 | 41.3 | 7.5-224.9 |
| V | ppm | 36.5 | 56 | 5.0*-395.0 | 43.5 | 96 | 5.0*-399.0 | 57 | 89 | 5.0*-384.0 | 36 | 67.5 | 5.0*-301.0 | 24 | 29.4 | 5.0*-129.0 |
| W | ppm | 0.5* | 1.78 | 0.5*-27.0 | 0.5* | 1.4 | 0.5*-11.0 | 0.5* | 1.13 | 0.5*-9.0 | 0.5* | 0.89 | 0.5*-5.0 | 0.5* | 0.74 | 0.5*-3.0 |
| Zn | ppm | 25 | 30.5 | 0.5*-249.0 | 37.5 | 58.4 | 1.0-480.0 | 29.5 | 49.4 | 3.0-247.0 | 24 | 38.8 | 0.5*-272.0 | 15 | 28 | 0.5*-179.0 |
| Zr | ppm | 130 | 159 | 3.0-818 | 137.5 | 169.8 | 2.0-509 | 118.5 | 133.9 | 24.0-437.0 | 87 | 98 | 1.0-409.0 | 28 | 47.7 | 3.0-153.0 |
| La | ppm | 42.7 | 71 | 1.5-1038 | 49.7 | 71 | 2.6-392.0 | 55.5 | 101.1 | 4.6-751.0 | 84 | 169 | 5.0-1618 | 87.8 | 137.6 | 18.6-647.0 |
| Ce | ppm | 85.3 | 129 | 2.0-1560 | 106 | 136 | 8.2-773 | 131.6 | 201.5 | 8.3-1249 | 188 | 338 | 25.0-2727 | 225.4 | 291.1 | 44.0-1138 |
| Pr | ppm | 9.2 | 13.4 | 0.38-149.0 | 12 | 14.6 | 1.5-76.0 | 13.9 | 21.6 | 1.16-114.5 | 21.5 | 34.2 | 1.6-229.0 | 25 | 31.1 | 5.47-107.8 |
| Nd | ppm | 31.35 | 43.12 | 1.2-384.0 | 38.2 | 47.7 | 5.7-207.0 | 45.3 | 68.3 | 4.2-356.0 | 63 | 102 | 5.9-571.0 | 82.6 | 95.8 | 19.2-293.0 |
| Sm | ppm | 5.79 | 7.06 | 0.23-39.9 | 6.75 | 7.9 | 1.2-24.5 | 6.7 | 9.8 | 1.2-38.3 | 8.7 | 12.6 | 1.2-46.3 | 11.79 | 11.9 | 2.79-31 |
| Eu | ppm | 1.05 | 1.29 | 0.09-4.94 | 1.3 | 1.6 | 0.08-5.32 | 1.3 | 1.7 | 0.3-6.4 | 1.3 | 1.8 | 0.16-10.47 | 1.11 | 1.49 | 0.26-6.54 |
| Gd | ppm | 4.46 | 5.18 | 0.11-19.8 | 5.49 | 6.04 | 0.84-15 | 4.75 | 6.55 | 1.1-21.6 | 6 | 7.7 | 0.8-25.5 | 7.1 | 7.1 | 1.7-18.9 |
| Tb | ppm | 0.68 | 0.75 | 0.02-3.2 | 0.85 | 0.9 | 0.09-2.14 | 0.71 | 0.93 | 0.15-3.33 | 0.79 | 1.02 | 0.12-2.4 | 0.86 | 0.92 | 0.25-2.54 |
| Dy | ppm | 3.67 | 4.24 | 0.07-20.1 | 5.34 | 5.27 | 0.5-11.8 | 4.15 | 5.3 | 0.94-21.0 | 4.2 | 5.5 | 0.7-22.2 | 4.64 | 4.82 | 1.4-12.3 |
| Ho | ppm | 0.77 | 0.87 | 0.03-4.25 | 1.06 | 1.09 | 0.12-2.3 | 0.82 | 1.06 | 0.18-4.37 | 0.8 | 1.1 | 0.17-4.5 | 0.92 | 0.97 | 0.3-2.63 |
| Er | ppm | 1.97 | 2.33 | 0.12-12.04 | 2.89 | 3.02 | 0.3-7.3 | 2.28 | 2.9 | 0.5-12.8 | 2.27 | 2.87 | 0.4-12.6 | 2.33 | 2.5 | 0.8-6.2 |
| Tm | ppm | 0.29 | 0.33 | 0.25-1.7 | 0.43 | 0.44 | 0.025*-1.18 | 0.34 | 0.43 | 0.06-1.74 | 0.35 | 0.42 | 0.025*-1.68 | 0.34 | 0.36 | 0.1-0.88 |
| Yb | ppm | 1.93 | 2.16 | 0.07-11.34 | 2.77 | 2.95 | 0.45-8.97 | 2.39 | 2.86 | 0.47-11.34 | 2.23 | 2.74 | 0.42-10.26 | 2.32 | 2.31 | 0.73-5.06 |
| Lu | ppm | 0.29 | 0.32 | 0.01*-1.71 | 0.43 | 0.47 | 0.01*-1.76 | 0.38 | 0.45 | 0.05-1.73 | 0.35 | 0.43 | 0.01*-1.47 | 0.32 | 0.35 | 0.06-0.63 |
| Y | ppm | 21.7 | 24.8 | 0.7-119.1 | 30.05 | 30.75 | 3.0-66.5 | 23.1 | 29.5 | 5.9-120.0 | 24.6 | 30.3 | 4.4-121.0 | 25.4 | 26.45 | 8.9-70.6 |

**Appendix 2.** Summary geochemical data for hematite-dominated IOCG samples analyzed in .this study. Asterisk denotes values below the limit of detection

| | | Unmineralized <100 ppm Cu n=740 | | | Anomalous 100–299 ppm Cu n=253 | | | Weakly mineralized 300–999 ppm Cu n=238 | | | Moderately mineralized 1000–3000 ppm Cu n=102 | | | Mineralized >3000 ppm Cu n=141 | | |
|---|---|---|---|---|---|---|---|---|---|---|---|---|---|---|---|---|
| | | Median | Mean | Range | Median | Mean | Range | Median | Mean | Range | Median | Mean | Range | Median | Mean | Range |
| Cu | ppm | 22 | 31.3 | 0.5*-99.0 | 177 | 185.6 | 100.0-299.0 | 557.5 | 571.1 | 301.0-991.0 | 1707 | 1817 | 1000-2998 | 7263 | 12305 | 3011-98015 |
| Au | ppb | 0.5 | 6 | 0.5*-710.0 | 3 | 39.4 | 0.5*-3107 | 7 | 31.3 | 0.5*-986 | 31 | 48.1 | 0.5*-318.0 | 178.5 | 337.3 | 0.5*-3120 |
| Ag | ppm | 0.1 | 0.21 | 0.005*-11.7 | 0.2 | 0.8 | 0.005*-34.2 | 0.35 | 0.76 | 0.005*-7.9 | 0.47 | 1.65 | 0.02-16.5 | 2.5 | 4.2 | 0.12-52.2 |
| As | ppm | 6.7 | 17.8 | 0.25*-368.0 | 15.8 | 75 | 0.25*-6519.7 | 19.1 | 112.4 | 1.0-5760 | 44.7 | 139.8 | 1.0-3863.6 | 37.3 | 87 | 4.1-2324 |
| Ba | ppm | 1110 | 2099 | 6.4-44983 | 1125.4 | 1831 | 4.6-16994 | 869.5 | 1678 | 2.4-25243 | 871 | 1558 | 5.4-11872.1 | 893 | 2179 | 4.6-18690 |
| Be | ppm | 2.6 | 2.8 | 0.25*-11.9 | 2.9 | 3.4 | 0.25*-12.4 | 2.7 | 3.6 | 0.25*-28 | 3.3 | 3.6 | 0.25*-32.5 | 2.6 | 3 | 0.25*-11.9 |
| Bi | ppm | 0.5 | 1.3 | 0.02-27.2 | 0.9 | 3 | 0.005*-77.0 | 1.3 | 6.3 | 0.04-201.3 | 2.4 | 17.45 | 0.07-709.0 | 5.7 | 14.8 | 0.3-338.7 |
| Cd | ppm | 0.05 | 0.2 | 0.01*-10.4 | 0.05 | 0.2 | 0.01*-4.51 | 0.09 | 0.6 | 0.01*-20.9 | 0.11 | 1.49 | 0.01*-25.9 | 0.08 | 4.3 | 0.01*-65.7 |
| Co | ppm | 11.1 | 22 | 0.5-986.3 | 21.3 | 73.5 | 2.4-5064 | 30.9 | 96 | 0.9-4670.8 | 35.7 | 98.2 | 3.1-2995.5 | 36.3 | 80.2 | 2.6-1445.8 |
| Cr | ppm | 24 | 36.1 | 2.0*-1005.0 | 26 | 33.6 | 3.0*-258.0 | 27 | 31.1 | 1.0*-124.0 | 25 | 32.8 | 1.0*-305.0 | 18 | 26.7 | 2.5*-297.0 |
| Cs | ppm | 4.1 | 6 | 0.025*-105.5 | 2.8 | 4.8 | 0.025*-55.0 | 1.6 | 3.1 | 0.025*-23.4 | 1.5 | 2.4 | 0.025-19.3 | 1.76 | 3 | 0.1-20.7 |
| F | ppm | 1130 | 1304 | 90.0-8665 | 1008 | 1844 | 25.0*-46523 | 1138 | 2714 | 184.0-38709 | 1669 | 2608 | 266.0-24181 | 2131 | 4000 | 118.0-76476 |
| Ga | ppm | 17.4 | 16.1 | 1.6-66.9 | 17.8 | 17.5 | 1.2-51.19 | 17.2 | 17.7 | 0.6-50.9 | 17.5 | 17.13 | 2.2-38.3 | 13.7 | 14.7 | 0.05-50.07 |
| Ge | ppm | 0.65 | 0.7 | 0.025*-4.0 | 1 | 1 | 0.025*-3.4 | 1.11 | 1.2 | 0.05-3.8 | 1.1 | 1.2 | 0.025*-5.7 | 1.1 | 1.2 | 0.025*-4.9 |
| Hf | ppm | 4.7 | 5.3 | 0.05*-35.0 | 4.7 | 5.1 | 0.2-16.8 | 4 | 4.6 | 0.05*-16.7 | 3.1 | 3.4 | 0.2-15.3 | 2.6 | 2.9 | 0.05*-10.5 |
| In | ppm | 0.1 | 0.2 | 0.0025*-3.0 | 0.23 | 0.4 | 0.008-4.42 | 0.25 | 0.4 | 0.011-2.85 | 0.41 | 0.5 | 0.005-1.528 | 0.5 | 0.76 | 0.014-9.4 |
| Li | ppm | 24.8 | 36.5 | 1.4-325.8 | 23.4 | 33.4 | 0.4-441.9 | 25.7 | 38.2 | 1.7-467.0 | 25 | 35.5 | 2.3-187.0 | 30.1 | 51.6 | 3.1-482.0 |
| Mn | ppm | 934 | 2388 | 77.5*-23776 | 2246 | 4340 | 77.5*-90458 | 2603 | 4900 | 77.5*-71794 | 3060 | 9039 | 77.5*-66697 | 1659 | 3817 | 77.5*-27107 |
| Mo | ppm | 0.9 | 3.4 | 0.05*-291.4 | 1.4 | 8.6 | 0.05*-969.6 | 1.9 | 7.6 | 0.2-500.5 | 3.1 | 7.5 | 0.3-76.5 | 5.6 | 16.5 | 0.2-199.7 |
| Nb | ppm | 11 | 12.2 | 0.025*-73.9 | 12 | 12.1 | 0.025*-46.3 | 11.1 | 11 | 0.025*-38.0 | 7.3 | 8.2 | 0.025*-23.0 | 9.6 | 13 | 0.05-122.9 |
| Ni | ppm | 9 | 15 | 0.5*-207.0 | 16 | 22.4 | 0.5*-168.0 | 19 | 29.4 | 0.5*-254.0 | 29 | 39.6 | 3.0-272.0 | 29 | 51.7 | 0.5*-412.0 |
| Pb | ppm | 15 | 31.4 | 1.9-1522 | 16 | 47.3 | 2.5-1641 | 15 | 71.9 | 2.5-1627 | 22.1 | 171.2 | 2.1-2400 | 23.6 | 305.1 | 2.5-5098 |
| Pd | ppb | 0.5 | 0.9 | 0.5*-71.0 | 0.5 | 1.8 | 0.5*-20.0 | 0.5 | 3.1 | 0.5*-34.0 | 0.5 | 1.3 | 0.5*-4.0 | 0.5 | 1 | 0.5*-7.0 |
| Pt | ppb | 0.5 | 0.7 | 0.5*-21.0 | 0.5 | 1 | 0.5*-13.0 | 0.5 | 1.6 | 0.5*-16.0 | 0.5 | 0.8 | 0.5*-2.0 | 0.5 | 0.8 | 0.5*-4.0 |
| Rb | ppm | 242.9 | 237.6 | 0.3-836.6 | 199.9 | 203.3 | 0.8-578.0 | 151.3 | 165.9 | 0.4-730.0 | 83.2 | 125.7 | 0.3-528.1 | 72.9 | 111.9 | 0.6-622.7 |
| Re | ppm | 0.001 | 0.002 | 0.001*-0.07 | 0.002 | 0.005 | 0.001*-0.18 | 0.003 | 0.011 | 0.001*-0.475 | 0.003 | 0.009 | 0.001*-0.134 | 0.007 | 0.039 | 0.001*-1.25 |
| S | ppm | 345.5 | 1052 | 25*-32143 | 900 | 2152 | 25*-22740 | 1880 | 5244 | 25*-45726 | 4212 | 8462 | 25*-77700 | 10758 | 15487 | 909-133700 |
| Sb | ppm | 1.3 | 2.1 | 0.025*-33.6 | 1.9 | 2.9 | 0.025*-28.82 | 2 | 3.1 | 0.025*-26.3 | 2.2 | 3.5 | 0.6-33.64 | 2.8 | 4.6 | 0.9-48.6 |
| Sc | ppm | 10 | 11 | 0.005*-74 | 9 | 12.1 | 0.8-131.0 | 8.3 | 10.6 | 0.97-76.0 | 6.8 | 7.5 | 0.005*-24.1 | 5.8 | 6.9 | 0.005*-23.4 |
| Se | ppm | 0.13 | 1.1 | 0.13*-10.0 | 0.6 | 1.1 | 0.13*-9.0 | 0.8 | 1.5 | 0.13*-25.0 | 1.6 | 1.7 | 0.13*-5.2 | 3.7 | 5.7 | 0.13*-57.5 |
| Sn | ppm | 4 | 5.8 | 0.5*-56.0 | 5 | 7.8 | 0.5*-53.0 | 5 | 7.1 | 1.0-35.0 | 6 | 8 | 1.0-40.0 | 10 | 13.6 | 1.0-140.0 |
| Sr | ppm | 49.2 | 73.4 | 0.1*-576.8 | 47 | 65.8 | 0.1*-545.0 | 40.3 | 53.6 | 1.8-477.8 | 47.5 | 55.2 | 0.1*-269.7 | 64.2 | 111.2 | 0.1*-945.8 |
| Ta | ppm | 1.15 | 1.3 | 0.05*-11.1 | 1 | 1.1 | 0.05*-7.2 | 0.9 | 1 | 0.05*-8.1 | 0.7 | 0.7 | 0.05*-2.2 | 0.6 | 0.6 | 0.05*-1.7 |
| Te | ppm | 0.01 | 0.1 | 0.01*-7.3 | 0.1 | 0.6 | 0.01*-31.82 | 0.11 | 0.4 | 0.01*-14.24 | 0.1 | 0.5 | 0.01*-7.4 | 0.39 | 1 | 0.01*-11.4 |
| Th | ppm | 15.7 | 19.6 | 0.22-190.8 | 15.4 | 17.8 | 0.29-58.36 | 13.6 | 15.9 | 0.37-107.65 | 10.8 | 12.5 | 1.6-39.2 | 13 | 15.7 | 0.13-76.8 |
| Tl | ppm | 1 | 1.2 | 0.01*-6.2 | 0.78 | 0.9 | 0.01*-4.07 | 0.6 | 0.8 | 0.01*-5.07 | 0.5 | 0.7 | 0.01*-3.8 | 0.4 | 0.6 | 0.01*-4.1 |
| U | ppm | 5.2 | 5.9 | 0.58-43.8 | 6.9 | 9.3 | 0.22-76.7 | 6.7 | 10.4 | 0.69-168.8 | 6.8 | 14.2 | 1.2-162.6 | 10.6 | 47.1 | 1.33-972.9 |
| V | ppm | 51 | 68.7 | 5.0*-486.0 | 63 | 89.9 | 5.0*-493.0 | 65 | 92.2 | 5.0*-602.0 | 68.5 | 88.9 | 17-379.0 | 59 | 65.7 | 5.0*-216.0 |
| W | ppm | 4 | 10.1 | 0.5*-437.0 | 7 | 15.8 | 0.5*-279.0 | 7 | 15.1 | 0.5*-188.0 | 11 | 27.1 | 0.5*-253.0 | 27 | 47.5 | 0.5*-581.0 |
| Zn | ppm | 88 | 212.9 | 3.0-7038 | 127 | 217.1 | 5.0-2263 | 161 | 323.6 | 3.0-6903 | 213 | 657.8 | 5.0-8620 | 163 | 1641.3 | 0.5*-35404 |
| Zr | ppm | 169 | 201.3 | 6.0-1097.0 | 165 | 189.2 | 8.0-631.0 | 144.5 | 167.2 | 2.0-645.0 | 108.5 | 122.5 | 7.0-534.0 | 94 | 106.2 | 9.0-414.0 |
| La | ppm | 44.9 | 65.8 | 0.8-1669.1 | 50.5 | 119.4 | 1.4-2094.2 | 42.15 | 87.6 | 1.2-1988.4 | 37.9 | 104.3 | 7.3-1235.0 | 55.6 | 452.2 | 0.6-4528.8 |
| Ce | ppm | 87.2 | 117.8 | 1.8-2353.3 | 101.2 | 192.2 | 3.3-2972.4 | 79.65 | 145.5 | 2.1-3246.7 | 69.6 | 169.3 | 17.9-1862.6 | 94.7 | 727.9 | 1.4-8903.8 |
| Pr | ppm | 9.93 | 12.6 | 0.23-217.9 | 11.5 | 18.5 | 0.34-255.7 | 9.68 | 15.3 | 0.28-360.0 | 8 | 16.4 | 1.8-145.3 | 10.84 | 65.6 | 0.21-979.5 |
| Nd | ppm | 36 | 42.4 | 0.8-607.4 | 42.1 | 57.5 | 1.5-700.0 | 34.5 | 51.8 | 1.2-1350 | 29 | 51.7 | 6.9-530.1 | 40.8 | 192.9 | 1.0-3404.9 |
| Sm | ppm | 6.61 | 7.5 | 0.18-53.9 | 7.9 | 9 | 0.43-57.4 | 6.7 | 9.7 | 0.48-266.0 | 5.6 | 8.3 | 1.3-114.8 | 7.21 | 22.3 | 0.38-476.4 |
| Eu | ppm | 1.27 | 1.5 | 0.025*-11.7 | 1.64 | 2.1 | 0.08-10.8 | 1.6 | 2.5 | 0.025*-76.7 | 1.5 | 2.3 | 0.2-38.9 | 1.9 | 6.1 | 0.12-116.1 |
| Gd | ppm | 5.69 | 6.3 | 0.26-37.4 | 6.61 | 7.3 | 0.56-35.0 | 5.95 | 8.2 | 0.73-197 | 4.9 | 6.4 | 0.9-94.2 | 6.4 | 13.3 | 0.62-249.4 |
| Tb | ppm | 0.85 | 0.9 | 0.04-7.5 | 1 | 1.1 | 0.11-5.5 | 0.94 | 1.2 | 0.09-23.3 | 0.72 | 0.9 | 0.07-11.9 | 1 | 1.7 | 0.08-23.4 |
| Dy | ppm | 5.18 | 5.8 | 0.28-47.2 | 5.7 | 6.5 | 0.76-29.3 | 5.5 | 6.7 | 0.67-92.2 | 4.22 | 5.1 | 0.9-52.0 | 5.8 | 10 | 0.46-114.3 |
| Ho | ppm | 1.02 | 1.2 | 0.06-9.4 | 1.11 | 1.3 | 0.1-4.97 | 1.1 | 1.3 | 0.12-11.4 | 0.78 | 1 | 0.2-7.1 | 1.1 | 2 | 0.09-20.8 |
| Er | ppm | 2.78 | 3.3 | 0.15-24.7 | 3.05 | 3.6 | 0.39-11.1 | 2.9 | 3.4 | 0.39-15.4 | 2.18 | 2.6 | 0.4-11.9 | 3.06 | 5.3 | 0.25-53.6 |
| Tm | ppm | 0.42 | 0.52 | 0.025*-3.23 | 0.45 | 0.52 | 0.025*-1.7 | 0.43 | 0.52 | 0.025*-2.5 | 0.33 | 0.39 | 0.025*-1.7 | 0.46 | 0.8 | 0.025*-8.7 |
| Yb | ppm | 2.7 | 3.2 | 0.19-18.6 | 2.9 | 3.5 | 0.41-11.9 | 2.79 | 3.5 | 0.39-12.7 | 2.26 | 2.57 | 0.26-10.6 | 2.9 | 5 | 0.23-53.3 |
| Lu | ppm | 0.42 | 0.5 | 0.025*-2.7 | 0.46 | 0.5 | 0.025*-1.7 | 0.41 | 0.5 | 0.03-2.3 | 0.37 | 0.4 | 0.05-1.5 | 0.47 | 0.8 | 0.06-7.3 |
| Y | ppm | 29.1 | 33.5 | 1.6-263.5 | 31.9 | 36.5 | 4.4-122.1 | 29.75 | 36.2 | 3.7-300.4 | 22.45 | 27.5 | 2.7-184.1 | 29.8 | 53.3 | 2.7-554.3 |

# Geochemical Signatures of Metasomatic Ore Systems Hosting IOCG, IOA, Albitite-hosted Uranium and Affiliated Deposits: A Tool for Process Studies and Mineral Exploration

**Olivier Blein**
*Bureau de recherches géologiques et minières, Orléans, France.*
*o.blein@brgm.fr*

**Louise Corriveau**
*Geological Survey of Canada, Québec, Canada*

**Jean-François Montreuil**
*Red Pine Exploration, Sudbury, Canada*

**Kathy Ehrig**
*BHP-Olympic Dam, Adelaide, Australia*

**Adrian Fabris and Anthony Reid**
*Geological Survey of South Australia, Adelaide, Australia*

**Dipak C. Pal**
*Department of Geological Sciences, Jadavpur University, Kolkata, India*

*Recommended citation: Blein, O., Corriveau, L., Montreuil, J.-F., Ehrig, K., Fabris, A., Reid, A., and Pal, D., 2022, Geochemical signatures of metasomatic ore systems hosting IOCG, IOA, albitite-hosted uranium and affiliated deposits: A tool for process studies and mineral exploration, in Corriveau, L., Potter, E.G. and Mumin, A.H., eds., Mineral systems with iron oxide copper-gold (IOCG) and affiliated deposits: Geological Association of Canada, Special Paper 52, p. 263-298.*

## Abstract

Iron oxide copper-gold (IOCG) deposits include a wide range of hydrothermal alteration types that intensely replace their host rocks. These deposits and affiliated deposits, notably iron oxide-apatite (IOA), IOCG, skarn, albitite-hosted uranium or Au–Co–U, and polymetallic vein deposits, form through prograde, tectonically telescoped, and cyclical metasomatic paths within regional-scale iron oxide and alkali-calcic alteration (IOAA) ore systems. From the roots of the systems at the base of the upper crust to the epithermal caps, these alteration types form distinct alteration facies that prograde from: 1) Na (albitite) and local skarn to 2) high-temperature Ca-Fe, 3) high-temperature K-Fe, 4) transitional K (brecciated felsite) and K-Ca-Mg (potassic skarn), 5) low-temperature hydrolytic K-Fe and Ca-Mg-Fe, and 6) epithermal alteration. Each alteration facies has a distinct chemical composition from which to assess system maturity and potential fertility. The best geochemical discriminants for each alteration facies are the Na-Ca-Fe-K-Mg molar proportions. In parallel, the proportions of (Si + Al) in lieu of Mg best discriminates IOAA systems from those hosting epithermal, porphyry, volcanogenic massive sulphide and sedimentary-exhalative deposits. Reporting molar barcodes of characteristic cations on the IOCG discriminant diagram yields a first-order identification of metasomatic processes that affect whole-rock composition and ore deposition.

In this contribution, we investigate the footprints of key metasomatic systems from Olympic Dam, Acropolis, Punt Hill and other systems of the Olympic Copper-Gold Province, as well as similar systems from the Great Bear magmatic zone, Romanet Horst, and Singhbhum Shear Zone. The footprints of these systems provide novel tools to discriminate least-altered rocks from metasomatites, assess alteration intensity and probable protoliths, follow the incremental alteration of a host at a specific alteration facies, characterize the sequential depth-to-surface development of intense alteration, and identify tectonically telescoped metasomatic paths. Metal contents vary significantly according to alteration facies, and can be used to record metal pathways from sources to deposits. The results provide innovative exploration vectors for IOCG and affiliated deposits, and the means to assess the mineral potential of prospective settings. In addition, distinct signatures emerge for each system, enhancing the ability to model and detect these mineral systems, particularly through the processing of large corporate databases.

## Résumé

Les gîtes à oxydes de fer cuivre-or (IOCG) comportent une large gamme de faciès d'altération hydrothermale qui transforment intensément les roches hôtes. Ces gîtes et leurs gîtes affiliés, notamment ceux à oxydes de fer-apatite (IOA), IOCG, skarn, albitite uranifère ou à Au–Co–U, et veines polymétalliques se forment au cours de parcours métasomatiques progrades, télescopés, et cycliques au sein de systèmes minéralisés à oxydes de fer et altération alcali-calcique d'échelle régionale. De la racine de ces systèmes à la base de la croûte supérieure jusqu'à leurs toits épithermaux, ces types d'altération forment des faciès d'altération distincts qui évoluent de : 1) Na (albitite) et skarn local, 2) Ca-Fe à haute température, 3) K-Fe à haute température, 4) transitionnelle à K (felsite bréchifiée) ou K-Ca-Mg (skarn potassique), 5) hydrolytique à K-Fe ou Ca-Mg-Fe de faible température et 6) épithermale. Chaque faciès d'altération a des compositions chimiques distinctes à partir desquelles il est possible d'évaluer la maturité des systèmes et leur fertilité potentielle. Les compositions molaires en Na-Ca-Fe-K-Mg sont utilisées comme discriminants pour identifier les différents faciès d'altération. Les proportions molaires en silice et aluminium sont également utilisées pour discriminer les zones d'altération liées à des gîtes épithermaux, des porphyres, des sulfures massifs volcanogènes ou des systèmes sédimentaires exhalatifs. L'utilisation de ces compositions molaires au sein de codes-barres permet une visualisation rapide des différents processus métasomatiques affectant les différents encaissants.

Dans cette publication, les empreintes de systèmes métasomatiques clés de la Laurentie au Canada, du craton Gawler en Australie et d'autres exemples globaux sont décrits en utilisant des milliers d'analyses d'Olympic Dam, d'Acropolis, de Punt Hill et d'autres systèmes de la province cuivre-or d'Olympic ainsi que des données de la zone magmatique du Grand Lac de l'Ours, du Horst de Romanet et de la zone de cisaillement de Singhbhum en Inde. Les empreintes de ces systèmes fournissent de nouveaux outils pour discriminer les roches peu altérées et altérées, d'évaluer l'intensité de l'altération et la nature des protolites probables, de suivre le degré d'altération d'une roche hôte à un faciès d'altération spécifique, de caractériser le développement séquentiel depuis la profondeur jusqu'à la surface d'altération très intense et d'identifier les parcours métasomatiques télescopés tectoniquement. Les teneurs en métaux varient suivant le faciès d'altération et enregistrent les parcours métasomatiques des métaux de leurs sources jusqu'aux gîtes. Les résultats fournissent des vecteurs d'exploration innovants pour les gîtes IOCG et affiliés, et des moyens plus globaux pour évaluer le potentiel minéral de contextes d'exploration. De plus, des signatures distinctes émergent d'un système minéral à l'autre, améliorant les capacités de modélisation et de détection des systèmes minéralisés grâce au traitement de vastes bases de données.

## Introduction

Iron oxide and alkali-calcic alteration ore systems (IOAA), as defined by Porter (2010) and Corriveau et al. (2016), form through a self-propagating series of alteration facies each associated with or serving as host to distinct deposit types: iron oxide-apatite (IOA), iron oxide copper-gold (IOCG), skarn, K-skarn and albitite-hosted polymetallic deposits as well as their REE, Co, Bi, Mo, Re and U-rich variants (Corriveau et al., 2022a–e). The last decade of mapping and exploration of these mineral systems have greatly enhanced the understanding of their evolution and the range of deposits types they form as well as their global distribution and ages (Fig. 1; Hitzman et al., 1992; Barton and Johnson, 1996; Hitzman and Valenta, 2005; Williams et al., 2005; Chen, 2013; Wilde, 2013; Barton, 2014; Montreuil et al., 2015; Corriveau et al., 2016, 2018b, 2022c).

The alteration facies are defined by diagnostic mineral assemblages that show a progressive, systematic evolution from the roots of the IOAA systems to the paleosurface epithermal caps distal from heat sources (Corriveau et al., 2016). This systematic evolution is marked by significant changes in bulk-rock compositions from one facies to another (Fabris et al., 2013; Montreuil et al., 2013; Corriveau et al., 2022b; Fabris, 2022). Disruption to the prograde metasomatic path (e.g. heat or external fluid ingress to the main fluid plume) resets the physicochemical conditions of the fluid plume and results in permutations of the prograde alteration facies. Faulting can lead to telescoping or repetition of alteration facies and local disruption of the prograde sequence. The juxtaposition, overprinting, tectonic telescoping, renewal and retrogression of alteration facies can be identified and mapped using diagnostic chemical signatures (Montreuil et al., 2013, 2015, 2016a–c; Corriveau et al., 2016, 2022a–d). Mineralization formed through prograde metasomatism consists first of IOA and local iron skarn deposits that mark the most intense development of magnetite-dominant high-temperature (HT) Ca-Fe alteration after early Na and HT Na-Ca-Fe alteration. Rare earth element (REE)-rich variants form within systems that were able to evolve to potassium-bearing facies. Other deposit types include: 1) cobalt-rich IOCG variants that are coeval with transitional HT Ca-Fe-K alteration; 2) magnetite-group IOCG deposits that form during HT K-Fe alteration; 3) polymetallic K-skarn and magnetite-to-hematite group IOCG deposits that form at the magnetite-to-hematite HT to LT transition during K-Fe alteration; and 4) hematite-group IOCG deposits that form at the LT K-Fe to LT Ca-Mg-Fe facies (Williams, 2010a; Corriveau et al., 2022c).

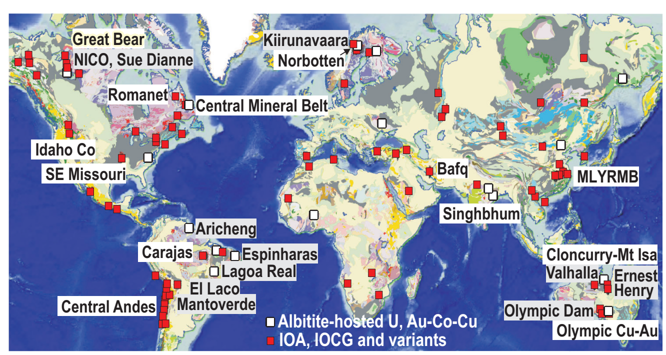


**Figure 1.** Distribution of IOCG, IOA and affiliated deposits (red squares) and albitite-hosted uranium deposits (white squares) (Williams et al., 2005; Corriveau et al., 2018b and references therein) on geological map of the world (Chorlton, 2007). *MLYRMB*: Middle-Lower Yangtze River metallogenic belt.

The chemical evolution of IOAA systems does not conform to simple zoning models such as porphyry systems. Instead, the hydrothermal alteration zones have kilometre-scale vertical and lateral dimensions that show significant variation in geometry, largely as a function of depth, rock composition, and orientation of regional scale discontinuities and more permeable zones. In IOAA systems, bulk chemical and mineral assemblage changes in host rocks are extensive and pervasive. The systems chemically and texturally transform host rocks over hundreds of square kilometres and depths reaching 10–15 km (Mumin et al., 2007; Hayward, 2013; Corriveau et al., 2016), in response to the evolving physicochemical conditions of the ascending fluid plume (Corriveau et al., 2022c). As in other deposit types and ore systems (e.g. Franklin, 1997; Large et al., 2001; Warren et al., 2007; Madeisky and Stanley, 2010), whole-rock composition provides a useful tool to detect prospective hydrothermal alteration at regional scales and to vector towards mineralization (this work; Montreuil et al., 2013).

In IOAA systems, each alteration facies has a diagnostic chemical signature illustrated by molar barcodes calculated from whole-rock geochemical analyses (Appendix 1; Corriveau et al., 2016, 2017, 2018a). On the IOCG geochemical alteration discrimination diagram of Montreuil et al. (2013), the molar barcodes (Na-Ca-Fe-K-Mg and/or Na-Ca-Fe-K-(Si + Al)/10) allow metasomatic rocks to be distinguished from least-altered rocks, even when they plot within the least-altered fields of the diagram. The molar barcodes make it easy to recognize the main alteration types, and to discriminate complex alteration types associated with telescoped, superimposed, prograde to retrograde or cyclical metasomatic paths. Though the barcodes serve as very useful proxies for the diagnostic minerals of the alteration facies, they are not generated from automated mineralogy or petrography scans and as such do not represent the quantitative proportion of minerals.

In this paper, we present the chemical metasomatic footprints of prospects and deposits of the Great Bear magmatic zone, the Olympic Copper-Gold Province of the Gawler Craton (Australia), the Mantoverde district in the Central Andes (Chile), the Singhbhum shear zone (India) and the Romanet Horst in the Labrador Trough (Quebec) (Fig. 1). The metasomatic footprints of these districts track the chemical evolution of the ore systems that form magnetite- and hematite-group IOCG, magnetite-rich Au-Co-Bi-Cu deposits, and albitite-hosted uranium deposits.

## Mineral Systems

Iron oxide and alkali-calcic alteration systems and their iron oxide-apatite (IOA), iron oxide copper-gold (IOCG) and affiliated deposits form through the ascent of an evolving fluid plume that intensely alters host rocks regionally into a series of distinctive alteration facies, each with their own set of mineral assemblages and chemical composition (Mumin et al., 2010; Corriveau et al., 2016, 2022a–c and references therein). Where most intense, the composition of alteration becomes largely independent of the composition of the host rocks whether they were volcanic, volcaniclastic, hypabyssal intrusive or sedimentary in origin (Montreuil et al., 2013, 2016a–c).

Six main alteration facies form as highly saline fluid columns rise towards surface and cool. From high to low temperatures (HT to LT) the facies are: Facies 1, Na (albite, scapolite); Facies 2, HT Ca-Fe (amphibole, magnetite, apatite ± clinopyroxene; transient skarn with clinopyroxene and garnet; and Na-Ca-Fe assemblages with albite, amphibole ± scapolite, magnetite, clinopyroxene and apatite); Facies 3, HT K-Fe (K-feldspar, biotite, magnetite); Facies 4, HT K-skarn (clinopyroxene, garnet, K-feldspar) and K-felsite (K-feldspar); Facies 5, LT hydrolytic K-Fe to Ca-Mg-Fe (K-feldspar, white mica, hematite, carbonates, chlorite, barite, fluorite); and Facies 6, epithermal alteration types and late stage veins.

Epithermal alteration develops late and at higher structural levels than the IOAA systems or can be superimposed on any component of a system if the temperature regime of the system collapses, as described by Mumin et al. (2010) and Kreiner and Barton (2017). Silicification, and phyllic, argillic and advanced argillic alteration are included within the GBMZ, Olympic Dam deposit and Romanet Horst sample sets.

### *Early Albitization, HT Na-Ca-Fe and Skarn Alteration*

Early alteration facies (Na, Fe-skarn, HT Ca-Fe, and transitional Na-Ca and HT Na-Ca-Fe) are laterally extensive at the deepest levels of alteration systems (commonly above subvolcanic intrusions), and along regional fault zones and splays. Skarn (clinopyroxene- to calcic garnet-dominant Ca-Mg ± Fe assemblages) can be the earliest alteration type where early intrusions were emplaced prior to IOAA metasomatism, such as at the Mary Kathleen uranium-REE deposit in Australia (Oliver et al., 1999) and in the Middle-Lower Yangtze River metallogenic belt in China (Yu et al., 2011). Skarn alteration is also coeval with or postdates albitization in the presence of carbonate rocks, and is generally spatially associated with zones of albitite, not intrusions (Corriveau et al., 2022d). Skarn assemblages evolve to and are replaced by amphibole or magnetite-rich HT Ca-Fe alteration in the Great Bear magmatic zone (GBMZ) and Middle-Lower Yangtze River metallogenic belt (Hu et al., 2019; Corriveau et al., 2022c). In IOA and IOCG districts, skarn zones can also form without significant precipitation of iron oxides, such as at Punt Hill in Australia (Reid et al., 2011; Fabris et al., 2018a, b).

The Na, HT Na-Ca-Fe and skarn facies are largely barren in terms of metals and are not the immediate host to IOCG deposits unless tectonically telescoped to higher crustal levels and infiltrated by lower temperature fluids that form breccias, replacement zones, vein systems and mineralized zones displaying K-skarn, HT to LT K-Fe and/or LT Ca-Mg-Fe alteration (Corriveau et al., 2014, 2016; Montreuil et al., 2015, 2016b; Hayward et al., 2016). Consequently, these early facies are typically under-represented in corporate geochemical databases, particularly in districts devoid of albitite-hosted U, Au, Co or Au-Co-U deposits. In some cases, they can also be misinterpreted as common unaltered rocks such as syenite, quartzite, amphibolite, etc., and not systematically sampled (Corriveau et al., 2022b).

*High-temperature Ca-Fe Alteration*

The HT Ca-Fe alteration facies can host IOA mineralization. Rare earth elements (REE) precipitate during IOA mineralization within systems that mature to K-Fe alteration facies (Corriveau et al., 2016, 2022a). Although commonly drilled due to their prominent magnetic anomalies (Mumin et al., 2007), early exploration programs rarely analyzed these units for REE and other critical metal contents (Potter et al., 2019).

*Transitional HT Ca-K-Fe Alteration*

The HT Ca-K-Fe alteration facies hosts cobalt- and bismuth-rich variants of IOCG deposits that commonly include arsenopyrite as the dominant sulphide. This facies is most extensive in sedimentary sequences that include carbonate rocks; within such sequences, mineralization is largely stratabound (e.g. NICO deposit of the Idaho Cobalt Belt: Slack, 2013; Montreuil et al., 2016b).

*High- to Low-temperature K-Fe Alteration*

The HT and LT K-Fe alteration facies host polymetallic magnetite- and hematite-group IOCG deposits such as their respective archetypes, the Ernest Henry and Olympic Dam deposits in Australia (Williams et al., 2005; Williams, 2010a; Corriveau et al., 2022d).

Within the HT K-Fe facies, biotite (with magnetite) may crystallize, but K-feldspar is most commonly the dominant potassic phase (e.g. Ernest Henry deposit; Williams, 2010b; Zhao et al., 2017). As this alteration intensifies, magnetite contents increase gradually and replace earlier K-feldspar and biotite (Corriveau et al., 2022d). Zones of magnetite alteration are also present at depth and as relics throughout the deposits at Olympic Dam and Acropolis in the Olympic Copper-Gold Province, and Sue Dianne in the GBMZ (Mumin et al., 2010; Ehrig et al., 2012, 2017a, b).

During LT K-Fe alteration, which hosts the most heavily mineralized zones, hydrothermal K-feldspar is gradually replaced by sericite, while hematite content increases. Hematite precipitation above a certain threshold results in largely barren zones with quartz at the Olympic Dam deposit (Ehrig et al., 2012), and in gold mineralization barren of copper at the Prominent Hill deposit in the Olympic Copper-Gold Province (Schlegel and Heinrich, 2015). The coupling of these mineral variations with ore grades led Schlegel and Heinrich (2015) to define a hematite-quartz index and prospective ranges of K/Al and Fe/Si in iron oxide breccias. Barite, fluorite and carbonates can be abundant in the late stages of LT K-Fe alteration.

Magnetite to hematite-group IOCG deposits form through three main evolutionary pathways: 1) early magnetite-bearing alteration that evolves to hematite-bearing alteration, creating zoned deposits; 2) replacement of magnetite by hematite during evolution of a single system (e.g. through changes in temperatures and degree of oxidation related to cooling of fluids, fluid mixing or magma emplacement); and 3) hydrothermal alteration of magnetite-rich ironstones, resulting in the precipitation of hematite and sulphides. This process is also common where ironstones, formed through early stratabound magnetite-rich alteration, have been subsequently hematized (e.g. by being thrust into the field of hematite precipitation, or where fluid mixing induces crystallization of hematite-bearing alteration facies).

Types 1 and 2 above are end members in a spectrum of deposits that form under spatial and/or temporal variations in hydrothermal conditions. For example, Olympic Dam is the archetype of hematite-group IOCG deposits, but the discovery of magnetite-rich zones at depth (Apukhtina et al., 2017) illustrates that giant hematite-group IOCG deposits can be the upper-level end member of systems that also crystallized magnetite in abundance at depth.

*Potassic-skarn and Low-temperature Ca-Mg-Fe Alteration*

Potassic skarn and associated polymetallic mineralization forms at the magnetite-to-hematite transition where carbonate and carbonaceous host rocks are present (e.g. Wang and Williams, 2001), or within earlier-formed carbonate alteration zones by cooling of fluids after magnetite crystallization, such as the Mile Lake prospect in the GBMZ (Mumin et al., 2010; Corriveau et al., 2022d). Zones of K-feldspar-rich felsite form at this transition or as envelopes around iron oxide-rich breccias and ore zones (e.g. Ernest Henry deposit: Mark et al., 2006; Rusk et al., 2010; Sue Dianne deposit: Mumin et al., 2010; Montreuil et al., 2016b). In some cases, K-feldspar-rich alteration can be orthomagmatic, or constitute the upper parts of the IOAA system, leading to extensive potassic haloes that typically are not brecciated or spatially associated with iron oxides. Such potassic haloes have been observed to be intense and extensive above the NICO deposit (Shives et al., 2000), irregular and of weak-to-moderate intensity above and within dioritic subvolcanic intrusions, and locally strong in an albitite corridor in the GBMZ (Mumin et al., 2010; Montreuil et al., 2015, 2016b). The development of large-scale potassic alteration is well illustrated in the classic model of Hitzman et al. (1992) and is represented in the Great Bear and the Olympic Dam databases.

Many systems evolve to iron oxide-rich, iron oxide-poor, and iron-poor LT Ca-Mg-Fe alteration with highly variable metal associations (Corriveau et al., 2022c). The albitite-hosted uranium-gold mineralization of the Romanet Horst in Quebec (Canada) serves as a case example in which the LT Ca-Mg-Fe facies is dominated by dolomitization, whereas the Scadding albitite-hosted gold deposit in Ontario (Canada) features intense LT Ca-Mg-Fe alteration dominated by chlorite (Corriveau et al., 2022c).

*Additional Alteration Types*

Overprinting of alteration types induced by active tectonics or magma emplacement during metasomatism can generate deposit types with hybrid metal associations in addition to deposits formed through prograde metasomatism. For example, albitite zones overprinted by HT to LT K-Fe and LT Ca-Mg-Fe and epithermal facies form preferential traps for the precipitation of U and Au-Co-U. This telescoping leads to albitite-hosted U and Au-Co-U deposits (Montreuil et al., 2015; Potter et al., 2019, 2022).

## Chemical Discriminants of Metasomatic Reaction Paths

*Molar Barcodes*

The main alteration facies of IOAA systems have distinctive and diagnostic molar proportions of sodium (Na), calcium (Ca), potassium (K), iron (Fe), and magnesium (Mg) that differ significantly from common igneous, metamorphic or sedimentary rocks (Montreuil et al., 2013, 2016b). These proportions are portrayed as barcodes, in which cations act as proxies for minerals that characterize the main alteration facies (Fig. 2; Appendix 1; Corriveau et al., 2016, 2017). Sodium, shown in pink, reflects early Na alteration that is light pink to white in its most intense expression (albitite). Calcium proportions are dark green for the diagnostic dark-green amphibole of the HT Ca-Fe alteration zone. Iron proportions are black, reflecting the presence of iron oxides within HT Ca-Fe and K-Fe alteration facies, and potassium proportions are red as per the brick-red K-feldspar that characterizes K-Fe alteration zones. Finally, magnesium proportions are bright green, reflecting the abundant chlorite in some late hydrolytic LT Ca-Mg-Fe alteration facies.

As displayed in Figures 2 to 5, one or two elements dominate the molar proportions of metasomatic rocks in contrast to the molar proportions of elements in common volcanic and intrusive rocks (Figs. 2, 3) or sedimentary rocks (Fig. 4) which are comparatively equal. Common rocks with only one or two dominant cations include rhyolite, trondhjemite, ultramafic rocks, quartzite and quartz-rich sandstone (Figs. 2, 4, 5).

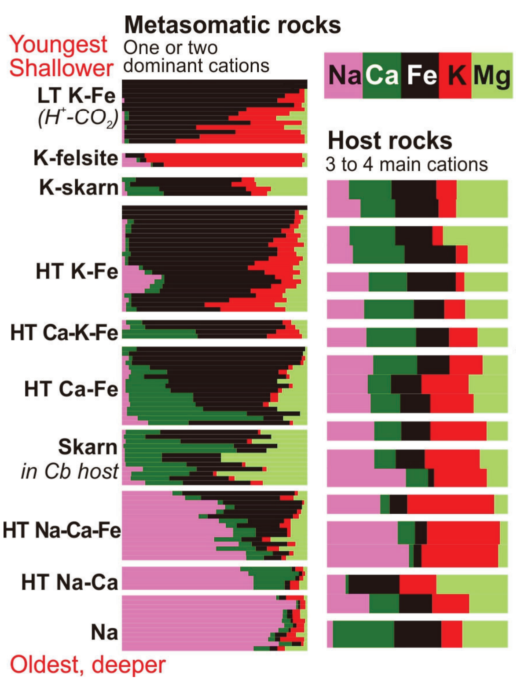


FIGURE 2. Na-Ca-Fe-K-Mg molar barcodes of sedimentary, volcanic and plutonic rocks versus barcodes of IOAA metasomatites from the GBMZ (diagram from Corriveau et al., 2018b; dataset from Corriveau et al., 2015). Barcodes of high and low temperature K-Fe metasomatites can be similar.

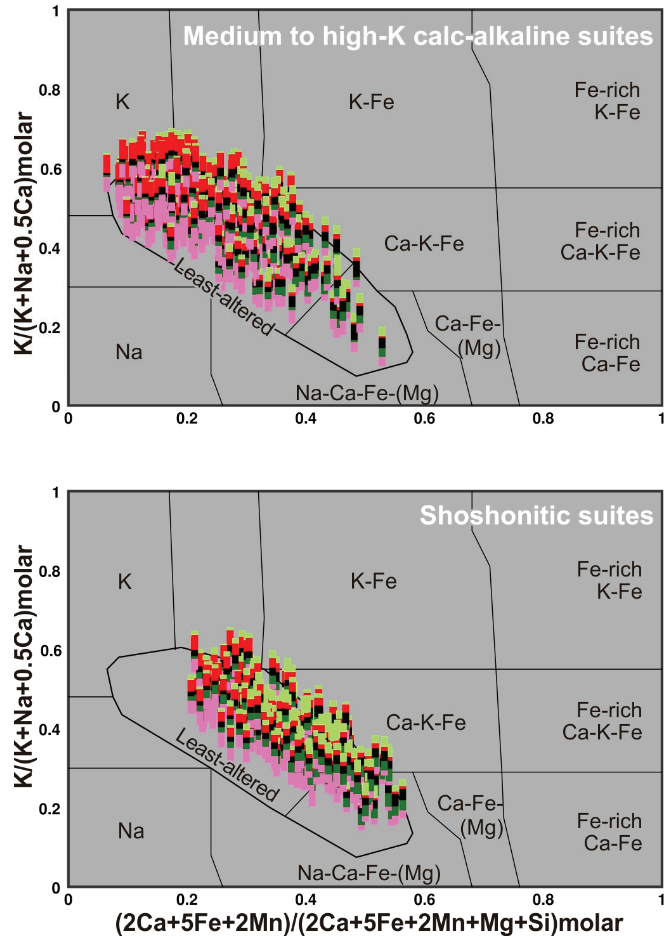


FIGURE 3. Molar proportion barcodes of igneous rocks on the AIOCG diagram of Montreuil et al. (2013). **A.** Medium to high-potassium calc-alkaline suites. **B.** Shoshonitic suites. Calc-alkaline and shoshonitic suites data compiled from GEOROC database (http://georoc.mpch-mainz.gwdg.de/georoc/).

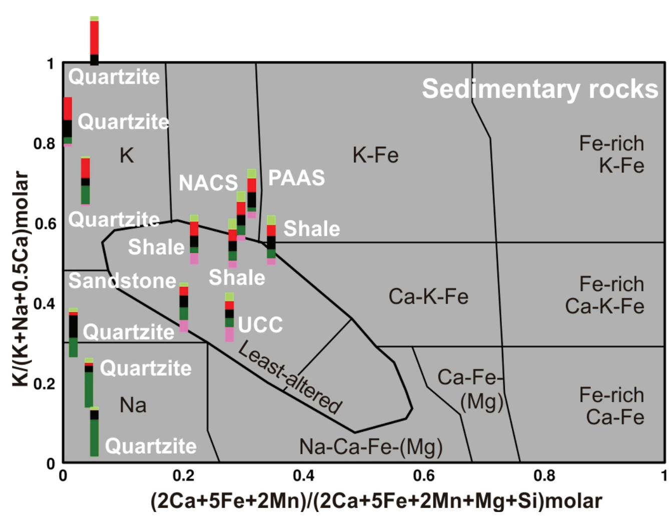


FIGURE 4. Molar proportion barcodes of sedimentary rocks plotted on the AIOCG diagram of Montreuil et al. (2013). Data compiled from Pettijohn (1975), Gromet et al. (1984), and Baiyegunhi et al. (2017).

The barcodes can be used to map alteration facies at regional or deposit scales (Montreuil et al., 2016b), display evolving alteration in boreholes, or supplement chemical discriminant diagrams such as the Montreuil et al. (2013) alteration indices for iron oxide copper-gold alteration facies (AIOCG) plot. The effective use of barcodes stems from the significant changes induced in host rock compositions as a main fluid plume ascends through the upper crust to form IOAA systems (Fig. 6), and the very distinct signatures of deposit types (Fig. 7). For example, iron oxide and alkali-calcic alteration facies can be distinguished from alteration types in epithermal, porphyry or VMS deposit types by their respective molar proportions of (Si + Al)/10 (Corriveau et al., 2018a, 2022a). In IOAA systems, each alteration facies corresponds to a marked change in major element composition and to distinct ore mineral deposits having characteristic suites of barcodes (Fig. 7). However, the molar proportions of the defining cations in the mineral assemblages composing each alteration facies may vary due to variations in alteration intensity, mineral contents of the protoliths and metasomatites, and physicochemical conditions of the fluids (Figs. 2, 6).

*AIOCG Discriminant Diagram*

Field assessment of alteration intensity and extent using qualitative terminology such as weak, moderate, strong, intense, megascopically complete or selective-patchy-pervasive, are essential to understand and map IOAA alteration zones (Corriveau et al., 2022b). In addition, quantitative tools abound for measuring and discriminating alteration intensity (Leitch and Lentz, 1994; Large et al., 2001; Benavides et al., 2008; Montreuil et al., 2013; Schlegel and Heinrich, 2015). Alteration indexes and discriminant diagrams allow characterization of specific types of alteration and quantification of elemental gains and losses.

In IOAA systems, each alteration facies has distinct mineral assemblages, hence distinct major element compositions, associated metal associations and enrichments (this work; Corriveau et al., 2022a). HT Ca-Fe alteration may evolve to precipitate massive quantities of fluorine, phosphorus and REE as magnetite ± phosphate and REE-bearing minerals, forming IOA deposits. Mineralized zones formed at the HT Ca-K-Fe facies are enriched in As, Au, Co, and variably enriched in Bi,

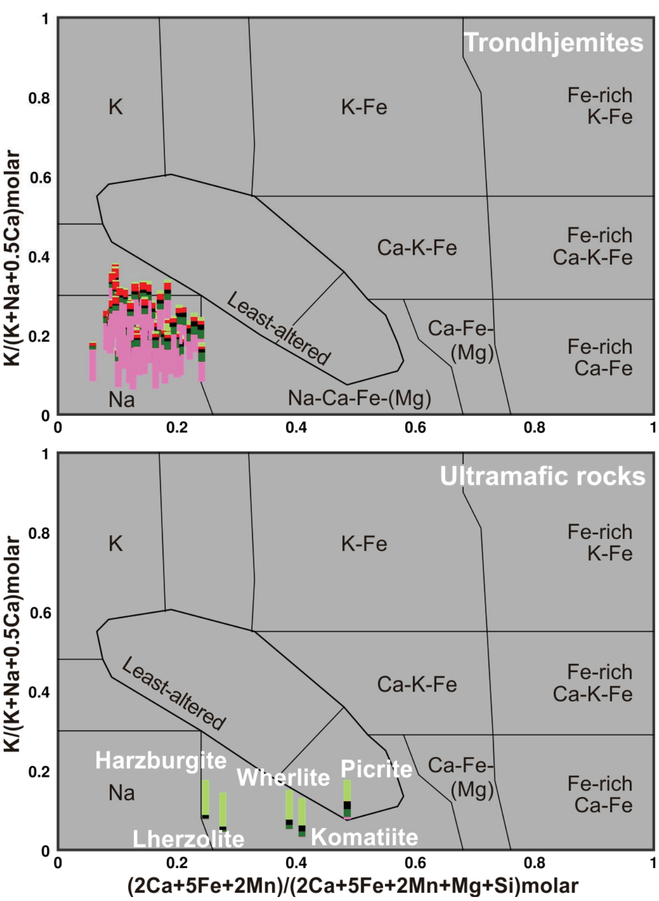


**FIGURE 5.** Molar proportion barcodes of trondhjemite and ultramafic rocks plotted on the AIOCG diagram of Montreuil et al. (2013). **A.** Trondhjemites of tonalite-trondhjemite and granodiorite (TTG) suites. **B.** Ultramafic rocks. TTG suites and ultramafic rocks data compiled from GEOROC database (http://georoc.mpch-mainz.gwdg.de/georoc/).

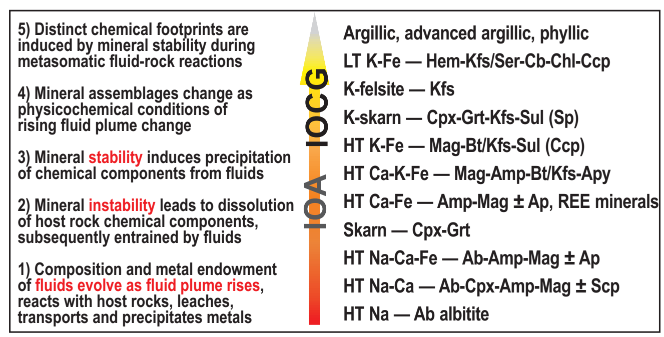


**FIGURE 6.** Processes leading to the distinctive alteration facies (Corriveau et al., 2018b). Sul: sulphides; other mineral abbreviations in Whitney and Evans (2010).

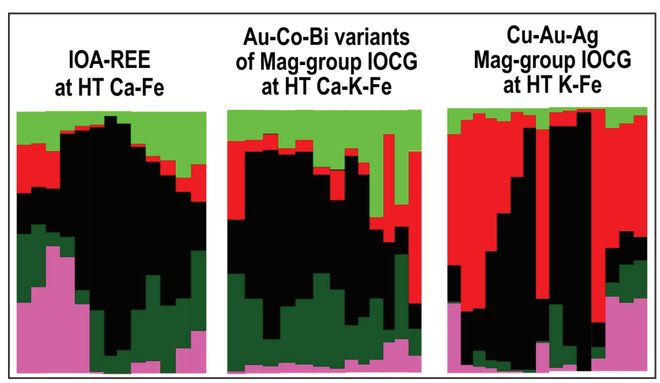


**FIGURE 7.** Representative molar Na-Ca-Fe-K-Mg barcodes of IOA mineralization (Terra mine), cobalt-rich IOCG variant (NICO deposit) and IOCG mineralization (Summit Peak showing in volcanic rocks overlying the NICO deposit) from the Great Bear magmatic zone. Each deposit type displays barcodes with a very high molar proportion of iron.

Cu, Ni, REE including HREE and W. HT K-Fe alteration zones are variably enriched in As, Ag, Au, Co, Cu, REE, and U., and finally, mineralization types possible at the LT K-Fe/LT Ca-Mg-Fe facies include hematite-group Cu-Ag-Au-(light REE, U) IOCG mineralization; iron-rich Au-(Co, Cu, Bi, U) mineralization; iron-poor Cu-Zn-Pb-(Ag, Au) mineralization; iron-poor Mo-Re mineralization; and iron-rich Cu-Ag-Au-(Zn-Pb) mineralization hosted in variably potassic skarn.

Major element whole-rock geochemical data provide significant information on the evolution of mineral systems and deposits, helps optimize mineral exploration strategies and mineral potential mapping, and can provide vectors to areas of more intense alteration and mineralization.

The AIOCG alteration index of Montreuil et al. (2013) uses molar concentrations calculated from whole rock analyses to create a visual representation of the geochemical signature and mineralogy of a rock (Pearce, 1968; Stanley and Madeisky, 1994; Grunsky and Bacon-Shone, 2011). The major elements in the IOCG alteration index encompass all the geochemical variations observed in IOCG-related ore systems. Moreover, these elements are commonly and precisely determined during whole-rock geochemical analysis, allowing reprocessing of large historical datasets to better guide mineral exploration in prospective settings.

The first index (AIOCG 1), or y-axis of the AIOCG diagram, is based on Principal Component Analysis (PCA) results demonstrating that potassium, sodium and calcium are key elements in discriminating Na, K and Ca-Fe alteration, combined with a modified Madeisky (1996) index (K/(K+Na+2Ca)molar), used to quantify potassium metasomatism. The weight of calcium is reduced in comparison to the Madeisky (1996) index to accentuate the contrast between sodium- and potassium-rich alteration (e.g. Ernest Henry deposit, Mark et al., 2006; Hitzman et al., 1992). The second index, AIOCG2, defined as (2Ca+5Fe+2Mn)/(2Ca+5Fe+2Mn+Mg+Si)molar and x-axis of the AIOCG diagram, is designed to discriminate alkali (Na-K) alteration from Ca-Fe, K-Fe and Fe alteration. The addition of molar barcodes to the Montreuil et al. (2013) plot further discriminates the main alteration facies and provides a means to identify increasing alteration intensity, and prograde or overprinting prograde to retrograde alteration (Corriveau et al., 2017, 2022a).

On the AIOCG diagram and in the molar barcodes, sodium serves as a proxy for sodium-rich minerals formed during Na alteration (albite and scapolite). Calcium is a proxy for calcium-rich minerals usually formed during HT Ca-Fe alteration (amphibole, apatite), in skarn (clinopyroxene, and andradite to grossular garnet), and in calcium-bearing scapolite formed during Na-Ca and Na-Ca-Fe alteration. Manganese may also act as a proxy for HT Ca-Fe alteration. In addition, calcium enables identification of LT Ca-Mg-Fe alteration and fluorite enrichment associated with LT K-Fe to iron-dominant facies (e.g. Olympic Dam: Ehrig et al., 2012). Iron is a proxy for iron oxides and for the commonly iron-rich nature of ferromagnesian silicates. Potassium is a proxy for potassium-rich minerals (K-feldspar, biotite, sericite) of the K, K-Fe, phyllic and sericitic alteration facies. K-feldspar, biotite, and sericite have high AIOCG 1 index values (greater than 0.95), and diverse AIOCG 2 index values related to varying iron and magnesium contents (Fig. 8). Silica is a proxy for sodium- and potassium-bearing minerals because of the positive covariation of silica with those elements.

In Figure 8, chemical data for some hydrothermal minerals from the NICO deposit in the GBMZ (Sidor, 2000) are plotted on the AIOCG diagram. Amphiboles have low AIOCG 1 index values (less than 0.30) because of high calcium and low potassium contents, whereas AIOCG 2 index values range from 0.45 to 0.80, depending on magnesium content (Fig. 8). Clinopyroxenes are characterized by very low AIOCG 1 index values (less than 0.05), and AIOCG 2 index values between 0.60 and 0.80 (Fig. 8).

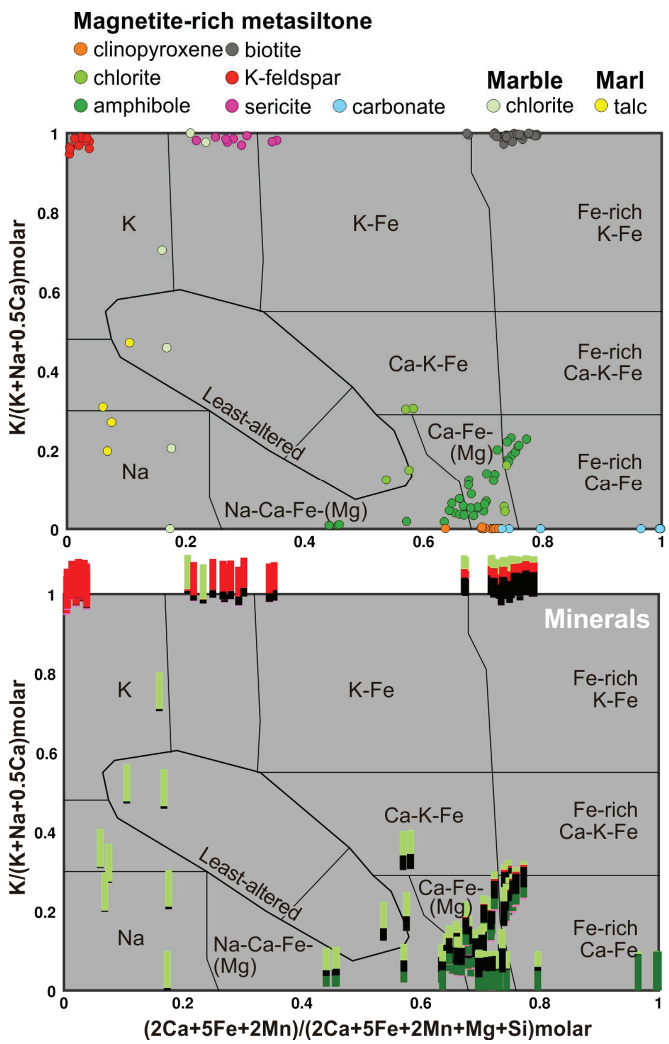


**FIGURE 8.** Minerals common in IOAA systems plotted on the AIOCG diagram of Montreuil et al. (2013). **A.** Minerals from marls, carbonates, skarn, HT Ca-Fe metasomatites and magnetite-altered metasiltstones, analyzed by Sidor (2000). **B.** Na-Ca-Fe-K-Mg molar barcodes of minerals in A.

Magnetite-rich or hematite-rich K-Fe and Ca-Fe alteration types become increasingly depleted in silica and aluminum as the alteration matures to iron end-members. The Fe/Mg ratio is used to discriminate HT Ca-Fe and Fe alteration from unaltered mafic rocks by emphasizing enrichment of iron over magnesium in HT Ca-Fe and K-Fe IOCG alteration. This enrichment in iron results in Fe/Mg ratios considerably greater than those normally observed in unaltered or weakly altered mafic rocks because of the abundance of iron oxides, iron-rich amphibole, iron-rich chlorite and iron-rich biotite in the altered rocks. In sedimentary rocks, chlorites have barcodes dominated by magnesium (Fig. 8), whereas in ironstones, chlorite barcodes are dominated by magnesium and iron (Fig. 8). In mineralized zones, chlorite is commonly rich in iron (e.g. Olympic Dam deposit and Emmie Bluff prospect: Huntington et al., 2004; Mauger et al., 2016).

*Data Processing*

Geochemical databases were processed from the GBMZ (Corriveau et al., 2015), Olympic Dam deposit (Ehrig et al., 2012; Dmitrijeva et al., 2019; BHP-Olympic Dam, unpublished data), Olympic Copper-Gold Province (Geological Survey of South Australia; via South Australian Resources Information Gateway https://map.sarig.sa.gov.au/), Mantoverde district (Benavides et al., 2008), Singhbhum Shear Zone (Pal et al., 2011a), and Romanet Horst (McLaughlin et al., 2016).

In order to track the geochemical evolution of hydrothermal alteration and metal associations within IOAA systems, attempts were made to avoid samples that could be laden with later veins or superimposed alteration, such as silicification, and argillic (or advanced argillic) alteration. In some cases, it was impossible to avoid overprints, especially in mineralized zones such as albitite-hosted uranium deposits. The use of barcodes provides an efficient method to identify superimposed alteration and propose a first-order characterization of alteration end-members involved. Samples affected by argillic to advanced argillic alteration, or silicification, are characterized by Na-Ca-Fe-K-(Si + Al)/10 barcodes in which (Si + Al)/10 constitutes more than 75% of the barcodes.

## Prograde and Telescoped Reaction Paths across Systems of the Great Bear Magmatic Zone

In IOAA ore systems with a simple prograde path, the metasomatic footprints are vertically zoned from deeper Na (albite), through HT Ca-Fe (amphibole-magnetite-apatite), K-Fe (magnetite-biotite-K feldspar to shallower hematite-K feldspar-sericite-chlorite-carbonate) and epithermal or phyllic alteration facies. The preserved prograde development of these systems was observed in the Great Bear magmatic zone along tilted sections, representing a few kilometres in paleo-depth (Corriveau et al., 2016, 2022d), or assessed at district scales using borehole data and large-scale lithogeochemical databases (e.g. Olympic Copper-Gold Province in Australia: Ehrig et al., 2012, 2017b; Dmitrijeva et al., 2019; this work).

Mineral deposits of the Great Bear magmatic zone (Canada) were among the Proterozoic case examples used to develop the classic genetic models for hydrothermal IOCG and iron oxide-apatite (IOA) deposits of Hitzman et al. (1992). The onset of continental arc volcanism at ca. 1.87 Ga was largely andesitic in the northern portion of the arc, and andesitic to rhyolitic and uranium-rich in the south (Fig. 9; Hildebrand et al., 2010; Ootes et al., 2013). Late Great Bear magmatism consists of a belt of 1.85 Ga, A-type granite

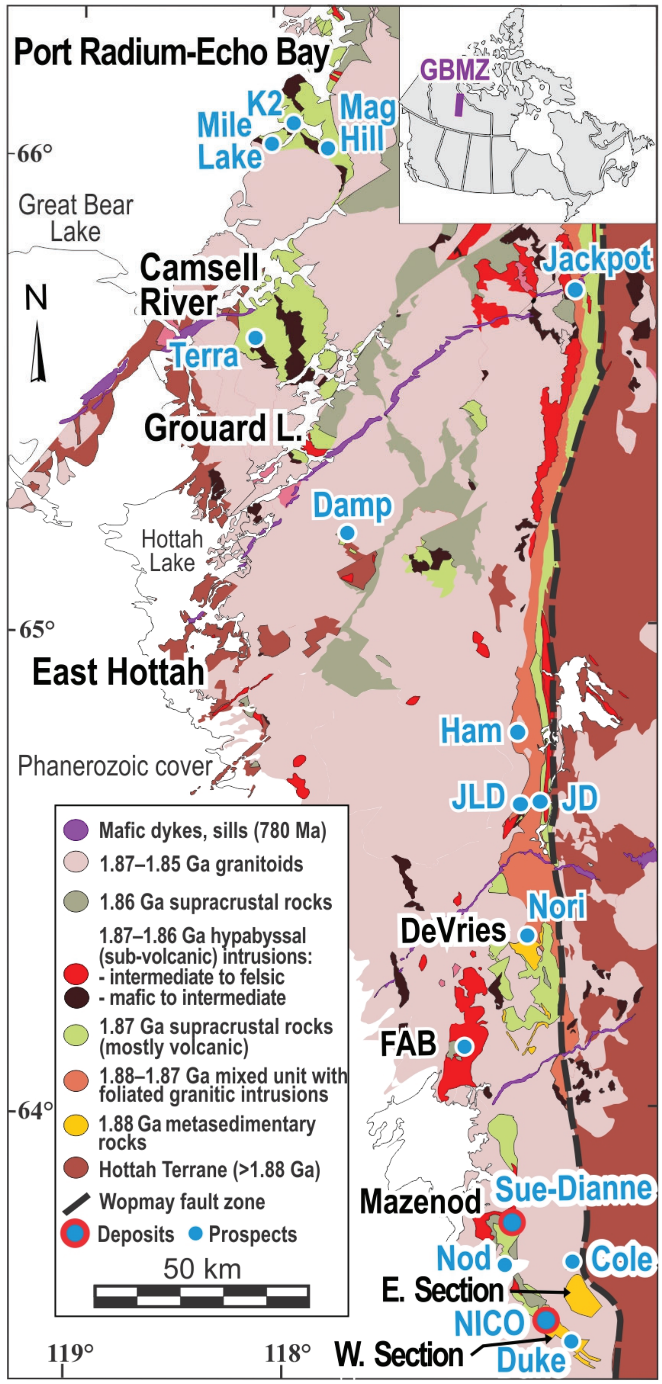


**Figure 9.** Regional geology and main mineral systems of the GBMZ (modified from Corriveau et al., 2016). Inset locates the belt in Canada.

plutons (Hildebrand et al., 2010; Davis et al., 2011). Throughout the belt, 1.87 Ga units and older basement rocks host mineral occurrences and deposits having metal associations and gangue minerals typical of IOCG, IOA, skarn, albitite-hosted uranium, and epithermal deposits. The IOAA-related mineralization includes a wide range in morphology (replacement zones, veins, stockworks, breccias, mantos), host rocks (volcanic, volcaniclastic, siliciclastic, carbonate, hypabyssal-intrusive, plutonic rocks), metals, and alteration assemblages. Mineral modes can be highly variable even though the alteration facies are regular.

In the GBMZ, Na, Na-Ca-Fe, and HT Ca-Fe facies are early and, laterally extensive; they are located at the deepest levels of alteration systems, along fault zones and above subvolcanic intrusions. The Na facies consists mostly of albite. Scapolite and residual protolith minerals other than quartz are rare. In sedimentary rocks, albitized domains are layer-selective and dominantly stratabound, or form patchy to variegated alteration fronts that coalesce into large, pervasively albitized zones (Corriveau et al., 2016, 2022b, d). Albitization creates microporosity that remains well preserved in fine-grained albitite that has not been recrystallized (Engvik et al., 2008; Putnis, 2009; Montreuil et al., 2012). This porosity, combined with brittle deformation associated with faulting, make this facies a highly favorable pathway for fluid migration and mineralization in tectonically active settings.

Skarn occurs within carbonate rocks at the base of the 1.87 Ga volcanic sequence or within underlying 1.88 Ga sedimentary rocks. The zones of skarn are commonly intermixed with, overprint, or lie in close proximity to earlier albitite (Montreuil et al., 2016b; Corriveau et al., 2022d).

Within the GBMZ, HT Ca-Fe, HT Ca-K-Fe, HT K-Fe, and K alteration facies are well represented, and clearly define a prograde metasomatic path of intense alteration (Fig. 10A). HT Ca-Fe alteration assemblages of amphibole, amphibole-magnetite, amphibole-magnetite-apatite and magnetite, replace both sedimentary- and volcanic-dominant sequences, skarn, and breccia fragments, and form the cement in many albitite breccias. Amphibole-dominant assemblages occur as replacements, veins and breccias, and most commonly precede magnetite-dominant alteration zones and veins (Corriveau et al., 2022d).

High temperature K-Fe alteration zones typically consist of K-feldspar-magnetite, biotite-magnetite, and/or K-feldspar-biotite ± magnetite assemblages. The predominant potassium mineral is K-feldspar in altered felsic rocks and sodic-altered units, whereas biotite dominates in HT Ca-Fe alteration zones, sedimentary rocks with elevated clay and silt fractions, and mafic to ultramafic rocks (Corriveau et al., 2014, 2016, 2022c). These magnetite-bearing assemblages evolve structurally upward to, or are cut by, hematite-bearing K-Fe alteration zones containing abundant K-feldspar, white mica (sericite), chlorite, carbonate, and/or quartz, becoming hydrolytic in the process as described by Hitzman et al. (1992) and Skirrow (2022) for hematite-group deposits worldwide. Products of epithermal alteration and vein type mineralization are located peripheral to, structurally above, and within K-Fe alteration zones, but can also occur in IOA mineralized bodies (Mumin et al., 2010).

Plotting the element barcodes on the AIOCG geochemical alteration discrimination diagram of Montreuil et al. (2013) visually illustrates the prograde evolution of the Great Bear iron oxide and alkali-calcic alteration systems. In Figure 10A, B, the prograde evolution of the main alteration facies of the GBMZ defines a counter-clockwise trend from the Na to HT Ca-Fe, HT K-Fe and K alteration facies. Typically, one or two cations dominate the barcodes of these metasomatic rocks (Fig. 2). Samples with lower temperature alteration, such as LT K-Fe, may also plot in these fields; their mineral assemblages differ significantly although their barcodes may be similar. Generally, LT K-Fe alteration facies are characterized by an AIOCG 1 index higher than normally seen in HT K-Fe alteration facies (Fig. 10A).

Overprinting of Na facies rocks by K-Fe ± Ca-Mg alteration causes a shift in the composition of altered rocks to higher AIOCG 1 and AIOCG 2 index values, resulting in some compositions plotting in the least-altered field (Fig. 10C, D). The barcodes are, however, distinct from those of the least-altered rocks in having atypical molar proportions or combinations of elements, in particular higher iron and lower magnesium proportions relative to least-altered rocks (Figs. 3, 10C, D). Such signatures stem from the collapse of systems (when the system cools down) or the telescoping of high-temperature alteration facies to higher structural levels where low-temperatures prevail, corresponding to the two-fluid or two-stage models of Skirrow (2022) for IOCG deposits.

## Prograde and Telescoped Reaction Paths across Systems of the Olympic Copper-Gold Province

### *Olympic Copper-Gold Province, Gawler Craton*

The Olympic Copper-Gold Province is a mineralized belt that formed within the eastern part of the Gawler Craton in southern Australia. Its various domains are defined by their lithostratigraphic and geophysical characteristics (Ferris et al., 2002). The craton hosts significant IOCG ± uranium deposits (Skirrow et al., 2007; Ehrig et al., 2012; Skirrow, 2022); it also has resources of iron ore and gold, and potential for other styles of mineralization such as skarn, epithermal and mafic-ultramafic-related nickel-copper sulphide deposits (Daly et al., 1998; Hand et al., 2007; Fabris et al., 2013, 2018a, b; Gum, 2019). The Olympic Dam U-Cu-Au and other IOCG deposits occur within the Olympic Copper-Gold Province (Skirrow et al., 2002, 2007; Reid, 2019) along the eastern margin of the Gawler Craton (Fig. 11).

The Gawler Craton consists of Archean and Paleoproterozoic granitoids, metamorphic complexes and metasedimentary formations, and records a long and complex evolution (Hand et al., 2007; Reid and Hand, 2012). The final, Paleoproterozoic magmatic phases of the Gawler Craton are represented by two suites: the ca. 1620–1605 Ma St. Peter Suite and the ca. 1595–1570 Ma comagmatic Gawler Range Volcanics and Hiltaba Suite. The lower Gawler Range

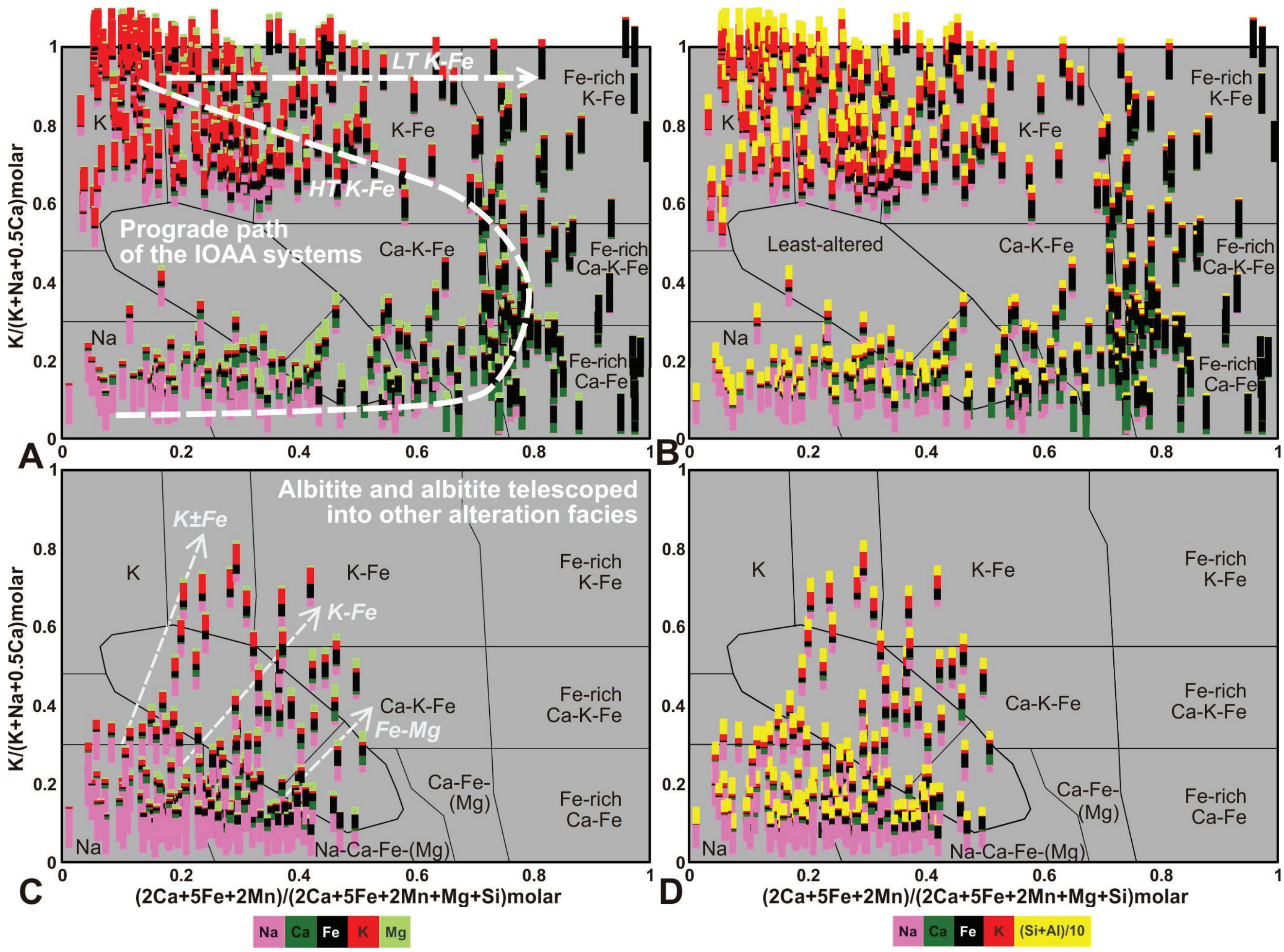


**FIGURE 10.** Samples of the GBMZ mineral systems plotted on the AIOCG diagram of Montreuil et al. (2013). **A, B.** Distribution of the facies along the prograde path of IOAA systems highlights the IOA-IOCG-epithermal footprints. Only samples with a single alteration type were chosen from the Corriveau et al. (2015) dataset (see Montreuil et al., 2013). **C, D.** Path of albitite replaced by and telescoped into subsequent alteration facies have increasing intensity trends that plot in the least-altered field. Data compiled from Corriveau et al. (2015).

Volcanics (1594–1589 Ma) predate the IOAA systems of the region, whereas the upper Gawler Range Volcanics (1587.5–1587.2 Ma) postdates them (Jagodzinski et al., 2016). Such a two-stage volcanic event also characterizes the GBMZ. However, in the GBMZ, the first stage is coeval with IOAA metasomatism. In addition, plutonic rocks in the GBMZ similarly comprise two main suites — early subvolcanic intrusions within small volcanic centers coeval with IOAA metasomatism, and subsequent voluminous batholiths that postdate IOAA metasomatism (Hildebrand et al., 2010; Ootes et al., 2017; Montreuil et al., 2016a–c; Corriveau et al., 2022d).

The St. Peter Suite is magnesian and calc-alkaline, with moderately evolved to relatively juvenile Nd isotopic compositions, which suggest derivation in part from contemporary mantle (Reid et al., 2020). In contrast, the Gawler Range Volcanics and Hiltaba Suite (which includes the RDG; Fig. 12) are dominated by A-type felsic compositions with a subordinate mafic component and variable Nd isotopic compositions reflecting crustal contamination of a mafic source by a heterogeneous crustal column (Flint et al., 1993; Allen et al., 2008; Belousova et al., 2009; Wade et al., 2012). The Gawler Range Volcanics and Hiltaba Suite were associated with a regional deformation event and widespread hydrothermal alteration and mineralization in the Olympic Copper-Gold Province and the Central Gawler Gold Province (Fraser et al., 2007; Skirrow et al., 2007; Hayward and Skirrow, 2010).

Skirrow et al. (2002, 2007) recognized four major groupings of hydrothermal alteration assemblages in the Olympic Copper-Gold Province: 1) vein and replacement alteration comprising magnetite-albite-amphibole; 2) K-feldspar-bearing magnetite-calc-silicate alteration known mainly from the Olympic Dam district, where early albite alteration has been almost entirely replaced by K-feldspar (Bastrakov et al., 2007); 3) magnetite-biotite alteration recognized in the Mount Woods region and Moonta-Wallaroo district, South Australia (Fig. 11); and 4) hematite-sericite-chlorite-carbonate alteration observed at many prospects in the Olympic Dam district, including Emmie Bluff, Torrens, and Titan prospects (Skirrow et al., 2002; Bastrakov et al., 2007; Davidson et al., 2007).

Borehole samples from across the Olympic Copper-Gold Province, including magnetite- and hematite-rich rocks that display varying degrees of alteration intensity and mineralization (barren to strongly mineralized) were analyzed for their major element compositions (Geological Survey of South Australia data). Three examples are discussed in this section: the Olympic Dam deposit, the Emmie Bluff prospect, and the Mt. Woods region (Fig. 11).

*Olympic Dam Deposit*

Hematite-group IOCG deposits typically consist of hematite, sericite (± K-feldspar) and chlorite (± quartz-albite-carbonate) alteration. They form at temperatures in the range of 200–350°C, are restricted to shallow crustal levels, and are commonly coeval with volcanic activity (Williams, 2010a).

The Olympic Dam Cu-U-Au-Ag deposit is hosted by the Olympic Dam Breccia Complex (ODBC), which occurs entirely within the Mesoproterozoic Roxby Downs Granite (RDG; Reeve et al., 1990). The RDG is part of the 1.59 Ga Hiltaba Suite granites, which intruded Paleoproterozoic metasedimentary rocks (and minor iron formation) of the Hutchison and Wallaroo groups, the Donington Suite granitoids, and predominantly felsic volcanic rocks of the Gawler Range Volcanics (Hand et al., 2007).

The ODBC consists of weakly to intensely altered and brecciated RDG, as well as subordinate clastic, volcanic, and mafic-ultramafic intrusive rocks (Ehrig et al., 2012, 2017b; McPhie et al., 2016). The ODBC contact with the least-altered to weakly-altered RDG is gradational and geochemically defined by RDG with <5 wt% Fe (Fig. 12; Ehrig et al., 2012). Alteration intensity and brecciation increase from the outer edges of the funnel-shaped ODBC towards the core of the deposit.

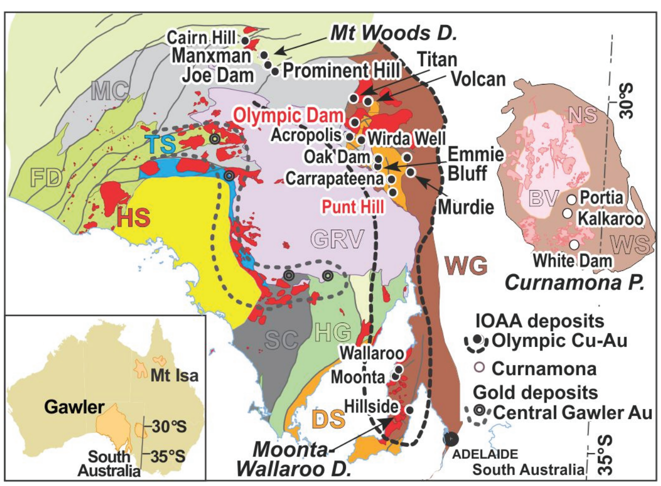


**FIGURE 11.** Schematic map indicating the distribution of major stratigraphic groups in the Gawler Craton (after Reid and Hand, 2012). *BV*: Benagerie Volcanic Suite; *DS*: Donington Suite; *FD*: Fowler Domain; *HG*: Hutchison Group; *HS*: Hiltaba Suite; *GRV*: Gawler Range Volcanics; *MC*: Mulgathing Complex; *SC*: Sleaford Complex; *TS*: Tunkillia Suite; *SPS*: St Peter Suite; *NS*: Ninnerie Supersuite; *WG*: Wallaroo Group; *WS*: Willyama Supergroup.

Alteration zonation in the RDG from deposit-distal to deposit-core consists of: 1) distal and at-depth albitization; 2) distal hydrothermal K-feldspar; 3) progressive sericitization and hematization proximal to mineralization, with ore grades generally positively correlating with increases in hematization; and 4) barren hematite-quartz-barite breccias in the core of the deposit. Alteration mineral zoning from depth to surface and across the deposit, including zoning of ore minerals (chalcopyrite, bornite, chalcocite), barium, $CO_2$ and fluorite, are provided in Ehrig et al. (2012, 2017b) and Dmitrijeva et al. (2019).

Within the ODBC, all igneous plagioclase is replaced by sericite, primary mafic minerals are not preserved, and the overall abundance of hematite and copper sulphides increases gradually upwards and towards the deposit centre (Ehrig et al., 2012, 2017b). Most igneous K-feldspar is replaced by hydrothermal K-feldspar and sericite; highly porous albite is partially preserved at depth and in least-altered RDG (Kontonikas-Charos et al., 2017). Petrographic observation and whole-rock geochemistry indicate that hydrothermal albite and K-feldspar formed within the RDG without the need for an external source of alkalis (Kontonikas-Charos et al., 2017). Remobilization and sodium-depletion occur in the least-altered RDG; whereas mineralized RDG is associated with iron- and potassium-enrichment, albitization, K-feldspar-sericite-hematite alteration, and overprinting iron oxide-Cu–Au–REE–Mo–U mineralization (Kontonikas-Charos et al., 2017; this study).

Figure 13 display the statistical means of Ehrig et al. (2012) lithogeochemical data from variably altered and copper-mineralized ODBC host rocks (granite, picrite). Picrites are strongly carbonate-hematite-altered (Ehrig et al., 2012) and plot in the Ca-K-Fe alteration field, in contrast to fresh picrites, which plot in the least-altered rock field (Fig. 5). Sericitization of plagioclase decreases the Na/K in barcodes. Increasing hematite alteration for mineralized and unmineralized samples of ODBC (and relics of magnetite) increases the iron proportion in the barcodes.

Unmineralized and mineralized samples with less than 5 wt% Fe yield barcodes indicating iron proportions of ~30%, whereas unmineralized and mineralized samples containing 5 to 10 wt% Fe yield renormalized iron proportions of approximately 45%. In samples containing 10 to 20 wt% Fe, the iron proportions of the barcodes is ~80% of the barcodes; however, it is only 65% in mineralized samples, which have a higher proportion of potassium. Similarly, in samples with 20 to 30 wt% Fe, iron proportions represent 93% of the barcode in unmineralized samples, and 85% in mineralized samples. In samples with 30 to 40 wt% Fe, iron proportions represent 95% of the barcodes in unmineralized samples, and 90% in mineralized samples. Finally, in unmineralized samples with 40 to 50 wt% Fe, iron proportions represent 97% of the barcodes, and 93% in mineralized samples.

In Figure 13, chlorite-bearing laminated sandstones and mudstones (KASH) and chloritized dolerite are characterized by barcodes with magnesium proportions of 25% and 50%, respectively. Sphalerite-bearing granite-rich breccias (Bx-Zn), magnetite-hematite breccias (Bx-Mag) and hematite-rich

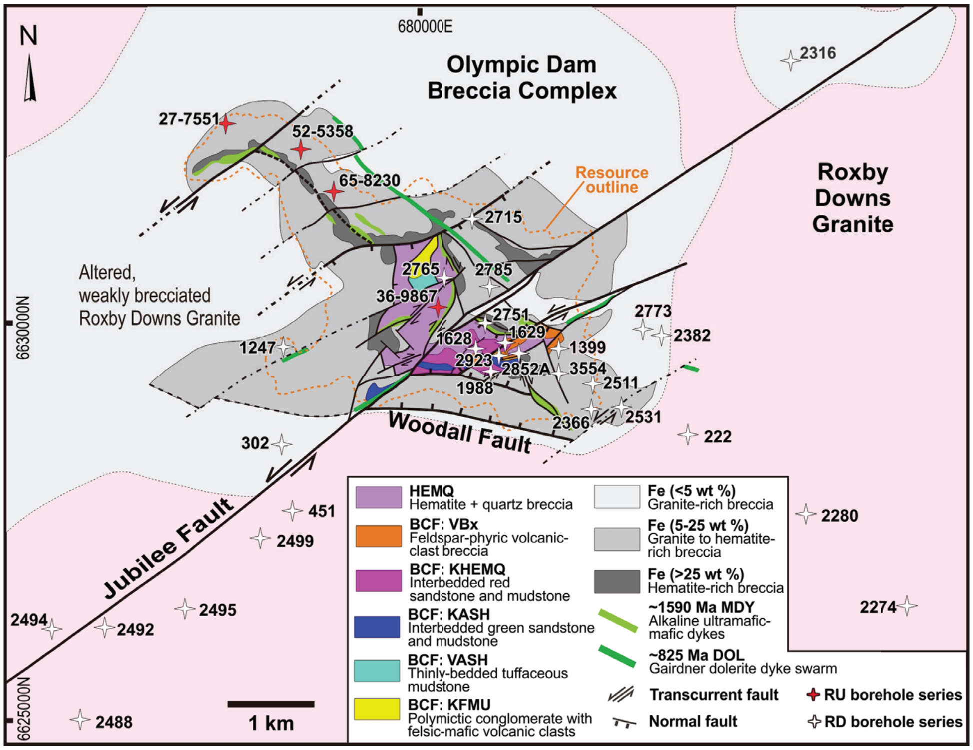


**FIGURE 12.** Simplified geology at -350 mRL (metres Relative sea Level) of the Olympic Dam Breccia Complex (Clark et al., 2017; Corriveau et al., 2022d), showing the distribution of Roxby Downs Granite, outer limits of significant brecciation and iron metasomatism (biotite-out limit), granite-rich (<5 wt% Fe), and hematite-rich breccias (>20 wt% Fe). The area with less than 5 wt% Fe corresponds to the external zone of the ODBC whereas the area with more than 20 wt% of Fe represents the core zone. Boreholes, from the RD and RU series, at depth from the external area may cut zones with higher iron concentrations. *BCF*: Bedded Clastic Facies.

breccias from mineralized zones at depth (Bx-Mo) are characterized by calcium-rich barcodes (between 5 to 10%) relative to unmineralized or mineralized hematite breccias (calcium proportions lower than 3% in mineralized samples, and lower than 2% in unmineralized samples).

In Figures 14 and 15, borehole samples from the Olympic Dam area are grouped according to their location (see -350 level on geologic map, Fig. 12) and plotted in the Montreuil et al. (2013) AIOCG diagram. Figure 14 illustrates the alteration of the RDG (Hiltaba Suite) and Donington suite in boreholes outside of the ODBC (Fig. 14A–D) and at the biotite 'out' boundary (Fig. 14E, F). Figure 15, on the other hand, illustrates the alteration of samples in boreholes inside of the ODBC in three different areas (Fig. 12): i) an external zone characterized by granite-rich breccias (5 wt% Fe contour at -350 mRL; Fig. 15A, B); ii) an intermediate zone comprising hematite breccias (5–20 wt% Fe contour at -350 mRL; Fig. 15C, D); and iii) a core zone characterized by hematite-rich breccias (>20 wt% Fe contour at -350 mRL; Fig. 15E, F).

In the most distal boreholes (>5 km from the deposit), host rocks are least-altered granites with local moderate potassic alteration (Fig. 14A, B). In samples three to five km from the deposit (Fig. 14C, D), sericitization of least-altered granites produces a trend of decreasing sodium and increasing potassium proportions. Some samples record albitization. Replacement of ferromagnesian minerals by magnesium-chlorite in altered RDG

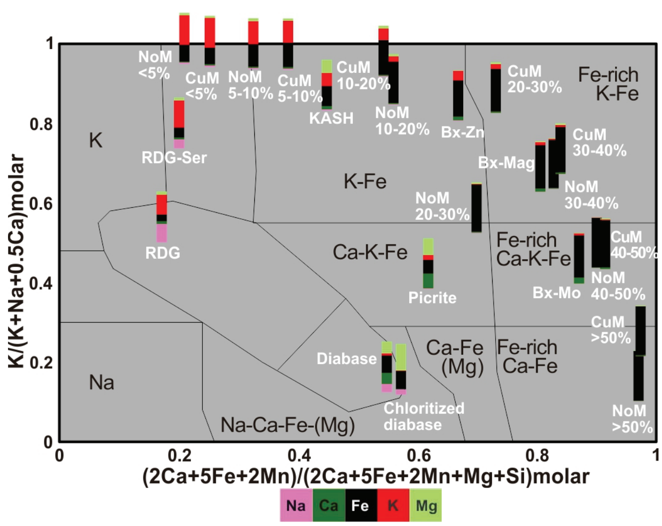


**FIGURE 13.** Representative samples of least-altered Roxby Downs Granite, sericite-altered RDG, and Olympic Dam Breccia Complex from Ehrig et al. (2012) plotted on the AIOCG diagram of Montreuil et al. (2013). *RDG*: Roxby Downs Granite; *RDG-Ser*: sericite altered RDG; *KASH*: chlorite-bearing laminated sandstone and mudstone; *Bx-Zn*: sphalerite-bearing granite-rich breccias; *Bx-Mag*: magnetite+hematite breccias; *Bx-Mo*: hematite-rich breccias from deep zone of mineralization; *NoM*: unmineralized samples; *CuM*: Cu-mineralized samples. Percentage ranges below NoM and CuM barcodes are iron contents.

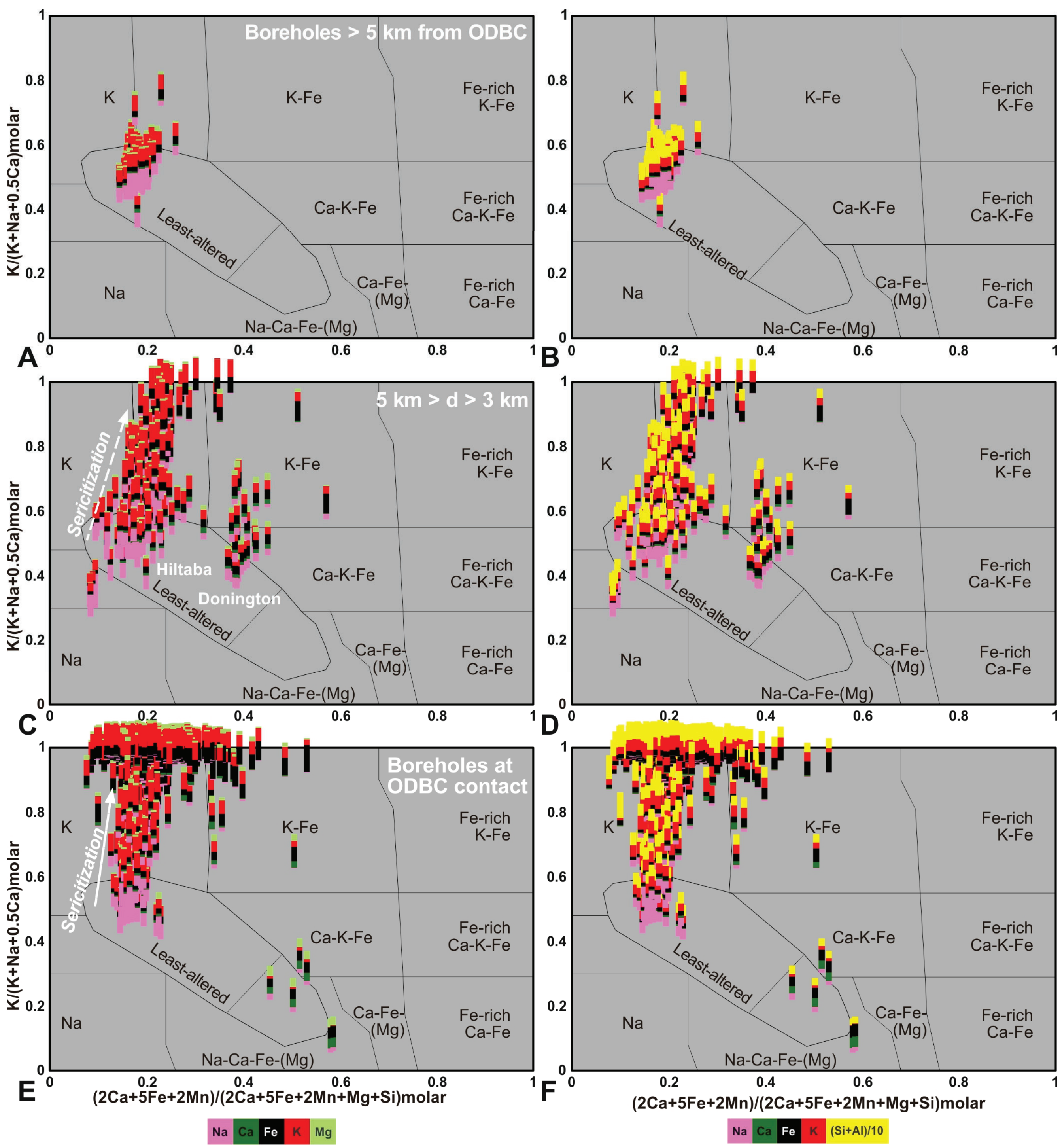


**FIGURE 14.** Samples of the Roxby Downs Granite and the Olympic Dam Breccia Complex plotted on the AIOCG diagram of Montreuil et al. (2013). **A, B.** Borehole samples more than 5 km from ODBC (RD2488). **C, D.** Borehole samples between 3 and 5 km from ODBC (RD451, RD2274, RD2280, RD2492, RD2494, RD2499). **E, F.** Borehole samples at the OBDC contact with altered granites and least-altered mafic rocks (RD302, RD2382). Data compiled from BHP Billiton (unpublished data).

increases the magnesium proportions in barcodes. In addition, Donington granitoids are weakly to moderately K-Fe altered.

The contact of the ODBC is gradational and defined by chlorite alteration of igneous biotite and hematite alteration of igneous magnetite (Ehrig et al., 2012). From this contact inward, the intensity of LT K-Fe alteration increases. Intense sericitization and increasing hematite contents removed sodium from the host rocks, and produced molar barcodes with high potassium proportions (~60%), moderate iron proportions (25–30%), low magnesium proportions (5–10%) and extremely low sodium proportions. The horizontal K-Fe trend with high AIOCG 1 index (>0.95; Fig. 14E, F) is typical of LT K-Fe alteration.

In the external zone of the ODBC (Fe<5 wt%), barcodes of altered samples indicate proportions of potassium, iron, and magnesium of ~58–60%, ~33%, and ~3–5%, respectively (Fig. 13). This zone is characterized at depth by rare less-altered RDG samples that display two trends —one toward highly sericitized granites (generally observed outside of the ODBC at -350 mRL), and the other between least-altered granite and iron-rich K-Fe alteration field (Fig. 15A, B). With increasing hematite alteration within the ODBC, alteration evolves to iron-rich fields. Two trends are observed: i) low Ca and high Fe proportions which evolve to the iron-rich Ca-K-Fe field (trend 1, Fig. 15A); and ii) moderate Ca and high Fe proportions (related to fluorite) which evolve towards the iron-rich Ca-Fe field (trend 2, Fig. 15A). This evolution shows a continuous increase of hydrothermal alteration toward the core of the deposit.

In the intermediate zone of the ODBC (Fig. 15C, D), there are no relics of granite that plot in the field of least-altered rocks, and iron-rich facies are very abundant. In areas with iron concentration between 5 and 20 wt%, barcode plots indicate proportions of potassium, iron and magnesium of 10–45%, 45–80%, and ~5%, respectively (Fig. 13). There is a continuum between sericitized RDG, typical of the outer limit of ODBC (barcode plots with potassium proportions up to 75%), and hematite-rich breccias characterized by barcodes with iron proportions higher than 80% (Fig. 15C, D). This continuum clearly defines an alteration path from K to Ca-Fe alterations fields.

In the core zone (Fig. 15E, F), there are no barcodes with less than 35% Fe. Barcodes indicate potassium proportions <10%, and iron proportions >85%, and follow curving trends (Fig. 15C, D). However, higher proportions of calcium are observed in boreholes that intersect the fluorine-rich zone. Barcodes with potassium proportions >10%, and iron proportions <85% represent the marginal zone of the ODBC (K-feldspar-sericite-hematite breccia) at depth (see Fig. 11 in Corriveau et al., 2022d).

Around the ODBC, the RDG becomes increasingly altered through sericite-dominant LT K-Fe alteration, and within the ODBC, it becomes increasingly brecciated. The geochemical footprints evolve from the least-altered field, through the K, K-Fe, Ca-K-Fe and Ca-Fe alteration fields to the iron-rich fields on the AIOCG diagram (Figs. 14, 15). This alteration path, deflected by low-temperature alteration, is distinct from the alteration path defined by high-temperature alteration within the GBMZ (Fig. 10).

*Emmie Bluff Prospect*

At the Emmie Bluff prospect, mineralization occurs within a highly fractured zone of magnetite-rich alteration, developed in both the Gawler Range Volcanics and the underlying metasedimentary Wallaroo Group. These metasedimentary rocks include fine-grained laminated siltstones, coarse-grained arkosic rocks, siltstones, cherts, mudstones and carbonate-facies sediments. Coarse-grained iron oxide mineralization mainly consists of hematite, although many of the hematite aggregates contain magnetite cores indicating that hematite replaced magnetite. Gow et al. (1994) interpreted the magnetite to be a relic of earlier magnetite-K-feldspar-amphibole (HT Ca-K-Fe) alteration.

Boreholes located in areas with more than 2 vol% of magnetite are characterized by HT Ca-Fe, iron-rich HT Ca-Fe, HT Ca-K-Fe and HT to LT K-Fe alteration facies that plot along the IOAA prograde metasomatic path (Fig. 16A). Current exploration has not identified Na, transitional Na-Ca and Na-Ca-Fe facies. The Ca-Fe alteration facies is poorly developed, but the iron-rich Ca-Fe, Ca-K-Fe and K-Fe alteration facies are abundant. Many samples that fall within the K-Fe alteration facies have high AIOCG 1 index values and form a horizontal band that transitions into the K alteration facies. The significant proportion of chlorite, represented by magnesium in the barcodes, is more typical of LT K-Fe than HT K-Fe alteration.

In Figure 16A, many samples from the Ca-Fe, Ca-K-Fe and K-Fe alteration facies plot to the left of the main prograde metasomatic path (i.e. those with lower AIOCG 2 index values), reflecting higher molar proportions of Mg, Ca and K. Such proportions suggest that low-temperature Mg-Ca-Fe alteration overprints iron-rich Ca-Fe, Ca-K-Fe or K-Fe alteration facies (Mg-Ca-Fe trend line, Fig. 16A). These overprinting relationships are compatible with a hematite-sericite-chlorite-carbonate alteration superimposed on an earlier prograde magnetite-K-feldspar-amphibole alteration (and skarn). Locally, in the K-alteration field, some samples are characterized by high molar proportions of silica (Fig. 16B). The high silica contents suggest either K-alteration of quartz-rich units (e.g. host sandstone or siltstone) and/or K-Fe alteration cut by quartz veining.

Boreholes in areas outside the magnetite-rich zone (<2 vol%) are characterized by high proportions of least-altered rocks, including picrite, quartz-rich sedimentary rocks and carbonates, K ± Fe altered rocks, and iron-rich Ca-Fe facies (Fig. 16C, D). Samples define trends between least-altered rocks and Na and K-Fe metasomatic end-members. In these boreholes, picrites exhibit Ca-K-Fe alteration.

*Mount Woods Region*

The Mount Woods region is a geologically complex area that is underlain by Paleoproterozoic metasedimentary rocks and Mesoproterozoic orthogneisses intruded by granitic intrusions of the Hiltaba Suite. It hosts the Cairn Hill and Prominent Hill IOCG deposits (Belperio et al., 2007; Clark, 2014), and the Manxman and Joes Dam prospects (Hampton, 1997).

Boreholes located between the Manxman, Joes Dam and Cairn Hill prospects have been divided into two distinct groups, those having abundant iron-rich facies, and those having few iron-rich facies. High proportions of K-Fe, iron-rich K-Fe, and iron-rich Ca-Fe alteration facies characterize the first group. These facies define a prograde IOAA metasomatic path (Fig. 17A, B), like that documented at the Emmie Bluff prospect (Fig. 16A) in altered facies containing more than 2 vol% of magnetite.

The Mount Woods boreholes also contain strongly albitized and albite-amphibole-apatite-magnetite units (Clark, 2014) that plot within the Na and Na-Ca-Fe fields (Fig. 17). Due to the intense albitization, samples plotting in the iron-rich Ca-Fe fields preserve some molar proportion of sodium in their barcodes.

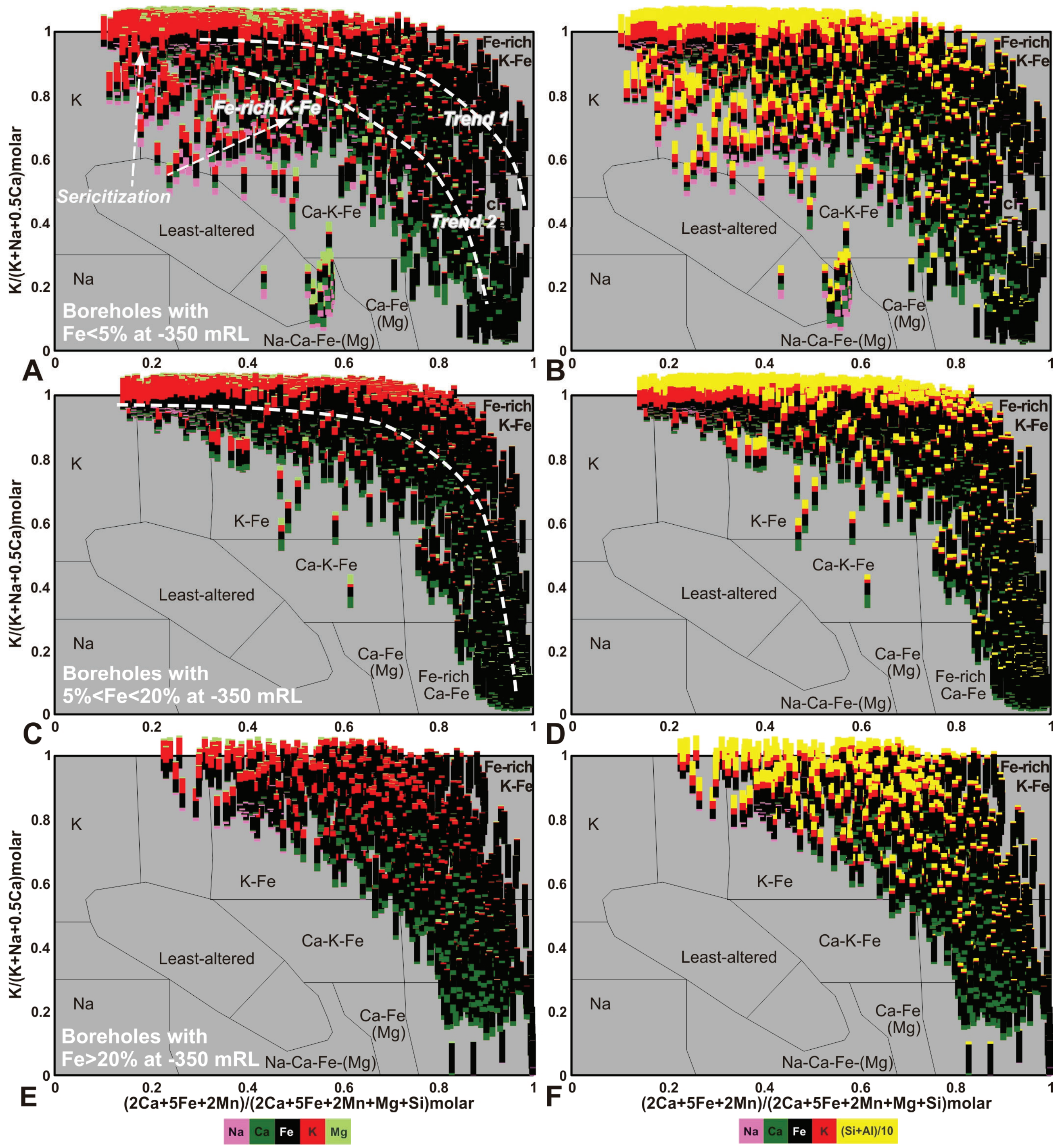


**Figure 15.** Borehole samples of the ODBC plotted on the AIOCG diagram of Montreuil et al. (2013). **A, B.** Borehole samples in areas with iron concentrations lower than 5 wt% at -350 mRL (external zone) (RD2511, RD2531, RD2773, RD2785, RD3554, RU27-7551, RU65-8230; Fig. 12). **C, D.** Borehole samples in areas with iron concentrations between 5 and 20 wt% at -350 mRL (intermediate zone) (RD1399, RD2715, RD2366, RD2751, RD2765, RU36-9867). **E, F.** Borehole samples in areas with iron concentrations higher than 20 wt% at -350 mRL (core zone) (RD1629, RD1988, RD2852A). Data compiled from BHP Billiton (unpublished data).

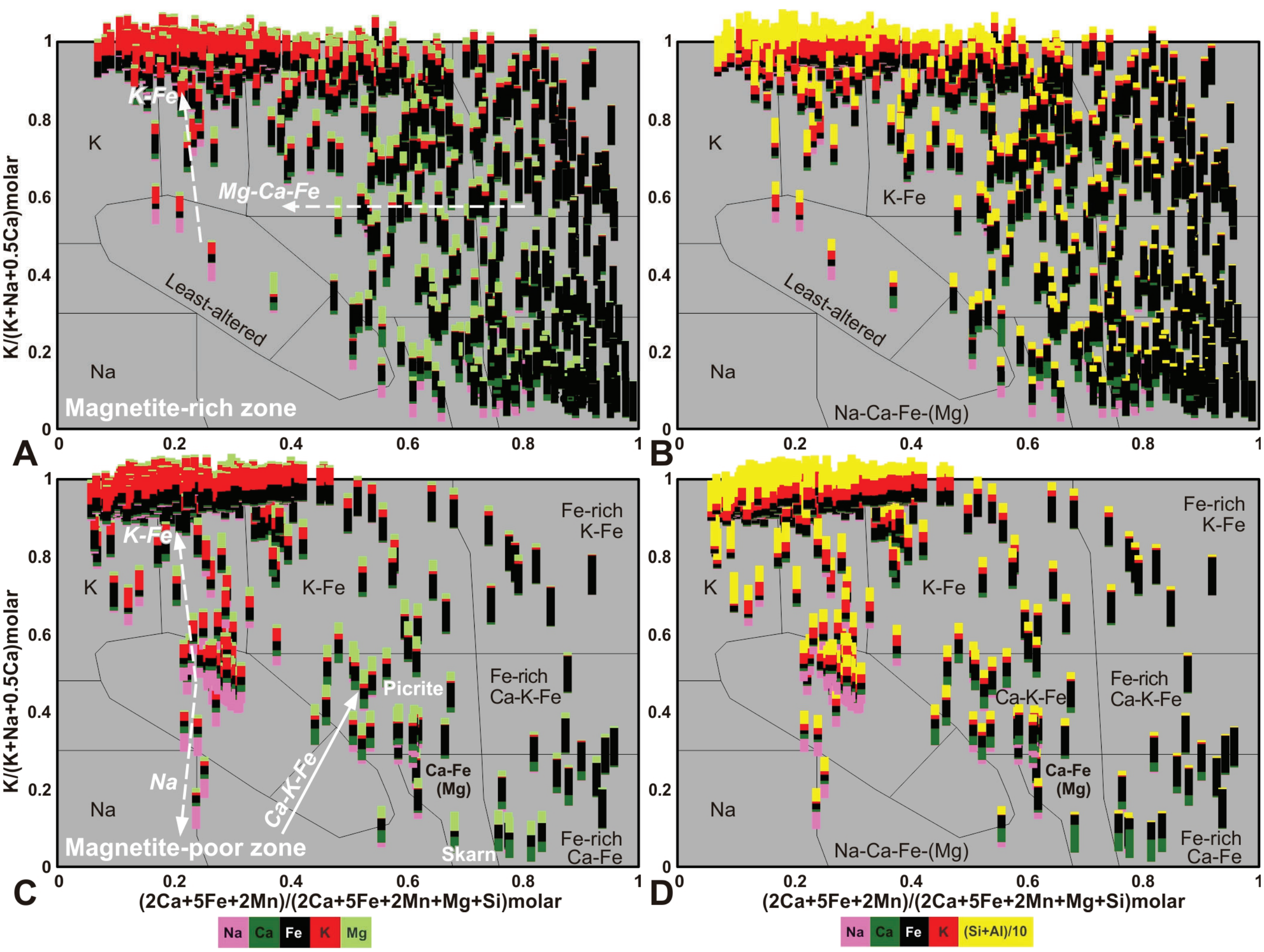


**Figure 16.** Samples of the Emmie Bluff prospect, Gawler Craton, Australia, plotted on the AIOCG diagram of Montreuil et al. (2013). **A, B.** Samples from boreholes intersecting area with more than 2 vol% of magnetite (AD8, IHAD2, IHAD3, IHAD5, SAE3, SAE4, SAE7, SAE11, WJD1). **C, D.** Borehole samples from outside of the magnetite-rich zone (AD2, ASD1, ASD2, IHAD1, IHAD6, SAE8, SAE9, SAE10). Data compiled from the Geological Survey of South Australia, via South Australian Resources Information Gateway (https://map.sarig.sa.gov.au/).

Samples with low molar proportions of sodium (5–15%) and high molar proportions of iron also plot in the Ca-K-Fe, K-Fe and least-altered sample fields (Fig. 17A). Equivalent samples with low molar proportions of sodium were not observed at the Emmie Bluff prospect nor in the central part of the ODBC (Fig. 15E, F). In the Ca-K-Fe field, barcodes with low molar proportions of sodium suggest that iron-rich HT K-Fe alteration overprinted Na and/or Na-Ca-Fe alteration facies (Fig. 17A, B). Similarly, in the least-altered sample field, barcodes with high molar proportions of iron are typical of iron-rich HT K-Fe alteration of albitized rocks (Fig. 17A, B). These observations suggest that albitization within the Mount Woods region largely developed prior to high-temperature alteration facies within the IOAA systems.

These lithogeochemical data support thin section interpretations at the Manxman prospect (Hampton, 1997) indicating that the magnetite-biotite assemblage overprints the albite-diopside-amphibole assemblage. Moreover, according to Clark (2014), the host rocks of the Cairn Hill deposit record an early Na-Ca alteration, composed of albite + scapolite + diopside, overprinted by localized zones of intense HT K-Fe (magnetite-biotite) alteration.

Borehole samples with low iron-oxide contents (<2 vol% magnetite), are characterized by Na, Na-Ca-Fe and Ca-Fe alteration, minor K-Fe alteration, and lack of iron-rich alteration (Fig. 17C, D). Furthermore, few of the iron-rich samples plot in the iron-rich fields. High magnesium proportions in these samples suggest that the magnesium enrichment is superimposed on iron-rich alteration facies, a feature typical of late chloritization.

Molar barcodes show that the samples from the Mount Woods region do not present a clear single prograde path, in contrast to the ODBC or the Emmie Bluff prospect. The chemical footprints are instead interpreted as an array of telescoped metasomatic paths, involving K-Fe alteration of earlier Na, Na-Ca-Fe, Ca-Fe and iron-rich Ca-Fe alteration assemblages.

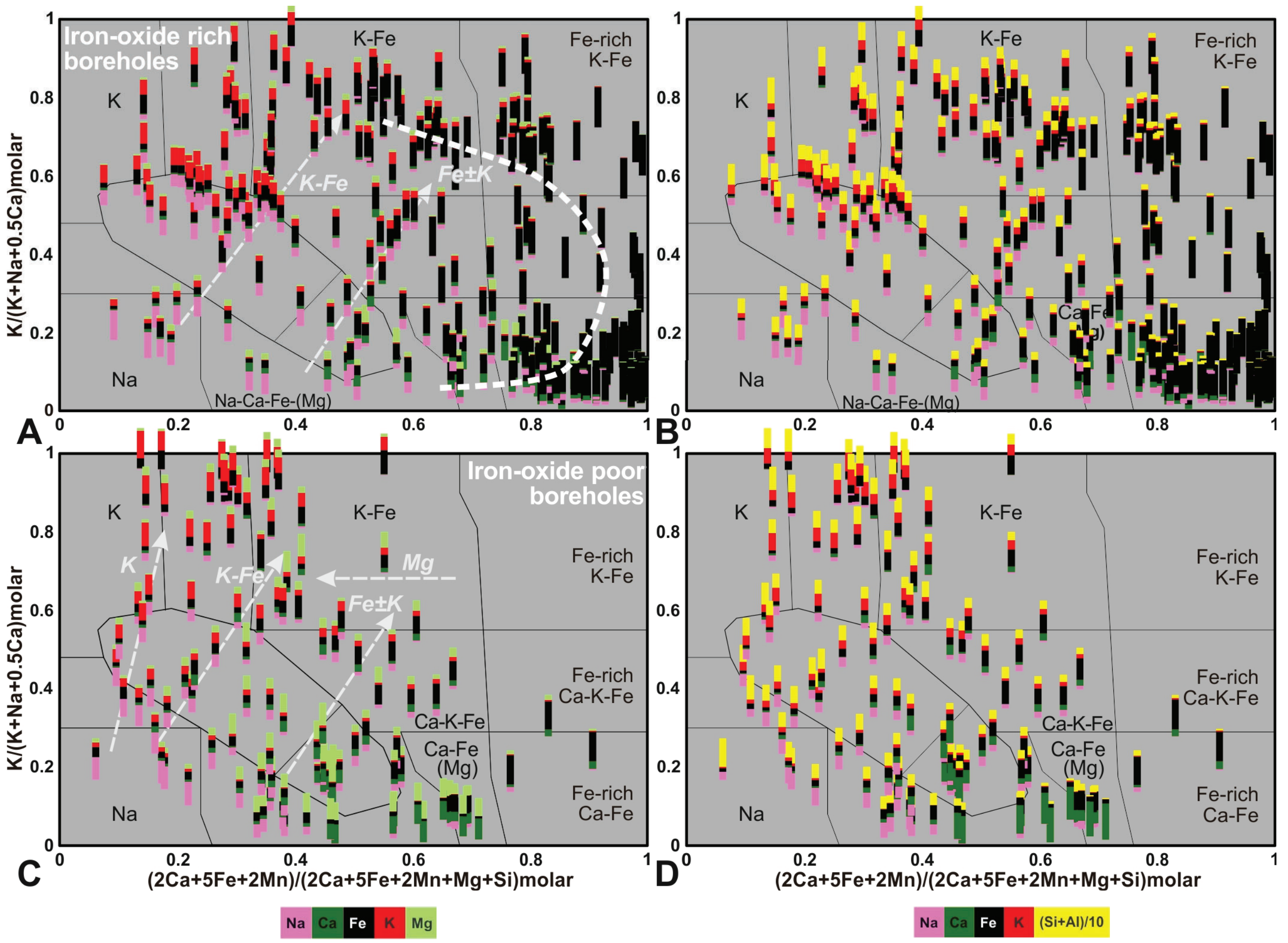


**FIGURE 17.** Borehole samples from the Mount Woods region, Gawler Craton, Australia plotted on the AIOCG diagram of Montreuil et al. (2013). **A, B.** Borehole samples with Fe-rich altered rocks. **C, D.** Borehole samples without Fe-rich altered rocks. Data compiled from the Geological Survey of South Australia, via South Australian Resources Information Gateway (https://map.sarig.sa.gov.au/).

Along the northwest-southeast trend between the Murdie Murdie and Titan prospects (Fig. 11), few alteration zones display greater than 2 vol% iron oxides. In these areas, alteration occurs as two distinct groups, those containing >2 vol% magnetite, and those from outside magnetite-rich zones. High molar proportions of iron-rich skarn, iron-rich Ca-Fe, and magnesium-rich alteration facies characterize the first group (Fig. 18A, B). A few samples in the Ca-K-Fe and iron-rich Ca-K-Fe alteration facies have barcodes with significant sodium proportions (> 10%), whereas sodium proportions are lower or lacking in the HT Ca-Fe and iron-rich Ca-Fe alteration facies (Fig. 18A, B). In a classic prograde metasomatic path, such as the Emmie Bluff prospect, Ca-K-Fe and iron-rich Ca-K-Fe alteration facies have less than 5% sodium in their barcodes (Fig. 16A, B). Hence, the presence of significant sodium in alteration facies in the Mt. Woods region suggests that albitized host rocks were overprinted by iron-rich Ca-K-Fe alteration. As observed at the Emmie Bluff prospect, later magnesium alteration overprints iron-rich Ca-K-Fe and K-Fe facies samples (Figs. 16, 18). However, the LT K-Fe alteration facies observed at the Emmie Bluff prospect are lacking in the Murdie Murdie and Titan prospects, and iron-rich alteration facies are less abundant.

The second alteration group, comprising samples from outside of magnetite-rich zones, is characterized by Na and Na-Ca-Fe alteration facies overprinted by a later K-Fe alteration, creating a continuum between least-altered rocks and LT K-Fe alteration (Fig. 18C, D).

In summary, within the Olympic Copper-Gold Province, IOAA systems are characterized by clear prograde metasomatic paths (Olympic Dam Breccia Complex or Emmie Bluff prospect), or by telescoped reaction paths characterized by albitization overprinted by later HT or LT K-Fe alteration (Mount Woods region, Murdie Murdie and Titan prospects).

## Magnetite to Hematite-group IOCG Deposits

*Mantoverde District, Chile*

Located in the forearc of the Andean Central Volcanic Zone, the Mantoverde IOCG district comprises a Jurassic to Lower Cretaceous magmatic arc developed on a basement of Devonian to Carboniferous metasedimentary and Permo-Triassic plutonic

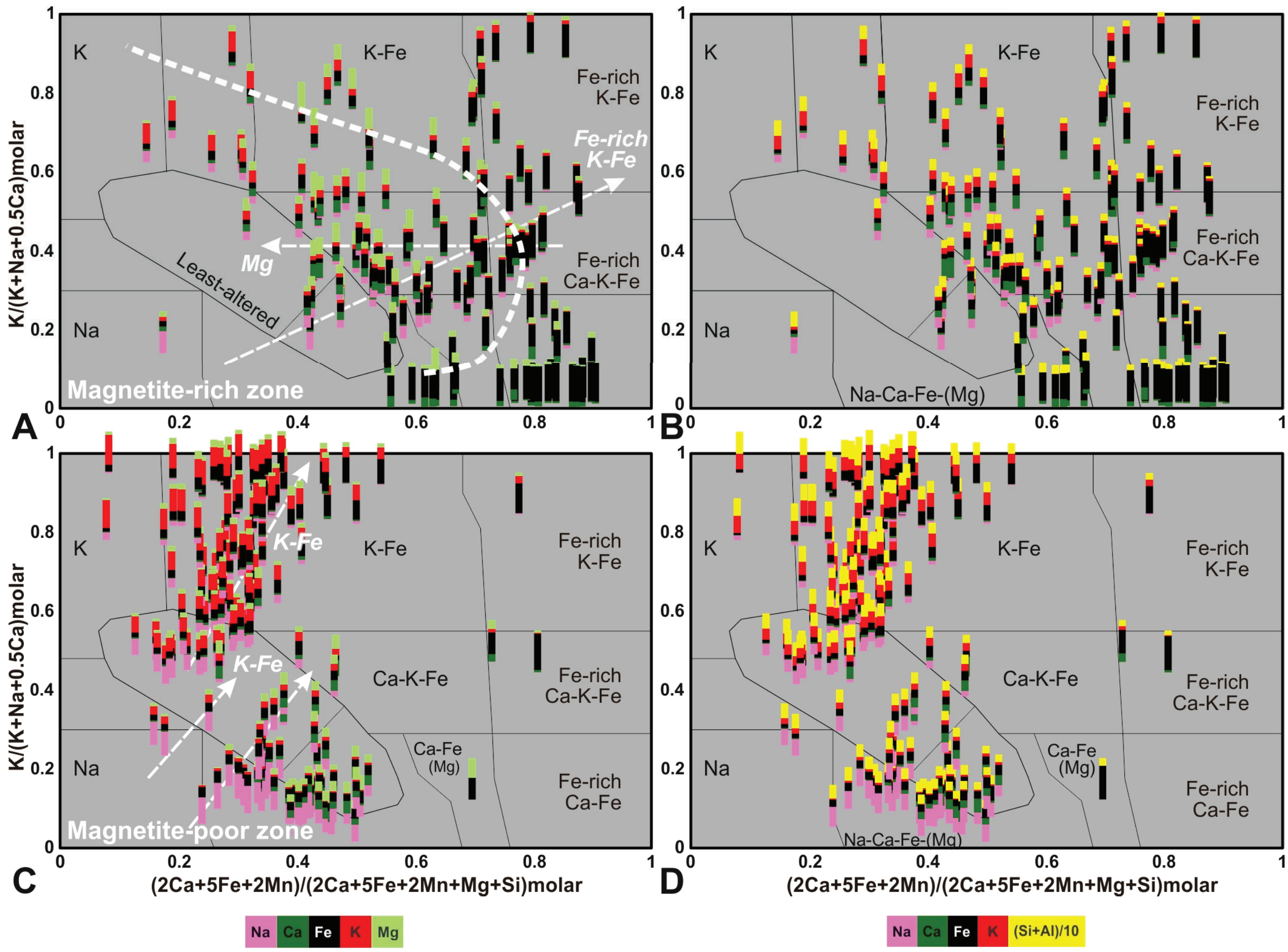


**FIGURE 18.** Samples of Murdie Murdie to Titan prospects, Gawler Craton, Australia plotted on the AIOCG diagram of Montreuil et al. (2013). **A, B.** Samples with more than 2 vol% of magnetite. **C, D.** Samples from outside of magnetite-rich zones. Data compiled from the Geological Survey of South Australia, via South Australian Resources Information Gateway (https://map.sarig.sa.gov.au/).

and volcaniclastic rocks (Fig. 19; Dallmeyer et al., 1996; Lara and Godoy, 1998; Grocott and Taylor, 2002). Mineralization in the Mantoverde district developed within an intensely fractured structural block delimited by the subvertical central and eastern branches of the Atacama Fault System (AFS). The AFS is a north-south striking, plate boundary-parallel strike-slip fault (Brown et al., 1993).

Rieger et al. (2010) subdivided the paragenetic sequence at Mantoverde into three hydrothermal stages: early K-Fe alteration and brecciation followed by sulphide mineralization, and late hydrothermal veining. According to Rieger et al. (2010), the iron oxide stage is characterized by intense iron metasomatism along fractures and in the matrix of breccias, associated with pervasive K-feldspar alteration of breccia fragments. Silicification and hydrolytic alteration of the host rocks also occurs. Crystallization of early specular hematite was followed by precipitation of magnetite and pyrite. Chalcopyrite mineralization is associated with silicification, and with quartz, K-feldspar + quartz, or sericite ± quartz veining. The late hydrothermal stage is characterized by pervasive carbonatization, the formation of calcite ± specularite veins and veinlets, specularite ± calcite veinlets, and minor quartz or sericite veinlets.

In Figure 20, geochemical data from the Mantoverde district mostly fall within the Na-Ca-Fe, K-Fe and K alteration facies, and have high molar proportions of magnesium, typical of late-stage chloritization of hematite-dominated IOCG deposits. In the process, chloritized iron-rich K-Fe alteration facies shift to the left towards the K-Fe alteration field, and chloritized Ca-K-Fe and Ca-Fe alteration facies plot within the least-altered rocks field. Silica-rich samples falling in the K alteration field are likely quartz veins (Fig. 20B). As a result of these silica- and magnesium-rich alteration overprints (Fig. 20), data for the Mantoverde district are slightly offset from the simple prograde metasomatic path of magnetite-dominated IOCG settings (e.g. compare Fig. 14 with Fig. 10).

*Singhbhum Shear Zone, India*

In India, the Singhbhum Shear Zone (SSZ) is an important polymetallic mineral district located at the boundary between an Archean cratonic nucleus to the south and a Proterozoic fold

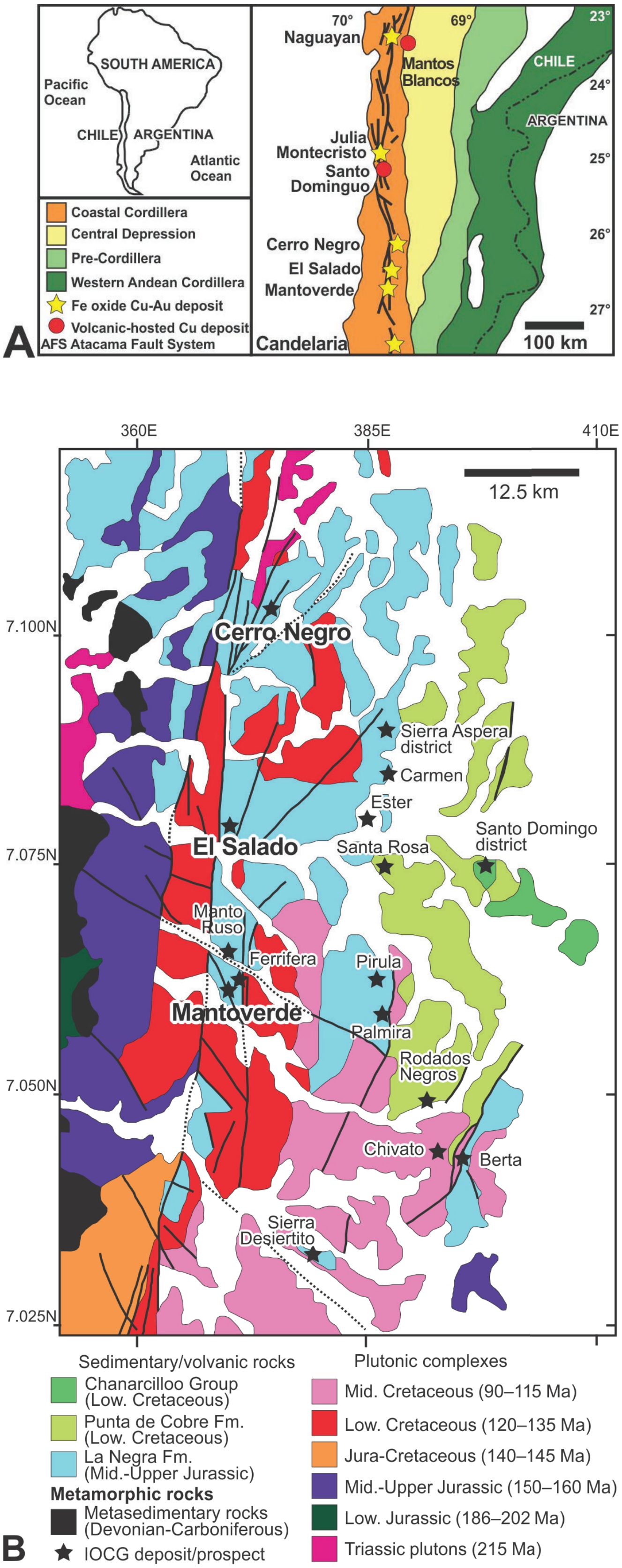


**Figure 19. A.** Map of the Central Andes forearc in northern Chile. **B.** Geology of the Mantoverde area, modified from Lara and Godoy (1998).

belt to the north (Fig. 21). The Archean craton is a granite-greenstone terrain comprising large, composite granite-tonalite batholiths known as the Singhbhum granite complex (with enclaves of older metamorphic and metaplutonic rocks), and metamorphosed sedimentary and volcanic rocks, mafic sills and dykes (Iron Ore Group; Mukhopadhyay et al., 2008). Several Proterozoic volcano-sedimentary basins surround the cratonic nucleus.

The SSZ was subjected to multiple hydrothermal events. It is the largest repository of uranium, and one of the most important copper-producing regions in India (Sarkar, 1984; Pal et al., 2009a, b, 2010, 2011b; Pal and Rhede, 2013). In addition, several small apatite-magnetite deposits occur in the SSZ. Uranium and copper ores are commonly enriched in Ni, Co, Mo, Te, Au and Fe (magnetite), which have been recovered as by-products of uranium and copper mining. The SSZ also holds potential for significant light and heavy REE mineralization (Sarkar, 1982; Pal et al., 2011a; Sarkar and Gupta, 2012).

The zones of polymetallic mineralization are hosted by highly deformed, metamorphosed and variably altered meta-sedimentary and meta-volcanic rocks, including feldspathic

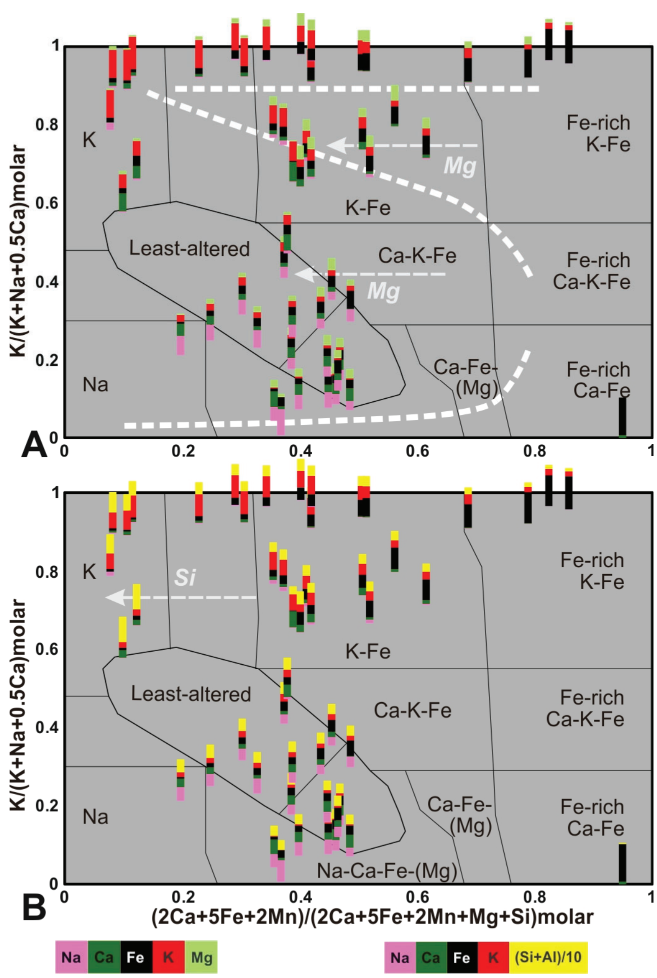


**Figure 20.** Samples from the Mantoverde district in Chile (Benavides et al., 2008; Rieger et al., 2010) plotted on the AIOCG diagram of Montreuil et al. (2013). Data compiled from Benavides et al. (2008).

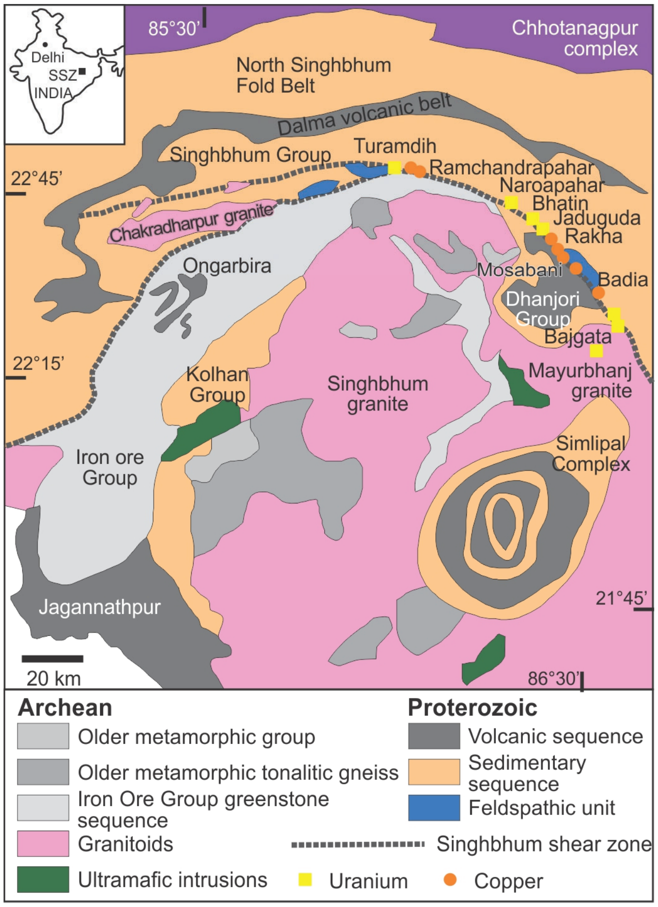


**FIGURE 21.** Regional geologic map of the eastern Indian Craton, illustrating the location of the North Singhbhum fold belt, Singhbhum shear zone and Juduguda deposit (modified from Saha, 1994).

schist/'soda granite' (Dunn, 1942), biotite schist and chlorite schist (Sarkar and Gupta, 2012; Pal et al., 2009 a, b, 2011a, b; Pal and Rhede, 2013; Pal and Chaudhuri, 2016). The feldspathic schist is composed dominantly of albite and quartz overprinted in variable proportions by chlorite, sericite and biotite. The biotite and chlorite schists contain variable modal percentages of quartz, biotite, chlorite, sericite, apatite, magnetite and tourmaline. They may be intensely altered, locally exceeding 70–80 vol% of biotite or chlorite and forming nearly monomineralic rocks. Alteration textures include replacement of albite by chlorite, alkali amphibole by biotite, and biotite by chlorite. Variable chloritization of pre-existing alteration assemblages is widespread. Integrated studies of the mode of occurrences, microtexture, microstructure and mineral dating collectively indicate that most mineralization formed prior to or at a very early stage of shear deformation and metamorphism (Pal et al., 2009b, 2011a, b; Ghosh et al., 2013; Pal and Rhede, 2013). In situ U-Pb dating of allanite suggests that LREE and uranium mineralization took place at ~1.88 Ga and ~1.8–1.9 Ga, respectively, and were later (1.66 Ga and ~1.0 Ga) remobilized during metamorphism and reactivation of the SSZ (Pal et al., 2011a; Pal and Rhede, 2013).

The metal associations (U-Cu-Fe-P-Co-Ni-Mo-REE), structural control, presence of widespread regional potassic and sodic alteration collectively provide evidence in favor of a Fe-oxide (U-Cu-REE) IOCG model. In addition, the discrete zones of mineralization, involvement of high-temperature (exceeding 450°C; Pal et al., 2008; Pal and Bhowmick, 2015) and high-salinity brines (presumably derived from modified seawater/evaporite dissolution), have been collectively interpreted as evidence in favour of the IOCG model (Pal et al., 2009b, 2010, 2011a, b).

Figure 22 illustrates the distribution of alteration facies in the Singhbhum Shear Zone. Felsic and intermediate rocks record sodic, potassic and iron-potassic alteration, and overprinting of albitized facies by iron-magnesium alteration (Fig. 22). These samples are characterized by barcodes with high iron (>35%) and moderate sodium proportions (>10%), yet plot in the least-altered or Ca-K-Fe fields. Magnesium alteration superimposed on the iron-rich Ca-K-Fe and K-Fe alteration facies creates barcodes with magnesium proportions higher than 25%, suggesting systematic late chloritization

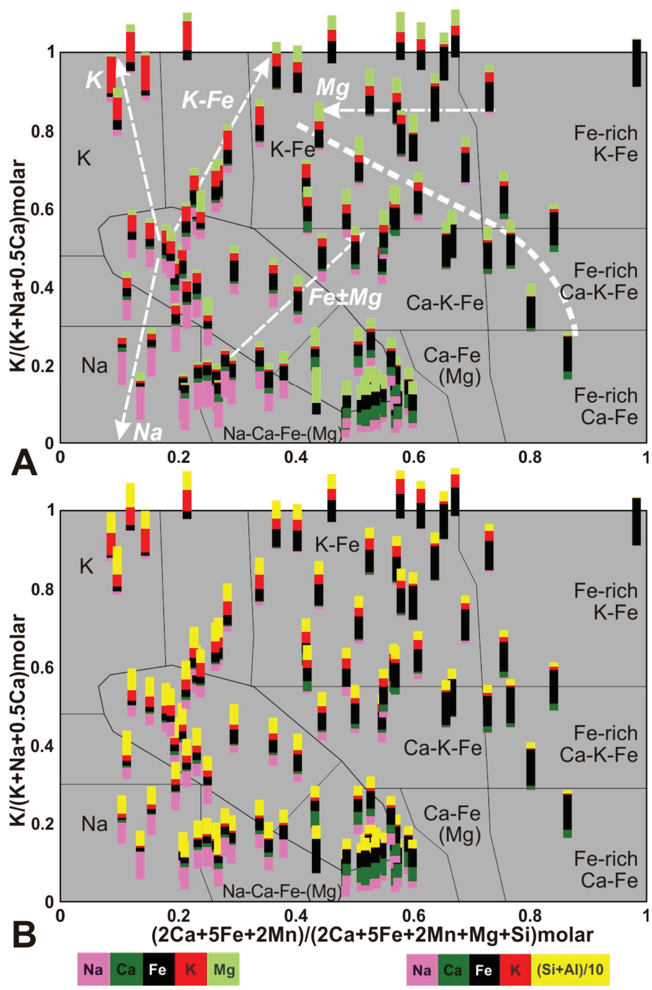


**FIGURE 22.** Samples of the Singhbhum shear zone deposit, India plotted on the AIOCG diagram of Montreuil et al. (2013). Data compiled from Sarkar et al. (1984), Pal et al. (2011a), De et al. (2015) and unpublished data of D.C. Pal.

superimposed on HT K-Fe alteration facies. Overall, the sample suite from the Singhbhum Shear Zone defines a prograde path up to the HT K-Fe alteration facies, whereas K and LT K-Fe alteration facies are lacking.

### Polymetallic Skarn: Punt Hill, Australia

The Olympic Copper-Gold Province is best known for sericite-hematite breccia-hosted IOCG deposits such as the Olympic Dam and Prominent Hill deposits (Williams et al., 2005; Skirrow, 2022). However, within geological sequences rich in carbonate rocks, skarn, K-skarn and iron oxide alteration and veins are present. Examples include the Cu-Au-Ag-Zn-Pb-REE skarn-hosted mineralization in the Punt Hill district (Reid et al., 2011; Fabris et al., 2018a, b), and the Hillside copper-gold skarn deposit in the Moonta-Wallaroo district (Conor et al., 2010; Ismail et al., 2014) (Fig. 11).

In the Moonta-Wallaroo district, the magnetite-dominant Cu-Au ± Mo mineralization and skarn-type alteration at Hillside is interpreted to represent hydrothermal activity at a relatively deep crustal level, contrasting with shallower, brecciated hematite-sericite-dominant mineralization at Olympic Dam (Conor et al., 2010; Ismail et al., 2014).

At the Punt Hill prospect, skarn alteration is layer-controlled and developed within the Wandearah Formation, which comprises a sequence of laminated dolomitic micaceous siltstone, fine-grained micaceous sandstone, and minor dolomite and conglomeratic greywacke (Cowley et al., 2003). Hematite and minor magnetite replace earlier prograde grossular garnet and clinopyroxene within veins; however, much of the iron in the system is accommodated in skarn minerals (e.g. andraditic garnet) (Reid et al., 2011; Fabris et al., 2018a, b). The host sequence unconformably overlies sericitized and hematite-altered granite of the Donington Suite, and is overlain by crystal-lithic tuff-dominated felsic volcaniclastic units of the GRV (Reid et al., 2011).

Figure 23 illustrates the alteration facies present in felsic tuffs (upper part of system) within and more than four km away from the Punt Hill prospect. Felsic tuffs near the mineralized zone are K and K-Fe altered, and none of the samples plot in

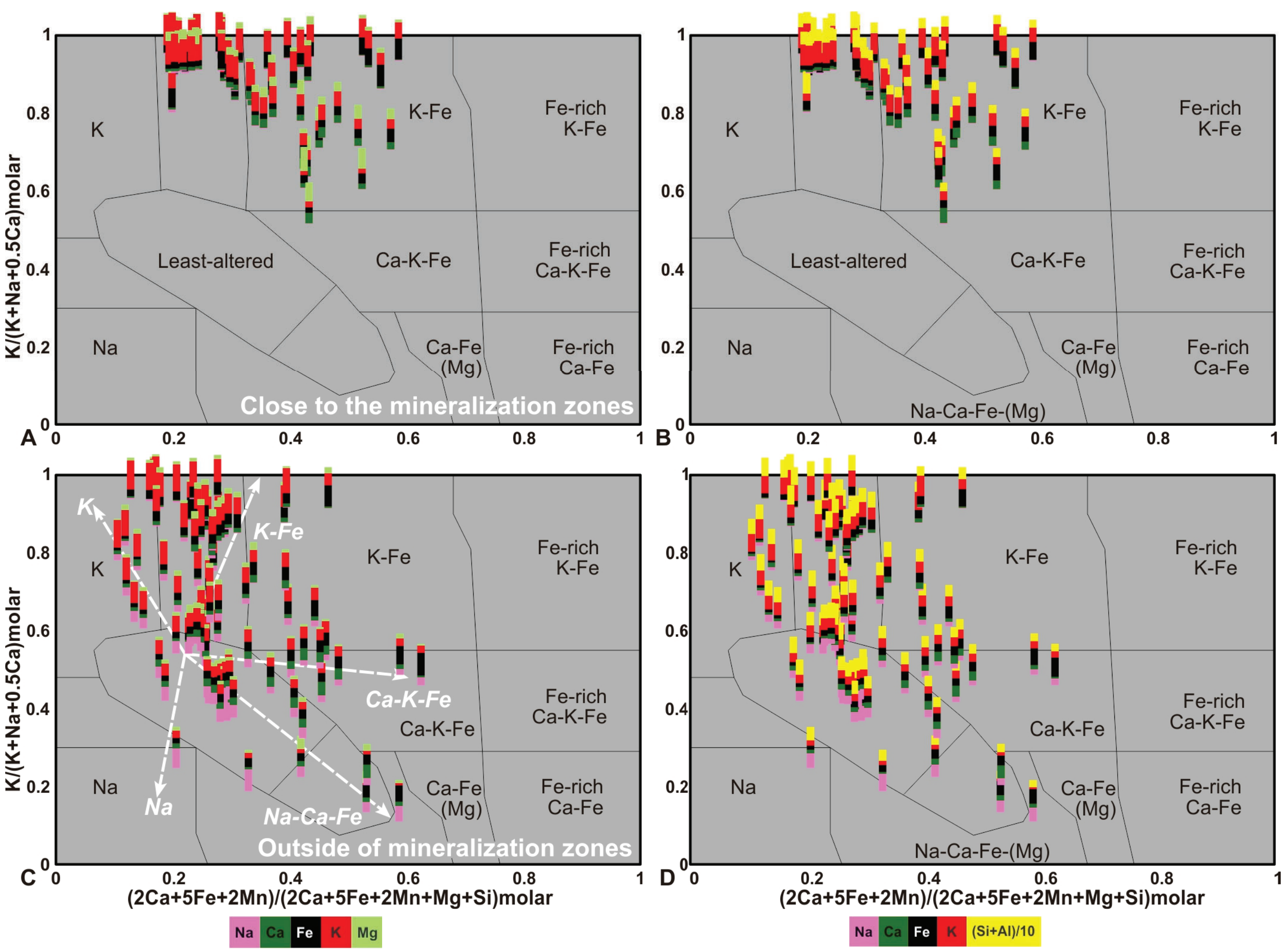


**FIGURE 23.** Samples of felsic tuffs (GRV) of the Punt Hill skarn prospect plotted on the AIOCG diagram of Montreuil et al. (2013). **A, B.** Close to the mineralized zones. **C, D.** Outside of the mineralized zones. Data compiled from the Geological Survey of South Australia, via South Australian Resources Information Gateway (https://map.sarig.sa.gov.au/).

the least-altered field (Fig. 23A, B). The felsic volcaniclastic rocks are characterized by four main barcode groupings: 1) potassium (K proportions: 60–75%); 2) potassium-iron (K: 25–50%; Fe: 30–50%); 3) potassium-magnesium with subordinate calcium and iron (K: 25–55%; Mg: 20–35%; Ca and Fe 15–20%); and 4) magnesium with subordinate calcium and iron (Mg: 45–60%; Ca and Fe: 15–25%).

Higher magnesium proportions, likely representing some of the skarn alteration zones, characterize the base of the upper (volcaniclastic) part of the system. In boreholes far from skarn, felsic volcaniclastic rocks define trends that deviate from the least-altered end-member (Fig. 23C, D): 1) K-Fe; 2) K; 3) Ca-K-Fe; 4) Na + Ca-Fe; and 5) Na. The association of these alteration zones is diagnostic of IOAA systems.

In mineralized skarn within laminated metasedimentary rocks, there is a continuum between potassium-rich and calcium-rich end-members (Fig. 24A, B). The potassium-rich end-members have barcodes with potassium proportions greater than 40%. Data that plot in the K alteration facies reflect prominent, selectively-replaced feldspathic marker units within the skarn. Samples that plot in the K-Fe field display three or four main elements in the barcodes, which is atypical of K-Fe alteration; they may correspond to less-altered laminated sedimentary rocks. Higher molar proportions of magnesium, suggesting chloritization of earlier skarn, characterize laminated sedimentary rocks associated with mineralized skarn. Sulphides, hematite and gold formed late in the paragenetic sequence (Reid et al., 2011). Veins related to the later assemblage are quartz-feldspar-chlorite-hematite-dominant and display alteration selvages of chlorite-hematite-calcite (Reid et al., 2011).

Outside of the mineralized zones, data plots for laminated metasedimentary rocks consistently display a continuum between K-Fe alteration and iron oxide-rich skarn, and K-feldspar alteration in the marker horizon is less developed (Fig. 24C). Unmineralized metasedimentary rocks exhibit more variable AIOCG 2 index values due to significant variation in magnesium and silica contents. Their barcodes display lower molar proportions of magnesium and higher molar proportions of sodium than in laminated metasedimentary rocks associated with mineralized skarn (Fig. 24C, D).

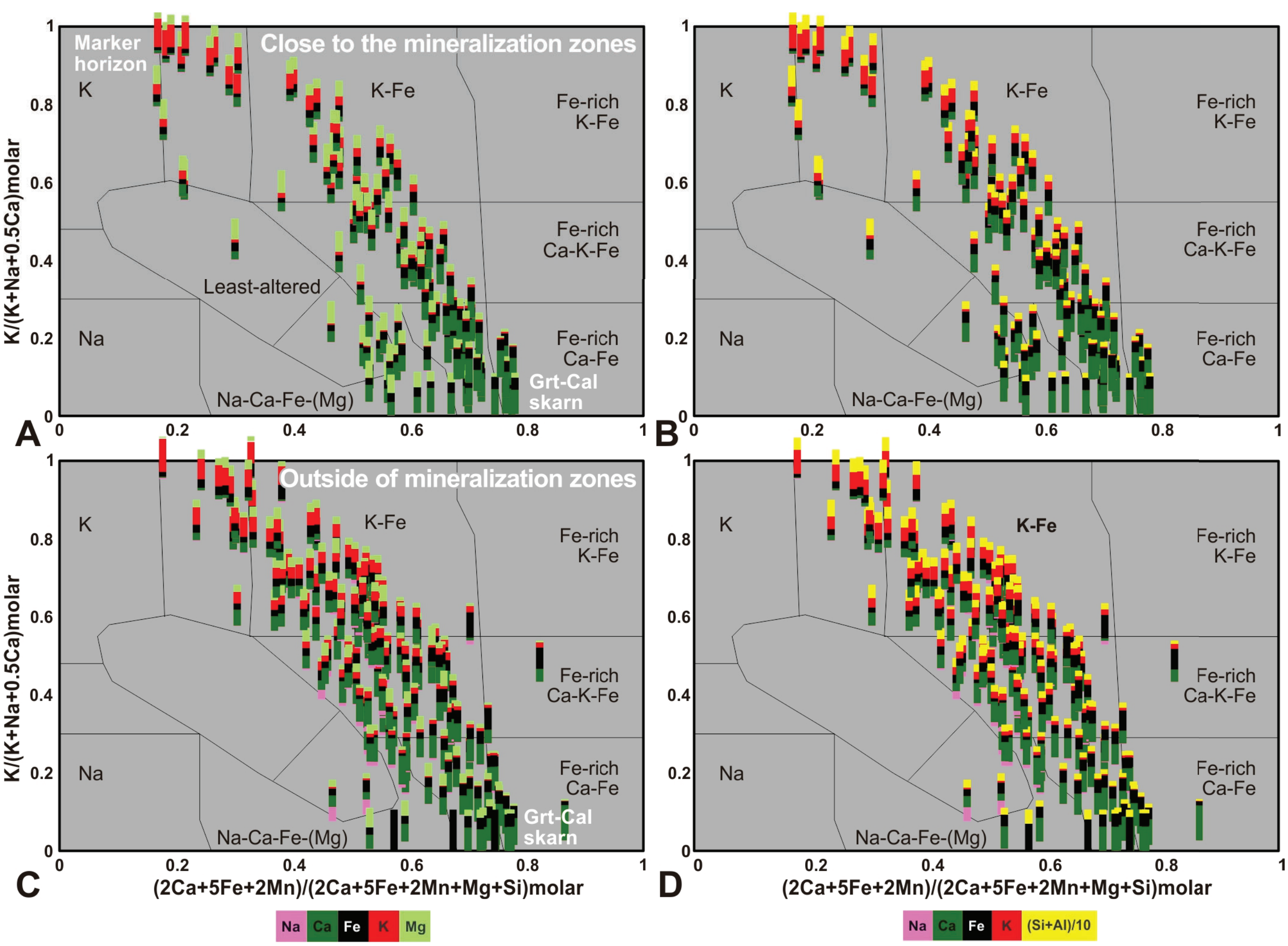


**FIGURE 24.** Samples of the laminated metasedimentary rocks of the Punt Hill skarn prospect plotted on the AIOCG diagram of Montreuil et al. (2013). **A, B.** Close to the mineralized zones. **C, D.** Outside of mineralized zones. Data compiled from the Geological Survey of South Australia, via South Australian Resources Information Gateway (https://map.sarig.sa.gov.au/).

### Albitite-hosted Uranium Deposits

*The Southern Breccia Prospect and Host IOAA System, Great Bear Magmatic Zone*

In the southern GBMZ, uranium and polymetallic uranium mineralization is hosted within a brecciated albitite corridor, one km south of the magnetite-rich Au-Co-Bi-Cu NICO deposit, a cobalt-rich variant of magnetite-group IOCG deposits, and overlying *bona fide* IOCG mineralization (Summit Peak and Chalco prospects). The regional IOAA system hosting both the NICO deposit and the Southern Breccia mineralization is herein termed the Lou IOAA system.

The Lou system is hosted in a tilted section of 1.88 Ga metasedimentary rocks that are unconformably overlain by unmetamorphosed (sub-greenschist facies) 1.87 Ga volcanic rocks (Goad et al., 2000a, b; Gandhi et al., 2001). The 1.88 Ga sedimentary sequence consists of: 1) a lower siltstone unit, 2) a middle carbonate unit with siltstone and wacke interbeds, 3) a massive quartz arenite unit, and 4) an upper siltstone unit. The main mineralized zones of the Lou IOAA system are hosted by the lower siltstone, carbonate and quartz arenite units.

The Southern Breccia albitite corridor (3 by 0.5 km) comprises albitized metasedimentary rocks, albitite, and local porphyritic dykes that are replaced, cut and brecciated by HT to LT K-Fe alteration facies hosting concentrations of up to 1 wt% U in representative hand and channel samples (Corriveau et al., 2015; Montreuil et al., 2015). Early porphyritic rhyolite dykes, granite and subvolcanic intrusions are also locally albitized (Montreuil et al., 2016b).

The Southern Breccia corridor demonstrates that the large albitization zones associated with the evolution of IOAA systems are potential hosts of albitite-hosted uranium deposits (Montreuil et al., 2015; Potter et al., 2019; see also Wilde, 2013). Similarities between the Southern Breccia and other major albitite-hosted uranium deposits like Valhalla (Australia), Aricheng (Guyana), Espinharas and Lagoa Real (Brazil) include: a large-scale albitization event that predates the uranium-thorium mineralization, and ore deposition during the transition from brittle-ductile to brittle deformation (Porto da Silveira et al., 1991; Polito et al., 2009; Alexandre, 2010).

In Figure 25A and B, altered samples from the Southern Breccia corridor are characterized by three distinct barcodes:

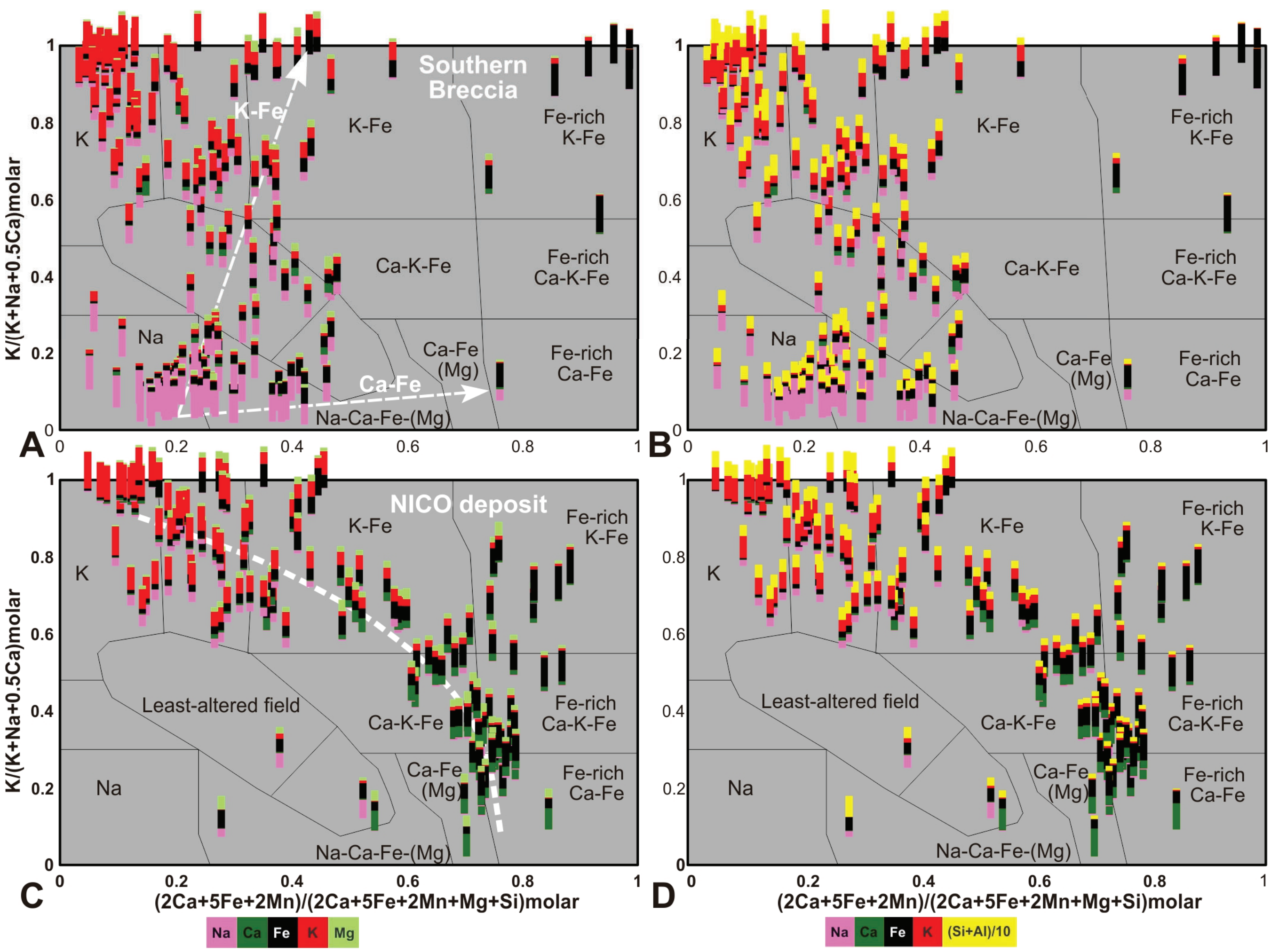


**FIGURE 25.** Samples of the Lou IOAA system, Great Bear magmatic zone, Canada, plotted on the AIOCG diagram of Montreuil et al. (2013). **A, B.** Southern Breccia albitite corridor and uranium mineralization. **C, D.** NICO deposit. Data compiled from Corriveau et al. (2015).

1) sodium-dominated (Na: 70–85%); 2) potassium-iron dominated (K: 30–65%, Fe: 25–50%); and 3) potassium dominated (K: >75%). Sodium-dominated with subordinate iron (Na: 45–75%, Fe: 20–40%) is the most common barcode type. The data as a whole form a continuum between the Na and K-Fe alteration facies (Fig. 25A, B). These latter two facies are characterized by a progressive decrease in sodium proportions (from 80% to <5%), and a progressive increase in the potassium and iron proportions. These behaviours are typical of K or K-Fe overprints on albitite.

In contrast, within the NICO deposit, altered samples exhibit a continuum between Ca-Fe rich and K-rich end-members. Four main types of barcodes characterize this continuum: 1) iron-calcium dominated (Fe: 40–65%; Ca: 15–25%); 2) iron dominated with subordinate potassium and calcium (Fe: 25–45%; K: 15–30%; Ca: 15–25%); 3) potassium dominated with subordinate iron (K: 40–65%; Fe: 15–25%); and 4) potassium dominated (K >70%).

Along the Southern Breccia corridor, albitite is abundant and, in contrast to other albitite corridors of the GBMZ, the albitite is in sharp contact with HT Ca-Fe alteration zones – without the typical amphibole veining and HT Na-Ca-Fe facies (Montreuil et al., 2015). High-temperature Ca-Fe veining is weakly developed along the faulted (inferred) northern margin, closest to the NICO deposit. In Southern Breccia showings, the uraninite-bearing mineralization postdates albitization and is coeval with HT K-Fe (biotite-magnetite ± K-feldspar) alteration and LT K-Fe ± Mg (hematite ± K-feldspar ± chlorite) alteration. The chemistry of uraninite correspondingly evolves from high- to low-temperature signatures (Montreuil et al., 2015; Potter et al., 2019, 2022).

Within the NICO deposit, the prograde Au-Co-Bi ± Cu mineralization occurred during pulsating HT Ca-K-Fe and HT K-Fe alteration with late stage mineralization being coeval with LT K-Fe alteration. All these alteration facies occur as stratabound replacement, localized breccia cements and as veins within the earlier, intense and pervasive HT Ca-Fe alteration zones in metasiltstone (Acosta-Góngora et al., 2015; Corriveau et al., 2016; Montreuil et al., 2016b). Above the deposit, overlying volcanic rocks are intensely K-altered and locally cut by HT K-Fe breccias and associated chalcopyrite-bearing IOCG mineralization (Acosta-Góngora et al., 2015; Corriveau et al., 2016; Montreuil et al., 2016b).

Field relationships, geochronology and geochemical signatures demonstrate that the Southern Breccia and NICO deposit developed as part of a single IOAA system (Davis et al., 2011; Montreuil et al., 2016a; Potter et al., 2019). In addition, field relationships indicate that evolution of K-Fe and K metasomatism in the Southern Breccia corridor was coeval with the development of these facies in the volcanic rocks above the NICO deposit. The evolution of Southern Breccia alteration, with characterized by early albitization that was cut and replaced by K-Fe alteration facies, provides an example of tectonic telescoping of system components; i.e. tectonic thrusting of earlier-formed albitite into the fields of HT K-Fe, K, and finally LT K-Fe-Mg metasomatism (Montreuil et al., 2015; Enkin et al., 2016; Hayward et al., 2016).

*Romanet Horst, Labrador Trough: Albitite-hosted Uranium-Gold Mineralization within an Iron Oxide-poor System*

The Labrador Trough is a Paleoproterozoic collisional fold and thrust belt of the New Quebec Orogen (NQO) (Fig. 26). It consists of four principal parautochthonous and allochthonous lithotectonic zones composed of Paleoproterozoic sedimentary, volcanic and plutonic rocks: Schefferville, Howse, Gerido-Doublet and Rachel-Laporte (Fig. 27; Dimroth, 1978; Clark and Wares, 2004; Konstantinovskaya et al., 2019).

In the Central Labrador Trough, the autochthonous Cambrien zone and parautochthonous Schefferville zone are composed of ironstone and sedimentary rocks. The allochthonous Howse zone is composed of voluminous sills of gabbro and pillows of basalt with subordinate sedimentary rocks. The sedimentary rocks of the Wheeler zone are exposed

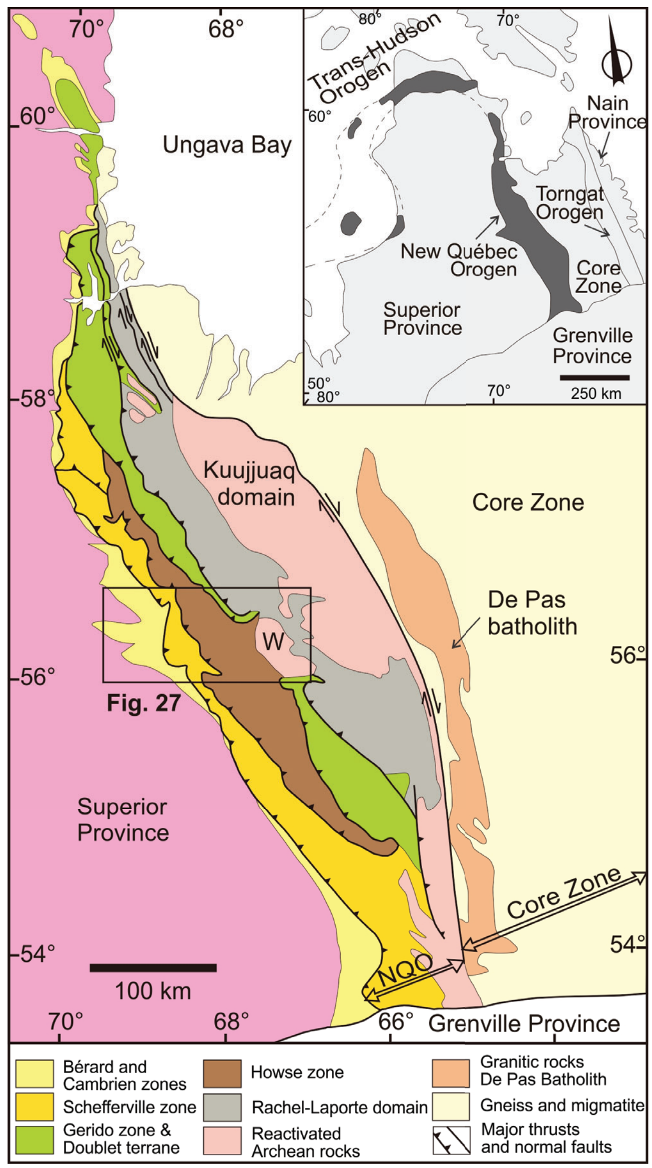


**Figure 26.** Major tectonic zones of the New Quebec Orogen modified after Wardle et al. (2002), Clark and Wares (2004) and Corrigan et al. (2018). *NQO*: New Québec Orogen; *W*: Wheeler.

between two nappes of mafic rocks of the Howse zone (Fig. 27) in a structure delimited by the Bertin and Romanet faults and known as the Romanet horst (Le Gallais and Lavoie, 1982; Chevé, 1985; Clark, 1986). The Gerido and Doublet zones are composed of pyroclastic and sedimentary rocks with basaltic lava flows and sills of mafic and ultramafic rocks. The hinterland of the Central Labrador Trough is composed of gneiss, migmatite, migmatized sedimentary schist and amphibolite of the Rachel-Laporte zone (Fig. 26), grading into reworked Archean basement rocks and granitic plutons of the Kuujjuaq domain (Charette et al., 2017; Rayner et al., 2017).

The Romanet Horst records the development of metasomatic iron and alkali-calcic systems that are generally poor in iron oxides and dominated by albitite-hosted uranium-gold mineralization. The information gained from this system complements that available for the albitite corridor within IOAA systems of the GBMZ. Volcanic and sedimentary rocks of the Romanet horst form a regional-scale albitite corridor along bounding and transverse fault zones (Corriveau et al., 2014; McLaughlin et al., 2016). Recent exploration has focused on this corridor and adjacent hosts within the Sagar property (Desrochers, 2014). Metasomatism was synchronous with alkaline magmatism within the Trough and emplacement of the 1835–1800 Ma De Pas batholith to the east of the Trough (Fig. 26; Clark and Wares, 2004).

Within the horst, coeval intermediate to felsic magmatism is lacking. High-grade gold and uranium mineralization occur within sericitized and brecciated albitite cut by dolomite veins. In albitite corridors, iron preferentially occurs as sulphides rather than oxide form, and graphitic schists are common associates (Clark, 1986; Clark and Wares, 2004; Corriveau et al., 2014).

Host sedimentary and fine-grained mafic rocks are pervasively and intensely albitized whereas carbonate units are cut by sharply defined albitite veins. The albitite zones are cut by very regular, parallel fractures that host amphibole and sulphide veins, and veinlets of quartz and dolomite, all brecciated and locally folded. These veins are associated with locally pervasive hydrolytic LT K-Fe alteration (carbonates, chlorite, hematite, K-feldspar, white mica), silicification (quartz), sericitization and phyllic alteration (white mica, pyrite), LT Ca-Mg-Fe (chlorite-epidote), carbonatization, and sulphate (Ca-SO4) alteration that host the Au, Co, Cu and U mineralization and Mo and REE enrichments (Corriveau et al., 2014; McLaughlin et al., 2016).

Albitized mafic rocks are locally cut by HT Ca-Fe (magnetite-amphibole) and copper-mineralized HT K-Fe alteration (biotite-magnetite-chalcopyrite), which is typical of magnetite-group IOCG deposits (Corriveau et al., 2014). Dolomitic beds display locally intense stratabound alteration to specular hematite. Detailed alteration mapping identified up to nine alteration types, including Na, HT Ca-Fe, HT K-Fe, and LT K-Fe alteration, followed by silicification, sericitization/phyllic alteration, LT Ca-Fe alteration, carbonatization, and sulphate alteration (Corriveau et al., 2014). To date, skarn, K-feldspar felsite, and K-feldspar-bearing skarn have not been observed even though carbonate rocks are abundant. Some zones display transitional Na-Ca-Fe or HT Ca-Fe-K alteration.

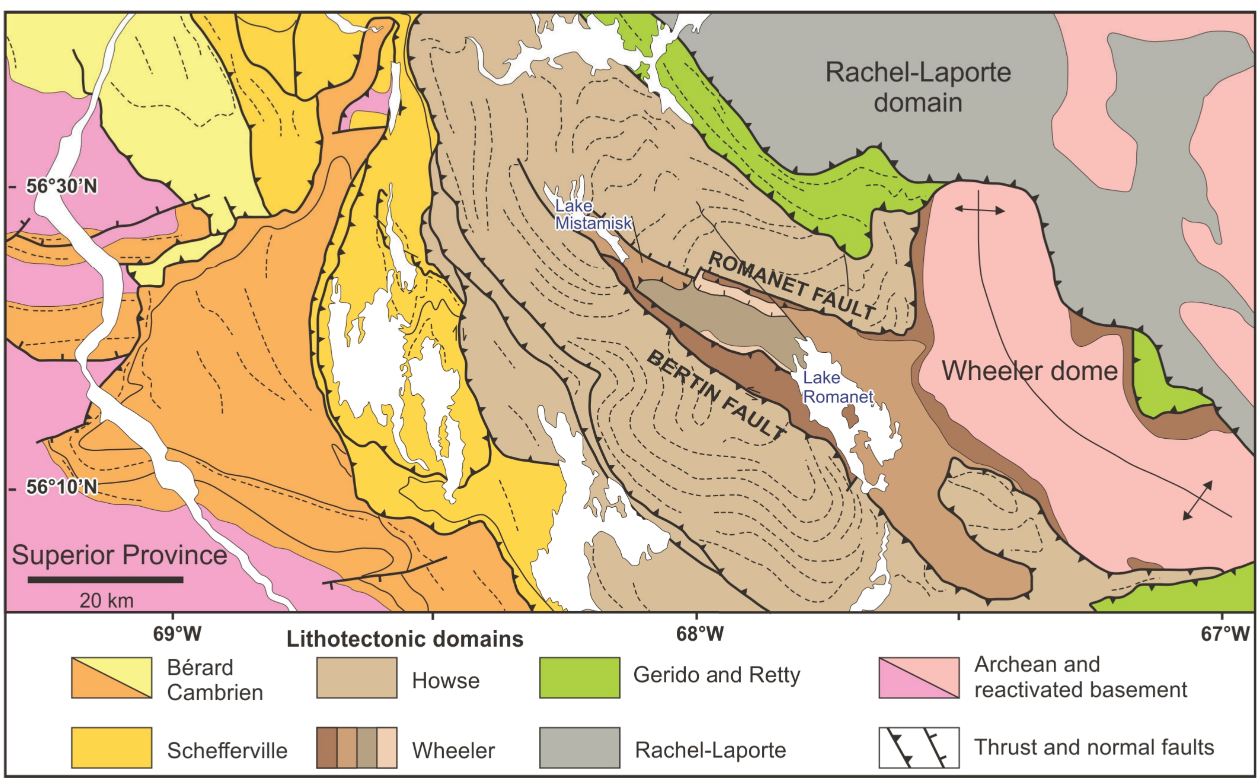


**FIGURE 27.** Map of tectonic zones of the Central Labrador Trough, modified after Dimroth (1978), Clark (1986) and Clark and Wares (2004).

Figure 28 illustrates the distribution of alteration facies in the Romanet Horst. Albitized volcano-sedimentary rocks form albitite, which plots within the Na field. Some K ± Fe and K-Fe veins and replacement zones cut or overprint albitized and mafic rocks, forming two distinct trends on the AIOCG diagram, both if which may plot within the least-altered field (Fig. 28). Abundant dolomite and quartz veining and local chloritization have led to magnesium and silica overprints that shift the HT Ca-Fe and HT Ca-K-Fe samples towards the left (Fig. 28), whereas it shifts albitite toward the right.

The barcodes and their distribution (Fig. 28) provide a good case example of the footprint of IOAA systems dominated by albitite-hosted uranium-gold mineralization, in which albitite is overprinted by low-temperature carbonate alteration and chlorite- and dolomite-bearing veins. The additional alteration facies indicate that, overall, the system has followed a prograde path but that the footprint of albitite tectonically telescoped to lower temperature facies dominates, a feature also observed in the Central Mineral Belt of Labrador (Acosta-Góngora et al., 2019).

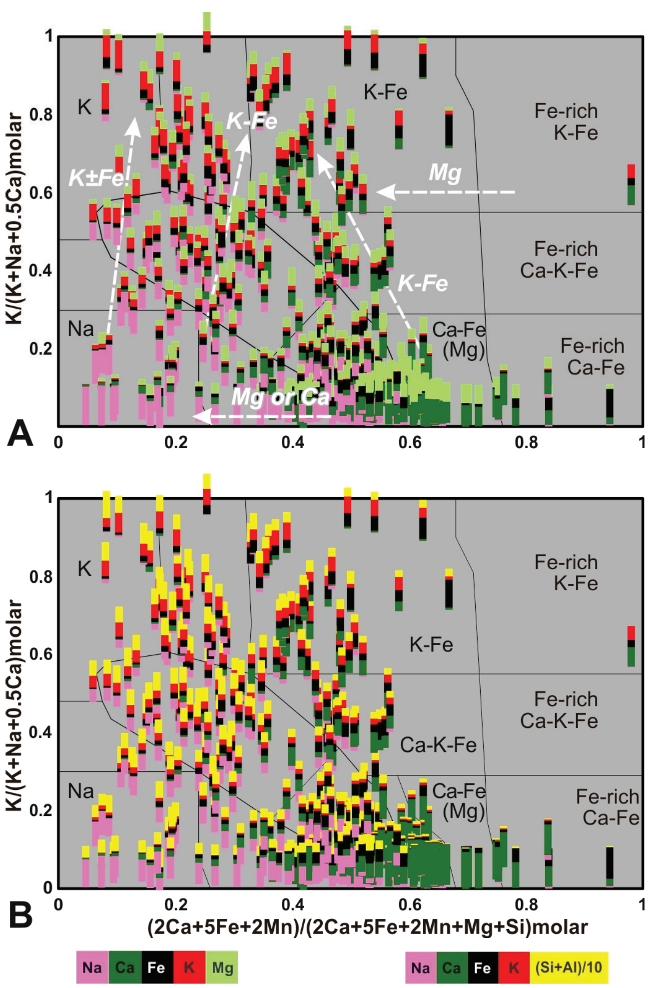


**Figure 28.** Samples of the Romanet Horst deposit, Canada, plotted on the AIOCG diagram of Montreuil et al. (2013). Data compiled from McLaughlin et al. (2016).

## Mineralization and Metal Endowments

*Olympic Dam Deposit*

Figure 29 is a graphic representation of alteration (using molar barcodes) and concentrations of select metals and trace elements from borehole samples of the ODBC. The main purpose is to visualize the associations between metal and cation fluxing and alteration facies.

For each selected metal and trace element, four equal composition intervals (quartiles) are portrayed based upon all the values from the ODBC. Dark green dots represent the first quartile: the quarter of the dataset with the lowest concentration range for that element. Pale green dots represent the second quartile: between 25.1% and 50% of the dataset. Yellow dots represent the third quartile: between 50.1% and 75% of the dataset. Orange and red dots represent the fourth quartile. Red dots represent the 5% of the dataset with the highest concentrations.

Outside of the ODBC, metals are generally at background levels; ytterbium is the only element having consistently elevated values; it has been proposed (Kontonikas-Charos et al., 2018) that ytterbium mobility is linked to potassic alteration. The K-alteration facies does not show significant enrichment in metal and trace elements (Fig. 29). In borehole RD2316, metal and trace elements, such as Cu, Au, Ag, Bi, Co, and Ce, are in the first quartile in terms of concentration (Fig. 29). By contrast, ytterbium contents are in the third quartile, suggesting a light enrichment (Fig. 29).

Within the ODBC, the abundance of selected elements (Cu, Au, Ag, Bi, Co, Ce and Yb) either increases or decreases from one alteration facies to another, and each alteration facies has distinct metal assemblages (Fig. 29). Downhole comparisons show that variations in concentrations of metals and trace elements define very clear boundaries that correspond to changing alteration facies.

Within the ODBC, zones where potassium and iron alteration are coeval show a diversity in metal and cation fluxing. Iron-rich hydrothermal facies (iron proportions greater than 75% in barcodes) are characterized by enrichments in Cu, Au, Ag, Co and Ce, so that metal and trace element contents are generally in the fourth quartile. These zones have molar barcodes largely dominated by iron and associated potassium and calcium. This link between enrichment in Cu, Au, Ag, Co and Ce, and iron-rich K-Fe ± Ca alteration facies is observed in boreholes RD2785 (at 360 m and 575 m), RD1247 (630 m), RD2715 (at 420 m and 560 m), RD2751 (at 720 m and 960 m), and RD1998 (>810 m).

In K-Fe and iron-rich K-Fe alteration facies, enrichments in Cu, Au, Ag, Co and Ce are not as great as in iron-rich Ca-K-Fe alteration facies, as metal and trace element contents fall mainly in the second and third quartiles. Significant differences in Cu, Au, Ag, Co and Ce enrichment exist between the iron-rich K-Fe ± Ca and K or K-Fe alteration facies, and between K-Fe and K alteration facies. For example, contrasting enrichments between the K and K-Fe facies are evident in borehole RD2316 at 440 m depth (Fig. 29), as data for the K facies fall mainly in the first quartile, whereas data for the K-Fe facies fall partly in the third and fourth quartiles. Similarly, in borehole RD2715, at 460 and 560 m depth, marked differences in enrichment are observed between iron-rich K-Fe ± Ca and K-Fe alteration facies (Fig. 29). In this borehole, K-Fe-altered samples fall essentially in the second quartile. By contrast, in the K-Fe ± Ca alteration facies, data fall in the third and fourth quartiles. This contrast in metal enrichments is most significant where fluids transition from K to K-Fe alteration facies, and from K-Fe to iron-rich K-Fe ± Ca alteration facies (Corriveau et al., 2022a).

*Southern Breccia Corridor versus the NICO Deposit*

Figure 30 illustrates variations in Bi, Co, Cu and U in the NICO deposit and within the Southern Breccia corridor. In the Southern Breccia, albitite and some samples altered to the K-Fe alteration facies are enriched in uranium and copper. This is in agreement with the genetic relationship observed between uranium mineralization and K-Fe assemblages in the Southern Breccia albitite-hosted uranium showings (Montreuil et al., 2015; Potter et al., 2019). At the NICO deposit, enrichments in Bi, Co, and Cu follow the prograde path from iron-rich HT Ca-Fe through progressively more intensely mineralized HT Ca-K-Fe to HT K-Fe alteration facies. Zones of HT Ca-K-Fe alteration are associated with higher Bi-Co-Cu contents and minor Cu. In the NICO deposit, the Au-Bi-Cu mineralization is within a high-temperature Ca-K-Fe alteration assemblage (Montreuil et al., 2016b). This observation highlights the typical association between potassium-bearing alteration facies and enrichment in base, precious and some critical metals in deposits formed in IOAA systems.

## A Predictive Exploration Tool

Iron-oxide and alkali-calcic alteration systems are characterized by a wide variety of mineral deposits, including iron oxide-apatite (IOA), iron oxide-copper-gold (IOCG), iron oxide Co/Bi/REE/U, skarn, and albitite-hosted U and Au-Co ± U.

Using whole-rock geochemical data, the evolution of the most intense alteration in IOAA systems is shown to follow a regular evolutionary trend that is attributed to the consecutive reactions of a voluminous fluid plume with host rocks as it ascends through the crust (Corriveau et al., 2022a–e). The prograde metasomatic sequence of IOAA systems results in distinct variations in the molar proportions of Na, Ca, Fe, K, Mg, and (Si + Al)/10 in different alteration facies. By combining molar barcodes with the alteration indices Na-Ca-Fe-K-Mg and Na-Ca-Fe-K-(Si + Al/10) on the AIOCG discriminant diagram of Montreuil et al. (2013), clear identification of hydrothermal alteration processes of IOAA systems is possible.

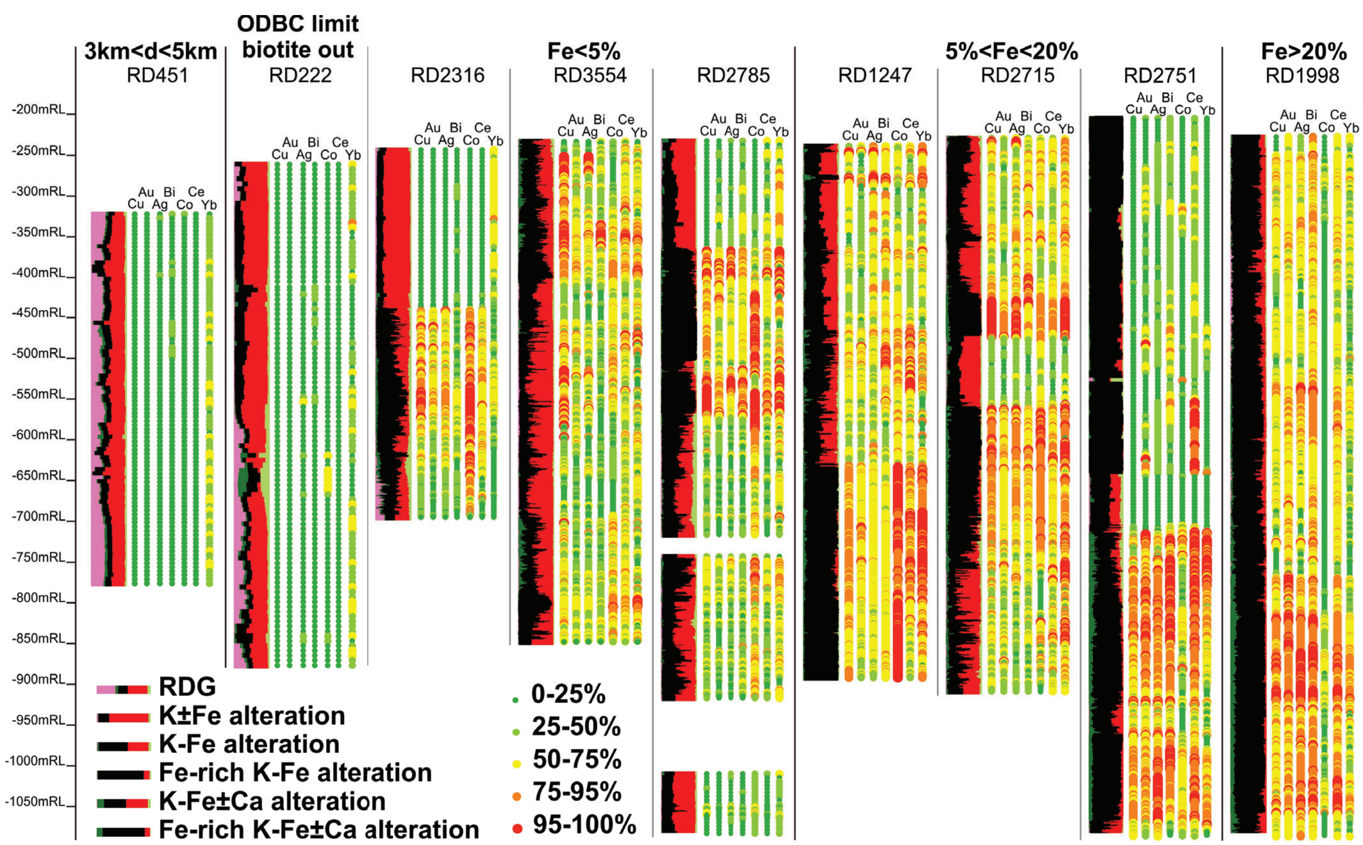


FIGURE 29. Graphic representation of hydrothermal alteration and concentrations of Cu, Au, Ag, Bi, Co, Ce and Yb in borehole samples from the ODBC. Hydrothermal alteration is illustrated using molar proportions of Na, Ca, Fe, K and Mg: Boreholes are arranged in distal to proximal order (left to right) with respect to mineralization. See text for explanation of coloured dots used for elemental abundances (quartiles).

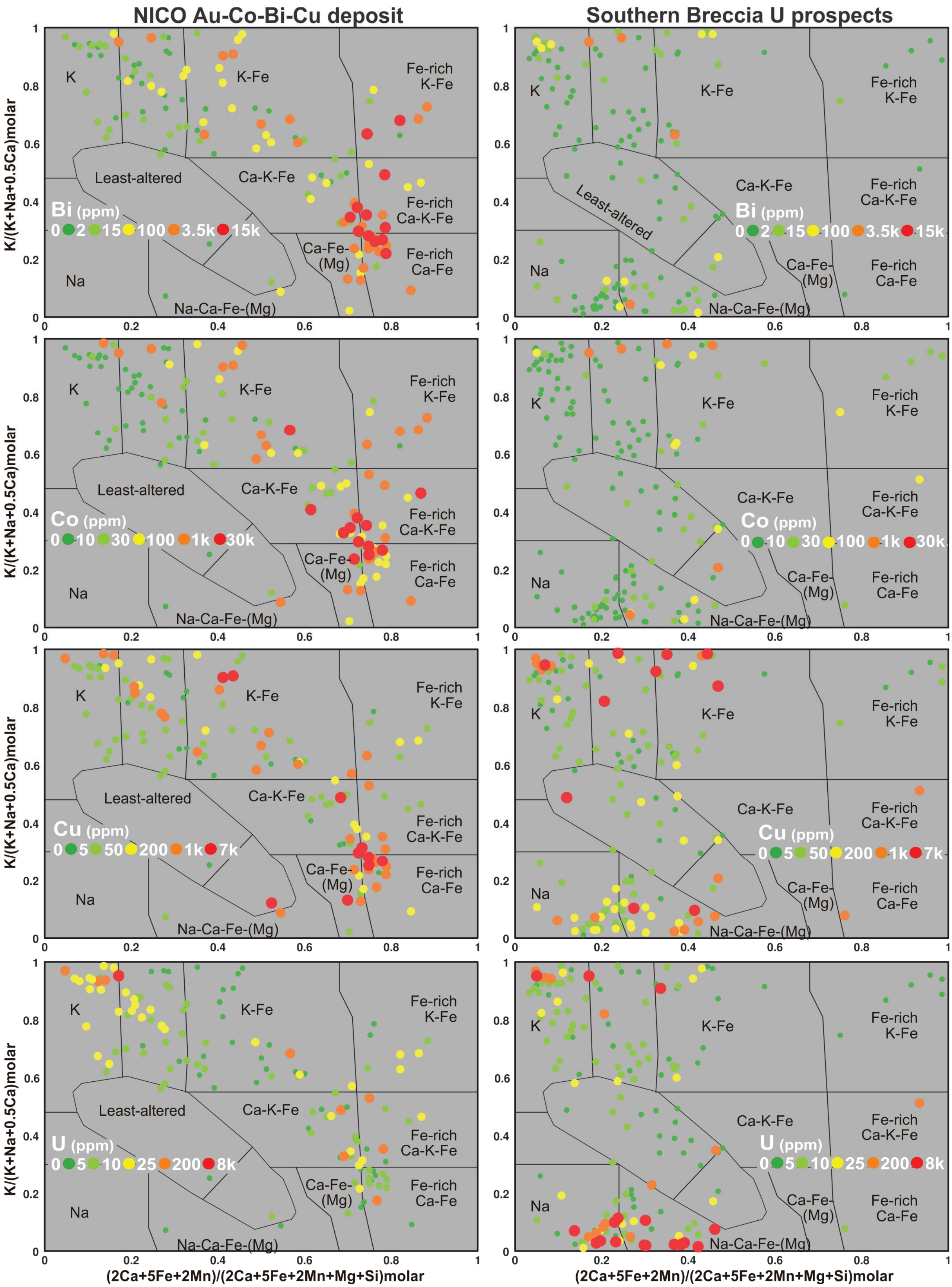


**Figure 30.** Bismuth, cobalt, copper, and uranium contents from samples of the NICO deposit and Southern Breccia areas plotted on the AIOCG diagram of Montreuil et al. (2013). The percentile ranges are from the entire dataset of the GBMZ. Data compiled from Corriveau et al. (2015).

In the AIOCG diagram, a classic prograde metasomatic path characterized by the five main alteration facies (Na, HT Ca-Fe, HT K-Fe, K felsite, and LT hydrolytic K-Fe) defines a counter-clockwise trend culminating in the LT K-Fe alteration facies, as illustrated by a plot of highly altered samples from the GBMZ (Fig. 31A). However, the lower temperature facies, such as LT K-Fe, are under-represented in the GBMZ dataset. Weakly to moderately altered samples plot between least-altered rocks and the classic prograde metasomatic path.

In cases where IOAA systems do not follow a linear evolution, the resulting metasomatic path relates to tectonic telescoping, renewed magmatism, influx of externally derived fluids or a combination of multiple geological processes. Molar barcodes enable the recognition of such superimposed hydrothermal alteration. For example, faulting can telescope albitite zones to levels with HT and/or LT K-Fe ± Ca fluids (Fig. 31B), and occasionally precipitate uranium. In host sedimentary rocks of the Southern Breccia corridor in the GBMZ, normal faulting has juxtaposed HT K-Fe facies U-Cu-Mo mineralization against uranium-bearing LT K-Fe alteration facies in albitite at shallower crustal levels (Potter et al., 2019). The overprinting of albitite by K, K-Fe or Ca-K-Fe alteration produces alteration trends that overlap the field of least altered samples, yet exhibit atypical molar barcodes relative to least altered rocks (Fig. 31B).

In hematite-group IOCG deposits, Na, HT Ca-Fe and HT K-Fe alteration facies are rarely exposed and/or preserved (as illustrated by the Olympic Dam deposit), and are therefore under-represented. In the Olympic Dam Breccia Complex, the recorded metasomatic path of intense alteration extends from the K alteration field to the iron-rich alteration fields (e.g. boreholes RD2366 and RD2715 close to the Olympic Dam deposit; Fig. 32A).

Other metasomatic paths characteristic of hematite-group IOCG environments define continuous trends between protoliths and K or K-Fe alteration facies. Outside of the mineralized zone, sericitization defines a clear vertical trend characteristic of a K ± Fe alteration (Fig. 32B). In contrast, in mineralized zones, borehole samples at depth define an oblique trend between least-altered protoliths and K-Fe alteration facies (Fig. 32B).

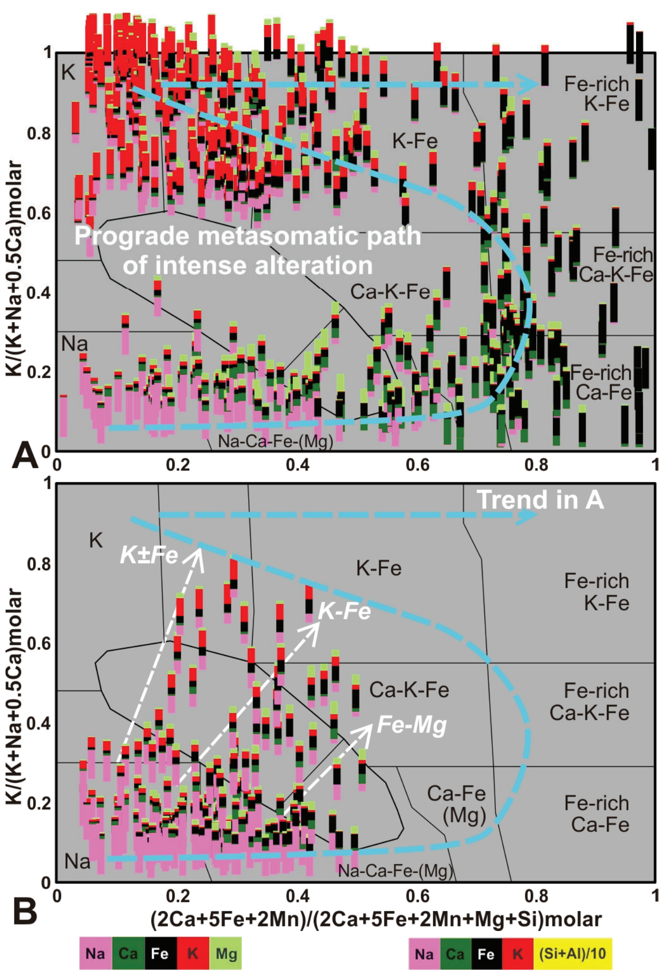


**FIGURE 31.** Chemical evolution of alteration facies in IOAA systems of the GBMZ. **A.** Prograde metasomatic path of intense alterations. **B.** Trends from albitite to subsequent alteration facies. Data compiled from Corriveau et al. (2015).

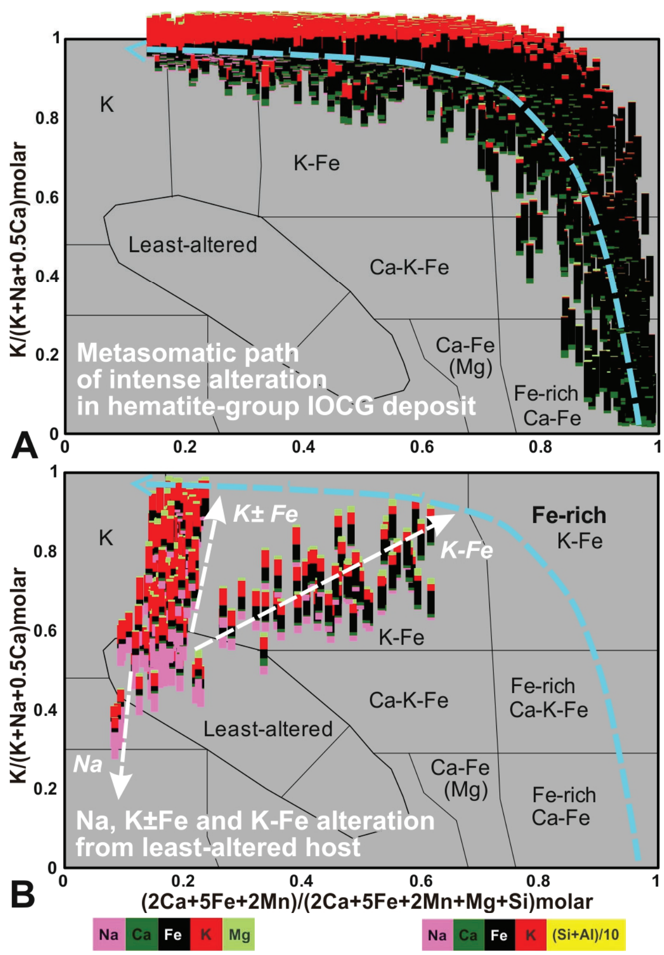


**FIGURE 32.** Chemical evolution of alteration facies in IOAA systems of the Olympic Dam area. **A.** Metasomatic path of intense alteration in boreholes RD2366 and RD2715 in the Olympic Dam deposit. **B.** Trends from least-altered hosts to Na, K±Fe and Fe-K alteration facies, ODBC.

In conclusion, the molar barcodes define metasomatic paths, identify hydrothermal alteration processes, and indicate alteration trends that do not display the complete sequence of alteration facies. When coupled with discrimination plots, the barcodes can therefore identify juxtaposition, overprinting, or telescoping alteration in IOAA systems. The transfer of metals and cations from sources to ore zones can be observed at regional to deposit scale, depending on the dataset. Furthermore, combining trace element concentrations with the AIOCG discriminant diagram of Montreuil et al. (2013) enables an understanding of the behaviour of elements in the development of each alteration facies (see Corriveau et al., 2022a).

To summarize:

1) Most elements are depleted relative to least-altered rocks during albitization;
2) HT Ca-Fe alteration facies give rise to IOA deposits;
3) Enrichment in Co and Au and onset of Cu precipitation is coupled with Ca-K-Fe facies. Iron-oxide Au-Co-Bi ± Cu deposits form at the iron-rich end members of the high-temperature Ca-K-Fe facies (e.g. NICO deposit, GMBZ);
4) HT K-Fe alteration facies lead to the development of breccia or replacement zones hosting copper-gold mineralization. HT K-Fe facies with biotite can also be rich in Co and As, whereas HT K-Fe facies with K-feldspar is marked by precipitation of Ag, Au, Bi, Cu, Mo, REE and U;
5) K alteration facies, such as K-felsite, are largely barren, whereas K-skarn can host polymetallic lead-zinc mineralization.
6) LT K-Fe and Ca-Mg-Fe (± K) alteration facies can produce a wide range of polymetallic mineral deposits, including hematite-group IOCG deposits and uranium or critical metals;
7) Finally, low-temperature alteration facies (Si, Al, K) encompass epithermal alteration/mineralization and polymetallic veins, including five-element veins.

Within IOAA systems, metasomatic alteration facies can be discriminated using Na-Ca-Fe-K-Mg molar proportions, and from other ore systems by proportions of Al-Si. Each facies has distinct paragenetic and chemical characteristics, and their metasomatic reaction paths vector to specific deposit types (IOA, IOCG, skarn, albitite-hosted U or Au-Co-U, and polymetallic vein deposits).

## Acknowledgments

This paper is a collaborative effort between the Geological Survey of Canada and the Institute Carnot BRGM. Data are derived from the Geomapping for Energy and Minerals and the Targeted Geoscience Initiative programs of the Geological Survey of Canada as well as from BHP-Olympic Dam for the Olympic Dam and Acropolis deposits. Other data from South Australian examples are available via South Australian Resources Information Gateway https://map.sarig.sa.gov.au.

Fieldwork and sample collections were conducted in collaboration with the Northwest Territories Geoscience Survey South Wopmay Bedrock Mapping project, Alberta Star Development Corporation, Fortune Minerals Limited, Honey Badger Exploration Inc., Energizer Resources Inc., graduate and undergraduate students, and industry, university and government colleagues from across Canada who generously contributed time, effort, logistical infrastructures or funding for this research. Permission to publish on the Olympic Dam deposit and other BHP prospects and deposits was granted by BHP-Olympic Dam. The authors thank INRS for hosting O. Blein in their department and Chris Lawley, Eric Potter, Sophie Decrée and Adrienne Brotodewo, and Reginal Wilson editor of the Geological Association of Canada (GAC) for their thorough reviews of this paper. NRCan contribution 20200491.

## References

Acosta-Góngora, P., Gleeson, S., Samson, I., Corriveau, L., Ootes, L., Taylor, B.E., Creaser, R.A. and Muehlenbachs, K., 2015, Genesis of the Paleoproterozoic NICO iron-oxide-cobalt-gold-bismuth deposit, Northwest Territories, Canada: evidence from isotope geochemistry and fluid inclusions: Precambrian Research, v. 268, p. 168-193.

Acosta-Góngora, P., Potter, E.G., Corriveau, L., Lawley, C.J.M. and Sparkes, G.W., 2019, Geochemistry of U±Cu±Mo±V mineralization, Central Mineral Belt, Labrador: differentiating between mineralization styles using a principal component analysis approach, *in* Rogers, N., ed., Targeted Geoscience Initiative: 2018 report of activities: Geological Survey of Canada, Open File 8549, p. 381-391.

Alexandre, P., 2010, Mineralogy and geochemistry of the sodium metasomatism-related uranium occurrence of Aricheng South, Guyana: Mineralium Deposita, v. 45, p. 351-367.

Allen, S.R., McPhie, J., Ferris, G., and Cadd, A.G., 2008, Evolution and architecture of a large felsic igneous province in western Laurentia: the 1.6 Ga Gawler Range Volcanics, South Australia: Journal of Volcanology and Geothermal Research, v. 172, p. 132-147.

Apukhtina, O.B., Kamenetsky, V. S., Ehrig, K., Kamenetsky, M.B., Maas, R., Thompson, J., McPhie, J., Ciobanu, C.L., and Cook, N.J., 2017, Early, deep magnetite-fluorapatite mineralization at the Olympic Dam Cu-U-Au-Ag deposit, South Australia: Economic Geology, v. 112, p. 1531-1542.

Baiyegunhi, C., Liu, K., and Gwavava, O., 2017, Geochemistry of sandstones and shales from the Ecca Group, Karoo Supergroup, in the Eastern Cape Province of South Africa: implications for provenance, weathering and tectonic setting: Open Geosciences, v. 9, p. 340-360.

Barton, M.D., 2014, Iron oxide(-Cu-Au-REE-P-Ag-U-Co) systems, *in* Holland, H.D. and Turekian, K.K., eds., Treatise on geochemistry: Elsevier, 2nd ed., v. 13, p. 515-541.

Barton, M.D. and Johnson, D.A., 1996, Evaporitic source model for igneous-related Fe-oxide (REE-Cu-Au-U) mineralization: Geology, v. 24, p. 259-262.

Bastrakov, E.N., Skirrow, R.G., and Davidson, G.J., 2007, Fluid evolution and origins of iron oxide Cu-Au prospects in the Olympic Dam district, Gawler Craton, South Australia: Economic Geology, v. 102, p. 1415-1440.

Belousova, E.A., Reid, A., Griffin, W.L., and O'Reilly, S.Y., 2009, Rejuvenation vs. recycling of Archean crust in the Gawler Craton, South Australia: evidence from U–Pb and Hf isotopes in detrital zircon: Lithos, v. 113, p. 570-582.

Belperio, A.P., Flint, R., and Freeman, H., 2007, Prominent Hill—a hematite-dominated, iron oxide copper-gold system: Economic Geology, v. 102, p. 1499-1510.

Benavides, J., Kyser, T.K., Clark, A.H., Stanley, C., and Oates, C.J., 2008, Exploration guidelines for copper-rich iron oxide-copper-gold deposits in the Mantoverde area, northern Chile: the integration of host-rock molar element ratios and oxygen isotope compositions: Geochemistry: Exploration Environment Analysis, v. 8, p. 343-367.

Brown, M., Diaz, F., and Grocott, J., 1993, Displacement history of the Atacama Fault System, 25°S-27°S, northern Chile: Geological Society of America Bulletin, v. 105, p. 1165-1174.

Charette, B., Lafrance, I., and Mathieu, G., 2017, Géologie de la région du Lac Jeannin (SNRC 24Bb): Ministère de l'Energie et des Ressources naturelles, Québec, BG 2015-01, available at https://gq.mines.gouv.qc.ca.

Chen, H., 2013, External sulphur in IOCG mineralization: implications on definition and classification of the IOCG clan: Ore Geology Reviews, v. 51, p. 74-78.

Chevé, S.R., 1985, Les indices minéralisés du lac Romanet, Fosse du Labrador : Ministère de l'Energie et des Ressources naturelles, Québec, ET 83–13, 60 p.

Chorlton, L.B. (compiler), 2007, Generalized geology of the world: bedrock domains and major faults in GIS format: Geological Survey of Canada, Open File 5529, 1 CD-ROM.

Clark, J.M., 2014, Defining the style of mineralisation at the Cairn Hill magnetite-sulphide deposit, Mount Woods Inlier, Gawler Craton South Australia: Unpublished B.Sc. thesis, University of Adelaide, Australia, 69 p.

Clark, J.M., Passmore, M., and Poznik, N., 2017, Olympic Dam rock quality designation model – an integrated approach. Tenth International Mining Geology Conference 2017, Hobart, Tasmania, 20-22 September 2017.

Clark, T., 1986, Géologie et minéralisations de la région du lac Mistamik et de la rivière Romanet: Ministère des Ressources naturelles et de la Faune, Québec, ET 83-22, 56 p.

Clark, T., and Wares, R., 2004, Synthèse lithotectonique et métallogénique de l'Orogène du Nouveau-Québec (Fosse du Labrador): Ministère des Ressources naturelles et de la Faune, Québec, MM 2004-01, 177 p.

Conor, C.C.H., Raymond, O., Baker, T., Teale, G.S., Say, P., and Lowe, G., 2010, Alteration and mineralisation in the Moonta-Wallaroo copper-gold mining field region, Olympic Domain, South Australia, *in* Porter, T.M., ed., Hydrothermal iron oxide copper-gold and related deposits: a global perspective, volume 3: PGC Publishing, Adelaide, p. 1-24.

Corrigan, D., Wodicka, N., McFarlane, C., Lafrance, I., van Rooyen, D., Bandyayera, D., and Bilodeau, C., 2018, Lithotectonic framework of the Core Zone, southeastern Churchill Province, Canada: Geoscience Canada, v. 45, p. 1-24.

Corriveau, L., Nadeau, O., Montreuil, J.-F., and Desrochers, J.-P., 2014, Report of activities for the Core Zone: strategic geomapping and geoscience to assess the mineral potential of the Labrador Trough for multiple metals IOCG and affiliated deposits, Canada: Geological Survey of Canada, Open File 7714, 12 p.

Corriveau, L., Lauzière, K., Montreuil, J.-F., Potter, E., Prémont, S., and Hanes, R., 2015, Dataset of new lithogeochemical analysis in the Great Bear magmatic zone, Northwest Territories, Canada: Geological Survey of Canada, Open File 7643, 19 p.

Corriveau, L., Montreuil, J.-F., and Potter, E.G., 2016, Alteration facies linkages among IOCG, IOA and affiliated deposits in the Great Bear magmatic zone, Canada, *in* Slack, J., Corriveau, L. and Hitzman, M., eds., Proterozoic iron oxide-apatite (± REE) and iron oxide-copper-gold and affiliated deposits of Southeast Missouri, USA, and the Great Bear magmatic zone, Northwest Territories, Canada: Economic Geology, v. 111, p. 2045-2072.

Corriveau, L., Potter, E.G., Acosta-Góngora, P., Blein, O., Montreuil, J.-F., De Toni, A.F., Day, W., Slack, J.F., Ayuso, R.A., and Hanes, R., 2017, Petrological mapping and chemical discrimination of alteration facies as vectors to IOA, IOCG, and affiliated deposits within Laurentia and beyond: Proceedings of the 14th SGA Biennial Meeting, 20-23 August 2017, Quebec City, p. 851-855.

Corriveau, L., Blein, O., Gervais, F., Trapy, P.H., De Souza, S., and Fafard, D., 2018a, Iron-oxide and alkali-calcic alteration, skarn and epithermal mineralizing systems of the Grenville Province: the Bondy gneiss complex in the Central Metasedimentary Belt of Quebec as a case example – a field trip to the 14th Society for Geology Applied to Mineral Deposits (SGA) biennial meeting: Geological Survey of Canada, Open File 8349, 136 p.

Corriveau, L., Potter, E.G., Montreuil, J.-F., Blein, O., Ehrig, K., and De Toni, A., 2018b, Iron oxide and alkali-calcic alteration ore systems and their polymetallic IOA, IOCG, skarn, albitite-hosted U±Au±Co, and affiliated deposits: a short course series. Part 2: overview of deposit types, distribution, ages, settings, alteration facies, and ore deposit models: Geological Survey of Canada, Scientific Presentation 81, 154 p.

Corriveau, L., Montreuil, J.-F., Blein, O., Ehrig, K., Potter, E.G., and Fabris, A., 2022a, Mineral systems with IOCG and affiliated deposits: part 2 – geochemical footprint, *in* Corriveau, L., Potter, E.G. and Mumin, A.H., eds., Mineral systems with iron oxide copper-gold (IOCG) and affiliated deposits: Geological Association of Canada, Special Paper 52, p. 159-204.

Corriveau, L., Montreuil, J.-F., De Toni, A.F., Potter, E.G., and Percival, J.B., 2022b, Mapping mineral systems with IOCG and affiliated deposits: a facies approach, *in* Corriveau, L., Potter, E.G., and Mumin, A.H., eds., Mineral systems with iron oxide copper-gold (IOCG) and affiliated deposits: Geological Association of Canada, Special Paper 52, p. 69-111.

Corriveau, L., Montreuil, J.-F., Potter, E.G., Blein, O., and De Toni, A.F., 2022c, Mineral systems with IOCG and affiliated deposits: part 3 – metal pathways and ore deposit model, *in* Corriveau, L., Potter, E.G., and Mumin, A.H., eds., Mineral systems with iron oxide copper-gold (IOCG) and affiliated deposits: Geological Association of Canada, Special Paper 52, p. 205-245

Corriveau, L., Montreuil, J.-F., Potter, E.G., Ehrig, K., Clark, J., Mumin, A.H., and Williams, P.J., 2022d, Mineral systems with IOCG and affiliated deposits: part 1 – metasomatic footprints of alteration facies, *in* Corriveau, L., Potter, E.G., and Mumin, A.H., eds., Mineral systems with iron oxide copper-gold (IOCG) and affiliated deposits: Geological Association of Canada, Special Paper 52, p. 113-158.

Corriveau, L., Mumin, A.H., and Potter, E.G., 2022e, Mineral systems with iron oxide copper-gold (IOCG) and affiliated deposits: introduction and overview, *in* Corriveau, L., Potter, E.G., and Mumin, A.H., eds., Iron oxide copper-gold (Ag-Bi-Co-U-REE) and affiliated deposits: Geological Association of Canada, Special Paper 52, p. 1-26.

Cowley, W.M., Conor, C., and Zang, W., 2003, New and revised Proterozoic stratigraphic units on northern Yorke Peninsula: MESA Journal, v. 29, p. 46-58.

Dallmeyer, R.D., Brown, M., Grocott, J., Taylor, G.K., and Treolar, P.J., 1996, Mesozoic magmatic and tectonic events within the Andean plate boundary zone, 26°-27°30' S, north Chile: constraints from $^{40}Ar/^{39}Ar$ mineral ages: Journal of Geology, v. 104, p. 19-40.

Daly, S.J., Fanning, C.M., and Fairclough, M.C., 1998, Tectonic evolution and exploration potential of the Gawler Craton, South Australia: AGSO Journal of Australian Geology & Geophysics, v. 17, p. 145-168.

Davidson, G.J., Paterson, H., Meffre, S., and Berry, R.F., 2007, Characteristics and origin of the Oak Dam East breccia-hosted, iron oxide Cu-U-(Au) deposit: Olympic Dam region, Gawler craton, South Australia: Economic Geology, v. 102, p. 1471-1498.

Davis, W.J., Corriveau, L., van Breemen, O., Bleeker, W., Montreuil, J.-F., Potter, E., and Pelleter, E., 2011, Timing of IOCG mineralising and alteration events within the Great Bear magmatic zone, *in* Fischer, B.J. and Watson, D.M., comps., 39th Annual Yellowknife Geoscience Forum Abstracts: Northwest Territories Geoscience Office, Abstracts Volume 2011, p. 97.

De, S., Mazumder, R., Ohta, T., Hegner, E., Yamada, K., Bhattacharrya, T., Chiarenzelli, J., Altermann, W., and Arima, M., 2015, Geochemical and Sm-Nd isotopic characteristics of the Late Archean-Paleoproterozoic Dhanjori and Chaibasa metasedimentary rocks, Singhbhum craton, E. India: implications for provenance, and contemporary basin tectonics: Precambrian Research, v. 256, p. 62-78.

Desrochers, J.-P., 2014, Technical report on the Sagar property, Romanet Horst, Labrador Trough, Quebec, Canada (latitude, 56°22'N and longitude 68°00'W; NTS map sheets 24B/05 and 24C/08): National Instrument 43–101 Technical Report prepared for Honey Badger Exploration Inc., available at www.sedar.com.

Dimroth, E., 1978, Région de la Fosse du Labrador (54˚30'–56˚30'): Ministère de l'Energie et des Ressources naturelles, Quebec, RG–193, 396 p.

Dmitrijeva, M., Ehrig, K., Ciobanu, C.L., Cook, N., Verdugo-Ihl, M.R., and Metcalfe, A.V., 2019, Defining IOCG signatures through compositional data analysis: a case study of lithogeochemical zoning from the Olympic Dam deposit, South Australia: Ore Geology Reviews, v. 105, p. 86-101.

Dunn, J.A., 1942, Geology and petrology of Eastern Singhbhum and surrounding areas: Geological Survey of India, Memoir 69, p. 261-456.

Ehrig, K., McPhie, J., and Kamenetsky, V., 2012, Geology and mineralogical zonation of the Olympic Dam iron oxide Cu-U-Au-Ag deposit, South Australia, *in* Hedenquist, J.W., Harris, M. and Camus, F., eds., Geology and genesis of major copper deposits and districts of the world: a tribute to Richard H. Sillitoe: Society of Economic Geologists Special Publication, v. 16, p. 237-267.

Ehrig, K., Kamenetsky, V.S., McPhie, J., Apukhtina, O., Ciabanu, C.L., Cook, N., Kontonikas-Charos, A., and Krneta, S., 2017a, The IOCG-IOA Olympic Dam Cu-U-Au-Ag deposit and nearby prospects, South Australia: Proceedings of the 14th SGA Biennial Meeting, 20-23 August 2017, Quebec City, p. 823-827.

Ehrig, K., Kamenetsky, V.S., McPhie, J., Apukhtina, O., Cook, N., and Ciabanu, C.L., 2017b, Olympic Dam iron oxide Cu-U-Au-Ag deposit, *in* Phillips, G.N., ed., Australian ore deposits: The Australasian Institute of Mining and Metallurgy, Melbourne, p. 601-610.

Engvik, A., Putnis, A., Fitz Gerald, J.D., and Austrheim, H., 2008, Albitization of granitic rocks: the mechanism of replacement of oligoclase by albite: The Canadian Mineralogist, v. 46, p. 1401-1415.

Enkin, R.J., Corriveau, L., and Hayward, N., 2016, Metasomatic alteration control of petrophysical properties in the Great Bear magmatic zone (Northwest Territories, Canada), *in* Slack, J., Corriveau, L. and Hitzman, M., eds., Proterozoic iron oxide-apatite (± REE) and iron oxide-copper-gold and affiliated deposits of Southeast Missouri, USA, and the Great Bear magmatic zone, Northwest Territories, Canada: Economic Geology, v. 111, p. 2073-2085.

Fabris, A., 2022, Geochemical characteristics of IOCG deposits from the Olympic Copper-Gold Province, South Australia, *in* Corriveau, L., Potter, E.G., and Mumin, A.H., eds., Mineral systems with iron oxide copper-gold (IOCG) and affiliated deposits: Geological Association of Canada, Special Paper 52, p. 247-262.

Fabris, A.J., Halley, S., van der Wielen, S., Keeping, T., and Gordon, G., 2013, IOCG-style mineralisation in the central eastern Gawler Craton, SA: characterisation of alteration, geochemical associations and exploration vectors: Department of Innovation, Manufacturing, Trade, Resources and Energy, South Australia, Report Book 2013/00014, 49 p.

Fabris, A., Katona, L., Gordon, G., Reed, G., Keeping, T., Gouthas, G., and Swain, G., 2018a, Characterisation and mapping of Cu-Au skarn systems in the Punt Hill region, Olympic Cu-Au Province: MESA Journal, v. 87, p. 15-27.

Fabris, A., Katona, L., Gordon, G., Reed, G., Keeping, T., Gouthas, G., and Swain, G., 2018b, Characterising and mapping alteration in the Punt Hill region: a data integration project: Government of South Australia. Department of the Premier and Cabinet. Report Book, 2018/00010, 604 p.

Ferris, G.M., Schwarz, M.P., and Heithersay, P., 2002, The geological framework, distribution and controls of Fe-oxide Cu-Au deposits in the Gawler craton. Part I. Geological and tectonic framework, *in* Porter, T.M., ed., Hydrothermal iron oxide copper-gold and related deposits, volume 2: PGC Publishing, Adelaide, p. 9-31.

Flint, R.B., Blissett, A.H., Conor, C.H.H., Cowley, W.M., Cross, K.C., Creaser, R.A., Daly, S.J., Krieg, G.W., Major, R.B., Teale, G.S., and Parker, A.J., 1993, Mesoproterozoic, *in* Drexel, J.F., Preiss, W.V. and Parker, A.J., eds., The geology of South Australia, volume 1, The Precambrian: Geological Survey of South Australia, Bulletin 54, p. 106-169.

Franklin, J.M., 1997, Lithogeochemical and mineralogical methods for base metal and gold, *in* Gubins, A.G., ed., Proceedings of Exploration 97: Fourth Decennial International Conference on Mineral Exploration, p. 191-208.

Fraser, G., Skirrow, R.G., and Holm, O., 2007, Mesoproterozoic gold in the central Gawler Craton, South Australia: geology, alteration, fluids and timing: Economic Geology, v. 102, p. 1511-1539.

Gandhi, S.S., Mortensen, J.K., Prasad, N., and van Breemen, O., 2001, Magmatic evolution of the southern Great Bear continental arc, northwestern Canadian Shield: geochronological constraints: Canadian Journal of Earth Sciences, v. 38, p. 767-785.

Ghosh, D., Dutta, T., Samanta, S.K., and Pal, D.C., 2013, Texture, microstructure and geochemistry of magnetite from the Banduhurang uranium mine, Singhbhum Shear Zone, India — implications for physico-chemical evolution of magnetite mineralization: Journal of the Geological Society of India, v. 81, p. 101-112.

Goad, R.E., Mumin, A.H., Duke, N.A., Neale, K.L., and Mulligan, D.L., 2000a, Geology of the Proterozoic iron oxide-hosted NICO cobalt-gold-bismuth, and Sue-Dianne copper-silver deposits, southern Great Bear magmatic zone, Northwest Territories, Canada, *in* Porter, T.M., ed., Hydrothermal iron oxide copper-gold and related deposits: a global perspective, volume 1: PGC Publishing, Adelaide, p. 249-267.

Goad, R.E., Mumin, A.H., Duke, N.A., Neale, K.L., Mulligan, D.L., and Camier, W.J., 2000b, The NICO and Sue-Dianne Proterozoic, iron oxide hosted, polymetallic deposits, Northwest Territories: application of the Olympic Dam model in exploration: Exploration and Mining Geology, v. 9, p. 123-140.

Gow, P.A., Wall, V.J., Oliver, N.H.S., and Valenta, R.K., 1994, Proterozoic iron oxide (Cu-U-Au-REE) deposits: further evidence of hydrothermal origins: Geology, v. 22, p. 633-636.

Grocott, J., and Taylor, G., 2002, Magmatic arc fault systems, deformation partitioning and emplacement of granitic complexes in the Coastal Cordillera, north Chilean Andes (25°30’ to 27°00’ S): Journal of the Geological Society of London, v. 159, p. 425-442.

Gromet, L.P., Dymek, R.F., Haskin, L.A., and Korotev, R.L., 1984, The North American shale composite. Its compilation, major and trace element characteristics: Geochimica et Cosmochimica Acta, v. 48, p. 2469-2482.

Grunsky, E.C., and Bacon-Shone, J., 2011, The stoichiometry of mineral compositions: Conference Proceedings, CodaWork11, May 9-13, 2011, Saint Feliu de Guixols, Spain.

Gum, J., 2019, Gold mineral systems and exploration, Gawler Craton, South Australia: MESA, v. 91, p. 51-65.

Hampton, S., 1997, A study of the paragenesis and controls on Proterozoic (Cu-Fe-Au-REE) mineralization at the Manxman A1 and Joes Dam South prospects, Mount Woods inlier, South Australia: Unpublished B.Sc. thesis, Australia, Department of Economic Geology, James Cook University of North Queensland, 146 p.

Hand, M., Reid, A., and Jagodzinski, E., 2007, Tectonic framework and evolution of the Gawler Craton, South Australia: Economic Geology, v. 102, p. 1377-1395.

Hayward, N., and Skirrow, R., 2010, Geodynamic setting and controls on iron oxide Cu-Au (±U) ore in the Gawler Craton, South Australia, *in* Porter, T.M., ed., Hydrothermal iron oxide copper-gold and related deposits: a global perspective, volume 3: PGC Publishing, Adelaide, p. 105-131.

Hayward, N., 2013, 3D magnetic inversion of mineral prospects in the Great Bear magmatic zone, NT, Canada: Geological Survey of Canada, Open File 7421.

Hayward, N., Corriveau, L., Craven, J., and Enkin, R., 2016, Geophysical signature of the NICO Au-Co-Bi-Cu deposit and its iron oxide-alkali alteration system, Northwest Territories, Canada, *in* Slack, J., Corriveau, L. and Hitzman, M., eds., Proterozoic iron oxide-apatite (± REE) and iron oxide-copper-gold and affiliated deposits of Southeast Missouri, USA, and the Great Bear magmatic zone, Northwest Territories, Canada: Economic Geology, v. 111, p. 2087-2110.

Hildebrand, R.S., Hoffman, P.F., Housh, T., and Bowring, S.A., 2010, The nature of volcano-plutonic relations and shapes of epizonal plutons of continental arcs as revealed in the Great Bear magmatic zone, northwestern Canada: Geosphere, v. 6, p. 812-839.

Hitzman, M.W., and Valenta, R.K., 2005, Uranium in iron oxide-copper-gold (IOCG) systems: Economic Geology, v. 100, p. 1657-1661.

Hitzman, M.W., Oeskes, N., and Einaudi, M.T., 1992, Geological characteristics and tectonic settings of Proterozoic iron oxide (Cu-Au-U-REE) deposits: Precambrian Research, v. 58, p. 241-258.

Hu, H., Li, J.W., Harlov, D.E., Lentz, D.R., McFarlane, C.R.M., and Yang, Y.-H., 2019, A genetic link between iron oxide-apatite and iron skarn mineralization in the Jinniu volcanic basin, Daye district, eastern China: evidence from magnetite geochemistry and multi-mineral U-Pb geochronology: Geological Society of America Bulletin, v. 132, p. 899-917.

Huntington, J., Mauger, A., Skirrow, R., Bastrakov, E., Connor, P., Mason, P., Keeling, J., Coward, D., Berman, M., Phillips, R., Whitbourn, L., and Heithersay, P., 2004, Automated mineralogical logging of core from the Emmie Bluff, iron oxide copper–gold prospect, South Australia: AusIMM Publication Series No.5/2004, PACRIM 2004, Adelaide SA, 19–22 September 2004, p. 223-230.

Ismail, R., Ciobanu, C.L., Cook, N.J., Giles, D., Schmidt-Mumm, A., and Wade, B., 2014, Rare earths and other trace elements in minerals from skarn assemblages, Hillside iron oxide–copper–gold deposit, Yorke Peninsula, South Australia: Lithos, v. 184-187, p. 456-477.

Jagodzinski, E.A., Reid, A., Crowley, J., McAvaney, S., and Wade, C., 2016, New CA-TIMS dates for the Gawler Range Volcanics: implications for the duration of volcanism: Geological Survey of South Australia, Report Book 2016/00032, p. 17-18.

Konstantinovskaya, E., Ivanov, G., Feybesse, J.L., and Lescuyer, J.L., 2019, Structural features of the Central Labrador Trough: a model for strain partitioning, differential exhumation and late normal faulting in a thrust wedge under oblique shortening: Geoscience Canada, v. 46, p. 5-30.

Kontonikas-Charos, A., Ciobanu, C.L., Cook, N.J., Ehrig, K., Krneta, S., and Kamenetsky, V.S., 2017, Feldspar evolution in the Roxby Downs Granite, host to Fe-oxide Cu-Au-(U) mineralisation at Olympic Dam, South Australia: Ore Geology Reviews, v. 80, p. 838-859.

Kontonikas-Charos, A., Ciobanu, C.L., Cook, N.J., Ehrig, K., Ismail, R., and Krneta, S., 2018, Feldspar mineralogy and rare-earth element (re)mobilization in iron-oxide copper gold systems from South Australia: a nanoscale study: Mineralogical Magazine, v. 82(S1), p. S173-S197.

Kreiner, D., and Barton, M.D., 2017, Sulfur-poor intense acid hydrothermal alteration: a distinctive hydrothermal environment: Ore Geology Reviews, v. 88, p. 174-187.

Lara, L., and Godoy, E., 1998, Hoja Quebrada Salitrosa, III Región de Atacama: Santiago, Chile, Servicio Nacional de Geología y Minería, Mapas Geológicos 4, escala 1:100.000.

Large, R.R., Gemmell, J.B., Paulick, H., and Huston, D.L., 2001, The alteration box plot-A simple approach to understanding the relationship between alteration mineralogy and lithogeochemistry associated with volcanic-hosted massive sulfide deposits: Economic Geology, v. 96, p. 957-971.

Le Gallais, C.J., and Lavoie, S., 1982, Basin evolution of the Lower Proterozoic Kaniapiskau Supergroup, central Labrador miogeocline (Trough), Quebec: Bulletin of Canadian Petroleum Geology, v. 30, p. 150-166.

Leitch, C.H.B., and Lentz, D.R., 1994, The Gresens approach to mass balance constraints of alteration systems-methods, pitfalls, examples, *in* Lentz, D.R., ed., Alteration and alteration processes associated with ore-forming systems: Geological Association of Canada, Short Course Notes, No. 11, p. 161-192.

Madeisky, H.E., 1996, A lithogeochemical and radiometric study of hydrothermal alteration and metal zoning at the Cinola epithermal gold deposit. Queen Charlotte Islands. British Columbia, *in* Coyner, A.R., and Fahey, P.L., eds., Geology and ore deposits of the American Cordillera: Geological Society of Nevada, USA, v. 3, p. 1153-1185.

Madeisky, H.E., and Stanley, C.R., 2010, Lithogeochemical exploration of metasomatic zones associated with volcanic-hosted massive sulfide deposits using Pearce element ratio analysis: International Geology Review, v. 35, p. 1121-1148.

Mark, G., Oliver, N.H.S., and Williams, P.J., 2006, Mineralogical and chemical evolution of the Ernest Henry Fe oxide-Cu-Au ore system, Cloncurry district, northwest Queensland, Australia: Mineralium Deposita, v. 40, p. 769-801.

Mauger, A.J., Ehrig, K., Kontonikas-Charos, A., Ciobanu, C.L., Cook, N.J., and Kamenetsky, V.S., 2016, Alteration at the Olympic Dam IOCG–U deposit: insights into distal to proximal feldspar and phyllosilicate chemistry from infrared reflectance spectroscopy: Australian Journal of Earth Sciences, v. 63, p. 959-972.

McLaughlin, B., Montreuil, J.-F., and Desrochers, J.-P., 2016, Exploration report (summer and fall 2014 drill program) on the Sagar Property, Romanet Horst, Labrador Trough, Québec, Canada: Ministère des Ressources naturelles et de l'Énergie, Québec, GM 69734, 65 p.

McPhie, J., Orth, K., Kamenetsky, V.S., Kamenetsky, M.B., and Ehrig, K., 2016, Characteristics, origin and significance of Mesoproterozoic bedded clastic facies at the Olympic Dam Cu-U-Au-Ag deposit, South Australia: Precambrian Research, v. 276, p. 85-100.

Montreuil, J.-F., Corriveau, L., and Long, B., 2012, Porosity in albitites and the development of albitite-hosted U deposits: insights from X-ray computed tomography: CT scan workshop, development on non-medical environment-state of the art, INRS-ETE, Quebec City, Program, p. 5.

Montreuil, J.-F., Corriveau, L., and Grunsky, E.C., 2013, Compositional data analysis of IOCG systems, Great Bear magmatic zone, Canada: to each alteration types its own geochemical signature: Geochemistry: Exploration, Environment, Analysis, v. 13, p. 229-247.

Montreuil, J.-F., Corriveau, L., and Potter, E., 2015, Formation of albitite-hosted uranium within IOCG systems: the Southern Breccia, Great Bear magmatic zone, Northwest Territories, Canada: Mineralium Deposita, v. 50, p. 293-325.

Montreuil, J.-F., Corriveau, L., and Davis, W., 2016a, Tectonomagmatic evolution of the southern Great Bear magmatic zone (Northwest Territories, Canada) – Implications on the genesis of iron oxide alkali-altered hydrothermal systems, *in* Slack, J., Corriveau, L. and Hitzman, M., eds., Proterozoic iron oxide-apatite (± REE) and iron oxide-copper-gold and affiliated deposits of Southeast Missouri, USA, and the Great Bear magmatic zone, Northwest Territories, Canada: Economic Geology, v. 111, p. 2111-2138.

Montreuil, J.-F., Corriveau, L., Potter, E.G., and De Toni, A.F., 2016b, On the relation between alteration facies and metal endowment of iron oxide–alkali-altered systems, southern Great Bear magmatic zone (Canada), *in* Slack, J., Corriveau, L. and Hitzman, M., eds., Proterozoic iron oxide-apatite (± REE) and iron oxide-copper-gold and affiliated deposits of Southeast Missouri, USA, and the Great Bear magmatic zone, Northwest Territories, Canada: Economic Geology, v. 111, p. 2139-2168.

Montreuil, J.-F., Potter, E., Corriveau, L., and Davis, W.J., 2016c, Element mobility patterns in magnetite-group IOCG systems: the Fab IOCG system, Northwest Territories, Canada: Ore Geology Reviews, v. 72, p. 562-584.

Mukhopadhyay, J., Beukes, N.J., Armstrong, R.A., Zimmermann, U., Ghosh, G., and Medda, R.A., 2008, Dating the oldest greenstone in India: A 3.51 Ga precise U-Pb SHRIMP zircon age for dacitic lava of the southern Iron Ore Group, Singhbhum Craton: Journal of Geology, v. 116, p. 449-461.

Mumin, A.H., Corriveau, L., Somarin, A.K., and Ootes, L., 2007, Iron oxide copper-gold-type polymetallic mineralisation in the Contact Lake Belt, Great Bear magmatic zone, Northwest Territories, Canada: Exploration and Mining Geology, v. 16, p. 187-208.

Mumin, A.H., Somarin, A.K., Jones, B., Corriveau, L., Ootes, L., and Camier, J., 2010, The IOCG-porphyry-epithermal continuum of deposits types in the Great Bear Magmatic Zone, Northwest Territories, Canada, *in* Corriveau, L. and Mumin, A.H., eds., Exploring for iron oxide copper-gold deposits: Canada and global analogues: Geological Association of Canada, Short Course Notes, No. 20, p. 59-78.

Oliver, N.H.S., Pearson, P.J., Holcombe, R.J., and Ord, A., 1999, Mary Kathleen metamorphic–hydrothermal uranium–rare-earth element deposit: ore genesis and numerical model of coupled deformation and fluid flow: Australian Journal of Earth Sciences, v. 46, p. 467-484.

Ootes, L., Harris, J., Jackson, V.A., Azar, B., and Corriveau, L., 2013, Uranium-enriched bedrock in the central Wopmay orogen: implications for uranium mineralization, *in* Potter, E.G., Quirt, D., and Jefferson, C.W., eds., Uranium in Canada: geological environments and exploration developments: Exploration and Mining Geology, v. 21, p. 85-103.

Ootes, L., Snyder, D., Davis, W.J., Acosta-Góngora, P., Corriveau, L., Mumin, A.H., Montreuil, J.-F., Gleeson, S.A., Samson, I.A. and Jackson, V.A., 2017, A Paleoproterozoic Andean-type iron oxide copper-gold environment, the Great Bear magmatic zone, Northwest Canada: Ore Geology Reviews, v. 81, p. 123-139.

Pal, D.C., and Bhowmick, T., 2015, Petrography and microthermometry of fluid inclusions in apatite in the Turamdih uranium deposit, Singhbhum shear zone, eastern India – an insight into ore forming fluid: Journal of the Geological Society of India, v. 86, p. 253-262.

Pal, D.C., and Chaudhuri, T., 2016, Radiation damage-controlled localization of alteration haloes in albite: implications for alteration types and patterns vis-à-vis mineralization and element mobilization: Mineralogy and Petrology, v. 110, p. 823-843.

Pal, D.C., and Rhede, D., 2013, Geochemistry and chemical dating of uraninite in the Jaduguda uranium deposit, Singhbhum Shear Zone, India – Implications for uranium mineralization and geochemical evolution of uraninite: Economic Geology, v. 108, p. 1499-1515.

Pal, D.C., Saravanan, S., and Mishra, B., 2008, Involvement of high temperature oxidized brine in pre-shearing hydrothermal alteration: evidence from fluid inclusions in tourmaline in feldspathic schist, Pathargora area, Singhbhum shear zone, eastern India: Second meeting of the Asian Current Research on Fluid Inclusions (ACROFI-2), Abstracts with program, IIT, Kharagpur, India.

Pal, D.C., Banerjee, A., and Dutta, A., 2009a, Hydrothermal alteration and ore mineralization in the Narwapahar uranium mine, Singhbhum shear zone, eastern India: International Conference on Paleoproterozoic Supercontinents and Global Evolution, International Association for Gondwana Research Conference Series no. 9, Indian Statistical Institute, Kolkata, India, 26-18 October, 2009, Proceedings, p. 28-29.

Pal, D.C., Barton, M.D., and Sarangi, A.K., 2009b, Deciphering a multistage history affecting U-Cu (-Fe) mineralization in the Singhbhum shear zone, eastern India using pyrite textures and compositions in the Turamdih U-Cu (-Fe) deposit: Mineralium Deposita, v. 44, p. 61-80.

Pal, D.C., Trumbull, R.B., and Wiedenbeck, M., 2010, Chemical and boron isotope compositions of tourmaline from the Jaduguda U (-Cu-Fe) deposit, Singhbhum shear zone, India: implications for the sources and evolution of mineralizing fluids: Chemical Geology, v. 277, p. 245-260.

Pal, D.C., Chaudhuri, T., McFarlane, C., Mukherjee, A., and Sarangi, A.K., 2011a, Mineral chemistry and in situ dating of allanite, and geochemistry of its host rocks in the Bagjata uranium mine, Singhbhum Shear Zone, India – implications for the chemical evolution of REE mineralization and mobilization: Economic Geology, v. 106, p. 1155-1171.

Pal, D.C., Sarkar, S., Mishra, B., and Sarangi, A.K., 2011b, Chemical and Sulphur isotope compositions of pyrite in the Jaduguda U (-Cu-Fe) deposit, Singhbhum shear zone, eastern India-implications for sulphide mineralization: Journal of Earth System Sciences, v. 120, p. 475-488.

Pearce, T.H., 1968, A contribution to the theory of variation diagrams: Contributions to Mineralogy and Petrology, v. 19, p. 142-157.

Pettijohn, F.J., 1975, Sand and sandstones: Harper and Row, New York, 3rd edition, 628 p.

Polito, P.A., Kyser, T.K., and Stanley, C., 2009, The Proterozoic, albitite-hosted, Valhalla uranium deposit, Queensland, Australia: a description of the alteration assemblage associated with uranium mineralization in diamond drill hole V39: Mineralium Deposita, v. 44, p. 11-40.

Porter, T.M., 2010, Current understanding of iron oxide associated-alkali altered mineralised systems. Part 1 - an overview, *in* Porter, T.M., ed., Hydrothermal iron oxide copper-gold and related deposits: a global perspective, volume 3: PGC Publishing, Adelaide, p. 5-32.

Porto da Silveira, C.L., Schorscher, H.D., and Miekeley, N., 1991, The geochemistry of albitization and related uranium mineralization, Espinharas, Paraiba (PB), Brazil: Journal of Geochemical Exploration, v. 40, p. 329-347.

Potter, E.G., Montreuil, J.-F., Corriveau, L., and Davis, W., 2019, The Southern Breccia metasomatic uranium system of the Great Bear magmatic zone, Canada: iron oxide-copper-gold (IOCG) and albitite-hosted uranium linkages, *in* Decrée, S. and Robb, L., eds., Ore deposits: origin, exploration, and exploitation: Geophysical Monograph 242, First Edition, American Geophysical Union, John Wiley & Sons, Inc., p. 109-130.

Potter, E.G., Acosta-Góngora, P., Corriveau, L., Montreuil, J.-F., and Yang, Z., 2022, Uranium enrichment processes in iron oxide and alkali-calcic alteration systems as revealed by trace element signatures of uraninite, *in* Corriveau, L., Potter, E.G. and Mumin, A.H., eds., Mineral systems with iron oxide copper-gold (IOCG) and affiliated deposits: Geological Association of Canada, Special Paper 52, p. 325-345.

Putnis, A., 2009, Mineral replacement reactions: Reviews in Mineralogy and Geochemistry, v. 70, p. 87-124.

Rayner, N.M., Lafrance, I., Corrigan, D., and Charette, B., 2017, New U–Pb zircon ages of plutonic rocks from the Jeannin Lake area, Quebec: an evaluation of the Kuujjuaq domain and Rachel–Laporte Zone: Geological Survey of Canada, Current Research, 2017–4, 17 p.

Reeve, J.S., Cross, K.C., Smith, R.N., and Oreskes, N., 1990, Olympic Dam copper-uranium-gold-silver deposit: Geology of the mineral deposits of Australia Papua New Guinea, v. 2, p. 1009-1035.

Reid, A.J., 2019, The Olympic Cu-Au Province, Gawler Craton: a review of the lithospheric architecture, geodynamic setting, alteration systems, cover successions and prospectivity: Minerals, v. 9, 371.

Reid, A.J., and Hand, M., 2012, Mesoarchean to Mesoproterozoic evolution of the southern Gawler Craton, South Australia: Economic Geology, v. 35, p. 216-225.

Reid, A.J., Swain, G., Mason, D., and Maas, R., 2011, Nature and timing of Cu–Au–Zn–Pb mineralisation at Punt Hill, eastern Gawler Craton: MESA Journal, v. 60, p. 7-27.

Reid, A.J., Pawley, C., Wade, C., Jagodzinski, E.A., Dutch, R.A., and Armstrong, R., 2020, Resolving tectonic settings of ancient magmatic suites using structural, geochemical and isotopic constraints: the example of the St Peter Suite, southern Australia: Australian Journal of Earth Sciences, v. 67, p. 31-58.

Rieger, A.A., Marschik, R., Diaz, M., Hölzl, S., Chiaradia, M., Akker, B., and Spangenberg, J.E., 2010, The hypogene iron oxide copper-gold mineralization in the Mantoverde district, northern Chile: Economic Geology, v. 104, p. 1271-1299.

Rusk, B.G., Oliver, N.H.S., Cleverley, J.S., Blenkinsop, T.G., Zhang, D., Williams, P.J., and Habermann, P., 2010, Physical and chemical characteristics of the Ernest Henry iron oxide copper gold deposit, Australia: implications for IOCG genesis, *in* Porter, T.M., ed., Hydrothermal iron oxide copper-gold and related deposits: a global perspective, volume 4: PGC Publishing, Adelaide, p. 201-218.

Saha, A.K., 1994, Crustal evolution of Singhbhum-North Orissa, eastern India: Memoirs of the Geological Society of India, v. 27, p. 341.

Sarkar, S.C., 1982, Uranium (-nickel-cobalt-molybdenum) mineralization along the Singhbhum copper belt, India, and the problem of ore genesis: Mineralium Deposita, v. 17, p. 257-278.

Sarkar, S.C., 1984, Geology and ore mineralization along the Singhbhum copper-uranium belt, eastern India: Calcutta, Jadavpur University Press, 263 p.

Sarkar, S.C., and Gupta, A., 2012, Crustal evolution and metallogeny in India: Cambridge University Press, 840 p.

Schlegel, T.U., and Heinrich, C.A., 2015, Lithology and hydrothermal alteration control the distribution of copper grade in the Prominent Hill iron oxide-copper-gold deposit (Gawler Craton, South Australia): Economic Geology, v. 110, p. 1953-1994.

Shives, R.B.K., Charbonneau, B.W., and Ford, K.L., 2000, The detection of potassic alteration by gamma-ray spectrometry-recognition of alteration related to mineralization: Geophysics, v. 65, p. 2001-2011.

Sidor, M., 2000, The origin of Black Rock alteration overprinting iron-rich sediments and its genetic relationship to disseminated polymetallic sulphide ores, Lou lake, Northwestern Territories, Canada: Unpublished M.Sc. thesis, University of Western Ontario, 190 p.

Skirrow, R., 2022, Hematite-group IOCG ± U deposits: an update on their tectonic settings, hydrothermal characteristics, and Cu-Au-U mineralizing processes, *in* Corriveau, L., Potter, E.G., and Mumin, A.H., eds., Mineral systems with iron oxide copper-gold (IOCG) and affiliated deposits: Geological Association of Canada, Special Paper 52, p. 27-51.

Skirrow, R.G., Bastrakov, E., Davidson, G.J., Raymond, O., and Heithersay, P., 2002, Geological framework, distribution and controls of Fe-oxide Cu-Au deposits in the Gawler craton, Part II, Alteration and mineralization, *in* Porter, T.M., ed., Hydrothermal iron oxide copper-gold and related deposits: a global perspective, volume 2: PGC Publishing, Adelaide, p. 33-47.

Skirrow, R.G., Bastrakov, E.N., Barovich, K., Fraser, G.L., Creaser, R.A., Fanning, C.M., Raymond, O.L., and Davidson, G.J., 2007, Timing of iron oxide Cu-Au-(U) hydrothermal activity and Nd isotope constraints on metal sources in the Gawler Craton, South Australia: Economic Geology, v. 102, p. 1441-1470.

Slack, J., 2013, Descriptive and geoenvironmental model for cobalt–copper–gold deposits in metasedimentary rocks: U.S. Geological Survey Scientific Investigations Report 2010–5070–G, 218 p.

Stanley, C.R., and Madeisky, H.E., 1994, Lithogeochemical exploration for hydrothermal ore deposits using Pearce element ratio analysis, *in* Lentz, D.R., ed., Alteration and alteration processes associated with ore-forming systems: Geological Association of Canada, Short Course Notes, No. 11, p. 193-211.

Wade, C.E., Reid, A.J., Wingate, M.T.D., Jagodzinski, E.A., and Barovich, K., 2012, Geochemistry and geochronology of the c. 1585 Ma Benagerie Volcanic Suite, southern Australia: relationship to the Gawler Range Volcanics and implications for the petrogenesis of a Mesoproterozoic silicic large igneous province: Precambrian Research, v. 206-207, p. 17-35.

Wang, S., and Williams, P.J., 2001, Geochemistry and origin of Proterozoic skarns at the Mount Elliott Cu-Au (-Co-Ni) deposit, Cloncurry district, NW Queensland, Australia: Mineralium Deposita, v. 36, p. 109-124.

Wardle, R.J., James, D.T., Scott, D.J., and Hall, J., 2002, The southeastern Churchill Province: synthesis of a Paleoproterozoic transpressional orogen: Canadian Journal of Earth Sciences, v. 39, p. 639-663.

Warren, I., Simmons, S.F., and Mauk, J.L., 2007, Whole-rock geochemical techniques for evaluating hydrothermal alteration, mass change, and compositional gradients associated with epithermal Au-Ag mineralization: Economic Geology, v. 102, p. 923-948.

Whitney, D.L., and Evans, B.W., 2010, Abbreviations for names of rock-forming minerals: American Mineralogist, v. 95, p. 185-187.

Wilde, A., 2013, Towards a model for albitite-type uranium deposit model: Minerals, v. 3, p. 36-48.

Williams, P.J., 2010a, Classifying IOCG deposits, *in* Corriveau, L. and Mumin, A.H., eds., Exploring for iron oxide copper-gold deposits: Canada and global analogues: Geological Association of Canada, Short Course Notes, No. 20, p. 13-21.

Williams, P.J., 2010b, "Magnetite-group" IOCGs with special reference to Cloncurry and Northern Sweden: settings, alteration, deposit characteristics, fluid sources, and their relationship to apatite-rich iron ores, *in* Corriveau, L. and Mumin, A.H., eds., Exploring for iron oxide copper-gold deposits: Canada and global analogues: Geological Association of Canada, Short Course Notes, No. 20, p. 23-38.

Williams, P.J., Barton, M.D., Johnson, D.A., Fontboté, L., de Haller, A., Mark, G., Oliver, N.H.S., and Marschik, R., 2005, Iron-oxide copper-gold deposits: geology, space-time distribution, and possible modes of origin, *in* Hedenquist, J.W., Thompson, J.F.H., Goldfarb, R.J. and Richards, J.P., eds., Society of Economic: Economic Geology 100$^{th}$ anniversary volume, p. 371-405.

Yu, J., Chen, Y., Mao, J., Pirajno, F., and Duan, C., 2011, Review of geology, alteration and origin of iron oxide–apatite deposits in the Cretaceous Ningwu basin, Lower Yangtze River Valley, eastern China: implications for ore genesis and geodynamic setting: Ore Geology Reviews, v. 43, p. 170-181.

Zhao, X.F., Zhou, M.F., Su, Z.K., Li, X.C., Chen, W.T., and Li, J.W., 2017, Geology, geochronology, and geochemistry of the Dahongshan Fe-Cu-(Au-Ag) deposit, southwest China: implications for the formation of iron oxide copper-gold deposits in intracratonic rift settings: Economic Geology, v. 112, p. 603-628.

## Appendix 1

In the Montreuil et al. (2013) discriminant plot, alteration indexes are based on molar proportions in order to directly represent the geochemical signature and mineralogy of the rocks (Pearce, 1968; Stanley and Madeisky, 1994; Grunsky and Bacon-Shone, 2011). In this diagram, whole-rock geochemical data are plotted using a coloured barcode derived from whole-rock molar concentrations of Na, Ca, Fe, K, Mg, Si and Al. For example, (Molar concentration) Na = (wt% $Na_2O$ * (atomic mass of 2Na/ atomic mass of $Na_2O$))/atomic mass of Na.

Sodium is a proxy for sodium-rich minerals formed during Na alteration (albite and scapolite). Calcium is a proxy for calcium-rich minerals present in HT Ca-Fe alteration (amphibole, apatite), skarn (clinopyroxene, and andradite to grossular garnet) and calcium-bearing scapolite present in Na-Ca and Na-Ca-Fe alteration. Calcium is also a proxy for epidote, calcite and fluorite in LT Ca-Mg-Fe alteration. Iron is a proxy for iron oxides, iron silicates, iron sulphides and iron carbonates. Potassium is a proxy for potassium-rich phases (K-feldspar, biotite, sericite) of the K, HT and LT K-Fe, phyllic and sericitic alteration facies. Magnesium is a proxy for chlorite and/or talc in LT Ca-Mg-Fe alteration and some late hydrolytic LT alteration facies. Finally, the sum of silica + aluminum is a proxy for advanced argillic alteration and quartz enrichment and for the intensity of iron oxide alteration.

Two main types of barcodes are used: 1) Na-Ca-Fe-K-Mg; and 2) Na-Ca-Fe-K-(Si+Al)/10. Each element or combination of elements ([Si+Al]/10) is normalized with respect to the sum of the elements used in the barcode. The molar proportions of cations are similar in common volcanic, intrusive or sedimentary rocks in which alteration is lacking. In contrast, one or two cations dominate the molar proportions of metasomatic rocks. One exception, unaltered rhyolites, are generally characterized by a barcode dominated by two cations, Na and K.

ArcMap was used to construct the diagrams. The diagram corresponds to a rectangle of 150 meters by 100 meters, with the AIOCG 1 index expressed in latitude and the AIOCG 2 index in longitude. In an excel table, we assign a latitude and a longitude for each analysis. The latitude (in metres) corresponds to the AIOCG1 index multiplied by 100, and the longitude to the AIOCG2 index multiplied by 150. Once the file is imported into ArcMap, these coordinates are used to plot the analyses in the diagram. To create barcodes, we use the stacked chart function in the symbology tab of ArcMap. Once the stacked chart panel appears, we set the display properties, such as chemical element in molar concentrations, color ramps, and so on, to generate the barcodes for each analysis.

Disproportions in the normalized molar concentrations of Na, Ca, Fe, K or Mg highlight alteration types, whereas the amplitude of the disproportions provides a semi-quantitative measurement of alteration intensity.

# Defining Geophysical Signatures of IOCG Deposits in the Olympic Copper-Gold Province, South Australia, using Geophysics, GIS and Spatial Statistics

**Laszlo Katona**
*Geological Survey of South Australia, Department for Energy and Mining, Adelaide, Australia; Laz.Katona@sa.gov.au*

**Adrian Fabris**
*Geological Survey of South Australia, Department for Energy and Mining, Adelaide, Australia*

*Katona, L.F., and Fabris, A., 2022, Defining geophysical signatures of IOCG deposits in the Olympic Copper-Gold Province, South Australia, using geophysics, GIS and spatial statistics, in Corriveau, L., Potter, E.G. and Mumin, A.H., eds., Mineral systems with iron oxide copper-gold (IOCG) and affiliated deposits: Geological Association of Canada, Special Paper 52, p. 299-313.*

## Abstract

Iron oxide copper-gold deposits (IOCG) contain significant quantities of iron, such that they produce gravity responses that are distinct from the surrounding country rock, and in most cases, magnetic anomalies, resulting from associated magnetite. South Australia's Olympic Copper-Gold Province contains numerous examples of IOCG deposits; however, prospective ground encompasses thousands of gravity and magnetic anomalies. Efficient mineral exploration requires a method that can delineate, map and classify geophysical anomalies in order to prioritize potential drill targets.

Residual Bouguer gravity and variable-reduced-to-pole total magnetic intensity grids over the Gawler Craton were vectorized, generating polygon datasets representing regions of locally anomalous gravity and magnetic intensity. Statistics from potential field grids were embedded into each polygon, which enabled calculation of anomaly magnitude. Known IOCG-type deposits were found to be consistently associated with coincident to semi-coincident magnetic and gravity anomalies. Ground-based gravity data acquired at 1 km or closer spacing were found to be desirable for mapping gravity anomalies associated with IOCG deposits located from the near surface to over 1 000 m, while airborne magnetic data acquired at 400 m or better line spacing are sufficient to map magnetic anomalies at a scale that permits IOCG site selection. Analysis of spatial clustering and the identification of outliers using the Anselin Local Morans I statistical method has resulted in the delineation of geographic regions, spatially correlating with the Mount Woods, Moonta and Olympic Domains within the eastern Gawler Craton. These regions exhibit either high magnitude spatial clusters or high magnitude spatial outliers. High magnitude spatial outliers are of particular interest, as they include a high proportion of currently identified IOCG deposits and mineral occurrences. The statistical approach defining spatial clustering of high magnitude gravity features defined a threshold of 0.4 mGals as a statistically significant magnitude threshold for residual gravity features associated with IOCG deposits in the Gawler Craton. However, this threshold is very likely to be dependent on the population of anomalies in the study area and the method used to produce the residual dataset. Results from this study suggest IOCG deposits do not occur in isolation and a number of additional, untested spatially coincident magnetic and gravity anomalies exist that warrant further investigation.

## Résumé

Les gîtes à oxydes de fer cuivre-or (IOCG) contiennent d'importantes quantités de fer ce qui fait en sorte qu'ils ont une réponse gravimétrique distincte de celle de la roche environnante et que, dans la plupart des cas, ils produisent des anomalies magnétiques qui résultent de leur contenu en magnétite. La province cuivre-or d'Olympique, en Australie méridionale, contient de nombreux exemples de gîtes IOCG mais la région d'intérêt renferme des milliers d'anomalies gravimétriques et magnétiques. Une exploration minérale efficace nécessite une méthode permettant de délimiter, cartographier et classifier les anomalies géophysiques afin de hiérarchiser les cibles de forage potentielles.

La gravité de Bouguer résiduelle et les grilles d'intensité magnétique totale variable réduite au pôle du craton de Gawler ont été vectorisées, générant des jeux de données de polygones représentant des régions de gravité et d'intensité magnétique localement anormales. Les statistiques des grilles de champs potentiels ont été intégrées à chaque polygone, ce qui a permis de calculer la magnitude des anomalies. Les gîtes IOCG connus sont systématiquement associés à des anomalies magnétiques et gravimétriques coïncidentes à semi-coïncidentes. Les données gravimétriques au sol acquises avec un espacement de 1 km ou moins sont idéales pour cartographier les anomalies gravimétriques associées aux gisements IOCG, tandis que les données magnétiques aéroportées acquises à un espacement de ligne inférieur ou égal à 400 m suffisent pour cartographier les anomalies magnétiques à une échelle permettant la sélection de cibles IOCG. Les statistiques spatiales définissent un seuil de 0.4 mGals comme seuil d'amplitude statistiquement significatif pour les entités gravimétriques résiduelles associées aux gîtes IOCG du craton de Gawler; ce seuil dépend toutefois du nombre d'anomalies dans la zone d'étude et de la méthode utilisée pour produire le jeu de données résiduel. L'analyse du regroupement spatial et l'identification des valeurs isolées à l'aide d'Anselin Local Morans I ont permis de délimiter des régions géographiques présentant des grappes de grande magnitude ou des valeurs isolées de grande magnitude, correspondant à des domaines géologiques régionaux. Dans l'est du craton Gawler, les valeurs isolées de grande magnitude revêtent un intérêt particulier dans la mesure où elles incluent une forte proportion de gisements IOCG et de zones minéralisées actuellement identifiés. Les résultats de cette étude suggèrent que les gisements IOCG ne se produisent pas isolément et qu'il existe un certain nombre d'anomalies magnétiques et gravimétriques coïncidentes dans l'espace, non vérifiées, qui méritent d'être étudiés plus en profondeur.

## Introduction

Potential field geophysical techniques characterize iron oxide copper-gold (IOCG) deposits as positive gravity anomalies that are spatially coincident, but commonly offset from, an associated positive magnetic anomaly (Gow et al., 1993; Esdale et al., 2003; Hart and Freeman, 2003; Porter, 2010; van der Wielen et al., 2013). These anomalies are a representation of the magnetic and density properties of iron-bearing minerals within the IOCG system. The Olympic Copper-Gold Province of the Gawler Craton, South Australia is the type location of the hematite-rich end member of the IOCG deposit clan, being the location of the Olympic Dam deposit along with others such as Prominent Hill and Carrapateena (Skirrow et al., 2002; Belperio et al., 2007; Porter, 2010; Skirrow, 2022). However, the vast majority of the prospective Gawler Craton basement in this region is covered by a thick veneer of younger sedimentary rocks, meaning mineral exploration relies heavily on geophysical targeting. There are thousands of gravity and magnetic anomalies within and adjacent to the Olympic Copper-Gold Province. Efficient mineral exploration requires a method that can delineate, map and classify these anomalies in order to prioritize potential drill targets.

The aim of this paper is to demonstrate how gravity and magnetic data can be processed to highlight areas likely to host IOCG deposits, based on the known geophysical character of example deposits or prospects within the Gawler Craton. A methodology using GIS and spatial statistics to delineate gravity and magnetic anomalies suitable for IOCG targeting has been developed that highlights those geophysical features that warrant further, detailed investigation. Geoprocessing of residual Bouguer gravity and reduced-to-pole total magnetic intensity (RTP-TMI) grids is used to identify both known and potential IOCG deposits and occurrences within the Olympic Copper-Gold Province. This paper describes the geophysical signatures of five of these deposits: Carrapateena, Khamsin, Olympic Dam, Wirrda Well and Oak Dam (Fig. 1), while detailing the use of spatial statistics for mapping other known and potential IOCG deposits within the province. These methodologies are applicable to exploration regardless of whether target areas are at the surface or below thick cover, provided geophysical coverage is sufficient.

## Geological and Geophysical Setting

*The Olympic Copper-Gold Province*

The Olympic Copper-Gold Province (Fig. 1) is a metallogenic province that has been delineated using geophysical interpretation (primarily magnetic), drillhole information, and the locations of copper and gold deposits and mines (Skirrow et al., 2002, 2007). Much of the province is covered by at least 100 m of barren sedimentary rocks (Fig. 1), which obscure the prospective crystalline basement. With no surficial indication of mineral endowment beneath the cover, geophysical data and drill samples are the main explanatory datasets used by mineral explorers targeting IOCG deposits and interpreting basement geology (i.e. the explanatory variables that best explain the existence of the mineral potential). Reviews of the geology of the Olympic Copper-Gold Province and Gawler Craton can be found in Ferris et al. (2002), Hand et al. (2007) and Reid and Fabris (2015).

*Geophysical Data from the Gawler Craton*

Ground-based Bouguer gravity and airborne total magnetic intensity (TMI) survey coverage of the Olympic Copper-Gold Province consists of a combination of regional, government funded surveys and smaller but usually higher-resolution private sector surveys. The gravity and TMI coverage for the Gawler Craton is shown in Figure 2. Within this region, the gravity station spacing varies from 100 m to 4 000 m in the central and eastern portion (which includes the Olympic Copper-Gold Province), with stations spaced up to 8 000 m apart in the western Gawler Craton. The TMI surveys are more consistent, with the majority of the Gawler Craton survey line spacing 400 m or closer.

## Methodology

A residual Bouguer gravity grid with a 100 m grid interval was produced (Fig. 3) by subtracting a 1 000 m upward-continued Bouguer gravity grid from the Bouguer gravity grid. By removing the regional effect of the gravity signal, the residual represents the locally derived gravitational effect and more accurately defines individual gravity anomalies. The same process was applied to the variable reduced to pole TMI (referred to in this paper as VRTP-TMI, RTP-TMI or TMI) with a grid interval of 80 m (Fig. 3). This processing attenuates anomalies related to deeper sources (McCafferty et al., 2016; Katona et al., 2018) and sharpens the detail on anomalies associated with shallower magnetic and density sources. The value ranges of the grids are changed as a consequence of subtracting the upward-continued grids; ranges of data values for both the residual and non-residual gravity and TMI grids were tabulated (Table 1). A geoprocessing routine (equivalent to a script) was applied to each grid (Katona et al., 2018), producing GIS polygons positioned over localized geophysical anomalies (Fig. 4). The routine used distance thresholds for

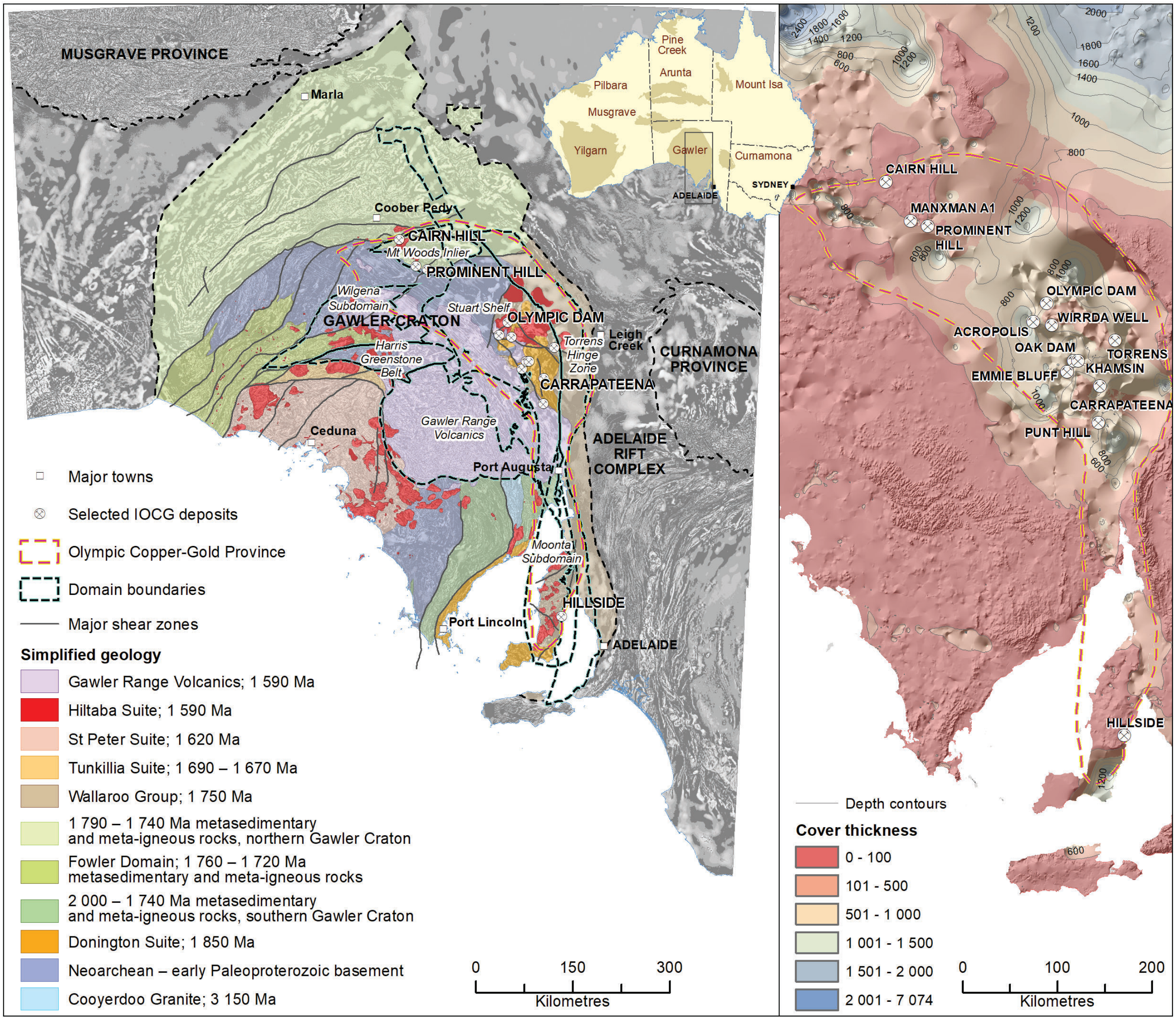


**FIGURE 1.** Simplified Gawler Craton geology showing the extent of the Olympic Copper-Gold Province, South Australia.

the maximum perimeter distance of the polygons (25 km for gravity and 50 km for TMI), with information of the underlying grid embedded in the polygon attributes. Attributes captured during the processing included perimeter contour values of each anomaly plus minimum, maximum and mean values of the grid underlying each anomaly. An anomaly 'magnitude' was calculated by subtracting the maximum anomaly value from the contour value. A geophysical anomaly was accepted if the mean value within the polygon was greater than the value of the contour defining it. The offshore anomaly polygons for gravity and TMI were discarded due to the very low resolution of the offshore data. The number of gravity and TMI anomalies coincident with each other at three distance thresholds was logged and tabulated (Table 2).

**TABLE 1.** Gravity and TMI grid value ranges.

| Dataset | Potential Field values |
|---|---|
| Bouguer gravity range | -92 – 50 mGals |
| Residual Bouguer gravity range | -16 – 12 mGals |
| Reduced to pole TMI range | -2 936 – 21 718 nTeslas |
| Residual reduced to pole TMI range (nTeslas) | -4 733– 18 733 nTeslas |

Spatially coincident magnetic and gravity features were displayed for interrogation and comparison to known IOCG deposits. The number of copper-gold deposits within the three distance thresholds of TMI and gravity anomalies (i.e. threshold one: within an anomaly, threshold two: within 500m of an anomaly margin, threshold three: within 1000m of an anomaly margin, Fig. 3)

The gravity and TMI polygons were checked for spatial clustering based on the magnitude attribute, using the

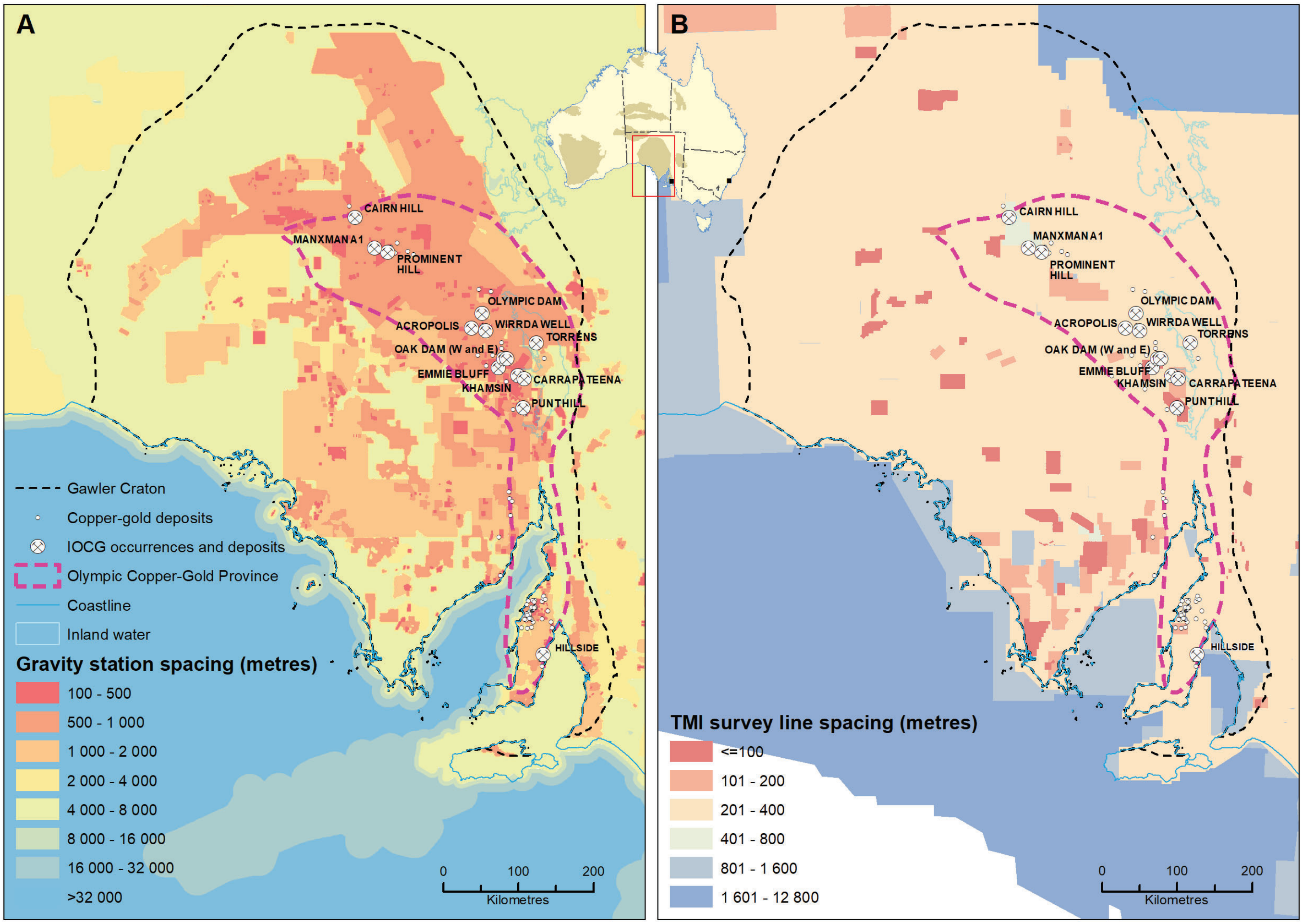


**FIGURE 2.** Gravity and magnetic survey density within the Olympic Copper-Gold Province. **A.** Gravity survey. **B.** Magnetic survey.

Getis-Ord General G (Getis and Ord, 1992) analysis in ArcGIS (Fig. 5). A cluster and outlier analysis (Anselin Local Morans I; Anselin, 1995) was then applied separately to the gravity and TMI polygons to show which high and low magnitude gravity and magnetic features are spatially clustering and which are spatial outliers (Fig. 6). An overlay proximity analysis was applied on the gravity and magnetic features to determine spatial coincidence between gravity and corresponding magnetic anomalies, with non-coincident features discarded (Fig. 7). The gravity anomalies identified as high by the cluster and outlier analysis were used to determine a threshold magnitude that can be associated with both known and undiscovered deposits and occurrences. Value ranges of residual gravity and TMI were tabulated (Table 4), and anomalies that were higher than the magnitude threshold but displaying no spatial clustering were plotted separately (Fig. 8).

**TABLE 2.** Residual gravity and TMI coincident features within the Gawler Craton, South Australia.

| Feature type | Feature Count |
|---|---|
| Onshore TMI anomalies | 39 047 |
| Onshore TMI anomalies with a coincident gravity anomaly | 12 104 |
| Onshore TMI anomalies within 500 m of a gravity anomaly | 16 434 |
| Onshore TMI anomalies within 1 000 m of a gravity anomaly | 20 345 |
| Onshore Gravity anomalies | 10 259 |
| Onshore Gravity anomalies with a coincident TMI anomaly | 6 937 |
| Onshore Gravity anomalies within 500 m a coincident TMI anomaly | 7 901 |
| Onshore Gravity anomalies within 1 000 m a coincident TMI anomaly | 8 510 |

## Results

### *Input Gravity and TMI Grids*

While the focus of the study was the Olympic Copper-Gold Province, the gravity and TMI data used covers the entire onshore portion of the Gawler Craton (Fig. 1). Figure 2 shows that for most of the province, the coverage of the onshore gravity and TMI meet the criteria of gravity station spacing ≤ 1 000 m and airborne TMI flight line spacing ≤ 400 m. Outside of the province, particularly in the west of the Gawler Craton, the gravity station coverage is sparse, with stations spaced from 2 000 m to 8 000 m apart, diminishing the capacity of the gravity data to accurately map the magnitude and size of density sources. Although the coarsely-spaced data are

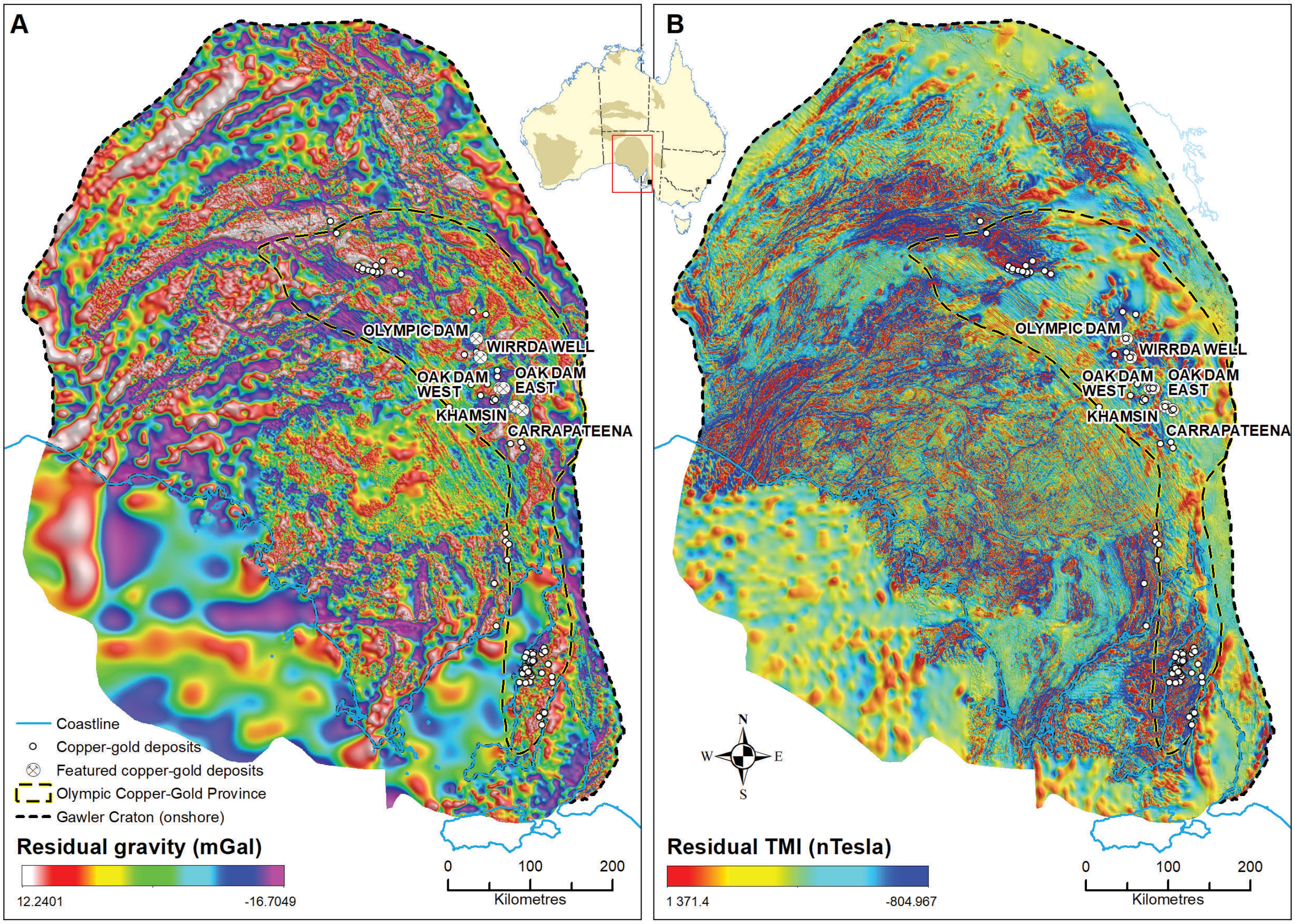


**Figure 3.** Residual gravity and residual reduced to pole TMI grids. **A.** Residual gravity. **B.** Residual reduced to pole.

**Table 3.** Basement hosted copper-gold deposits and their proximity to residual gravity and magnetic anomalies.

| Proximity attribute | Deposit Count | Percent |
|---|---|---|
| Total number of copper-gold deposits | 104 | 100.0 |
| ...within a TMI anomaly | 65 | 62.5 |
| ...within 500 m of a TMI anomaly | 89 | 85.5 |
| ...within 1 000 m of a TMI anomaly | 101 | 97.1 |
| ...within a gravity anomaly | 54 | 51.9 |
| ...within 500 m of a gravity anomaly | 82 | 78.8 |
| ...within 1 000 m of a gravity anomaly | 97 | 93.2 |
| ...within a TMI anomaly coincident with a gravity anomaly | 65 | 62.5 |
| ...within a 500 m of a TMI anomaly coincident with a gravity anomaly | 88 | 84.6 |
| ...within a 1 000 m of a TMI anomaly coincident with a gravity anomaly | 100 | 96.2 |
| ...within a gravity anomaly coincident with a TMI anomaly | 47 | 45.2 |
| ...within 500 m of a gravity anomaly coincident with a TMI anomaly | 64 | 61.5 |
| ...within 1 000 m of a gravity anomaly coincident with a TMI anomaly | 73 | 70.2 |

almost exclusively outside of the area of interest in this study, the data nevertheless contribute to the overall population of anomalies used in statistical analyses. The Gawler Craton RTP-TMI and Bouguer gravity grids used in this study were clipped from the publicly available South Australian regional grids produced by the Geological Survey of South Australia.

Ranges of gravity and TMI grids, both before and after computing the residuals, are displayed in Table 1. The residual transform has reduced the overall gravity value range by 114 mGals to 28 mGals and the TMI value range by 1 188 nTeslas to 23 466 nTeslas.

*GIS Polygons as Representations of Geophysical Anomalies*

The distance thresholds of 25 km for gravity and 50 km for TMI effectively capture the geometry of the respective anomalies as displayed in Figure 4 and the anomalies associated with five known IOCG deposits (Fig. 9). The larger distance threshold for TMI features was necessary because the geometry of the TMI features of interest tend to be more complex and spread out than the gravity features, which are commonly smaller and more compact. Table 2 shows the number of TMI and gravity anomaly polygons produced for the Gawler Craton

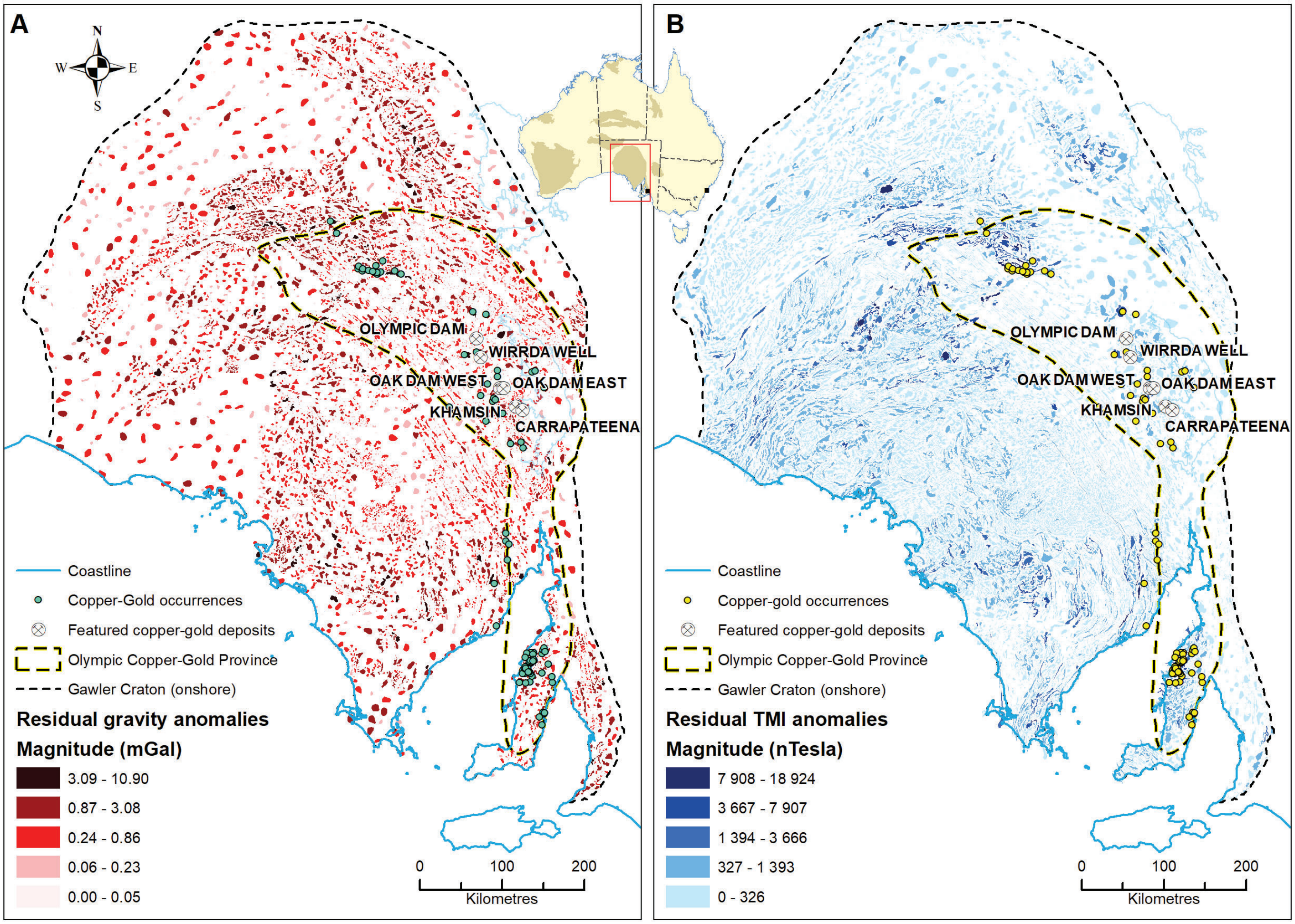


**FIGURE 4.** Gravity and TMI anomalies recovered by the GIS processing. **A.** Gravity anomalies. **B.** TMI anomalies.

along with the results of a proximity analysis of coincident and near-coincident TMI and gravity features. Within the Gawler Craton there were 39 047 onshore TMI anomalies of which 12 104 were overlapping a gravity anomaly; 16 434 were within 500 m of a gravity anomaly and 20 345 were within 1 000 m of a gravity anomaly. There were 10 259 onshore gravity anomalies in total, of which 6 937 were overlapping a TMI anomaly; 7 901 were within 500 m of a TMI anomaly and 8 510 were within 1 000 m of a TMI anomaly.

*Locations of Geophysical Anomalies in Relation to Copper-gold Deposits in the Olympic Copper-Gold Province*

The 104 known crystalline basement-hosted copper-gold occurrences in the study (Department for Energy and Mining, 2019) were used as search criteria to obtain a count of significant TMI and gravity anomaly highs overlapping or in close proximity of the known deposits. These results are displayed in Table 3 and reveal 97% of deposits were within 1 000 m of a TMI anomaly and 93.2% were within 1 000 m of a gravity anomaly; 96.2% of deposits were within 1 000 m of a TMI anomaly that is coincident (within 1 000 m) with a gravity anomaly and 70.2% of deposits were within 1 000 m of a gravity anomaly that is coincident (within 1 000 m) with a TMI anomaly.

The known copper-gold occurrences cluster into three distinct groups: one located in the northwestern part of the province, with 18 deposits; one in the central part of the province, with 28 deposits; and the third in the southern part of the province, with 58 deposits (Fig. 7). For these three groups, the majority of the northwestern and central groups (77% and 82%, respectively) are associated with gravity and magnetic highs. For copper-gold deposits occurring in the southern group, there is less of an association with potential field highs, with only 29% associated with a gravity high and 48% with a magnetic high.

*Spatial Clustering of Gravity and TMI*

The likelihood that observed spatial clustering of gravity and magnetic anomalies are the result of random chance was tested using Getis-Ord General G analysis (Fig. 5). Using the anomaly magnitude attribute as the input numeric parameter, the High-Low clustering report indicates that a z-score of 2.58 specifies at a 99% confidence level that the high magnitude values are clustering. The value of the z-scores from the gravity

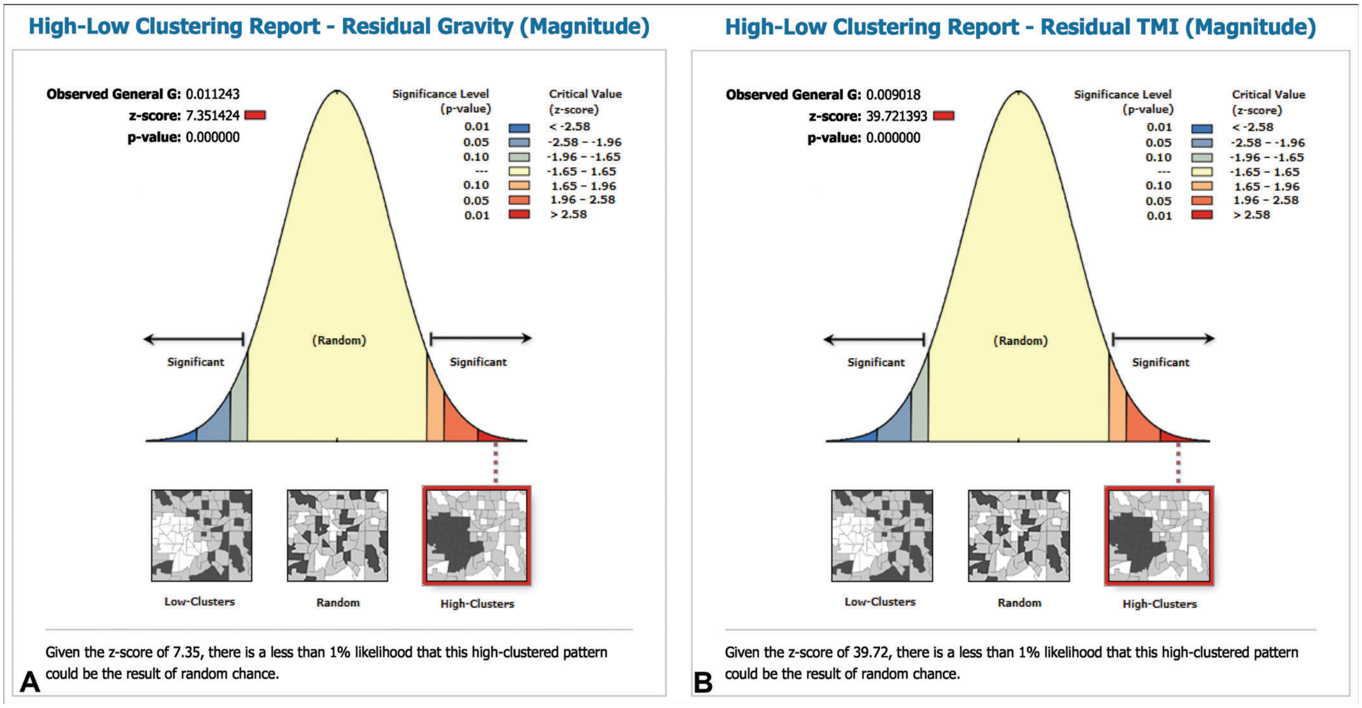


FIGURE 5. Clustering results – The Getis-Ord General G indicates spatial clustering of high magnitude anomalies for **(A)** gravity and **(B)** TMI that is not the result of random chance.

and TMI returned 7.35 and 39.72 respectively. These z-scores indicate that there is less than 1% likelihood that the high-clustered patterns could be the result of random chance.

*Cluster and Outlier Analysis*

Satisfied that there is significant clustering of high-magnitude values evident in both the gravity and TMI polygons, a cluster and outlier analysis (Anselin Local Morans I; Anselin, 1995) was performed on the gravity and TMI polygons to map the magnitude of each feature as clusters or outliers. This analysis tags each anomaly feature with a z-score and pseudo p-value to determine whether to accept or reject the null hypothesis that the apparent similarity, or spatial clustering of high-magnitude values is what would be expected in a random distribution (ESRI, 2018). There are four specific types of clusters and outliers produced by the analysis. High clusters (a statistically significant cluster of high-magnitude features), high-low outliers (a statistically significant high-magnitude feature, surrounded by features with low values), low-high outliers (a low-magnitude feature surrounded by statistically significant high values), low clusters (a statistically significant cluster of low-magnitude features) and a 'not significant' class of features that satisfies the null hypothesis and displays no statistically significant clustering.

Figure 6 displays the cluster and outlier map of gravity and TMI for the Gawler Craton. The spatial distribution of high gravity and TMI clusters in many parts of the craton are similar. There are also similarities in the spatial distribution of high-low outliers (along with low clusters) between the TMI and gravity in the central Gawler Craton, with two exceptions being the northwestern Gawler Craton, which hosts a region of high-low TMI outliers and the northeastern Olympic Copper-Gold Province, which hosts more high-low gravity outliers than high-low TMI outliers.

The distribution of high-low outliers (and associated low clusters) is of principal significance in the gravity data because these outliers appear to be contained within and contiguous with to the central part of the Olympic Copper-Gold Province, which hosts many known deposits and occurrences including Olympic Dam and Carrapateena (Fig. 7). This suggests that many of the IOCG deposits within the central Olympic Copper-Gold Province are associated with the high-low outlier gravity features, while the TMI features occupying the same region as these gravity outliers have either clusters of moderate to low magnitude features, or do not show any statistically significant clustering.

The high gravity clusters in the northwest and south of the Olympic Copper-Gold Province are also associated with IOCG deposits; however, they show a distinct distribution and character. The differing nature of gravity anomaly clustering suggests a fundamental difference between these regions when compared with the central zone. In addition, unlike the central zone, several deposits in these regions are associated with gravity anomalies that do not exhibit significant clustering and lie between the high and low clusters.

*Determination of a Gravity Anomaly Threshold Using Spatial Statistics*

Table 4 displays the ranges of magnitude values attributed to the five statistical clustering classes. For gravity, both the

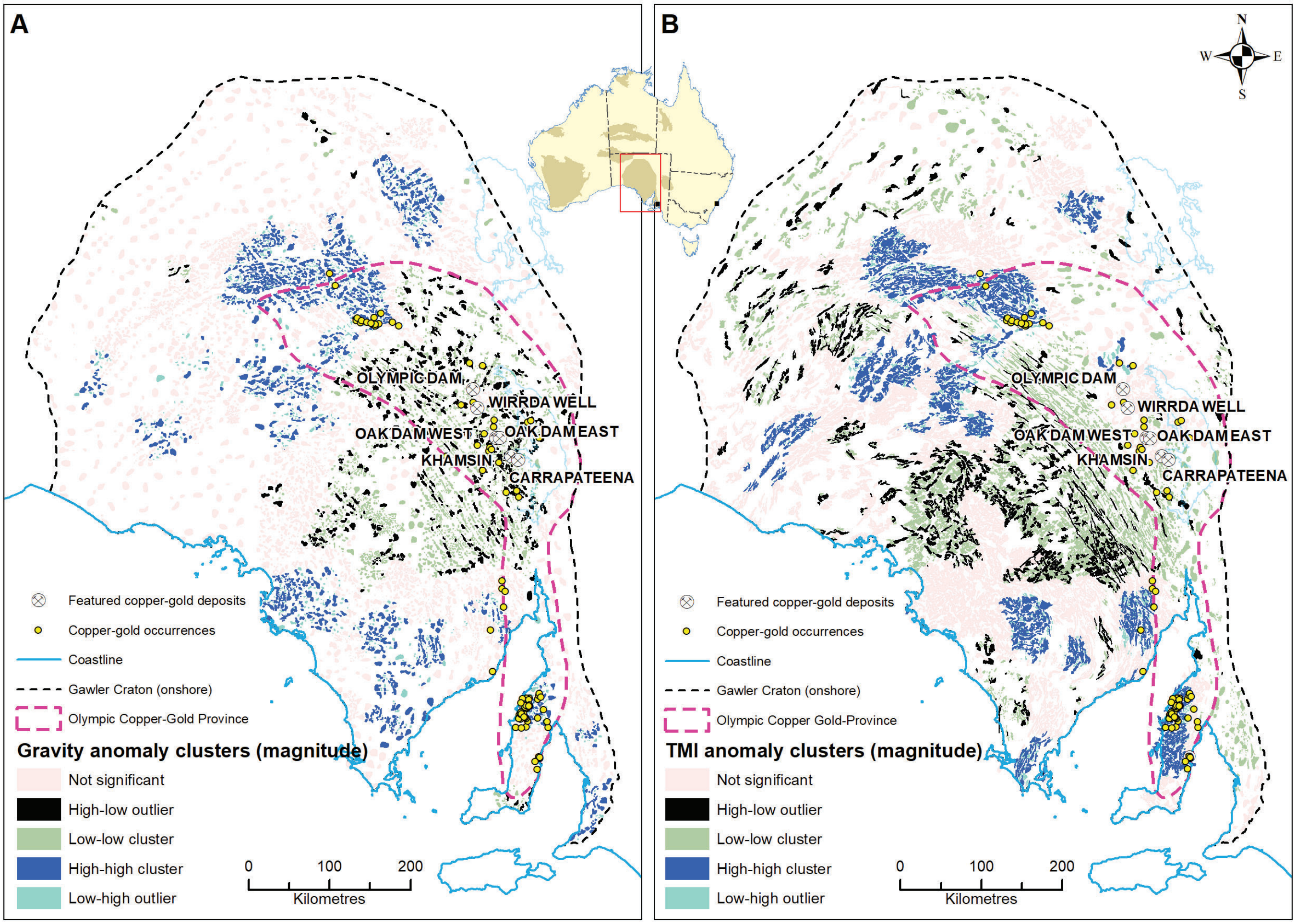


**Figure 6**. **(A)** Gravity clusters and outliers, and **(B)** magnetic clusters and outliers of the Gawler Craton.

**Table 4.** Ranges of gravity and TMI values in the four cluster and outlier types, for coincident gravity and TMI features (within 1,000m).

| Cluster-outlier type | Value range | No. of Features |
|---|---|---|
| Gravity High Cluster (HH) | 0.400 – 10.90 mGals | 1 112 |
| Gravity High-Low Outlier (HL) | 0.400 – 9.17 mGals | 530 |
| Gravity Low-High Outlier (LH) | 0.099 – 0.399 mGals | 1 259 |
| Gravity Low Cluster (LL) | 0.001 – 0.130 mGals | 2 442 |
| Gravity No Significant Clustering | 0.001 – 7.95 mGals | 3 167 (1 193 ≥0.4mGals) |
| TMI High Cluster (HH) | 136 – 18 923 nTeslas | 1 830 |
| TMI High-Low Outlier (HL) | 136 – 4 754 nTeslas | 1 047 |
| TMI Low-High Outlier (LH) | 0.5 – 135.8 nTeslas | 2 301 |
| TMI Low Cluster (LL) | 0.09 – 135.9 nTeslas | 6 876 |
| TMI No Significant Clustering | 0.17 – 13 070 nTeslas | 8 291 |

high clusters and the high-low outliers have a minimum anomaly value of 0.4 mGals. This is a statistically significant threshold and is regarded as a residual gravity anomaly of sufficient magnitude to make it a valid IOCG target. The gravity anomalies that exhibit no significant clustering have a value range of 0.001 to 7.95 mGals. Assuming the residual gravity features in the Olympic domain above the 0.4 mGal threshold are of interest as potential IOCG deposits, any of the features not exhibiting significant spatial clustering with a magnitude >=0.4 mGals may also be taken as a candidate IOCG. Within the Olympic Copper-Gold Province, many of these non-clustering features are located around known deposits in the northwest and south of the study area (Fig. 8). There are 193 such features within the province.

Since there is no clear correlation between high-magnitude TMI anomalies and the presence of IOCG deposits, we are more interested in the presence of a TMI anomaly than its magnitude. For completeness, Figure 8 also displays the TMI features within the 'no significant clustering' group. There are 1 289 high-magnitude (>136 nTeslas) TMI features of this class within the Olympic Copper-Gold Province.

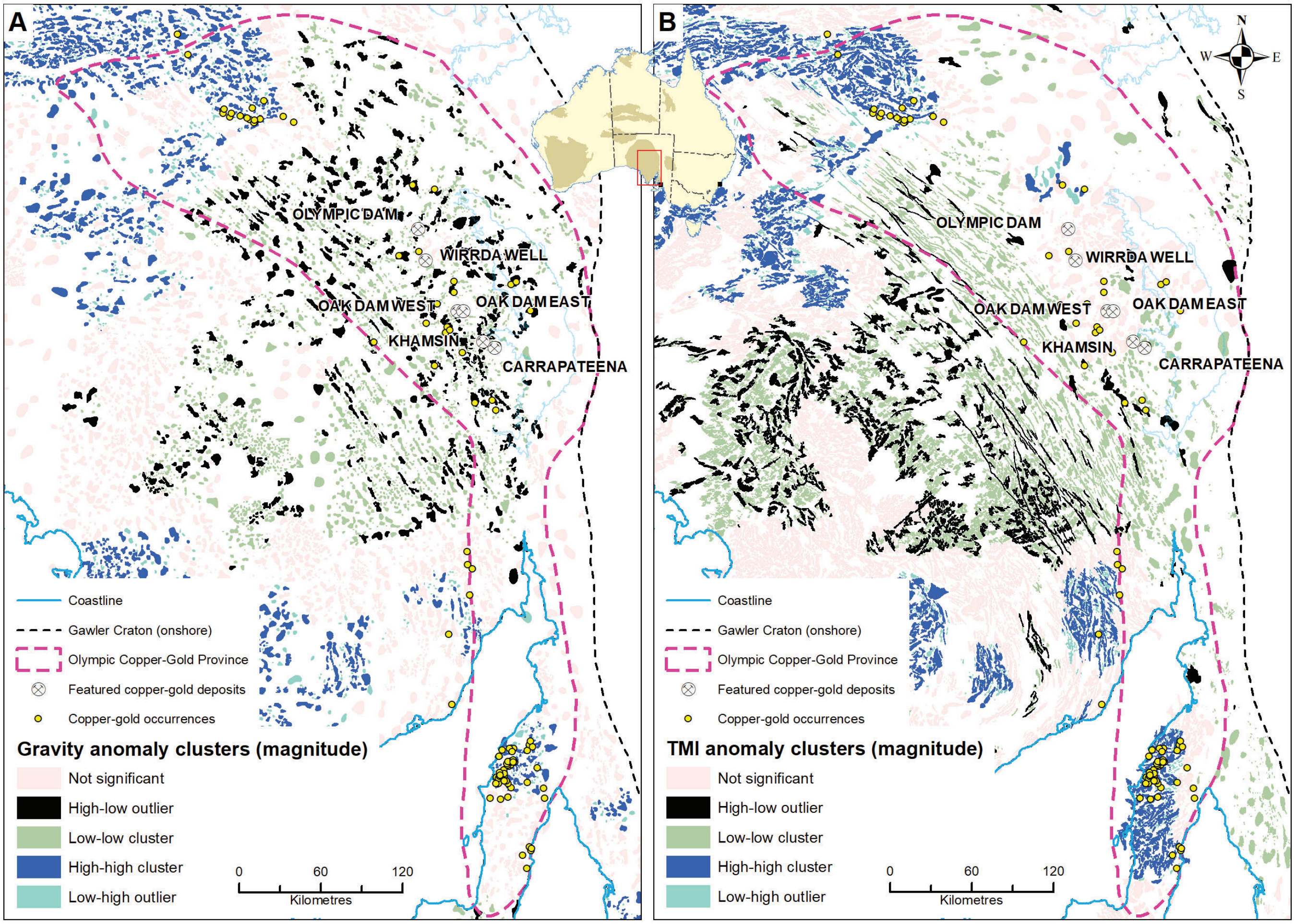


**Figure 7.** Olympic Copper-Gold Province spatially coincident **(A)** gravity clusters and outliers, **(B)** magnetic clusters and outliers, 1 000m threshold used to determine spatial coincidence.

*Geophysical Characteristics of Known IOCG Deposits*

Figure 9 displays the residual gravity and TMI signatures of IOCG deposits in the Olympic Copper-Gold Province. For each of the deposits the residual TMI grid is shown on the left and the residual gravity grid is shown on the right, with gravity stations superimposed. In the centre, the TMI and gravity features are displayed, with the cluster status of local gravity features shown as the boundary of local features, and contours overlaid to show internal anomaly detail. The label on the main gravity feature is the range of residual gravity within the feature. The resource figures for each of the five deposits are presented in Table 5. Beginning with the Olympic Dam deposit (Fig. 9), the extent of the residual gravity signature is approximately 8 km in width, and an almost coincident residual TMI anomaly has a width of about 10 km. This deposit is located at a depth of ~350 m and defines the hematite breccia-style IOCG±U type for South Australia, containing a resource of 10.1 Bt of ore (BHP, 2018a). The geophysical footprint of the Wirrda Well prospect is smaller, with coincident residual gravity and TMI features of approximately 5 km width. Significant intercepts into mineralization start at a depth of 419 m (Hayward and Skirrow, 2010). The Carrapateena deposit is more compact, residing within a residual gravity feature of approximately 4 km width, and a broader (8 km) TMI anomaly. This deposit begins at a depth of 473 m and has a current resource of 970 Mt (OZ Minerals, 2019), however a previous resource

**Table 5.** Resource estimates for the IOCG deposits highlighted in this paper.

| Deposit | Total Resource Estimates |
|---|---|
| Olympic Dam | 10.1 Bt @ 0.78% Cu, 0.33g/t Au, 1g/t Ag, 0.25kg/t $U_3O_8$ (BHP, 2018a) |
| Wirrda Well | 248 m @ 0.86% Cu, 4.6 g/t Ag from 419 m (Hayward and Skirrow, 2010) |
| Carrapateena | 970 Mt @ 0.5% Cu, 0.2g/t Au, 3g/t Ag (+U) (OZ Minerals, 2019) |
| Khamsin | 202 Mt @ 0.6% Cu, 0.1g/t Au, 1.7g/t Ag when considered as a block caving mining method (OZ Minerals, 2016) |
| Oak Dam (East and West) | Oak Dam East - ~560 Mt @ 41 to 56% Fe, and 300 Mt @ 0.2% Cu (Davidson et al., 2007). Oak Dam West – best drill intercept of 425.7 m @ 3.04% Cu, 0.59 g/t Au and 6.03 g/t Ag from 1063 m (BHP, 2018b) |

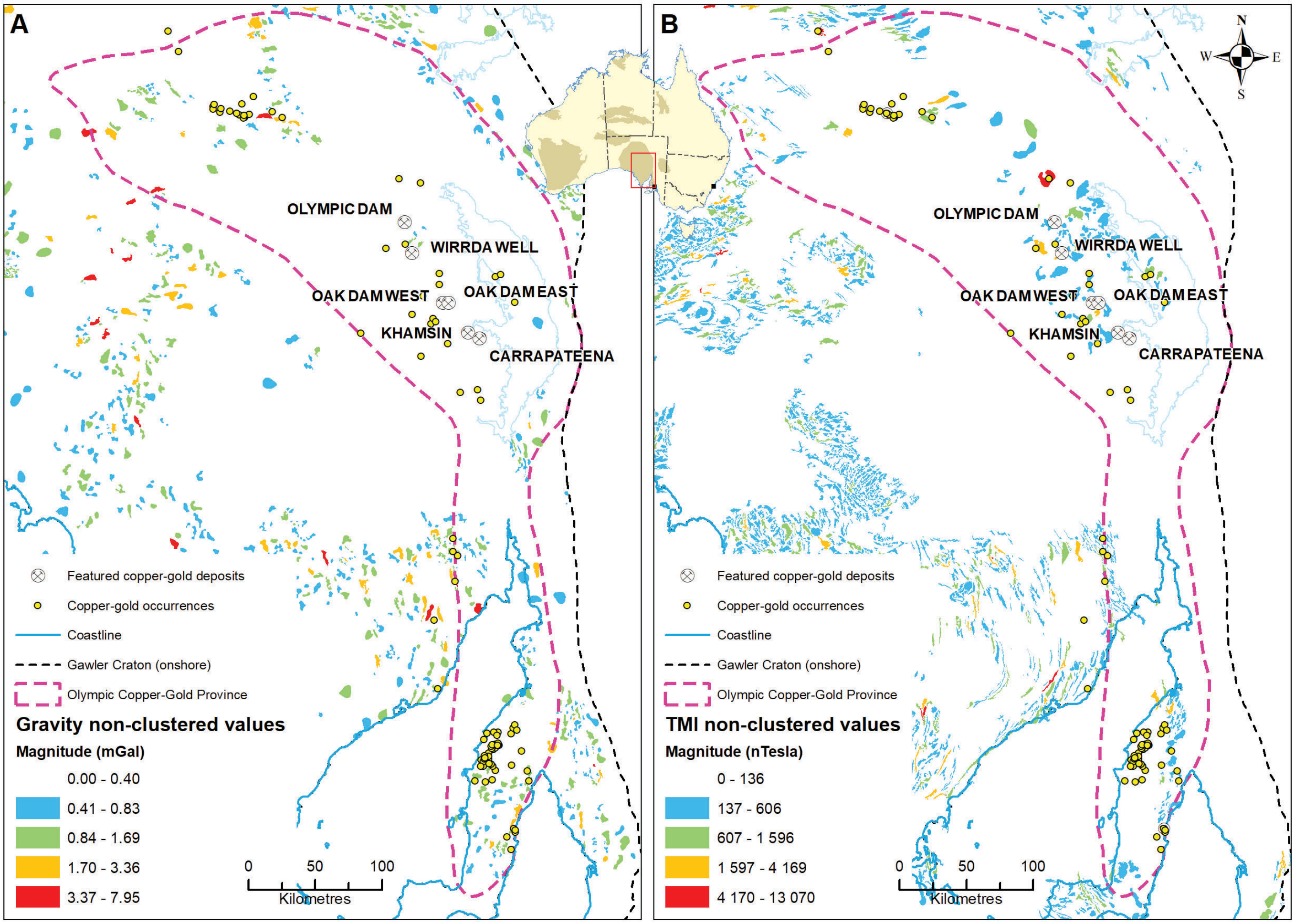


**FIGURE 8.** Anomalies tagged as having no significant clustering of the magnitude attribute in the cluster and outlier analysis. Gravity anomalies within the Olympic Copper-Gold Province >=0.4m Gal are considered to be potential IOCG targets. **A.** Gravity anomalies. **B.** TMI anomalies.

estimate was 800 Mt when the deposit was considered as a block caving proposal (OZ Minerals, 2017). The Khamsin deposit, approximately 480 m below the surface, has a residual gravity footprint of approximately 3 km and a narrow (~2 km wide) TMI feature comprising three discreet 'bullseye' type features, the central one being spatially coincident with mineralization. Khamsin has a resource estimate of 202 Mt (OZ Minerals, 2016). The Oak Dam prospects (Davidson et al., 2007) comprise two discrete residual gravity features, Oak Dam West and Oak Dam East (4 km and 2 km in width, respectively). The Oak Dam East residual gravity anomaly is coincident with the maximum gradient of an elongate magnetic feature. Drill intercepts to significant mineralization are ~850 m and ~600 m for the Oak Dam West and Oak Dam East prospects, respectively.

## Discussion

*Input Gravity and TMI Grids*

Our analyses have shown that a gravity station coverage of 1 km or closer is required for regional scale targeting of IOCG deposits, as this is considered to be the minimum resolution needed to spatially locate the peaks of the gravity features with reasonable accuracy at depths from near surface to greater than 1 000 m. For airborne magnetic data, 400 m line spacing or better are the South Australian standard of regional TMI resolution and are considered herein to be suitable for targeting IOCG deposits located at depths from the near surface to greater than 1 000m. The onshore gravity and TMI coverage meet the necessary criteria for geophysical targeting for most of the Olympic Copper-Gold Province; however, it is good practise to check any results against the source data to qualify those results. In addition, while such datasets permit recognition of potential targets, they are not intended to refine final drill targets where explorers rely on such geophysical data for their exploration.

The input grids used for this study were clipped to the boundary of the Gawler Craton, from the South Australian state-wide VRTP TMI and Bouguer gravity so the investigation could be performed within the context of the Gawler Craton. Although this paper is focused on the Olympic Copper-Gold Province, the results suggest there is further IOCG potential outside of the current interpreted extent of the metallogenic province.

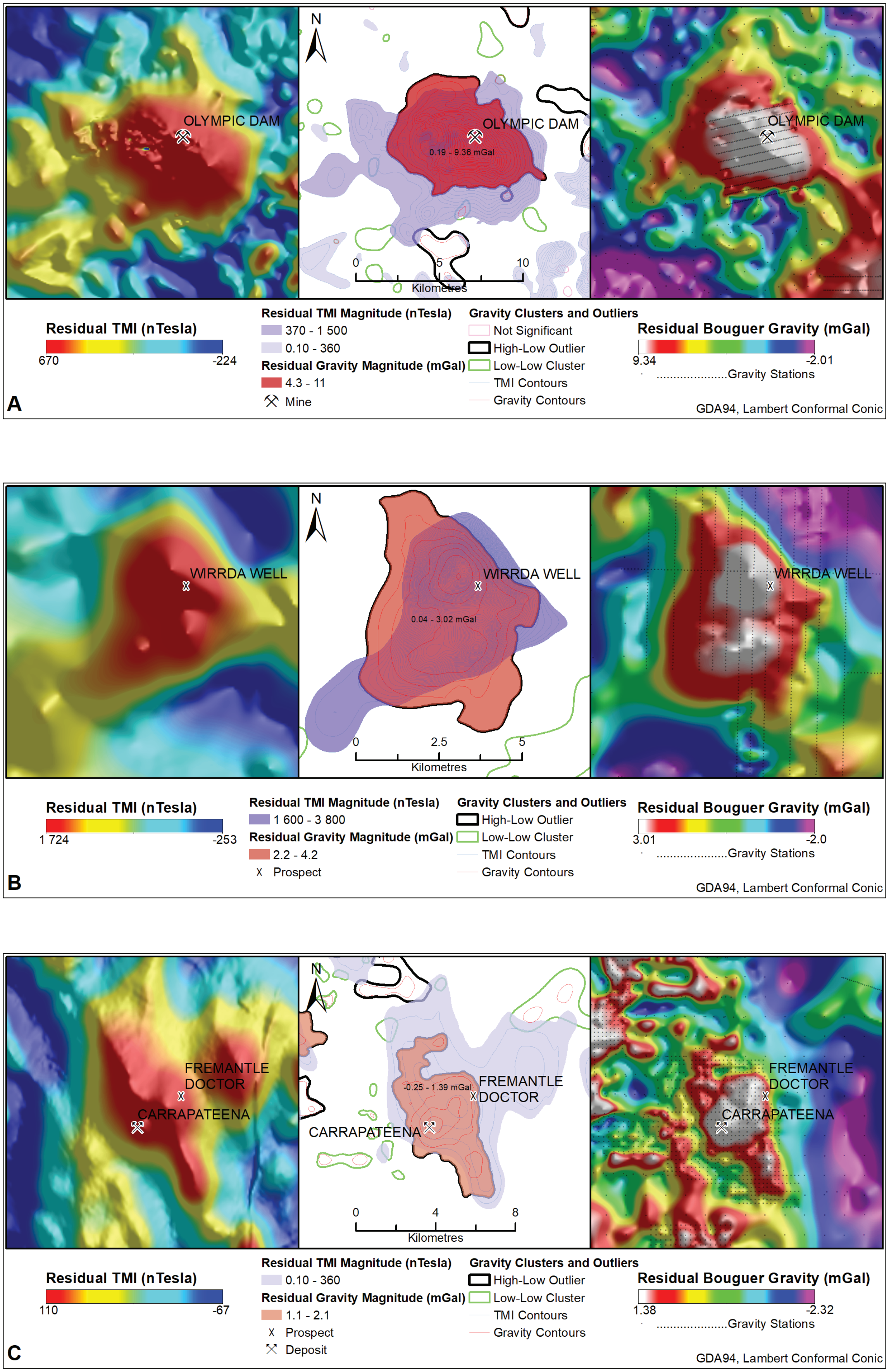
OLYMPIC DAM
N
0.19 - 9.36 mGal
0
5
10
Kilometres
Residual TMI (nTesla)
670
-224
Residual TMI Magnitude (nTesla)
370 - 1 500
0.10 - 360
Residual Gravity Magnitude (mGal)
4.3 - 11
Mine
Gravity Clusters and Outliers
Not Significant
High-Low Outlier
Low-Low Cluster
TMI Contours
Gravity Contours
Residual Bouguer Gravity (mGal)
9.34
-2.01
Gravity Stations
GDA94, Lambert Conformal Conic
A
WIRRDA WELL
0.04 - 3.02 mGal
0
2.5
5
Kilometres
Residual TMI (nTesla)
1 724
-253
Residual TMI Magnitude (nTesla)
1 600 - 3 800
Residual Gravity Magnitude (mGal)
2.2 - 4.2
Prospect
Gravity Clusters and Outliers
High-Low Outlier
Low-Low Cluster
TMI Contours
Gravity Contours
Residual Bouguer Gravity (mGal)
3.01
-2.0
Gravity Stations
GDA94, Lambert Conformal Conic
B
FREMANTLE DOCTOR
CARRAPATEENA
-0.25 - 1.39 mGal
0
4
8
Kilometres
Residual TMI (nTesla)
110
-67
Residual TMI Magnitude (nTesla)
0.10 - 360
Residual Gravity Magnitude (mGal)
1.1 - 2.1
Prospect
Deposit
Gravity Clusters and Outliers
High-Low Outlier
Low-Low Cluster
TMI Contours
Gravity Contours
Residual Bouguer Gravity (mGal)
1.38
-2.32
Gravity Stations
GDA94, Lambert Conformal Conic
C

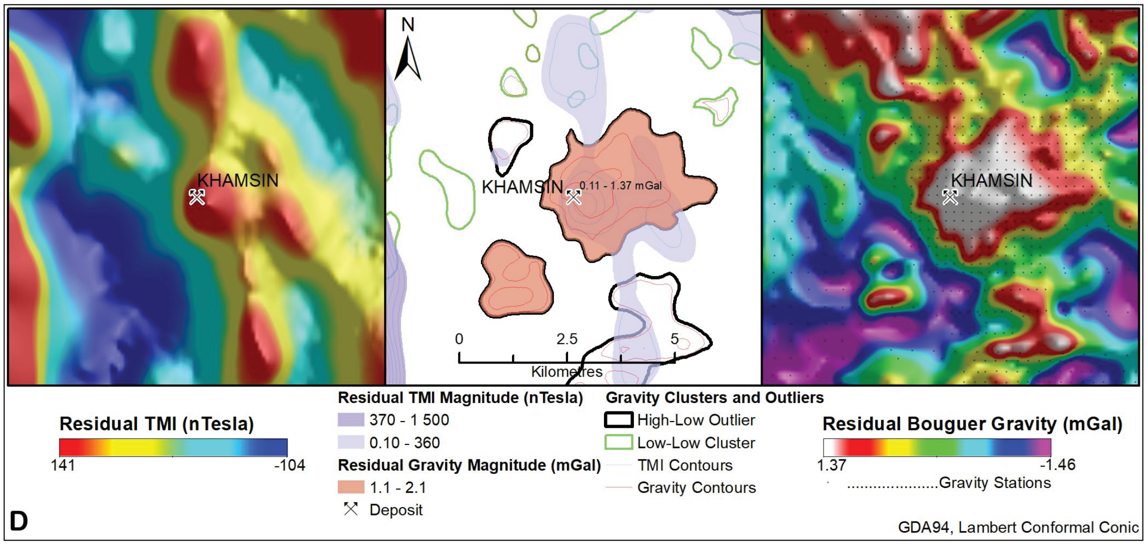


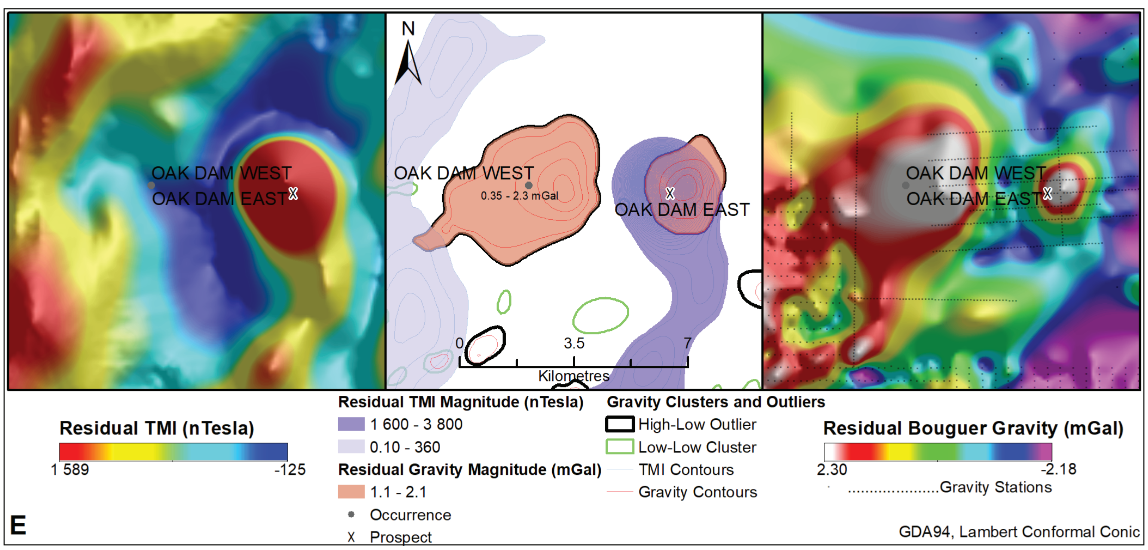


FIGURE 9. Gravity and magnetic signatures of IOCG deposits within the Gawler Craton. Residual TMI is shown at left; at right is the residual gravity with station locations; at the centre are the vectorized TMI and gravity anomalies with the range of the residual TMI magnitude features (nTesla) in purple and the residual gravity feature (mgal) shown in red. The bold outline of the gravity features shows the cluster type, black for High-Low outliers and green for Low-Low clusters. **A.** Olympic Dam IOCG deposit. **B.** Wirrda Well IOCG deposit. **C.** Carrapateena/Fremantle Doctor IOCG deposit. **D.** Khamsin IOCG deposit. **E.** Oak Dam East/Oak Dam West IOCG deposit.

The RTP of the TMI is an important transformation for interpretation because this Fast Fourier Transform (FFT) corrects the magnetization direction, repositioning features from a steeply inclined field to a vertical field (Foss et al., 2018). Assuming the direction of magnetization and the specified geomagnetic field direction are both correct, the RTP image is better suited for magnetic field interpretation than the TMI image (Foss et al., 2018). The variable RTP (VRTP) is used for RTP transformation performed on large areas because it accounts for lateral variations in the earth's geomagnetic field, reducing distortions in the resulting RTP image. For mapping geophysical characteristics of IOCG occurrences, the expression of the TMI and gravity features at the deposit scale are assumed to represent the distribution of ferromagnetic minerals within the IOCG system. Alternative explanations for similar geophysical signatures in the Gawler Craton include mafic units, iron formations and the development of skarn related to metamorphism and hydrothermal alteration.

Removing the regional signal from the gravity and TMI grids resulted in geometrically and geologically plausible residual anomalies (Fig. 9) that more clearly delineate the known IOCG deposits than the un-transformed grids.

The upward continuation method for producing the regional grid is one of a number of possible methods that will produce similar results. The decision to use the 1 000 m upward continuation was the result of testing a number of alternative upward continuation distances. The resulting range within the residual gravity grid was considerably reduced (by about 80%) by the subtraction of the upward continued image, while the same process applied to the TMI reduced the range by about 5%. These differences do not appear to have diminished the effectiveness of the method or results. For both the gravity and TMI, there are subtle features sharpened by the residual images. In some cases, this allows the differentiation between the response related to the IOCG deposit and other geological features (Fig. 9C). For example, the subtle perturbation in the residual TMI at the Carrapateena deposit is directly related to mineralization and is superimposed on a linear, northwest-southeast trending feature related to a suspected mafic intrusion.

*Geophysical Characteristics of Known IOCG Deposits*

Interesting features of known IOCG deposits are that the deposit location in all cases is proximal but not coincident with the peak of the gravity anomaly. The area returning the highest gravity signal commonly relates to the unmineralized hematitic core of the deposit. The corresponding TMI anomaly commonly has greater complexity than the coincident gravity feature with multiple TMI peaks within the bounds of the gravity feature (Olympic Dam, Carrapateena, Wirrda Well). As with the gravity anomalies, the deposit locations are typically adjacent to a magnetic peak. The magnitude of TMI features cannot be used as a measure of prospectivity in hematite-dominated deposits as the response varies as a function of the degree to which magnetite has been converted to hematite within the deposit.

*GIS Polygons as Representations of Geophysical Anomalies: Calibrating Results with Known Occurrences*

There are several advantages to generating polygons as representation of geophysical features, including the ability to filter and rank the data, perform overlay operations and generate spatial statistics. Taken as simple anomaly polygons, there are a very large number of such features across the Gawler Craton (>39 000 TMI and >10 000 gravity). Superimposing mineral deposits over these features shows a clear spatial correlation between IOCG deposits and occurrences, and anomalies (>90% of deposits within 1 000 m of an anomaly), but leaves thousands of anomalies of varying magnitudes that cannot all be related to IOCG mineralization. Eliminating TMI and gravity anomalies with a spacing of more than 1 000 m reduces the search space to ~20 000 TMI features and ~8 500 gravity features. Of these remaining gravity features, the search space can be reduced further by eliminating features below a certain magnitude threshold, which we assume to be too low to relate to an IOCG system. Limiting the search to 0.4 mGal anomalies, the exploration space was reduced to 798 gravity features with coincident TMI features within the Olympic Copper-Gold Province. The 0.4 mGal magnitude related to the statistically-derived gravity threshold. This is regarded as a useful way of identifying potential IOCG targets across the Gawler Craton. Where a similar workflow is followed, this method should be applicable to similar IOCG districts.

*Spatial Clustering of Gravity and TMI: Relationships to Regional Geology*

The emphasis on linking the distribution of IOCGs and the spatial clustering of gravity features in the Gawler Craton comes from the observed spatial relationship between the population of 104 Gawler Craton copper-gold deposits (displayed as white dots in Figure 3) and associated discrete gravity anomalies (spatial outliers). Although there is a clear spatial relationship, the way in which the gravity anomaly clusters are spatially distributed provides additional information that can be related to differing basement geology and deposit style. The largest grouping of spatial gravity outliers is in the eastern Gawler Craton (Figs. 6, 7). This group of gravity outliers forms the central (and currently most endowed) part of the Olympic Copper-Gold Province, where 23 out of the 28 basement-hosted copper-gold deposits are coincident with a mapped gravity anomaly that was classified as a spatial outlier. In this region, IOCG deposits are primarily hematite-dominant, and hosted in felsic intrusive rocks of the Donington and Hiltaba Suite (Flint, 1993; Ferris et al., 2002; Schwarz, 2003) or overlying low metamorphic grade metasedimentary rocks of the Wallaroo Group (Cowley et al., 2003), all of which have relatively low background magnetite content. In this region, hydrothermally derived iron oxides therefore form clear gravity outliers (high magnitude features surrounded by features with low values). Alternative explanations for gravity high outliers include mafic intrusive units and the development of skarn, both of which are known in the region and commonly occur in close proximity to IOCG deposits. Although it is difficult to distinguish these alternatives, particularly where thick basement-cover units can significantly generalize the margins of individual bodies, this style of analysis is meant as a method of identifying geophysical characteristics that are permissive of IOCG deposits, rather than a method that will only map IOCG deposits. Interestingly, high gravity and TMI outliers, common in the central Olympic Copper-Gold Province, also extend over the Gawler Range Volcanics, potentially extending the area of prospectivity. Historically, limited exploration has taken place for IOCG deposits in this region due to the prohibitive thickness of upper Gawler Range Volcanics (greater than 1 100 m and locally beyond 2 000 m). Although isolated mafic volcanic units within the volcanic pile provide an alternative source of gravity and magnetic features to IOCG deposits, the results from this study indicate that there are many features that warrant closer investigation.

In the northwestern end of the Olympic Copper-Gold Province, 14 of the 18 deposits and occurrences (including the Prominent Hill mine) are coincident with gravity anomalies; however, these are of the high-cluster type of gravity anomalies (i.e. a statistically significant cluster of high-magnitude features). The extent of the region identified by the cluster analysis of both gravity and magnetic data coincides with relatively shallow (<150 m), high metamorphic grade rocks of the Mount Woods Inlier, Coober Pedy ridge, and Mabel Creek ridge. In this region, basement rocks are generally magnetite-stable and include sources of gravity and magnetic anomalies other than IOCG deposits, such as iron formation and magnetite-bearing orthogneiss (Chalmers, 2007). Mineral occurrences in the region are magnetite-dominant but represent a spectrum of deposits, from those containing significant copper (e.g. Manxman A1) to those that are copper-poor and locally contain apatite (e.g. Cairn Hill; iron oxide-apatite style of deposit after Williams, 2010). Regardless, hydrothermal iron oxide is interpreted to have formed at higher temperatures and deeper in the crust than IOCG deposits of the central Olympic Copper-Gold Province (Clarke et al., 2014). Importantly, this contrast in deposit style and common occurrence of magnetite-rich iron formation is readily distinguishable from hematite-rich deposits of the central Olympic Copper-Gold Province based on the spatial distribution of gravity and magnetic features.

The southern-most part of the Olympic Copper-Gold Province, exposed on the Yorke Peninsula, is also dominated by gravity high clusters. Only 17 of the 58 copper-gold deposits are located over a gravity anomaly; however, 42 are in close proximity to gravity high-clusters, indicating some spatial association with high density sources. The remaining 16 deposits are associated with gravity features in the not-significant clustering class. Unlike the central eastern Gawler Craton, where many of the copper-gold occurrences relate to discrete, pipe-like magnetic and high gravity bodies, much of the metasomatic iron in the Moonta Domain is structurally controlled and located along shear zones. The spatial distribution of introduced iron is heavily influenced by prior, upper greenschist to amphibolite facies metamorphism and deformation (Conor et al., 2010). In addition, as in the northern Olympic Copper-Gold Province, iron formations in the region present an alternative source of geophysical features.

Gravity and magnetic high outliers and clustering is also evident in areas outside of the Olympic Copper-Gold Province (Fig. 6). In these instances, high gravity and TMI clusters coincide with geological terranes that are known to include significant magnetite-rich lithotypes and basaltic units (e.g. Wilgena Domain, Harris Greenstone Belt). Spatial clustering of gravity and magnetic features can therefore be used to define geological domains having a similar geophysical character, related to a shared tectonic history and basement geology. Since these factors may influence the style of mineralization, spatial clustering provides an additional means of regional exploration area selection.

## Conclusions

Mineral exploration relies upon accurate drill targeting, especially in terranes with significant barren cover. The application of potential field geophysical methods to characterize rock packages beneath barren cover is a critical element in any mineral exploration workflow. In this paper, we have shown that the conversion of residual TMI and gravity data to vector GIS layers assist the joint interpretation of complex TMI and gravity grids. High-magnitude spatial outliers of residual gravity delineate IOCG deposits within the Olympic Copper-Gold Province and suggest the existence of a significant number of unexplored or under-explored gravity anomalies of similar tenor to those that host IOCG deposits.

Based on analysis of the potential field data in this study, a gravity station coverage of 1 km or closer is sufficient to locate the peaks of gravity features related to IOCG deposits and is therefore necessary for regional scale targeting. For airborne magnetic data, 400 m line spacing or better is considered suitable for targeting IOCG deposits.

Spatial statistics defined a threshold of 0.4 mGals as a statistically significant magnitude threshold for residual gravity features associated with IOCG deposits and identified the central Olympic Copper-Gold Province as containing a distinct gravity response, with many spatial outliers of high-magnitude gravity features. The residual gravity threshold of 0.4 mGals should only be considered appropriate for this study as it is dependent on the population of anomalies in the study area and the method used to produce the residual dataset. However, the statistical approach explained in this contribution can be applied elsewhere, and used to define a local threshold.

The spatial clustering of gravity (and to some degree TMI) anomalies has helped define three sub-regions of the Olympic Copper-Gold Province whose geophysical character are explained by corresponding changes in the fundamental geology within the sub-regions. The main group of high-magnitude gravity outliers suggests that the style of high-density sources found in the central part of the province extends beyond the Olympic Domain, and includes large portions of the Gawler Range Volcanics. Exploration strategies for each of the three sub-provinces should be considered separately, to maximize the chance of success within each region.

This type of analysis and interpretation is an early step in identifying possible location of copper-gold mineralization. A thorough understanding of the specific style of IOCG system should be coupled with analyses such as this in order to identify appropriate relationships between potential deposits and magnetic and gravity data, leading to identification of plausible IOCG targets.

## Acknowledgments

All geophysical data used in this analysis are publically available and accessible via the Geological Survey of South Australia's South Australian Resources Information Geoserver (https://map.sarig.sa.gov.au/). This paper is published with permission of the Director, Geological Survey of South Australia. The authors would like to thank Dr. Anne McCafferty and Dr. Louise Corriveau for their valuable input and suggestions. Anthony Reid is thanked for his support and encouragement that led to this paper.

## References


Anselin, L., 1995, Local indicators of spatial association – LISA: Geographical Analysis, v. 27, p. 93-115.

Belperio, A., Flint, R., and Freeman, H., 2007, Prominent Hill: a hematite-dominated, iron oxide Cu-Au system: Economic Geology, v. 102, p. 1 499-1 510.

BHP, 2018a, BHP annual report, September 2018: Available at https://www.bhp.com/investor-centre/annual-report-2018.

BHP, 2018b, BHP copper exploration program update, 27 November 2018: Available at https://www.bhp.com/media-and-insights/news-releases/2018/11/bhp-copper-exploration-program-update.

Chalmers, N.C., 2007, Mount Woods Domain: Proterozoic metasediments and intrusives: Department State Development, Adelaide, Report Book 2007/20.

Clarke, J.M., Cook, N.J., Ciobanu, C.L., Reid, A.J., and Hill, P., 2014, Defining the style of mineralisation at the Cairn Hill magnetite-sulphide deposit; Mount Woods Inlier, Gawler Craton, South Australia: Gold14@Kalgoorlie, International Symposium, Kalgoorlie, Western Australia, 2014, Extended Abstracts, p. 19-20.

Conor, C., Raymond, O., Baker, T., Teale, G., Say, P., and Lowe, G., 2010, Alteration and mineralisation in the Moonta-Wallaroo copper-gold mining field region, Olympic Domain, South Australia, *in* Porter, T.M., ed., Hydrothermal iron oxide copper-gold & related deposits: a global perspective, v. 3: PGC Publishing, Adelaide, p. 147-170.

Cowley, W.M., Connor, C.H.H., and Zang, W., 2003, New and revised Proterozoic stratigraphic units on northern Yorke Peninsula: MESA Journal, v. 29, p. 46-58.

Davidson, G.J., Paterson, H., Meffre, S., and Berry, R.F., 2007, Characteristics and origin of the Oak Dam East breccia-hosted, iron oxide Cu-U-(Au) deposit: Olympic Dam region, Gawler Craton, South Australia: Economic Geology, v. 102, p. 1471-1498.

Department for Energy and Mining, 2019, MINDEP online: Department for Energy and Mining: Accessed 19 March 2019 at http://www.energymining.sa.gov.au/minerals/online_tools/online_databases_and_products/mindep_online

Esdale, D., Pridmore, D.F., Coggon, J., Muir, P., Williams, P., and Fritz, F., 2003, The Olympic Cu-U-Au-Ag-REE deposit, South Australia: a geophysical case study, *in* Dentith, M.C., ed., Geophysical signatures of South Australian mineral deposits: Centre for Global Metallogeny, University of Western Australia, Publication No. 31.

ESRI, 2018, Cluster and outlier analysis (Anselin Local Moran's I): Environmental Systems Research Institute (ESRI), ArcMap 10.6, available at http://desktop.arcgis.com/en/arcmap/latest/tools/spatial-statistics-toolbox/cluster-and-outlier-analysis-anselin-local-moran-s.htm.

Ferris, G.M., Schwarz, M.P., and Heithersay, P., 2002, The geological framework, distribution and controls of Fe-oxide and related alteration, and Cu-Au mineralisation in the Gawler Craton, South Australia. Part I: geological and tectonic framework, *in* Porter, T.M., ed., Hydrothermal iron oxide copper-gold and related deposits: a global perspective, v. 2: PGC Publishing, Adelaide, p. 9-31.

Flint, R.B., 1993, Hiltaba Suite, *in* Drexel, J.F., Preiss, W.V. and Parker, A.J., eds., The geology of South Australia, volume 1, the Precambrian: Geological Survey of South Australia, Bulletin 54, p. 127-131.

Foss, C.A., Gouthas, G., Wise, T., Katona, L.F., Hutchens, M.F., and Reed, G.D., 2018, Gawler Craton airborne geophysical survey region 2A, Murloocoppie – Enhanced geophysical imagery and magnetic source depth models: Department of the Premier and Cabinet, South Australia, Adelaide, Report Book 2018/00015.

Getis, A., and Ord, J.K., 1992, The analysis of spatial association by use of distance statistics: Geographical Analysis, v. 24, p. 189-206.

Gow, P.A., Wall, V.J., and Valenta, R.K., 1993, The regional geophysical response of the Stuart Shelf, South Australia: Exploration Geophysics, v. 24, p. 513-520.

Hand, M., Reid, A., and Jagodzinski, L., 2007, Tectonic framework and evolution of the Gawler Craton, South Australia: Economic Geology, v. 102, p. 1 377-1 395.

Hart, J., and Freeman, H., 2003, Geophysics of the Prominent Hill prospect, South Australia, *in* Dentith, M.C., ed., Geophysical signatures of South Australian mineral deposits: Australian Society of Exploration Geophysicists, Special Publication 12, p. 93-100.

Hayward, N., and Skirrow, R.G., 2010, Geodynamic setting and controls on iron oxide Au-Au (+/-U) ore in the Gawler Craton, South Australia, *in* Porter, T.M., ed., Hydrothermal iron oxide Cu-Au and related deposits: a global perspective, v. 3: PGC Publishing, Adelaide, p. 119-146.

Katona, L.F., Wise, T., and Reid, A., 2018, Vectorisation of residual gravity and TMI data in the northern Gawler Craton: implications for exploration targeting and GIS analysis: Department for Energy and Mining, South Australia, Adelaide, Report Book 2016/00037.

McCafferty, A.E., Phillips, J.D., and Driscoll, R.L., 2016, Magnetic and gravity gradiometry framework for Mesoproterozoic iron oxide-apatite and iron oxide-copper-gold deposits, Southeast Missouri, *in* Slack, J., Corriveau, L. and Hitzman, M., eds., Proterozoic iron oxide-apatite (± REE) and iron oxide-copper-gold and affiliated deposits of Southeast Missouri, USA, and the Great Bear magmatic zone, Northwest Territories, Canada: Economic Geology, v. 111, p. 1859-1882.

OZ Minerals, 2016, Annual and sustainability report, 2016, p. 117: Available at https://www.ozminerals.com/uploads/media/170420_OZMinerals_AnnualSustainabilityReport.pdf.

OZ Minerals, 2017, Annual and sustainability report, February 2018: Available at https://www.ozminerals.com/uploads/media/OZMinerals_2017_Annual_and_ Sustainability_Report.pdf.

OZ Minerals, 2019, Carrapateena 2019 mineral resources and ore reserves statement and explanatory notes as at 30 June 2019: Available at https://www.ozminerals.com/uploads/media/OZL_Carrapateena_MROR.pdf.

Porter, T.M., 2010, The Carrapateena iron oxide copper gold deposit, Gawler Craton, South Australia: a review, *in* Porter, T.M., ed., Hydrothermal iron oxide copper gold and related deposits: a global perspective, v. 3: PGC Publishing, Adelaide, p. 191-200.

Reid, A.J., and Fabris, A., 2015, Influence of pre-existing low metamorphic grade sedimentary successions on the distribution of copper-gold mineralisation in the Olympic Cu-Au Province, Gawler Craton: Economic Geology, v. 110, p. 2 147-2 157.

Schwarz, M.P., 2003, LINCOLN, South Australia, 1:250 000 geological series explanatory notes, sheet SI53-11: Department of Primary Industries and Resources South Australia, Adelaide.

Skirrow, R.G., 2022, Hematite-group IOCG±U ore systems: an update on tectonic settings, hydrothermal characteristics, and Cu-Au and U mineralizing processes, *in* Corriveau, L., Potter, E.G. and Mumin, A.H., eds., Mineral systems with iron oxide copper-gold (IOCG) and affiliated deposits: Geological Association of Canada, Special Paper 52, p. 27-51.

Skirrow, R.G., Bastrakov, E., Davidson, G., Raymond, O.L., and Heithersay, P., 2002, The geological framework, distribution and controls of Fe-oxide and related alteration, and Cu-Au mineralisation in the Gawler Craton, South Australia. Part II: alteration and mineralisation, *in* Porter, T.M., ed., Hydrothermal iron oxide copper-gold and related deposits: a global perspective, v. 2: PGC Publishing, Adelaide, p. 33-47.

Skirrow, R.G., Bastrakov, E.N., Barovich, K., Fraser, G.L., Creaser, R.A., Fanning, C.M., Raymond, O.L., and Davidson, G.J., 2007, Timing of iron oxide Cu-Au-(U) hydrothermal activity and Nd isotope constraints on metal sources in the Gawler Craton, South Australia: Economic Geology, v. 102, p. 1441-1470.

van der Wielen, S.E., Fabris, A.F., Halley, S.H., Keeling, J.K., Mauger, A.J., Gordon, G.A., Keeping, T., Giles, D., and Hill, S.M., 2013, An exploration strategy for IOCG mineral systems under deep cover: MESA Journal, v. 71, p. 18-30.

Williams, P.J., 2010, Classifying IOCG deposits, *in* Corriveau, L. and Mumin, A.H., eds., Exploring for iron oxide copper-gold deposits: Canada and global analogues: Geological Association of Canada, Short Course Notes, No 20, p. 13-22.

# Use of Breccias in IOCG Exploration: An Updated Review

**Michel Jébrak**
*Université du Québec à Montréal, Montréal, QC; jebrak.michel@uqam.ca*

*Recommended citation: Jébrak, M., 2022, Use of breccias in IOCG exploration: an updated review, in Corriveau, L., Potter, E.G., and Mumin, A.H., eds., Mineral systems with iron oxide copper-gold (IOCG) and affiliated deposits: Geological Association of Canada, Special Paper 52, p. 315-324.*

## Abstract

Breccias are key elements of polymetallic iron oxide Cu-Au ± Co-Ag-Bi-U (IOCG) deposits worldwide. However, their use in exploration or production mapping has been limited due to lack of a systematic method of categorizing and interpreting their physical and compositional parameters. Recent studies on breccias in magmatic-hydrothermal systems show that genetic information may be determined from quantitative geometric parameters (shape and spatial organization of fragments) and composition. Breccia maturity can be determined from several parameters that can be used to help target mineralization. In IOCG deposits, breccias occur in all geological environments and at depths ranging from plutonic sources to surface. Corroded breccia fragments and chaotic particle size distributions are more abundant in IOCGs than in most other types of ore deposits, due to the extreme dynamics and solution processes at work in this class of deposits.

## Résumé

Les brèches sont des éléments essentiels des gîtes polymétalliques à oxydes de fer à Cu-Au ± Co-Ag-Bi-U (IOCG). Leur utilisation en exploration régionale et pour la cartographie au cours de la production minière demeure cependant limitée en raison de l'absence d'une méthode systématique de catégorisation et d'interprétation de leurs paramètres physiques et compositionnels. Les études récentes sur les brèches dans les systèmes magmatiques-hydrothermaux démontrent qu'il est possible d'obtenir de multiples informations génétiques à partir d'analyses géométriques détaillées sur la forme et l'organisation spatiale des fragments de même qu'à partir de la composition. La maturité d'une brèche peut se mesurer selon différents paramètres et peut servir de vecteur vers la minéralisation. Dans les gîtes IOCG, les brèches apparaissent dans tous les environnements et à diverses profondeurs allant des sources plutoniques à la surface. Des fragments de brèches corrodés et une granulométrie chaotique sont plus courants que dans d'autres types de gisements, en raison d'une dynamique de bréchification extrême et de l'importance des processus de dissolution dans ces gisements.

## Introduction

Iron-oxide copper-gold (± Co-Ag-Bi-U) deposits (IOCG) are recognized as an increasingly important type of ore globally (Williams, 2010). These copper-gold deposits are characterized by numerous variations in their geological setting and composition and by their abundance of iron oxides (magnetite, hematite). Iron, uranium, cobalt, bismuth, rare-earths, barium, fluorine constitute additional possible economic elements. The emplacement of the ore is associated with various styles of permeability, such as veins, breccias or replacements, controlled by chemical, structural and plutonic factors. Alteration is ubiquitous, and is mostly alkali- and or iron-rich, with local calcium, silica, phosphate, $CO_2$, Cl, F and other metals (Hitzman et al., 1992; Corriveau et al., 2010, 2016, 2022a, b; Mumin et al., 2010; Richards and Mumin, 2013a).

IOCGs constitute a rather diverse class of ore deposits, sharing mineralogical and geochemical assemblages rather than a common lithological package or a specific geodynamic context (Hitzman et al., 1992; Corriveau et al., 2022a, b). Early descriptions of this association may be found in the 'Eisen-Baryt-Formation' ('eba') paragenesis described in Central Europe (Bernard, 1980). However, it was only after the discovery of the Olympic Dam deposit in South Australia that the necessity to distinguish this class of ore deposit grew (Hitzman et al., 1992). Several other significant deposits were subsequently discovered, such as Salobo (Brazil, in 1977), Starra (Australia, in 1980), La Candelaria (Chile, in 1987), Osborne (Australia, in 1988), Ernest Henry (Australia, in 1991) and Alemao (Brazil, in 1996; Ronze et al., 2000). Several apatite-rich deposits were also linked to the group, including the Kiruna and Bayan Obo deposits. While IOCG deposits represent less than 5% of the copper and 1% of the gold produced worldwide, they nevertheless play a major economic role. For example, Olympic Dam is the world's largest single uranium source, Bayan Obo is the world's largest REE producer, and Kiruna is the largest underground iron mine in Europe.

Breccias are very abundant in IOCG deposits (sensu lato), and host most of the mineralization in most deposits such as Olympic Dam, Prominent Hill and Ernest Henry (Australia), and La Candelaria (Chile); many examples are presented in this volume (Corriveau et al., 2022a, b; Skirrow, 2022; Williams, 2022) and for the Kwyjibo deposit in Québec, in Clark et al. (2010) and Prominent Hill deposit in Australia in Schlegel and Heinrich (2015). Such breccias have been considered one of the key elements of this family of deposits (Hitzman et al., 1992). Breccia formation has been related to numerous processes, from physical (explosion, comminution) to chemical (dissolution). Several hypotheses have been proposed to explain their formation from explosive alkaline magmatism to faulting to dissolution by surface waters (Hitzman et al., 1992; Barton and Johnson, 1996; Williams, 1999; Mark et al., 2006). However, most of these breccias display complex relationships to the ore, due to multiple episodes of fragmentation and alteration. Consistent recognition and mapping of breccias in a large orebody is extremely challenging, particularly where several geologists are involved and where the variability of facies at all scales leads to shortcuts in their description.

This paper presents a semi-quantitative methodology for the description and the interpretation of breccias in IOCG deposits. The approach has been developed for field geologists, either in exploration or production, and does not require any specific instrumentation.

*Previous Work*

A variety of approaches has been used in the classification of breccias, ranging from purely descriptive to genetic, and based on a wide variety of criteria. Sibson (1986) reviewed the structural brecciation processes in fault zones and proposed a classification for the definition of fault rocks using textural features (e.g. roundness), internal clast deformation, clast size distribution, and clast and matrix composition.

Sillitoe (1985) used a practical classification for breccias in plutonic and hydrothermal systems within magmatic-arc environments based on the abundance and petrographic composition of the matrix or cement, the shape of the breccia elements, and the overall organization of the brecciated units. Laznicka (1988) undertook a thorough review of breccia structures and associated rocks. He examined the wide range of settings for breccias in different geological environments and proposed a fully genetic classification and a descriptive approach.

Taylor and Pollard (1993) and Taylor (2009a, b) developed a field approach focusing on intrusive and extrusive breccias, beautifully illustrated by photographs showing specific characteristics such as discrete pressurized slurry veins, onion skin textures (probably hypogene exfoliation), decompressive shock textures, sheeted fractures, shingle texture, and collapse.

Jébrak (1997) used a quantitative approach similar to the one used in sedimentology. Although it was developed for hydrothermal breccias, it can be used for different styles of fragmentation processes. Five key physical parameters were recognized and should, with the varied alteration imprints, completely describe a breccia (Fig. 1). They include particle size distribution, fragment shape, dilation ratio, fragment fabric and matrix. Fragmentation may occur in response to either physical constraints or to chemical disequilibrium. The same approach was used by Clark et al. (2006) for understanding the formation of magmatic-hydrothermal breccias in the Curnamona Province (eastern South Australia). Mineralogy, fractal analysis of clast shape, and clast size distribution analysis were used to distinguish two styles of breccias and to indicate whether fluid pressure fluctuations played a significant role in the initiation of the brecciation process. Billi and Storti (2004) showed the fractal distribution of the fragments in a fault zone, whereas Storti et al. (2007) studied in great detail the shape of the fragments in faults within limestone and detailed the mechanisms related to the interactions between clasts.

Loucks (1999) suggested a classification for cave breccias and sediment fills. Loucks et al. (2004) demonstrated a means to analyse paleocaverns in limestone in terms of paleocave-facies classification, from disturbed strata facies to fine and coarse chaotic breccias. The same approach was transferred to the Dent fault, England, by Woodcock et al. (2007) where chaotic breccias are related to incremental void formation in a reverse-oblique fault. Eliassen and Talbot (2005) recognized two main styles of breccia in sedimentary evaporitic reservoirs: 1) horizontal stratabound, and 2) thick, crosscutting breccias. Some of the facies encountered show strong similarities with breccias in IOCG deposits.

*Descriptive Approach*

The author advocates a multi-faceted, descriptive approach for the practical applied study and documentation of brecciated rocks. Three variables are proposed: 1) composition of the clasts and of the matrix, 2) shape of the clasts, and 3) spatial organization of the clasts. From an initial rigorous description of a breccia, different styles of brecciation can be defined based on the dominant process and its intensity, allowing maturation characterization of the studied breccia.

*Composition of Clasts and Matrix*

The nature of clasts and matrix is the first key element of a description of brecciated rocks. A breccia may be monomict or polymict, with different degrees of heterogeneity. Monomict breccias can be in situ or transported (Fig. 2A). Polymict breccias (e.g. Fig. 2B) usually indicate some amount of transport

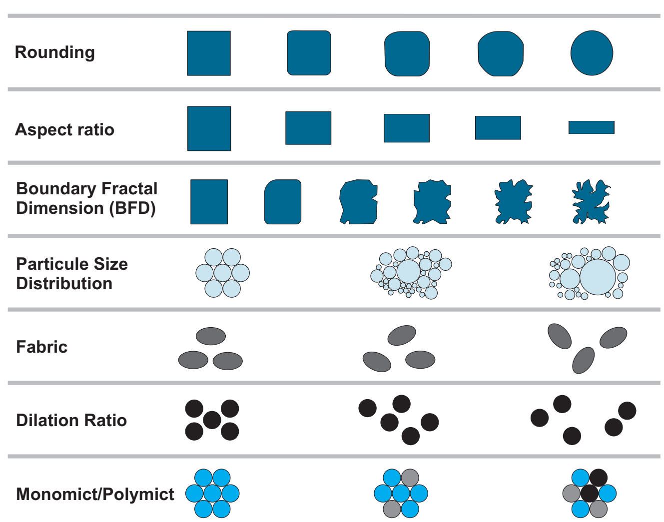


**Figure 1.** Graphical evolution of six geometric parameters is needed for an efficient description of brecciated rocks; the distinction between monomict and polymict breccias is also essential and needs to take into account selective alteration of clasts when defining the polymictic character of breccias (Corriveau et al., 2022a, b).

of the clasts, either up- or downward or lateral. However, the distance of transport is usually difficult to assess, particularly in areas with significant variability in the host rocks. Transport of several hundred vertical metres has been documented in some fault and breccia-pipe systems.

Breccia matrix can be crushed, hydrothermal (cement), or magmatic. In the case of a crushed matrix, it can be difficult to distinguish breccia clasts from the matrix because of the fractal character and the similarities of the fragments.

*Shape of Clasts*

The shape of clasts in a breccia may be defined using aspect ratio (length vs. width), roundness, and complexity. Aspect ratios can vary from equidimensional to very elongate (see for example Fig. 2C, D).

Roundness (or sphericity) is related to the general shape of the fragments whereas complexity describes the detailed structure of the shape. Although there is a mathematical continuity between these two shape parameters, a gap in scale

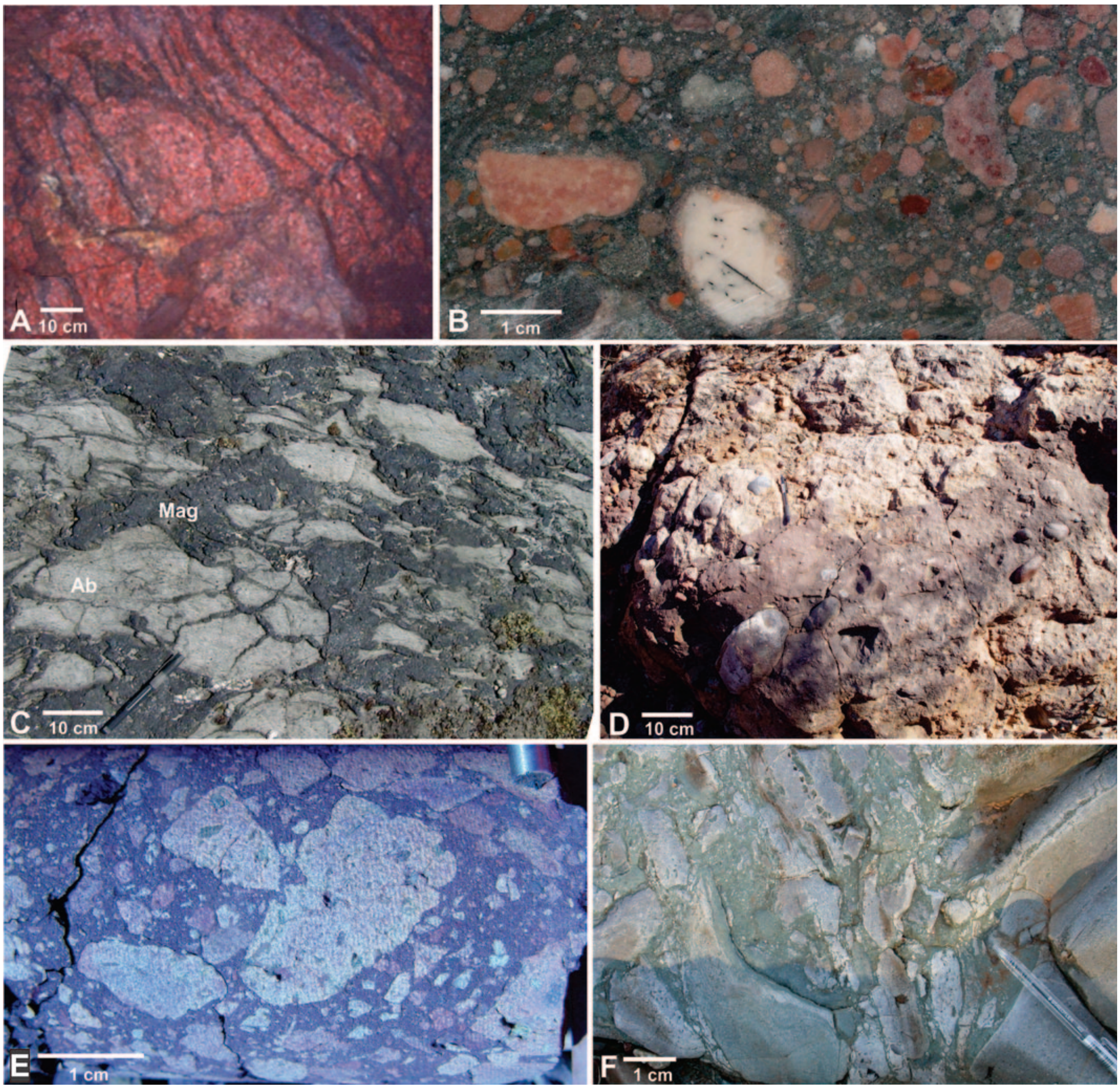


**Figure 2.** Compositional variations: **A**. Monomict breccia, Olympic Dam (South Australia). **B.** Polymict breccia, Olympic Dam (South Australia). Roundness variations: **C**. Low roundness, Kwyjibo (Québec). **D**. High roundness, pebble dyke, Mt Gee (South Australia). Complexity variations: **E.** Lobate fragment, Olympic Dam (South Australia), core. **F.** Fragments without corrosion, straight contour, Roxmere (Australia). All photographs from M. Jébrak, except F (courtesy of M. Gauthier).

may occur, resulting in a bi-fractal distribution (Orford and Whalley, 1983; Jébrak, 1997). It is practical for field applications to describe the overall shape (roundness) of a clast and the detail of its boundary (complexity) separately.

Roundness can be either of mechanical or chemical origin. In the former, it is related to abrasion processes such as milling. Pebble dykes are exceptional examples of this process (Fig. 2D). Chemical dissolution processes are recognized by the formation of indentations, lobes and cupules on the clast surface (Fig. 2E) that contrast with the sharp and straight clast contours in Figure 2F. Experiments show that such dissolution may take several tens to thousands of years to occur; except in pseudotachylite where round clasts indicate flash frictional melting (Lin, 1999; Ganor et al., 2005).

Complexity is almost completely related to solution processes affecting the surface of the fragments, although some granular rocks have rough original surfaces. A clast's complexity can be computed by several methods, such as Fourrier Transform (FFT) or fractal analysis (Fig. 3). The boundary fractal dimension is a relatively easy parameter to measure and it evaluates the complexity of the outline. The Euclidean Distance Mapping method (Bérubé and Jébrak, 1999) is a robust method whereby ribbons of increasing thickness are computed from the particle outline. A high fractal dimension value indicates a high complexity related to dissolution where a kinetic regime is dominant (Sahimi and Tsotsis, 1987). Such kinetic regimes are characterized by a consumption rate that is limited only by the chemical reaction rate. The concentration of reactants outside clasts are the same everywhere and the external surface of clasts are totally exposed to the reactants. This regime leads to a progressive increase in the complexity of the external surface. In contrast, a diffusion-limited regime is governed by the diffusion rate of the reactants; corners provide greater exposure relative to the bulk internal mass. This regime is therefore surface dependant and may lead to rounding or smoothing of the external surface (Jébrak, 1997; Lalonde et al., 2010).

*Spatial Organization of Clasts*

The spatial organization of clasts in a breccia can be described by three parameters: dilation ratio, particle size distribution (PSD), and fabric.

Dilation ratio corresponds to the volumetric percentage of the matrix, giving an approximation of the porosity at the time of formation. A low dilation-ratio corresponds to a 'clast-supported' model whereas a high dilation-ration is equivalent to the 'matrix-supported' model (Fig. 4A, B). Dilation ratio is the more useful of the three spatial organization parameters for distinctions between crackle breccia, mosaic breccia and chaotic breccia (Mort and Woodcock, 2008). The breccia class is strongly related to the rotation of the clasts: crackle breccia involves less than 10° average rotation, mosaic breccia, 10-20°, and chaotic breccia more than 20° rotation. Mort and Woodcook (2008) provided comparison charts for semi-quantitative classification of fault breccias.

Particle size distribution (PSD) varies from normal to log-normal/fractal distribution (Jébrak, 1997). It can be summarized by another fractal dimension, Ds, that represents the slope of the cumulative particle size distribution in a log-log diagram, or more intuitively the ratio between small particles and large fragments. High Ds values correspond to breccias with large clast size distributions such as volcanic breccias, whereas low Ds values occur where clasts have roughly the same size. Figure 4C and 4D show two end members with fractal and almost isometric distribution in IOCG deposits. Fabric describes the orientation(s) of breccia clasts. A single orientation corresponds to a low fabric value, whereas randomly-oriented clasts are assigned a high fabric value (Fig. 4E, F).

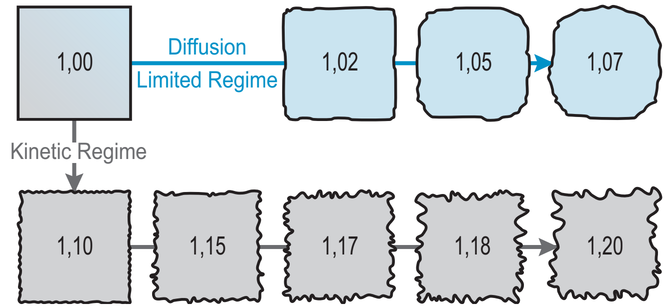


**FIGURE 3.** Two types of evolution during chemical corrosion of a particle. Diffusion Limited Regime increases rounding and indicates a slow process. Kinetic regime increases complexity and indicates a strong chemical disequilibrium. Numbers indicate the value of the Boundary Fractal Dimension, computed by the method of Bérubé and Jébrak (1999).

*Brecciation Maturity*

During breccia formation, clasts evolve in such a way that their shapes reflect the intensity of the brecciation processes, physical and/or chemical. Such maturity of breccia is an important character to determine because mineralization is usually associated with the most evolved part of a breccia system. Even where a sequence of formation processes may be proposed (e.g. Fig. 5), there is no general consensus for the best parameters to observe for targeting ore. Ore formation depends on the nature of the processes involved in breccia formation, and many other physical and chemical parameters.

In the Athabasca sandstone, ball zones are hydrothermal breccias developed in sandstones some tens of metres from some unconformity-type uranium ore bodies. They are composed of altered sandstone fragments wrapped in red, green, yellow and/or white massive clay (illite), locally displaying flow texture. Their maturity, as characterized by the matrix percentage, increases toward the unconformity and at fault intersections (Lorrilleux et al., 2003). They formed during peak diagenesis at temperatures between 240 and 280°C.

In a fault zone, the evolution of a breccia system can be followed using particle size distribution. Billi and Storti (2004) studied carbonate cataclastic rocks in detail from the Mattinata Fault, Southern Apennines, Italy. They showed that the PSD follows a fractal law with fractal dimensions (D) clustering around a value of f2.5. Low D-values characterize immature cataclastic breccias. Intermediate D-values are typical of the

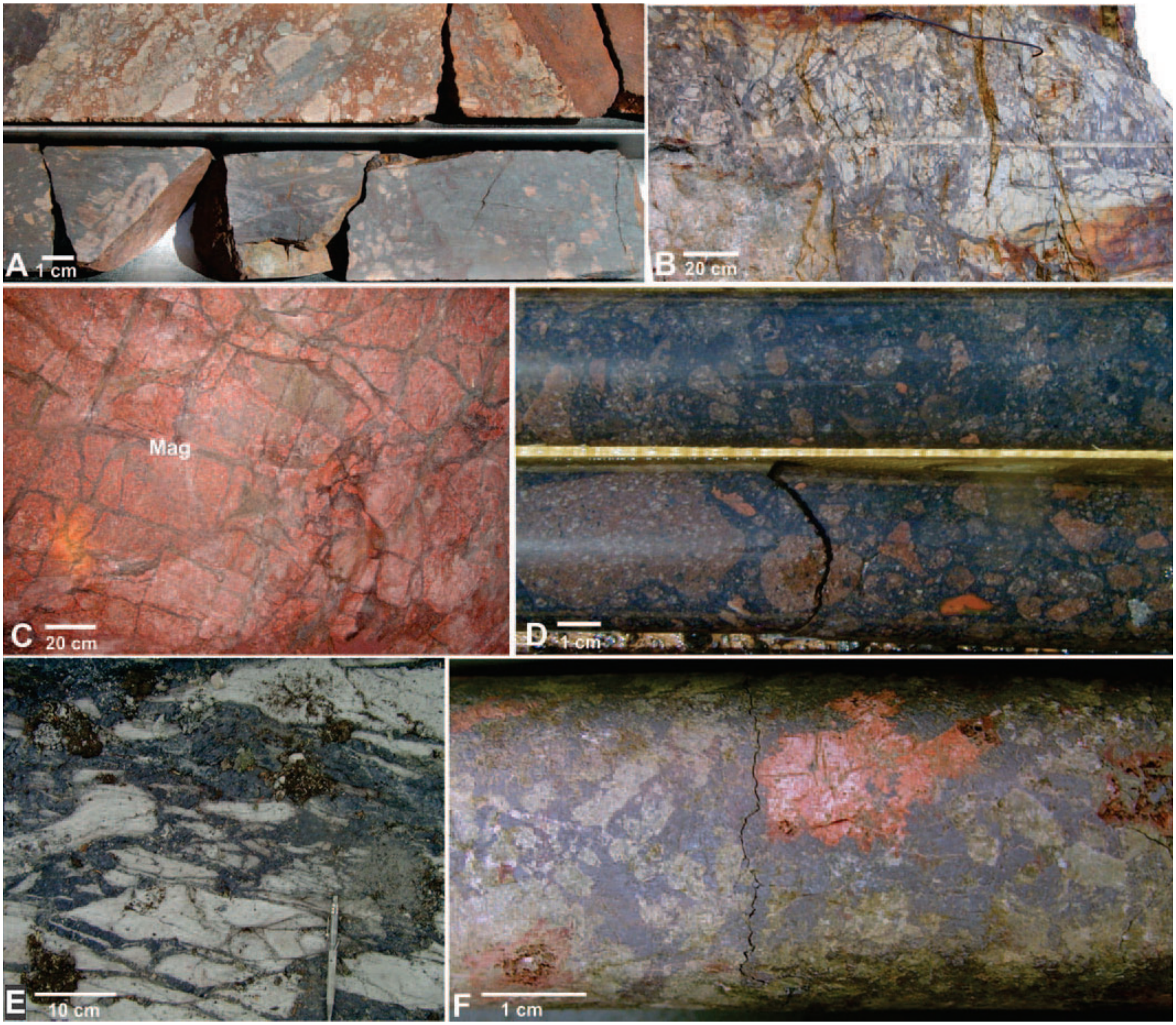


**Figure 4.** Dilation variations: **A**. High dilation: Prominent Hill (South Australia), core. **B.** Low dilation: Mary Kathleen (Australia). Particle Size Distribution variations: **C.** Fragments of similar size, Olympic Dam (South Australia). **D**. Fractal distribution of fragments, Kourou Diako, KKKI, Faleme (Senegal), core. Fabric variations: **E.** Orientated fragments, Kwyjibo (Québec). **F.** Random orientation, Murdie Well (South Australia), core. All photographs from M. Jébrak, except B (courtesy of M. Gauthier).

bulk fault core. High D-values pertain to gouge in shear bands where cataclastic rocks of the fault core have been brecciated again. The development of particle size distributions with D>2.6–2.7 in shear bands occurred via a preferential relative increase of fine particles rather than selective decrease of coarse particles. This results from intense comminution enhanced by the rolling of coarse particles whose consequent smoothing produced a large number of fine particles.

Mort and Woodcock (2008) used a geometric classification of fault breccia in the Dent Fault, northwest England. They demonstrated that maturity can be quantified by clast rounding correlated with surface roughness. However, PSD shows no correlation with the breccia classes.

## Breccia Processes

Breccia genesis in magmatic-hydrothermal systems may be related to numerous processes (Fig. 6). In order to have a full analysis of the processes of breccia formation, the stage of propagation and mobility should be distinguished (Fig. 5). Propagation is a pure fragmentation process controlling the primary PSD, fabric and composition, and overall aspect ratio of the clasts. Mobility indicates the level of maturity, controls the secondary PSD (classification), fabric and heterogeneity of the fragments. It defines also the detailed shape of the clast (roundness, complexity).

During the propagation stage, initial PSD is a function of the energy of fragmentation that can be computed from the

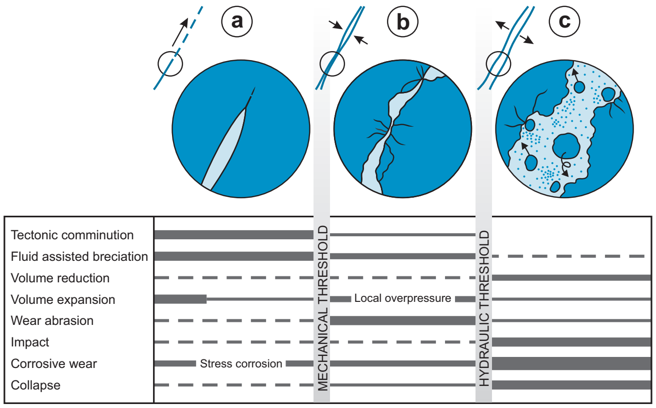


**FIGURE 5.** Maturity in a breccia system and evolution of fragmented rocks. The three stages of the fragmentation process, with the different styles of associated breccia (from Jébrak, 1997): (a) represents the initiation of the fragmentation, with mechanical continuity; (b) represents the stage of mechanical discontinuity and hydraulic continuity (propagation stage); (c) represents both mechanical and hydraulic discontinuities (mobility stage). Bars represent the relative frequency of the process.

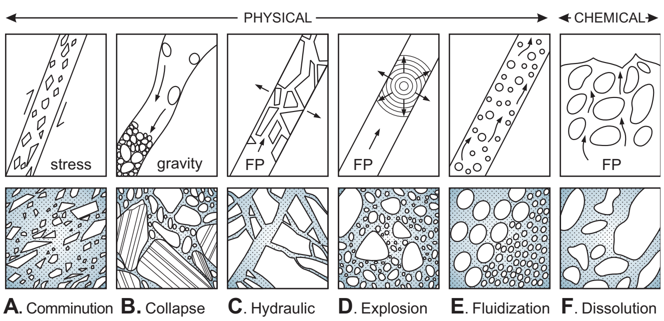


**FIGURE 6.** Main processes involved in breccia formation. All have been observed in IOCG deposits. FP = Fluid pressure

amount of newly created surface. Four processes are distinguished:

1) Very low energy processes: Thermo-elastic decompression or cooling retraction, as observed in surficial environment (mud cracks, columnar basalts, some gels in epithermal environments). In such slow processes, homogeneous nucleation follows a Delaunay tessellation (Courrioux et al., 2001). The typical values of geometric parameters are summarized in Table 1;
2) Low energy processes: Hydraulic brecciation related to an increase of fluid pressure, or a decrease of the effective pressure in a low permeability environment. Such breccia will be preferentially developed under a sealed cap rock such as impermeable shale or a siliceous or silicified layer (Li et al., 2002). Hydraulic breccias are frequent in transtensional environments due to rapid pressure variations;
3) Medium energy processes: Stress-related rupture (Andersonian stress), which generates fragments that are angular and often elongated;
4) High energy process: Explosion breccias (Herzian stress) that could be produced by cratering (Buhl et al., 2013), magmatic, phreato-magmatic or phreatic explosions (Bertelli and Baker, 2010).

**TABLE 1.** Relation between the processes involved in the propagation stage of breccia formation and geometric parameters.

| Parameters | Decompression | Hydraulic | Tectonic | Explosion |
|---|---|---|---|---|
| Dilation | High | High | Low | High |
| Fabric | - | - | Medium | Low |
| PSD | Non-fractal | Normal | Fractal High | Fractal Low |
| Aspect ratio | variable | - | Medium | Low |
| Complexity | Low | - | - | Low |

During the mobility stage (Table 2), four processes may occur, including solid- or fluid-dominated processes:

1) Grinding and milling in the fault, with transport of small particles more limited than could occur in a polymict breccia. In this situation, particle abrasion increases the sphericity values (Mair and Abe, 2011; Storti et al., 2007). Extreme milling and tumbling may result in the formation of pebble-dykes and breccia pipes;
2) Fluidization, or liquefaction, results in the conversion of the granular fault from a static solid-like state to a dynamic fluid-like state. It is related to acoustic energy released during rupture (Melosh, 1996) or/and dilation of close-packed particulate material as fault zones widen during slip (Monzawa and Otsuki, 2003). It could be turbulent or linear and could produce grain size sorting. It has been described in IOCG deposits (Oliver et al., 2006), kimberlites (Walters et al., 2006), breccia pipes (Davies et al., 2008), and Columbian emerald deposits (Branquet et al., 1999);
3) Collapse is frequent in normal faults. It corresponds to a sudden pressure drop in the fault zone. This has been mainly observed in sedimentary environments (Loucks, 1999; Mort and Woodcock, 2008), but may also occur at the top of intrusions (Ross et al., 2002) and in orogenic gold deposits. It is also a common component of volcanoclastic rocks in kimberlites (Barnett, 2003);
4) Dissolution may be simultaneous with both grinding and collapse and contribute to the mobility stage. It could occur in any environment, including carbonate and silicate rocks. In IOCG deposits, such processes are frequently observed

**TABLE 2.** Relation between the processes involved in the mobility stage of breccia formation and geometric parameters.

| Parameters | Grinding Milling | Collapse | Fluidization | Dissolution |
|---|---|---|---|---|
| Dilation | Low | Variable | Low | Variable |
| Fabric | None | None (except for slate) | None to high | None |
| PSD | Increase fractal dimension | Locally | Fractal | |
| Aspect ratio | Decrease | - | - | Decrease |
| Complexity | Decrease | Decrease | Decrease | Increase |

because of the high dissolution capacity of associated fluorine-rich, among other types, hydrothermal solutions (Hecht and Cuney, 2000; Landtwing et al., 2005; Le Carlier de Veslud et al., 2009; Ehrig et al., 2012).

## From Field to Laboratory

Field mapping is an absolute requisite for any breccia study, and therefore most of the steps for breccia identification should be applied in the field. Mapping of breccias remains difficult because of the variability of facies, the numerous styles of brecciation, and the multiplicity of classifications.

In the field, the following steps should be followed:

1) Look for major evolution and gradients in the eight geometric parameters described above and in the composition of fragments and matrix;
2) Search for less evolved breccia in order to define the end members, which usually means mapping beyond the main zone of mineralization;
3) Organize observations by giving explicit names to the different styles of breccias, connecting geometric and compositional observations;
4) Search for the limit of breccia units and define the overall organization of the breccia system, as numerous hydrothermal systems and IOCG deposits display several generations of breccias.
4) Determine relative chronology, determined by breccia in breccia and crosscutting relationships;
5) Document observations with samples and photographs.

Back in the lab, it may be necessary to prepare polished slabs and thin sections to better observe the sample textures, composition of the cement, the nature of the dissolution processes, and the relationship between ore deposition and breccia formation.

More detailed work can be performed using semi-quantitative or quantitative approaches. Geoscientists have been trying for a long time to develop automatic recognition of breccias, including Fourier transform analysis, computation of fractal dimensions, fabric analysis, etc. (Bérubé and Jébrak, 1999; Heilbronner and Keulen, 2006; Storti et al., 2007). The success of these approaches has been limited to date because of difficulty distinguishing the fragments and complexities of the matrix.

From an evaluation of the processes occurring during the propagation and mobility stages in a fault, it is possible to develop a diagnostic table where typical vein-, karst- and pipe-environments could be recognized (Fig. 7).

## Application to IOCG Deposits

The IOCG clan of deposits includes a wide range of affiliated deposits (Williams, 2010; this volume). One of the main characteristics of IOCG deposits is their strong relation to high permeability domains of the crust, illustrated by the abundance of faults and breccias. IOCG deposits may occur at different levels of the crust, in different environments, and are associated with different styles of brecciation, including:

1) Directly in association with plutons (Kiruna, Aitik) where breccias are characterized by hydraulic fracturing, and occasionally by explosive processes;
2) Iron-skarn and other iron-rich metasomatic breccias (Faleme, Candelaria, Pea Ridge) that show evidence of polyphase emplacement, including an early, inner magnetite and potassium-calcium assemblage followed by an outer hematite and sodic assemblage. These metasomatic breccias are largely chemical pseudobreccias;
3) Breccias in stratabound style deposits (Tennant Creek, Bayan Obo, Kwyjibo) that are characterized by hydraulic and dissolution-collapse processes;
4) Both structural and chemical breccias that are associated with vein systems (Ernest Henry, Wallaroo, Andes); and
5) Epithermal deposit (Tapajos, Mt. Painter, Olympic Dam, Great Bear Magmatic Zone, Wernecke, or Pea Ridge in southeast Missouri) breccia pipes and veins. Pipes can be subvolcanic, phreatomagmatic or hydrothermal, and associated breccias are usually of multiple origins (Ross et al., 2017).

The style of brecciation in IOCG deposits was compared to those of other deposits. Three levels of comparison were performed: between different types of mineral deposits, between different deposits within a deposit type, and within a single deposit. Some differences appear between different types of deposits. For instance, the IOCG breccias display a wide range of particle size distribution whereas orogenic gold deposits are characterized by a more limited size range of particles in associated breccias. This reflects the variety of processes occurring in IOCG deposits. Other results showed that particle roundness in IOCG deposits is similar to breccias in copper-molybdenum porphyry deposits, but higher than what is found in typical shear zones. Fabrics are commonly characterized by a near absence of orientation in IOCG deposits in contrast to many other types of ores. Finally, complexity can be very high (Fig. 8); it reflects the high capacity of dissolution of F-rich fluid. The only type of ore deposits that host breccia with such high values are magmatic breccias in PGE deposits (Lac-des-Iles, Ontario; Lavigne and Michaud, 2001). Within the IOCG class, differences in breccia styles are also significant

| Propagation \ Mobility | Grinding | Collapse | Fluidization | Dissolution |
|---|---|---|---|---|
| Thermo-elastic | | ● | | ● |
| Hydraulic | | Vein | | |
| Tectonic | ● | ● | ● | Karst |
| Explosion | Breccia pipe | | Breccia pipe | |

**FIGURE 7.** Table of processes in the formation of hydrothermal breccia showing the likely occurrence of main process combinations: vein, karst and breccia pipe are the main IOCG environment. Other possible combinations are indicated by blue dots. Fragmentation processes shown on the vertical axis; Mobility processes shown on the horizontal axis.

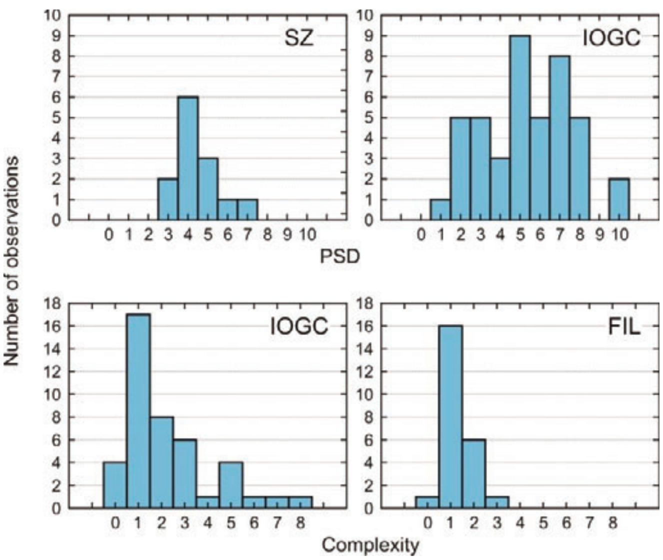


**Figure 8.** Comparison of two geometric parameters of breccias in IOCG vs. other deposit types. Upper histograms: comparison of particle size distribution for IOCG (South Australia, mainly Olympic Dam) and Au shear zone (SZ, Abitibi greenstone belt) breccias; 0 represents equal size distribution, and 10 a high fractal value. Lower histograms: comparison of complexity of breccia clasts between IOCG (South Australia, mainly Olympic Dam) and low temperature fluorite-barite vein type deposits (FIL, French Massif Central, mainly Le Rossignol); 0 corresponds to lack of corrosion and 10 to highly corroded particles.

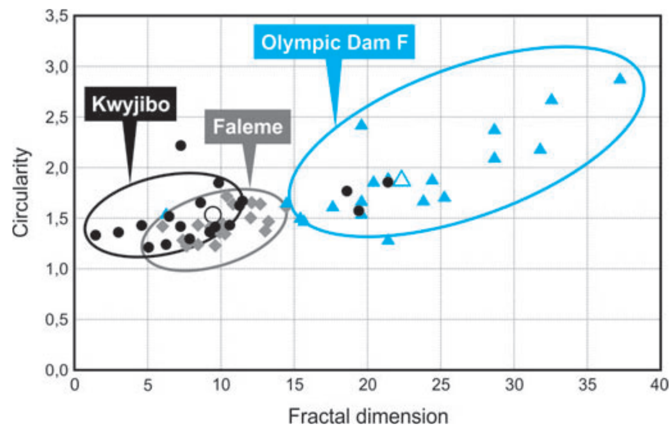


**Figure 9.** Comparison of two geometric parameters of breccias in three IOCG deposits: Kwyjibo (Québec), Faleme (Senegal) and Olympic Dam (F zone, South Australia). Fractal dimension represents the complexity (BFD-1). Circularity (= sphericity in 2D) varies from angular (0) to rounded (maximum of 10). Large symbols represent average value for each deposit.

between deposits. For instance, a quantitative analysis of the shape of fragments using roundness (value of sphericity) and complexity (BFD) shows that the F zone in the northwestern part of the Olympic Dam deposit displays much more corrosion than other deposits (Fig. 9). Such values are significantly higher than what occurs in a breccia pipe dominated by explosive processes, such as in an epithermal system, and suggests that much or all of the breccia in the F zone is related to solution processes within a tectonic zone.

Within a single deposit, a large variation in particle shape distribution can also be observed. For instance, several deposits show an evolution from magmatic to hydraulic and solution breccias (Corbett and Leach, 1998). Magmatic breccias are generally early features that are associated with pluton emplacement. Hydraulic breccias are associated with the subsequent expulsion of hydrothermal fluids. Explosive breccias occur in many systems, depending on the dynamics of pressure build-up and release. Solution breccias displaying evidence of dissolution and collapse are associated with the development of hydrothermal systems having high water: rock ratios. Tectonic breccias may occur before, during or after mineralization.

Recognition of the degree of evolution of breccias (mixing and corrosion) can be applied to an early assessment of their economic potential. For example, a cross section in the Olympic Dam deposit shows that fragment complexity increases strongly from the in situ hydraulic-style monomict breccia in the outer zone of the deposit (Fig. 2A) to highly corroded polymict fragments at the core of the orebody (Lei et al., 1995; Corriveau et al., 2022b). Such criteria can be used easily in the field.

## Conclusions

The recognition and proper interpretation of breccias can provide key elements in the exploration for IOCG deposits. Composition and geometric parameters allow recognition of the different generations and evolution of each breccia. Observations may be semi-quantified in the field or quantified in the lab in order to define more precisely the maturity of brecciation and help define vectors to mineralization.

Due to the extensive and dynamic magmatic-hydrothermal processes at work over long periods of time in IOCG systems (Richards and Mumin, 2013a, b; this paper), a wide diversity of processes that cause fragmentation can disrupt host rocks. Consequently, an abundance of breccias of different types are produced, each related to the specific dynamics and environment in which they form. Most important, it has been shown that potential ore-proximal breccias can be distinguished from those that are more likely barren.

## Acknowledgments

The study of fragmentation processes associated with ore deposits have been supported mainly by NSERC, FQRNT, DIVEX and numerous mining exploration companies including Areva (now Orano), Soquem, Sirios, Osisko, Goviex, and Iamgold. A.H. Mumin, L. Corriveau and R. Wilson are thanked for their detailed reviews of the paper.

## References

Barnett, W., 2003, Subsidence breccias in kimberlite pipes – an application of fractal analysis, *in* Heaman, L.M., Stachet, T., Scott, B.H., Smith, H., Grûther, H.S. and Mitchell, R.H., eds., 8th International kimberlite conference: The C. Roger Clement Volume, vol. 1 Long abstract, 5 p., Elsevier.

Barton, M.D., and Johnson, D.A., 1996, Evaporitic-source model for igneous related Fe-oxide-(REE-Cu-Au) mineralization: Geology, v. 24, p. 259-262.

Bernard, J.H., 1980, Paragenetic units of the Variscan megazone: Freiberger Forschungshefte Reihe C, v. 352, p. 55-71.

Bertelli, M., and Baker, T.A., 2010, Fluid inclusion study of the Suicide Ridge Breccia Pipe, Cloncurry district, Australia: implication for breccia genesis and IOGC mineralization: Precambrian Research, v. 179, p. 69-87.

Bérubé, D., and Jébrak, M., 1999, High precision boundary fractal analysis for shape characterization: Computers & Geosciences, v. 25, p. 1059-1071.

Billi, A., and Storti, F., 2004, Fractal distribution of particle size in carbonate cataclastic rocks from the core of a regional strike-slip fault zone: Tectonophysics, v. 384, p. 115-128.

Branquet, Y., Cheilletz, A., Giuliani, G., Laumonier, B., and Blanco, O., 1999, Fluidized hydrothermal breccia in dilatant faults during thrusting: the Colombian emerald deposits, *in* McCaffrey, K.J.W., Lonergan, L. and Wilkinson, J.J., eds., Fractures, fluid flow and mineralization: Geological Society of London, Special Publication, v. 155, p. 183-195.

Buhl, E., Kowitz, A., Eibelshausen, D., Sommer, F., Dressen, G., Poelchau, M.H., Reimold, W.U., Schmitt, R.T., and Kenkmann, T., 2013, Particle size distribution and strain rate attenuation in hypervelocity impact and shock recovery experiments: Journal of Structural Geology, v. 56, p. 20-33.

Clark, C., Schmidt Mumm, A., and Collins, A.S., 2006, A coupled micro- and macrostructural approach to the analysis of fluid induced brecciation, Curnamona Province, South Australia: Journal of Structural Geology, v. 28, p. 745-761.

Clark, T., Gobeil, A., and Chevé, S., 2010, Alterations in IOCG-type and related deposits in the Manitou Lake area, Eastern Grenville Province, Québec, *in* Corriveau, L. and Mumin, A.H., eds., Exploring for iron oxide copper-gold deposits: Canada and global analogues: Geological Association of Canada, Short Course Notes, No. 20, p. 127-146.

Corbett, G.J., and Leach, T.M., 1998, Southwest Pacific gold-copper systems: structure, alteration and mineralization: Society of Economic Geologists, Special Publication 6, 238 p.

Corriveau, L., Williams, P.J., and Mumin, A.H., 2010, Alteration vectors to IOCG mineralization from uncharted terranes to deposits, *in* Corriveau, L. and Mumin, A.H., eds., Exploring for iron oxide copper-gold deposits: Canada and global analogues: Geological Association of Canada, Short Course Notes, No. 20, p. 89-110.

Corriveau, L., Montreuil, J.-F., and Potter, E.G., 2016, Alteration facies linkages among IOCG, IOA and affiliated deposits in the Great Bear magmatic zone, Canada, *in* Slack, J., Corriveau, L. and Hitzman, M., eds., Proterozoic iron oxide-apatite (± REE) and iron oxide-copper-gold and affiliated deposits of Southeast Missouri, USA, and the Great Bear magmatic zone, Northwest Territories, Canada: Economic Geology, v. 111, p. 2045-2072.

Corriveau, L., Montreuil, J.-F., De Toni, A.F., Potter, E.G., and Percival, J.B., 2022a, Mapping mineral systems with IOCG and affiliated deposits: a facies approach, *in* Corriveau, L., Potter, E.G. and Mumin, A.H., eds., Mineral systems with iron oxide copper-gold (IOCG) and affiliated deposits: Geological Association of Canada, Special Paper 52, p. 69-111.

Corriveau, L., Montreuil, J.-F., Potter, E.G., Ehrig, K., Clark J., Mumin, A.H., and Williams, P.J., 2022b, Mineral systems with IOCG and affiliated deposits: part 1 – metasomatic footprints of alteration facies, *in* Corriveau, L., Potter, E.G. and Mumin, A.H., eds., Mineral systems with iron oxide copper-gold (IOCG) and affiliated deposits: Geological Association of Canada, Special Paper 52, p. 113-158.

Courrioux, G., Nullans, S., Guillen, A., Boissonnat, J.D., Repusseau, P., Renaud, X., and Thibaut, M., 2001, 3D volumetric modeling of Cadomian terranes (Northern Brittany, France): an automatic method using Voronoı diagrams: Tectonophysics, v. 331, p. 181-196.

Davies, A.G.S., Cooke, D.R., Gemmell, J.B., van Leewen, T., Cesare, P., and Hartshorn, G., 2008, Hydrothermal breccias and veins in the Kelian gold mine, Kalimantan, Indonesia: genesis of a large epithermal gold deposit: Economic Geology, v. 102, p. 717-758.

Ehrig, K., McPhie, J., and Kamenetsky, V., 2012, Geology and mineralogical zonation of the Olympic Dam iron oxide Cu-U-Au-Ag deposit, South Australia. Chapter 11, *in* Hedenquist, J.W., Harris, M. and Camus, F., eds., Geology and genesis of major copper deposits and districts of the world: a tribute to Richard H. Sillitoe: Society of Economic Geologists, Special Publication n. 16, p. 237-267.

Eliassen, A., and Talbot, M.R., 2005, Solution-collapse breccias of the Minkinfjellet and Wordiekammen Formations, Central Spitsbergen, Svalbard: a large gypsum palaeokarst system: Sedimentology, v. 52, p. 775-794.

Ganor, J., Roueff, E., Erel, Y., and Blum, J.D., 2005, The dissolution kinetics of a granite and its minerals – Implications for comparison between laboratory and field dissolution rates: Geochimica Cosmochimica Acta, v. 69, p. 607-621

Hecht, L., and Cuney, M., 2000, Hydrothermal alteration of monazite in the Precambrian basement of the Athabasca basin: implications for the genesis of unconformity related deposits: Mineralium Deposita, v. 35, p. 791-795.

Heilbronner, R., and Keulen, N., 2006, Grain size and grain shape analysis of fault rocks: Tectonophysics, v. 27, p. 199-216.

Hitzman, M.W., Oreskes, N., and Einaudi, M.T., 1992, Geological characteristics and tectonic setting of Proterozoic iron oxides (Cu-U-Au-REE) deposits: Precambrian Research, v. 58, p. 241-287.

Jébrak, M., 1997, Hydrothermal breccias in vein-type ore deposits: a review of mechanisms, morphology and size distribution: Ore Geology Reviews, v. 12, p. 111-134.

Lalonde, M., Tremblay, G., and Jébrak, M., 2010, Modeling virtual breccias using cellular automata – application to rounding in hydrothermal breccias: Computer & Geosciences, v. 36, p. 827-838.

Landtwing, M.R., Pettke, T., Halter, W.E., Heinrich, C.A., Redmond, P.B., Einaudi, M.T., and Kunze, K., 2005, Copper deposition during quartz dissolution by cooling magmatic-hydrothermal fluids: the Bingham porphyry: Earth and Planetary Science Letter, v. 235, p. 229-243.

Lavigne, M.J., and Michaud, M.J., 2001, Geology of the North American Palladium Ltd.'s Roby Zone deposit, Lac des Iles: Exploration and Mining Geology, v. 10, p. 1-17.

Laznicka, P., 1988, Breccias and coarse fragmentites: petrology, environments, associations, ores: Developments in Economic Geology, v. 25, 832 p.

Le Carlier de Veslud, C., Cuney, M., Lorilleux, G., Royer, J.J., and Jébrak, M., 2009, 3D modelling of uranium-bearing solution-collapse breccias in Proterozoic sandstone (Athabasca Basin, Canada). Metallogenic interpretations: Computers & Geosciences, v. 35, p. 92-107.

Lei, Y., Jébrak, M., and Danty, K., 1995, Structural evolution of the Olympic Dam deposit, South Australia: International conference on tectonics and metallogeny of Earth/mid Precambrian orogenic belts, Montréal, Canada, Program with Abstracts, p. 100.

Li, J.W., Zhou, M.F., Li, X.F., Li, Z.J., and Fu, Z.R., 2002, Origin of a large breccia-vein system in the Sanerlin uranium deposit, southern China: a reinterpretation: Mineralium Deposita, v. 37, p. 213-225.

Lin, A., 1999, Roundness of clasts in pseudotachylytes and cataclastic rocks as an indicator of frictional melting: Journal of Structural Geology, v. 21, p. 473-478.

Lorilleux, G., Cuney, M., Jébrak, M., Rippert, J.C., and Portella, P., 2003, Chemical brecciation processes in the Sue unconformity-type deposit: Journal of Geochemical Exploration, v. 80, p. 241-258.

Loucks, R.G., 1999, Paleocave carbonate reservoirs: origins, burial-depth modifications, spatial complexity, and reservoir implications: American Association of Petroleum Geologists Bulletin, v. 83, p. 1795-1834.

Loucks, R.G., Mescher, P.K., and McMehan, G.S., 2004, Three-dimensional architecture of a coalesced, collapsed-paleocave system in the Lower Ordovician Ellenburger Group, central Texas: American Association of Petroleum Geologists Bulletin, v. 88, p. 545-564.

Mair, K., and Abe, S., 2011, Breaking up: comminution mechanisms in sheared simulated fault gouge: Pure and Applied Geophysics, v. 168, p. 2277-2288.

Mark, G., Oliver, N.H.S., and Williams, P.J., 2006, Mineralogical and chemical evolution of the Ernest Henry Fe oxide-Cu-Au ore system, Cloncurry district, northwest Queensland, Australia: Mineralium Deposita, v. 40, p. 769-801.

Melosh, H.J., 1996, Acoustic fluidization: a new geological process?: Journal of Geophysical Research, v. 84, p. 7513-7520.

Monzawa, N., and Otsuki, K., 2003, Comminution and fluidization of granular materials: implications for fault slip behavior: Tectonophysics, v. 167, p. 127-143.

Mort, K., and Woodcock, N.H., 2008, Quantifying fault breccia geometry: Dent Fault, NW England: Journal of Structural Geology, v. 30, p. 701-709.

Mumin, A.H., Somarin, A.K., Jones, B., Corriveau, L., Ootes, L., and Camier, J., 2010, The IOCG-porphyry-epithermal continuum of deposits types in the Great Bear Magmatic Zone, Northwest Territories, Canada, *in* Corriveau, L. and Mumin, A.H., eds., Exploring for iron oxide copper-gold deposits: Canada and global analogues: Geological Association of Canada, Short Course Notes, No. 20, p. 59-78.

Oliver, N.H.S., Rubenach, M.J., Baker, B.F., Blenkinsop, T.G., Cleverley, J.S., Marshall, L.J., and Ridd, P.J., 2006, Granite-related overpressure and volatile release in the mid crust: fluidized breccias from the Cloncurry district, Australia: Geofluids, v. 6, p. 346-358.

Orford, J.D., and Whalley, W.B., 1983, The use of fractal dimension to characterize irregular-shaped particles: Sedimentology, v. 30, p. 655-668.

Richards, J.P., and Mumin A.H., 2013a, Magmatic-hydrothermal processes within an evolving Earth: iron oxide-copper-gold and porphyry Cu±Mo±Au deposits: Geology, v. 41, p. 767-770.

Richards, J.P., and Mumin A.H., 2013b, Lithospheric fertilization and mineralization by arc magmas: genetic links and secular differences between porphyry copper±molybdenum±gold and magmatic-hydrothermal iron oxide copper-gold deposits, *in* Colpron, M., Bissig, T., Rusk, B.G. and Thompson, J.F.H., eds., Tectonics, metallogeny, and discovery: the North American Cordillera and similar accretionary settings: Society of Economic Geologists, Special Publication 17, p. 277-299.

Ronze, P.C., Soares A.D.V., dos Santos D.G.V., and Barreira, D.F., 2000, Alemao copper-gold (-U-REE) deposit, Carajas, Brazil, *in* Porter, T.M., ed., Hydrothermal iron oxide copper-gold and related deposits: a global perspective, v. 1: PGC Publishing, Adelaide, p. 191-202.

Ross, P.S., Jébrak, M., and Walker, B., 2002, Discharge of hydrothermal fluids from a magma chamber and concomitant formation of a stratified breccia zone at the Questa porphyry molybdenum deposit, New Mexico: Economic Geology, v. 97, p. 1679-1699.

Ross, P.S., Nunez, G.C., and Hayman, P., 2017, Felsic maar-diatreme volcanoes: a review: Bulletin of Volcanology, v. 79, Paper 20, 33 p.

Sahimi, M., and Tsotsis, T.T., 1987, Dynamic scaling for fragmentation of reactive porous medias: Physical Review Letters, v. 59, p. 888-891.

Schlegel, T.U., and Heinrich, C.A., 2015, Lithology and hydrothermal alteration control the distribution of copper grade in the Prominent Hill iron oxide-copper-gold deposit (Gawler Craton, South Australia): Economic Geology, v. 110, p. 1953-1994.

Sibson, R.H., 1986, Earthquakes and rock deformation in crustal fault zones: Annual Reviews of Earth and Planetary Sciences, v. 14, p. 149-175.

Sillitoe, R.H., 1985, Ore related breccias in volcanoplutonic arcs: Economic Geology, v. 80, p. 1467-1814.

Skirrow, R.G., 2022, Hematite-group IOCG ± U deposits: an update on their tectonic settings, hydrothermal characteristics, and Cu-Au-U mineralizing processes, *in* Corriveau, L., Potter, E.G. and Mumin, A.H., eds., Mineral systems with iron oxide copper-gold (IOCG) and affiliated deposits: Geological Association of Canada, Special Paper 52, p. 27-51.

Storti, F., Balsamo, F., and Salvini, F., 2007, Particle shape evolution in natural carbonate granular wear material: Terra Nova, v. 19, p. 1-9.

Taylor, R., 2009a, Broken rocks – breccia 1, *in* Ore textures: recognition and interpretation: Springer, Berlin, Heidelberg, p.163-219.

Taylor, R., 2009b, Broken rocks – breccia 2, *in* Ore textures: recognition and interpretation: Springer, Berlin, Heidelberg, p. 223-282.

Taylor, R.G., and Pollard, P.J., 1993, Mineralized breccia systems: methods of recognition and interpretation: Economic Geology Research Unit, Key Center in Economic Geology, James Cook University of North Queensland, Townsville, Australia, Contribution 46, 31 p.

Walters, A.I., Phillips, J.C., Brown, R.J., Field, M., Gernon, T., Stripp, G., and Sparks, R.S.J., 2006, The role of fluidisation in the formation of volcaniclastic kimberlite: grain size observations and experimental investigation: Journal of Volcanology and Geothermal Research, v. 115, p. 119-137.

Williams, P.J., 1999, Fe-oxide-Au deposits of the Olympic Dam/Ernest Henry-type, *in* Hodgson, C.J. and Franklin, J.M., eds., New developments in the geological understanding of some major ore types and environments, with implications for exploration: Toronto, Prospectors and Developers Association of Canada, p. 1-43.

Williams, P.J., 2010, Classifying IOCG deposits, *in* Corriveau, L. and Mumin, A.H., eds., Exploring for iron oxide copper-gold deposits: Canada and global analogues: Geological Association of Canada, Short Course Notes, No. 20, p. 13-21.

Williams, P.J., 2022, Magnetite-group IOCGs with special reference to Cloncurry and Northern Sweden: settings, alteration, deposit characteristics, fluid sources, and their relationship to apatite-rich iron ores, *in* Corriveau, L., Potter, E.G. and Mumin, A.H., eds., Mineral systems with iron oxide copper-gold (IOCG) and affiliated deposits: Geological Association of Canada, Special Paper 52, p. 53-67.

Woodcock, N.H., Dickson, J.A.D., and Tarasewicz, J.P.T., 2007, Transient permeability and reseal hardening in fault zones, *in* Lonergan, K., Jolly, R.J.H., Rawnsley, K. and Sanderson, D.J., eds., Evidence from dilation breccia textures: Geological Society of London, Special Publication 270, p. 43-53.

# Uranium Enrichment Processes in Metasomatic Iron Oxide and Alkali-calcic Systems as Revealed by Uraninite Trace Element Chemistry

**Eric G. Potter**
*Geological Survey of Canada, 601 Booth St., Ottawa, ON*
*eric.potter@NRCan-RNCan.gc.ca*

**Pedro Acosta-Góngora**
*Geological Survey of Canada, 601 Booth St., Ottawa, ON*

**Louise Corriveau**
*Geological Survey of Canada, 490 rue de la Couronne, Quebec, QC*

**Jean-François Montreuil**
*formerly Institut national de la Recherche scientifique (INRS), Quebec, QC.*
*Current address: Red Pine Exploration Inc., Toronto, ON.*

**Zhaoping Yang**
*Geological Survey of Canada, 601 Booth St., Ottawa, ON*

*Recommended citation: Potter, E.G., Acosta-Góngora, P., Corriveau, L., Montreuil, J.-F., and Yang, Z., 2022, Uranium enrichment processes in metasomatic iron oxide and alkali-calcic systems as revealed by uraninite trace element chemistry, in Corriveau, L., Potter, E.G. and Mumin, A.H., eds., Mineral systems with iron oxide copper-gold (IOCG) and affiliated deposits: Geological Association of Canada, Special Paper 52, p. 325-345.*

## Abstract

Uranium enrichment is relatively common in metasomatic iron oxide and alkali-calcic systems that can host iron oxide-apatite (IOA), magnetite-, magnetite-hematite and hematite-group iron oxide-copper-gold (IOCG) and albitite-hosted uranium and Au-Co-U deposits. In Canada, the best exposed and studied IOCG and affiliated occurrences are those of the Great Bear magmatic zone in the Northwest Territories. Trace element concentrations in uraninite from these occurrences produce relatively flat chondrite-normalized rare earth element (REE) patterns with negative europium anomalies, lanthanum depletion and mild heavy-REE depletion. In one of the occurrences, mild light-REE (LREE) depletion is linked to co-precipitation of LREE-bearing allanite (Nori showing). The high REE and thorium concentrations and negative europium anomalies are interpreted to reflect precipitation from high-temperature, reduced fluids that evolved and equilibrated through extensive Na alteration (albite), then Ca-Fe (amphibole+magnetite±apatite) and ultimately K-Fe (K-feldspar/biotite+iron-oxides) metasomatic facies. In most systems, field observations, petrography, and geochemistry indicate precipitation of primary uraninite during the transition from high temperature Ca-Fe to K-Fe facies in magnetite-dominant (reduced) assemblages. Unlike models proposed for hematite-group deposits, primary uranium enrichment in magnetite-dominant systems was likely sourced and transported as chloride complexes in high-temperature, reducing fluids rather than oxidized brines. Uranium precipitation was likely triggered by cooling of the fluids and/or changes in fluid chemistry induced by extensive fluid-rock interactions. Alteration of primary uraninite caused significant changes in major element chemistry (e.g. Pb, Ca, Fe, Si, etc.) but the chondrite-normalized REE patterns only deviate slightly, primarily through changes to LREE abundances. As observed in both magnetite- and hematite-group deposits globally, the remobilization of uranium indicates that although IOCG systems may have primary magmatic-hydrothermal origins, multiple generations of uranium mineralization occur through alteration, dissolution and re-precipitation as the hydrothermal cells collapse and surface-derived waters interact with the ores.

## Résumé

L'enrichissement de l'uranium est relativement courant dans les systèmes alcali-calcique à oxydes de fer qui peuvent renfermer des gîtes à oxyde de fer-apatite (IOA), à oxydes de fer cuivre-or (IOCG) des groupes à magnétite, magnétite-hématite et hématite et des gîtes à uranium et Au-Co-U encaissés dans de l'albitite. Au Canada, les occurrences de gîtes IOCG et gîtes affiliés les mieux exposées et les mieux étudiées sont celles de la zone magmatique du Grand lac de l'Ours, dans les Territoires du Nord-Ouest. Les concentrations d'éléments traces dans l'uraninite de ces zones minéralisées produisent des patrons relativement plats d'éléments des terres rares (ETR) normalisés aux chondrites, avec des anomalies négatives d'europium, un appauvrissement du lanthane et un léger appauvrissement des terres rares lourdes. Dans l'une des zones, un appauvrissement léger en terres rares légères est lié à la coprécipitation d'allanite contenant des terres rares légères (indice Nori). Les concentrations élevées d'ÉTR et de thorium et les anomalies négatives d'europium sont interprétées comme reflétant la précipitation de fluides réduits à haute température qui ont évolué et se sont équilibrés au sein de vastes zones d'altération sodique (albite), puis à Ca-Fe (amphibole+magnétite±apatite) et finalement à K-Fe (feldspath potassique/biotite+oxydes de fer). Dans la plupart des systèmes, les observations de terrain, la pétrographie et la géochimie indiquent la précipitation d'uraninite primaire pendant la transition des faciès à haute température Ca-Fe à K-Fe dans des assemblages à dominance de magnétite (réduite). Contrairement aux modèles proposés pour les gîtes IOCG du groupe de l'hématite, l'enrichissement primaire en uranium dans les systèmes à dominance de magnétite provenait probablement du transport de l'uranium sous forme de complexes de chlorure dans des fluides réducteurs à haute température plutôt que dans des saumures oxydées. La précipitation de l'uranium a probablement été déclenchée par le refroidissement des fluides et/ou par des changements dans la chimie des fluides induits par les interactions importantes entre les fluides et les roches. L'altération de l'uraninite primaire a causé des changements importants dans la chimie des éléments principaux (p. ex. Pb, Ca, Fe, Si, etc.), mais les modèles d'ÉTR normalisés aux chondrites ne varient que légèrement, principalement par des changements dans les abondances des terres rares légères. Tel qu'observé dans les gîtes IOCG des groupes à magnétite et à hématite à l'échelle mondiale, la remobilisation de l'uranium indique que même si les systèmes minéralisateurs hôtes ont des origines magmatiques-hydrothermales primaires, de multiples générations de minéralisation d'uranium se produisent par altération, dissolution et re-précipitation à mesure que les cellules hydrothermales s'effondrent et que les eaux de surface interagissent avec les minerais.

## Introduction

Iron oxide-copper-gold (IOCG) deposits represent some of the world's largest recoverable resources of uranium (e.g. Olympic Dam with 10,100 Mt at 250 ppm $U_3O_8$; BHP, 2018), yet little is known about the sources and processes of uranium enrichment in these deposits. More importantly, the behaviour of uranium in the broader iron oxide and alkali-calcic alteration systems that host IOCG and affiliated deposits remains poorly defined (Corriveau et al., 2016). Hitzman and Valenta (2005) were the first to propose models for uranium enrichment in IOCG deposits and recognize the potential for significant uranium resources within these systems. Uranium enrichment in the systems hosting IOCG deposits was proposed to be linked to the presence of uranium-rich, felsic host rocks (primary uranium source), and mixing between low-temperature (100–200°C), oxidizing, uranium-bearing fluids and reduced, magnetite-forming fluids along major structural pathways in extensional or transtensional settings (Hitzman and Valenta, 2005; Skirrow, 2010).

Although the total uranium tonnage at Olympic Dam is unique, elevated uranium contents occur in several IOCG and affiliated deposits globally and it remains an undervalued uranium exploration target (Table 1). In parallel, albitite-hosted uranium (also termed Na-metasomatic U, U-Cu and Au-Co-U) deposits have metal associations, alteration assemblages, and mineral compositions that fall within the range of published data from IOCG deposits. Furthermore, in places, the host albitite in these deposits is part of regional-scale iron oxide and alkali-calcic systems featuring IOCG, iron oxide-apatite (IOA) and affiliated deposits (Pal et al., 2009; Corriveau et al., 2011, 2016, 2018; Gosh et al., 2013; Wilde, 2013; Montreuil et al., 2015; Potter et al., 2019).

The formation of IOCG deposits worldwide is regularly associated with igneous processes, but this does not necessarily mean direct precipitation from a magmatic fluid (Barton, 2014). The bulk of fluid inclusion and stable and radiogenic isotopic data indicate that most IOCG provinces resulted from the mixing of magmatic and non-magmatic (metamorphic and crustal) fluids (e.g. Williams et al., 2005, 2010; Barton, 2014). However, the actual origin of the polymetallic and uranium ore remains elusive as most interpretations about their sources

**Table 1.** IOCG deposits with reported uranium contents.

| Deposit | Resources[1] | Grades/Commodities | Reference |
|---|---|---|---|
| Olympic Dam | 10,100 Mt | 0.78 % Cu, 0.33 g/t Au, 250 ppm $U_3O_8$, 1 ppm Ag | BHP, 2018 |
| Monakoff & Monakoff East | 3 Mt | 1.33% Cu, 0.4g/t Au + 112 ppm $U_3O_8$[2] | Xstrata, 2012 |
| E1 group (Mt Margaret) | 48.1 Mt | 0.72% Cu, 0.21 g/t Au + 112 ppm $U_3O_8$[2] | Xstrata, 2012 |
| Prominent Hill | 285Mt[3] | 0.90%Cu, 0.8g/t Au, 103 ppm U | OZ Minerals, 2010 |
| Oak Dam East | 560 Mt[4] | 41–56% Fe, 0.2%Cu, 690 ppm U | Davidson and Patterson, 1993; Davidson et al., 2007 |
| Carrapateena | 292 Mt[5] | 1.29% Cu, 0.48g/t Au, 5.4 g/t Ag, 207 ppm U | OZ Minerals, 2012 |
| Mt Gee | 51 Mt | 0.11% Cu, 525 ppm U | Marathon Resources, 2009 |
| Salobo | 1122.6 Mt[6] | 0.72% Cu, 0.38 g/t Au, 16–26 ppm U | Osmond et al., 2012 |
| Igarape Bahia-Alemao | 219 Mt | 1.4% Cu, 0.86 g/t Au + U + REE | Tallarico et al., 2005 |
| Sue Dianne | 8.4 Mt[7] | 0.80% Cu, 0.07 g/t Au, 3.2 g/t Ag + U | Henessey and Puritch, 2008 |
| Hangaslampi-gold | 0.4 Mt[8] | 0.06% Co, 5.1 g/t Au, 50–260 ppm U | Dragon Mining, 2012 |
| Hangaslampi-cobalt | 0.18 Mt[9] | 0.09% Co, 0.20 g/t Au, 50–260 ppm U | Dragon Mining, 2012 |
| Guelb Moghrein | 43.57 Mt[10] | 0.86% Cu, 0.74 g/t Au, 143 g/t Co +U | Gray et al., 2016; Kolb et al., 2006 |

Notes: 1- Indicated + inferred resources; 2- Average in situ recoverable grade; 3- Combined copper-gold and gold-only measured, indicated and inferred resources; 5- Indicated and inferred resources at 0.7 % Cu cut-off; 4- Estimated tonnage; 6- Mineral reserves; 7- Indicated resources only; 8- Grade reported at 1 g/t Au cut-off; 9-Separate, additional grade reported at 0.05% Co cut-off; 10- Measured + indicated resources.

come from S, H, C and O isotopes, which are disturbed by the telescoping and overprinting nature of the systems, and may be associated with different stages of fluid migration. It then becomes imperative to develop new geochemical approaches capable of directly fingerprinting the ore minerals. In this sense, uraninite chemistry can provide some genetic information about the source of uranium in IOCG deposits.

In this study, uraninite from IOCG and affiliated mineral occurrences from the Great Bear magmatic zone in Canada was examined to gain insights on the metal sourcing and precipitation mechanisms in the deposits. This setting (Fig. 1) is an ideal natural laboratory to study uranium enrichment in these metasomatic systems, as excellent glaciated exposures of the weakly to non-deformed and unmetamorphosed occurrences illustrate the evolution from IOA (Hildebrand, 1986) to magnetite, magnetite-hematite and hematite group IOCG deposits (Corriveau et al., 2010, 2016; Mumin et al., 2010; Ootes et al., 2010; Potter et al., 2013; Richards and Mumin, 2013; Montreuil et al., 2016a, b). The regional-scale systems also host a wide spectrum of affiliated deposits such as albitite-hosted uranium (Montreuil et al., 2015, 2016b; Potter et al., 2019), skarn (Gandhi, 2003; Williams, 2010a; Corriveau et al., 2022) and epithermal-style veins (Mumin et al., 2010; Somarin and Mumin, 2012; Gandhi et al., 2018). As documented by several authors (e.g. Fryer and Taylor, 1987; Pagel et al., 1987; Maas and McCulloch, 1990; Hidaka et al., 1992; Fayek and Kyser, 1997; Hidaka and Gauthier-Lafaye, 2001; Cuney, 2010; Mercadier et al., 2011; Frimmel et al., 2014), the trace element chemistry of uraninite is unique to the deposit type and provenance associated with its formation, and reflects the conditions under which the mineral crystallized (combination of fluid chemistry, temperature, source materials, etc.). As such, the chemistry of uraninite, coupled with field relationships and petrography, can provide insights on the sourcing and precipitation of uranium in these systems.

## The Great Bear Magmatic Zone

*Regional Setting*

Located on the western margin of the Slave craton, the Great Bear magmatic zone is one of four geotectonic provinces of the Wopmay orogen that are split by the north-south trending Wopmay Fault Zone: the Coronation Margin and reworked Slave basement in the east and the Hottah terrane and Great Bear magmatic zone to the west (Fig. 1; Hildebrand et al., 2010a; Jackson et al., 2013). The Hottah terrane is a 1.93–1.89 Ga volcanic arc that likely developed south of the Slave craton, and moved northward along the proto-Wopmay Fault Zone to its present location on the western margin of the Slave craton in response to rifting and translation at ca. 1.91−1.88 Ga (Davis et al., 2015; Ootes et al., 2015). Following translation, renewed subduction at ca. 1880 Ma generated the ca. 1875−1850 Ma dominantly calc-alkaline volcanic and plutonic magmas of the Great Bear magmatic zone (Bowring, 1984; Gandhi et al., 2001; Hildebrand et al., 2010b; Davis et al., 2015; Ootes et al., 2015; Montreuil et al., 2016a). The main plutonic-volcanic sequences of the Great Bear magmatic zone form the McTavish Supergroup, which is subdivided into the LaBine, Sloan, Dumas and Faber groups. The Faber Group is only exposed in the southern part of the belt, where it unconformably overlies a platform-type sedimentary sequence termed the Treasure Lake Group. The Treasure Lake Group was metamorphosed at greenschist to amphibolite facies (grade increases towards the Wopmay Fault Zone), deformed, and tilted

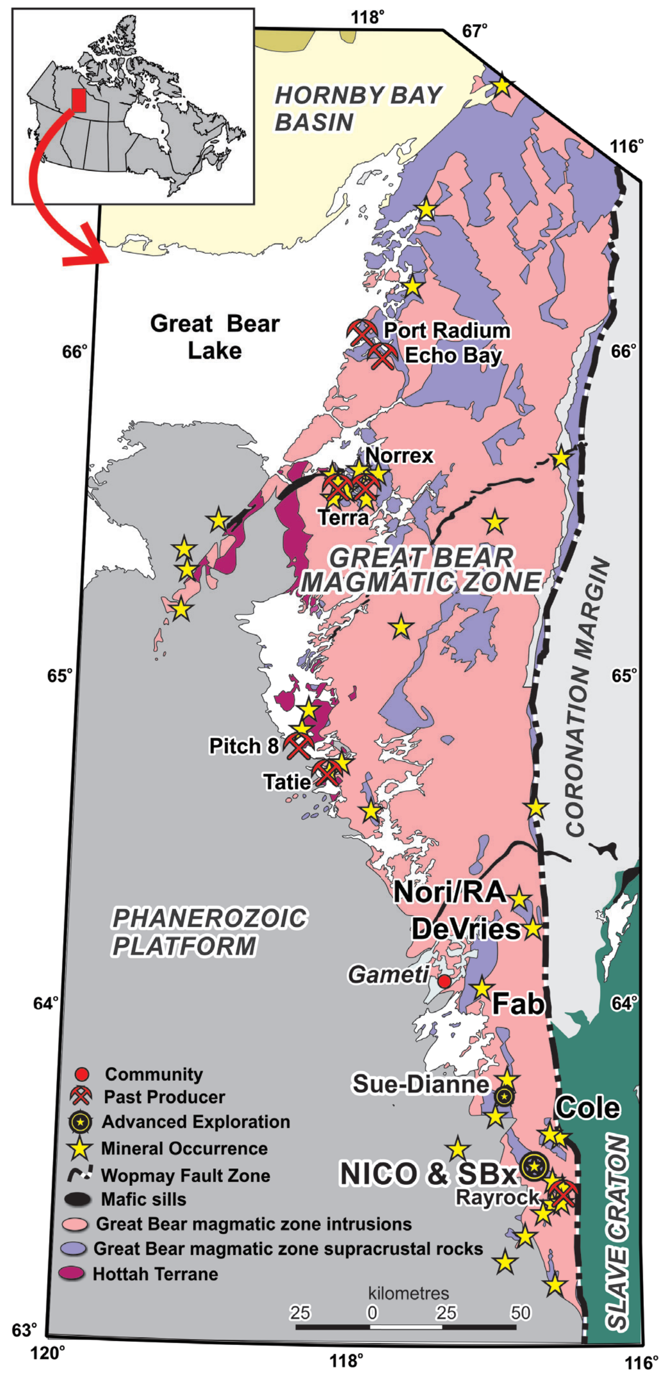


**Figure 1.** Location of the Great Bear magmatic zone and mineral occurrences examined in this study (bold font). Geology after Hoffman and Hall (1993) and mineral occurrences from the NORMIN database (www.nwtgeoscience.ca/normin).

before extrusion of the Faber Group volcanic sequence (Gandhi and van Breemen, 2005; Montreuil et al., 2016a). The ca. 1876−1873 Ma LaBine Group comprises mainly andesitic volcanic rocks erupted from large caldera complexes. The ash flow tuffs of the younger (ca. 1862 Ma; Ootes et al., 2015) Sloan Group underlie the north-central part of the magmatic zone. The LaBine, Dumas, and Faber groups are spatially and temporally associated with ca. 1.87 Ga subvolcanic intrusions, and the Sloan Group with granodioritic batholiths (Hildebrand et al., 2010b; Ootes et al., 2013; Montreuil et al., 2016a). Syn- to post-tectonic syenogranites intruded the volcanic rock ca. 1858–1850 Ma and form a large belt in the Great Bear magmatic zone (Bowring, 1984; Gandhi et al., 2001; Somarin and Mumin, 2012; Jackson et al., 2013; Hayward and Corriveau, 2014).

The Treasure Lake and Faber groups and ca. 1870 Ma synvolcanic intrusions are the principal hosts of the IOCG and affiliated deposits and prospects of the central-southern Great Bear magmatic zone, such as NICO, Sue Dianne, Southern Breccia, Brooke, Mar, Nod, Fab, and Nori/RA (Gandhi, 1994; Goad et al., 2000a, b; Camier, 2002; Mumin et al., 2010). Many of the Great Bear granitic phases and syn-volcanic intrusions that host mineralization contain elevated uranium contents relative to average continental crust, providing a fertile source of uranium for the ore systems (Ootes et al., 2013). In addition, some of the 1.85 Ga granites that host localized vein uranium mineralization are characterized by high radiogenic heat production, possibly indicating a genetic relationship between the intrusions and some of the uranium mineralization (Somarin and Mumin, 2012).

The Great Bear magmatic zone is cut by numerous brittle, northeast-trending, dextral transcurrent faults that formed during the interval 1850–1750 Ma, either by accretion of the Nahanni-Fort Simpson terranes to the western margin of the Hottah terrane, or related to an event well to the west of the Nahanni terrane (Hildebrand et al., 1987; Ootes et al., 2015). The faults are vertical to steeply dipping, have strike lengths up to 90 km, and host quartz veins, stockworks, and multiple generations of quartz ± uranium and copper (Furnival, 1935; Gandhi et al., 2000; Byron, 2010).

*Iron Oxide and Alkali-calcic Systems in a Continental Magmatic Arc at 1.87 Ga*

This study employs the metasomatic iron oxide and alkali-calcic classification of Porter (2010; revisited by Corriveau et al., 2016, 2022), which encompasses not only IOCG deposits (magnetite-, magnetite-hematite and hematite-group classes of Williams, 2010a), their alteration and breccia zones, but also the wide spectrum of affiliated deposits that can form within such systems, such as IOA deposits (Williams, 2010a, b), albitite-hosted uranium (Montreuil et al., 2015; Potter et al., 2019), iron oxide-uranium (IOU; Hitzman and Valenta, 2005; Skirrow, 2010; Skirrow et al., 2011), some skarns (Gandhi, 2003; Corriveau et al., 2010; Williams, 2010a), alkaline intrusion-hosted IOCG deposits (Groves et al., 2010), and alkaline-intrusion-related IOA and affiliated deposits (Corriveau et al., 2018, 2022). In this framework, IOCG deposits senso stricto are defined as polymetallic hydrothermal mineral occurrences that contain elevated copper, with or without elevated gold, abundant hydrothermal low-Ti iron-oxide (magnetite, hematite) gangue minerals or associated alteration, and sulphide-deficient ore consisting of native elements and low-sulphur base-metal sulphides and arsenides such as chalcopyrite, bornite, chalcocite, pyrrhotite and arsenopyrite (Corriveau, 2007; Corriveau et al., 2018). IOCG deposits range widely in age, but many prospective regions are associated with Archean to Proterozoic orogenic belts formed at the margins of Archean cratons (Skirrow, 2010). All IOCG deposits occur within broad-scale, chemically and mineralogically complex iron oxide and alkali-calcic metasomatic systems. The IOU deposits include U-REE-Mo mineralization closely associated with chlorite-hematite alteration and brecciation that overprint early hydrothermal magnetite such as at the Armchair deposit (Skirrow et al., 2011). Within this deposit, uranium exhibits spatial and genetic relationships to the precipitation of iron oxides. These deposits are distinct from IOCG and albitite-hosted uranium deposits as they are devoid of significant Cu-Au mineralization and are not directly hosted by sodic-altered zones. The term albitite-hosted uranium is preferred over “Na-metasomatic uranium”, as the mineralization postdates formation of the albitite.

The nomenclature used to describe the hydrothermal-metasomatic alteration in this study is taken from Corriveau et al. (2016, 2022), which follows the criteria of Schmid et al. (2007) and Zharikov et al. (2007) for the definition of metamorphic/metasomatic facies: systematic sets of mineral assemblages, repeatedly associated in time and space, and showing a regular relationship between mineral composition and bulk chemical composition, such that different alteration facies appear to be related to different physico-chemical conditions,

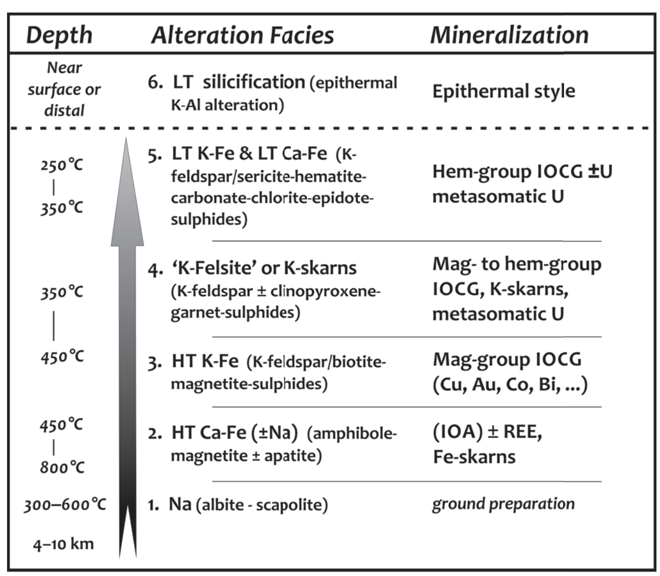


**Figure 2.** Metasomatic iron oxide and alkali-calcic system model, after Corriveau et al. (2010, 2016, 2022). *HT* = high temperature, *LT* = Low temperature.

**Table 2.** Characteristics of the Great Bear magmatic zone mineral occurrences examined in this study.

| Name | Host Rocks | Alteration* | Alteration Mineralogy | Accessory Minerals |
|---|---|---|---|---|
| Fab | Faber Gp porphyritic dacite | Na, Ca-Fe, Ca-Fe-K, K-Fe (HT) | Ab, Act, Mag, Bt, Kfs, Hem, Ap | Py, Urn, Ccp |
| Southern Breccia | Treasure Lake Gp meta-siltstones | Na, K-Fe (HT), K-Fe (LT) | Ab, Kfs, Bt, Mag, Hem, Chl | Py, Urn, Ccp, Ap, Rt, Ilm, Thr |
| DeVries | Treasure Lake Gp feldspathic quartzite | Na, Ca-Fe, K-Fe (HT) | Ab, Act, Mag, Ap, Kfs, late Qz | Urn, Aln, REE-Cb, |
| Nori/RA | Treasure Lake Gp meta-siltstones | Na, Ca-Fe, K-Fe (HT) | Ab, Act, Mag, Ap, Kfs, late Qz | Drv, Mol, Aln, Py, Ccp, Urn |
| Cole | Faber Gp rhyolite | Na, Ca-Fe-K, K, K-Fe (LT), Ca-Fe (LT) | Ab, Act, Mag, Ap, Kfs, Ep, Chl | Urn, Aln, Mnz, Cof, Zrn |

Mineral abbreviations from Whitney and Evans (2010).

especially temperature. The idealized regional- to deposit-scale facies are subdivided into (earliest to latest and broadly highest to lowest temperature): Na; high-temperature (HT) Ca-Fe (±Na); HT K-Fe; K-skarn and K-felsite; low-temperature (LT) K-Fe; and epithermal-type veins as summarized in Figure 2. Due to the dynamic nature of these systems, transitional facies (e.g. HT Na-Ca-Fe and HT Ca-Fe-K) and overprinting of facies are common.

The Great Bear magmatic zone currently hosts the only IOCG deposits in Canada with known or indicated reserves. The magnetite-group NICO deposit contains National Instrument 43-101-compliant proven and probable reserves of 33,077 Kt at 1.03 g/t Au, 0.11% Co, 0.14% Bi and 0.04% Cu (Burgess et al., 2014), and the Sue Dianne magnetite- to hematite-group deposit contains National Instrument 43-101-compliant indicated resources of 8.4 Mt grading at 0.80% Cu, 0.07 g/t Au and 3.2 g/t Ag (Hennessey and Puritch, 2008; Mumin et al., 2010).

Mineral occurrences examined in this study include Fab, DeVries, Nori/RA, Southern Breccia and Cole Lake (Table 2). Samples from DeVries Lake, Nori/RA, and Ridley (East Arm, Northwest Territories) were analyzed from archival material collected by S.S. Gandhi and housed within the Geological Survey of Canada radioactive rock storage facility. S.S. Gandhi samples from the Damp, Bode and BL prospects and the Sue Dianne deposit were examined but did not yield uraninite grains suitable for analysis (i.e. uraninite grains were either too fine-grained or significantly altered).

*Fab Magnetite-group IOCG Prospect*

The Fab system is located in the south-central part of the Great Bear magmatic zone (Figs. 1, 3; Table 2) within a succession of undifferentiated high-K calc-alkaline to shoshonitic porphyries (Azar, 2007; Hildebrand et al., 2010b). The porphyries represent the northernmost extension of the Faber Group of the McTavish Supergroup, which comprises all the volcanic sequences and hypabyssal intrusions within the Great Bear magmatic zone (Gandhi, 1988; Gandhi et al., 2001). Gandhi et al. (2001) interpreted the Fab Lake porphyry complex hosting the mineral occurrences as being a transitional sequence intercalated between the Mazenod and Lou assemblages; this was confirmed by recent geochronology of the porphyries, which yielded ages between 1870–1869 Ma (Montreuil et al., 2016c). The Fab Lake porphyry complex is bordered by ca. 1866 Ma Great Bear batholiths to the north and east, and the western and southern margins are defined by the 1856 +2/−3 Ma Faber Lake rapakivi granite (Gandhi et al., 2001; Jackson and Ootes, 2012). Within the porphyry complex, numerous 1866.8 ± 1.3 Ma porphyritic monzonite dykes and 1858 ± 6.1 Ma coarse-grained granitic bodies intrude the Fab Lake porphyries and post-date hydrothermal alteration (Azar, 2007; Potter et al., 2013; Montreuil et al., 2016c). Geochronology of unaltered porphyritic monzonite dykes and least-altered host rocks bracket hydrothermal alteration in the Fab system to 1870–1866 Ma, supporting a spatial, temporal, and genetic linkage between magmatism and formation of the Fab system (Montreuil et al., 2016b, c).

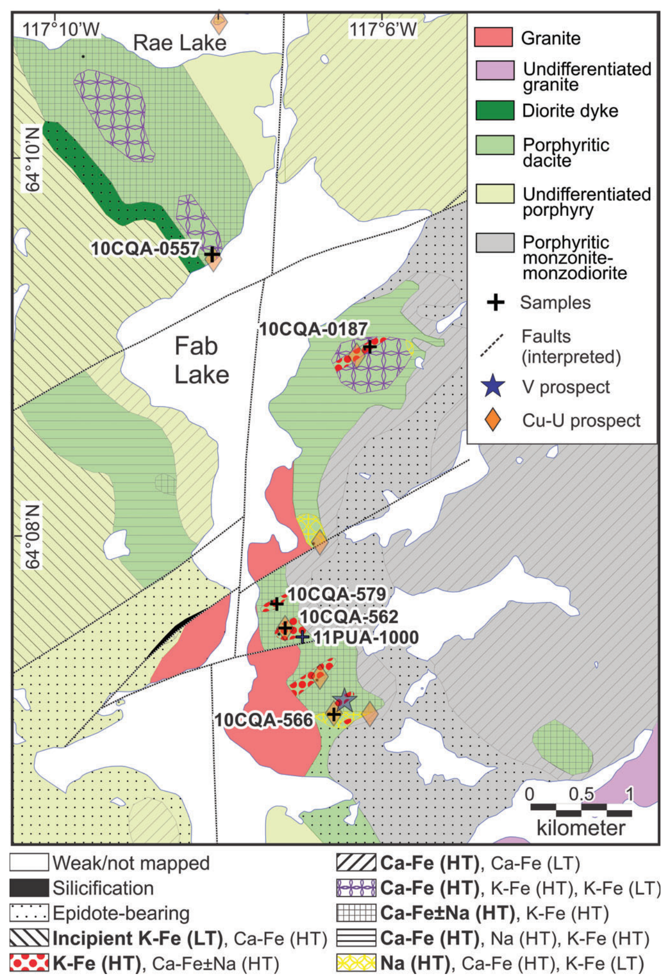


**Figure 3**. Generalized bedrock geology and alteration facies of the Fab system, after Potter et al. (2013) and Montreuil et al. (2016c) and references therein. Bold font alteration indicates the dominant facies, as most of the rocks record multiple phases of alteration.

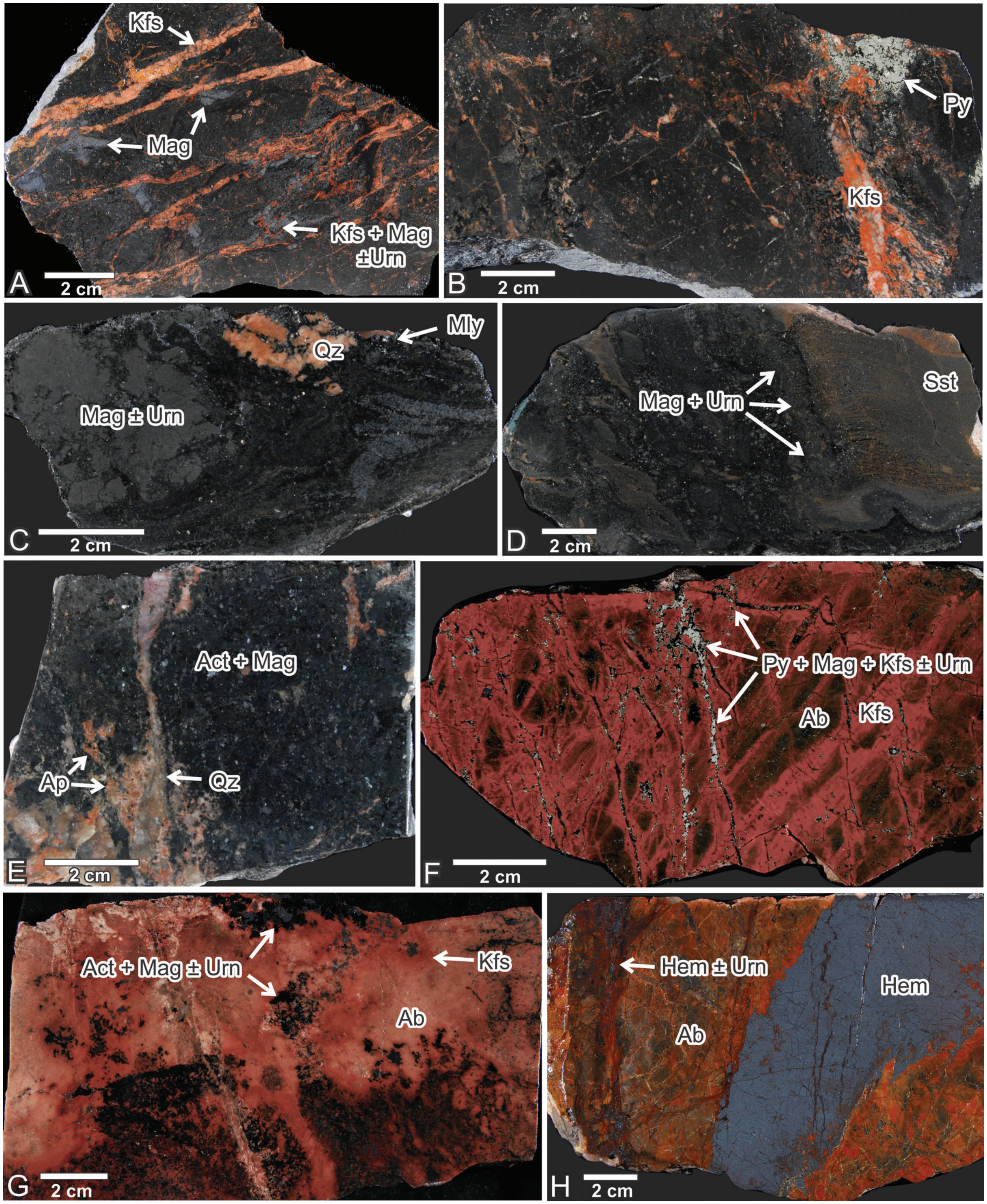


FIGURE 4. Photographs of representative samples examined in this study. **A, B.** Sulphide-bearing K-feldspar + magnetite veins cutting an intensely amphibole-magnetite altered porphyritic dacite from the Fab system, samples 10CQA-562C3 and 11PUA-1000H2. **C, D.** Stratabound to discordant amphibole + magnetite + biotite altered metasandstones from the Nori/RA occurrences, with trace contents of molybdenite. Samples GFA-291 and GFA-301. SSt= metasandstone clast rimmed by magnetite. **E.** Albite, amphibole(actinolite)+magnetite+apatite, and K-feldspar altered metasedimentary rocks from the DeVries showing cut by quartz veinlets. Sample 82GFA-255. **F.** Albite altered metasedimentary rocks of the Treasure Lake Group, altered and brecciated by magnetite+K-feldspar veins containing pyrite, chalcopyrite, uraninite and molybdenite from the Southern Breccia occurrences. Sample 10CQA-1705C1. **G.** Albite, amphibole+magnetite+K-feldspar altered volcanic rock from the Cole uranium showing. Sample 10CQA-511E3. **H.** Albite altered metasedimentary rocks cut by massive specular hematite vein and earthy hematite+K-feldspar veinlets containing uraninite at the Southern Breccia. Sample 11PUA-526D2.

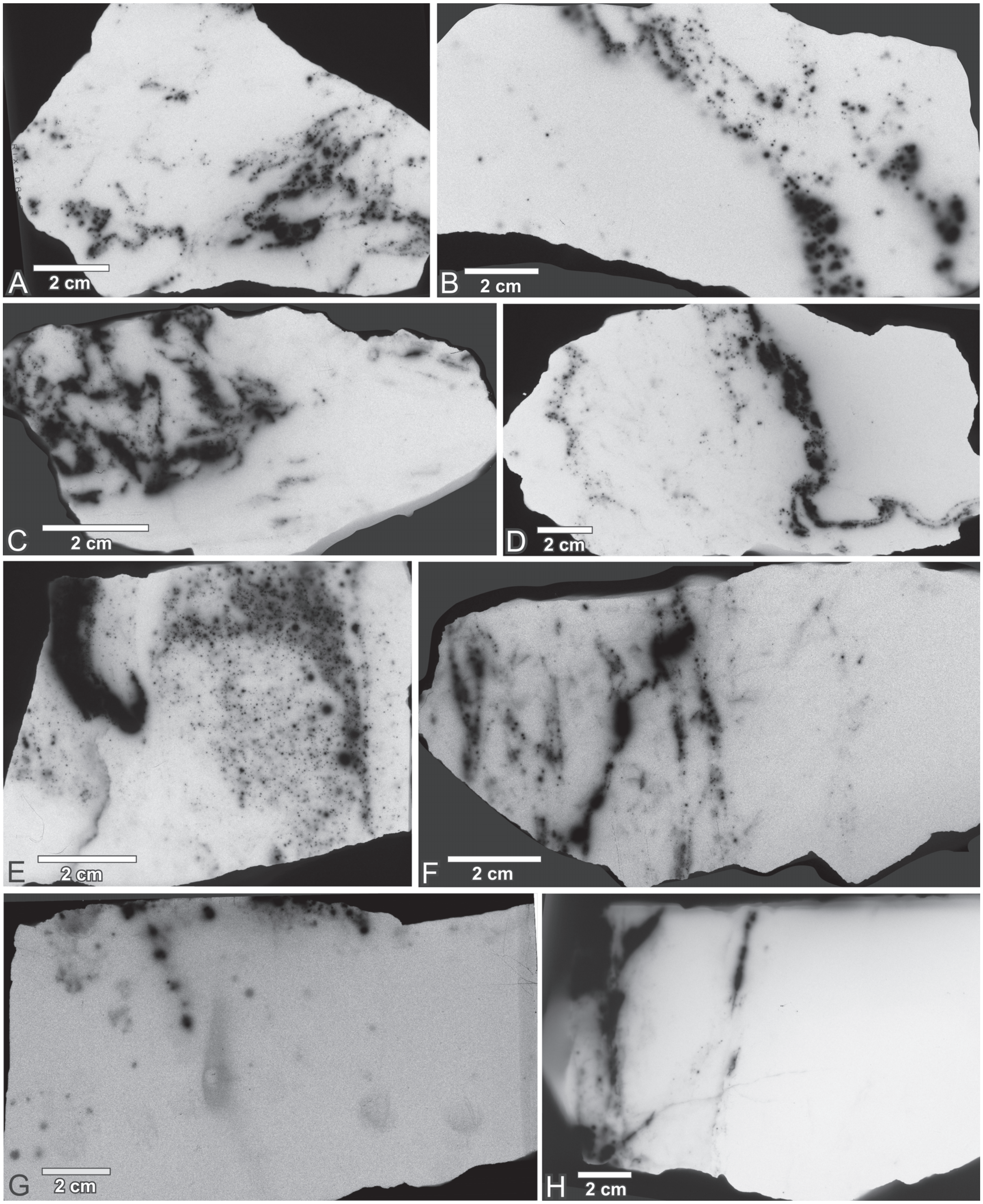


**FIGURE 5. A–H.** Autoradiographs (negatives) of the same samples from Figure 4. Radioactive minerals are denoted by black spots, primarily associated with magnetite + K-feldspar alteration and veinlets.

Alteration zones and historic U-Cu-Fe showings are observed in exposed sections of a homogeneous porphyritic dacite intrusion (Figs. 1, 3). Mineralization primarily occurs along the eastern shoreline of Fab Lake, within magnetite-cemented hydrothermal crackle breccias, zones of biotite-magnetite replacement, or within extensive amphibole-magnetite-bearing replacement fronts and K-feldspar-magnetite alteration zones (Figs. 3, 4, 5; Potter et al., 2013). These mineralized zones are characterized by the presence of magnetite, chalcopyrite, pyrite, and fine-grained uraninite that is variably altered to coffinite. Accessory minerals include titanite, ilmenite, fluorapatite, scheelite, thorite and fluorite (Gandhi, 1988; De Toni, 2016;

this study). Historical (1969–1977) exploration yielded grades of 0.010–0.065% U and 0.01–0.13% Cu, with minor Zn and trace Au, from composite trench samples 0.75 to 1.50 m in width (Morris, 1977). Mineralized grab samples from bedrock collected during this study returned values of 227–3010 ppm U, 36.8–109 ppm Th, 665 to 2067 ppm Cu and 5.44–14.7% Fe (Potter et al., 2013; Montreuil et al., 2016c).

*Southern Breccia Albitite-hosted Uranium Showings*

The Southern Breccia zone represents the southern component of the Lou iron oxide and alkali-calcic system, which also hosts the NICO deposit, an Au-Co-Bi-rich magnetite-group IOCG deposit (Montreuil et al., 2015; Corriveau et al., 2016; Potter et al., 2019). The southeast-trending, 500 m wide and 3 km long albitite corridor is characterized by a series of uranium-rich, polymetallic (U±Th-Cu-Mo-Bi-Au-REE) showings located 1 km south of the NICO deposit (Figs. 1, 6; Table 2). The corridor is hosted by metasiltstones of the Treasure Lake Group and bounded by local-scale faults. An albitized granitic intrusion truncates the metasedimentary rocks to the south and provides a maximum age of 1873 ±2 Ma for both the NICO and Southern Breccia (Gandhi et al., 2001). An unaltered, 1868 ±0.74 Ma porphyritic quartz monzonite dyke cuts all mineralization and alteration in the Southern Breccia corridor, constraining the age of the Southern Breccia. A similar porphyritic dike with a preliminary age of 1869 ± 1.3 Ma cuts the main iron oxide and alkali-calcic alteration at the NICO deposit (Davis et al., 2011), bracketing development of both NICO and the Southern Breccia corridor to a 5 Ma window from 1873–1868 Ma (Montreuil et al., 2016b).

At the main uranium showings in the corridor, primary uraninite (SB1) occurs with K-feldspar in magnetite-rich veinlets and crackle breccias. Uranium deposition is accompanied by thorium enrichment ± minor sulphides. In sulphide-poor magnetite+K-feldspar+biotite veins and breccias, uraninite is the dominant uranium mineral and occurs with accessory to minor chlorite, ilmenite, rutile, apatite, thorite, galena, titanite and zircon (Figs. 4, 5). Trace minerals present include: monazite, allanite, arsenopyrite, barite, wolframite, xenotime, ferrocolumbite and titanian ferrocolumbite. Less abundant uranium-bearing minerals include brannerite and coffinite, which occur in trace to minor concentrations as primary subhedral crystals and as alteration products of uraninite, respectively. In sulphide-rich samples, uraninite, brannerite and coffinite are accompanied by pyrite, chalcopyrite, bornite and molybdenite (Potter et al., 2019). Zoning of trace modal copper minerals in the halo of the uranium showings records an evolution to more oxidizing conditions, with the sequence chalcopyrite, bornite, chalcocite, and covellite (Montreuil et al., 2015, 2016b).

On the southwestern edge of the corridor, fine-grained uraninite (SB2), coffinite, becquerelite and fine-grained uranium-potassium-silicates (possibly compreignacite, boltwoodite or weeksite) occur in later, northeast-trending earthy hematite-chlorite-K-feldspar veins that cut the albitized host rocks. These veins are adjacent to the Lou Lake fault zone that lies parallel to northeast-trending regional faults, many of which host giant quartz-hematite-uraninite veins such as at the past-producing Rayrock and Eldorado mines (Fig. 1; Mumin et al., 2010). In Miller (1982), U–Pb analyses of uraninite from the Rayrock mine yielded ages indicating that some of these regional faults remained periodically active from the Paleoproterozoic to the Late Ordovician.

In terms of alteration facies, the uranium mineralized zones of the Southern Breccia corridor record several cycles of stratabound to discordant replacement alteration, veining and brecciation. Multiple early and intense Na alteration episodes completely transformed the host metasiltstone into albitite. Albitization, on relatively un-weathered exposures, is first expressed as dull white albite, followed by rose-colour albite on both weathered and freshly exposed samples. Next, particularly along the northern margin of the corridor, high-temperature Ca-Fe (amphibole-magnetite-arsenopyrite) veins cut the early Na alteration. The high-temperature Ca-Fe facies increases in intensity to the north and does not extend more than a few metres into the main albitite corridor. Finally,

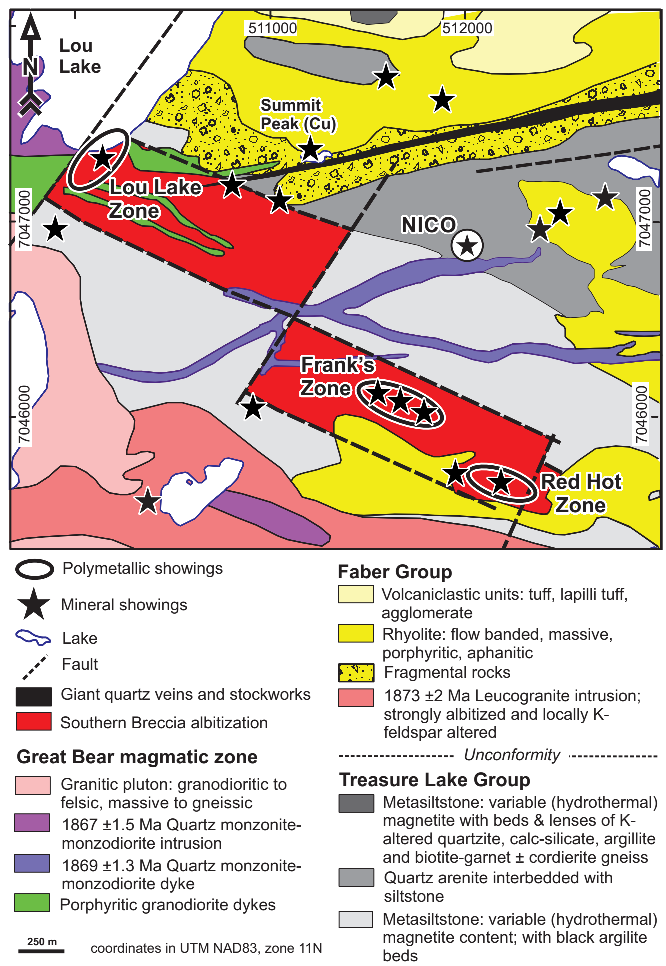


**Figure 6.** Location of the Southern Breccia corridor, NICO (a Co-rich magnetite-group IOCG deposit), and mineral showings sampled for this study (circled). Geology after Montreuil et al. (2015) and geochronology from Gandhi et al. (2001) and Montreuil et al. (2016a).

several generations of high- to low-temperature K-Fe assemblages imparted the diagnostic brick-red colour to the showings of the Southern Breccia corridor (Fig. 4). The uranium and polymetallic mineralization took place during the latest stage of high-temperature K-Fe (magnetite) veining and brecciation, which transitions into a hematite-bearing low-temperature K-Fe assemblage. Later uranium remobilization along brittle northeast-trending faults resulted in the formation of veinlets associated with, and trending parallel to, the Lou Lake fault near the southeast shoreline of Lou Lake (Potter et al., 2019).

*Cole Uranium Showing*

Located ~16 km northeast of NICO (Figs. 1, 7), the Cole volcanic complex includes volcanic and volcaniclastic rocks of the Cole assemblage of the Faber Group, feldspar-phyric intrusions and dykes, and quartz monzonite–monzodiorite intrusions (Gandhi et al., 2014). The Cole assemblage consists primarily of feldspar-amphibole-phyric andesite, local rhyolite, and volcaniclastic rocks.

Plutons of the Marian River batholith, which lack hydrothermal alteration, nearly surround the entire Cole volcanic complex and provide a minimum age of 1866 Ma for the volcanic complex and alteration (Montreuil et al., 2016a). Porphyritic dykes cutting the regional alteration were dated at 1866.4 ± 1.3 Ma while another dyke, directly cutting the Cole Breccia, was dated at 1865.9 ± 0.9 Ma (Montreuil et al., 2016b).

In terms of iron oxide and alkali-calcic alteration, the prevailing regional alteration in the Cole Lake area is a pervasive high-temperature Ca-Fe (amphibole-magnetite) impregnation of the porphyritic andesite groundmass that generally preserves host rock textures and is overprinted by an intense and texture-destructive Na alteration (Table 1). This Na alteration episode was followed by renewed high-temperature Ca-Fe, K, localized high-temperature Ca-Fe±K, low-temperature K-Fe (chlorite ± hematite), and low-temperature Ca-Fe-Mg (epidote) alteration and silicification (Montreuil et al., 2016a). The Cole uranium showing (Cole U; Figs. 1, 7) occurs in a zone of strong Na alteration superimposed over early high-temperature Ca-Fe alteration of the Cole assemblage andesite. Uranium mineralization is hosted by high-temperature Ca-Fe±K veins surrounded by localized K-feldspar (K-altered), low-temperature K-Fe and epidote with low modal contents of pyrite and traces of chalcopyrite (Fig. 4). However, the K-feldspar and epidote alteration postdate the uranium-bearing Ca-Fe±K facies veins. The mineralogy of uranium mineralization consists of uraninite in magnetite-amphibole-apatite ± K-feldspar veins containing trace chlorite, zircon, monazite, chalcopyrite, titanite and rutile in an intensely albite-altered, and weakly brecciated volcanic host.

## Nori/RA and DeVries Occurrences

The Nori/RA Cu-Mo-U (±REE, W) occurrences at DeVries Lake (Figs. 1, 8; Table 2) occur within foliated and altered Treasure Lake metasiltstones in the central Great Bear magmatic zone, roughly 1.5 km from the contact of ca. 1865 Ma porphyritic granites (Gandhi and Prasad, 1993; Gandhi, 1994;

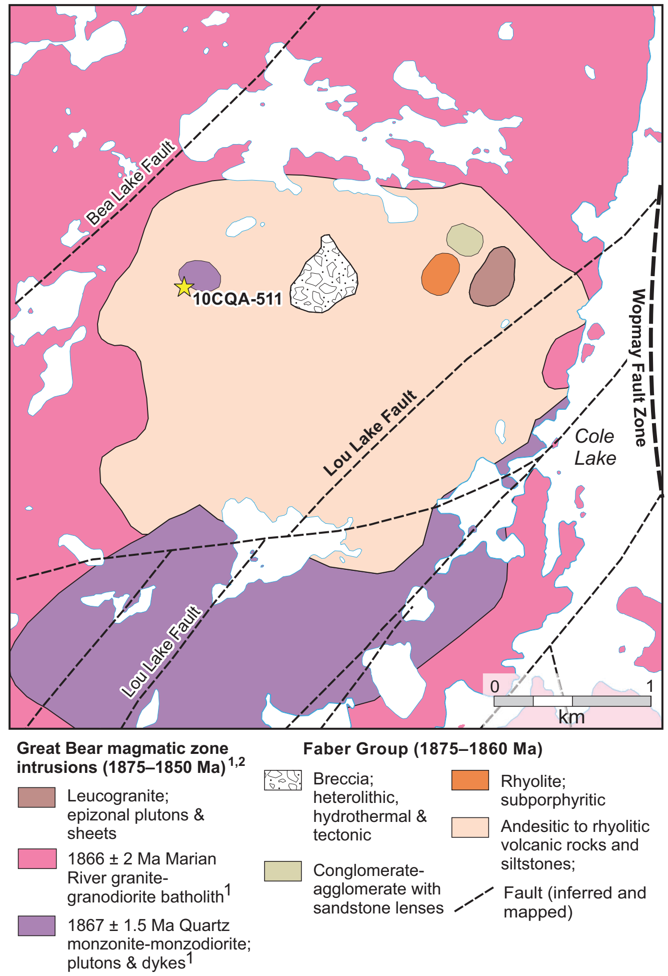


**FIGURE 7.** Regional geology of the Cole Lake complex, after Gandhi et al. (2014). Location of the uranium-bearing showing indicated by the star (station ID 10CQA-511). Geochronology from 1- Montreuil et al. (2016a) and 2- Gandhi et al. (2001).

Ootes et al., 2010; Jackson and Ootes, 2012). Alteration in metasedimentary rocks consists of an intense stratabound to discordant biotite-K-feldspar-magnetite assemblage cut by 10 cm to 1 m wide tourmaline-biotite-quartz-K-feldspar veins (Ootes et al., 2010). Uraninite occurs within the biotite-magnetite veins along with K-feldspar, dravitic tourmaline, molybdenite, allanite, chalcopyrite and pyrite (Fig. 4; Gandhi, 1994; Ootes et al., 2010; Acosta-Góngora et al., 2011). The showings contain abundant tourmaline, which is somewhat atypical for an iron oxide and alkali-calcic alteration system; however, hydrothermal tourmaline has been reported from IOA and IOCG occurrences in the Great Bear magmatic zone (Mumin et al., 2007; Montreuil et al., 2015, 2016a; Mumin, 2015; Kelly et al., 2020), Coastal Cordillera of Chile (Marschik and Fontboté, 2001; Benavides et al., 2007; Tornos et al., 2010, 2012), Dahongshan group in China (Su et al., 2016), and the Carajás Mineral Province of Brazil (Xavier et al., 2008). Molybdenite Re–Os dating of the Nori/RA veins by Ootes et al. (2010) yielded ages (1874.4 ±8.7 and 1872.4 ±8.8 Ma) within error of the Great Bear magmatic zone IOA and IOCG occurrences. Mineralization is hosted by a regional-scale system that includes: 1) stratabound Na (albite) and high-temperature Ca-Fe (amphibole, amphibole-magnetite and magnetite) alteration, as well as albitite and albitite breccia filled with amphibole; 2) stratabound and anastomosing K-feldspar overprints; and 3) high-temperature K-Fe (magnetite+K-feldspar) breccia zones and sulphide mineralization in the metasedimentary rocks (Corriveau et al., 2010). A late-stage potassic (K-feldspar) to propylitic (K-feldspar-epidote-chlorite-sericite) alteration forms well-developed networks of parallel veins and selvages (Landry, 2006) that cut the earlier stratabound alteration facies. Furthermore, the ca. 1872 Ma metavolcanic rocks that overlie the Treasure Lake metasiltstone in the DeVries Lake area have localized Na and K-Fe alteration, host magnetite-actinolite-apatite (IOA) veins, and contain local magnetite alteration superimposed by uranium mineralization indicative of a regional iron oxide and alkali-calcic system (Gandhi and Prasad, 1993; Gandhi, 1994; Ootes et al., 2010; Jackson and Ootes, 2012; V. Bennett, V. Jackson, L. Corriveau and S. Bowring, unpublished data). These observations led Ootes et al. (2010) to suggest that the showings represent an early expression of IOCG development.

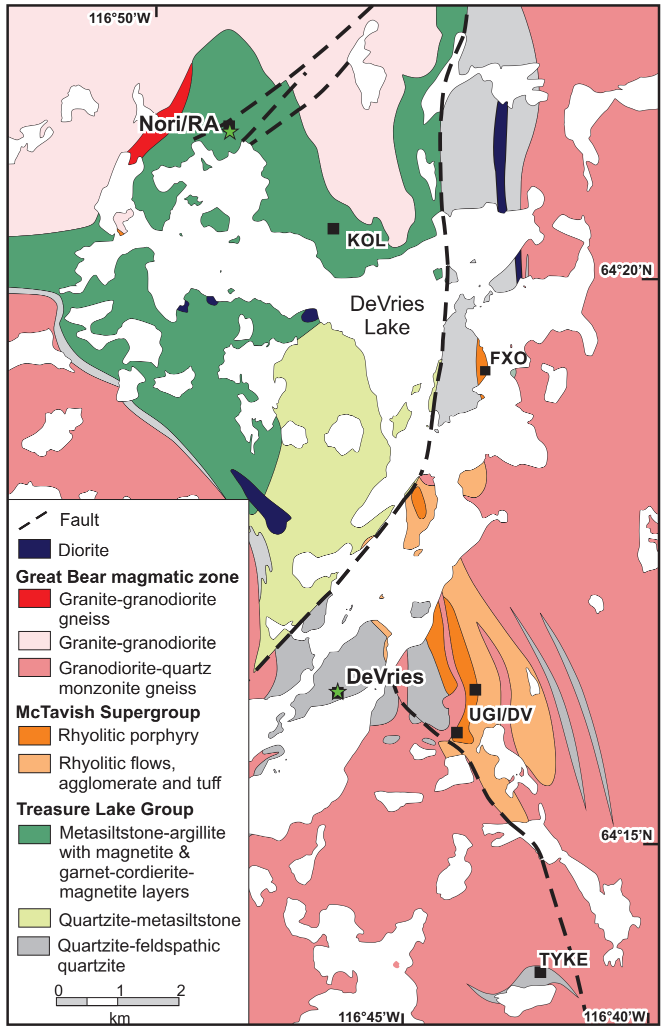


**FIGURE 8**. Geology and select mineral occurrences of the DeVries Lake region, after Gandhi and Prasad (1993) and Jackson et al. (2013).

## Methods

Thick (~200 µm) polished thin sections were prepared from polished sample slabs, using autoradiographs to target uraninite grains (Figs. 4, 5). The target grains were examined using a Zeiss EVO 50 series Scanning Electron Microscope (SEM) equipped with a Backscattered Electron Detector at the Geological Survey of Canada (GSC) in Ottawa. The Oxford energy dispersive spectrometry (EDS) system includes the X-MAX 150 Silicon Drift Detector, the INCA Energy 450 software and the latest AZtec microanalysis software. The SEM was operating at 20 kV with a beam current of 400 pA to 1 nA. Uraninite grains were analyzed with a Cameca SX50 electron microprobe at the GSC and a JEOL 8230 electron microprobe at the University of Ottawa. Operating conditions were 20 kV accelerating voltage and 10 nA current, with 20 s on peak and 10 s off-peak counting times. A mixture of natural and synthetic pure metal, simple oxides and simple compounds were used as standards. Data reduction was accomplished with a ZAF matrix correction using Probe For Windows software (Armstrong, 1988) and Pouchou and Pichoir (1984) using JEOL software. For elements with concentrations <1 wt%, typical detection limits during analysis were: 0.17 wt% $ThO_2$, 0.08 wt% $Y_2O_3$, 0.25 wt% $La_2O_3$, 0.03 wt% CaO, and 0.04 wt% FeO.

Trace element concentrations were analyzed using in situ laser ablation inductively coupled plasma mass spectrometry (LA-ICP-MS) on polished thick sections at the GSC. The system consists of a Teledyne Photon-Machines Analyte G1 excimer laser (193 nm) ablation system with a Helex dual-volume ablation cell and an Agilent 7700x quadrupole ICP-MS equipped with a second rotary vacuum pump that improves instrument sensitivity across the mass range by ~2 times (Jackson and Cabri, 2011). Analyses were done using a 26 µm spot size at repetition rate of 10 Hz, and a fluence of 4.53 J/cm$^2$ for the 200 µm thick polished sections. Helium gas was used to transport ablated sample material from the ablation cell. The sample and He mixture was mixed with argon (flow rate of 1.05 L/min) before entering the ICP-MS. Data acquisition time was 100 s in length, including 40 s of background signal prior to ablation and 60 s of sample signal. A USGS doped basaltic glass GSE-1G standard (Guillong et al., 2005) was used as calibration standard, while BCR-2G was used as a quality control standard, following methods outlined in Jackson (2008). The data reduction was performed using GLITTER (Griffin et al., 2008). The "GeoReM preferred values" (as of February 2010) from the on-line geological and environmental reference materials database (GeoReM; Jochum et al., 2005) were used for the concentrations of the elements in GSE-1G and BCR-2G. Most elements were within 5–10% of the accepted values for GSE-1G, except for Tb, Tm and Lu which within 15%. Average lower detection limits for REE during uraninite analyses were (in ppm): La=0.004, Ce=0.009, Pr=0.004, Nd=0.025, Sm=0.022, Eu=0.006, Gd=0.032, Tb=0.002, Dy=0.011, Ho=0.004, Er=0.021, Tm=0.002, Yb=0.012, Lu=0.003. The uranium content determined by electron probe microanalysis (EPMA) was used as an internal standard. The integrated region of sample signal was selected carefully to exclude regions associated with inclusions and/or ablation of surrounding minerals. In addition to the aforementioned standards, trace element concentrations were verified against a well-characterized uraninite from Mistamisk, Quebec (Bonhoure et al., 2007; Mercadier et al., 2011; Lach et al., 2013).

## Results

*Major and Minor Element Concentrations*

At most of the occurrences, electron probe microanalyses of uraninite yielded consistent major element concentrations — omitting extensively altered uraninite and coffinite grains. Two generations of uraninite were noted from differences in major element chemistry (e.g. $UO_2$, PbO, $ThO_2$, CaO, etc.) at the Southern Breccia (denoted SB1 and SB2) and Nori/RA (Nori-1 and Nori-2) showings (Fig. 9). At many of the occurrences, alteration of uraninite to coffinite points to increasing silica activity in the fluids.

The median concentrations of $UO_2$ in the samples studied vary from 52.93 to 80.7 wt%, with a mean of 65.29 wt% for the entire data suite. Aside from the Southern Breccia and Nori occurrences, intra-occurrence variability (in terms of standard deviation, 1σ) was generally <2.0 wt% $UO_2$.

In the analyzed samples, thorium (as $ThO_2$) had a mean value of 3.05 wt%, and ranged in concentration from below the EPMA detection limits (<0.17 wt% $ThO_2$) to 13.03 wt% (Fig. 9C). The highest mean $ThO_2$ concentrations were observed in the Cole (6.43 wt%) and the Southern Breccia (SB1=4.66 wt%) prospects, whereas secondary uraninite from the Southern Breccia (SB2) occurrence had $ThO_2$ values <0.17 wt% $ThO_2$. The intra-occurrence variability ranged from 0.1 (Nori-2) to 2.8 wt% (SB1), with most samples rarely exceeding 1.5 wt%.

The U/Th ratios were calculated from both EPMA (as $UO_2$ and $ThO_2$) and LA-ICP-MS ($ThO_2$) techniques. U/Th calculations based on EMPA data relied only on data points having $ThO_2$ >0.1 wt%, and were verified against the LA-ICP-MS results. The median U/Th ratio (EMPA and LA-ICP-MS) for the dataset is 26.9 with ~80% of the data having U/Th < 102 (Fig. 10). The lowest median values were obtained in the Cole (U/Th = 8.4) and highest from the SB2 phase of the Southern Breccia (U/Th = 39,414) prospects. In the Southern Breccia and Nori occurrences, different generations of uraninite have U/Th ratios that differ by up to 3 orders of magnitude (Nori-1 vs. Nori-2 and SB1 vs. SB2; Fig. 10).

The median concentrations of Pb can be separated into high (17.5 to 20.1 wt% PbO) and low (2.1 to 3.4 wt% PbO) groups; the entire dataset has a mean value of 17.86 wt%. The high PbO group comprises uraninite from the Cole, Fab, Nori (Nori-2), Southern Breccia (SB1) and DeVries Lake prospects, whereas the low PbO group is composed of uraninite from the

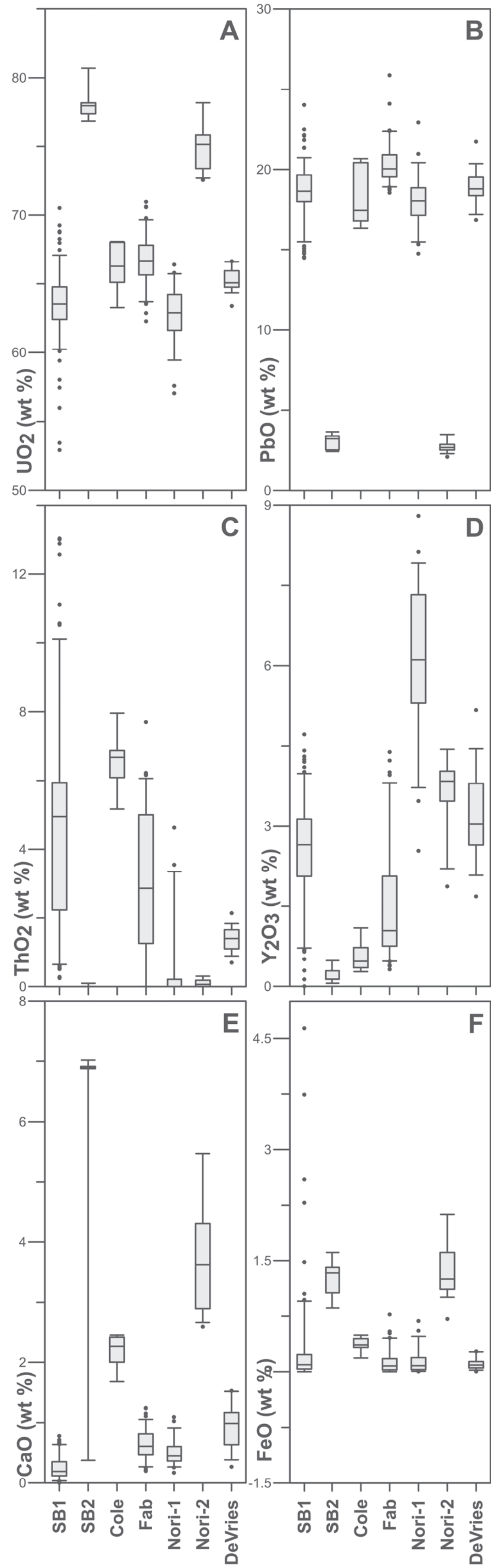


**FIGURE 9. A–G.** Major element concentrations of uraninite from the Great Bear magmatic zone occurrences, determined by EPMA.

Nori-1 and SB2 uraninite phases of the Nori and Southern Breccia prospects, respectively (Fig. 9B). The intra-occurrence variability was typically <1 wt%, but it can be up to 1.92 wt% in samples from the Cole occurrence.

Calcium is present in the majority of uraninite EPMA analyses and varies from below detection limit (<0.03 wt% CaO) up to 7.2 wt% CaO in SB2 (Fig. 9E). Similar to PbO, CaO data can be roughly separated into a low-concentration group (0.1 to 1.5 wt% CaO) and a more ill-defined high-concentration group (1.7 to 7.2 wt% CaO). The former group comprises uraninite from the Fab, DeVries Lake, Nori (Nori-2) and Southern Breccia (SB2) prospects, whereas the latter group includes uraninite from the Cole and Nori (Nori-1) prospects (Fig. 9E). Within-sample variability is commonly <0.5 wt%.

Yttrium concentrations vary from below detection limit (<0.06 wt% $Y_2O_3$) up to 8.8 wt%, with an overall mean $Y_2O_3$ value of 2.82 wt%. The Nori-2 uraninite grains have the highest (6.07 wt %) mean values, while SB2 has the lowest mean value (0.22 wt%). In the same way, the Fe concentrations varied greatly (from <detection limit to 4.64 wt% FeO), but unlike Y, most analyses are <1.0 wt%; the overall mean of the dataset is 0.27 wt% FeO. The concentration of Fe and Y in samples from the Nori and Southern Breccia prospects differentiates uraninite populations within each showing, i.e. Nori-1 versus Nori-2, and SB1 versus SB2 (Fig. 9D, 9F). A plot of $SiO_2$+CaO+FeO versus Pb in uraninite from the Great Bear magmatic zone occurrences (Fig. 11) demonstrates the presence of at least two generations of uraninite from the Nori/RA and Southern Breccia occurrences, plus PbO loss related to alteration, as reflected in increased CaO, FeO and $SiO_2$.

*Trace and Rare Earth Element Concentrations*

Trace element concentrations were determined by LA-ICP-MS. For the entire dataset, concentrations of Mn (median = 122 ppm), Mg (median = 66 ppm), Ti (median = 123 ppm) and V (median = 10 ppm) in uraninite vary from tens to thousands of ppm (Fig. 12). The Fab prospect uraninite has the lowest median values (<100 ppm). Trace element concentrations of uraninite from the Southern Breccia prospect illustrate the presence of two generations or populations: SB2 has systematically higher (up to two orders of magnitude) Mn, Mg, Ti, and V median values compared to SB1 (Fig. 12). In the Nori prospect, geochemical differences between the Nori-1 and Nori-2 populations are less marked, but in general, Nori-1 has higher Mn, Mg, Ti, and V than Nori-2.

Concentrations of ΣREE in uraninite from the Great Bear magmatic zone vary from 2.15 wt% up to 11.98 wt%. The overall ΣREE median value is 5.15 wt%, with uraninite from the Nori (Nori-1= 6.54 wt% and Nori-2= 6.43 wt%) and Southern Breccia (SB2= 2.40 wt%) prospects having the highest and lowest median values (Figs. 10, 12), respectively. In the Southern Breccia zone, median values of SB1 population have greater ΣREE (5.25 wt%), and HREE (1.76 wt%) contents relative to SB2 (ΣREE = 2.40 wt% and ΣHREE= 1,566 ppm). In the Nori prospect, Nori-1 (ΣLREE= 2.57 wt%) and Nori-2 (ΣLREE= 2.94 wt%) have comparable LREE contents.

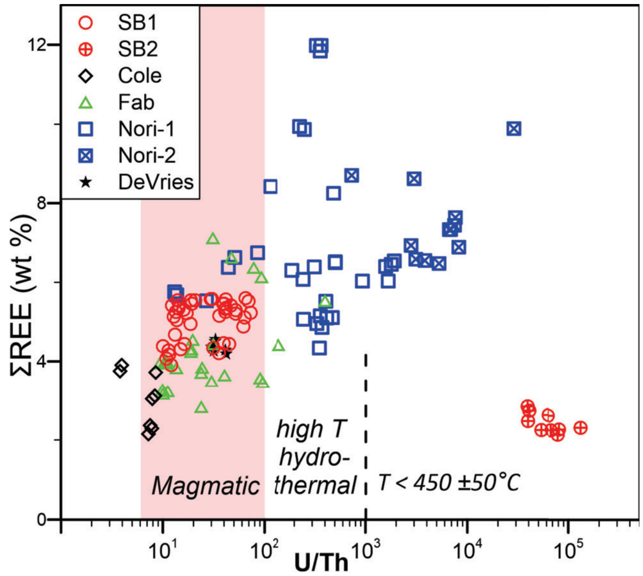


**FIGURE 10.** Total rare earth element (ΣREE) concentrations versus U/Th values in IOA-IOCG occurrences of the Great Bear magmatic zone, illustrating the high-temperature nature (low U/Th) of primary uraninite and the lower-temperature signature (higher U/Th) of the secondary phases (SB2 and Nori-2). Modified from Frimmel et al. (2014).

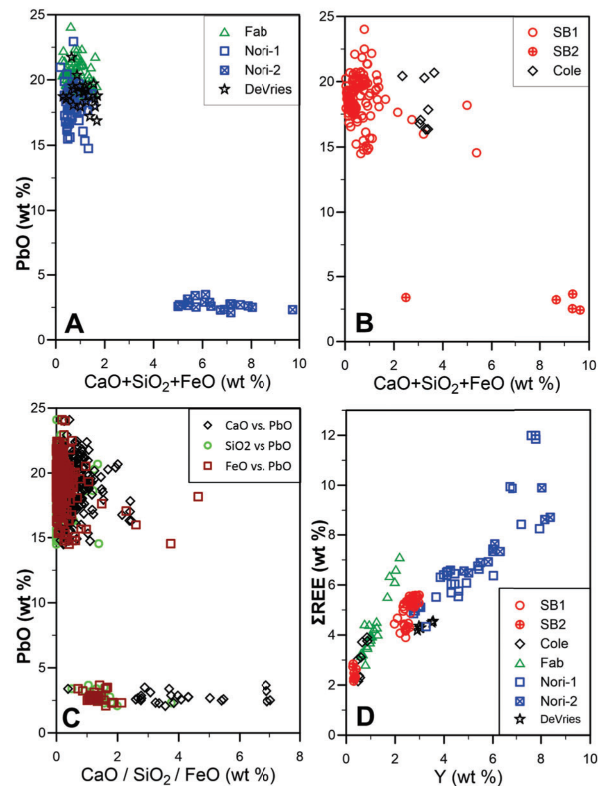


**FIGURE 11. A, B.** Variation in major elements illustrating the presence of two uraninite populations based on PbO versus CaO+FeO+$SiO_2$ (wt.%) contents. **C.** Plot indicating that the uraninite population with lower PbO contents contain greater CaO contents. **D.** Rare earth element versus yttrium concentrations in uraninite from the Great Bear magmatic zone.

Chondrite-normalized REE profiles of uraninite can be separated into three main groups based on their Ce/Yb ratios (Fig. 13). Uraninites with low Ce/Yb ratios (<4) occur in the Nori (Nori-1 and Nori-2), Southern Breccia SB1 phase and DeVries Lake prospects, and have slightly positive to flat REE patterns. Intermediate Ce/Yb ratios (7–21) include the Cole and Fab prospects, which have slightly negatively sloped REE patterns. The highest Ce/Yb ratios (up to 76) are recorded in the Southern Breccia SB2 phase, which also records the most negatively sloped REE profiles. Except for SB2, uraninite grains have negative Eu anomalies that vary in intensity.

## Discussion

*Signatures of the Major and Rare Earth Elements*

The incorporation of Si, Ca and Fe into the uraninite crystal structure is generally minor in high-temperature systems (e.g. magmatic), but tends to increase in uraninite formed at lower temperatures (Alexandre et al., 2015). Irrespective of the deposit type (high or low temperature), Pb versus Si+Fe+Ca plots of uraninite typically have an overall negative correlation, which is attributed to the incorporation of the latter elements into the crystal lattice in order to balance the loss of radiogenic lead during alteration events (Janeczek and Ewing, 1992; Alexandre and Kyser, 2005; Alexandre et al., 2015). In the Great Bear magmatic zone, most data exhibit a weak negative correlation between Pb and Si+Ca+Fe and cluster into two groups (Fig. 11), with higher CaO, FeO and $SiO_2$ in the altered or secondary uraninite populations. In the Southern Breccia occurrences, the early SB1 uraninite precipitated during high-temperature K-Fe alteration, and it contains significantly lower Si, Ca and Fe relative to SB2, which occurs in distinctively younger and lower temperature, chlorite-rich veinlets (Montreuil et al., 2015; Potter et al., 2019). At the Nori/RA prospect, the chemistry of the Nori-1 and Nori-2 uraninite populations (e.g. Ca, Fe and Si) is not influenced by the mineralization types (disseminated in hydrothermally altered metasiltstone, versus cross-cutting vein), and mineralogical evidence suggesting that these uraninite phases represent distinct hydrothermal events is scarce. However, the local development of Nori-2-type rims around larger pyrite crystals that elsewhere co-precipitated with Nori-1 and the higher Si+Ca+Fe and Pb contents indicate that the Nori-2 population corresponds to a later remobilization or alteration event. While the timing of these remobilization/alteration events is not defined, it is clear that uraninite in the IOCG showings precipitated during the primary ore-forming processes, but were subsequently altered.

Frimmel et al. (2014) proposed that the crystallization temperatures of uraninite could be estimated using U/Th ratios: if the ratio is >1000, low-temperature, epithermal conditions are inferred, but if U/Th <100, then amphibolite-facies or magmatic (granitic/pegmatitic) temperatures and conditions are inferred. The ΣREE content may also serve as a tool to discriminate between low and high crystallization temperatures; for example, ΣREE contents of >1 % in uraninite are indicative of crystallization temperatures >350°C (Frimmel et al., 2014). In the Great Bear magmatic zone, uraninite from the Cole, DeVries, and Fab occurrences (except for one outlier with U/Th=139) and the SB1 population of the Southern Breccia occurrences have U/Th <100, consistent with crystallization from high temperatures (e.g. >450°C in Fig. 10). These temperature estimates based on REE and Th/U values are consistent with precipitation of uraninite during the transition from high-temperature Ca-Fe to K-Fe alteration at temperatures >350°C (Fig. 2). In contrast, the higher and much more

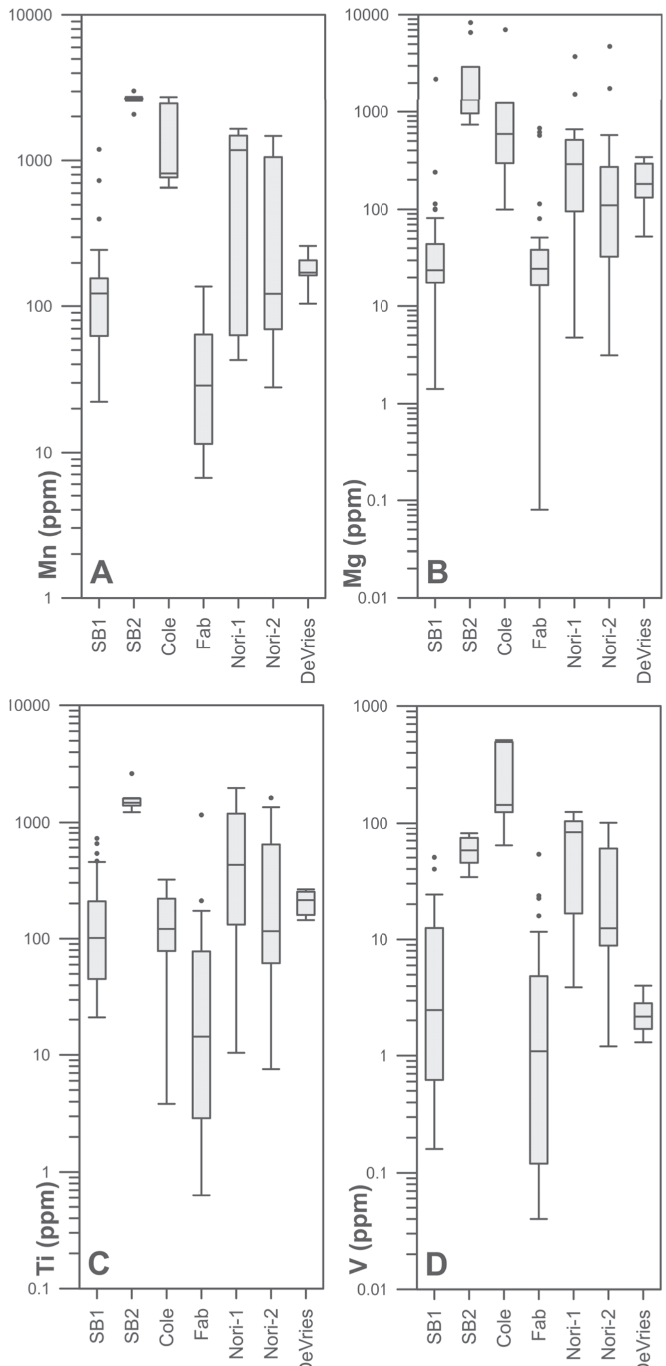


**FIGURE 12. A–D.** Trace element concentrations in uraninite as determined by LA-ICP-MS.

variable U/Th ratios in uraninite from the Southern Breccia SB2 population and Nori prospect (Nori-1 and Nori-2) suggest lower crystallization temperatures. Even though the SB2 population has ΣREE contents >1 wt %, the population plots close to the low-temperature hydrothermal fluids field defined by Frimmel et al. (2014) (Fig. 10). The 045°-trending earthy hematite-chlorite-K-feldspar veins that host SB2 uraninite transect the albitized host rocks and are consistent with a lower-temperature fluid distinct from that of the SB1 phase. Given the similarity in REE patterns between the SB2 uraninite and Southern Breccia Corridor whole-rock data (Potter et al., 2019), it is likely that the SB2 fluids sourced metals from the corridor during a post-iron oxide and alkali-calcic alteration event. As noted by Potter et al. (2019), the vein orientation parallels the late-stage (1850–1750 Ma) transcurrent faults found throughout the Great Bear magmatic zone. In the Nori prospect, the overall higher U/Th ratios of the Nori-2 uraninite phase may indicate lower temperatures of crystallization relative to Nori-1, consistent with the higher Ca+Fe+Si contents of Nori-1. However, the high ΣREE contents (>4 wt %) of both uraninite phases suggest precipitation within an overall high-temperature system (Fig. 10). This agrees with fluid inclusion work done by Ootes et al. (2010) on the uraninite-rich tourmaline-apatite veins, in which total homogenization (liquid-vapor-solid) temperatures of >400°C were recorded.

*Genetic Implications of the Rare Earth Element Profiles*

In general, analyses of uraninite from the Great Bear IOA-IOCG occurrences have chondrite-normalized profiles similar to uraninite that crystallized from high-temperature systems such as igneous intrusions and the Mistamisk veins reported in Mercadier et al. (2011) (Fig. 13). Although Kish and Cuney (1981) proposed that the Mistamisk occurrences formed in response to regional metamorphism (hence the term 'syn-metamorphic' in Mercadier et al., 2011), recent work by Corriveau et al. (2014) proposed that albite veins containing chlorite, hematite and uraninite occur within regional-scale corridors of albitite (Na alteration). When coupled with the presence of regional amphibole, magnetite, biotite, K-feldspar, hematite, carbonates, and white mica (i.e. high-temperature Ca-Fe, and K-Fe and low-temperature K-Fe alteration), this suggests that the district might host a previously unrecognized iron oxide and alkali-calcic system.

At the Nori prospect, the Nori-1 and Nori-2 uraninite populations display REE patterns similar to those of the DeVries Lake and SB1 prospects. However, Nori-1 exhibits stronger LREE depletion and HREE enrichment relative to Nori-2 (Fig. 13D), together with lower U/Th ratios and Ca+Fe+Si concentrations (Figs. 10, 11). Despite these differences, the similarity between Nori-1 and Nori-2 uraninite REE patterns, and abundances of Y and trace elements (Figs. 11D, 12, 13) supports a common source for both uraninite populations at Nori. The implication is that the REE signature of uraninite was preserved during remobilization and alteration (unlike major to minor elements such as Pb, Si, Ca, Fe, etc.), which increases the potential of this mineral to be used as a source indicator. This is consistent with experimental work on REE, O isotope and U-Pb systematics in uraninite that illustrate the preservation of chondrite-normalized REE profiles despite fluid-induced resetting of O and U-Pb isotopic systematics (Shabaga et al., 2021).

Although Frimmel et al. (2014) proposed that the Mary Kathleen U-REE deposit – in the Mary Kathleen Fold Belt of the Mt. Isa district in Australia – is a prime example of high-temperature uranium mineralization related to a major IOCG district, the classification and genesis of the deposit remains controversial as it lacks significant Cu and Au mineralization. Oliver et al. (1999) proposed that the deposit formed through interaction between regional metamorphic-hydrothermal fluids and 1750–1730 Ma calcic skarn (Oliver, 1995; Oliver et al., 2004), under amphibolite-facies conditions during a phase of the 1600–1580 Ma Isan orogeny (Oliver et al., 1991; Laing, 1998; Gauthier et al., 2001; Giles and Nutman, 2002; Hand and Rubatto, 2002). However, in the parallel Cloncurry district of the Mt. Isa block (which hosts the majority of the IOCG deposits), Mark et al. (2004), Marshall and Oliver (2006) and Oliver et al. (2008) have proposed that predominantly magmatic fluids drove metasomatism, with fluid-rock interactions along fluid flow paths explaining some of the diversity in alteration and mineralization styles in the district. Available U–Pb and Sm–Nd ages for the Mary Kathleen mineralization range from 1550 to 1470 Ma (Oliver et al., 1999). This is much younger than the primary calcic skarn and overlaps the age of thermal metamorphism in the Mt. Isa Block, which was driven by intrusion of the 1550–1500 Ma Williams Batholith (Page and Sun, 1998; Pollard et al., 1998; Mark et al., 1999; Davis et al., 2001). The age of the Mary Kathleen deposit also falls within error of the reported ages for the IOCG and affiliated deposits in the Cloncurry district (Oliver et al., 1999; Mark et al., 2004). Despite the possible involvement of somewhat analogous magmatic-hydrothermal fluids, the chondrite-normalized REE patterns of uraninite from Mary Kathleen are distinct from those of the Great Bear IOA-IOCG deposits, as they show a pronounced depletion in HREE (Frimmel et al., 2014; Fig. 13). The HREE depletion is especially critical when considering the association of uraninite and allanite at Mary Kathleen. In hydrothermal fluids, REE profiles rely on the REE budget of the mineralizing fluid (depending on the REE source), co-precipitating minerals capable of incorporating REE, and the oxidation state (Mercadier et al., 2011). As allanite preferentially incorporates LREE over HREE into its crystal structure (ΣLREE/ΣHREE >25,000), the presence of allanite should have caused LREE-depletion in the co-precipitating uraninite at Mary Kathleen – opposite to the pattern reported by Frimmel et al. (2014). Co-precipitating allanite is likely responsible for the slight LREE depletion of the Nori-1 and Nori-2 uraninite relative to other Great Bear occurrences (Fig. 13; Potter et al., 2014). Although geochronology indicates a significant time gap between mineralization and the clinopyroxene-garnet skarn bodies hosting the Mary Kathleen deposit, crystallization of a second generation of garnet during the main ore stage (Oliver et al., 1999), could have caused HREE depletion in the Mary Kathleen uraninite REE patterns as garnet has an affinity for HREE (Glaser et al., 1999).

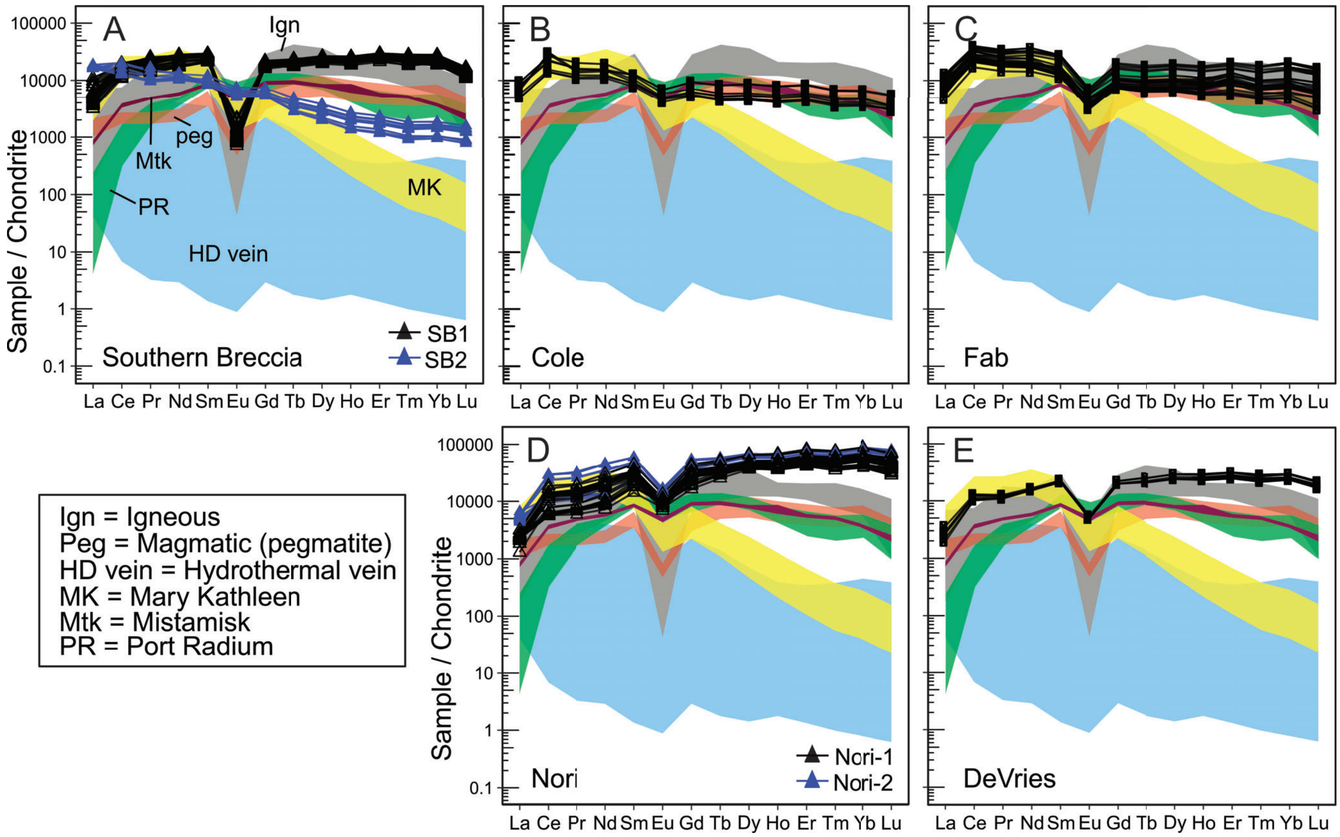


FIGURE 13. A–E. Chondrite-normalized REE plots of uraninite from IOA-IOCG occurrences of the Great Bear magmatic zone, plotted with reference to published data from Mercadier et al. (2011), Frimmel et al. (2014), Gandhi et al. (2018) and Potter et al. (2019). Normalized to McDonough and Sun (1995).

Uraninite grains from the Cole and Fab prospects are slightly enriched in LREE relative to HREE. Overall, these uraninite grains have MREE-HREE contents and Eu anomalies comparable to magmatic and high-temperature metasomatic uraninites, but with slightly higher LREE. The uranium-bearing assemblages in the Cole and Fab prospects do not include any REE-rich mineral (e.g. allanite) capable of influencing the partitioning of REE into uraninite, suggesting that the fluids that precipitated the uraninite were either originally enriched in LREE or had become enriched in LREE through evolving fluid-rock reactions, as described in Corriveau et al. (2016).

## Fingerprinting Uraninite Sources: Magmatic versus Non-magmatic Fluids in Formation of Iron oxide-copper-gold Deposits

The Great Bear magmatic zone is an unmetamorphosed Precambrian continental arc comparable to the younger Andean Cordillera (Ootes et al., 2017), in which early magmatism exhibits a direct link with formation of IOA-IOCG deposits (Hildebrand, 1986; Mumin et al., 2007, 2010; Corriveau et al., 2010, 2016; Somarin and Mumin, 2014; Montreuil et al., 2016a, b). The IOA-IOCG deposits in the southern portion of the Great Bear magmatic zone resulted from interaction between the Treasure Lake Group and exsolved fluids from the Faber Group volcanic and porphyritic intrusions, and/or from the magma chambers that crystallized the early albitized granitoids (Acosta-Góngora et al., 2015; Montreuil et al., 2016a, b). Variations in elemental associations and overprinting alteration assemblages reflect the evolution of fluid columns in systems that were periodically rejuvenated by magmatic-hydrothermal fluids (Montreuil et al., 2016b). Recent work by Acosta-Góngora et al. (2015, 2018) has shown that sulphide minerals from the Great Bear magmatic zone exhibit a dominantly magmatic sulphur isotope signature, contrary to sulphide minerals from the Andean cordillera IOCG deposits, where the input of non-magmatic sulphur ($\delta^{34}S > \sim 10$ and/or $\delta^{34}S < \sim -10$) is more prominent (Barton, 2014 and references therein). Similarly, a boron isotope study of tourmaline that precipitated within the iron oxide-alkali-calcic alteration from the Nori/RA and Southern Breccia occurrences have yielded boron isotopic values consistent with volcanic and plutonic sequences globally ($\delta^{11}B = -15‰$ to $-5‰$; Kelly et al., 2020). The negative $\delta^{11}B$ values indicate that the boron isotopic composition of the fluids was not contaminated by marine sequences, and are in contrast to tourmaline compositions from IOCG systems of the Coastal Cordillera of Chile ($\delta^{11}B = -10‰$ to $+6‰$; Tornos et al., 2012), the Dahongshan group in China ($\delta^{11}B = -14‰$ to $+6‰$; Su et al., 2016) and the Carajás Mineral Province of Brazil ($\delta^{11}B = +14‰$ to $+26‰$, $+6‰$ to $+9‰$, and $-8‰$ to $+11‰$; Xavier et al., 2008). Overall, the uraninite chemistry presented in this study suggests precipitation from high-temperature fluids, similar to uraninite precipitated in magmatic systems. However, the extensive metasomatic footprints of these systems and evolving fluid chemistries indicate that the magmatic fluids evolved through extensive fluid-rock interactions as hydrothermal cells formed over the magmatic heat sources. This is consistent with previous studies and emphasizes the significant role of magmatic-hydrothermal fluids in the formation of the Great Bear magmatic zone IOA-IOCG occurrences (e.g. Richards and Mumin, 2013; Somarin and Mumin, 2014; Acosta-Góngora et al., 2015, 2018; Montreuil et al., 2016a, b; Ootes et al., 2017; Kelly et al., 2020). Alteration of uraninite to coffinite at most of the occurrences also points to increasing silica activity in the later ore-forming fluids, consistent with field observations noting the presence of quartz-rich epithermal-style veining peripheral to the IOA-IOCG deposits (Potter et al., 2014).

Recent experimental work by Timofeev et al. (2018) has highlighted the presence of a previously unrecognized uranium chloride species ($UCl_4^0$) in reduced, acidic and high-temperature fluids. This new species increases uranium concentrations by up to 4 ppm at 400°C (Cl- = 0.10 and pH = 2.5), is more stable under reducing conditions, and reverses the long-standing notion that $U^{4+}$ is immobile. In modelling the behavior of this species in IOCG systems at 400°C, Timofeev et al. (2018) reported that increasing the oxygen fugacity via fluid mixing and gradually decreasing the temperature of the fluids did not lead to uraninite precipitation, but instead changed the uranium species in solution. However, increasing the pH of the oxidizing solution through interaction with wall rocks or mixing with meteoric waters led to precipitation of uranium minerals. Furthermore, under more reducing ($\log fO_2 = -35$) conditions, a decrease in temperature promoted uraninite deposition. While the modelling was completed at 400°C, increasing the temperature of the fluids to temperatures recorded in IOCG deposits worldwide (Fig. 2) would increase the concentration of dissolved uranium chloride species by orders of magnitude — thereby providing a mechanism to transport significant quantities of uranium under reduced conditions during formation of IOCG deposits (Timofeev et al., 2018).

All of the IOA-IOCG occurrences of the Great Bear magmatic zone are temporally and spatially associated with shoshonitic to high K, calc-alkaline intrusions (Montreuil et al., 2016a). The solubility of chlorine in silicate melts is higher in alkali-rich magmas (Webster and DeVivo, 2002), and chlorine preferentially partitions into aqueous fluids rather than silicate melts (Kilinc and Burnham, 1972; Metrich and Rutherford, 1992; Kravchuk and Keppler, 1994; Webster, 1997, 2004), indicating that fluids exsolved from the alkaline intrusions may have be chlorine-rich. As proposed by Montreuil et al. (2016c) in a geochemical study of the Fab system, high fluorine and chlorine contents of the country rocks and unusual element mobility recorded in the alteration facies provide strong evidence of high halogen activities ($F^-$ and $Cl^-$) in the magmatic-hydrothermal fluids. Sulphide mineral precipitation during the high-temperature, magnetite-bearing K-Fe facies alteration, followed by precipitation of hematite during lower-temperature K-Fe alteration, reflects decreasing temperatures, pressures, and ligand activities, increasing $fO_2$ and changing pH conditions as the fluids evolved and interacted with the host rocks. Therefore, geological mapping and geochemical modelling support cooling of a reduced fluid, or destabilization of chloride-species in solution through fluid mixing or fluid-rock interactions, as a trigger for uraninite precipitation in magnetite-bearing IOA-IOCG deposits.

The presence of distinct compositions of uraninite at Nori and the Southern Breccia attests to the potential for multiple generations of uranium enrichment within the systems. For example, in an examination of uraninite from Olympic Dam, Macmillan et al. (2016) highlighted at least four main classes of uraninite based on major element chemistry, reflecting at least two mineralization events plus numerous dissolution and re-precipitation events. However, as shown by the composition of uraninite from the Nori occurrence, remobilization and alteration of primary uraninite (indicated by lower Pb and increased Ca, Si, Fe contents plus formation of coffinite) has only a minor effect on the chondrite-normalized REE patterns. Other than the Southern Breccia occurrence, most systems record one primary uranium event, followed by alteration that removed radiogenic Pb and increased Ca, Si and Fe contents. At the Southern Breccia, later brittle faulting and veining unrelated to the primary IOA-IOCG mineralization produced uraninite generations having distinct trace element patterns (SB2, Fig. 13; Potter et al., 2019). Despite multiple generations of uraninite recorded at Olympic Dam, uranium isotopes also suggest that uranium was derived either directly from magmatic fluids or leached from the volcanic and/or volcanogenic country rocks, and precipitated under high-temperature conditions (Bopp et al., 2009; Brennecka et al., 2010; Hiess et al., 2012; Kirchenbaur et al., 2016). Furthermore, in a geochemical study of both magnetite- and hematite-group deposits and prospects from the Gawler province, Fabris (2022) noted that uranium enrichment in samples from magnetite-dominated occurrences are commonly similar or greater in magnitude than in hematite-dominated occurrences, indicating that primary uranium mineralization occurs early in the development of these ore systems (i.e. during magnetite alteration).

## Concluding Remarks

Uraninite from the Great Bear magmatic zone IOA-IOCG occurrences has generally low U/Th ratios (<100), high ΣREE (>2 wt%) contents and relatively flat, chondrite-normalized REE patterns (Ce/Yb <21) consistent with crystallization from high-temperature (>400°C) fluids. Slight REE enrichments and/or depletions in the uraninite relative to the fluid reservoir might result from co-precipitation of uraninite with other REE-rich mineral phases (e.g. allanite at the Nori prospect) or due to the REE-enriched nature of the source (e.g. LREE enrichments in Fab and Cole). The most notable exception is the Southern Breccia SB2 uraninite phase, which is hosted by chlorite-rich veinlets in a shear zone. SB2 uraninite has up to

3 orders of magnitude higher U/Th ratios (> 39000), lower ΣREE values (~2 wt%) and negatively sloped (median Ce/Yb >31) chondrite-normalized REE patterns, suggesting precipitation during a distinct, lower-temperature event unrelated to the iron oxide and alkali-calcic system. Much like vein-type deposits (Mercadier et al., 2011), the chondrite-normalized REE patterns of the SB2 uraninite mirror those of the host whole-rock data (Potter et al., 2019).

At the Nori prospect, alteration of Nori-1 uraninite apparently results in the formation of the Nori-2 uraninite, as recorded by their distinct Ca, Si, Fe and Pb contents. Despite variations in these elements, Nori-1 and Nori-2 uraninite phases yield indistinguishable REE patterns. The preservation of a primary REE signature in Nori-2 uraninite supports previous studies proposing that hydrothermal overprints have a limited or negligible impact on uraninite REE chemistry, and thus, it may constitute a viable tool for fingerprinting uranium sources (Frimmel et al., 2014).

The chemistry of uraninite from the Great Bear magmatic zone IOA-IOCG occurrences is interpreted to reflect (a) scavenging of metals (country rock metal fluxing of Richards and Mumin, 2013) by magmatic-driven fluids during reduced Na alteration, and (b) subsequent precipitation from fluids that evolved and equilibrated through progressive Na (albite), high temperature Ca-Fe (amphibole + magnetite) and ultimately high-temperature K-Fe (K-feldspar/biotite + iron oxides) metasomatism/alteration. In most systems, petrography, field observations and geochemistry indicate precipitation of primary uraninite during the transition from high-temperature Ca-Fe to high-temperature K-Fe facies in magnetite-dominant (reduced) assemblages. Unlike two-fluid models proposed for certain hematite-group IOCG ± U deposits (Skirrow, 2022), primary uranium enrichment in the Great Bear magmatic zone magnetite-dominant systems was likely sourced and transported as chloride species by high-temperature, reducing fluids rather than by oxidized brines. The results of this study are supported by recently published works on the stability of uranium chloride species, tourmaline boron isotope chemistry, and sulphur isotopes from the Great Bear magmatic zone. Uranium precipitation was likely triggered by cooling of the fluids and/or changes in fluid chemistry induced by extensive fluid-rock interactions. Finally, alteration of uraninite to coffinite at many of the occurrences also points to increasing silica activity in the residual fluids, consistent with field observations noting the presence of quartz-rich epithermal-style veining peripheral to IOA-IOCG deposits and the metasomatic iron oxide and alkali-calcic ore system model of Corriveau et al. (2016, 2022).

## Acknowledgments

This Natural Resources Canada (NRCan) contribution stems from the Targeted Geoscience Initiative (TGI) program and builds on data and results of the IOCG/Multiple Metals Great Bear Region project of the Geo-mapping for Energy and Minerals program conducted under collaborative agreements with the Northwest Territories Geoscience Office, the Community Government of Gamèti and Fortune Minerals Limited. Fieldwork and research was permitted under the Aurora Research Institute Scientific Research licenses 14548, 14649, Fortune Minerals Limited land use permit and NRCan land use permit W2010J0004 granted by the Wek'èezhìi Land and Water Board, and NWT archaeological sites database agreement # DR2009-335 and # DR2010-390. Field logistics fall in part under the Polar Continental Shelf Program project 00410. The authors would like to acknowledge the significant logistical support provided by Fortune Minerals Limited and field support from D. Apple, A. Arrowmaker, C. Arrowmaker, V. Boulanger-Martel, A. De Toni, C. Fontaine, L.-P. Gélinas, C. Gon, F. Gon, P. Normandeau and E. Williah. Technical assistance was provided by P. Hunt, K. Venance and J.-S. Comeau. Charlie Jefferson, Hamid Mumin, Duane Petts and Reginald Wilson are thanked for their thorough reviews and editorial handling of the manuscript. NRCan contribution number 20210044.

Supplementary data are available at https://doi.org/10.4095/328300 (Geological Survey of Canada, Open File 8798).

## References

Acosta-Góngora, P., Gleeson, S.A., Ootes, L., Jackson, V.A., Lee, M., and Samson, I., 2011, Preliminary observations on the IOCG mineralogy at the Damp, Fab, and Nori showings and Terra-Norex mines, Great Bear magmatic zone: N.W.T. Geoscience Office, Open File Report 2011-01, 11 p.

Acosta-Góngora, P., Gleeson, S.A., Samson, I.M., Corriveau, L., Ootes, L., Taylor, B.E., Creaser, R.A., and Muehlenbachs, K., 2015, Genesis of the Paleoproterozoic NICO iron-oxide-cobalt-gold-bismuth deposit, Northwest Territories, Canada: evidence from isotope geochemistry and fluid inclusions: Precambrian Research, v. 268, p. 168-193.

Acosta-Góngora, P., Gleeson, S.A., Samson, I.M., Corriveau, L., Ootes, L., Jackson, S.E., Taylor, B.E., and Girard, I., 2018, Origin of sulfur and crustal recycling of copper in polymetallic (Cu-Au-Co-Bi-U±Ag) iron-oxide-dominated systems in the Great Bear Magmatic Zone, NWT, Canada: Mineralium Deposita, v. 53, p. 353-376.

Alexandre, P., and Kyser, T.K., 2005, Effects of cationic substitutions and alteration in uraninite, and implications for the dating of uranium deposits: The Canadian Mineralogist, v. 43, p. 1005-1017.

Alexandre, P., Kyser, K., Layton-Matthews, D., and Brian, J., 2015, Chemical compositions of natural uraninite: The Canadian Mineralogist, v. 53, p. 595-622.

Armstrong, J.T., 1988, Quantitative analysis of silicates and oxide minerals: comparison of Monte-Carlo, ZAF and Phi-Rho-Z procedures, *in* Newbury, D.E., ed., Microbeam analysis: San Francisco Press, p. 239-246.

Azar, B., 2007, The lithogeochemistry of volcanic and subvolcanic rocks of the Fab Lake area, Great Bear magmatic zone, Northwest Territories, Canada: B.Sc. thesis, University of Toronto, Toronto, 96 p.

Barton, M.D., 2014, Iron oxide-(-Cu-Au-REE-P-Ag-U-Co) systems, *in* Turekian, K., Holland, H. and Scott, S.D., eds, Treatise on Geochemistry, v. 13, 2nd edition., Elsevier, New York, p. 515-541.

Benavides, J., Kyser, T.K., Clark, A.H., Oates, C.J., Zamora, R., Tarnovschi, R., and Castillo, B., 2007, The Mantoverde iron oxide-copper-gold district, III Región, Chile: the role of regionally derived, non magmatic fluids in chalcopyrite mineralization: Economic Geology, v. 102, p. 415-440.

BHP, 2018, BHP Billiton Limited annual report 2018, 300 p. available at: www.bhp.com/investor-centre.

Bonhoure, J., Kister, P., Cuney, M., and Deloule, E., 2007, Methodology for rare earth element determinations of uranium oxides by ion microprobe: Geostandards and Geoanalytical Research, v. 31, p. 209-225.

Bopp, IV, C.J., Lundstrom C.C., Johnson, T.M., and Glessner J.J.G., 2009, Variations in $^{238}U/^{235}U$ in uranium ore deposits: isotopic signatures of the U reduction process?: Geology v. 37, p. 611-614.

Bowring, S.A., 1984, Uranium–lead zircon geochronology of Early Proterozoic Wopmay Orogen, Northwest Territories, Canada: an example of rapid crustal evolution: Ph.D. thesis, University of Kansas, Lawrence, 148 p.

Brennecka, G.A., Borg, L.E., Hutcheon, I.D., Sharp, M.A., and Anbar, A.D., 2010, Natural variations in uranium isotope ratios of uranium ore concentrates: understanding the $^{238}U/^{235}U$ fractionation mechanism: Earth and Planetary Science Letters, v. 291, p. 228-233.

Burgess, H., Gowans, R.M., Hennessey, B.T., Lattanzi, C.R., and Puritch, E., 2014, Technical report on the feasibility study for the NICO gold–cobalt–bismuth–copper deposit, Northwest Territories, Canada: Fortune Minerals Ltd., NI 43-101 Technical Report No. 1335, 385 p., available at: www.sedar.com

Byron, S.J., 2010, Giant quartz veins of the Great Bear magmatic zone, Northwest Territories, Canada: M.Sc. thesis, University of Alberta, Edmonton, Alberta, 146 p.

Camier, J., 2002, The Sue-Dianne Fe-oxide Cu-Ag-Au breccia complex, southern Great Bear Magmatic Zone, Northwest Territories, Canada: M.Sc. thesis, University of Western Ontario, London, Ontario, 210 p.

Corriveau, L., 2007, Iron oxide copper–gold deposits: a Canadian perspective, *in* Goodfellow, W.D., ed., Mineral deposits of Canada: a synthesis of major deposit-types, district metallogeny, the evolution of geological provinces and exploration methods: Geological Association of Canada, Mineral Deposits Division, Special Publication 5, p. 307-328.

Corriveau, L., Williams, P.J., and Mumin, A.H., 2010, Alteration vectors to IOCG mineralisation – from uncharted terranes to deposits, *in* Corriveau, L. and Mumin, A.H., eds, Exploring for iron oxide copper-gold deposits: Canada and global analogues: Geological Association of Canada, Short Course Notes, No. 20, p. 89-110.

Corriveau, L., Mumin, A.H., and Montreuil, J.-F., 2011, The Great Bear magmatic zone: the IOCG spectrum and related deposit types: Proceedings of the 11th SGA Biennial Meeting, Antofagasta, Chile, p. 524-526.

Corriveau, L., Nadeau, O., Montreuil, J.-F., and Desrochers, J.-P., 2014, Report of activities for the Core Zone: strategic geomapping and geoscience to assess the mineral potential of the Labrador Trough for multiple metals IOCG and affiliated deposits, Canada: Geological Survey of Canada, Open File 7714, 12 p.

Corriveau, L., Montreuil, J.-F., and Potter, E.G., 2016, Alteration facies linkages among IOCG, IOA and affiliated deposits in the Great Bear magmatic zone, Canada, *in* Slack, J., Corriveau, L. and Hitzman, M., eds, Proterozoic iron oxide-apatite (± REE) and iron oxide-copper-gold and affiliated deposits of Southeast Missouri, USA, and the Great Bear magmatic zone, Northwest Territories, Canada: Economic Geology, v. 111,p. 2045-2072.

Corriveau, L., Potter, E.G., Montreuil, J.-F., Blein, O., Ehrig, K., and De Toni, A., 2018, Iron-oxide and alkali-calcic alteration ore systems and their polymetallic IOA, IOCG, skarn, albitite-hosted U±Au±Co, and affiliated deposits: a short course series. Part 2: overview of deposit types, distribution, ages, settings, alteration facies, and ore deposit models: Geological Survey of Canada, Scientific Presentation 81, 154 p.

Corriveau, L., Mumin, A.H., and Potter, E.G., 2022, Mineral systems with iron oxide-copper-gold (Ag-Bi-Co-U-REE) and affiliated deposits: introduction and overview, *in* Corriveau, L., Potter, E.G. and Mumin, A.H., eds., Mineral systems with iron oxide-copper-gold (IOCG) and affiliated deposits: Geological Association of Canada, Special Paper 52, p. 1-25.

Cuney, M., 2010, Evolution of uranium fractionation processes through time: driving the secular variation of uranium deposits: Economic Geology, v. 105, p. 553-569.

Davidson, G.J., and Paterson, H.L., 1993, Oak Dam East: a prodigious uranium-bearing, massive oxide body on the Stuart shelf: Geological Society of Australia Abstracts, v. 34, p. 18-19.

Davidson, G.J., Paterson, H., Meffre, S., and Berry, R.F., 2007, Characteristics and origin of the Oak Dam East breccia-hosted, iron oxide Cu-U-(Au) deposit: Olympic Dam region, Gawler Craton, South Australia: Economic Geology, v. 102, p. 1471-1498.

Davis, B.K., Pollard, P.J., Lally, J.H., McNaughton, N.J., Blake, K., and Williams, P.J., 2001, Deformation history of the Naraku batholith, Mount Isa inlier, Australia: implications for pluton ages and geometries from structural studies of the Dipvale Granodiorite and Levian Granite: Australian Journal of Earth Sciences, v. 48, p. 131-150.

Davis, W.J., Corriveau, L., van Breemen, O., Bleeker, W., Montreuil, J.-F., Potter, E.G., and Pelleter, E., 2011, Timing of IOCG mineralizing and alteration events within the Great Bear magmatic zone, *in* Fischer, B.J. and Watson, D.M., eds., 39th Annual Yellowknife Geoscience Forum Abstracts: Northwest Territories Geoscience Office, p. 97.

Davis, W.J., Ootes, L., Newton, L., Jackson, V., and Stern, R.A., 2015, Characterization of the Paleoproterozoic Hottah terrane, Wopmay Orogen using multi-isotopic (U-Pb, Hf and O) detrital zircon analyses: an evaluation of linkages to northwest Laurentian Paleoproterozoic domains: Precambrian Research, v. 269, p. 296-310.

De Toni, A.F., 2016, Les paragénèses à magnétite des altérations associées aux systèmes à oxydes de fer et altérations en éléments alcalins, zone magmatique du Grand lac de l'Ours: M.Sc. thesis, Institut national de la Recherche scientifique, Quebec, 534 p.

Dragon Mining, 2012, Resource update for the Hangaslampi deposit, Kuusamo gold project, 10 p., available at: www.dragonmining.com/asx-releases-2012.

Fabris, A., 2022, Geochemical characteristics of IOCG deposits from the Olympic Copper-gold Province, South Australia, *in* Corriveau, L., Potter, E.G. and Mumin, A.H., eds., Mineral systems with iron oxide-copper-gold (IOCG) and affiliated deposits: Geological Association of Canada, Special Paper 52, p. 247-262.

Fayek, M., and Kyser, T.K., 1997, Characterization of multiple fluid-flow events and rare-earth-element mobility associated with formation of unconformity-type uranium deposits in the Athabasca Basin, Saskatchewan: The Canadian Mineralogist, v. 35, p. 627-658.

Frimmel, H.E., Schedel, S., and Brätz, H., 2014, Uraninite chemistry as forensic tool for provenance analysis: Applied Geochemistry, v. 48, p. 104-121.

Fryer, B.J., and Taylor, R.P., 1987, Rare earth elements distributions in uraninites: implications for ore genesis: Chemical Geology, v. 63, p. 101-108.

Furnival, G.M., 1935, Large quartz veins of the Great Bear Lake, Canada: Economic Geology, v. 30, p. 843-859.

Gandhi, S.S., 1988, Volcano-plutonic setting of U-Cu bearing magnetite veins of FAB claims, southern Great Bear magmatic zone, Northwest Territories: Geological Survey of Canada, Paper 88-1C, p. 177-187.

Gandhi, S.S., 1994, Geological setting and genetic aspects of mineral occurrences in the southern Great Bear Magmatic Zone, Northwest Territories: Geological Survey of Canada, Bulletin 475, p. 63-96.

Gandhi, S.S., 2003, An overview of the Fe oxide-Cu-Au deposits and related deposit types: Canadian Institute of Mining and Metallurgy Conference, Montreal, Canada.

Gandhi, S.S., and Prasad, N., 1993, Regional metallogenic significance of Cu, Mo, and U occurrences at DeVries Lake, southern Great Bear magmatic zone, Northwest Territories: Geological Survey of Canada, Paper 93-1C, p. 29-39.

Gandhi, S.S., and van Breemen, O., 2005, SHRIMP U-Pb geochronology of detrital zircons from the Treasure Lake Group; new evidence for Paleoproterozoic collisional tectonics in the southern Hottah Terrane, northwestern Canadian Shield: Canadian Journal of Earth Sciences, v. 42, p. 833-845.

Gandhi, S.S., Carrière, J.J., and Prasad, N., 2000, Implications of a preliminary fluid-inclusion study of giant quartz veins of the southern Great Bear magmatic zone, Northwest Territories: Geological Survey of Canada, Paper 2000-1C, 13 p.

Gandhi, S.S., Mortensen, J.K., Prasad, N., and van Breemen, O., 2001, Magmatic evolution of the southern Great Bear continental arc, northwestern Canadian Shield: geochronological constraints: Canadian Journal of Earth Sciences, v. 38, p. 767-785.

Gandhi, S.S., Montreuil, J.-F., and Corriveau, L., 2014, Geology and mineral occurrences, Mazenod Lake-Lou Lake area, Northwest Territories: Geological Survey of Canada, Canadian Geoscience Map 148, scale 1:50 000.

Gandhi, S.S., Potter, E.G., and Fayek, M., 2018, New constraints on genesis of the polymetallic veins at Port Radium, Great Bear Lake, Northwest Canadian Shield: Ore Geology Reviews, v. 96, p. 28-47.

Gauthier, L., Hall, G., Stein, H., and Schaltegger, U., 2001, The Osborne deposit, Cloncurry district: a 1595 Ma Cu-Au skarn deposit: James Cook University, School of Earth Sciences, Economic Geology Research Unit Contribution, v. 59, p. 58-59.

Giles D., and Nutman, A.P., 2002, SHRIMP U–Pb monazite dating of 1600–1580 Ma amphibolite facies metamorphism in the southeastern Mt Isa Block, Australia: Australian Journal of Earth Sciences, v. 49, p. 455-465.

Glaser, S.M., Foley, S.F., and Gunther, D., 1999, Trace element compositions of minerals in garnet and spinel peridotite xenoliths from the Vitim volcanic field, Transbaikalia, eastern Siberia: Lithos, v. 48, p. 263-285.

Goad, R.E., Mumin, A.H., Duke, N.A., Neale, K.L., and Mulligan, D.L., 2000a, Geology of the Proterozoic iron oxide-hosted, NICO cobalt-gold-bismuth, and Sue Dianne copper-silver deposits, southern Great Bear magmatic zone, Northwest Territories, Canada, *in* Porter T.M., ed., Hydrothermal iron oxide copper-gold and related deposits. A global perspective, volume 1: PGC Publishing, Adelaide, p. 249-267.

Goad, R.E., Mumin, A.H., Duke, N.A., Neale, K.L., Mulligan, D.L., and Camier, W.J., 2000b, The NICO and Sue-Dianne Proterozoic, iron oxide-hosted, polymetallic deposits, Northwest Territories. Application of the Olympic Dam model in exploration: Exploration and Mining Geology, v. 9, p. 123-140.

Gosh, D., Dutta, T., Samanta, S.K., and Pal, D.C., 2013, Texture, microstructure and geochemistry of magnetite from the Banduhurang uranium mine, Singhbhum Shear Zone, India – Implications for physico-chemical evolution of magnetite mineralization: Journal Geological Society of India, v. 81, p. 101-112.

Gray, D., Cameron, T., and Briggs, A., 2016, Guelb Moghrein copper gold mine, Inchiri, Mauritania: NI43-101 Technical Report, 109 p., available at: www.first-quantum.com.

Griffin, W.L., Powell, W.J., Pearson, N.J., and O'Reilly, S.Y., 2008, GLITTER: data reduction software for laser ablation ICP-MS, *in* Sylvester, P., ed., Laser Ablation ICP-MS in the Earth Sciences: current practices and outstanding issues: Mineralogical Association of Canada, Short Course Series, v. 40, p. 307-311.

Groves, D.I., Bierlein, F.P., Meinert, L.D., and Hitzman, M.W., 2010, Iron oxide copper-gold (IOCG) deposits through Earth history. Implications for origin, lithospheric setting, and distinction from other epigenetic iron oxide deposits: Economic Geology, v. 105, p. 641-654.

Guillong, M., Hametner, K., Reusser, E., Wilson, S.A., and Günther, D., 2005, Preliminary characterisation of new glass reference materials (GSA-1G, GSC-1G, GSD-1G and GSE-1G) by laser ablation-inductively coupled plasma-mass spectrometry using 193 nm, 213 nm and 266 nm wavelengths: Geostandards and Geoanalytical Research, v. 29, p. 315-331.

Hand, M., and Rubatto, D., 2002, The scale of the thermal problem in the Mount Isa inlier: Geological Society of Australia Abstracts, v. 67, p. 173.

Hayward, N., and Corriveau, L., 2014, Fault reconstructions using aeromagnetic data in the Great Bear magmatic zone, Northwest Territories, Canada: Canadian Journal of Earth Sciences, v. 51, p. 1-16.

Hennessey, B.T., and Puritch, E., 2008, A technical report on a mineral resource estimate for the Sue-Dianne deposit, Mazenod Lake area, Northwest Territories, Canada: Fortune Minerals Limited, National Instrument 43-101 Technical Report, available at www.sedar.com.

Hidaka, H., and Gauthier-Lafaye, F., 2001, Neutron capture effects on Sm and Gd isotopes in uraninites: Geochimica et Cosmochimica Acta, v. 65, p. 941-949.

Hidaka, H., Hollinger, P., Shimuzu, H., and Masuda, A., 1992, Lanthanide tetrad effect observed in the Oklo and ordinary uraninites and implication for their forming processes: Geochemistry Journal, v. 26, p. 337-346.

Hiess, J., Condon, D.J., McLean, N., and Noble, R., 2012, $^{238}U/^{235}U$ systematics in terrestrial uranium-bearing minerals: Science, v. 335, p. 1610-1614.

Hildebrand, R.S., 1986, Kiruna-type deposits: their origin and relationship to intermediate subvolcanic plutons in the Great Bear magmatic zone, Northwestern Canada: Economic Geology, v. 81, p. 640-659.

Hildebrand, R.S., Hoffman, P.F., and Bowring, S.A., 1987, Tectono-magmatic evolution of the 1.9 Ga Great Bear magmatic zone, Wopmay Orogen, Northwestern Canada: Journal of Volcanology and Geothermal Research, v. 32, p. 99-118.

Hildebrand, R.S., Hoffman, P.F., and Bowring, S.A., 2010a, The Calderian orogeny in Wopmay orogen (1.9 Ga), northwest Canadian Shield: Geological Society of America Bulletin, v. 122, p. 794-814.

Hildebrand, R.S., Hoffman, P.F., Housh, T., and Bowring, S.A., 2010b, The nature of volcano-plutonic relations and shapes of epizonal plutons of continental arcs as revealed in the Great Bear magmatic zone, northwestern Canada: Geosphere, v. 6, p. 812-839.

Hitzman, M.W., and Valenta, R.K., 2005, Uranium in iron oxide-copper-gold (IOCG) systems: Economic Geology, v. 100, p. 1657-1661.

Hoffman, P., and Hall, L., 1993, Geology, Slave craton and environs; District of Mackenzie, Northwest Territories: Geological Survey of Canada, Open File 2559, scale 1: 1,000,000.

Jackson, S.E., 2008, Calibration strategies for elemental analysis by LA-ICP-MS, *in* Sylvester, P., ed., Laser ablation-ICP-mass spectrometry in the Earth sciences: current practices and outstanding issues: Mineralogical Association of Canada, Short Course Series, v. 40, p. 169-188.

Jackson, S.E., and Cabri, L.J., 2011, Progress in quantitative determination and mapping of trace elements in sulfides minerals using LAICPMS: Geological Association of Canada-Mineralogical Association of Canada joint annual meeting, Ottawa, Program with Abstracts, v. 34, p. 101-102.

Jackson, V.A., and Ootes, L., 2012, Preliminary geologic map of the south-central Wopmay Orogen (parts of NTS 86B, 86C, and 86D); results from 2009 to 2011: Northwest Territories Geoscience Office, NWT Open Report 2012-004, 1 map, 1:100,000 scale.

Jackson, V.A., van Breemen, O., Ootes, L., Bleeker, W., Bennett, V., Davis, W.J., Ketchum, J., and Smar, L., 2013, U-Pb zircon ages and field relationships of Archean basement and Paleoproterozoic intrusions, south-central Wopmay Orogen, NWT: implications for tectonic assignments: Canadian Journal of Earth Sciences, v. 50, p. 979-1006.

Janeczek, J., and Ewing, R.C., 1992, Structural formula of uraninite: Journal of Nuclear Materials, v. 190, p. 128-132.

Jochum, K.P., Willbold, M., Raczek, I., Stoll, B., and Herwig, K., 2005, Chemical characterisation of the USGS reference glasses GSA-1G, GSC-1G, GSD-1G, GSE-1G, BCR-2G, BHVO-2G and BIR-1G using EPMA, ID-TIMS, ID-ICP-MS and LA-ICP-MS: Geostandards and Geoanalytical Research, v. 29, p. 285-302.

Kelly, C., Davis, W.J., Potter, E.G., and Corriveau, L., 2020, Geochemistry of hydrothermal tourmaline from IOCG occurrences in the Great Bear magmatic zone: implications for fluid source(s) and fluid composition evolution: Ore Geology Reviews, v. 118, 103329.

Kilinc, I.A., and Burnham, C.W., 1972, Partitioning of chloride between a silicate melt and coexisting aqueous phase from 2 to 8 kilobars: Economic Geology, v. 67, p. 231-235.

Kirchenbaur, M., Mass, R., Ehrig, K., Kamenetsky, V.S., Strub, E., Ballhaus, C., and Munker, C., 2016, Uranium and Sm isotope studies of the supergiant Olympic Dam Cu–Au–U–Ag deposit, South Australia: Geochimica et Cosmochimica Acta, v. 180, p. 15-32.

Kish, L., and Cuney, M., 1981, Uraninite-albite veins from the Mistamisk Valley of the Labrador Trough, Quebec: Mineralogical Magazine, v. 44, p. 471-483.

Kolb, J., Sakellaris, G.A., and Meyer, F.M., 2006, Controls on hydrothermal Fe oxide–Cu–Au–Co mineralization at the Guelb Moghrein deposit, Akjoujt area, Mauritania: Mineralium Deposita, v. 41, p. 68-81.

Kravchuk, I.F., and Keppler, H., 1994, Distribution of chloride between aqueous fluids and felsic melts at 2 kbar and 800 degrees C: European Journal of Mineralogy, v. 6, p. 913-923.

Lach, P., Mercadier, J., Dubessy, J., Boiron, M-C., and Cuney, M., 2013, In situ quantitative measurement of rare earth elements in uranium oxides by laser ablation-inductively coupled plasma-mass spectrometry: Geostandards and Geoanalytical Research, v. 37, p. 277-296.

Laing, W.P., 1998, Structural-metasomatic environment of the East Mount Isa block base-metal-gold province: Australian Journal of Earth Sciences, v. 45, p. 413-428.

Landry, J.Y., 2006, Detailed relationships of iron oxide copper-gold type alteration zones at DeVries Lake, southern Great Bear Magmatic Zone, NWT: B.Sc thesis, University of Ottawa, Ottawa, Ontario, 68 p.

Maas, R., and McCulloch, M.T., 1990, A search for fossil nuclear reactors in the Alligator River uranium field, Australia: constraints from Sm, Gd and Nd isotopic studies: Chemical Geology, v. 88, p. 301-315.

Macmillan, E., Cook, N.J., Ehrig, K., Ciobanu, C.L., and Pring, A., 2016, Uraninite from the Olympic Dam IOCG-U-Ag deposit: linking textural and compositional variation to temporal evolution: American Mineralogist, v. 101, p. 1295-1320.

Marathon Resources, 2009, Annual Report 2009. No longer available online – also reported *in* Skirrow et al. (2011).

Mark, G., Darvall, M., Tolman, J., Foster, D.R.W., Williams, P.J., and Pollard, P.J., 1999, Magmas and regional Na-Ca alteration, Cloncurry district, Australia, *in* Stanley, C.J. et al., eds., Mineral deposits: processes to processing: Rotterdam, Balkema, p. 385-388.

Mark, G., Foster, D.R.W., Pollard, P.J., Williams, P.J., Tolman, J., Darvall, M., and Blake, K.L., 2004, Stable isotope evidence for magmatic fluid input during large-scale Na–Ca alteration in the Cloncurry Fe oxide Cu–Au district, NW Queensland, Australia: Terra Nova, v. 16, p. 54-61.

Marschik, R., and Fontboté, L., 2001, The Candelaria-Punta del Cobre iron oxide Cu-Au(-Zn-Ag) deposits, Chile: Economic Geology, v. 96, p. 1799-1826.

Marshall, L.J., and Oliver, N.H.S., 2006, Monitoring fluid chemistry in iron oxide–copper–gold-related metasomatic processes, eastern Mt Isa Block, Australia: Geofluids, v. 6, p. 45-66.

McDonough, W.F., and Sun, S-S., 1995, The composition of the Earth: Chemical Geology, v. 120, p. 223-253.

Mercadier, J., Cuney, M., Lach, P., Boiron, M.-C., Bonhoure, J., Richard, A., Leisen, M., and Kister, P., 2011, Origin of uranium deposits revealed by their rare earth element signature: Terra Nova, v. 23, p. 264-269.

Metrich, N., and Rutherford, M.J., 1992, Experimental study of chlorine behaviour in hydrous silicic melts: Geochimica et Cosmochimica Acta, v. 56, p. 607-616.

Miller, R.G., 1982, The geochronology of uranium deposits in the Great Bear batholith, Northwest Territories: Canadian Journal of Earth Sciences, v. 19, p. 1428-1448.

Montreuil, J.-F., Corriveau, L., and Potter, E.G., 2015, Formation of albitite-hosted uranium within IOCG systems: the Southern Breccia, Great Bear magmatic zone, Northwest Territories, Canada: Mineralium Deposita, v. 50, p. 293-325.

Montreuil, J.-F., Corriveau, L., and Davis, W., 2016a, Tectonomagmatic evolution of the southern Great Bear magmatic zone (Northwest Territories, Canada) – Implications on the genesis of iron oxide alkali-altered hydrothermal system, *in* Slack, J., Corriveau, L. and Hitzman, M., eds., Proterozoic iron oxide-apatite (± REE) and iron oxide-copper-gold and affiliated deposits of Southeast Missouri, USA, and the Great Bear magmatic zone, Northwest Territories, Canada: Economic Geology, v. 111, p. 2111-2138.

Montreuil, J.-F., Corriveau, L., Potter, E.G., and De Toni, A.F., 2016b, On the relation between alteration facies and metal endowment of iron oxide–alkali–altered systems, southern Great Bear magmatic zone (Canada), *in* Slack, J., Corriveau, L. and Hitzman, M., eds., Proterozoic iron oxide-apatite (± REE) and iron oxide-copper-gold and affiliated deposits of Southeast Missouri, USA, and the Great Bear magmatic zone, Northwest Territories, Canada: Economic Geology, v. 111, p. 2139-2168.

Montreuil, J.-F., Potter, E.G., Corriveau, L., and Davis, W.J., 2016c, Element mobility patterns in magnetite-group IOCG systems: the Fab IOCG system, Northwest Territories, Canada: Ore Geology Reviews, v. 72, p. 562-584.

Morris, A., 1977, Geology of parts of the FAB option (FAB, MAC, RON, TED claims), Rae Lakeare, N.W.T., Claim Sheet 86-C-3, Ryowa-Rayrock Joint Venture: Department of Indian and Northern Affairs, Document No. 080803.

Mumin, A.H. (editor), 2015, Echo Bay IOCG thematic map series: geology, structure and hydrothermal alteration of a stratovolcano complex, Northwest Territories, Canada: Geological Survey of Canada, Open File 7807, 19 p., 18 maps.

Mumin, A.H., Corriveau, L., Somarin, A.K., and Ootes, L., 2007, Iron oxide copper-gold-type polymetallic mineralization in the Contact Lake Belt, Great Bear Magmatic Zone, Northwest Territories, Canada: Exploration and Mining Geology, v. 16, p. 187-208.

Mumin, A.H., Somarin, A.K., Jones, B., Corriveau, L., Ootes, L., and Camier, J., 2010, The IOCG-porphyry-epithermal continuum of deposits types in the Great Bear magmatic zone, Northwest Territories, Canada, *in* Corriveau, L. and Mumin, A.H., eds., Exploring for iron oxide copper-gold deposits: Canada and global analogues: Geological Association of Canada, Short Course Notes, No. 20, p. 59-78.

Oliver, N.H.S., 1995, The hydrothermal history of the Mary Kathleen fold belt, Mount Isa block, Queensland, Australia: Australian Journal of Earth Sciences, v. 42, p. 267-280.

Oliver, N.H.S., Holcombe, R.J., Hill, E.J., and Pearson, P.J., 1991, Tectono-metamorphic evolution of the Mary Kathleen fold belt, northwest Queensland: a reflection of mantle plume processes?: Australian Journal of Earth Sciences, v. 38, p. 425-455.

Oliver, N.H.S., Pearson, P.J., Holcombe, R.J., and Ord, A., 1999, Mary Kathleen metamorphic-hydrothermal uranium – rare-earth element deposit: ore genesis and numerical model of coupled deformation and fluid flow: Australian Journal of Earth Sciences, v. 46, p. 467-484.

Oliver, N.H.S., Mark, G., Pollard, P.J., Rubenach, M.J., Bastrakov, E., Williams, P.J., Marshall, L.C., Baker, T., and Nemchin, A.A., 2004, The role of sodic alteration in the genesis of iron oxide-copper–gold deposits: geochemistry and geochemical modelling of fluid-rock interaction in the Cloncurry district, Australia: Economic Geology, v. 99, p. 1145-1176.

Oliver, N.H.S., Butera, K.M., Rubenach, M.J., Marshall, L.J., Cleverley, J.S., Mark, G., Tullemans, F., and Esser, D., 2008, The protracted hydrothermal evolution of the Mount Isa Eastern Succession: a review and tectonic implications: Precambrian Research, v. 163, p. 108-130.

Ootes, L., Goff, S., Jackson, V.A., Gleeson, S.A., Creaser, R.A., Samson, I.M., Evensen, N., Corriveau, L., and Mumin, A.H., 2010, Timing and thermochemical constraint on multi-element mineralization at the Nori/RA Cu-Mo-U prospect, Great Bear magmatic zone, Northwest Territories, Canada: Mineralium Deposita, v. 45, p. 549-566.

Ootes, L., Harris, J., Jackson, V.A., Azar, B., and Corriveau, L., 2013, Uranium-enriched bedrock in the central Wopmay orogen: implications for uranium mineralization, *in* Potter, E.G., Quirt, D. and Jefferson, C.W., eds., Uranium in Canada: geological environments and exploration developments: Exploration and Mining Geology, v. 21, p. 85-103.

Ootes, L., Davis, W.J., Jackson, V.A., and van Breemen, O., 2015, Chronostratigraphy of the Hottah terrane and Great Bear magmatic zone of Wopmay Orogen, Canada, and exploration of a terrane translation model: Canadian Journal of Earth Sciences, v. 52, p. 1062-1092.

Ootes, L., Snyder, D., Davis, W.J., Acosta-Góngora, P., Corriveau, L., Mumin, A.H., Gleeson, S., Samson, I.M., Montreuil, J.F., Potter, E.G., and Jackson, V.A., 2017, A Paleoproterozoic Andean-type iron oxide-copper-gold environment, the Great Bear magmatic zone, Northwest Canada: Ore Geology Reviews, v. 81, p. 123-139.

Osmond, J.C., Foo, B., Turner, J., and Jacobs, C., 2012, Technical report on the mineral reserves and mineral resources of the Salobo copper-gold mine Carajás, Pará State, Brazil: NI43-101 Technical Report, 200 p., available at www.sedar.com.

OZ Minerals Ltd., 2010, Prominent Hill June 2010 mineral resource and ore reserves statement and exploration update, 21 p., available at: www.ozminerals.com/operations/resources-reserves/resources-and-reserves-previous-statements/.

OZ Minerals Ltd., 2012, Carrapateena resource upgrade, and a significant new regional exploration copper discovery, 4 p., available at: www.ozminerals.com/operations/resources-reserves/resources-and-reserves-previous-statements/.

Page, R.W., and Sun, S-S., 1998, Aspects of geochronology and crustal evolution in the Eastern fold belt, Mount Isa inlier: Australian Journal of Earth Sciences, v. 45, p. 343-362.

Pagel, M., Pinte, G., and Rotach-Toulhoat, N., 1987, The rare earth elements in natural uranium oxides: Monograph Series on Mineral Deposits, v. 27, p. 81-85.

Pal, D.C., Barton, M.D., and Sarangi, A.K., 2009, Deciphering a multistage history affecting U–Cu(–Fe) mineralization in the Singhbhum Shear Zone, eastern India, using pyrite textures and compositions in the Turamdih U–Cu(–Fe) deposit: Mineralium Deposita, v. 44, p. 61-80.

Pollard, P.J., Mark, G., and Mitchell, L.C., 1998, Geochemistry of post-1540 Ma granites in the Cloncurry district, northwest Queensland: Economic Geology, v. 93, p. 1330-1344.

Porter, T.M., 2010, Current understanding of iron oxide associated-alkali altered mineralised systems. Part 1 - An overview, *in* Porter, T.M., ed., Hydrothermal iron oxide copper-gold and related deposits: a global perspective, volume 3: PGC Publishing, Adelaide, p. 5-32.

Potter, E.G., Montreuil, J.-F., Corriveau, L., and De Toni, A., 2013, Geology and hydrothermal alteration of the Fab Lake region, Northwest Territories: Geological Survey of Canada, Open File 7339, 26 p.

Potter, E.G., Corriveau, L., Montreuil, J.-F., Yang, Z., and Comeau, J.-S., 2014, Geochemical signatures of uraninite from iron oxide-copper-gold (IOCG) systems of the Great Bear magmatic zone, Canada: Geological Survey of Canada, Open File 7545, 1 poster.

Potter, E.G., Montreuil, J.-F., Corriveau, L., and Davis, W.J., 2019, The Southern Breccia metasomatic uranium system of the Great Bear magmatic zone, Canada: iron oxide-copper-gold (IOCG) and albitite-hosted uranium linkages, *in* Decrée, S. and Robb, L., eds., Ore deposits: origin, exploration, and exploitation: Geophysical Monograph 242, First Edition, John Wiley and Sons Inc., p. 109-132.

Pouchou, J.L., and Pichoir, F., 1984, Un nouveau modèle de calcul pour la microanalyse quantitative par spectrométrie de rayons X – Partie II : application à l'analyse d'échantillons hétérogènes en profondeur: La Recherche Aérospatiale, v. 5, p. 349-367.

Richards, J.P., and Mumin, A.H., 2013, Lithospheric fertilization and mineralization by arc magmas: genetic links and secular differences between porphyry copper ± molybdenum ± gold and magmatic-hydrothermal iron oxide copper-gold deposits, *in* Colpron, M., Bissig, T., Rusk, B.G. and Thompson, J.F.H., eds., Tectonics, metallogeny, and discovery: the North American Cordillera and similar accretionary settings: Society of Economic Geologists, Special Publication 17, p. 277-299.

Schmid, R., Fettes, D., Harte, B., Davis, E., and Desmons, J., 2007, How to name a metamorphic rock. Recommendations by the IUGS subcommission on the systematics of metamorphic rocks: Web version 01/02/07, available at www.bgs.ac.uk/scmr/home.html.

Shabaga, B.M., Fayek, M., McNeil, A., Linnen, R.L., Potter, E.G., 2021, Rare earth element partitioning between fluids and uraninite at 50–700°C: The Canadian Mineralogist, v. 59, p. 869-884.

Skirrow, R., 2010, "Hematite-group" IOCG±U ore systems. Tectonic settings, hydrothermal characteristics, and Cu-Au and U mineralizing processes, *in* Corriveau, L. and Mumin, A.H., eds., Exploring for iron oxide copper-gold deposits: Canada and global analogues: Geological Association of Canada, Short Course Notes, No. 20, p. 39-58.

Skirrow, R.G., 2022, Hematite-group IOCG ± U deposits: an update on their tectonic settings, hydrothermal characteristics, and Cu-Au-U mineralizing processes, *in* Corriveau, L., Potter, E.G. and Mumin, A.H., eds., Mineral systems with iron oxide-copper-gold (IOCG) and affiliated deposits: Geological Association of Canada, Special Paper 52, p. 27-51.

Skirrow, R.G., Creaser, R., and Hore, S.B., 2011, Mt Gee-Armchair U-REE deposits, South Australia, *in* Skirrow, R.G., ed., Uranium mineralisation events in Australia: geochronology of the Nolans Bore, Oasis, Kintyre, Mt Gee-Armchair, and Maureen uranium deposits: Geoscience Australia, Record 2011/12, p. 36-58.

Somarin, A.K., and Mumin, A.H., 2012, The Paleoproterozoic high heat production Richardson granite, Great Bear magmatic zone, Northwest Territories, Canada: source of U for Port Radium?: Resources Geology, v. 62, p. 227-242.

Somarin, A.K., and Mumin, A.H., 2014, P–T-composition and evolution of paleofluids in the Paleoproterozoic Mag Hill IOCG hydrothermal system, Contact Lake belt, Northwest Territories, Canada: Mineralium Deposita, v. 49, p. 199-215.

Su, Z., Zhao, X.F., Li, X.C., and Zou, M.F., 2016, Using elemental and boron isotopic compositions of tourmaline to trace fluid evolutions of IOCG systems: the world class Dahongshan Fe-Cu deposit in SW China: Chemical Geology, v. 441, p. 265-279.

Tallarico, F.H.B., Figueiredo, B.R., Groves, D.I., Kositcin, N., McNaughton, N.J., Fletcher, I.R., and Rego, J.L., 2005, Geology and SHRIMP U-Pb Geochronology of the Igarapé Bahia deposit, Carajás copper-gold belt, Brazil: an Archean (2.57 Ga) example of iron-oxide Cu-Au-(U-REE) mineralization: Economic Geology, v. 100, p. 7-28.

Timofeev, A., Migdisov, A.A., Williams-Jones, A.E., Roback, R., Nelson, A.T., and Xu, H., 2018, Uranium transport in acidic brines under reducing conditions: Nature Communications, v. 9, 1469.

Tornos, F., Velasco, F., Barra, F., and Morata, D., 2010, The Tropezón Cu-Mo-(Au) deposit, Northern Chile: the missing link between IOCG and porphyry copper systems?: Mineralium Deposita, v. 45, p. 313-321.

Tornos, F., Wiedenbeck, M., and Velasco, F., 2012, The boron isotope geochemistry of tourmaline-rich alteration in the IOCG systems of northern Chile: implications for a magmatic-hydrothermal origin: Mineralium Deposita, v. 47, p. 483-499.

Webster, J.D., 1997, Exsolution of magmatic volatile phases from Cl-enriched mineralizing granitic magmas and implications for ore metal transport: Geochimica et Cosmochimica Acta, v. 61, p. 117-1029.

Webster, J.D., 2004, The exsolution of magmatic hydrosaline melts: Chemical Geology, v. 210, p. 33-48.

Webster, J.D., and De Vivo, B., 2002, Experimental and modeled solubilities of chlorine in aluminosilicate melts, consequences of magma evolution, and implications for exsolution of hydrous chloride melt at Mt. Somma–Vesuvius: American Mineralogist, v. 87, p. 1046-1061.

Whitney, D.L., and Evans, B.W., 2010, Abbreviations for names of rock-forming minerals: American Mineralogist, v. 95, p. 185-187.

Wilde, A., 2013, Towards a model for albitite-type uranium: Minerals, v. 3, p. 36-48.

Williams, P.J., 2010a, Classifying IOCG deposits, *in* Corriveau, L. and Mumin, A.H., eds., Exploring for iron oxide copper-gold deposits: Canada and global analogues: Geological Association of Canada, Short Course Notes, No. 20, p. 13-22.

Williams, P.J., 2010b, "Magnetite-group" IOCGs with special reference to Cloncurry (NW Queensland) and Northern Sweden. Settings, alteration, deposit characteristics, fluid sources, and their relationship to apatite-rich iron ores, *in* Corriveau, L. and Mumin, A.H., eds., Exploring for iron oxide copper-gold deposits: Canada and global analogues: Geological Association of Canada, Short Course Notes, No. 20, p. 23-38.

Williams, P.J., Barton, M.D., Johnson, D.A., Fontboté, L., de Haller, A., Mark, G., Oliver, N.H.S., and Marschik, R., 2005, Iron oxide copper-gold deposits: geology, space-time distribution, and possible modes of origin, *in* Hedenquist, W., Thompson, J.F.H., Goldfarb, R.J. and Richards, J.P., eds., One hundredth anniversary economic geology special volume: Society of Economic Geologists, v. 100, p. 371-409.

Williams, P.J., Kendrick, M., and Xavier, R.P., 2010, Sources of ore fluid components in IOCG deposits, *in* Porter, T.M., ed., Hydrothermal iron oxide copper–gold and related deposits: a global perspective, volume 3: PGC Publishing, Adelaide, p. 107-116.

Xavier, R., Wiedenbeck, M., Trumbull, R.B., and Torresi, I., 2008, Tourmaline B-isotopes fingerprint marine evaporites as the source of high-salinity ore fluids in iron oxide copper-gold deposits, Carajás mineral province (Brazil): Geology, v. 36, p. 743-746.

Xstrata, 2012, Mineral resources and ore reserves, 53 p., available at: www.glencore.com/en/investors/reports-results/report-archive.

Zharikov, V.A., Pertsev, F.N., Rusinov, V.L., Callegari, E., and Fettes, D.J., 2007, Metasomatism and metasomatic rocks. Recommendations by the IUGS Subcommission on the Systematics of Metamorphic Rocks: Web version 01.02.07, available at www.bgs.ac.uk/scmr/home.html.

# Iron-oxide Trace Element Fingerprinting of Iron Oxide Copper-gold and Iron Oxide-apatite Deposits: A Review

**Xiao-Wen Huang**
*State Key Laboratory of Ore Deposit Geochemistry, Institute of Geochemistry, Chinese Academy of Sciences, China*
*E4m Center, Department of Geology and Geological Engineering, Laval University, Québec, Canada*
*huangxiaowen@mail.gyig.ac.cn*

**Georges Beaudoin**
*E4m Center, Department of Geology and Geological Engineering, Laval University, Québec, Canada*

**Anthony Franco De Toni**
*SOQUEM inc., Val-d'Or, Canada*

**Louise Corriveau**
*Geological Survey of Canada, Natural Resources Canada, Québec, Canada*

**Sheida Makvandi**
*Department of Geology and Geological Engineering, Laval University, Québec, Canada*

**Émilie Boutroy**
*Agnico Eagle Mines Limited, Val d'Or, Canada*

*Recommended citation: Huang, X.-W., Beaudoin, G., De Toni, A.-F., Corriveau, L., Makvandi, S., and Boutroy, E., 2022, Iron-oxide trace element fingerprinting of iron oxide copper-gold and iron oxide-apatite deposits: a review, in Corriveau, L., Potter, E.G. and Mumin, A.H., eds., Mineral systems with iron oxide copper-gold (IOCG) and affiliated deposits: Geological Association of Canada, Special Paper 52, p. 347-364.*

## Abstract

Iron oxide copper-gold (IOCG) and iron oxide-apatite (IOA) deposits are two important deposit types formed in iron oxide and alkali-calcic alteration ore systems. They are important copper, gold, uranium, rare earth element and iron resources. These deposits commonly occur in spatially and temporally associated districts (e.g. Chilean Iron Belt and Canadian Great Bear magmatic zone), are characterized by significant amounts of magnetite and/or hematite, and form within systems that generate the same alteration facies (e.g. Na, high-temperature Ca-Fe and K-Fe, and low-temperature K-Fe). Magnetite and hematite form a wide range of partial to complete solid-solutions, are resistant to supergene weathering, and their trace element chemistry varies according to deposit types/subtypes and host alteration facies (barren and fertile). They thus have significant potential as a mineral exploration tool. Temporal and spatial variations of trace elements in iron oxides at the mineral, alteration assemblage and deposit scales can shed light on fluid evolution and thus help understand ore-forming processes, especially when combined with studies of iron, oxygen, and osmium isotopes of iron oxides and associated minerals. However, recent research demonstrates that iron oxides can re-equilibrate during metasomatism through coupled dissolution-reprecipitation processes characteristic of these systems, and as such, can have mixed signatures. As alteration facies are best assessed at the megascopic scale, *in situ* chemical analysis of iron oxides needs to be combined with detailed textural characterization and paragenetic studies at the thin section to outcrop scale. Future work on iron oxide fingerprinting should include the discrimination of ore-related and barren alteration facies and linking iron oxide chemistry with physical properties related to geophysical exploration.

## Résumé

Les gisements à oxydes de fer, cuivre-or (IOCG) et à oxydes de fer-apatite (IOA) sont deux types de gisements importants formés dans les systèmes minéralisateurs à oxydes de fer et altération alcalino-calcique. Ils contiennent des ressources importantes en cuivre, or, uranium, terres rares et fer. Ces gîtes sont généralement associés dans l'espace et le temps (p. ex., la ceinture de fer chilienne et la zone magmatique du Grand lac de l'Ours, Canada). Ils contiennent d'abondantes quantités de magnétite et / ou d'hématite, et se forment au sein de systèmes partageant les mêmes faciès d'altération (p. ex., Na, Ca-Fe et K-Fe à haute température et K-Fe à basse température). La magnétite et l'hématite forment une vaste gamme de solutions solides et sont résistants à l'altération supergène. Leurs éléments traces varient en fonction des types / sous-types de gîtes et faciès d'altération (stériles et fertiles). Ils représentent donc des minéraux indicateurs potentiels en exploration minérale. De plus, les variations temporelles et spatiales des éléments traces dans les oxydes de fer aux échelles du minéral, de la paragenèse et des gîtes apportent d'importantes contraintes sur l'évolution des fluides et des processus de formation du minerai, en particulier lorsque leur étude est combinée à des études d'isotopes de fer, d'oxygène et d'osmium sur les oxydes de fer et minéraux associés. Cependant, certains oxydes de fer peuvent se rééquilibrer durant le métasomatisme par processus de dissolution-reprécipitation couplée. Par conséquent, les roches affectées par plusieurs faciès d'altération peuvent avoir des signatures d'éléments traces mixtes et l'interprétation des analyses chimiques in situ se doit d'être combinée à une caractérisation texturale et paragénétique tant à l'échelle de la lame mince que de l'affleurement, la caractérisation des faciès d'altération étant optimale à l'échelle mégascopique et non pas microscopique. Les travaux futurs sur la signature des oxydes de fer devraient inclure la distinction entre faciès d'altération fertile et stérile, et les liens entre chimie minérale et propriétés physiques liées à l'exploration géophysique.

## Introduction

Iron oxide-copper-gold (IOCG) deposits (e.g. Olympic Dam) are characterized by Cu-sulphides ± Au hydrothermal mineralization associated with abundant magnetite or hematite. They occur in rocks ranging in age from the late Archean to the Mesozoic (Williams et al., 2005). These deposits show a great variation in geological settings and alteration systematics as well as mineralizing fluid compositions (Hitzman et al., 1992; Hitzman, 2000; Barton and Johnson, 2004; Williams et al., 2005; Corriveau, 2007). Iron oxide apatite (IOA) deposits comprise iron ores with or without significant rare earth element mineralization, but lack copper, gold and polymetallic mineralization (Naslund et al., 2002; Williams, 2010a). Kiruna-type IOA deposits are characterized by magnetite with low to moderate contents of titanium, a distinguishing feature from nelsonites and magmatic Fe-Ti-V deposits (Zhou et al., 2005; Chen et al., 2013).

IOCG and IOA deposits are commonly spatially and temporally associated; both form within iron oxide and alkali-calcic alteration ore systems developed during coeval magmatism (Fig. 1). IOCG and IOA deposits can be subdivided into hematite, hematite + magnetite, and magnetite groups based on the principal iron oxides present (Fig. 1; Williams, 2010a). Magnetite-group and hematite-group IOCG deposits form in a variety of hydrothermal environments, across distinct temperature ranges and fluid evolution processes (Skirrow, 2010; Williams, 2010b). Magnetite-group IOCG deposits represent the higher temperature part of the IOCG spectrum compared to hematite-group deposits such as Olympic Dam, which are characterized by lower temperature hematite and white mica-dominated alteration (Williams, 2010a). IOA deposits occur in a number of regions worldwide, where they generally display an association with calc-alkaline arc magmatism such as in the Andes, the Middle-Lower Yangtze River metallogenic belt and the Great Bear magmatic zone (GBMZ) in the Northwest Territories of Canada (Williams et al., 2005; Mao et al., 2011; Ootes et al., 2017). Both magnetite-group and magnetite + hematite-group IOA deposits are commonly enveloped by magnetite ± hematite ± actinolite breccias within large scale Na ± Ca and high-temperature Ca-Fe alteration zones (Corriveau et al., 2010, 2016; Williams, 2010a; Tornos et al., 2016). Both IOCG and IOA deposits are closely associated with extensive hydrothermal alteration, which occurs as several high- to low-temperature types including high-temperature (HT) Na to Na-Ca, Ca-Fe, and K-Fe, and low-temperature (LT) K-Fe and Ca-Mg (Fig. 1; Corriveau et al., 2010, 2016). The alteration stages have characteristic mineral assemblages, chemical footprints and signatures, metal associations, formation temperatures, and fluid compositions (Corriveau et al., 2010, 2016; Montreuil et al., 2013, 2016a, b).

Iron oxides, including magnetite and hematite, are present in a range of rocks and mineral deposits (Ramdohr, 1980; Dupuis and Beaudoin, 2011). Magnetite has an inverse spinel structure and can incorporate a series of elements, including Al, Ti, Mg, Mn, Zn, Cr, V, Ni, Co and Ga (Buddington and Lindsley, 1964; Frost and Lindsley, 1991; Dupuis and Beaudoin, 2011; Nadoll et al., 2014). Some elements can also occur as nanometre mineral inclusions (e.g. diopside, clinoenstatite, amphibole, mica, ulvöspinel, and titanium-rich magnetite) in trace element-rich hydrothermal magnetite (Deditius et al., 2018).

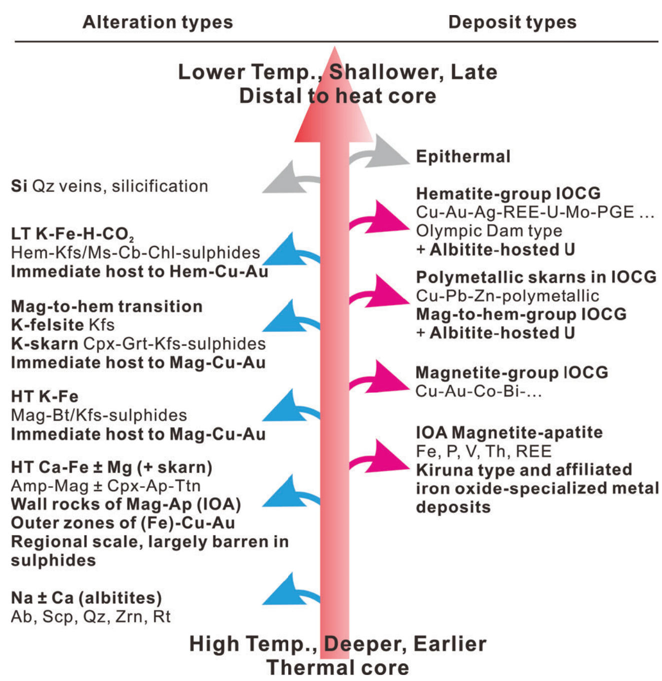


**FIGURE 1.** Main alteration facies and deposit types within evolving iron oxide and alkali-calcic alteration ore systems responsible for IOA and IOCG genesis (modified from Corriveau et al., 2016). Abbreviations: Ab = albite, Amp = amphibole, Ap = apatite, Bt = biotite, Chl = chlorite, Cpx = clinopyroxene, Grt = garnet, Hem = hematite, Kfs = K-feldspar, Mag = magnetite, Ms = muscovite, Cb = carbonate, Rt = rutile, Qz = quartz, Scp = scapolite, Ttn = titanite, Zrn = zircon. HT = high temperature, LT = low temperature.

The composition of magnetite and hematite is controlled by the composition of magmas (Dare et al., 2012, 2014; Liu et al., 2015) and/or hydrothermal fluids, their sources and the rock sequence along the fluid flow path (Carew, 2004; Dupuis and Beaudoin, 2011; Dare et al., 2014; Nadoll et al., 2014; Huang et al., 2016). The composition is also controlled by co-crystallizing minerals and the physical and chemical conditions that influence partition coefficients of elements, such as temperature, pressure, rate of cooling, oxygen fugacity, and silica activity (Goldschmidt, 1958; Buddington and Lindsley, 1964; Fleet, 1981; Wechsler et al., 1984; Whalen and Chappell, 1988; Ghiorso and Sack, 1991; Carew, 2004; Righter et al., 2006; Dare et al., 2012; Boutroy et al., 2014; Huang et al., 2014; Nadoll et al., 2014; Sievwright et al., 2017).

Magnetite can preserve its chemical composition during physical transport and chemical weathering and thus can be used for source discrimination (Grigsby, 1990; Dare et al., 2014), as well as a mineral indicator for mineral exploration (Dupuis and Beaudoin, 2011; McMartin et al., 2011a, b; Boutroy et al., 2014; Sappin et al., 2014; Makvandi et al., 2015, 2016a, b; Pisiak et al., 2017). Iron oxides are also widely used to fingerprint deposit types and ore-forming processes (Müller et al., 2003; Carew, 2004; Singoyi et al., 2006; Rusk et al., 2009b; Beaudoin and Dupuis, 2010; Dupuis and Beaudoin, 2011; Dare et al., 2012; Nadoll et al., 2012; Huang et al., 2013, 2015a, b; Chen et al., 2015; Knipping et al., 2015a, b). However, some studies show that igneous magnetite in altered granitoids (Wen et al., 2017), hydrothermal magnetite in skarn (Hu et al., 2015; Yin et al., 2017; Huang et al., 2018) and IOA deposits (Heidarian et al., 2016) can be reequilibrated in terms of their textures and chemical compositions by coupled dissolution-reprecipitation (CDR) processes (Hu et al., 2015; Heidarian et al., 2016; Wen et al., 2017; Yin et al., 2017; Huang et al., 2018). Evaporitic fluid infiltration was considered to induce CDR replacement of magnetite in skarn (Hu et al., 2014; Huang et al., 2018) and IOA (Heidarian et al., 2016) deposits. Wen et al. (2017) proposed that crystallization of titanite leads to fracturing and dissolution of igneous magnetite through pressure solution and formation of hydrothermal magnetite. Such processes also affect the textures and compositions of magnetite from IOCG and IOA deposits. Hence the study of iron oxides in these systems promises to shed light on the factors controlling mineral crystallization processes such as CDR and ore genesis.

In this paper, we review recent advances in trace element fingerprinting of iron oxides in IOCG and IOA deposits. These studies demonstrate that iron oxide chemistry can be used to discriminate deposit types and alteration facies, and serve as efficient mineral indicators for mineral exploration. Iron oxide chemistry combined with iron, oxygen, and osmium isotope systematics help constrain fluid evolution and sources, and thus provide new insights on the formation of IOCG and IOA deposits. However, some magnetite grains have experienced one or multiple re-equilibration processes during or after magnetite formation. Therefore, in situ chemical compositions of magnetite should be combined with detailed textural observations in order to better understand the origin of magnetite in IOCG and IOA deposits.

## Sample Selection and Data Collection

Samples used in this review include worldwide IOCG and IOA deposits described in Huang et al. (2019) and Canadian IOCG and IOA deposits and prospects from the GBMZ (Corriveau et al., 2016; De Toni, 2016). Deposits in the GBMZ include Contact Lake, McLeod, Port Radium Grouard, Terra, Fab, Ham, JLD, Sue Dianne, Cole Hump, NICO, Southern Breccia, LP's and Duke. The detailed sample information can be found in De Toni (2016). In addition to reusing published electron probe micro-analyzer (EPMA) data in Huang et al. (2019), 469 unpublished EPMA data from De Toni (2016) are also used to construct new diagrams.

## Analytical Methods for EPMA Analyses

Electron microprobe data in De Toni (2016) and Huang et al. (2019) were acquired by a CAMECA SX-100 EPMA at Université Laval using the same conditions. Detailed analytical procedures can be found in Boutroy et al. (2014) and Huang et al. (2019). The analyses were performed using a 10 µm beam 15 kV voltage, and 100 nA current. Thirteen elements were measured, including K, Ca, Al, Si, Ti, Mg, Mn, Cr, V, Sn, Cu, Zn, and Ni. Simple oxides (GEO Standard Block of P and H Developments) and natural minerals (Mineral Standard Mount MINM 25-53, Astimex Scientific) (Jarosewich et al., 1980) were used to calibrate the analyses. The background peak collection time was 15 s for V and 20 s for other elements. The counting time was 40 s for Mg and Si, 60 s for V and Cr, and 20 s for other elements. Most elements have detection limits lower than ~50 ppm, whereas Ni, Cu, and Zn have higher detection limits of ~60–100 ppm.

## Statistical Methods

### *Estimation of Average Composition*

Because electron microprobe datasets contain censored data that are below the detection limits (Helsel, 2005), we calculate the average composition of magnetite using the Nondetects and Data Analysis (NADA) package in R software, employing the nonparametric Kaplan-Meier (K-M) method (Lee and Helsel, 2007). This method can avoid higher average values caused by excluding the censored data.

### *Data Preprocessing*

In order to examine the relationships between iron oxide chemistry, alteration, and deposit types, the individual EPMA analyses were investigated by partial least squares-discriminant analysis (PLS-DA). PLS-DA also helps identify the best discriminant elements. Seven of thirteen elements in the EPMA data were investigated by PLS-DA; however, K, Sn, Cu, Zn, Ni, and Cr were not included in PLS-DA because censored data for each of these elements exceeds 40% of the studied dataset.

Similar to Makvandi et al. (2016b), censored data were estimated using robCompositions package in R software based on the k-nearest neighbours' function with the Aitchison distance (Hron et al., 2010; Makvandi et al., 2016b). The concentration data thus obtained were further transformed to centered-log ratio (CLR; Aitchison, 1986; Egozcue et al., 2003; Makvandi et al., 2016b), in order to eliminate the 'closure problem' caused by a constant sum of 100% for the concentration calculation (Aitchison, 1986; Whitten, 1995).

*Partial Least Squares-discriminant Analysis*

Statistical analysis was carried out using the PLS-DA method as described in Makvandi et al. (2016b) and Huang et al. (2019). As a supervised classification method using labeled data (e.g. groups of samples), PLS-DA can maximize the separation between pre-defined sample groups by rotating principal components and identifying the key elements responsible for the separation (Wold et al., 2001; De Iorio et al., 2008; Eriksson et al., 2013; Brereton and Lloyd, 2014).

Following Makvandi et al. (2016b), coupled loadings biplots (qw×1-qw×2) and score scatter plots (t1-t2) were used to interpret the results. Loadings biplots indicate the correlation among elements and the relationship between elements and defined sample groups (e.g. deposit type/alteration type). Score scatter plots show the distribution of samples and the relationship among labelled sample groups, and should be interpreted in combination with loading plots of elements. Samples in one quadrant of score plots are characterized by higher concentrations of elements in the same quadrant of loading plots than the average composition of the studied dataset. Samples plotting in the opposite quadrant of score scatter diagrams have contrasting element features. Projection of unknown samples in the PLS-DA model constructed by known samples was performed using the same regression parameters. The formulas for the scores of tested samples are:

$$t_1 = (\mathrm{CLR(a)}-\mathrm{average(a)})/\mathrm{stdev(a)} \times W_1 \times \mathrm{(a)} + (\mathrm{CLR(b)}-\mathrm{average(b)})/\mathrm{stdev(b)} \times W_1 \times \mathrm{(b)} + \ldots\ldots + (\mathrm{CLR(i)}-\mathrm{average(i)})/\mathrm{stdev(i)} \times W_1 \times \mathrm{(i)};$$

$$t_2 = (\mathrm{CLR(a)}-\mathrm{average(a)})/\mathrm{stdev(a)} \times W_2 \times \mathrm{(a)} + (\mathrm{CLR(b)}-\mathrm{average(b)})/\mathrm{stdev(b)} \times W_2 \times \mathrm{(b)} + \ldots\ldots + (\mathrm{CLR(i)}-\mathrm{average(i)})/\mathrm{stdev(i)} \times W_2 \times \mathrm{(i)};$$

where a, b and i represent element variables, CLR (i) is the CLR value of element i for tested sample, average(i) and stdev(i) are average value and standard deviation of element i for training sample, W1 × (i) and W2 × (i) represent weightings of element i for training sample in the first and second PLS-DA components.

## Discrimination of Deposit Types

Numerous diagrams based on trace element concentrations are used to discriminate IOCG and IOA magnetite from other types of deposits: 1) Dupuis and Beaudoin (2011) proposed binary plots using Ca+Al+Mn or Ni/(Cr+Mn) as y axis and Ti+V as x axis to discriminate IOCG and IOA deposits from banded iron formation (BIF), magmatic Fe-Ti-V, porphyry Cu and skarn Fe-Cu deposits. In these diagrams, lower Ti+V contents in iron oxides discriminate IOCG from IOA deposits; 2) Knipping et al. (2015b) used a V vs. Cr diagram to distinguish IOA deposits from magmatic Fe-Ti-V, porphyry Cu and IOCG deposits, based on the lower Cr but higher V concentrations in magnetite from IOA deposits compared to IOCG deposits; 3) Loberg and Horndahl (1983) proposed V vs. Ti, V vs. Ni+Co, V vs. Ni, and V/Ti vs. Ni/Ti diagrams to discriminate IOA deposits from magmatic Fe-Ti deposits and BIF based on bulk composition of iron ores. Heidarian et al. (2016) and Broughm et al. (2017) evaluated the diagrams of Loberg and Horndahl (1983) and demonstrated that these diagrams can be also used for in situ trace element analysis of magnetite; and 4) Huang et al. (2019) showed that iron oxides from IOA deposits can be discriminated from those of IOCG deposits by higher Mg, Ti, V, Pb, and Sc contents. Although the above diagrams are very efficient in discriminating the related deposit types in individual studies, all of them should be used with caution in terms of significant overlaps (e.g. Broughm et al., 2017).

Binary score plots based on PLS-DA are used to discriminate IOCG and IOA deposits from porphyry, Ni-Cu, VMS deposits, and VMS-related BIF (Makvandi et al., 2016b). Higher Si contents discriminate IOCG magnetite, whereas higher titanium and cobalt concentrations characterize IOA magnetite (Makvandi et al., 2016b). Similarly, Huang et al. (2019) show that IOCG and IOA deposits can be discriminated from porphyry Cu, Ni-Cu, VMS deposits and VMS-related BIF due to higher Si, Ca, Al, Ti, Co, and Ni contents in magnetite.

In addition to discrimination of IOCG and IOA deposits from other types of deposits, iron oxide chemistry can also be used to discriminate IOCG and IOA deposit subtypes (Huang et al., 2019). PLS-DA results show that higher Nb, Cu, Mo, W, and Sn contents discriminate iron oxides from hematite-group IOCG deposits from those of the magnetite-hematite-group and magnetite-group IOA deposits. Iron oxides from magnetite-group IOA deposits have relatively high Mg, Co, and V and low Si, K, Ca, W, Sn, Nb, and Mo contents, whereas those from magnetite-hematite-group IOA deposits have relatively high Zr, W, Sn, Sc, and Ti, but low Al and Mg contents. The compositional differences between iron oxides from magnetite-group and magnetite-hematite-group IOA deposits may reflect their formation under different temperatures and oxygen fugacities. Magnetite-group IOCG deposits show large compositional variations and overlap with the three other deposit subtypes, which probably results from the progressive formation of HT Ca-Fe and K-Fe alteration that are responsible for some magnetite-group IOCG deposits and their variants.

The EMPA trace element data for magnetite from IOCG and IOA deposits in the GBMZ (De Toni, 2016) are used to test a PLS-DA model in which the four deposit-subtype fields are also based on EPMA analyses (Si, Ca, Mg, Al, Mn, Ti, and V contents) (Fig. 2). Iron oxides with IOA-IOCG affinity plot in both IOA and IOCG fields (Fig. 2B), consistent with their transitional origin. Iron oxides from magnetite-hematite-group IOCG deposits in the GBMZ plot in the fields of magnetite-group and hematite-group IOCG deposits (with minor outliers), whereas iron oxides from the IOA prospects plot mainly in the field of magnetite-hematite-group IOA deposits (Fig. 2C). Iron oxides from magnetite-group IOCG deposits in the GBMZ are scattered among all fields except the field of magnetite-group IOA deposits (Fig. 2D), consistent with the highly varied chemical composition of such IOCG deposits (Huang et al., 2019). These results indicate that the defined PLS-DA model diagrams discriminate IOCG from IOA deposits but are not efficient at discriminating IOCG and IOA subtypes. The limitation of the diagrams may be due to the number of elements (7) available from EPMA data; PLS-DA models based on more elements (21) analysed by LA-ICP-MS have led to better discrimination (Huang et al., 2019).

Huang et al. (2017) proposed binary diagrams of Si+Ca vs. Mn+V and Si+Ca vs. Mg+Mn+V+Ni to discriminate magnetite-group from hematite-group IOCG deposits, and magnetite-group from magnetite-hematite-group IOA deposits. However, large overlaps occur between the two IOCG deposit subtypes. Based on the discriminant elements determined through PLS-DA (Huang et al., 2019), two ternary diagrams, Si+Ca-Mn-Mg+V and Si+Ca-Al+Mn-V, are proposed for IOCG and IOA subtype discrimination (Fig. 3). These diagrams are efficient in discriminating hematite-group IOCG deposits and magnetite-group IOA and magnetite + hematite-group IOA deposits but cannot discriminate magnetite-group IOCG deposits from the other deposit types (Fig. 3A, B).

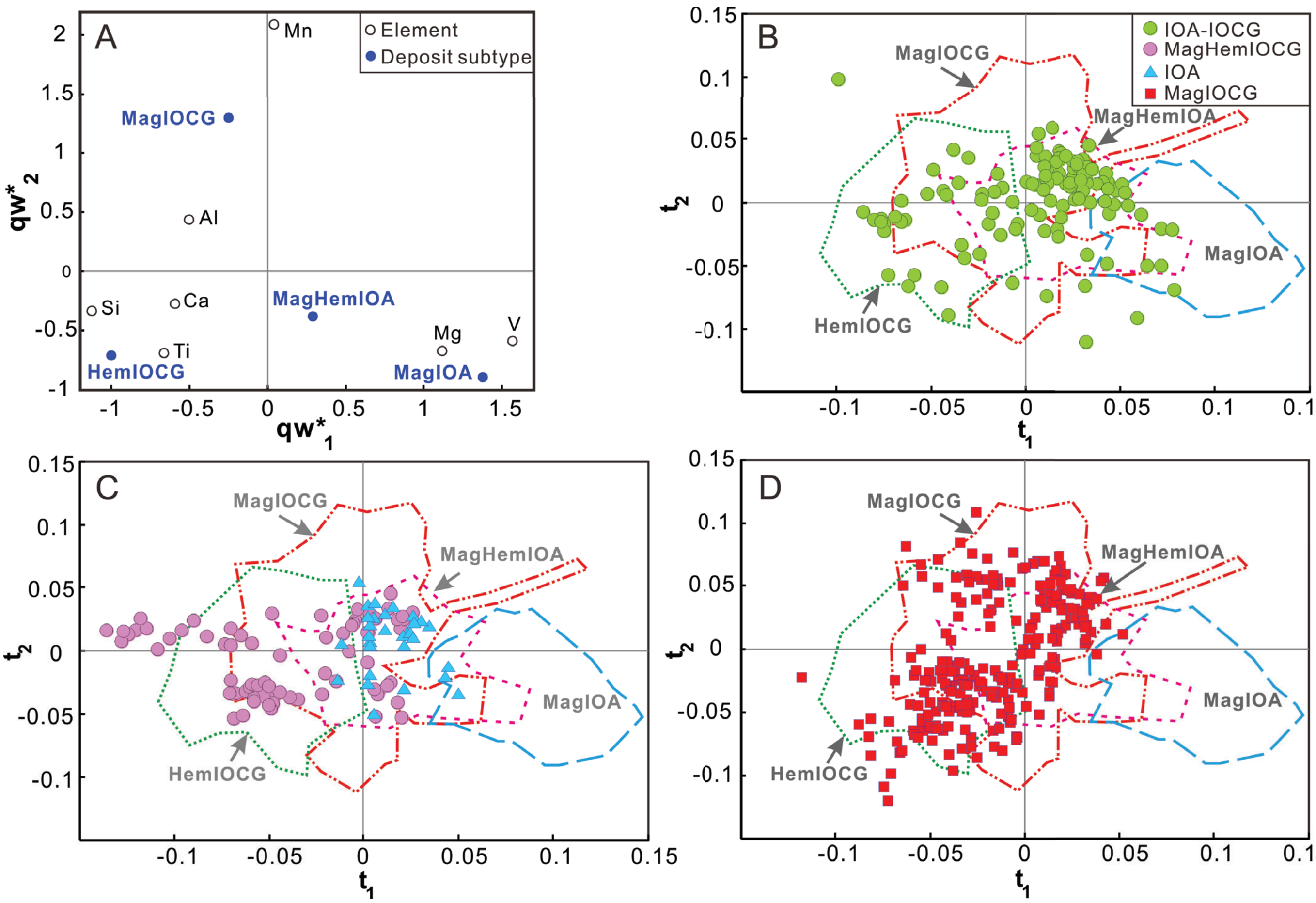


**FIGURE 2.** PLS-DA results of EPMA data of iron oxides from different subtypes of IOCG and IOA deposits (Huang et al., 2019). **A.** Plot of first and second loadings showing correlations among element variables and deposit subtypes. **B-D.** Plot of first and second scores showing the compositional range of samples from different deposit subtypes in the latent variable space defined by qw*1-qw*2 in A. Four fields are defined, i.e. MagIOCG, HemIOCG, MagIOA, and MagHem IOA. Data points in **B**, **C**, and **D** are individual EPMA analyses of magnetite from IOCG and IOA deposits in the GBMZ, Canada (De Toni, 2016). The formulas for plotting new samples in B, C, and D are: $t_1$ = (CLR(Si)+0.008)/0.4898 × (-0.0154) + (CLR(Ca)+0.6123)/0.3600 × (-0.0081) + (CLR(Al)-0.3378)/0.3533 × (-0.0069) + (CLR(Mn)-0.0658)/0.4857 × 0.00054 + (CLR(Mg)+0.3135)/0.4349 × 0.0152 + (CLR(Ti)-0.3054)/0.4969 × (-0.0091) + (CLR(V)-0.2248)/0.4940 × 0.0213; $t_2$ = (CLR(Si)+0.008)/0.4898 × (-0.0056) + (CLR(Ca)+0.6123)/0.3600 × (-0.0045) + (CLR(Al)-0.3378)/0.3533 × 0.00751 + (CLR(Mn)-0.0658)/0.4857 × 0.0355 + (CLR(Mg)+0.3135)/0.4349 × (-0.0112) + (CLR(Ti)-0.3054)/0.4969 × (-0.0116) + (CLR(V)-0.2248)/0.4940 × (-0.0098).

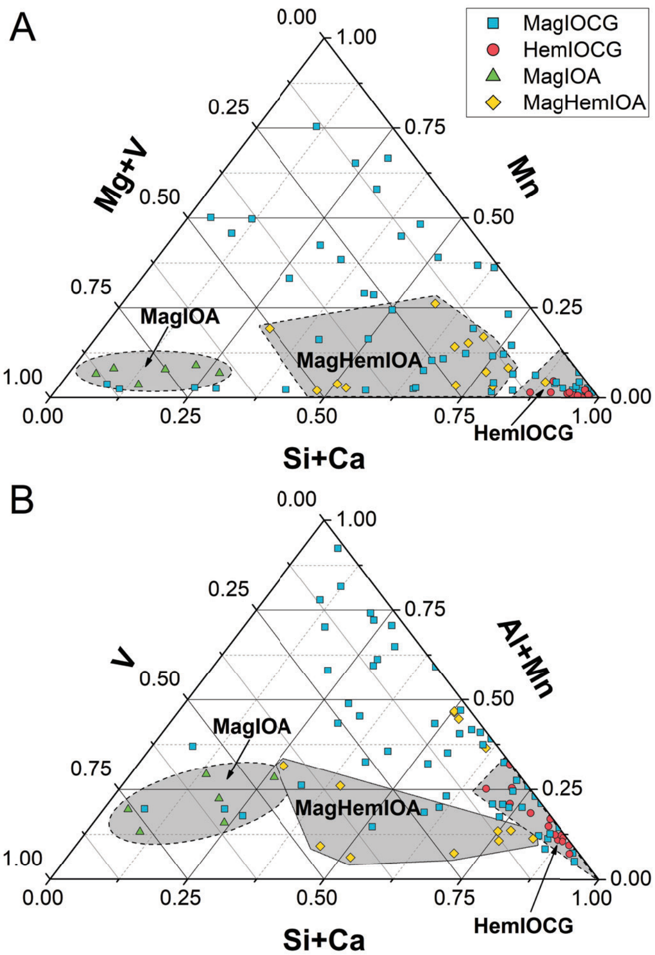


**FIGURE 3.** Ternary Si+Ca-Mn-Mg+V **(A)** and Si+Ca-Al+Mn-V **(B)** discrimination diagrams for IOCG and IOA subtypes. Data points are the average trace element composition of iron oxides from each sample (EPMA and LA-ICP-MS data of Huang et al., 2019).

## Alteration Vectors

Each alteration facies within iron oxide and alkali-calcic alteration systems of the GBMZ has a systematic and diagnostic geochemical signature largely independent of protolith (Corriveau et al., 2010, 2016; Montreuil et al., 2013, 2016b). In general, the K and K-Fe alteration facies are rich in K, Ba, Rb, Zr, Ta, Nb, Th and U, whereas the HT Ca-Fe alteration facies are rich in Ca, Fe, Mn, Mg, Zn, Ni and Co (Montreuil et al., 2013). Transitional alteration facies (HT Ca-K-Fe, skarns, and K-skarns) also have distinct mineral and metal associations (Corriveau et al., 2016, 2017; Blein and Corriveau, 2017). Finally, the Al and Si contents in all alteration facies are generally lower than those of common igneous and siliciclastic rocks, and alteration zones within other deposit types (Blein and Corriveau, 2017).

*Discrimination for Different Alteration Types*

Acosta-Góngora et al. (2014) and De Toni (2016) linked the trace element chemistry of magnetite from IOCG and affiliated mineralization in the GBMZ to specific alteration facies. They found that: a) the V, Ni, and Co contents of magnetite from the magnetite-amphibole and magnetite-apatite assemblages of HT Ca-Fe alteration zones are distinctive, and b) Si, K, Ca, ±Al ±Mg concentrations increase and V and Mn concentrations decrease in magnetite as iron oxide and alkali-calcic alteration systems evolve.

Huang et al. (2019) analyzed the chemical compositions of magnetite and hematite from nine IOCG and seven IOA deposits and demonstrated that they vary according to alteration facies, i.e. iron oxides from the HT Ca-Fe (including some transitional HT Ca-K-Fe), HT K-Fe, and LT K-Fe alteration facies have distinctive trace element compositions. The relative enrichment of Mg, Co, and Ni in iron oxides from the HT Ca-Fe alteration facies is consistent with the fluids being not only rich in Ca, Fe, Mn, Mg, Zn, Ni and Co, but also present at physicochemical conditions that allowed precipitation of these elements (Montreuil et al., 2013; Childress et al., 2016; Corriveau et al., 2016). Similarly, the relative enrichment of Si, K, and Al in iron oxides from the HT and LT K-Fe alteration facies is consistent with fluids having evolved to a composition rich in K, Al, Ba, Si, Rb, Zr, Ta, Nb, Th and U, and to physicochemical conditions that allowed precipitation of these elements (Montreuil et al., 2013; Corriveau et al., 2016). PLS-DA results show that iron oxides from the HT Ca-Fe alteration can be discriminated from HT and LT K-Fe alteration because of their higher Mg and V but lower Si, Al, and Mn contents. Additionally, iron oxides from LT K-Fe alteration can be discriminated from HT K-Fe alteration by their higher W, Sn, Nb, Mo, and Zr contents.

Magnetite data from the variety of alteration facies in the GBMZ are used herein to test the PLS-DA model of Huang et al. (2019). The model is also based on EPMA Si, Ca, Mg, Al, Mn, Ti, and V contents. Three alteration facies are discriminated (Fig. 4A). Magnetite associated with HT Na-Ca-Fe alteration plots in the "HT Ca-Fe" field, consistent with their origin (Fig. 4B). However, magnetite data from HT Ca-Fe, Ca-K-Fe, and K-Fe alteration zones are scattered throughout the diagram (Fig. 4B–D). This indicates that the chemical composition of magnetite is controlled not only by the host alteration type but also by other factors such as host rock buffering, fluid chemistry, and co-precipitating mineral phases (Acosta-Góngora et al., 2014; Huang et al., 2019).

Huang et al. (2017) proposed two binary diagrams, Si+Ca vs. Mn+Mg+V+Ni and Si+Ca vs. Mn+Cr (not shown), to discriminate alteration types. A plot of Si+Ca vs. Mn+Mg+V+Ni has been shown to discriminate LT K-Fe from HT Ca-Fe and HT K-Fe alteration, but cannot discriminate HT Ca-Fe from HT K-Fe alteration. In contrast, a plot of Si+Ca vs. Mn+Cr can discriminate the three alteration types from each other in spite of minor overlap. Based on the discriminant elements of Huang et al. (2019), two ternary diagrams have been developed: Si+Ca-V+Ni-Mn+Cr and Si+Ca-Mg+V-Mn+Cr (Fig. 5). These diagrams roughly separate three alteration types, although the composition of magnetite associated with HT Ca-Fe alteration may overlap with those

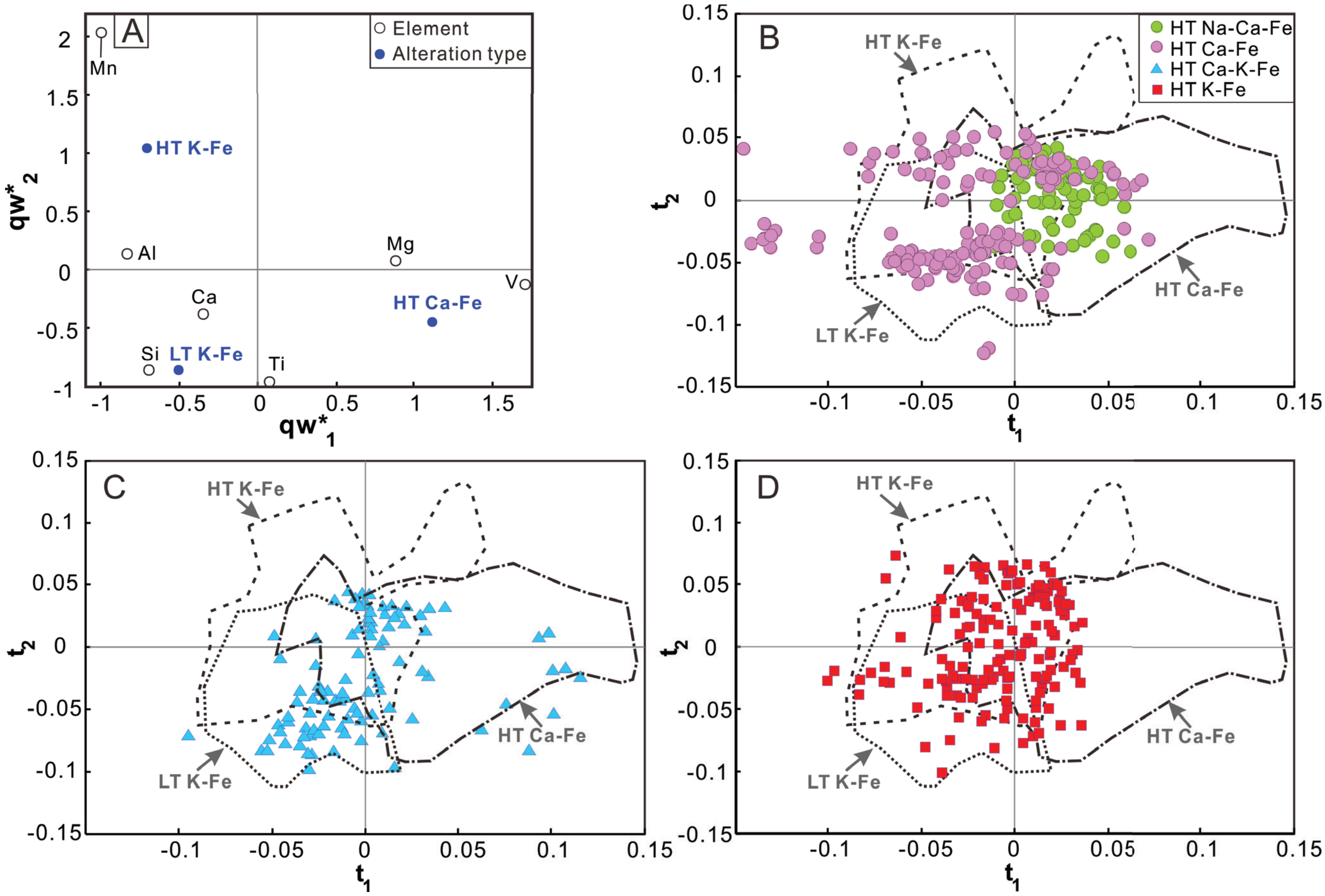


**FIGURE 4.** PLS-DA results of EPMA data of iron oxides from different alteration facies in IOCG and IOA deposits (Huang et al., 2019). **A**. Plot of qw×1 vs. qw×2 (first and second loadings) based on EPMA data showing correlations among element variables and alteration types. **B–D**. Plot of t1 vs. t2 (first and second scores) showing the compositional range of samples from different alteration facies in the latent variable space defined by qw×1-qw×2 in A. Three fields are defined, i.e. HT Ca-Fe, HT K-Fe, and LT K-Fe. Data points in B, C, and D are individual EPMA analyses of magnetite from the GBMZ (De Toni, 2016). HT = high temperature, LT = low temperature. The formulas for plotting new samples in B, C, and D are: t1 = (CLR(Si)+0.008)/0.4902 × (-0.0108) + (CLR(Ca)+0.6123)/0.3600 × (-0.0055) + (CLR(Al)-0.3378)/0.3522 × (-0.0129) + (CLR(Mn)-0.0658)/0.4858 × (-0.0155) + (CLR(Mg)+0.3135)/0.4350 × 0.0135 + (CLR(Ti)-0.3054)/0.4951 × 0.000996 + (CLR(V)-0.2248)/0.4940 × 0.0263; t2 = (CLR(Si)+0.008)/0.4902 × (-0.0132) + (CLR(Ca)+0.6123)/0.3600 × (-0.0058) + (CLR(Al)-0.3378)/0.3522 × 0.00234 + (CLR(Mn)-0.0658)/0.4858 × 0.0317 + (CLR(Mg)+0.3135)/0.4350 × 0.00137 + (CLR(Ti)-0.3054)/0.4951 × (-0.0148) + (CLR(V)-0.2248)/0.4940 × (-0.0018).

from HT K-Fe alteration. There is also a partial overlap between magnetite from the LT and HT K-Fe alteration facies.

Montreuil et al. (2013) defined two alteration indices based on bulk rock molar concentrations, (2×Ca+2×Mn+5×Fe)/(2×Ca+2×Mn+5×Fe+Mg+Si) and K/(K+Na+0.5×Ca), to discriminate iron oxide and alkali-calcic alteration facies. De Toni (2016) modified this diagram to discriminate iron oxides within the diagnostic alteration facies by removing Fe from the first index (x axis) and Na from the second index (y axis). As a result, iron oxides from HT Na-Ca-Fe and HT Ca-Fe alteration zones in the GBMZ mainly plot in the fields of Na-Ca-Fe-(Mg), Ca-K-Fe, Ca-Fe-(Mg), Fe-rich Ca-K-Fe, and Fe-rich Ca-Fe alteration (Fig. 6A). Iron oxides from HT K-Fe in the GBMZ mainly plot in the fields of K, K-(Fe), K-Fe, and Fe-rich K-Fe alteration (Fig. 6A). Similarly, iron oxides from HT and LT K-Fe alteration in worldwide IOCG deposits plot in K-related fields, whereas those from HT Ca-Fe alteration plot mainly in the field of the weakly altered rocks (Fig. 6B). However, iron oxides from HT Ca-K-Fe alteration zones in the GBMZ are scattered in nearly all fields of the discrimination plot (Fig. 6A). The foregoing indicates that the proposed discrimination diagram can be used to roughly distinguish HT Ca-Fe and K-Fe alteration, but it is difficult to distinguish transitional alteration types such as the HT Ca-K-Fe facies. These facies are commonly the sites of overprinted HT Ca-Fe, HT Ca-K-Fe and HT K-Fe alteration, such as described for the NICO deposit in the GBMZ (Corriveau et al., 2016; Montreuil et al., 2016a). In such zones, different generations of iron oxides are common (De Toni, 2016).

*Discrimination between Ore-related and Barren Alteration*

Ore-related and barren alteration facies are derived from different hydrothermal fluids or from an evolving fluid column with changing physicochemical conditions, both of which can

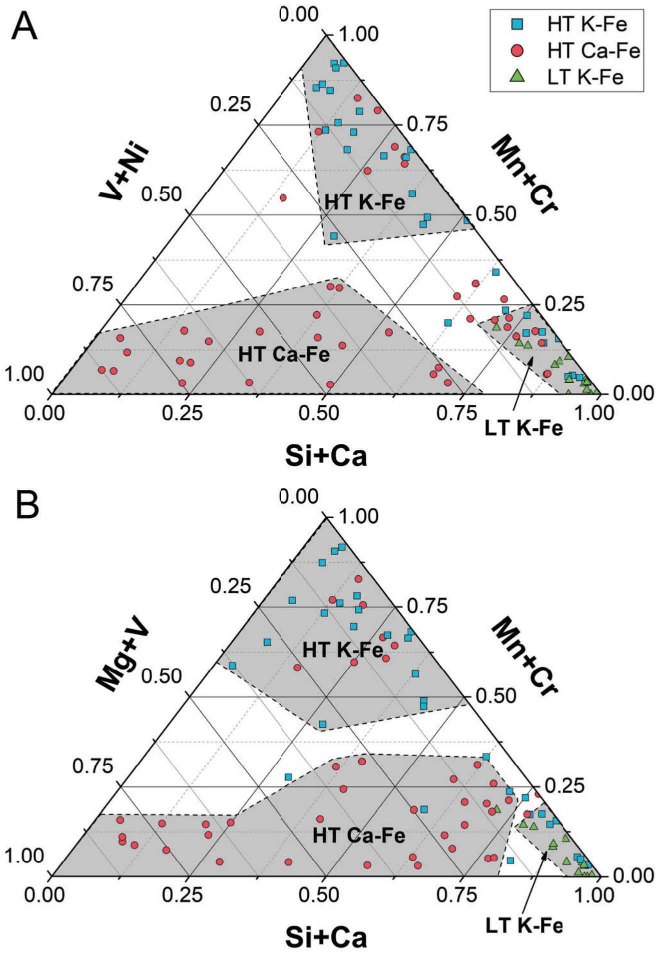


**FIGURE 5.** Ternary discriminant diagrams for alteration facies associated with IOCG and IOA deposits. Data points are average EPMA and LA-ICP-MS trace element compositions of iron oxides from each sample analyzed by Huang et al. (2019).

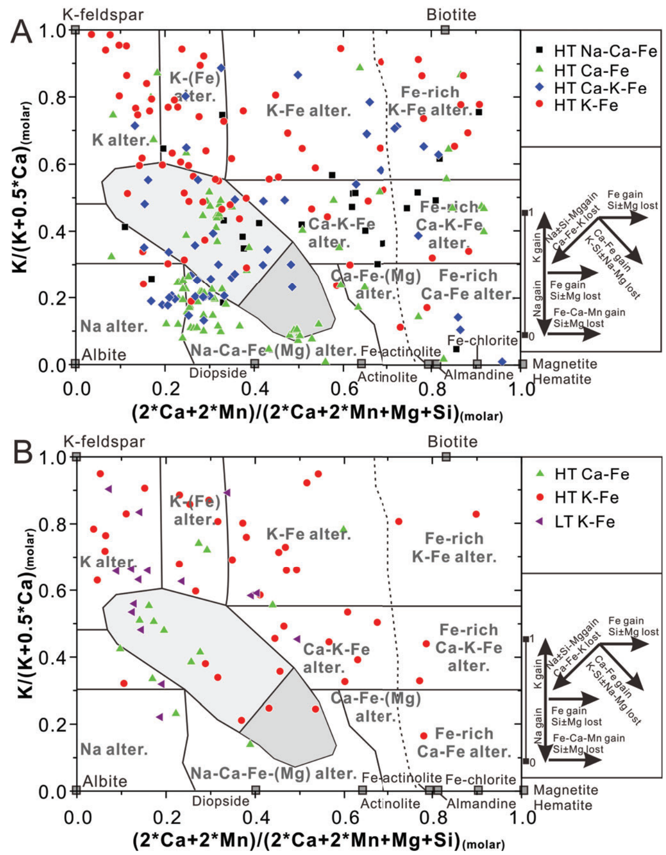


**FIGURE 6.** Trace element contents of iron oxides plotted on a modified version of the Montreuil et al. (2013) IOCG discriminant diagram. **A**. Analyses from the main alteration facies of the GBMZ. **B**. Analyses from global IOCG and IOA deposits (Huang et al., 2019). The pale and darker grey fields are for least-altered felsic to intermediate and mafic rocks, respectively. Rocks combining alteration facies also fall within these fields. Data here are EPMA analyses, excluding those below detection limits.

impact the chemical composition of magnetite. For example, Carew (2004) documents that Mo, W, U, and Th were relatively enriched in magnetite from weakly mineralized Na-Ca assemblages compared to magnetite in barren iron oxide-rich rocks and regional Na-Ca assemblages. He interprets the chemical differences between copper-gold mineralized and barren hydrothermal systems as the results of different magmatic sources and/or physicochemical conditions (e.g. T, $fO_2$). De Toni (2016) compared mineralized (Cu-Fe sulphide, U or REE) and barren alteration types (e.g. HT Ca-Fe, Ca-K-Fe, and K-Fe) and found that there is a general Mn and V impoverishment trend in magnetite from the mineralized alteration zones. For example, magnetite in mineralized and barren alteration facies can be discriminated by $t_1$, based on the relatively high Si, Ca, and Mg but low Ti, V, and Mn contents of magnetite associated with mineralization (Fig. 7A). This result is consistent with the conclusion of De Toni (2016). However, significant overlap between mineralized and barren alteration is observed (Fig. 7B). This may be due to the limited number of elements used for PLS-DA, preservation of several magnetite generations in samples with overprinting alteration facies, variations in fluid composition through fluid mixing, or changes in physicochemical conditions of the evolving fluid column responsible for fertile and barren alteration facies.

*Application for Mineral Exploration*

One of the most important aspects of iron oxide chemistry studies is to identify efficient indicator minerals for mineral exploration. Comparing magnetite chemistry from mineralized and barren rocks affords an opportunity to define the critical factors that control economic copper-gold or REE mineralization. Rusk et al. (2009a) analyzed trace elements in magnetite from the Cloncurry district, Australia, and documented that magnetite from barren hydrothermal breccias is enriched in vanadium and depleted in manganese relative to ore-related magnetite from the Ernest Henry deposit, known for having a significant manganese halo. They concluded that the difference in magnetite chemistry probably reflects mineral equilibrium at the site of magnetite deposition rather than different fluid compositions. They also analyzed

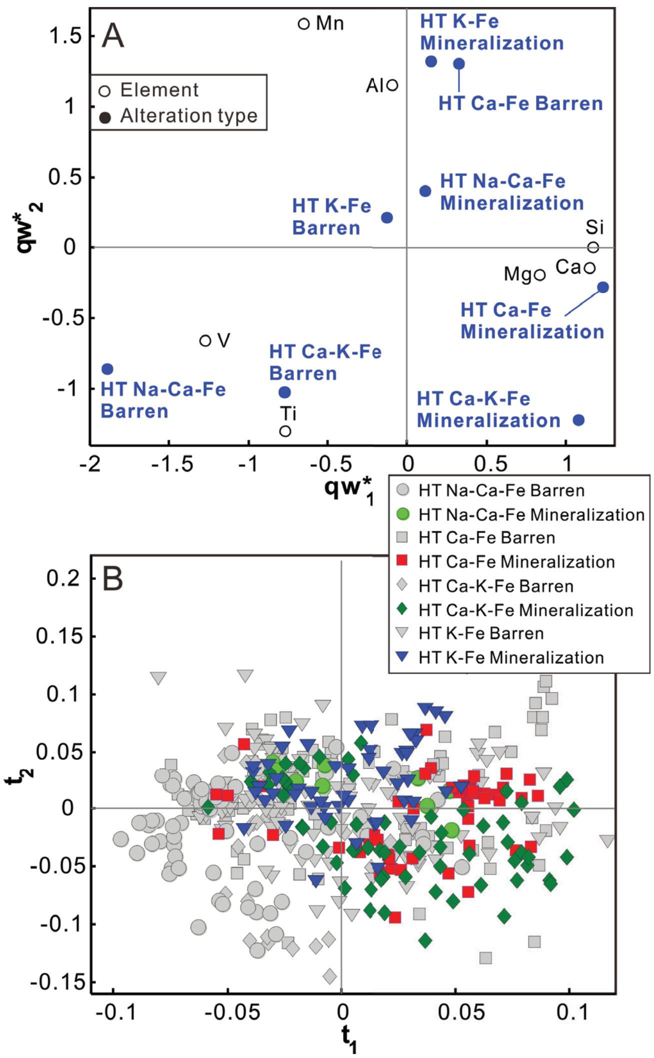


FIGURE 7. PLS-DA results of EPMA data of iron oxides from different alteration-mineralization types of IOCG and IOA deposits from the GBMZ, Canada. **A**. Plot of first and second loadings based on EPMA data showing correlations among element variables and alteration-mineralization types. **B**. Plot of first and second scores showing the distribution of individual analyses from different alteration and mineralization types in the latent variable space defined by qw*1-qw*2 in A. Data are from De Toni (2016). The formulas for plotting unknown samples in B are: t1 = (CLR(Si)-0.2281)/0.4927 × 0.0115 + (CLR(Ca)+0.3283)/0.4847 × 0.0113 + (CLR(Al)-0.1031)/0.3191 × (-0.000938) + (CLR(Mn)-0.0708)/0.4683 × (-0.0065) + (CLR(Mg)+0.505)/0.3582 × 0.00819 + (CLR(Ti)-0.1817)/0.4630 × (-0.00764) + (CLR(V)-0.2494)/0.5721 × (-0.0126); t2 = (CLR(Si)-0.2281)/0.4927 × 0.0000941 + (CLR(Ca)+0.3283)/0.4847 × (-0.00303) + (CLR(Al)-0.1031)/0.3191 × 0.0253 + (CLR(Mn)-0.0708)/0.4683 × 0.0348 + (CLR(Mg)+0.505)/0.3582 × (-0.0042) + (CLR(Ti)-0.1817)/0.4630 × (-0.0285) + (CLR(V)-0.2494)/0.5721 × (-0.0144).

magnetite and sulphides from the Starra, Mt. Elliot, and Osborne IOCG deposits to assess whether these minerals could be useful chemical vectors to proximal IOCG-style mineralization. The results show that the compositions of magnetite and sulphides from copper-gold ores are indistinguishable from those of regional unmineralized hydrothermal magnetite-matrix breccias.

Dupuis and Beaudoin (2011) proposed two diagrams, Ca+Al+Mn vs. Ti+V and Ni/(Cr+Mn) vs. Ti+V (not shown), to discriminate magnetite compositions in IOCG and IOA deposits from those in banded iron formation (BIF), magmatic Fe-Ti-V, porphyry and skarn deposits. These diagrams are very useful in preliminary discrimination of iron oxides having an unknown origin, e.g. those from till samples (McMartin et al., 2011a, b; Pisiak et al., 2017). However, all the magnetite grains used in this study are related to copper-gold or REE mineralization and the Dupuis and Beaudoin (2011) diagrams cannot be used to discriminate mineralized from barren samples.

Acosta-Góngora et al. (2014) showed that overlap exists in the Ti+V contents of magnetite from the barren metasedimentary host sequence and ore-related samples from the NICO deposit and other polymetallic prospects of the GBMZ. In contrast, magnetite elemental ratios such as Cr/Co, V/Co, Co/Ni, and V/Ni are likely more diagnostic than Ti+V contents. Pre-ore magnetite and magnetite in barren metasedimentary rocks have higher Cr/Co ratios (Cr/Co>1) than magnetite coeval with ore minerals and/or hosted by iron oxide (±sulphide)-dominated breccias and veins (Acosta-Góngora et al., 2014). However, some mineralization-related magnetite has elevated Cr/Co similar to that of magnetite unrelated to mineralization. This indicates that a transitional composition between the barren and ore-associated magnetite, such that binary diagrams based on these ratios should be used carefully when identifying magnetite related to mineralization.

De Toni (2016) illustrated that magnetite from mineralized alteration facies has lower concentrations of V and Mn than magnetite from barren alteration facies. As shown in Figure 7, magnetite from ore-related alteration zones can be discriminated from those in barren alteration zones by higher Si, Ca, and Mg but lower Ti, V, and Mn contents, as indicated by positive, higher loadings (qw×1) of these elements for ore-related alteration. This indicates that the composition of magnetite can be used as part of an indicator mineral method of exploring for IOCG and IOA deposits. It is worth noting that there is significant compositional overlap between fertile and barren magnetite (Fig. 7B). Therefore, more data are needed to assess the factors controlling the composition of magnetite from barren and fertile hydrothermal systems.

The intense metasomatic alteration in these systems influences rock physical properties (Enkin et al., 2016). In particular, changes in the composition of magnetite in alteration zones (De Toni, 2016) can modify the geophysical signatures magnetic susceptibility, electrical resistivity) of iron oxide-related alteration (Clark, 2014). For example, the introduction of silica during magnetite alteration affects its magnetic susceptibility. For three mineralized alteration facies (HT Ca-Fe, Ca-K-Fe, K-Fe), magnetic susceptibility is relatively high compared to barren alteration facies (De Toni, 2016). For a sample from a HT Ca-Fe alteration containing about 5% magnetite, the silica concentration in the magnetite is higher than in the magnetite of a HT Ca-Fe alteration vein (De Toni, 2016), which may explain a lower magnetic susceptibility.

### Constraints on Formation of IOCG and IOA Deposits

Numerous studies provide constraints on the genesis of IOCG and IOA deposits. IOCG deposits are considered to form from high-temperature magmatic-hydrothermal fluids exsolved from volatile-rich calc-alkaline to A-type granitic melts (Hitzman et al., 1992; Pollard, 2000; Sillitoe, 2003; Groves et al., 2010; Tornos, 2011; Ootes et al., 2017) or non-magmatic fluids, particularly from evaporitic sources driven by igneous or other heat sources (Barton and Johnson, 1996, 2000). A mixed source of magmatic fluids, basinal brines, and/or meteoric water was also proposed for the formation of IOCG deposits (Haynes et al., 1995; Kendrick et al., 2007, 2008; Baker et al., 2008; Zhao and Zhou, 2011; Chen, 2013; Huang et al., 2015b; Zhao et al., 2015).

Three main genetic models are invoked for the formation of IOA deposits: (1) crystallization of magnetite from high-temperature, volatile-rich oxide melts (Nyström and Henríquez, 1994; Frietsch and Perdahl, 1995; Henríquez and Nyström, 1998; Naslund et al., 2002; Henríquez et al., 2003; Velasco et al., 2016); (2) replacement of host rocks by iron-rich hydrothermal fluids (Hitzman et al., 1992; Rhodes et al., 1999; Hitzman, 2000; Sillitoe and Burrows, 2002; Edfelt et al., 2005; Valley et al., 2010; Dare et al., 2015; Corriveau et al., 2016; Broughm et al., 2017); and (3) magnetite flotation induced by exsolution of magmatic fluids and nucleation on magnetite microlites associated with hydrothermal alteration (Knipping et al., 2015a, b; Simon et al., 2018). A combination of the first two models is also proposed wherein igneous magnetite crystallizes from iron-rich melt and is overprinted by hydrothermal magnetite derived from magmatic-hydrothermal fluids (Tornos et al., 2016). In some iron oxide deposits associated with carbonatite (e.g. Phalabowra in South Africa, Bayan Obo in China; Groves and Vielreicher, 2001; Smith and Wu, 2000), magnetite is considered to form by autometasomatic oxidation of an extremely fractionated, salt-rich, carbonate melt separated from carbonated peralkalic silicate melt via liquid immiscibility (Lentz, 2014, 2018).

An important aspect that needs to be taken into account in constraining the origin of IOCG and IOA deposits using the trace element content of iron oxide is our current inability to distinguish igneous and high-temperature metasomatic magnetite solely based on composition. Some examples demonstrate that high-temperature metasomatic magnetite can have a trace element composition similar to that of igneous magnetite. For example, some magnetite grains from high-temperature Na-Ca-Fe and Ca-K-Fe alteration associated with IOA mineralization and iron oxide and alkali-calcic alteration systems in the Canadian GBMZ have Ti+V and Ca+Al+Mn contents similar to magnetite from magmatic Fe-Ti-V deposits (De Toni, 2016). In addition, magnetite and hematite from the Rektorn IOA deposit (Sweden) has Ti+V contents obviously higher than other IOA deposits worldwide (Huang et al., 2019), but similar to the composition of magmatic magnetite (Broughm et al., 2017). However, magnetite from the Rektorn and GBMZ deposits, with trace element signatures typical of igneous magnetite, have been demonstrated to be metasomatic, and formed within iron oxide and alkali-calcic alteration systems that host IOA mineralization (e.g. field observations and study of rock slabs and thin sections in Corriveau et al., 2016; De Toni, 2016; Montreuil et al., 2016a). Moreover, hydrothermally re-equilibrated igneous magnetite from granitic rocks can also have trace element signatures similar to magmatic magnetite from Fe-Ti-V deposits (Wen et al., 2017). Therefore, high-temperature hydrothermal and metasomatic magnetite cannot be discriminated from igneous magnetite solely by trace element composition, and detailed characterization of mineral assemblages associated with magnetite at field or thin section scale is necessary to assess crystallization processes at this time. In the remainder of this section, we focus on the ore genesis studies constrained by the trace element composition of iron oxides.

*Magmatic-associated IOCG and IOA Deposits*

Chen et al. (2015) analyzed trace element compositions of magnetite from the Lala, Dahongshan, and Yinachang IOCG deposits in the Kangdian Fe-Cu metallogenic province, southwestern China. High nickel contents of magnetite in the Lala and Dahongshan deposits suggest that the ore-forming fluids were genetically related to the crystallization of coeval mafic intrusions. Magnetite grains in iron oxide facies of the Yinachang deposit have much lower V and Ni but higher Sn and Mo contents than those of the Lala and Dahongshan deposits. They are interpreted as having precipitated from more oxidized and Mo-Sn-rich fluids that may have evolved from relatively felsic magmas. Though it is possible that the chemical composition of magnetite can be used to distinguish ore-forming fluids related to mafic or felsic magmas, it is also possible that such signatures result from preferential leaching of mafic and felsic igneous rocks.

Numerous IOA deposits occur in the Cretaceous Ningwu volcano-sedimentary basin in the Middle–Lower Yangtze River metallogenic belt (China), including the Ningwu, Washan, Nanshan, Heshangqiao, Taocun, Zhongjiu, and Gushan deposits (Mao et al., 2011; Yu et al., 2011). These deposits are called "porphyry-type iron deposit" in China because they are spatially and temporally associated with subvolcanic porphyries of intermediate to mafic composition. Triassic evaporites are considered to play an important role in the formation of the IOA and co-existing skarn deposits in this belt (e.g. Li et al., 2015). Hou et al. (2011) interpreted the massive magnetite orebody at Gushan as crystallized from iron-rich melts based on vesicle-rich, melt flow-like, brecciated ore structures and mineral chemistry of pyroxene phenocrysts and magnetite. Duan et al. (2012) showed that most magnetite grains in different types of ores from the Washan deposit have trace element compositions similar to magmatic magnetite, whereas minor grains have compositions similar to porphyry copper deposits. They interpreted the Washan magnetite as crystallized from high-temperature iron-rich fluids evolved from late magmas rather than hydrothermal replacement of the host diorite porphyry. Similar observations were made at the Heshangqiao deposit, where magnetite ranges in composition from that of magmatic Fe-Ti-V deposits to porphyry, and skarn deposits. Here, magnetite was interpreted as having crystallized from high-temperature iron-rich fluids with the involvement of evaporites (Duan et al., 2017). The Ti+V and the Ca+Al+Mn contents of magnetite in these IOA deposits are commonly higher than those of other global IOA deposits (Duan et al., 2012, 2017; Huang et al., 2019).

*Deposits with Mixed Magmatic and Hydrothermal-Metasomatic Features: El Laco, Chile*

The world-class El Laco iron deposit in Chile consists of more than 98% magnetite but the ore genesis remains controversial. It is considered to derive from an effusive iron oxide liquid or from replacement of andesite flows. Nyström and Henriquez (1994) interpreted the magnetitites on the flanks of the volcano El Laco as magnetite lavas and feeder dykes based on textures typical of rapid crystal growth from supersaturated melts. In particular, they suggest that the presence of columnar magnetite is diagnostic of a magmatic origin. Magnetite from El Laco has trace element compositions similar to those from the Kiruna deposit in Sweden with the exception of Mg values that are about five times higher at El Laco (4,000–8,000 ppm Mg). Dare et al. (2015) documented that magnetite from massive, lava-like magnetitite has trace-element features similar to magnetite from high-temperature (>500ºC) magmatic-hydrothermal deposits (e.g. IOCG and porphyry copper deposits) and argue for metasomatic replacement of andesite lava flows through dissolution and precipitation of magnetite from high-temperature fluids. Features interpreted as evidence for a metasomatic origin of the lava-looking units include: (1) depletion in elements that are relatively immobile in hydrothermal fluids (e.g. Ti, Al, Cr, Zr, Hf and Sc); (2) enrichment in elements that are highly incompatible with magmatic magnetite (REE, Si, Ca, Na and P) and normally present in very low abundance in magmatic magnetite; and (3) high Ni/Cr ratios that are typical of hydrothermal magnetite. In addition, magnetite also shows oscillatory zoning of Si, Ca, Mg, REE and most high field strength elements, and zoning truncations indicating dissolution, similar to that formed in hydrothermal iron skarn deposits.

Velasco et al. (2016) identified three types of magnetite in El Laco, based on differences in chemical compositions and host type: Type 1 magnetite in the andesite matrix is characterized by higher titanium and vanadium contents. Type 2 magnetite occurs as inclusions in phenocrysts or as daughter crystals of melt inclusions in andesite rocks, whereas type 3 magnetite represents the main magnetite mineralization and related hydrothermal alteration. Type 2 and 3 magnetite grains have lower titanium and vanadium contents but higher iron contents than type 1 magnetite. Combined with the mineralogy and chemistry of melt inclusions in pyroxene and plagioclase phenocrysts within the andesites, the trace element composition of the magnetite was interpreted to support a magmatic origin for the El Laco magnetite.

Broughm et al. (2017) observed that chemical zonation patterns in the El Laco magnetite do not correlate with those of iron-rich skarn magnetite (Dare et al., 2015). For example, the El Laco ore magnetite has zonation of incompatible large-ion lithophile element (e.g. strontium) and high field strength elements (e.g. Y, Nb, Ce, and Th) that are all elevated or depleted in the same crystal layers. In addition, some compatible elements (e.g. V and Ni) are homogenous across the magnetite grains. Therefore, they proposed that the magnetite at El Laco has crystallized from a volatile-rich, iron oxide melt that was fluctuating in physicochemical conditions rather than from replacement of the host rocks by pulses of hydrothermal fluids.

Ovalle et al. (2018) reported depth-dependent textural and geochemical variations in magnetite from outcrops and drill cores at El Laco. Seven generations of magnetite, all having different textures, were identified from shallow/surface, intermediate, and deep zones. Magnetite in the shallow/surface zone is coarse grained and transformed to hematite and goethite to various degrees. Magnetite in the intermediate zone is characterized by dissolution-reprecipitation and overgrowth textures, whereas magnetite in the deeper zone shows well-developed ilmenite exsolution lamellae. Moreover, from shallower to deeper zones, Ti, V, Al, and Mn concentrations in magnetite increase. The systematic variations in texture and chemical composition of magnetite with depth are interpreted to indicate the ore system evolved from purely magmatic to magmatic-hydrothermal environments. This study emphasizes the role of magmatic process during the evolution of caldera-related explosive volcanic systems in the formation of massive iron deposits.

*Carbonatite-associated Hydrothermal-metasomatic IOA Deposits: Bayan Obo, China*

The Bayan Obo Fe-REE-Nb deposit in China is the world's largest light REE deposit and is commonly grouped as a sub-type of the IOCG family (e.g. Corriveau, 2007; Smith and Wu, 2000). Though Bayan Obo is associated with carbonatites it is here regrouped with the IOA deposits because of the nature of its metasomatic system and the fact that ultimately, these deposits may have diverse sources of fluids while sharing similar ore system attributes. At Bayan Obo, magnetite and hematite ore bodies replace carbonate units (dolomite and limestone) coeval with alkaline magmatism, followed by remobilization and renewed hydrothermal activity (Drew et al., 1990; Smith and Wu, 2000). The iron oxide bodies form stratabound to massive alteration zones characterized by fluorite, Na-pyroxene or amphibole, biotite, dolomite or barite, and REE-bearing minerals including apatite and monazite (Smith and Wu, 2000). The stratabound alteration layers have been deformed and veined by renewed mineralization. Albitites occur as relicts within the pervasively K-feldspar-altered shale unit forming the hanging wall of the deposit (Drew et al., 1990). Contents of $K_2O$ reach 16 wt% (Drew et al., 1990). Breccias with K-feldspar-altered fragments and infills that include biotite, magnetite and K-feldspar form at the base of the previously albitized shale unit within the East ore zone. As such, Bayan Obo displays all metasomatic attributes of iron oxide and alkali-calcic alteration systems reviewed herein, and are best regrouped within IOA deposit types.

Most studies of the Bayan Obo deposit focus on REE, whereas studies on iron are sparse. Zeng et al. (1981) identified three generations of magnetite based on ore structures and magnetite textures. They analyzed the physical properties such as lattice parameter and reflectance, trace element composition, and temperature of magnetite formation, and interpreted that the three generations of magnetite are mainly metamorphic and sedimentary in origin, but have hydrothermal overprints. Oxygen isotopes in magnetite and hematite also support metasedimentary and hydrothermal origins for the iron (Wei and Shangguan, 1983). Huang et al. (2015b) showed that magnetite grains from the three types of ores have different trace element compositions: magnetite grains in banded ores have Al+Mn and Ti+V contents similar to BIF, whereas those from massive and disseminated ores have trace element compositions similar to IOCG and skarn deposits, respectively. The trace element signatures of magnetite from Bayan Obo are similar to those of the hydrothermally modified (metamorphosed) Tianhu sedimentary iron deposit in the Eastern Tianshan Orogenic Belt (Huang et al., 2015a). However, the banded ores in Bayan Obo cannot be interpreted as sedimentary in origin because these ores are mainly composed of aegirine, fluorite, barite, and REE minerals that are hydrothermal in origin. Based on REE contents in magnetite, Huang et al. (2015b) interpreted at least two stages of iron and REE mineralization. Sedimentary carbonates provide part of the REE content and were further metasomatized by REE-rich hydrothermal fluids to form the giant REE deposit. However, the trace element results are inconsistent with iron isotopes from iron ores, iron oxides, and related rocks that support a magmatic origin for the iron (Sun et al., 2013). Lentz (2014) proposes a model of magnetite formation by auto-oxidization and destabilization of $FeCO_3$ in the fractionated, salt-rich, carbonate melt.

*Deposits Linked to Flotation of Magmatic Magnetite*

Knipping et al. (2015a, b) analyzed trace element, iron and oxygen isotope compositions of magnetite from the Cretaceous Los Colorados IOA deposit in the northern Chilean Iron Belt. Textural and compositional variations define three types of magnetite that are interpreted as magmatic and hydrothermal in origin. Based on high-temperature experiments on melt inclusions in magnetite, published experimental data, and the geochemistry of magnetite and host rocks, they propose the flotation of magmatic magnetite suspensions for the formation of IOA deposits. In this model, the ore formation involves crystallization of magnetite microlites from a silicate melt, nucleation of aqueous fluid bubbles on magnetite surfaces, and formation and ascent of buoyant fluid bubble-magnetite aggregates. Simon et al. (2018) further illustrate this model by combining studies of trace elements and Fe-O-H-Re-Os isotopes of magnetite and other minerals. The magnetite flotation model is also supported by recent decompression experiments on silicate melts (Knipping et al., 2019; Pleše et al., 2019). The model explains the globally observed temporal and spatial relationship between magmatism and IOA and IOCG deposits but fails to account for the formation of the regional-scale albitite corridors that are an intrinsic early stage in the formation of these deposits worldwide. Nevertheless the model provides valuable concepts to define exploration strategies.

## Re-equilibration Processes in IOCG and IOA Magnetite

Magnetite can be used as an indicator mineral in glaciated terrain because it is resistant to low-temperature chemical weathering and mechanical abrasion during transport (McMartin et al., 2011a; Makvandi et al., 2017). Its ferromagnetic properties and characteristic chemical compositions in different geological environments have been used in mineral exploration. However, in high-temperature igneous and hydrothermal environments, the texture and composition of magnetite can be re-equilibrated by oxy-exsolution, coupled dissolution-reprecipitation (CDR), and recrystallization (Ciobanu and Cook, 2004; Hu et al., 2015; Makvandi et al., 2015; Heidarian et al., 2016; Broughm et al., 2017; Wen et al., 2017; Yin et al., 2017; Huang et al., 2018). The dissolution of magnetite has been demonstrated by solution experiments in which magnetite interacts with chloride-rich hydrothermal fluids (Chou and Eugster, 1977; Whitney et al., 1985; Ilton and Eugster, 1989). Simon et al. (2004) show that considerable amounts of iron can also be transported as vapor-phase metal complexes in the magmatic-hydrothermal system. Only a few studies focus on re-equilibrium processes in IOCG and IOA magnetite.

Heidarian et al. (2016) present textural and compositional data for three generations of magnetite in the Chadormalu IOA deposit. Primary magnetite is characterized by abundant porosity and a dark appearance under backscattered electron imaging, whereas a second generation of magnetite replacing primary magnetite shows a lighter appearance. The two generations of magnetite are related to CDR processes. Infiltration of high saline fluids was considered to have changed the physicochemical conditions of ore-forming fluids, which led to CDR reactions that formed secondary magnetite. A third generation of magnetite was formed by recrystallization of the previous two generations. The second generation of magnetite has lower Ca+Al+Mn contents than the primary magnetite, but the third generation of magnetite has higher V content than other two generations. Heidarian et al. (2016) attribute variations in the chemical composition of different generations of magnetite to the evolution of ore-forming fluids from magmatic-hydrothermal to moderately brine-dominated meteoric fluids. Broughm et al. (2017) show that magnetite at Kiruna displays complex textures and is largely influenced by subsequent metamorphism and/or metasomatic alteration. Thus, the chemical composition of the modified magnetite cannot be used to determine whether magnetite-apatite ores formed via hydrothermal fluids or through post-ore metamorphic or metasomatic alteration.

Textural and compositional data for magnetite from the Sossego, Alemao, and Candelaria IOCG and El Romeral IOA deposits in Brazil show that some magnetite grains have been modified by oxy-exsolution, CDR, and/or recrystallization (Fig. 8). Three generations of magnetite are identified in the Sossego deposit of the Carajás district in Brazil (Fig. 8A). The first generation of magnetite (Mag-1) is characterized by exsolution lamellae of ilmenite, which was overgrown by inclusion-poor Mag-2. The third generation of magnetite (Mag-3) replaced Mag-2 along grain margins and fractures. The Alemao magnetite shows a CDR texture with inclusion-rich core and an inclusion-poor rim

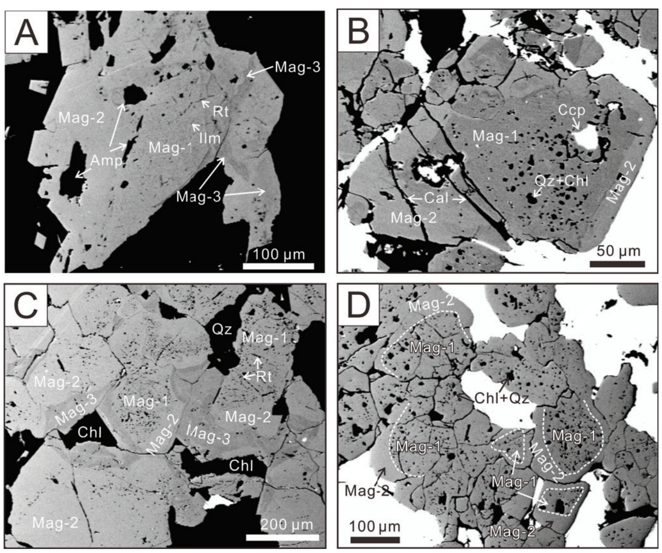


**Figure 8.** Backscattered electron images showing textures of magnetite from the Sossego, Alemao, and Candelaria IOCG and El Romeral IOA deposits (modified from Huang and Beaudoin, 2019). **A**. Three generations of magnetite in sample 080 from the Sossego IOCG deposit. Rutile and ilmenite-rich magnetite (Mag-1) was overgrown by smooth, light gray magnetite (Mag-2). Dark gray magnetite (Mag-3) replaced Mag-2 along grain boundaries or fractures. **B**. Two generations of magnetite in the Alemao IOCG deposit characterized by inclusion-rich core (Mag-1) and inclusion-free rim (Mag-2). Quartz, chlorite, and chalcopyrite inclusions are widespread in Mag-1. **C**. Three generations of magnetite in the El Romeral IOA deposit. The first generation of magnetite (Mag-1) is an inclusion-rich core and was replaced by an inclusion-poor magnetite in the rim (Mag-2). Mag-3 with darker BSE contrast replaced Mag-2 along the grain boundaries. **D**. Magnetite grains in sample PC98102 from the Candelaria IOCG deposit composed of inclusion (chlorite and quartz)-rich Mag-1 and inclusion-poor Mag-2. Abbreviations: *Amp* = amphibole, *Cal* = calcite, *Ccp* = chalcopyrite, *Chl* = chlorite, *Ilm* = ilmenite, *Mag* = magnetite, *Qz* = quartz, *Rt* = rutile.

(Fig. 8B). Similarly, three generations of magnetite have been identified at the El Romeral IOA deposit in Chile (Fig. 8C). The first contains abundant rutile and quartz inclusions and is overgrown by inclusion-poor magnetite (Mag-2) that was further replaced by inclusion-poor, darker magnetite (Mag-3). In the Candelaria IOCG deposit, the first generation of magnetite is rich in inclusions of chlorite and quartz (Mag-1) while the second generation consists of inclusion-poor (Mag-2) domains (Fig. 8D). Many magnetite grains show well-defined 120° triple junctions characteristic of recrystallization (Fig. 8D).

The oxy-exsolution of ilmenite in Sossego magnetite (Fig. 8A) is attributed to increasing oxygen fugacity and decreasing temperature with alteration and mineralization, resulting in product magnetite with lower titanium and higher vanadium contents (Huang and Beaudoin, 2019). CDR textures are widespread in magnetite grains from the Sossego, Alemao, and El Romeral deposits (Fig. 8A–C). Two types of CDR processes can be distinguished by textures and chemical compositions of different generations of magnetite (Huang and Beaudoin, 2019). The Type 1 CDR process is represented by the Alemao magnetite, in which an inclusion-rich and trace element-rich core (Mag-1) was replaced by inclusion-free and trace element-poor rim (Mag-2) (Fig. 8B). Type 2 CDR processes responsible for the third generation of magnetite (Mag-3) in the Sossego and El Romeral deposits occurs as veins replacing Mag-2 along fractures or grain margins (Fig. 8A, C). The Type 1 CDR process (transforming Mag-1 to Mag-2) is more extensive than Type 2 CDR in the studied samples and is similar to those reported in skarn deposits elsewhere (Hu et al., 2015). During Type 1 CDR processes, Si, K, Ca, Mg, Al, Mn, and Ti are excluded from parent magnetite as Fe contents increase, in contrast to the Type 2 CDR process (Huang and Beaudoin, 2019). Evolving fluid composition and/or decreasing temperature during ore formation may be responsible for Type 1 CDR processes, whereas post-ore replacement by magmatic-hydrothermal fluids may induce Type 2 CDR process (Huang and Beaudoin, 2019). Recrystallization of some magnetite grains (Fig. 8D) in Candelaria IOCG deposit is commonly due to high-temperature annealing during crystal growth that preserved chemical compositions of primary magnetite (Huang and Beaudoin, 2019).

The examples presented here further demonstrate that magnetite in magmatic-hydrothermal systems such as IOCG and IOA deposits can be modified in terms of textures and chemical compositions. The secondary magnetite grains, particularly those formed by CDR processes, have chemical composition that may be different from their primary parent magnetite, complicating the application of discrimination plots based on trace elements (Fig. 9). For example, magnetite that has experienced the Type 2 CDR process has trace element compositions similar to porphyry copper magnetite (Fig. 9A, B), whereas magnetite that experienced the Type 1 CDR process has lower Ca+Al+Mn contents (Fig. 9C). Recrystallization produced no significant change in the trace

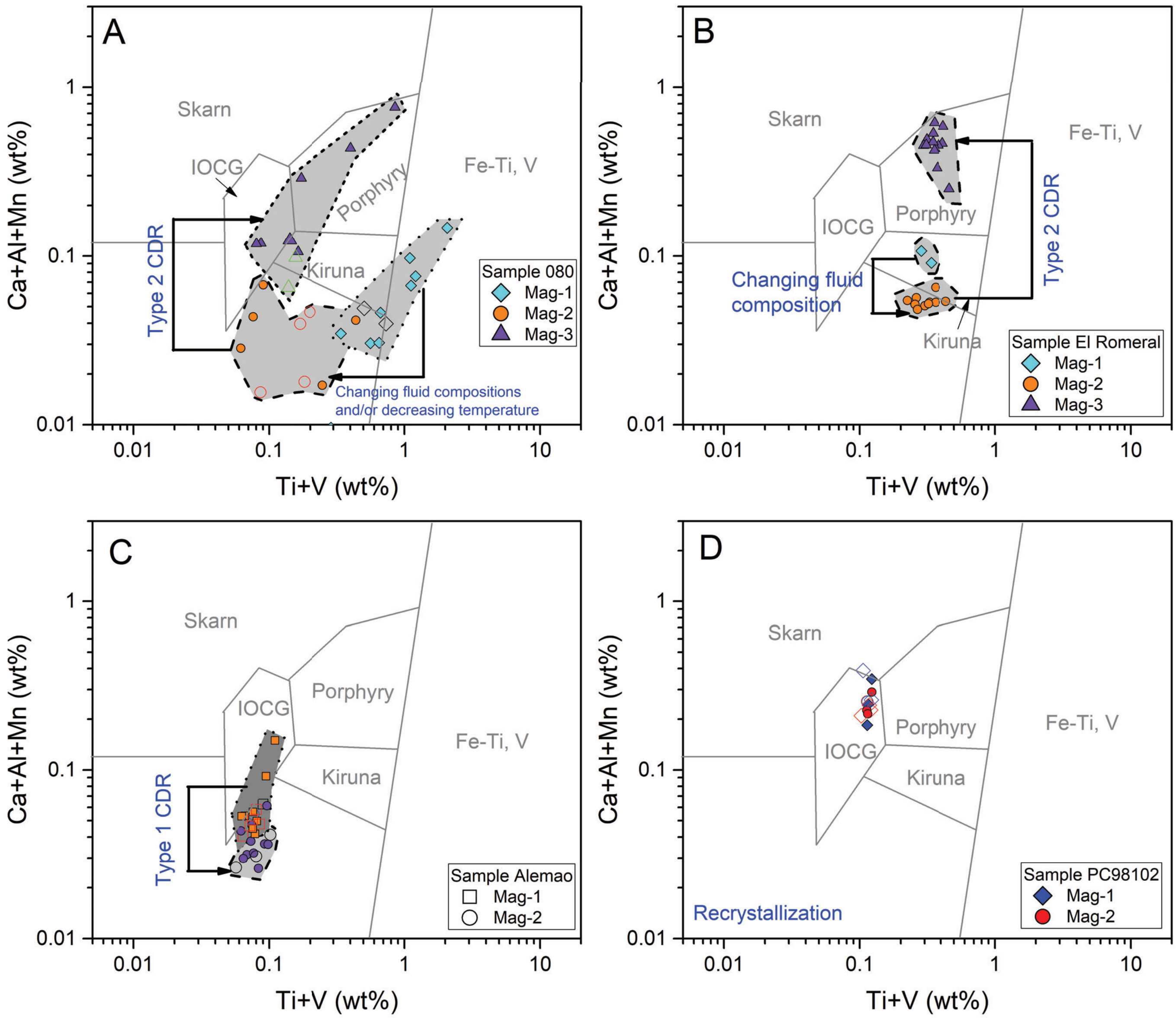


**Figure 9.** Plot of EPMA data of magnetite from Sossego IOCG (**A**), El Romeral IOA (**B**), Alemao (**C**) and Candelaria (**D**) IOCG deposits in the Ti+V vs. Ca+Al+Mn diagram (modified from Huang and Beaudoin, 2019). Data below the detection limit are plotted as hollow symbol. The deposit type fields are based on Dupuis and Beaudoin (2011). Deposit type abbreviations: Skarn = Fe-Cu skarn deposits, Porphyry = porphyry Cu deposits; Kiruna = Kiruna-type magnetite-apatite deposits.

element composition of magnetite (Fig. 9D). Therefore, the in situ chemical composition of magnetite should be interpreted together with textural observation to better constrain the origin of magnetite in IOCG and IOA deposits.

Widespread CDR textures in magnetite from IOCG deposits and, to a lesser extent, IOA deposits imply that hydrothermal alteration is crucial to the formation of these deposits. This is consistent with the widespread development of iron oxide and alkali-calcic alteration in association with both the IOCG and IOA deposit types (Corriveau et al., 2016). Moreover, magnetite is not formed by one pulse of hydrothermal fluids, as indicated by multiple generations of magnetite. Evolving fluid and metasomatic rock compositions as metasomatism proceeds results in the observed variations in alteration types and magnetite compositions, forming different types of iron oxide deposits (Fig. 1). Therefore, CDR textures further support the formation of IOCG and IOA deposits via hydrothermal metasomatism of host rocks through intensive fluid-rock interaction (Hitzman et al., 1992; Rhodes et al., 1999; Hitzman, 2000; Sillitoe and Burrows, 2002; Edfelt et al., 2005; Valley et al., 2010; Dare et al., 2015; Corriveau et al., 2016; Broughm et al., 2017).

## Concluding Remarks

Trace element geochemistry of iron oxides in IOCG and IOA deposits has been used to discriminate deposit and alteration types, and thus has important implications in mineral exploration. Identification of ore-related alteration from barren alteration will be an important aspect in the iron oxide fingerprinting of these deposits. Trace element compositions of iron oxides, combined with the study of Fe, O, and Os isotopes in iron oxides or other minerals, will be very efficient in constraining the genesis of IOCG and IOA deposits. Temporal and spatial variations of trace elements in iron oxides at mineral, alteration facies, and deposit scales provide fluid evolution information that is very helpful in understanding the formation of minerals and deposits. As there are commonly several generations of iron oxides in IOCG and IOA deposits, *in situ* chemical analysis of iron oxides should be combined with detailed textural observations in order to accurately understand their origin. Future work in iron oxide fingerprinting may include discrimination of ore-relation alteration from barren alteration, and linking iron oxide chemistry to physical properties amenable to geophysical exploration.

## Acknowledgments

This project was funded by “CAS Hundred Talents Program” project (Y9CJ034000) to XWH, the Natural Science and Engineering Research Council (NSERC) of Canada, Agnico Eagle Mines Limited, and Ministère de l’Énergie et des Ressources Naturelles du Québec within the NSERC-Agnico Eagle Industrial Research Chair in Mineral Exploration. The paper was also conducted in collaboration with the Targeted Geoscience Initiative of the Geological Survey of Canada; NRCan contribution number 20190058. We thank Marc Choquette (Laval U.) for his assistance with EPMA analyses, Isabelle McMartin and Pedro Acosta-Góngora for their reviews of this manuscript and Eric Potter for editorial handling of the manuscript.

## References

Acosta-Góngora, P., Gleeson, S.A., Samson, I.M., Ootes, L., and Corriveau, L., 2014, Trace element geochemistry of magnetite and its relationship to Cu-Bi-Co-Au-Ag-U-W mineralization in the Great Bear magmatic zone, NWT, Canada: Economic Geology, v. 109, p. 1901-1928.

Aitchison, J., 1986, The statistical analysis of compositional data: Chapman and Hall Ltd., London, 416 p.

Baker, T., Mustard, R., Fu, B., Williams, P.J., Dong, G., Fisher, L., Mark, G., and Ryan, C.G., 2008, Mixed messages in iron oxide–copper–gold systems of the Cloncurry district, Australia: insights from PIXE analysis of halogens and copper in fluid inclusions: Mineralium Deposita, v. 43, p. 599-608.

Barton, M.D., and Johnson, D.A., 1996, Evaporitic-source model for igneous-related Fe oxide–(REE-Cu-Au-U) mineralization: Geology, v. 24, p. 259-262.

Barton, M.D., and Johnson, D.A., 2000, Alternative brine sources for Fe-oxide (-Cu-Au) systems: implications for hydrothermal alteration and metals, *in* Porter, T.M., ed., Hydrothermal iron oxide copper-gold and related deposits: a global perspective, v. 1: PGC Publishing, Adelaide, p. 43-60.

Barton, M.D., and Johnson, D.A., 2004, Footprints of Fe oxide (-Cu-Au) systems: University of Western Australia Special Publication, v. 33, p. 112-116.

Beaudoin, G., and Dupuis, C., 2010, Iron-oxide Trace Element Fingerprinting of mineral deposit types, *in* Corriveau, L. and Mumin, A.H., eds., Exploring for iron oxide copper-gold deposits: Canada and global analogues: Geological Association of Canada, Short Course Notes, No. 20, p. 107-121.

Blein, O., and Corriveau, L., 2017, Recognizing IOCG alteration facies at granulite facies in the Bondy gneiss complex of the Grenville Province: Proceedings of the 14th SGA Biennial Meeting, 20-23 August, Québec City, p. 907-911.

Boutroy, E., Dare, S.A.S., Beaudoin, G., Barnes, S.-J., and Lightfoot, P.C., 2014, Magnetite composition in Ni-Cu-PGE deposits worldwide and its application to mineral exploration: Journal of Geochemical Exploration, v. 145, p. 64-81.

Brereton, R.G., and Lloyd, G.R., 2014, Partial least squares discriminant analysis: taking the magic away: Journal of Chemometrics, v. 28, p. 213-225.

Broughm, S.G., Hanchar, J.M., Tornos, F., Westhues, A., and Attersley, S., 2017, Mineral chemistry of magnetite from magnetite-apatite mineralization and their host rocks: examples from Kiruna, Sweden, and El Laco, Chile: Mineralium Deposita, v. 52, p. 1223-1244.

Buddington, A., and Lindsley, D., 1964, Iron-titanium oxide minerals and synthetic equivalents: Journal of Petrology, v. 5, p. 310-357.

Carew, M.J., 2004, Controls on Cu-Au mineralisation and Fe oxide metasomatism in the Eastern Fold Belt, NW Queensland, Australia: Ph.D. thesis, James Cook University, 308 p.

Chen, H., 2013, External sulphur in IOCG mineralization: implications on definition and classification of the IOCG clan: Ore Geology Reviews, v. 51, p. 74-78.

Chen, W.T., Zhou, M.-F., and Zhao, T.-P., 2013, Differentiation of nelsonitic magmas in the formation of the ~1.74 Ga Damiao Fe–Ti–P ore deposit, North China: Contributions to Mineralogy and Petrology, v. 165, p. 1341-1362.

Chen, W.T., Zhou, M.-F., Gao, J.-F., and Hu, R.Z., 2015, Geochemistry of magnetite from Proterozoic Fe-Cu deposits in the Kangdian metallogenic province, SW China: Mineralium Deposita, v. 50, p. 795-809.

Childress, T.M., Simon, A.C., Day, W.C., Lundstrom, C.C., and Bindeman, I.N., 2016, Iron and oxygen isotope signatures of the Pea Ridge and Pilot Knob magnetite-apatite deposits, southeast Missouri, USA: Economic Geology, v. 111, p. 2033-2044.

Chou, I.-M., and Eugster, H.P., 1977, Solubility of magnetite in supercritical chloride solutions: American Journal of Science, v. 277, p. 1296-1314.

Ciobanu, C.L., and Cook, N.J., 2004, Skarn textures and a case study: the Ocna de Fier-Dognecea orefield, Banat, Romania: Ore Geology Reviews, v. 24, p. 315-370.

Clark, D.A., 2014, Magnetic effects of hydrothermal alteration in porphyry copper and iron-oxide copper–gold systems: a review: Tectonophysics, v. 624, p. 46-65.

Corriveau, L., 2007, Iron oxide copper-gold deposits: a Canadian perspective, *in* Goodfellow, W., ed., Mineral deposits of Canada: a synthesis of major deposit-types, district metallogeny, the evolution of geological provinces, and exploration methods: Geological Association of Canada-Mineral Deposits Division, Special Volume 5, p. 307-328.

Corriveau, L., Williams, P.J., and Mumin, A.H., 2010, Alteration vectors to IOCG mineralization – From uncharted terranes to deposits, *in* Corriveau, L. and Mumin, A.H., eds., Exploring for iron oxide copper-gold deposits: Canada and global analogues: Geological Association of Canada, Short Course Notes, No. 20, p. 89-110.

Corriveau, L., Montreuil, J.-F., and Potter, E.G., 2016, Alteration facies linkages among iron oxide copper-gold, iron oxide-apatite, and affiliated deposits in the Great Bear magmatic zone, Northwest Territories, Canada: Economic Geology, v. 111, p. 2045-2072.

Corriveau, L., Potter, E.G., Acosta-Góngora, P., Blein, O., Montreuil, J.-F., De Toni, A.F., Day, W., Slack, J.F., Ayuso, R.A., and Hanes, R., 2017, Petrological mapping and chemical discrimination of alteration facies as vectors to IOA, IOCG, and affiliated deposits within Laurentia and beyond: Proceedings of the 14th SGA Biennial Meeting, 20-23 August, Québec City, p. 851-855.

Dare, S.A.S., Barnes, S.-J., and Beaudoin, G., 2012, Variation in trace element content of magnetite crystallized from a fractionating sulfide liquid, Sudbury, Canada: implications for provenance discrimination: Geochimica et Cosmochimica Acta, v. 88, p. 27-50.

Dare, S.A.S., Barnes, S.-J., Beaudoin, G., Méric, J., Boutroy, E., and Potvin-Doucet, C., 2014, Trace elements in magnetite as petrogenetic indicators: Mineralium Deposita, v. 49, p. 785-796.

Dare, S.A.S., Barnes, S.-J., and Beaudoin, G., 2015, Did the massive magnetite "lava flows" of El Laco (Chile) form by magmatic or hydrothermal processes? New constraints from magnetite composition by LA-ICP-MS: Mineralium Deposita, v. 50, p. 607-617.

De Iorio, M., Ebbels, T.M.D., and Stephens, D.A., 2008, Statistical techniques in metabolic profiling: Handbook of Statistical Genetics, John Wiley & Sons, Ltd, p. 347-373.

De Toni, A.F., 2016, Les paragenèses à magnétite des altérations associées aux systèmes à oxydes de fer et altérations en éléments alcalins, zone magmatique du Grand lac de l'Ours: M.Sc. thesis, Institut national de la Recherche scientifique-Centre Eau Terre Environnement, 549 p.

Deditius, A.P., Reich, M., Simon, A.C., Suvorova, A., Knipping, J., Roberts, M.P., Rubanov, S., Dodd, A., and Saunders, M., 2018, Nanogeochemistry of hydrothermal magnetite: Contributions to Mineralogy and Petrology, v. 173, 46.

Drew, L.J., Meng, Q., and Sun, W., 1990, The Bayan Obo iron-rare-earth-niobium deposits, Inner Mongolia, China: Lithos, v. 26, p. 43-65.

Duan, C., Li, Y.H., Yuan, S.D., Hu, M.Y., Zhao, L.H., Chen, X.D., Zhang, C., and Liu, J.L., 2012, Geochemical characteristics of magnetite from Washan iron deposit in Ningwu ore district and its constraints on ore-forming: Acta Petrologica Sinica, v. 28, p. 243-257. (in Chinese with English abstract)

Duan, C., Li, Y.H., Mao, J.W., Wang, C.L., Yang, B.Y., Hou, K.J., Wang, Q., and Li, W., 2017, Study on the ore-forming process of the Heshangqiao IOA deposit in the Ningwu ore district: insight from magnetite LA-ICP-MS in-situ analysis data: Acta Petrologica Sinica, v. 33, p. 3471-3483. (in Chinese with English abstract)

Dupuis, C., and Beaudoin, G., 2011, Discriminant diagrams for iron oxide trace element fingerprinting of mineral deposit types: Mineralium Deposita, v. 46, p. 1-17.

Edfelt, Å., Armstrong, R.N., Smith, M., and Martinsson, O., 2005, Alteration paragenesis and mineral chemistry of the Tjårrojåkka apatite–iron and Cu (-Au) occurrences, Kiruna area, northern Sweden: Mineralium Deposita, v. 40, p. 409-434.

Egozcue, J.J., Pawlowsky-Glahn, V., Mateu-Figueras, G., and Barcelo-Vidal, C., 2003, Isometric logratio transformations for compositional data analysis: Mathematical Geology, v. 35, p. 279-300.

Enkin, R.J., Corriveau, L., and Hayward, N., 2016, Metasomatic alteration control of petrophysical properties in the Great Bear magmatic zone (Northwest Territories, Canada, *in* Slack, J., Corriveau, L. and Hitzman, M., eds., Proterozoic iron oxide-apatite (± REE) and iron oxide-copper-gold and affiliated deposits of Southeast Missouri, USA, and the Great Bear magmatic zone, Northwest Territories, Canada: Economic Geology, v. 111, p. 2073-2086.

Eriksson, L., Byrne, T., Johansson, E., Trygg, J., and Vikström, C., 2013, Multi- and megavariate data analysis: basic principles and applications: Sweden, MKS Umetrics AB, 1-521 p.

Fleet, M.E., 1981, The structure of magnetite: Acta Crystallographica Section B, Structural Science Crystal Engineering Materials, v. 37, p. 917-920.

Frietsch, R., and Perdahl, J.-A., 1995, Rare earth elements in apatite and magnetite in Kiruna-type iron ores and some other iron ore types: Ore Geology Reviews, v. 9, p. 489-510.

Frost, B.R., and Lindsley, D.H., 1991, Occurrence of iron-titanium oxides in igneous rocks, *in* Lindsley, D.H., ed., Oxide minerals: petrologic and magnetic significance: Reviews in Mineralogy and Geochemistry, v. 25, p. 433-468.

Ghiorso, M.S., and Sack, O., 1991, Fe-Ti oxide geothermometry: thermodynamic formulation and the estimation of intensive variables in silicic magmas: Contributions to Mineralogy and Petrology, v. 108, p. 485-510.

Goldschmidt, V.M., 1958, Geochemistry: Oxford University Press, London.

Grigsby, J.D., 1990, Detrital magnetite as a provenance indicator: Journal of Sedimentary Research, v. 60, p. 940-951.

Groves, D.I., and Vielreicher, N.M., 2001, The Phalaborwa (Palabora) carbonatite-hosted magnetite-copper sulfide deposit, South Africa: an end-member of the iron-oxide copper-gold-rare earth element deposit group?: Mineralium Deposita, v. 36, p. 189-194.

Groves, D.I., Bierlein, F.P., Meinert, L.D., and Hitzman, M.W., 2010, Iron oxide copper-gold (IOCG) deposits through Earth history: implications for origin, lithospheric setting, and distinction from other epigenetic iron oxide deposits: Economic Geology, v. 105, p. 641-654.

Haynes, D.W., Cross, K.C., Bills, R.T., and Reed, M.H., 1995, Olympic Dam ore genesis: a fluid-mixing model: Economic Geology, v. 90, p. 281-307.

Heidarian, H., Lentz, D., Alirezaei, S., Peighambari, S., and Hall, D., 2016, Using the chemical analysis of magnetite to constrain various stages in the formation and genesis of the Kiruna-type Chadormalu magnetite-apatite deposit, Bafq district, Central Iran: Mineralogy and Petrology, v. 110, p. 927-942.

Helsel, D.R., 2005, Nondetects and data analysis: statistics for censored environmental data: New York, Wiley-Interscience, 228 p.

Henríquez, F., and Nyström, J.O., 1998, Magnetite bombs at El Laco volcano, Chile: GFF, v. 120, p. 269-271.

Henríquez, F., Naslund, H.R., Nyström, J.O., Vivallo, W., Aguirre, R., Dobbs, F.M., and Lledó, H., 2003, New field evidence bearing on the origin of the El Laco magnetite deposit, northern Chile—a discussion: Economic Geology, v. 98, p. 1497-1500.

Hitzman, M.W., 2000, Iron oxide-Cu-Au deposits: what, where, when, and why, *in* Porter, T.M., ed., Hydrothermal iron oxide copper-gold & related deposits: a global perspective, v. 1: PGC Publishing, Adelaide, p. 9-25.

Hitzman, M.W., Oreskes, N., and Einaudi, M.T., 1992, Geological characteristics and tectonic setting of Proterozoic iron oxide (Cu ± U ± Au ± REE) deposits: Precambrian Research, v. 58, p. 241-287.

Hou, T., Zhang, Z., and Kusky, T., 2011, Gushan magnetite–apatite deposit in the Ningwu basin, Lower Yangtze River Valley, SE China: hydrothermal or Kiruna-type?: Ore Geology Reviews, v. 43, p. 333-346.

Hron, K., Templ, M., and Filzmoser, P., 2010, Imputation of missing values for compositional data using classical and robust methods: Computational Statistics & Data Analysis, v. 54, p. 3095-3107.

Hu, H., Li, J.-W., Lentz, D., Ren, Z., Zhao, X.-F., Deng, X.-D., and Hall, D., 2014, Dissolution–reprecipitation process of magnetite from the Chengchao iron deposit: insights into ore genesis and implication for in-situ chemical analysis of magnetite: Ore Geology Reviews, v. 57, p. 393-405.

Hu, H., Lentz, D., Li, J.-W., McCarron, T., Zhao, X.-F., and Hall, D., 2015, Reequilibration processes in magnetite from iron skarn deposits: Economic Geology, v. 110, p. 1-8.

Huang, X.-W., and Beaudoin, G., 2019, Textures and chemical composition of magnetite from iron oxide-copper-gold (IOCG) and Kiruna-type iron oxide-apatite (IOA) deposits and their implications for ore genesis and magnetite classification schemes: Economic Geology, v. 114, p. 1-28.

Huang, X.-W., Zhou, M.-F., Qi, L., Gao, J.-F., and Wang, Y.-W., 2013, Re-Os isotopic ages of pyrite and chemical composition of magnetite from the Cihai magmatic-hydrothermal Fe deposit, NW China: Mineralium Deposita, v. 48, p. 925-946.

Huang, X.-W., Qi, L., and Meng, Y.-M., 2014, Trace element geochemistry of magnetite from the Fe(-Cu) deposits in the Hami region, Eastern Tianshan Orogenic Belt, NW China: Acta Geologica Sinica, v. 88, p. 176-195.

Huang, X.-W., Gao, J.-F., Qi, L., and Zhou, M.-F., 2015a, In-situ LA-ICP-MS trace elemental analyses of magnetite and Re–Os dating of pyrite: the Tianhu hydrothermally remobilized sedimentary Fe deposit, NW China: Ore Geology Reviews, v. 65, p. 900-916.

Huang, X.-W., Zhou, M.-F., Qiu, Y.-Z., and Qi, L., 2015b, In-situ LA-ICP-MS trace elemental analyses of magnetite: the Bayan Obo Fe-REE-Nb deposit, North China: Ore Geology Reviews, v. 65, p. 884-899.

Huang, X.-W., Gao, J.-F., Qi, L., Meng, Y.-M., Wang, Y.-C., and Dai, Z.-H., 2016, In-situ LA-ICP-MS trace elements analysis of magnetite: the Fenghuangshan Cu-Fe-Au deposit, Tongling, Eastern China: Ore Geology Reviews, v. 72, p. 746-759.

Huang, X.-W., Boutroy, E., Beaudoin, G., Makvandi, S., Corriveau, L., and De Toni, A.F., 2017, Trace element composition of iron oxides from IOCG and IOA deposits, and relationships to hydrothermal alteration and deposit subtypes: Proceedings of the 14th SGA Biennial Meeting, 20-23 August, Québec City, p. 931-934.

Huang, X.-W., Zhou, M.-F., Beaudoin, G., Gao, J.-F., Qi, L., and Lyu, C., 2018, Origin of the volcanic-hosted Yamansu Fe deposit, Eastern Tianshan, NW China: constraints from pyrite Re-Os isotopes, stable isotopes, and in situ magnetite trace elements: Mineralium Deposita, v. 53, p. 1039-1060.

Huang, X.-W., Boutroy, E., Makvandi, S., Beaudoin, G., Corriveau, L., and De Toni, A.F., 2019, Trace element composition of iron oxides from IOCG and IOA deposits: relationship to hydrothermal alteration and deposit subtypes: Mineralium Deposita, v. 54, p. 525-552.

Ilton, E.S., and Eugster, H.P., 1989, Base metal exchange between magnetite and a chloride-rich hydrothermal fluid: Geochimica et Cosmochimica Acta, v. 53, p. 291-301.

Jarosewich, E., Nelen, J., and Norberg, J.A., 1980, Reference samples for electron microprobe analysis: Geostandards Newsletter, v. 4, p. 43-47.

Kendrick, M., Mark, G., and Phillips, D., 2007, Mid-crustal fluid mixing in a Proterozoic Fe oxide–Cu–Au deposit, Ernest Henry, Australia: evidence from Ar, Kr, Xe, Cl, Br, and I: Earth and Planetary Science Letters, v. 256, p. 328-343.

Kendrick, M., Baker, T., Fu, B., Phillips, D., and Williams, P., 2008, Noble gas and halogen constraints on regionally extensive mid-crustal Na–Ca metasomatism, the Proterozoic Eastern Mount Isa Block, Australia: Precambrian Research, v. 163, p. 131-150.

Knipping, J.L., Bilenker, L.D., Simon, A.C., Reich, M., Barra, F., Deditius, A.P., Lundstrom, C., Bindeman, I., and Munizaga, R., 2015a, Giant Kiruna-type deposits form by efficient flotation of magmatic magnetite suspensions: Geology, v. 43, p. 591-594.

Knipping, J.L., Bilenker, L.D., Simon, A.C., Reich, M., Barra, F., Deditius, A.P., Wälle, M., Heinrich, C.A., Holtz, F., and Munizaga, R., 2015b, Trace elements in magnetite from massive iron oxide-apatite deposits indicate a combined formation by igneous and magmatic- hydrothermal processes: Geochimica et Cosmochimica Acta, v. 171, p. 15-38.

Knipping, J.L., Webster, J.D., Simon, A.C., and Holtz, F., 2019, Accumulation of magnetite by flotation on bubbles during decompression of silicate magma: Scientific Reports, v. 9, 3852.

Lee, L., and Helsel, D., 2007, Statistical analysis of water-quality data containing multiple detection limits II: S-language software for nonparametric distribution modeling and hypothesis testing: Computers & Geosciences, v. 33, p. 696-704.

Lentz, D., 2014, Reexamination of the genesis of the Bayan Obo Fe-REE-Nb deposit: autometasomatic oxidation of an extremely fractionated ferrocarbonatite: Acta Geologica Sinica-English Edition, v. 88, p. 361-363.

Lentz, D., 2018, Iron oxide copper-gold (IOCG) systems: examination of end-member models, physiochemical processes, and possible modern analogies: Proceedings of the 15th Quadrennial IAGOD International Association on the Genesis of Ore Deposits Symposium, Salta, p. 373-374.

Li, W., Audétat, A., and Zhang, J., 2015, The role of evaporites in the formation of magnetite–apatite deposits along the Middle and Lower Yangtze River, China: evidence from LA-ICP-MS analysis of fluid inclusions: Ore Geology Reviews, v. 67, p. 264-278.

Liu, P.-P., Zhou, M.-F., Chen, W.T., Gao, J.-F., and Huang, X.-W., 2015, In-situ LA-ICP-MS trace elemental analyses of magnetite: Fe–Ti–(V) oxide-bearing mafic–ultramafic layered intrusions of the Emeishan Large Igneous Province, SW China: Ore Geology Reviews, v. 65, p. 853-871.

Loberg, B.E.H., and Horndahl, A.K., 1983, Ferride geochemistry of Swedish Precambrian iron ores: Mineralium Deposita, v. 18, p. 487-504.

Makvandi, S., Beaudoin, G., McClenaghan, B.M., and Layton-Matthews, D., 2015, The surface texture and morphology of magnetite from the Izok Lake volcanogenic massive sulfide deposit and local glacial sediments, Nunavut, Canada: application to mineral exploration: Journal of Geochemical Exploration, v. 150, p. 84-103.

Makvandi, S., Ghasemzadeh-Barvarz, M., Beaudoin, G., Grunsky, E.C., McClenaghan, M.B., and Duchesne, C., 2016a, Principal component analysis of magnetite composition from volcanogenic massive sulfide deposits: case studies from the Izok Lake (Nunavut, Canada) and Halfmile Lake (New Brunswick, Canada) deposits: Ore Geology Reviews, v. 72, p. 60-85.

Makvandi, S., Ghasemzadeh-Barvarz, M., Beaudoin, G., Grunsky, E.C., McClenaghan, M.B., Duchesne, C., and Boutroy, E., 2016b, Partial least squares-discriminant analysis of trace element compositions of magnetite from various VMS deposit subtypes: application to mineral exploration: Ore Geology Reviews, v. 78, p. 388-408.

Makvandi, S., Beaudoin, G., McClenaghan, M.B., and Quirt, D., 2017, Geochemistry of magnetite and hematite from unmineralized bedrock and local till at the Kiggavik uranium deposit: implications for sediment provenance: Journal of Geochemical Exploration, v. 183, p. 1-21.

Mao, J., Xie, G., Duan, C., Pirajno, F., Ishiyama, D., and Chen, Y., 2011, A tectono-genetic model for porphyry–skarn–stratabound Cu–Au–Mo–Fe and magnetite–apatite deposits along the Middle–Lower Yangtze River Valley, Eastern China: Ore Geology Reviews, v. 43, p. 294-314.

McMartin, I., Corriveau, L., and Beaudoin, G., 2011a, An orientation study of the heavy mineral signature of the NICO Co-Au-Bi deposit, Great Bear magmatic zone, Northwest Territories, Canada: Geochemistry: Exploration, Environment, Analysis, v. 11, p. 293-307.

McMartin, I., Corriveau, L., Beaudoin, G., Jackson, S.E., and Normandeau, P.X., 2011b, Magnetite composition applied to drift prospecting methods for IOCG exploration in the Great Bear magmatic zone, Canada: results from the NICO Au-Co-Bi deposit, *in* Sarala, P., Ojala, V.J. and Porsanger, M.-L., eds., Final programme and abstracts: 25th International Applied Geochemistry Symposium, Rovaniemi, 22-26 August, p. 90-91.

Montreuil, J.-F., Corriveau, L., and Grunsky, E.C., 2013, Compositional data analysis of hydrothermal alteration in IOCG systems, Great Bear magmatic zone, Canada: to each alteration type its own geochemical signature: Geochemistry: Exploration, Environment, Analysis, v. 13, p. 229-247.

Montreuil, J.-F., Corriveau, L., Potter, E.G., and De Toni, A.F., 2016a, On the relation between alteration facies and metal endowment of iron oxide–alkali –altered systems, southern Great Bear magmatic zone (Canada), *in* Slack, J., Corriveau, L. and Hitzman, M., eds., Proterozoic iron oxide-apatite (± REE) and iron oxide-copper-gold and affiliated deposits of Southeast Missouri, USA, and the Great Bear magmatic zone, Northwest Territories, Canada: Economic Geology, v. 111, p. 2139-2168.

Montreuil, J.-F., Potter, E.G., Corriveau, L., and Davis, W.J., 2016b, Element mobility patterns in magnetite-group IOCG systems: the Fab IOCG system, Northwest Territories, Canada: Ore Geology Reviews, v. 72, p. 562-584.

Müller, B., Axelsson, M.D., and Öhlander, B., 2003, Trace elements in magnetite from Kiruna, northern Sweden, as determined by LA-ICP-MS: GFF, v. 125, p. 1-5.

Nadoll, P., Mauk, J.L., Hayes, T.S., Koenig, A.E., and Box, S.E., 2012, Geochemistry of magnetite from hydrothermal ore deposits and host rocks of the Mesoproterozoic Belt Supergroup, United States: Economic Geology, v. 107, p. 1275-1292.

Nadoll, P., Angerer, T., Mauk, J.L., French, D., and Walshe, J., 2014, The chemistry of hydrothermal magnetite: a review: Ore Geology Reviews, v. 61, p. 1-32.

Naslund, H.R., Henríquez, F., Nyström, J.O., Vivallo, W., and Dobbs, F.M., 2002, Magmatic iron ores and associated mineralization: examples from the Chilean high Andes and coastal Cordillera, *in* Porter, T.M., ed., Hydrothermal iron oxide copper-gold and related deposits: a global perspective, v. 2: PGC Publishing, Adelaide, p. 207-226.

Nyström, J.O., and Henríquez, F., 1994, Magmatic features of iron ores of the Kiruna type in Chile and Sweden; ore textures and magnetite geochemistry: Economic Geology, v. 89, p. 820-839.

Ootes, L., Snyder, D., Davis, W.J., Acosta-Góngora, P., Corriveau, L., Mumin, A.H., Gleeson, S.A., Samson, I.A., Montreuil, J.-F., Potter, E.G., and Jackson, V.A., 2017, A Paleoproterozoic Andean-type iron oxide copper-gold environment, the Great Bear magmatic zone, Northwest Canada: Ore Geology Reviews, v. 81, p. 123-139.

Ovalle, J.T., La Cruz, N.L., Reich, M., Barra, F., Simon, A.C., Konecke, B.A., Rodriguez-Mustafa, M.A., Deditius, A.P., Childress, T.M., and Morata, D., 2018, Formation of massive iron deposits linked to explosive volcanic eruptions: Scientific Reports, v. 8, 14855.

Pisiak, L.K., Canil, D., Lacourse, T., Plouffe, A., and Ferbey, T., 2017, Magnetite as an indicator mineral in the exploration of porphyry deposits: a case study in till near the Mount Polley Cu-Au deposit, British Columbia, Canada: Economic Geology, v. 112, p. 919-940.

Pleše, P., Higgins, M.D., Baker, D.R., Lanzafame, G., Prašek, M.K., Mancini, L., and Rooyakkers, S.M., 2019, Production and detachment of oxide crystal shells on bubble walls during experimental vesiculation of andesitic magmas: Contributions to Mineralogy Petrology, v. 174, 21.

Pollard, P.J., 2000, Evidence of a magmatic fluid and metal source for Fe-oxide Cu-Au mineralization, *in* Porter, T.M., ed., Hydrothermal iron oxide copper-gold and related deposits: a global perspective, v. 2: PGC Publishing, Adelaide, p. 27-41.

Ramdohr, P., 1980, The ore minerals and their intergrowths: Pergamon Press, New York, 2nd edition, 1269 p.

Rhodes, A.L., Oreskes, N., and Sheets, S.A., 1999, Geology and rare earth element (REE) geochemistry of magnetite deposits at El Laco, Chile, *in* Skinner, B.J., ed., Geology and ore deposits of the Central Andes: Society of Economic Geologists Special Publications, v. 7, p. 299-332.

Righter, K., Sutton, S.R., Newville, M., Le, L., Schwandt, C.S., Uchida, H., Lavina, B., and Downs, R.T., 2006, An experimental study of the oxidation state of vanadium in spinel and basaltic melt with implications for the origin of planetary basalt: American Mineralogist, v. 91, p. 1643-1656.

Rusk, B., Oliver, N.H.S., Brown, A., Lilly, R., and Jungmann, D., 2009a, Barren magnetite breccias in the Cloncurry region, Australia; comparisons to IOCG deposits: Proceedings of the 10th Biennial Meeting, 17-20 August, Townsville, p. 656-658.

Rusk, B.G., Oliver, N.H.S., Zhang, D., Brown, A., Lilly, R., and Jungmann, D., 2009b, Compositions of magnetite and sulfides from barren and mineralized IOCG deposits in the eastern succession of the Mt Isa Inlier, Australia: Proceedings of GSA Annual Meeting, 18-21 October, Portland, p. 84.

Sappin, A.-A., Dupuis, C., Beaudoin, G., Pozza, M., McMartin, I., and McClenaghan, M., 2014, Optimal ferromagnetic fraction in till samples along ice-flow paths: case studies from the Sue-Dianne and Thompson deposits, Canada: Geochemistry: Exploration, Environment, Analysis, v. 14, p. 315-329.

Sievwright, R.H., Wilkinson, J.J., O'Neill, H.S.C., and Berry, A.J., 2017, Thermodynamic controls on element partitioning between titanomagnetite and andesitic–dacitic silicate melts: Contributions to Mineralogy and Petrology, v. 172, p. 1-33.

Sillitoe, R.H., 2003, Iron oxide-copper-gold deposits: an Andean view: Mineralium Deposita, v. 38, p. 787-812.

Sillitoe, R.H., and Burrows, D.R., 2002, New field evidence bearing on the origin of the El Laco magnetite deposit, northern Chile: Economic Geology, v. 97, p. 1101-1109.

Simon, A.C., Pettke, T., Candela, P.A., Piccoli, P.M., and Heinrich, C.A., 2004, Magnetite solubility and iron transport in magmatic-hydrothermal environments: Geochimica et Cosmochimica Acta, v. 68, p. 4905-4914.

Simon, A.C., Knipping, J., Reich, M., Barra, F., Deditius, A.P., Bilenker, L., and Childress, T., 2018, Kiruna-type iron oxide-apatite (IOA) and iron oxide copper-gold (IOCG) deposits form by a combination of igneous and magmatic-hydrothermal processes: evidence from the Chilean Iron Belt: Economic Geology Special Publications, v. 21, p. 89-114.

Singoyi, B., Danyushevsky, L., Davidson, G.J., Large, R., and Zaw, K., 2006, Determination of trace elements in magnetites from hydrothermal deposits using the LA ICP-MS technique: SEG Keystone Conference, Denver, USA, CD-ROM, 2006.

Skirrow, R.G., 2010, "Hematite-group" IOCG±U ore systems: tectonic settings, hydrothermal characteristics, and Cu-Au and U mineralizing processes, *in* Corriveau, L. and Mumin, A.H., eds., Exploring for iron oxide copper-gold deposits: Canada and global analogues: Geological Association of Canada, Short Course Notes, No. 20, p. 39-58.

Smith, M., and Wu, C., 2000, The geology and genesis of the Bayan Obo Fe-REE-Nb deposit: a review, *in* Porter, T. M., ed., Hydrothermal iron oxide copper-gold and related deposits: a global perspective, v. 1: PGC Publishing, Adelaide, p. 271-281.

Sun, J., Zhu, X., Chen, Y., and Fang, N., 2013, Iron isotopic constraints on the genesis of Bayan Obo ore deposit, Inner Mongolia, China: Precambrian Research, v. 235, p. 88-106.

Tornos, F., 2011, Magnetite-apatite and IOCG deposits formed by magmatic-hydrothermal evolution of complex calcalkaline melts: Proceedings of 11th Biennial SGA Meeting, 26-29 September, Antofagasta, p. 443-445.

Tornos, F., Velasco, F., and Hanchar, J.M., 2016, Iron-rich melts, magmatic magnetite, and superheated hydrothermal systems: the El Laco deposit, Chile: Geology, v. 44, p. 427-430.

Valley, P.M., Fisher, C.M., Hanchar, J.M., Lam, R., and Tubrett, M., 2010, Hafnium isotopes in zircon: a tracer of fluid-rock interaction during magnetite–apatite ("Kiruna-type") mineralization: Chemical Geology, v. 275, p. 208-220.

Velasco, F., Tornos, F., and Hanchar, J.M., 2016, Immiscible iron- and silica-rich melts and magnetite geochemistry at the El Laco volcano (northern Chile): evidence for a magmatic origin for the magnetite deposits: Ore Geology Reviews, v. 79, p. 346-366.

Wechsler, B.A., Lindsley, D.H., and Prewitt, C.T., 1984, Crystal structure and cation distribution in titanomagnetites (Fe3-xTixO4): American Mineralogist, v. 69, p. 754-770.

Wei, J., and Shangguan, Z., 1983, Oxygen isotope composition of magnetite and hematite in Baiyun Ebo iron deposit, Inner Mongolia: Scientia Geologica Sinica, p. 217-224. (in Chinese with English abstract)

Wen, G., Li, J.-W., Hofstra, A.H., Koenig, A.E., Lowers, H.A., and Adams, D., 2017, Hydrothermal reequilibration of igneous magnetite in altered granitic plutons and its implications for magnetite classification schemes: insights from the Handan-Xingtai iron district, North China Craton: Geochimica et Cosmochimica Acta, v. 213, p. 255-270.

Whalen, J.B., and Chappell, B.W., 1988, Opaque mineralogy and mafic mineral chemistry of I-and S-type granites of the Lachlan fold belt, southeast Australia: American Mineralogist, v. 73, p. 281-296.

Whitney, J.A., Hemley, J.J., and Simon, F.O., 1985, The concentration of iron in chloride solutions equilibrated with synthetic granitic compositions; the sulfur-free system: Economic Geology, v. 80, p. 444-460.

Whitten, E.H.T., 1995, Open and closed compositional data in petrology: Mathematical Geology, v. 27, p. 789-806.

Williams, P.J., 2010a, Classifying IOCG deposits, *in* Corriveau, L. and Mumin, A.H., eds., Exploring for iron oxide copper-gold deposits: Canada and global analogues: Geological Association of Canada, Short Course Notes, No. 20, p. 13-22.

Williams, P.J., 2010b, "Magnetite-group" IOCGs with special reference to Cloncurry (NW Queensland) and Northern Sweden: settings, alteration, deposit characteristics, fluid sources, and their relationship to apatite-rich iron ores, *in* Corriveau, L. and Mumin, A.H., eds., Exploring for iron oxide copper-gold deposits: Canada and global analogues: Geological Association of Canada, Short Course Notes, No. 20, p. 23-38.

Williams, P.J., Barton, M.D., Johnson, D.A., Fontbote, L., De Haller, A., Mark, G., Oliver, N.H.S., and Marschik, R., 2005, Iron oxide copper-gold deposits: geology, space-time distribution and possible modes of origin, *in* Hedenquist, J.W., Thompson, J.F.H., Goldfarb, R.J. and Richards, J.P., eds., Economic Geology 100th Anniversary Volume: Littelton, Colorado, USA: Society of Economic Geologists, p. 371-405.

Wold, S., Sjöström, M., and Eriksson, L., 2001, PLS-regression: a basic tool of chemometrics: Chemometrics and Intelligent Laboratory Systems, v. 58, p. 109-130.

Yin, S., Ma, C., and Robinson, P.T., 2017, Textures and high field strength elements in hydrothermal magnetite from a skarn system: implications for coupled dissolution-reprecipitation reactions: American Mineralogist, v. 102, p. 1045-1056.

Yu, J., Chen, Y., Mao, J., Pirajno, F., and Duan, C., 2011, Review of geology, alteration and origin of iron oxide–apatite deposits in the Cretaceous Ningwu basin, Lower Yangtze River Valley, eastern China: implications for ore genesis and geodynamic setting: Ore Geology Reviews, v. 43, p. 170-181.

Zeng, J., Wang, M., and Qu, W., 1981, The genesis of magnetite from the Bayan Obo Fe deposit: Journal of Mineralogy and Petrology, p. 44-58. (in Chinese)

Zhao, X.-F., and Zhou, M.-F., 2011, Fe-Cu deposits in the Kangdian region, SW China: a Proterozoic IOCG (iron-oxide–copper–gold) metallogenic province: Mineralium Deposita, v. 46, p. 731-747.

Zhao, X.-F., Zhou, M.-F., Gao, J.-F., Li, X.-C., and Li, J.-W., 2015, In situ Sr isotope analysis of apatite by LA-MC-ICPMS: constraints on the evolution of ore fluids of the Yinachang Fe-Cu-REE deposit, Southwest China: Mineralium Deposita, v. 50, p. 871-884.

Zhou, M.-F., Robinson, P.T., Lesher, C.M., Keays, R.R., Zhang, C.-J., and Malpas, J., 2005, Geochemistry, petrogenesis and metallogenesis of the Panzhihua gabbroic layered intrusion and associated Fe–Ti–V oxide deposits, Sichuan Province, SW China: Journal of Petrology, v. 46, p. 2253-2280.

# Mineralization, alteration, and fluid compositions in selected Andean IOCG deposits

**Huayong Chen**
*Key Laboratory of Mineralogy and Metallogeny, Guangzhou Institute of Geochemistry, Chinese Academy of Sciences*
*CAS Center for Excellence in Deep Earth Science, huayongchen@gig.ac.cn*

**Liandang Zhao**
*School of Earth Science and Resources, Chang'an University*

*Recommended citation: Chen, H., and Zhao, L., 2022, Mineralization, alteration, and fluid compositions in selected Andean IOCG deposits, in Corriveau, L., Potter, E.G. and Mumin, A.H., eds., Mineral systems with iron oxide copper-gold (IOCG) and affiliated deposits: Geological Association of Canada, Special Paper 52, p. 365-381.*

**Abstract**

The Mesozoic iron oxide copper-gold (IOCG) deposits in the Central Andes are well preserved along the western margin of the South America continental arc. This contribution summarizes and updates the development of four typical Mesozoic IOCG deposits "sensu stricto" in this belt — Mina Justa in southern Perú, and Mantoverde, Candelaria, and El Espino in northern Chile. The detailed paragenetic studies on all examples present a large variety of alteration and mineralization patterns in which distinct styles of magnetite and copper (-gold) mineralization form. Fluid inclusion data and isotope tracing of ore-forming fluids indicate involvement of a magmatic-hydrothermal end-member in the formation of the early magnetite mineralization, whereas basinal brines or residual seawater end-member fluids were involved in copper (-gold) mineralization by reaction with andesitic host rocks. The relatively narrow age range (ca. 120–90 Ma) for the IOCG mineralization corresponds well with the ages of basin inversion along the Central Andean continental margin. This tectonic setting is commonly characterized by extensive magmatism and large-scale movement of fluids external to magmas, and is interpreted as a key control on access to the variety of fluid sources needed to form the Mesozoic IOCG ore systems, a variety that contrasts with other known deposit types.

**Résumé**

Les gisements à oxydes de fer cuivre-or (IOCG) mésozoïques des Andes centrales sont bien préservés le long de la marge ouest de l'arc continental sud-américain. Cette contribution résume et met à jour les patrons d'évolution de quatre gisements mésozoïques IOCG (au sens stricte) typiques de cette ceinture, Mina Justa dans le sud du Pérou, et Mantoverde, Candelaria et El Espino dans le nord du Chili. Les études paragénétiques détaillées de tous les exemples présentent une grande variété de patrons d'altération et de minéralisation qui mènent à la formation de minéralisation distincte à magnétite et à cuivre (-or). Les données d'inclusion des fluides et le traçage isotopique des fluides minéralisateurs indiquent un pôle d'origine magmatique-hydrothermal pour la minéralisation précoce à magnétite et un pôle de saumure de bassin ou d'eau de mer résiduelle qui a réagi avec les roches volcaniques andésitiques encaissantes pour la minéralisation à cuivre (-or). La plage d'âge relativement étroite (environ 120-90 Ma) de la minéralisation IOCG correspond aux âges d'inversion du bassin le long de la marge continentale des Andes centrales. Ce cadre tectonique peut conduire à un magmatisme étendu et à un mouvement de fluides externes à grande échelle, et est interprété comme un contrôle clé pour l'accès à la variété de sources de fluides nécessaires pour former les systèmes minéralisateurs à IOCG du Mésozoïque, une variété qui contraste avec d'autres types de gisements connus.

## Introduction

The iron oxide copper-gold (IOCG) deposits in the Central Andes, e.g. Mina Justa in southern Perú and Candelaria and Mantoverde in northern Chile, represent rare examples of Phanerozoic (Mesozoic) IOCG provinces, compared to almost all other large IOCG deposits and provinces, which are Precambrian in age. Although there is ongoing debate regarding ore deposit classification and genetic processes for some of the Mesozoic iron-copper (-gold) deposits in the Central Andes, such as whether some skarn deposits are affiliated (or not) with IOCG deposits (e.g. the Candelaria IOCG deposit has garnet alteration; Marschik and Fontboté, 2001), most large iron-copper (-gold) deposits of the region are included within the IOCG deposit "sensu stricto" clan without controversy. In the shadow of the many famous and giant Tertiary porphyry copper deposits in southern Perú and northern Chile, the Mesozoic IOCG deposits (which are also large copper resources; Lundin Mining, 2020) remained significantly under-studied in the 20th century. Since then, many IOCG deposits have been characterized in detail in both Perú and Chile, such as Candelaria (Marschik and Fontboté, 2001; del Real et al., 2018) and Mantoverde (Benavides et al., 2007; Rieger et al., 2010, 2012) in northern Chile, and Mina Justa (Chen et al., 2010, 2011) and Raúl-Condestable (de Haller et al., 2006; de Haller and Fontboté, 2009) in southern Perú.

Additional research and discoveries of IOCG deposits have occurred since the 2010s, such as acquisition of new isotope data on ore-forming fluids for the Mina Justa deposit (Li et al., 2018), and detailed studies of the newly-explored El Espino deposit, the youngest IOCG deposit in the Central Andes (Lopez et al., 2014). These recent studies have tremendously contributed to our knowledge of the Mesozoic Central Andean IOCG deposits and enlarged the IOCG family with significant young representatives. Moreover, recent studies on iron oxide ± apatite deposits (IOA; also known as magnetite-apatite or Kiruna-type deposits) have also proposed a genetic connection between IOA and IOCG deposits, i.e. the two types form a continuum produced by a combination of igneous and magmatic-hydrothermal processes (e.g. Knipping et al., 2015a, b; Reich et al., 2016; Simon et al., 2018; Palma et al., 2019; Rodriguez-Mustafa et al., 2020). It is thus timely to review current advances on Central Andean IOCG deposits "sensu stricto", piggy-backing on and updating early syntheses by Sillitoe (2003). These syntheses predated the detailed studies of key IOCG deposits (e.g. Mantoverde and Mina Justa) by Chen (2010), who reviewed the IOCG deposits of the Central Andes and compared them with spatially associated IOA deposits.

In this synthesis, we review some of the major Mesozoic IOCG deposits "sensu stricto", without referring to IOA deposits, although the latter have recently been included in the IOCG clan as part of a continuous evolutionary process (e.g. Barra et al., 2017; Simon et al., 2018). This contribution mainly focuses on descriptions of alteration and mineralization parageneses, their evolution within the ore systems, and the nature and evolution of ore-forming fluids, leading to a proposed general ore deposit model for the Central Andes IOCG deposits "sensu stricto". This review of the large Central Andean IOCG deposits sheds light on the genesis of the broad IOCG ore family, and complements papers in this special volume that focus on the evolution of the iron oxide and alkali-calcic alteration facies that define these ore systems and their IOCG and affiliated deposits. As such, we regroup our alteration descriptions to conform with the diagnostic alteration facies described by Corriveau et al. (2016, 2018, 2022a).

## Mesozoic IOCG Deposits in the Central Andes

The Central Andean IOCG deposits (Fig. 1) occur within a linear array of interconnected Mesozoic continental margin rift basins that record a major phase of extension accompanying subduction along the western margin of Gondwana (Chen et al., 2013). The Andean IOCG deposits formed between the Middle Jurassic (~165 Ma; e.g. Guaillos, Tocopilla, and Julia; Ruiz and Peebles, 1988; Boric et al., 1990) and the Upper Cretaceous (~88 Ma; e.g. El Espino; Lopez et al., 2014), but most of the ores formed during Lower Cretaceous tectonic inversion of the extensional basins (120–100 Ma; Chen et al., 2013). Some of the large, copper-rich IOCG examples, including Mina Justa (Perú), Mantoverde

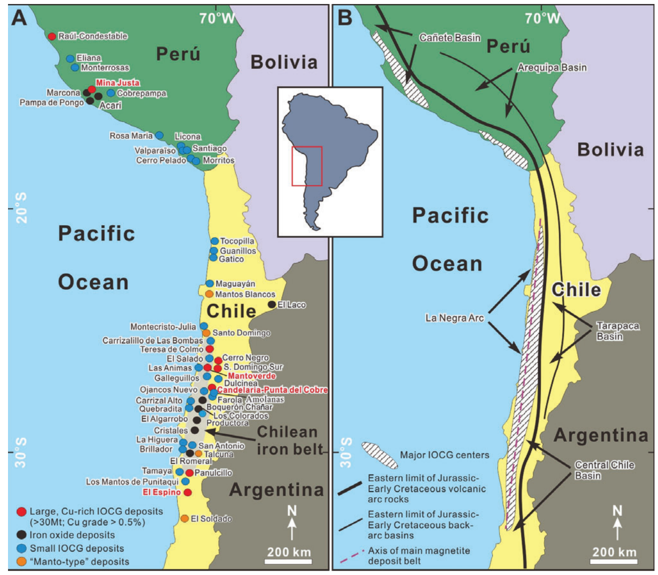


**FIGURE 1**. Location of copper-rich IOCG deposits, large iron oxide deposits, and manto-type copper-silver deposits in the Central Andes (**A**; modified from Chen et al., 2013 and references therein) and position of the Central Andean IOCG belt of northern Chile and southern Perú (**B**; modified from Chen et al., 2013 and references therein).

(Chile), and Candelaria (Chile), have economic copper-gold mineralization. For example, at Candelaria, the total estimated measured and indicated mineral resource is 1179.3 Mt at 0.64% Cu (Lundin Mining, 2020). These deposits can be used as important case examples to explore some unsolved scientific problems in IOCG studies.

The Andean IOCG deposits discussed herein are mainly hosted by volcanic and volcaniclastic rocks of Jurassic to Cretaceous age. The Mina Justa and Mantoverde deposits (Fig. 2A, B) are hosted by the Jurassic Río Grande and La Negra formations, whereas the Candelaria and El Espino deposits (Fig. 2C, D) are hosted by the Cretaceous Punta del Cobre, Arqueros, and Quebrada Marquesa formations. These formations constitute an arc- and basin-related (including intra-arc basin and back-arc basin) domain in southern Perú and northern Chile. Plutonic complexes with mafic to felsic compositions (e.g. gabbro, diorite, and granodiorite) occur throughout the Jurassic to Cretaceous formations and are irregular in outline or elongated belts parallel to the orogen (Sillitoe, 2003). In the vicinity of IOCG districts, syn-mineralization plutons, which predominantly comprise granodiorite, tonalite, quartz diorite, and monzogranite, have contributed to the formation of economic mineralization (e.g. El Espino; Lopez et al., 2014). The Atacama Fault System, a major orogen-parallel fault system, has exerted a structural control on regional metamorphism and pluton emplacement (Sillitoe, 2003). It follows the axis of the Coastal Cordillera for >1000 km between latitudes 20° and 30°S, where it consists of a series of concave-west segments of NNW-, N-, and NNE-striking ductile and brittle faults. In the Upper

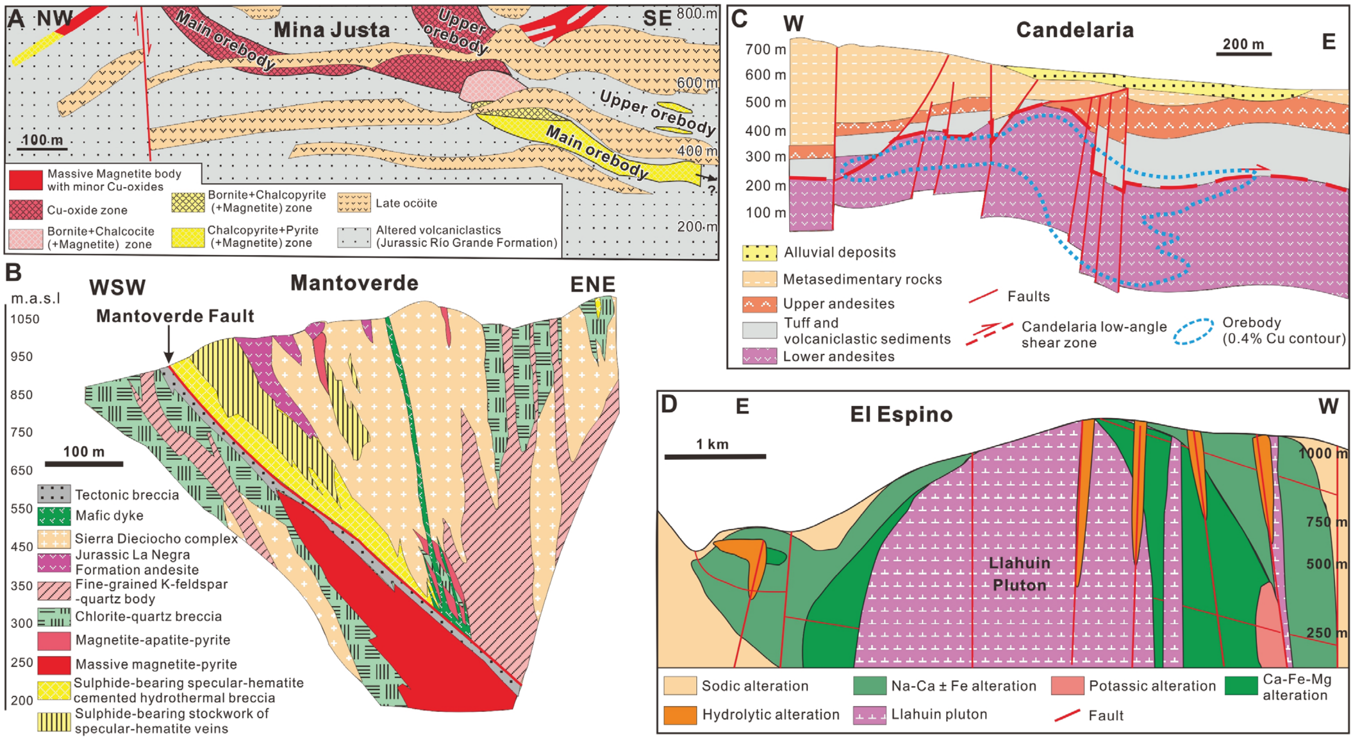


**FIGURE 2.** Geological sections of major IOCG deposits in the Central Andes. **A.** Mina Justa copper (-silver) deposit, Perú (modified from Chen et al., 2010). **B.** Mantoverde copper (-gold) deposit, Chile (modified from Benavides et al., 2007). **C.** Candelaria copper-gold deposit, Chile (modified from Arévalo et al., 2006). **D.** El Espino copper-gold deposit, Chile (modified from Lopez et al., 2014).

Cretaceous, the opening of the Atlantic Ocean basin to the east was the geodynamic trigger that led to tectonic inversion of the formerly extensional back-arc basins and reactivation of fault systems in a transpressive regime (e.g. the Chivato Fault; Taylor et al., 1998; Grocott and Taylor, 2002). This likely promoted contemporary pluton emplacement and associated mineralization, considering that the locations and shapes of orebodies are mainly controlled by normal fault systems (e.g. Mina Justa Fault and Mantoverde Fault; Fig. 2B) and/or shear zones (e.g. Candelaria low angle shear zone; Fig. 2C).

## Ore Deposit Geology: Alteration and Mineralization Paragenesis

The Mina Justa, Mantoverde, Candelaria, and El Espino IOCG deposits share many similarities in alteration and mineralization types, but differences also occur (Fig. 3; Marschik and Fontboté, 2001; Benavides et al., 2007; Chen et al., 2010, 2011; Rieger et al., 2010, 2012; Lopez et al., 2014; del Real et al., 2018). In this section, we describe the alteration and mineralization of each deposit in detail.

### *Mina Justa*

Based on crosscutting relationships, the paragenetic sequence of alteration and mineralization at the Mina Justa IOCG deposit (Chen et al., 2010; Li et al., 2018) evolved from sodic metasomatism (Stage I), through high-temperature (HT) K-Fe metasomatism (Stage II), HT Ca-Fe metasomatism (Stage III), early hematite-calcite alteration (Stage IV), HT K-Fe magnetite-pyrite alteration (Stage V), and lower-temperature (LT) copper mineralization (Stage VI), to late hematite (Stage VII) (Fig. 3A).

*Sodic metasomatism*: The widespread sodic metasomatic event is documented in andesitic lavas and volcaniclastic interbeds, in which albite and minor actinolite replace both plagioclase phenocrysts and andesite matrix (Fig. 4A).

*HT K-Fe metasomatism*: Both fresh and previously albitized plagioclase are replaced by extremely small K-feldspar grains (< 0.05 mm), whereas aggregates of magnetite and K-feldspar form the matrix (Fig. 4B–E). This HT K-Fe metasomatic event was contemporaneous with the development of stratabound to slightly discordant lenses of sulphide-free magnetite that are locally cut by massive magnetite-pyrite bodies (Chen et al., 2010).

*HT Ca-Fe metasomatism*: Alteration assemblages consist of diopside, actinolite, and magnetite. Diopside is spatially associated with and locally replaced by actinolite in the albitized and K-Fe-metasomatized host rocks. Actinolite is commonly associated with minor magnetite, with which it forms massive aggregates and (locally) the matrix of hydrothermal breccias. Actinolite replaced earlier albite and K-feldspar-magnetite assemblages (Fig. 4C, D), and is replaced by chlorite, carbonate, and quartz (Fig. 4F).

*Early hematite-calcite alteration*: This stage is characterized by hematite and calcite; the hematite is entirely replaced by mushketovite in the main magnetite bodies, indicating that a now obliterated hematite-dominant stage

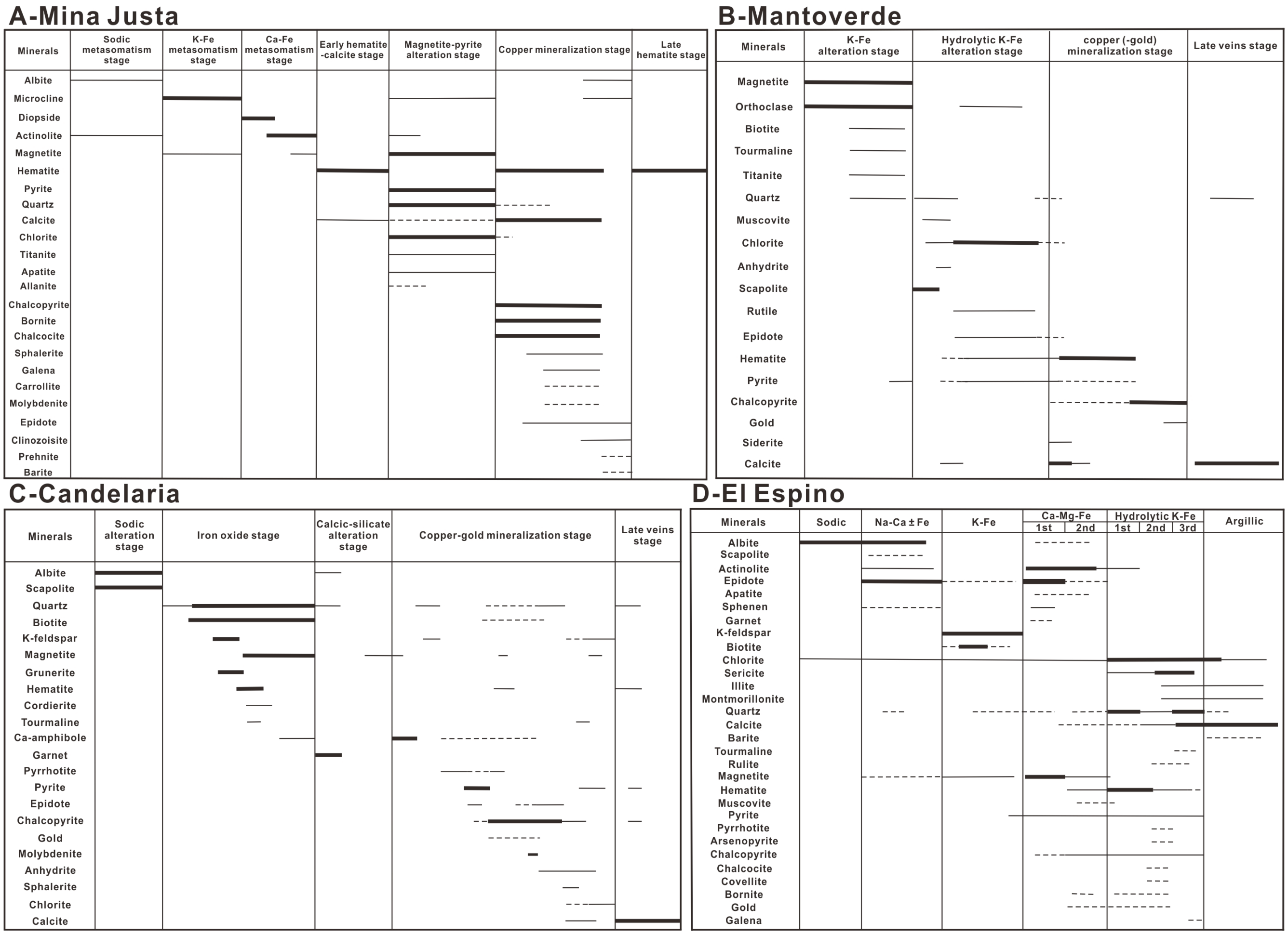


**Figure 3.** Alteration and mineralization paragenesis of the major Central Andean IOCG deposits. **A.** Mina Justa (modified from Chen et al., 2010). **B.** Mantoverde (modified from Benavides et al., 2007). **C.** Candelaria (modified from Marschik and Fontboté, 2001; Ullrich and Clark, 1999). **D.** El Espino (modified from Lopez, 2012).

existed before development of the main massive magnetite body (Fig. 4G; Chen et al., 2010).

*HT K-Fe magnetite-pyrite alteration*: This magnetite-rich iron mineralization stage also includes pyrite, quartz, and chlorite. Magnetite occurs as granular or tabular aggregates (Fig. 4G, H) and locally as veins (Li et al., 2018), and is intergrown with pyrite to form massive, lensoid, and brecciated magnetite-pyrite bodies (Fig. 2A; Chen et al., 2010). Hydrothermal breccias, commonly present at the margins of the magnetite bodies, comprise a magnetite-pyrite-dominant matrix and angular clasts of andesite altered to microcline or actinolite (Chen et al., 2010). Moreover, microcline, chlorite, and abundant subhedral to euhedral quartz coexist with magnetite-pyrite ± actinolite, and can be observed in the main magnetite bodies.

*Copper mineralization*: Major metallic minerals of this stage include copper sulphides (e.g. chalcopyrite, bornite, chalcocite, and digenite; Fig. 4I–K), sphalerite, and galena (Li et al., 2018). The copper sulphides and associated assemblages most commonly occur in massive magnetite-pyrite bodies or veins. Locally, chalcocite, digenite, and bornite form large patches with complex vermicular intergrowths (Chen et al., 2010) that can be interpreted as exsolution textures formed at low temperature (< 250 °C; Brett, 1964). Commonly, fine-grained platy hematite is associated with chalcopyrite and bornite-chalcocite aggregates around copper sulphides (Chen et al., 2010). Other minerals associated with copper mineralization include calcite, albite, microcline, epidote, chlorite, clinozoisite, and barite, typical of LT Ca-Mg-Fe facies (Corriveau et al., 2016, 2022b).

*Late hematite*: Late hematite that locally develops in the upper parts of orebodies is medium- to coarse-grained and replaces or cuts earlier alteration and/or mineralization minerals, such as actinolite related to HT Ca-Fe metasomatism, magnetite related to HT K-Fe alteration, and chalcopyrite associated with the copper mineralization stage (Chen et al., 2010; Li et al., 2018).

*Mantoverde*

Several detailed paragenetic studies of alteration and mineralization have been undertaken on the Mantoverde IOCG deposit in the past two decades, including those of

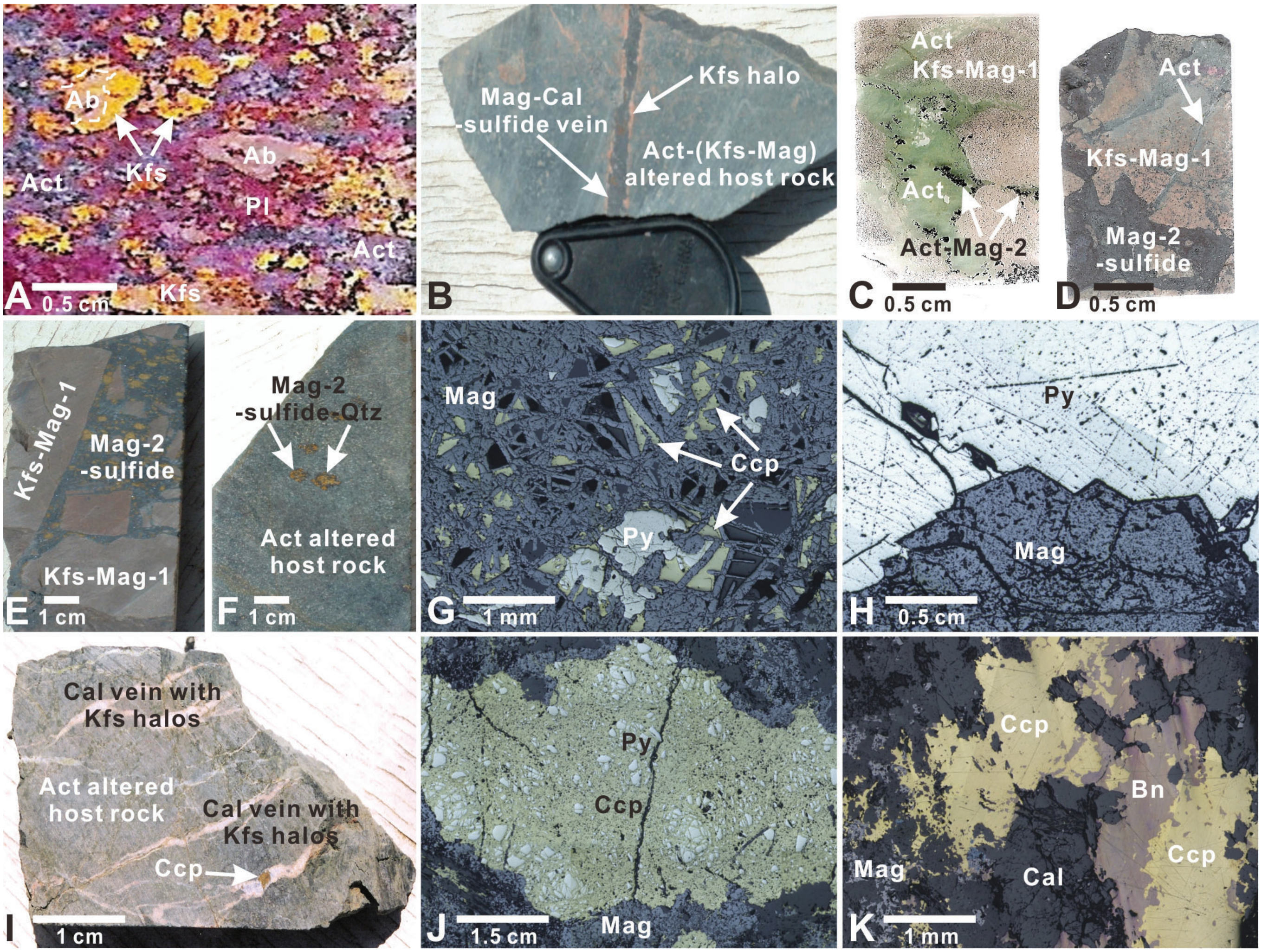


**FIGURE 4.** Representative photographs of alteration/mineralization paragenesis of the Mina Justa deposit (Chen, 2008; Li et al., 2018). **A.** Light-pink albite (not stained by hematite) and fine-grained actinolite extensively replacing original phenocrystic and groundmass plagioclase (stained pink to red by hematite). Albite is replaced by K-feldspar, and then both are replaced by actinolite. **B.** Magnetite-calcite-sulphide veins with K-feldspar haloes cutting Stage II K-feldspar-magnetite and Stage III actinolite alteration. **C.** Stage III actinolite matrix cementing clasts of Stage II K-feldspar-magnetite (Mag-1), and coarse-grained Stage V magnetite (Mag-2) occurring with actinolite and locally as veins. **D.** Stage II magnetite (Mag-1)-K-feldspar is cut by Stage III actinolite veins, and is cemented by Stage V magnetite (Mag-2)-sulphide (bornite and chalcocite). **E.** Stage V magnetite (Mag-2)-sulphide occurring as a matrix around Stage II K-feldspar-magnetite (Mag-1) clasts. **F.** Spotty magnetite-chalcopyrite-quartz mineralization in earlier actinolite and microcline-magnetite-altered host rocks. **G.** Tabular magnetite coexisting with pyrite, and both replaced by chalcopyrite of the copper mineralization stage. Such tabular magnetite is typical of mushketovite where magnetite replaced earlier hematite. **H.** Stage V magnetite and pyrite. **I.** Chalcopyrite-calcite veins cutting altered host rocks, and K-feldspar haloes around calcite veins. **J.** Stage V pyrite is replaced by Stage VI chalcopyrite. **K.** Chalcopyrite-bornite-calcite assemblage of the copper mineralization stage replacing earlier magnetite of Stage V HT K-Fe magnetite-pyrite-K-feldspar alteration stage. Abbreviations: *Ab*: albite, *Act*: actinolite, *Bn*: bornite, *Cal*: calcite, *Ccp*: chalcopyrite, *Kfs*: K-feldspar, *Mag*: magnetite, *Pl*: plagioclase, *Py*: pyrite, *Qz*: quartz.

Vila et al. (1996), Cornejo at al. (2000), López (2002), Benavides et al. (2007), Rieger et al. (2010, 2012), and Marschik and Kendrick (2015). Based on crosscutting relationships, the results of these studies can be synthesized as a sequence of alteration and mineralization assemblages as follows: sodic alteration (Stage I), HT K-Fe alteration (Stage II), hydrolytic LT K-Fe alteration (Stage III), copper (-gold) mineralization (Stage IV), and late veins (Stage V) (Fig. 3B). These are described below.

*Sodic alteration*: Albite observed in some clasts within a chloritic hydrothermal breccia was extensively replaced by orthoclase (not shown in Fig. 3B; Benavides et al., 2007).

*HT K-Fe alteration*: Intense potassic alteration is recorded by widespread hydrothermal K-feldspar, accompanied by subordinate biotite, tourmaline, and titanite. K-feldspar has selectively replaced plagioclase in the andesitic and plutonic host rocks (Fig. 5A, B), whereas biotite is mainly observed in the andesite groundmass

(Benavides et al., 2007). Magnetite (Fig. 5C–E) has also replaced the host rocks (e.g. andesite and tuff), and coexists with K-feldspar. Collectively, the paragenesis is typical of the HT K-Fe alteration facies of Corriveau et al. (2016). In the Mantoverde district, iron mineralization consists of fine-grained magnetite-pyrite that commonly forms massive, tabular, and subvertical bodies (Fig. 2B), which are cut by veinlets of chlorite, quartz, orthoclase, and calcite (Benavides et al., 2007). Within the magnetite zone, pseudomorphous replacement of early hematite by magnetite (mushketovite) is also common (Rieger et al., 2010). In the eastern branch of the Atacama Fault System, iron oxide-apatite mineralization consisting of equigranular magnetite, fluorapatite, and pyrite (Benavides et al., 2007) is typical of the HT Ca-Fe facies of Corriveau et al. (2016).

*Hydrolytic LT K-Fe alteration*: Major minerals of this stage of alteration include chlorite, quartz (Fig. 5B), sericite, and minor scapolite, epidote, pyrite, rutile, and hematite (Fig. 5F), collectively forming a LT K-Fe to LT Ca-Mg-Fe facies. Chlorite is intergrown with quartz and sericite and replaces earlier hydrothermal minerals (e.g. K-feldspar and scapolite) or volcanic host rocks. Pyrite is mainly euhedral as isolated grains and coexists with chlorite, sericite, and quartz. Locally observed scapolite that has extensively replaced plagioclase phenocrysts in andesite or occurs as remnants in chlorite aggregates may represent a Na-Cl metasomatic event in the

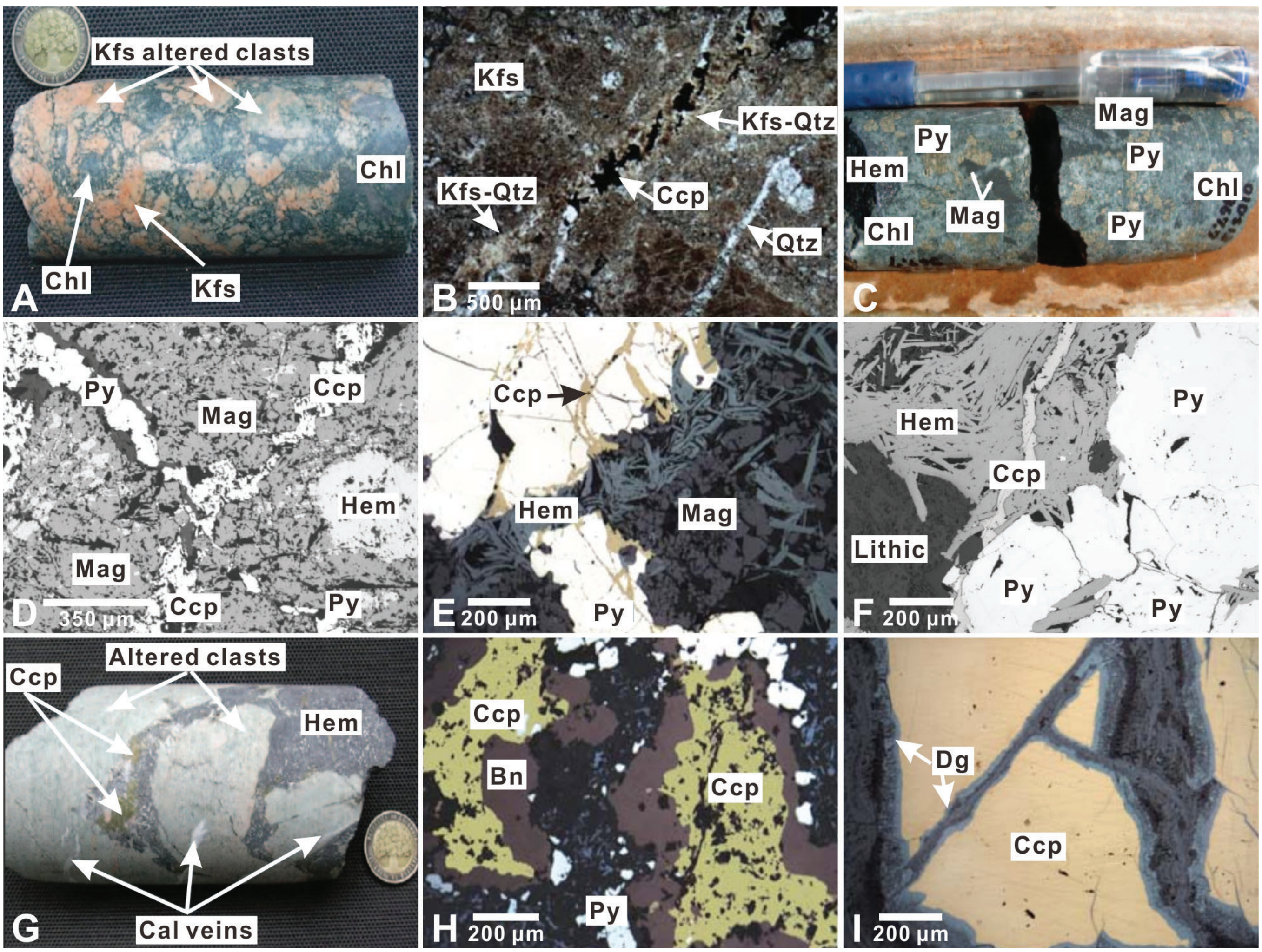


**Figure 5.** Representative photographs of alteration/mineralization paragenesis of the Mantoverde deposit (Benavides et al., 2007; Rieger et al., 2010). **A.** Chlorite-bearing hydrothermal breccia containing fragments of K-feldspathized host rock. **B.** Pervasive K-feldspar alteration is cut by K-feldspar-quartz or quartz veinlets, with chalcopyrite as a late infill. **C.** Magnetite is enclosed in a pyrite-bearing, chlorite-dominated assemblage, which is then cut by a hematite vein. **D.** Chalcopyrite veins cutting pyrite-magnetite, with magnetite replaced by irregular patches of hematite. **E.** Pyrite veinlets cut magnetite, and then pyrite is cut by chalcopyrite veinlets, with a hematite vein cutting the aforementioned minerals. **F.** A chalcopyrite vein cutting hematite and pyrite of the copper (-gold) mineralization stage. **G.** Chalcopyrite is intergrown with hematite replacing K-feldspar- and chlorite-altered host rock, and chalcopyrite is cut by a late calcite vein. **H.** Chalcopyrite replaced by bornite along margins. **I.** Chalcopyrite marginally converted to digenite. Abbreviations: *Bn*: bornite, *Cal*: calcite, *Ccp*: chalcopyrite, *Chl*: chlorite, *Dg*: digenite, *Hem*: hematite; *Kfs*: K-feldspar, *Mag*: magnetite, *Py*: pyrite, *Qz*: quartz.

early hydrolytic alteration stage (Benavides et al., 2007). This is supported by the presence of scapolite that postdates magnetite formed during previous HT K-Fe alteration and is overprinted by chlorite that dominates the early hydrolytic LT K-Fe alteration (Benavides et al., 2007).

*Copper (-gold) mineralization*: Sulphide-rich, hematite-cemented hydrothermal breccias and mineralogically identical veins represent the main ore stage in the Mantoverde district (Benavides et al., 2007). In breccia and vein-type ores, chalcopyrite coexists with pyrite or hematite, filling fractures in earlier K-feldspar- and chlorite-altered host rocks (Fig. 5G). Subangular to subrounded pyrite associated with hematite-cemented breccias generally occurs as fractured grains or (less commonly) aggregates up to a few millimetres in diameter, whereas chalcopyrite precipitated in open-space fillings up to a few centimetres wide or in thin, discontinuous veinlets of massive to porous chalcopyrite aggregates (Benavides et al., 2007). Locally, sulphides and calcite are intergrown with quartz and specular hematite in vein-type ores, in which pyrite is subangular to subrounded, and chalcopyrite occurs as irregular and rounded aggregates replaced by bornite (Fig. 5H, I). Gold commonly coexists with chalcopyrite and specular hematite, with gold grades increasing towards the Mantoverde Fault (Fig. 2B) (Vila et al., 1996; López, 2002).

*Late veins*: Late hydrothermal veins of calcite ± quartz (up to a few metres wide) are observed throughout the Mantoverde district and are abundant in the northern centres of the Mantoverde district (Benavides et al., 2007).

*Candelaria*

The paragenetic sequence of alteration and mineralization at the Candelaria IOCG deposit has been described in detail by Ullrich and Clark (1999), Marschik and Fontboté (2001), Williams et al. (2005), and del Real et al. (2018). Here we synthesize the findings of previous paragenetic studies; from early to late, the sequence comprises sodic alteration (Stage I), iron metasomatism associated with potassic alteration and iron oxide mineralization (Stage II), calc-silicate alteration (Stage III), copper-gold mineralization (Stage IV), and late veins (Stage V) (Fig. 3C). Each stage and assemblage is described below.

*Sodic alteration* that predated intense iron metasomatism accompanied by potassic alteration is widespread in the Candelaria district (Fig. 6A) (Marschik and Fontboté, 2001). This stage is characterized by pervasive albite and scapolite.

*HT K-Fe alteration (or iron metasomatism)* featured crystallization of specular hematite (inferred from pseudomorphic replacement of bladed hematite by magnetite to form mushketovite) and massive magnetite mineralization (Fig. 6B–G). In foliated domains of the Candelaria deposit, magnetite mineralization is closely associated with biotite, which was ascribed to an iron oxide mineralization stage by Marschik and Fontboté (2001). In the deeper parts of the deposit, mineralization is concentrated within an east-dipping zone of magnetite-biotite-K-feldspar-calcic amphibole (or actinolite; del Real et al., 2018).

*Calc-silicate alteration*: Garnet (mainly andradite) postdates scapolite and cuts biotitized rocks, but is in turn cut by calcic amphibole and pyrite ± chalcopyrite veinlets, indicating that calc-silicate alteration (skarnification) occurred between the iron oxide and main copper mineralization stages (Marschik and Fontboté, 2001). This has been interpreted as a contact metamorphic (or HT Na-Ca ± Fe alteration) event by Marschik and Fontboté (2001).

*The main copper mineralization stage* postdates the iron oxide stage (or iron mineralization stage), and is represented by chalcopyrite ± pyrite-bearing assemblages in veins that cut, or masses that replace earlier iron oxide minerals (e.g. magnetite, mushketovite, and hematite; Fig. 6C–G). The chalcopyrite ± pyrite is accompanied by alteration or veins composed of albite ± scapolite, amphibole, and quartz ± K-feldspar (Fig. 6C, H, I). Commonly, in the copper mineralization stage, calcic amphibole associated with chalcopyrite and pyrite cuts previously formed albite veins (Fig. 6A, H), or coexists with epidote as veins cutting pervasive K-feldspar ± albite alteration (Fig. 6I; Marschik and Fontboté, 2001). Chalcopyrite is commonly observed as infilling skeletal and cataclastic pyrite, suggesting that most pyrite formed earlier than chalcopyrite, although minor pyrite postdates chalcopyrite as indicated by pyrite veinlets cutting massive chalcopyrite (Marschik and Fontboté, 2001). Pyrrhotite is, in part, contemporaneous with the first stage of main chalcopyrite mineralization (Ullrich and Clark, 1999). In the Candelaria district, anhydrite displays complex relationships with chalcopyrite, and can be inferred as having multiple generations that are pre- (Fig. 6G), syn-, and post-chalcopyrite. The earliest generation of anhydrite locally has sphalerite inclusions that are spatially associated with epidote-allanite-chalcopyrite-pyrite alteration (Marschik and Fontboté, 2001). Gold is mainly observed as inclusions in chalcopyrite and pyrite (Hopf, 1990; Ryan et al., 1995), whereas locally observed molybdenite, tourmaline, and apatite are interpreted to have formed towards the end of the main chalcopyrite stage (Hopf, 1990; Ryan et al., 1995; Marschik and Fontboté, 2001).

*Late veins*: Late stages of hydrothermal activity are represented by hematite, which may correlate with specularite ± calcite veins that locally contain minor pyrite and rare chalcopyrite (Marschik and Fontboté, 2001).

*El Espino*

The paragenetic sequence of alteration and mineralization at the El Espino IOCG deposit consists of sodic alteration (Stage I), HT Na-Ca ± Fe alteration (Stage II), HT K-Fe alteration and associated iron oxide mineralization (Stage III), LT Ca-Mg-Fe alteration (Stage IV), LT hydrolytic K-Fe alteration (Stage V), and argillic alteration (Stage VI). The LT Ca-Mg-Fe and LT hydrolytic K-Fe alteration are accompanied by copper sulphide mineralization and copper-gold mineralization, respectively (Fig. 3D; Lopez et al., 2014).

*Sodic alteration*: Sodic alteration is extensive in the El Espino district (Fig. 2D), and comprises albite ± chlorite that replace host rock minerals (e.g. plagioclase, amphibole, and pyroxene) or matrix and clasts. Albite veins can be up to 1 cm in width and cut intrusive rocks (Fig. 7A).

*HT Na-Ca ± Fe alteration*: This alteration facies has a more limited extent than sodic alteration. It is characterized by epidote-albite (Fig. 7B), actinolite-albite, epidote-actinolite-chlorite-albite ± titanite, and actinolite-scapolite-albite assemblages, commonly intergrown with minor magnetite (Lopez et al., 2014). These alteration minerals partially or totally replace phenocrysts (e.g. plagioclase, hornblende, and pyroxene) in host rocks. Alteration of different types of host rocks may produce different mineral assemblages with varied textures. In siltstone, epidote occurs as irregular veinlets (commonly < 1 mm width) cutting albite-altered beds, whereas scapolite is restricted to zones within a leucodiorite intrusion. Magnetite is subhedral and commonly partially to totally martinized (Lopez et al., 2014).

*HT K-Fe alteration*: K-feldspar-magnetite-hematite ± biotite alteration is locally and weakly developed in the El Espino district, and is overprinted by subsequent LT Ca-Mg-Fe and hydrolytic LT K-Fe alteration (Lopez et al., 2014). In the HT K-Fe alteration stage, biotite is commonly replaced by chlorite. Generally, K-feldspar either replaces original plagioclase or albite from the sodic and/or Na-Ca ± Fe alteration stage, or is replaced by sericite, clays, and chlorite of the LT hydrolytic K-Fe alteration stage. K-feldspar alteration is selective, commonly expressed as alteration bands

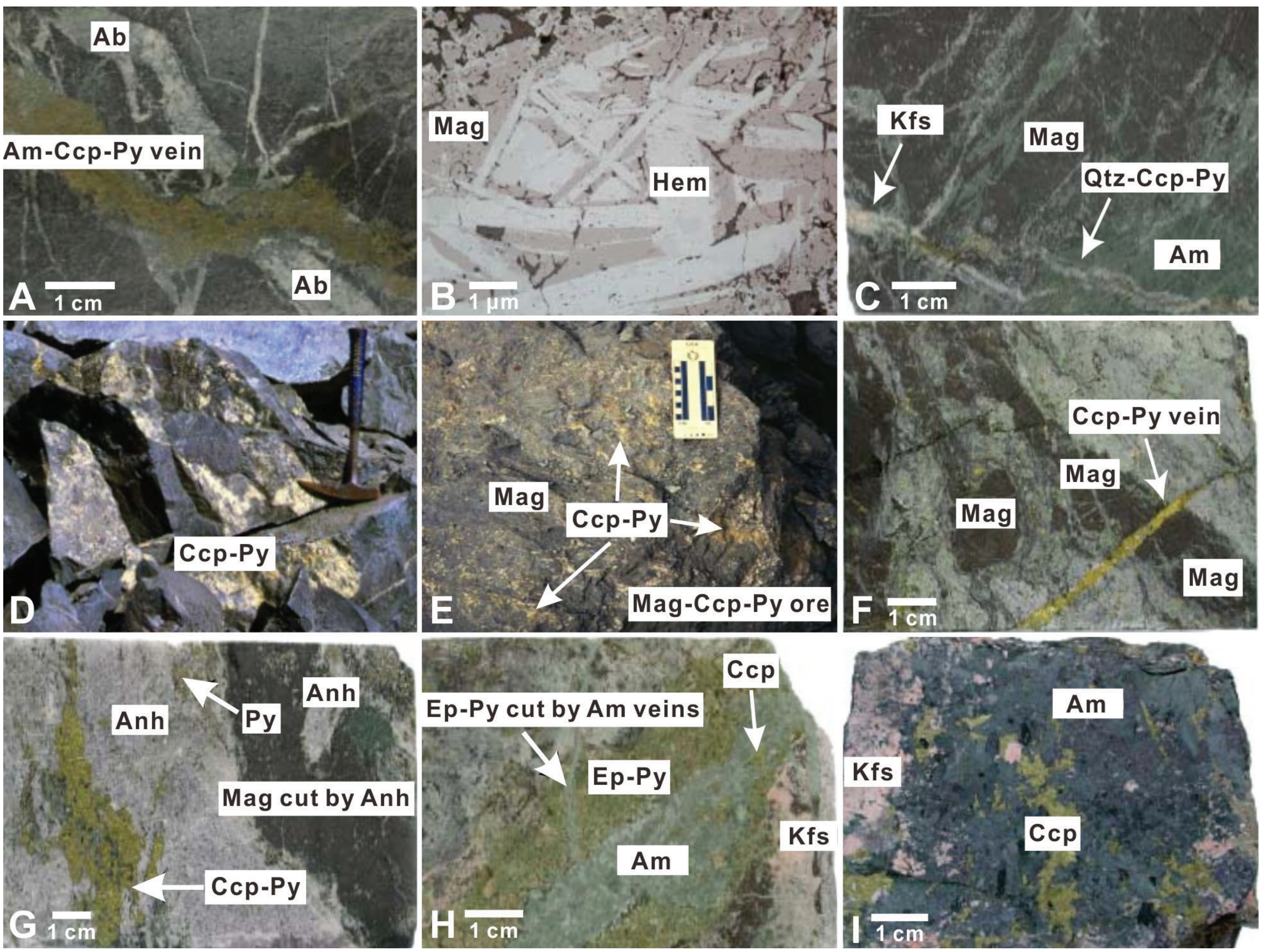


**Figure 6.** Representative photographs of alteration/mineralization paragenesis of the Candelaria deposit (Marschik and Fontboté, 2001). **A**. A chalcopyrite-pyrite-amphibole vein cutting albite veinlets. **B.** Magnetite replacing and overgrowing hematite during the main iron oxide mineralization. **C.** K-feldspar and quartz-chalcopyrite-pyrite veins cutting magnetite and amphibole. **D.** Chalcopyrite-pyrite in intensely iron-metasomatized volcanic or volcaniclastic rocks. **E.** Massive magnetite replaced by chalcopyrite-pyrite. **F.** Chalcopyrite-pyrite veinlets cutting magnetite replacement zones in host rocks (mainly andesitic to dacitic in composition), illustrating that iron oxide crystallized prior to the late stage sulphide mineralization. **G.** Magnetite cut by anhydrite that is replaced by chalcopyrite-pyrite. **H.** K-feldspar cut by epidote-pyrite veins, then replaced or cut by an amphibole-chalcopyrite assemblage. **I.** Amphibole and chalcopyrite (veins) replacing K-feldspar. Abbreviations: *Ab*: albite, *Am*: amphibole, *Anh*: anhydrite, *Ccp*: chalcopyrite, *Ep*: epidote, *Hem*: hematite; *Kfs*: K-feldspar, *Mag*: magnetite, *Py*: pyrite, *Qz*: quartz.

in thin bedded siltstone or rims around clasts. Locally, K-feldspar pervasively replaces all the primary minerals in clastic sedimentary rocks (Fig. 7C; Lopez et al., 2014). In the El Espino district, secondary biotite and disseminated magnetite (Fig. 7D) form HT K-Fe alteration aggregates a few metres in diameter that have been intersected in several deep drill holes (Lopez et al., 2014).

*LT Ca-Mg-Fe alteration*: Epidote, actinolite, chlorite, subordinate calcite, titanite, apatite, quartz, and minor garnet (andradite) replace calcareous sedimentary rocks. The most common mineral associations are epidote-actinolite (Fig. 7E) and epidote-chlorite (Lopez et al., 2014), typical of the LT Ca-Mg-Fe alteration facies (Corriveau et al., 2016, 2022b). This alteration event was divided into two sub-stages by Lopez et al. (2014): (1) partial replacement in volcanic rocks, and pervasive replacement that locally obliterates primary textures in sedimentary rocks; followed by (2) iron oxide- and sulphide-bearing veinlets with actinolite selvages that cut earlier Ca-Mg-Fe, Na-Ca ± Fe, and Na alteration facies. Early replacement by epidote and actinolite is associated with abundant magnetite or lesser hematite, as well as with ilmenite, pyrite, and chalcopyrite, minor bornite and covellite, and local calcite. Commonly, sulphides (e.g. chalcopyrite and bornite) replace iron oxide minerals (Fig. 7F) or form minute inclusions in quartz. Veinlets (1–10 cm width) in the second stage of the LT Ca-Fe-Mg alteration facies contain actinolite, epidote, quartz, either magnetite or specular hematite, pyrite, and chalcopyrite (Lopez et al., 2014).

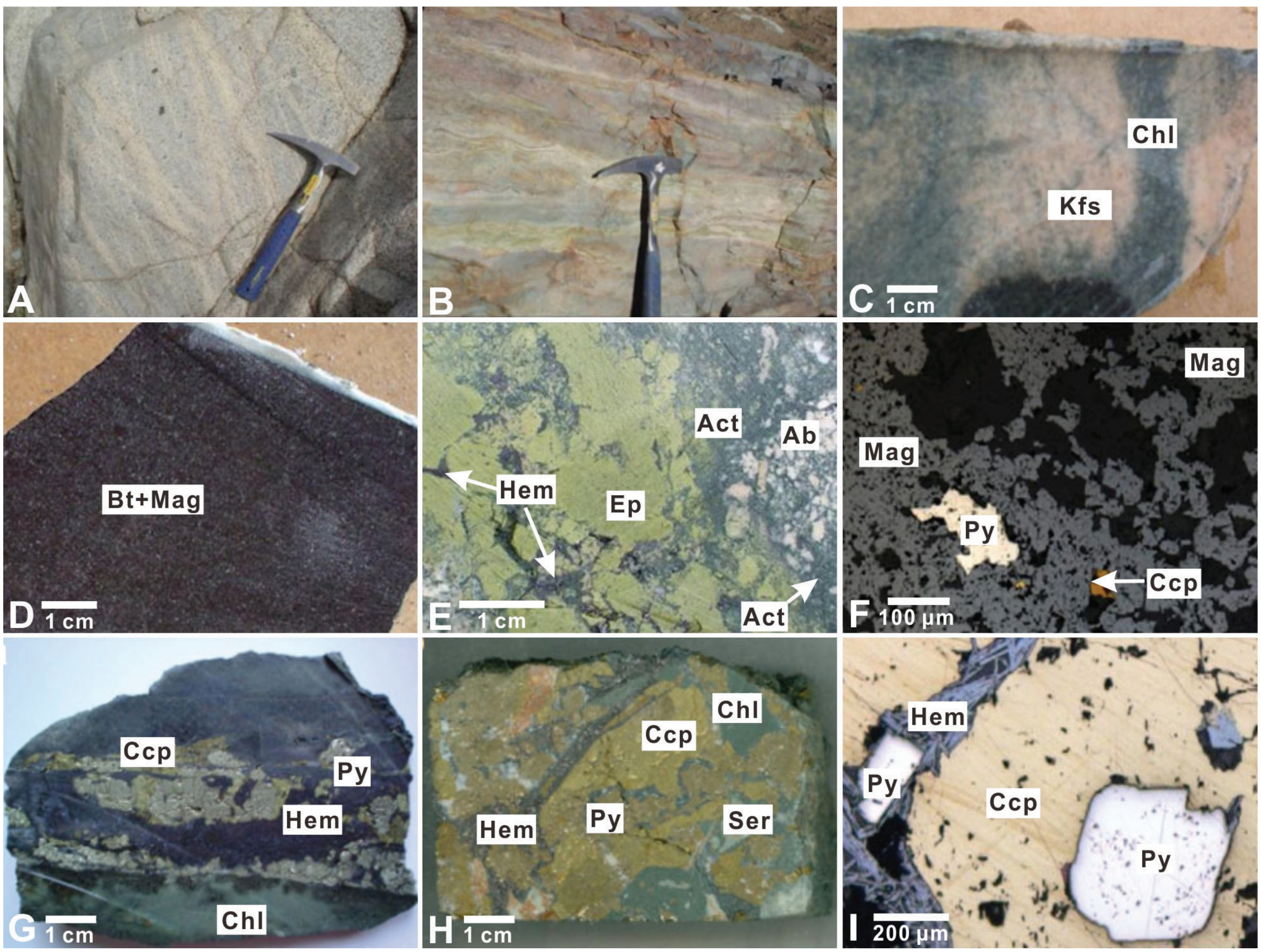


**Figure 7.** Representative photographs of alteration/mineralization paragenesis of the El Espino deposit (Lopez et al., 2014). **A.** Albite veinlets showing sodic alteration in quartz diorite. **B**. Albite- and epidote-altered sandstone showing sodic-calcic alteration. **C.** K-feldspar and chlorite alteration in andesite host rock. **D.** Biotite and magnetite assemblage showing potassic-iron alteration in sandstone. **E.** Conglomerate altered by early albite, which was then overprinted by actinolite and epidote. The actinolite and epidote are cut by later hematite. **F.** Pyrite and chalcopyrite replacing magnetite-actinolite-epidote alteration facies. **G.** Hematite-sulphide veinlets with chlorite selvages in sandstone. **H.** Massive chalcopyrite, accompanied by chlorite and sericite, cut by hematite veinlets. **I.** Chalcopyrite and hematite replacing pyrite. Abbreviations: *Ab*: albite, *Act*: actinolite, *Bt*: biotite, *Ccp*: chalcopyrite, *Chl*: chlorite, *Ep*: epidote, *Hem*: hematite, *Kfs*: K-feldspar, *Mag*: magnetite, *Py*: pyrite, *Ser*: sericite.

*LT hydrolytic K-Fe alteration*: This facies forms hydrothermal breccia and veins containing quartz, calcite, sericite, chlorite, and iron oxides (dominantly hematite; Fig. 7G–I), and hosts the vast majority of the sulphides in the El Espino district (Lopez et al., 2014). Based on crosscutting relationships among veins, three sub-stages are recognized (Lopez et al., 2014): the earliest quartz and sulphide veins are cut by later two types of veins containing hematite, sulphides, and variable amounts of quartz. The earlier hematite-sulphide veins have well-developed to poorly-developed selvages of muscovite and chlorite typical of LT K-Fe alteration (Fig. 7H, I), whereas the latest veins contain quartz, calcite, sulphide, and minor iron oxide. Locally, minor amounts of bornite, galena, and hypogene chalcocite replace chalcopyrite. Gold was locally observed as inclusions in chalcopyrite associated with the hydrolytic alteration, or in earlier quartz grains coexisting with chalcopyrite, bornite, pyrite, and actinolite and accompanied by LT Ca-Mg-Fe alteration (Lopez et al., 2014).

*Argillic alteration*: Argillic alteration is characterized by calcite-barite-quartz veins that may record the final hypogene alteration and mineralization event in the El Espino hydrothermal system. These veins commonly have selvages of late hydrothermal and clay-bearing minerals (e.g. chlorite, quartz, calcite, illite, and montmorillonite), and are observed in the upper levels of the mineralizing system (Lopez et al., 2014).

### Ore-forming Fluids: Nature and Evolution

The nature and proposed sources of ore-forming fluids for IOCG deposits globally are varied, and include magmatic-hydrothermal (Pollard, 2000, 2001, 2006) and non-magmatic (Barton and Johnson, 2004; Xavier et al., 2008; Chen et al., 2011) end-members. Non-magmatic fluid sources are proposed to be surface or basin-derived (e.g. basinal brines, seawater, and meteoric water), as well as potentially of metamorphic origin (Williams et al., 2005), which is plausible where evaporite-bearing sedimentary sequences are present during metamorphism. Ore-forming fluids for the iron and copper (-gold) mineralization stages in the Mesozoic Andean IOCG deposits also vary, based on available fluid inclusion and stable isotope data (Fig. 8; Table 1). These data were mainly obtained from mineralization-related gangue and metallic minerals, e.g. quartz and calcite for fluid inclusions; quartz, apatite, and magnetite for oxygen isotopes; and pyrite and chalcopyrite for sulphur isotopes. Moreover, fluid isotope data were used to trace the sources of ore-forming fluids, based on the isotope compositions of minerals and mineral assemblages, and their formation temperature (Table 1; e.g. Mina Justa; Chen et al., 2011).

At Mina Justa, the iron mineralization fluids (Stage V) are high-temperature (540–600 °C) and high-salinity (inferred by low final ice melting temperatures ($T_{m(ice)}$) of fluid inclusions; $T_{m(ice)}$ = −41.8 to −0.1°C; Chen, 2008), with magmatic-like oxygen ($\delta^{18}O_{fluid}$ = 9.5–11.5‰) and sulphur isotopes ($\delta^{34}S_{fluid}$ = 0.8–3.9‰), whereas the copper mineralization

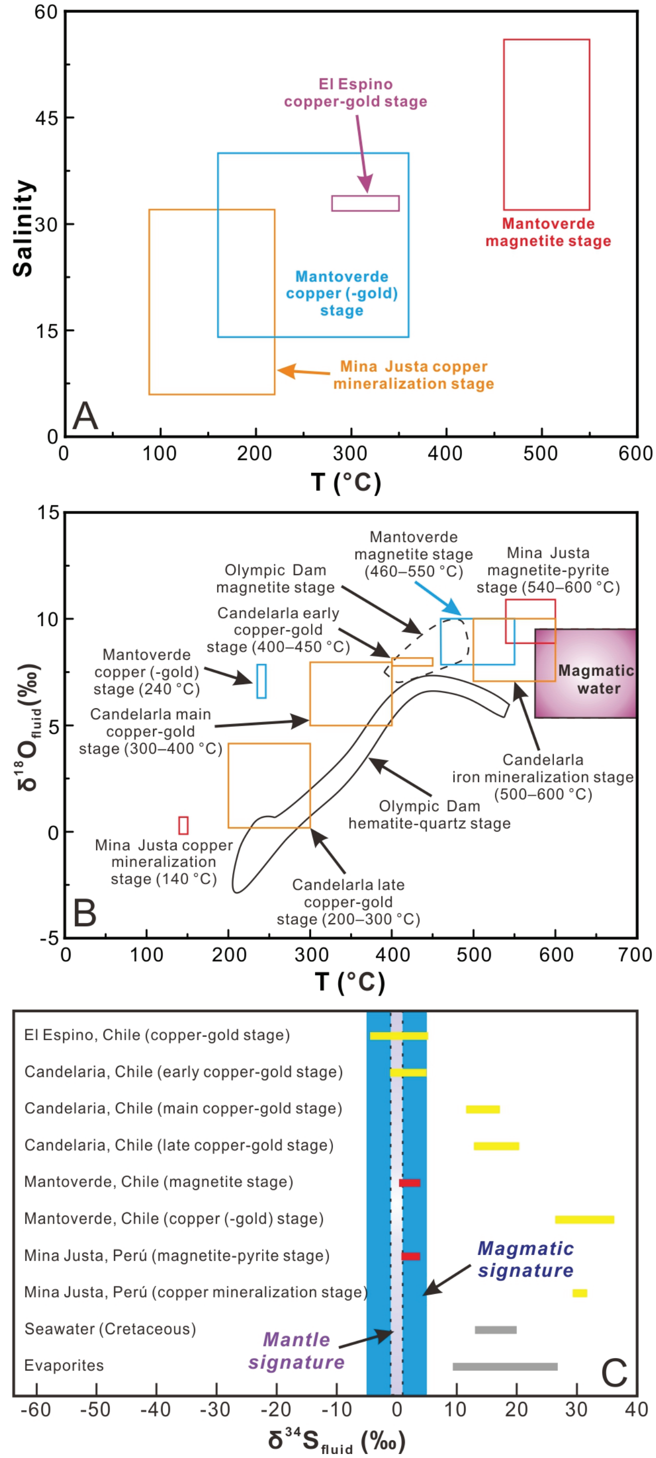


**FIGURE 8.** Comparison of ore-forming fluid characteristics of the major IOCG deposits in the Central Andes. **A.** Salinity vs. temperature diagram (salinity is weight percent NaCl equiv. or weight percent NaCl + $CaCl_2$ equiv. as Table 1 illustrates). **B.** $\delta^{18}O_{fluid}$ values and temperature relationships of ore-forming fluids. **C.** $\delta^{34}S_{fluid}$ values of ore-forming fluids. Data are from Chen et al. (2011) for the Mina Justa copper (-silver) deposit; from Benavides et al. (2007) for the Mantoverde copper (-gold) deposit; from Ullrich and Clark (1999), Ullrich et al. (2001), and Marschik and Fontboté (2001) for the Candelaria copper-gold deposit; and from Lopez et al. (2014) for the El Espino copper-gold deposit

fluids (Stage VI) have low temperatures (88–220 °C), medium to high salinities (6–32 wt% NaCl equiv.; mean 24 wt% NaCl equiv.), and are rich in calcium (Fig. 8; Table 1; Chen et al., 2011; Li et al., 2018). The latter fluids are proposed to be of basinal brine origin, and to have attained their copper and sulphur via leaching of andesitic volcanic rocks and earlier magmatic pyrite associated with the iron mineralization. Evidence of a basinal brine origin for the copper mineralizing fluids is based on the lower $\delta^{18}O_{fluid}$ (0.1‰) and higher $\delta^{34}S_{fluid}$ values (29.3–31.7‰) when compared with iron mineralizing fluids (Fig. 8). Similar conclusions can be reached for distinct inherited sources of copper mineralizing fluids based on in-situ chalcopyrite sulphur isotopes; for example, chalcopyrite that has not replaced pyrite has $\delta^{34}S$ values clustering around 1.0‰ (associated with leaching of andesitic wall rocks), whereas chalcopyrite that

**Table 1.** Comparison of salient features of the major Mesozoic IOCG deposits in the Central Andes as illustrated in Figure 9.

| **Deposits** | **Mina Justa, Perú** | **Mantoverde, Chile** | **Candelaria, Chile** | **El Espino, Chile** |
|---|---|---|---|---|
| **Tonnage** | 346.6 Mt @ 0.71% Cu, 3.8 g/t Ag and 0.03 g/t Au | 400 Mt @ 0.52% Cu and 0.11 g/t Au | 470 Mt @ 0.95% Cu, 0.22 g/t Au and 3.1 g/t Ag | 123 Mt @ 0.66% Cu and 0.24 g/t Au |
| **Host rocks** | plagioclase-phyric andesite and andesitic volcaniclastic rock | andesitic lava and volcaniclastic rock | volcanic and volcaniclastic rock | volcanic, volcaniclastic, and sedimentary rocks |
| **Alteration**[a] | (1) sodic and K-Fe (albite, actinolite, microcline, and magnetite) metasomatism (2) Ca-Fe metasomatism and early hematite alteration (3) K-Fe metasomatism with magnetite-pyrite mineralization (4) copper mineralization with calcite-hematite | (1) sodic alteration (2) K-Fe alteration with magnetite mineralization (3) hydrolytic K-Fe alteration (4) copper (-gold) mineralization with hematite-calcite | (1) sodic metasomatism (2) K-Fe alteration with iron oxide mineralization (3) calcic-silicate (garnet, albite, and quartz) alteration (4) copper-gold mineralization | (1) sodic alteration (2) Na-Ca ± Fe alteration (3) K-Fe alteration with iron mineralization (4) Ca-Fe-Mg alteration with copper sulphide mineralization (5) hydrolytic K-Fe alteration with copper-gold mineralization |
| **Mineral assemblages**[b, c] | mag-py-*qz*-chl<br>ccp-bn-*cal*-hem-cc | mag-kfs+bt<br>ccp-hem-*cal*-*qz*+Au | mag-bt-kfs-bt-qz+act<br>ccp-hem-cal-chl+Au | hem-kfs+bt+act+ep and bt-mag<br>*qz*-hem-ccp-py+Au |
| **Temperature (°C)**[b] | 540–600<br>88–220 (140[d]) | 460–550<br>160–360 (240) | 500–600<br>early: 400–450 middle: 300–400 late: 200–300 | /<br>280–350 |
| **Salinity**[b, e] | /<br>6–32 (24) | 32–56<br>14–40 | high<br>high | /<br>32–34 |
| **Fluid composition**[b] | Na<br>Ca | Ca<br>Na (Ca?) | /<br>Na (Ca) | /<br>Na |
| **$\delta^{18}O_{fluid}$ (‰)**[b] | 9.5–11.5<br>0.1 | 7.9–9.9<br>6.3–7.9 | 7.0–10.0<br>early: 8.0 middle: 5.0–8.0 late: 0.2–4.0 | /<br>/ |
| **$\delta^{34}S_{fluid}$(‰)**[b] | 0.8–3.9<br>29.3–31.7 | 0.4–4.0<br>26.4–36.2 | /<br>early: 1.0–5.7 middle: 9.0–13.0 late: 12.0–20.2 | /<br>−4.4 to 6.2 |
| **Fluid source**[b] | magmatic–hydrothermal<br>basinal brines | magmatic–hydrothermal<br>seawater | magmatic–hydrothermal<br>basinal brines or seawater | /<br>magmatic–hydrothermal (incorporation of seawater) |
| **Age (Ma)**[b] | 104–101 (microcline Ar-Ar)<br>99–95 (microcline Ar-Ar) | /<br>116 (magnetite Re-Os) | 114.2 ± 0.8 (biotite Ar-Ar)<br>111.7 ± 0.8 (biotite Ar-Ar) | 88.4 ± 1.2 (actinolite Ar-Ar)<br>87.9 ± 0.6 (muscovite Ar-Ar) |
| **References** | Chen et al., 2010, 2011 | Mathur et al., 2002<br>Benavides et al., 2007<br>Rieger et al., 2012 | Ullrich and Clark, 1999<br>Marschik and Fontboté, 2001<br>Ullrich et al., 2001 | Lopez, 2012<br>Lopez et al., 2014 |

Mineral abbreviations: *act*, actinolite; *bn*, bornite; *bt*, biotite; *cal*, calcite; *cc*, chalcocite; *ccp*, chalcopyrite; *chl*, chlorite; *ep*, epidote; *hem*, hematite; *kfs*, K-feldspar; *mag*, magnetite; *py*, pyrite; *qz*, quartz.

a Numbers indicate approximate stages in the paragenetic sequence

b Above the line: iron mineralization; below the line: copper (-gold) mineralization

c Italicized mineral used for fluid inclusion study

d The majority

e Weight percent NaCl equiv. or weight percent NaCl + $CaCl_2$ equiv.

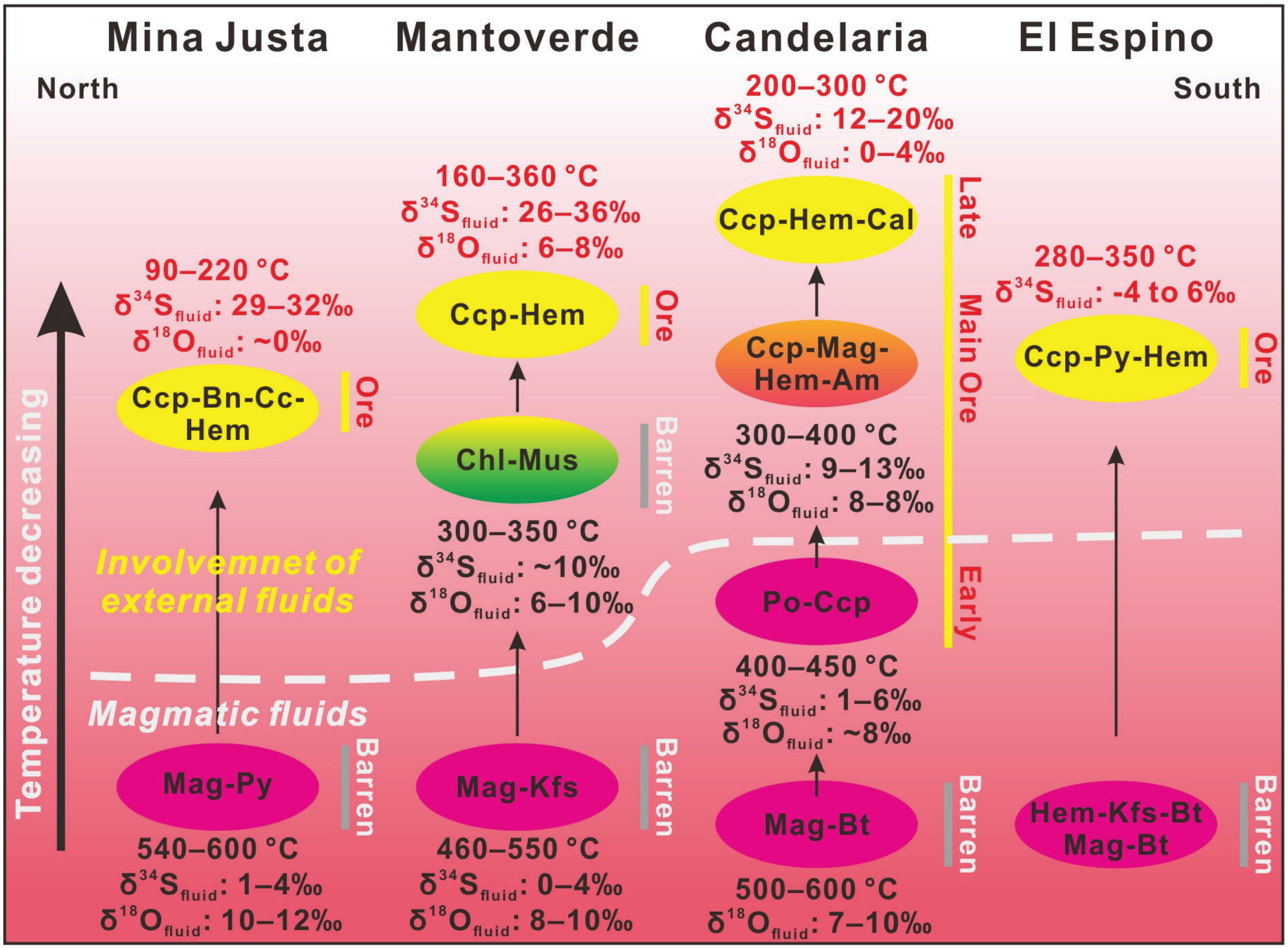


**FIGURE 9.** Comparison of mineralization for the major Central Andean IOCG deposits (data and references for each deposit can be found in Table 1). Abbreviations: *Am*: amphibole, *Bn*: bonite, *Bt*: biotite, *Cal*: calcite, *Cc*: chalcocite, *Ccp*: chalcopyrite, *Chl*: chlorite, *Hem*: hematite, *Kfs*: K-feldspar, *Mag*: magnetite, *Mus*: muscovite, *Po*: pyrrhotite, *Py*: pyrite

replaced pyrite has $\delta^{34}S$ values and trace element patterns comparable to those of the pyrite (Li et al., 2018).

At Mantoverde, ore-forming fluids generally have characteristics similar to those of the Mina Justa deposit (Table 1). Fluid inclusion studies indicate that the Mantoverde iron mineralization (Stage II) crystallized from high-temperature (460–550 °C) and high-salinity (32–56 wt% NaCl equiv.) fluids, whereas the copper (-gold) mineralization (Stage IV) crystallized from low- to medium-temperature (150–360 °C; mean 240 °C) and medium- to high-salinity (14–40 wt% NaCl equiv.) fluids (Fig. 8A, B; Benavides et al., 2007 and references therein). Oxygen isotopes show a decreasing trend from the iron mineralizing to copper (-gold) mineralizing fluids ($\delta^{18}O_{fluid}$ = 7.9–9.9‰ to 6.3–7.9‰, respectively; Fig. 8B), and sulphur isotopes show an increasing trend ($\delta^{34}S_{fluid}$ = 0.4–4.0‰ to 26.4–36.2‰; Fig. 8C), again indicating respective magmatic-hydrothermal and seawater sources of oxygen and sulphur in the fluids (Benavides et al., 2007; Rieger et al., 2012; Marschik and Kendrick, 2015).

The Candelaria iron mineralizing fluids (Stage II iron oxide) are characterized by high temperatures (500–600 °C), whereas copper-gold mineralizing fluids (Stage IV) have a wide range of temperatures (200–450 °C); fluid salinities are high in both mineralization stages (Table 1; Marschik and Fontboté, 2001). The high $\delta^{18}O_{fluid}$ values (7.0–10.0‰) suggest that fluids for the magnetite mineralization are magmatic-hydrothermal in origin (Fig. 8B). Fluids responsible for subsequent copper-gold mineralization may have been of basinal brine or seawater origin based on the wide ranges of oxygen and sulphur isotope compositions (Table 1; Fig. 8B, C): (1) $\delta^{18}O_{fluid}$ values from the early, through the main to the late copper-gold mineralization stages decrease, with values of 8.0‰, 5.0–8.0‰, and 0.2–4.0‰, respectively, and (2) correspon-ding $\delta^{34}S_{fluid}$ values are 1.0–5.7‰, 9.0–13.0‰, and 12.0–20.2‰ (Ullrich and Clark, 1999; Marschik and Fontboté, 2001; Ullrich et al., 2001).

At El Espino, fluid inclusion studies suggest that hydrothermal fluids responsible for hematite and sulphide mineralization (Stage V) have low to medium temperatures (280–350 °C) and high salinities (32–34 wt% NaCl equiv.), with an estimated depth for the mineralization of 3–4 km (Fig. 8A; Lopez et al., 2014). Moreover, sulphur isotope data for Stage IV LT Ca-Mg-Fe alteration ($\delta^{34}S_{fluid}$ = −4.0‰ to 2.4‰; mean −1‰) and Stage V LT K-Fe hydrolytic alteration ($\delta^{34}S_{fluid}$ = −4.4‰ to 6.2‰; mean 0‰) are comparable. However, the latter stage displays a broader range and higher values, possibly indicating two sources via mixing, i.e. a magmatic source and a variably reduced sulphate source (Fig. 8C; Lopez et al., 2014).

In summary, the Mesozoic Andean IOCG deposits show distinctly different characteristics for the fluids that formed the main iron oxide assemblages compared to those responsible for the copper (-gold) mineralization. Low-temperature, medium- to high-salinity fluids of probable basinal brine or seawater origin played predominant roles in the genesis of economic copper (-gold) mineralization (Fig. 9).

## Ore Deposit Modelling: Genetic and Exploration Models

In addition to the varied sources of fluids, the sources of metals are also diverse in IOCG deposits (Williams et al., 2005). Although the major Mesozoic Andean IOCG deposits, including Mina Justa, Mantoverde, Candelaria, and El Espino display distinct iron (including IOA-type) and copper (-gold) mineralization (e.g. Mina Justa and Mantoverde), they share similar regional to deposit-scale alteration (including pre-ore Na, Na-Ca-Fe, and HT Ca-Fe alteration). The principal IOCG deposits are Cretaceous (115–88 Ma; Table 1) and formed within arc-related basins, largely during their tectonic inversion between 120–100 Ma (e.g. Mina Justa, Mantoverde, and Candelaria). The El Espino deposit in northern Chile is one of the youngest (ca. 88 Ma) and southernmost IOCG systems. It formed in an active magmatic arc, also possibly during the waning stages of basin inversion, later than the Mina Justa, Mantoverde, and Candelaria deposits, thus the El Espino deposit is not included in the Central Andes ore deposit model shown in Figure 10.

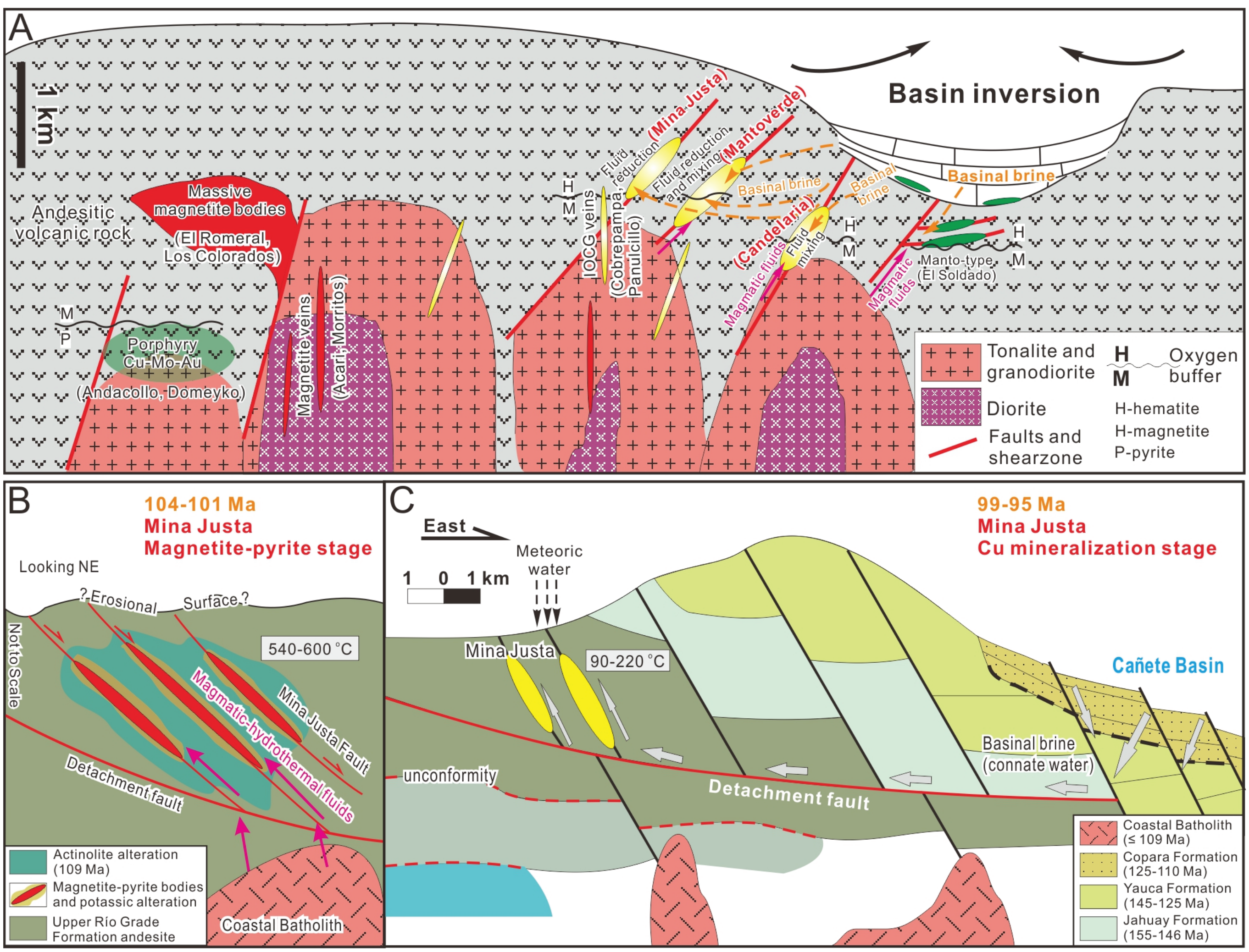


**Figure 10. A.** Models of the Mesozoic Andean IOCG mineralization in relation to other mineralization styles (modified from Chen, 2010). **B–C.** Genetic model for the Mina Justa magnetite-pyrite and copper mineralization stages (modified from Chen et al., 2011).

The IOCG deposits are spatially associated with IOA (e.g. El Romeral), manto-type (e.g. El Soldado), and porphyry Cu-Mo-Au deposits (e.g. Andacollo) deposits (Fig. 10A; Sillitoe, 2003; Chen, 2010; Chen et al., 2013). Although some differences are observed among the Mesozoic IOCG deposits in terms of alteration, mineralization, and the evolution, nature, and sources of ore-forming fluids, they clearly share similar ore-forming processes at system and deposit scales (Fig. 9). In particular, the fluids responsible for iron mineralization are high-temperature and high-salinity magmatic-hydrothermal fluids that were mainly derived from magmas of largely intermediate composition (e.g. Coastal Batholith for Mina Justa and Llahuin pluton for El Espino; Chen et al., 2011; Lopez et al., 2014), whereas fluids responsible for the subsequent economic copper (-gold) mineralization were low-temperature, medium- to high-salinity, basinal brine or seawater-derived sources. Here we illustrate our mineralization model for the Mesozoic Andean IOCG deposits using the Mina Justa deposit as an example.

At Mina Justa, as back-arc extension led to formation of the Cañete Basin (Fig. 10C), high-salinity magmatic-hydrothermal fluids pooled towards the top(s) of magma chamber(s), and ascended along fault zones to form the early Na, Na-Ca, and Na-Ca-Fe alteration facies. During inversion of the extensional basin, early high-temperature magmatic-hydrothermal fluids evolved to an iron-rich composition through early fluid-rock reactions, and ascended along the Mina Justa Fault, replacing previous extensive alteration zones and/or minerals (e.g. 110 Ma actinolite alteration; Chen et al., 2010) and forming magnetite-pyrite bodies in the HT K-Fe (K-feldspar-magnetite) alteration facies (Fig. 10B). With inversion of the Cañete Basin, low-temperature Ca-rich basinal brines began to play a more predominant role in leaching and precipitating additional economic metals (e.g. copper and sulphur) from volcanic rocks (probably andesitic volcanic or volcaniclastic rocks that host the Central Andean IOCG deposits; Table 1). These brines migrated along earlier normal and detachment faults (now inverted) in the Mina Justa ore system, replacing early-formed minerals (e.g. magnetite and pyrite), and at ca. 99–95 Ma generated economic copper orebodies. These deposits were dominated by copper sulphides, such as chalcopyrite, bornite, chalcocite, and digenite within the LT K-Fe and LT Ca-Mg-Fe alteration facies (Fig. 10C; Chen et al., 2010, 2011; Li et al., 2018).

Temporal separation of early iron and subsequent economic copper (-gold) mineralization in Mesozoic Andean IOCG deposits is common (Chen, 2010, this study), and is typical of the evolution of iron oxide and alkali-calcic alteration systems that generate IOA and/or IOCG mineralization worldwide (Corriveau et al., 2010, 2016, 2022a). This characteristic evolution of fluid systems is in turn commonly associated with changes in geodynamic settings (Skirrow, 2010; Montreuil et al., 2016a, b; Corriveau et al., 2022b). The compositional end-members of the fluids responsible for iron oxide versus copper (-gold) mineralization is also different, with major contributions from fluids of non-magmatic origin (e.g. basinal brines and/or seawater) playing a key role in the formation of economic copper (-gold) mineralization (Fig. 9; Table 1).

The Mesozoic Andean IOCG deposits commonly have a protracted history of alteration and mineralization, as well as a spatial and temporal association with porphyry Cu (-Mo-Au), manto-type copper, and Chilean iron deposits (Fig. 10A; Sillitoe, 2003; Chen, 2010; Chen et al., 2010, 2013). During the culminated hydrothermal alteration and mineralization period (ca. 125–110 Ma), ore-related magmatic-hydrothermal fluids in the northern Chile formed porphyry Cu (-Mo-Au) deposits, K-Fe metasomatism around some Chilean iron deposits, and early magnetite orebodies of the IOCG deposits (Sillitoe, 2003; Benavides et al., 2007; Chen, 2010). This spatial association can provide clues for mineral prospecting, not only for IOCG deposits (although other iron oxide and alkali-calcic alteration systems in the Andean Mesozoic may in fact represent credible exploration targets), but associated deposit types (e.g. porphyry and manto-type deposits). For example, El Espino, the youngest and southernmost deposit, is similar to the Raúl-Condestable IOCG deposit in Perú (Fig. 1) in terms of host rocks, paragenetic sequence, and alteration patterns (Lopez et al., 2014). However, El Espino currently does not have iron resources as pervasive and high-grade as those of the Raúl-Condestable deposit, potentially indicating that significant undiscovered magnetite deposits may exist where the deeper HT Ca-Fe alteration zones at El Espino evolve to the fertile HT and LT K-Fe alteration, LT Ca-Mg-Fe facies, and their variants. In addition, similar tectonic settings involving a spatial and temporal association with extensional basins and basin inversion occur throughout the Central Andes and may indicate prospectivity for additional Mesozoic IOCG deposits along the margin of the former arc-basin systems (Chen et al., 2013).

## Implications for the Ore Genesis and Tectonic Setting of the Global IOCG Family

The genesis of IOCG deposits has long been debated in terms of ore-forming fluids and tectonic settings, which represent two different but associated geological paradigms for modelling ore deposits, as stressed by many researchers, including Skirrow (2010) and Chen et al. (2013). The early studies of the giant Olympic Dam deposit triggered such debates in the 1980s and 1990s and these arguments have continued in the following decades for other IOCG deposits and provinces. In a comprehensive review of global IOCG deposits, Williams et al. (2005) compared ore deposit geology, ore-forming fluids, and known tectonic settings. However, several alternative models were included in Williams' review, and two major aspects of IOCG ore genesis are still not fully resolved. First, the tectonic settings of IOCG deposits have remained unclear, partly due to the fact that most of the major IOCG deposits are hosted by rocks of Precambrian age, in which deciphering tectonic settings can be difficult. A broad range of tectonic settings was proposed by Hitzman (2000) for both Precambrian and younger IOCG deposits, including extensional and "orogenic basin collapse" scenarios. Groves et al. (2010) proposed different tectonic settings for Precambrian IOCG deposits (e.g. intracontinental, largely anorogenic, at fossil craton margins above metasomatized lithospheric mantle) and Phanerozoic IOCG deposits (e.g. Andean-type continental margins). Chen et al. (2013) proposed that initial Central Andean IOCG mineralization was coeval with the early stage of Gondwana breakup (i.e. extension), and peak Mesozoic IOCG mineralization occurred during inversion of the extensional basins (compression/transpression). They also predicted that more Mesozoic IOCG deposits would be discovered around the margin of the former Gondwana Supercontinent (Chen et al., 2013). More recently, Skirrow et al. (2018) and Tiddy and Giles (2020) have re-examined the geodynamic evolution of the Olympic copper-gold province, which hosts the Olympic Dam deposit. Skirrow et al. (2018) proposed that IOCG mineralization occurred in a post-subduction setting distal (inboard) from a former magmatic arc, above previously metasomatized lithospheric mantle, during a switch from compression to extension, whereas Tiddy and Giles (2020) have significantly advanced an alternative model based on a suprasubduction environment.

In contrast to the cryptic Precambrian IOCG settings, the tectonic setting and evolution of the Mesozoic Central Andean IOCG deposits is much better understood and relatively simple because of their young formation ages and good rock exposure of the host basins and fault systems. This means that it is possible to describe the nature and evolution of ore-forming fluids within the context of a relatively well-understood geodynamic framework. The clarity afforded by the Mesozoic Central Andean IOCG systems can therefore enhance our understanding of IOCG ore-forming systems globally, at least for IOCG deposits formed in ancient continental margin settings. Based on our synthesis, we are now able to clarify a second aspect of IOCG ore genesis, namely the differing roles of magmatic-hydrothermal and non-magmatic fluids. In the Central Andean IOCG systems, iron (magnetite) mineralization and copper (-gold) mineralization are temporally distinct, and involve both magmatic-hydrothermal and non-magmatic mineralizing fluids (basinal brines or seawater having reacted with andesitic volcanic rocks), respectively. Combined with recent accurate isotope age dating for the mineralization and magmatism (Marschik and Fontboté, 2001; Mathur et al., 2002; Chen et al., 2010; Lopez, 2012; Cochrane et al., 2014), the available data indicate that the IOCG deposits of the Central Andes formed during the inversion (transpression) of extensional basins in the Early Cretaceous. The two distinct ore-forming fluid sources also match this tectonic setting: i.e. magmatism that sourced the early magmatic-hydrothermal ore-forming fluids and basinal brines and/or residual seawater that reacted with the volcanic host rocks are both common and play major roles in such a tectonic setting. However, compared with the major IOCG deposits formed at the peak of basin inversion, the younger IOCG deposits in the Central Andes (such as El Espino) may have formed during the waning stage or termination of basin inversion, to be followed by a new magmatic arc system during the Central Andes "porphyry period".

## Conclusions

The Mesozoic IOCG deposits in the Central Andes provide good examples to resolve the decades-long arguments about ore-forming fluids and tectonic settings of other "Andean type" IOCG deposits. Clearly, both magmatic-hydrothermal and non-magmatic fluids are important in generating these deposits, playing different roles in the high- to low-temperature evolution of the hydrothermal systems that form iron oxide and alkali-calcic alteration systems and their ore deposits. We speculate that the larger and higher-grade copper (-gold) IOCG deposits may have formed where and when the tectonic and geological setting permitted "external" or non-magmatic fluids to affect the same volumes of crust as earlier fluids of magmatic-hydrothermal origin. This may have involved fluid mixing and/or overprinting of one fluid system by the other, which hasn't been discussed in detail herein and is beyond the scope of this paper. The extent to which high volumes of end-member fluids can mix within single ore systems could be related to their unique tectonic setting, i.e. inversion of extensional basins along continental margins characterized by extensive magmatism and large-scale movement of non-magmatic fluids. These insights about the genesis of IOCG deposits in the Central Andes have significant implications for our understanding of and deposit modelling of the global IOCG family, and complements current work being carried out globally on these topics.

## Acknowledgments

The authors thank Dr. Louise Corriveau for inviting us to participate in this special publication and for her review and editorial handling of the manuscript. We also thank Roger Skirrow, Fernando Barra, and Reginald Wilson for their insightful comments.

Financial supports from the National Natural Science Foundation of China (41725009 and 42002083) are appreciated.

## References

Arévalo, C., Grocott, J., Martin, W., and Pringle, M., 2006, Structural setting of the Candelaria Fe oxide Cu-Au deposit, Chilean Andes (27°30'S): Economic Geology, v. 101, p. 819-841.

Barra, F., Reich, M., Selby, D., Rojas, P., Simon, A.C., Salazar, E., and Palma, G., 2017, Unraveling the origin of the Andean IOCG clan: a Re-Os isotopes approach: Ore Geology Reviews, v. 81, p. 62-78.

Barton, M.D., and Johnson, D.A., 2004, Footprints of Fe-oxide (-Cu-Au) systems: University of Western Australia Special Publication, v. 33, p. 112-116.

Benavides, J., Kyser, T., Clark, A.H., Oates, C.J., Zamora, R., Tarnovschi, R., and Castillo, B., 2007, The Mantoverde iron oxide–copper–gold district, III Región, Chile: the role of regionally derived, nonmagmatic fluids in chalcopyrite mineralization: Economic Geology, v. 102, p. 415-440.

Boric, P.R., Díaz, F.F., and Maksaev, J.V., 1990, Geología y yacimientos metalíferos de la Región de Antofagasta: Servicio Nacional de Geología y Minería Boletín, v. 40, p. 246.

Brett, R., 1964, Experimental data from the system Cu-Fe-S and their bearing on exsolution textures in ores: Economic Geology, v. 59, p. 1241-1269.

Chen, H.Y., 2008, The Marcona-Mina Justa district, south-central Perú: implications for the genesis and definition of the iron oxide-copper (-gold) ore deposit clan: Unpublished Ph.D. thesis, Queen's University, 266 p.

Chen, H.Y., 2010, Mesozoic IOCG mineralization in the Central Andes: an updated review, *in* Porter, T.M., ed., Hydrothermal iron oxide copper–gold and related deposits: a global perspective, volume 4: PGC Publishing, Adelaide, p. 259-272.

Chen, H.Y., Clark, A.H., Kyser, T.K., Ullrich, T.D., Baxter, R., Chen, Y.M., and Moody, T.C., 2010, Evolution of the giant Marcona-Mina Justa iron oxide–copper–gold district, south-central Perú: Economic Geology, v. 105, p. 155-185.

Chen, H.Y., Kyser, T.K., and Clark, A.H., 2011, Contrasting fluids and reservoirs in the contiguous Marcona and Mina Justa iron oxide–Cu (–Ag–Au) deposits, south-central Perú: Mineralium Deposita, v. 46, p. 677-706.

Chen, H.Y., Cook, D.R., and Baker, M.J., 2013, Mesozoic iron oxide copper-gold mineralization in the central Andes and the Gondwana Supercontinent breakup: Economic Geology, v. 108, p. 37-44.

Cochrane, R., Spikings, R., Gerdes, A., Winkler, W., Ulianov, A., Mora, A., and Chiaradia, M., 2014, Distinguishing between in-situ and accretionary growth of continents along active margins: Lithos, v. 202, p. 382-394.

Cornejo, P., Matthews, S., Orrego, M., and Robles, W., 2000, Etapas de mineralización asociadas a alteración potásica en un sistema Fe-Cu-Au: Yacimiento Mantoverde, III Región de Atacama, Chile: IX Congreso Geológico Chileno, Puerto Varas, Actas, p. 97-101.

Corriveau, L., Williams, P.J., and Mumin, A.H., 2010, Alteration vectors to IOCG mineralization – from uncharted terranes to deposits, *in* Corriveau, L. and Mumin, A.H., eds., Exploring for iron oxide copper-gold deposits: Canada and global analogues: Geological Association of Canada, Short Course Notes, No. 20, p. 89-110.

Corriveau, L., Montreuil, J.-F., and Potter, E.G., 2016, Alteration facies linkages among iron oxide copper-gold, iron oxide-apatite, and affiliated deposits in the Great Bear magmatic zone, Northwest Territories, Canada: Economic Geology, v. 111, p. 2045-2072.

Corriveau, L., Potter, E.G., Montreuil, J.-F., Blein, O., Ehrig, K., and De Toni, A., 2018, Iron-oxide and alkali-calcic alteration ore systems and their polymetallic IOA, IOCG, skarn, albitite-hosted U±Au±Co, and affiliated deposits: A short course series. Part 2: overview of deposit types, distribution, ages, settings, alteration facies, and ore deposit models: Geological Survey of Canada, Scientific Presentation 81, 154 p.

Corriveau, L., Montreuil, J.-F., Blein, O., Ehrig, K., Potter, E.G., and De Toni, A.F., 2022a, Mineral systems with iron oxide and alkali-calcic alteration: part 3 – metal pathways and ore deposit model, *in* Corriveau, L., Potter, E.G. and Mumin, A.H., eds., Mineral systems with iron oxide copper-gold (IOCG) and affiliated deposits: Geological Association of Canada, Special Paper 52, p. 205-245.

Corriveau, L., Mumin, A.H., and Potter, E.G., 2022b, Iron oxide copper-gold (Ag-Bi-Co-U-REE) and affiliated deposits: introduction and overview, *in* Corriveau, L., Potter, E.G. and Mumin, A.H., eds., Mineral systems with iron oxide copper-gold (IOCG) and affiliated deposits: Geological Association of Canada, Special Paper 52, p. 1-25.

de Haller, A., and Fontboté, L., 2009, The Raúl-Condestable iron oxide copper-gold deposit, central coast of Perú: ore and related hydrothermal alteration, sulfur isotopes, and thermodynamic constraints: Economic Geology, v. 104, p. 365-384.

de Haller, A., Corfu, F., Fontboté, L., Schaltegger, U., Barra, F., Chiaradia, M., Frank, M., and Alvarado, J.Z., 2006, Geology, geochronology, and Hf and Pb isotope data of the Raúl-Condestable iron oxide–copper–gold deposit, central coast of Perú: Economic Geology, v. 101, p. 281-310.

del Real, I., Thompson, J.F.H., and Carriedo, J., 2018, Lithological and structural controls on the genesis of the Candelaria-Punta del Cobre Iron Oxide Copper Gold district, Northern Chile: Ore Geology Reviews, v. 102, p. 106-153.

Grocott, J., and Taylor, G.K., 2002, Magmatic arc fault systems, deformation partitioning and emplacement of granitic complexes in the Coastal Cordillera, northern Chilean Andes (25°30′ S to 27°00′ S): Journal of the Geological Society, v. 159, p. 425-442.

Groves, D.I., Bierlein, F.P., Meinert, L.D., and Hitzman, M.W., 2010, Iron oxide copper-gold (IOCG) deposits through Earth history: implications for origin, lithospheric setting, and distinction from other epigenetic iron oxide deposits: Economic Geology, v. 105, p. 641-654.

Hitzman, M.W., 2000, Iron oxide-Cu-Au deposits: what, where, when, and why, *in* Porter, T.M., ed., Hydrothermal iron oxide copper-gold and related deposits: a global perspective, volume 1: PGC Publishing, Adelaide, p. 9-26.

Hopf, S., 1990, The Agustina mine: a volcanic-hosted copper deposit in northern Chile: Society for Geology Applied to Mineral Deposits Special Publication, v. 8, p. 421-434.

Knipping, J.L., Bilenker, L.D., Simon, A.C., Reich, M., Barra, F., Deditius, A.P., Wälle, M., Heinrich, C.A., Holtz, F., and Munizaga, R., 2015a, Trace elements in magnetite from massive iron oxide-apatite deposits indicate a combined formation by igneous and magmatic-hydrothermal processes: Geochimica et Cosmochimica Acta, v. 171, p. 15-38.

Knipping, J.L., Bilenker, L.D., Simon, A.C., Reich, M., Barra, F., Deditius, A.P., Lundstrom, C., Bindeman, I., and Munizaga, R., 2015b, Giant Kiruna-type deposits form by efficient flotation of magmatic magnetite suspensions: Geology, v. 43, p. 591-594.

Li, R.C., Chen, H.Y., Xia, X.P., Yang, Q., Danyushevshy, L.V., and Lai, C., 2018, Using integrated in-situ sulfide trace element geochemistry and sulfur isotopes to trace ore-forming fluids: example from the Mina Justa IOCG deposit (southern Perú): Ore Geology Reviews, v. 101, p. 165-179.

López, E., 2002, Caracterización petrográfica y estudio de la alteración hidrotermal y mineralización del distrito Mantoverde, Provincia de Chañaral, Tercera Región, Chile: Unpublished B.Sc. thesis, Antofagasta, Chile, Universidad Católica del Norte, 119 p.

Lopez, G.P., 2012, The El Espino iron oxide copper gold (IOCG) district, Coastal Cordillera of North-Central Chile: Unpublished Ph.D. thesis, Colorado School of Mines, Golden, Colorado, 120 p.

Lopez, G.P., Hitzman, M.W., and Nelson, E.P., 2014, Alteration patterns and structural controls of the El Espino IOCG mining district, Chile: Mineralium Deposita, v. 49, p. 235-259.

Lundin Mining, 2020, Lundin Mining announces 2020 mineral resource and reserve estimates: News provided by Lundin Mining on September 8th, 2020.

Marschik, R., and Fontboté, L., 2001, The Candelaria-Punta del Cobre iron–oxide Cu–Au (–Zn–Ag) deposits, Chile: Economic Geology, v. 96, p. 1799-1826.

Marschik, R., and Kendrick, M.A., 2015, Noble gas and halogen constraints on fluid sources in iron oxide-copper-gold mineralization: Mantoverde and La Candelaria, Northern Chile: Mineralium Deposita, v. 50, p. 357-371.

Mathur, R., Marschik, R., Ruiz, J., Munizaga, F., Leveille, R.A., and Martin, W., 2002, Age of mineralization of the Candelaria iron oxide Cu–Au deposit, and the origin of the Chilean Iron Belt based on Re–Os isotopes: Economic Geology, v. 97, p. 59-71.

Montreuil, J.-F., Corriveau, L., and Davis, W.J., 2016a, Tectonomagmatic evolution of the southern Great Bear magmatic zone (Northwest Territories, Canada) – Implications on the genesis of iron oxide alkali-altered hydrothermal systems, *in* Slack, J., Corriveau, L. and Hitzman, M., eds., Proterozoic iron oxide-apatite (± REE) and iron oxide-copper-gold and affiliated deposits of Southeast Missouri, USA, and the Great Bear magmatic zone, Northwest Territories, Canada: Economic Geology, v. 111, p. 2111-2138.

Montreuil, J.-F., Corriveau, L., Potter, E.G., and De Toni, A.F., 2016b, On the relation between alteration facies and metal endowment of iron oxide–alkali–altered systems, southern Great Bear Magmatic Zone (Canada), *in* Slack, J., Corriveau, L. and Hitzman, M., eds., Proterozoic iron oxide-apatite (± REE) and iron oxide-copper-gold and affiliated deposits of Southeast Missouri, USA, and the Great Bear magmatic zone, Northwest Territories, Canada: Economic Geology, v. 111, p. 2139-2168.

Palma, G., Barra, F., Reich, M., Valencia, V., Simon, A.C., Vervoort, J., Leisen, M., and Romero, R., 2019, Halogens, trace element concentrations, and Sr-Nd isotopes in apatite from iron oxide-apatite (IOA) deposits in the Chilean iron belt: evidence for magmatic and hydrothermal stages of mineralization: Geochimica et Cosmochimica Acta, v. 246, p. 515-540.

Pollard, P.J., 2000, Evidence of a magmatic fluid and metal source for Fe-oxide Cu–Au mineralization, *in* Porter TM, ed., Hydrothermal iron oxide–copper–gold and related deposits: a global perspective, volume 1: PGC Publishing, Adelaide, p. 27-41.

Pollard, P.J., 2001, Sodic (–calcic) alteration associated with Fe-oxide–Cu–Au deposits: an origin via unmixing of magmatic-derived $H_2O$–$CO_2$–salt fluids: Mineralium Deposita, v. 36, p. 93-100.

Pollard, P.J., 2006, An intrusion-related origin for Cu–Au mineralization in iron oxide–copper–gold (IOCG) provinces: Mineralium Deposita, v. 41, p. 179-187.

Reich, M., Simon, A.C., Deditius, A., Barra, F., Chryssoulis, S., Lagas, G., Tardani, D., Knipping, J., Bilenker, L., Sánchez-Alfaro, P., Roberts, M.P., and Munizaga, R., 2016, Trace element signature of pyrite from the Los Colorados iron oxide-apatite (IOA) deposit, Chile: a missing link between Andean IOA and iron oxide copper-gold systems: Economic Geology, v. 111, p. 743-761.

Rieger, A.A., Marschik, R., Díaz, M., Holzl, S., Chiaradia, M., Akker, B., and Spangenberg, J.E., 2010, The hypogene iron oxide copper-gold mineralization in the Mantoverde district, northern Chile: Economic Geology, v. 105, p. 1271-1299.

Rieger, A.A., Marschik, R., and Díaz, M., 2012, The evolution of the hydrothermal IOCG system in the Mantoverde district, northern Chile: new evidence from microthermometry and stable isotope geochemistry: Mineralium Deposita, v. 47, p. 359-369.

Rodriguez-Mustafa, M.A., Simon, A.C., del Real, I., Thompson, J.F.H., Bilenker, L., Barra, F., Bindeman, I., and Cadwell, D., 2020, A continuum from iron oxide copper-gold to iron oxide-apatite deposits: evidence from Fe and O stable isotopes and trace element chemistry of magnetite: Economic Geology, v. 115, p. 1443-1459.

Ruiz, F.C., and Peebles, L.F., 1988, Geología, distribución y génesis de los yacimientos metalíferos Chilenos: Unpublished Ph.D. thesis, Santiago, Editorial Universitaria, 334 p.

Ryan, P.J., Lawrence, A.L., Jenkins, R.A., Matthews, J.P., Zamora, J.C., Marino, E., and Urqueta, I., 1995, The Candelaria copper-gold deposit, Chile: Arizona Geological Society Digest, v. 20, p. 625-645.

Sillitoe, R.H., 2003, Iron oxide-copper-gold deposits: an Andean view: Mineralium Deposita, v. 38, p. 787-812.

Simon, A.C., Knipping, J., Reich, M., Barra, F., Deditius, A.P., Bilenker, L., and Childress, T., 2018, Kiruna-type iron oxide-apatite (IOA) and iron oxide copper-gold (IOCG) deposits form by a combination of igneous and magmatic-hydrothermal processes: evidence from the Chilean iron belt: Society of Economic Geologists Special Publication, v. 21, p. 89-114.

Skirrow, R.G., 2010, "Hematite-group" IOCG ± U ore systems: tectonic settings, hydrothermal characteristics, and Cu-Au and U mineralizing processes: Geological Association of Canada, Short Course Notes, No. 20, p. 39-58.

Skirrow, R.G., van der Wielen, S.E., Champion, D.C., Czarnota, K., and Thiel, S., 2018, Lithospheric architecture and mantle metasomatism linked to iron oxide Cu-Au ore formation: multidisciplinary evidence from the Olympic Dam region, South Australia: Geochemistry, Geophysics, Geosystems, v. 19, p. 2673-2705.

Taylor, G.K., Grocott, J., Pope, A., and Randall, D.E., 1998, Mesozoic fault systems, deformation and fault block rotation in the Andean forearc: a crustal scale strike-slip duplex in the Coastal Cordillera of northern Chile: Tectonophysics, v. 299, p. 93-109.

Tiddy, C.J., and Giles, D., 2020, Suprasubduction zone model for metal endowment at 1.60–1.57 Ga in eastern Australia: Ore Geology Reviews, v. 122, 103483.

Ullrich, T.D., and Clark, A.H., 1999, The Candelaria Cu–Au deposit, III Región, Chile: paragenesis, geochronology and fluid composition, *in* Stanley, C.J., ed., Mineral deposits: processes to processing: Balkema, Rotterdam, p. 201-204.

Ullrich, T.D., Clark, A.H., and Kyser, T.K., 2001, The Candelaria Cu–Au deposit, III Región, Chile: product of long-term mixing of magmatic–hydrothermal and evaporite-sourced fluids: Geological Society of America Annual Meeting, Boston, Abstracts with Programs, p. A-3.

Vila, T., Lindsay, N., and Zamora, R., 1996, Geology of the Mantoverde copper deposit, northern Chile: a specularite-rich hydrothermal-tectonic breccia related to the Atacama fault zone: Society of Economic Geologists Special Publication, v. 5, p. 157-170.

Williams, P.J., Barton, M.D., Johnson, D.A., Fontboté, L., Halter, A.D., Mark, G., Oliver, N.H.S., and Marschik, R., 2005, Iron oxide copper–gold deposits: geology, space-time distribution, and possible modes of origin: Economic Geology 100th Anniversary Volume, p. 371-405.

Xavier, R.P., Wiedenbeck, M., Trumbell, R.B., Dreher, A.M., Monteiro, L.V.S., Rhede, D., Araújo, C.E.G., and Torresi, I., 2008, Tourmaline B-isotopes fingerprint marine evaporites as the source of high-salinity ore fluids in iron-oxide-copper-gold deposits, Carajás Mineral Province (Brazil): Geology, v. 36, p. 743-746.

# Linkages among IOA, Skarn, and Magnetite-group IOCG Deposits in China: From Deposit Studies to Mineral Potential Assessment

**Xin-Fu Zhao**
*State Key Laboratory of Geological Processes and Mineral Resources, and School of Earth Resources, China University of Geosciences (Wuhan), xfzhao@cug.edu.cn*

**Huayong Chen**
*Key Laboratory of Mineralogy and Metallogeny, Guangzhou Institute of Geochemistry, Chinese Academy of Sciences*

**Liandang Zhao**
*School of Earth Science and Resources, Chang'an University*

**Mei-Fu Zhou**
*State Key Laboratory of Geological Processes and Mineral Resources, and School of Earth Resources, China University of Geosciences (Wuhan)*
*Department of Earth Sciences, The University of Hong Kong*

*Recommended citation: Zhao, X.-F., Chen, H., Zhao, L., and Zhou, M.-F., 2022, Linkages among IOA, skarn, and magnetite-group IOCG deposits in China: from deposit studies to mineral potential assessment, in Corriveau, L., Potter, E.G. and Mumin, A.H., eds., Mineral systems with iron oxide copper-gold (IOCG) and affiliated deposits: Geological Association of Canada, Special Paper 52, p. 383-407.*

## Abstract

Genesis of iron oxide-copper-gold (IOCG) and iron oxide-apatite (IOA) deposits is framed by a variety of models that have rarely considered the insights provided by deposits from China. This paper synthesizes studies on IOA, skarn, and IOCG deposits from China, and links the different types of deposits to their alteration facies and tectonic settings. Mesozoic IOA deposits (ca. 130 Ma) from eastern China are spatially and temporally associated with subvolcanic dioritic intrusions. The orebodies are situated in the roof zones of the associated intrusions and along the contacts between the intrusions and overlying volcanic rocks. They are commonly associated with extensive brecciation and show a zonation of alteration from Na and high-temperature Ca-Fe alteration facies to low-temperature Ca-Mg facies. The magnetite-apatite assemblages formed from extremely high-temperature, highly saline magmatic-hydrothermal liquids that interacted with the country rocks of the subvolcanic intrusions. Slightly older (143–130 Ma) skarn Fe-(Cu-Au) deposits were formed in the same metallogenic belt, but are generally not spatially associated with the IOA deposits. However, they share similar hydrothermal alteration and paragenetic sequences, indicating that both types of deposits are derived from similar high-temperature magmatic-hydrothermal systems.

IOCG deposits in southwestern China are hosted by late Paleoproterozoic metasedimentary and metavolcanic rocks in a rift-related basin at the continental margin of the Yangtze block. Orebodies are generally stratabound and (or) structurally controlled. Some deposits contain both bona fide IOCG and magnetite-only orebodies. The ore-forming fluids for the iron-oxide stage are dominantly magmatic in origin, possibly derived from deep-seated magmas, whereas non-magmatic fluids were involved at various degrees during the Cu-sulphide stage. Late Paleozoic Fe-Cu(-Au) deposits are hosted by mafic to intermediate volcanic rocks in eastern Tianshan and eastern Junggar, northwestern China. They are interpreted to have formed during a tectonic transition from basin extension to inversion, and show fluid evolution typical of IOCG deposits in the central Andes. However, these deposits also have mineral assemblages and alteration sequences similar to skarn deposits. We suggest that IOA and skarn deposits form under high temperature regimes proximal to intrusions within magmatic-hydrothermal systems, whereas IOCG deposits are derived from magmatic fluids that have significantly circulated into host country rocks and have potentially mixed with external brine sources.

## Résumé

La formation des gîtes à d'oxydes de fer-cuivre-or (IOCG) et à oxydes de fer-apatite (IOA) est cadrée par divers modèles qui ont rarement pris en compte les connaissances découlant des études sur les gîtes de Chine. Cet article synthétise les études sur les gîtes IOA, skarn et IOCG de Chine, et lie les différents types de gîtes à leurs séquences d'altération et à leurs contextes tectoniques. Les gîtes IOA mésozoïques (ca. 130 Ma) de la Chine orientale sont associés dans le temps et dans l'espace à des intrusions dioritiques subvolcaniques. Ils sont localisés au toit des intrusions et à leur contact avec les roches volcaniques sus-jacentes. Ces gîtes sont généralement associés à une bréchification extensive, et montre une zonation des faciès d'altération de Na à Ca-Fe de haute température. Les assemblages à magnétite-apatite se sont formés à partir de fluides magmatiques-hydrothermaux salins et de températures extrêmement élevées qui ont interagi avec l'encaissant des intrusions subvolcaniques. Des gisements à skarn à Fe-(Cu-Au) légèrement plus anciens (143–130 Ma) sont associés spatialement aux gisements IOA et en partagent les types et séquences d'altération hydrothermale, indiquant que les deux types de gîtes sont dérivés de fluides magmatiques-hydrothermaux de haute température similaires.

Les gîtes IOCG du sud-ouest de la Chine sont situés dans des roches métasédimentaires et métavolcaniques du Paléoprotérozoïque tardif au sein d'un bassin associé à un rift à la marge continentale du bloc Yangtze. Les corps minéralisés sont généralement concordants à la stratification et / ou présentent des évidences d'un contrôle structural. Certains gisements contiennent des corps minéralisés à la fois de type IOCG et de type à magnétite seulement (IOA). Les fluides minéralisateurs pour le stade à oxydes de fer sont essentiellement magmatiques, probablement issus de magmas profonds, tandis que des fluides non magmatiques sont intervenus à divers degrés au stade des sulfures de cuivre. Les gisements Fe-Cu(-Au) du Paléozoïque tardif sont encaissés dans des roches volcaniques mafiques à intermédiaires dans l'est du Tianshan et l'est du Junggar, dans le nord-ouest de la Chine. Ils sont interprétés comme ayant été formés dans un contexte de transition tectonique de l'extension du bassin hôte à son inversion, et montrent une évolution de fluides typique des gisements IOCG des Andes centrales. Cependant, ces gisements présentent également des assemblages de minéraux et des séquences d'altération similaires aux gisements de type skarn. Nous suggérons que les gîtes IOA et à skarn se forment sous des régimes de températures élevées à proximité d'intrusions au sein de systèmes de fluides magmatiques-hydrothermaux, tandis que les gîtes IOCG sont dérivés de fluides magmatiques qui ont circulé de manière significative dans les roches encaissantes et se sont éventuellement mélangés à des sources de fluides externes.

## Introduction

When Hitzman et al. (1992) proposed the first synthesis of the Proterozoic Fe-(Cu-U-Au-REE) deposits (an initial concept of iron oxide-copper-gold (IOCG) deposits), iron oxide-apatite (IOA) deposits were included as the iron-rich end member of this group. A key question is whether a magmatic-hydrothermal fluid that precipitates massive magnetite (IOA ores) will continue transporting significant amounts of dissolved Fe, Cu, and Au to form true IOCG ores. Based on exceptional field exposures and structurally controlled depth to surface profiles, Corriveau et al. (2016, 2018) demonstrate that IOA and IOCG deposits in the Great Bear magmatic zone of Canada share the same sequence of iron oxides and alkali-calcic alteration facies and that each facies or their superposition produces distinct deposit types. This possible genetic link between IOA and IOCG deposits has only been documented in a few settings. In most cases, they remain obscure and controversial (Williams, 2010). In the central Andes and the Great Bear magmatic zone, several studies proposed that IOA deposits may represent the deeper roots of iron oxide and alkali-calcic alteration systems that can also form IOCG deposits (e.g. Sillitoe, 2003; Mumin et al., 2010; Barton, 2014; Corriveau et al., 2016; Reich et al., 2016). However, Groves et al. (2010) have suggested that IOCG deposits have different temporal distribution and tectonic settings than IOA deposits, although both types of deposits are characterized by Na-Ca alteration zones and common association with brecciated rocks. In addition, IOA deposits have also been considered to form from a volatile-rich iron-oxide melt (Tornos et al., 2016) or magnetite-bubble pairs (Knipping et al., 2015) separated from conjugate silicate melts, which were subsequently overprinted by hydrothermal alteration. These different models obscure the shared attributes of IOCG and affiliated deposits, and sustain debates on ore genesis.

This paper provides an overview of deposit geology and alteration sequences of IOA, skarn, and IOCG deposits from China, including the Mesozoic IOA and skarn deposits from the Middle and Lower Yangtze River Metallogenic Belt of eastern China, the Paleozoic IOCG-like deposits in the Xinjiang province of northwestern China, and the Proterozoic IOCG deposits in the Kangdian district of southwestern China (Fig. 1). A comparison of the alteration sequences for these deposits documents significant commonalities that provide constraints on ore genesis, as well as for mineral exploration.

## IOCG and Affiliated Deposits in China

Systematic studies of IOCG deposits from China were not available until about 10 years ago. Dozens of Fe-Cu-(Au-REE) deposits hosted in late Paleoproterozoic strata in southwestern China define the Proterozoic Kangdian IOCG metallogenic belt (Fig. 1; Zhao and Zhou, 2011; Zhou et al., 2014). Several

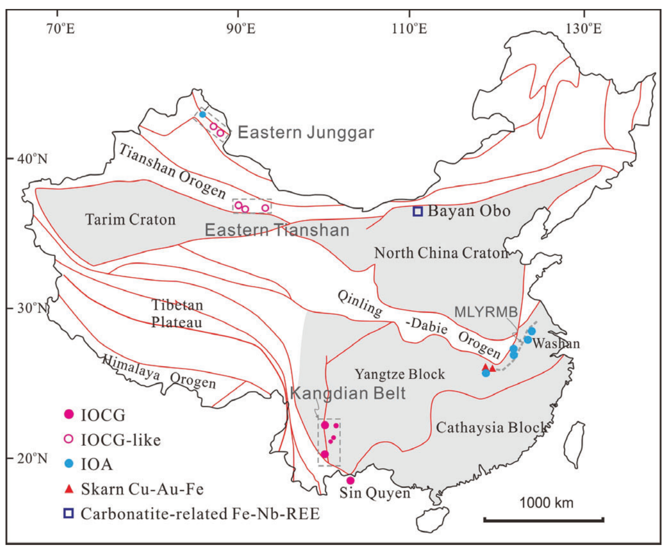


**FIGURE 1.** Simplified geotectonic map of China with locations of Proterozoic IOCG deposits in the Kangdian metallogenic province, Paleozoic IOCG-like deposits in eastern Tianshan and eastern Junggar, and Mesozoic IOA and skarn deposits in the Middle and Lower Yangtze River Metallogenic Belt (MLYRLB) (modified from Zhao XF et al., 2019a).

of the most important deposits of the district, including Dahongshan, Lala, and Yinachang, have been well documented in international journals (e.g. Zhao and Zhou, 2011; Chen and Zhou, 2012; Li X et al., 2015; Su et al., 2016; Zhao XF et al., 2017; Zhu et al., 2017), making them the most well-known IOCG deposits in China.

Recently, late Paleozoic iron-copper deposits in the Aqishan-Yamansu belt, eastern Tianshan, and northern margin of eastern Junggar, in northwestern China, have been shown to have affinities with IOCG deposits in the central Andes, and also with skarn deposits (Zhao LD et al., 2017a; Jiang et al., 2018; Liang et al., 2018, 2019; Zhang et al., 2018). They may represent new examples of Phanerozoic IOCG deposits formed during basin inversion in a continental arc setting (Zhang et al., 2017; Zhao LD et al., 2018b). Early Cretaceous IOA deposits in the MLYRMB are the best studied deposits in China since the classic work and modelling of the Ningwu Research Group (1978) (Fig. 1). In the introductory chapter of this special paper, these deposits are considered prime examples of IOA mineralization (Corriveau et al., 2022), and may provide critical evidence for the linkage between IOCG, IOA, and skarn deposits.

## Late Paleoproterozoic IOCG Deposits in the Kangdian Metallogenic Province

### *Geological Background*

The Kangdian metallogenic province, including the Fe-Cu-(Au-REE) deposits in southwestern China and northern Vietnam, is a recently defined Proterozoic IOCG belt located in the southwestern part of the Yangtze block (Zhao and Zhou, 2011; Zhou et al., 2014; Figs. 1, 2). The Yangtze block has very limited exposure of Archean basement due to a thick cover of Proterozoic and Phanerozoic rocks. Paleoproterozoic strata, including the Dahongshan, Dongchuan, and Hekou groups, are distributed mainly in the Kangdian region of the western Yangtze block (Wu et al., 1990; Zhao et al., 2010). These strata comprise arenaceous to argillaceous metasedimentary rocks with minor metavolcanic rocks, all of which have undergone greenschist to lower amphibolite facies metamorphism during a Neoproterozoic orogenic event at ca. 830 Ma (Wu et al., 1990; Yang et al., 2013; Zhou et al., 2014).

The IOCG deposits in the Kangdian metallogenic belt are hosted by late Paleoproterozoic (1.74 to 1.68 Ga) metasedimentary and metavolcanic rocks (Fig. 2; Zhao and Zhou, 2011; Zhou et al., 2014). The ore-hosting rocks formed in a rift-related basin at the continental margin of the Yangtze block. Orebodies are generally stratabound and/or structurally controlled, and have thicknesses ranging from several metres to tens of metres. They are spatially associated with slightly younger 1.69 to 1.65 Ga mafic intrusions and various sizes of hydrothermal breccia bodies. The paragenetic sequence of the deposits includes pre-ore Na-(Ca) alteration (stage I), iron-oxide mineralization dominated by magnetite and siderite with subsidiary apatite (stage II high-temperature Ca-Fe alteration), and Cu-(Au-REE) mineralization comprising chalcopyrite, ankerite, biotite, chlorite, and possible bornite and REE minerals (stage III K-Fe alteration). In many deposits, except for the true IOCG ores, there are also massive and/or banded magnetite ores without copper sulphides. These magnetite-only ores commonly contain minor apatite, are similar to IOA ores in other districts such as the Great Bear magmatic zone, and likely represent the earlier stage of an ore system that evolved to IOCG mineralization, but without significant overprint by sulphide assemblages.

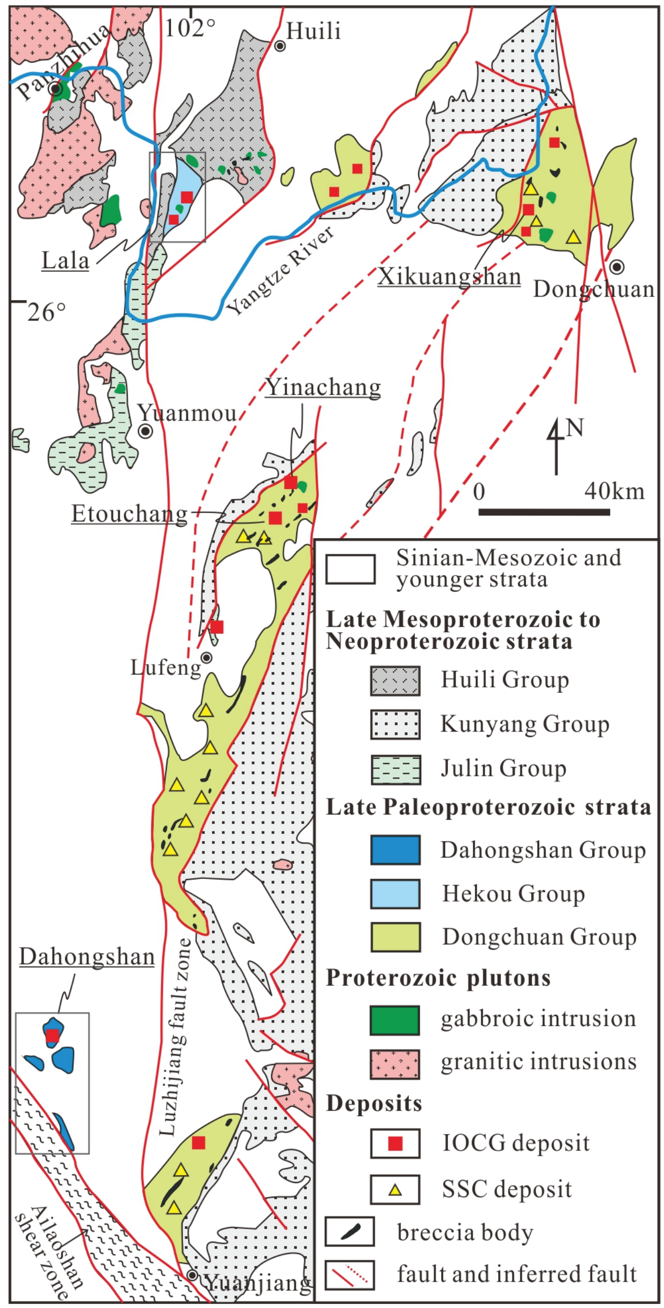


FIGURE 2. Simplified geological map of the Kangdian district, showing the location of representative IOCG deposits (modified from Zhao and Zhou, 2011). Sedimentary rock-hosted stratiform copper (SSC) deposits formed within the same late Paleoproterozoic sequence, but in different lithotypes.

The Kangdian belt has experienced multiple tectonothermal-hydrothermal events (Zhou et al., 2014; Zhao XF et al., 2019a). The most important mineralizing event is associated with late Paleoproterozoic (1.66–1.65 Ga) magmatism, although a late Mesoproterozoic magmatic event (1.08–1.03 Ga) is possibly responsible for another significant mineralization/remobilization in the northern part of the district. Widespread Neoproterozoic magmatic-metamorphic events in the Kangdian belt have led to remobilization of Cu-(Au-REE) ores (Zhao XF et al., 2019a).

*Deposit Geology*

Here we use the Dahongshan deposit as an example to introduce the mineralization and alteration features of the Kangdian belt. The Dahongshan Fe-Cu-(Au-Ag) deposit was discovered by aeromagnetic survey in the 1960s. It was explored by the No. 9 Geological Brigade of the Yunnan Bureau of Geology and Mineral Resources (N9GBYBGMR) in the 1970s, but industrial mining did not begin until 1997. It has a reserve of 458.3 Mt of ore grading 41.0% Fe and 1.35 Mt Cu (metal) in ore grading 0.78% Cu, and contains approximately 16 t Au, 141 t Ag, 18,156 t Co, and 2.1 t Pd+Pt (N9GBYBGMR, 1983). The deposit is particularly interesting because both massive iron and stratabound copper-iron orebodies are present, although they are hosted by different lithotypes (Fig. 3). Thus, this deposit provides an excellent opportunity to examine ore-forming processes and the role of magmatism in the formation of IOCG deposits.

Orebodies are hosted within least-altered to altered rocks of the Dahongshan Group, which consists mainly of metaconglomerate, meta-arenite, quartz-mica schist and gneiss, albitite, marble, amphibolite, and local migmatite (Wu et al., 1990). The metapelitic rocks and amphibolite commonly have garnet porphyroblasts and display a prominent foliation parallel to sedimentary bedding. Most of the rocks have undergone extensive albitization during ore formation and possibly also postore metamorphic events.

Briefly, the deposit has two types of ore: (1) iron ore, which consists of massive or banded magnetite, local hematite, and minor to no sulphides; and (2) copper-iron ore that forms disseminations, stockworks, and stratabound layers of magnetite-chalcopyrite within biotite schist. Most iron orebodies are hosted in extensively sodic-metasomatized brecciated rocks, and are localized just above a large gabbroic intrusion (Fig. 3). These iron orebodies are chiefly lens-shaped, and generally contain 40–60% Fe and have very little or no chalcopyrite, but may contain minor amounts of fine-grained pyrite. They are hosted within either the albitized rocks or high-temperature (HT) Ca-Fe-altered rocks containing abundant amphibole and magnetite. Albite, apatite, siderite, and quartz are common gangue minerals, which are disseminated in the ores. In contrast, the copper-iron orebodies are roughly stratabound and sheet-like in shape (Fig. 3), and hosted mainly by garnet-biotite schist. Detailed petrographic observations have shown that the garnet-biotite schists are likely hydrothermally altered argillaceous siltstone and dolostone. Replacement of albite by K-feldspar can be observed in these country rocks. Abundant biotite and K-feldspar indicate a K-Fe alteration associated with copper-sulphide mineralization. Characteristic ores are disseminations or stockworks of magnetite and chalcopyrite, plus local minor bornite, overall having an average grade of ~1% Cu (0.3–1.5%) and 20–30% Fe. Gold and silver, by-products in the copper-iron orebodies, have average grades of 0.1 ppm and 3 ppm, respectively (N9GBYBGMR, 1983). In addition to the two types of ores, pervasive magnetite alteration has affected the country rocks, resulting in iron contents that are generally greater than 10%. Locally, low-grade magnetite-hematite ores with 20–30% Fe are present above the massive No. II iron orebody.

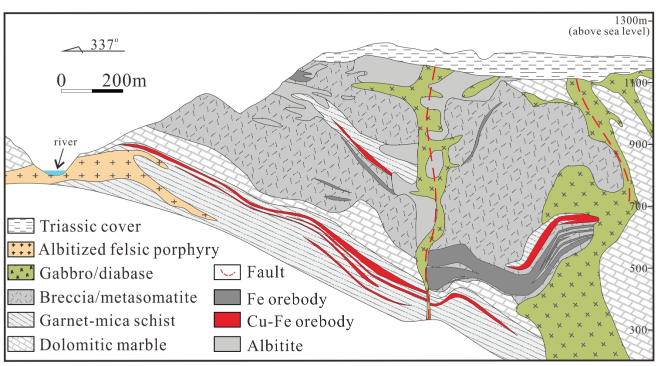

**Figure 3.** Geological cross-section of No. 38 exploration line of Dahongshan deposit (modified from N9GBYBGMR, 1983), showing spatial relationship between massive iron and stratabound iron-copper orebodies. Also note close association of massive iron orebodies, breccias, and gabbroic intrusions.

Although the assemblage of ore minerals is slightly different, the massive iron and stratabound copper-iron ores have similar paragenetic sequences and alteration assemblages (Figs. 4, 5). The Dahongshan Group and gabbro intrusions have both undergone pervasive stage I Na-(Ca) alteration, which is characterized by widespread and abundant albite, actinolite, and local scapolite. In places, both volcanic and sedimentary rocks are completely replaced and metasomatically altered to albitite (Figs. 4, 5). Albitization can either preserve the structures of the protoliths (Figs. 4A, 5A, B, E) or obscure them by complete recrystallization (Fig. 4B, C). Multiple albitization events are observed as late-stage albite veins locally cut albitite (Fig. 5B). Some albite grains have rims that are slightly more enriched in calcium than cores (Fig. 6), suggesting that the fluids gradually evolved to produce the stage II HT Ca-Fe alteration facies.

Magnetite is the predominant ore mineral of stage II, and is closely associated spatially with apatite, amphibole, and minor albite. Disseminated apatite is widespread in the magnetite ores and is the most important accessory mineral. Amphiboles, including actinolite, ferro-pargasite, cummingtonite, and tschermakite, are widespread in different lithotypes. Minor amounts of fine-grained pyrite also formed during this stage, being texturally coeval with magnetite. Hematite formed during the latter parts of stage II alteration and texturally postdates magnetite and pyrite; it is spatially associated with sericite, K-feldspar,

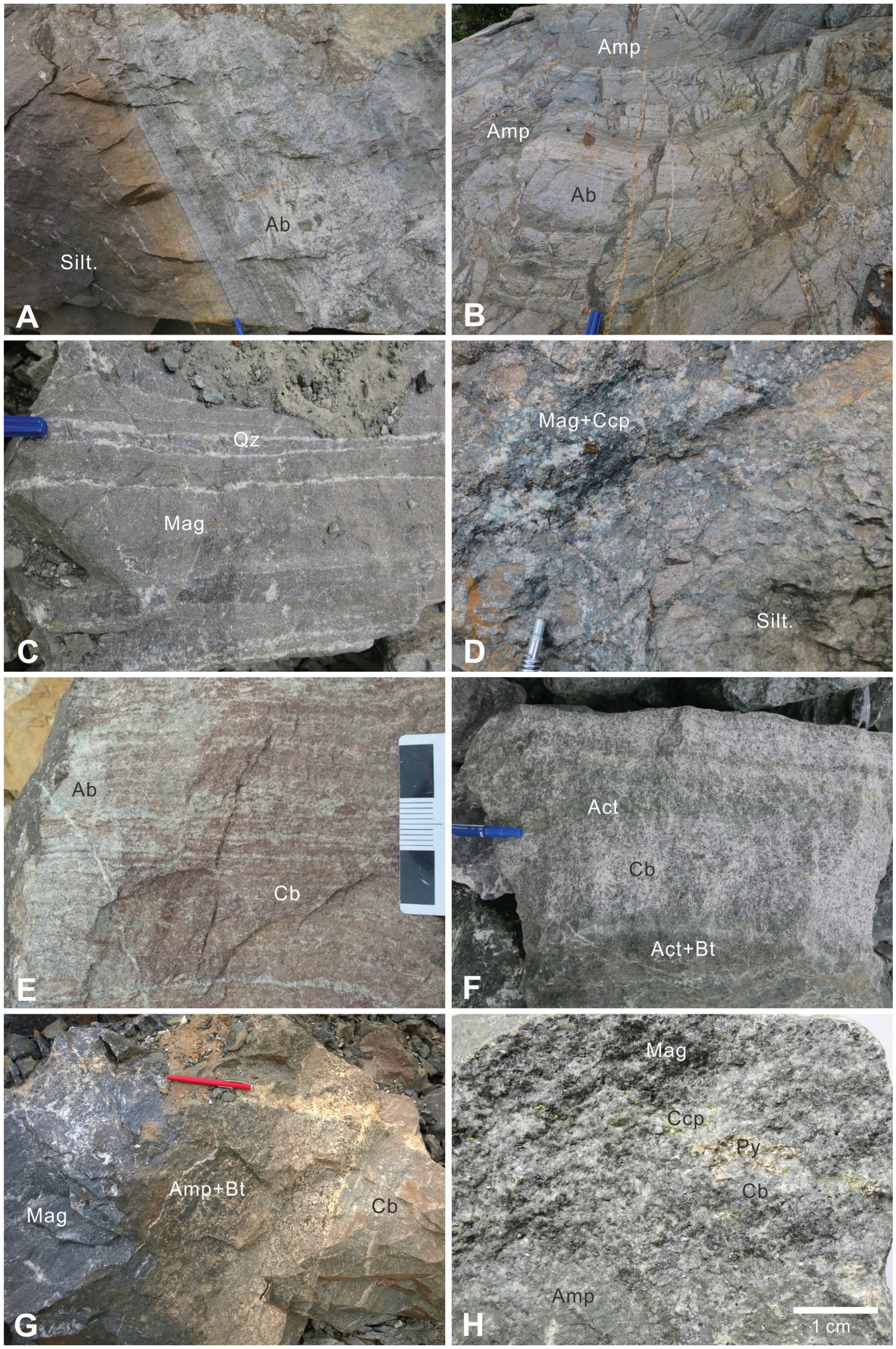


**FIGURE 4.** Field photographs of country rocks showing representative alteration in siltstone (A–D) and dolostone (E–H) in the Dahongshan deposit. **A.** Intensely albitized siltstone and less altered siltstone have sharp contacts. **B.** Amphibole ± magnetite overprint on albitized siltstone either along bedding planes or as veinlets. **C.** Intensely magnetite±amphibole-altered siltstone; note the quartz bands along the bedding planes. **D.** Veins of magnetite-amphibole-chalcopyrite cutting albitized siltstone. **E.** Albitized arenaceous dolostone with preserved sedimentary bedding structure. **F.** Actinolite and biotite alteration along the bedding of arenaceous dolostone. **G.** Sharp contact between extensive magnetite alteration and actinolite-biotite altered dolostone; note the progressively decreasing amphibole+biotite trend towards albitized arenaceous carbonate. **H.** Disseminated amphibole- and amphibole-magnetite-altered -magnetite-altered carbonate rocks cut by chalcopyrite-pyrite veinlets. Mineral and rock-type abbreviations in this paper: *Act* = actinolite, *Ab* = albite, *Amp* = amphibole, *Ap* = apatite, *Bt* = biotite, *Cal* = calcite, *Cb* = carbonate, *Ccp* = chalcopyrite, *Chl* = chlorite, *Clay* = clay mineral, *Elc* = electrum, *Ep* = epidote, *Grt* = garnet, *Hem* = hematite, *Kfs* = K-feldspar, *Mag* = magnetite, *Pl* = plagioclase, *Py* = pyrite, *Qz* = quartz, *Scp* = scapolite, *Ser* = sericitic white mica, *Silt* = siltstone, *Sp* = sphalerite, *Ttn*: titanite, *Tur* = tourmaline.

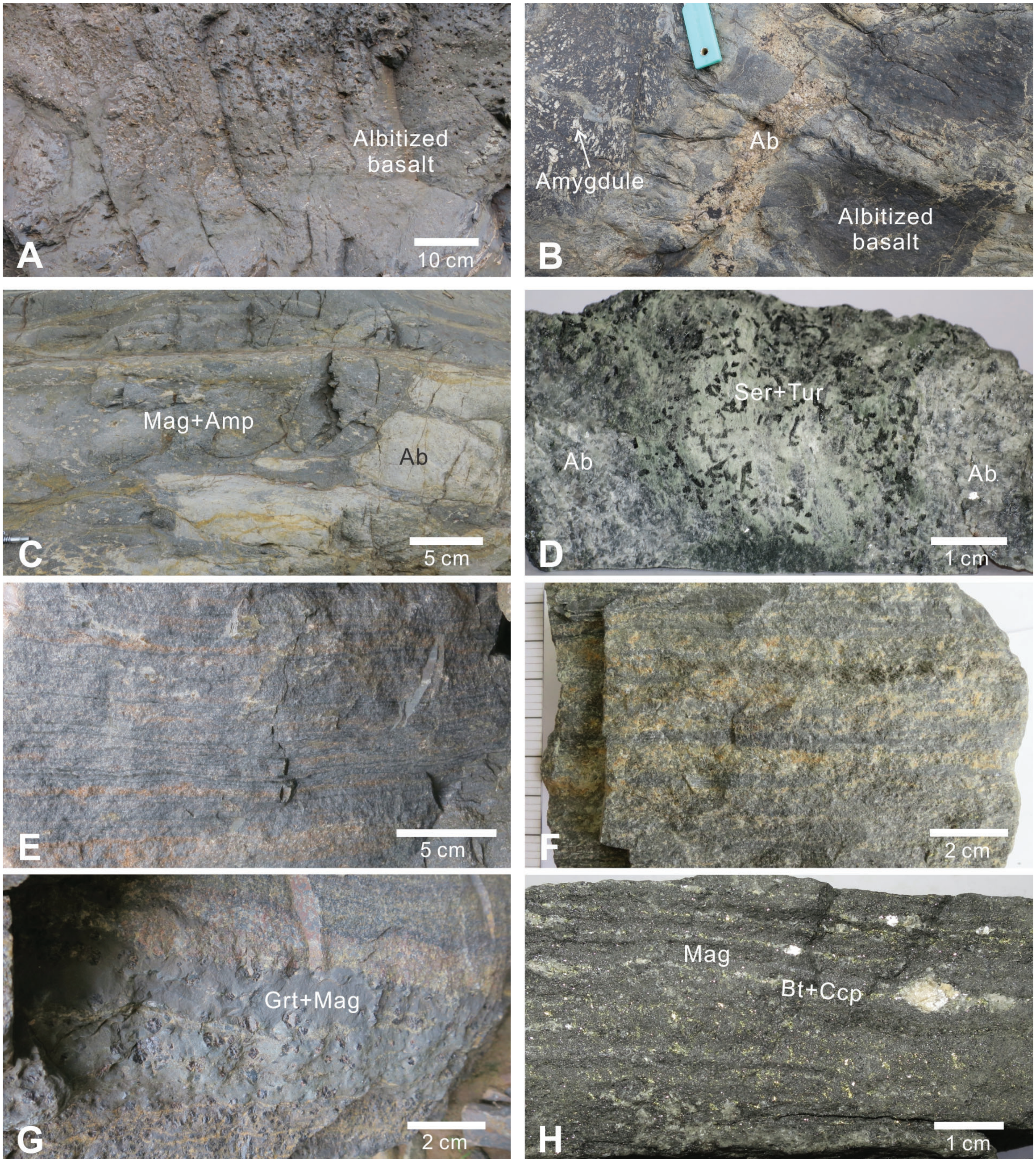


**FIGURE 5.** Photographs of representative alteration of basalt and interbedded argillaceous siltstone and dolostone (IASD) in the Dahongshan deposit. **A.** Extensively Na-Fe altered basaltic rocks showing relict amygdaloidal textures. **B.** Albitized, amygdaloidal basalt (dark) overprinted by albite-magnetite veins, implying multiple albitization. The amygdules consist of a mineral association of albite-magnetite-amphibole-apatite-biotite±chalcopyrite. **C.** Intensely albitized volcanic rocks overprinted by slightly younger magnetite and amphibole alteration. **D.** Coarse-grained albitite is overprinted by sericite-tourmaline-(hematite)-chlorite alteration. **E, F.** Variously Na-Fe altered IASD, still preserving the sedimentary bedding. Note that the thin layers ranging from 0.5 cm to few centimetres in width have protoliths of siltstone, argillaceous siltstone, pelite, to dolostone. **G.** Magnetite alteration layer in albitized IASD. In many places, grains of poikiloblastic manganese-rich almandine are observed within massive magnetite layers. **H.** Laminated, biotite-altered IASD composed of albite, magnetite, apatite, biotite, chalcopyrite and ankerite are the main host rocks for copper-iron orebodies.

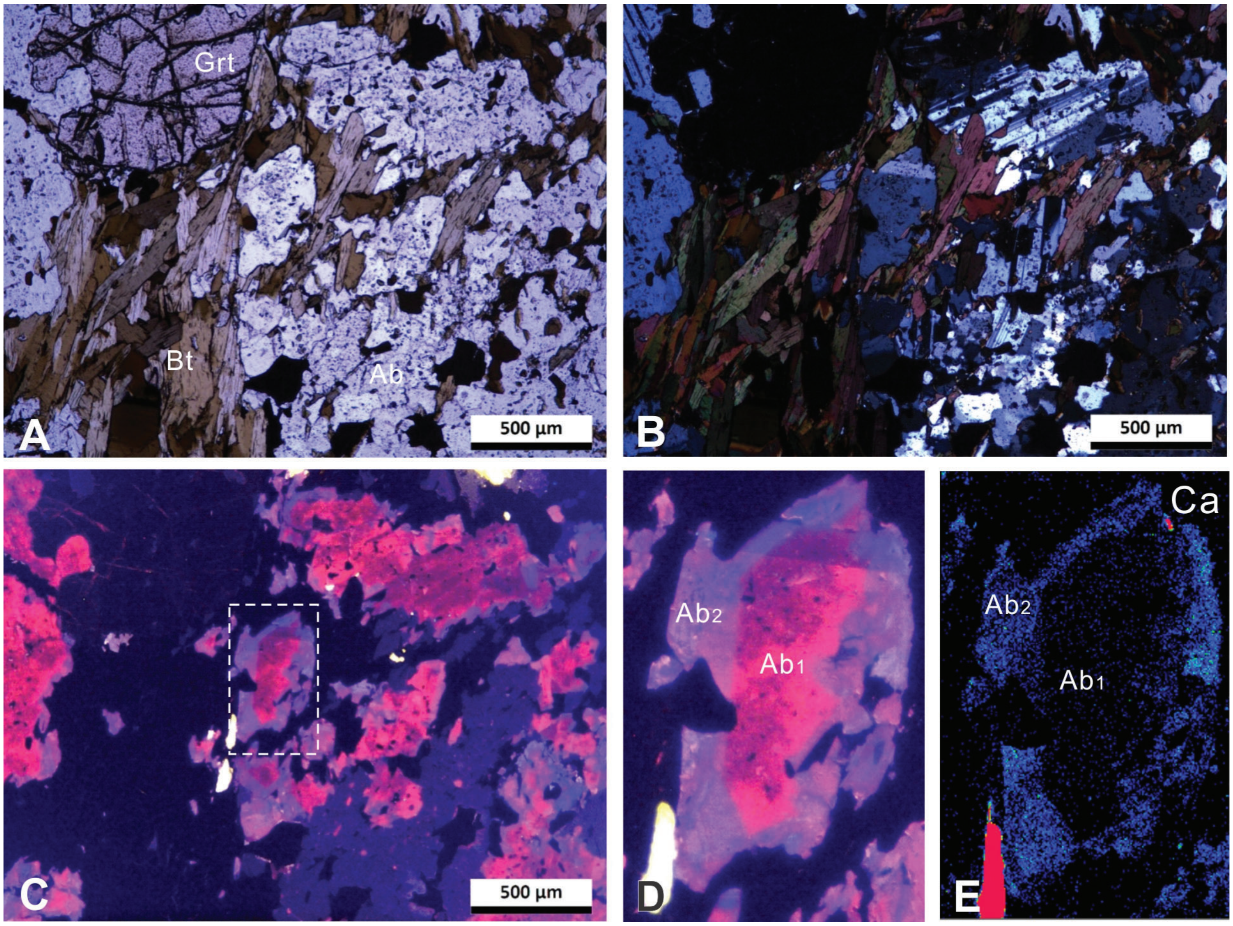


**FIGURE 6. A, B.** Photomicrograph of plane (A) and crossed (B) light microscopy for representative garnet-biotite schist, the main ore-hosting rock for copper-iron orebodies in the Dahongshan deposit. Pervasive stage I albite is overprinted by garnet and biotite. **C, D.** Microscopic cathodoluminescence (CL) images showing that the earlier stage albite (Ab1) is partially replaced by Ab2 with different CL colours along grain margins. **E.** Electron microprobe EDS mapping shows that Ab2 contains higher calcium than Ab1, implying that the fluid conditions evolved to a calcium-stable trend.

and quartz, forming a typical low-temperature K-Fe alteration assemblage. Field and microscopic observations suggest that stage III chalcopyrite paragenetically postdates magnetite (Fig. 4H), and is likely coeval with quartz, biotite, chlorite, sericite, and locally K-feldspar. Pyrite, pyrrhotite, and minor bornite also formed during this stage in the copper-iron orebodies. Biotite and chlorite are the most abundant alteration minerals, aside from the Ca-Fe assemblages of stage II. Stage IV alteration produced quartz, calcite, and chlorite veins. Ankerite and siderite are pervasive in all rock types; they may have formed over a prolonged period, in which siderite and ankerite likely precipitated during stages II and III, respectively.

*A Genetic Model for the Kangdian District IOCG Deposits*

The IOCG deposits of the Kangdian district (Fig. 7) have the following features: a significant volume of breccia, regional-scale sodic alteration zones, and structurally controlled and/or stratabound orebodies. Fluid inclusions and stable and radiogenic isotopes have shown that the early-stage ore fluids are dominantly magmatic in origin, possibly derived from deep-seated magmas (Fig. 7). However, non-magmatic fluids were involved

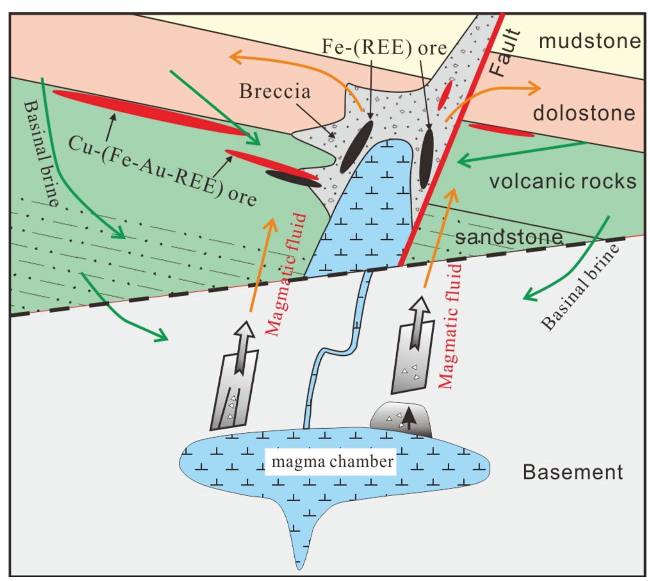


**FIGURE 7.** Conceptual genetic model of mixing magmatic fluids and basinal brines in the formation of IOCG deposits in the Kangdian metallogenic province, southwestern China (Zhao XF et al., 2017).

at various degrees during the copper sulphide stage (Zhao X.F. et al., 2017). We suggest that mixing of ascending hot magmatic fluids with cooler non-magmatic fluids effectively led to the saturation and deposition of ore minerals. Iron first precipitated as magnetite, and locally as hematite, mainly within the brecciated zones or preferential structures of the hosting rocks; copper and gold were more mobile and subsequently became saturated in the country rocks where externally derived sulphur was available (Fig. 7). Orebodies with different mineral associations may have complex controls in terms of their depth, ore-hosting country rocks, degree of fluid mixing, and alteration facies.

## Mesozoic IOA Deposits in Eastern China

*Geological Background*

The Middle-Lower Yangtze River Metallogenic Belt (MLYRMB) is situated in the northeastern part of the Yangtze Block (Figs. 1, 8) and is one of the most important Fe-Cu-Au metallogenic belts in China. It contains numerous early Cretaceous Fe-Cu-Au deposits, including skarn Cu-Au-(Fe), porphyry copper-gold, and IOA deposits (Zhai et al., 1996; Pan and Dong, 1999; Mao et al., 2011; Zhou et al., 2013). The belt is divided into several ore districts termed, from west to east, Daye, Jiurui, Anqing-Guichi, Tongling, Luzong, Ningwu, and Ningzhen districts. The Ningwu and Luzong districts are famous in China for their ca. 130 Ma IOA deposits (Fig. 8). Other ore districts mostly contain copper-gold skarn and copper-molybdenum porphyry polymetallic deposits that range in age from 143 to 137 Ma. Iron-only (ca. 130 Ma) skarn deposits also occur in some districts (Fig. 8).

These deposits are genetically associated with two episodes of magmatism: (1) high-K calc-alkaline granitoids (156–137 Ma, mostly between 143–137 Ma) associated with porphyry, skarn, and stratabound Cu-Au-(Fe) deposits (Mao et al., 2011); (2) shoshonitic to high-K calc-alkaline intermediate volcanic rocks and equivalent intrusions (133–130 Ma) that host IOA deposits (Mao et al., 2011; Chen et al., 2016). A-type granitoids and associated alkaline volcanic rocks (127 to 122 Ma) mark a waning stage of the extensive early Cretaceous magmatism (Zhou et al., 2013), and are mostly barren.

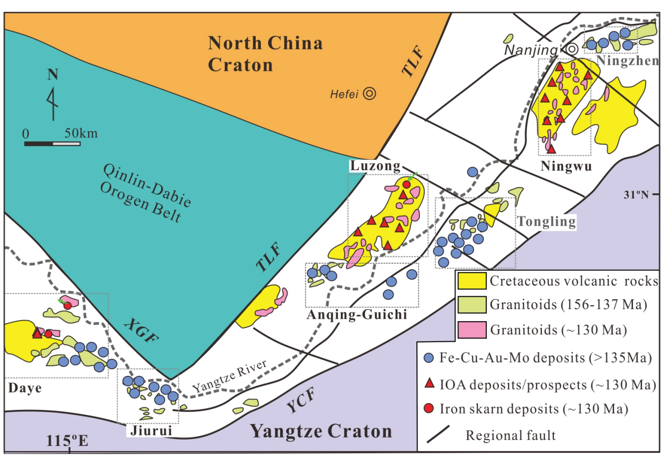


**FIGURE 8.** Distribution of late Mesozoic intrusions and major districts hosting large skarn Cu-Au-(Fe-Mo) and iron-oxide apatite (IOA) deposits in the Middle-Lower Yangtze River Metallogenic Belt (modified from Mao et al., 2011; Xie et al., 2011; Hu et al., 2020). Abbreviations: TLF: Tan-Lu Fault; XGF: Xiangfan-Guangji Fault; YCF: Yangxing-Changzhou Fault.

The igneous rocks and mineral deposits of the MLYRMB are interpreted as having formed during an episode of regional lithospheric extension and thinning in a back-arc setting during roll-back of the paleo-Pacific plate; magmas were sourced from enriched subcontinental lithospheric mantle (Zhou et al., 2013; Chen et al., 2016). Previous geochemical studies have suggested that the 133–130 Ma intermediate volcanic and intrusive rocks have a geochemical affinity to continental arc magmatism (Tang et al., 2013; Chen et al., 2016).

The Ningwu ore district is characterized by northeast-striking regional faults and a thick sequence of Lower Cretaceous volcanic rocks that are underlain by Triassic to Jurassic marine sedimentary rocks (Ningwu Research Group, 1978). The sedimentary sequence consists of lagoon- to platform-facies carbonate rocks in the lower part and arenaceous to argillaceous rocks in the upper part. The lagoon-facies carbonate rocks locally contain thick gypsum-anhydrite layers, with a total thickness ranging from tens of metres up to 350 m. The sedimentary sequence is unconformably overlain by Lower Cretaceous intermediate volcanic rocks that cover an area of ~1000 km$^2$ (Ningwu Research Group, 1978). The volcanic sequence is divided into the Longwangshan, Dawangshan, Gushan, and Niangniangshan formations (Fig. 9). Previous studies have shown that there is a disconformity between the Dawangshan and Gushan formations. The basal Longwangshan (133–131 Ma) and Dawangshan formations (132–130 Ma) are mainly composed of trachybasalt, trachyandesite, basaltic andesite, and andesite (Zhou et al., 2011). The Gushan Formation (130 Ma to 128 Ma) crops out locally in the northernmost and southernmost parts of the basin, and consists of trachyandesitic lava, breccia, and tuff (Zhou et al., 2011). The uppermost Niangniangshan Formation (ca. 127 Ma) consists of peralkaline nosean phonolite, minor trachydacite, and corresponding pseudoleucite porphyry (Zhou et al., 2011). The lower two formations are intruded by subvolcanic intrusions, including gabbro-diorite porphyry, and consistently have zircon U-Pb ages of ca. 130 Ma (Zhou et al., 2013).

Over 30 IOA deposits are hosted within the early Cretaceous Ningwu volcanic field; the total resource consists of 2700 Mt grading 20–50 wt% Fe (Masteel Mining Co. Ltd., 2012). These deposits display a close spatial and temporal association with porphyritic diorite intrusions (Figs. 9, 10; Ningwu Research Group, 1978). Orebodies are mainly hosted in volcanic rocks of the lower two formations and the apical portions of <1 km-wide intrusions, but also locally occur along the contact with underlying Triassic sedimentary rocks. Depending on their spatial relationship to diorite intrusion(s), different styles of deposits have been described by the Ningwu Research Group (1978), which, taken together, were considered to form a "porphyry iron system". All the deposits have consistent isotopic ages at 131–130 Ma, contemporaneous with the emplacement of the porphyritic diorite intrusions (Mao et al., 2011; Zhou et al., 2013). The deposits are interpreted as having formed under regional lithospheric extension and thinning with ore metals derived from basaltic melts sourced from enriched lithospheric mantle (Zhou et al., 2013). The regional extensional event was possibly related to roll-back and rotation of the paleo-Pacific plate (Mao et al., 2011).

The deposits are commonly brecciated (Fig. 10), have similar alteration assemblages, and share a common paragenetic sequence, which includes an early stage of pervasive albitization followed by precipitation of magnetite, actinolite (±diopside or garnet), and fluorapatite (Figs. 11, 12A–G). Breccias contain fragments of albitized intrusive and volcanic rocks, and are commonly cemented by a magnetite-actinolite assemblage (Figs. 10D, 11G). Kilometre-wide alteration halos extend hundreds of metres to a few kilometres along strike, and feature both vertical and horizontal zonation around the ore-hosting intrusion (Ningwu Research Group, 1978). The inner zone I within the intrusion is characterized by incipient to pervasive albite and, in places, possible scapolite alteration. It grades toward an intermediate zone II dominated by actinolite, albite, epidote, apatite, and chlorite. The outer zone III is marked by

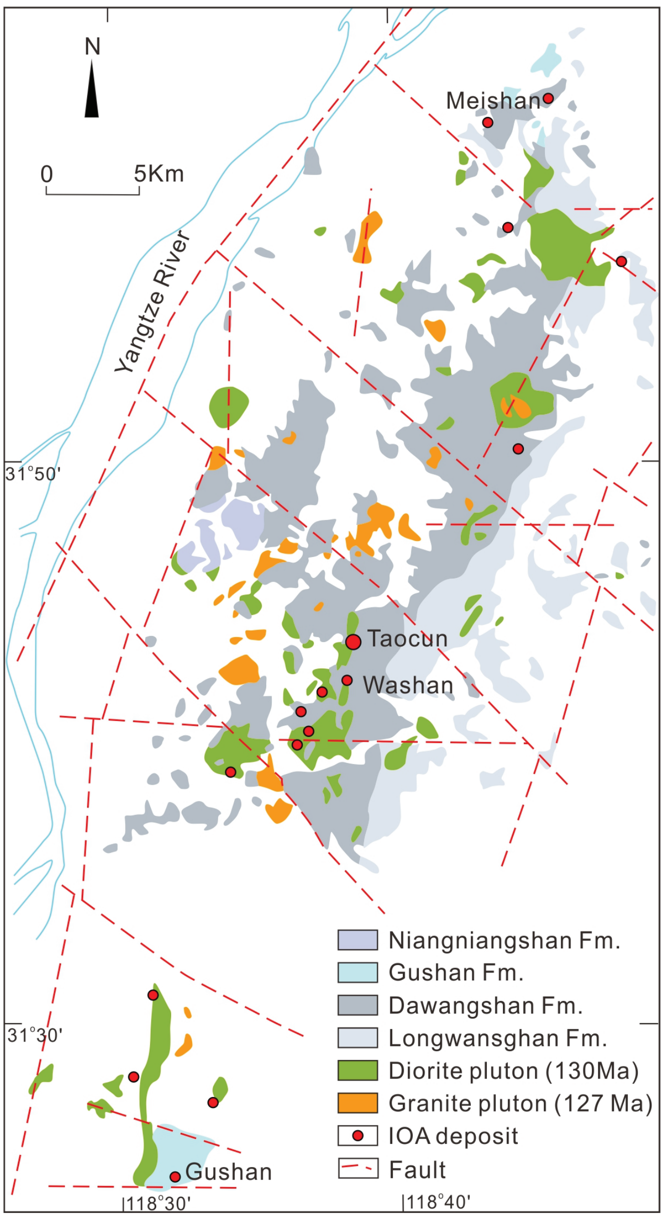


**Figure 9.** Simplified map of the Ningwu volcanic field, MLYRMB (modified from Ningwu Research Group, 1978). Note the close spatial association between IOA deposits and subvolcanic diorite intrusions.

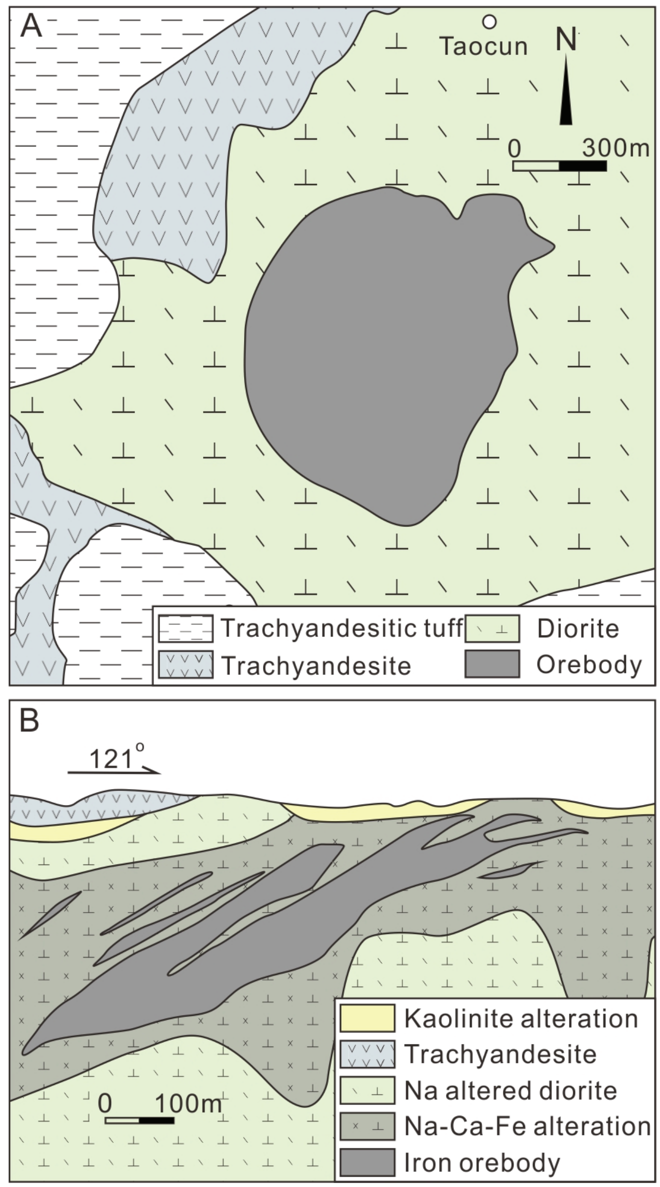


**Figure 10. A.** Geologic map of the Taocun deposit. The orebody is at the top of a dioritic intrusion (modified from Masteel Mining Co. Ltd., 2012; Zeng et al., 2016). **B.** Cross-section of the Taocun deposit showing the distribution of alteration types and iron orebodies. Sodic alteration consists of albite ± scapolite. The Na-Ca-Fe alteration comprises scapolite, magnetite, apatite, and actinolite. Kaolinite alteration near the surface may be supergene in origin.

abundant carbonate, pyrite, and chlorite. Iron orebodies typically occur in the intermediate alteration zone II, where magnetite is spatially associated with actinolite-apatite and/or diopside-anhydrite assemblages. Pyrite orebodies are present in zone III in some deposits. Deposits formed at the contact between intrusive and carbonate rocks show many similarities to skarn iron deposits and contain abundant skarn minerals, e.g. garnet and diopside (Ningwu Research Group, 1978).

*Geology of the Taocun Deposit*

The Taocun deposit, located in the central part of the Ningwu basin (Fig. 9), is representative of mineralization and alteration in the Ningwu region. The orebodies are mainly hosted within the apical zone of an extensively altered diorite intrusion and its volcanic host rocks of the Dawangshan Formation (Fig. 10). The ore zone, which is approximately 1000–1600 m long, 500 m wide, and 10–150 m thick, contains 360 Mt ore at an average grade of 20–26 wt% Fe, 0.06–0.17 wt% V, 0.32–3.96 wt% S, and 0.01–3.08 wt% P (Masteel Mining Co. Ltd., 2012). Most of the individual orebodies strike northeast and are stratabound or lens-shaped in cross section (Fig. 10). The Taocun deposit consists mainly of two types of ore: (1) a disseminated ore composed of magnetite, apatite, actinolite, and albite (Fig. 12C), and (2) a vein-type ore with coarse-grained to pegmatitic, magnetite-actinolite-apatite assemblages (Figs. 11C, D, 12F). Disseminated ores constitute the major orebody, whereas vein-type ores are locally developed along fractures or joints of the albitized country rocks (Fig. 11A–C). Magnetite-actinolite-apatite veins commonly infill fractures in both the disseminated ores and altered intrusive rocks, demonstrating that the vein-type mineralization postdated the disseminated mineralization (Zeng et al., 2016).

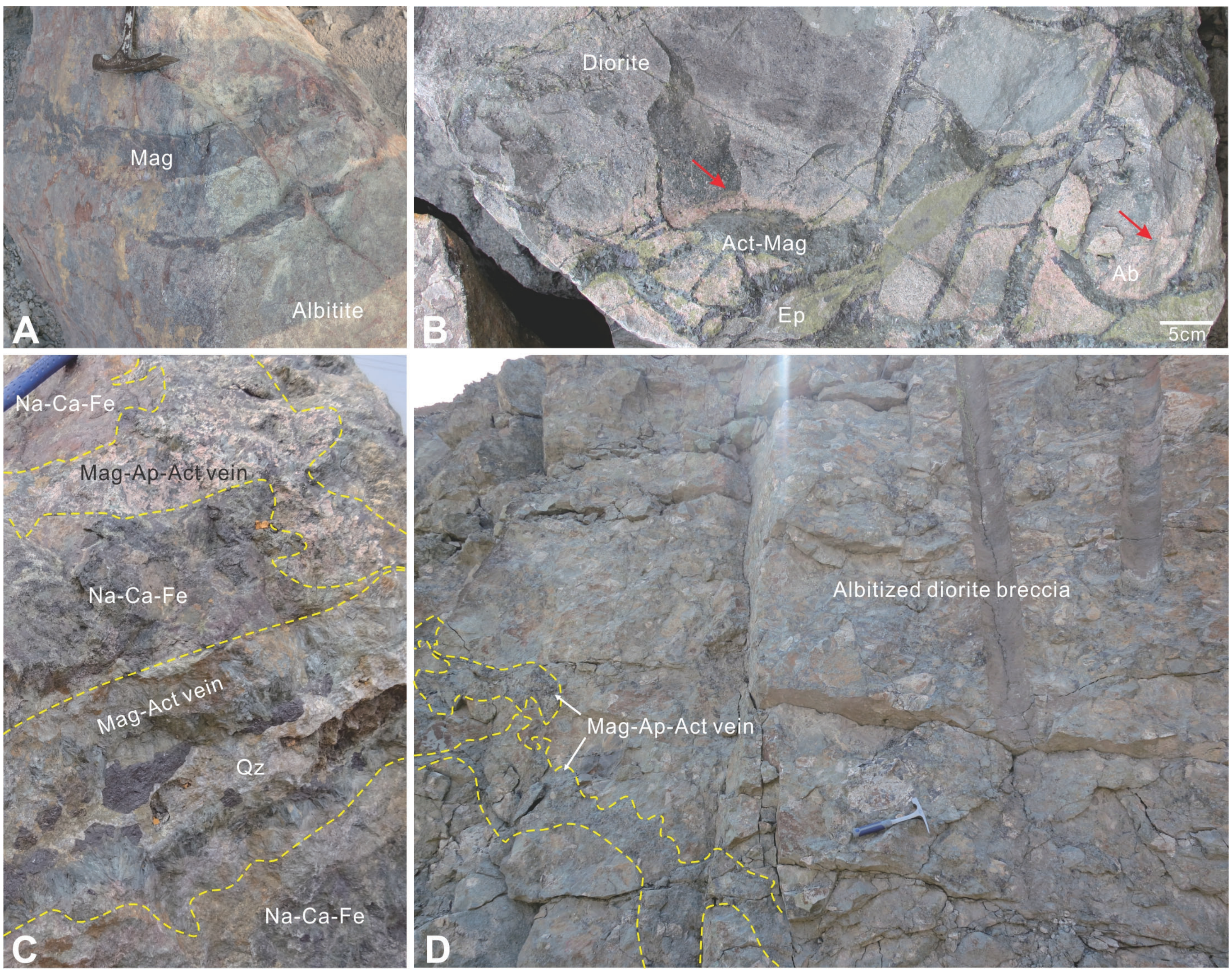


**FIGURE 11.** Field photographs showing representative alteration in the Taocun IOA deposit. **A.** Volcanic rocks have been completely altered to albitite and subsequently cut by magnetite-actinolite veins, indicating that magnetite postdates albitization. **B.** The diorite porphyry is variably albitized and cut by magnetite-actinolite veins; note the epidote halo along the veins. **C.** Extensively Na-Ca-Fe-altered rocks are cut by multiple phases of magnetite-actinolite-(apatite) veins; one vein has later-stage quartz in the central part. **D.** The albitized diorite has been brecciated, and the breccia body cut by magnetite-apatite-actinolite veins.

Hydrothermal alteration is extensive in the Taocun deposit and has a well-defined spatial zonation (Fig. 10). The inner and deeper zone of pervasive sodic alteration occurs mainly within the ore-hosting intrusion. The sodic alteration (stage I) consists mainly of albite and scapolite (Figs. 11A–C, 12A–D). Metasomatism gradually evolved to form interstitial magnetite (Fig. 13C, D) intergrown with apatite and actinolite (stage II), typical of HT Na-Ca-Fe alteration. Veins of magnetite-apatite-actinolite (Fig. 12E, F) are common and cut across the altered rocks and orebodies, indicating possible multiple metasomatic events.

A lower-temperature Ca-Mg alteration, consisting of epidote, chlorite, and minor albite (stage III) (Figs. 11B, 12G), variably overprints the HT Ca-Fe alteration zone. It texturally postdates deposition of magnetite and may occur as an envelope of Fe-oxide-apatite veins (Figs. 11B, 12G). It was possibly responsible for the observed pseudomorphic replacement of scapolite by albite (Figs. 12D, 13C, D) and diopside by actinolite (Zeng et al., 2016), as HT Ca-Fe alteration can be retrograded to epidote and chlorite (Fig. 12E, G). Hematite is locally present at this stage also. Quartz and carbonate minerals (siderite and calcite) mark the last stage of alteration (stage IV) (Figs. 12I, 13K, L), which is most extensive in the outer zone within the volcanic rocks. Kaolinite occurs locally along the contact between the volcanic rocks and diorite intrusion (Fig. 10), but may be supergene in origin.

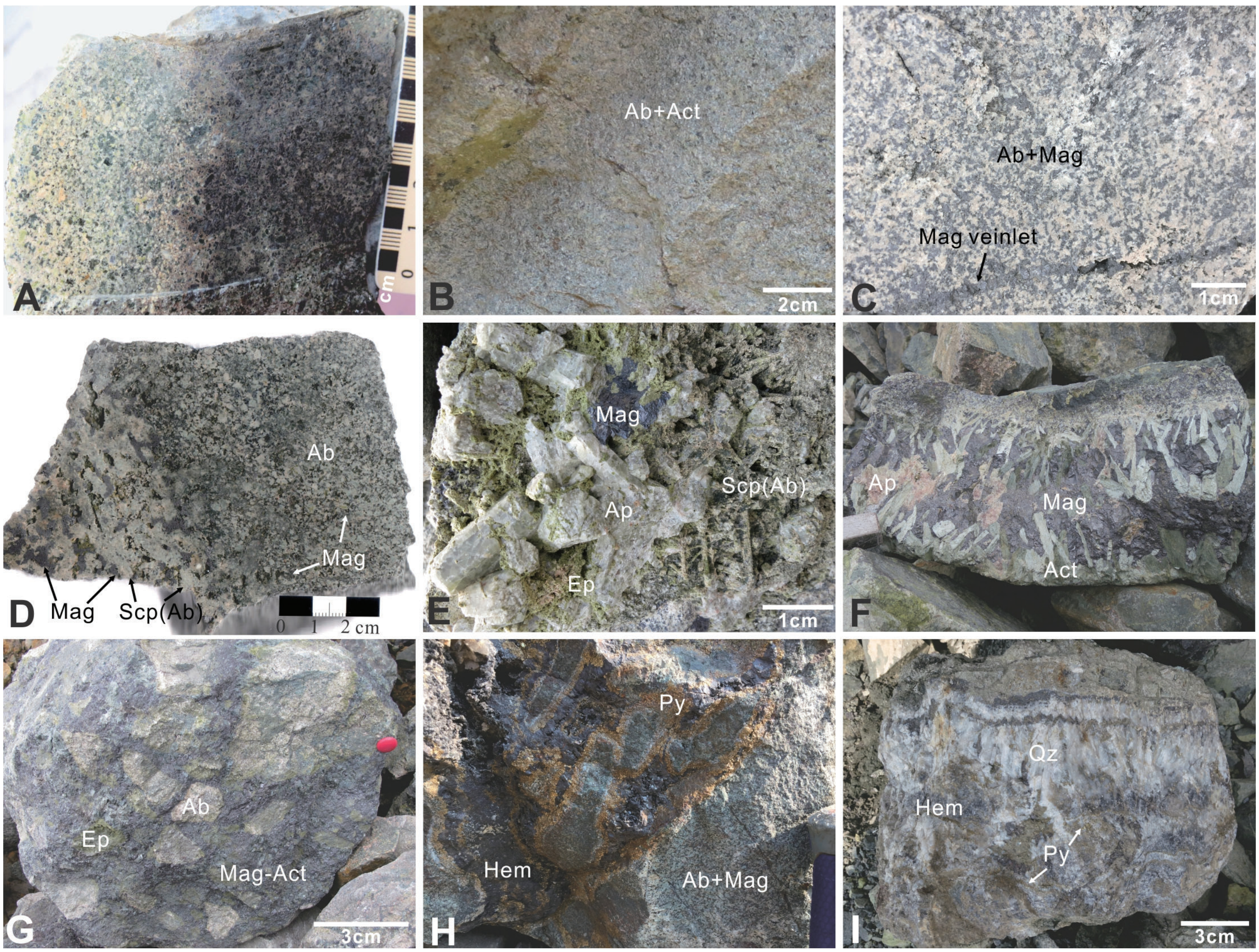


**Figure 12.** Field photographs of representative ores and alteration types in the Taocun deposit. **A.** Sodic alteration of a diorite porphyry intrusion on the left side of the photo. **B.** Completely albitized diorite intrusion with local actinolite alteration. **C.** Anhedral magnetite grains are interstitial to albite crystals and form disseminated magnetite ore, suggesting precipitation of magnetite subsequent to albitization; note the late-stage magnetite veinlet. **D.** Larger albite crystals (possible scapolite pseudomorph) have been replaced by slightly younger albite and magnetite, possibly implying multiple albitization. Abundant voids remained after the rocks were albitized. **E.** The transitional HT Na-Ca-Fe alteration association consists of euhedral scapolite (replaced by albite), apatite, and magnetite. It is overprinted by epidote alteration. **F.** A typical vein assemblage consisting of euhedral magnetite, apatite, and actinolite. **G.** Albitized diorite porphyry and volcanic rocks have been brecciated and cemented by matrix of magnetite and actinolite, which are overprinted by epidote alteration. **H.** A brecciated ore overprinted by low-temperature mineral assemblage of hematite and pyrite. The fragments of magnetite ore are enveloped by pyrite crystals and cemented by acicular hematite. **I.** Late-stage hematite-pyrite-quartz vein representing low-temperature alteration.

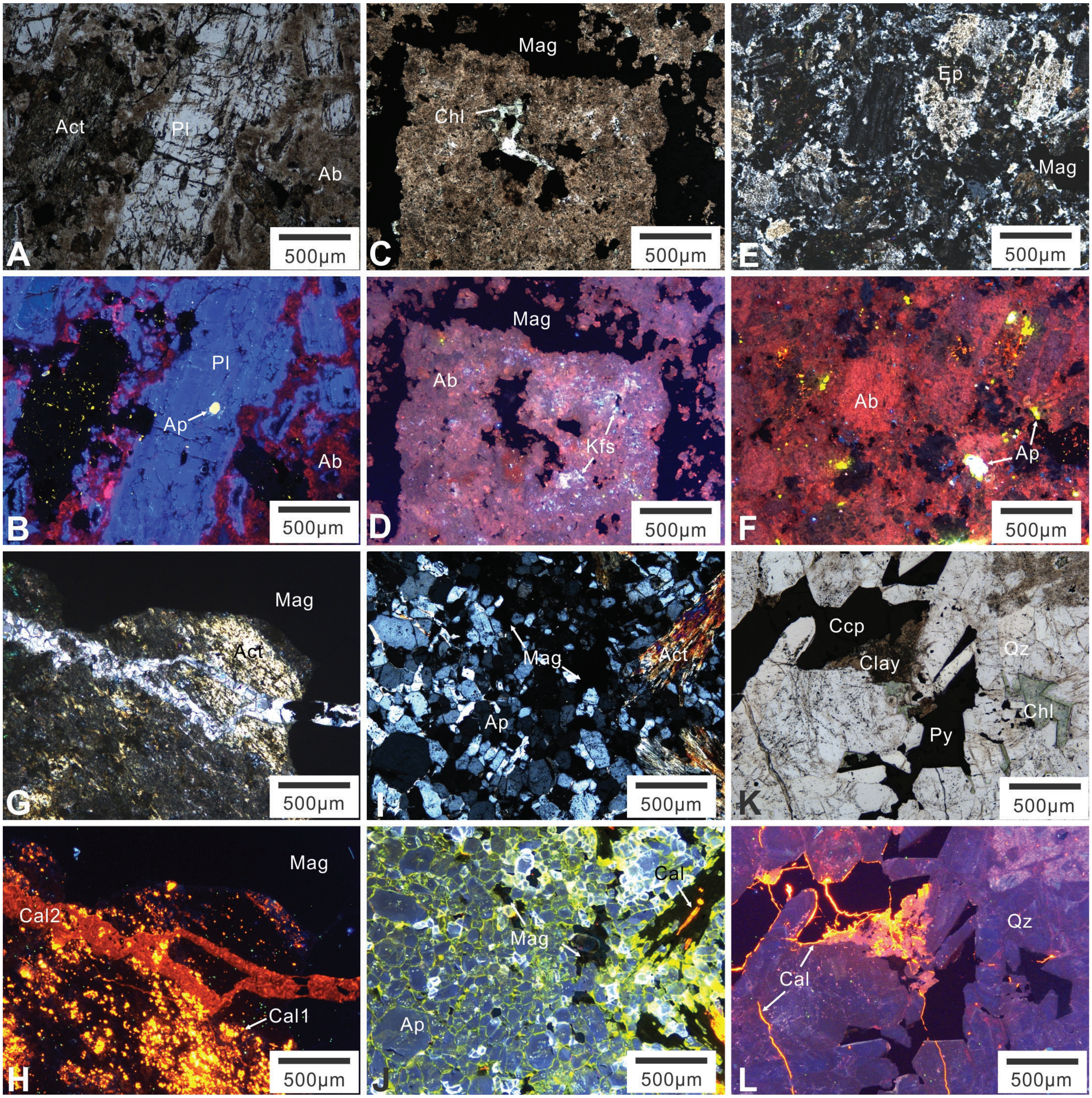


**Figure 13.** Representative photomicrographs and microscopic cathodoluminescence (CL) images showing the replacement textures in the Taocun deposit. **A, B.** Partly albitized diorite porphyry intrusion showing corroded plagioclase partly replaced by albite and pyroxene replaced by actinolite. **C, D.** Possibly precursor euhedral scapolite is completely altered to fine-grained albite and subsequently overprinted by minor K-feldspar (light blue). Magnetite is interstitial to fine-grained albite, illustrating that magnetite is later than scapolite and albite. **E, F.** Extensive Na-Ca-Fe alteration comprising albite, magnetite, apatite, and actinolite, overprinted by late epidote. Minor fine-grained apatite grains are interstitial to albite. **G, H.** Magnetite and actinolite assemblages overprinted by two stages of calcite alteration. Earlier calcite (Cal1) locally replaces actinolite heterogeneously, whereas later calcite (Cal2) occurs as veinlets. **I, J.** Typical magnetite-actinolite-apatite assemblage. Euhedral apatite grains show blue cores and variably altered rims appearing yellow under CL. **K, L.** Sulphide minerals (pyrite and chalcopyrite) and chlorite interstitial to euhedral quartz grains and cut by a calcite veinlet. Note that quartz shows oscillatory zoning under CL.

*Proposed Genetic Model*

The IOA deposits in the Ningwu region have been mined actively since the beginning of the 20th century and have been extensively studied by Chinese geologists. However, most of the results are published in Chinese. Among them is the classic synthesis book of the Ningwu Research Group (1978) that proposed an integrated genetic model (Fig. 14). The key point of this model attributes the ore-forming processes to the evolution of a magmatic-hydrothermal system above subvolcanic intrusions; most of the orebodies are considered to form by these processes. The deposits have many similarities to iron skarn deposits: skarn assemblages of garnet and diopside are preserved in some deposits, but most deposits are characterized by magnetite-apatite-actinolite mineral assemblages. Orebodies mainly occur within Ca-Fe-Mg alteration zones along the contact between altered diorite and country rocks (Fig. 14). The IOA deposits in the Ningwu district most likely formed from high-temperature magmatic fluids (Ningwu Research Group 1978; Li W et al., 2015; Hu et al., 2020) that altered the apical part of the diorite intrusion as well as their host rocks. This interpretation is similar to the models proposed by Hildebrand (1986), Mumin et al. (2010) and Montreuil et al. (2016) for systems with IOA and IOCG deposits in the Great Bear magmatic zone, Canada. Although Ningwu Research Group (1978) did not preclude the possibility of iron oxide melts, they consider that this style of iron ores was not significant in the Ningwu district.

Recent studies on fluid inclusions and stable isotopes have shown that the earliest ore fluids were highly saline and extremely high temperature (740–840ºC; e.g. Li W et al., 2015) and high salinity (up to 90% NaCl equiv.). Therefore, magnetite was likely precipitated from a volatile-rich salt system during a magmatic-hydrothermal transition (Zhao et al., 2016; hydrosaline liquid in Zhao XF et al., 2019b). This interpretation is consistent with field and textural data showing that magnetite formed slightly later than albitization, but coeval with apatite and actinolite, which is typical of IOA deposits in many settings (see also Corriveau et al., 2016). However, the properties of such a salt system and how it formed are still not well understood. Evaporites have been considered to be the source of the salt, as evidenced by the chemical compositions of fluid inclusions and highly positive sulphur isotope values in pyrite (Li W et al., 2015). The possible role of evaporite in these deposits is currently being investigated.

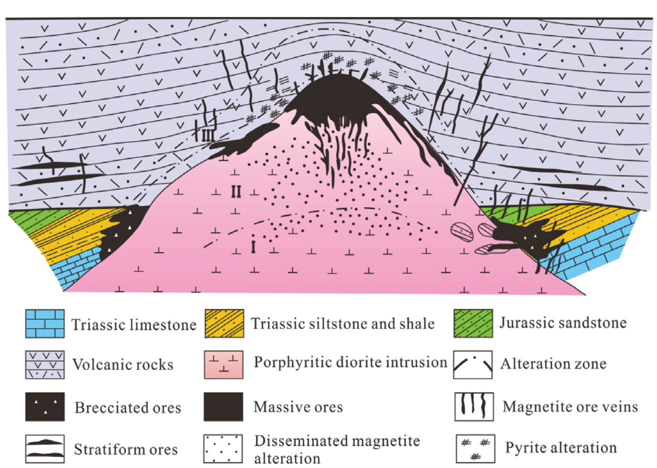


**Figure 14.** Conceptually integrated genetic model for the IOA deposits in eastern China, as proposed by the Ningwu Research Group (1978). Note that the orebodies mainly occur at the apical zones of the intrusion and/or at the contact zones between the intrusion and country rocks. I, II, and III indicate alteration zonation, see text for details.

## IOCG-like Deposits in Northwestern China

*Geological Background*

The Xinjiang province in northwestern China is partly assigned to the Central Asian Orogenic Belt (CAOB), one of the largest accretionary orogenic belts in the world. The CAOB is located southeast of the Eastern European Craton, south of the Siberian Craton, and north of the Kalakumu, Tarim, and North China cratons (Fig. 15A; Zhao LD et al., 2019). The CAOB is an ideal natural laboratory not only for researching the processes of formation of accretionary orogens and continental growth, but also ore deposits (e.g. Au, Ag, Fe, Cu, and Mo). The northern Xinjiang province of the CAOB (Fig. 15B) has some iron-dominated deposit belts, such as eastern Tianshan, western Tianshan, and the northern margin of eastern Junggar. Some deposits also have economic copper-gold mineralization. Recently published works document that some Fe-Cu (-Au) deposits in eastern Tianshan (e.g. Heijianshan, Duotoushan, and Shaquanzi) and along the northern margin of eastern Junggar (e.g. Qiaoxiahala and Laoshankou) have features in common with central Andean IOCG deposits in terms of alteration, mineral assemblages, nature and sources of ore-forming fluids, and tectonic settings, suggesting that these Fe-Cu (-Au) deposits are IOCG or IOCG-like deposits (Zhao LD et al., 2017a; Jiang et al., 2018; Liang et al., 2018, 2019; Zhang et al., 2018). The following sections describe the different hydrothermal alteration and mineralization stages and the ore-forming processes of the IOCG-like deposits in northwestern China.

*Eastern Tianshan District*

The eastern Tianshan district is subdivided, from north to south, into the Dananhu-Tousuquan island arc belt, Kangguer shear zone, Aqishan-Yamansu belt, and central Tianshan terrane. The deep crustal, east-west-trending Kangguer, Yamansu, and Aqikekuduke faults form the boundaries between the respective belts (Fig. 15C). The Aqishan-Yamansu belt was a Carboniferous fore-arc basin during southward subduction of the Kangguer oceanic slab beneath the Yili-Central Tianshan block (Zhang et al., 2016; Zhao LD et al., 2018b, 2019). It comprises Carboniferous volcanic, volcaniclastic, and clastic rocks overlain by Permian clastic and volcanic rocks and local carbonate interbeds (Mao et al., 2005). The Aqishan-Yamansu belt also features abundant late Carboniferous to Middle Triassic felsic intrusions (Zhou et al., 2010) and hosts many significant iron (e.g. Hongyuntan, Bailingshan, Chilongfeng, and Yamansu) and iron-copper deposits (e.g. Heijianshan, Duotoushan, Shuanglong, and Shaquanzi). The belt underwent fore-arc basin extension and inversion during the early and late Carboniferous, respectively, and during the basin inversion stage, emplacement of voluminous intermediate to felsic intrusions was accompanied by formation of many iron and iron-copper deposits (Zhao LD et al., 2019).

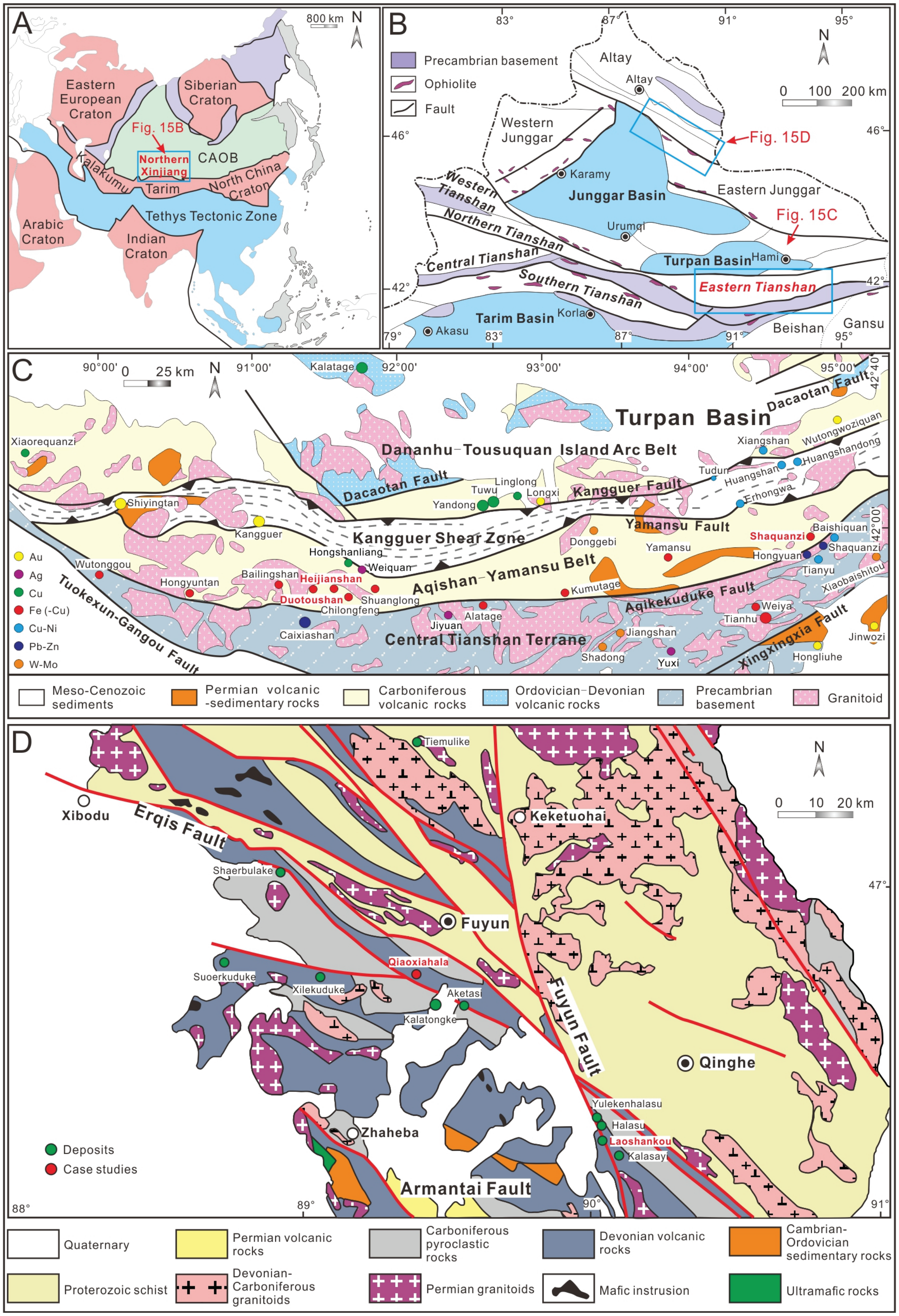


**FIGURE 15. A.** Simplified tectonic framework of the Central Asian Orogenic Belt (CAOB; simplified after Sengör and Natal'in, 1996). **B.** Sketch map showing the tectonic framework of northern Xinjiang (simplified after Chen et al., 2012). **C.** Geologic map of the eastern Tianshan Orogenic Belt and distribution of major ore deposits (modified after Deng et al., 2014). **D.** Regional geologic and mineralization map of the southeastern Chinese Altay and the northeastern part of the eastern Junggar district (modified after Liang et al., 2019).

*Geology of the Heijianshan Deposit*

Exposed rocks at Heijianshan consist of the lower three members of the late Carboniferous Matoutan Formation, which comprises mafic to intermediate tuff, basalt, felsic brecciated tuff, and basaltic andesite. The Matoutan Formation at Heijianshan was intruded by intermediate to felsic intrusive rocks, including quartz syenite porphyry, quartz diorite, diorite porphyry, and minor monzogranite and granodiorite (Zhao LD et al., 2017a). These intrusions belong to the dominantly late Carboniferous Bailingshan intrusive complex (ca. 329–297 Ma) (Zhao LD et al., 2019). Three fault systems and a small syncline have been documented at Heijianshan. The oldest faults trend northwest to north-northwest; they cut the tuff, basalt, and brecciated tuff sequences and are probably coeval with the Heijianshan iron mineralization. Younger, north-northeast to northeast-trending faults are locally truncated by quartz diorite intrusions, whereas the youngest (east-northeast-trending) fault transects diorite porphyry, quartz diorite, quartz syenite porphyry, and monzogranite intrusions (Zhao LD et al., 2017a). Tabular or stratabound orebodies are commonly hosted by mafic to intermediate tuff and brecciated tuff of the middle member of the Matoutan Formation. The largest orebody is 30–50 m long and 8–10 m wide in the open pit. Based on the differing spatial distributions of iron and copper mineralization, ores can be divided into sulphide, oxide, and mixed oxide-sulphide ores, with the latter two being predominant and mainly occurring as massive, disseminated, and 'brecciated' (magnetite-clast breccia) ores (Fig. 16A–F; Zhao LD et al., 2017a, 2018a).

Five alteration and mineralization stages have been established for the Heijianshan Fe-Cu (-Au) deposit: epidote alteration (Stage I), magnetite/iron mineralization (Stage II), pyrite alteration (Stage III), copper (-gold) mineralization (Stage IV), and miscellaneous late veins (Stage V) (Zhao LD et al., 2017a).

Stage I—Epidote alteration: Epidote is widespread in the Heijianshan host rocks, commonly replacing plagioclase and amphibole phenocrysts in mafic tuff, or intergrown with calcite as veins cutting volcanic rocks of the Matoutan Formation. Other Stage I minerals include tourmaline and sericite, inferred to have replaced primary igneous minerals. The epidote-calcite assemblage is replaced by the Stage II amphibole-magnetite assemblage, and collectively the Stage I minerals may record an early Ca-Mg alteration that evolves towards HT Ca-Fe alteration (Zhao LD et al., 2017a).

Stage II—Magnetite/iron mineralization: Fine-grained magnetite constitutes the main iron ore mineral in the Heijianshan deposit; the style of mineralization varies from massive to disseminated, 'brecciated', and vein-type (Fig. 16A–F). The magnetite is hydrothermal in origin and each type has a distinct signature on trace element discrimination diagrams such as Cr vs. Co/Ni, Cr vs. Ti, V vs. Cr, and Ni vs. Cr (Zhao LD et al., 2018a). The magnetite is closely associated with calcic amphibole (tremolite, actinolite, and magnesio-hornblende; Figs. 16A, B, F, 17A), and this assemblage has replaced or cross-cut host rocks and earlier-formed epidote (Fig. 17A), calcite, and locally tourmaline. Quartz, K-feldspar, and titanite locally coexist with magnetite and amphibole. Hematite formed locally and now consists of mushketovite (magnetite pseudomorph of hematite), indicating higher $fO^2$ during the iron mineralization stage. Fluid inclusions from quartz, oxygen isotope geothermometry, and H-O-S isotopic results indicate that the iron mineralizing fluids were of high temperature (~590°C) and high salinity, and had a magmatic-hydrothermal origin (Zhao LD et al., 2017a, b).

Stage III—Pyrite alteration: Pyrite crystallized with quartz and minor hematite, pyrrhotite, and chalcopyrite, forming two assemblages: pyrite-hematite and pyrite-pyrrhotite-chalcopyrite (Zhao LD et al., 2017a). Pyrite occurs as disseminated or massive bodies or as veinlets within sulphide and mixed oxide-sulphide ores. Stage III pyrite is commonly observed to replace Stage II magnetite, and to be replaced or cross-cut by Stage IV chalcopyrite ± electrum veinlets (Fig. 17B).

Stage IV—Copper (-gold) mineralization: Major minerals include quartz, chalcopyrite, and chlorite, with minor hematite and electrum. The presence of electrum is atypical of the deposits in the district, being only observed in the Heijianshan deposit. The chalcopyrite-electrum, chalcopyrite-chlorite, and minor quartz-chalcopyrite-hematite veins cut zones of massive pyrite and magnetite (Fig. 17B, C). Mineralizing fluids formed at low temperature (constrained by chlorite geothermometry at ~240°C) and have a magmatic-hydrothermal origin, but also interacted with basinal brines and volcanic rocks (Zhao LD et al., 2017a).

Stage V—Late veins: Late-stage hydrothermal veins are abundant. Epidote and calcite veins are widespread, cutting host rocks and other mineral assemblages, whereas veins of quartz, (specular) hematite, tourmaline, chlorite, and albite cut host rocks and sulphides (Zhao LD et al., 2017a).

*Geology of the Duotoushan Deposit*

At Duotoushan, the exposed rocks are assigned to the late Carboniferous Matoutan Formation (also named Tugutublak Formation or Shaquanzi Formation in the eastern section of the Aqishan-Yamansu belt; ca. 324–306 Ma; Zhang XH et al., 2012; Zhang et al., 2016). The formation mainly consists of andesitic to dacitic flows and brecciated flows; orebodies are mainly hosted by the andesitic tuff-breccia (Zhang et al., 2018). Felsic intrusions are also documented in the Duotoushan deposit area, including monzogranite (318.3 ± 3.0 Ma), granodiorite (317.7 ± 1.8 Ma), albite granite porphyry (316.3 ± 8.1 Ma), and dacite porphyry (197.2 ± 3.5 Ma) (Zhang et al., 2016, 2017). The Duotoushan iron-copper deposit is a medium-sized deposit lacking calculated reserves but having a grade of 45–53% Fe and 0.7–1.0% Cu. The seven stratabound orebodies range from 50 to 248 m long and 4 to 70 m wide (Sang et al., 2003). At Duotoushan, iron mineralization is massive and disseminated (Fig. 16G–K), whereas sub-economic copper mineralization is disseminated and in veins (Zhang et al., 2018).

Five alteration and mineralization stages have been established: albite-amphibole alteration (Stage I), garnet-clinopyroxene alteration (Stage II), main magnetite mineralization (Stage III), late sulphides (Stage IV), and late veins (Stage V) (Zhang et al., 2018).

Stage I—Albite-amphibole alteration: Abundant albite and minor amphibole are observed in dacitic tuff at the Duotoushan deposit; this alteration is commonly intersected by magnetite veins, indicating a Na ± Ca metasomatism event before magnetite mineralization (Fig. 17D). Considering that the Na ± Ca metasomatism occurs only in the groundmass of dacitic tuff in contact with sodic granite porphyry, it is inferred that Stage I alteration was caused by fluid evolved from the porphyry (Zhang et al., 2018).

Stage II—Garnet-clinopyroxene alteration: Coarse-grained, light brown to yellowish-green garnet (mainly andradite) and minor clinopyroxene are commonly observed beneath the massive magnetite ores (Zhang et al., 2018). These anhydrous minerals are replaced by amphibole and epidote, and locally by magnetite (Fig. 16I–K), indicating that the garnet and clinopyroxene alteration predated magnetite mineralization.

Stage III—Main magnetite mineralization: Minerals in Stage III are magnetite (locally as mushketovite), amphibole, epidote, quartz, and minor titanite and pyrite. Based on mineral assemblages, replacement textures, and spatial distribution of minerals, three sub-stages can be recognized, including mushketovite-amphibole ± pyrite ± titanite (Stage III-A), magnetite-epidote-amphibole ± titanite (Stage III-B; Figs. 16G, 17E), and magnetite-quartz-epidote ± amphibole ± pyrite (Stage III-C; Fig. 16H) (Zhang et al., 2018). The association of epidote, quartz, and magnetite without amphibole, and especially quartz-magnetite veins cutting amphibole, are commonly observed, indicating that amphibole formed largely before quartz. Hydrogen isotope analysis and oxygen isotope geothermometry indicate that Stage III fluids had a high-temperature (400–520°C) magmatic origin in early Stage III, then mixed with basinal brines during late Stage III (Zhang et al., 2018).

Stage IV—Late sulphides: Stage IV sulphides consist of pyrite and chalcopyrite, coexisting with amphibole and chlorite. Pyrite-rich veins cut Stage III massive magnetite (Fig. 16H), and are locally cut by chalcopyrite veinlets (Fig. 17F). Given that chlorite and chalcopyrite veinlets both formed later than pyrite veinlets and were then transected by late veins, it is speculated that chlorite and chalcopyrite precipitated during the late stage of sulphide mineralization (Zhang et al. 2018). Fluids of Stage IV were low-temperature (183–232°C, average 215°C) and had a magmatic-hydrothermal origin (probably basinal brines), based on chlorite geothermometry and stable isotope analysis, respectively (Zhang et al., 2018).

Stage V—Late veins: Hydrothermal veins, including quartz, calcite, and minor hematite and epidote, are abundant and crosscut earlier-stage minerals (e.g. Stage III quartz and epidote).

*Geology of the Shaquanzi Deposit*

The Shaquanzi orebodies are hosted by andesite and volcaniclastic rocks of the Shaquanzi Formation (ca. 315–305 Ma; Huang et al., 2013, 2014; Jiang et al., 2017). Diorite porphyry, granite porphyry, and diorite (ca. 299 Ma; Jiang et al., 2017) locally intruded the Shaquanzi Formation, and some Permian pyroxene diorites were also documented in the Shaquanzi deposit. The major fault systems at Shaquanzi are the mineralization-related east-trending faults (possible satellites of the regional deep-seated Aqikekuduke-Shaquanzi Fault), and postmineralization north-trending faults that intersect the orebodies (Jiang et al., 2018).

The Shaquanzi iron-copper deposit contains a reserve of 2.49 Mt Fe metal in ore grading 26–49%, and 2040 t Cu metal in ore grading 0.23–1.58% (No. 6 GPXBGM, 2008). The iron orebodies are 50–500 m long, 1–17 m wide, and 1–14 m thick; the copper orebodies (300 m long, 2–8 m thick; No. 6 GPXBGM, 2008) are located below and within the iron orebodies. The east-trending iron-copper orebodies are lensoidal to tabular. Magnetite ores are disseminated, massive or banded (Fig. 16L–P), whereas chalcopyrite ores are mainly disseminated (Jiang et al., 2018).

Five alteration and mineralization stages have been established, including early skarn alteration (Stage I), HT Ca-Fe alteration (Stage II), main magnetite mineralization (or HT K-Fe alteration; Stage III), chalcopyrite mineralization (Stage IV), and late veins (Stage V) (Jiang et al., 2018).

Stage I—Skarn alteration: Alteration minerals are garnet and minor diopside. Garnet is typically euhedral and replaced by Stage II amphibole and Stage III magnetite, K-feldspar, epidote, and quartz (Fig. 16L, P; Jiang et al., 2018).

Stage II—Epidote-bearing HT Ca-Fe alteration: Euhedral to subhedral amphibole is intergrown with epidote and magnetite, and subsequently replaced by chlorite. The assemblage is replaced by Stage III K-feldspar and quartz, as well as local Stage III magnetite along amphibole cleavage planes (Fig. 17G).

Stage III—Main magnetite mineralization: Major minerals in this stage are mushketovite, magnetite, pyrite, epidote, K-feldspar, and quartz, collectively suggesting an overall HT K-Fe facies. This stage can be further divided into hematite mineralization (Stage III-A), K-feldspar-epidote alteration (Stage III-B), and magnetite-pyrite mineralization (Stage III-C). Stage III-A mushketovite commonly occurs in the main magnetite orebodies, evidence for a now-obliterated hematite-dominant stage, although some relict hematite is preserved (Jiang et al., 2018). Stage III-B is characterized by anhedral to subhedral K-feldspar, fine-grained epidote, and minor magnetite (Fig. 16O), and Stage III-C is dominated by magnetite, pyrite, quartz, and subsequent chalcopyrite replacements (Fig. 17H). Recent studies of H-O-S isotopes indicate that Stage III fluids for main magnetite mineralization were of magmatic-hydrothermal origin and mixed with formation water (Jiang et al., 2018).

Stage IV—Chalcopyrite mineralization: Chalcopyrite is associated with hematite, bornite, sphalerite, epidote, chlorite, calcite, and minor quartz. Stage IV euhedral epidote coexists with minor chalcopyrite and quartz or fine-grained magnetite as veins cutting earlier-stage minerals. Hematite is euhedral and acicular, suggesting a primary origin. Locally, calcite-chlorite-chalcopyrite-hematite-sphalerite veins cut Stage III-C pyrite (Fig. 17I). Stage IV fluids were low-temperature (~160°C), low-medium salinity, and calcium-rich; a non-magmatic origin involving basinal brines is supported by fluid inclusion study and S-C isotope analysis (Jiang et al., 2018).

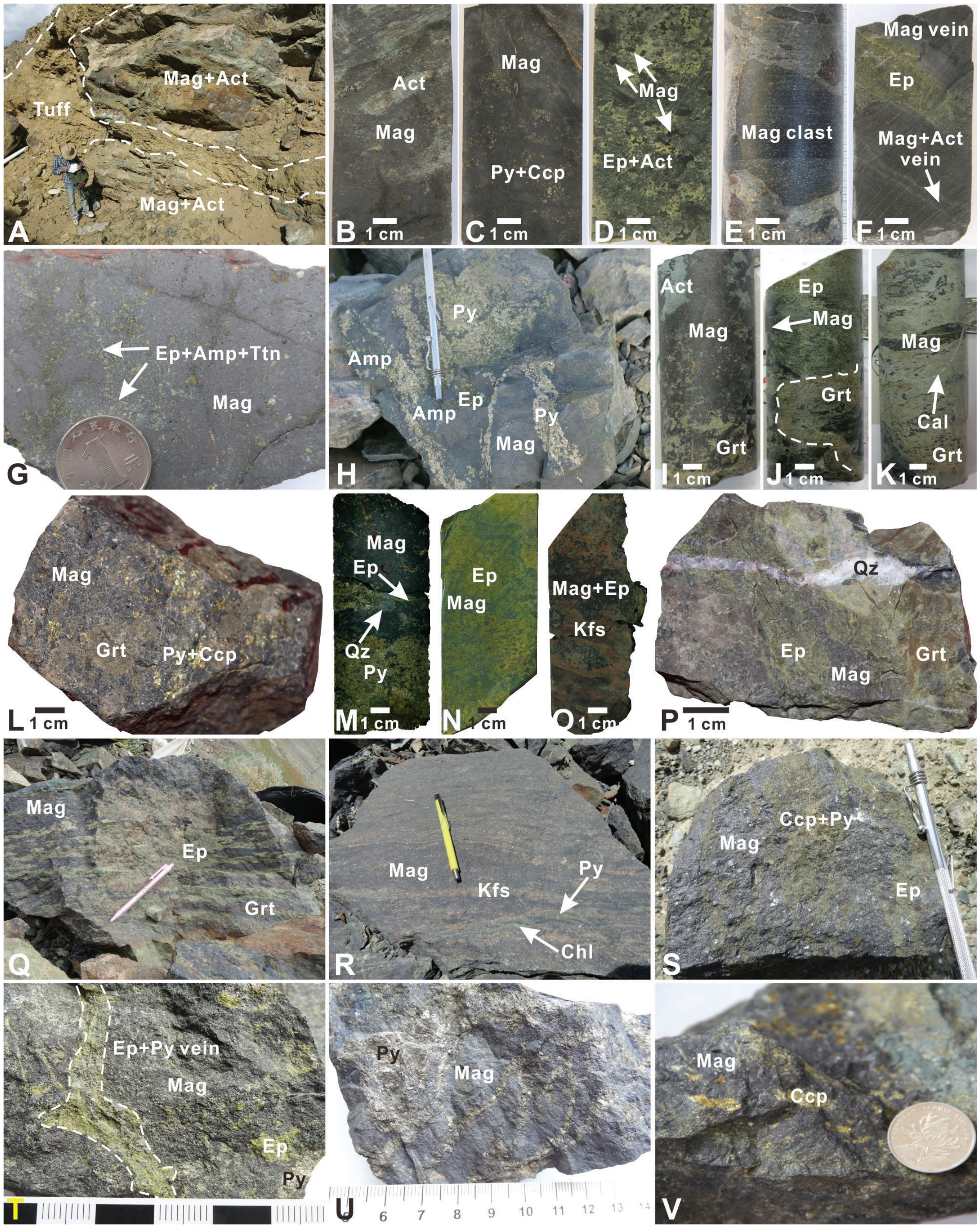


**FIGURE 16.** Representative photographs of ores and ore-related mineral assemblages of IOCG-like deposits in northwestern China. **A.** Massive magnetite (with actinolite) orebody hosted by tuff of the Matoutan Formation. **B.** Massive magnetite coexisting with actinolite. **C.** Massive magnetite replaced by pyrite and chalcopyrite. **D.** Magnetite in disseminated magnetite ores replaced epidote. **E.** Magnetite clasts ores. **F.** Magnetite (with/without actinolite) veins cutting epidote-altered host rocks. **G.** Massive magnetite coexisting with epidote, amphibole, and titanite. **H.** Massive magnetite intergrown with minor amphibole and epidote, and subsequently cross-cut by pyrite veins. **I.** Massive magnetite with actinolite-replaced garnet. **J.** Disseminated magnetite with epidote-replaced garnet. **K.** Magnetite vein replacing garnet, and subsequently cut by a calcite vein. **L.** Massive magnetite with sulphides (pyrite and chalcopyrite) replacing garnet. **M.** Massive magnetite with pyrite and minor quartz and epidote. **N.** Disseminated magnetite and epidote. **O.** Disseminated magnetite with epidote and K-feldspar. **P.** Disseminated magnetite with epidote-replaced garnet, subsequently cut by a quartz vein. **Q.** Banded magnetite-skarn (garnet and epidote) ore. **R.** Banded magnetite-K-feldspar-pyrite ore, with magnetite cut by a chlorite vein. **S.** Taxitic magnetite-epidote-sulphide ore. **T.** Massive magnetite ore with epidote, cross-cut by an epidote-pyrite vein. **U.** Massive magnetite ore with vein-like pyrite. **V.** Massive magnetite-chalcopyrite ore. Figures A–F are from the Heijianshan Fe-Cu (-Au) deposit (Zhao L.D. et al., 2017a, 2018a), G–K from the Duotoushan iron-copper deposit (Zhang et al., 2018), L–P from the Shaquanzi iron-copper deposit (Jiang et al., 2018), Q–S from the Qiaoxiahala Fe-Cu (-Au) deposit (Liang et al., 2018), and T–V from the Laoshankou Fe-Cu (-Au) deposit (Liang et al., 2019).

Stage V—Late veins: Some calcite, quartz, and epidote-amphibole veins cross-cut earlier-stage minerals and host rocks.

*Northern Margin of the Eastern Junggar District*

The eastern Junggar district, located between the Chinese Altay orogen and the Harlik arc, is bounded by the Erqis Fault to the north and the Kelameili Fault to the south (Liang et al., 2016a). The margins of the district are composed of the Dulate arc in the north and the Yemaquan arc in the south (Liang et al., 2019). The district dominantly comprises late Paleozoic volcano-sedimentary rocks ranging in age from the Lower Devonian to the Permian (Fig. 15D). Abundant intrusions with compositions varying from (dominantly) felsic to (rarely) mafic-intermediate are exposed along the northern margin of eastern Junggar (Li and Chen, 2004). Relations between magmatism, tectonic setting, and mineralization can be summarized as follows (Liang et al., 2019 and references therein): (1) Cambrian to Lower Ordovician mafic to ultramafic rocks (ca. 500–480 Ma) formed in a mid-ocean ridge setting; (2) Middle to Upper Devonian (ca. 390–370 Ma) arc-related felsic intrusions are genetically associated with Fe-Cu (-Au) and porphyry copper deposits; (3) Carboniferous to Permian (ca. 330–280 Ma) felsic intrusions formed in a postcollisional or intraplate extensional setting and are linked to skarn copper-molybdenum, porphyry copper-molybdenum, and hydrothermal gold deposits.

*Geology of the Qiaoxiahala Deposit*

The Qiaoxiahala Fe-Cu (-Au) deposit is located just south of the Erqis Fault (Fig. 15D). Exposed strata at Qiaoxiahala are the Middle Devonian Beitashan and Yundukala formations, early Carboniferous Nanmingshui Formation, and Quaternary sediments. The Beitashan Formation contains three members, with the upper member being composed of tuffaceous conglomerate, mafic tuff, basalt, andesite, and minor sandstone, siltstone, marble, and chert. These rocks host most of the iron and copper-gold orebodies (Liang et al., 2018). The overlying Yundukala Formation consists of mafic tuff, tuffaceous siltstone, and sandstone interlayered with tuffaceous conglomerate, felsite, and mafic crystal tuff. The Nanmingshui Formation consists of sandstone, tuffaceous sandstone, and slate intercalated with chert and limestone lenses (Liang et al., 2018).

Intrusive rocks are widely exposed in the central and eastern sections of the Qiaoxiahala deposit, including granodiorite, diorite, diorite porphyry (380–378 Ma; Liang et al., 2016b), and aplite (331 Ma; Liang et al., 2016b). The diorite porphyry has a close spatial relationship with Fe-Cu (-Au) mineralization. Northwest-trending faults associated with the nearby Erqis Fault are regarded as the ore-controlling structures (Ying, 2007). Mineralization at Qiaoxiahala is clearly zoned: the upper, middle, and lower mineralization zones are dominated by magnetite, copper-gold-bearing magnetite, and copper-gold orebodies, respectively (Liang et al., 2018). Iron orebodies are tabular and stratabound, and form lenticular zones or veins; they are 100–620 m long, 1–41 m wide, and extend 75–302 m down-dip. Copper-gold orebodies consist of veins or lenticular replacement zones and are 30–70 m long, 2–9 m wide, and 60–288 m down-dip; the ores are variously massive, taxitic, banded, disseminated, or brecciated (Fig. 16Q–S; Liang et al., 2018).

Six alteration and mineralization stages have been documented, including calcic-skarn alteration (Stage I), epidote-bearing HT Ca-Fe alteration (Stage II), magnetite mineralization (Stage III), magnetite-pyrite mineralization (Stage IV), chalcopyrite mineralization (Stage V), and late veins (Stage VI) (Liang et al., 2018).

Stage I—Calcic skarn alteration: This stage is characterized by local euhedral to subhedral andradite in the volcanic wall rocks or along the contact between the volcanic wall rocks and massive magnetite orebodies. The andradite has clear zoning and is commonly replaced by magnetite, epidote, and calcite (Fig. 17J; Liang et al., 2018).

Stage II—Epidote-bearing HT Ca-Fe alteration: The main alteration minerals are subhedral to anhedral epidote and anhedral amphibole, which were locally replaced by late magnetite.

Stage III—Magnetite mineralization in the HT Ca-K-Fe alteration facies: This main iron mineralization stage largely consists of magnetite-epidote-quartz-calcite and magnetite-K-feldspar-quartz-calcite assemblages. The anhedral magnetite is fine-grained, and forms aggregates with epidote, titanite, apatite, K-feldspar, quartz, and calcite, or is intergrown with subhedral to anhedral epidote and K-feldspar (Figs. 16Q–S, 17K; Liang et al., 2018). Quartz, calcite, and apatite are commonly subhedral to anhedral, and host many fluid inclusions that constrain the temperature and salinity to 354–386°C, 9.9–14.7 wt% NaCl equivalent, respectively (Liang et al., 2018).

Stage IV—Magnetite-pyrite mineralization: Major minerals in this stage are garnet, quartz, magnetite, pyrite, and calcite. Pyrite is widely replaced by chalcopyrite, whereas magnetite postdates pyrite and has a platy, anhedral to subhedral shape resembling mushketovite. Zoning of magnetite in backscattered electron (BSE) images also supports the replacement of hematite by magnetite (Liang et al., 2018). Fluid inclusion study documents that Stage IV fluids were of medium-high temperature (272–453°C), low-medium salinity (2.9–19.5 wt% NaCl equivalent), and Mg-Fe-rich (Liang et al., 2018).

Stage V—Chalcopyrite mineralization: This stage is characterized by a chalcopyrite-chlorite assemblage that commonly coexists with minor calcite and quartz and replaces Stage IV quartz, pyrite, and magnetite (Fig. 17L). Chlorite occurs as fine needles. Native gold has been tentatively identified in sulphide assemblages (Ying et al., 2009; Li et al., 2014 ). Fluids of this stage were low-medium temperature (186–270°C), low-medium salinity (1.4–21.8 wt% NaCl equivalent), and calcium- or sodium-rich. Mineralization depth has been estimated at 1–2 km (Liang et al., 2018).

Stage VI—Late veins: Late veins are common and include epidote, quartz, calcite, and hematite.

*Geology of the Laoshankou Deposit*

At Laoshankou, exposed strata are the Lower Devonian Tuoranggekuduke Formation, the Middle Devonian Beitashan

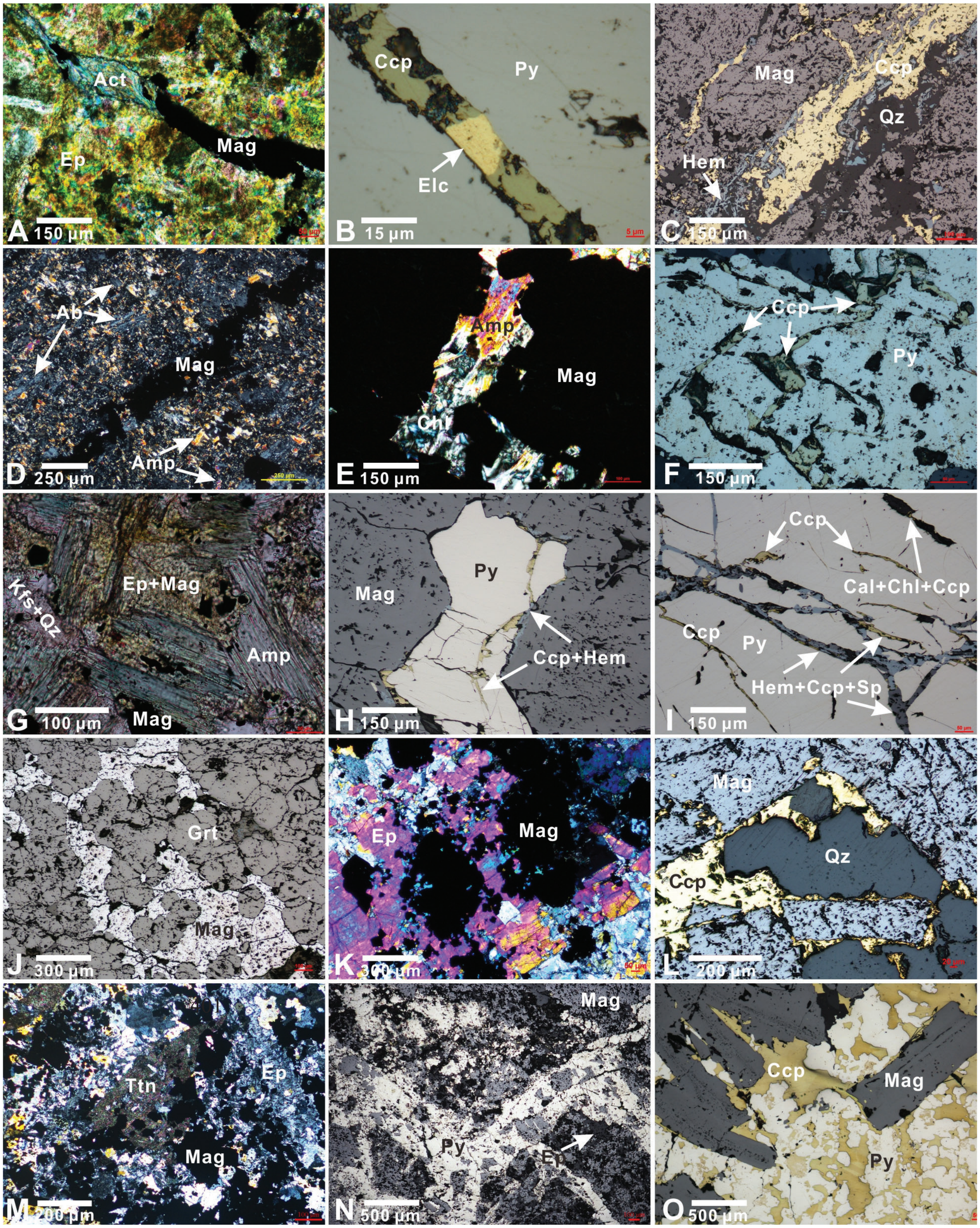


**Figure 17.** Representative photographs of alteration/mineralization paragenesis of IOCG-like deposits in northwestern China. **A.** Epidote cut by an actinolite-magnetite vein. **B.** Massive pyrite cut by a chalcopyrite and electrum vein. **C.** Massive magnetite cut by quartz-chalcopyrite-hematite veins. **D.** An amphibole-albite assemblage cut by a magnetite veinlet. **E.** Magnetite coexisting with amphibole that is replaced by chlorite. **F.** Pyrite cut by chalcopyrite veins. **G.** Amphibole-magnetite-epidote assemblage replaced by K-feldspar-quartz. **H.** Magnetite coexisting with pyrite that is partially replaced by chalcopyrite-hematite veins. **I.** Pyrite cut by chalcopyrite, hematite-chalcopyrite-sphalerite, and calcite-chlorite-chalcopyrite veins. **J.** Granular garnet replaced by magnetite. **K.** Epidote intergrown with magnetite. **L.** Magnetite coexisting with quartz and replaced by chalcopyrite. **M.** Magnetite intergrown with epidote and titanite. **N.** Pyrite veins cutting magnetite-epidote assemblage. **O.** Magnetite cut/replaced by pyrite and chalcopyrite. Figures of A–C are from the Heijianshan Fe-Cu (-Au) deposit (Zhao LD et al., 2017a), D–F from the Duotoushan iron-copper deposit (Zhang et al., 2018), G–I from the Shaquanzi iron-copper deposit (Jiang et al., 2018), J–L from the Qiaoxiahala Fe-Cu (-Au) deposit (Liang et al., 2018), and M–O from the Laoshankou Fe-Cu (-Au) deposit (Liang et al., 2019).

Formation, and Quaternary sediments. The Beitashan Formation hosts the Laoshankou deposit, and mainly contains basaltic/andesitic breccias and tuff intercalated with fossiliferous limestone (Liang et al., 2019). Magmatism at Laoshankou is mainly represented by diorite porphyry (380 Ma; Lu et al., 2012), biotite diorite (381 Ma; Liang et al., 2016a), quartz syenite intrusions (376 Ma; Liang et al., 2016a), and diorite dykes (354 Ma; Lu et al., 2012). Two large northwest-trending faults control the distribution of volcanic edifices and magmatism in the Laoshankou deposit area, viz. the Fuyun Fault in the north (Fig. 15D) and the Shanqian Fault in the south (Liang et al., 2019). There are also subsidiary east-west-striking faults that cross-cut or displace components of the Laoshankou deposit (Liang et al., 2019).

The Laoshankou deposit has a metal reserve of 3.26 Mt Fe, 9800 t Cu, and 0.14 t Au. Ore grades are 33.5–36.4% Fe, 0.2–0.4% Cu, and 0.5–1.3 g/t Au (Liang et al., 2019). Orebodies are mainly stratabound and parallel to late faults, and can be divided into two ore zones — upper magnetite orebodies with minor copper-gold mineralization (36.42–53.35% Fe, 0.28–1.57% Cu, and 0.49–1.90 g/t Au), and lower copper-gold orebodies (0.41–1.67% Cu and 1.31–9.11 g/t Au; Liang et al., 2019). Ores are mainly massive (Fig. 16T–V), and locally banded, disseminated, taxitic, or vein-like.

Four alteration and mineralization stages have been established: skarn alteration (Stage I), HT Ca-Fe alteration/mineralization (Stage II), pyrite-chalcopyrite mineralization (Stage III), and late hydrothermal veining (Stage IV) (Liang et al., 2019).

Stage I—Skarn alteration: Stage I minerals are mainly garnet (andradite and grossularite), scapolite and minor pyroxene. The garnet is coarse-grained, and locally replaced by magnetite, epidote, K-feldspar, and carbonate. Columnar scapolite is commonly replaced by epidote and quartz, whereas coarse-grained pyroxene (calcic pyroxene and diopside) is locally replaced by magnetite and epidote (Liang et al., 2019).

Stage II—High-temperature Ca-Fe alteration/mineralization: As the main iron mineralization stage, it can be further divided into Stage II-A and Stage II-B. Stage II-A is dominated by amphibole and minor albite, whereas Stage II-B is characterized by major amphibole, magnetite, titanite, epidote, and quartz (Figs. 16T, 17M), and minor albite and K-feldspar. Magnetite is subhedral to anhedral, granular, massive or vein-hosted, and locally shows distinct compositional zoning (Liang et al., 2019). Fluid inclusion and isotope analytical results show that iron mineralizing fluids of this stage were high-temperature (~530°C) magmatic fluids mixed with seawater (Liang et al., 2019).

Stage III—Pyrite-chalcopyrite mineralization: This stage features abundant sulphide minerals, and can be divided into Stage III-A and Stage III-B according to the dominant mineral assemblage — pyrite-epidote-quartz-garnet and chalcopyrite-amphibole-chlorite, respectively (Liang et al., 2019). Commonly, pyrite-epidote and pyrite-quartz-garnet veins cross-cut massive magnetite (Fig. 16T) and epidote-altered wall rocks (Fig. 17N). Epidote in Stage III-A and Stage II-B is texturally and compositionally similar. Stage III-A garnet is yellowish, euhedral to subhedral, and homogenous. Chalcopyrite commonly occurs as disseminations, patches or veins that locally cut altered host rocks, or replace Stage II-B magnetite and Stage III-A pyrite (Fig. 16O; Liang et al., 2019). Sphalerite has vermicular texture and chalcocite commonly occurs as replacement rims around chalcopyrite. Stage III-B chlorite compositions range from ripidolite to pycnochlorite, constraining the temperature of this stage to ~236–272°C (Liang et al., 2019). Native gold occurs in pyrite and chalcopyrite (Li Q et al., 2015). The economic copper mineralizing fluids were probably formed by the mixing of meteoric water-dominated fluid and Ca-rich formation water (Liang et al., 2019).

Stage IV—Late hydrothermal veining: Late-stage hydrothermal veins are abundant and include amphibole, K-feldspar, epidote, pyrite, hematite, chlorite, quartz, calcite, and tourmaline.

*Ore Genesis*

The Heijianshan, Duotoushan, and Shaquanzi deposits of eastern Tianshan are geologically very similar, e.g. volcanic/volcaniclastic host rocks, pre-mineralization alteration types, and distinct iron and copper (-gold) mineralization stages. Moreover, they share similar tectonic settings (basin inversion stage at ca. 320–300 Ma; Zhao LD et al., 2019), and age of mineralization (ca. 310–300 Ma; Huang et al., 2013, 2014; Jiang et al., 2018; Zhang et al., 2018; Zhao, 2018). However, the iron and copper (-gold) stages of mineralization incorporate distinct assemblages of ore minerals (magnetite ± amphibole ± quartz ± K-feldspar ± epidote, and chalcopyrite-chlorite ± quartz ± electrum ± hematite, respectively) and alteration assemblages (amphibole ± K-feldspar ± epidote, and chlorite ± hematite, respectively) (Zhao LD et al., 2017a; Jiang et al., 2018; Zhang et al., 2018). Iron mineralizing fluids were high-temperature, medium to high salinity, and had a magmatic-hydrothermal origin attributed to intermediate to felsic intrusions. In contrast, copper (-gold) mineralizing fluids were low-temperature, low to medium salinity, and had an external magmatic-hydrothermal origin contributed by basinal brines that interacted with volcanic and volcaniclastic rocks (Zhao, 2018). The alteration styles, mineral assemblages, nature and sources of fluids, and tectonic settings of deposits in the Aqishan-Yamansu belt of eastern Tianshan are similar to central Andean IOCG deposits, indicating these deposits in the Aqishan-Yamansu belt of eastern Tianshan can be classified as late Paleozoic IOCG-like deposits. Similar conclusions can also be drawn for the Qiaoxiahala and Laoshankou Fe-Cu (-Au) deposits at the northern margin of eastern Junggar (details can be found in Liang et al., 2018, 2019).

Ore-forming processes for the IOCG-like deposits in northwestern China are summarized using the Heijianshan Fe-Cu (-Au) deposit as an example. At Heijianshan, extensive epidote alteration may have formed from the reaction of late Carboniferous seawater with volcanic/volcaniclastic host rocks, and heat sourced from cooling of mafic magma (Fig. 18A; Zhao

LD et al., 2017a). Iron-rich magmatic-hydrothermal fluids evolved from intermediate to felsic intrusions and ascended along faults, interacting with host rocks and earlier (Stage I) epidote alteration. Magnetite precipitated from the high-temperature and medium- to high-salinity fluids, leading to formation of the Heijianshan magnetite orebodies (Fig. 18B). With continuing basin closure, evaporation, and fluid evolution within the system, basinal brines may have started to leach limited amounts of sulphur and copper from the host rocks, and mixed with the fluid system to initiate Stage III pyrite alteration (Fig. 18C). Further leaching and water-rock reaction between the basinal brines that interacted with host rocks, and mixing with the magmatic-hydrothermal fluids, produced low-temperature and medium- to high-salinity fluids that precipitated copper and gold ores (dominantly chalcopyrite + quartz + chlorite ± electrum ± hematite; Fig. 18D). In the postmineralization stage at Heijianshan, abundant late-hydrothermal veins cross-cut the earlier-stage hydrothermal and mineralization mineral assemblages.

*Summary*

The eastern Tianshan and northern margin of eastern Junggar districts in northwestern China have undergone tectonic transition either from basin extension to inversion or from basin-related to arc-related settings, and these areas develop several late Paleozoic Fe-Cu (-Au) deposits including Heijianshan, Duotoushan, and Shaquanzi in the eastern Tianshan district, and Qiaoxiahala and Laoshankou at the northern margin of the eastern Junggar district. These Fe-Cu (-Au) deposits are hosted by mafic to andesitic volcanic rocks (some with albite alteration, e.g. the Duotoushan deposit; Zhang et al., 2018) and their orebodies are parallel to stratigraphy. Although most of these Fe-Cu (-Au) deposits display skarn alteration (e.g. garnet and pyroxene), their mineral assemblages, alteration types, nature and sources of fluids point to distinct styles of iron versus copper (-gold) mineralization. Their tectonic settings are similar to central Andean IOCG deposits, implying that the late Paleozoic Fe-Cu (-Au) deposits in northwestern China are best interpreted as IOCG-like deposits.

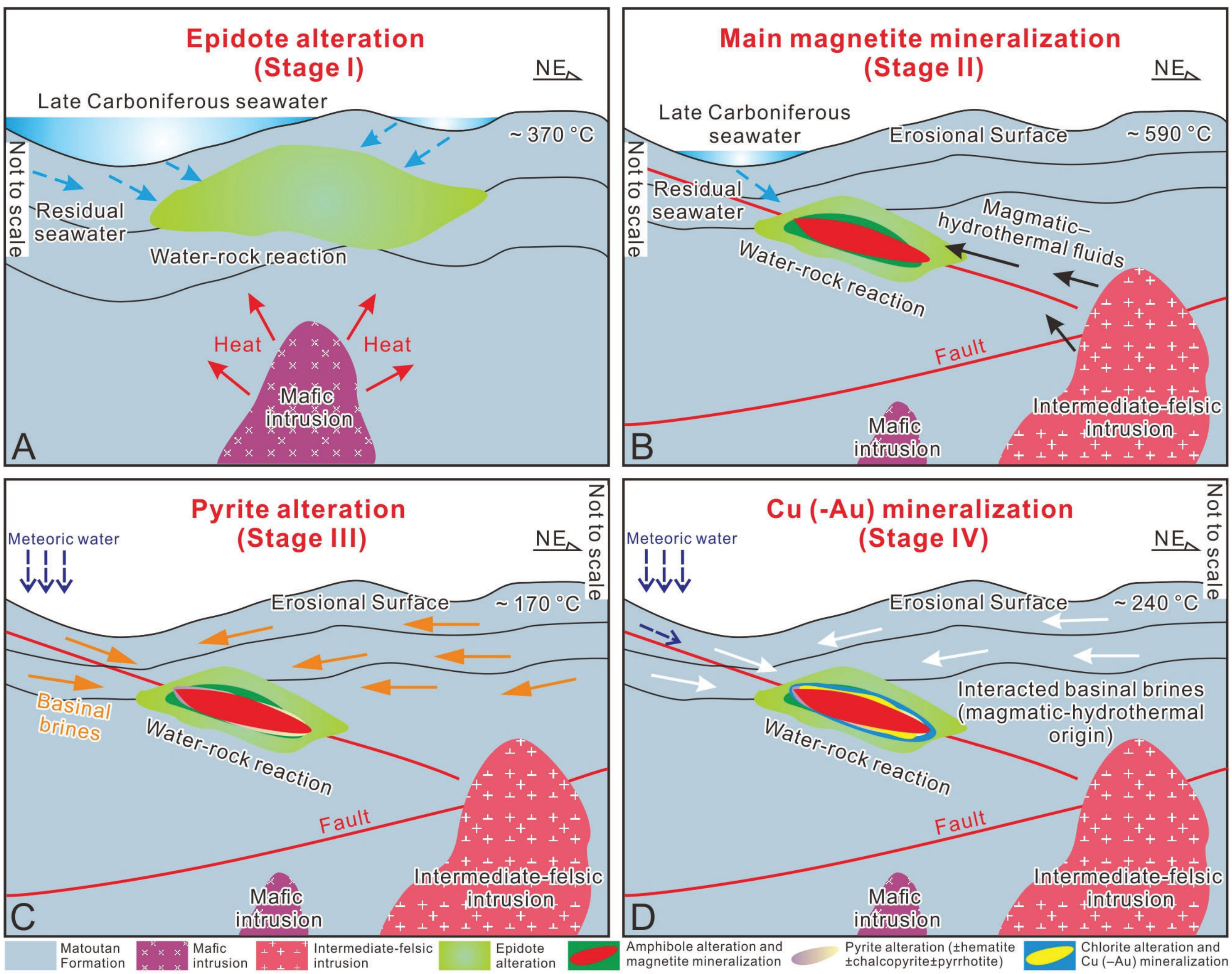


**FIGURE 18.** Schematic ore-forming diagram of the Heijianshan Fe-Cu (-Au) deposit (modified after Zhao LD et al., 2017a).

## Discussion and Implications

*Ore Genesis of IOA Deposits*

Iron-oxide apatite deposits display remarkably similar styles of alteration and mineralization from district to district and throughout geologic time (Hitzman, 2000). Many of the IOA deposits in eastern China display spatial, temporal, and hence genetic relationships to dioritic intrusions in shallow subvolcanic settings (Ningwu Research Group, 1978). This association is typical of IOA deposits worldwide (Hildebrand, 1986; Groves et al., 2010). Initiation of an extremely high-temperature, highly saline, magmatic-hydrothermal system (>800ºC) that interacts with country rocks in the vicinity of intermediate intrusions is required to produce magnetite-apatite ores (Fig. 14), a model similar to that proposed and illustrated by Corriveau et al. (2016). The consistent enrichment of iron, phosphorous, and commonly LREE in IOA deposits worldwide argues for a common ore-forming process. We suggest, therefore, that IOA deposits form in a magmatic-hydrothermal system proximal to intermediate subvolcanic intrusions within a specific tectonic setting and/or condition. For this reason, IOA deposits in China have been referred to as dioritic porphyry iron deposits (Ningwu Research Group, 1978).

*Genetic Link among IOA, IOCG, and Skarn Deposits*

Various styles of ore deposits may form from a magmatic-hydrothermal system, e.g. porphyry copper-gold mineralizing system commonly includes porphyry, skarn, epithermal, and carbonate replacement copper-gold deposits. Therefore, identification of a possible genetic link between different ore types in a region is not only of critical importance for a better understanding of the magmatic-hydrothermal processes, but can also help in successful mineral exploration. Both iron oxide-apatite (IOA) and iron skarn deposits in the MLYRMB are closely associated with intermediate intrusive rocks. Some IOA deposits can also contain abundant diopside and/or garnet as gangue minerals. The similar alteration facies and contemporaneous ages strongly imply a genetic link between the two. For example, Hu et al. (2020) reported a newly identified subsurface IOA orebody located at the apex of a diorite porphyry at the Wangbaoshan deposit, where previously known iron skarn orebodies are located immediately above the IOA mineralization. Hu et al. (2020) propose that IOA and skarn ores are products of consecutive mineralizing stages in the same magmatic-hydrothermal system, in which high-temperature, hypersaline fluids coexisting with diorite porphyry magma formed IOA ores, and subsequent hydrothermal fluids, diluted by circulating meteoric water, were responsible for retrograde iron skarn ore at lower temperatures.

There are also many similarities between systems hosting IOA and IOCG deposits, e.g. HT Na-(Ca)-Fe alteration facies and common association with albitite breccia (e.g. Corriveau et al., 2016; Montreuil et al., 2016). Many researchers have argued whether IOA deposits represent an iron-rich end member or represent the deep parts of a large IOCG system. However, in contrast to true IOCGs, typical IOA deposits lack economic copper and gold. It has been proposed that copper-sulphides are not saturated/precipitated at the time these systems formed (Corriveau et al., 2016; Reich et al., 2016). Alternatively, high-temperature (800–900ºC), saline magmatic-hydrothermal fluids fail to transport copper and gold in IOA systems, hence fluids capable of forming IOCG deposits are lacking. Such fluids have been interpreted as exsolved magmatic hydrosaline liquids (Zhao et al., 2016) or hydrous immiscible iron-oxide melts (Tornos et al., 2016).

In contrast to IOA deposits, early-stage ore-forming fluids for IOCG deposits may have temperatures of 500–600ºC or higher, but were effectively and quickly mixed with external low-temperature fluids in a larger-scale ore-forming system. In any case, fluids that form IOCG deposits are significantly lower in temperature than those recorded in IOA deposits. They can be derived from a deep-seated magma chamber (Fig. 7), therefore orebodies may not show a spatial association with igneous intrusions. In contrast, IOA deposits require shallow-level emplacement of porphyry intrusion(s) and are located in proximity to those intrusions.

Some IOCG deposits, e.g. the Dahongshan deposit in the Kangdian belt, contain both iron and copper-iron orebodies. A question arises as whether the massive, magnetite-only ores of Dahongshan should be considered IOA ores, as they commonly contain lower abundances of titanium and phosphorus than typical IOA deposits. In situ elemental analyses of Dahongshan magnetite show that the magnetite grains have titanium and vanadium contents lower than typical IOA ores (Chen et al., 2015; our unpublished data), implying they formed from relatively lower temperature hydrothermal fluids. We suggest, therefore, that IOA and IOCG deposits formed by somewhat similar processes from related magmatic-hydrothermal systems, but may not constitute a single system transitional from IOA to IOCG deposits. Tectonic settings may have a first-order control on which types of deposits formed (Groves et al., 2010; Montreuil et al., 2016).

The central Andes metallogenic belt contains large, roughly contemporaneous IOA and IOCG deposits (Sillitoe 2003), although their temporal distributions are slightly different (Groves et al., 2010). Several other major IOCG metallogenic belts include both IOA and IOCG deposits; however, they either contain large- to small-sized IOCG deposits and relatively small IOA deposits (e.g. Gawler, Cloncurry, Carajás, and Great Bear magmatic zone districts; Hitzman et al., 1992; Groves et al., 2010; Corriveau et al., 2016), or large IOA deposits and small IOCG deposits/prospects (e.g. Norrbotten region; Groves et al., 2010; Martinsson et al., 2016). In all cases, IOA deposits predate IOCG deposits in those districts. Again, this may imply a tectonic control on the two types of deposits (Groves et al., 2010; Montreuil et al., 2016), but the details on this issue are not well understood.

The possible genetic link between IOCG and skarn deposits has been noticed for a long time. The IOCG deposits in southwestern China and the central Andes metallogenic belt have previously been classified as skarn type, before the definition of IOCG was proposed. However, it is apparent that external basinal fluids played critical roles in the precipitation of copper-sulphides in IOCG deposits (Groves et al., 2010; Barton, 2014). Hence, the large-scale alteration zones and involvement of basinal fluids can be used as criteria to distinguish IOCG from skarn deposits. The similar paragenetic sequences typically observed in the two types of deposits imply that each formed from a magmatic-hydrothermal system, but IOCG is probably more distal from the ore-related intrusions.

## Acknowledgments

We thank Jian-Wei Li and Hao Hu for their useful discussions, Li-Ping Zeng, Zhi-Kun Su, Weifeng Zhang, Pei Liang, and Hongjun Jiang for preparing/providing some figures, and Louise Corriveau, David Lentz and Xiaowen Huang for reviewing this manuscript. Financial supports from NSFC (41822203, 41972074, 41472068, and 42002083), the Fundamental Research Funds for the Central Universities (CUG140618 and CUGCJ1711) are appreciated.

## References

Barton, M.D., 2014, Iron oxide(-Cu-Au-REE-P-Ag-U-Co) systems, *in* Scott, S.D., ed., Treatise on Geochemistry, 13: Amsterdam, Elsevier, p. 515-541.

Chen, L., Zheng, Y.-F., and Zhao, Z.-F., 2016, Geochemical constraints on the origin of late Mesozoic andesites from the Ningwu basin in the Middle–Lower Yangtze Valley, South China: Lithos, v. 254-255, p. 94-117.

Chen, W.T., and Zhou, M.-F., 2012, Paragenesis, stable isotopes, and molybdenite Re-Os isotope age of the Lala iron-copper deposit, southwest China: Economic Geology, v. 107, p. 459-480.

Chen, W.T., Zhou, M.-F., Gao, J.-F., and Hu, R., 2015, Geochemistry of magnetite from Proterozoic Fe-Cu deposits in the Kangdian metallogenic province, SW China: Mineralium Deposita, v. 50, p. 795-809.

Chen, Y.J., Pirajno, F., Wu, G., Qi, J.P., and Xiong, X.L., 2012, Epithermal deposits in north Xinjiang, NW China: International Journal of Earth Sciences, v. 101, p. 889-917.

Corriveau, L., Montreuil, J.-F., and Potter, E.G., 2016, Alteration facies linkages among iron oxide copper-gold, iron oxide-apatite, and affiliated deposits in the Great Bear magmatic zone, Northwest Territories, Canada: Economic Geology, v. 111, p. 2045-2072.

Corriveau, L., Potter, E.G., Montreuil, J.-F., Blein, O., Ehrig, K., and De Toni, A., 2018, Iron-oxide and alkali-calcic alteration ore systems and their polymetallic IOA, IOCG, skarn, albitite-hosted U±Au±Co, and affiliated deposits: a short course series. Part 2: overview of deposit types, distribution, ages, settings, alteration facies, and ore deposit models: Geological Survey of Canada, Scientific Presentation 81, 154 p.

Corriveau, L., Mumin, A.H., and Potter, E.G., 2022, Mineral systems with iron oxide copper-gold (IOCG) and affiliated deposits: introduction and overview, *in* Corriveau, L., Potter, E.G. and Mumin, A.H., eds., Mineral systems with iron oxide copper-gold (IOCG) and affiliated deposits: Geological Association of Canada, Special Paper 52, p. 1-25.

Deng, X.H., Wang, J.B., Wang, Y.W., Li, Y.C., Fang, T.H., and Mao, Q.G., 2014, Geological characteristics of the Hongshi Cu-Au deposit, eastern Tianshan, Xinjiang and discussion of the deposit genesis: Mineral Exploration, v. 5, p. 159-168 (in Chinese with English abstract).

Groves, D.I., Bierlein, F.P., Meinert, L.D., and Hitzman, M.W., 2010, Iron oxide copper-gold (IOCG) deposits through Earth history: implications for origin, lithospheric setting, and distinction from other epigenetic iron oxide deposits: Economic Geology, v. 105, p. 641-654.

Hildebrand, R.S., 1986, Kiruna-type deposits; their origin and relationship to intermediate subvolcanic plutons in the Great Bear magmatic zone, Northwest Canada: Economic Geology, v. 81, p. 640-659.

Hitzman, M.W., 2000, Iron oxide-Cu-Au deposits: what, where, when, and why, *in* Porter, T.M., ed., Hydrothermal iron oxide copper-gold & related deposits: a global perspective, volume 1: PGC Publishing, Adelaide, p. 9-25.

Hitzman, M.W., Oreskes, N., and Einaudi, M.T., 1992, Geological characteristics and tectonic setting of Proterozoic iron oxide (Cu-U-Au-REE) deposits: Precambrian Research, v. 58, p. 241-287.

Hu, H., Li, J.W., Harlov, D.E., Lentz, D.R., McFarlane, C.R.M., and Yang, Y.-H., 2020, A genetic link between iron oxide-apatite and iron skarn mineralization in the Jinniu volcanic basin, Daye district, eastern China: evidence from magnetite geochemistry and multi-mineral U-Pb geochronology: GSA Bulletin, v. 132, p. 899-917.

Huang, X.W., Qi, L., Gao, J.F., and Zhou, M.F., 2013, First reliable Re-Os ages of pyrite and stable isotope compositions of Fe (-Cu) deposits in the Hami region, Eastern Tianshan Orogenic Belt, NW China: Resource Geology, v. 63, p. 166-187.

Huang, X.W., Qi, L., Wang, Y.C., and Liu, Y.-Y., 2014, Re-Os dating of magnetite from the Shaquanzi Fe-Cu deposit, eastern Tianshan, NW China: Science China: Earth Sciences, v. 57, p. 267-277.

Jiang, H.J., Han, J.S., Chen, H.Y., Zheng, Y., Lu, W.J., Deng, G., and Tan, Z.X., 2017, Intra-continental back-arc basin inversion and Late Carboniferous magmatism in Eastern Tianshan, NW China: constraints from the Shaquanzi magmatic suite: Geoscience Frontiers, v. 8, p. 1447-1467.

Jiang, H.J., Han, J.S., Chen, H.Y., Zheng, Y., Zhang, W.F., Lu, W.J., Deng, G., and Tan, Z.X., 2018, Hydrothermal alteration, fluid inclusions and stable isotope characteristics of the Shaquanzi Fe-Cu deposit, Eastern Tianshan: implications for deposit type and metallogenesis: Ore Geology Reviews, v. 100, p. 385-400.

Knipping, J.L., Bilenker, L.D., Simon, A.C., Reich, M., Barra, F., Deditius, A.P., Lundstrom, C., Bindeman, I., and Munizaga, R., 2015, Giant Kiruna-type deposits form by efficient flotation of magmatic magnetite suspensions: Geology, v. 43, p. 591-594.

Li, H.Q., and Chen, F.W., 2004, Isotopic geochronology of regional mineralization in Xinjiang, NW China: Beijing: Geological Publishing House, 391 p. (in Chinese with English abstract).

Li, Q., Lu, S.J., Yang, F.Q., Geng, X.X., and Chai, F.M., 2015, Geological characteristics and genesis of the Laoshankou Fe-Cu-Au deposit in Junggar, Xinjiang, Central Asian Orogenic Belt: Ore Geology Reviews, v. 68, p. 59-78.

Li, W., Audétat, A., and Zhang, J., 2015, The role of evaporites in the formation of magnetite–apatite deposits along the Middle and Lower Yangtze River, China: evidence from LA-ICP-MS analysis of fluid inclusions: Ore Geology Reviews, v. 67, p. 264-278.

Li, X., Zhao, X.-F., Zhou, M.-F., Chen, W.T., and Chu, Z., 2015, Fluid inclusion and isotopic constraints on the origin of the Paleoproterozoic Yinachang Fe-Cu-(REE) deposit, southwest China: Economic Geology, v. 110, p. 1339-1369.

Liang, P., Chen, H.Y., Hollings, P., Wu, C., Xiao, B., Bao, Z.W., and Xu, D.R., 2016a, Geochronology and geochemistry of igneous rocks from the Laoshankou district, North Xinjiang: implications for the late Paleozoic tectonic evolution and metallogenesis of East Junggar: Lithos, v. 266-267, p. 115-132.

Liang, P., Chen, H.Y., Hollings, P., Xiao, B., Wu, C., Bao, Z.W., and Cai, K.D., 2016b, The Paleozoic tectonic evolution and metallogenesis of the northern margin of East Junggar, Central Asia Orogenic Belt: geochronological and geochemical constraints from igneous rocks of the Qiaoxiahala Fe-Cu deposit: Journal of Asian Earth Sciences, v. 130, p. 23-45.

Liang, P., Chen, H.Y., Wu, C., Zhang, W.F., Xu, D.R., Xia, X.P., Liu, Z.J., and Zhang, Z.J., 2018, Mineralization and ore genesis of the Qiaoxiahala Fe-Cu-(Au) deposit in the northern margin of East Junggar terrane, Central Asian Orogenic Belt: constraints from fluid inclusions and stable isotopes: Ore Geology Reviews, v. 100, p. 360-384.

Liang, P., Chen, H.Y., Han, J.S., Wu, C., Zhang, W.F., Xu, D.R., Lai, C.K., and Kyser, K., 2019, Iron oxide-copper-gold mineralization of the Devonian Laoshankou deposit (Xinjiang, NW China) in the Central Asian Orogenic Belt: Ore Geology Reviews, v. 104, p. 628-655.

Lu, S.J., Yang, F.Q., Chai, F.M., Zhang, X.B., Jiang, L.P., Liu, F., Zhang, Z.X., Geng, X.X., and Ouyang, L.J., 2012, Zircon U-Pb dating for intrusions in Laoshankou ore district in northern margin of East Junggar and their significances: Geological Review, v. 58, p. 149-164 (in Chinese with English abstract).

Mao, J.W., Goldfarb, R.J., Wang, Y.T., Hart, C.J., Wang, Z.L., and Yang, J.M., 2005, Late Paleozoic base and precious metal deposits, East Tianshan, Xinjiang, China: characteristics and geodynamic setting: Episodes, v. 28, p. 23-30.

Mao, J.W., Xie, G.Q., Duan, C., Pirajno, F., Ishiyama, D., and Chen, Y.C., 2011, A tectono-genetic model for porphyry–skarn–stratabound Cu–Au–Mo–Fe and magnetite–apatite deposits along the Middle–Lower Yangtze River Valley, Eastern China: Ore Geology Reviews, v. 43, p. 294-314.

Martinsson, O., Billström, K., Broman, C., Weihed, P., and Wanhainen, C., 2016, Metallogeny of the Northern Norrbotten ore province, northern Fennoscandian Shield with emphasis on IOCG and apatite-iron ore deposits: Ore Geology Reviews, v. 78, p. 447-492.

Masteel Mining Co. Ltd., 2012, The secondary stage exploration report of resources and reserves of the Gaocun iron deposit, Ma'anshan city, Anhui Province: Masteel Mining Co. Ltd., Unpublished report, p. 106.

Montreuil, J.-F., Corriveau, L., Potter, E.G., and De Toni, A.F., 2016, On the relationship between alteration facies and metal endowment of iron oxide-alkali-altered systems, southern Great Bear magmatic zone (Canada): Economic Geology, v. 111, p. 2139-2168.

Mumin A.H., Somarin A.K., Jones B., Corriveau L., Ootes L., and Camier J., 2010, The IOCG-porphyry-epithermal continuum of deposit types in the Great Bear magmatic zone, Northwest Territories, Canada, *in* Corriveau, L. and Mumin, A.H., eds., exploring for iron oxide copper-gold deposits: Canada and global analogues: Geological Association of Canada, Short Course Notes, No. 20, p. 59-78.

N9GBYBGMR (No. 9 Geological Brigade of the Yunnan Bureau of Geology and Mineral Resources), 1983, Report of exploration and prospecting of the Dahongshan iron and copper deposits, Xinping County, Yunnan Province: Unpublished report, p. 377.

Ningwu Research Group, 1978, Ningwu porphyry iron ore deposits: Geological Publishing House, Beijing.196 p. (in Chinese).

No. 6 GPXBGM (No. 6 Geological Party Xinjiang Bureau of Geology and Mineral Resource), 2008, Supplementary report for geological exploration of the Shaquanzi Fe-Cu deposit in Hami city, Xinjiang Uygur Autonomous Region: Xinjiang Bureau of Geology and Mineral Resource, 104 p. (in Chinese).

Pan, Y., and Dong, P., 1999, The Lower Changjiang (Yangzi/Yangtze River) metallogenic belt, east central China: intrusion- and wall rock-hosted Cu-Fe-Au, Mo, Zn, Pb, Ag deposits: Ore Geology Reviews, v. 15, p. 177-242.

Reich, M., Simon, A.C., Deditius, A., Barra, F., Chryssoulis, S., Lagas, G., Tardani, D., Knipping, J., Bilenker, L., Sánchez-Alfaro, P., Roberts, M.P., and Munizaga, R., 2016, Trace element signature of pyrite from the Los Colorados iron oxide-apatite (IOA) deposit, Chile: a missing link between Andean IOA and iron oxide copper-gold system?: Economic Geology, v. 111, p. 743-761.

Sang, S.J., Peng, M.X., and Guo, Y.H., 2003, Optimized target areas and evaluation report of resource in the Caixiashan to Jinyan area: Xingjiang Institute of Geology Investigation, p. 42-44 (in Chinese).

Sengör, A.M.C., and Natal'in, B.A., 1996, Paleotectonics of Asia: fragments of synthesis, *in* Yin, A. and Harrison, T.M., eds., The tectonic evolution of Asia: Cambridge University Press, Cambridge, p. 486-640.

Sillitoe, R.H., 2003, Iron oxide-copper-gold deposits: an Andean view: Mineralium Deposita, v. 38, p. 787-812.

Su, Z.-K., Zhao, X.-F., Li, X.-C., and Zhou, M.-F., 2016, Using elemental and boron isotopic compositions of tourmaline to trace fluid evolutions of IOCG systems: the worldclass Dahongshan Fe-Cu deposit in SW China: Chemical Geology, v. 441, p. 265-279.

Tang, Y.-J., Zhang, H.-F., Ying, J.-F., Su, B.-X., Li, X.-H., and Santosh, M., 2013, Rapid eruption of the Ningwu volcanics in eastern China: response to Cretaceous subduction of the Pacific plate: Geochemistry, Geophysics, Geosystems, v. 14, p. 1703-1721.

Tornos, F., Velasco, F., and Hanchar, J.M., 2016, Iron-rich melts, magmatic magnetite, and superheated hydrothermal systems: the El Laco deposit, Chile: Geology, v. 44, p. 427-430.

Williams, P.J., 2010, "Magnetite-group" IOCGs with special reference to Cloncurry (NW Queensland) and northern Sweden: settings, alteration, deposit characteristics, fluid sources, and their relationship to apatite-rich iron ores, *in* Corriveau, L. and Mumin, A.H., eds., Exploring for iron oxide copper-gold deposits: Canada and global analogues: Geological Association of Canada, Short Course Notes, No. 20, p 23-38.

Wu, M.-D., Duan, J.-S., Song, X.-L., Chen, L., and Dan, Y., 1990, Geology of Kunyang Group in Yunnan Province: Scientific Press of Yunnan Province, Kunming, China, 265 p. (in Chinese with English abstract).

Xie, G., Mao, J., Xiongwei, L., Duan, C., and Yao, L., 2011, Late Mesozoic bimodal volcanic rocks in the Jinniu basin, Middle-Lower Yangtze River Belt (YRB), East China: age, petrogenesis and tectonic implications: Lithos, v. 127, p. 144-164.

Yang, H., Liu, F., Liu, P., and Wang, F., 2013, $^{40}Ar/^{39}Ar$ dating for muscovite in garnet muscovite-felsic schist of the Dahongshan Group in southwestern Yangtze block: Acta Petrologica Sinica, v. 29, p. 2161-2170 (in Chinese with English abstract).

Ying, L.J., 2007, Geology, geochemistry and discussion on the origin of the Qiaoxiahala Fe-Cu-Au deposit in Xinjiang: Master thesis, Chinese Academy of Geological Sciences, Beijing, China, 112 p. (in Chinese with English abstract).

Ying, L.J., Wang, D.H., Liang, T., and Zhou, R.H., 2009, Ore genesis and metallogenic model of Qiaoxiahala Fe-Cu-Au deposit in Xinjiang: Mineral Deposits, v. 28, p. 211-217 (in Chinese with English abstract).

Zeng, L.-P., Zhao, X.-F., Li, X.-C., Hu, H., and McFarlane, C., 2016, In situ elemental and isotopic analysis of fluorapatite from the Taocun magnetite-apatite deposit, Eastern China: constraints on fluid metasomatism: American Mineralogist, v. 101, p. 2468-2483.

Zhai, Y.-S., Xiong, Y.-l., Yao, S., and Lin, X., 1996, Metallogeny of copper and iron deposits in the Eastern Yangtse Craton, east-central China: Ore Geology Reviews, v. 11, p. 229-248.

Zhang, W.F., Chen, H.Y., Han, J.S., Zhao, L.D., Huang, J.H., Yang, J.T., and Yan, X.L., 2016, Geochronology and geochemistry of igneous rocks in the Bailingshan area: implications for the tectonic setting of late Paleozoic magmatism and iron skarn mineralization in the eastern Tianshan, NW China: Gondwana Research, v. 38, p. 40-59.

Zhang, W.F., Chen, H.Y., Jiang, H.J., Lu, W.J., Liang, P., Xu, C., Yan, X.L., and Yang, J.T., 2017, Geochronology, geochemistry and petrogenesis of granitoids in the Duotoushan Fe-Cu deposit, Eastern Tianshan, Xinjiang province: implications on tectonic setting of late Paleozoic magmatism: Geotectonica et Metallogenia, v. 14, p. 1171-1191 (in Chinese with English abstract).

Zhang, W.F., Chen, H.Y., Peng, L.H., Zhao, L.D., Lu, W.J., Zhang, Z.J., Yang, J.T., and Sun, J., 2018, Ore genesis of the Duotoushan Fe-Cu deposit, Eastern Tianshan, NW China: constraints from ore geology, mineral geochemistry, fluid inclusion and stable isotopes: Ore Geology Reviews, v. 100, p. 401-421.

Zhang, X.H., Huang, X., Chen, J.P., Liao, Q.A., and Duan, X.F., 2012, Stratigraphic sequence of carboniferous marine volcanic-deposit rock and its geological age in Juotage Area, Eastern Tianshan: Earth Science - Journal of China University of Geosciences, v. 6, p. 1305-1314 (in Chinese with English abstract).

Zhao, L.D., 2018, Tectonic evolution and metallogenesis of the Aqishan-Yamansu metallogenic belt, Eastern Tianshan: case studies of the Heijianshan Fe-Cu (-Au) and Hongshanliang Cu deposits: Ph.D. thesis, Beijing, China, University of Chinese Academy of Sciences, 350 p. (in Chinese with English abstract).

Zhao, L.D., Chen, H.Y., Zhang, L., Xia, X.P., Zhang, W.F., Li, D.F., Lu, W.J., Liang, P., Li, R.C., Yang, J.T., and Yan, X.L., 2017a, Geology and ore genesis of the late Paleozoic Heijianshan Fe oxide-Cu (-Au) deposit in the Eastern Tianshan, NW China: Ore Geology Reviews, v. 91, p. 110-132.

Zhao, L.D., Chen, H.Y., Zhang, L., Zhang, Z.J., Li, D.F., Zhang, W.F., Lu, W.J., Yang, J.T., and Yan, X.L., 2017b, H-O isotope characteristics and geological significance of the Heijianshan Fe-Cu (-Au) deposit in the Eastern Tianshan, Xinjiang: Mineral Deposits, v. 36, p. 38-56 (in Chinese with English abstract).

Zhao, L.D., Chen, H.Y., Zhang, L., Li, D.F., Zhang, W.F., Wang, C.M., Yang, J.T., and Yan, X.L., 2018a, Magnetite geochemistry of the Heijianshan Fe-Cu (-Au) deposit in Eastern Tianshan: metallogenic implications for submarine volcanic-hosted Fe-Cu deposits in NW China: Ore Geology Reviews, v. 100, p. 422-440.

Zhao, L.D., Chen, H.Y., Zhang, L., Zhang, W.F., Yang, J.T., and Yan, X.L., 2018b, The Late Paleozoic magmatic evolution of the Aqishan-Yamansu belt, Eastern Tianshan: constraints from geochronology, geochemistry and Sr-Nd-Pb-Hf isotopes of igneous rocks: Journal of Asian Earth Sciences, v. 153, p. 170-192.

Zhao, L.D., Chen, H.Y., Hollings, P., and Han, J.S., 2019, Late Paleozoic magmatism and metallogenesis in the Aqishan-Yamansu belt, Eastern Tianshan: constraints from the Bailingshan intrusive complex: Gondwana Research, v. 65, p. 68-85.

Zhao, X.-F., and Zhou, M.-F., 2011, Fe–Cu deposits in the Kangdian region, SW China: a Proterozoic IOCG (iron-oxide–copper–gold) metallogenic province: Mineralium Deposita, v. 46, p. 731-747.

Zhao, X.-F., Zhou, M.-F., Li, J.-W., Sun, M., Gao, J.-F., Sun, W.-H., and Yang, J.-H., 2010, Late Paleoproterozoic to early Mesoproterozoic Dongchuan Group in Yunnan, SW China: implications for tectonic evolution of the Yangtze Block: Precambrian Research, v. 182, p. 57-69.

Zhao X.-F., Zeng L.-P., Hu H., and Li, X.-C., 2016, Iron-oxide apatite deposits in eastern China formed by accumulation of magmatic hydrosaline chloride liquids: 34th IGC Meeting Proceedings, Cape Town.

Zhao, X.-F., Zhou, M.-F., Su, Z.-K., Li, X.-C., Chen, W.T., and Li, J.-W., 2017, Geology, geochronology, and geochemistry of the Dahongshan Fe-Cu-(Au-Ag) deposit, SW China: implications for the formation of IOCG deposits in intracratonic rift settings: Economic Geology, v. 112, p. 603-628.

Zhao, X.-F., Chen, W.-T., Li, X.-C., and Zhou, M.-F., 2019a, Iron oxide copper-gold deposits in China: a review and perspectives on ore genesis, *in* Goldfarb, R. and Chang, Z., eds., Mineral deposits of China: Society of Economic Geologists Special Publication, v. 22, p. 553-580.

Zhao, X.-F., Zeng, L.-P., Hu, H., and Hofstra, A.H., 2019b, Iron oxide-apatite deposits form from hydrosaline liquids exsolved from subvolcanic intrusions: Geological Association of Canada-Mineralogical Association of Canada, Program with Abstract, v. 42, p. 199.

Zhou, M.-F., Zhao, X.-F., Chen, W.T., Li, X.-C., Wang, W., Yan, D.-P., and Qiu, H.-N., 2014, Proterozoic Fe-Cu metallogeny and supercontinental cycles of the southwestern Yangtze Block, southern China and northern Vietnam: Earth-Science Reviews, v. 139, p. 59-82.

Zhou, T.F., Yuan, F., Zhang, D.Y., Fan, Y., Liu, S., Peng, M.X., and Zhang, J.D., 2010, Geochronology, tectonic setting and mineralization of granitoids in Jueluotage area, eastern Tianshan, Xingjiang: Acta Petrologica Sinica, v. 26, p. 478-520 (in Chinese with English abstract).

Zhou, T.F., Fan, Y., Yuan, F., Zhang, L.J., Ma, L., Qian, B., and Xie, J., 2011, Petrogenesis and metallogeny study of the volcanic basins in the Middle and Lower Yangtze metallogenic belt: Acta Geologica Sinica, v. 85, p. 712-730 (in Chinese with English abstract).

Zhou, T.F., Fan, Y., Yuan, F., Zhang, L.J., Qian, B., Ma, L., and Yang, X.F., 2013, Geology and geochronology of magnetite–apatite deposits in the Ning-Wu volcanic basin, eastern China: Journal of Asian Earth Sciences, v. 66, p. 90-107.

Zhu, Z., Tan, H., Liu, Y., and Li, C., 2017, Multiple episodes of mineralization revealed by Re-Os molybdenite geochronology in the Lala Fe-Cu deposit, SW China: Mineralium Deposita, v. 53, p. 311-322.

# Early Cambrian IOA-REE, U-Th and Cu(Au)-Bi-Co-Ni-Ag-As-Sulphide Deposits of the Bafq District, East-central Iran

**Farahnaz Daliran, Heinz-Günter Stosch**
*Institute for Applied Geosciences, Karlsruhe Institute of Technology, Karlsruhe, Germany*
*farahnaz.daliran@partner.kit.edu*

**Patrick J. Williams**
*Formerly at School of Earth and Environmental Sciences, James Cook University, Townsville, Australia*

**Heymat Jamali**
*Department of Geology, University of Isfahan, Isfahan, Iran*
*Formerly at the Geological Survey of Iran, Tehran, Iran*

**Mohammad-Bagher Dorri**
*Geological Survey of Iran, Tehran, Iran*

*In memory of Pat*

*Recommended citation: Daliran, F., Stosch, H.-G., Williams, P.J., Jamali, H., and Dorri, M.-B., 2022, Early Cambrian IOA-REE, U-Th and Cu(Au)-Bi-Co-Ni-Ag-As-sulphide deposits of the Bafq district, East-central Iran, in Corriveau, L., Potter, E.G. and Mumin, A.H., eds., Mineral systems with iron oxide copper-gold (IOCG) and affiliated deposits: Geological Association of Canada, Special Paper 52, p. 409-424.*

## Abstract

The Bafq metallogenic province hosts major (~1.8 Gt) sulphide-poor and REE-bearing, iron oxide-apatite (IOA) deposits that are transitional to REE- and apatite-rich rocks called 'apatitites'. The deposits are hosted by early Cambrian volcanic rocks (dominantly leucocratic rhyolites) and by volcano-sedimentary sequences of the Kashmar-Kerman Tectonic Zone in the eastern Central Iran structural province. The host rhyolites, along with equivalent Zarigan-Narigan type subvolcanic leucogranites, spilitic basalts and rare undersaturated rocks (nephelinite/basanite), form part of a felsic-mafic bimodal association that was modified by sodic and potassic metasomatism prior to REE-bearing, IOA mineralization and intrusion of late diabase dyke swarms. The sodic and potassic metasomatism dominantly resulted in the formation of sodic and potassic feldspars, along with local development of albitite. The ore fluids evolved from a high temperature, anhydrous mineral assemblage consisting of Ca-Mg-Fe-silicates (including calcium-rich pyroxene and REE-bearing calcium-rich garnet), to a magnetite ± hematite + LREE-fluorite-rich apatite assemblage. Apatite contains abundant monazite inclusions. Multistage actinolite is the most common ore-related alteration phase and formed instead of pyroxene at lower temperatures, locally accompanied by quartz. At lower temperatures, chlorite formed instead of actinolite, along with abundant quartz. The late-stage $CO_2$-$SiO_2$ fluids precipitated calcite and quartz, but were enriched in REE and formed LREE-bearing phosphates and silicates, as well as HREE-bearing phosphates, carbonates, silicates and oxides. Locally, abundant zircon ± baddeleyite, thorite/calcium-thorianite, uranium- and thorium-oxides, davidite, titanite and rutile formed with progressing metasomatism. Minor pyrite ± chalcopyrite characterizes the post-oxide, sulphide ore-stage, followed by talc alteration. Common late alteration phases include chlorite and tourmaline. Post-IOA mineralization formed economic concentrations of uranium-thorium at the Sagand deposit and Cu(± Au)-Mo-Bi-Co-Ni-Ag-As(Zn, Pb)-sulphide ore with pyrite + uranium-thorium oxide ore systems in the Narigan district.

A close spatial relationships between rhyolitic volcanism and mineralization, and the similar radiometric ages (ca. 528 Ma) of the host rhyolites and ore-related apatite and monazite support a direct relationship between early Cambrian high level magmatism and mineralization. The Bafq IOA deposits, their extension south to the Zarand area and to the Persian Gulf, regional ore-related alkali metasomatism, and association with bimodal volcanism that includes undersaturated alkaline rock components, together indicate a large-scale tectonomagmatic control on the mineralization related to short-lived early Cambrian extension along the volcanic arc of the Kashmar-Kerman Tectonic Zone. Geochemical signatures indicate input of ore-related alkali fluids from the mantle during extensional tectonic activity. Recent discoveries of Cu ± Au-Mo-Bi-Co-Ni-Ag-As-(Zn, Pb)-sulphide-pyrite ore and uranium-thorium ore systems, in association with high-temperature metasomatism, extend hundreds of kilometres south to the Persian Gulf, suggesting that additional economic IOCG deposits could occur within the Kashmar-Kerman Tectonic Zone.

## Résumé

La province métallogénique de Bafq renferme d'importants gisements (~1.8 Gt) à oxydes de fer-apatite (IOA), pauvres en sulfures et contenant des terres rares (ETR) qui évoluent vers des gîtes riches en terres rares et en apatite appelés 'apatitites'. Ces gîtes sont encaissés par les roches volcaniques à dominante rhyolitique du Cambrien précoce et les séquences volcanosédimentaires de la zone tectonique de Kashmar-Kerman dans le centre-est de l'Iran. Les rhyolites hôtes et leurs équivalents leucogranitiques sub-volcaniques de type Zarigan-Narigan, des basaltes spilitiques et de rares roches sous-saturées (néphélinite/basanite) font partie d'une association bimodale felsique-mafique qui a été modifiée par un métasomatisme sodique et potassique avant la minéralisation IOA à ETR et la mise en place d'essaims de dykes de diabase tardifs. Le métasomatisme sodique et potassique a principalement entraîné la crystallisation de feldspaths sodique et potassique et localement d'albitite. Les fluides minéralisés ont évolué d'un assemblage minéral anhydre à haute température composé de silicates à Ca-Mg-Fe (pyroxène riche en calcium et grenat riche en calcium et contenant des ETR) à un assemblage à magnétite±hématite+ETR légère-fluorine riche en apatite. L'apatite contient d'abondantes inclusions de monazite. L'actinolite est la phase d'altération la plus souvent liée au minerai et s'est formée à la place du pyroxène en plusieurs stages et à des températures plus basses (localement avec du quartz). La chlorite s'est formée à la place de l'actinolite à des températures encore plus basses et ce avec du quartz en abondance. Les fluides tardifs à $CO_2$-$SiO_2$ sont enrichis en ETR et ont formé des phosphates à terres rares légères et des silicates, ainsi que des phosphates à terres rares lourdes, carbonates, silicates et oxydes avec de la calcite et du quartz. Localement, une abondance de zircon ±baddeleyite, thorite/calcium-thorianite, oxydes d'uranium et de thorium, davidite, titanite et rutile se sont formés lors du métasomatisme. De la pyrite ±chalcopyrite mineure s'est formée au stade du minerai sulfuré postérieur aux oxydes suivi d'une altération en talc. Les phases d'altération tardives les plus courantes comprennent la chlorite et la tourmaline. Des concentrations économiques d'uranium-thorium au gîte de Sagand et du minerai à sulfures de Cu(±Au)-Mo-Bi-Co-Ni-Ag-As(Zn, Pb), pyrite et oxydes d'uranium-thorium du district de Narigan constituent les types de minéralisation postérieure aux gîtes IOA.

Des relations spatiales étroites entre le volcanisme rhyolitique et la minéralisation et les âges radiométriques similaires de l'apatite et de la monazite associées au minerai et les rhyolites hôtes à environ 528 Ma, appuient une relation directe entre le magmatisme hypabyssal du Cambrien inférieur et la minéralisation. Les gîtes IOA de Bafq, leur extension vers le sud jusqu'à la région de Zarand et au golfe Persique, le métasomatisme régional lié à la mineralization, l'association avec un volcanisme bimodal à composantes alcalines sous-saturées et un métasomatisme riches en éléments alcalins indiquent qu'un contrôle tectonomagmatique sur la minéralisation était lié à une brève période d'extension au Cambrien inférieur le long de l'arc volcanique de la zone tectonique de Kashmar-Kerman. Les signatures géochimiques enregistrent un apport de fluides minéralisateurs mantelliques riches en éléments alcalins pendant l'activité tectonique d'extension. Les découvertes récentes de systèmes minéralisés à sulfures à Cu±Au-Mo-Bi-Co-Ni-Ag-As(Zn, Pb) et à pyrite et de minerai d'uranium-thorium en association avec un métasomatisme à haute température s'étendant sur des centaines de kilomètres au sud du Golfe Persique suggèrent que des gisements économiques d'IOCG pourraient se trouver dans la ceinture tectonique Kashmar-Kerman du Cambrien précoce.

## Introduction

The Bafq district in the eastern part of the Central Iran structural province (Fig. 1) is one of the few global geological settings hosting distinctive occurrences of REE-rich iron oxide-apatite ores commonly referred to as 'Kiruna-type' (e.g. Geijer, 1930; Hildebrand, 1986; Nyström and Henriquez, 1994) or as iron oxide-apatite (IOA) deposits (Daliran et al., 2010; Williams, 2010). The IOA ores in the Bafq district are hosted by early Cambrian rhyolite and volcano-sedimentary units (ECVSU) that exhibit a large variety of high-temperature metasomatic alteration assemblages.

The early Cambrian IOA mineralization in the region of Bafq is localized along a major early Cambrian tectonic suture that extends from the Robat-Posht-Badam area in the north to the Jalal Abad-Zarand area in the Kerman region in the south, and hundreds of kilometres further to Hormuz Island in the Persian Gulf (Daliran, 1990) (Fig. 2). Although late-stage sulphides overprint the IOA ore stage in almost all deposits and form minor amounts of pyrite ± chalcopyrite mineralization, the IOA deposits of the Bafq district have not been historically known to display a regional association with economic copper-gold sulphide ores (IOCG deposits; Hitzman, 2000). This is in contrast with other well-known IOA districts such as the Norrbotten district in northern Sweden (Kiruna deposit) and the Andean Coastal Ranges (e.g. Williams et al., 2005; Barton, 2014). Enrichment in uranium and thorium, which overprints

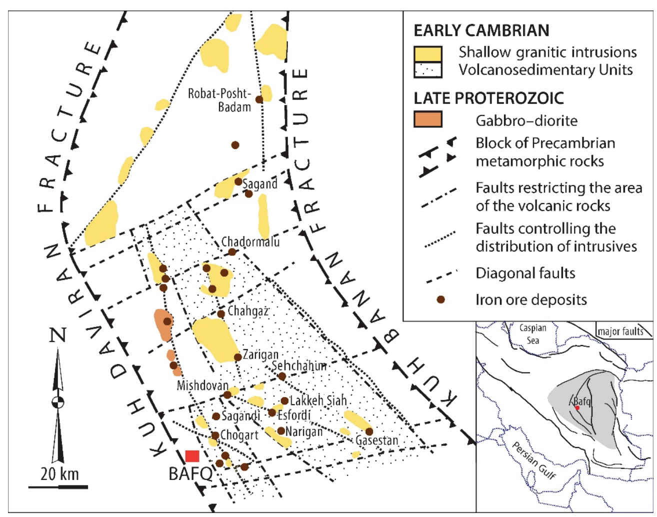


**FIGURE 1.** Distribution of IOA, phosphate (apatitite) (Zarigan, Esfordi), U-Th (Sagand), and Cu (± Au)-Mo-Bi-Co-Ni-Ag-As (Zn, Pb) sulphide-pyrite-U-Th (Narigan) ore deposits of the Bafq district, hosted by early Cambrian rhyolites and volcano-sedimentary units of the ECVSU. Note the structural control of the deposits imposed by the Kuh Daviran and Kuh Banan crustal faults, here referred to as the "Block of Precambrian metamorphic rocks". Shallow granitic intrusions are the Narigan-Zarigan-type leucogranites, and the "Precambrian gabbro-diorite" corresponds to earlier, ca. 533 Ma (Early Cambrian), unmineralized granodiorite-tonalite composite plutons of Ramezani and Tucker (2003) (modified from NISCO, 1980).

the IOA mineralization as trace amounts of oxide minerals (see below) in almost all of the Bafq IOA deposits, appears to have locally resulted in the formation of uranium-thorium deposits in the Bafq district. Thus, similar to the IOA deposits, the Sagand uranium-thorium deposit occurs in early Cambrian albite-actinolite ± Na-pyroxene-altered rocks in paragenetic association with high temperature K-feldspar-phlogopite and magnetite ± REE-apatite-carbonate metasomatism (NISCO, 1976, 1980; Samani, 1988; Samani and Talezadeh Lari, 1988; Gharesi and Karimi, 2011; Fazeli et al., 2014; Deymar et al., 2018). Recently, Cu-Au-Mo-Bi-Co-Ni-Ag-As(Zn, Pb)-sulphide + pyrite ore associated with uranium-thorium ore at the Narigan deposit (Gharesi and Karimi, 2011; Fazeli et al., 2014), and phosphorous-poor, IOA-type magnetite ore at the Jalal Abad deposit (200 Mt iron ore) were discovered within similarly metasomatically altered ECVSU (Gotlov and Esev, 1976; Karimi-Shahraki et al., 2016). The presence of native gold associated with the sulphide ore, currently only confirmed at the Jalal Abad deposit, supports the potential for undiscovered, economic IOCG mineralization elsewhere in the

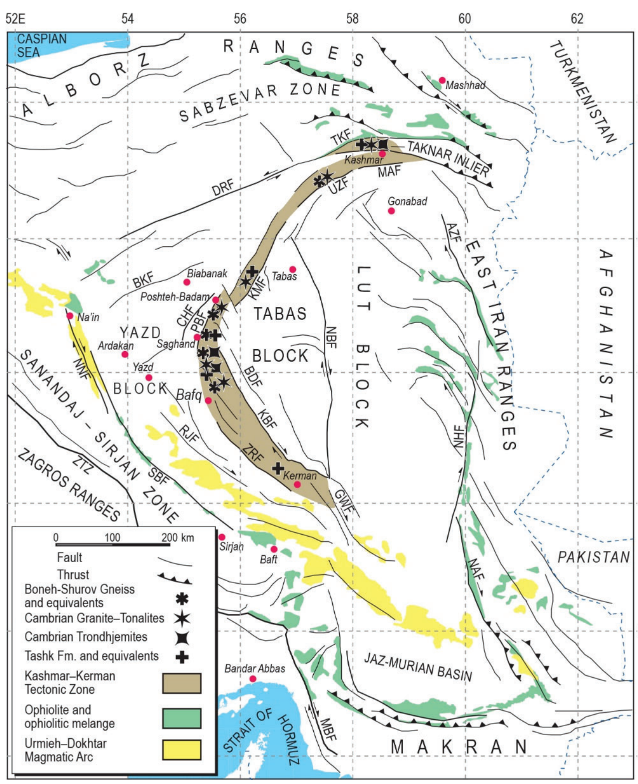


**Figure 2.** The metallogenic province of Bafq in the N-S-trending central section of the KKTZ is bordered by the major Kuhbanan (KBF) and Zarand (ZRF) crustal faults and extends southeastwards to Zarand in the Kerman region (Ramezani and Tucker, 2003). AZF: Abiz Fault; BDF: Behabad Fault; BKF: Biabanak Fault; CHF: Chapedony Fault; DRF: Doruneh Fault; GWF: Gowk Fault; KMF: Kalmard Fault; MAF: Mehdiabad Fault; MBF: Minab Fault; NAF: Nostratabad Fault; NHF: Nehbandan Fault; NNF: Na'in Fault; PBF: Posht-Badam Fault; RJF: Rafsanjan Fault; SBF: Shahre-Babak Fault; TKF: Taknar Fault; UZF: Uzbak-Kuh Fault; and ZTZ: Zagros Thrust Zone.

early Cambrian Kashmar-Kerman Tectonic Zone. As seen in the uranium-thorium ore, the formation of these sulphide ore minerals (±gold) is the result of overprinting of the IOA mineralization by a late sulphide stage (Daliran, 1990). Consequently, to the extent that metallogenic associations are currently known, the Bafq district provides an opportunity to study metasomatic events associated with IOA metallogeny. Specifically, it allows an understanding of how these systems evolve at regional scales to form IOA-REE, uranium-thorium and Cu±Au-Mo-Bi-Co-Ni-Ag-As(Zn,Pb)-sulphide-pyrite ore and associated uranium-thorium ore systems, and which economic metals will be ultimately deposited during district-scale metasomatic alteration. SEDEX lead-zinc mineralization occurs independently of IOA mineralization in separate sedimentary basins at the Kushk, Chahmir and Cheshmeh Firuz deposits (Gibbs, 1976; Rajabi et al., 2014).

This work is an update of a previous paper (Daliran et al., 2010) and presents the results of decades of studies of IOA mineralization in the southern sector of the Bafq-Robat Posht Badam region, including the Chogart deposit in the south and the Sagandi (North Anomaly), Mishdovan, Narigan, Esfordi, Lakkeh Siah, Gasestan, Sehchahun, Zarigan, Chadormalu and Chahgaz deposits in the north (Fig. 1). (Note variable English spelling of the local names in the literature.)

The metasomatic alteration-mineralization described in this work serves as a basic scheme to study other IOA±REE, uranium-thorium deposits of the Bafq district and, in part, the lead-zinc mineralization (e.g. Bonyadi et al., 2011; Fazeli et al., 2014; Rajabi et al., 2014; Heidarian et al., 2017; Khoshnoodi et al., 2017; Deymar et al., 2018). Close attention is paid to the small number and quality of geochemical analyses, particularly the whole-rock analyses of metasomatized rhyolites, as modification of original rock chemistry has led to the erroneous designation of these rhyolites as more mafic species such as dacite, andesite or trachyandesite, and to unjustified petrological interpretations. The general term alkali metasomatism is also used herein when sodic- and/or potassic-metasomatism were not specified in the original studies.

## The Bafq District

### *Regional Geology, Geodynamic Setting and Timing Relationships*

The Bafq district encompasses the 150 km, roughly north-south striking eastern domain of the early Cambrian Kashmar-Kerman Tectonic Zone in east-central Iran (Haghipour, 1974; Ramezani and Tucker, 2003). This zone is bordered by two major crustal faults that extend from Bafq in the south to Robat-Posht-Badam in the north (Fig. 2). The Bafq district comprises a substratum of Neoproterozoic metamorphic complexes and plutonic rocks, early Cambrian composite granite to diorite-gabbro plutons (533 ± 1 Ma granite-tonalite of Ramezani and Tucker, 2003), and younger, early Cambrian high-level magmatic and volcano-sedimentary units (ECVSU) that are largely unmetamorphosed. The high-level magmatism was largely explosive and mainly consists of felsic volcanic rocks of rhyolitic composition (528.2 ± 0.8 Ma; Ramezani and Tucker, 2003) that host the IOA and slightly younger, Narigan-Zarigan-type leucogranites that form large, subvolcanic bodies (525 ± 7 Ma trondhjemite of Ramezani and Tucker, 2003) intruding the host rhyolites. Rhyolites occur as voluminous subaerial pyroclastic tuffs and welded ash flow tuffs, and less commonly as lava flows and domes. The rhyolites are locally interstratified with fine-grained tuffaceous shale, dolomitic limestone and minor evaporites within the ECVSU. Basalts, commonly spilitic, locally occur in the ECVSU, and an extensive flow unit tens of metres thick extends over some kilometres along a north-south striking structure south of Zarigan. Rare, undersaturated basalts (nephelinite/basanite) were found in close association with spilitic basalts at Narigan and were followed by swarms of late diabase dykes. A different, sedimentary rock-dominated facies of the ECVSU, mainly consisting of slightly metamorphosed fine-grained clastic rocks and an upper carbonate member, occurs in the vicinity of several deposits and is unmineralized (Daliran, 1990; Jami, 2005). The large variation in thickness of the ECVSU to more than 1000 m records the development of horst-graben rift structures during the early Cambrian (Haghipour, 1974). A small (1–2 $km^2$) body of pinkish, syenite-like rocks at the quarry west of the Lakkeh Siah deposit has formerly been interpreted as granite (GSI, 1991); however, as it consists of perthitic albite with local transitions to coarse-grained, sodic pyroxene-sodic amphibole-bearing rocks (Fig. 4C-E), we suggest that this body represents a metasomatic rock, i.e. an albitite. Transitional facies containing apatite-magnetite ± titanite ± zircon overgrown by baddeleyite ± monazite and allanite, similar to the metasomatized rhyolites, also indicate a link with the regional albite metasomatism (see below). Peculiar, metre-scale bodies of coarse-grained gabbroic rocks intrude the uppermost, sedimentary rock-dominated, unmineralized ECVSU at Gasestan to the north of the mineralized rhyolites.

The IOA deposits display an intimate spatial and temporal association with early Cambrian high-level magmatism. The ca. 528 Ma age of the host rhyolites overlaps with ages obtained for the ore-related apatite (Bonyadi et al., 2011; Stosch et al., 2011) and associated monazite (Torab and Lehmann, 2007), indicating that mineralization took place within a short time span during the 528 Ma felsic volcanism and prior to the emplacement of diabase dykes that intrude the mineralized rocks. An erosional channel filled with detrital iron ore (sand and blocks) that dissects the ore body at Mishdovan (Daliran, 1990), and iron oxide ore pebbles in basal conglomerate of the early Cambrian formations (Haghipour, 1974), mark the presence of an unconformity and indicate that IOA mineralization terminated prior to uplift and erosion that marked the onset of a new tectonic cycle in the early Cambrian.

The tectonomagmatic setting of mineralization in the Bafq district has long been a matter of debate. This structural zone was previously considered to have developed during Pan-African crustal extension (Haghipour, 1974; Berberian and King, 1981; Samani, 1988; Daliran, 1990; Daliran et al., 2009, 2010), and was recently interpreted as a magmatic arc that formed during the early Cambrian along the Proto-Tethyan margin of Gondwana (i.e. the KKTZ; Ramezani and Tucker, 2003). However, the petrochemical study supporting this magmatic arc model was based on samples of metasomatized rhyolite and the Zarigan leucogranite; the extensive spilitic basalts and undersaturated rocks, the late diabase dykes, alkali metasomatism, and the huge amounts of the Fe-P-REE-U introduced during this period were not considered in this tectonomagmatic model.

Early Cambrian high-level magmatism encompassed a variety of rocks ranging from rare undersaturated alkali basalts, basalts, and host felsic volcanic rocks (rhyolite) (Fig. 3). The shift of felsic host rock composition from an original rhyolite to rhyodacite-dacite is due to the metasomatic exchange with external fluids during IOA metallogenesis, i.e. a result of alteration. In the study area, rocks with intermediate composition (andesites) were only found at a single location at Sehchahun district, within a distinct, unmineralized volcano-sedimentary sequence. This indicates that early Cambrian volcanism was bimodal, largely consisting of rhyolites and basalts. These data and the petrochemistry of the early Cambrian magmatic rocks (Daliran and Stosch, unpublished data) strongly support a phase of back-arc extension in close proximity to the active continental margin of Ramezani and Tucker (2003), confirming the long advocated extensional tectonics in the region. In this model, geochemical data indicate that a major mantle-derived component was intruded into the host rhyolites, inducing pervasive alkali metasomatism along with IOA and related mineralization.

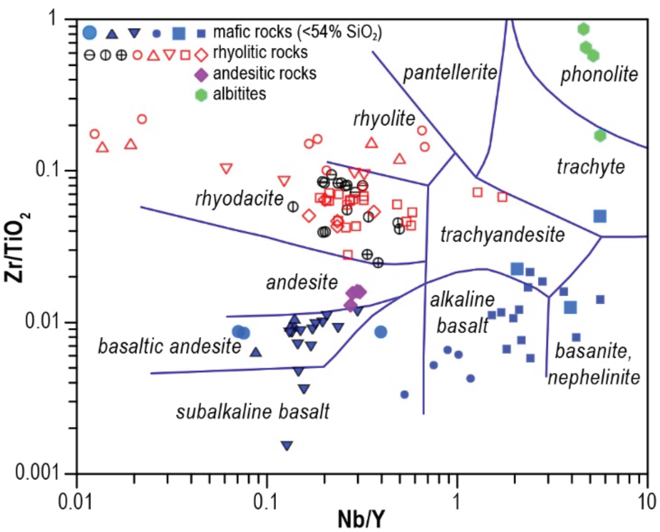


**FIGURE 3.** Nb/Y versus $Zr/TiO_2$ diagram of Winchester and Floyd (1977) for early Cambrian volcanic rocks between Chogart and Zarigan in the Bafq region. Concentrations of elements typically assumed to be immobile have been modified during ore-related metasomatic processes, resulting in displacement of the host rhyolites towards the dacite-rhyodacite and trachyandesite fields. Unmineralized andesite and mafic rocks plot normally, and metasomatic "albitite" plot in the field of trachyte-phonolite.

*Protoliths*

In all the deposits examined in this study (e.g. Chogart, Sagandi, Mishdovan, Narigan, Esfordi, Lakkeh Siah, Gasestan, Zarigan, Chadormalu and Chahgaz), rhyolites are the most common rocks at regional- to deposit-scales, and also host the ore. They occur as voluminous pyroclastic rocks, or are intercalated with other strata in the ECVSU. As mentioned above, the upper ECVSU sedimentary member, which occurs in the hanging wall of many of the studied deposits, is unmineralized. Spilitic basalts are locally intercalated with sedimentary rocks of the ECVSU, such as at the Mishdovan deposit, but their stratigraphic position relative to the host rhyolites is unclear. Small concentrations of iron oxide lenses in spilitic basalts result from alteration of the iron-magnesium minerals (Haghipour, 1974; Daliran, 1990); however, the iron oxide lenses are not associated with the distinctive mineral assemblages of IOA deposits such as apatite and REE-minerals, indicating that they are unrelated to the IOA.

Rhyolites form tuffs and thick sheets of welded ash flow tuff up to a few hundred metres thick. They are very leucocratic, having no ferromagnesian minerals, and display aphanitic textures with variable amounts of tiny quartz and feldspar phenocrysts. These high alkali-silica volcanic rocks were commonly termed 'keratophyres' by Soviet geologists (NISCO, 1980), who recognized that their strong alkaline character was induced by alkali feldspar metasomatism. Individual sheets of the welded ash flow tuffs display relics of flow lineation, pumice and glass shards in a large number of deposits, indicating that the early Cambrian volcanism in the Bafq district was largely explosive. The welded ash flow tuffs are recognizable by their flattened glass shards and the micropoikilitic quartz devitrification texture under the microscope (Figs. 4A, 8D–F). Lavas are not abundant and commonly exhibit perlitic and spherulitic devitrification textures. Lava domes intrude the host rhyolites and the ECVSU at a few localities but are unmineralized, e.g. Mishdovan (Daliran, 1990) and Esfordi (Jami, 2005).

## Metasomatic Alteration

The IOA of the Bafq district formed by successive, multistage, metasomatic processes, consisting of an early, pre-ore regional alkali alteration, and district-scale, REE-bearing, iron oxide-apatite and apatite-rich (forming apatitites) metasomatism (Daliran et al., 2007, 2009, 2010).

*Regional Pre-ore Alkali Alteration*

In the region of Bafq, the early Cambrian rhyolites display a strong alkaline affinity, incorporating a range of sodic to potassic compositions induced by extensive, pre-mineralization albitization and K-feldspar alteration (Fig. 4B-D). The regional-scale alkali metasomatism happened prior to introduction of the ore fluids. Relicts of albite (if of metasomatic origin) in the K-feldspar suggests that sodic-metasomatism predated potassic-metasomatism. The intensity of sodic relative to potassic metasomatism varies in different deposits, but the controlling factors of this variation remain to be studied.

Albitization associated with formation of scapolite and phlogopite in relation to IOA mineralization in the region of Bafq-Biabanak was recognized by Haghipour (1974), but the observation of such metasomatism in the rhyolites did not gain significant attention by subsequent workers. Haghipour (1974) attributes formation of scapolite to the transformation of earlier plagioclase to scapolite + albite by influx of $CO_2$ and calcium-bearing metasomatic fluids. Albitization of ferric pyroxene and amphibole, causing the liberation of iron, was proposed as a source of iron for the IOA ores.

Welded ash flow tuffs at Gasestan are extremely rich in potassium (10 wt% $K_2O$, 0.2 wt% $Na_2O$), a result of K-feldspar alteration. This is displayed by K-feldspar replacement of feldspar phenocrysts and by a K-feldspar-rich matrix that imparts a reddish hue to the rhyolites (augmented by a 'dusting' of iron oxide) (Fig. 8D). Most samples of alkali metasomatized rhyolite from the Chogart deposit are rich in sodium (7.2 wt% $Na_2O$, 0.2 wt% $K_2O$), whereas Lakkeh Siah samples have variable Na/K ratios. Although changes in Na/K values within the pyroclastic units could locally reflect eruption from chemically zoned magmas as suggested by Daliran (1990), our recent studies indicate extensive overprinting of the host rhyolites by regional sodic- and potassic-metasomatism. Texture-destructive albitization has locally led to the formation of coarse-grained albitites having very low quartz contents (Fig. 4B–D). Although albitites in some instances resemble syenite-like igneous rocks, as mentioned above, features such as transitional facies from fine-grained alkali metasomatized rhyolites to coarse-grained albitites, and to Fe-Mg-Ca-silicate-bearing albite rocks with magnetite-apatite and monazite (Fig. 4E), support their metasomatic origin. It also indicates an evolution from sodic, to high-temperature Na-Ca-Fe and Ca-Fe alteration and IOA mineralization, as commonly observed in ore systems with iron oxide and alkali-calcic alteration (cf. paragenetic model of Corriveau et al., 2016, 2018, 2022).

*Ore-related Metasomatism: Iron Oxide-apatite-REE Ores and Apatitites*

Major (1.8–2 Gt), high-grade (up to 65 wt% Fe), sulphide-poor, iron oxide-apatite ores, mainly consisting of magnetite with subordinate hematite, occur within a 150 km-long, narrow structural corridor from Bafq in the south to Robat-Posht-Badam in the north, and are distributed over 34 major aeromagnetic anomalies, some shown in Figure 1. Resources in individual deposits vary from 20 Mt at Mishdovan to over 500 Mt at Chogart and Chadormalu (NISCO, 1980). The iron oxide ore is commonly associated with and transitional to apatite-rich rocks termed "apatitites", which locally form small LREE-rich phosphate deposits such as at Esfordi and Zarigan. Apatite concentrations display large variations within the IOA deposits of the Bafq district, leading to their classification as apatite-poor and apatite-rich ores for ore processing purposes and for classification of the IOA (NISCO, 1980).

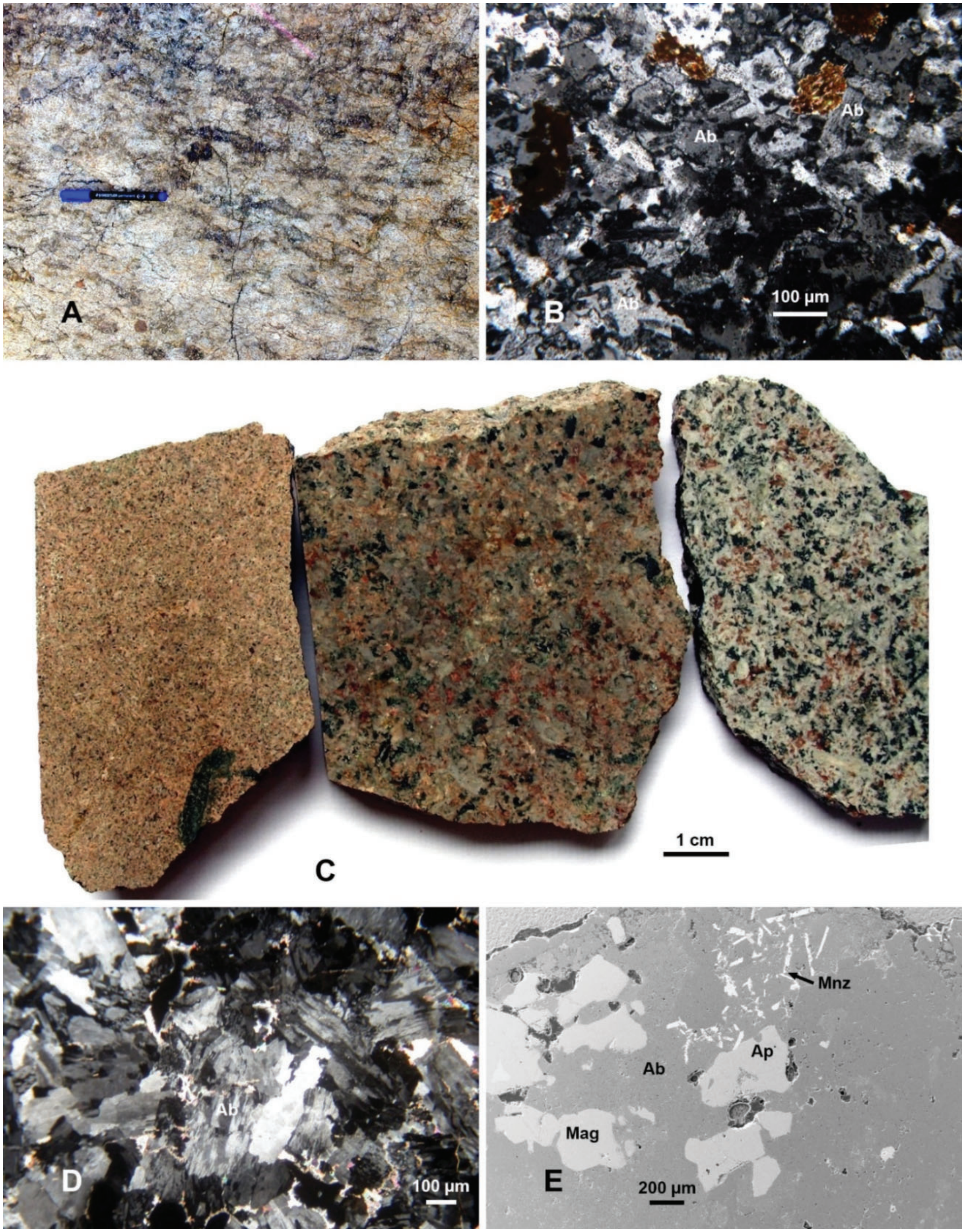


Figure 4. **A.** Rhyolitic welded ash flow tuff displaying flattened pumice shards (Lakkeh Siah deposit). **B.** Photomicrograph of the albitized host rhyolites (keratophyres) displaying fine-grained microperthitic albite with minor quartz (Chogart deposit). **C.** Rock slabs of syenite-like albitites and sodic-calcic alteration zones from the quarry between Lakkeh Siah and Sehchahun. The samples are albite-rich, perthitic rocks ranging from a fine-grained, Fe-Mg-silicate free, pink albitite (left), to coarse-grained aegirine-albite metasomatites with accessory apatite, magnetite, titanite, zircon-baddeleyite, REE minerals and late calcite (right). **D.** Photomicrograph showing advanced albitization (albitite) comprising coarse-grained chessboard albite (Chogart deposit). E. Backscatter electron (BSE) image of an albitite overprinted by the ore-related, metasomatic mineral assemblage of magnetite, apatite, and monazite, in a matrix of metasomatic albite. *Ab*=albite, *Ap*=apatite, *Mag*=magnetite, *Mnz*=monazite.

## Deposit Morphologies and Mineralization Styles

Diverse IOA mineralization styles and shapes of ore bodies are observed in the Bafq district, a result of multistage metasomatic processes within the subaerial rhyolite tuffs and the ECVSU as a whole. The alteration style can vary within a given deposit according to a variety of parameters that appear to reflect the mode of replacement of subaerial tuffs and submarine ECVSU, as well as the prevailing local ore fluid composition and temperature. Ore bodies within the ECVSU display stratabound as well as stratiform-like geometries. The geological map (Fig. 5) displays a typical example of IOA mineralization within the ECVSU, although in some instances, it is difficult to ascertain the primary nature of the ore beds. Stratiform-like ore bodies form fine-laminae (Fig. 6A), layers, and lenses of magnetite and hematite ore, and occasionally exhibit slumped and overturned ore beds and reworked ore (Daliran, 1990; Jami, 2005). These features have been taken as evidence of a submarine sedimentary environment during ore precipitation and interpreted as evidence of synvolcanic-sedimentary ores. However, recent work on global iron oxide and alkali-calcic alteration systems has shown that magnetite- or hematite-rich layers with regular to irregular thicknesses, tapered layering, and anastomosing features, are more typical of stratabound replacement (cf. Mumin et al., 2010; Corriveau et al., 2022). Ores within the ECVSU occur, in some instances, such as at Mishdovan and Lakkeh Siah deposits, in association with brownish carbonate lenses of undefined origin (Fig. 6B). These carbonate lenses are filled with millimetre-scale, yellow apatite crystals at Mishdovan deposit (Daliran, 1990). Local jaspilitic ore (with no apatite) in the area of the Gasestan deposit (Fig. 6C), where the host rhyolite is also intensively silicified (and chloritized), as well as at Esfordi (Jami, 2005), has been regarded as syn-sedimentary, but could also be metasomatic in origin. The iron-manganese oxyhydroxide ore at Narigan is another example of iron oxide deposits in the Bafq district that have been classified as syn-volcanic sedimentary ores poor in phosphorous (NISCO, 1980). Authigenic minerals such as quartz, alkali feldspar and anhydrite are locally observed in ore deposits hosted by the ECVSU (Fig. 6D).

Metasomatic replacement, during or shortly after sedimentation, is advocated for the stratabound ores within the ECVSU. Stratabound ore bodies occur within the subaerial rhyolite tuffs, as well as the ECVSU, and exhibit relicts of metasomatized and mineralized tuff beds. Stratabound apatite-magnetite ore having clear replacement features occurs in rhyolite tuffs,

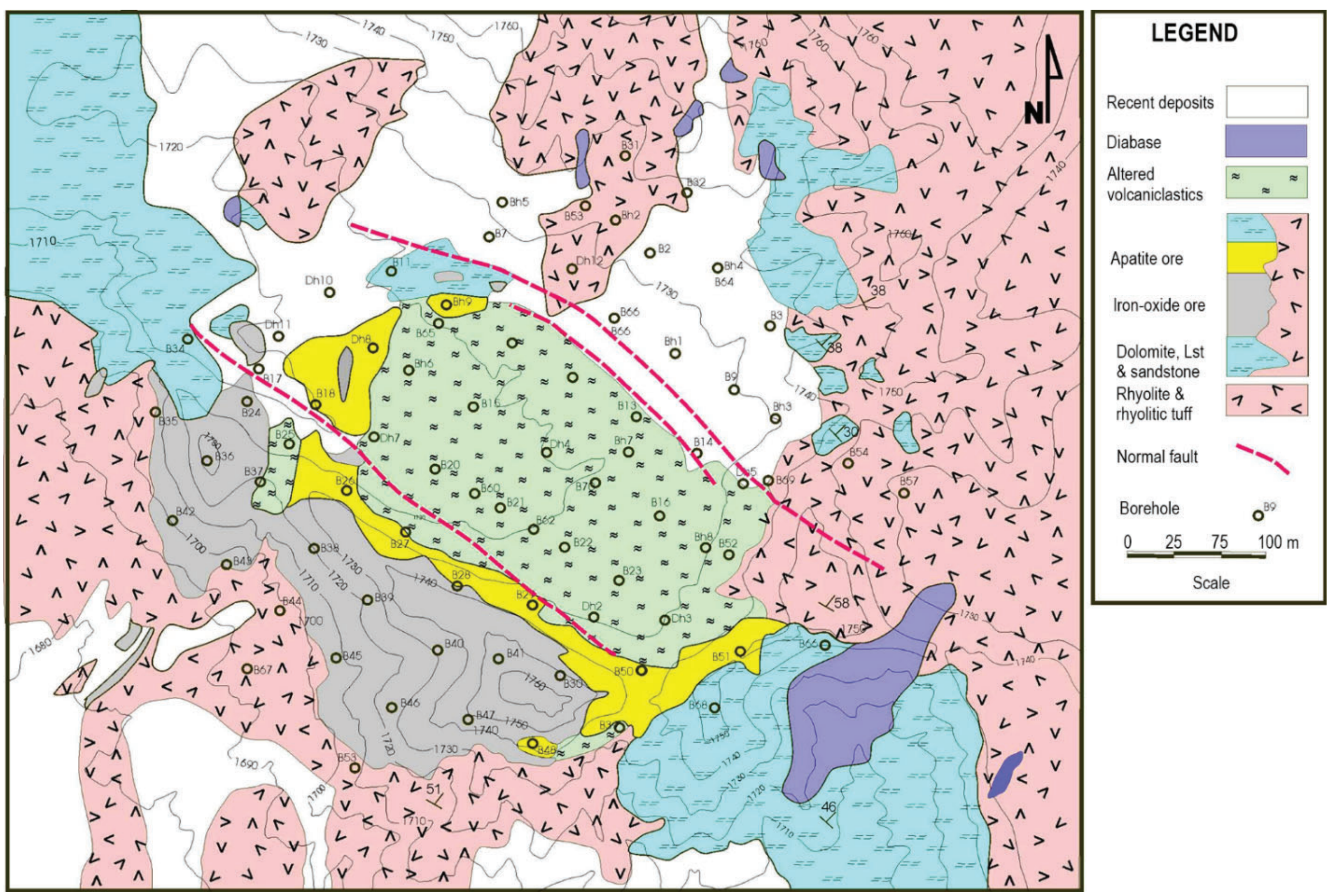


**FIGURE 5.** Geological map of the Esfordi iron oxide-apatite and apatite ore (apatitite) deposit, representative of a sedimentary rock hosting IOA in the ECVSU (from Jami, 2005). Other deposits such as at Mishdovan have similar settings (see Daliran, 1990). See Figure 1 for location.

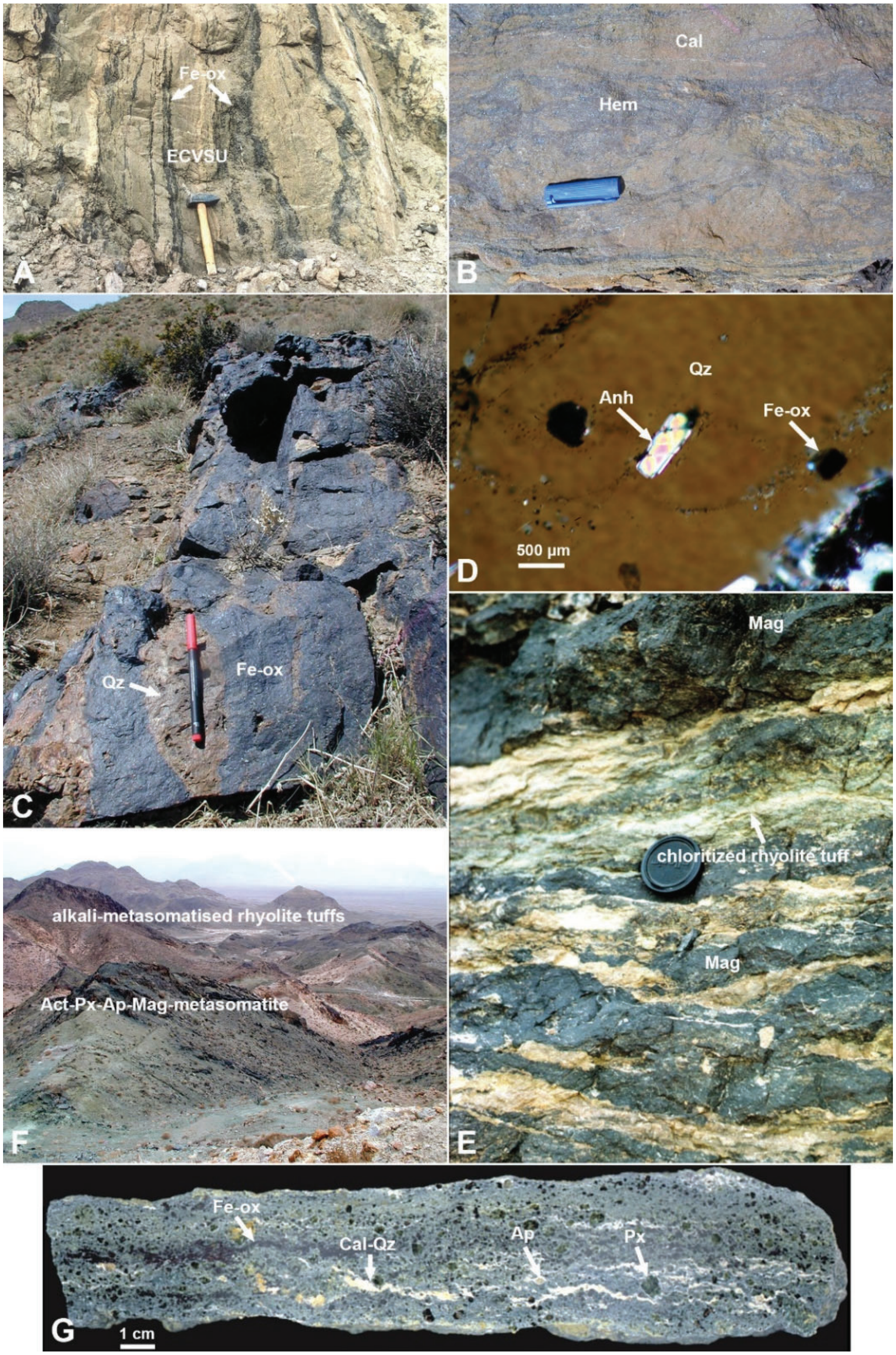


FIGURE 6. **A.** Stratiform-looking laminae of reworked iron oxide ore in vertical strata of the ECVSU at the Esfordi deposit (from Jami, 2005). **B.** Finely laminated specular hematite ore in carbonate lenses (Lakkeh Siah deposit). **C.** Jaspilitic iron oxide ore with brownish chert lenses (Gasestan deposit). **D.** Photomicrograph of anhydrite and hematite in authigenic quartz displaying growth zoning marked by iron oxide pigmentation in reworked ore (Lakkeh Siah deposit). **E.** Stratabound magnetite ore in chloritized rhyolite tuffs in ECVSU, below the massive magnetite-apatite ore (Mishdovan deposit). **F.** Alkali-feldspar metasomatized host rhyolite tuff, seemingly subaerial, displaying bedding in actinolitized sectors (Lakkeh Siah ore body no. II). **G.** Polished slab of the actinolitized tuff in (F) displaying stratabound, replacement ore consisting of a fine-grained actinolite matrix containing dispersed tiny crystals of pyroxene and apatite, discrete iron oxide, and late carbonate seams. *Act*=actinolite, *Anh*=anhydrite, *Ap*=apatite, *Cal*=calcite, *Fe-ox*=iron oxide, *Hem*=hematite, *Qz*=quartz, *Mag*=magnetite, *Px*=pyroxene.

e.g. at the Lakkeh Siah and Mishdovan deposits (Fig. 6E–G). Both the stratabound and stratiform-like ore bodies may occur at a single deposit (e.g. Mishdovan, Gasestan, Lakkeh Siah), although in some cases, where there is a strong alteration overprint, it is difficult to ascertain if a particular ore body is stratiform or stratabound.

Non-stratabound epigenetic ore occurs as very large podiform bodies of over 500 Mt (e.g. Chogart and Chadormalu deposits), as large lensoidal bodies (e.g. Gasestan deposit) in which the host, alkali-metasomatized rhyolite was variably mineralized by iron oxide-apatite ore fluids. More rarely, such as at Zarigan, apatite-rich rocks form dyke-like pegmatoidal bodies of apatitite a few metres in diameter. Apatitites also occur at the contact zone between the IOA ore body and host rhyolites at the Esfordi phosphate deposit (Fig. 5), as well as in strongly brecciated zones at the Chogart deposit, where they also cut the ore body itself. Such ore bodies appear to have formed along major structures that could have served as ore fluid conduits, such as at the Chogart deposit, where the apatitite is emplaced along a 0.5 km zone parallel to a major northwest-southeast fault (G. Dehghani, personal communication, 2008). Likewise, the extension of the alteration zone at Gasestan, where ore lenses are located along the east-west valley bordering the mineralization to the north, could be related to a cryptic structure.

*Ore Breccias*

A variety of breccias occur in the IOA deposits of the Bafq district; brecciation ranges in scale from hand specimen to microscopic. Aside from brecciation reflecting the multiple stages of metasomatism and mineralization, many breccias form part of IOA ore itself.

The ore breccia at the Gasestan deposit resembles hydrothermal brecciation consisting of fragments of silicified-chloritized host rhyolite cemented by apatite-magnetite ore (Fig. 7A–B), whereas local reworked ore clasts in reworked ores at the Mishdovan and Esfordi deposits are considered to be a product of syn-sedimentary brecciation (Daliran, 1990; Jami, 2005). In many other cases, such as at the Chogart deposit, ore breccias are apatite-rich rocks (apatitites) that are largely confined to the milled zones at the contact of the ore body with the albite-metasomatized host rhyolites. These apatitites also cross-cut the orebody itself, and occur as an interlayering of laminae and brecciated and fluidized apatite crystals (Fig. 7C–E). The dyke-like, pegmatoidal apatite-pyroxenite at Zarigan consists of large "shattered" crystals of early stage pyroxene and apatite in a matrix of late calcite. In these breccias, the early stage minerals (pyroxene, apatite, magnetite, actinolite) locally occur as a segregation of crystal fragments typical of fluidized breccias, whereas the late calcite-quartz matrix is undisturbed (Figs. 7D–E, 9A). A variety of breccias recording multiple stages of metasomatism and mineralization are displayed in Figure 8A–B, and can be inferred from Figures 9A–C and 10A–D, G.

The mechanism(s) of diverse ore brecciation are still not well understood, but many breccias do share characteristics of the fluidized breccias described by Jébrak (2010). Restriction of the ore breccias to the ore bodies suggests that brecciation was triggered by the ore fluids and the physicochemical conditions at the time of ore formation. The intensity of brecciation appears to increase with increasing apatite and locally with increasing late-stage calcite, implying a build-up of fluid pressure because of the increase in volatile components. Daliran (2002) proposed that this type of brecciation resulted from transport of earlier-formed solid crystals to shallower crustal levels by supercritical fluids.

*Mineral Assemblage-mineralization Style*

In both groups of ore deposits, i.e. those formed within the ECVSU and those in subaerial tuffs, varied mineralization styles can be distinguished by their early mineral assemblages, which reflects the temperature of the ore-forming fluids. Formation of high-temperature actinolite ± diopside, or alternatively chloritization, started during the early ore-stage alteration. The high-temperature mineral assemblage commonly comprises diopside in pod-like ore bodies and in the apatitites at Chogart, as well as in dyke-like pegmatoidal apatitites at Zarigan. At Esfordi and at Lakkeh Siah, the high-temperature assemblage includes garnet. Actinolite occurs instead of pyroxene in a number of deposits, such as at Mishdovan (Daliran, 1990), reflecting the evolution of high-temperature calcium-iron assemblages in which diopside is early and gradually replaced by, or gives way to, the crystallization of amphibole (Corriveau et al., 2016). At the Sagandi deposit, formation of actinolite is associated with silicification of the alkali metasomatized rhyolites. At the Gasestan deposit, the extremely apatite-rich iron oxide ore is associated with chloritization and silicification instead of high-temperature pyroxene-actinolite, suggesting lower temperatures during metasomatic alteration of this deposit.

In the IOA deposits of the Bafq district, magnetite largely dominates over hematite, and apatite + REE contents vary in individual deposits. The Sagandi deposit contains relatively apatite-poor, iron oxide ore. The Narigan iron oxide ore deposit, which comprises almost apatite-free, jaspilitic iron ± manganese oxyhydroxide ores, is an example of what has been characterized as low-temperature sedimentary ore. The controlling factors on the formation of magnetite or hematite and the relative abundance of apatite are not yet well understood, but appear to be, in part, controlled by local physicochemical conditions of the ore fluids.

Ore-related, incipient metasomatism is best represented by discrete, selective, texture-preserving actinolitization and by iron oxide replacement of alkali-altered welded ash flow tuffs distal to the ore bodies (Fig. 8D–F). Modification of the original rhyolite composition by this type of discrete metasomatism is commonly not recognized, leading to misinterpretation of the rhyolites as dacite, andesite, trachyandesite, etc. Two or more alteration-mineralization styles are locally present within the area of a given deposit (e.g. REE-apatite-magnetite ore, as well as jaspilitic iron ore at Gasestan), although their relationships may be unclear.

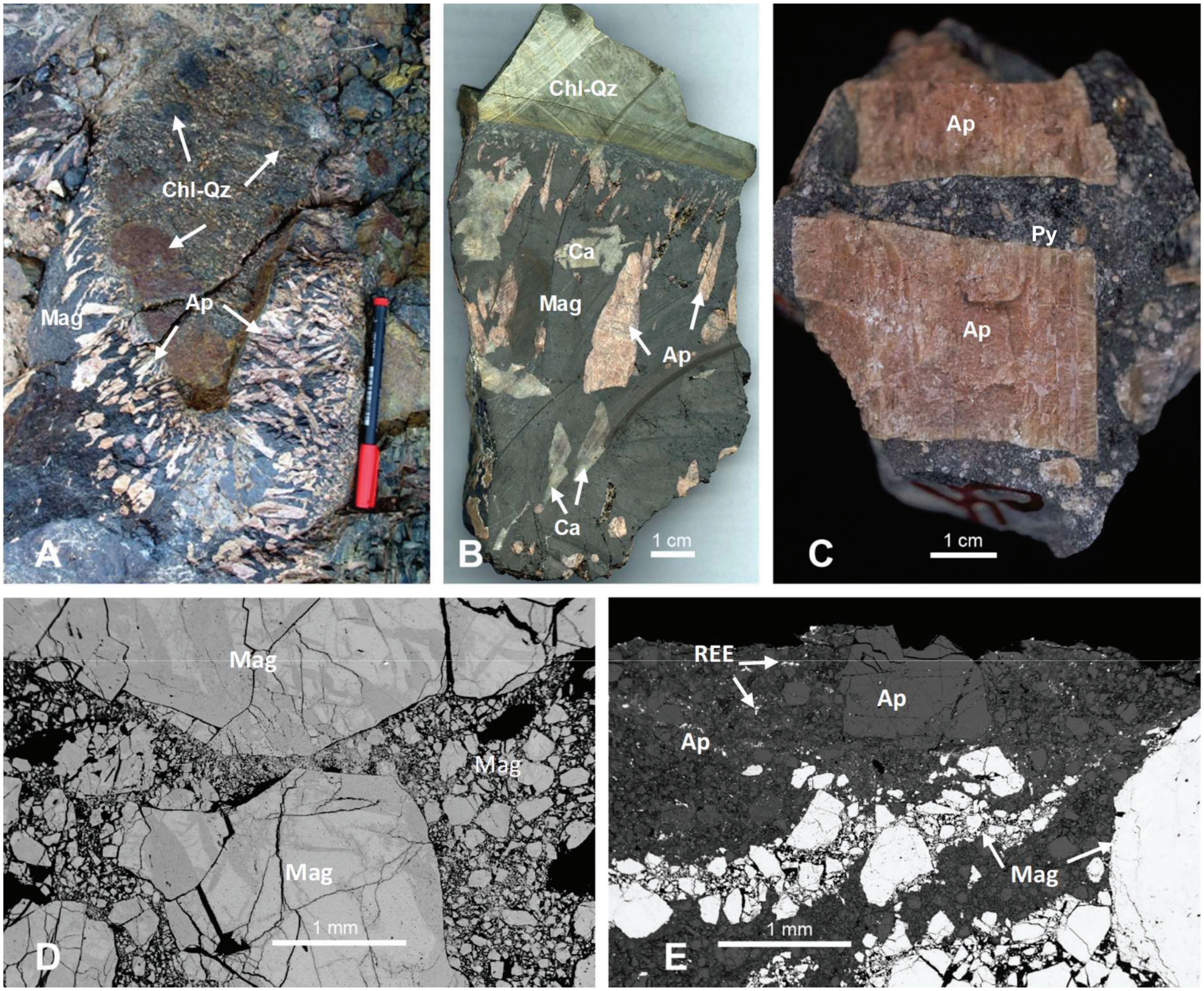


**FIGURE 7. A.** Apatite-magnetite ore displaying multistage "hydrothermal" brecciation. Small fragments of silicified-chloritized tuff in the core are cemented by fine-grained apatite-magnetite. A thick rim of later, coarse-grained apatite-magnetite where apatite exhibits unidirectional growth mantles the core fragment (Gasestan deposit). **B.** Close-up of (A) displaying the unidirectional growth of apatite crystals on a very compact and fine-grained silicified-chloritized tuff clast. Light gray patches consist of late calcite. **C.** Two large fragments of pegmatoidal apatite and milled apatite crystals in a matrix of post-oxide sulphide-stage pyrite (Chogart deposit). **D.** BSE image showing milled magnetite grains (martitized) in the magnetite ore (Mishdovan deposit). **E.** BSE image displaying laminar segregation of milled apatite crystals and magnetite in a matrix of late calcite that is associated with minute dispersed grains of REE-minerals (Mishdovan deposit). *Ap*=apatite, *Cal*=calcite, *Chl*=chlorite, *Qz*=quartz, *Py*=pyrite, *REE*= rare earth element minerals.

### Mineral Chemistry and Fluid Evolution

Almost all ore types display a similar evolution pattern represented by the following paragenetic stages: The early ore-stage mineral assemblage consists of high temperature, commonly anhydrous, calcium-rich silicates consisting of diopsidic pyroxene $(Fe_{0.2}Mg_{0.8}Ca_{0.9}Na_{0.1})Si_2O_6$ ± andradite-grossular garnet $(Ca\text{-}REE)_3Fe_2(SiO_4)_3$, followed by actinolite $(Ca_{1.8}Na_{0.2}Fe_{0.8}Mg_{4.2})(\pm Al_{0.2})Si_8O_{22}(OH)_2$ (Fig. 9A–C). The actinolite formed either by metasomatism of the earlier pyroxene, or crystallized independently at lower temperatures than pyroxene. At Sagandi (an apatite-poor, magnetite-hematite deposit), actinolitization is associated with silicification of alkali-metasomatized rhyolites. At the Gasestan deposit, extremely apatite-rich magnetite ore overprints K-feldspar-altered, chloritized-silicified rhyolite instead of high-temperature pyroxene and actinolite. Such chlorite-quartz-altered, alkali-metasomatized rhyolites, which are very fine-grained, compact and extremely hard, do not display any relicts of earlier pyroxene or actinolite, indicating lower temperatures of metasomatic alteration.

Following the introduction of REE-F-Cl(OH)-P-Fe ore fluids, large, euhedral, yellow, transparent or whitish crystals of apatite up to 30 cm long formed at the Chogart, Mishdovan, Esfordi, Lakkeh,

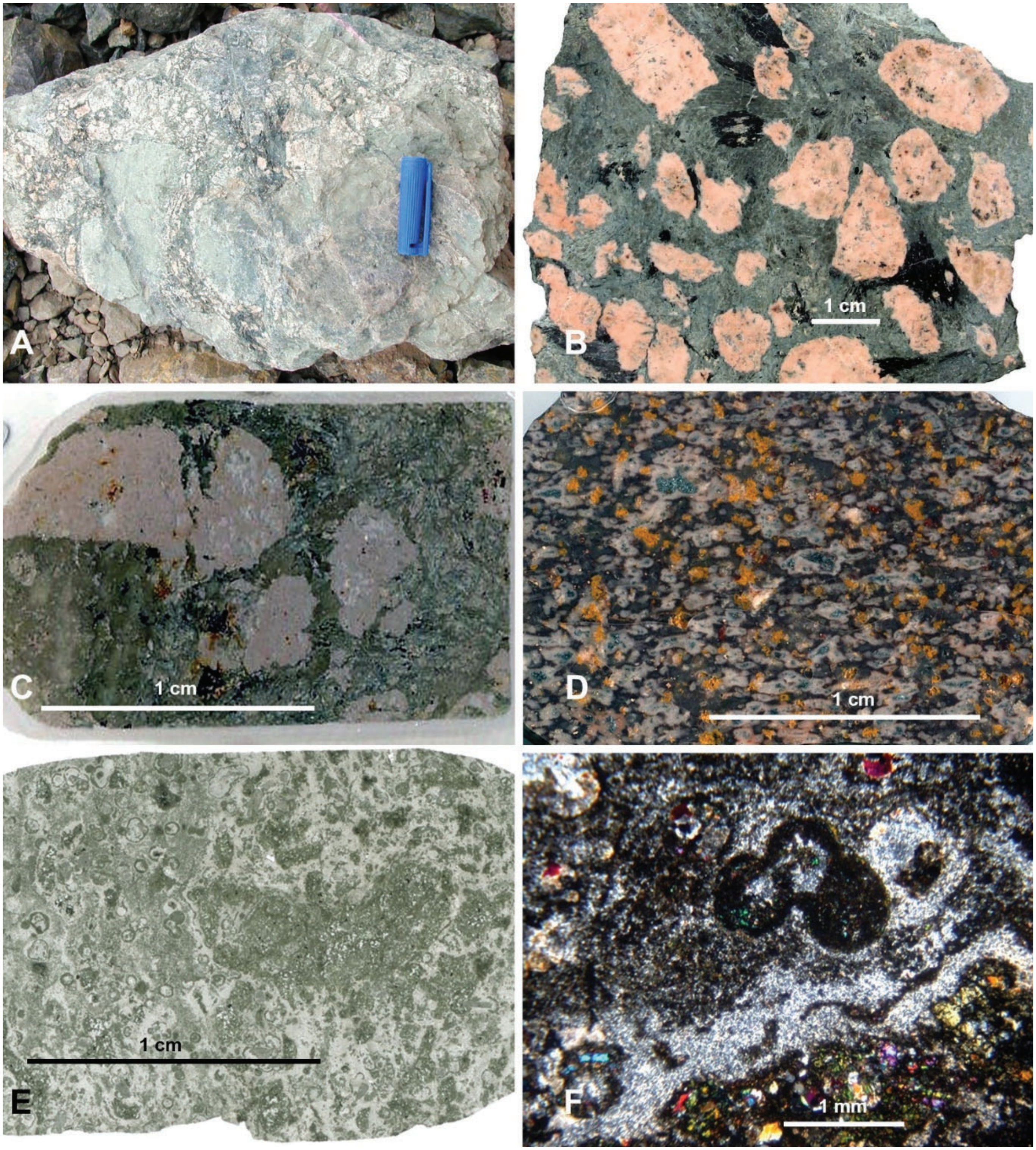


**Figure 8. A.** Multistage metasomatism associated with brecciation, displayed by fragments of alkali-altered rhyolite overprinted by actinolite and crosscut by a younger, breccia-matrix actinolite (Chogart deposit). **B.** Polished slab displaying actinolite ± pyroxene alteration and brecciated, alkali-altered rhyolite (pink fragments) from (A). **C.** Polished thin section showing relicts of alkali feldspar-altered rhyolite overprinted by actinolite ± pyroxene alteration in (B). **D.** Rock slab displaying incipient iron oxide metasomatism of K-feldspar-altered welded ash flow tuff along flow lineation, here displayed horizontally by flattened pumice shards and by feldspar phenocrysts. Iron oxide metasomatism has resulted in a red wine coloration to the Gasestan rhyolites. **E.** Polished thin section showing non-destructive replacement of an ash flow tuff by actinolite, as displayed by preserved glass and pumice shards (Chogart deposit). **F.** Photomicrograph of non-destructive actinolitization in the ash flow tuff from (E), displaying preserved flow lineation and round micropoikilitic quartz grains (Chogart deposit).

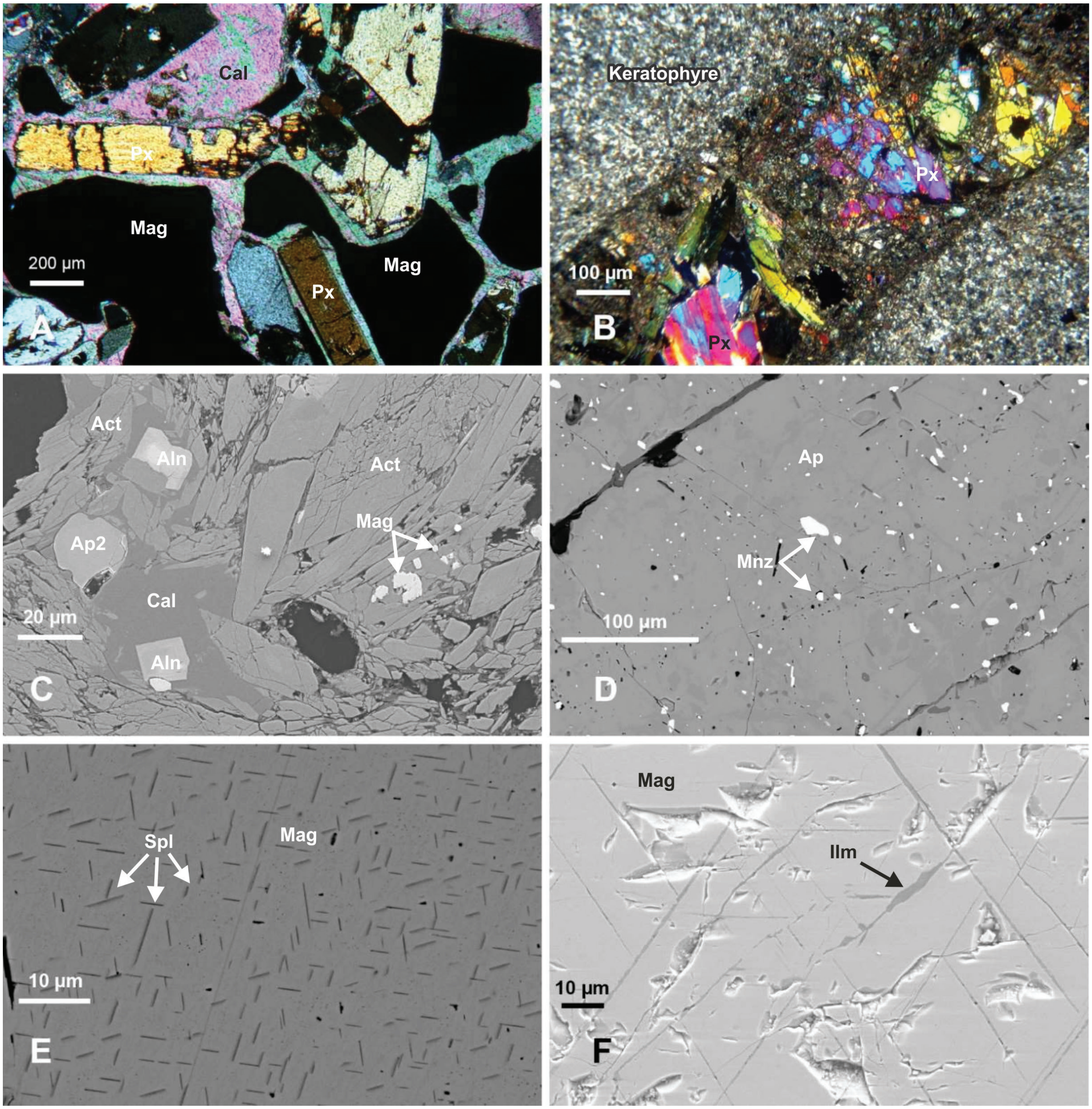


**Figure 9. A.** Photomicrograph showing large, euhedral, early-stage diopside and magnetite crystals, brecciated and overprinted by late-stage calcite (Chogart deposit). **B.** Photomicrograph of an intensively "crushed" pyroxene-actinolite vein crosscutting albitized rhyolite ("keratophyre", Chogart deposit). **C.** BSE image showing pervasive actinolitization, tiny magnetite grains, second-stage apatite2, and zoned allanite crystals with REE-rich cores in late calcite-quartz matrix (Lakkeh Siah deposit). **D.** BSE image showing abundant monazite inclusions exsolved from the early-stage apatite (Gasestan deposit). **E.** BSE image showing exsolved lamellae and blebs of spinel in magnetite ore (Mishdovan deposit). **F.** BSE image showing ilmenite trellis exsolved from Ti-bearing magnetite (Lakkeh Siah deposit). *Act*=actinolite, *Aln*=allanite, *Ap*=apatite, *Cal*=calcite, *Ilm*=ilmenite, *Mag*=magnetite, *Mnz*=monazite, *Px*=pyroxene, *Sp*=spinel.

Siah, Zarigan and Chadormalu deposits. Apatite crystals at Gasestan are reddish and can be extremely large (metre-scale); occasionally, they display unidirectional growth resembling gas escape channels as shown in Figure 7A–B. The reddish color is caused by microscopic trails of iron oxide and fluid inclusions along microcracks.

Bafq apatites are rich in fluorine (2–3 wt% F vs. 0.5–0.7 wt% Cl), enriched in LREE (0.7 wt% at Chahgaz to 1.8 wt% at Mishdovan and Zargian), contain traces of arsenic (~200 ppm As), and their chondrite-normalized REE patterns are characterized by a negative europium anomaly (NISCO,

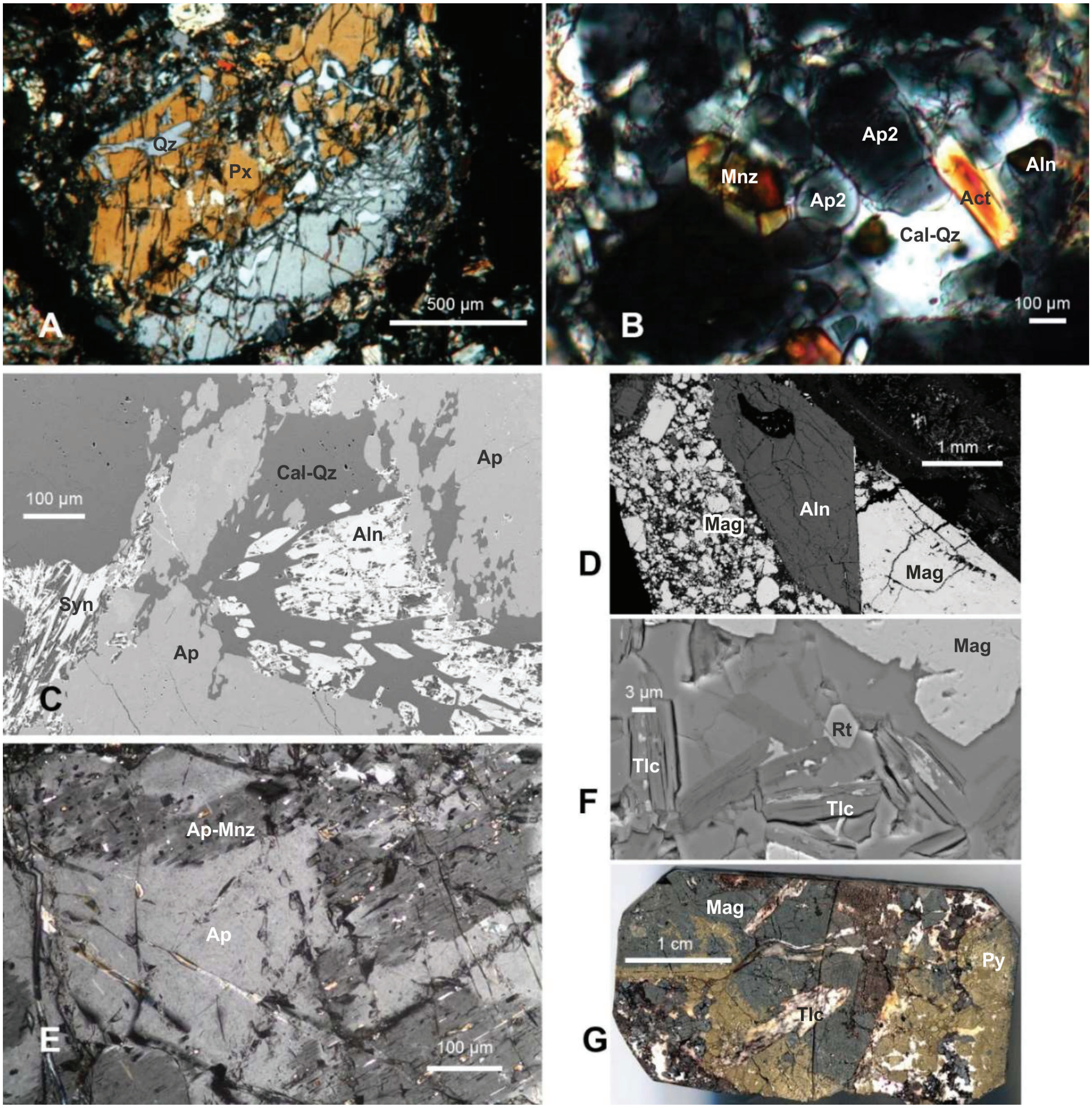


FIGURE 10. **A.** Photomicrograph of an early-stage, twinned pyroxene crystal, fragmented and overprinted by late-stage quartz (Chogart deposit). **B.** Photomicrograph showing tiny second-stage crystals of apatite, monazite and allanite in late-stage quartz (Chogart deposit). **C.** BSE image showing lozenge crystals of allanite and an acicular HREE mineral, probably synchysite, associated with late calcite-quartz. Early-stage apatite displays a patchy appearance because of variation in REE, F, Cl concentrations during metasomatic leach (Gasestan deposit). **D.** BSE image of a large, lozenge-shaped, late-stage allanite crystal in milled magnetite ore (Chahgaz deposit). **E.** Photomicrograph showing REE-depleted areas of apatite (dark), where REE has been metasomatically extracted from the apatite lattice and reprecipitated as abundant monazite grains in parallel trails along the C-axis of the apatite (Lakkeh Siah deposit). **F.** BSE image of the post-ore alteration assemblage, talc and rutile (Lakkeh Siah deposit). **G.** Ore slab displaying post-oxide, sulphide-stage ore, here represented by pyrite veins, overprinting the iron oxide ore. Note the complete talc pseudomorph after an earlier, lath-shaped fibrous mineral, probably actinolite (Lakkeh Siah deposit). *Act*=actinolite, *Aln*=allanite, *Ap*=apatite, *Cal*=calcite, *Mnz*=monazite, *Px*=pyroxene, *Py*=pyrite, *Qz*=quartz, *Rt*=rutile, *Syn*=synchysite, *Tlc*=talc.

1980; Daliran, 1990, 2002). They exhibit local oscillatory growth zoning, but patchy zoning is more common because of changes in the concentrations of REE, fluorine and chlorine. Dark areas (in thin section; Fig. 10E) are depleted in REE as a result of continuous metasomatism and extraction of REE from the apatite lattice. The extracted REE are reconstituted in abundant monazite (LREE)$PO_4$ inclusions that commonly occur along the C-axis of the apatite crystals (Figs. 9D, 10D). Oxygen stable isotope compositions obtained from apatite crystals (Vennemann and Daliran, unpublished data) indicate a predominantly magmatic source.

Iron oxide-apatite ores commonly consist of magnetite ± hematite. Hematite is more common in low-temperature ores, in ores apparently formed in sedimentary environments, and in ores with lower phosphate contents such as the jaspilitic and iron-manganese oxide ores. The iron oxide is low in titanium and vanadium (commonly <1–2 wt% $TiO_2$ and $V_2O_3$). Magnetite contains rare traces of chalcopyrite and commonly exhibits ilmenite trellis as well as spinel blebs exsolved from the magnetite during continuous cooling and metasomatism (Fig. 9E–F). Iron oxide-apatite ore formed at temperatures close to and below 500–550°C, based on the composition of ilmenite-magnetite pairs, as well as fluid inclusion data from the Mishdovan (Daliran, 1990 and unpublished data) and Esfordi (Jami, 2005) deposits.

With progressive metasomatism, fluids became enriched in $CO_2$-$SiO_2$ and HREE. This resulted in pervasive formation of calcite and quartz and growth of a large variety of accessory and trace minerals, including apatite, REE-phosphates and LREE-rich silicates (e.g. monazite and allanite) and a number of HREE minerals such as HREE-fluorine-carbonates (synchysite and bastnaesite), yttrium-rich phosphates (xenotime), yttrium-calcium-britholite, uranium-thorium oxides, calcium-thorianite, zircon (abundant at the Sagandi deposit), titanite, rutile, and the REE-U-Ti-Fe oxyhydroxide mineral davidite (Daliran et al., 1994). These processes can be inferred from a number of photographs (Figs. 9A–F, 10A–F).

The Sagand deposit comprises economic concentrations of uranium and thorium formed in association with high-temperature K-feldspar-phlogopite and magnetite ± REE-apatite-carbonate metasomatism in albite-actinolite ± Na-pyroxene rocks. Indications of uranium and thorium enrichment also occur at Gachin, close to the Hormuz IOA deposit near the Persian Gulf (e.g. www.mindat.org).

Sulphides associated with the IOA deposits of the Bafq district commonly consist of minor amounts of late pyrite ± chalcopyrite clearly overprinting the oxide ore stage (Fig. 10G). At Narigan, the Cu ± Au-Mo-Bi-Co-Ni-Ag-As-(Zn, Pb)-sulphide+pyrite mineralization in association with uranium-thorium oxides appears to be part of the late sulphide ore stage. This is also the case at the extension of the Bafq district to the south at Zarand, where large quantities of pyrite had been long observed in outcrops. Barite (with variable Sr) may have formed as an accessory mineral at the end of this stage. The presence of trace amounts of anhydrite associated with authigenic quartz and feldspar in some ECVSU deposits requires detailed study to understand their paragenetic associations and relationships with the diverse styles of IOA mineralization.

Post ore-stage alteration includes formation of tourmaline, chlorite and talc (Figs. 6E, 10F). Sericite, a common hydrothermal alteration mineral, is unrelated to the IOA mineralization. Pb-Zn SEDEX ore deposits also formed independently of the IOA mineralization in individual sedimentary basins, as initially noted by Daliran (1990).

## Concluding Remarks

Iron oxide-apatite mineralization and apatitites forming the phosphate deposits of the Bafq district occur within the southern sectors of the narrow, early Cambrian, Kashmar-Kerman Tectonic Zone. The deposits, as well as their extension south to the Zarand area and to the Persian Gulf, are coeval with early Cambrian high-level arc magmatism (Ramezani and Tucker, 2003). Geochemical signatures strongly support the long advocated extensional setting of the Bafq IOA deposits during the early Cambrian, in close proximity to back-arc volcanism. During volcanism, a major mantle-derived component was introduced into the system, inducing pervasive alkali and ore-related metasomatism (Daliran and Stosch, unpublished data). “Evidence for mantle derivation of at least the mafic end members of the magmatic rocks and the release of deep, volatile-rich magmatic fluids through devolatization of causative, mantle-derived magmas and variable degrees of mixing of these magmatic fluids with other crustal fluids along regional-scale fluid flow paths” was recently advocated for IOCG deposits (Groves et al., 2010).

The time interval during which regional sodic- and potassic-alteration and mineralization took place was short, and coeval with ca. 528 Ma rhyolite volcanism that terminated before early Cambrian barren basalt volcanism. Subsequent uplift and erosion is indicated by the presence of iron oxide ore pebbles in basal conglomerates of post-ore formations; this post-mineralization unconformity supports the formation of the IOA and related mineralization prior to the onset of a new tectonic cycle in the early Cambrian. The IOA ore formed at temperatures close to and below 500–550°C, based on the composition of ilmenite-magnetite pairs and fluid inclusion data from the Mishdovan (Daliran, 1990 and unpublished data) and Esfordi (Jami, 2005) deposits. Oxygen stable isotope compositions obtained from apatite (Vennemann and Daliran, unpublished data) additionally indicates a predominantly magmatic source for the apatite. Following extensive sodic-metasomatism and local development of albitites, and/or K-feldspar metasomatism, the ore-bearing high-temperature fluids metasomatized the already alkali-metasomatized host rocks resulting in the formation of high-temperature calcium-iron assemblages comprising early stage ± diopside ± garnet-actinolite, or alternatively actinolite-quartz and chlorite-quartz. The IOA deposits consist of low titanium-vanadium magnetite ± hematite, LREE-fluorine-rich apatite and predominantly LREE-minerals, mainly monazite. Late ore-stage metasomatism is represented by subordinate amounts of a calcite-quartz assemblage associated with a large number of LREE- and HREE-fluorine phosphates (including a new generation of apatite), silicates and carbonates, and a number of other minerals such as zircon-baddeleyite, davidite, titanite, rutile and uranium-thorium oxides that locally form the uranium-thorium deposits. Minor to trace amounts of sulphides, commonly pyrite ± chalcopyrite, overprinted the IOA at the post-oxide ore stage and were followed by talc and chlorite alteration.

Our decades of studies document that the metasomatic alteration-mineralization at the Bafq IOA district, and extending to the Zarand region to the south, share the characteristic features of global IOA deposits. The high-temperature mineral assemblages in the IOA deposits of the Bafq district are in line with other, worldwide IOA and IOCG districts that formed following albitization and/or K-feldspar alteration and high-temperature calcium-iron alteration, in accordance with the prograding metasomatic reaction path of iron oxide and alkali-calcic alteration systems described in Corriveau et al. (2010, 2016, 2022). Although high-temperature minerals are a prominent part of the mineralization at the Bafq IOA deposits, we could not locate evidence of ore melt inclusions (Daliran and Davidson, unpublished data). The high-temperature assemblages are not interpreted as skarns because of their regional extent and the association with sodic- and potassic-metasomatism and ore-related mineral assemblages diagnostic of IOA deposits. A genetic relationship between evaporites as the source of ore brines (Torab and Lehmann, 2005), following the global model presented by Barton and Johnson (1996), seems to be speculative. Evaporites are uncommon in the Bafq region and those that are known were coeval with the host ECVSU; hence, they could not have been involved in generating the ore fluids. Diversities in the mode of formation, i.e. syn-sedimentary versus epigenetic ores, need to be studied further to explain possible discrepancies.

Although the Bafq district has not been explored for copper and gold, extensive exploration at surface and at depth has not revealed economic copper-gold ores. However, the recent discovery of Cu ± Au-Mo-Bi-Co-Ni-Ag-As(Zn, Pb)-sulphide-pyrite ore in association with uranium-thorium oxide ore at Narigan and at the southerly Zarand area indicate that the ore systems have locally evolved to sulphide-rich mineralization and that further exploration may discover economic IOCG-related copper-gold deposits. These discoveries, the extension of the IOA province hundreds of kilometres south to Hormuz Island in the Persian Gulf, and the uranium-thorium ore indications at Gachin, provide new opportunities to study the conditions that led to formation of the IOA, uranium-thorium, and copper-gold-sulphide ores within the Kashmar-Kerman Tectonic(-magmatic) Zone.

## Acknowledgments

Part of this work was funded by the German Research Foundation (DFG), Grant STO 173/8, and was conducted in cooperation with the Geological Survey of Iran. Logistic support by the Iran Central Iron Ore Company is greatly appreciated. We would like to thank J. Ramezani for his valued scientific discussions on the geology of the Bafq region and L. Corriveau and E. Potter for continued interest and discussions of the Bafq deposits.

## References

Barton, M.D., 2014, Iron oxide (-Cu-Au-REE-P-Ag-U-Co) systems, *in* Holland, H.D. and Turekian, K.K., eds., Treatise on Geochemistry, second edition, volume 13: Elsevier Inc., p. 515-541.

Barton, M.D., and Johnson, D.A., 1996, Evaporitic-source model for igneous-related Fe oxide-(REE-Cu-Au-U) mineralisation: Geology, v. 24, p. 259-262.

Berberian, M., and King, G.C., 1981, Towards a paleogeography and tectonic evolution of Iran: Canadian Journal of Earth Sciences, v. 18, p. 210-265.

Bonyadi, Z., Davidson, G.J., Mehrabi, B., Sebastien Meffre, S., and Ghazban, F., 2011, Significance of apatite REE depletion and monazite inclusions in the brecciated Sehchahun apatite deposit, Bafq district, Iran: insights from paragenesis and geochemistry: Chemical Geology, v. 281, p. 253-269.

Corriveau, L., Williams, P.J., and Mumin, A.H., 2010, Alteration vectors to IOCG mineralisation – from uncharted terranes to deposits, *in* Corriveau, L. and Mumin, A.H., eds., Exploring for iron oxide copper-gold deposits: Canada and global analogues: Geological Association of Canada, Short Course Notes, No. 20, p. 89-110.

Corriveau, L., Montreuil, J.-F., and Potter, E.G., 2016, Alteration facies linkages among IOCG, IOA and affiliated deposits in the Great Bear magmatic zone, Canada, *in* Slack, J., Corriveau, L. and Hitzman, M., eds., Proterozoic iron oxide-apatite (± REE) and iron oxide-copper-gold and affiliated deposits of Southeast Missouri, USA, and the Great Bear magmatic zone, Northwest Territories, Canada: Economic Geology, v. 111, p. 2045-2072.

Corriveau, L., Potter, E.G., Montreuil, J.-F., Blein, O., Ehrig, K., and De Toni, A., 2018, Iron-oxide and alkali-calcic alteration ore systems and their polymetallic IOA, IOCG, skarn, albitite-hosted U±Au±Co, and affiliated deposits: a short course series. Part 2: overview of deposit types, distribution, ages, settings, alteration facies, and ore deposit models: Geological Survey of Canada, Scientific Presentation 81, 154 p.

Corriveau, L., Mumin, A.H., and Potter, E.G., 2022, Iron oxide copper-gold (Ag-Bi-Co-U-REE) and affiliated deposits: introduction and overview, *in* Corriveau, L., Potter, E.G. and Mumin, A.H., eds., Mineral systems with iron oxide copper-gold (IOCG) and affiliated deposits: Geological Association of Canada, Special Paper 52, p. 1-25.

Daliran, F., 1990, The magnetite–apatite deposit of Mishdovan, East-Central Iran. An alkali rhyolite hosted, “Kiruna-type” occurrence in the Infracambrian Bafg metallotect: Unpublished Ph.D. Thesis, Heidelberger Geowissenschaftliche Abhandlungen, 37, 248 p.

Daliran, F., 2002, Kiruna-type iron oxide-apatite ores and ‘apatites’ of the Bafq district, Iran, with an emphasis on the REE geochemistry of their apatites, *in* Porter, T.M., ed., Hydrothermal iron oxide copper gold and related deposits: a global perspective, v. 2: PCG Publishing, Adelaide, Australia, p. 303-320.

Daliran, F., Tarkian, M., and Tavaf-Djalali, F., 1994, A new occurrence of davidite from the apatite-magnetite ore deposit of Chogart, Bafg district, East Central Iran: Neues Jahrbuch für Mineralogie Monatshefte, v. 3, p. 138-144.

Daliran, F., Stosch, H.-G., and Williams, P.J., 2007, Multistage metasomatism and mineralisation at hydrothermal Fe oxide-REE-apatite deposits and “apatitites” of the Bafq District, Central-East Iran, *in* Andrew, C.J. et al., eds., Digging deeper: Proceedings of the 9th SGA Biennial Meeting, Dublin, 2007, p. 1501-1504.

Daliran, F., Stosch, H.-G., and Williams, P.J., 2009, A review of the early Cambrian magmatic and metasomatic events and their bearing on the genesis of the Fe oxide-REE-apatite deposits (IOA) of the Bafq district, Iran, *in* Williams et al., eds., Smart science for exploration and mining: Proceedings of the 10th SGA Biennial Meeting, Townsville, Australia, p. 623-625.

Daliran, F., Stosch, H.-G., Williams, P.J., Jamali, H., and Dorri, M.-B., 2010, Lower Cambrian iron oxide-apatite-REE (U) deposits of the Bafq district, east-Central Iran, *in* Corriveau, L. and Mumin, A.H., eds., Exploring for iron oxide copper-gold deposits: Canada and global analogues: Geological Association of Canada, Short Course Notes, No. 20, p. 147-159.

Deymar, S., Yazdi, M., Rezvanianzadeh, M.R., and Behzadi, M., 2018, Metasomatism as a process for Ti–REE–Y–U–Th mineralisation in the Saghand Anomaly 5, Central Iran: insights from geochemical, mineralogical, and stable isotope data: Ore Geology Reviews, v. 93, p. 308-336.

Fazeli, A., Azizaliabad, M., and Iranmanesh, J., 2014, Petrography, metasomatism and mineralisation of uranium and other radioactive mineral, *in* Symposium on uranium raw material for the nuclear fuel cycle: exploration, mining, production, supply and demand, economics and environmental issues: IAEA, Book of Abstracts, IAEA-CN-216, Abstract 083.

Geijer, P., 1930, The iron ores of the Kiruna type: geographical distribution, geological characters, and origin: Sveriges Geologiska Undersökning, Ser. C, No. 367, 39 p.

Gharesi, M., and Karimi, M., 2011, Five element vein type mineralisation and the role of secondary boiling during mineralisation process in the Narigun area, Central Iran: Proceedings of the 13th SGA Biennial Meeting, Uppsala, Abstract A075.

Gibbs, A., 1976, Geology and genesis of the Bafq lead-zinc deposit, Iran: Institute of Mining and Metallurgy, v. 85, p. B205-B220.

Gotlov, V.I., and Esev, Y.M., 1976, Report on the result of preliminary survey of the Zarand iron ore deposit: NISCO, TECNO-EXPORT, UDSSR, 1104 p. (in Persian).

Groves, D.I., Bierlein, F.P., Meinert, L.D., and Hitzman, M.H., 2010, Iron oxide copper-gold (IOCG) deposits through Earth history: implications for origin, lithospheric setting, and distinction from other epigenetic iron oxide deposits: Economic Geology, v. 105, p. 641-654.

GSI (Geological Survey of Iran), 1991, Geological map of Esfordy: Geological Survey of Iran, 1:100,000 Series, Sheet 7153.

Haghipour, A., 1974, Étude géologique de la région de Biabanak-Bafq (Iran Central): pétrographie et tectonique du socle précambrien et de sa couverture: Doctorat d'État, Université de Grenoble, 403 p.

Heidarian, H., Alirezaei, S., and Lentz, D.R., 2017, Chadormalu Kiruna-type magnetite-apatite deposit, Bafq district, Iran: insights into hydrothermal alteration and petrogenesis from geochemical, fluid inclusion, and sulfur isotope data: Ore Geology Reviews, v. 83, p. 43-62.

Hildebrand, R.S., 1986, Kiruna-type deposits: their origin and relationship to intermediate subvolcanic plutons in the Great Bear magmatic zone, Northwest Canada: Economic Geology, v. 81, p. 640-659.

Hitzman, M.W., 2000, Iron oxide–Cu–Au deposits: what, where, when and why, *in* Porter, T.M., ed., Hydrothermal iron oxide copper-gold and related deposits: a global perspective, v. 1: PCG Publishing, Adelaide, p. 9-25.

Jami, M., 2005, Geology, geochemistry and evolution of the Esfordi phosphate - iron deposit, Bafq area, Central Iran: Unpublished Ph.D. thesis, University of New South Wales, 355 p.

Jébrak, M., 2010, Use of breccias in IOCG(U) exploration, *in* Corriveau, L. and Mumin, A.H., eds., Exploring for iron oxide copper-gold deposits: Canada and global analogues: Geological Association of Canada, Short Course Notes, No. 20, p. 79-88.

Karimi Shahraki, B., Mehrabi, M., and Masoudi, F., 2016, Iron oxide-copper-gold mineralisation (IOCG) at Jalalabad deposit, NW Zarand: Iran Journal of Crystallography and Mineralogy, v. 2, p. 283-296 (in Persian).

Khoshnoodi, K., Behzadi, M., Gannadi-Maragheh, M., and Yazdi, M., 2017, Alkali metasomatism and Th-REE mineralisation in the Choghart deposit, Bafq district, Central Iran: Geologia Croatica, v. 70, p. 53-69.

Mumin, A.H., Somarin, A.K., Jones, B., Corriveau, L., Ootes, L., and Camier, J., 2010, The IOCG-porphyry-epithermal continuum of deposits types in the Great Bear Magmatic Zone, Northwest Territories, Canada, *in* Corriveau, L. and Mumin, A.H., eds., Exploring for iron oxide copper-gold deposits: Canada and global analogues: Geological Association of Canada, Short Course Notes, No. 20, p. 59-78.

NISCO (National Iranian Steel Corporation), 1976, Report on the first phase of uranium exploration project in Saghand area: NISCO, Internal Report, 225 p.

NISCO, 1980, Report on results of search and evaluation works at magnetic anomalies of the Bafq iron ore region during 1976-1979: NISCO, Internal Report, 260 p.

Nyström, J.O., and Henriquez, F., 1994, Magmatic features of iron ores of the Kiruna-type in Chile and Sweden: ore textures and magnetite geochemistry: Economic Geology, v. 89, p. 820-839.

Rajabi, A., Canet, C., Rastad, E., and Alfonso, P., 2014, Basin evolution and stratigraphic correlation of sedimentary-exhalative Zn–Pb deposits of the early Cambrian Zarigan–Chahmir Basin, Central Iran: Ore Geology Reviews v. 64, p. 328-353.

Ramezani, J., and Tucker, R.D., 2003, The Saghand region, Central Iran: U–Pb geochronology, petrogenesis and implications for Gondwana tectonics: American Journal of Sciences, v. 303, p. 622-665.

Samani, B.A., 1988, Metallogeny of the Precambrian in Iran: Precambrian Research, v. 39, p. 85-106.

Samani, B., and Talezadeh Lari, Y., 1988, Report of the first phase of uranium exploration project in Saghand area: AEOI Report No. 225.

Stosch, H.-G., Romer, R.-L., Daliran, F., and Rhede, D., 2011, Uranium–lead ages of apatite from iron oxide ores of the Bafq district, east-Central Iran: Mineralium Deposita, v. 46, p. 9-21.

Torab, F.M., and Lehmann, B., 2007, Magnetite-apatite deposits of the Bafq district, Central Iran: monazite geochronology and ore formation, *in* Andrew, C.J. et al., eds., Digging deeper: Proceedings of the 9th SGA Biennial Meeting, Dublin, p. 439-442.

Williams, P.J., 2010, Classifying IOCG deposits, *in* Corriveau, L. and Mumin, A.H., eds., Exploring for iron oxide copper-gold deposits: Canada and global analogues: Geological Association of Canada, Short Course Notes, No. 20, p. 13-21.

Williams, P. J., Barton, M.D., Johnson, D.A., Fontboté, L., De Haller, A., Mark, G., Oliver, N.H.S., and Marschik, R., 2005, Iron oxide copper-gold deposits: geology, space-time distribution, and possible modes of origin: Economic Geology, v. 100, p. 371-405.

Winchester, J.A., and Floyd, P.A., 1977, Geochemical discrimination of different magma series and their differentiation products using immobile elements: Chemical Geology, v. 20, p. 325-435.